



UNIVERSITY OF CHEMISTRY AND TECHNOLOGY, PRAGUE
Faculty of Chemical Engineering
Department of Chemical Engineering

Habilitation thesis

Design of advanced functional polymeric materials from
environmentally benign methodologies

Fatima Hassouna

Prague, January 30, 2019

I hereby declare that I have worked out this thesis independently while noting all the resources employed as well as co-authors of the presented results.

Prague, January 30, 2019

Fatima Hassouna

Summary

This habilitation thesis gives an overview of my research activities conducted on the design of high performance polymeric materials with tailored morphology and properties using eco-friendly methodologies. This area has been motivated by environmental concerns and governmental directives to move from solvent-based to water-borne systems or free-solvent processes as well as the scientific challenges that still need to be addressed.

The habilitation thesis is divided into two main parts. In the first part, my research activities related to the development of a new methodology for preparing high-performance polylactide (PLA) materials by the reactive-extrusion, a solvent free process, are commented. The proposed methodology is based on reactive grafting and compatibilization of PLA with low molecular (bio)-plasticizers whose implementation resulted in a significant improvement of the mechanical properties of PLA based materials. Many of the prepared materials whose preparation is described in this section exhibited outstanding mechanical properties.

The second part of the habilitation thesis outlines my research activities devoted to the preparation of novel nanocomposite materials with tunable properties by environmentally benign concept based on waterborne systems. Following this approach, three types of nanocomposites were designed for different applications: i) nanocomposites based on combination of core-shell latex nanoparticles (NPs) and cellulose nanocrystals, ii) hierarchically porous materials from low-cost precursors – polyaniline (PANI) and polystyrene latex NPs (PS NPs), and iii) reduced graphene oxide (RGO)/ doped PANI nanocomposites. The above mentioned nanocomposite materials can find application in a wide range of domains including CO₂ capture processes or manufacturing electrodes for supercapacitors.

In the last section, selected research activities I have recently initiated in our research group are briefly depicted along with an outlook to future studies. A list of references providing more details about my research activities can be found in Appendix A. Copies of my scientific articles are enclosed in Appendix B.

Table of contents

1. Introduction	5
2. High performance polylactide (PLA)	7
2.1 Super-tough PLA materials synthesized by reactive extrusion and their thermo-mechanical recycling aptitude	7
2.1.1 Reactive extrusion grafting and plasticizing of PLA	8
2.1.2 Thermal and mechanical properties	9
2.1.3 Structure-property relationships.....	10
2.1.4 Thermo-mechanical degradation of the produced high performance PLA (PLA/AcrylPEG/L101) after multiple reprocessing to simulate recycling	11
2.2. Green plasticization: design of new cardanol derivative as potential biobased plasticizer for PLA	13
3. Advanced functional nanocomposite materials	16
3.1 Polymer nanocomposites reinforced by cellulose nanocrystals	16
3.2 New approach on the development of polyaniline/reduced graphene oxide nanocomposites via sacrificial surfactant-stabilized reduced graphene oxide	19
3.2.1 Preparation of nanocomposites	20
3.2.2 Structure properties relationships	20
3.3 Nitrogen-rich hierarchically porous polyaniline-based sorbents for carbon dioxide (CO₂) capture	23
3.3.1 Synthesis of the 3-D Microclusters	23
3.3.2 Morphology of the 3-D Microclusters.....	25
3.3.3 Capture performance and consideration for industrial applications:	25
4. Research perspectives	27
4.1. Design of flexible hybrid supercapacitors from renewable resources	27
4.2. Development of novel biodegradable porous nanocomposite materials for bio-medical applications	27
4.3. Amorphous solid dispersions: formulation and prediction of phase diagrams drug-polymer	28
References	29
Appendices	32
Appendix A: List of author's articles in impacted journals	32
Appendix B: Author's articles in impacted journals	35

Chapter 1

Introduction

Due to their wide variety, versatility, profitability, highly desirable properties, synthetic polymers found a central place in the modern lifestyle. Their applications cover many sectors, namely packaging, building and construction, automotive, electrical and electronic, and some other applications. They have experienced an exceptional and tremendous growth over the past six decades. Until last decade, most synthetic polymers were produced from non-renewable crude oil (fossil) and natural gas resources. This heavy dependence on fossil fuels has reached a perilous situation as the world's oil resources will inevitably be depleted. Moreover, the use of crude oil is not without consequences for the environment. Numerous environmental impacts associated with the production and with the use of petroleum based materials were pointed out: air emissions, including both greenhouse gases (contributing to global warming out of which anthropogenic CO₂ emissions have been implicated) and air pollutants, and so on. In addition, most of petroleum based polymers are robust and are usually non-biodegradable, and end-up as waste in the environment for centuries, thereby posing risks to human and animal health as well as the environment. Paradoxically, one of the most desirable features of plastics - their durability and resistance to degradation - is also the source of one of their biggest and most dangerous liabilities when it comes to their disposal.

These issues can be tackled from various perspectives, including:

- Development of valorization routes, namely polymer recycling, return to oil (depolymerization and reuse of the monomers), incineration (energetic valorization by combustion), carbon capture and storage technologies as immediate solution to minimize CO₂ emissions.
- Replacement of petroleum-based materials with renewable resources as an answer to the environmental concerns and the depletion of petroleum resources. Progressively, scientists and industrials are shifting away from petroleum polymers towards polymers with renewable content in the form of biobased polymers (biodegradable and non-biodegradable polymers), polymer blends, and/or bio-fillers, with the inherent challenge to both reduce the overall environmental impact and to retain suitable properties.
- Development of environmentally benign technologies based on water-borne systems (aqueous colloidal suspension etc.) or free-solvent processes (thermal-processing methods (e.g. extrusion, compression molding, injection molding), living free radical methodologies etc.)

When properly combined, the above mentioned techniques can lead to the design of high performance polymeric materials with reduced environmental impact.

This habilitation thesis gives an overview of the research activities conducted on the design of high performance polymeric materials with tailored morphology and properties using environmentally benign methodologies that were developed during the years 2009–2018 by myself together or with the PhD and master students under my supervision or co-supervision. **Chapter 2** deals mostly with the main advances achieved in the design of high performance polylactide (PLA) from green plasticization to super-tough PLA materials synthesized by (reactive) extrusion, followed by study of their thermo-mechanical recycling. In **Chapter 3**, divided into three sub-chapters, main advances carried out in the design of novel functional nanocomposites using waterborne approach are described. More specifically, in the sub-chapters, three different nanocomposites are presented: i) nanocomposite films based on combination of core-shell latex nanoparticles and cellulose nanocrystals, ii) preparation of reduced graphene oxide/doped polyaniline nanocomposites for applications in supercapacitors, and iii) hierarchically porous materials from low-cost precursors for applications in CO₂ capture.

Finally, my scientific articles are gathered in the appendices A and B, as follows:

Appendix A: List of author's articles in impacted journals

Appendix B: Author's articles in impacted journals

Chapter 2

High performance polylactide (PLA)

2.1 Super-tough PLA materials synthesized by reactive extrusion and their thermo-mechanical recycling aptitude

PLA is a biodegradable thermoplastic derived from renewable sources (mainly starch and sugar). As a consequence of increasing feedstock prices for traditional petroleum derived polymers and a reduction in industrial grade PLA cost due to production improvements, PLA is now being commercially produced for commodity applications. Since PLA is compostable and derived from sustainable sources, it has been viewed as a promising material to reduce the societal solid waste disposal problem. PLA is mainly marketed for a variety of fiber and packaging products. In the next years, PLA production and consumption is expected to increase exponentially. Therefore, there is a need to better understand and improve its properties. PLA exhibits inherent brittleness which can limit its application. Due to this characteristic, PLA displays many drawbacks related to its properties and processability including i) poor impact strength (26 J m^{-1}), ii) low elongation at break (few %), another aspect of its brittle nature, iii) low heat deflection temperature (HDT) ($<60 \text{ }^{\circ}\text{C}$), and iv) poor processability¹. The brittleness of PLA limits its use in applications where mechanical toughness, such as plastic deformation at high impact rates or high elongation is required (i.e. car parts, appliance casings, etc.).

In order to enhance the mechanical properties of PLA, plasticization with low molecular weight compounds has been intensively investigated¹. To get all the benefits in terms of its processability, flexibility/ductility and impact strength, the plasticizer should be miscible with the polymer at the required loadings. Depending on their molecular weight, two main classes of plasticizers can be distinguished, i.e. the first type includes monomers or small molecule plasticizers and the second one includes oligomeric or polymeric plasticizers. Many small molecules/monomeric biodegradable compounds, mainly based on the family of citrate derivatives and lactide (LA) monomer, have been investigated. By comparison with oligomeric or polymeric plasticizers, the small molecule plasticizers are more miscible and efficient in decreasing the glass transition temperature (T_g) of the PLA polymer due to their higher mixing entropy contribution. However, because of their low boiling points, small molecule plasticizers can get evaporated during melt processing²⁻⁵ as well as have a strong tendency to migrate toward the surface of the polymeric material,^{2, 5-7} reducing the toughness of PLA-based materials. This can be explained by the tendency of the plasticized

PLA to crystallize overtime, which reduces the amorphous fraction able to retain the plasticizer molecules in the polymer. In addition, the plasticizer migration can result in food contaminations in packaging applications. In this regard, oligomeric and polymeric plasticizers are preferred for plasticization of polymer matrix as they are significantly less prone to the migration within the prepared material. However, the plasticization extent with oligomeric and polymeric plasticizers has not been satisfactory yet, because they can yield micro- to macro-phase separation at high loadings overtime in the PLA-based blends.

To overcome these issues, we developed a new strategy based on the *in situ* solvent-free chemical modification of PLA via reactive grafting of different types of functionalized plasticizers, e.g. PEG derivatives, cardanol derivatives as well as citrate derivatives, by reactive extrusion in order to create more interactions between the so-functionalized polyester matrix and the remaining fraction of non-grafted plasticizer, and therefore minimizing or even ideally suppressing the propensity of the plasticizer to phase-separate in the blends. Interestingly, reactive extrusion has proven to be an ecological, cost-effective and versatile process to design novel and high performance bioplastics. In this habilitation thesis, I describe solely the achievements related to reactive-plasticization of PLA with low molecular weight poly(ethylene glycol) (PEG) derivatives bearing (meth)acrylates moieties.

2.1.1 Reactive extrusion grafting and plasticizing of PLA

To finely tune the toughness of PLA, a novel and original pathway to chemically modify PLA in presence of “reactive” PEG derivatives via reactive extrusion was designed. Polyethylene glycol methyl ether methacrylate (MAPEG) and polyethylene glycol methyl ether acrylate (AcrylPEG) were melt-mixed and extruded with PLA in presence of 2,5-dimethyl-2,5-di-(tert-butylperoxy)hexane (L101) as a free-radical initiator using a co-rotating twin screw micro-compounder (DSM Xplore Research) under nitrogen atmosphere. Both MAPEG and AcrylPEG were successfully homo-oligomerized and grafted onto PLA chains. This was demonstrated by the increase of the melt viscosity during the melt-processing (increase of the extrusion force), the decrease of the plasticizer extracted fraction from the so-produced materials (Soxhlet extraction with methanol), and finally by an extensive molecular characterization (infrared spectroscopy (FTIR), gel permeation chromatography (GPC), nuclear magnetic resonance spectroscopy (^1H NMR)), indicating that the presence of optimum amount (0.5 - 1 wt.%) of L101 in the ternary PLA/MAPEG/L101 and PLA/AcrylPEG/L101 blends played a key role in grafting the plasticizers onto PLA backbone. In fact, L101, being a difunctional di-tertiary alkyl peroxide, free-radicals are generated during its thermal decomposition, promoting free-radical reactions which take place in the melt during reactive extrusion. In addition, the plasticizer functional end-group displayed a significant effect on the grafting efficiency mainly because of the difference in the reactivity between the methacrylic and the acrylic functional groups. Accordingly, a much higher grafting efficiency was reached when using AcrylPEG.

Based on the molecular characteristics of the as-produced materials, a mechanism of reactive grafting of MAPEG and AcrylPEG onto PLA chains was suggested.⁸⁻¹⁰

2.1.2 Thermal and mechanical properties

The impact of the reactive plasticization of PLA on the thermal and thermo-mechanical properties of the investigated blends was evaluated by means of differential scanning calorimetry (DSC) and dynamical mechanical thermal analysis (DMTA), respectively. The mechanical performances, namely, impact strength and tensile properties, were assessed using Notched Izod impact and tensile tests, respectively.

The overall properties of the main materials are gathered in **Table 1**.^{8, 10}

Both MAPEG and AcrylPEG exhibited efficient plasticization for PLA highlighted by the shift of the T_g to lower values with respect to neat PLA. By comparison to the “conventionally” plasticized binary blends (PLA/MAPEG and PLA/AcrylPEG), “reactive grafting” the plasticizers on PLA increased the T_g of the plasticized reactive blends, thus permitting to regain a part of PLA stiffness, evidenced by relatively high storage modulus values (**Table 1**). In fact, addition of L101 to PLA/MAPEG and PLA/AcrylPEG allowed a remarkable increase of the storage modulus. Besides, regardless the added amount of L101, the presence of optimum amount of reactive plasticizer (20 wt. % MAPEG and AcrylPEG), intrinsically modified the uniaxial deformation (tensile elongation) of the modified PLA-based materials to highly ductile behavior evidenced by very high elongation at break. The reactive grafting had also a positive effect on the improvement of the impact strength of the plasticized PLA. It even further enhanced with the increase of the L101 amount. The best improvement was achieved in the case of PLA/AcrylPEG/L101 containing the highest amount of L101. Overall, this latter ternary system exhibited the desired properties, namely, very high elongation at break and impact toughness while maintaining a high tensile strength and modulus. Finally, identification of the strain-induced deformation mechanism of the most promising material (PLA/AcrylPEG/L101) such as chain orientation, phase transformation and possible damage mechanisms, during drawing performed at different temperatures and strain rates, was possible thanks to combination of several techniques (DSC, scanning electron microscopy (SEM) and X-ray diffraction (XRD)).^{8, 11-13} Overall, it was found that orientation of amorphous and crystalline chains, crystallization, and destruction of crystals were involved during the drawing of the plasticized PLA. It was also found that below 50 °C, crystal formation and crystal destruction were in permanent competition, thus leading to a constant or slightly decreasing crystallinity with strain. Increased crystal formation and restricted crystal destruction was observed when increasing temperature, leading to an enhanced crystallinity with the strain level.

Table 1: Overall thermal and mechanical properties of all the investigated materials

Blend composition (wt. %)	T_g^a (°C)	T_α^b (°C)	E'^c (MPa)	ϵ^d (%)	I.E. ^e (kJ/m ²)
Extruded PLA	61	59	1776 ± 17	4 ± 1	2.8 ± 0.3
PLA/MAPEG 80/20	16	17	72 ± 3	313 ± 15	39.9 ± 6.3
PLA/MAPEG/L101 79.5/20/0.5	25	29	302 ± 51	279 ± 3	77.5 ± 11.0
PLA/AcrylPEG 80/20	29	35	643 ± 46	230 ± 35	86.0 ± 8.6
PLA/AcrylPEG/L101 79.5/20/0.5	ND	41	827 ± 109	199 ± 47	102.6 ± 16.3

^a Glass transition temperature from the second heating DSC scans

^b Alpha transition temperature at maximum $\tan\delta$ peak (DMTA)

^c Storage modulus at 20°C (DMTA)

^d Tensile elongation at break at 20°C according to ASTM D638 (test speed 5 mm/min)

^e Notched Izod impact energy at 20°C according to ASTM D256

ND: Not Detected

2.1.3 Structure-property relationships

Combination of different techniques is usually required to generate fundamental understanding of relationships between the process of material preparation and their final properties.

Morphological and structural characterizations by means of SEM, Quantitative Nanomechanical Peak Force Atomic Force Microscopy (QNM-PF-AFM) and DMTA carried out on the most promising system in terms of thermo-mechanical and mechanical performance, i.e. PLA/AcrylPEG/L101, revealed that the grafting of AcrylPEG on PLA resulted in an *in situ* generation of rubbery poly(acrylic) micro-domains (less than 1 µm of diameter) finely dispersed in the PLA matrix. These domains are built on soft poly(AcrylPEG)-rich cores ($T_g = -59$ °C) having an “immiscibility gradient” with surrounding PLA (**Figure 1**). The rubbery inclusions appeared as star-shaped domains on the fractured section after notched Izod impact testing at room temperature (**Figure 2**). As a result, much more limited migration of the plasticizer out of the material was observed overtime. Based on these findings, we suggested that together with the plasticized PLA matrix ($T_g = 41$ °C), the rubbery inclusions must be acting as an effective stress concentrators and fracture propagation inhibitors by absorbing the energy during the impact test, evidenced by the outstanding enhancement of both the tensile elongation at break and the impact strength in comparison with neat PLA.

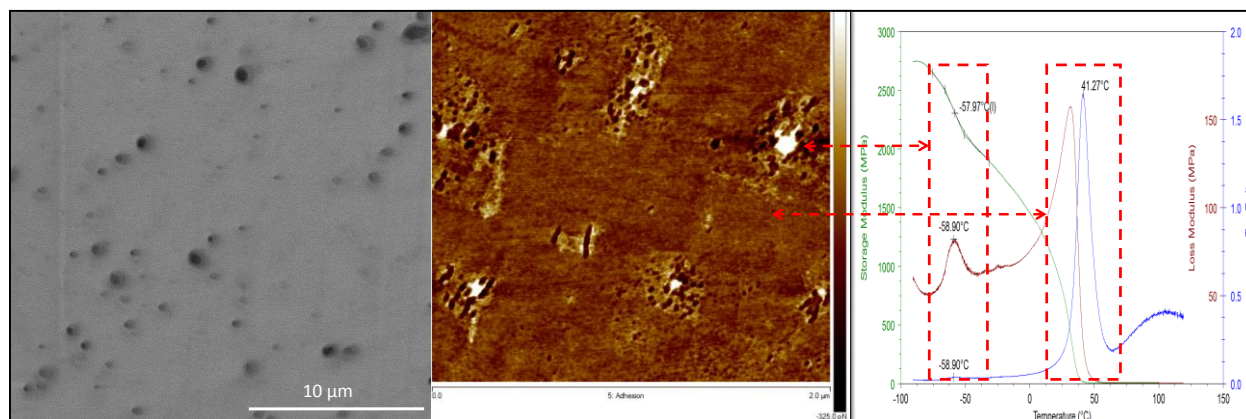


Figure 1: SEM image (left), Peak force AFM image (middle), and DMTA curves (right) of PLA/AcrylPEG/L101 : 79.5/20/0.5 wt. %

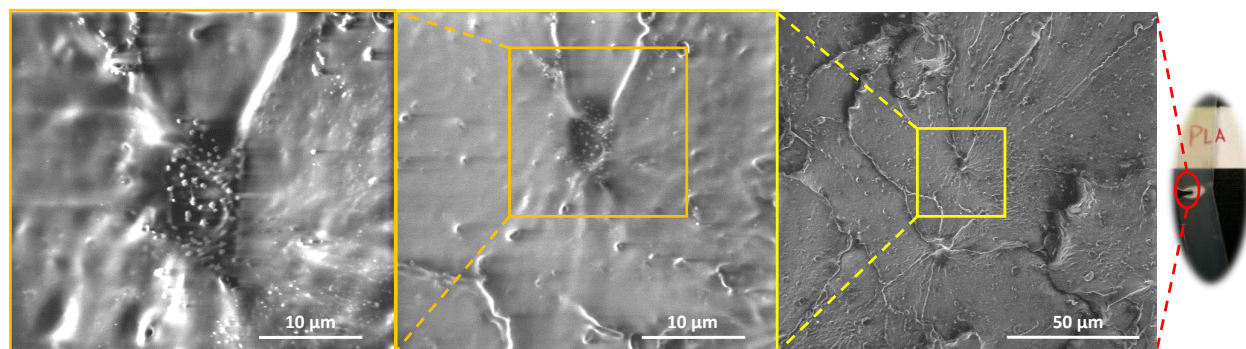


Figure 2: SEM images on cryofractured surface of PLA/AcrylPEG/L101: 79.5/20/0.5 wt. %

2.1.4 Thermo-mechanical degradation of the produced high performance PLA (PLA/AcrylPEG/L101) after multiple reprocessing to simulate recycling

Over the last decade, recycling of PLA by thermo-mechanical reprocessing has been considered as a new scenario of end-of-life for this biobased and biodegradable polyester. With this respect, the degradation mechanisms occurring during the thermo-mechanical recycling of our most promising plasticized PLA, i.e. PLA/AcrylPEG/L101 ((p)PLA), were identified *via* multiscale approach, and were compared to those of neat PLA. Both PLA and (p)PLA materials were characterized at the macroscopic scale by mechanical and thermal testing, at the microstructure scale, and at their molecular scale after 1, 3 and 5 processing cycles (Figure 3).

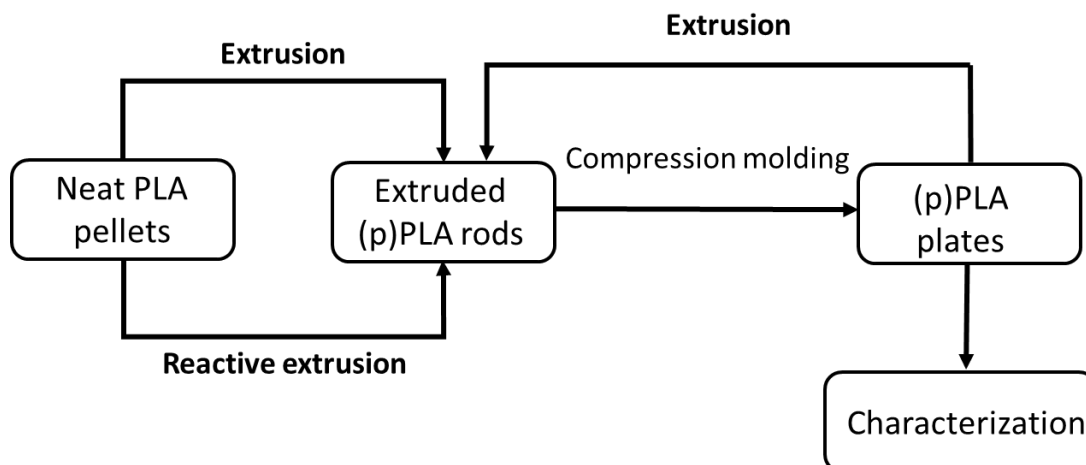


Figure 3: Processing and reprocessing routes of (p)PLA

For PLA, a thermo-mechanical degradation occurred during reprocessing by a random chain scission as highlighted by GPC. This led to a higher chain mobility that was confirmed by a higher ability of cold crystallization in DSC. At the same time, PLA remained amorphous as revealed by DSC measurements. According to chemical structure analysis carried out by means of FTIR and ^1H NMR, no additional chemical function was detected when compared to the non-recycled PLA. Thus, random chain scission was the main active mechanism during PLA recycling and was probably responsible for the decrease of storage modulus and tensile modulus, decrease of tensile resistance and decrease of toughness.

Due to the complexity of (p)PLA, differentiated look at different components interacting with each other was necessary to elucidate the degradation mechanisms. The mechanical properties deteriorated strongly from the first to the third processing, resulting in a brittle material since it noticeably lost tensile ductility and its toughness dropped down. Interestingly, the viscoelastic properties of (p)PLA were not affected by the recycling (constant storage modulus and tensile modulus). Morphological analysis by SEM and AFM imaging showed that the inclusions of poly(AcrylPEG) underwent a noticeable transformation with reprocessing evidenced by a deformation of their shape, damaging mechanisms through the formation of porosity, and fibrillation leading to a reduction of their size. For the highest number of processing, SEM showed the appearance of cracks in the polymer matrix. The origin of these cracks can be due to the coupling of poly(AcrylPEG) phase size reduction and porosity formation that may decrease the physical interactions between the matrix and poly(AcrylPEG). They can also be due to chain scission mechanisms of the polymer matrix inducing chain shrinkage and then cracks. As for PLA, chemical structure characterization of (p)PLA did not show any change in the chemical functions before and after recycling. In addition, due to cross-linking that survived reprocessing up to 5 times, it was not possible to conduct GPC measurements. The increase of crystallinity after reprocessing attested for a higher mobility due to chain scission. Nonetheless the lack of cold crystallization noticed in DSC measurements supports the

assumption that cross-linking may endure the reprocessing. At the same time, rheology measurements undoubtedly highlighted the decrease of the viscosity for (p)PLA with the recycling, indicating that the degradation of the PLA matrix in (p)PLA by a chain scission mechanism was probably dominant here as well. By the calculation of the chain scission number from the rheology data, it was revealed that the (p)PLA matrix underlies a stronger degradation than the neat PLA. The chain scission number was nearly double for (p)PLA compared to PLA. As a conclusion, due to its severe degradation during reprocessing, it is not convenient to reuse recycled-(p)PLA for its initial application. The proposed degradation mechanisms of (p)PLA is summarized in **Figure 4** ¹⁴.

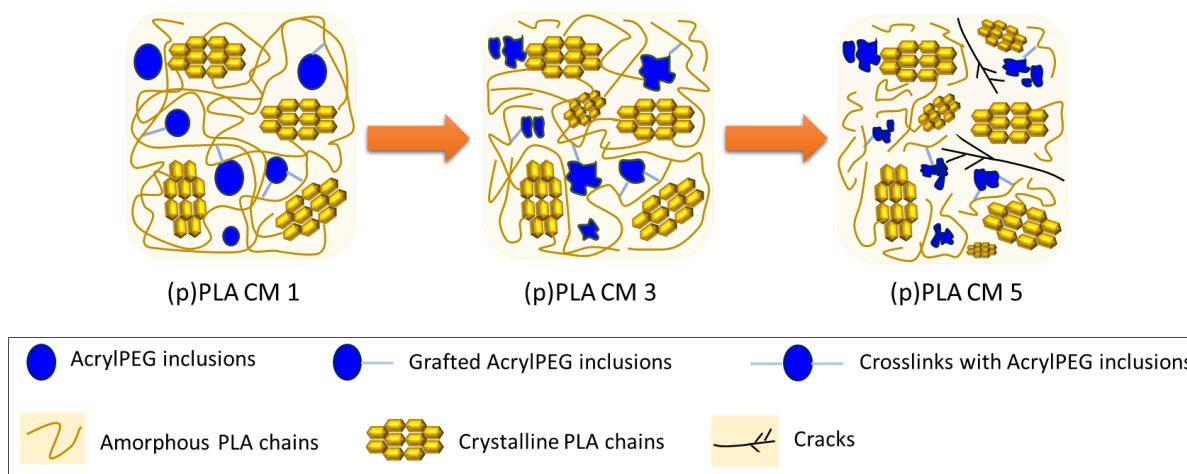


Figure 4: Schematic representation of the degradation of pPLA after 1, 3, and 5 processing cycles

.For more details about the research activities presented in the section 2.1, refer to the articles **7, 11, 14, 16, 18, 19** and **20** in the Appendix B.

I would to mention that the properties of the materials developed in the frame of this study (section 2.1) attracted the interest of industrial companies such as PolyOne Inc. with whole I launched a collaboration (2012-2015) with the purpose to scale-up the most promising material.

2.2. Green plasticization: design of new cardanol derivative as potential biobased plasticizer for PLA

Cardanol oil is a renewable and organic natural resource produced by vacuum distillation of roasted cashew nut shell liquid obtained from the spongy mesocarp of cashew nut shells, a byproduct of cashew nut processing ¹⁵. Due to its versatile chemical structure and cost-effectiveness, cardanol and its derivatives are considered as a promising raw material to develop novel derived biobased materials. Particular properties of cardanol and its derivatives, namely the relatively high solubility in non-polar environments and good processability, are attributed to the presence of the C15 chain attached to the meta position of the phenolic

ring¹⁶. The intrinsically reactive alkyl chain constitutes an interesting platform for chemical modification and functionalization¹⁷⁻¹⁹. In particular, synthesis of a new family of biobased plasticizers made of cardanol for brittle biodegradable polymers such as PLA would be highly beneficial. In fact, as most plasticizers of PLA enhancing its mechanical properties (as described in the section 2.1) are petroleum-based compounds²⁰, there is a need to look at alternative sources of plasticizers derived from biobased resources to design fully renewable polymeric blends. In this context, we synthesized a novel cardanol-derived plasticizer through methoxylation of the double bonds on the side chain of cardanol (C15 chain attached to the meta position of the phenolic ring). The main motivation for designing methoxylated cardanol, i.e., methoxylated hydroxyethyl cardanol (MeCard), lied in the enhancement of the compatibility properties with PLA since a lack of miscibility between the commercial hydroxyethyl cardanol (pCard) and PLA was clearly observed. MeCard was synthesized via a five-step synthetic route²¹. Afterwards, all melt blends PLA-pCard and PLA-MeCard were performed using a co-rotating twin screw micro-compounder (DSM Xplore Research). Molecular characterizations revealed that both cardanol derivatives (pCard and MeCard) did not alter the processability of PLA after blending. Interestingly, the plasticizer performances were highlighted using DMTA and DSC measurements. Addition of optimum amount of pCard led to the shift of the T_g as well as the cold crystallization peak (T_{cc}) due to the presence of a high amount of low molecular weight plasticizer. The decrease of T_{cc} was directly related to the higher PLA chain ability. More interestingly, melt blending of PLA with MeCard resulted in the shift of T_g and T_{cc} to even lower values as compared to PLA-pCard. Such behavior can be explained by the improved miscibility between PLA and MeCard due to the methoxylation of the double bonds on the side chain of cardanol as shown by SEM (**Figure 5**). Indeed, morphological analysis of PLA-pCard showed clearly the presence of two distinct phases, in which fine and regular pCard droplets are dispersed in PLA matrix. On the other hand, homogeneous morphological features without any phase separation were noted in PLA-MeCard, confirming that the interaction between PLA and MeCard was probably sufficient for providing good miscibility. It is believed that this interaction takes place between the methyl side groups present on PLA chains and the methoxy groups on the side chain of cardanol. The plasticization efficiency of MeCard was also demonstrated by a substantial decrease of the storage modulus, loss modulus, tensile modulus, together with a significant increase of the elongation at break as compared to PLA (**Table 2**). Moreover, higher plasticization performances than those of pCard toward PLA were noted (**Table 2**). The enhanced ductility of blends containing MeCard was related again to the improved miscibility and compatibility between PLA and MeCard.

Table 2: Overall thermal and mechanical properties of all the materials investigated

Blend composition (wt. %)	T_g^a (°C)	E'^b (MPa)	E_t^c (MPa)	ε_b^d (%)
Extruded PLA	60	1850	1860	5.7
PLA-pCard; 80/20	38	1435	1035	12
PLA-MeCard; 80/20	27	1235	710	198

^a Glass transition temperature from the second heating DSC scans

^b Storage modulus at 20°C (DMTA)

^c Tensile modulus at 20°C according to ASTM D638 (test speed 5 mm/min)

^d Tensile elongation at break at 20°C according to ASTM D638 (test speed 5 mm/min)

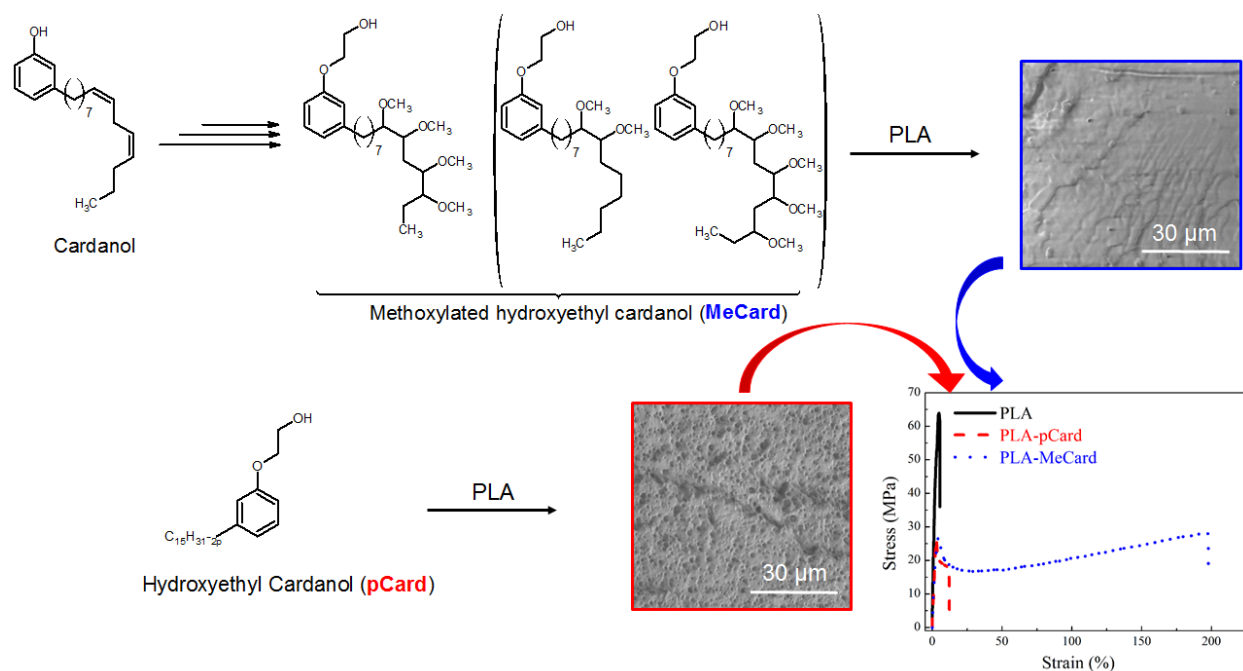


Figure 5: Morphology and mechanical properties of PLA-pCard and PLA-MeCard

For more details about the study presented in the section 2.2, refer to the article **21** in the Appendix B.

Chapter 3

Advanced functional nanocomposite materials

A part of my research activities focused on the development of environmentally benign methodologies based on waterborne systems for preparation of advanced functional novel nanocomposite materials with tunable properties. The concept of waterborne system is considered as an attractive green alternative to the conventional organic solvents thanks to water solvency, reusability, ease of use, non-toxicity, relatively low environmental impact, and cost-effectiveness. Following this approach, several types of nanocomposites were designed for different applications, including:

1. Elaboration of novel nanocomposites with tunable properties, from a combination of core-shell latex nanoparticles and cellulose nanocrystals, without any further chemical modification of the nanofiller while assuring good compatibility between both entities. This novel material can find applications in different domains.
2. Preparation of reduced graphene oxide/doped polyaniline nanocomposites using new approach based on sacrificial surfactant-stabilized reduced graphene oxide. Thanks to its outstanding electrical conductivity, application of the prepared nanocomposites as electrode materials for supercapacitors was tested.
3. Hierarchically porous materials from low-cost precursors – polyaniline and polystyrene latex nanoparticles using an easy and new concept based on the removal of the polystyrene nanoparticles during a pre-carbonization step followed by chemical activation. Outstanding CO₂ capture capacity of the optimum material was attained.

The above mentioned nanocomposite materials are discussed in details in a form of three sub-chapters (sections 3.1, 3.2 and 3.3 below).

3.1 Polymer nanocomposites reinforced by cellulose nanocrystals

In the frame of the eco-development vision, the biobased nanofillers i.e. cellulose nanocrystals (CNC), extracted from cellulose, have emerged as promising materials for the design of environmentally friendly materials thanks to their biodegradability, renewability, low specific density, needle-like morphology, and exceptional mechanical properties²². Due to their outstanding mechanical properties, nanoscale size and high aspect ratios, CNC fulfill all desired characteristics for ideal nanofiller for preparation of polymeric

based nanocomposites²³. Despite these attractive features, CNC are difficult to disperse in hydrophobic polymeric matrices or in non-polar solvents due to polar nature of their surface, which results in the aggregation of the nanofillers. This presents a major disadvantage associated to the utilization of CNC for preparation of polymer nanocomposites as a reinforcement material. To overcome this issue, chemical modification of the surface of CNC has been employed, such as polymer chain grafting that may act as a compatibilizer with the matrix, and thus enhancing the final mechanical properties of the nanocomposite materials. However, the disadvantage of this approach is the use of many toxic chemicals. Therefore, a new methodology based on incorporation CNC aqueous suspension into polymeric latex suspension (matrix) has been investigated.²⁴⁻²⁷ The advantage of this methodology is the incorporation of CNC aqueous suspension into latex suspension, without any further chemical modification of the nanofiller to assure a good compatibility. Besides, the final nanocomposites can be prepared using conventional processing methods. In this context, we developed new nanocomposite materials based on combination of core-shell latex nanoparticles (NPs), characterized by hard core and soft shell, as a matrix, CNC as a reinforcing agent, and polyethylene glycol (PEG) as a plasticizer. The combination of the three components exhibiting different properties (thermal, rheological, mechanical etc.) were expected to tailor the properties of the final ternary nanocomposites, without requiring any further chemical modification of the surface of CNC while assuring good compatibility between the components. The second motivation behind this study was to elucidate the fundamental aspects governing the behavior of such hybrid polymer nanocomposites, which are still not well understood since they were barely investigated.

Core-shell NPs were synthesized from copolymer (methyl methacrylate-ethylene glycol dimethacrylate)-core and copolymer (methyl methacrylate-butyl acrylate)-shell (CS15) using starved emulsion polymerization. CNC were extracted from bleached ramie fibers by acidic hydrolysis. Using CS15 as a matrix, CNC as a reinforcing agent as well as a biobased source and PEG as a plasticizing agent, new nanocomposite materials with different component ratios were designed. The nanocomposite films were processed following three different methods, i.e. i) solution casting, ii) solution casting followed by compression molding at 165 °C, and iii) freeze drying followed by compression molding at 165 °C. Morphological characterization (SEM) showed that the methods involving compression molding displayed the highest degree of coalescence of CS15 NPs. However, in presence of PEG or PEG/CNC, the maximum level of compaction of the material was reached as PEG or PEG/CNC fully occupied the interstitial spaces and the interface. In addition, visual observation of the films indicated that the presence of PEG helped protecting CNC from thermal degradation at relatively high temperature (**Figure 6**). It was shown that this protective effect was very much dependent on the ratio between CNC and PEG. Thermal analysis (DSC) revealed that PEG was very well confined between the NPs and at the interstitial spaces and was present in amorphous form in all CS15 based materials containing less than 30 wt. % of PEG. Nevertheless, XRD,

owing to its higher sensitivity, showed the presence of residual crystals of PEG, which were probably formed during the cooling step of the compression molded specimen in the hydraulic press. Moreover, good conservation of CNC in presence of PEG during the melt processing at 165 °C, even at higher CNC loading, was highlighted by the appearance of the crystalline peaks of cellulose-I structure, thus confirming the visual observations. The structure and the properties of the ternary nanocomposite films CS15/PEG/CNC were tailored by fine-tuning the concentration of the three components. As expected, the plasticizing effect of PEG was revealed by a noticeable decrease of the storage modulus of the materials and the shift of the T_g of the shell to lower values, both measured by DMTA. This effect was more pronounced with increasing PEG content. Concerning the level of reinforcement of CNC, DMTA measurement showed that this latter was very much dependent on the ratio CNC/PEG. By controlling this ratio, one can control the thermo-mechanical properties of the final film. This reinforcement effect was correlated with the creation of percolating CNC network capable of increasing the overall storage modulus of the system. Unbalanced ratio between CNC and PEG can compromise the formation of the percolating network because of the adsorption of PEG at the surface of most of CNC.

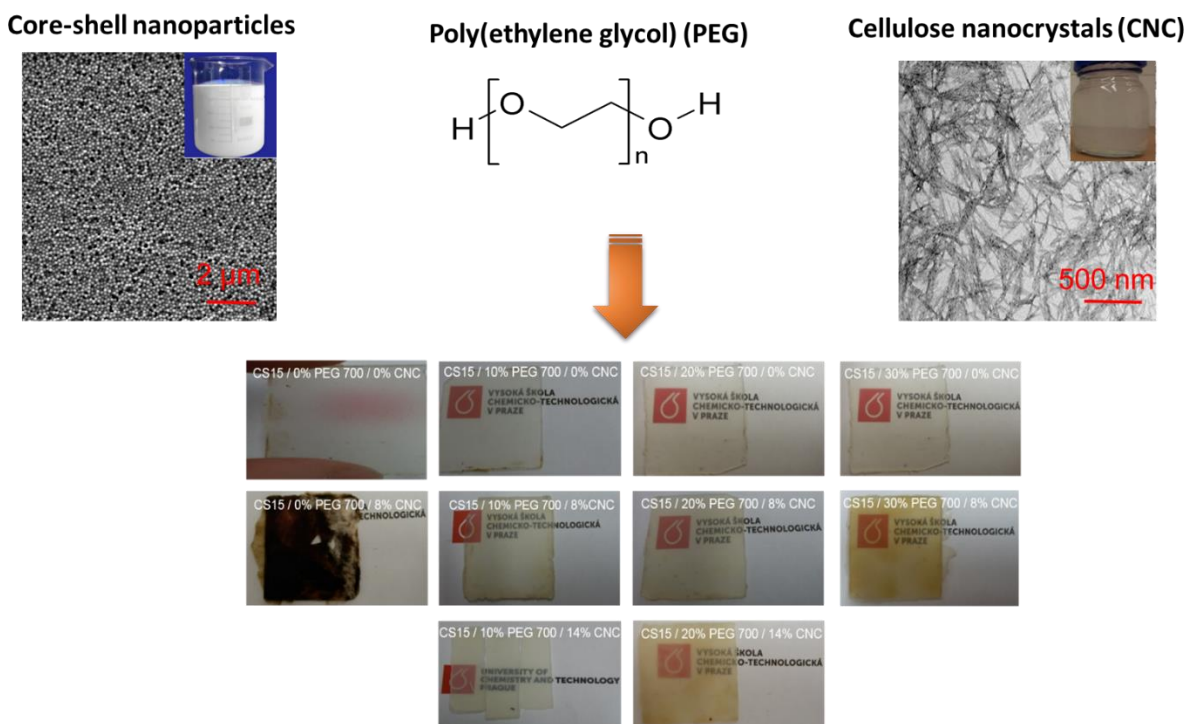


Figure 6: CS15/PEG/CNC specimen prepared by freeze drying followed by compression molding

For more details about the study presented in the section 2.2, refer to the article **23** in the Appendix B.

3.2 New approach on the development of polyaniline/reduced graphene oxide nanocomposites via sacrificial surfactant-stabilized reduced graphene oxide

There is a high demand for high-performance energy storage systems, due to the rapidly growing market in wearable and portable electronics ²⁸. Some principal requirements of these energy storage devices are low-cost, light-weight, stretchability, environmentally friendliness, excellent durability and high power and energy densities. In this context, supercapacitors made of electrochemically active materials, as one of most promising emerging energy storage devices, have received considerable interest ²⁹. This is due to their high power densities combined with high mechanical performances, fast charging and discharging, long lasting stability, safe handling and excellent cycle life. Recent years have witnessed the development of electrically conductive polymers as a promising class of materials for supercapacitor electrodes due to their relatively high theoretical capacities, stretchability, and versatility, as well as their light weight and cost-effectiveness. Among them, polyaniline (PANI) is perhaps the most extensively studied electrically conductive polymer thanks to its unique properties such as different oxidation states, high specific capacitance, good electrical properties, biocompatibility, good chemical and thermal stability, and relative ease of synthesis by electrochemical or chemical methods ^{30, 31}. Nevertheless, PANI suffers from several drawbacks as poor cycle stability and degradation at relatively high potentials. It is expected that loading of PANI with various conductive metals or/and nanocarbonaceous materials can lead to some improvement ³⁰. In particular, graphene, a prominent member of nanocarbonaceous materials, is a promising candidate for developing highly functional graphene-PANI nanocomposite materials, thanks to its outstanding properties as excellent electrical and thermal conductivity, flexibility, mechanical strength and large specific surface area ³². Recently, various kinds of graphene-PANI nanocomposites were developed, showing enhanced electrochemical characteristics as electrode materials for energy storage ³³. Most of the reported studies employed *in situ* polymerization methods of aniline in the presence of reduced graphene oxide (RGO) or graphene oxide (GO) ³⁴⁻³⁹. Due to its electrical resistance, GO combined with PANI does not improve the electrical conductivity of the nanocomposites and the overall electrochemical performances in supercapacitor electrode. To overcome this issue, reduction of the nanocomposite GO-PANI is carried out which simultaneously converts GO into the conductive RGO and PANI to non-conductive form. This is followed by a reoxidation step, aiming to recover PANI to its conductive form, i.e. emeraldine salt state. Though the reoxidation step can help a partial recovery of the electrical conductivity of the nanocomposites, it dramatically affects the chemical and electronic structure of both PANI and RGO, thus degrading the capacitor performances. Another issue, which needs to be addressed during the polymerization of aniline monomers at the surface of GO is the colloidal instability of GO under acidic conditions of the polymerization reaction. The approach consisting of *in situ* polymerization of

aniline in presence of RGO showed other limitations associated with aggregation of RGO during the step of reduction of GO and the subsequent lack of colloidal stability in aqueous solution, thus leading to obstruction of the electrochemical performances of the related nanocomposites. In this regard, we designed a novel approach based on sacrificial surfactant-stabilization of reduced graphene oxide to prepare RGO/PANI nanocomposites from well exfoliated RGO ⁴⁰.

3.2.1 Preparation of nanocomposites

We designed an easy, inexpensive and optimal route of synthesis of RGO/doped PANI nanocomposites with controllable morphologies and properties, following the approach named “*ex situ* reduction”, which consists of reduction of GO (GO was obtained by chemical oxidation of expanded graphite (EG)) in the presence of a sacrificial surfactant (polyvinylpyrrolidone (PVP)) followed by *in situ* polymerization of aniline monomers in the presence of RGO. For a sake of comparison and understanding of the structure-properties relationships, another approach, named “*in situ* reduction” consisting of *in situ* polymerization of aniline monomers in the presence of sacrificial surfactant stabilized-GO sheets in acidic medium followed by reduction of GO in GO-PANI nanocomposites was carried out. Both approaches are illustrated in **Figure 7**.

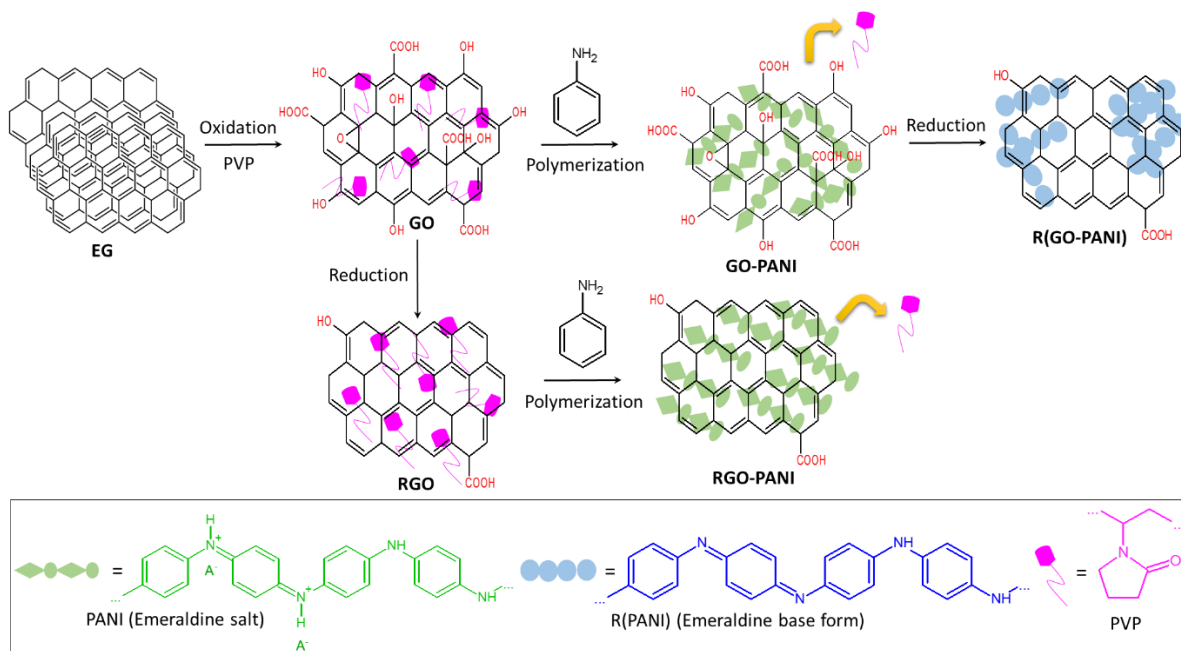


Figure 7: Schematic illustration of the preparation routes of RGO/PANI nanocomposites

3.2.2 Structure properties relationships

The comparative study between the properties of RGO-PANI and R(GO-PANI) was necessary to better understand the complex interactions occurring between PANI and RGO, by putting closer look at the rich states of oxidation and protonation of PANI in combination with different surface chemistries of graphene

derivatives (GO/RGO). It also allowed understanding the colloidal stability of RGO in water, essential to controlling the subsequent morphology and properties of RGO-PANI nanocomposites.

SEM, transmission electron microscopy (TEM) and AFM revealed different morphological structures between R(GO-PANI) and RGO-PANI. While the former exhibits a discontinuous PANI coating in the form of droplets, the latter displays a homogeneous thin coating of PANI at the surface of RGO sheets. In addition, RGO-PANI exhibits a sandwich like-structure in which the nanosheets of RGO coated with PANI overlap in ordered manner whereas this distribution is random in R(GO-PANI) and GO-PANI. Meanwhile, XRD patterns indicate a loss of crystallinity of PANI in R(GO-PANI) connected with the simultaneous reduction of GO and PANI. Nonetheless, the crystalline structures of PANI is retained in RGO-PANI. The morphological and physical structure discrepancies noticed between R(GO-PANI) and RGO-PANI highlight differences in their chemical structures (FTIR, Raman spectroscopy, X-Ray Photoelectron Spectroscopy (XPS) and UV-visible) and therefore differences in the mode of interaction between the polymer and the nanofiller, which in turn affects the related properties. As a result of the simultaneous reduction of GO and PANI when following *in situ* reduction approach, transition of PANI from its emeraldine salt oxidative state to emeraldine base form occurs. Polymerization of PANI at the surface of RGO sheets via *ex situ* reduction approach allows retaining its emeraldine salt form. As a consequence, R(GO-PANI) exhibits much higher thermal stability (using thermogravimetric analysis (TGA)) and poor electrical conductivity ($\sigma = 0.01 \text{ S/m}$) attributed to the decrease of the doping degree of PANI and to morphology changes of the nanocomposites during the reduction process with respect to GO-PANI ($\sigma = 0.18 \text{ S/cm}$) and to neat PANI ($\sigma = 0.11 \text{ S/cm}$). The trend of these properties is more pronounced with the increase of the reduction time. In contrast, RGO-PANI displays thermal properties comparable to those of neat PANI and superior electrical properties ($\sigma = 76 \text{ S/cm}$), which can be further improved by milling of the nanocomposite ($\sigma = 280 \text{ S/cm}$). Such enhancement of the electrical conductivity were attributed to the particular morphology of RGO-PANI obtained under well-controlled processing conditions, which are due to the establishment of strong interactions including π - π stacking, electrostatic and hydrogen bonding between PANI and RGO sheets. Elaboration of RGO-PANI with such electrical conductivity features was possible only thanks to the excellent colloidal stability of RGO in water, achieved via effective stabilization of GO during the reduction process, and to the subsequent morphology of RGO-PANI.

The electrochemical characterization of the selected nanocomposites was performed by cycling voltammetry (CV) and constant current charge-discharge cycling (CC) to see the effect of the above mentioned physico-chemical properties on their capacitive and redox characteristics. The electrochemical properties of the most promising material, i.e. RGO-PANI were compared with the results of GO, PANI and GO-PANI (**Figure 8**). Qualitatively, the cyclovoltammograms of all the PANI-containing electrodes showed all the characteristic peaks of PANI. Both nanocomposites GO-PANI and RGO-PANI showed

greater intensities of the middle peak, most probably due to the fact that they bring more quinone and hydroquinone species to the system originating from graphene-based phase.⁴¹ However, all PANI-based electrodes indicated poor electrochemical cycling stability of the nanocomposites. A summary of the decay of the capacitance (**Figure 8E**) showed continuous capacitance decrease during the stabilization experiment. In the case of GO, an increase of its capacitance was observed as it got reduced during the experiment, which increased the conductivity due to partial restoration of the sp^2 hybridization. The data from the stabilization experiment suggested that no protection against degradation was provided by GO or RGO. It rather seems that pure PANI exhibits the best cycling stability of all the materials. However, if one look carefully at the three points in the bottom part of Figure 8E, which are relative capacitances calculated from the CV experiment performed after examining the effect of scan rate, one can see that the capacitance of the nanocomposites in fact converged to some value, while pure PANI degrades further. Overall, though significant advances were made on these materials in the frame of this study, the cycling stability obtained is still not satisfactory. Optimization of the material composition will be done in the future to enable further opportunities for the development of novel electrically active materials.

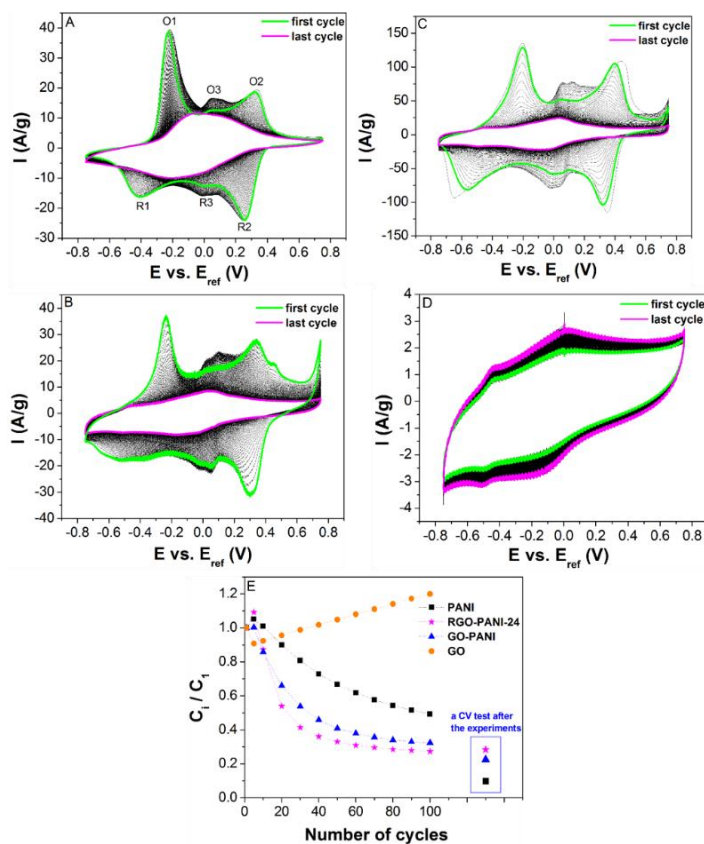


Figure 8: Cyclic voltammograms of the materials A) PANI, B) PANI-GO, C) RGO-PANI-24, D) GO, E) Evolution of relative specific capacitance as a function of number of cycles

A scientific article describing the findings presented in the section 3.2 was submitted to journal of Colloid and Interface Science ⁴⁰.

3.3 Nitrogen-rich hierarchically porous polyaniline-based sorbents for carbon dioxide (CO₂) capture

Energy-driven consumption of fossil fuels has led to a dramatic rise in CO₂ emissions, disturbing the global carbon cycle. Carbon capture and storage technologies are considered as immediate and most realistic solution to reduce CO₂ emissions. Among the CO₂ capture options available, post-combustion capture is the most widely adopted method. ^{42, 43} For more than six decades, amine absorption has been an efficient and most advanced technology for the removal of CO₂ from natural gas. ^{42, 44} Though well-established, this approach consumes an enormous amount of energy, results in corrosion of equipment, inherent regeneration costs and toxic emissions. To date, the main challenge for the large scale application of post-combustion capture to coal fired power plants remains the cost of CO₂ capture. A number of solid sorbents such as molecular sieves, porous carbon, porous silica, metal organic frameworks etc., are emerging as promising alternatives to replace liquid amine, thanks to their well-developed porosity, ease in handling and their low energy requirements for regeneration. ⁴⁵⁻⁴⁷ CO₂ adsorption capacity and selectivity of porous carbons can further be improved by incorporating nitrogen groups into the framework as these functional groups can act as Lewis base sites for sequestering CO₂.⁴⁸ As a result, there is an accentuated interest to investigate the CO₂ capture performance of nitrogen doped porous carbons. According to latest reported studies, it has been found that efficient CO₂ sorption performance depends on a combination of diffusion and adsorption selectivity. Although the incorporation of amines or nitrogen groups enhances the CO₂ sorption capacity, the functionalization step usually results in the blockage of the diffusion channels to the active sites present on the materials. Moreover, there have been reports of amine degradation and leaching after multiple CO₂ capture cycles. A more promising approach is the direct carbonization and activation of nitrogen-containing polymers. This method allows better control over the chemical composition and avoids complicated post-treatments to incorporate nitrogen groups. However, it still remains a challenge to design the optimum combination of surface chemistry and a material framework comprising all three types of pores i.e. abundant micropores (for high CO₂ adsorption), mesopores and macropores (to facilitate efficient CO₂ diffusion into and out of the adsorption sites). ^{49, 50} Based on these findings, we designed stable hierarchically porous materials with high surface areas and high nitrogen content and tested their application in CO₂ capture⁵¹.

3.3.1 Synthesis of the 3-D Microclusters

The proposed strategy for designing the stable hierarchically porous materials was aimed at creating a range of pore sizes in the same material while retaining a good amount of nitrogen functionalities on the carbon

framework, due to its affinity towards CO₂. The creation of different pore sizes was necessary to facilitate efficient gas diffusion and simultaneously enhancing the CO₂ adsorption capacity. PANI was selected as a starting polymer, thanks to its high nitrogen content, ease of synthesis and low cost. The intrinsic presence of nitrogen in the molecule of aniline (monomer), guaranteed the homogenous distribution of nitrogen groups in the carbon based final materials. The spherical polystyrene latex nanoparticles (PS NPs) were chosen as building blocks, based on their high T_g , which gave rigid and non-deformable support to the 3-D framework⁵²⁻⁵⁶ and later on as sacrificial template. Upon carbonization and removal of PS NPs, we expected to create additional pores and increase the surface area and pore volume of the final materials. The crosslinking of the polymer using phytic acid with the purpose to create hierarchical porosity was also investigated.

The PS-NP building blocks were prepared by radical emulsion polymerization.⁵¹ Aniline (ANI) was polymerized by chemical oxidative route in aqueous medium in the presence of the PS NPs. Polymerization of aniline was done without or with PS NPs, without or with phytic acid as crosslinker for comparison. The resulting suspensions of microclusters were freeze dried and then carbonized under controlled conditions. Finally, they underwent chemical activation using KOH at different ratios of KOH/Carbonized material (KOH/C), followed by another cycle of carbonization. The synthesis procedure is depicted in **Figure 9**.

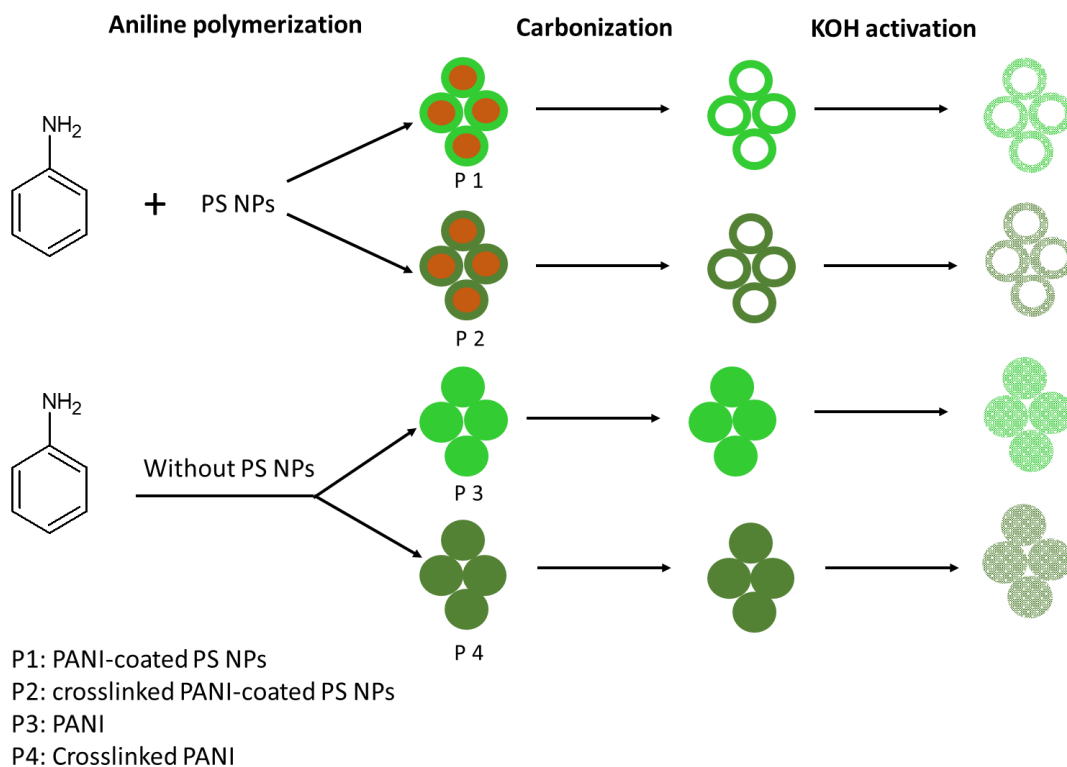


Figure 9: Procedure of synthesis of the 3-D porous materials

3.3.2 Morphology of the 3-D Microclusters

Overall, a higher carbon mass remained for all the crosslinked materials in comparison to non-crosslinked materials, measured by TGA. The weight difference is due to the thermal stability of the crosslinker, phytic acid, which undergoes dehydration and carbonization and therefore slightly increasing the weight of the crosslinked materials. SEM analysis showed that the skeleton of the PS-PANI microclusters contain interconnected spherical pores left by the removal of PS NPs, which created additional porosity for easy diffusion of CO₂. Comparatively, the PANI microclusters prepared without PS NP building blocks showed globular rather than the hierarchically porous structures. The adsorption isotherms further evidenced the creation of the high surface area hierarchically porous materials after the carbonization and activation steps (micropores and some mesopores). In addition, TEM images clearly showed the porosity of the carbon, which is important for efficient gas diffusion.

The trend in evolution of Brunauer–Emmett–Teller (BET) surface areas with different KOH treatments showed that increasing the KOH/C ratio from 1 to 3 resulted in the formation of new pores and thus to higher surface areas. This effect was more pronounced for the materials, which were crosslinked with phytic acid. The phytic acid networks guaranteed greatest KOH adsorption of the carbonized material, and therefore a well-developed porosity in the following activation step thanks to the property of KOH to generate pores. When the ratio KOH/C = 3 was used for the crosslinked materials, optimum pore size distribution was achieved.

3.3.3 Capture performance

The optimized material i.e. PS coated crosslinked PANI activated using KOH/C = 3 achieved very high CO₂ capacity (9.14 mmol/g) at 273.15 K and 1 bar, which is among the highest reported for carbon-based sorbents in the literature. It is clear that this high CO₂ capture capacity was principally due to the hierarchical pore structure, which increased the diffusion of CO₂ into the inner micropores. After examining the CO₂ capture capacity of the so-produced materials with varying textural properties and nitrogen amount, we found out that the CO₂ capture capacity at low pressure is mainly controlled by the presence of micropores with diameter smaller than 0.7 nm. However, when elaborating materials for concrete applications, it is primordial to tune both the pore structure and surface chemistry, at the same time to combine their advantages.

By taking into consideration possible industrial application of our material, sorbent regeneration capability test was carried out on our optimized material⁵¹. The obtained results of regeneration indicated the highest reduction in sorption capacity after the first cycle, whilst further cycles (within statistical uncertainty of the measured data) did not show important reduction of the sorption capacity. CO₂ sorption isotherms measured after each regeneration cycle showed a change in pore size distributions after the first regeneration whereas

other distributions were quasi-identical to each other independent on the number of regeneration cycle. There was no significant difference for the composition of all tested materials, indicating that physical adsorption in ultramicropores (physisorption) is the main binding mode. Nevertheless, the loss in sorption capacity, despite no change in composition suggested that there were small changes to the material porosity. Basically, since the binding mechanism of our materials is only by physisorption, we believe this requires lower amount of energy for regeneration compared to aqueous amine absorption process, where CO₂ is reacting with amine molecules (chemisorption). In addition, it was already reported that amine solutions are less stable and undergo degradation, which is not the case of solid sorbents, which are durable over several cycles.

For more details about the study presented in the section 2.2, refer to the article **25** in the Appendix B.

Chapter 4

Research perspectives

I have recently launched several research activities in our research group. The main ones include:

4.1. Design of flexible hybrid supercapacitors from renewable resources

In the frame of my research activities related to the design of high performance supercapacitors, I launched few months ago a new project aiming at designing a novel type of highly flexible, thermally stable and lightweight electrodes based on materials suitable for sustainable development for high performance supercapacitors, with tailored structure and high capacitance. Herein, the emerging biosourced cellulose nanofibrils (CNF) is employed as a substrate to prepare supercapacitor electrodes with electrically conductive polymers (ECP) and/or nanocarbonaceous materials (graphene derivatives or carbon nanotubes (CNT)) using bottom-up approaches. New methodologies of polymer/nanofiller compatibilization and homogenization are being investigated to combine together different materials and different properties into free-standing CNF-ECP based porous electrodes with optimal dispersion of the nanosized fillers, porosity, and thickness. In this regard, surface functionalization of the CNF and nanocarbonaceous materials with well-selected functional groups will be performed. The electrodes exhibiting the best capacitances, high flexibility and thermal stability will be used in fabrication and testing of supercapacitor devices. This study is motivated by i) a high need to develop environmentally benign, lightweight and flexible supercapacitors with enhanced capacitance retention at high charge–discharge rates, and ii) a significant lack of fundamental understanding of the structure-properties relationships governing such hybrid supercapacitors.

4.2. Development of novel biodegradable porous nanocomposite materials for bio-medical applications

The project deals with the investigation of novel approach of generating biodegradable and biocompatible composite like-porous materials as potential scaffolds or drug delivery carriers. Porous materials with desired porosity, high and tunable mechanical stability and degradation kinetics will be designed. In this context, polymeric biodegradable porous materials with controlled pore structures and chemical compositions have engendered substantial interest due of their attractive characteristics, such as large specific surface area, low density, and well-defined porosity. They can find applications in biomacromolecule trapping, drug delivery or tissue engineering. Among potential biodegradable polymers,

poly(lactic-co-glycolic acid) (PLGA) has been used as a tissue engineering scaffold, as well as a carrier for the delivery of proteins, drugs, and other macromolecules, as the degradation rate of the polymer can be controlled. In the frame of this project, we already started the synthesis of PLGA bearing various functional groups. Synthesized polymers are currently explored for preparation of two types of particles, i.e. i) nanoparticles with different surface charges, which will open new possibilities for construction of nano- to micro-clusters based nanoparticles by self-assembly, and ii) porous microspheres, which can serve either for construction of solid porous scaffolds in combination with reinforcing agents (CNT, CNF etc.), or as drug delivery carriers. Entrapment of model molecules inside the nanoparticles/porous microspheres are also ongoing. Detailed material characterization will be carried out to understand the structure-properties relationship. Finally, in vitro tests will be performed on the most suitable materials. This study will be later extended to other biodegradable polymers such as polycaprolactone and polylactide.

4.3. Amorphous solid dispersions: formulation and prediction of phase diagrams drug-polymer

The therapeutic efficiency of a drug, so-called active pharmaceutical ingredient (API) depends upon its bioavailability, which is directly associated to its solubility in water. Recent studies reported that up to 70% of investigational new drugs and up to 40% of marketed drugs exhibit poor solubility in water, resulting in low bioavailability and often results in variable dissolution rates. A promising way to improve the bioavailability of poorly soluble API is their integration into polymer matrices and formation of so-called amorphous solid dispersions (ASD), or co-amorphization with amino-acids and formation of co-amorphous. The most used techniques to create ASD are spray drying and hot melt extrusion. ASD is created by molecularly dispersed API within the carrier forming single-phase. Physical stability or API recrystallization tendency of an ASD formulation depends mainly on the solubility of the crystalline API in the polymer at the storage temperature. Taking into consideration the above mentioned, before the preparation of ASD, such parameters as the solubility of the API in the polymer, T_g , T_m , and many others should be calculated and subsequently used in theoretical modeling. In the frame of a collaboration between our laboratory and Laboratory of applied thermodynamics, we started an activity related to preparation of ASD by means of hot melt extrusion and freeze drying using model drugs. To predict the stability of the prepared ASD formulations at storage conditions, the phase diagrams are constructed based on calorimetric measurements with mixtures of different compositions in connection with the modeling using the Flory-Huggins theory and recently developed molecular-based equations of state. The long-term stability of the prepared ASD formulations is systematically assessed for pharmaceutically relevant time periods. In parallel to this study, we plan also to study the formulation and long term physical stability of co-amorphous API-amino acid systems, as another promising approach of API amorphization.

References

1. K. Anderson, K. Schreck and M. Hillmyer, *Polyme Review*, 2008, **48**, 85-108.
2. N. Ljungberg and B. Wesslén, *Polymer*, 2003, **44**, 7679-7688.
3. L. V. Labrecque, R. A. Kumar, V. Davé, R. A. Gross and S. P. McCarthy, *Journal of Applied Polymer Science*, 1997, **66**, 1507–1513.
4. V. P. Martino, A. Jiménez and R. A. Ruseckaite, *Journal of Applied Polymer Science*, 2009, **112**, 2010-2018.
5. N. Ljungberg, T. Andersson and B. Wesslén, *Journal of Applied Polymer Science*, 2003, **88**, 3239–3247.
6. V. P. Martino, R. A. Ruseckaite and A. Jiménez, *Journal of Thermal Analysis and Calorimetry*, 2006, **86**, 707-712.
7. N. Ljungberg, D. Colombini and B. Wesslén, *Journal of Applied Polymer Science*, 2005, **96**, 992-1002.
8. G. Kfoury, J.-M. Raquez, F. Hassouna, P. Leclère, V. Toniazzo, D. Ruch and P. Dubois, *Polymer Engineering & Science*, 2015, **55**, 1408-1419 (**reference 18/25 in Appendix B**).
9. G. Kfoury, J. M. Raquez, F. Hassouna, J. Odent, V. Toniazzo, D. Ruch and P. Dubois, *Frontiers in Chemistry*, 2013, **1**, 32 (**reference 14/25 in Appendix B**).
10. G. Kfoury, F. Hassouna, J.-M. Raquez, V. Toniazzo, D. Ruch and P. Dubois, *Macromolecular Materials and Engineering*, 2014, **299**, 583-595 (**reference 16/25 in Appendix B**).
11. K. Wang, B. Brüster, F. Addiego, G. Kfoury, F. Hassouna, D. Ruch, J.-M. Raquez and P. Dubois, *Polymer International*, 2015, **64**, 1544-1554 (**reference 19/25 in Appendix B**).
12. F. Hassouna, J.-M. Raquez, F. Addiego, V. Toniazzo, P. Dubois and D. Ruch, *European Polymer Journal*, 2012, **48**, 404-415 (**reference 11/25 in Appendix B**).
13. F. Hassouna, J.-M. Raquez, F. Addiego, P. Dubois, V. Toniazzo and D. Ruch, *European Polymer Journal*, 2011, **47**, 2134-2144 (**reference 7/25 in Appendix B**).
14. B. Brüster, F. Addiego, F. Hassouna, D. Ruch, J. M. Raquez and P. Dubois, *Polymer Degradation and Stability*, 2016, **131**, 132-144 (**reference 20/25 in Appendix B**).
15. G. Vasapollo, G. Mele and R. Del Sole, *Molecules*, 2011, **16**, 6871-6882.
16. E. Bloise, L. Carbone, G. Colafemmina, L. D'Accolti, S. E. Mazzetto, G. Vasapollo and G. Mele, *Molecules*, 2012, **17**, 12252-12261.
17. J. Chen, Z. Liu, J. Jiang, X. Nie, Y. Zhou and R. E. Murray, *RSC Advances*, 2015, **5**, 56171-56180.

18. V. S. Balachandran, S. R. Jadhav, P. K. Vemula and G. John, *Chemical Society Reviews*, 2013, **42**, 427-438.
19. C. Voirin, S. Caillol, N. V. Sadavarte, B. V. Tawade, B. Boutevin and P. P. Wadgaonkar, *Polymer Chemistry*, 2014, **5**, 3142-3162.
20. W. M. Gramlich, M. L. Robertson and M. A. Hillmyer, *Macromolecules*, 2010, **43**, 2313-2321.
21. F. Hassouna, I. Mihai, L. Fetzter, T. Fouquet, J.-M. Raquez, A. Laachachi, H. Ibn Al Ahrach and P. Dubois, *Macromolecular Materials & Engineering*, 2016, **301**, 1267-1278 (**reference 23/25 in Appendix B**).
22. G. Siqueira, J. Bras and A. Dufresne, *Polymers*, 2010, **2**, 728-765.
23. Y. Habibi, L. A. Lucia and O. J. Rojas, *Chemical Reviews*, 2010, **110**, 3479–3500.
24. P. K. Annamalai, K. L. Dagnon, S. Monemian, E. J. Foster, S. J. Rowan and C. Weder, *ACS applied materials & interfaces*, 2014, **6**, 967-976.
25. D. Dubief, E. Samain and A. Dufresne, *Macromolecules*, 1999, **32**, 5765-5771.
26. V. Favier, G. R. Canova, J. Y. Cavaillé, H. Chanzy, A. Dufresne and C. Gauthier, *Polymers for Advanced Technologies*, 1995, **6**, 351-355.
27. V. Favier, H. Chanzy and J. Y. Cavaille, *Macromolecules*, 1995, **28**, 6365-6367.
28. H. Nishide and K. Oyaizu, *Science*, 2008, **319**, 737-738.
29. A. González, E. Goikolea, J. A. Barrena and R. Mysyk, *Renewable and Sustainable Energy Reviews*, 2016, **58**, 1189-1206.
30. H. Wang, J. Lin and Z. X. Shen, *Journal of Science: Advanced Materials and Devices*, 2016, **1**, 225-255.
31. C. H. B. Silva, N. A. Galiote, F. Huguenin, É. Teixeira-Neto, V. R. L. Constantino and M. L. A. Temperini, *Journal of Materials Chemistry*, 2012, **22**, 14052.
32. M. J. Allen, V. C. Tung and R. B. Kaner, *Chemical Reviews*, 2010, **110**, 132-145.
33. S. Stankovich, D. A. Dikin, G. H. Dommett, K. M. Kohlhaas, E. J. Zimney, E. A. Stach, R. D. Piner, S. T. Nguyen and R. S. Ruoff, *Nature*, 2006, **442**, 282-286.
34. C. Vallés, P. Jiménez, E. Muñoz, A. M. Benito and W. K. Maser, *The Journal of Physical Chemistry C*, 2011, **115**, 10468-10474.
35. K. Zhang, L. L. Zhang, X. S. Zhao and J. Wu, *Chemistry of Materials*, 2010, **22**, 1392-1401.
36. O. D. Iakobson, O. L. Gribkova, A. R. Tameev, V. V. Kravchenko, A. V. Egorov and A. V. Vannikov, *Synthetic Metals*, 2016, **211**, 89-98.
37. D. Gui, C. Liu, F. Chen and J. Liu, *Applied Surface Science*, 2014, **307**, 172-177.
38. M. Mitra, C. Kulsi, K. Chatterjee, K. Kargupta, S. Ganguly, D. Banerjee and S. Goswami, *RSC Advances*, 2015, **5**, 31039-31048.

39. M. H. Mohamadzadeh Moghadam, S. Sabury, M. M. Gudarzi and F. Sharif, *Journal of Polymer Science Part A: Polymer Chemistry*, 2014, **52**, 1545-1554.
40. T. Bautkinová, F. Hassouna, A. Sifton, E. M. Kutorglo, M. Dendisová, P. Mazúr, D. Kopecký, L. Fišer, P. Ulbrich and M. Šoós, *Submitted to Journal of Colloidal and Interface Science*, 2019.
41. F. Regisser, M.-A. Lavoie, G. Y. Champagne and D. Bélanger, *Journal of Electroanalytical Chemistry*, 1996, **415**, 47-54.
42. B. Dutcher, M. Fan and A. G. Russell, *ACS Appl Mater Interfaces*, 2015, **7**, 2137-2148.
43. A. L. Yaumi, M. Z. A. Bakar and B. H. Hameed, *Energy*, 2017, **124**, 461-480.
44. J. C. Abanades, B. Arias, A. Lyngfelt, T. Mattisson, D. E. Wiley, H. Li, M. T. Ho, E. Mangano and S. Brandani, *International Journal of Greenhouse Gas Control*, 2015, **40**, 126-166.
45. L. Liu, Q.-F. Deng, X.-X. Hou and Z.-Y. Yuan, *Journal of Materials Chemistry*, 2012, **22**, 15540.
46. Z. Liu, Z. Du, H. Song, C. Wang, F. Subhan, W. Xing and Z. Yan, *Journal of Colloid Interface and Science*, 2014, **416**, 124-132.
47. H. A. Patel, J. Byun and C. T. Yavuz, *ChemSusChem*, 2017, **10**, 1303-1317.
48. J. Wang, I. Senkovska, M. Oschatz, M. R. Lohe, L. Borchardt, A. Heerwig, Q. Liu and S. Kaskel, *Journal of Materials Chemistry A*, 2013, **1**, 10951.
49. J. H. Lee, H. J. Lee, S. Y. Lim, B. G. Kim and J. W. Choi, *Journal of American Chemical Society*, 2015, **137**, 7210-7216.
50. B. Li, Y. Duan, D. Luebke and B. Morreale, *Applied Energy*, 2013, **102**, 1439-1447.
51. E. M. Kutorglo, F. Hassouna, A. Beltzung, D. Kopecký, I. Sedlářová and M. Šoós, *Chemical Engineering Journal*, 2018, DOI: <https://doi.org/10.1016/j.cej.2018.10.133> (**reference 25/25 in Appendix B**).
52. E. M. Kutorglo, F. Hassouna, D. Kopecký, L. Fišer, I. Sedlářová, A. Zdražil and M. Šoós, *Colloids and Surfaces A: Physicochemical and Engineering Aspects*, 2018, **557**, 137-145 (**reference 24/25 in Appendix B**).
53. D. Kim, Y. Tian and H. J. Choi, *RSC Advances*, 2015, **5**, 81546-81553.
54. S. Bousalem, S. Benabderrahmane, Y. Y. C. Sang, C. Mangeney and M. M. Chehimi, *Journal of Materials Chemistry*, 2005, **15**, 3109.
55. C. F. Mangeney, M.; Bousalem, S.; Zhicai, M. Ammar, S.; Herbst, F.; Beaunier, P.; Elaissari, A. and Chehimi, M. M. , *Langmuir*, 2007, **23**, 10940 - 10949.
56. D. B. Cairns, M. A. Khan, C. Perruchot, A. Riede and S. P. Armes, *Chemical Materials*, 2003, **15**, 233 - 239.

Appendices

Appendix A: List of author's articles in impacted journals

1. Maerten E, Hassouna F, Couve-Bonnaire S, Mortreux A, Carpentier JF, Castanet Y. Direct synthesis of benzoylpyridines from chloropyridines via a palladium-carbene catalyzed carbonylative Suzuki cross-coupling reaction. *Synlett*. 2003(12):1874-1876.
2. Hassouna F, Morlat-Therias S, Mailhot G, Gardette JL. Influence of water on the photodegradation of poly(ethylene oxide). *Polymer Degradation and Stability*. 2007;92(11):2042-2050.
3. Hassouna F, Mailhot G, Morlat-Therias S, Gardette JL. Photochemical behaviour of poly(ethylene oxide) (PEO) in aqueous solution: Influence of iron salts. *Journal of Photochemistry and Photobiology a-Chemistry*. 2008;195(2-3):167-174.
4. Hassouna F, Therias S, Mailhot G, Gardette JL. Photooxidation of poly(N-vinylpyrrolidone) (PVP) in the solid state and in aqueous solution. *Polymer Degradation and Stability*. 2009;94(12):2257-2266.
5. Hassouna F, Mailhot G, Morlat-Therias S, Gardette JL. Influence of iron salts on the photooxidation of poly(N-vinylpyrrolidone) in aqueous solution. *Journal of Photochemistry and Photobiology a-Chemistry*. 2011;218(2-3):239-246.
6. Baniassadi M, Addiego F, Laachachi A, Ahzi S, Garmestani H, Hassouna F, et al. Using SAXS approach to estimate thermal conductivity of polystyrene/zirconia nanocomposite by exploiting strong contrast technique. *Acta Materialia*. 2011;59(7):2742-2748.
7. Hassouna F, Raquez JM, Addiego F, Dubois P, Toniazzi V, Ruch D. New approach on the development of plasticized polylactide (PLA): Grafting of poly(ethylene glycol) (PEG) via reactive extrusion. *European Polymer Journal*. 2011;47(11):2134-2144.
8. Baniassadi M, Laachachi A, Hassouna F, Addiego F, Muller R, Garmestani H, et al. Mechanical and thermal behavior of nanoclay based polymer nanocomposites using statistical homogenization approach. *Composites Science and Technology*. 2011;71(16):1930-1935.
9. Hassouna F, Laachachi A, Chapron D, El Mouedden Y, Toniazzi V, Ruch D. Development of new approach based on Raman spectroscopy to study the dispersion of expanded graphite in poly(lactide). *Polymer Degradation and Stability*. 2011;96(12):2040-2047.
10. Mertz G, Hassouna F, Toniazzi V, Dahoun A, Ruch D. Effect of Coated Rutile TiO₂ and Disazopyrazolone Dye Additives on Unvulcanized Styrene Butadiene Rubber During Photo-Ageing. *Journal of Engineering Materials and Technology-Transactions of the Asme*. 2011;134(1): 010903-010903-7.
11. Hassouna F, Raquez JM, Addiego F, Toniazzi V, Dubois P, Ruch D. New development on plasticized poly(lactide): Chemical grafting of citrate on PLA by reactive extrusion. *European Polymer Journal*. 2012;48(2):404-415.

12. Hassouna F, Kashyap S, Laachachi A, Ball V, Chapron D, Toniazzi V, et al. Peculiar reduction of graphene oxide into graphene after diffusion in exponentially growing polyelectrolyte multilayers. *Journal of Colloid and Interface Science*. 2012;377:489-496.
13. Mertz G, Hassouna F, Leclerc P, Dahoun A, Toniazzi V, Ruch D. Correlation between (nano)-mechanical and chemical changes occurring during photo-oxidation of filled vulcanised styrene butadiene rubber (SBR). *Polymer Degradation and Stability*. 2012;97(11):2195-2201.
14. Kfoury G, Raquez JM, Hassouna F, Odent J, Toniazzi V, Ruch D, Dubois P. Recent advances in high performance poly(lactide): from "green" plasticization to super-tough materials via (reactive) compounding. *Frontiers in Chemistry*. 2013;1(32):1-46.
15. Mortazavi B, Hassouna F, Laachachi A, Rajabpour A, Ahzi S, Chapron D, et al. Experimental and multiscale modeling of thermal conductivity and elastic properties of PLA/expanded graphite polymer nanocomposites. *Thermochimica Acta*. 2013;552:106-113.
16. Kfoury G, Hassouna F, Raquez JM, Toniazzi V, Ruch D, Dubois P. Tunable and durable toughening of polylactide materials via reactive extrusion. *Macromolecular Materials and Engineering*. 2014;299(5):583-595.
17. Ibarra-Gomez R, Muller R, Bouquey M, Rondin J, Serra CA, Hassouna F, et al. Processing of nanocomposites PLA/graphite using a novel elongational mixing device. *Polymer Engineering and Science*. 2015;55(1):214-222.
18. Kfoury G, Raquez JM, Hassouna F, Leclerc P, Toniazzi V, Ruch D. Toughening of poly(lactide) using polyethylene glycol methyl ether acrylate: Reactive versus physical blending. *Polymer Engineering and Science*. 2015;55(6):1408-1419.
19. Wang K, Bruster B, Addiego F, Kfoury G, Hassouna F, Ruch D et al. Strain-induced deformation mechanisms of polylactide plasticized with acrylated poly(ethylene glycol) obtained by reactive extrusion. *Polymer International*. 2015;64(11):1544-1554.
20. Brüster B, Addiego F, Hassouna F, Ruch D, Raquez JM, Dubois P. Thermo-mechanical degradation of plasticized poly(lactide) after multiple reprocessing to simulate recycling: Multi-scale analysis and underlying mechanisms. *Polymer Degradation Stability*. 2016;131:132-144.
21. Hassouna F, Mihai I, Fetzer L, Fouquet T, Raquez JM, Laachachi A, Ibn Al Ahrach H, Dubois P. Design of new cardanol derivative: synthesis and application as potential biobased plasticizer for poly(lactide), *Macromolecular Materials and Engineering*. 2016;301:1267-1278.
22. Mihai I, Hassouna F, Fouquet T, Laachachi A, Raquez JM, Ibn El Ahrach H, Dubois P. Reactive plasticization of poly(lactide) with epoxy functionalized cardanol. *Polymer Engineering and Science*. 2018; 58 (S1): E64-E72.
23. Hassouna F, Korbelářová J, Jaquet B, Kutorglo EM, Kopecký D, Ulbrich P, Fulem M, Hrdlička Z, Šoos M. An environmentally benign methodology to elaborating polymer nanocomposites with tunable properties using core-shell nanoparticles and cellulose nanocrystals. *Colloids and Surfaces A: Physicochemical and Engineering Aspects*. 2018;553: 169-179.
24. Kutorglo EM, Hassouna F, Kopecký D, Fišer L, Sedlářová I, Zdražil A, Šoos M. Synthesis of conductive macroporous composite polymeric materials using porogen-free method. *Colloids and Surfaces A: Physicochemical and Engineering Aspects*. 2018;557:137-145.

- 25.** Kutorglo EM, Hassouna F, Beltzung A, Kopecký D, Sedlářová I, Šoóš M. Nitrogen-rich hierarchically porous polyaniline-based sorbents for carbon dioxide (CO₂) capture. *Chemical Engineering Journal*. 2018; doi.org/10.1016/j.cej.2018.10.133.

Appendix B: Author's articles in impacted journals

Direct Synthesis of Benzoylpyridines from Chloropyridines via a Palladium-Carbene Catalyzed Carbonylative Suzuki Cross-Coupling Reaction

Eddy Maerten,^a Fatima Hassouna,^a Samuel Couve-Bonnaire,^a André Mortreux,^a Jean-François Carpentier,^b Yves Castanet^{*a}

^a Laboratoire de Catalyse de Lille, UMR 8010 CNRS, Université de Lille 1, ENSCL, BP 108, 59652, Villeneuve d'Ascq Cedex, France
Fax +33(3)20436585; E-mail: yves.castanet@enscl-lille.fr

^b Organométalliques et Catalyse, UMR 6509 CNRS, Université de Rennes 1, Institut de Chimie, Campus de Beaulieu, 35042, Rennes Cedex, France

Received 17 June 2003

Abstract: The use of N-heterocyclic carbene-type ligands with palladium catalysts allows the activation of chloropyridines and chloroquinoline towards carbonylative cross-coupling with phenylboronic acid for the synthesis of unsymmetrical biaryl ketones.

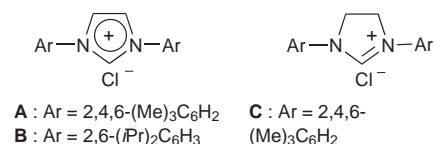
Key words: palladium, N-heterocyclic carbene ligand, pyridyl chloride

Palladium-catalyzed Suzuki cross-coupling reactions of boranes, boronic esters or boronic acids with aryl halides or pseudo-halides to form biaryl derivatives have emerged over the past two decades as an extremely powerful tool in organic synthesis.¹ In particular, remarkable progress has been achieved recently to enlarge the scope of these reactions to aryl chlorides, which are less reactive but much cheaper and more readily available substrates than aryl iodides and bromides.² Closely related to the Suzuki reaction, the palladium-catalyzed three-component cross-coupling of aryl halides, carbon monoxide and aryl boronic acid provides also a straightforward access to unsymmetrical biaryl ketones.³ The main drawback of this approach lies sometimes in the formation of biaryl side-products, which results from direct coupling, i.e. without carbon monoxide insertion, in particular with electron-deficient aryl halides. Also, whereas aryl iodides and bromides are usually coupled efficiently under carbonylative conditions, aryl chlorides suffer from the same lack of reactivity as aforementioned and, until now, to our knowledge, there is no example of carbonylative cross-coupling involving aryl chloride.

We have recently reported the selective transformation of various mono- and di-iodo and bromopyridines into α -pyridyl ketones using such methodology.⁴ In this study, it was found that both the reactivity and selectivity for the ketone product increased when PCy₃ was used instead of PPh₃. This fact prompted us to investigate other types of sterically demanding electron-rich ligands. In this paper, we report that the use of palladium-catalysts based on N-heterocyclic carbene ligands derived from commercially available imidazolium salts (Scheme 1), which have prov-

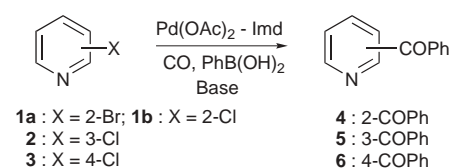
en successful in direct Suzuki coupling of chloroarenes,⁵ allows the effective carbonylative coupling of various chloro- and dichloroazines (pyridine and quinoline) with phenylboronic acid.

As the use of such ligands in carbonylation reactions has not been described previously,⁶ the reaction was first explored with 2-bromopyridine (**1a**) and phenylboronic acid (Scheme 2).



Scheme 1 Imidazolium salts (Imd)

Various solvents and bases were used in combination with Pd(II) acetate and 1,3-bis(2,4,6-trimethylphenyl)-imidazolium chloride (**A**) as the catalyst precursors. Table 1 shows that 1,4-dioxane is the best solvent, which enables complete conversion of **1a** within reasonable time and high selectivity for 2-benzoyl-pyridine (**4**) (entry 2). In other ether type solvents such as anisole and THF, both the reactivity and selectivity were slightly lower (entries 1, 3).



Scheme 2 Carbonylative Suzuki cross-coupling of pyridyl halides

On the other hand, no conversion was observed in DMF (entry 4). The base affected also greatly the efficiency of the process. Best results were obtained with Cs₂CO₃ and K₂CO₃ (entries 2, 5). KF, an effective base for direct Suzuki coupling,⁷ led to low conversion and the only products observed (mainly biphenyl) resulted from direct coupling (entry 6). A strong base such as Mg(OEt)₂ proved totally ineffective though alkoxide anions are known to reduce imidazolium salts into the corresponding

N-heterocyclic carbene (entry 8).⁸ The reaction was affected little by the CO pressure; only a slight decrease in selectivity occurred on lowering the pressure from 50 to 5 bar (entries 9, 10). In fact, the reactivity and selectivity for ketone with this N-heterocyclic carbene system are slightly better than those obtained with PCy₃ under the same reaction conditions.⁴

Table 1 Palladium-Imidazolium-Catalyzed Carbonylative Coupling of 2-Bromopyridine (**1a**) with Phenylboronic Acid^a

En-try	Solvent	Base	P (CO) (bar)	Time (h) ^b	Conversion 1a (%)	Selectivity 4 (%) ^c
1	Anisole	Cs ₂ CO ₃	50	24	83	93
2	1,4-Dioxane	Cs ₂ CO ₃	50	21	100	95
3	THF	Cs ₂ CO ₃	50	22	88	89
4	DMF	Cs ₂ CO ₃	50	22	0	–
5	1,4-Dioxane	K ₂ CO ₃	50	22	95	95
6	1,4-Dioxane	KF	50	22	35	0
7	1,4-Dioxane	K ₂ CO ₃ /CsCl	50	22	67	94
8	1,4-Dioxane	Mg(OEt) ₂	50	22	7	0
9	1,4-Dioxane	Cs ₂ CO ₃	5	21	100	91
10	1,4-Dioxane	Cs ₂ CO ₃	10	21	100	94

^a General conditions: **1a** = 2.1 mmol, PhB(OH)₂ = 2.2 mmol, base = 4.0 mmol, Pd(OAc)₂ = 0.06 mmol, **A** = 0.12 mmol, solvent = 15 mL, T = 100 °C.

^b Reaction time was not necessarily optimized.

^c Selectivity for carbonylated product **4**; 2-phenylpyridine accounts for the balance.

The catalytic performance of Pd-imidazolium salt systems towards various chloropyridines was next examined under the conditions optimized for **1a**, i.e. using 1,4-dioxane as solvent and Cs₂CO₃ as base (Table 2). At 120 °C, catalyst system **A** appeared somewhat sluggish with 2-chloropyridine (**1b**) but the selectivity into **4** was excellent (entry 11). Increasing the temperature to 140 °C led, as expected, to a great increase in the activity and, interestingly, the selectivity was almost unaffected (entry 12, see typical procedure). On the other hand, at 150 °C, the catalyst system apparently reached its stability limits as the overall conversion decreased (entry 13).

The influence of the palladium-to-ligand ratio was also investigated. Deviation from the 1:2 ratio induced a dramatic drop in activity (entries 14, 15). Most likely, for lower amounts of ligand, the system is not stable enough over long periods to reach a satisfactory conversion.⁹ On the contrary, when higher amounts of ligand are used, the coordination sphere of the palladium center is likely too hindered to allow a good activity. Likewise, bulky imidazolium salts **B** and **C** were found much less effective than **A** (entries 16, 17). Decreasing the CO pressure resulted in both lower conversion and selectivity (entries 18,

Table 2 Palladium-Imidazolium-Catalyzed Carbonylative Coupling of Chloropyridines with Phenylboronic Acid^a

En-try	Sub-strate	Ligand Imd ^b	T (°C)	P (CO) (bar)	Time (h)	Conversion (%)	Selectivity (%) ^c
11	1b	A (2)	120	50	40	63	93
12	1b	A (2)	140	50	16	72	90
13	1b	A (2)	150	50	24	60	87
14	1b	A (1)	140	50	30	32	84
15	1b	A (4)	140	50	30	49	87
16	1b	B (2)	140	50	30	48	89
17	1b	C (2)	140	50	30	39	90
18	1b	A (2)	140	25	30	69	91
19	1b	A (2)	140	5	30	63	71
20 ^d	1b	A (2)	140	50	22	88	91
21 ^e	1b	A (2)	140	50	60	40	92
22	2	A (2)	140	50	24	4	50
23	3	A (2)	140	50	47	43	42

^a General conditions: substrate = 2.1 mmol, PhB(OH)₂ = 2.2 mmol, Pd(OAc)₂ = 0.06 mmol, Cs₂CO₃ = 4.0 mmol, dioxane = 15 mL.

^b The values in parentheses refer to the imidazolium salt: Pd ratio.

^c Selectivity for carbonylated product; phenylpyridine accounts for the balance.

^d Dioxane was percolated just before use through freshly activated alumina.

^e 0.2 mL of water was added in the reaction medium.

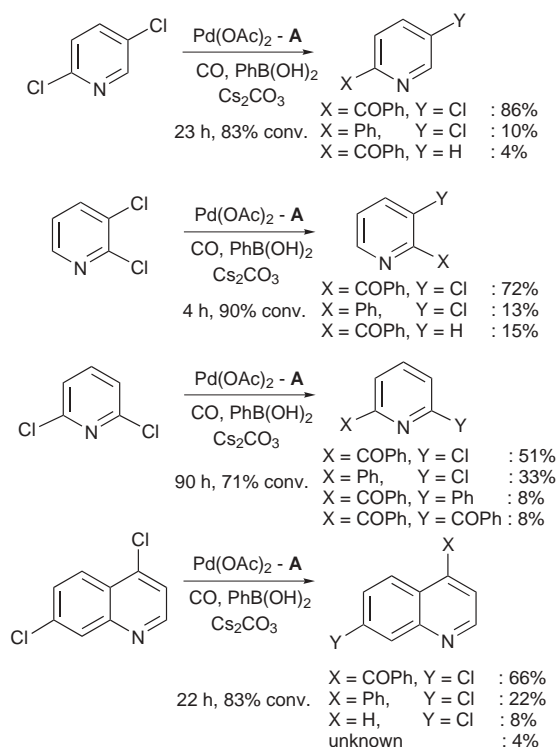
19). Remarkably, much better results in terms of conversion were obtained when 1,4-dioxane was percolated just before use through freshly activated alumina (TOF = 10 h⁻¹; entry 20),¹⁰ whereas addition of small amounts of water into the reaction medium had a detrimental effect (entry 21).

The halogen in 2-position in halopyridines is well known to be more reactive than the one in 4-position towards nucleophilic substitution and, hence, oxidative addition of such a C-Cl bond onto palladium should be facilitated. Indeed, the reaction with 4-chloropyridine (**3**) proceeded more slowly than with **1b** (entry 23). This is consistent with an oxidative addition as the rate-determining step of the catalytic cycle for chlorides.² The poor reaction rate with 3-chloropyridine (**2**) was thus not unexpected considering the unactivated 3-position of the pyridyl ring (entry 22). In both cases, the low reactivity proved also detrimental for the ketone selectivity.

The reactivity of other dichloroazines was also tested using the conditions optimized for **1b**: Pd(OAc)₂-**A** (1:2) as catalyst, 1,4-dioxane as solvent, Cs₂CO₃ as base, at 140 °C under 50 bar CO (Scheme 3). Consistent with the results described above, the 2-position in dichloropyridines reacts selectively with respect to the 3-position, to give the corresponding 2-aryl derivatives in valuable yields over

reasonable times (TOF = 20 h⁻¹ with 2,3-dichloropyridine).¹⁰ Small amounts of the diketone product were also formed from 2,6-dichloropyridine (two activated positions). Only the activated 4-position of 4,7-dichloroquinoline reacted to form ketone adduct (TOF = 7 h⁻¹).¹⁰ As usually observed with chloride substrates and Pd catalysts, some reduction compounds were also obtained.

In summary, we have extended the scope of the carbonylative coupling reaction to the attractive heteroaryl chlorides. The use of N-heterocyclic carbene ligand enables to overcome the poor reactivity of this class of substrates and leads to good selectivities towards ketones. Other substrates are currently being tested to generalize this method and reaction conditions are still under investigation to optimize the process.



Scheme 3 Carbonylative Suzuki cross-coupling of dichloroazines

Typical Procedure

In a typical experiment, a 50 mL stainless steel autoclave equipped with a magnetic stirring bar was charged with Pd(OAc)₂ (13.5 mg, 0.06 mmol), the imidazolium salt (0.12 mmol) (**A** and **B** from Strem Chemical, **C** from Acros), **1b** (200 μ L, 2.1 mmol), Cs₂CO₃ (1.3 g, 4.0 mmol) and 1,4-dioxane (10 mL). After flushing the atmosphere

with N₂, the autoclave was heated to 80 °C under stirring for 40 min. Then, the autoclave was cooled to 20 °C and a solution of phenylboronic acid (268 mg, 2.2 mmol) in dioxane (5 mL) was added under N₂. The autoclave was flushed with CO, pressurized to 50 bar and heated to 140 °C for 22 h. After cooling to 20 °C, the solution was analyzed by quantitative GLC. For isolating the products, CH₂Cl₂ (15 mL) was added to the reaction mixture, the solution was washed with aq brine and dried over MgSO₄. The solvent was removed in vacuo and the residue was purified by silica gel chromatography to give analytically pure (¹H and ¹³C NMR, MS) ketone products.

References

- (1) For reviews, see: (a) Miyaura, N.; Suzuki, A. *Chem. Rev.* **1995**, *95*, 2457. (b) Suzuki, A. In *Handbook of Organopalladium Chemistry for Organic Synthesis*, Vol 1; Negishi, E. I., Ed.; John Wiley and Sons, Inc.: Hoboken, **2002**, 249–262.
- (2) For a recent review, see: Littke, A. F.; Fu, G. C. *Angew. Chem. Int. Ed.* **2002**, *41*, 4176.
- (3) (a) Ishiyama, T.; Kizaki, H.; Miyaura, N.; Suzuki, A. *Tetrahedron Lett.* **1993**, *34*, 7595. (b) Ishiyama, T.; Kizaki, H.; Hayashi, T.; Suzuki, A.; Miyaura, N. *J. Org. Chem.* **1998**, *63*, 4726.
- (4) (a) Couve-Bonnaire, S.; Carpentier, J.-F.; Mortreux, A.; Castanet, Y. *Tetrahedron Lett.* **2001**, *42*, 3689. (b) Couve-Bonnaire, S.; Carpentier, J.-F.; Mortreux, A.; Castanet, Y. *Tetrahedron* **2003**, *59*, 2793.
- (5) (a) Zhang, C.; Huang, J.; Trudell, M. T.; Nolan, S. P. *J. Org. Chem.* **1999**, *64*, 3804. (b) Grasa, G. A.; Viciu, M. S.; Huang, J.; Zhang, C.; Trudell, M. L.; Nolan, S. P. *Organometallics* **2002**, *21*, 2866. (c) McGuinness, D.; Cavell, K. J. *Organometallics* **2000**, *19*, 741.
- (d) Gstöttmayr, C. W. K.; Böhn, V. P. M.; Herdtweck, E.; Grosche, M.; Herrmann, W. A. *Angew. Chem. Int. Ed.* **2002**, *41*, 1363.
- (6) As our investigations neared completion, palladium-imidazolium carbonylative coupling of more activated aryl diazonium ions with aryl boronic acids was reported: Andrus, M. B.; Ma, Y.; Zang, Y.; Song, C. *Tetrahedron Lett.* **2002**, *43*, 9137.
- (7) (a) Littke, A. D.; Dai, C.; Fu, G. C. *J. Am. Chem. Soc.* **2000**, *122*, 4020. (b) Yin, J.; Rainka, M. P.; Zhang, X.-X.; Buchwald, S. L. *J. Am. Chem. Soc.* **2002**, *124*, 1162.
- (8) Arduengo, A. J. III; Krafczyk, R.; Schmutzler, R.; Craig, H. A.; Goerlich, J. R.; Marshall, W. J.; Unverzagt, M. *Tetrahedron* **1999**, *55*, 14523.
- (9) In a number of coupling reactions of aryl chlorides, it was found that a 1:1 Pd-ligand ratio (ligand = N-heterocyclic carbene, phosphine, ...) led to optimum reaction rates (see ref. 2 and ref. 5b for N-heterocyclic carbene ligands).
- (10) TOF: turnover frequencies defined as the number of moles of substrate transformed per mole of catalyst and per hour calculated after one hour of reaction.



Influence of water on the photodegradation of poly(ethylene oxide)

F. Hassouna, S. Morlat-Thérias*, G. Mailhot, J.L. Gardette

Laboratoire de Photochimie Moléculaire et Macromoléculaire (UMR CNRS-UBP 6505), Université Blaise Pascal, 63177 AUBIERE Cedex, France

Received 21 June 2007; accepted 30 July 2007

Available online 9 August 2007

Abstract

The UV-light degradation of polyethylene oxide (PEO) in aqueous solution was investigated operating under long wavelengths ($\lambda > 300$ nm) at 20 °C in different pH conditions varying from 2.3 to 12.0 and at two different concentrations. Thermo-oxidation experiments on PEO aqueous solution at 50 °C are also reported and compared to photo-oxidation results. The formation of oxidation products was followed by infrared analysis of deposits obtained by evaporation of aliquots of irradiated polymer solution. Photo-oxidation led to formates and esters but a third product was also identified, formic acid ions formed by partial hydrolysis of formates. The degradation of PEO in water led to the acidification of the aquatic medium. Size exclusion chromatography (SEC) was used to monitor the changes in molar weight and intrinsic viscosity with irradiation time. It was shown that the photo-oxidation produced a dramatic decrease of the average molar weights which is more important in acidic medium. Total organic carbon (TOC) measurements of the aged aqueous solutions showed that the mineralization of PEO could not be achieved in these photo-oxidative conditions.

© 2007 Elsevier Ltd. All rights reserved.

Keywords: Photodegradation; Water; Poly(ethylene oxide); SEC

1. Introduction

Water-soluble polymers are produced in large volumes and are widely used in a variety of industrial and consumer products. These polymers find use in polymeric surfactant, pigment dispersants, mining oil drilling, detergents, etc. After use, depending on their characteristics and particular applications, water-soluble polymers are discarded into solid waste disposal systems or as dilute aqueous solutions and they are potential contributors to environmental problems [1]. Their photochemical degradation in aqueous solution gives insight of their impact on environment in outdoor conditions. The knowledge of their degradation is then of prime importance to evaluate their fate and their long term behaviour.

Among polyethers, PEO with PVME are the only one that are readily soluble in water [2]. PEO is biocompatible, biodegradable, non-ionic and a water-soluble polymer of considerable industrial significance. PEO finds applications in many

different branches of industry, cosmetics, pharmacy and medicine. For example it is typically used as a surfactant, lubricant, textile size, hydraulic fluid, and water-soluble packaging film [3–6].

Poly(ethylene oxide) (PEO) has a simple chemical structure. It is built from flexible linear macrochains consisting of elements with different electronegativity, carbon and oxygen ($-\text{CH}_2-\text{CH}_2-\text{O}-$). In the crystalline solid state, PEO exists mainly in the form of a regular helix. The characterisation of the spatial configuration of PEO shows an arrangement with *trans* ($\text{O}-\text{CH}_2$), *gauche* (CH_2-CH_2) and *trans* ($\text{O}-\text{CH}_2$) conformations [7,8]. In aqueous solution PEO conformation shifts to a random coil with statically placed residual helix segments [2,4,9,10], the helix structure being conserved. According to experimental and theoretical studies realised on water–PEO systems [4,11–13], hydrogen bonding plays an important role in the interactions between PEO and water. PEO in water adopts the local conformations ($-\text{O}-\text{C}-\text{C}-\text{O}-$ dihedral sequences) *tgt*, *tgg*, *ttt*,...etc. (with *t* = *trans* and *g* = *gauche*). The conformations *tgt* and *tgg* are favoured under low concentration and low temperature conditions whereas the population

* Corresponding author. Tel.: +33 (0)73 40 71 43; fax: +33 (0)73 40 77 00.
E-mail address: sandrine.therias@univ-bpclermont.fr (S. Morlat-Thérias).

of the hydrophobic conformers increases with concentration and temperature. These two conformers exhibit a substantial hydrophilic character while the rest are essentially hydrophobic. Hydrogen bonds play an important role in the preferential conformation *tgt* characterised by O–C–C–O– dihedral angle of 85.4°.

This study of photo-oxidation of PEO is part of a general study of water-soluble polymers carried out in our laboratory [14,15]. The mechanism of photo-oxidation of PEO in the solid state has already been studied under irradiation at long wavelengths ($\lambda > 300$ nm, 35 °C) in presence of oxygen [14]. This previous study has shown that PEO is very sensitive to oxidation. Hydroperoxides (POOH) are formed as primary products within a classical chain oxidation reaction that involves hydrogen abstraction which occurs on methylene groups in α -position of the oxygen atom. These primary hydroperoxides readily decompose to form macroalkoxy radicals PO• and hydroxyl radical •OH. In photo-oxidative conditions, the main route of decomposition of macroalkoxy radicals is a β -scission, which generates formates in a 5/1 ratio against chain esters. In contrast, in conditions of thermo-oxidation, the situation is different. The hydroxy radicals •OH formed by decomposition of the hydroperoxides mainly react with the macroalkoxy radicals in a cage reaction, producing esters. A same amount of esters and formates is then observed.

A first approach of the photodegradation of PEO in aqueous solution has been carried out [15]. Irradiation of PEO aqueous solutions leads to the formation of macromolecular esters, formate end groups and a third photoproduct was identified, HCOO[−]. The main difference observed between the photoproducts formed in photo-oxidation conditions either in solid state or in aqueous solution concerns the formation of formic acid ions (HCOO[−]) released in solution. A strong influence of the pH of aqueous solution was observed on the photochemical behaviour of PEO, which could not have been explained. The chemical structure of the polymer cannot explain the influence of pH on the mechanism of oxidation, and the importance of radical or ionic reactions occurring in water was still questionable.

The present paper is mainly focused on the influence of pH of the aquatic medium on the mechanism of photo-oxidation of PEO; a specific attention is being paid to the analysis of photoproducts and to the characterisation of the rate of photo-oxidation. Photo-oxidation experiments were carried out in different pH conditions. The modifications of the chemical structure of the polymer were followed by IR spectrometry and by SEC analysis in order to characterise the changes of molar weight distribution and the evolution of the viscosity of the solution. The aqueous solutions were also characterised by measuring the variations of pH during irradiation. The influence of the pH on the stability of the photoproducts was also studied. Moreover, an evaluation of the possibility to achieve the mineralization of PEO in photo-oxidation conditions was also carried out by measuring the Total Organic Carbon (TOC) concentration of the irradiated solution.

2. Experimental

2.1. Materials

Poly(ethylene oxide) was obtained from Scientific Polymer Products and used without further purification. Average molar weight of the polymer was 100 000 g mol^{−1}. PEO solutions of 5 wt.% and 0.5 wt.% (respectively, 50 gm mL^{−1} and 5 mg mL^{−1}) were prepared by dissolving PEO into a distilled and deionized water with mild stirring overnight at room temperature. The pH value was measured with an ORION pH meter to ± 0.1 pH unit. Dissolution of PEO in deionized ultrapure water (at concentration of 50 mg mL^{−1} or 5 mg mL^{−1}) results in a solution with a pH value of 8.4. Solutions in acidic or basic medium (pH = 2.3 or 3.1 and 12.0) were, respectively, obtained by adding drops of diluted HClO₄ or NaOH (HClO₄ was chosen to acidify the aqueous solution because ClO₄[−] is photochemically stable contrary to Cl[−]). No buffer was used in order to avoid making the system too complex by adding too many species.

2.2. Irradiation

Irradiations of PEO in solid state (as films) were carried out in a SEPAP 14/24 unit. This apparatus has been designed for the study of polymer photodegradation in artificial ageing corresponding to medium accelerated conditions [14,16].

Irradiation of PEO aqueous solutions was carried out in an elliptical chamber which is equipped with one medium-pressure mercury lamp (Mazda MA 400) in a vertical position at one focal axis of the chamber [15]. Wavelengths below 300 nm are filtered by a glass envelope. The aqueous solution of PEO was irradiated in a Pyrex reactor cooled by water circulation. The temperature of the solution was maintained at 15 °C in order to avoid water evaporation. This reactor was placed at the second focal axis of the chamber. The solutions were continuously stirred with a magnetic stirrer and a Teflon bar.

Thermo-oxidation experiments were carried out at 50 °C in a 100-mL round bottom flask equipped with reflux condenser. This temperature was chosen to keep the aqueous solution at a temperature below the cloud point temperature (CPT = 100 °C) [17,18]. The reactor was therefore placed into an oil bath.

2.3. Chemical characterisations

PEO solutions of 5 wt.% concentration were chosen in order to follow the chemical modifications of the irradiated solutions by IR analysis of deposits on CaF₂ windows. Thin deposits of oxidized samples of PEO obtained by evaporation of aliquots of irradiated aqueous solution of PEO were analysed in transmission mode before infrared analysis. The samples were dried at room temperature for 24 h. In the manuscript, the figures of FTIR spectra are limited to the range 4000–1000 cm^{−1} due to the opacity of the CaF₂ plate between 1000 cm^{−1} and 400 cm^{−1}. Infrared spectra were recorded with a Nicolet FTIR 760 spectrometer, working with OMNIC software.

Spectra were obtained using 32 scan summations and 4 cm^{-1} resolution. In order to take into account the variations of thickness resulting from the mode of preparation of the samples, a calibration of the photo-oxidized samples was performed at 1965 cm^{-1} , which corresponds to a combination band of (COC) stretching modes and (CH_2) rocking modes. The thickness dependence of the absorbance obeyed the equation: $e = \text{absorbance at } 1965\text{ cm}^{-1} \times 1/0.00405$ [14].

Chemical treatments with SF_4 and NH_3 carried out to identify the photoproducts were performed following the procedure previously described [14,19–21].

2.4. SEC

The changes of molar weight (M_w , M_n), molar weight distribution (polydispersity index (M_w/M_n)) and the intrinsic viscosity (IV) were measured by size exclusion chromatography (SEC) with double distilled deionized water as eluent at a flow rate of 1 mL min^{-1} . A linear column was used for physical separation (TSK/Ref: GMPWXL). The refractive index was monitored continuously with a differential refractometer (Viscotek VE 3580) and the intrinsic viscosity with a viscometer (Viscotek TriSec Model 270).

2.5. Ion chromatography

Ion chromatographic analyses were performed in a clean room (class 10 000). Aqueous solutions were injected directly without filtration to avoid further contamination. Working conditions are similar to those detailed by Jaffrezo et al. [22]. A DX 320 chromatograph equipped with an AS11 (4 mm) column for the anions was used in order to detect HCOO^- or HCOOH in aqueous solutions after ageing.

2.6. Total organic carbon

Total Organic Carbon (TOC) measurements of aqueous solution were obtained with a Total Organic Carbon (TOC) analyzer Shimadzu model TOC-5050A. The Shimadzu TOC-5050A is able to perform Total Carbon (TC) analyses by combustion and Inorganic Carbon (IC) analyses by oxidation. TOC measurements were obtained by calculating the difference between TC and IC measurements.

3. Results and discussion

3.1. Photo-oxidation of PEO in water (concentration 50 mg mL^{-1} , $\text{pH} = 8.4$)

3.1.1. IR analysis

The concentration of PEO aqueous solution was 50 mg mL^{-1} . As recalled above, this “high” concentration was chosen because it permits obtaining well calibrated deposits around $16\text{ }\mu\text{m}$ that can be used to observe the formation of photoproducts by infrared analysis. The pH of the solution at this concentration was 8.4.

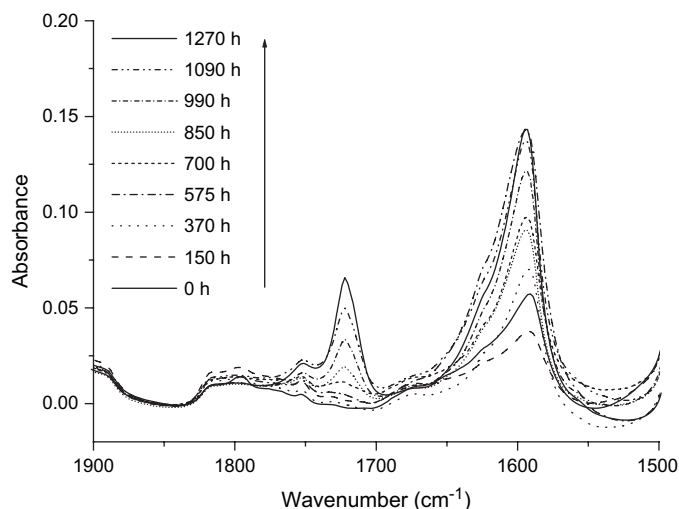


Fig. 1. Infrared spectra deposits obtained from irradiated aqueous solutions of PEO ($[\text{PEO}] = 50\text{ mg mL}^{-1}$, $\text{pH}_{\text{initial}} = 8.4$).

Fig. 1 shows the changes in the carbonyl region of spectra obtained from aqueous solutions for several irradiation times ranging from 0 h to 1272 h. Monitoring each spectrum necessitated that a sample was prepared, following the procedure described in the experimental part. In the carbonyl region, three absorption bands develop at 1750 cm^{-1} and 1720 cm^{-1} , and at 1590 cm^{-1} . The two absorption bands at 1750 cm^{-1} and 1720 cm^{-1} have already been observed in the case of irradiation of PEO in solid state [14]. On the basis of chemical derivatisation (NH_3 , SF_4 and formic acid), these absorption bands have been attributed to formate end groups (1720 cm^{-1}) and macromolecular ester groups (1750 cm^{-1}). The intense band that develops at 1590 cm^{-1} has also been observed and attributed to formic acid ions [15] (Scheme 1). It is recalled that this band is not observed in the case of the photo-oxidation of PEO in the solid state (film).

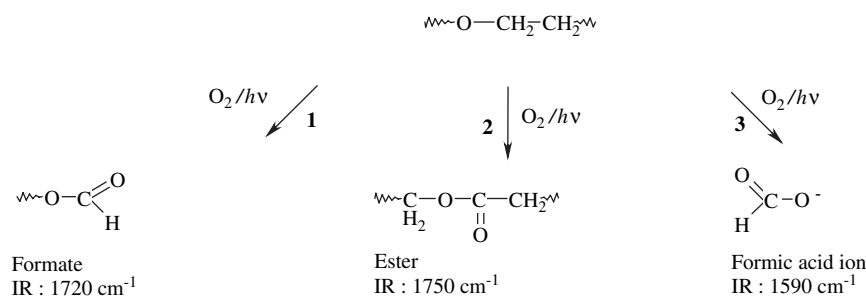
If one considers the same absorption coefficients for the two $\text{C}=\text{O}$ stretches at 1750 cm^{-1} and 1720 cm^{-1} , it can be deduced that the photo-oxidation of PEO in aqueous solution results in the formation of four formate groups to one ester function (ratio: 4/1).

3.1.2. Evolution of pH

The variations of the pH of PEO aqueous solution during irradiation are reported in Fig. 2. For a PEO concentration of 50 mg mL^{-1} , the initial pH value of the water solution is 8.4. Irradiation of this aqueous solution of PEO leads to a dramatic acidification of the solution, with a pH that decreases from 8.4 to 4.5 after 1200 h of irradiation.

The dramatic decrease of the pH of the PEO solution reveals an acidification of the medium that could be correlated with the release of formic acid ions (HCOO^-). In order to confirm this hypothesis, formic acid and formic acid ions were measured and quantified by Ionic Chromatography (IC) (Fig. 2).

An intense peak corresponding to formic acid ions appeared in the IC chromatogram of the irradiated solutions. As shown in



Scheme 1. Photoproducts formed by photo-oxidation of PEO in aqueous solutions.

Fig. 2, the concentration of formic acid and formic acid ions increased from 0.075 mol L⁻¹ to 0.503 mol L⁻¹ after 660 h of irradiation.

This result confirms that formic acid formed is responsible for the acidification of the medium. This is an important result in terms of toxicity because acidification of the aquatic medium could contribute to a drastic perturbation of the ecosystems.

3.2. Influence of the pH of the aquatic medium

In order to understand the effect of pH on the photo-oxidation of PEO in aqueous solution, irradiations were carried out at different pHs: 2.3, 3.1 and 12.0 and compared with the results reported above in the case of pH = 8.4.

3.2.1. Analysis by infrared spectroscopy

3.2.1.1. pH = 12.0. The modifications of the infrared spectra of PEO provoked by irradiations of solutions at pH = 12 are different from those reported above in the case of pH = 8.4. After 300 h of irradiation, two maxima developed at 1610 cm⁻¹ and 1665 cm⁻¹ and a shoulder around 1600 cm⁻¹. After 500 h, a wide band centred over 1600 cm⁻¹ developed. This

maximum was progressively shifted towards 1590 cm⁻¹. After 700 h of irradiation, two new absorption bands were observed at 1720 cm⁻¹ and 1750 cm⁻¹. This clearly indicates that different photoproducts are formed, in comparison with the results given above. In parallel, the pH of the solution decreased during irradiation and reached a value around 6.0 after 400 h and 4.6 after 1200 h.

The modifications of the chemical structure of the photo-products can result in the decrease of the pH of the medium during the photo-oxidation. Absorption bands observed at 1610 cm⁻¹ and 1665 cm⁻¹ could correspond to carboxylate acid ions, which can explain the first phase with the decrease of pH from 12.0 to 6.0. In the second phase, from pH ≤ 6, formates (1720 cm⁻¹) and esters (1750 cm⁻¹) (with the ratio of formate/ester = 4/1), as well as formic acid ions (1590 cm⁻¹) appear.

3.2.1.2. pH = 3.1. Fig. 3 shows the changes in the carbonyl region of the IR spectra for deposits obtained from PEO aqueous solutions acidified to pH 3.1 for irradiation times ranging from 0 h to 790 h. In the first stage of irradiation, an absorption band with a maximum at 1720 cm⁻¹ appears, which indicates the formation of formates. A shoulder around 1750 cm⁻¹ due to

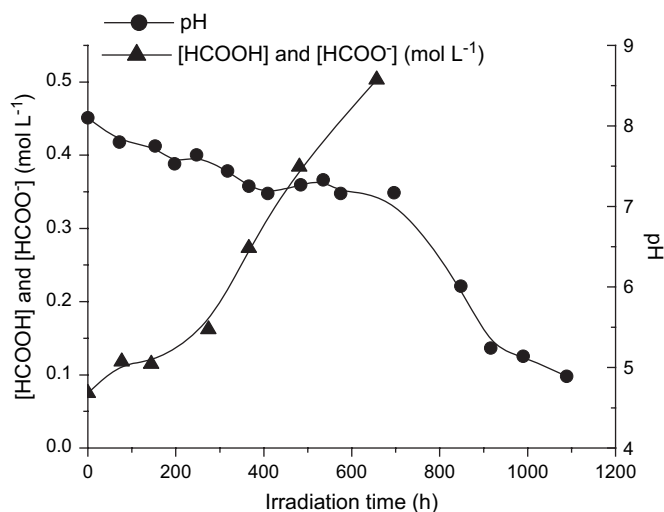


Fig. 2. Variations versus irradiation time of the concentration of formic acid and formic acid ions and of the pH of PEO aqueous solution ([PEO] = 50 mg mL⁻¹, pH_{initial} = 8.4).

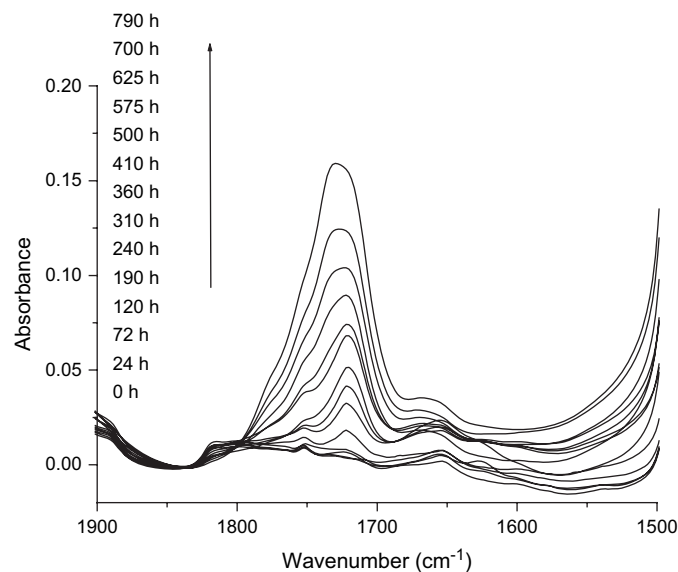


Fig. 3. FTIR spectra of PEO deposit from an acidic aqueous solution at pH = 3.1 during photo-oxidation, [PEO] = 50 mg mL⁻¹.

the formation of esters is also observed. After 400 h of irradiation, this absorption band widens and the absorption maximum is shifted towards 1735 cm^{-1} with two shoulders at 1750 cm^{-1} and 1770 cm^{-1} . These two absorption maxima (1735 cm^{-1} and 1770 cm^{-1}) indicate the formation of secondary products resulting from the degradation of the photoproducts in acidic medium. Considering the frequencies, lactones with five and six atoms are good candidates [23]. Opposite to the case of the solutions with pH 8.4 or 12.0, the absorption band at 1590 cm^{-1} corresponding to the formic acid ions is not observed. In fact, at pH = 3.1, the equilibrium between the ionic and the acidic form is shifted to the acidic form and formic acid ions are no more detected. It is recalled that $\text{p}K_{\text{a}}(\text{HCOOH}/\text{HCOO}^-) = 3.78$, HCOOH is not detected in the analysed deposit because it migrates out of the polymer [15].

The variations of the pH during irradiation only reveal a slight decrease from 3.1 to 2.8, which however indicates that a large amount of H^+ coming from formic acid is released into the solution after 800 h of irradiation.

3.2.1.3. pH = 2.3. From the beginning of the irradiation, a broad absorption band appears in the carbonyl region ($1900\text{--}1500\text{ cm}^{-1}$) with a maximum at 1720 cm^{-1} (formate) and a shoulder around 1750 cm^{-1} (ester) (ratio of formate/ester = 4/1). After 120 h of irradiation, two maxima develop at 1735 cm^{-1} and 1770 cm^{-1} . As reported above in the case of irradiations at pH = 3.1, formic acid ions are not detected as the equilibrium is shifted to the acidic form. In addition, strong modifications of the IR spectra between 1600 cm^{-1} and 1200 cm^{-1} after 100 h of irradiation were noticed. The absorption bands are no more of those characteristics of PEO, which means that the PEO polymer is highly degraded in such an acidic medium (pH = 2.3).

3.2.2. Analysis by size exclusion chromatography (SEC)

Fig. 4a shows the variations of the molar weights of PEO during irradiation of aqueous solution at different initial pH.

At pH = 8.4, the changes caused by irradiation of the PEO aqueous solution are characterised by a shift of the molar weight distribution curves towards lower molar weights. The average molar weight decreases by about 50% after 700 h of irradiation and 82% after 1664 h. This decrease in the average molar weight can be attributed to the chain scissions resulting from the photo-oxidation of PEO. This indicates that a dramatic degradation process takes place during the oxidation of the polymer.

The intrinsic viscosity (IV) drops during irradiation as shown in Fig. 4b. This decrease in viscosity and in molar weight is correlated to the chain scissions due to the formation of formate end groups.

Table 1 reports the evolution of the polydispersity index of PEO during photo-oxidation in aqueous solution. The evolution of the polydispersity index versus irradiation time shows a decrease of polydispersity during irradiation corresponding to more uniform mass distribution of degraded PEO. This reveals that the mechanism of chain scissions is predominant.

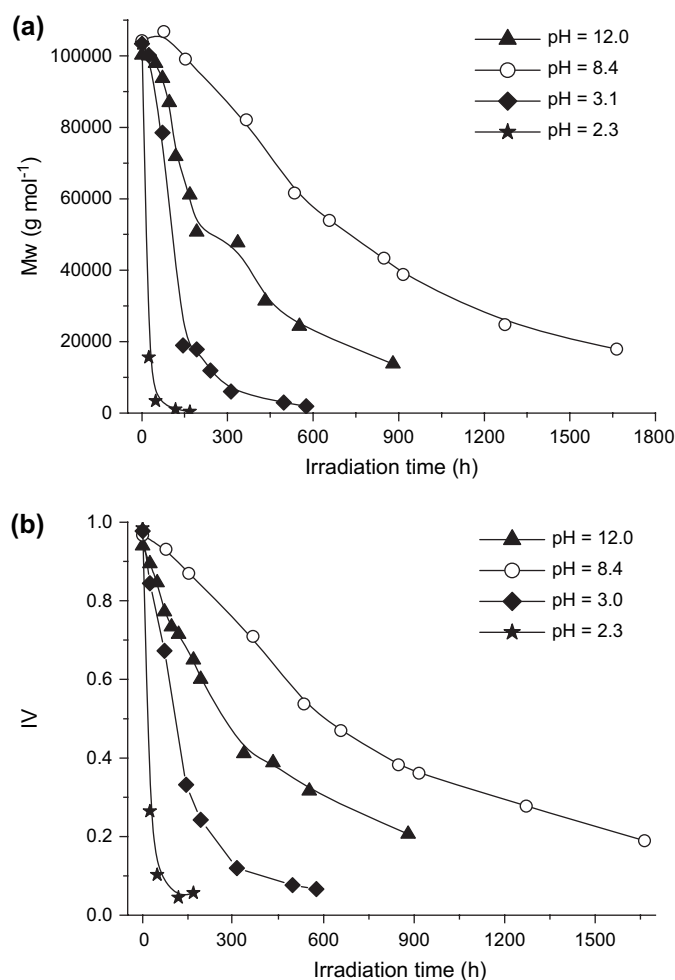


Fig. 4. (a) Evolution of PEO molar weight (M_w) as a function of irradiation time and in different pH conditions (12.0, 8.4, 3.1 and 2.3), $[\text{PEO}] = 50\text{ mg mL}^{-1}$ and (b) evolution of PEO intrinsic viscosity of the solution as a function of irradiation time.

At pH = 12, after 24 h of induction period, the average molar weights and intrinsic viscosity starts to decrease. The rate of degradation of PEO is faster in very basic medium (pH = 12.0).

SEC analysis of PEO aqueous solution at pH = 3.1 shows also the decrease of the average molar weights and the intrinsic viscosity. However, the rate of degradation of PEO is faster and without induction period at this pH. Indeed, the average molar weight decreases by about 82% only after 145 h of

Table 1

Evolution of PEO polydispersity index of the solution as a function of irradiation time (pH = 8.4)

Irradiation time (h)	IP
0	3.8
150	3.2
370	2.6
535	2.5
660	1.9
850	1.7
920	1.6
1664	1.2

irradiation and by 94% after 310 h. These results confirm that chain scission is the main way of degradation implied in the mechanism during photo-oxidation in acidic medium.

At pH = 2.3, a spectacular decrease of average molar weights and of intrinsic viscosity is observed. Indeed, the average molar weight decreases by about 86% only after 24 h of irradiation and by 99% after 120 h. After 120 h, the molar weights are too low and out of range of the column separation, then the polymer can be considered as highly degraded. Possible candidates could be oligomers, formic acid and lactones. The correlation of the results obtained by SEC with those obtained with IR indicates that after 120 h of irradiation, the polymer is completely degraded. The absorption bands at 1735 cm^{-1} and 1770 cm^{-1} correspond to secondary products resulting from the degradation or from the transformation of formate and ester at pH lower than 3.

All the results obtained by SEC analysis (M_w , IV, IP) show that the degradation of PEO in aqueous solution leads to a mechanism of chain scissions.

3.3. Stability of the photoproducts

In order to study the influence of pH on the photo-oxidation of PEO, it is important to characterise the stability of PEO photoproducts in water. Fig. 5 compares the IR spectrum of a photo-oxidized PEO film (after 42 h of irradiation) and the spectrum of a deposit of the same film dissolved in water (pH = 8).

It is recalled that photo-oxidation of PEO as a film in solid state leads to the formation of two products, formate (1720 cm^{-1}) and ester (1750 cm^{-1}). The IR spectrum of a deposit obtained after dissolution of the photo-oxidized film of PEO in water shows a third absorption band at 1590 cm^{-1} and a decrease of intensity of the absorption band at 1720 cm^{-1} corresponding to formate. This band can be attributed to formic acid ions, which suggests that a partial hydrolysis of formate occurs in water, leading to the formation of HCOO^- .

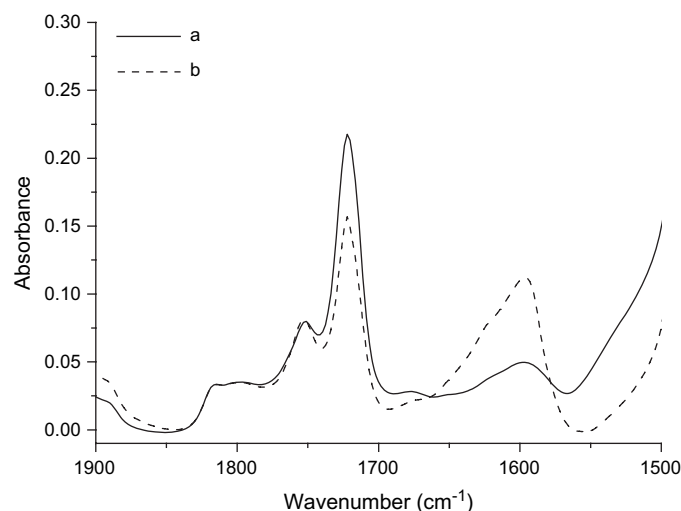


Fig. 5. FTIR spectra of PEO after 40 h of photo-oxidation in solid state (a) as a film and (b) a deposit after dissolution of this film in water (pH = 8).

This confirms that the absorption band at 1595 cm^{-1} observed for the photo-oxidation of PEO in water at pH 12.0 and 8.4 comes from a partial hydrolysis of formate in water.

The pH of the solution can be adjusted to different values. A PEO film photo-oxidized for the same time (42 h) was dissolved in water and the pH was adjusted to values ranging from 2.6 to 11.4. The IR spectra of deposits obtained from these solutions are shown in Fig. 6.

In a basic medium, when the pH of the solution (in which the PEO film is dissolved) is adjusted to 9.6, the intensity of the absorption band corresponding to formates (1720 cm^{-1}) decreases whereas that corresponding to formic acid ions (1590 cm^{-1}) increases. In a more basic medium, pH = 11.4, the absorption bands of formates and esters disappear and two new bands centred at 1610 cm^{-1} and 1665 cm^{-1} appear. As reported above, these two bands have been already observed during the first time of irradiation of PEO in basic aqueous solution at pH = 12.0.

In an acidic medium, at pH = 4.0, the IR spectrum of deposit shows the decrease of intensity of the bands at 1720 cm^{-1} and 1750 cm^{-1} (formate and ester) and a band at 1590 cm^{-1} with a shoulder at around 1620 cm^{-1} is observed. In a more acidic medium, pH = 2.6, the absorption bands at 1720 cm^{-1} and 1590 cm^{-1} almost disappear. Indeed, the pH being lower than pK_a ($\text{HCOOH}/\text{HCOO}^-$), the disappearance of formate groups by hydrolysis leads to formic acid.

These results thus show the instability of formate and ester groups in acidic and basic media. Formate groups are hydrolysed in an acidic medium leading to the formation of formic acid, which however are not detected by IR analysis because it evaporates during the drying of the deposit. In a basic medium formic acid ions are formed [15]. Ester groups can be hydrolysed in basic medium to form carboxylate ions (1665 cm^{-1} or 1620 cm^{-1}).

Scheme 2 summarizes the comments made above concerning the reactivity of ester and formate groups under different pH conditions. Formates are hydrolysed in acidic medium

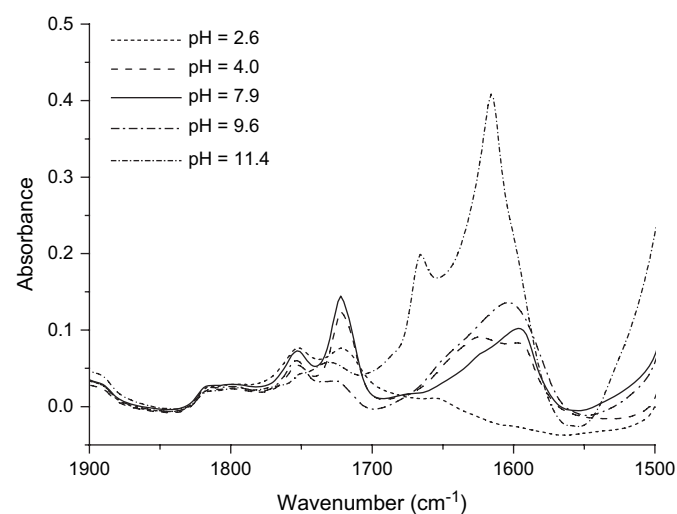
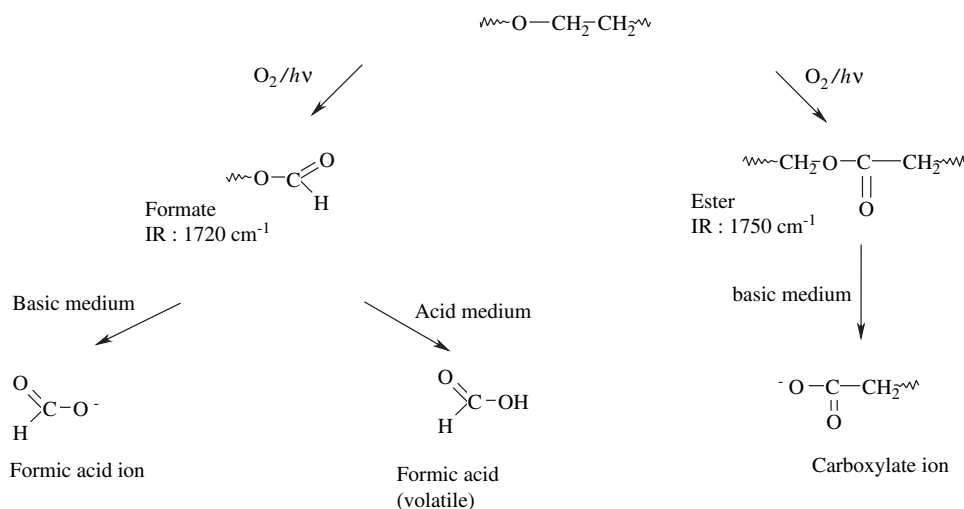


Fig. 6. Infrared spectra of deposits obtained after dissolution in water at different pHs of a PEO solid film photo-oxidized for 42 h.



Scheme 2. Stability of formates and esters in aqueous solution at different pHs.

into formic acid which is likely to migrate out of the deposit and into formic acid ions (1590 cm^{-1}) in basic medium. The ester is hydrolysed into carboxylate ions (1665 cm^{-1}) at very basic medium ($\text{pH} > 11$).

3.4. Photo-oxidation rate

The kinetics of photo-oxidation of PEO irradiated in aqueous solutions at different pH can be compared by following the increase of the infrared absorbance at 1720 cm^{-1} as a function of irradiation time (Fig. 7).

According to the initial pH of the solution, the rate of accumulation of formates is different. The absorbance increases very quickly in acidic media whereas in basic media ($\text{pH} = 12.0$ and 8.4) formates are not detected by infrared analysis of the deposits before 500 h and 700 h for the solutions of $\text{pH} = 12.0$ and 8.4 , respectively. This can be explained by the fact that in basic medium ($\text{pH} > 6-7$), macromolecular

formates undergo hydrolysis. This explains in turn the presence of HCOO^- detected in the medium.

3.5. Influence of polymer concentration

The concentration of PEO in the solution can influence both the polymer concentration and the rate of degradation of the polymer. The comparison of the behaviour of PEO aqueous solutions of concentration 50 mg mL^{-1} and 5 mg mL^{-1} at different pH conditions (12.0, 8.4, 3.1 and 2.3). The change of pH during the irradiation was also followed.

It is important to underline that the thickness of the deposits obtained from solutions at 5 mg mL^{-1} was limited to $2\text{ }\mu\text{m}$ whereas the thickness for deposit from PEO solutions at a concentration of 50 mg mL^{-1} was $16\text{ }\mu\text{m}$. Comparison of the rates of photo-oxidation based on the infrared analysis would be meaningless because no reliable results would be obtained by considering the correction factor of 8 that has to be used for comparing the absorbances.

At $\text{pH} = 8.4$, within the first 1000 h of irradiation, three absorption bands develop at 1750 cm^{-1} (formate), 1720 cm^{-1} (ester), and at 1590 cm^{-1} (formic acid ion). The formate/ester ratio is equal to 4/1. The pH of the solution was observed to dramatically decrease, from the value of 8 to 2.9 after 1000 h of irradiation. After 1000 h, the intensity of the absorption at 1720 cm^{-1} band decreases. The proportion of formate/ester is then 1/1. This decrease can be related to the evolution of the pH of the solution during irradiation. At the same time, the band at 1590 cm^{-1} corresponding to formic acid ions is progressively shifted towards 1605 cm^{-1} . This can be explained by the protonation of HCOO^- ions into formic acid ($\text{pH} < \text{pK}_a (\text{HCOOH}/\text{HCOO}^-) = 3.8$).

The comparison with the IR spectra of deposits obtained for PEO concentration (50 mg mL^{-1}) shown in Fig. 1 indicates that the photoproducts formed are the same with the similar proportion during the first 1000 h of irradiation. However, after 1000 h of irradiation, as the pH of the diluted solution is lower ($\text{pH} = 2.9$) than that of the concentrated solution

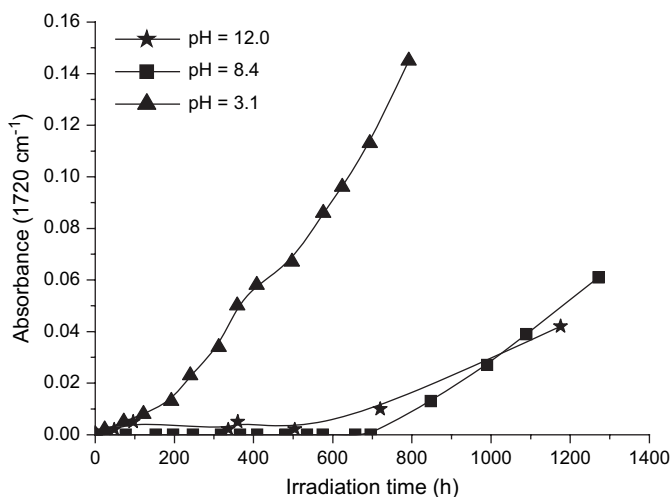


Fig. 7. Evolution of absorbance at 1720 cm^{-1} as a function of irradiation time for PEO aqueous solutions and in different pH conditions, $[\text{PEO}] = 50\text{ mg mL}^{-1}$.

(pH = 4.0), the partial hydrolysis of formate is then more important in the diluted solution than in the concentrated one and explains the discrepancy observed.

In parallel, the solutions were characterised by SEC during irradiation. Fig. 8 compares the solutions of PEO at concentration of 5 mg mL⁻¹ or 50 mg mL⁻¹. This figure clearly shows a higher degradation rate in the case of a diluted solution at 5 mg mL⁻¹. This behaviour can be directly correlated with the change of the pH of the solution.

The degradation of PEO could be higher in diluted solution than a more concentrated solution because the mobility of polymer chains is higher in a less viscous solution [24]. Moreover, this difference could be explained by the fact that for a concentration of 50 mg mL⁻¹, PEO aqueous solutions present a notable diffusion of light. This diffusion effect could contribute to the decrease of the PEO phototransformation rate.

In acidic medium, pH = 2.3, in the carbonyl region, a new absorption band at 1718 cm⁻¹ appears in IR spectra from the beginning of the irradiation and a shoulder around 1750 cm⁻¹ corresponding to macromolecular esters. On the basis of NH₃ and SF₄ chemical treatments the absorption band at 1718 cm⁻¹ can be attributed to the formation of carboxylic acids.

The absence of macromolecular formates in these conditions of concentration and pH ([PEO] = 0.5 mg mL⁻¹, pH = 2.3) can be explained by the complete hydrolysis of formate groups to formic acid. As shown in Table 2, the quantification of formic acid during irradiation by ionic chromatography analysis confirmed this hypothesis.

3.6. Evolution of the total organic carbon (TOC)

The measurements of the quantity of carbon present in solution during irradiation of PEO aqueous solutions in different pH conditions (pH = 2.3, 8.4 and 12.0) were carried out by TOC analysis and the results are about 5 mg mL⁻¹. The obtained results show that no change of the carbon quantity

Table 2

Formic acid concentration during irradiation (pH = 2.3, [PEO] = 5 mg mL⁻¹)

Time of irradiation (h)	Concentration of formic acid (mol L ⁻¹)
0	5.2×10^{-3}
410	0.239
840	0.343

was observed during 850 h of irradiation. This means that even low concentration PEO aqueous solutions cannot be mineralized during the photo-oxidation.

3.7. Thermo-oxidation

Thermo-oxidation at 50 °C of PEO aqueous solution at various pHs was carried out.

At pH 8.4 and 12.0, no significant evolution was detected after 900 h at 50 °C contrarily to acidic media (pH = 3.1 and 2.3).

At pH = 3.1, the evolution of IR spectra shows the formation of two absorption bands at 1720 cm⁻¹ and 1750 cm⁻¹ corresponding to the two previously identified oxidation products, respectively, formate and ester. However, the relative proportion of ester is much higher in the case of thermo-oxidation than in the case of photo-oxidation, and one observed the formation of esters and formates to the same extent whereas photo-oxidised solutions develop four formate end groups for one ester function. The same observation was made in the case of PEO in solid state [14].

In parallel, the pH of the solution decreased, from 3.1 to 2.4 after 500 h of heating, and stabilized at 2.4. After 400 h, the absorption band of formate (1720 cm⁻¹) became a shoulder while the ester band (1750 cm⁻¹) was still increasing. The behaviour of formates results from their hydrolysis that becomes more important when pH is under 3.0.

Fig. 9 shows the evolution of the molar weight of PEO in aqueous solution at pH = 3.1 in conditions of thermo-oxidation.

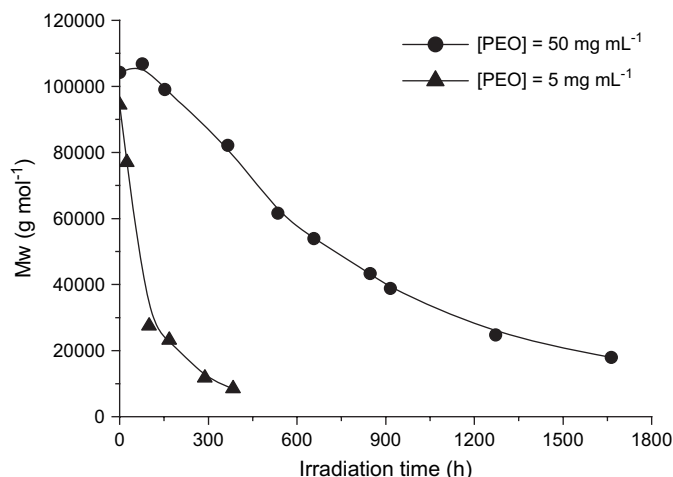


Fig. 8. Evolution of molar weight (M_w) as a function of irradiation time of PEO aqueous solutions (pH = 8.4, [PEO] = 50 mg mL⁻¹ and 5 mg mL⁻¹).

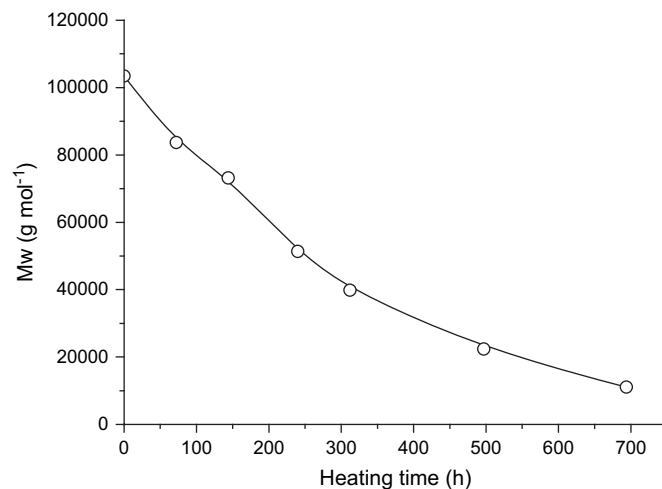


Fig. 9. Evolution of PEO molar weight (M_w) as a function of heating time and irradiation time at pH = 3.1.

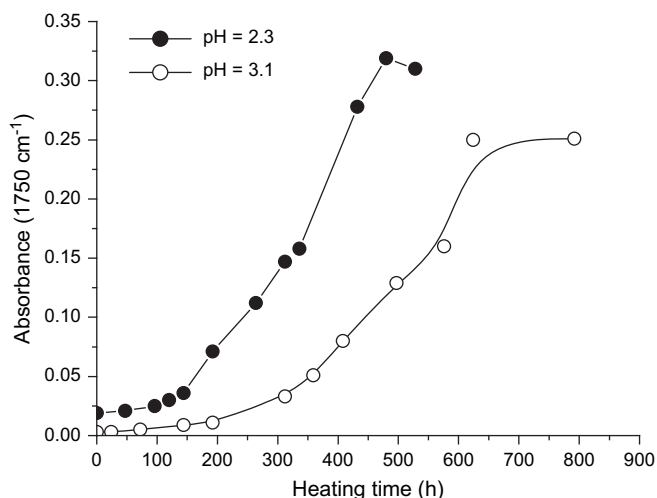


Fig. 10. Variations of the absorbance at 1750 cm^{-1} as a function of heating time; pH = 2.3 and 3.1.

A decrease of the molar weight is observed; the average molar weight decreases by about 50% only after 240 h of heating and by 90% after 700 h. This result shows that chain scissions occur during thermo-oxidation in acidic medium.

Fig. 10 compares the rates of oxidation of PEO measured at 1750 cm^{-1} (ester) at two different pHs (3.1 and 2.3). It can be observed that the rate of formation of esters (rate of oxidation) is faster when the solution is more acidic. The same behaviour has been observed for ageing in condition of photo-oxidation.

4. Conclusion

It can be recalled that photo-oxidation of PEO in solid state occurs through a conventional radical mechanism [14] involving the formation of macromolecular formate end groups and esters. The photo-oxidation of PEO in aqueous solution (concentration 50 mg mL^{-1} or 5 mg mL^{-1} , $\text{pH}_{\text{initial}} = 8.4$) leads also to the formation of formate end groups and esters but a third product has also been identified, formic acid ions or formic acid depending on the pH of the medium. Formic acid ions or formic acid might come from partial acidic or basic hydrolysis of formate end groups of the polymer matrix. The release of formic acid is mainly responsible for the acidification of the medium. For very advanced time of irradiation in acidic medium, secondary products appear.

The oxidation products depend on the pH of the medium, due to the instability of formate and ester in acidic and basic media. Formates are hydrolysed in acidic medium with the release of formic acid, in basic medium with the production of formic acid ions. Ester groups are also hydrolysed in basic and acidic media to give carboxylate ions/carboxylic acids.

SEC analysis of PEO aqueous solutions shows that in all pH conditions the photo-oxidation of PEO aqueous solution leads to the decrease of molar weights, which means that the degradation of PEO implies a chain scissions mechanism. SEC analysis also shows that the rate of degradation is much higher in acidic medium, because of the partial hydrolysis of formate.

The influence of the medium, aqueous solution in regard to solid state, lies in the stability of the photoproducts which is different depending also on the pH of the medium in aqueous solution but the mechanism of oxidation of PEO is not modified. Indeed, the differences observed are connected to hydrolysis reactions of photoproducts in aqueous solution.

The experiments of thermo-oxidation, at $50\text{ }^{\circ}\text{C}$, of PEO aqueous solution do not show the degradation of PEO in solution of initial pH 12.0 and 8.4 while in acidic medium, the formation of oxidation products is observed.

The comparison of results obtained either in thermo-oxidation or in photo-oxidation of PEO aqueous solution shows a different ratio of formate/ester as already observed in solid state. Thermo-oxidation of PEO aqueous solution produces equal amounts of esters and formates whereas photo-oxidation generates formates in a ratio of 4/1 against chain esters.

The next step of our study on PEO deals with the influence of Fe(III) on the photodegradation of PEO aqueous solutions.

Acknowledgements

The authors are grateful to Marius Parazols, Ph.D. student at the “Laboratoire de Photochimie Moléculaire et Macromoléculaire” for his kind collaboration in ion chromatographic experiments.

References

- [1] Swift G. *Polym Degrad Stab* 1998;59:19–24.
- [2] Molyneux P. *Water-soluble synthetic polymers: properties and behavior*, vol. 1. Boca Raton: CRC Press; 1983 [Chapter 2].
- [3] Al-Saigh ZY. *Polymer* 1999;40:3479–85.
- [4] Aray Y, Marquez M, Rodriguez J, Vega D, Simon-Manso Y, Coll S, et al. *J Phys Chem B* 2004;108:2418–24.
- [5] Scheirs J, Bigger SW, Delatycki O. *Polymer* 1991;32(11):2014–9.
- [6] Bjordal CG, Nilsson T, Daniel G. *Int Biodeterior Biodegrad* 1999;43:63.
- [7] da Costa VM, Fiske TG, Coleman LB. *J Phys Chem* 1994;101:2746–51.
- [8] Miyazawa T, Fukushima K, Ideguchi Y. *J Chem Phys* 1962;37(12):2764–76.
- [9] Begum R, Matsuura H. *J Chem Soc Faraday Trans* 1997;93(21):3839–48.
- [10] Takahashi Y, Tadokora H. *Macromolecules* 1973;6:672–5.
- [11] Bedrov D, Pekny M, Smith GD. *J Phys Chem B* 1998;102:996–1001.
- [12] Dormidontova EE. *Macromolecules* 2002;35:987–1001.
- [13] Smith GD, Bedrov D, Borodin O. *J Am Chem Soc* 2000;122:9548–9.
- [14] Morlat S, Gardette JL. *Polymer* 2001;42:6071–9.
- [15] Morlat S, Gardette JL. *Polymer* 2003;44:7891–7.
- [16] Philippart JL, Sinturel C, Gardette JL. *Polym Degrad Stab* 1997;58:261–8.
- [17] Pang P, Englezos P. *Fluid Phase Equilib* 2002;194:1059–66.
- [18] Bailey Jr FE, Callard RW. *J Appl Polym Sci* 1959;1:56–62.
- [19] Wilhelm C, Gardette JL. *J Appl Polym Sci* 1994;51:1411–20.
- [20] Morlat S, Cezard N, Loubineux B, Philippart JL, Gardette JL. *Polym Degrad Stab* 2001;72(2):199–208.
- [21] Gauvin P, Philippart JL, Lemaire J. *Makromol Chem* 1985;186:1167–80.
- [22] Jaffrezzo JL, Calas N, Bouchet M. *Atmos Environ* 1998;32:2705–8.
- [23] Lin-Vin D, Colthup NB, Fateley WG, Grasselli JG. *The handbook of infrared Raman characteristic of organic molecules*. San Diego: Academic Press; 1991.
- [24] Vijayalakshmi SP, Senapati D, Madras G. *Polym Degrad Stab* 2005;87:521–6.



Photochemical behaviour of poly(ethylene oxide) (PEO) in aqueous solution: Influence of iron salts

Fatima Hassouna, Gilles Mailhot*, Sandrine Morlat-Thérias, Jean-Luc Gardette

Laboratoire de Photochimie Moléculaire et Macromoléculaire, Université Blaise Pascal, UMR CNRS-UBP 6505, F-63177 Aubiere Cedex, France

Received 28 June 2007; received in revised form 28 September 2007; accepted 29 September 2007

Available online 5 October 2007

Abstract

The degradation of poly(ethylene oxide) (PEO) photoinduced ($\lambda \geq 300$ nm) by Fe(III) (6.0×10^{-4} mol L⁻¹) in aqueous solution in the presence of oxygen at 15 °C has been investigated in various experimental conditions of pH and concentrations: pH 3.1 and 7.8 and at three different concentrations of PEO: 0.1, 5.0 and 50.0 g L⁻¹. The formation of oxidation products was followed by infrared analysis of deposit obtained by evaporation of aliquots of irradiated polymer solutions. The photooxidation of PEO aqueous solutions both in the presence and in the absence of Fe(III) leads to the formation of macromolecular formates and esters. Formate ions are formed by the hydrolysis of macromolecular formates leading to the acidification of the medium. The presence of Fe(III) modifies the rate of oxidation especially in weakly acidic medium. The photogenerated •OH radicals from iron species accelerate the oxidation of PEO. Thermooxidation experiments of PEO in aqueous solution in the presence of Fe(III) at 50 °C are also reported and compared with photooxidation results.

© 2007 Elsevier B.V. All rights reserved.

Keywords: Poly(ethylene oxide) (PEO); Iron; Photodegradation; Aqueous solution; Mineralisation

1. Introduction

PEO is widely used in many applications such as detergents, paints, drug delivery, etc. At the end of its useful life, it is generally discarded into the aqueous environment simply because it is unrecoverable. This polymer is not biodegradable and its fate in the environment is not well known in terms of PEO concentration really present, degradation and toxicity. Moreover, the potential pollution from this polymer is not visible. Consequently it has received less attention in the media than packaging plastics which visibly litter the countryside and contribute to landfill overland.

A previous paper reported a study carried out to understand the photooxidation ($\lambda \geq 300$ nm) and the thermooxidation at 50 °C of poly(ethylene oxide) (PEO) in the solid state [1]. It was concluded that the mechanism of photodegradation of PEO in the solid state mainly led to the formation of macromolecular formates and esters. Similar studies were carried out in aqueous solution [2,3] in presence of oxygen at 15 °C at different pH's

(2.3, 3.1, 7.8, 8.4 and 12.0) and at different PEO concentrations. It has been shown that the photodegradation of PEO in aqueous solution, beside formation of macromolecular formates and esters, results in the formation of formate ions or formic acid depending on the pH of the medium. This product comes from a partial hydrolysis in aqueous solution of formate end groups in the polymer matrix. This process of hydrolysis contributes to the acidification of the medium.

The main objective of the present work is to study the influence of Fe(III) salt, which is a transition metal and an efficient photochemical source of hydroxyl radicals, on the photochemical and thermal degradation of PEO in aqueous solution. The photochemical degradation of PEO in the solid state in presence of oxygen with the introduction of transition metal ions (FeCl₃, NiCl₂, CoCl₂ and CuCl₂) into polymers has been investigated [4–8]. It was concluded that the photostability of PEO was dramatically reduced in the presence of metal ions and a significant formation of carbonyl, carboxyl and hydroxy/hydroperoxy groups was observed.

The hydrolysis of Fe(III) is a complex phenomenon and a number of equilibria yield numerous species [9]. Previous works have shown that the hydrolysis depends mainly on pH, initial concentration of Fe(III), temperature, ionic strength and

* Corresponding author. Tel.: +33 73 40 71 73; fax: +33 73 40 77 00.
E-mail address: gilles.mailhot@univ-bpclermont.fr (G. Mailhot).

nature of anions [10]. These different species have distinct chemical reactivity and behaviour under irradiation in aqueous solution. Among the Fe(III) aquacomplexes, $\text{Fe}(\text{OH})^{2+}$ (or $[\text{Fe}(\text{H}_2\text{O})_5(\text{OH})]^{2+}$) is the most photoreactive in terms of hydroxyl radical formation [11] and is the dominant species in moderately acidic solutions (pH 2.5–5.0) [9].

Photoexcitation of $\text{Fe}(\text{OH})^{2+}$ forms $\bullet\text{OH}$ radicals following ligand-to-metal charge transfer excitation (reaction 1). These radicals are considered to be the oxidant species which are capable to react with most organic compounds.



The present article reports a study of the degradation of PEO photoinduced by Fe(III) aquacomplexes until its complete mineralisation. The role of Fe(III) species is identified and a mechanism of PEO degradation is proposed. The influence of the pH of the aqueous solution is also studied by comparing the photo- and thermo-degradation of PEO at two pH's 3.1 and 7.8.

2. Experimental

2.1. Materials

All reagents were of the purest grade commercially available and were used without further purification.

Poly(ethylene oxide) was obtained from Scientific Polymer Products and used without further purification. The average molecular weight of the polymer was 100,000. Ferric perchlorate nonahydrate ($\text{Fe}(\text{ClO}_4)_3 \cdot 9\text{H}_2\text{O}$; >97%) was a Fluka product kept in a dessicator. Water was purified by a Millipore Ultra-Pure System ($\rho = 18.2 \text{ M}\Omega \text{ cm}$). Irradiations of PEO in solid state (as films) were carried out in a SEPAP 14/24 unit. This apparatus has been designed for the study of polymer photodegradation in artificial ageing corresponding to medium accelerated conditions [12]. The irradiation of PEO aqueous solutions was carried out in an elliptic chamber which is equipped with one medium-pressure mercury lamp (Mazda MA 400, polychromatic emission with an intensity of 22 W m^{-2}) in a vertical position at one focal axis of the chamber. A glass envelope filters wavelengths below 300 nm. The aqueous solution of PEO was irradiated in a pyrex reactor cooled by water circulation. The temperature of the solution was maintained at 15°C in order to avoid water evaporation. This reactor was placed at the second focal axis of the chamber. The solutions were continuously stirred with a magnetic stirrer and a Teflon bar.

Thermooxidation experiments were carried out at 50°C in a 100 mL round bottled flask equipped with reflux condenser. This temperature was chosen to keep the aqueous solution at a temperature below cloud point temperature (CPT = 100°C). The reactor was therefore placed into an oil bath.

PEO solutions of 5.0% (50.0 g L^{-1}), 0.5% (5.0 g L^{-1}) and 0.01% (0.1 g L^{-1}) of wt.% were prepared by dissolving PEO into distilled and deionized water with mild stirring overnight at room temperature. The aqueous solutions of PEO are not completely homogeneous and that can lead to high TOC variations (cf. Fig. 6a). This polymer has tendency to

agglomerate (formation of soluble aggregate) in aqueous solution.

To reach the total dissolution of iron, PEO aqueous solution was first acidified to obtain a pH of 3.5 or 4.0 with HClO_4 . $\text{Fe}(\text{ClO}_4)_3$ was dissolved in these PEO solutions at the concentration of $6 \times 10^{-4} \text{ mol L}^{-1}$ and $1.2 \times 10^{-3} \text{ mol L}^{-1}$, respectively. After iron addition, the pH of the solutions decreased from 3.5 to 3.1. In order to test the influence of the pH, Fe(III) has been dissolved in PEO aqueous solution without further acidification. In these conditions the pH of the solution changed from 8.4 to 7.8 after the addition of $\text{Fe}(\text{ClO}_4)_3$ ($6 \times 10^{-4} \text{ mol L}^{-1}$).

Relatively concentrated solutions of PEO (5.0 and 0.5%) had to be used in order to follow the chemical modifications of the irradiated solutions by IR analysis of deposits on CaF_2 windows. FTIR transmission spectra were recorded for thin deposits of oxidised samples of PEO, which were obtained by evaporation of aliquots of irradiated aqueous solution of PEO. The samples were dried at room temperature for 24 h. No buffer was used in order to avoid any contamination of the solution and any interaction with iron.

2.2. Chemical and spectrophotometric analysis

Chemical treatments of SF_4 and NH_3 were performed following the experimental procedure described previously [1].

Fe(II) concentration was determined by complexometry with *ortho*-phenanthroline, using $\varepsilon_{510} = 1.118 \times 10^4 \text{ L mol}^{-1} \text{ cm}^{-1}$ for Fe(II)-phenanthroline complex [13].

The pH was measured with an ORION pH-meter to ± 0.1 pH unit.

Ion chromatographic analyses were performed. Aqueous solutions were injected directly without filtration. Working conditions are similar with those described in detail by Jaffrezzo et al. [14]. DX 320 chromatograph (DIONEX) is equipped with an AS11 (4 mm) column for the anions in order to detect HCOO^- .

Infrared spectra were recorded with a Nicolet FTIR 760 spectrometer, working with OMNIC software. Spectra were obtained using 32 scans summation and 4 cm^{-1} resolution. The calibration of the thickness (in μm) of samples was performed at 1965 cm^{-1} , which corresponds to a band combining (COC) stretching modes and (CH_2) rocking modes. The thickness (e) dependence on the absorbance at 1965 cm^{-1} (OD) obeyed the equation: $\text{OD} = 0.00405 \times e$ [1]. UV-absorption spectra were recorded on a Varian spectrophotometer Cary 3.

The changes of molar weight (M_w , M_n), molar weight distribution (polydispersity index $\text{PI} = M_w/M_n$) and the intrinsic viscosity (IV) were obtained by size exclusion chromatography (SEC) analyses. Double distilled de-ionized water was used as eluent at a flow rate of 1 mL min^{-1} . A column was used for physical separation (TSK/Ref: GMPWXL). The refractive index was monitored continuously with a differential refractometer (Viscotek VE 3580) and the intrinsic viscosity with viscometer (Viscotek TriSec Model 270).

Total organic carbon (TOC) measurements in aqueous solution were obtained with a total organic carbon (TOC) analyzer Shimadzu model TOC-5050A. The Shimadzu TOC-5050A is

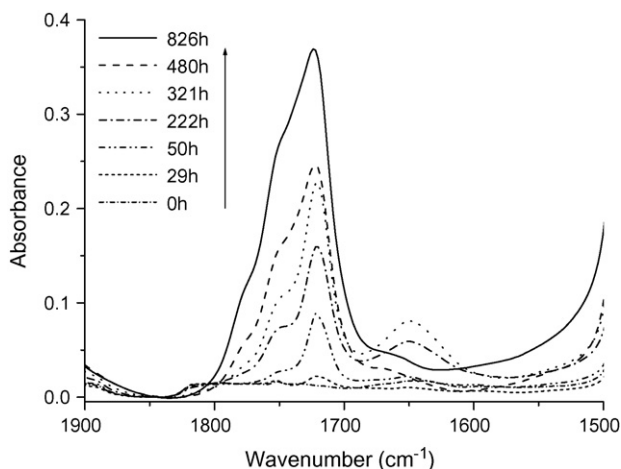


Fig. 1. FTIR spectra of deposits obtained from a PEO aqueous solution in the carbonyl domain ($1900\text{--}1500\text{ cm}^{-1}$) in the presence of Fe(III) during photooxidation (pH 3.1, $[\text{PEO}] = 50.0\text{ g L}^{-1}$, $[\text{Fe(III)}] = 6 \times 10^{-4}\text{ mol L}^{-1}$).

capable of performing total carbon (TC) analyses by combustion and inorganic carbon (IC) analyses by oxidation. TOC measurements were obtained by calculating the difference between TC and IC measurements. Calibration curves within the range of $0\text{--}500\text{ mg L}^{-1}$ for TC and $0\text{--}100\text{ mg L}^{-1}$ for IC were obtained using potassium hydrogen phthalate for total carbon and sodium hydrogen carbonate with potassium carbonate for inorganic carbon.

3. Results and discussion

The oxidation of PEO photoinduced by Fe(III) ($6 \times 10^{-4}\text{ mol L}^{-1}$) ($\lambda \geq 300\text{ nm}$) in aqueous solution in the presence of oxygen at 15°C was investigated at two different pH conditions: 3.1 and 7.8. First of all it is important to notice that no interaction between iron and PEO was observed in the medium.

3.1. pH 3.1

3.1.1. Analysis by IR spectroscopy

The FTIR spectra are limited to the domain of $4000\text{--}1000\text{ cm}^{-1}$ due to the opacity of the CaF_2 plate between 1000 and 400 cm^{-1} . Irradiation under wavelengths ($\lambda \geq 300\text{ nm}$, 15°C) of PEO aqueous solution at pH 3.1 in the presence of Fe(III) leads to significant modifications of the IR spectrum (Fig. 1) characterised by the appearance of an absorption band at 1720 cm^{-1} (formate) and a shoulder around 1750 cm^{-1} (ester) in the carbonyl vibration region ($1900\text{--}1500\text{ cm}^{-1}$).

For irradiation times below 480 h, one can observe a preponderance of formates. After 480 h, a shoulder appears near 1770 cm^{-1} . This absorption band could indicate the formation of a secondary product resulting from hydrolysis or rearrangements of the photoproducts when pH is lower than 3.1. Indeed, the pH of the solution was observed to decrease after 480 h of irradiation from 3.1 to 2.5, as a result of the partial hydrolysis of formates in acid medium. Moreover, in the domain ($1600\text{--}1200\text{ cm}^{-1}$), the absorption bands of PEO are no more recognizable after 480 h

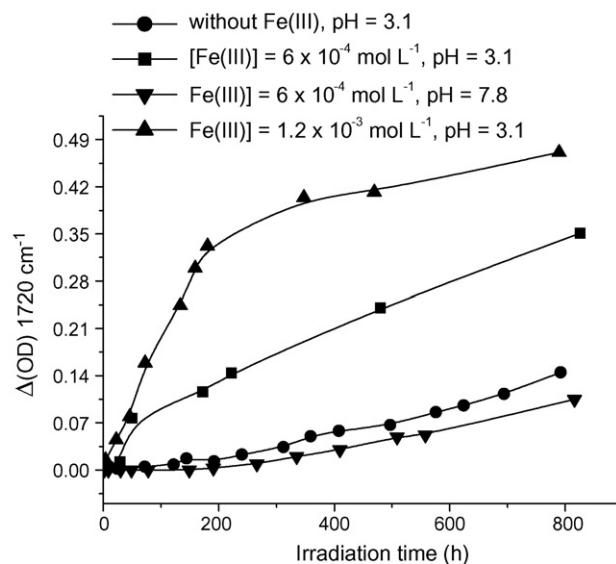


Fig. 2. Evolution of the absorbance at 1720 cm^{-1} as function of irradiation time in the absence or in the presence of Fe(III) at 6×10^{-4} and $1.2 \times 10^{-3}\text{ mol L}^{-1}$, $[\text{PEO}] = 50.0\text{ g L}^{-1}$.

of irradiation, which indicates that the structure of the polymeric backbone is drastically modified.

Comparison with the results previously obtained in the case of PEO aqueous solution irradiated in the absence of Fe(III) at pH 3.1 [3] shows that the same photoproducts are formed. If one considers the same absorption coefficients for the two C=O bands at 1750 and 1720 cm^{-1} , one can deduce from the previous results that the photooxidation of PEO in aqueous solution in the presence of Fe(III) results in the formation of four formate (end groups) to one ester (in the macromolecular chain) (ratio: 4/1). The same ratio is observed in the absence of Fe(III). These observations allow us to conclude that the mechanism of photooxidation of PEO in the absence as well as in the presence of Fe(III) is the same.

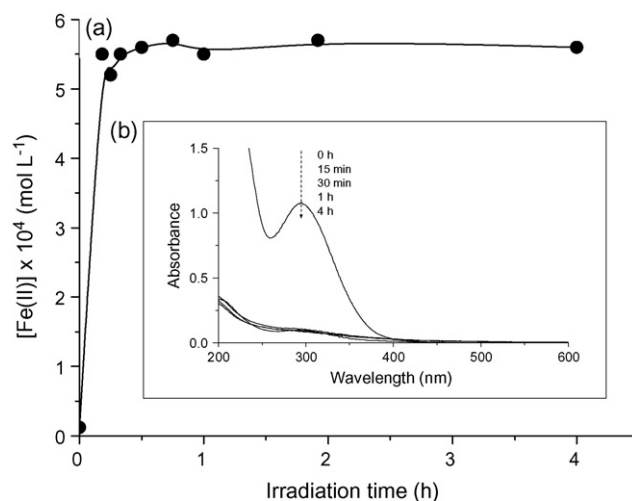


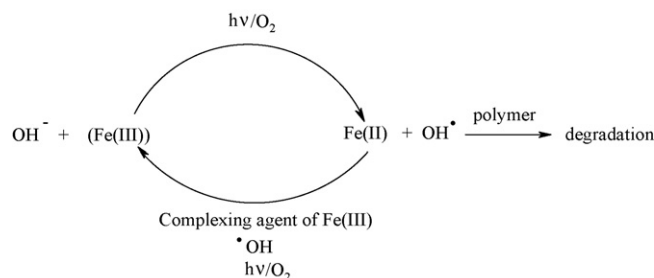
Fig. 3. (a) Fe(II) formation upon irradiation of PEO aqueous solution in presence of Fe(III) (initial pH 3.1, $[\text{PEO}] = 0.1\text{ g L}^{-1}$, $[\text{Fe(III)}] = 6 \times 10^{-4}\text{ mol L}^{-1}$) during photooxidation and (b) UV-vis spectra of PEO aqueous solution in presence of Fe(III) (initial pH 3.1, $[\text{PEO}] = 0.1\text{ g L}^{-1}$, $[\text{Fe(III)}] = 6 \times 10^{-4}\text{ mol L}^{-1}$) during photooxidation.

3.1.2. Kinetic of photooxidation of PEO

The variations of absorbance at 1720 cm^{-1} in presence and in absence of Fe(III) as a function of irradiation time in the case of the PEO aqueous solution at pH 3.1 are presented in Fig. 2 (this figure shows also the results concerning other pH and concentrations of iron, presented below in the manuscript). In order to compare different experiments, it was necessary to calibrate the thickness (e , in μm) of each deposit of the photooxidised sample. First of all, the curves show in Fig. 2 clearly that the rate of formation of carbonyl groups is much higher when the concentration of Fe(III) increases. In presence of Fe(III), two different slopes are observed on the kinetic curves of carbonyl groups formation.

Fig. 3 shows a very fast increase of the concentration of Fe(II) at the beginning of the irradiation which mainly results from the photoredox process of $\text{Fe}(\text{OH})^{2+}$ species. Fe(III) is mainly transformed into Fe(II). This photoreduction mainly leads to the production of $\bullet\text{OH}$ radicals. After the first period of irradiation, Fe(II) concentration is constant and reaches an apparent-constant value corresponding to a photostationary equilibrium between Fe(III) and Fe(II) ($[\text{Fe}(\text{II})] \approx 5.7 \times 10^{-4}\text{ mol L}^{-1}$ at the plateau) [15]. This photocatalytic process based on the couple Fe(III)/Fe(II) is presented in Scheme 1.

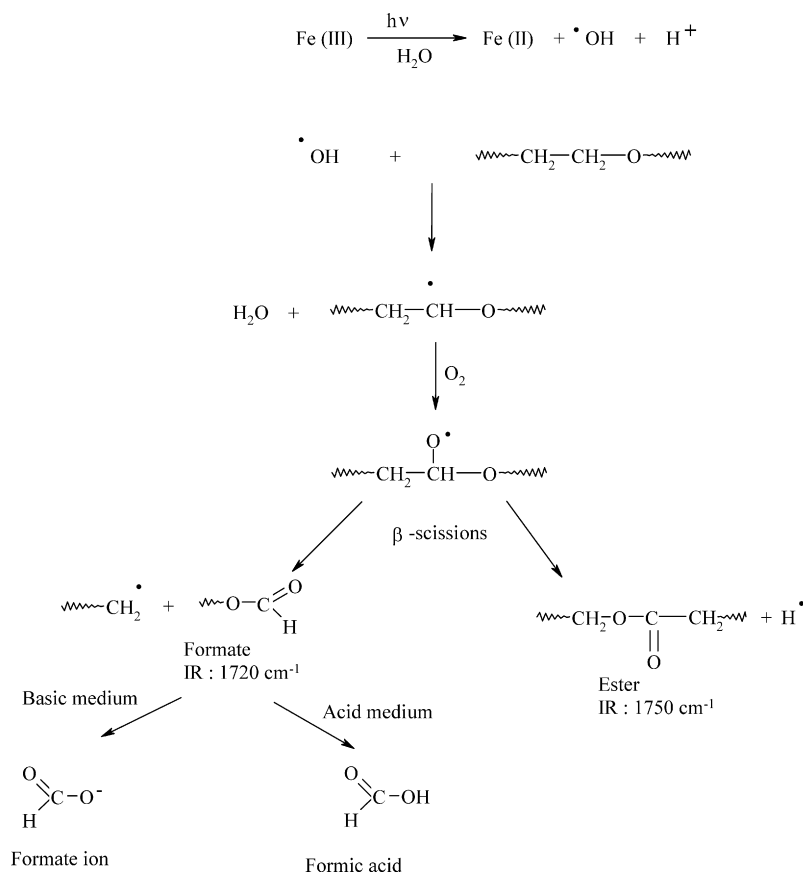
The first part of the photooxidation process, which is very fast, is then explained by the presence at $t = 0\text{ h}$ of $\text{Fe}(\text{OH})^{2+}$ which is an important photochemical source of $\bullet\text{OH}$ radicals production (reaction 1). The concentration of Fe(II) was measured all along the irradiation (Fig. 3).



Scheme 1. Photostationary equilibrium between Fe(III) and Fe(II) in the presence of organic compounds, (Fe(III)) represents all species of ferric iron during the cycle Fe(III)/Fe(II).

The second phase of the kinetic curves of the photooxidation of PEO aqueous solution in presence of Fe(III) (Fig. 2) corresponds to a decrease in the rate of formation of formate groups. This could be explained by the presence, after the first period where $\text{Fe}(\text{OH})^{2+}$ is photodegraded, of a photocatalytic cycle of Fe(III)/Fe(II) in which radical species ($\bullet\text{OH}$) are regularly formed in less important amount and also of the inherent photooxidation of PEO in aqueous solution.

The $\bullet\text{OH}$ radicals react on PEO by hydrogen abstraction during the first step of oxidation mechanism. After reaction with oxygen alkoxy radical can lead to the formation of macromolecular formate and ester by β -scissions [16]. The partial hydrolysis of formate groups can occur, leading to formate ions. The following scheme summarizes the PEO photooxidation mechanism in the presence of iron:



3.1.3. Characterisation by SEC

The evolutions of the molar weight distribution during photooxidation are reported in Fig. 4. The changes caused by irradiation of the PEO aqueous solution in presence of Fe(III) are characterised by a shift of the molar weight distribution curves towards the lower molar weights. The number average molar weight decreased by about 70% after 50 h of irradiation and 94% after 170 h (Fig. 4). In PEO aqueous solution without Fe(III), Mw decreased about 10% after 50 h and 95% after 312 h. This decrease in the number average molar weight indicates that chain scissions occur.

The results show that chain scissions in PEO are dramatically accelerated by the presence of Fe(III) during the first hours of irradiation. As a consequence, this suggests that $\bullet\text{OH}$ radicals are involved in the photooxidation process.

These results can be correlated to the kinetics of photooxidation of PEO in aqueous solution shown in Fig. 2. They show the photoinductive effect of Fe(III) in water by formation of $\bullet\text{OH}$ radicals, which accelerates the photooxidation of the polymer and as a consequence, scissions of the macromolecular backbone.

3.1.4. Influence of the Fe(III) concentration

As recalled above the rate of photooxidation of PEO aqueous solution is strongly dependent on Fe(III) concentration. Fig. 2 shows that the formation of carbonyl products, and as a consequence the chain scissions, became faster when the concentration of Fe(III) increases. This effect can be correlated with the increase of the monomeric species present in Fe(III) solution. Indeed, the $\text{Fe}(\text{OH})^{2+}$ species are the major light-absorbing species at 300 nm and the amount of $\bullet\text{OH}$ radicals produced is much higher for the Fe(III) concentration equal to $1.2 \times 10^{-3} \text{ mol L}^{-1}$.

3.1.5. Influence of polymer concentration

The influence of the polymer concentration on the mechanism of degradation has been studied in the aqueous solution at pH 3.1, by comparison of PEO aqueous solutions at 50.0 and 5.0 g L^{-1} . The evolution of the pH during the irradiation has been also measured.

(a) Analysis by infrared spectroscopy

Solutions of PEO of two different concentrations (5.0 and 50.0 g L^{-1}) in presence of Fe(III) ($6 \times 10^{-4} \text{ mol L}^{-1}$) at pH 3.1 were irradiated. The comparison of the infrared spectra shows that the same photoproducts are formed in both cases. This indicates that the mechanism of photooxidation of PEO is not depending on the concentration of PEO in the solution.

(b) Characterisation by SEC

For both concentrations, the average number molar weight decreases as a function of irradiation time (Fig. 4). This can be attributed to chain scissions occurring in PEO macromolecular chains. The degradation of the polymer is accelerated in dilute aqueous solutions. Indeed, after 20 h of irradiation of the PEO aqueous solution at 5.0 g L^{-1} , the peak was shifted to longer retention time, which can be attributed to the formation of products with

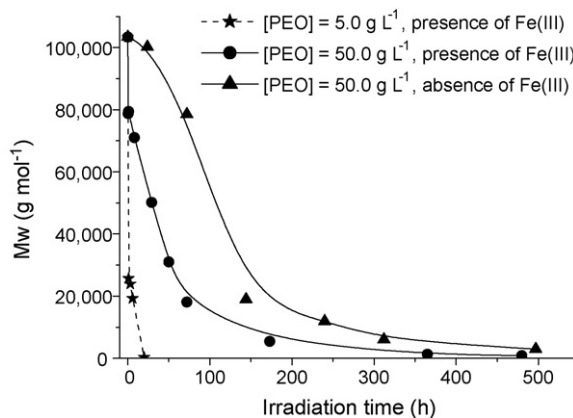


Fig. 4. Evolution of PEO molar weight (Mw) as a function of irradiation time in presence and in absence of iron ($[\text{Fe}(\text{III})] = 6 \times 10^{-4} \text{ mol L}^{-1}$, pH 3.1, $[\text{PEO}] = 5.0$ and 50.0 g L^{-1}).

lower molar weight. However, this measure was out of range of the column separation. The degradation of PEO could be higher in diluted solution than in more concentrated solution because the mobility of polymer chains is higher in less viscous solution [2]. Moreover, this difference could be also explained by the fact that for a concentration of 50 g L^{-1} , PEO aqueous solution presents a notable diffusion of light. This diffusion effect could contribute to the decrease of the PEO phototransformation rate.

3.2. pH 7.8

Aqueous solutions of PEO were irradiated without acidification of the medium in the presence of Fe(III) in order to study the influence of the initial pH of the medium on the photodegradation of PEO in presence of iron. The initial pH of the PEO aqueous solution (50.0 g L^{-1}) changed from 8.4 to 7.8 after the addition of $\text{Fe}(\text{ClO}_4)_3$ ($6 \times 10^{-4} \text{ mol L}^{-1}$).

3.2.1. Analysis by infrared spectroscopy

UV-light irradiation of aerated PEO in aqueous solution (concentration 50.0 g L^{-1} , $\text{pH}_{\text{initial}}$ 8.4) in absence of Fe(III) leads also to the formation of formate end groups and esters and also to formate ions [3]. At a pH of 7.8, the same absorption bands are formed in the carbonyl region with the same stoichiometry.

3.2.2. Evolution of pH

The pH value decreased from 7.8 to 4.4 after 840 h of irradiation. In absence of Fe(III) at pH 8.4, the same dramatic decrease of the pH in the solution has been noticed [2]. This decrease has been correlated with the accumulation of formate ions (HCOO^-).

3.2.3. Effect of the presence of Fe(III)

Fig. 5 shows the variations of the absorbance at 1720 cm^{-1} and at 1750 cm^{-1} both in presence and in absence of Fe(III) as a function of irradiation time. It is observed that degradation of PEO appears more rapidly in presence of Fe(III). The degrada-

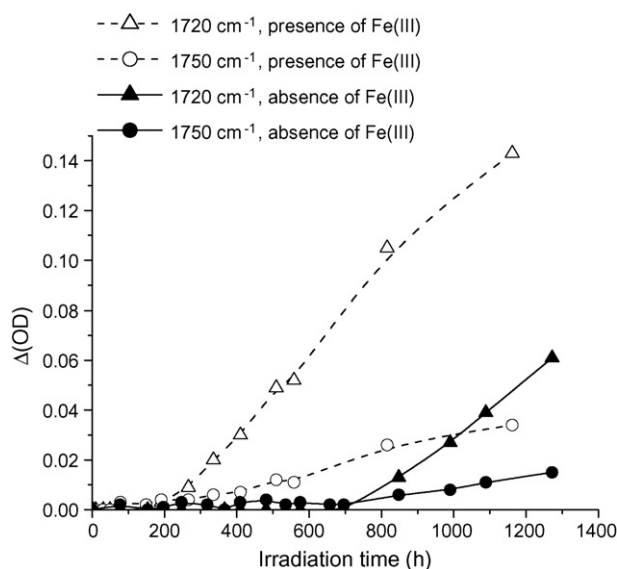


Fig. 5. Evolution of the absorbance at 1720 and 1750 cm^{-1} as function of irradiation time in presence and in absence of Fe(III) at pH 7.8 and 8.4, respectively ($[\text{PEO}] = 50.0 \text{ g L}^{-1}$, $[\text{Fe(III)}] = 6 \times 10^{-4} \text{ mol L}^{-1}$).

tion of PEO in presence of Fe(III) can be observed after 200 h when the pH of the solution becomes lower than 7.0. This can be explained by the dissolution of Fe(III) when the pH of the solution decreases which increases the concentration of iron in water.

3.3. Influence of the pH in presence of Fe(III)

The rate of PEO photooxidation in aqueous solution in presence of Fe(III) is faster at pH 3.1 than at pH 7.8 at the beginning of irradiation (Fig. 2). Indeed, the rate of PEO photooxidation is strongly affected by the pH of the solution which controls the solubility and the speciation of Fe(III) monomeric species present in the solution. At pH 7.8, iron is not solubilised in aqueous solution. But the Fe(III) starts to be soluble in a weakly acidic medium (pH lower than 6.0) [9].

The nature and the concentration of Fe(III) species in the solution give evidences for the importance of iron speciation and consequently for photooxidoreduction process leading to Fe(II) formation and to oxidation of the PEO polymer present in aqueous solution [17].

3.4. Mineralisation of PEO

One of the aims of the present work was to test the efficiency of PEO removal from water solution, when the degradation was photoinduced by Fe(III). Total organic carbon experiments were undertaken in order to make evidence for the mineralisation of PEO. Relatively diluted polymer solutions (0.5 and 0.1 g L^{-1}) were chosen in order to point out the mineralisation of the polymer. As shown in Fig. 6a, total mineralisation of PEO was reached after 70 h of irradiation when the concentration of the solution was of 0.1 g L^{-1} and the pH 3.1. At higher concentration of PEO (0.5 g L^{-1}) (Fig. 6b), the mineralisation is slower and total after 320 h of irradiation. The complete mineralisation is obtained due to the continuous formation of radical species ($\bullet\text{OH}$), which is the result of a photocatalytic cycle (Scheme 1), in homogeneous phase, based on the couple Fe(III)/Fe(II) and assisted by oxygen [15]. In the absence of Fe(III), no decrease of TOC concentration mineralisation was observed after 340 h of irradiation.

The rate of mineralisation under irradiation of PEO in aqueous solution in presence of iron was also examined. The results show the same rate of carbon disappearance ($0.9 \text{ mg L}^{-1} \text{ h}^{-1}$) for both concentrations of polymer solutions (0.1 and 0.5 g L^{-1}). This can be explained by the fact that the rate of degradation of PEO depends only on the initial concentration of Fe(III) species presents in the solution, in particular Fe(OH)^{2+} species.

3.5. Thermooxidation

Thermooxidation at 50°C of PEO aqueous solution in different pH conditions in presence of iron was studied in order to evaluate an eventual thermal effect on the degradation of

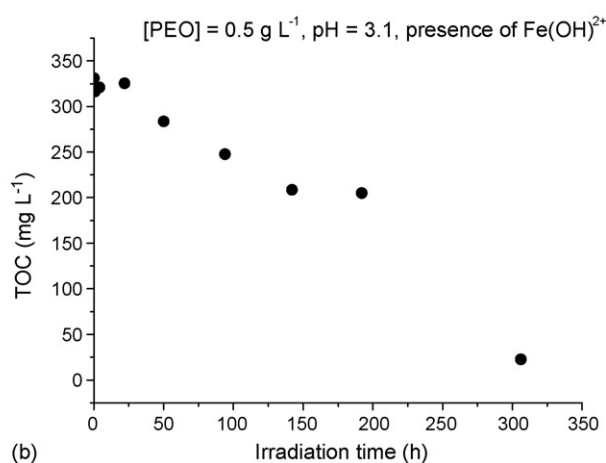
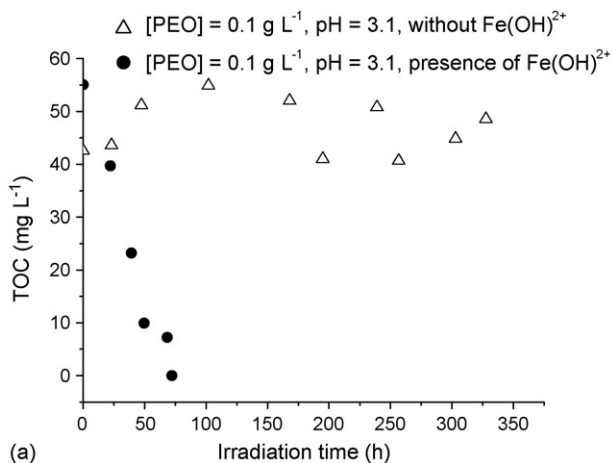


Fig. 6. TOC evolution of PEO aqueous solution during irradiation ($\lambda \geq 300 \text{ nm}$) (pH 3.1, $[\text{Fe(III)}] = 6 \times 10^{-4} \text{ mol L}^{-1}$), (a) $[\text{PEO}] = 0.1 \text{ g L}^{-1}$ and (b) $[\text{PEO}] = 0.5 \text{ g L}^{-1}$.

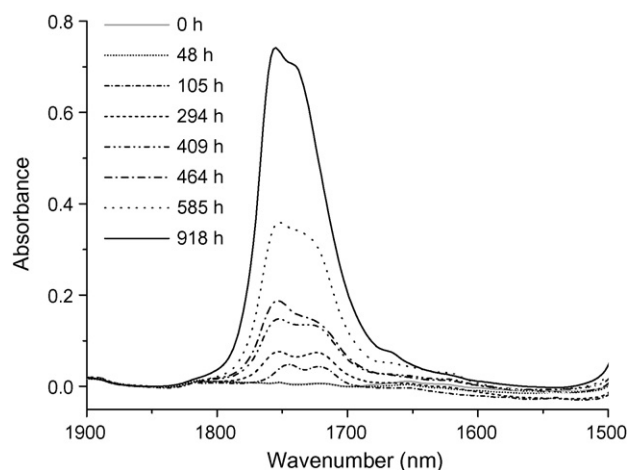


Fig. 7. FTIR spectra of deposits obtained from a PEO aqueous solution in presence of Fe(III) during thermooxidation (50 °C) ([PEO] = 50.0 g L⁻¹, [Fe(III)] = 6 × 10⁻⁴ mol L⁻¹, pH 3.1).

PEO aqueous solution. It is important to note that no significant oxidation of PEO, in the presence or in the absence of Fe(III), was observed even after 900 h at room temperature (20–25 °C).

At pH 7.8, in the absence and the presence of Fe(III), no significant evolution has been observed after 400 h of heating (50 °C) by infrared analysis contrary to pH 3.1.

3.5.1. Analysis by infrared spectroscopy

At pH 3.1, in the carbonyl region, two bands with an absorption maximum at 1750 cm⁻¹ (ester) and 1720 cm⁻¹ (formate) developed with similar intensities. For very long duration (900 h) a shoulder around 1735 cm⁻¹ can be observed whereas the maximum at 1720 cm⁻¹ is no more visible. For advanced times of irradiation, secondary products are observed (1735 cm⁻¹).

The comparison between the photooxidation and the thermooxidation of PEO in aqueous solution shows that the photooxidation generates formates in a ratio 4/1 against chain esters whereas thermooxidation produces equal amounts of esters and formates as already observed without iron [2,3] and in solid state [1] (Fig. 7).

3.5.2. Rate of thermooxidation of PEO at pH 3.1

The evolutions of absorbance at 1720 cm⁻¹ in presence and in absence of Fe(III) as a function of heating time in the case of the PEO aqueous solution at pH 3.1 are reported in Fig. 8. This figure shows that the rate of carbonyl groups formation is much higher in PEO aqueous solution with Fe(III). It is probable that in presence of Fe(III), the redox mechanism (reaction 2) between iron species and the polymer with production of macroradicals is favoured by the temperature [18]. These macroradicals participate in the photooxidation of the polymer.

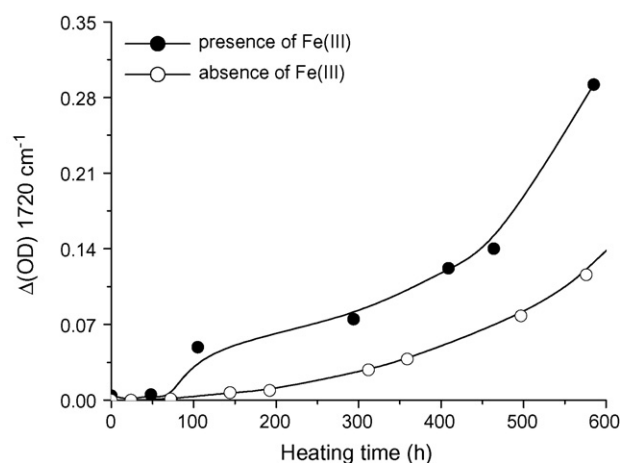
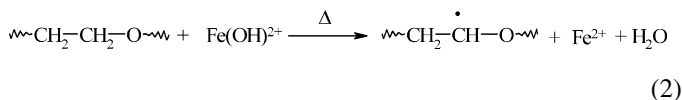


Fig. 8. Evolution of absorbance at 1720 cm⁻¹ as a function of heating (50 °C) time in presence and in absence of Fe(III) ([PEO] = 50.0 g L⁻¹, [Fe(III)] = 6 × 10⁻⁴ mol L⁻¹, pH 3.1).

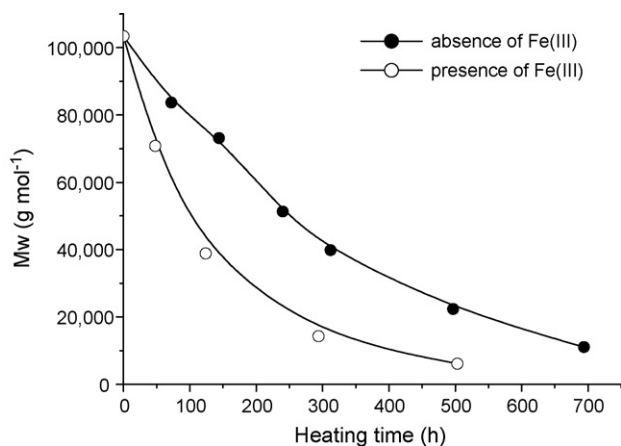


Fig. 9. Evolution of PEO molar weight (Mw) as a function of heating time ([PEO] = 50.0 g L⁻¹, [Fe(III)] = 6 × 10⁻⁴ mol L⁻¹, pH 3.1).

3.5.3. Characterisation by SEC

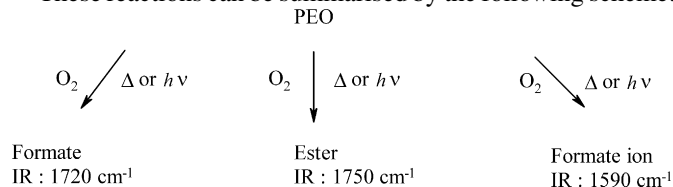
The evolutions of PEO during thermooxidation of aqueous solution at pH 3.1 in presence of Fe(III) was also characterised by SEC. Fig. 9 shows the decrease of the molar weight with no induction period both in presence and in absence of Fe(III). This decrease is attributed to chain scissions occurring in PEO chains, which indicate a dramatic degradation process during the thermal oxidation of the polymer. In presence of iron, the process of chain scissions is faster. This result shows again the efficiency of ferric salts in the acceleration of the degradation (oxidation) of PEO.

4. Conclusion

The results reported in this article show that the mechanism of photooxidation of PEO at different pH, concentration, in the presence or in the absence of Fe(III) is the same. Indeed, three photoproducts are observed: formate, ester and formate ions or formic acid. The formation of these last species depends on the pH of the medium. Formate ions or formic acid might come from partial hydrolysis of formate end groups of the polymer

matrix, which explains the acidification of the medium. In conditions of thermooxidation, the same behaviour was observed. However, a difference in the ratio ester/formate was detected. In photooxidation, formate (end) groups were generated in a ratio 4/1 against (chain) esters, whereas in thermooxidation, equal amounts of esters and formates were produced.

These reactions can be summarised by the following scheme:



The presence of iron was observed to accelerate the rate of photooxidation or thermooxidation and as a consequence the degradation of the polymer. The addition of Fe(III), which increases the rate of PEO oxidation, is essential for the mineralisation of the polymer. Indeed, these results confirm that Fe(III) can act as an efficient photoinducer (at acidic pH) of PEO elimination from aqueous solution and that the photodegradation leads to the complete mineralisation. However, this study also demonstrates the importance of the Fe(III)/Fe(II) couple correlated with the pH of the medium during the photodegradation, and it is clear that at pH more relevant to aquatic environment (6–8) the effect of iron is very weak. Anyway, this work is the first one demonstrating that a water-soluble polymer can be completely mineralised in certain conditions (pH, iron and polymer concentrations).

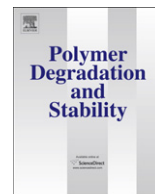
References

- [1] S. Morlat, J.L. Gardette, *Polymer* 42 (2001) 6071–6079.
- [2] F. Hassouna, S. Morlat-Théris, G. Mailhot, J.L. Gardette, *Polym. Degrad. Stab.* 92 (2007) 2042–2050.
- [3] S. Morlat, J.L. Gardette, *Polymer* 44 (2003) 7891–7897.
- [4] H. Kaczmarek, A. Kamińska, J. Kowalonek, A. Szalla, J. Photoch. Photobio. A 128 (1999) 121–127.
- [5] H. Kaczmarek, J.F. Rabek, *Angew. Makromol. Chem.* 247 (1997) 11–130.
- [6] H. Kaczmarek, A. Sionkowska, A. Kamińska, J. Kowalonek, M. Świątek, A. Szalla, *Polym. Degrad. Stab.* 73 (2001) 437–441.
- [7] A.L. Lindén, J.F. Rabek, H. Kaczmarek, A. Kamińska, M. Scoconi, *Coord. Chem. Rev.* 125 (1993) 195–218.
- [8] J.F. Rabek, A.L. Lindén, H. Kaczmarek, B.J. Qu, W.F. Shi, *Polym. Degrad. Stab.* 37 (1992) 33–40.
- [9] C.M. Flynn Jr., *Chem. Rev.* 84 (1984) 31–41.
- [10] R.N. Sylva, *Rev. Pure. Appl. Chem.* 22 (1972) 115–132.
- [11] H.J. Benkelberg, P. Warneck, *J. Phys. Chem.* 99 (1995) 5214–5221.
- [12] S.C. Philippart, J.L. Gardette, *Polym. Degrad. Stab.* 58 (1997) 261–268.
- [13] J.G. Calvert, J.M. Pitts, *Photochemistry*, Wiley, New York, 1966, pp. 783–786.
- [14] J.L. Jaffrezo, N. Calas, M. Bouchet, *Atmos. Environ.* 32 (1998) 2705–2708.
- [15] L. Poulain, G. Mailhot, P. Wong-Wah-Chung, *J. Photoch. Photobio. A* 159 (2003) 81–88.
- [16] C. Von-Sonntag, H.P. Schuchmann, *Angew. Chem. Int. Ed. Engl.* 30 (1991) 1229–1253.
- [17] H. Měšt'ánková, G. Mailhot, J.F. Pilichowski, J. Krýsa, J. Jirkovský, M. Bolte, *Chemosphere* 57 (2004) 1307–1315.
- [18] P. Mazellier, M. Bolte, *Chemosphere* 35 (1997) 2181–2192.



Contents lists available at ScienceDirect

Polymer Degradation and Stability

journal homepage: www.elsevier.com/locate/polydegstab

Photooxidation of poly(N-vinylpyrrolidone) (PVP) in the solid state and in aqueous solution

Fatima Hassouna^{a,b}, Sandrine Therias^{a,b,*}, Gilles Mailhot^{a,b}, Jean-Luc Gardette^{a,b}

^a Clermont Université, Université Blaise Pascal, Laboratoire de Photochimie Moléculaire et Macromoléculaire UMR, F-63000 Clermont-Ferrand, France

^b CNRS, LPMM UMR 6505, F-63177 Aubière, France

ARTICLE INFO

Article history:

Received 25 June 2009

Accepted 18 August 2009

Available online 23 August 2009

Keywords:

PVP

Water

Photooxidation

Infrared

SEC

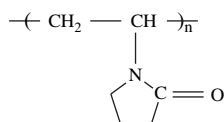
ABSTRACT

The photooxidation of poly(N-vinylpyrrolidone) (PVP) in the solid state and in an aqueous solution has been studied under irradiation at long wavelengths (at $\lambda \geq 300$ nm) and in the presence of oxygen, as these conditions of irradiation are those of natural outdoor aging. Infrared spectroscopy was used to follow the photochemical evolution of the polymer either for solid films of PVP or for PVP irradiated in an aqueous solution. Chemical treatments (NH_3 , SF_4) were carried out on the photooxidized samples, and aqueous solutions of PVP were characterized by viscometry and size exclusion chromatography (SEC). Based on photooxidation results obtained in both the solid state and in an aqueous solution, a general mechanism that accounts for the main routes of oxidation is proposed. It was shown that the rates of oxidation and the stoichiometries of the reactions were strongly influenced by the physical state of the polymer (solid state or aqueous solution).

© 2009 Elsevier Ltd. All rights reserved.

1. Introduction

Poly(N-vinylpyrrolidone) (PVP) belongs to the class of water-soluble polymers. From a chemical point of view, PVP is a polymeric lactam with an internal amide bond [1].



Considering the structure of the monomer unit, PVP has amphiphilic character since it contains a highly polar amide group that confers hydrophilic and polar-attracting properties, and also non-polar methylene groups in the backbone and in the ring that confer hydrophobic properties [2].

PVP is used in a wide variety of applications. PVP is interesting from a biological point of view, since it has structural features similar to those of proteins, and has great potential for applications in the medical domain. Specifically, PVP is a bio- and hemocompatible polymer with very low toxicity, so that materials coated with this polymer can be used as medical devices intended for implanting in the human body [3]. Since PVP is physiologically

inactive, it has been used as a plasma substitute [4]. PVP forms a stable complex with iodine, in which this water-soluble complex retains the germicidal properties of iodine, but with reduced iodine toxicity to humans [5].

PVP is also interesting for technological applications. Its film forming and adhesive qualities are utilized in aerosol hair sprays, adhesives, and lithographic solutions. As a protective colloid, it is used in drug and detergent formulations, cosmetic preparations, polymerization reactions, and in pigment or dyestuff dispersions [5]. Moreover, PVP is miscible with hydroxyl-containing polymers, such as poly(vinyl alcohol) (PVA), and with polymers containing halogens, such as poly(vinyl chloride) (PVC).

Since water-soluble polymers are potential contributors to environmental problems, it is particularly important to determine their fate in conditions of natural weathering. After use, depending on the domains of application, PVP can be discarded into solid waste disposal systems or as a dilute aqueous solution. Moreover, biodegradability tests have shown that PVP is recalcitrant [6]. The effect of γ -irradiation on PVP [7,8,9] and the thermal behaviour of PVP [10] have been studied; however, the degradation of PVP when exposed to UV-light in the presence of oxygen has not been reported, and the mechanism of photooxidation of this water-soluble polymer is unknown.

This investigation of the photooxidation mechanism of PVP, both in the solid state and in an aqueous solution, is part of a general study of the photochemical behaviour of water-soluble polymers carried out in our research group with the aim of better understanding the potential contribution of these polymers to

* Corresponding author at: Clermont Université, Université Blaise Pascal, Laboratoire de Photochimie Moléculaire et Macromoléculaire UMR, F-63000 Clermont-Ferrand, France. Tel.: +33 (0) 73 40 71 43; fax: +33 (0) 73 40 77 00.

E-mail address: sandrine.therias@univ-bpclermont.fr (S. Therias).

environmental problems. The challenge of understanding the complex degradation mechanism of water-soluble polymers cannot be addressed by applying data obtained for the solid state to aqueous solutions of the polymers. The objectives of the present work are to elucidate the photooxidation mechanism of PVP in the solid state and to evaluate the influence of aqueous media on the “orientation” of the reaction leading to PVP degradation.

The photooxidation of PVP in the solid state will first be reported and then compared to PVP photochemical behaviour in an aqueous solution. Several chemical and physical aspects of PVP will be evaluated, including:

- The mobility of polymer segments, which is different in aqueous solutions. Changes in macrochain order (conformation and crystallinity) are considered, as well as the mobility, which is an important factor that influences reactivity. In particular, the ratio between the propagation and termination reactions that result from the recombination of radical species drastically modifies the mechanisms of oxidation.
- The influence of water on the reactive intermediates is likely to modify the reactions in terms of kinetics and mechanism. It must also be pointed out that the radical nature of PVP oxidation is questionable since, in a water solution, the interference of a radical mechanism with an ionic mechanism should be considered.
- The reaction of water with some of the intermediates or final products of oxidation that could occur.

The present article reports the photochemical behaviour of PVP in the solid state and in an aqueous solution under accelerated artificial aging ($\lambda \geq 300$ nm, in the presence of oxygen). These conditions of irradiation simulate and accelerate natural weathering. The oxidation products were characterized by FTIR spectroscopy coupled to chemical treatments in order to identify the photoproducts. Irradiated aqueous solutions have also been characterized by viscometry and size exclusion chromatography. On the basis of results obtained in the solid state compared to those obtained in an aqueous solution, a mechanism accounting for the main routes of PVP photooxidation is proposed.

2. Experimental

2.1. Materials

Poly(N-vinylpyrrolidone) (PVP) with $M = 360\,000$ g mol⁻¹ was supplied by Scientific Polymer Products. Thin, 20 μ m, films were obtained by the evaporation of polymer solutions prepared in methanol. All aqueous solutions were prepared with deionised ultra pure water ($\rho = 18.2$ M Ω cm). The study of PVP in solution was undertaken in aqueous solutions of 6.25% and 1.25% (w/w).

2.2. Irradiation

2.2.1. In aqueous solution

Irradiations were carried out in a SEPAP 14/24 unit at 20 °C for the PVP aqueous solutions investigated. The chamber consists of an elliptical reactor equipped with one medium-pressure mercury lamp (Mazda MA 400) in the vertical position at one focal axis of the chamber. Wavelengths below 300 nm are filtered by a glass envelope. At the second focal axis of the chamber, the aqueous solutions of PVP were placed in a Pyrex reactor cooled by water circulation. The temperature of the solution was maintained at 20 °C in order to avoid water evaporation.

2.2.2. In the solid state

Irradiations of PVP films were also performed at 20 °C: PVP films were placed in the aforementioned water-cooled Pyrex reactor in a SEPAP 14/24 (same device as for aqueous solutions).

2.3. Characterization methods

Infrared spectra were recorded using a Nicolet 760-FTIR spectrometer with OMNIC software. Spectra were obtained using a summation of 32 scans and a resolution of 4 cm⁻¹. A calibration of the thickness (e , μ m) of the non-photooxidized samples was performed by measuring the absorbance (OD) at 1370 cm⁻¹, which corresponds to a vibration band of the (C–H) bending mode. The thickness dependence of the absorbance obeyed the equation $OD = 0.0175 \times e$. FTIR transmission spectra were recorded for thin films of photooxidized samples of PVP, which were obtained on ZnSe plates by the evaporation of aliquots of the irradiated aqueous solution.

2.4. Size exclusion chromatography (SEC)

The changes of molar weight, viscosity, and molar weight distribution (polydispersity index, M_w/M_n) were obtained by size exclusion chromatography (SEC) using a Viscotek chromatograph working with a differential refractometer detector (Viscotek VE 3580), a viscometer detector (Viscotek TriSec Model 270), and a linear column (TSK/Ref: GMPWXL). The analyses were performed with an eluant of water containing 0.1 mol L⁻¹ NaNO₃ and CH₃CN (80/20v/v) at a flow rate of 0.7 mL min⁻¹. The detector was calibrated with PEO standards.

2.5. Analysis of volatiles by SPME

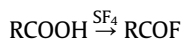
Films of PVP were irradiated in sealed vials in order to collect the volatile photodegradation products. Carboxen–PDMS fibre (75 μ m) was used to extract the volatile products. The extraction time was 5 min at 60 °C.

The volatile compounds were analyzed by gas chromatography/mass spectrometry (GC/MS) analysis with a 6890 Agilent GC coupled with a 5973 Agilent MS. The GC was equipped with a SupelcowaxTM 10 column (30 m \times 0.25 mm \times 0.25 μ m) from Supelco. Splitless injections were used (2 min). The temperature of the GC injector was 280 °C, while the oven temperature was programmed to be 35 °C for 10 min, and then raised to 200 °C with a heating rate of 10 °C min⁻¹. Mass spectra were acquired under the electron ionization mode (EI) at 70 eV, and recorded from 20 to 400 m/z at 1 Hz.

2.5.1. Chemical treatments

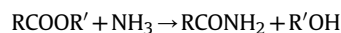
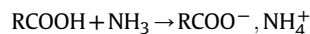
The photooxidized samples were submitted to various chemical treatments in order to identify the photoproducts. The irradiated films were exposed to reactive gas at room temperature in a simple flow system that could be sealed off to permit the reaction to proceed. SF₄ and NH₃ treatments were carried out in an all-Teflon system.

Acid groups react with SF₄ to give acid fluorides.



The absorption band $\nu(\text{C}=\text{O})$ of acid fluorides has a characteristic wavenumber between 1800 and 1850 cm⁻¹ [11,12]. SF₄ reacts with all –OH groups and, as a result, the absorption in the hydroxyl region decreases [13].

Acid groups also react with NH₃ to give ammonium carboxylates and esters by reacting with NH₃ to produce amide groups.



Ammonium carboxylates can be characterized by an infrared absorption band around 1550 cm^{-1} . Amide groups present, among others, two characteristic absorption bands around 1670 cm^{-1} (amide I band) and 1630 cm^{-1} (amide II band).

3. Results and discussion

3.1. Infrared analysis

Analysis of changes in the IR spectra requires that the absorption bands composing the spectrum of poly(N-vinylpyrrolidone) (PVP) before irradiation (Fig. 1) are identified. As poly(N-vinylpyrrolidone) is a highly hygroscopic polymer, an absorption band in the hydroxyl region corresponding to adsorbed water was observed on the infrared spectra, even after 20 min in the IR spectrometer bench, which is purged with dry air. The main spectral features of PVP are presented in Table 1.

3.1.1. Photooxidation in solid state

The photooxidation of PVP thin films was monitored by infrared spectroscopy (Fig. 2). In the carbonyl region (Fig. 2a), a band with an absorption maximum at 1770 cm^{-1} develops. The initial amide band centred at 1680 cm^{-1} becomes wider and a shoulder at 1735 cm^{-1} can be observed. Moreover, a broad band centred at 1540 cm^{-1} appears. Fig. 2b shows that, in the domain between 1100 and 700 cm^{-1} , new absorption bands appear at 1060 cm^{-1} , 985 cm^{-1} , 910 cm^{-1} , 820 cm^{-1} , and 785 cm^{-1} during irradiation. One can particularly notice that the decrease of the absorption bands at 845 and 930 cm^{-1} is correlated to the formation of new absorption bands at 820 and 910 cm^{-1} , respectively, with two isobestic points at 830 cm^{-1} and 925 cm^{-1} .

3.1.2. Photooxidation in aqueous solution

Photooxidation of a PVP aqueous solution at $20\text{ }^\circ\text{C}$ ([PVP] = 12.5 mg mL^{-1} , pH = 4.2), was also characterized by IR analysis. The modifications of the IR spectra of PVP deposits resulting from irradiation in aqueous solution (Fig. 3) were comparable to those of PVP in the solid state (Fig. 2); however, one

Table 1

Attribution of infrared absorption bands of PVP.

$\nu\text{ (cm}^{-1}\text{)}$	Attribution
3460	Stretching (OH)
2920	Antisym. stretching (CH_2)
2880	Sym. stretching (CH_2)
1670	Stretching ($\text{C}=\text{O}$)
1460	Bending (CH_2)
1425	Bending (CH_2) in α -position of $\text{C}=\text{O}$
1375	Bending (CH)
1285	Stretching ($\text{C}-\text{N}$)
1170, 1050	Stretching ($\text{C}-\text{C}$) of the ring
845	Ring "breathing" of pyrrolidone

can observe that, depending on the medium of irradiation and the physical state of the polymer, the relative intensities of the absorption bands are different.

Table 2 shows the absorbance ratios of IR bands calculated from the absorbance measured at 1770 cm^{-1} considered as the reference band for long irradiation times ($\approx 250\text{ h}$). The results show important discrepancies between the values obtained for the PVP solid state and PVP in an aqueous solution. The intensities of the absorption bands at 1060 , 985 , and 785 cm^{-1} that result from photooxidation are approximately 4–5 times more important in the

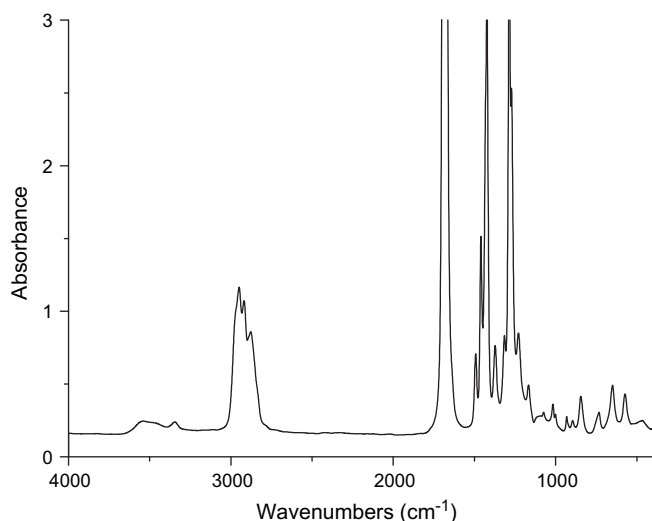


Fig. 1. FTIR spectrum of a PVP film before irradiation.

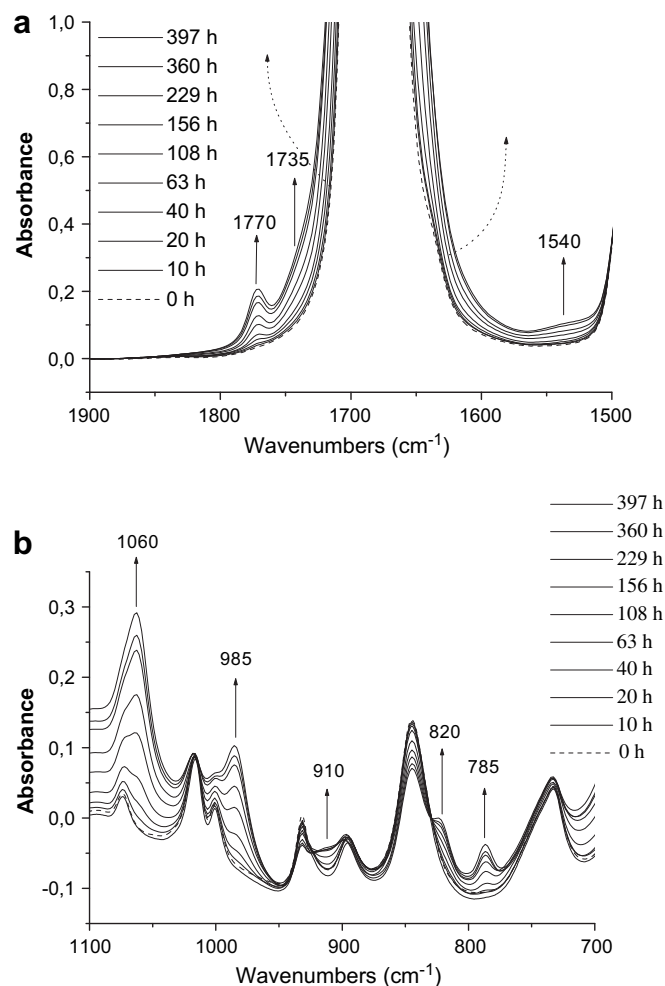


Fig. 2. FTIR spectra of a PVP film photooxidized at $\lambda \geq 300\text{ nm}$ and $20\text{ }^\circ\text{C}$ (film thickness of $20\text{ }\mu\text{m}$), a) in the domain of $1900\text{--}1500\text{ cm}^{-1}$, b) in the domain of $1100\text{--}700\text{ cm}^{-1}$.

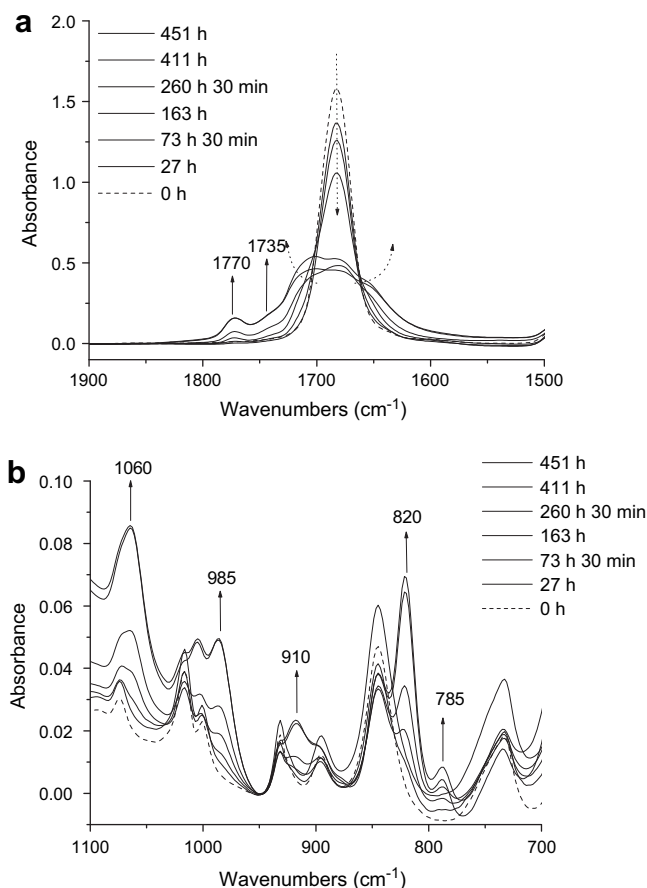


Fig. 3. FTIR spectra of deposits of a PVP aqueous solution photooxidized at $\lambda > 300$ nm and 20 °C (deposit thickness 5 μm), a) in the range of 1900–1500 cm^{-1} , b) in the range of 1100–700 cm^{-1} .

solid state than in the aqueous solution for equivalent durations of irradiation. These results underline that the photoproducts corresponding to these absorption bands are formed at a higher rate in the PVP solid state than in the PVP aqueous solution.

3.2. Identification of the photoproducts

The photooxidized samples were submitted to various chemical treatments that permit, by derivatisation, identification of the different photoproducts by IR spectrophotometry.

3.2.1. Chemical treatments

SF_4 treatments carried out on PVP films before photooxidation showed modifications of the IR spectrum in the carbonyl region, which makes this treatment unable to identify carboxylic acids.

Table 2

Ratios of absorbance of IR bands vs. absorbance at 1770 cm^{-1} for PVP photooxidation as a film or in an aqueous solution.

Absorption band (cm^{-1})	Absorbance ratios PVP aqueous solution [PVP] = 12.5 mg mL^{-1} $t_{\text{irradiation}} = 260$ h	Absorbance ratios PVP film $t_{\text{irradiation}} = 229$ h
785	0.04	0.2
820	0.35	0.25
910	0.1	0.3
985	0.25	0.9
1060	0.3	1.5
1770	1	1

In the case of NH_3 treatment, the results were more favourable. At first, it was verified that NH_3 treatment carried out on a PVP sample before photooxidation did not lead to any modification of the IR spectrum. In the case of a photooxidized PVP film, the appearance of a maximum at 1575 cm^{-1} (as a shoulder to the amide band) on the IR spectrum was observed after NH_3 treatment. This absorption band can be assigned to ammonium carboxylate groups, which confirms that carboxylic acids are formed as a result of photooxidation. The same modifications were observed in the case of NH_3 treatments of the deposits obtained from photooxidized PVP in aqueous solutions.

3.2.2. Comparison with IR features of succinimide

The increase of absorbance at 820 cm^{-1} of photooxidized PVP can be observed to be linked to a decrease in an absorption band at 845 cm^{-1} , demonstrating an isobestic point on the IR spectra (830 cm^{-1}) (Fig. 2b). Since the band at 845 cm^{-1} is characteristic of a pyrrolidone ring, this suggests that the photoproduct that corresponds to the IR band at 820 cm^{-1} results from the oxidation of the pyrrolidone ring.

Previous studies carried out in our laboratory on polyamides photooxidized at long wavelengths (at $\lambda \geq 300$ nm) [14] have shown that, among the numerous oxidation photoproducts, imides are the most easily identifiable. These products are characterized by IR absorption bands at 1735 and 1690 cm^{-1} . Analogously to polyamides, the formation of imides by the oxidation of PVP can be proposed. Additionally, the absorption band that develops upon photooxidation at 1770 cm^{-1} could correspond to a cyclic imide [15,16]. In the case of PVP, this band can be assigned to the succinimide ring that results from the oxidation of the pyrrolidone ring. In order to assess this hypothesis, a few drops of succinimide were added to the PVP aqueous solution ([PVP] = 62.5 mg mL^{-1}) and the deposit of this solution was analyzed by IR after water evaporation. The IR spectrum of this deposit (PVP + succinimide) was compared with that of a pure PVP deposit. As expected, in the presence of succinimide, two supplementary bands appear at 820 cm^{-1} and at 1770 cm^{-1} .

These observations suggest that the IR absorption bands at 820 and 1770 cm^{-1} can be attributed to a single photoproduct with a succinimide structure, which indicates that oxidation of the pyrrolidone ring occurs.

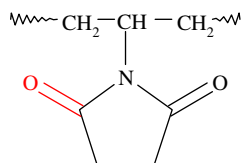
3.2.3. Identification of unsaturated photoproducts

The previously discussed results suggest that unsaturated photoproducts can be obtained. There are different possibilities of double bond formation according to the chemical structure of PVP. The IR spectra and the results reported in Table 2 indicate that the absorption bands at 785, 985, and 1060 cm^{-1} are correlated and could correspond either to the same photoproduct or to photoproducts coming from the same degradation reaction.

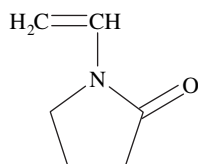
Several types of unsaturation can be considered: Vinyl, vinylene, and conjugated structures.

- **Vinyl unsaturation:** The formation of $\text{CH}_2=\text{CH}-\text{CH}_2-$ could account for the absorption bands observed at 910, 985, and 1060 cm^{-1} [1].
- **N-vinylpyrrolidone:** According to the chemical structure of PVP, one can consider the formation of N-vinylpyrrolidone (Schemes 1 and 2). N-vinylpyrrolidone presents a band at 985 cm^{-1} [deformation of (C–H) outside the plane (trans) of $=\text{CH}$].

In order to verify this hypothesis, N-vinylpyrrolidone was added to a PVP aqueous solution (concentration of 62.5 mg mL^{-1}), and a deposit of this solution was analyzed by IR after the water was



Scheme 1. Structure of the succinimide ring obtained after PVP photooxidation.



Scheme 2. Chemical structure of N-vinylpyrrolidone.

evaporated. The resultant spectrum shows an absorption band at 985 cm^{-1} , as well as another, less intense, band centred at 1040 cm^{-1} , corresponding to the (C–H) bending vibration in the plane of ($\text{CH}_2=$).

- **Vinylene unsaturation:** The absorption band at 785 cm^{-1} in photooxidized PVP samples can be attributed to vinylenes (HR-C=C-R_2) [16].

3.2.4. Evolution of pH in PVP aqueous solutions

Photooxidation of the PVP aqueous solution decreased the solution pH from 4.2 to 3.3 after 200 h of irradiation. The acidification of the solution can be explained by an accumulation of carboxylic acids during irradiation.

3.3. Rates of photooxidation

The rates of formation of PVP photoproducts were compared by plotting the increase of absorbance with the irradiation time for films and PVP aqueous solutions photooxidized at 20°C .

3.3.1. PVP in the solid state

Fig. 4a depicts the kinetic curves of PVP oxidized films irradiated in the SEPAP 14–24 unit at 20°C .

These curves show the formation of photoproducts from the beginning of irradiation without any induction time. After about 200 h, the absorbance values reach a quasi-stationary state.

3.3.2. PVP aqueous solution

Fig. 4b depicts the kinetic curves for deposits obtained from a PVP aqueous solution as a function of irradiation time. The rates of formation of the photoproducts obtained for the PVP aqueous solution can be compared to those of the PVP films (Fig. 4a) obtained from irradiations at 20°C .

Table 3 reports the irradiation times that are required to produce the same absorbance for a defined band in both physical states (for the same film and deposit thicknesses).

Table 3 shows that the bands at 1770 cm^{-1} and 820 cm^{-1} are correlated. Indeed, for the same irradiation times, either in film (40 h) or in solution (163 h), the absorbance values are equivalent. The same observation can be made for the bands at 1060, 985, and 785 cm^{-1} with the corresponding irradiation times of 63 h and 451 h in film and solution, respectively. These results suggest that these correlated bands correspond to either the same photoproduct or to photoproducts formed through the same route. Moreover, the ratio between the concentrations of the

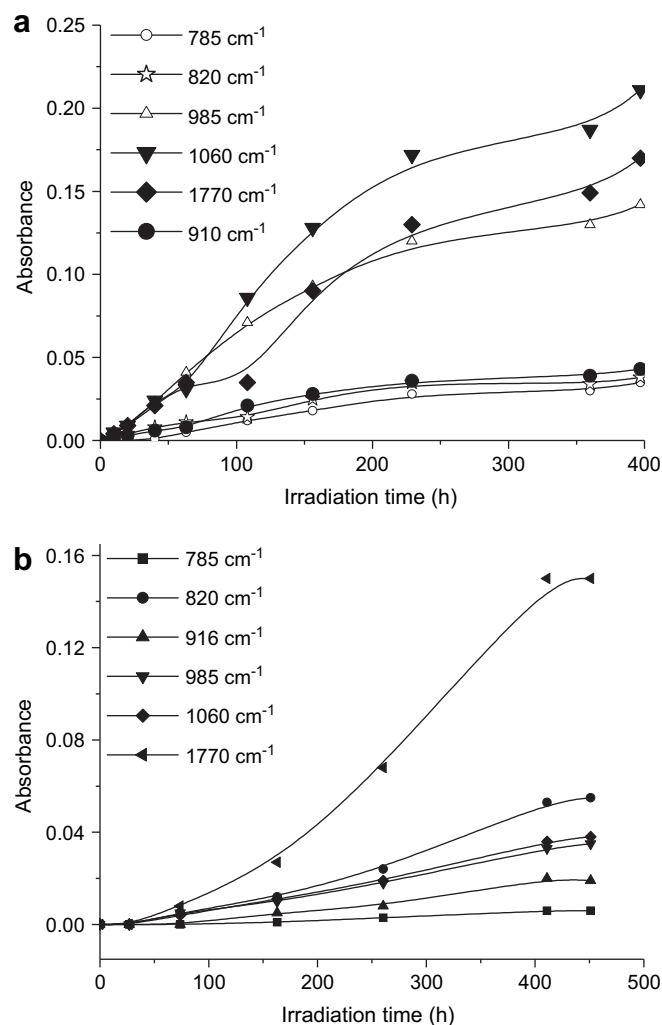


Fig. 4. a: Evolution of absorbance at 1770, 1060, 985, 910, 820, and 785 cm^{-1} as a function of irradiation time for a PVP film (thickness = $20\text{ }\mu\text{m}$) photooxidized at $\lambda \geq 300\text{ nm}$ and 20°C . b: Evolution of absorbance at 1770, 1060, 985, 910 cm^{-1} , 820, and 785 cm^{-1} as a function of irradiation time for PVP in an aqueous solution at 20°C ([PVP] = 12.5 mg mL^{-1}).

photoproducts in the solid and liquid states is not the same for both kinds of products: For identical irradiation times, a ratio of 4 is obtained for photoproduct(s) corresponding to 1770 and 820 cm^{-1} and a ratio of 7 for photoproduct(s) at 985, 785, and 1060 cm^{-1} . This observation also reflects the difference in stoichiometry for the formation of product(s) at 1770 and 820 cm^{-1} and product(s) at 785, 985, and 1060 cm^{-1} , depending on the solid state and the aqueous solution.

Table 3

Comparative results of the PVP film and PVP aqueous solution deposit with photooxidation at 20°C .

Wavenumber (cm^{-1})	Photooxidation	PVP films	Photooxidation	PVP solutions
	Absorbance	Irradiation time (h)	Absorbance	Irradiation time (h)
1770	0.021	40	0.027	163
820	0.008	40	0.012	163
1060	0.031	63	0.038	451
985	0.041	63	0.035	451
785	0.005	63	0.006	451

3.4. SEC analysis

A decrease of PVP solubility in water resulting from irradiation was observed. After only 40 h of irradiation, 70% of the PVP samples became insoluble.

3.4.1. SEC analysis of PVP in an aqueous solution

Modifications to the molar weight distribution of irradiated PVP in aqueous solutions were characterized by SEC, which provided the evolution of the intrinsic viscosity of PVP in aqueous solutions. Measurements were carried out on PVP in aqueous solutions at two different concentrations: 12.5 mg mL⁻¹ and 62.5 mg mL⁻¹ (Fig. 5a).

Chromatograms obtained by SEC analysis for irradiated PVP in aqueous solutions show that the polymer retains a monomodal distribution with a decrease in the molar weight distribution and a significant narrowing of the initial distribution. The average molar weight (M_w) decreases by about 80% after 27 h of irradiation. The intrinsic viscosity of the solution (IV) (Fig. 5b) shows a dramatic decrease. Furthermore, the polydispersity index decreases: The I_p ($= M_w/M_n$) value for PVP was 6.3 before irradiation, and decreased to 3.7 after 260 h of irradiation.

Computer models of degradation have been reported by Emsley et al. [17]. It is shown that I_p changes differently during aging, according to the processes that occur (random or systematic). In the case of the photooxidation of PVP in solution, the M_w/M_n ratio

decreases. This indicates that chain scissions are predominant and the macromolecular chains retain similar molecular weights. Viebke [18] has shown that the preferential scission of the longest chain leads to movement of the peak towards lower molar weights.

Our results indicate that the mechanism of photooxidation of PVP implies chain scission, as the molar weight and the viscosity of the solution dramatically decrease upon aging.

3.5. Analysis of the volatile products

UV-light-induced degradation of polymers produces a large variety of products. Most of the resultant products are trapped in the solid polymeric matrix. These products can be detected and easily identified by IR analysis of the polymer film. The situation is different in the case of low molecular weight products that result from multiple chain scissions, which are likely to migrate from the polymer matrix towards the atmosphere. Identification of these products requires the analysis of the gas phase that surrounds the exposed samples. This can be achieved through several techniques [19]. A simple method that can be used is solid-phase micro-extraction (SPME). This method consists of trapping the volatile products resulting from photooxidation with an SPME fibre, which is then analyzed by GC/MS [20,21]. In the case of PVP, the identification of the low molecular weight products in the gas phase was particularly necessary since one could suspect that photooxidation could provoke the formation of N-pyrrolidone. It was not possible to observe this product by IR analysis of PVP films, since it presents the same infrared characteristics as PVP. SPME analysis of the gas phase after irradiation revealed a peak at 85 that is characteristic of the mass spectrum of N-pyrrolidone (Fig. 6). This result indicates the release of molecular pyrrolidone, which confirmed that scissions of the C–N bond between the backbone and pyrrolidone group occurred during the irradiation of PVP in conditions of photooxidation.

3.6. Mechanism

Despite the fact that PVP does not absorb radiation of wavelengths longer than 300 nm, this polymer appears to be very sensitive to photooxidative degradation. Both in the solid state and in aqueous solution, photooxidation can be initiated by chromophoric impurities that absorb the UV-light and produce radicals that can react further with the polymer [22]. Based on commonly agreed upon photooxidation mechanisms, this first step is followed

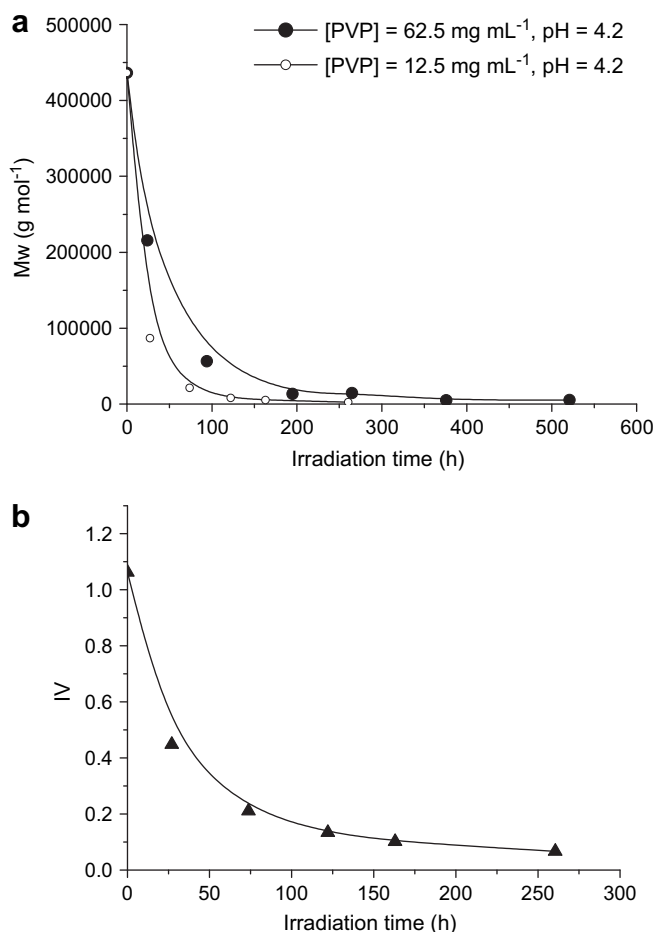


Fig. 5. a: Evolution of molar weight (M_w) as a function of irradiation time for PVP in aqueous solutions ([PVP] = 62.5 and 12.5 mg mL⁻¹). b: Evolution of intrinsic viscosity as a function of irradiation time for PVP in an aqueous solution (concentration of PVP 12.5 mg mL⁻¹).

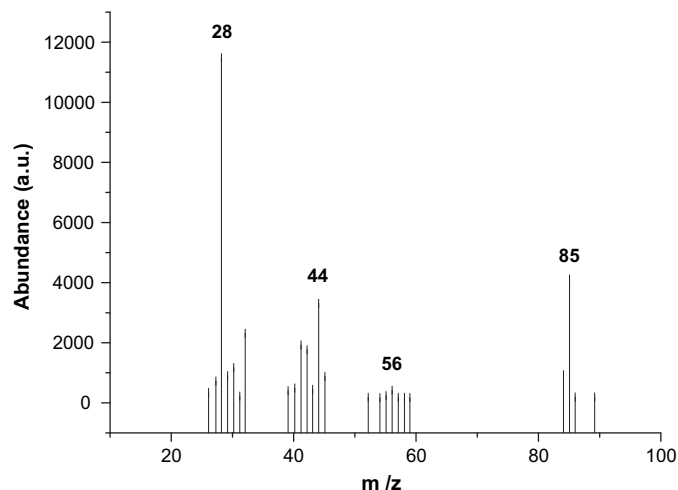
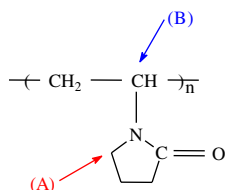


Fig. 6. Mass spectrum of N-pyrrolidone.

by hydrogen abstraction on the polymeric backbone by radicals. Macroradicals are then formed and react with oxygen, leading to peroxy radicals that give hydroperoxides by abstraction of a labile hydrogen atom, which then propagates the oxidation.

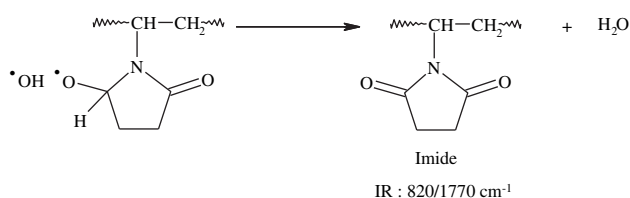
In the case of polyamides, photooxidation has been shown to result from an attack on the carbon atoms in the α -position of the amide group [14]. In the case of PVP, there are two carbon atoms in the α -position of the nitrogen atom, either a secondary carbon atom (A) or a tertiary one (B).



Two different routes can be proposed, which lead to the formation of two different hydroperoxides, as shown in Scheme 3. Hydroperoxides are thermally and photochemically unstable. The decompositions of these hydroperoxides occur through the homolysis of the peroxide bond and give hydroxyl radicals with either a secondary alkoxy radical (A') or a tertiary one (B').

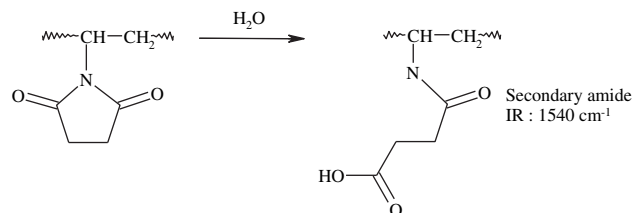
1) Evolution of alkoxy radical (A')

a) It has been shown in the case of aliphatic polyamides that the main route of evolution of an alkoxy radical (A') is hydrogen abstraction by the hydroxyl radical leading to imide group [14]. This reaction also produces water. In the case of PVP, the formation of imides would account for the increase of absorbance observed at 820 and 1770 cm^{-1} .

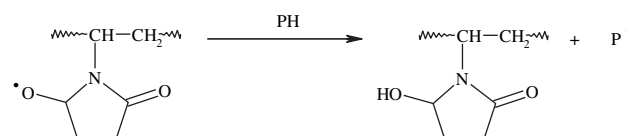


Imide groups are sensitive to hydrolysis and are likely to react with water formed *in situ* in close vicinity, which gives secondary amides. The absorption band at 1540 cm^{-1} that grows upon irradiation of PVP films can be attributed to the bending vibration of the N–H bond of the secondary amides coming from this reaction.

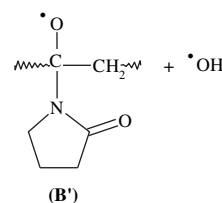
This reaction involves a ring opening [23]. The stretching vibration of the N–H bond that should appear at 3340 cm^{-1} is masked by the broad hydroxyl absorption band.



b) N-1-hydroxy groups could be formed through hydrogen abstraction by radical A', but this would be a minor route of evolution. There is no direct experimental evidence for the formation of these products. It should also be recalled that, if formed, N-1-hydroxy groups readily decompose above 60 °C [14].

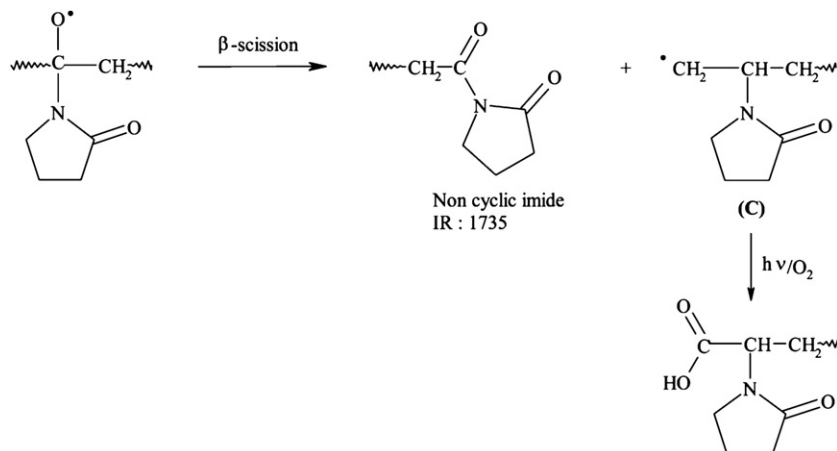


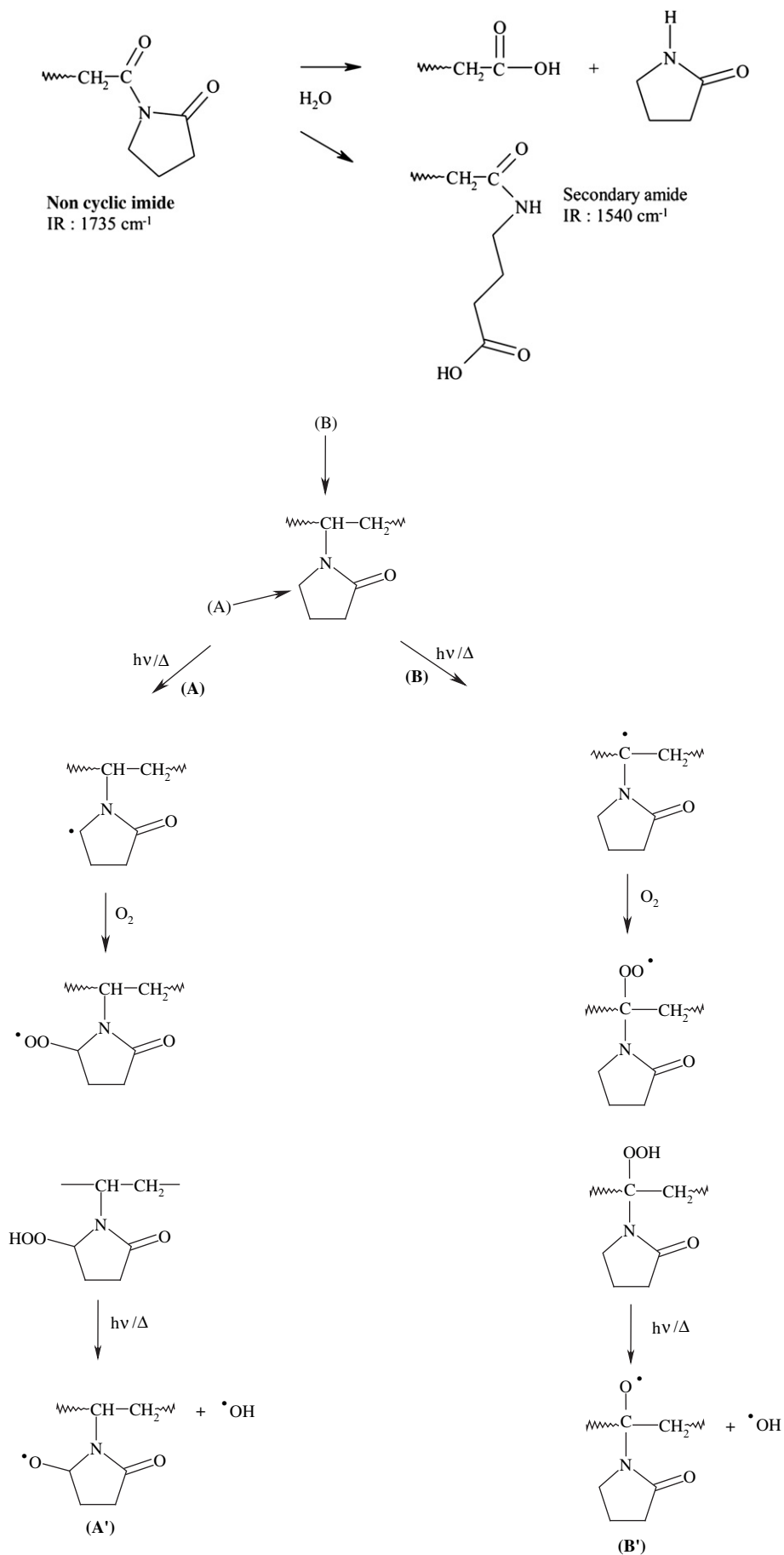
2) Evolution of alkoxy radical (B')



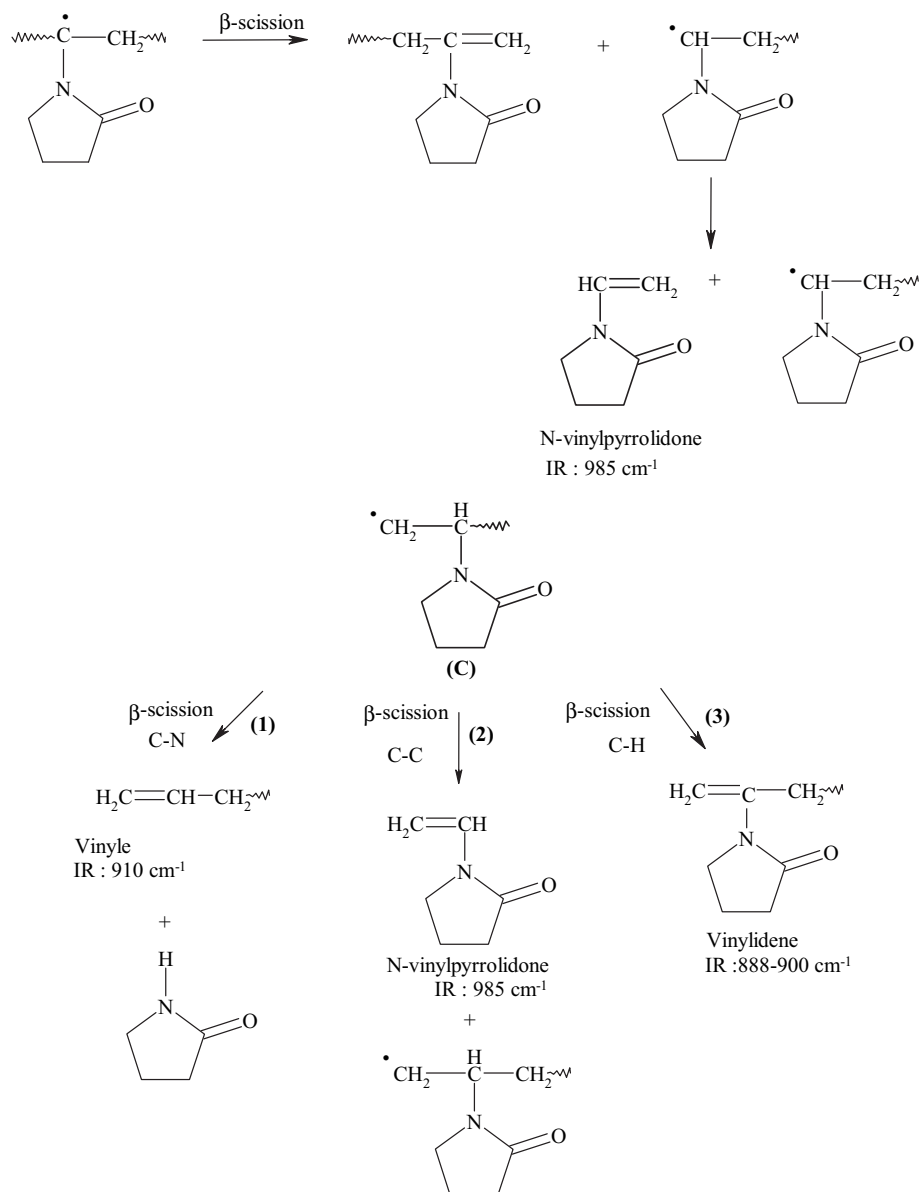
a) The evolution of the alkoxy radical B' by β -scission of the main chain produces imide groups (1735 cm^{-1}) and a primary alkyl radical (C). Reaction of this radical with oxygen leads to the formation of carboxylic acids.

Carboxylic acids are also obtained as end groups by hydrolysis of the non-cyclic imides. This reaction results in either the formation of 2-pyrrolidone or the ring opening of the pyrrolidone group.





Scheme 3. Mechanism of hydroperoxide formation.



Scheme 4. Possible evolutions of tertiary radical (B) and primary radical (C) without oxygen fixation.

There is another possible route concerning the tertiary alkyl radical (C), which could explain the formation of unsaturated products. As proposed in Scheme 4, the alkyl radical can indeed decompose through three different β -scission processes:

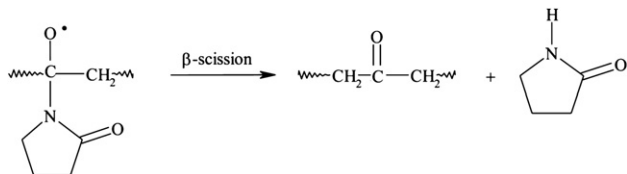
- 3) (C-N) (Route 1) giving a vinyl group and releasing 2-pyrrolidone.
- 4) (C-C) (Route 2) releasing molecules of N-vinylpyrrolidone.
- 5) (C-H) (Route 3) giving rise to macromolecular vinylidenes (this route might be unlikely due to the higher bond energy)

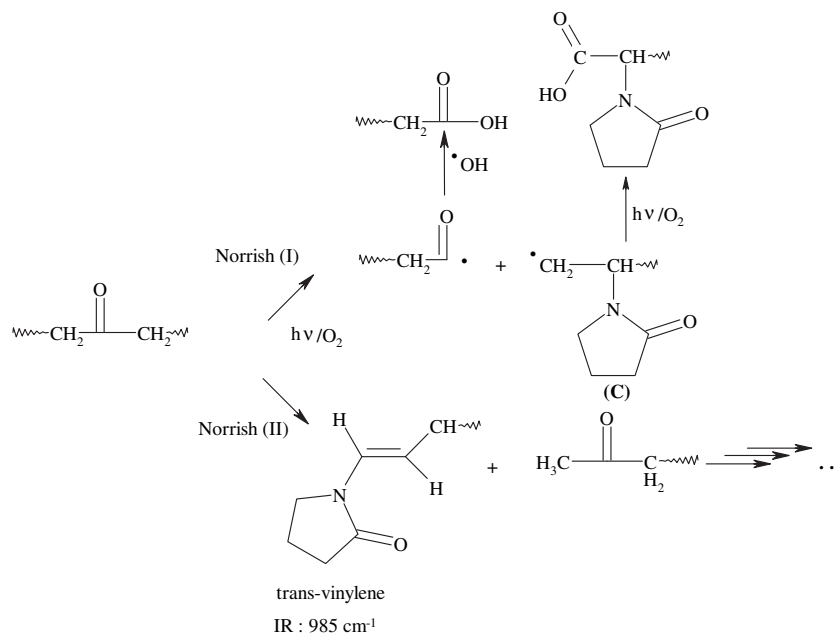
- b) A second route of evolution for the radical (B') is β -scission through the C-N bond, which leads to the formation of a macromolecular ketone and the release of 2-pyrrolidone.

Ketones are photochemically unstable and can decompose via Norrish I or Norrish II reactions. The Norrish I reaction leads to the formation of carboxylic acids, while the Norrish II reaction leads to the formation of the end-chain ketones and unsaturation (Scheme 5) detected at 985 cm⁻¹.

3.7. Influence of the physical state: solid vs. solution

The results reported above show that the reactions of PVP photooxidation strongly depend on the physical state of the polymer. The same photoproducts are formed in the solid state as in aqueous solution, but their relative concentrations are different. Photooxidation of PVP in the solid state leads to 70% of insoluble fractions, whereas, in aqueous solution, photooxidation primarily





Scheme 5. Norrish reactions.

produces chain scissions. Moreover, in the solid state, the relative rate of formation of the unsaturated photoproducts is more important than in aqueous solution, and the ratio of cyclic unsaturation vs. imides is higher (Table 2). This influence of the medium on the mechanism of PVP photooxidation can be explained by the differences between the mobility of the macromolecular chains in the solid state vs. in an aqueous solution. Moreover, the stationary concentration of oxygen is different in both media and oxygen diffusion is easier in the solution, which favours the formation of oxidation products in this case.

4. Conclusions

The results reported in this article show that PVP is very sensitive to photooxidation. UV-light-induced oxidation of PVP can be described as a succession of reactions that can occur in a concerted manner, and start with a radical attack on the carbon atom in the α -position of the nitrogen atom.

Two different alkoxy radicals can be formed: Secondary (A) and tertiary (B) radicals. The oxidation routes that involve the tertiary alkoxy radical (B) lead to macromolecular chain scissions, whereas the routes involving the secondary alkoxy radical (A) produce only bond scissions in the pyrrolidone ring and not in the macromolecular backbone.

Our results show that the degradation mechanisms of solid state PVP and PVP in an aqueous solution are significantly different. The main difference between the photoproducts formed under conditions of photooxidation for PVP in the solid state and in aqueous solution concerns the ratio of unsaturated products and cyclic imides. In addition, water was not observed to react with intermediate species or final products. Moreover, there was no evidence for the contribution of an ionic mechanism.

These conclusions concerning the photooxidation of PVP are different from those reported in a previous study investigating the photooxidation of poly(ethylene oxide) (PEO), which is also a water-soluble polymer [24]. In the case of PEO, the photoproducts formed in the solid state were shown to react with water, producing different final photoproducts when PEO was oxidized in

an aqueous medium. The comparison of these two polymers shows that, from a general point of view related to the photodegradation of water-soluble polymers in an aqueous solution, no universal rules and conclusions can be drawn, and each water-soluble polymer needs to be individually investigated.

Acknowledgements

The authors are grateful to Dr P. Wong Wah Chung and B. Legeret for the technical support of SPME experiments.

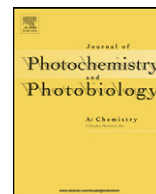
References

- [1] Frank HP, Polym J. Science 1954;12:565–76.
- [2] Polyvinylpyrrolidone – PVP in water-soluble synthetic polymers, 146–93.
- [3] Doneux C, Caudano R, Delhalle J, Leonard-Stibbe E, Charlier J, Bureau C, et al. Langmuir 1997;13:4898–905.
- [4] Frank HP, Polym J. Science 1953;10(4):371–8.
- [5] Blecher L, Lorenz DH, Lowd HL, Wood AS, Wyman DP. Handbook of water-soluble gums and resins. In: Davidson RL, editor. New-York: McGraw-Hill; 1980 [Chapter 21].
- [6] Trimpin S, Eichhorn P, Räder HJ, Müllen K, Knepper TP. J Chromatog A 2001;938(1–2):67–77.
- [7] Benamer S, Mahlous M, Boukrif A, Mansouri B, Larbi Youssef S. Nucl Instrum Methods Phys B 2006;248(2):284–90.
- [8] Charlshby A, Alexander P. Nature 1955:699–709.
- [9] Davis EJ, Senogles E. Aust J Chem 1981;34:1413–21.
- [10] Peniche C, Zaldivar D, Pazos M, Paz S, Bulay A, San Roman JJ. Appl Polym Sci 1993;50:485–93.
- [11] Gauvin P, Philippart JL, Lemaire J. Makromol Chem 1985;186:1167–80.
- [12] Gauvin P, Lemaire J. Makromol Chem 1987;188:971–86.
- [13] Gardette JL, Posada F, Philippart JL, Kappler P. Macromol Symp 1997;115: 53–67.
- [14] Roger A, Sallet D, Lemaire J. Macromolecules 1986;19(3):579–84.
- [15] Hall Jr HK, Zbinden RJ. Am Chem Soc 1958;80:6428.
- [16] Lin-Vien D, Colthup NB, Fateley WG, Grasselli JG. The handbook of infrared Raman characteristic of organic molecules. Academic Press, Inc.; 1991.
- [17] Emsley AM, Heywood RJ. Polym Degrad Stab 1995;49:145–9.
- [18] Viebke J, Elble E, Gedde UW. Polym Eng Sci 1996;36(4):458–66.
- [19] Philippart JL, Posada F, Gardette JL. Polym Degrad Stab 1995;49:285–90.
- [20] Hakkarainen M, Gröning M, Albertsson A-C. J Appl Polym Sci 2003;89:867–73.
- [21] Hakkarainen M. Adv Polym Sci 2008;211:23–50.
- [22] Rabek JF. Photodegradation of polymers. Berlin/Heidelberg: Springer; 1996.
- [23] Marchant RE, Yu D, Khoo CJ. Polym Sci Part A Polym Chem 1989;27:881–95.
- [24] Hassouna F, Morlat-Therias S, Maillhot G, Gardette JL. Polym Degrad Stab 2007;92:2042–50.



Contents lists available at ScienceDirect

Journal of Photochemistry and Photobiology A: Chemistry

journal homepage: www.elsevier.com/locate/jphotochem

Influence of iron salts on the photooxidation of poly(N-vinylpyrrolidone) in aqueous solution

Fatima Hassouna^{a,b,1}, Gilles Mailhot^{a,b,*}, Sandrine Morlat-Thélias^{a,b}, Jean-Luc Gardette^{a,b}^a Clermont université, Université Blaise Pascal, Laboratoire de Photochimie Moléculaire et Macromoléculaire, BP 10448, F-63000 Clermont-Ferrand, France^b CNRS, UMR 6505, BP 80026, F-63171 Aubière, France

ARTICLE INFO

Article history:

Received 3 November 2010

Received in revised form

17 December 2010

Accepted 12 January 2011

Available online 22 January 2011

Keywords:

Poly(N-vinylpyrrolidone) (PVP)

Iron

Photochemistry

Water

Hydrogel

Mineralisation

ABSTRACT

This article reports on the effect of UV–vis radiation ($\lambda \geq 300$ nm) on the degradation of poly(N-vinylpyrrolidone) PVP photoinduced by Fe(III) in aqueous solution and in the presence of oxygen. The formation of oxidation products was followed by infrared analysis of deposits obtained after evaporation of water and by UV–vis analysis of the irradiated polymer solutions. Size exclusion chromatography (SEC) was used for monitoring the variations of molar weight and intrinsic viscosity with irradiation time. Total organic carbon (TOC) measurements were performed with the aim of checking the mineralisation of aqueous solutions.

Depending on the concentration of Fe(III), the concentration of PVP and the pH of the solution, we were able to show that the photooxidation of PVP leads to a chain scission and to a cross-linking mechanism, contrary to photooxidation of PVP in the absence of Fe(III) which only involves a mechanism of chain scission. A mechanism of PVP photooxidation until its possible mineralisation is proposed, taking into account the concentration of Fe(III) in the solution.

© 2011 Elsevier B.V. All rights reserved.

1. Introduction

Because of its unique chemical and physical properties, Poly(N-vinylpyrrolidone) (PVP) has found significant use in pharmaceuticals, cosmetics (hairsprays), medicine (blood plasma extender), construction industry (in plywood, sealing composites, etc.), textiles, paper, detergents, etc. [1,2]. After use, depending on its domain of application, this polymer can be discharged as dilute aqueous solutions or into solid waste disposal systems. Effluents entering aqueous wastewater streams may enter the environment directly. Like the majority of synthetic polymers, PVP is not sensitive to biodegradation [3] so its fate in the environment is uncertain. Moreover, due to its water solubility, PVP has received less attention in the media than packaging plastics, which visibly litter the countryside and contribute to landfill overload.

The degradation of PVP in the environment may take place through several paths. Among the different abiotic degradation processes, solar irradiation is one of the main factors responsible for pollutant degradation in the aquatic environment. In a recent

paper [4], we reported work on the photooxidation of poly(N-vinylpyrrolidone) (PVP) under long wavelengths ($\lambda \geq 300$ nm) in solid state and in aqueous solution. Based on the results of photooxidation, a mechanism accounting for the main routes of oxidation can be proposed.

The photochemical evolution of PVP under oxidative conditions under long wavelengths ($\lambda \geq 300$ nm) involves two types of hydroperoxides. The oxidation path, leading to scission of the macromolecular chain, involves the formation of a tertiary hydroperoxide, whereas in the path involving the formation of a secondary product, the decomposition of these hydroperoxides leads only to bond scission of the pyrrolidone ring.

If we examine the role of water in the orientation of the photooxidation mechanism, we notice that in the solid state, the rate of formed unsaturation is higher than in aqueous solution. The ratio between unsaturations and cyclic imides is higher in the solid state. There is thus a significant influence of the medium on the PVP degradation mechanism.

In this paper, we have investigated the influence of Fe(III) salts, which is a transition metal naturally present in the aquatic compartments, on the photochemical behaviour of PVP in aqueous solution. The influence of Fe(III) chloride on the photodegradation under 254 nm irradiation of PVP aqueous solution has been studied by Kaczmarek et al. [5]. The efficiency of FeCl₃ on the rate of photooxidation was compared with the effect caused by H₂O₂. It was concluded that the photo-oxidative degradation of PVP was accelerated by either FeCl₃ or H₂O₂. However, •OH and •OOH radicals,

* Corresponding author at: Laboratoire de Photochimie Moléculaire et Macromoléculaire, Université Blaise Pascal, UMR CNRS-UBP 6505, BP 80026, F-63171 Aubière Cedex, France. Tel.: +33 0 73 40 71 73; fax: +33 0 73 40 77 00.

E-mail address: gilles.mailhot@univ-bpclermont.fr (G. Mailhot).

¹ Now at Centre de Recherche Public Henri Tudor, Site du technoport, 66, rue de Luxembourg, BP 144, L-4002 Esch-sur-Alzette, Luxembourg.

which are generated from the decomposition of H_2O_2 , were more efficient accelerating agents than Cl^\bullet radicals. Moreover, the high concentration of carbonyl groups detected by IR spectroscopy is in favour of efficient Norrish I and II type reactions leading to a fast decomposition of PVP. A relatively high amount of gel was formed in PVP solution in the presence of H_2O_2 , which points out that in this case recombination of macroradicals dominates the disproportionation or reaction between small radicals and macroradicals. It seems that in the presence of H_2O_2 , the occurrence of ring opening reaction in PVP is more likely and the macroradicals formed in this process also take part in the termination of degradation. Interestingly, both the competing and opposing reactions of chain scission and cross-linking are efficiently accelerated for PVP irradiated in H_2O_2 solution compared to pure PVP.

In previous works, the photodegradation of pollutants induced by Fe(III) has been reported [6–8]. It has been revealed that the attack by $\bullet\text{OH}$ radicals arising from Fe(III) species in the excited state is a very efficient process. Indeed, Fe(III) aquacomplexes can absorb solar light and undergo a photoredox process giving rise to Fe(II) and hydroxyl radicals [9,10]. Among the Fe(III) aquo-complexes, $\text{Fe}(\text{OH})^{2+}$ (which refers to $[\text{Fe}(\text{H}_2\text{O})_5(\text{OH})]^{2+}$) is photolysed with the highest quantum yield [10] according to the following reaction:



Hydroxyl radicals are known to be very reactive species, reacting with most organic substrates with rate constants that are limited by diffusion. The photodegradation of pollutants induced by Fe(III) [11,12] has been previously investigated and in all cases, it has been concluded that it was a useful process for the elimination of pollutants in water.

The present work deals with the photodegradation of PVP in aqueous solution induced by Fe(III) aquacomplexes until it is completely mineralised. The role of Fe(III) species is discussed and a mechanism of PVP degradation is proposed.

2. Materials and methods

2.1. Materials

All reagents were of the purest grade commercially available and were used without further purification.

Poly(N-vinylpyrrolidone) (PVP) sample was supplied by Scientific Polymer Products. The average molar weight of the polymer was $360,000 \text{ g mol}^{-1}$. Ferric perchlorate nonahydrate ($\text{Fe}(\text{ClO}_4)_3 \cdot 9\text{H}_2\text{O}$; >97%) was a Fluka product kept in a desiccator. Hydroxylamine chlorhydrate and ferrozine (3-(2-pyridyl)-5,6-diphenyl-1,2,4-triazine-4,4'-disulfonic acid, sodium salt, 97%) were purchased from Aldrich.

Water was purified by a Millipore Ultra-Pure System ($\rho = 18.2 \text{ M}\Omega \text{ cm}$). PVP solutions of 6.25% (62.5 mg mL^{-1}), 1.25% (12.5 mg mL^{-1}) and 0.1% (1.0 mg mL^{-1}) of wt.% were prepared by dissolving PVP into deionised water with mild stirring overnight at room temperature. The natural pH of aqueous solutions of PVP was around 4.2. Acidified solution (pH 3.1) was obtained by adding drops of diluted HClO_4 . HClO_4 was chosen for acidifying the aqueous solution because ClO_4^- is far less reactive and photosensitizer than Cl^- , and is the counter anion of the ferric salt used. No buffer was used in order to avoid any contamination of the solution and any interaction with iron.

Solutions with iron were prepared by dissolving $\text{Fe}(\text{ClO}_4)_3$ in PVP aqueous solutions. The pH of the solution changed from 4.2 to 3.1 or 4.2 to 2.95 after the addition to PVP aqueous solution ($[\text{PVP}] = 62.5 \text{ mg mL}^{-1}$) of $\text{Fe}(\text{ClO}_4)_3$ at a concentration of $6 \times 10^{-4} \text{ mol L}^{-1}$ or $1.2 \times 10^{-3} \text{ mol L}^{-1}$, respectively. Solutions with

hydrogen peroxide were prepared by adding different concentrations of H_2O_2 (10^{-1} , 10^{-2} , 10^{-3} , 1.2×10^{-3} and $6 \times 10^{-4} \text{ mol L}^{-1}$) into PVP aqueous solutions ($[\text{PVP}] = 62.5 \text{ mg mL}^{-1}$).

Relatively concentrated polymer solution (6.25%) was chosen in order to follow the chemical modifications of the irradiated solutions by IR analysis of deposits on ZnSe windows. FTIR transmission spectra were recorded for thin deposits of oxidised samples of PVP, which were obtained by evaporation of aliquots of irradiated aqueous solution of PVP. The samples were dried at room temperature for 24 h.

Unless otherwise noted, our experiments were performed with $[\text{PVP}] = 62.5 \text{ mg mL}^{-1}$ (6.25%) and $[\text{Fe}(\text{III})] = 6 \times 10^{-4} \text{ mol L}^{-1}$.

2.2. Irradiation

PVP aqueous solutions were irradiated in a SEPAP 14/24 unit at 20°C . The chamber is an elliptical reactor equipped with one medium-pressure mercury lamp (Mazda MA 400) in vertical position at one focal axis of the chamber. Wavelengths below 300 nm were filtered by a glass envelope. At the second focal axis of the chamber, the aqueous solution of PVP was placed in a Pyrex reactor cooled by water circulation. The temperature of the solution was maintained at 20°C in order to avoid water evaporation.

2.3. Chemical and spectrophotometric analysis

Fe(II) concentration was determined by complexometry with *ortho*-phenanthroline, using $\varepsilon_{510} = 1.118 \times 10^4 \text{ L mol}^{-1} \text{ cm}^{-1}$ for Fe(II)-phenanthroline complex [13]. Total iron concentration was determined after reduction of Fe(III) species with a solution of hydroxylamine chlorhydrate (3 mol L^{-1}) prepared by dissolution of 104.25 mg in a 500 mL flask into 200 mL 32% HCl and then completed with distilled water. Ferrozine forms a strong coloured complex with Fe(II). In a 5 mL flask were added 0.25 mL sample, 1.5 mL water and 0.5 mL of hydroxylamine solution (3 mol L^{-1}). After stirring vigorously and waiting for 10 min, it was added 0.5 mL of ferrozine (0.02 mol L^{-1}), 1 mL ammonium acetate buffer 0.1 N and water to complete to 5 mL. After stirring, absorbance was measured at 562 nm. The accuracy of the method is $\pm 0.1 \mu\text{mol L}^{-1}$.

Infrared spectra were recorded with a Nicolet 760-FTIR spectrometer, working with OMNIC Software. Spectra were obtained using 32 scans summation and 4 cm^{-1} resolution. The thickness (e , in μm) of the non-photooxidised samples was calibrated by measuring the absorbance (OD) at 1370 cm^{-1} , which corresponds to a vibrational band of (C–H) bending mode. The thickness dependence of the absorbance obeyed the equation $\text{OD} = 0.0175 \times e$. UV–vis spectra of solutions were recorded on a Cary 3 double beam spectrophotometer (Varian).

The variations of molar weight, viscosity and molar weight distribution (polydispersity index, Mw/Mn) were measured by size exclusion chromatography (SEC) using a Viscotek chromatograph working with a differential refractometer detection (Viscotek VE 3580), a viscometer detector (Viscotek TriSec Model 270) and a linear column (TSK/Ref: GMPWXL). The analyses were performed with NaNO_3 $0.1 \text{ mol L}^{-1}/\text{CH}_3\text{CN}$ (80/20) as eluent at a flow rate of 0.7 mL min^{-1} . The equipment was calibrated with PEO standards. Molar weight distributions were calculated with OMNISEC Software.

Total organic carbon (TOC) in aqueous solution was measured using a Total Organic Carbon analyzer Shimadzu model TOC-5050A. The Shimadzu TOC-5050A is capable of performing total carbon (TC) analyses by combustion and inorganic carbon (IC) analyses by oxidation in 25% H_3PO_4 solution. TOC measurements were obtained by calculating the difference between TC and IC measurements. Calibration curves within the range of 0–500 mg L^{-1} for TC and 0–100 mg L^{-1} for IC were obtained using potassium hydrogen phthalate for total carbon and sodium hydro-

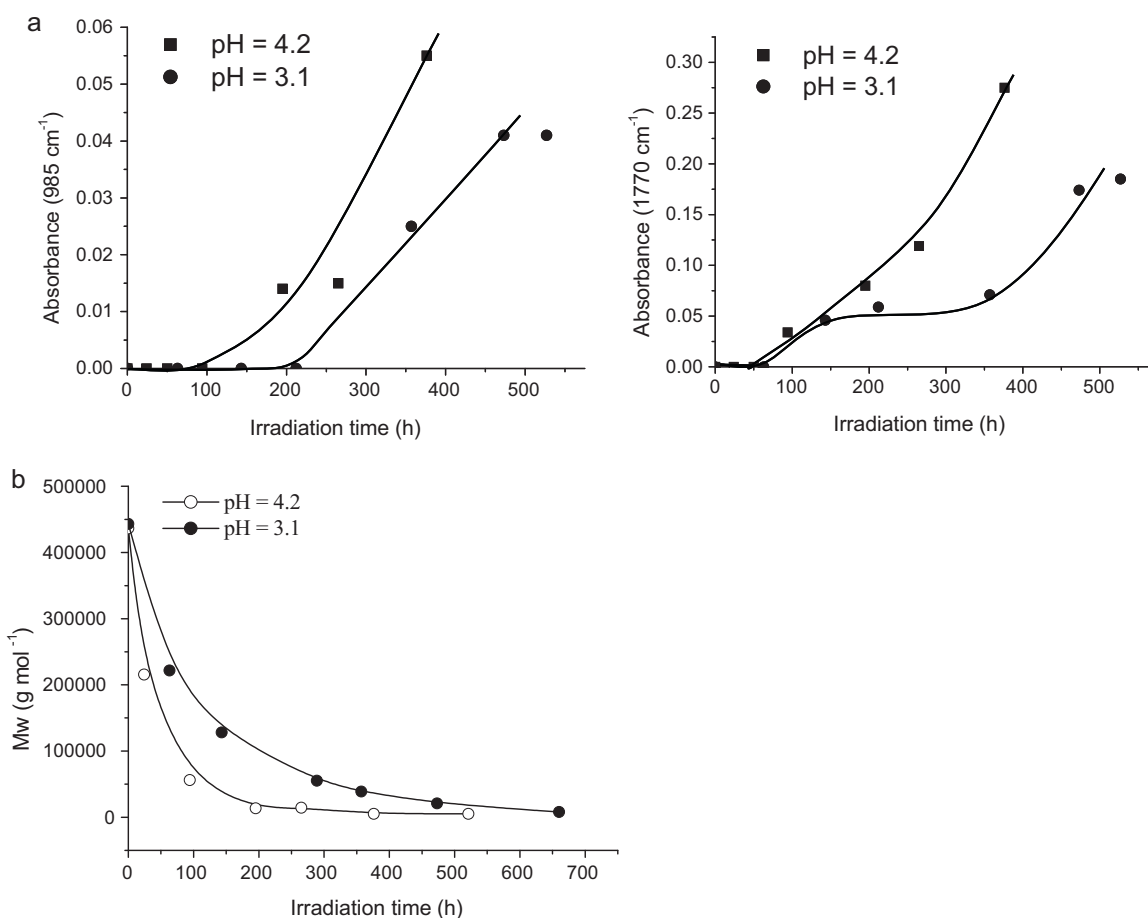


Fig. 1. (a) Evolution of absorbance at 1770, and 985 cm^{-1} , of PVP aqueous solutions as a function of irradiation time, $\text{pH}_{\text{initial}} = 4.2$ and 3.1, $[\text{PVP}] = 62.5 \text{ mg mL}^{-1}$. (b) Evolution of PVP molar weight (Mw) as a function of irradiation time for PVP aqueous solutions at pH 4.2 and 3.1, $[\text{PVP}] = 62.5 \text{ mg mL}^{-1}$.

gen carbonate with potassium carbonate for inorganic carbon.

The insoluble fraction of the samples was evaluated by gravimetric measurements for different times of irradiation. After each exposure time of PVP aqueous solution, the solutions were filtered and the insoluble fractions were dried outdoors. The films obtained were then put into a glass phial with water, a solvent of PVP. The amount of water was adjusted in order to obtain the same specific concentration for all the mixtures; typically $M_{\text{total}}/V_{\text{water}} = 3.5 \text{ mg mL}^{-1}$. The phials were then hermetically sealed and hidden from the daylight for 96 h. The gel obtained was dried until constant weight. The gel fraction is defined as the ratio between the weight of the dry gel ($M_{\text{insoluble}}$) and the weight of PVP (M_{total}).

$$\text{Gel fraction (G}_f\text{)} = \frac{[M_{\text{insoluble}}]}{[M_{\text{total}}]}$$

3. Results and discussion

Firstly, before approaching the study of the photooxidation of PVP aqueous solution in presence of Fe(III) (pH 3.1), the PVP photooxidation was studied at the same pH but without Fe(III). The solution was acidified with HClO_4 in order to study the effect of the pH on the photooxidation of PVP aqueous solution before investigating the effect of the Fe(III). Indeed, during the dissolution of $\text{Fe}(\text{ClO}_4)_3$, perchloric acid is formed in the aqueous solution. Moreover, a dark experiment at room temperature with PVP and Fe(III) in aqueous solution was performed. No degradation of PVP and no interaction between PVP and Fe(III) were observed after few days.

3.1. Photooxidation of PVP aqueous solution at $\text{pH}_{\text{initial}} = 3.1$

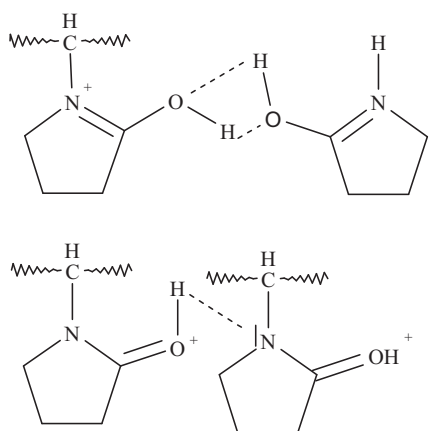
3.1.1. PVP aqueous solution in the presence of perchloric acid

The IR spectrum of PVP deposit obtained from aqueous solution in presence of HClO_4 shows two new absorption bands at 1095 and 620 cm^{-1} compared to IR spectrum of natural PVP aqueous solution. The intensity of these two bands increases with the concentration of HClO_4 . The same bands were observed in the spectrum of HClO_4 . These two bands are thus part from ClO_4^- vibrations.

3.1.2. Photooxidation process

During photooxidation of PVP aqueous solution in presence of oxygen at 20 °C (pH 3.1), chemical modifications of PVP were followed by IR analysis. Deposits, of about 20 μm , were obtained by casting from aqueous irradiated solutions onto ZnSe wafers. After evaporation of water, the thickness of the deposits was determined by IR. The general evolution of the IR spectra of PVP upon irradiation at pH 3.1 in aqueous solution is comparable to that of PVP aqueous solution at pH 4.2 [4]. Furthermore, the stoichiometries of the different photoproducts are identical. The pH of the solution decreased weakly during irradiation, from 3.1 to 3.0 after 300 h.

Kinetics of photoproducts formation at pH 4.2 and 3.1 were compared by studying the evolution of the absorbance measured at 1770 cm^{-1} (succinimide rings), and 985 cm^{-1} (unsaturations) (Fig. 1a). These rates are slower at pH 3.1 than at pH 4.2. At pH 3.1, an induction period of around 50 h is observed before the detection of photoproducts. This indicates that the rate of photooxidation of PVP decreases in the presence of HClO_4 .



Scheme 1. Possible hydrogen bonds to be formed between PVP chains in acidic solution (pH 3.1).

The evolution of average molar weights of PVP in aqueous solution (pH 3.1) during the photooxidation was characterized by SEC and compared with the trend observed at pH 4.2 (Fig. 1b). A decrease of the molar weight was observed during the irradiation, which implies a mechanism of chain scission, but the decrease of molar weight was faster when the initial pH of the solution was 4.2 rather than 3.1. This means that the mechanism of chain scissions slowed down in the presence of HClO_4 . This result is in agreement with the evolution of IR spectra commented previously.

One explanation of the slower photooxidation of PVP in presence of HClO_4 is that in relatively acidic solution, protonation of PVP takes place on the oxygen atom, whereas protonation on the nitrogen atom would destroy the conjugation [14]. Indeed, PVP can be considered as a Lewis polybase [15] and the electronic configuration of the polymer after protonation is consequently modified. Interactions by hydrogen bonding can take place between PVP macromolecular chains. The same behaviour was observed when carboxylic acids or polyacids were added to the PVP aqueous solution [15–17] (Scheme 1).

3.2. Photooxidation of PVP aqueous solution in the presence of Fe(III)

3.2.1. IR analysis

After dissolution of Fe(III) in PVP aqueous solution, the pH of the solution decreased from 4.2 to 3.2. Irradiation of this solution led to important modifications of IR spectra obtained on deposits of aliquots of the polymer aqueous solution on ZnSe plate.

Several absorption bands were observed from the beginning of irradiation (Fig. 2). Absorption bands corresponding to succinimide ring (1770 and 820 cm^{-1}) appeared from the first 8 h of irradiation while absorption bands corresponding to unsaturations (1060 , 985 and 785 cm^{-1}) were observed after an induction period of 25 h. These absorption bands are similar to those observed during the photooxidation of PVP aqueous solution in absence of Fe(III), which indicates that the oxidation products are identical. Furthermore, the photoproducts of PVP in water in presence and in absence of Fe(III) represent the same percentage as a function of degraded PVP. As a contrary, it is important to note that the pH increased from 3.2 to 3.4 after 400 h of photoageing and reached the value of 3.8 after 500 h. The pH of the aqueous solution PVP/Fe(III) tends to increase during the irradiation contrary to the behaviour under irradiation of the PVP aqueous solution in absence of Fe(III). This observation has an important consequence on the speciation of iron species present in aqueous solution.

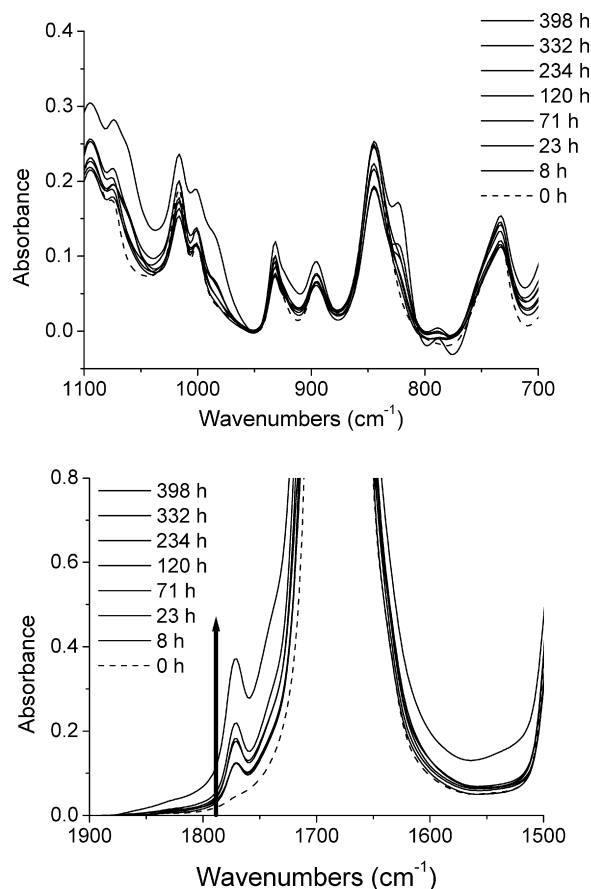


Fig. 2. FTIR spectra of deposits obtained from a PVP aqueous solution in the presence of Fe(III) during photooxidation (pH 3.2, [PVP] = 62.5 mg mL^{-1} , [Fe(III)] = $6 \times 10^{-4}\text{ mol L}^{-1}$).

3.2.2. Kinetics of photooxidation

The variations of absorbance at 1770 and 985 cm^{-1} as a function of irradiation time of PVP aqueous solution are plotted in Fig. 3. These results show that in the presence of Fe(III), the rate of formation of the photoproducts is faster during the first hours of irradiation. The degradation kinetics in the presence of Fe(III) allow confirming the correlations of the absorption bands at 1770 and 820 cm^{-1} assigned to succinimide rings [4] as well as unsaturations at 785 and 985 cm^{-1} . Indeed, oxidation products corresponding to the unsaturations appear after an induction period of 25 h and the oxidation products corresponding to the succinimide rings are detected from the beginning of the irradiation. In the absence of Fe(III), the different photoproducts can be observed beginning after 50–80 h of irradiation. In presence of Fe(III), during the first hours of irradiation, the rate of formation of the photoproducts is significant. Indeed, as shown in a previous article devoted to the influence of Fe(III) on the photodegradation of PEO [18], the monomeric species $\text{Fe}(\text{OH})^{2+}$ are predominant in aqueous solution at pHs between 2.5 and 5.0, and can be considered as the most important source of $\bullet\text{OH}$ radicals production (reaction 1) under exposure to light.

The concentration of Fe(II) was also measured all along the irradiation. The results show a very fast increase in the concentration of Fe(II) at the beginning of the irradiation, which mainly results from the photoredox process of $\text{Fe}(\text{OH})^{2+}$ species. Fe(III) is mainly transformed into Fe(II) and the formation of $\bullet\text{OH}$ is maximum. Then, Fe(II) concentration reaches a constant value corresponding to a photostationary equilibrium between Fe(III) and Fe(II) in the presence of organic compounds ($[\text{Fe(II)}] \approx 5.5 \times 10^{-4}\text{ mol L}^{-1}$ at the

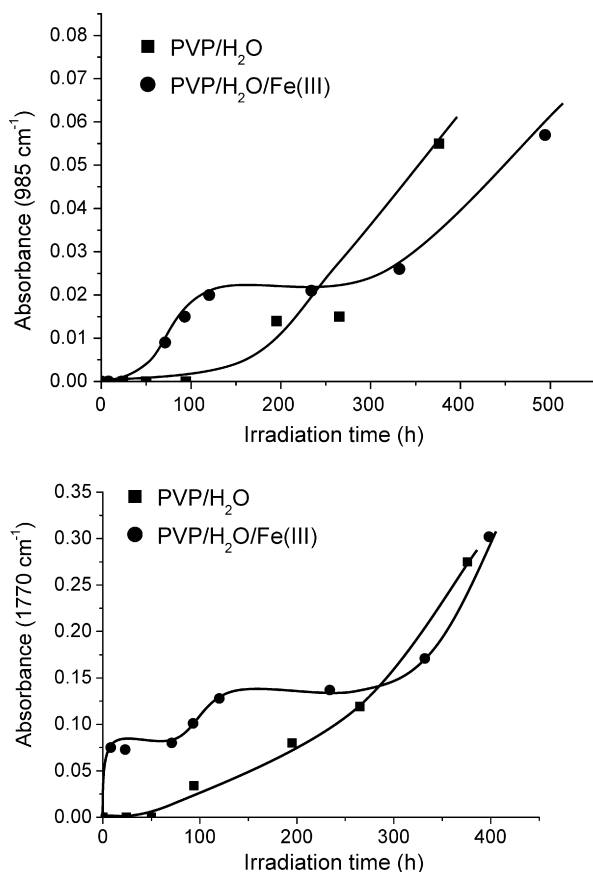


Fig. 3. Evolution of absorbance at 1770 and 985 cm^{-1} , of PVP aqueous solution as a function of irradiation time in presence of Fe(III) ($\text{pH}_{\text{initial}} = 3.1$, $[\text{PVP}] = 62.5 \text{ mg mL}^{-1}$, $[\text{Fe(III)}] = 6 \times 10^{-4} \text{ mol L}^{-1}$).

plateau), as reported in a previous study on PEO photodegradation [18]. This photostationary equilibrium can be explained by a photocatalytic cycle between Fe(III) and Fe(II) species [18].

The second phase of the kinetic curves of the photooxidation of PVP aqueous solution in presence of Fe(III) (between 100 h and 300 h) (Fig. 3) corresponds to a slowing down of the rate of formation of the photoproducts. This can be explained by the presence, after the first period where Fe(OH)^{2+} is photodegraded, of a photocatalytic cycle of Fe(III)/Fe(II) in which radical species ($\bullet\text{OH}$) are formed regularly in much smaller amount. This second phase can correspond also to the induction observed in the experiment without iron. After 350 h, the formation rate of the photoproducts increases again and resembles the kinetics obtained in the absence of iron. Iron has no more photochemical impact in the phototransformation of PVP.

3.2.3. SEC analysis

The changes provoked by the irradiation of PVP aqueous solution in the presence of Fe(III) (Fig. 4) can be characterized by the decrease in average molar weights, which implies several chain scissions. The decrease of molar weights is faster during the first hours of irradiation in presence of Fe(III). This result clearly shows the photoinductive effect of Fe(III) due to the production of $\bullet\text{OH}$ under irradiation. The mechanism of chain scissions is thus accelerated in presence of Fe(III). Between 8 and 100 h of irradiation, the average molar weight is almost constant. The invariance of the average molar weight can be correlated with the kinetics of formation of the photoproducts which show the same slow-down after 8 h of irradiation. This phenomenon can be attributed to the strong decrease of $\bullet\text{OH}$ hydroxyl radical production and/or to the

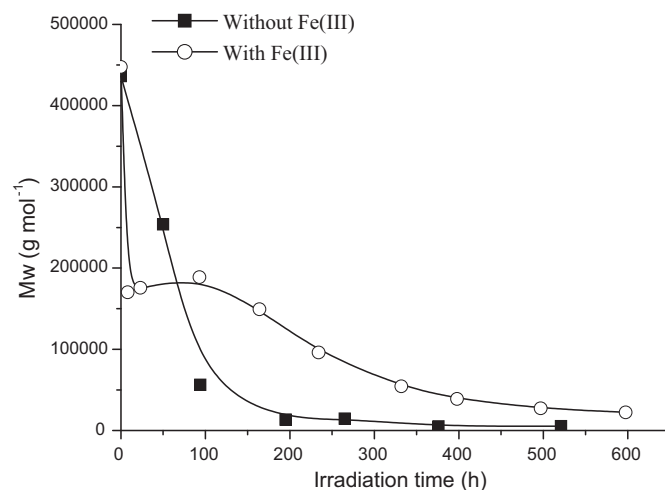


Fig. 4. Evolution of PVP molar weight (M_w) as a function of irradiation time in the presence and in the absence of iron ($[\text{Fe(III)}] = 6 \times 10^{-4} \text{ mol L}^{-1}$, $[\text{PVP}] = 62.5 \text{ mg mL}^{-1}$).

competition between a mechanism of chain scissions and cross-linking in which an equilibrium is established.

3.3. Influence of Fe(III) concentration

The influence of Fe(III) concentration on the photooxidation of PVP in water was followed by IR spectroscopy, UV-vis spectrophotometry and by SEC analyses for two concentrations of Fe(III): 6×10^{-4} and $1.2 \times 10^{-3} \text{ mol L}^{-1}$. The increase of Fe(III) concentration from 6×10^{-4} to $1.2 \times 10^{-3} \text{ mol L}^{-1}$ in PVP aqueous solution ($[\text{PVP}] = 62.5 \text{ mg mL}^{-1}$) leads to the formation of hydrogel after 350 h of irradiation. This hydrogel was not observed for concentration of Fe(III) equal to $6 \times 10^{-4} \text{ mol L}^{-1}$.

3.3.1. IR analysis

The presence of Fe(III) at a concentration of $1.2 \times 10^{-3} \text{ mol L}^{-1}$ in PVP aqueous solution leads to the decrease of the pH of the solution from 4.2 to 2.9. IR analysis did not show any evolution of PVP between 0 and 300 h of irradiation, which means that the presence of iron with higher concentration slows down considerably the appearance of the photoproducts as imides and unsaturations. It is important to note that after 350 h of photoageing, the solution became a hydrogel. The pH of the solution evolved during the photooxidation, it increased from 2.9 to 3.2 after 400 h of irradiation.

3.3.2. UV-vis analysis

The UV-vis spectra of PVP aqueous solution irradiated in the presence of Fe(III) ($1.2 \times 10^{-3} \text{ mol L}^{-1}$) showed mainly the disappearance of the absorption band at 297 nm corresponding to the transformation of Fe(III) to Fe(II). There were no significant changes in the absorption spectra of PVP in aqueous solution during 350 h of irradiation. After 350 h, the polymer in solution was a hydrogel and consequently it was not possible to continue its characterization by UV-vis spectrophotometry.

3.3.3. Hydrogel characterization

The cross-linking of PVP in aqueous solution was investigated by monitoring the insoluble fraction generated during irradiation. The nature of the hydrogel formed was also determined, namely reversible or permanent. The evolution of the insoluble fraction upon irradiation is represented in Fig. 5. During the first 200 h of irradiation, no insoluble fraction was measured. After that, an insoluble network of polymer appeared. The ratio of the insoluble part increased up to a plateau corresponding to 45% of insoluble fraction.

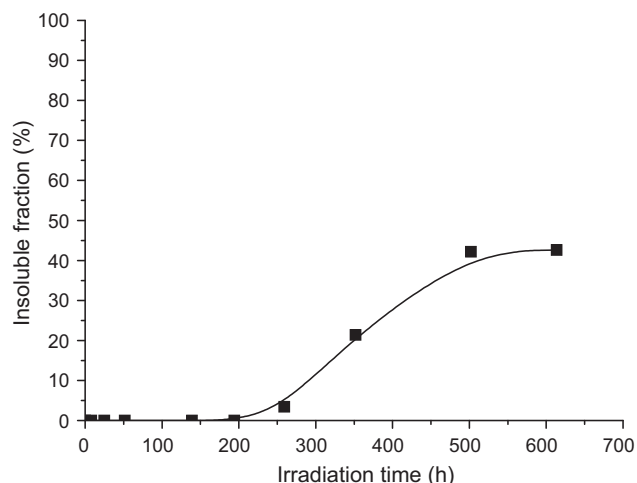


Fig. 5. Evolution of the insoluble fraction as a function of irradiation time ([PVP] = 62.5 mg mL⁻¹, [Fe(III)] = 1.2×10^{-3} mol L⁻¹, pH_{initial} = 2.9).

In order to determine the nature of the insoluble fraction, several tests were carried out. Indeed, several types of interactions can be at the origin of the formation of hydrogels. The cross-linking can proceed through the formation of covalent bonds involving the macroradical reactivity, through the formation of hydrogen bonds between the molecules of polymer or through iron chelation by the polymeric matrix. To elucidate the nature of the PVP cross-linking and the eventual involvement of iron species, three tests were performed: heating test, ferrozine test and the effect of H₂O₂.

3.3.4. Heating test

Heating a reversible hydrogel leads to the breaking of hydrogen bonds and consequently makes the polymer soluble, which constitutes a simple test. For that purpose, 0.81 g of the hydrogel was placed in 10 mL of ultra-pure water. The mixture was warmed at 80 °C hermetically during 10 h. After filtration of the mixture, the totality of the insoluble fraction was recovered. This result shows that the hydrogen bonds are not at the origin of the hydrogel formation.

3.3.5. Ferrozine test

The hypothesis according to which Fe(III) or Fe(II) was in interaction with photooxidized PVP leading to the formation of the reversible hydrogel was not dismissed even though this hypothesis remains not very probable. Indeed, UV–vis spectra recorded at various extents of the photochemical ageing did not show any absorption band which could correspond to the formation of a complex between iron and photooxidized PVP. Furthermore, chemical functions such as carboxylates or alcoholates susceptible to chelate iron were not observed by IR.

Nevertheless, a test that could allow us to definitively throw back the hypothesis of possible interaction of the photooxidised PVP with Fe(II) or Fe(III) was performed. This test consisted in a quantitative determination of the total iron using ferrozine, a very strong complexing agent of iron, in the hydrogel obtained after 500 h of irradiation. Indeed, if iron was responsible for the formation of the hydrogel by interaction with photooxidized PVP, the ferrozine would make PVP soluble again in water, since it can complex iron. However, the totality of the iron was recovered after this quantitative determination (1.2×10^{-3} mol L⁻¹) and the hydrogel was not dissolved in the aqueous solution in spite of drastic conditions of pH used in this titration of iron.

The two tests described above have shown that the hydrogel formed after irradiation of PVP aqueous solution in the presence of Fe(III) (1.2×10^{-3} mol L⁻¹) was not reversible. Neither the

hydrogen bonds nor the iron were responsible for the cross-linking of the polymer. This suggests that the formation of an hydrogel in presence of Fe(III) was probably due to intermolecular covalent bonds. Indeed, Fe(OH)²⁺ were the dominant species in moderately acidic aqueous solution (pH 2.9). The production of hydroxyl radicals •OH during initial periods of irradiation was very important as the concentration of Fe(III) was very high (1.2×10^{-3} mol L⁻¹). In PVP aqueous solution, hydroxyl radicals lead to the formation of macroalkyl radicals by the abstraction of hydrogen atom from macromolecules at backbone or on the pyrrolidone ring [4]. The macroradicals are likely to form covalent bond in an intermolecular cross-linking process, which involves recombination of radicals coming from two different macromolecules [19]. So, according to Fig. 5, the insoluble fraction for this concentration of Fe(III) during the first 200 h of irradiation is not observed. After that, the insoluble fraction increases very quickly and reaches a limit value corresponding to maximal insolubility, which suggests the presence of a cross-linked network in the polymeric matrix.

The photooxidation of PVP aqueous solution with two different concentrations of iron gives an evidence of the influence of the Fe(III) concentration. When the concentration of Fe(III) is more important (1.2×10^{-3} mol L⁻¹), the photoageing leads to the formation of a hydrogel while for a Fe(III) concentration of 6×10^{-4} mol L⁻¹, a mechanism of PVP degradation by chain scissions is predominant. In order to confirm the intervention of hydroxyl radicals (•OH) formed by direct photolysis of Fe(OH)²⁺ in the process of cross-linking of the polymer, aqueous solutions of PVP were irradiated in the presence of H₂O₂, which can be considered as another photochemical source of hydroxyl radicals.

3.3.6. Effect of H₂O₂

The photooxidation of PVP aqueous solution in the presence of H₂O₂ at different concentrations (10^{-1} , 10^{-2} , 10^{-3} , 6×10^{-4} mol L⁻¹) was investigated. Irradiation of PVP aqueous solution in presence of 10^{-1} mol L⁻¹ of H₂O₂ led to the appearance of three absorption bands, 785, 985 and 1060 cm⁻¹ after only 10 h of irradiation. The absorption bands corresponding to succinimide rings (820 and 1770 cm⁻¹) were not observed. After 10 h of irradiation, a hydrogel was formed. A deposit could be obtained by drying this hydrogel, but the IR spectra of the sample was too noisy. To obtain IR spectra of the hydrogel, the dry hydrogel was immersed in liquid nitrogen and crushed in a mortar to reduce it into powder. From this powder, KBr pellets were prepared. The IR spectra obtained from these pellets showed the absorption bands at 785, 985 and 1060 cm⁻¹, while the bands at 820 and 1770 cm⁻¹ were very weak.

UV–vis analysis did not show any evolution during the irradiation, which can be explained by the fact that the accumulation of unsaturated products is not significant. The pH of the aqueous solution remained constant during the first 10 h of irradiation. These experimental results (IR, UV–vis, pH measures) can be correlated. They show that the process leading to the formation of oxidation products is minor although photoproducts were observed by IR analysis.

The characterization of the hydrogel by measurement of the insoluble fraction as a function of irradiation time is presented in Fig. 6. At the highest concentration of H₂O₂ (10^{-1} mol L⁻¹) and after only 10 h of irradiation, 46% of the polymer became insoluble. After 13 h, the rate of insoluble fraction was maximal (67%) while from 100 h of irradiation a beginning of dissolution of the hydrogel was observed. At lower concentration of H₂O₂ (10^{-2} mol L⁻¹), the insoluble fraction of the polymer did not represent more than 20% and a complete dissolution was observed after 60 h of irradiation. When the concentration of H₂O₂ was divided by 10, the maximal rate of insoluble fraction decreased from 67% to 18%. Indeed, when the concentration of H₂O₂ decreased, the quantity of hydroxyl radicals

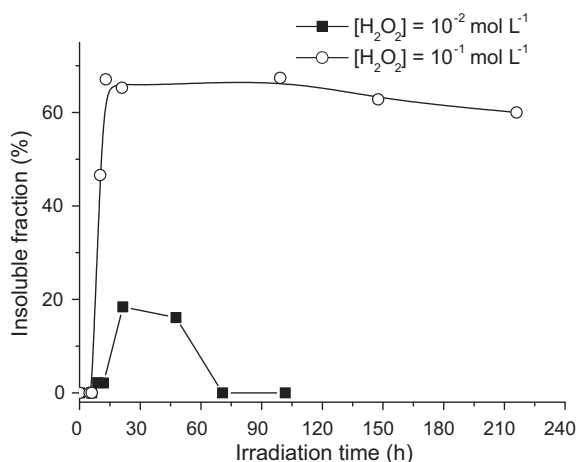


Fig. 6. Evolution of the insoluble fraction as a function of irradiation time ([PVP] = 62.5 mg mL⁻¹, [H₂O₂] = 10⁻¹ and 10⁻² mol L⁻¹).

formed by direct photolysis of H₂O₂ also decreased. These results suggest that hydroxyl radicals are responsible for the formation of the hydrogel. Furthermore, photoproducts previously observed during the irradiation of PVP in the water are not formed in a significant manner.

In the case where the concentration of H₂O₂ was between 10⁻³ and 6 × 10⁻⁴ mol L⁻¹, no hydrogel was formed during the irradiation. It was observed throughout the photooxidation course that no UV–vis absorption band appeared. Also, no bands corresponding to photoproducts were detected by IR over a period of 475 h. In addition, the pH of the solution remained constant and the average molar weight decreased only by 10% after 475 h.

As shown by the IR, UV–vis and SEC analysis, the presence of H₂O₂ at relatively low concentrations (≤10⁻³ mol L⁻¹) in PVP aqueous solution leads to a considerable decrease of the oxidation rate of the polymer. This indicates that H₂O₂ acts as a stabilizer at low concentration. A recent study showed that PVP is capable of forming a stable cyclic complex (during several months) with H₂O₂ by hydrogen bonds [20]. The formation of this complex when the concentration of H₂O₂ is lower could protect the polymer from the photochemical oxidation.

The immediate conclusions from these different experimental results concern the role of hydroxyl radicals in the formation of the hydrogel. Indeed, during the photooxidation of the PVP aqueous solution in the presence of relatively high concentration of H₂O₂ there is an important production of hydroxyl radicals generated by direct photolysis of H₂O₂. They abstract hydrogen atoms from macromolecules, thus macroradicals are formed. The most important reaction of macroalkyl radicals is the intermolecular cross-linking. Moreover, it is well known that only a small proportion of these radicals seems to evolve according to a mechanism of chain scissions [4].

3.4. Total organic carbon (TOC) concentration

TOC experiments were undertaken to prove the efficiency of Fe(III) salts in the elimination of PVP from the aqueous solution. Relatively diluted polymer solutions (0.1 mg mL⁻¹) were chosen in order to highlight the mineralisation process of the polymer. The evolution of organic carbon concentration in PVP aqueous solutions in the absence or in the presence of Fe(III) is illustrated in Fig. 7. In the presence of Fe(III) (pH 3.1), 70% of the TOC quickly disappeared during the first 40 h of irradiation but the total mineralisation of the polymer was not reached. Indeed, 13% of the organic carbon still remained in the aqueous solution after 118 h of irradiation. The

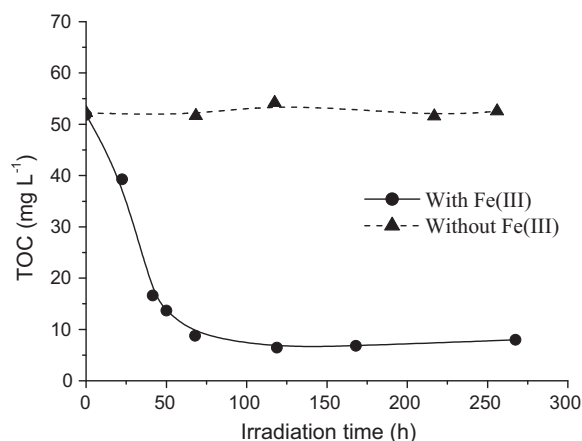


Fig. 7. TOC evolution of PVP aqueous solution during the irradiation, [PVP] = 0.1 mg mL⁻¹, [Fe(III)] = 6 × 10⁻⁴ mol L⁻¹, pH 3.1.

degradation products accumulated after 40 h are probably not or weakly photodegradable. On the contrary, in the absence of Fe(III), no decrease of the TOC was noticed after 270 h of irradiation. Therefore, the important mineralisation (87%) of PVP in presence of Fe(III) can be explained by the photoinductor effect of iron leading to the formation of hydroxyl radicals. In our experimental conditions, the presence of iron in PVP solutions gave an important mineralisation of PVP during photooxidation.

4. Conclusions

The present work illustrates the efficiency of PVP degradation in aqueous solution photoinduced by Fe(III). Through our study, we demonstrate that a couple Fe(III)–solar light can play an important role in the fate of PVP in water. According to the concentration of Fe(III), the concentration of PVP and the pH of the medium, photooxidation of PVP leads to a chain scission or to a cross-linking mechanism contrary to the photooxidation of PVP in the absence of Fe(III) where only the mechanism of chain scission was observed. Indeed, the influence of the presence of Fe(III) on the mechanism of photooxidation of PVP in relatively concentrated aqueous solution ([PVP] = 62.5 mg mL⁻¹) shows that:

- When Fe(III) is added at a concentration of 6 × 10⁻⁴ mol L⁻¹, iron is mainly present in the form of Fe(OH)²⁺, which is the most photoreactive species in terms of •OH radicals formation. In this case, hydroxyl radicals provoke the acceleration of the degradation process of the polymer by chain scissions.
- When the concentration of the Fe(III) is two times higher (1.2 × 10⁻³ mol L⁻¹), the same iron species (Fe(OH)²⁺) is present in aqueous solution but at higher concentration. In this case, the concentration of macroradical is also increased. So, the mechanism of cross-linking of the polymer is strongly favoured and the formation of a permanent hydrogel is observed. Effectively, the production of hydroxyl radicals is much more important during the first times of irradiation since the concentration of Fe(III) is higher. These radicals react with PVP macromolecular chains to give macroalkyl radicals that lead to the generation of cross-linked network. The formation of the hydrogel, therefore, is attributed to the recombination of macroalkyl radicals.

The incorporation of H₂O₂ into the PVP aqueous solution showed clearly the role of hydroxyl radicals in the formation of the hydrogel. The presence of H₂O₂ at high concentrations (10⁻¹ mol L⁻¹), which is also a photochemical source of hydroxyl radicals leads to the formation of a hydrogel.

During this work, we also demonstrated that iron species present in aqueous solution can oxidise the PVP until its partial mineralisation. The addition of Fe(III) ($6 \times 10^{-4} \text{ mol L}^{-1}$) into PVP diluted aqueous solution (0.1 mg mL^{-1}) leads to a high mineralisation (87%) of the polymer.

The mechanism of photooxidation of PVP in aqueous solution in the presence of Fe(III) depends strongly on the ratio between the concentrations of PVP and of Fe(III). At lower concentration of Fe(III), the presence of iron accelerates the photooxidation of PVP by a mechanism of chain scission identical to that observed in aqueous solution without iron, showing mainly the formation of succinimide rings and unsaturations. At higher concentration of iron, the photochemical reaction leads to a mechanism of polycondensation of macromolecular chains until the formation of insoluble hydrogel.

References

- [1] L. Blecher, D.H. Lorenz, H.L. Lowd, A.S. Wood, D.P. Wyman, in: R.L. Davidson (Ed.), *Handbook of Water-soluble Gums and Resins*, McGraw-Hill, New-York, 1980 (Chapter 21).
- [2] P.H. Molyneux, *Polyvinylpyrrolidone Water-soluble Synthetic Polymers: Properties and Behavior*, vol. I, CRC Press, Florida, 1983, pp. 146–193.
- [3] S. Trimpin, P. Eichhorn, H.J. Räder, K. Müllen, T.P. Knepper, Recalcitrance of poly(vinylpyrrolidone): evidence through matrix-assisted laser desorption–ionization time-of-flight mass spectrometry, *J. Chromatogr. A* 938 (1–2) (2001) 67–77.
- [4] F. Hassouna, S. Therias, G. Mailhot, J.L. Gardette, Photooxidation of poly(N-vinylpyrrolidone) (PVP) in the solid state and in aqueous solution, *Polym. Degrad. Stab.* 94 (12) (2009) 2257–2266.
- [5] H. Kaczmarek, A. Kaminska, M. Swiatek, J.F. Rabek, Photo-oxidative degradation of some water-soluble polymers in the presence of accelerating agents, *Angew. Makromol. Chem.* 261–262 (1998) 109–121.
- [6] O. Bajt, G. Mailhot, M. Bolte, Degradation of dibutylphthalate by homogeneous photocatalysis with iron(III) in aqueous solution, *Appl. Catal. B* 33 (2001) 239–248.
- [7] H. Kawaguchi, A. Inagaki, Kinetics of ferric ion promoted photodecomposition of 2-chlorophenol, *Chemosphere* 28 (1994) 57–62.
- [8] P. Mazellier, M. Bolte, 3-chlorophenol elimination upon excitation of dilute iron(III) solution: evidence for the only involvement of $\text{Fe}(\text{OH})^{2+}$, *Chemosphere* 42 (2001) 361–366.
- [9] H.J. Benkelberg, P. Warneck, Photodecomposition of iron(III) hydroxo and sulfato complexes in aqueous solution: wavelength dependence of OH and SO_4^- quantum yields, *J. Phys. Chem.* 99 (1995) 5214–5221.
- [10] B.C. Faust, J. Hoigné, Photolysis of Fe(III)-hydroxy complexes as sources of OH radicals in clouds, forest and rain, *Atmos. Environ.* 24A (1990) 79–89.
- [11] N. Brand, G. Mailhot, M. Bolte, Degradation and photodegradation of tetraacetylenediamine (TAED) in the presence of iron(III) in aqueous solution, *Chemosphere* 34 (1997) 2637–2648.
- [12] P. Mazellier, M. Bolte, Iron(III) promoted degradation of 2,6-dimethylphenol in aqueous solution, *Chemosphere* 35 (1997) 2181–2192.
- [13] J.G. Calvert, J.M. Pitts, *Photochemistry*, Wiley, New York, 1966, pp. 783–786.
- [14] G. Fraenkel, C. Franconi, Protonation of amides, *J. Am. Chem. Soc.* 82 (1960) 4478–4483.
- [15] B. Sébille, J. Néel, Interaction entre la polyvinylpyrrolidone et les composés acides: quelques considérations sur la coacervation, *J. Chim. Phys.* 60 (4) (1963) 475–491.
- [16] J. Shuping, M. Liu, S. Chen, Y. Chen, Complexation between poly(acrylic acid) and poly(vinylpyrrolidone): influence of the molecular weight of poly(acrylic acid) and small molecule salt on the complexation, *Eur. Polym. J.* 41 (2005) 2406–2415.
- [17] H. Kaczmarek, A. Szalla, A. Kaminska, Study of poly(acrylic acid)–poly(vinylpyrrolidone) complexes and their photostability, *Polymer* 42 (2001) 6057–6069.
- [18] F. Hassouna, G. Mailhot, S. Morlat-Therias, J.L. Gardette, Photochemical behaviour of poly(ethylene oxide) (PEO) in aqueous solution: influence of iron salts, *J. Photochem. Photobiol. A* 195 (2008) 167–174.
- [19] J.M. Rosiak, P. Ulanski, Synthesis of hydrogels by irradiation of polymers in aqueous solution, *Radiat. Phys. Chem.* 55 (1999) 139–151.
- [20] E.F. Panarin, K.K. Kalninsk, D.V. Pestov, Complexation of hydrogen peroxide with polyvinylpyrrolidone: ab initio calculations, *Eur. Polym. J.* 37 (2001) 375–379.



Using SAXS approach to estimate thermal conductivity of polystyrene/zirconia nanocomposite by exploiting strong contrast technique

M. Baniassadi^{a,b}, F. Addiego^{a,*}, A. Laachachi^a, S. Ahzi^b, H. Garmestani^c,
F. Hassouna^c, A. Makradi^a, V. Toniazio^a, D. Ruch^a

^a Public Research Centre Henri Tudor, Advanced Materials and Structures Department, 66 Rue de Luxembourg, L-4221 Esch-sur-Alzette, Luxembourg

^b Université de Strasbourg, Institut de Mécanique des Fluides et des Solides—CNRS, 2 Rue Boussingault, 67000 Strasbourg, France

^c Georgia Institute of Technology, School of Materials Science and Engineering, 771 Ferst Drive, NW, Atlanta, GA 30332-0245, USA

Received 1 June 2010; received in revised form 4 January 2011; accepted 5 January 2011

Abstract

In this study, the effective thermal conductivity of a polymer/ZrO₂ nanocomposite material has been calculated based on small-angle X-ray scattering (SAXS) data. These SAXS results have been used to calculate statistical two-point correlation functions of the nanostructure. A statistical continuum approach based on higher-order correlation functions has been utilized to estimate the effective thermal conductivity of this zirconia-filled polymer. A strong-contrast formulation was used to predict the effective conductivity of the nanocomposite by means of two- and three-point statistical functions with an approximation of the three-point probability functions for a two-phase media. The thermal conductivity of ZrO₂ particles is estimated using a semi-inverse application of the strong contrast technique for a buckypaper material sample. Comparison of the simulated results with our experimental results for polystyrene/ZrO₂ nanocomposite samples with different volume fractions shows satisfactory agreement. This supports the capability of our proposed methodology to predict effective thermal conductivity of nanocomposites.

© 2011 Acta Materialia Inc. Published by Elsevier Ltd. All rights reserved.

Keywords: Nanocomposite; Small-angle X-ray scattering; Thermal conductivity; Analytical methods; Strong contrast statistical approach

1. Introduction

Statistical continuum theory correlates the morphology of microstructures with the physical properties of heterogeneous materials through correlation functions. In this framework, statistical n -point correlation functions provide a mathematical representation of the morphology of heterogeneous materials [1]. In particular, one-point correlation functions give information about the volume fraction of each constituent (phase) of the heterogeneous material [1]. The distribution, orientation and shape of the heteroge-

neous material phases are described by two-point or higher-order correlation functions, which can in general be determined from appropriate microstructure measurements [2]. These measurements must be representative of the material morphology, i.e. the experimental information must reflect all the variations of phase distribution within the material. The heterogeneity, introduced through the polymer-based nanocomposites, can be represented by: (i) the overall distribution of the nanoparticles within the polymer matrix; and (ii) the local heterogeneity of the nanoparticles, which is called the dispersion state [3]. What dictates the material properties is actually the dispersion state of the nanoparticles. We therefore consider that the dispersion of the nanoparticles within the polymer matrix is the key distribution parameter to take into account in the statistical theory.

* Corresponding author. Tel.: +352 42 59 91 639; fax: +352 42 59 91 555.

E-mail address: frederic.addiego@tudor.lu (F. Addiego).

Transmission electron microscopy (TEM) or X-ray scattering can be used to obtain information about nanoparticle dispersion [4]. However, TEM images are only relevant when the entire dispersion gradients of the nanoparticles are represented [5]. In fact, uniform nanoparticle dispersion is not usually achieved, but rather a mixture of single particles and aggregates containing more than one particle (aggregation) exist. Note that the aggregate size of the nanoparticles can reach several hundred nanometers depending on the nanoparticle size, processing method and the chemical interactions between the nanoparticle and the matrix. Therefore, the calculated correlation functions strongly depend on the magnification at which the TEM images are recorded. Using a high magnification, the correlation function will be dictated by the position within the heterogeneous material where the microscopy images are taken (e.g. whether the images are chosen to include aggregates or not) [6]. In other words, the resolution can be high but the representative area (or volume) is much larger than the selected image [7]. However, using a low magnification, more representative information about the dispersion of the nanoparticles will be obtained. In this case, the statistics are high but the resolution is low. As an alternative method, the dispersion state of nanoparticles in polymer-based nanocomposites can be characterized by small-angle X-ray scattering (SAXS) measurement [8]. SAXS is an easy and fast method that is applied to a volume of the order of several cubic millimeters (high statistics) without compromising the resolution. The obtained scattering signal of the nanoparticles reflects the size distribution and shape of the nanoparticles (form factor) and their position with respect to each other (structure factor). For example, a high dispersion state of the nanoparticles within a polymer matrix will be characterized by an average particle size near that of a single particle and eventually a homogeneous interparticle distance. The SAXS signal can consequently be exploited to calculate two-point correlation functions (TPCFs) with great accuracy since it produces a very accurate representation of the material morphology [9–12].

The objective of this work is to estimate the thermal properties of a polymer nanocomposite from two- and three-point correlation functions. The selected material is polystyrene (PS) filled with zirconium oxide (ZrO_2) nanoparticles. The nanocomposite morphology was first examined by scanning transmission electron microscopy (STEM) and SAXS. The TPCFs were then calculated from SAXS measurements, while the three-point correlation functions are deduced from TPCFs using an analytical equation [13]. Our attention is focused on the effective thermal conductivity of the nanocomposites which was experimentally assessed by coupling different techniques. The experimental values of thermal conductivity were compared with predicted ones obtained using the strong contrast statistical continuum theory, where the morphology description is represented by two-point and three-point correlation functions.

2. Correlation between SAXS data and two-point correlation functions

The SAXS technique relies on electron density scattered from heterogeneities ranging from 1 to 1000 nm in size, depending on the equipment configuration [14–16]. The scattered intensity depends on the difference between the local electronic density ρ from the scattered heterogeneities and its surrounding, which can be represented by an average density $\bar{\rho}$. The local fluctuation η of the electronic density can be defined as follows:

$$\eta = \rho - \bar{\rho}. \quad (1)$$

Assuming a statistically isotropic system with no long-range order, a correlation function that considers the amplitude of the density fluctuations can be defined as:

$$\gamma(r)\langle\eta^2\rangle = \langle\eta_A\eta_B\rangle, \quad (2)$$

where A and B are two distinct points in the medium represented by the vectors r_1 and r_2 , and $\gamma(r)$ is the characteristic or autocorrelation function depending on the position r . $\gamma(r)$ can be defined as follows:

$$\gamma(r) = \langle\eta(r_1)\eta(r_2)\rangle. \quad (3)$$

For a random distribution of heterogeneities, the autocorrelation function $\gamma(r)$ satisfies the following conditions: $\gamma(r=0) = \eta^2$ and $\gamma(r \rightarrow \infty) = 0$. It is convenient to define the auto-covariance of phase 1 for a statistically homogeneous media as [1]:

$$\gamma(r) = \langle\eta(r_1)\eta(r_2)\rangle = P_2^1(r) - \phi_1^2, \quad (4)$$

where ϕ_1 is the volume fraction of phase 1 (fillers) and $P_2^1(r)$ is the two-point probability function. Recalling that $\rho(r)$ is the number of electrons per unit volume, a volume element $\rho(r)$ at position r will contain $\rho(r) \times dV$ electrons.

The intensity of the X-ray scattering I as a function of the scattering vector \vec{h} over the entire volume V is given by the following Fourier integral [17]:

$$\begin{aligned} I(\vec{h}) &= \int \int \int \int \int \int dV_1 dV_2 \rho(r_1) \rho(r_2) e^{-i\vec{h}r} \\ &= \int \int_V \rho(r_1) \rho(r_2) e^{-i\vec{h}r} dr_1 dr_2, \end{aligned} \quad (5)$$

Summing all pairs with the same relative distance, then integrating over all relative distances, seems to be a logical course. An autocorrelation function can be defined as:

$$\tilde{\rho}^2(r) = \int \int \int dV_1 \rho(r_1) \rho(r_2), \quad (6)$$

which allows $I(h)$ to be rewritten as:

$$I(\vec{h}) = \int \int \int dV \tilde{\rho}^2(r) e^{-i\vec{h}r}, \quad (7)$$

implying that the intensity distribution in h or reciprocal space is uniquely determined by the structure of the density field. Considering statistical isotropy, Debye et al. [10,11] proved that

$$\langle e^{-ihr} \rangle = \frac{\sin(hr)}{hr}. \quad (8)$$

As a result, the average scattering intensity reduces to:

$$I(h) = \int 4\pi r^2 dr \cdot \tilde{\rho}^2(r) \frac{\sin(hr)}{hr}. \quad (9)$$

Recalling the autocorrelation function, γ , the above equation can be rewritten:

$$I(h) = V n_0^2 \int 4\pi r^2 dr \cdot \gamma(r) \frac{\sin(hr)}{hr}, \quad (10)$$

where n_0 is the mean density of electrons. Or,

$$\gamma(r) = \frac{1}{2\pi^2 V n_0^2} \int_0^\infty I(h) \frac{\sin(hr)}{hr} h^2 dh, \quad (11)$$

Here, n_0 is a constant. Using Eq. (4), the Eq. (11) can be rewritten as follows:

$$\gamma(r) = P_2^1(r) - \phi_1^2 = \frac{1}{2\pi^2 V n_0^2} \int_0^\infty I(h) \frac{\sin(hr)}{hr} h^2 dh, \quad (12)$$

where $P_2^1(r)$ represents the two-point probability correlation function which measures the spatial distribution of the heterogeneities (phase 1) in the matrix (phase 2). $P_2^1(r)$ should verify the following condition:

$$P_2^1(r) = \phi_1 \quad \text{when} \quad r = 0 \quad (13)$$

$$P_2^1(r) = (\phi_1)^2 \quad \text{when} \quad r \rightarrow \infty. \quad (14)$$

The second condition in Eq. (14) is an indicator of the degree of homogeneity of the distribution of heterogeneities in the matrix (i.e. if the second condition is not verified, then the distribution of the heterogeneities is not homogeneous in the matrix).

3. Structural characterization

3.1. Materials

The polymer matrix of the studied nanocomposite, PS, was supplied by Scientific Polymer Products Inc. It has a molecular weight of about $120,000 \text{ g mol}^{-1}$. The ZrO_2 nanofiller was provided by Sigma Aldrich under the reference #544760 (average particle size $<100 \text{ nm}$ according to the datasheet). The specific surface area (measured by the Brunauer–Emmett–Teller method) and the density of ZrO_2 were $25 \text{ m}^2 \text{ g}^{-1}$ and 5.89 g cm^{-3} , respectively.

3.2. Preparation of the nanocomposites

All nanocomposites were prepared by melt mixing. The following material systems were extruded by means of a DSM microcompounder (reference Xplore 15 ml): neat PS, PS + 1 wt.% ZrO_2 , PS + 3 wt.% ZrO_2 , and PS + 5 wt.% ZrO_2 . During this procedure, each system was compounded for 5 min at 230°C with a screw co-rotating speed of 200 rpm. To avoid oxidation phenomena, the extrusion was carried out under argon gas. The produced

materials were extruded cylinders, 5 mm in diameter. Thermogravimetric analysis was performed after the processing step to measure the effective amount of nanoparticles within PS. The results indicated that the amounts of nanoparticles used for the processing are preserved.

3.3. Scanning transmission electron microscopy

We performed a structural characterization of the nanocomposites by STEM to verify the presence of aggregates within the polymer matrix. STEM analyses of the PS– ZrO_2 nanocomposites were carried out using a FEI Quanta FEG 200 scanning electron microscope at 7 kV. The STEM samples were ultra-thin films (70 nm thick) that were prepared with a Leica EM FC6 cryo-ultramicrotome at 25°C using a trimming diamond blade.

Fig. 1 shows some tendency to aggregation irrespective of the amount of filler. The size of the aggregates is much less than 200 nm except for a very few cases for which the size of the aggregates is in the micrometer range. The tendency to aggregation can be explained by the fact that the particles were not coated, which prevents an increase in the interaction between the oxide particle and the polymer matrix. It is also thought that the microcompounder used does not enable optimal dispersion to be achieved.

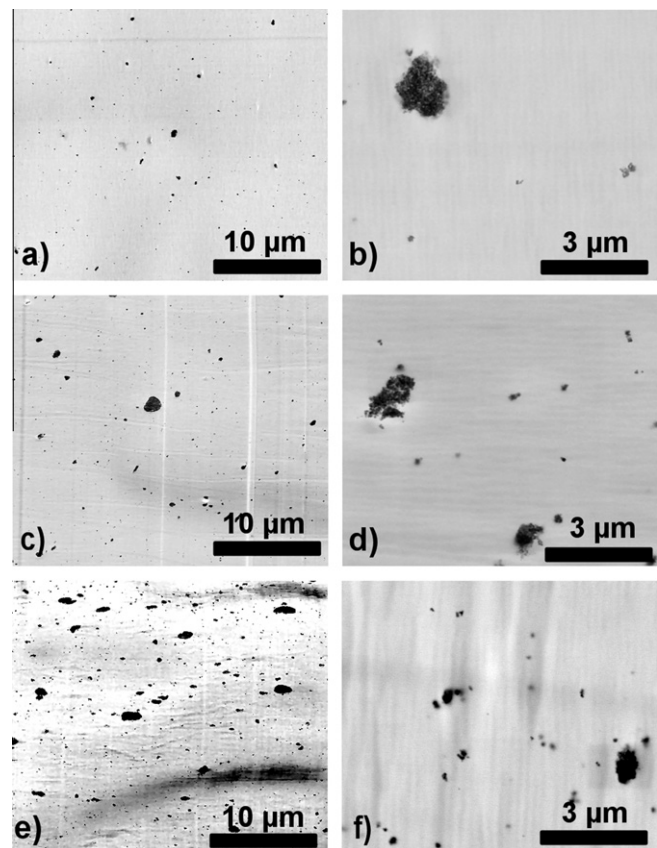


Fig. 1. STEM micrographs at two magnifications, 5000 (a, c, and e) and 50,000 (b, d, and f), of the composites PS + 1 wt.% ZrO_2 (a and b), PS + 3 wt.% ZrO_2 (c and d), and PS + 5 wt.% ZrO_2 (e and f).

This can be explained by the geometry of the extrusion screws that prevents an elongational flow high enough to completely break up the aggregates into primary particles. Moreover, the low beam energy of the scanning electron microscope means that it is not possible to observe the local distribution state of the nanoparticles, i.e. the dispersion state, with the transmission mode. To characterize this local distribution of the particles, the SAXS technique was used.

3.4. Small-angle X-ray scattering

SAXS tests were performed using a Panalytical X'Pert Pro MPD device to study the scattering signal of the nanoparticles within the polymer matrix, and hence to obtain physical and structural information. In particular, the analysis of the scattering signal enables the size and shape of the particles (form factor) to be characterized as well as their relative ordering (structure factor) [2]. The radiation used, $\lambda = 1.54 \text{ \AA}$ (Cu K), was generated by an X-ray tube operating at 40 kV and 45 mA. A focused parallel mirror and a PIXcel detector were employed with specific slits in order to obtain the highest resolution at small angles. In addition, to analyze the strong signal from the nanoparticles, the background noise from the SAXS curves, i.e. the scattering curve of neat PS, was systematically subtracted. The final treatment of the curves consisted of assessing the intensity of the primary beam that passes through the nanoparticles (absorption correction). The scattering intensity I is plotted as a function of scattering vector $h = (4\pi/\lambda) \sin(\theta)$, where θ is the scattering angle. Each SAXS test was repeated on three specimens.

Fig. 2 shows the representative scattered intensity $I(h)$ of ZrO_2 characterized both alone (as-received powder) and within the PS matrix (3 and 5 wt.% ZrO_2). A high reproducibility of the $I(h)$ curves was found for each material. It should be noted that no scattering signal was obtained for 1 wt.% of ZrO_2 within PS, and hence the scattering

curve of this system is not plotted in Fig. 2. This is certainly due to the resolution of the X-ray scattering equipment, which is not capable of characterizing such a low content of particles (1 wt.%) within a polymer matrix. For the other investigated ZrO_2 amounts, no long-range Bragg peak is noted on the scattering curves, indicating no ordering of ZrO_2 nanoparticles and hence no interaction between the particles as, for example, Van der Waals or hard-sphere interactions. Consequently, the scattering signal of the nanoparticles is only induced by the form factor. The initial parts of the $I(h)$ curves, below $h = 0.07 \text{ nm}^{-1}$, show a continuous decrease in intensity with h that suggests the presence of some large aggregates. This observation is in line with the aggregation tendency noted on STEM images (Fig. 1). It should be noted that in the case of a well-dispersed system, an initial “plateau” of scattering intensity at very low h would have been noted, followed by a gradual decrease in the intensity with h . Above $h = 0.07 \text{ nm}^{-1}$, the presence of some oscillation indicates the presence of scattering objects that have a relatively uniform size. These objects are most probably single particles and small aggregates constituted of a few single particles. By means of a Guinier plot ($\ln I$ as a function of h^2), we found a radius of gyration R_g (deduced from the slope of the $\ln(I)-h^2$ curve) of about 13.5 nm for as-received ZrO_2 , 5 wt.% ZrO_2 in PS and 3 wt.% of ZrO_2 in PS. Considering ZrO_2 nanoparticles as having a spherical shape, the average particle size (diameter), deduced from the relationship $2 \times R_g \times (5/3)^{0.5}$, is equal to 34.8 nm. Despite the presence of some large aggregates in the micrometer range (Fig. 1), we considered that the most representative information about the distribution of the particles is provided by SAXS. $I(h)$ curves (Fig. 2) are hence used for the calculation of the TPCFs.

The two-point probability functions representing the distribution of the ZrO_2 nanoparticles within the PS matrix are calculated using Eq. (12) and reported in Fig. 3. Note that since the SAXS diagram of 1 wt.% ZrO_2 in PS does not show any signal from the nanoparticles, the $P_2^1(r)$ curve presents negative values and does not verify the second

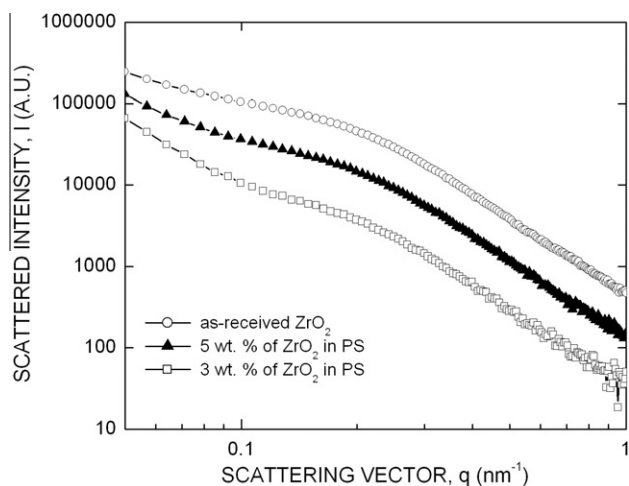


Fig. 2. The scattered intensity I as a function of scattering vector h for ZrO_2 nanopowder and PS– ZrO_2 composites (3 and 5 wt.%) (background- and absorption-corrected curves).

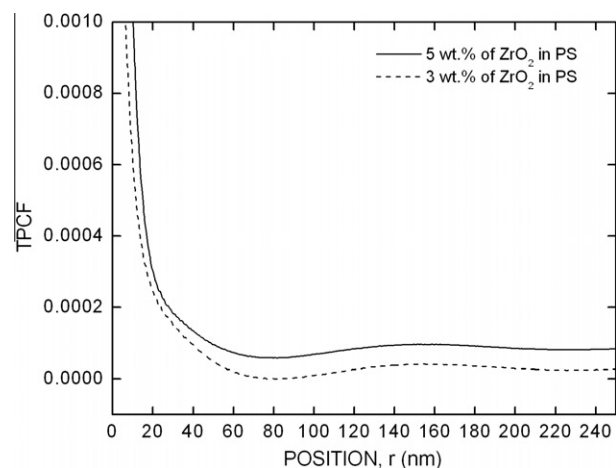


Fig. 3. TPCFs for PS– ZrO_2 composites (3 and 5 wt.% ZrO_2).

condition in Eq. (14). Therefore $P_2^1(r)$ for 1 wt.% ZrO_2 cannot be exploited to calculate the physical properties of the nanocomposite. However, the two-point probability function, $P_2^1(r)$, for 3 and 5 wt.% ZrO_2 (see Fig. 3) confirm the limits given in Eq. (14).

4. SAXS structural-based calculation of the thermal conductivity of PS– ZrO_2 nanocomposites

The thermal conductivity of PS– ZrO_2 nanocomposites is calculated using the SAXS-based probability function in conjunction with the strong-contrast formulation of the statistical continuum theory [18]. The predicted results are compared with the experimental thermal conductivity $\lambda(T)$, which is deduced from the thermal diffusivity $\alpha(T)$, the specific heat $C_p(T)$ and the bulk density $\rho_s(T)$ according to the following equation:

$$\lambda(T) = \rho_s(T) \times C_p(T) \times \alpha(T). \quad (15)$$

A short description of the experimental procedures used to measure the physical properties $\rho_s(T)$, $C_p(T)$ and $\alpha(T)$ is summarized below.

4.1. Thermal diffusivity

The thermal diffusivity $\alpha(T)$ of the studied materials was measured by the laser flash method. This technique entails heating the front side of a small, usually disk-shaped plane-parallel sample by a short laser pulse (≤ 1 ms). The temperature rise on the rear surface is measured vs. time using an infrared detector. The samples in the shape of discs, 12 mm in diameter and 1 mm thick, were prepared by compression molding. All samples were coated, on both faces, with a very thin layer of colloidal graphite. The measurements were carried out from room temperature to 140 °C under an argon flow. Three samples were tested for each systems and the uncertainty in the determination of the thermal diffusivity was evaluated at $\pm 3\%$. Fig. 4 shows the thermal diffusivity as a function of the temperature for the investigated materials. It can be seen that, as expected, the thermal diffusivity increases with the amount of filler and decreases with increasing temperature.

4.2. Specific density

The specific density ρ of the nanocomposite materials was determined using Archimedes' principle, where the volume is measured from the buoyancy in a fluid of known density. The weight and buoyancy measurements were performed with an electronic densimeter (X22B Wallace). Pure water was chosen as the fluid. The density measurement resolution is 0.001 g cm^{-3} .

4.3. Differential scanning calorimetry

Specific heat C_p measurements were performed using a differential scanning calorimeter (Netzsch 204 F1).

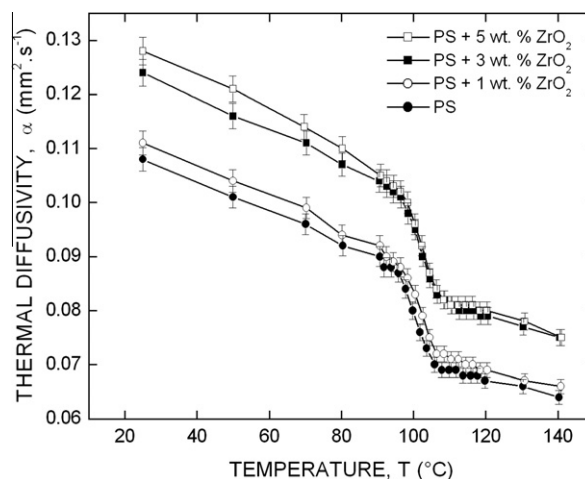


Fig. 4. Experimental thermal diffusivity α of two-phase composite as a function of temperature T for neat PS and its composites with ZrO_2 (1, 3 and 5 wt.%).

Measurements were carried out in the temperature range from 25 to 200 °C under a nitrogen flow and with a heating rate of 10 °C min^{-1} . The calorimeter was calibrated in the same temperature region before experiments, using a sapphire sample as standard, with a well-known specific heat. The deviation between the individual measurement results is generally less than $\pm 2\%$. The thermal conductivity λ of the materials, assessed using Eq. (15), is shown in Fig. 5. It can be seen that λ significantly increases with the amount of ZrO_2 in the studied temperature range.

4.4. Effective thermal conductivity of the polymer nanocomposite

The strong-contrast approach in statistical continuum theory is used in this work to predict the effective thermal conductivity of the two-phase isotropic media based on

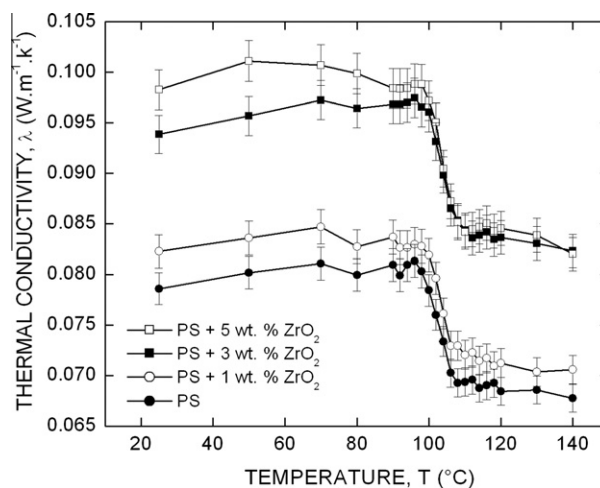


Fig. 5. Experimental thermal conductivity λ of two-phase composite as a function of temperature T for neat PS and its composites with ZrO_2 (1, 3 and 5 wt.%).

the work of Torquato [1], where the individual properties of phases are highly dissimilar. Assuming isotropic properties of the PS matrix and ZrO₂ nanoparticles, the effective conductivity tensor λ_e of the PS–ZrO₂ nanocomposites is determined using the strong-contrast formulation of the statistical continuum theory [1,18]:

$$\begin{aligned} \{\lambda_e - \lambda_R I_d\}^{-1} \{\lambda_e + (d-1)\lambda_R I_d\} &= \frac{1}{\beta_{SR} P_1^S(x)} I_d - \lambda_R d \\ &\times \int \left[\frac{P_2^S(x, x') - P_1^S(x) P_1^S(x')}{P_1^S(x) P_1^S(x')} \right] H^R(x - x') dx' - \lambda_R^2 d^2 \beta_{SR} \\ &\times \int \int \left[\frac{P_3^S(x, x', x'')}{P_1^S(x) P_1^S(x')} - \frac{P_2^S(x, x') P_2^S(x', x'')}{P_1^S(x) P_1^S(x') P_1^S(x'')} \right] H^R(x - x') \\ &\cdot H^R(x' - x'') dx' dx'' - \dots, \end{aligned} \quad (16)$$

where I_d is the second-order identity tensor, β_{SR} is the polarizability, λ_R is the reference conductivity, and $H^R(x - x')$ is a second-order tensor, defined below. The subscript R stands for the reference phase, which is chosen here to be the PS matrix, and the subscript/superscript S stands for the ZrO₂ phase.

The polarizability β_{SR} is expressed by:

$$\beta_{SR} = \frac{\lambda_S - \lambda_R}{\lambda_S + (d-1)\lambda_R}. \quad (17)$$

The second-order tensor $H^R(x - x')$ is defined by:

$$H^R(x - x') = \frac{1}{\Omega} \frac{d}{\lambda_R} \frac{nn - I_d}{(|x - x'|)^d}, \quad (18)$$

where Ω is the total solid angle contained in a d -dimensional sphere and $n = (x - x')/|x - x'|$. $P_1^S(x)$, $P_2^S(x, x')$ and $P_3^S(x, x', x'')$ are the probability functions that contain all the microstructure information. The one-point probability function, $P_1^S(x)$, is the volume fraction of the nanoparticles. The two-point probability function, $P_2^S(x, x')$, is calculated from the SAXS measurements. The three-point probability function, $P_3^S(x, x', x'')$, is calculated from $P_2^S(x, x')$ using an analytical approximation [13]. It should be noted that the calculated effective properties will depend significantly on the profile of the probability functions. In this context, we recently proved that electrical conductivity of fiber-filled polymer is markedly influenced by the TPCF profile [19]. In particular, TPCFs have been simulated for different orientations of generated media. The computed results showed that the directional TPCFs were related to fiber orientation direction and therefore the calculated effective conductivity showed high contrast between the directions parallel and perpendicular to the fiber axis [19]. These previous results indicate a high sensitivity of conductivity to the TPCF profile. Nevertheless, any approximation used should verify the limits and should reproduce the profile in an acceptable way, which is the case for our approximation for the three-point probability function [13,18,19].

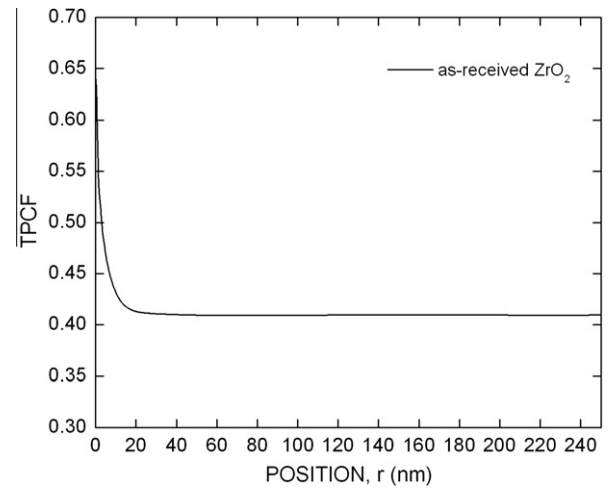


Fig. 6. TPCFs for the ZrO₂ nanopowder.

4.5. Semi-inverse calculation of the effective thermal conductivity of ZrO₂

The physical parameters needed for the computation of the effective conductivity are the individual conductivities of the PS matrix λ_R and the ZrO₂ nanoparticles λ_S . The conductivity of the PS matrix is deduced from the experimental thermal diffusivity using Eq. (15). The conductivity of the ZrO₂ nanoparticles is calculated from experimental conductivity of bucky ZrO₂ samples, using the strong-contrast formulation of the statistical continuum theory (Eq. (16)). These values are $\lambda_S = 4.13 \text{ W K}^{-1} \text{ m}^{-1}$ and $\lambda_R = 2 \text{ W K}^{-1} \text{ m}^{-1}$. The correlation functions needed in Eq. (16) are calculated from the SAXS data (Fig. 2) and reported in Fig. 6. Knowing the experimental thermal conductivity of the bucky ZrO₂ sample, the individual thermal conductivity of ZrO₂ nanoparticles is adjusted to obtain a predicted effective conductivity that is the same as the experimental values.

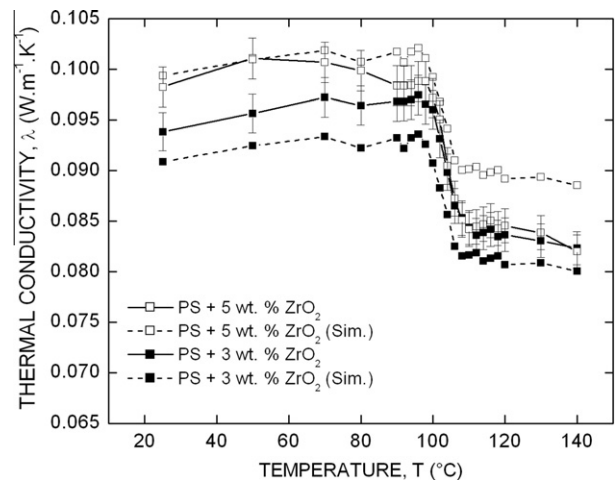


Fig. 7. Comparison of results between experimental and simulated thermal conductivity λ of two-phase composites as a function of temperature T , in the case of PS–ZrO₂ composites (3 and 5 wt.%).

The temperature dependence of the predicted effective thermal conductivity is compared to the experimental value and reported in Fig. 7. The predicted effective conductivity for both 3 and 5 wt.% ZrO₂ (Fig. 7) shows a good agreement with the experimental data.

5. Conclusions

PS nanocomposites were produced by the melt mixing technique using ZrO₂ as filler. The spatial dispersion of nanoparticles within the polymer matrix was characterized by STEM and SAXS measurements. A non-uniform dispersion of the nanoparticles within the polymer matrix with a tendency to aggregation is obtained. The SAXS signals are used to calculate the correlation functions that represent the spatial dispersion of the nanoparticles, which is considered to be the key distribution parameter in these heterogeneous materials. The calculated correlation functions were used in conjunction with the strong contrast version of the statistical continuum theory to predict the effective conductivity for both 3 and 5 wt.% ZrO₂. The predicted results are compared with the experimental results and a fairly good agreement is found. To improve this agreement, the modeling could be based on experimental data reflecting a wider range of sizes, which could be achieved by the combination of different techniques, e.g. SAXS and ultra-SAXS (USAXS). This agreement could be also improved if one takes into account the temperature effects on the thermal conductivity of the fillers. This effect is very difficult to characterize and may be evaluated by using molecular dynamics simulations, which is beyond the scope of the present work.

Acknowledgment

The authors thank Fonds National de la Recherche Luxembourg (FNR Luxembourg) for providing the PhD Grant of M.B.

References

- [1] Torquato S. Random heterogeneous materials: microstructure and macroscopic properties. New York: Springer Verlag; 2002.
- [2] Jiao Y, Stillinger FH, Torquato S. *Phys Rev E* 2007;76:031110.
- [3] Alexandre M, Dubois P. *Mater Sci Eng R-Rep* 2000;28:1.
- [4] Kashiwagi T, Harris RH, Zhang X, Briber RM, Cipriano BH, Raghavan SR, et al. *Polymer* 2004;45:881.
- [5] Kashiwagi T, Fagan J, Douglas JF, Yamamoto K, Heckert AN, Leigh SD, et al. *Polymer* 2007;48:4855.
- [6] Li D, Baniassadi M, Garmestani H, Ahzi S, Taha H, Ruch D. *J Comput Theor Nanos* 2010;7:1.
- [7] Lingaiah S, Sadler R, Ibeh C, Shivakumar K. *Compos Part B-Eng* 2008;39:196.
- [8] Bandyopadhyay J, Sinha Ray S. *Polymer* 2010;51:1437.
- [9] Gunier A, Fournet G. *Small angle scattering of X-rays*. New York: John Wiley; 1955.
- [10] Debye P, Anderson HR. *J Appl Phys* 1957;28:4.
- [11] Debye P, Anderson HR, Brumberger H. *J Appl Phys* 1957;28:679.
- [12] Frisch HL, Stillinger FH. *J Chem Phys* 1963;38:2200.
- [13] Mikdam A, Makradi A, Ahzi S, Garmestani H, Li DS, Remond Y. *Int J Solids Struct* 2009;46:3782.
- [14] Cullity BD, Stock SR. *Elements of X-ray diffraction*. Englewood Cliffs, NJ: Prentice Hall; 2001.
- [15] Brumberger H. *Modern aspects of small-angle scattering*. Boston: Kluwer; 1995.
- [16] Feigin LA, Svergun DI. *Structure analysis by small-angle X-ray and neutron scattering*. New York: Plenum Press; 1987.
- [17] Glatter O, Kratky O. *Small angle X-ray scattering*. New York: Academic Press; 1982.
- [18] Mikdam A, Makradi A, Ahzi S, Garmestani H, Li DS, Remond Y. *J Mech Phys Solids* 2009;57:76.
- [19] Mikdam A, Makradi A, Ahzi S, Garmestani H, Li DS, Remond Y. *Compos Sci Technol* 2010;70:510.



New approach on the development of plasticized polylactide (PLA): Grafting of poly(ethylene glycol) (PEG) via reactive extrusion

Fatima Hassouna^{a,*}, Jean-Marie Raquez^b, Frédéric Addiego^a, Philippe Dubois^b, Valérie Toniazzi^a, David Ruch^a

^a Department of Advanced Materials and Structures, Centre de Recherche Public Henri Tudor, Rue Luxembourg 66, L4221 Esch sur Alzette, Luxembourg

^b Laboratory of Polymeric and Composite Materials, Centre d'Innovation et de Recherche en Matériaux Polymères – CIRMAP – Université de Mons – UMONS, Place du Parc, 23, B-7000 Mons, Belgium

ARTICLE INFO

Article history:

Received 5 January 2011

Received in revised form 13 July 2011

Accepted 1 August 2011

Available online 16 August 2011

Keywords:

Poly(lactide)

Poly(ethylene glycol)

Ductility

Reactive extrusion

Crystallization

ABSTRACT

In this work, new ways of plasticizing polylactide (PLA) with low molecular poly(ethylene glycol) (PEG) were developed to improve the ductility of PLA while maintaining the plasticizer content at maximum 20 wt.% PLA. To this end, a reactive blending of anhydride-grafted PLA (MAG-PLA) copolymer with PEG, with chains terminated with hydroxyl groups, was performed. During the melt-processing, a fraction of PEG was grafted into the anhydride-functionalized PLA chains. The role of the grafted fraction was to improve the compatibility between PLA and PEG. Reactive extrusion and melt-blending of neat and modified PLA with PEG did not induce any dramatic drop of PLA molecular weight. The *in situ* reactive grafting of PEG into the modified PLA in PLA/PEG blends showed a clear effect on the thermal properties of PLA. It was demonstrated by DSC that the mobility gained by PLA chains in the plasticized blends yielded crystallization. The grafting of a fraction of PEG into PLA did not affect this process. However, DSC results obtained after the second heating showed an interesting effect on the T_g when 20 wt.% PEG were melt blended with neat PLA or 10 wt.% MAG-PLA. In the latter case, the T_g displayed by the reactive blend was shifted to even lower temperatures at around 14 °C, while the T_g of neat PLA and PLA blended with 20 wt.% PEG was around 60 and 23 °C, respectively. Regarding viscoelastic and viscoplastic properties, the presence of MAG-PLA does not significantly influence the behavior of plasticized PLA. Indeed, with or without MAG-PLA, elastic modulus and yield stress decrease, while ultimate strain increases with the addition of PEG into PLA.

© 2011 Elsevier Ltd. All rights reserved.

1. Introduction

In recent years, the increase in fossil energy costs and the environmental concerns result in new opportunities for the industrial production of biodegradable polymers based on renewable resources. The application of these biopolymeric materials is therefore growing very fast [1–4].

Aliphatic polyesters represent an important family of biodegradable polymers [3]. Poly(lactide) (PLA) is the best

known polymer of this family [3,5,6]. Until the last decade, the main uses of PLA have been limited to medical applications such as implant devices, tissue scaffolds, and internal sutures, because of its high cost, low availability and limited molecular weight. Recently, new techniques, which allow economical production of high molecular weight PLA polymer, have broadened its uses [1,6,7]. Its low toxicity, along with its environmentally benign characteristics, has made PLA an ideal material for food packaging and film wrap and for other consumer products [4,8,9]. PLA is characterized by excellent optical properties and high tensile-strength but unfortunately, it is rigid and brittle at room temperature due to its glass transition temperature (T_g)

* Corresponding author. Tel.: +352 42 59 91 594.

E-mail address: fatima.hassouna@tudor.lu (F. Hassouna).

close to ca. 55 °C [6]. Previous work suggested that the brittleness of PLA is due to the low entanglement density (V_e) and the high value of characteristic ratio (C_∞), a measure of chain stiffness [10,11], limiting its use and melt-processability for food packaging. Indeed, developing packaging materials requires high flexibility at room temperature and thus, there is no tolerance for the polymer film tearing or cracking when subjected to stresses during package manufacturing or use [6,12]. Other requirements include transparency and low crystallinity.

To improve the ductility of PLA-based materials, a large number of investigations have been made to modify PLA properties via plasticization. However, a great number of variables, i.e. nature of PLA matrix, type, and optimal percentage of plasticizer, thermal stability at the processing temperature, etc. must be considered. Unfortunately, poor mechanical properties are often reported or the relationship between the thermo-mechanical properties and molecular parameters has not been considered enough. Therefore, the choice of an adequate plasticizer is essential.

Rather than lactide, many kinds of ester-like plasticizers for PLA have been studied such as bishydroxymethyl malonate (DBM) [13], glucose monoesters and partial fatty acid esters, and citrates [14]. However, the low molecular weight plasticizers have the problem of migrating, owing to their high mobility within the PLA matrix. Therefore, plasticizers with rather high molecular weight and low mobility are necessary.

At least five kinds of plasticizers with high molecular weight and being miscible to PLA without any compatibilizer have been reported so far, i.e. polyethylene glycol (PEG) [14–16], poly(propylene glycol) (PPG) [17], atactic poly(3-hydroxybutyrate) (a-PHB) [18,19], polyester diol (PED) as poly(diethylene adipate) (PDEA) [20], tributyl citrate-oligoester (TbC-oligoesters), diethyl bishydroxymethyl malonate oligoester (DBM-oligoester) and oligoesteramide (DBM-oligoesteramide) [13,21,22].

On the other hand, the choice of plasticizer used as a modifier for PLA is limited by the legislative or technical requirements of the application, and in this context, its selection becomes more difficult [13,22]. In fact, the plasticizer used for PLA has to be biodegradable, non-toxic for food contact (for packaging) and/or biocompatible (for biomedical applications).

Typically, amounts ranging from 10 to 20 wt.% of plasticizers are required to provide both a substantial reduction of T_g of PLA matrix and adequate mechanical properties. In sustainable issues, the preferred plasticizer for PLA is biodegradable/bioresorbable, sufficiently non-volatile, with a relatively low molecular weight to produce the desired decrease of the Young's modulus value and increase of the impact strength. Moreover, the addition of more than 20–30% (depending on the plasticizer) of plasticizers into PLA matrix leads to a phase separation. The plasticization is thus limited by the amount of plasticizer to be blended with PLA.

Hydroxy-terminated PEG (400 g mol⁻¹) chosen as plasticizing agent for PLA in this study fulfills all these requirements. According to the literature, PEG had previously displayed excellent plasticizing abilities when blended with PLA the amount introduced in PLA has to be lower

or equal to 20 wt.% in each to avoid phase separation. This latter limitation reduces the possible impact of PEG on the PLA's T_g .

The objectives of the present work were hence to develop new means of plasticizing PLA with low molecular PEG in order to further improve PLA's ductility compared to what is done so far, while maintaining the plasticizer content at maximum 20 wt.% (to avoid phase separation). The strategy chosen consists in grafting a fraction of hydroxyl-functionalized PEG plasticizer onto a PLA backbone by reactive extrusion in order to create more interactions between the so-functionalized polyester matrix and the remaining fraction of non-grafted plasticizer. To this end, a reactive blending of maleic anhydride-grafted PLA (MAG-PLA) copolymer with hydroxyl-functionalized PEG was performed. Physico-chemical, thermal and mechanical properties of the extruded blends were studied in order to assess the compatibility of the plasticizer with the PLA matrix, the morphological stability of the plasticized material and the prevention/limitation of the plasticizer migrating from the bulk.

2. Experimental part

2.1. Materials

Poly(lactide) (PLA) (4042D) was provided by Nature-Works LLC. 2,5-Dimethyl-2,5-di-(tert-butylperoxy)hexane organic peroxide (Lupersol 101), Maleic anhydride (MA) and Poly(ethylene glycol) (PEG, M_n = 380–400 g/mol) were purchased from Sigma–Aldrich.

2.2. Processing

All melt (reactive) blending were performed on a Leistritz corotating intermeshing twin-screw extruder (L/D = 45). The die was two 3-mm-diameter holes. The temperature profile was 160/180/180/180/180/180/180/180/180/180 from the feed throat to the die, and the melt temperature was 181 °C. The screw speed employed was 80 rpm. A two-hole filament die of 3 mm in diameter, with a cooling sleeve was assembled to the extruder. PLA was dried overnight at 40 °C in a vacuum oven before processing. Dry PEG was used with any particular caution.

The maleation of polylactide (MAG-PLA) was carried out by reactive extrusion. PLA, MA and Lupersol 101 (L101) were hand-mixed together before extrusion.

The percentage of Lupersol added was on a PLA weight basis (0.5 wt.%), and 2 wt.% MA (PLA basis) chosen for this maleation study according to the literature [23]. Neat PLA and PLA + 10 wt.% MAG-PLA were mixed with poly(ethylene glycol) (PEG) plasticizer and submitted to extrusion in similar conditions as for the maleic anhydride grafting step. The contents of plasticizer were chosen to be: 10 and 20 wt.%. Table 1 summarizes the composition of each formulation.

For the mechanical study (tensile tests and dynamical mechanical analyses), 110 × 110 × 5 mm³ plates of PLA each sample were compression-molded using a Carver press and a specific mold. The procedure was as follows:

Table 1

Summary of (reactive) blending composition in wt.%.

	PLA	Maleic anhydride (MA)	Lupersol (L101)
Anhydride-grafted PLA (MAG-PLA)	97.5	2	0.5
PLA + PEG	PLA 90 80	MAG-PLA	PEG 10 20
PLA + MAG-PLA + PEG	80 70	10 10	10 20

% In weight.

(i) extruded sample pellets were introduced within the mold, (ii) PLA was heated at 190 °C for 3 min, (iii) the sample was compressed for 30 s with a pressure of 15 MPa, and (iv) under the same pressure (15 MPa) and then cooled by means of a room temperature water circulation.

2.3. Characterizations

Fourier transform infrared (FTIR), Nuclear Magnetic Resonance (NMR), potentiometric titration and soxhlet extraction are used to characterize the efficiency of the grafting reaction.

2.3.1. Fourier transform infrared (FTIR)

Chemical structure modification of PLA is evaluated by FTIR spectroscopy in transmission from 400 to 4000 cm⁻¹ with a Bruker Optics Tensor 27 spectrometer. Films of ≈100 μm thickness were obtained by compression-molding around 20 mg samples between poly(tetrafluoroethylene) (PTFE) Teflon® films by using a Carver press (Temperature: 180 °C, pressure: 5 MPa).

2.3.2. Potentiometric titration

The extent of maleation for samples grafted with MA has been determined by titration [23]. Since the initial percent of reacted MA is quite low (2 wt.%), it can be assumed that the actual percent of MA grafted onto the PLA backbone is very small. A direct titration of these samples would probably be inaccurate as a small discrepancy such as a contaminant could result in a large error; therefore, a back titration of the sample is necessary. A back titration consists of adding a known excess of base and then titrating the base with acid. The base reacts with both the maleated sample and the acid. The amount of anhydride groups attached to the PLA backbone can then be determined.

A potentiometric titration was done using a potentiometer. A first-derivative analysis was used to determine the equivalence point of the sample by the following method: (1) remove unreacted MA by drying in a vacuum oven at 80 °C for 24 h; (2) dissolve 1 g of the sample (containing a maximum of 2 wt.% MA) in 20 mL of CHCl₃-MeOH (5:1); (3) after 1 h, when the samples are completely dissolved, add 2.0 mL of morpholine solution (0.05 N in MeOH); (4) let the mixture reacting for 10 min; and (5) titrate the samples with 0.01 N HCl using the autotitrator. The HCl solution was titrated against a known NaOH standard. The morpholine solution was then titrated against

the HCl to get a blank reading. The calculation for determining the quantity of grafted anhydride is as follows:

$$\% \text{ Anhydride} = (V_{\text{mor}}N_{\text{mor}} - V_{\text{HCl}}N_{\text{HCl}}) \times \frac{98.06 \text{ g/mol}}{W_{\text{sample}}} \times 100$$

2.3.3. Size exclusion chromatography (SEC)

Size exclusion chromatography (SEC) used is an Agilent Technologies series 1200 working with a differential refractive index detection and a linear column (PLgel Mixed-D 5 and 3 μm, 200 Da < Mw < 200 kDa in chloroform 1 mL min⁻¹). SEC analyses were carried out to follow the evolution of the molecular weight of PLA before and after grafting and upon melt-blending with plasticizers. They were run at room temperature (concentration 2 mg mL⁻¹).

2.3.4. Tensile tests

Tensile behavior of PLA was investigated by means of a servo-hydraulic testing machine MTS 810 equipped with the optical extensometer “VidéoTraction” (7 markers mode). This special extensometer provided the true stress – true strain curve of the materials at constant strain rate. Mechanical tests were performed at the temperature of 23 °C and at the strain rate of 0.001 s⁻¹. Rectangular tensile specimens were machined from the 4 mm-thick plates using a computer-controlled milling machine (CharlyRobot CRA4). The calibrated zone of tensile specimens was a parallelepiped of 34 × 7.6 × 4 mm³. Note that the median region of the calibrated zone had a reduced width of 6.8 mm and a local radius of curvature of 15 mm to localize necking process in this zone. Seven black ink markers, were carefully printed in the form of a cross on the front flat face of the sample. More details about this method are given in a previous paper [24].

2.3.5. Dynamic mechanical analyzer (DMA)

The influence of the plasticizer on viscoelastic properties of PLA was analyzed by means of a dynamic mechanical analyzer (DMA) Netzsch DMA 242C. For this study, we used 50 × 10 × 4 mm³ rectangular specimens machined from the compression-molded plates. They were subjected to double cantilever mode of flexural loading with a maximum displacement of 40 μm in the temperature range –60 to 120 °C (rate 10 °C/min) and a frequency of 1 Hz.

2.3.6. Differential scanning calorimeter (DSC)

DSC scans were recorded on a Differential scanning calorimeter 204 F1 Phoenix[®] (Netzsch) in inert atmosphere (nitrogen), with a heating rate of 10 K min⁻¹. The samples (10–20 mg) were placed into alumina crucibles. After the first heating –100 °C to 200 °C, the samples were cooled to –100 °C and subsequently heated again and thermograms for second heating were recorded.

2.3.7. Thermogravimetric analyzer (TGA)

Thermogravimetric analyses were performed with a Netzsch TG 409 PC Luxx[®] device operating in nitrogen (80 mL min⁻¹) and oxygen (20 mL min⁻¹) environment in alumina crucibles (150 mL) containing 20–25 mg of sample. The runs were carried out in dynamic conditions. They were heated to 600 °C at the constant heating rate of 20 K min⁻¹.

2.3.8. Soxhlet extraction

The plasticizer was extracted from plasticized PLA using soxhlet to determine the amount and the nature of the extracted fraction. The samples were placed in a thimble-holder that is gradually filled with condensed fresh solvent (methanol) from a distillation flask. When the liquid reaches the overflow level, a siphon aspirates the solute from the thimble-holder and unloads it back into the distillation flask, thus carrying the extracts into the bulk liquid. This operation is repeated until extraction is complete. Solid fraction (PLA) was dried overnight at 60 °C and weighed. Methanol was then evaporated from the solution fraction and the obtained product was characterized by FTIR and NMR.

3. Results and discussion

3.1. Reactive extrusion modification and plasticizing of PLA

Maleic anhydride (MA) grafting onto PLA was carried out in an attempt to create functional groups [23] which would react with a fraction of hydroxylated PEG, and will be used here as the plasticizer, to improve the interfacial adhesion between PLA and PEG and therefore improve PLA ductility.

Grafting of MA into PLA by reactive extrusion was characterized by FTIR and quantified by titration after elimination of the unreacted MA. FTIR showed the appearance of additional peaks at 698 and 1850 cm⁻¹ after PLA maleation by reactive extrusion can be observed. The absorbance at 1850 cm⁻¹ corresponds to the asymmetric stretching of carbonyl band of the grafted anhydride and the absorbance at 698 cm⁻¹ is attributed to the out-of-plane bending vibration of the C–H bands of the anhydride ring.

The amount of anhydride attached to the PLA backbone was determined by back titration. The addition of 0.5 wt.% of L101 and 2 wt.% of MA to PLA leads to the melt-grafting of 0.6 wt.% of MA. Moreover, the addition of MA has a slight negative effect on the molecular weight of PLA. It leads to a slight decrease of the number average molecular weight (Mn) from 77,320 to 66,950 g mol⁻¹. Carlson et al attributed the decrease of the molecular weight to the β -scission

reactions mediated by free-radicals along the polyester chains (which increase as the initiator concentration increases) at 180 °C [23].

A mechanism of maleation reaction has been proposed by Carlson et al [23]. The formation of the radical is the first step in the maleation of PLA. Once the radical is formed, hydrogen abstraction can occur producing a PLA which may react with MA. Note that such an hydrogen abstraction on the PLA backbone was recently reported by Malincolino et al in the case of radical polymerization of butyl acrylate in the presence of preformed PLA [25]. The resulting polymer radical may then combine with another radical (MA, peroxide, or polymer radicals or hydrogen) and further undergo a β -scission as shown in Scheme 1. Chain scission by either back-biting or thermohydrolysis may also occur [23].

In order to react easily with the anhydride functions grafted in the resulting PLA chains, to improve the compatibility with PLA and to slow down the plasticizer from migrating from the bulk, PEG chains terminated with hydroxyl groups were selected.

It was shown by FTIR that the melt-blending of PEG (10% or 20%) with PLA + 10% MAG-PLA leads to the grafting of a fraction of PEG onto the anhydride functions (Scheme 1). Indeed, a decrease of the absorption band intensity at 1850 cm⁻¹ corresponding to anhydride functions evidencing the reaction between the anhydride functionalities and hydroxyl terminated groups of PEG was noticed (Fig. 1). The reaction between anhydride and hydroxyl groups by esterification reaction is very used for compatibilizing polymer blends [26].

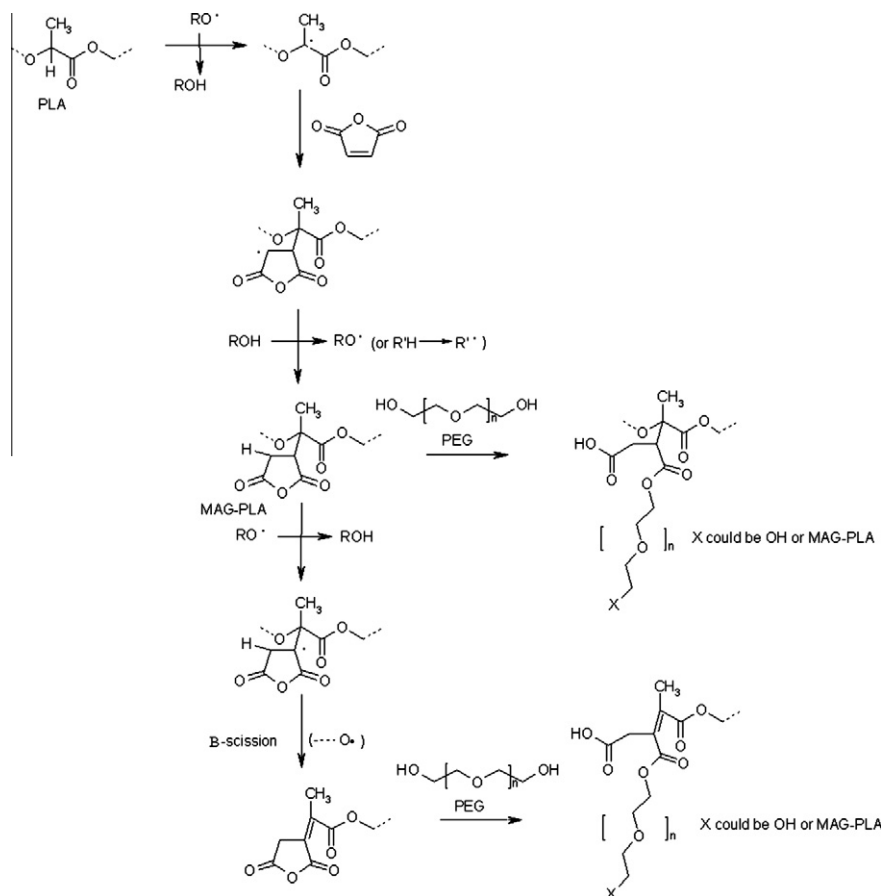
3.2. Modification of PLA molecular characteristics

PLA, as most of polyesters, is sensitive to its environment during melt processing (particularly to water, temperature and shear). In many cases the mixing of PLA with plasticizers or additives leads to a high decrease of the molecular weights, with negative impact on the thermo-mechanical properties of the polymer material.

Size exclusion chromatography (SEC) analysis used to estimate the apparent molecular weight (Mn and Mw) of all samples according to polystyrene standards are summarized in Table 2.

The grafting of maleic anhydride into PLA leads to a slight decrease of the molecular weight as already noticed above. Table 2 highlights also the effect of PEG on PLA molecular weight during processing. In fact, the increase of PEG amount from 10 to 20 wt.% showed a shift of Mn and Mw toward lower molecular weights. PLA chain scissions are however very limited. This might be attributed to hydroxyl terminated groups of PEG and PLA ester functions, acidity, catalysts or some impurities, etc [27].

The molecular weight characterization seems to evidence, that under adequate processing conditions, melt reactive extrusion and melt-blending of PLA with PEG 400 does not induce any dramatic drop of PLA molecular weight by thermal degradation or hydrolysis of polyester chains, while the polydispersity index is poorly affected by the chemical modification of PLA and by the presence of the plasticizer.



Scheme 1. Mechanism of PEG grafting onto MAG-PLA by reactive extrusion.

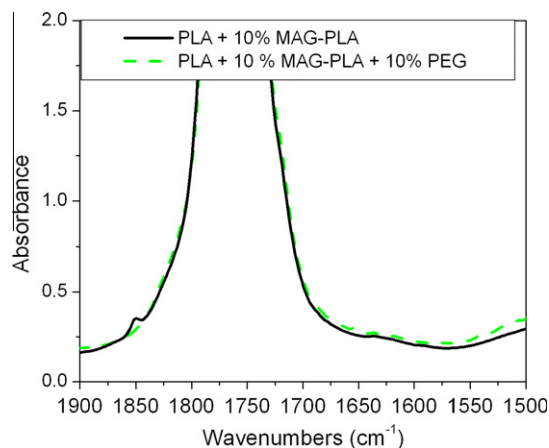


Fig. 1. Zoom over FTIR spectra of PLA films before and after reactive blending with PEG.

3.3. Thermal characterizations

3.3.1. Thermal stability

Thermal properties of PLA materials after extrusion were investigated by means of differential scanning calorimetry (DSC) and thermogravimetry analysis (TGA).

An issue not very often taken into account when studying a plasticized polymer is the impact of the plasticizer on the thermal stability of the polymeric matrix. To investigate the influence of the presence of PEG on the thermal stability of PLA matrix, TGA measurements were carried out on the different formulations (Fig. 2a). Fig. 2a reveals that the initial decomposition temperature of PEG is lower compared to neat PLA, while the kinetics of degradation is slower. Fig. 2a also shows that the modified and plasticized PLAs are stable within the range of interest (180 °C). However, the decomposition onset temperature as well as the decomposition temperature at 50% weight loss of PLA shifts systematically to lower temperatures when PEG is added. This shift is globally more important when the amount of plasticizer is higher. For example, a shift from 350 to 307 °C and from 365 to 345 °C is observed for the decomposition onset temperature and the decomposition temperature at 50% weight loss of the sample PLA/20% PEG, respectively. The decrease of the PLA thermal stability is mainly due to the presence of PEG as evidenced after extracting the plasticizer from PLA matrix. It leads to a back shift of the decomposition temperature from 345 to 365 °C, i.e. recovering the thermal behavior of neat PLA (Fig. 2b).

DTG curves show that the thermal decomposition mechanism of PLA is somehow modified in the presence

Table 2

Molecular weights (Mn and Mw) of all samples based PLA.

Sample	Mn (g mol ⁻¹)	Mw (g mol ⁻¹)	Polydispersity index
PLA	77,300	94,350	1.2
PLA after extrusion	77,850	93,850	1.2
MAG-PLA	66,950	87,300	1.3
PLA + 10%MAG-PLA	73,600	90,550	1.2
PLA + 10%PEG	61,200	87,800	1.4
PLA + 10%MAG-PLA + 10%PEG	62,550	87,500	1.4
PLA + 20%PEG	59,950	78,900	1.3
PLA + 10%MAG-PLA + 20%PEG	56,650	79,450	1.4

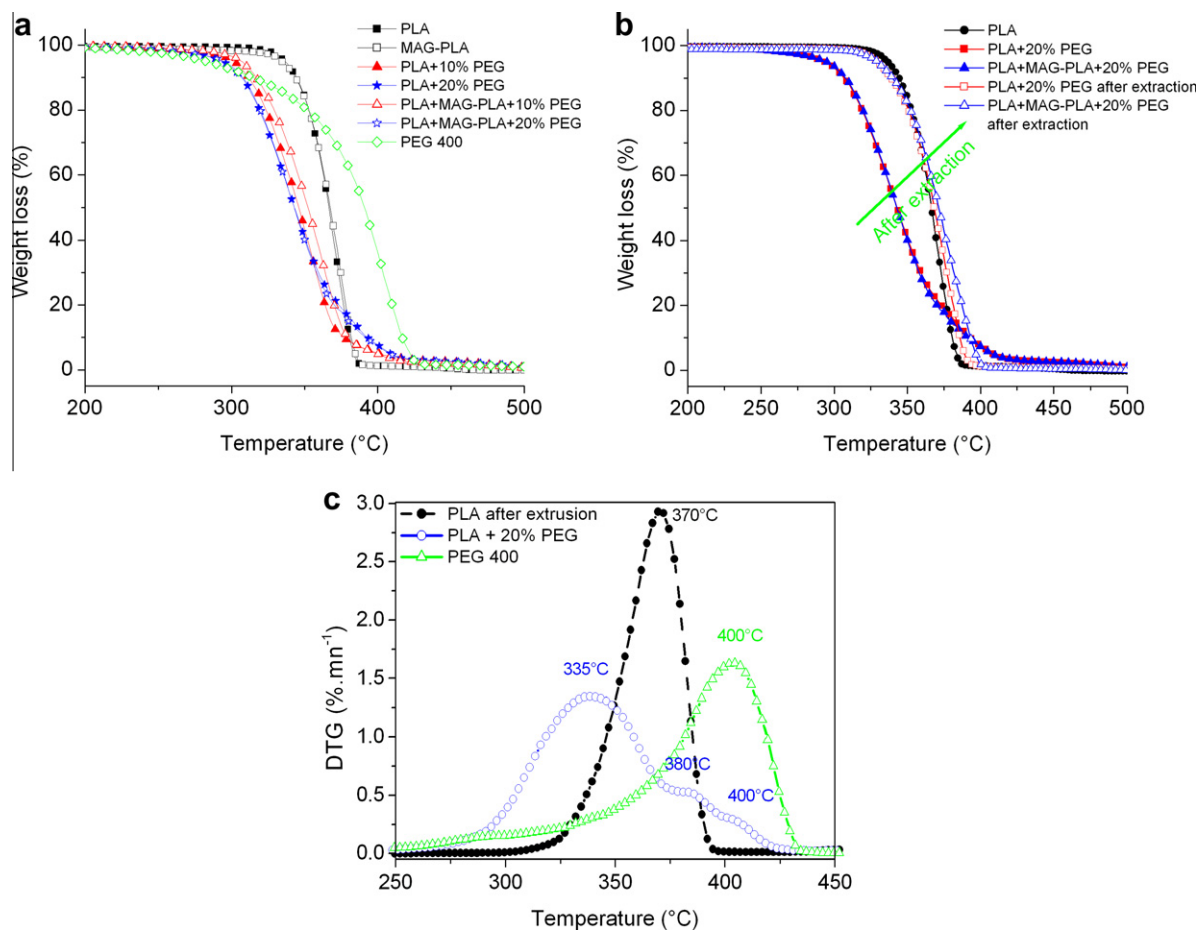


Fig. 2. TGA under N₂/O₂ flow of: (a) PEG 400, neat, modified and plasticized PLA. (b) Neat PLA, PLA + 20% PEG and PLA + MAG-PLA + 20% PEG before and after PEG extraction. (c) DTG curves for neat PLA, PEG 400 and PLA + 20% PEG.

of PEG (Fig. 2c). Different assumptions can be pointed out to explain the catalytic effect played by PEG to degrade PLA. The products of PEG degradation generated when the initial degradation temperature is reached (280 °C) can promote PLA degradation. The reaction between hydroxyl terminated groups of PEG and PLA ester functions, acidity, catalysts or some impurities could be the sources of such degradation, as already mentioned above. However, globally, the addition of PEG plasticizer makes certainly PLA more sensitive to thermal stability but at higher temperature ranges (higher than 300 °C) not

reached during the processing step. The grafting of PEG into MAG-PLA does not influence that much the thermal stability of the blend.

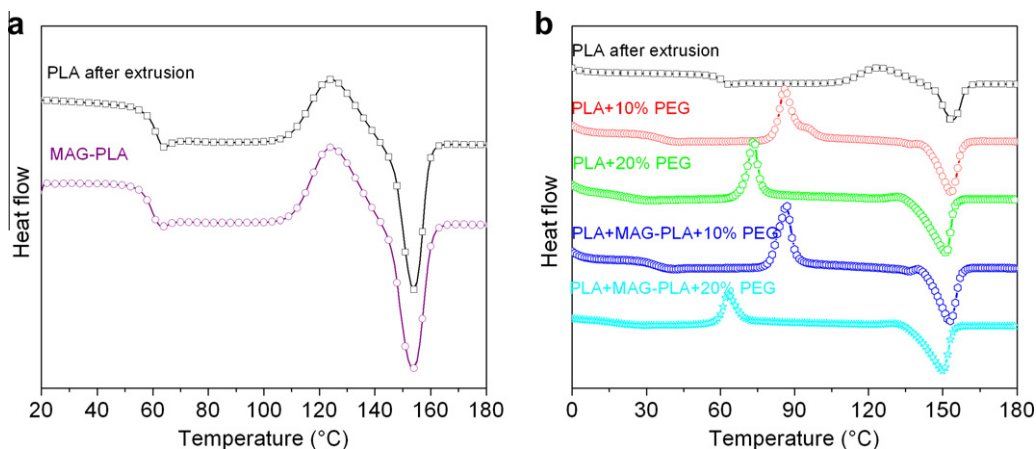
3.3.2. Thermal and morphology properties

Tables 3 and Fig. 3a and b summarize the thermal properties of neat, modified and blended PLA during the second heating scan using a cycle from –100 to 200 °C. The second heating removes the uncertainties that arise when the behavior of the material may depend on the thermal history of the samples.

Table 3Thermal data obtained by DSC measurements during the second heating at $10\text{ }^{\circ}\text{C min}^{-1}$ ($\pm 1\text{ }^{\circ}\text{C}$) for films of neat, modified and plasticized PLA.

Material	T_g ($^{\circ}\text{C}$) PLA	T_m ($^{\circ}\text{C}$)	ΔH_m (J/g)	T_{cc} ($^{\circ}\text{C}$)	ΔH_c (J/g)	d ΔH (J/g)
PLA after extrusion (reference)	60.0	154	−18	124	21	0
MAG-PLA	59.5	153.5	−21	124	24	0
PLA + 10%MAG-PLA	60.5	154.5	−21	126	24	0
PLA + 10%PEG	34.3	153	−25	86	25	0
PLA + 20%PEG	23.2	151	−33	73.5	21	12
PLA + 10%MAGPLA + 10%PEG	33.3	153	−27	86.5	26	0
PLA + 10%MAGPLA + 20%PEG	14.5	150	−29	63	20	9

T_g , glass transition temperature; T_m , melt temperature of PLA; T_{cc} , cold crystallization temperature of PLA; ΔH_m , heat of melting of PLA; ΔH_c , heat of cold crystallization of PLA; d ΔH : heat of melting of PLA determined by subtracting heat of cold crystallization from heat of melting.

**Fig. 3.** DSC traces recorded for (a) PLA and modified PLA and (b) PLA blends during the second heating.

DSC runs for the neat and modified PLA (Fig. 3a) show that the grafting of 0.6 wt.% of anhydride functions into PLA does not disturb significantly its thermal properties. Both PLA and MAG-PLA thermograms display a shift in the signal baseline related to the glass transition around $60\text{ }^{\circ}\text{C}$, an exothermic peak of cold crystallization at $124\text{ }^{\circ}\text{C}$ and an endothermic melting peak centered at $154\text{ }^{\circ}\text{C}$. The slight increase of ΔH_c from 21 to 24 J/g can be likely explained by the presence of higher amount of short chains that contribute to the crystallization of PLA. The comparison of crystallization enthalpy and melting enthalpy for neat and modified PLA after extrusion (Table 3) indicate an amorphous morphology for all the specimens, excepted for the materials containing 20% of PEG that contains a low amount of crystals. Since the crystallinity of PLA + 20% PEG and that of PLA + 10% MAG-PLA + 20% PEG are quite identical (same observation in the case of PLA + 10% PEG and PLA + 10% MAG-PLA + 10% PEG), the maleation process does not affect the thermal properties of the polymer itself.

The second heating curves (Fig. 3b and Table 3) of melt blended PLA, PLA + 10%MAG-PLA with PEG (10% and 20%) display only one glass transition temperature, stating the full miscibility of the polymer and the plasticizer as reported by Pillin et al. [28]. The T_g values obtained for the whole blends are lower than in neat PLA. In terms of efficiency, it has been observed that blends containing 20% of plasticizer exhibit the lowest values. Indeed all PLA and PLA + 10%MAG-PLA samples exhibit similar T_g value

around $34\text{ }^{\circ}\text{C}$ when blended with 10%PEG. The plasticizer grafting does not seem to have an impact on the T_g in this case. The increase of the amount of PEG from 10% to 20% in pristine PLA leads to a further decrease of T_g from 34 to $23\text{ }^{\circ}\text{C}$. More interesting, when 20% PEG are melt blended with PLA + 10% MAG-PLA, the T_g of the blends are shifted to even lower temperatures at around $14\text{ }^{\circ}\text{C}$ (instead of $23\text{ }^{\circ}\text{C}$ for PLA + 20%PEG). The supplementary decrease of T_g when mixed with modified PLA can be explained by the increase of PLA chain disentanglement due to presence of PLA-g-PEG chains leading to the enlargement of the free volume. The increase of PLA chain disentanglements could be related to the conformation of PLA-g-PEG. Other mechanisms such as physical interactions between grafted and free PEG could also be taken into account to explain the decrease of the T_g . Indeed, as shown above, the small amount of anhydride grafted onto PLA backbone reacted with a fraction of PEG, improving probably the interfacial adhesion and compatibility in PLA blends and therefore the plasticizing effect of PEG.

As already mentioned above, neat PLA exhibits an exothermic broad peak of cold-crystallization $T_{cc,PLA}$ from 105 to $145\text{ }^{\circ}\text{C}$ and centered at $124\text{ }^{\circ}\text{C}$. For PLA/PEG blends, this peak is shifted to lower temperatures. The shift to $86\text{ }^{\circ}\text{C}$ is observed for PLAs + 10% PEG blends. For blends containing 20% PEG, the shift is very much dependent on the presence or not of grafted PEG in the blend. Indeed, the $T_{cc,PLA}$ of PLA + 20% PEG is about $73\text{ }^{\circ}\text{C}$ and this value is even lower

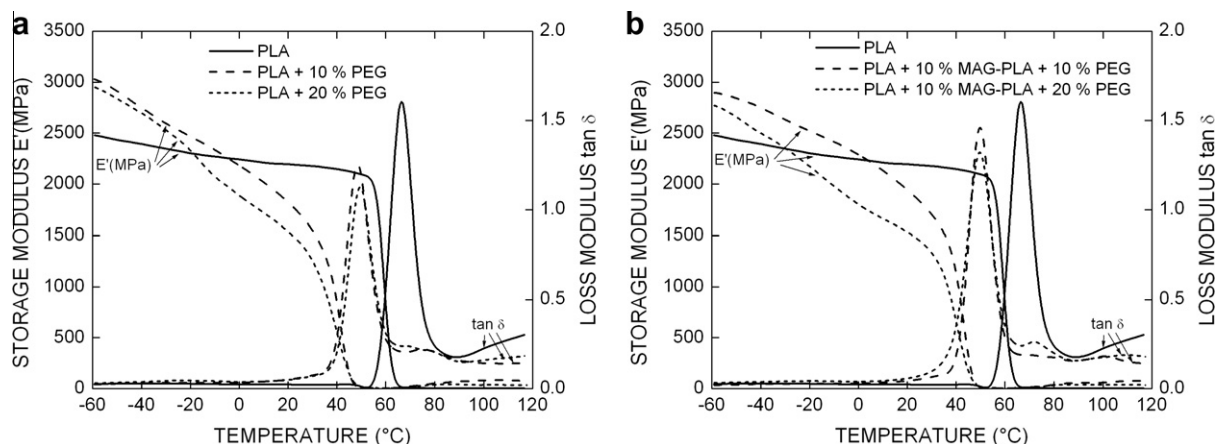


Fig. 4. Temperature dependence of storage modulus E' and loss factor $\tan \delta$ for neat PLA (a and b), PLA/PEG blends (a) and PLA/MAG-PLA/PEG blends (b) (DMA tests performed at 1 Hz).

Table 4

Mechanical features of neat PLA and plasticized PLA measured by DMA and tensile tests.

Material	Storage modulus E' (MPa) at 23 °C	Yield stress σ_{33}^y (MPa)	Yield strain ϵ_{33}^y	Ultimate stress σ_{33}^u (MPa)	Ultimate strain ϵ_{33}^u
Neat PLA	2190	67.8	0.02	55.3	0.07
PLA + 10% PEG	1750	15.1	0.03	67.0	1.12
PLA + 20% PEG	1460	14.6	0.03	>64.5	>1.30
PLA + 10% MAG-PLA + 10% PEG	1870	29.1	0.02	70.7	1.16
PLA + 10% MAG-PLA + 20% PEG	1480	15.8	0.03	>55.1	>1.27

in the presence of MAG-PLA, where $T_{cc,PLA}$ is the lowest recorded at 63 °C. The trend of $T_{cc,PLA}$ and T_g values as a function of PEG concentration and the presence or absence of grafted PEG are correlated. This result is considered to be directly related to the motion ability of the PLA chains. Indeed, the increase of PLA chain motion due to the amount of PEG (lower T_g) allows an easier rearrangement of polyester chains to crystallize. For instance, the higher the amount of PEG, the higher the motion and the lower the $T_{cc,PLA}$.

3.4. Mechanical properties

The effect of temperature on storage modulus, E' and loss factor, $\tan \delta$, is shown in Fig. 4 for neat and plasticized PLA. One can associate the glass transition temperature (T_g) as the maximum of the loss modulus ($\tan \delta$ obtained by DMA). Accordingly, neat PLA has a T_g equal to 60 °C and, as expected, all the plasticized PLA display a lower glass transition temperature compared to neat PLA. As already observed in DSC results, the presence of PEG chains grafted onto PLA in the blend PLA/PEG does have a significant effect on the glass transition temperature of PLA. These measurements of T_g are in line with those are obtained by DSC. In the temperature-dependent $\tan \delta$ curves of plasticized PLA, cold-crystallization processes are observed after the glass transition relaxation. This is evidenced by the presence of several low peaks between 65 and

120 °C. At the lowest investigated temperature, -60 °C, the plasticized PLA have a storage modulus E' between 2600 and 3030 MPa, while that of neat PLA is equal to 2500 MPa. With increasing temperature up to the onset of glass transition relaxation, a 50% decrease of the storage modulus of plasticized PLA is noted. In the same temperature range, a much less marked decrease in E' occurs for neat PLA (17%). The storage modulus E' measured at room temperature, 23 °C, is reported in Table 4 for the studied materials. Neat PLA has a modulus E' that is equal to 2190 MPa. As expected, when increasing the content of PEG, the elastic modulus of the material measured at 23 °C markedly decreases from 2190 MPa to a minimum of 1460 MPa for PLA + 20% PEG. We also note that the presence of MA-grafted PLA (MAG-PLA) has no significant effect on the elastic modulus when comparing PLA + 10% PEG with PLA + 10% MAG-PLA + 10% PEG or PLA + 20% PEG with PLA + 10% MAG-PLA + 20% PEG. After the glass transition relaxation, bumps are observed in the curves $\tan \delta$ – temperature for all the materials, while a weak but significant increase of E' occurs for plasticized PLA grades. Regarding the evolution of loss modulus E'' with temperature (curves not shown here), we observe the presence of a marked low temperature peak for PLA/PEG blends ranging between -60 and 0 °C, and a broadening of the E'' peak associated to the glass transition in the case of PLA/PEG and PLA/MAG-PLA/PEG blends with respect to neat PLA.

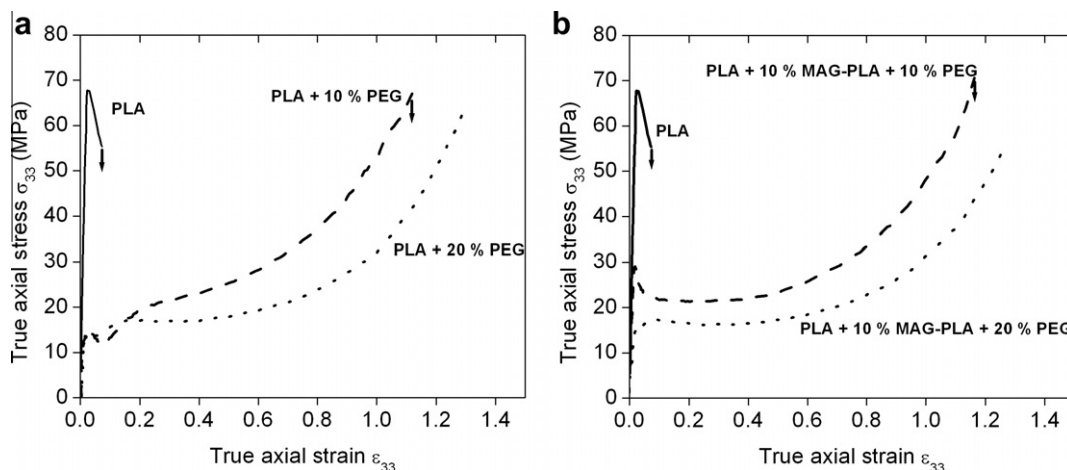


Fig. 5. True axial stress σ_{33} as a function of true axial strain ϵ_{33} for neat PLA (a and c), PLA/PEG blends (a) and PLA/MAG-PLA/PEG blends (b) (tensile tests performed at 23 °C and 10^{-3} s^{-1}).

True tensile behavior of neat PLA and plasticized PLA is collected in Fig. 5, while the measured characteristics (yield stress σ_{33}^y , yield strain ϵ_{33}^y , ultimate stress σ_{33}^u and ultimate strain ϵ_{33}^u) are listed in Table 4. Neat PLA is characterized by a high yield point ($\sigma_{33}^y = 67.8 \text{ MPa}$ and $\epsilon_{33}^y = 0.02$) and after this point is reached, a marked stress drop occurs until the material breaks at an ultimate strain of 0.07. As a result, neat PLA has a limited viscoplastic stage. When compared to neat PLA, plasticized PLA samples exhibit a lower yield stress, a higher yield strain and a longer viscoplastic stage. Indeed, for plasticized PLA, yield stress is comprised between 9.4 and 29.1 MPa, yield strain is ranging between 0.02 and 0.03, and ultimate strain is higher than 1.12. Moreover, the maximum elongation increases with the content of PEG for the blends PLA/PEG and PLA/MAG-PLA/PEG. For materials containing 20% PEG, it was not possible to deform the tensile specimen above the axial strain 1.3 due to a destruction of the dots. Furthermore, the yield stress and the stress drop occurring after the yield point decrease with increasing the amount of PEG. In this context, the material PLA + 10% MAG-PLA + 20% PEG does not present a yield peak during the viscoelastic/viscoplastic stages transition. The true stress – true strain curves of PLA/PEG blends (Fig. 5a) exhibit an irregularity. Indeed, a marked increase of stress at the beginning of viscoplastic stage followed by a gradual decrease of the slope until $\epsilon_{33} = 0.20$ is observed.

As shown by Figs. 4 and 5 and Table 4, the viscoelastic and viscoplastic behavior of PLA are drastically influenced by the plasticization methodology. To explain the viscoelastic features of PLA blends, the material composition and the intrinsic properties of each material component must be considered. Plasticized PLA blends are composed of (i) an amorphous phase with a rigidity dictated by the value of T_g , (ii) a PEG phase at liquid state to ensure a plasticization effect of PLA amorphous phase, and (iii) eventually rigid crystalline lamellae in the case of the material containing 20% of PEG as shown by DSC measurements (Table 3). At room temperature, the storage modulus E' is hence supposed to decrease with decreasing the index of

crystallinity [29], increasing the amount of PEG [30], and decreasing the glass transition temperature of PLA [30]. When 10% of PEG is added to PLA, the mechanisms (i) and (ii) are active, and hence, lead to a decrease of E' . When 20% of PEG is added to PLA, these three mechanisms are active, but the effect of the presence of crystalline lamellae seems to be widely overcome by the effect of the decrease of T_g and the presence of the PEG liquid phase on the elastic modulus. However, at the lowest temperature (-60°C), neat PLA has a lower elastic modulus than all the plasticized PLA, which is difficult to understand. The origin of this phenomenon is unclear, but we hypothesize that is maybe due to slight differences in the (i) specimen consolidation state or (ii) specimen dimensions when comparing neat and plasticized PLA grades. As indicated by Piorkowska et al [31], the curve loss modulus E'' – temperature (not shown here) provides information about the dispersion/distribution of PEG within amorphous PLA phase. The presence of an additional low temperature peak in the plasticized PLA grades suggests the formation of a PEG-rich phase. Furthermore, a broadening of the width of the peak reflecting the glass transition is due to a plasticizer concentration gradient in all the PLA blends. Regarding the increase of E' with temperature and the presence of bumps in the $\tan \delta$ – temperature curves after the glass transition, they are due to a cold-crystallization process [32]. This result proves that our processing conditions do not enable to achieve a complete crystallization of PLA. It is anticipated that this cold-crystallization will influence the tensile behavior of the PLA blends. Last, it is to be noted that the presence of MA-grafted PLA (MAG-PLA) does not significantly influence the viscoelastic properties of the materials.

The tensile behavior of the plasticized PLA developed in this study is in good accordance with that reported in literature in terms of yield and elongation at break as a function of PEG content [30,31]. The viscoelastic deformation is ascribed to an initial elastic expansion of the materials influenced by the phenomena described above. Subsequently, the stresses are dissipated by conformational changes of glassy amorphous PLA chains that lead to

segmental orientation [33]. In glassy amorphous polymer such as polycarbonate (PC) or polyvinyl chloride (PVC), the activation of plasticity is induced by the development of stable shear defects within amorphous matrix [34,35]. However, in the case of semi-crystalline polymers such as high-density polyethylene (HDPE), the plasticity is induced by the onset of shear mechanisms of crystalline lamellae [36]. As mentioned by Kulinski and Piorkowska [32], orientation also occurs in crystalline phase of PLA proving that shear mechanisms of crystalline lamellae are active in PLA. We hence conclude that activation of plasticity in semi-crystalline PLA is ascribed to the development of shear defects in amorphous phase and shear mechanisms of crystalline lamellae. Since the crystallinity is low in the present materials (0% of crystallinity for neat PLA and PLA containing 10% of PEG, and 9–12% of crystallinity for the other materials, see Table 3) the former mechanisms are mainly responsible for plasticity. The presence of plasticizer in the amorphous phase of PLA facilitates the conformational changes of PLA, which leads to an easier activation of plasticity. Yield stress consequently decreases with the content of plasticizer (Table 4). The yield drop is due to the multiplication of shear defects that locally accelerate the deformation [37]. As a result, the macroscopic stress decreases. The increase of the PEG amount triggers a diminution of yield drop (Fig. 5). One can suggest that the multiplication of shear defects is less marked with increasing the content of PEG, this mechanism being the less intense for PLA + 10% MAG-PLA + 20% PEG (no yield peak). The viscoplastic stage can be divided into cohesive mechanisms, as further deformation of amorphous network through the development of shear defects and further shearing of lamellae, and non-cohesive mechanisms as crazing [24,32]. The ability of amorphous network to the plastic deformation increases with the content of PEG, which induces an increase of elongation at break (Table 4). However, to ensure a high elongation, non-cohesive mechanisms may be limited. The development of crazes in amorphous layers is active in the PLA blends studied in this work since whitening phenomena were noted at macroscopic scale. Further investigations are required to study the competition between cohesive and non-cohesive mechanisms. This can be achieved through real-time structural characterization by SEM and XRD of PLA blends subjected to a tensile test. The irregularity observed in tensile curves of PLA/PEG blends (Fig. 5a) is probably due to the cold-crystallization process that induces a significant increase of stress at the beginning of viscoplastic stage. As indicated by DMA results, PLA/PEG blends may contain PEG rich phases. This PEG phase may be concentrated in interspherulitic regions, which can promote the development of non-cohesive mechanisms. We also observe here that the addition of MAG-PLA has no significant effect on the tensile behavior of PLA.

4. Conclusions

The *in situ* reactive grafting of hydroxy-terminated PEG plasticizer onto the maleic anhydride modified PLA in PLA/PEG blends:

- Does not lead to a dramatic drop of PLA molecular weight by thermal degradation or hydrolysis of ester chains.
- Lowers significantly the glass transition temperature compared to the blends where no grafting could occur (neat PLA + PEG).
- Has no significant effect on the viscoelastic and viscoplastic mechanical behaviors of PLA that are only influenced by the addition of PEG.

Future works on the ageing conditions will be carried out in order to assess the grafting effect of PEG on the stability of the plasticized material and the prevention/limitation of the plasticizer migrating from the bulk.

Acknowledgements

Authors from CIRMAP are grateful to the “Région Wallonne” and European Community (FEDER, FSE) in the frame of “Pôle d'Excellence Materia Nova” for their financial support. CIRMAP thanks the “Belgian Federal Government Office Policy of Science (SSTC)” for general support in the frame of the PAI-6/27. J.-M. Raquez is “chargé de recherche” by the F.R.S.-FNRS. Ph. Dubois thanks the Fonds National de la Recherche-Luxembourg and the Centre de Recherche Public Henri Tudor for financial supports. Thanks also go to Mr. Olivier Godard from the Institut Jean Lamour of Nancy (France) for providing mechanical tests.

References

- [1] Chandra R, Rustgi R. Biodegradable polymers. *Prog Polym Sci* 1998;23:1273–335.
- [2] Grodzinski JJ. Biomedical application of functional polymers. *React Funct Polym* 1999;39:99–138.
- [3] Vroman I, Tighzert L. Biodegradable polymers. *Materials* 2009;2:307–44.
- [4] Rabetafika HN, Paquot M, Dubois P. Les polymères issus du végétal: matériaux à propriétés spécifiques pour des applications ciblées en industrie plastique. *Biotechnol Agron Soc Environ* 2006;10(3):185–96.
- [5] Garlotta D. A literature review of poly(lactide). *J Polym Environ* 2001;9:63–84.
- [6] Lim LT, Auras R, Rubino M. Processing technologies for poly(lactide). *Prog Polym Sci* 2008;33:820–52.
- [7] Nair LS, Laurencin CT. Biodegradable polymers as biomaterials. *Prog Polym Sci* 2007;32:762–98.
- [8] Auras R, Harte B, Selke S. An overview of polylactides as packaging materials. *Macromolecular Bioscience* 2004;4:835–64.
- [9] Weber CJ, Haugaard V, Festersen R, Bertelsen G. Production and applications of biobased packaging materials for the food industry. *Food Addit Contam* 2002;19:172–7.
- [10] Grijpma DW, Penning JP, Pennings AJ. Chain entanglement, mechanical properties and drawability of poly(lactide). *Colloid Polym Sci* 1994;271:1068–81.
- [11] Tonelli AE, Flory PJ. The configuration statistics of random poly(lactide) chains I. Experimental results. *Macromolecules* 1969;2(3):225–7.
- [12] Anderson NS, Schreck KM, Hillmyer MA. Toughening polylactide. *Polymer Review* 2008;48(1):85–108.
- [13] Ljungberg N, Wesslén B. Preparation and properties of plasticized poly(lactide) films. *Biomacromolecules* 2005;6:1789–96.
- [14] Jacobsen S, Fritz HG. Plasticizing polylactide—the effect of different plasticizers on the mechanical properties. *Polym Eng Sci* 1999;39:1303–10.
- [15] Hu Y, Hu YS, Topolkaraev V, Hiltner A, Baer E. Crystallization and phase separation in blends of high stereoregular poly(lactide) with poly(ethene glycol). *Polymer* 2003;44:5681–9.

- [16] Hu Y, Rogunova M, Topolkaraev V, Hiltner A, Baer E. Ageing of poly(lactide)/poly(ethylene glycol) blends. Part 1. Poly(lactide) with low stereoregularity. *Polymer* 2003;44:5701–10.
- [17] Kulinski Z, Piorkowska E, Gadzinowska K, Stasiak M. Plasticization of poly(lactide) with poly(propylene glycol). *Biomacromolecules* 2006;7:2128–35.
- [18] Focarete ML, Dobrzynski MS, Kowalczyk M. *Macromolecules* 2002;35:8472–7.
- [19] Blumm E, Owen AJ. *Polymer* 1995;36:4077–81.
- [20] Okamoto K, Ichikawa T, Yokohara T, Yamaguchi M. Miscibility, mechanical and thermal properties of poly(lactide)/polyester diol blends. *Euro Polym J* 2009;45:2304–12.
- [21] Ljungberg N, Andersson T, Wesslén B. Film extrusion and film weldability of poly(lactide) plasticized with triacetone and tributyl citrate. *J Appl Polym Sci* 2003;88:3239–47.
- [22] Ljungberg N, Wesslén B. Tributyl citrate oligomers as plasticizers for poly(lactide): thermo-mechanical film properties and aging. *Polymer* 2003;44:7679–88.
- [23] Carlson D, Nie L, Narayan R, Dubois P. Maleation of poly(lactide) (PLA) by reactive extrusion. *J Appl Polym Sci* 1999;72:477–85.
- [24] Addiego F, Dahoun A, G'Sell C, Hiver JM. *Polymer* 2006;47:4387–99.
- [25] Avella M, Emco ME, Immirzi B, Malinconico M, Martuscelli E, Paolillo L, Falcigno L. Radical polymerization of poly(butyl acrylate) in the presence of poly(L-lactic acid). 1 synthesis, characterization and properties of blends. *Angew Makromol Chem* 1997;246:49–63.
- [26] Baker W, Scott C, Hu GH. *Reactive polymer blending*. Hanser Publishers; 2001.
- [27] DSFA Murariu M, Pluta M, Bonnaud L, Alexandre M, Dubois PH. Poly(lactide) (PLA)-CaSO₄ composites toughened with low molecular weight and polymeric ester-like plasticizers and related performances. *Eur Polym J* 2008;44:3842–52.
- [28] Pillin I, Montrelay N, Grohens Y. Thermo-mechanical characterization of plasticized PLA: Is the miscibility the only significant factor? *Polymer* 2006;46:4676–82.
- [29] Perego G, Cella GD, Bastioli C. Effect of molecular weight and crystallinity on poly(lactic acid) mechanical properties. *J Appl Polym Sci* 1996;59(1):37–43.
- [30] Baiardo M, Frisoni G, Scandola M, Rimelen M, Lips D, Ruffieux K, et al. Thermal and mechanical properties of plasticized poly(L-lactic acid). *J Appl Polym Sci* 2003;90(7):1731–8.
- [31] Piorkowska E, Kulinski Z, Galeski A, Masirek R. Plasticization of semicrystalline poly(lactide) with poly(propylene glycol). *Polymer* 2006;47(20):7178–88.
- [32] Kulinski Z, Piorkowska E. Crystallization, structure and properties of plasticized poly(L-lactide). *Polymer* 2005;46:10290–300.
- [33] Yang X, Kang S, Yang Y, Aou K, Hsu SL. Raman spectroscopic study of conformational changes in the amorphous phase of poly(lactic acid) during deformation. *Polymer* 2004;45(12):4241–8.
- [34] G'Sell C, Jonas JJ. Yield and transient effects during the plastic deformation of solid polymers. *J Mater Sci* 1981;16(7):1956–74.
- [35] Jo Perez. *Physics and mechanics of amorphous polymers*, Taylor & Francis, 1998.
- [36] Lin L, Argon AS. Structure and plastic deformation of polyethylene. *J Mater Sci* 1994;29(2):294–323.
- [37] Rezgui F, Swistek M, Hiver JM, G'Sell C, Sadoun T. Deformation and damage upon stretching of degradable polymers (PLA and PCL). *Polymer* 2005;46(18):7370–85.



Mechanical and thermal behavior of nanoclay based polymer nanocomposites using statistical homogenization approach

M. Baniassadi^{a,b}, A. Laachachi^a, F. Hassouna^a, F. Addiego^a, R. Muller^c, H. Garmestani^d, S. Ahzi^{b,d,*}, V. Toniazzi^a, D. Ruch^a

^a Centre de Recherche Public Henri Tudor, AMS, 66 Rue de Luxembourg, BP 144, L-4002 Esch/Alzette, Luxembourg

^b University of Strasbourg, IMFS, 2 Rue Boussingault, 67000 Strasbourg, France

^c University of Strasbourg, LIPHT-G2IP (EAc 4379), 25 Rue Becquerel F-67087 Strasbourg, France

^d School of Material Science & Engineering, Georgia Institute of Technology, 771 Ferst Drive, Atlanta, GA 30332-0245, USA

ARTICLE INFO

Article history:

Received 30 March 2011

Received in revised form 9 September 2011

Accepted 12 September 2011

Available online 17 September 2011

Keywords:

A. Nanoclays

A. Nanocomposites

A. Polymer-matrix composites (PMCs)

B. Thermomechanical properties

C. Multiscale modeling

ABSTRACT

In the present study, the effects of nanoclay additives on the effective mechanical and thermal properties of polymer/nanoclay composites have been investigated using experimental and simulation analyzes. In this research, we propose the use of strong contrast statistical continuum theory to predict the effective elastic and thermal properties. To validate our modeling approach, we conducted experimental measurements of these properties for polyamide/nanoclay nanocomposites with concentrations of 1, 3 and 5 wt.% of nanoclay particles. Three-dimensional isotropic nanocomposite samples with randomly oriented monolayer nanoclays were computer generated and used to calculate the statistical correlation functions of the realized model. These correlation functions have been exploited to calculate effective thermal and elastic properties of the nanocomposite. The simulation results have shown that effective stiffness can be increased significantly with small amounts of particle concentration for the exfoliated clay monolayers. The predicted effective conductivity and elastic modulus have been compared to our experimental results. Effective thermal conductivity shows satisfactory agreement with experimental data. However, the predicted results for the elastic modulus overestimate the experimental data, which might be due to the increasing intercalated structure for high concentration of nanofiller and to anisotropic properties of the nanoclay.

© 2011 Elsevier Ltd. All rights reserved.

1. Introduction

The improvement of mechanical, thermal, gas barrier and fire resistance properties of organic polymer materials is a major concern, particularly in the domains of transportation, building construction, and electrical engineering. Polymer nanocomposites often exhibit physical and chemical properties dramatically different from the corresponding pure polymers. Numerous and recent studies have shown the interest of the use of clay nanoparticles (above all modified montmorillonites) as nanofillers for several polymers [1,2]. The usual content of clay that has been used is in the range of 5–10 wt.% organo-modified montmorillonite. The reasons are the high aspect ratio (more than 1000), the high surface area (more than 750 m²/g) and the high modulus of these lamellar nanoparticles (176 GPa). Depending upon the processing conditions and characteristics of both the polymer matrix and organo-clay, the in situ dispersion of organoclay inside the host polymer

by melt blending can be more or less achieved, leading to intercalated or exfoliated nanocomposites.

Recently most of the researches about layered silicates are focused especially on montmorillonites (MMT), as the reinforcing phase due to availability and versatility of these types of nanofillers [3]. Depending on the process conditions and on the polymer/nanofiller affinity, the layered silicates dispersed into the polymer matrix can be observed in different states of intercalation and/or exfoliation [4]. The best performances are commonly achieved with the exfoliated structures [5]. Besides that, the insertion of clay materials into a polymer matrix led to a significant decrease of the diffusion coefficient of various gases into the composites [3,6]. Several homogenization methods have been used in the literature to predict effective properties of nanocomposite properties. For instance, the effective mechanical properties of such nanocomposites have been investigated using inclusion-based theories which call for the Eshelby solution for ellipsoidal inclusions in a homogeneous medium [7–15]. For example, the generalized Mori-Tanka model has been exploited to predict the effective elastic modulus of the starch/clay nanobiocomposites [16]. Similarly, the effective thermal

* Corresponding author at: University of Strasbourg, IMFS, 2 Rue Boussingault, 67000 Strasbourg, France. Tel.: +33 (0) 677 39 4011; fax: +33 (0)3 68 85 29 36.

E-mail address: ahzi@unistra.fr (S. Ahzi).

conductivity of composites with ellipsoidal inclusions have been widely considered using various micromechanical models in literature [17,18].

In this paper we used a strong contrast [19–22] multiscale statistical method to predict the overall modulus and thermal conductivity of montmorillonite polymer based nanocomposites. To take into account the geometrical information on inclusions and their distribution in the matrix, a statistical continuum approach has been developed based on statistical correlation functions [22]. In this study two-point and three-point correlation functions have been taken into account to describe the microstructure. Using Monte Carlo simulation, two-point correlation functions of the realized nanostructures have been extracted and in a following step three point correlation functions have been estimated based on the previously determined two point correlation functions [23]. From the two-point and three-point correlation functions, the effective thermal conductivity of the nanocomposites was calculated using a strong contrast expansion. To validate our proposed statistical approach, we conducted experimental tests to measure both the elastic and thermal properties for polyamide/MMT nanocomposites with 1, 3 and 5 wt.% of nanoparticles. We then we compared our simulate results to the experimental one.

2. Experimental part

2.1. Materials

The polyamide (PA) resin (viscosity 35p, at 240 °C) was supplied by Scientific Polymer. The PA density was 0.99 g cm⁻³ (at 23 °C). The filler was a commercial organo-modified montmorillonite, Cloisite 30B (OMMT) and was purchased from Southern Clay Co. The modifier was methyl bis-2-hydroxyethyl tallow ammonium and its concentration was 90 meq per 100 g of clay. This treatment leads to a good dispersion in the polar polymer matrix and allows preparing intercalated or exfoliated nanocomposites. The density of organo-modified montmorillonite was 1.98 g cm⁻³ (at 23 °C). We should note that the choice of the commercial organo-clay (cloisite 30B) was based on the good compatibility of the organic part of the cloisite 30B and the chemical structure of polyamide to promote a good dispersion.

2.2. Nanocomposites preparation

PA and OMMT were first dried at 80 °C during 4 h. PA–OMMT nanocomposites were then prepared by melt-mixing, the molten PA pellets and the OMMT at different weight fractions of clay, using a co-rotating twin-screw extruder (DSM Xplore), at 180 °C for 5 min, with a rotation speed of 150 rpm. The investigated weight fractions of OMMT in PA nanocomposites were 0, 1, 3 and 5 wt.%.

2.3. Transmission electron microscopy

Transmission electron microscopy (TEM) analyzes of PA–OMMT nanocomposites were carried out using a Carl Zeiss LEO 922 apparatus at 200 kV. The ultrathin films (70 nm thick) were prepared with a LEICA EM FC6 cryo-ultramicrotome at 25 °C.

2.4. X-ray diffraction

Wide-angle X-ray scattering (WAXS) experiments were performed in a PANalytical X'Pert Pro MPD equipment using Cu K α radiation (wavelength: 1.54 Å) generated at 45 kV and 40 mA. Tests were conducted with the transmission mode of this equipment and using a focus mirror (divergence slit 1/4°, anti-scatter slit 1/4°, soller slit 0.04 rad) as incident optics and PIXcel detector

(anti-scatter slit 1/32° and soller slit 0.04 rad) as secondary optics. This specific configuration enables to obtain a high resolution in the 2 theta range of interest (3–10°) providing information about crystalline structure of the nanoclay.

2.5. Mechanical properties

The evaluation of the mechanical properties of PA and its nanocomposites was carried out using a Dynamic Mechanical Analyzer (DMA 242C-Netzsch). Storage (E') and loss (E'') modulus were measured as a function of temperature (–175 °C to +70 °C) with a dynamic temperature ramp sweep at 2 K min⁻¹. Measurements were performed using the single cantilever bending mode at a frequency of 1 Hz. All DMA sample were hot-pressed and cut in the form of 9.70–10.40 mm-long, 1.15–1.47 mm-thick and 4.95–5.9 mm-wide specimens. To check the reproducibility of the experimental data and to ensure their consistency, three specimens were tested for each formulation.

2.6. Laser flash

Thermal diffusivity and thermal conductivity of studied materials were measured by the laser flash method. This technique entails heating the front side of a small, usually disk-shaped plane-parallel sample by a short (≤ 1 ms) laser pulse. The temperature rise on the rear surface is measured versus time using an infrared detector. All samples were coated on both faces with a very thin layer of colloidal graphite. The thermal diffusivity $a(T)$ values can then be converted to thermal conductivity $\lambda(T)$ by using the specific heat $C_p(T)$ and bulk density $\rho(T)$ of studied material according to:

$$\lambda(T) = \rho(T) \cdot C_p(T) \cdot a(T) \quad (1)$$

The samples in the shape of disks, 12 mm in diameter and 1 mm in thickness were prepared by hot-pressing. The measurements were carried out from room temperature to 100 °C under an argon flow. Three samples were tested for each system and the uncertainty for the determination of thermal diffusivity was evaluated to $\pm 3\%$.

3. Computer generated model

In this research, three-dimensional isotropic virtual samples with randomly oriented disks as mono-layer nanoclays are generated, using the soft-core approach, and used to calculate the statistical two point correlation functions of the realized nanostructure. These statistical correlation functions have been utilized as nanostructure descriptor to approximate the strong contrast solution for thermal and mechanical properties of nanocomposites. In this solution, two point and three point correlation functions have been used as input functions to solve the strong contrast equations for the effective thermal and elastic properties [22]. In this study, three point correlation functions have been approximated using two point correlation functions [23,24].

3.1. Statistical correlation function calculation

In this work, the Monte Carlo estimation of two-point correlation function are acquired by assigning a number of random vectors within the generated microstructure and examining the number fraction of the sets (of vectors) which satisfy the different types of correlation states [24]. Fig. 1 shows two point correlation functions for three composites with 1, 3 and 5 wt.% of nanoclay.

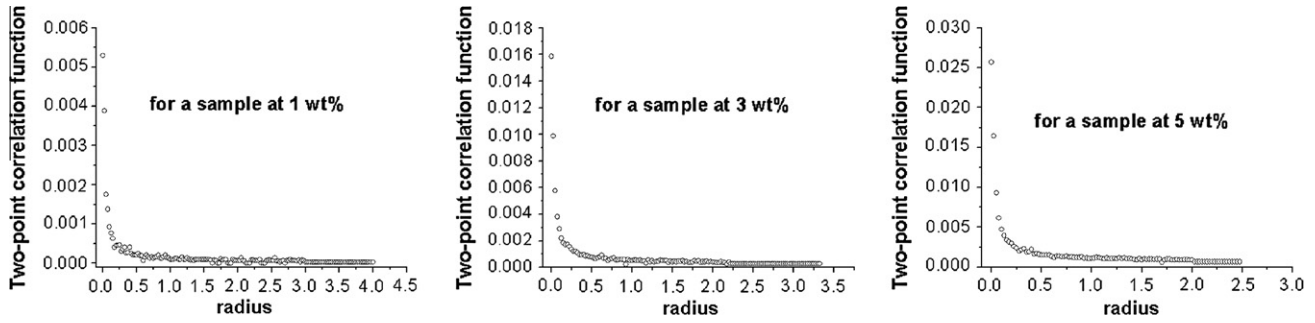


Fig. 1. Two point correlation function.

Similarly, three-point correlation functions for phase p can be interpreted as the probability that three points at positions x_1 , x_2 , x_3 are found in phase p and this interpretation can be generalized for N-point correlation functions [22].

3.2. Thermal conductivity

To evaluate the effective conductivity at macroscopically anisotropic two-phase composites, the strong-contrast expansion approach has been further improved by establishing an integral equation for the cavity intensity field [19,20,22]. The n th order tensorial expansions are expressed in terms of integrals over products of certain tensorial fields and a determinant of N-point statistical correlation functions which make the integrals convergent for the infinite volume limit. One of the salient aspects of this expansion is that when truncated, at finite order, they give reasonably accurate estimates at rather all concentrations even though the contrast between the conductivities is high.

Assuming isotropic properties of the PA matrix and nanoclay particles, the effective conductivity tensor λ_e of the nanocomposite is determined using the strong-contrast formulation of the statistical continuum theory [22]:

$$\{\lambda_e - \lambda_R \mathbf{I}\}^{-1} \cdot \{\lambda_e + 2\lambda_R \mathbf{I}\} = \frac{1}{\beta_{SR} S_1^S(\mathbf{x})} \mathbf{I} - 3\lambda_R \iint \left[\frac{S_2^S(1,2) - S_1^S(1)S_1^S(2)}{S_1^S(\mathbf{x})S_1^S(\mathbf{x}')} \right] \mathbf{M}^R(1,2) d\mathbf{2} - \lambda_R^2 d^2 \beta_{SR} \iint \left[\frac{S_3^S(1,2,3)}{S_1^S(\mathbf{x})S_1^S(\mathbf{x}')S_1^S(\mathbf{x}'')} - \frac{S_2^S(1,2)S_2^S(2,3)}{S_1^S(1)S_1^S(2)S_1^S(3)} \right] \mathbf{M}^R(1,2) \cdot \mathbf{M}^R(2,3) d\mathbf{2} d\mathbf{3} - \dots \quad (2)$$

Here, we have adopted the shorthand notation consisting in representing x_1 , x_2 , x_3 by 1 and 2, 3 respectively. In Eq. (2), \mathbf{I} is the second-order identity tensor, λ_R is the reference conductivity, $\mathbf{M}^R(1,2)$ is a second-order tensor defined below, and β_{SR} is the polarizability:

$$\beta_{SR} = \frac{\lambda_S - \lambda_R}{\lambda_S + (d-1)\lambda_R} \quad (3)$$

The subscript R stands for the reference phase, which is chosen here to be the nanoclay phase, and the subscript/superscript S stands for the PA matrix. The second order tensor $\mathbf{M}^R(1,2)$ is defined by:

$$\mathbf{M}^R(1,2) = \frac{1}{\Omega \lambda_R} \frac{3\mathbf{t}\mathbf{t} - \mathbf{I}}{(\mathbf{x}_1 - \mathbf{x}_2)^3} \quad (4)$$

$$\mathbf{t} = \frac{(\mathbf{x}_1 - \mathbf{x}_2)}{|\mathbf{x}_1 - \mathbf{x}_2|} \quad (5)$$

where Ω is the total solid angle contained in a 3-dimensional sphere.

$S_1^S(1)$, $S_2^S(1,2)$ and $S_3^S(1,2,3)$ are the probability functions that contain the microstructure information. The one-point probability function, $S_1^S(1)$, is the volume fraction of the nanoparticles. The

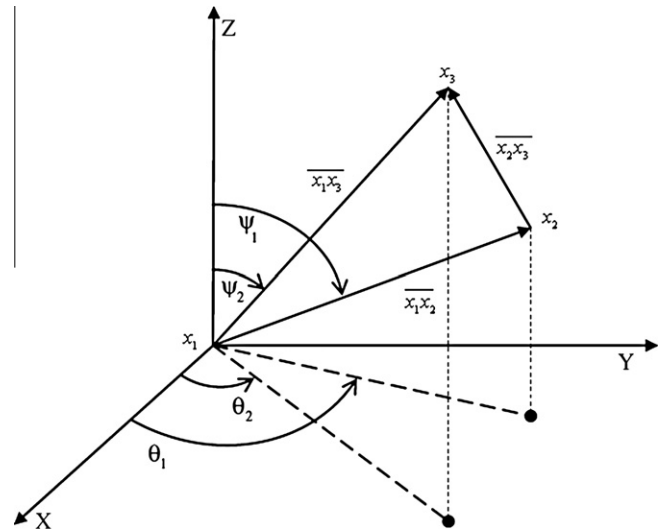


Fig. 2. Representation of vectors in spherical coordinate.

two-point probability function, $S_2^S(1,2)$, is calculated from the Monte Carlo simulation. The three-point probability function, $S_3^S(1,2,3)$, is calculated from the following analytical approximation [23]:

$$S_3^S(1,2,3) \cong \left[\frac{|\mathbf{x}_1 \mathbf{x}_2|}{|\mathbf{x}_1 \mathbf{x}_2| + |\mathbf{x}_1 \mathbf{x}_3|} S_2^p(1,3) + \frac{|\mathbf{x}_1 \mathbf{x}_3|}{|\mathbf{x}_1 \mathbf{x}_2| + |\mathbf{x}_1 \mathbf{x}_3|} S_2^p(1,2) \right] \frac{S_2^p(2,3)}{S_1^p(1)} \quad (6)$$

Fig. 2 defines the variables used in this approximation in local coordinates.

3.3. Mechanical model

In general, strong-contrast expansions take a larger radius of convergence than weak-contrast expansion for the same reference properties [21]. The statistical theory of strong contrast has been used to determine the effective stiffness tensor of macroscopically isotropic two-phase composites. In this approach, an integral equation for the strain field leads to an exact series expansions for the effective stiffness tensor of two-phase composite media. In this method, N-point correlation functions show up in the final equations that characterize the microstructure. The general term of the expansion for a reference phase q is written as follows [21]:

$$\varphi_p^2 L^{(q)} : [L_e^{(q)}]^{-1} = \varphi_p I - \sum_{n=2}^{\infty} B_n^{(p)} \quad (7)$$

where ϕ_p is the volume fraction of phase p and I is the fourth-order identity tensor.

In Eq. (7) the tensor coefficients (B_n) are the following integrals over products of the U Tensors and the S_n represent the N -point correlation functions for phase p :

$$B_2^{(p)} = \int_{\varepsilon} d2U^{(q)}(1,2)[S_2^{(p)}(1,2) - \varphi_p^2] \quad (8)$$

$$B_n^{(p)} = (1 - \varphi_p)^n \left(\frac{1}{\varphi_p}\right)^{n-2} \int d2... \int dn U^{(q)}(1,2) : U^{(q)}(2,3) \cdots U^{(q)}(n-1,n) \Delta_n^{(p)}(1,...,n), \quad n \geq 3, \quad (9)$$

$$\mathbf{r} = \mathbf{x} - \mathbf{x}', \quad \mathbf{t} = \frac{\mathbf{r}}{|\mathbf{r}|} \quad (10)$$

In Eq. (7) the effective tensor $L_e^{(q)}$ is given by:

$$L_e^{(q)} = \{C_e - C^{(q)}\} \{I + A^{(q)} : [C_e - C^{(q)}]\}^{-1} \quad (11)$$

where C_e is the effective stiffness tensor, C^q is the stiffness tensor of the reference phase and $A^{(q)}$ is a forth order constant tensor [22].

Here $\Delta_n^{(p)}(1,...,n)$ is a position-dependent determinant that is calculated using N -point correlation function for a given phase p [21].

The tensor U is calculated based on the position-dependent fourth-order $H(r)$ and the related tensor for phase q , $L^{(q)}$:

$$U_{ijkl}^{(q)}(\mathbf{r}) = L_{ijmn}^{(q)} H_{mnkl}^{(q)}(\mathbf{r}) = [dK_q + 2(d-1)G_q] \left\{ \left[K_{pq} - \frac{(d+2)G_q}{d(K_q + 2G_q)} \mu_{pq} \right] \frac{\delta_{ij}}{d} H_{mnkl}^{(q)}(\mathbf{r}) + \frac{(d+2)G_q}{d(K_q + 2G_q)} \mu_{pq} H_{ijkl}^{(q)}(\mathbf{r}) \right\} \quad (12)$$

where d is space dimension and the tensor $H(r)$ is the symmetrized double gradient tensor [21].

The constant tensor for phase q or $L^{(q)}$ is expressed as:

$$L^{(q)} = [dK_q + 2(d-1)G_q] \left[k_{pq} \Lambda_h + \frac{(d+2)G_q}{d(K_q + 2G_q)} \mu_{pq} \Lambda_s \right] \quad (13)$$

where d is space dimension and where k_{pq} and μ_{pq} are introduced as bulk and shear modulus polarizabilities [21], K_q and G_q are respectively the bulk modulus and the shear modulus of the reference phase and Λ_h and Λ_s are the projection tensors[21].

For macroscopically isotropic media, Eq. (7) can be simplified as [21]:

$$\varphi_p^2 \left[\frac{k_{pq}}{k_{eq}} \Lambda_h + \frac{\mu_{pq}}{\mu_{eq}} \Lambda_s \right] = \varphi_p I - \sum_{n=2}^{\infty} B_n^{(p)} \quad (14)$$

In this work, the calculations have been performed for the first and second terms of B and other terms have been neglected because of the complexity of the calculations:

$$\varphi_p^2 \left[\frac{k_{pq}}{k_{eq}} \Lambda_h + \frac{\mu_{pq}}{\mu_{eq}} \Lambda_s \right] = \varphi_p I - B_2^{(p)} - B_3^{(p)} \quad (15)$$

$$B_2^{(p)} = \int_{\varepsilon} d2U^{(q)}(1,2) [S_2^{(p)}(1,2) - \varphi_p^2] \quad (16)$$

$$B_3^{(p)} = \left(\frac{1}{\varphi_p} \right) \int d2... \int dn U^{(q)}(1,2) : U^{(q)}(2,3) \Delta_3^{(p)}(1,...,3) \quad (17)$$

$$\Delta_3^{(p)}(1,...,3) = \begin{vmatrix} S_2^{(p)}(1,2) & S_1^{(p)}(2) \\ S_3^{(p)}(1,2,3) & S_2^{(p)}(2,3) \end{vmatrix} \quad (18)$$

We recall that for three-point correlation functions, we are using the analytical approximation in Eq. (6).

4. Results and discussion

4.1. Thermal conductivity

Thermal conductivity of neat PA decreases from $0.127 \text{ W m}^{-1} \text{ K}^{-1}$ with increasing temperature (see Fig. 3). In our calculation, the thermal conductivity of nanoclay particles has been estimated using a semi-inverse strong contrast approach [25] for the compressed powder sample at about $0.55 (\text{W m}^{-1} \text{ K}^{-1})$. We have neglected the effect of temperature on this property. We analyzed the thermal conductivity for PA/nanoclay with 1, 3 and 5 wt.%. The corresponding volume fractions are obtained from the two point correlation functions (see Fig. 1) as 0.55%, 1.6% and 2.5%, respectively.

Our results show that the addition of nanoclay leads to an increase in thermal conductivity of PA. Moreover, the higher the amount of nanoclay, the higher the thermal conductivity becomes. As shown in Fig. 3, the thermal conductivity of the PA-OMMT composites predicted using the strong contrast approach fits quite well with the experimental results. The simulated curves are not smooth because we used non-smooth experimental data of conductivity for pure polymer as a function of temperature (see Fig. 3).

For comparison with the classical homogenization theories, we have used the Mori-Tanaka approach to estimate the effective

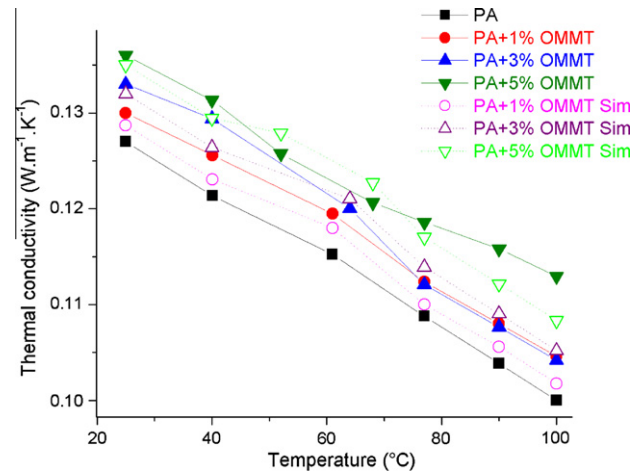


Fig. 3. Comparison between experimental and simulation thermal conductivity of PA and its nanocomposites with OMMT.

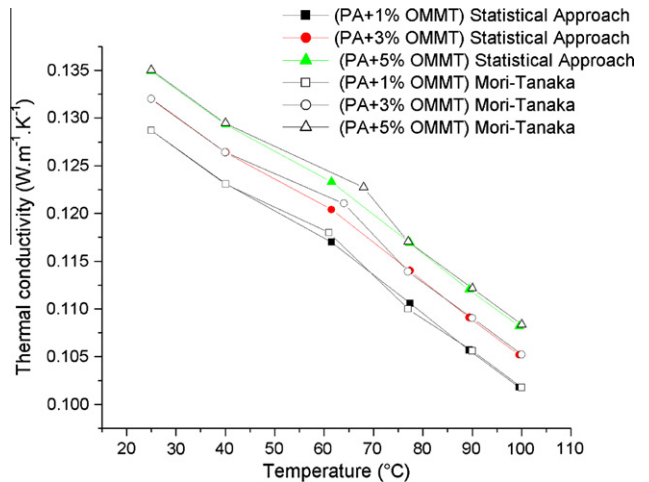


Fig. 4. Comparison between statistical approach and Mori-Tanaka homogenization technique for thermal conductivity of two phase composites as function of temperature T for PA/OMMT nanocomposites (1, 3 and 5 wt.%).

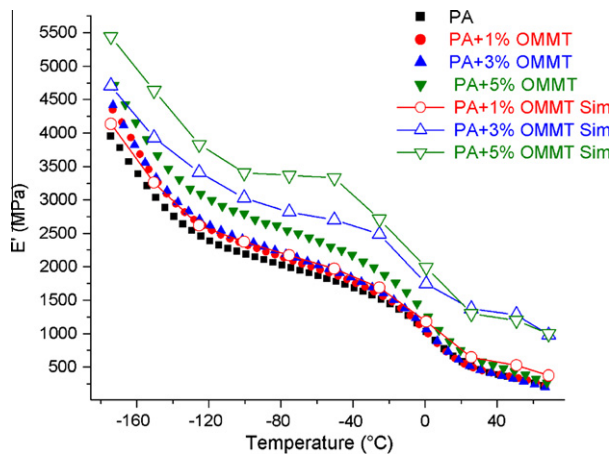


Fig. 5. Experimental and simulated elastic modulus of two phases composite as a function of temperature T for neat PA and its composites with OMMT (1, 3 and 5 wt.%).

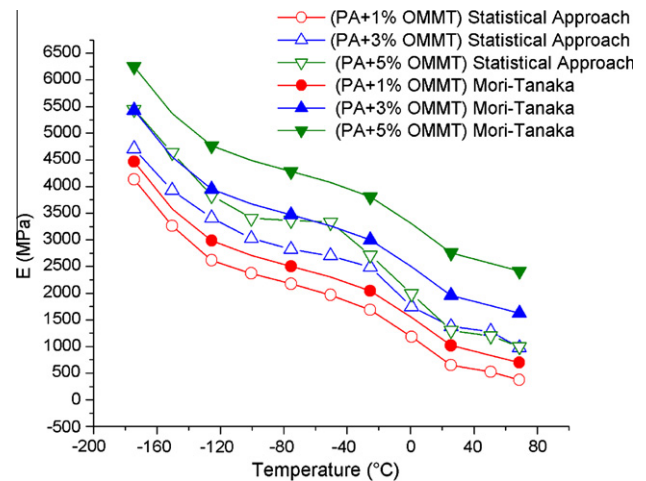


Fig. 6. Comparison between statistical approach and Mori-Tanaka homogenization technique for the elastic modulus of two phase composites as function of temperature T for PA/OMMT nanocomposites (1, 3 and 5 wt.%).

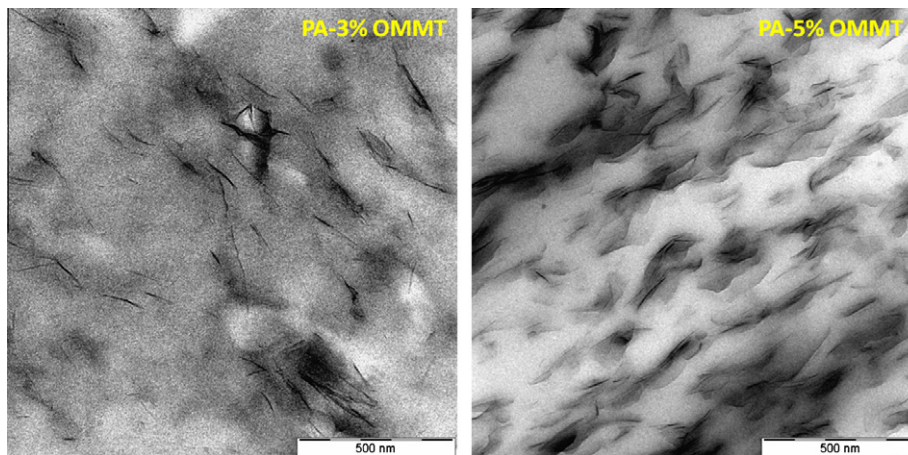


Fig. 7. TEM micrographs of PA-3%OMMT and PA-5%OMMT nanocomposite.

thermal conductivity [26]. The results are shown in Fig. 4 where they match both the statistical approach predictions.

4.2. Thermo-mechanical properties

Since montmorillonite can be used for improving thermal stability, it is important that it does not dramatically deteriorate the mechanical properties (stiffness). To predict the elastic modulus of the composite, values of the elastic modulus of nanoclay found in the literature was used, $E_{\text{nanoclay}} = 176$ GPa [27]. The elastic modulus of the PA matrix is shown in Fig. 4 as function of temperature. Fig. 5 shows the effect of the nanoclay on the mechanical properties (storage modulus E') obtained by DMA measurements as well as those obtained using statistical continuum theory. At room temperature, PA exhibits a significant storage modulus ($E'_{25^\circ\text{C}} = 550$ MPa). The addition of 1–5 wt.% nanoparticles did not have any impact on $E'_{25^\circ\text{C}}$. Below 0°C , the values of E' of the composites containing 1 or 3 wt.% nanoclay are similar. However E' increases by $\sim 20\%$ when 5 wt.% clay is added to PA.

In Fig. 6, we report a comparison of the estimated effective modulus by the statistical approach and a classical model based on the Mori-Tanaka homogenization approach [7]. As shown in this figure, the Mori-Tanaka based prediction exceeds the prediction by the sta-

tistical approach and the mismatch between the two predictions increases with fillers content.

It is found that E' of the composites predicted by our simulations fit well with the experimental data for 1 wt.%. However, simulated values of E' for the composites containing more than 1 wt.% nanoclay, are unfortunately higher than the experimental ones for the same composition. In the next, we will attempt to explain these discrepancies.

TEM analyzes of the PA-OMMT nanocomposites were performed in order to investigate the distribution and the dispersion of OMMT into the PA matrix. Fig. 7 shows two TEM images for two different nanofiller contents, 3 and 5 wt.%. The images show decreasing exfoliation state of nanofillers with increasing volume fraction of the fillers.

The discrepancies between the experimental and the theoretical results or the elastic modulus can be explained by the dispersion of the nanoclays in PA matrix. Indeed, the statistical continuum theory calculations assume that nanoclays in PA are in exfoliated state (Fig. 8). On the other hand, the experimental results showed that the nanoclays are in exfoliated state in the composites PA – 1 wt.% OMMT and in both exfoliated–intercalated state in the composites PA – 3 wt.% OMMT and PA – 5 wt.% OMMT.

In order to adjust the results of the statistical approach for the microstructures with partial exfoliation, one needs to have very

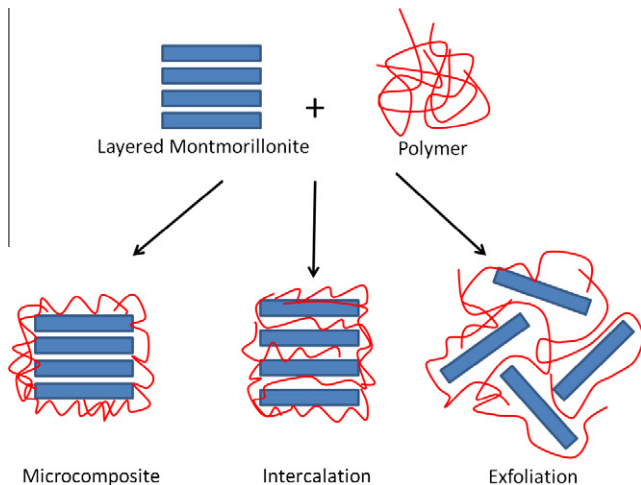


Fig. 8. Polymer/clay nanocomposite morphologies.

detailed information on the microstructure where all of the phases (matrix, exfoliated fillers, intercalated fillers and micro-fillers) are clearly identified. This requires, unfortunately, a lot of work which is out of the scope of the present paper. In addition, in the classical homogenization approaches such as the Mori–Tanaka approach, it is also possible to adjust the results knowing the volume fraction of each of the present phases. This has been addressed the literature by different authors (see for instance [15,16]).

5. Conclusion

In the present study, the effects of nanoclay additives on the effective mechanical and thermal properties of nanoclay based polymer composites have been investigated using experimental and simulation work. In the present study, Statistical continuum theory is used to predict the effective thermal conductivity and elastic modulus of nanoclay based polymer composites.

In this research, Monte Carlo simulations have been performed to find two-point probability functions of each phase. Two-point and three-point probability functions as statistical descriptor of inclusions have been used to solve strong contrast homogenization for the effective thermal and mechanical properties of nanoclay based polymer composites. The predicted thermal conductivity results have shown satisfactory agreement with experimental data. However, the effective elastic modulus results for high concentration of nanoclay overestimate the experimental data. This discrepancy is probably due to increasing intercalated structure of nanoclay for high nanofiller concentrations.

Acknowledgment

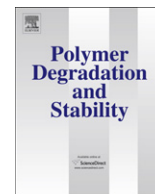
The authors would like to thank the Fond National de la Recherche Luxembourg (FNR Luxembourg) for providing the PhD Grant of Majid Baniassadi.

Reference

- [1] Gilman JW. Flammability and thermal stability studies of polymer layered-silicate (clay) nanocomposites. *Appl Clay Sci* 1999;15(1–2):31–49.
- [2] Matadi R, Gueguen O, Ahzi S, Gracio J, Muller R, Ruch D. Investigation of the stiffness and yield behaviour of melt-intercalated poly(methyl methacrylate)/organoclay nanocomposites: characterisation and modelling. *J Nanosci Nanotechnol* 2010;10:2956–61.
- [3] Sinha Ray S, Okamoto M. Polymer/layered silicate nanocomposites: a review from preparation to processing. *Prog Polym Sci* 2003;28(11):1539–641.
- [4] Vaia RA, Giannelis EP. Lattice model of polymer melt intercalation in organically-modified layered silicates. *Macromolecules* 1997;30(25):7990–9.
- [5] Pollet E, Delcourt C, Alexandre M, Dubois P. Organic–inorganic nanohybrids obtained by sequential copolymerization of ϵ -caprolactone and L,L-lactide from activated clay surface. *Macromol Chem Phys* 2004;205(16):2235–44.
- [6] Kojima Yoshitsugu, Usuki Arimitsu, Kawasumi Masaya, Okada Akane, Fukushima Yoshiaki, Kurauchi Toshio, et al. Mechanical properties of nylon 6-clay hybrid. *J Mater Res* 1993;8(5).
- [7] Benveniste Y. A new approach to the application of Mori–Tanaka's theory in composite materials. *Mech Mater* 1987;6(2):147–57.
- [8] Eshelby JD. The determination of the elastic field of an ellipsoidal inclusion, and related problems. *Proc Royal Soc London Ser A, Math Phys Sci* 1957;241(1226):376–96.
- [9] Hori M, Nemat-Nasser S. Double-inclusion model and overall moduli of multi-phase composites. *Mech Mater* 1993;14(3):189–206.
- [10] Hu GK, Weng GJ. The connections between the double-inclusion model and the Ponte Castaneda–Willis, Mori–Tanaka, and Kuster–Toksoz models. *Mech Mater* 2000;32(8):495–503.
- [11] Luo J-J, Daniel IM. Characterization and modeling of mechanical behavior of polymer/clay nanocomposites. *Compos Sci Technol* 2003;63(11):1607–16.
- [12] Mori T, Tanaka K. Average stress in matrix and average elastic energy of materials with misfitting inclusions. *Acta Metall* 1973;21(5):571–4.
- [13] Mura T. *Micromechanics of defects in solids*. 2nd rev. ed. Lancaster; 1987.
- [14] Nemat-Nasser S, Hori M. *Micromechanics: overall properties of heterogeneous materials*. 2nd rev. ed. Amsterdam; New York: Elsevier; 1999.
- [15] Sheng N, Boyce MC, Parks DM, Rutledge GC, Abes JJ, Cohen RE. Multiscale micromechanical modeling of polymer/clay nanocomposites and the effective clay particle. *Polymer* 2004;45(2):487–506.
- [16] Chivrac F, Gueguen O, Pollet E, Ahzi S, Makradi A, Averous L. Micromechanical modeling and characterization of the effective properties in starch-based nano-biocomposites. *Acta Biomater* 2008;4(6):1707–14.
- [17] Mercier S, Molinari A, El Mouden M. Thermal conductivity of composite material with coated inclusions: applications to tetragonal array of spheroids. *J Appl Phys* 2000;87(7):3511–9.
- [18] Milhans J, Ahzi S, Garmestani H, Khaleel MA, Sun X, Koepfel BJ. Modeling of the effective elastic and thermal properties of glass-ceramic solid oxide fuel cell seal materials. *Mater Des* 2009;30(5):1667–73.
- [19] Pham DC, Torquato S. Strong-contrast expansions and approximations for the effective conductivity of isotropic multiphase composites. *J Appl Phys* 2003;94(10):6591–602.
- [20] Sen AK, Torquato S. Effective conductivity of anisotropic two-phase composite media. *Phys Rev B* 1989;39(7):4504.
- [21] Torquato S. Effective stiffness tensor of composite media–I. Exact series expansions. *J Mech Phys Solids* 1997;45(9):1421–48.
- [22] Torquato S. *Random heterogeneous materials: microstructure and macroscopic properties*. New York; London: Springer; 2002.
- [23] Mikdam A, Makradi A, Ahzi S, Garmestani H, Li DS, Remond Y. A new approximation for the three-point probability function. *Int J Solids Struct* 2009;46(21):3782–7.
- [24] Baniassadi M, Garmestani H, Li DS, Ahzi S, Khaleel M, Sun X. Three-phase solid oxide fuel cell anode microstructure realization using two-point correlation functions. *Acta Mater* 2011;59(1):30–43.
- [25] Baniassadi M, Addiego F, Laachachi A, Ahzi S, Garmestani H, Hassouna F, et al. Using SAXS approach to estimate thermal conductivity of polystyrene/zirconia nanocomposite by exploiting strong contrast technique. *Acta Mater* 2011;59(7):2742–8.
- [26] Böhm HJ, Nogales S. Mori–Tanaka models for the thermal conductivity of composites with interfacial resistance and particle size distributions. *Compos Sci Technol* 2008;68(5):1181–7.
- [27] Chen B, Evans JRG. Elastic moduli of clay platelets. *Scr Mater* 2006;54(9):1581–5.

Contents lists available at [SciVerse ScienceDirect](http://www.sciencedirect.com)

Polymer Degradation and Stability

journal homepage: www.elsevier.com/locate/polydegstab

Development of new approach based on Raman spectroscopy to study the dispersion of expanded graphite in poly(lactide)

Fatima Hassouna^a, Abdelghani Laachachi^{a,*}, David Chapron^b, Yamna El Mouedden^a, Valérie Toniazzo^a, David Ruch^a^aAMS – Centre de Recherche Public Henri Tudor, 66 Rue de Luxembourg, BP 144, L-4002 Esch-sur-Alzette, Luxembourg^bLMOPS – Université Paul Verlaine Metz, Supélec, 2 Rue Edouard, Belin F-57070 Metz, France

ARTICLE INFO

Article history:

Received 26 August 2011

Received in revised form

30 September 2011

Accepted 4 October 2011

Available online 12 October 2011

Keywords:

Poly(lactide) (PLA)

Nanocomposite

Expanded graphite

Dispersion

Thermal properties

Raman

ABSTRACT

A new approach has been developed to study the dispersion/delamination of expanded graphite (EG) in poly(lactide) (PLA) by using Raman spectroscopy. This technique is more sensitive and therefore fully complementary to more standard dispersion characterization techniques like SEM, TEM and X-ray diffraction. The incorporation of EG into PLA was carried out by a twin-screw micro-extruder. The effects of the dispersion and delamination of EG on the thermal and thermo-mechanical properties of polylactide-EG nanocomposites were investigated. In contrast to the standard techniques, Raman spectroscopy was able to show a partial exfoliation, which could therefore explain the slight improvement of the PLA–EG thermal and thermo-mechanical properties.

© 2011 Elsevier Ltd. All rights reserved.

1. Introduction

Graphite is widely used as reinforcement for polymers because of its ability to modify their mechanical and electrical properties [1]. Indeed, the potentially high aspect ratio of single graphene sheets indicates that graphene can greatly improve mechanical and gas barrier properties if it is well dispersed in a polymer matrix [2,3]. If exfoliated and homogeneously dispersed, it can improve the properties at relatively small loading compared to conventional carbon fillers such as carbon black and carbon fibres [1]. However, to up to now, the exfoliation of graphite to graphene and its incorporation into polymers has not been fully successful. Because of strong interactions and small spacing between planes, it is very hard to achieve a fully separated state of graphene. Indeed, Van der Waals forces exist between the carbon layers with an interaction energy of about 2 eV/nm². Therefore, the order of magnitude of the force necessary to exfoliate the graphite is about 300 nN/μm² [4,5], which is very difficult to achieve.

Many researchers have recently attempted to exfoliate and optimize the dispersion of graphite sheets using intercalation with

alkali metals [6] or exposing them to strong acidic conditions [7–9]. The expansion of the layer spacing has been achieved *via* heat treatment [6,8] or exposure to microwave radiation followed by mechanical grinding [10]. As a result of the expansion, the surface area of graphite was considerably enhanced. Expanded graphite (EG) has been incorporated into polymer *via in situ* polymerization [9], solvent mixing [11], or coating onto polymer particles or by melt processing [10] leading to the improvement of the intrinsic properties of the polymer matrix.

We choose to incorporate commercially available EG in poly(lactide) (PLA). As a biodegradable thermoplastic derived from sustainable sources, PLA has received considerable attention for conventional uses.

Expanded graphite reinforced PLA has been already produced by melt-blending [12,13]. Thermo-mechanical and fire-retardant properties were evaluated. It has been shown that EG nanofillers provide PLA composites with competitive functional properties. The final composite exhibits a high rigidity, with Young's modulus and storage modulus increasing with EG content. The presence of EG improves significantly the thermal stability while preserving the glass transition and melting temperature of the original PLA matrix.

The purpose of the present paper is to investigate the dispersion of EG in PLA matrix melt-processed using DSM Xplore twin-screw

* Corresponding author. Tel.: +352 42 59 91 591.

E-mail address: abdelghani.laachachi@tudor.lu (A. Laachachi).

micro-extruder. To provide good and complete information about the dispersion and particularly the delamination of the EG occurring during the melt-blending, a new approach has been developed by using Raman spectroscopy to study the dispersion of EG in these nanocomposites and validated by conventional dispersion characterization techniques (SEM, TEM and X-ray diffraction). The influence of the dispersion state of EG on the thermal stability, thermo-mechanical properties and thermal diffusivity and conductivity of the composites is also reported.

2. Experimental part

2.1. Materials and processing method

Poly(lactide) (PLA) was provided by NatureWorks LLC under the reference 4042D. Expanded graphite (EG) was supplied by ECOPHIT G. According to the technical sheet, the principal characteristics of the specific grade of EG used GFG 5 are: real density = 2.25 g/cm³, mean diameter (d_{50} = 5–7 μ m). It was used without any further purification.

Before processing by melt-blending, PLA and EG were dried at 40 °C overnight under vacuum to minimize the water content for melt-blending. PLA–EG nanocomposites were prepared by mixing, in an appropriate ratio, the molten PLA pellets and the EG using a twin-screw extruder (DSM Xplore), at 180 °C. Three different speed rates were explored: 50, 100 and 150 rpm at two different residence times of 5 min and 10 min. The EG content into PLA nanocomposites was 3 wt%. For comparison, pure PLA was processed in similar conditions of melt-blending.

For the thermo-mechanical analyses by Dynamical Mechanical Analysis, 50 × 10 × 1 mm³ plates of PLA were compression-moulded using a Carver press and a specific mould. The utilized procedure was as follows: i) extruded PLA pellets were introduced within the mould, ii) PLA was heated at 190 °C during 3 min, iii) PLA was compressed during 30 s with a pressure of 15 MPa, and iv) under the same pressure (15 MPa), PLA was cooled by means of a room temperature water circulation.

2.2. Size exclusion chromatography

Size exclusion chromatography (SEC) analyses were carried out to follow the changes of the molecular weight of PLA upon melt-blending in absence and in presence of EG. SEC analyses were run at room temperature (concentration 2 mg mL^{−1}) in chloroform using differential refractive index detectors (RID). The apparent molecular weight (M_n and M_w) of all samples were obtained according to polystyrene standards.

2.3. Dynamic mechanical analysis

The influence of the expanded graphite on the viscoelastic properties of PLA was analyzed by means of a dynamic mechanical analyzer (DMA) Netzsch DMA 242 C. For this study, 50 × 10 × 1 mm³ rectangular specimens were machined from the compression-moulded plates. They were subjected to double cantilever mode of flexural loading with a maximum displacement of 40 μ m in the temperature range 25–100 °C (rate 2 °C/min) and a frequency of 1 Hz.

2.4. Differential Scanning Calorimetry

Differential Scanning Calorimetry thermograms of PLA were recorded by means of a Netzsch DSC 204 F1 Phoenix apparatus operating in inert atmosphere (nitrogen), and with a heating rate of 10 °C/min. The samples (10–20 mg) were placed into alumina

crucibles and were subjected to the following temperature program: i) a first heating step from 0 to 200 °C, ii) a cooling step from 200 to 0 °C and iii) a second heating step from 0 to 200 °C. Only the results arising from the second heating step are reported in this study since this second step is well-known to reflect the intrinsic thermal behaviour of a polymer.

2.5. Thermogravimetric analysis

Thermogravimetric analysis were performed with a on a Netzsch TG 409 PC Luxx device operating in air environment in alumina crucibles (150 mL) containing 20–25 mg of sample. The runs were carried out in dynamic conditions at constant heating rates of 2, 5, and 10 °C min^{−1}. The kinetic analysis of the degradation of the samples was made using an advanced thermokinetic software package developed by Netzsch Company.

2.6. Flash laser

The thermal diffusivity of PLA and its nanocomposites was measured from room temperature to 100 °C using a laser flash technique (Netzsch LFA 457 Microflash™) under inert atmosphere (argon flow: 100 mL min^{−1}).

Samples were machined in the shape of plane and parallel disks with 12.7 mm in diameter and about 1.1 mm thick. Their front side is heated by a short laser pulse (0.5 ms). The heat induced propagates through the sample and causes a temperature increase on the rear surface. This temperature rise is measured versus time using the IR-detector. The thermal diffusivity is then determined using the “half-rise-time” ($t_{1/2}$) corresponding to the time for the back face temperature to reach 50% of its maximum value and for which $\omega = 1.38$. The thermal diffusivity can be calculated using equation (1):

$$\alpha = \frac{1.38 \cdot L^2}{\pi^2 \cdot t_{1/2}} \quad (1)$$

where L is the specimen thickness.

For each sample and condition, measurements were repeated three times in order to collect meaningful data between room temperature and 100 °C.

Laser Flash Analysis is a direct measurement method for measuring thermal diffusivity and an indirect one for measuring thermal conductivity.

Thermal conductivity (k) can be determined using equation (2):

$$k(T) = \alpha(T) \cdot C_p(T) \cdot \rho(T) \quad (2)$$

where C_p is the heat capacity determined by Differential Scanning Calorimetry and ρ is the density measured with a densitometer.

2.7. Raman spectroscopy

Raman scattering experiments were performed at room temperature with a LabRam spectrometer (Horiba Jobin Yvon). All spectra were recorded in backscattered geometry using a 1800 groove mm^{−1} as the diffraction grating and a spectral resolution of 1 cm^{−1} was achieved. Both incident and scattered beams were collected through an Olympus confocal microscope using a 100× objective lens ($NA = 0.9$). Rayleigh scattering was blocked with a holographic Notch filter. The laser excitation wavelength was 514 nm and the laser power was less than 2 mW to avoid sample damage. The samples were analyzed without any preparation as they were at the extruder output.

2.8. Scanning electron microscopy

Scanning Electron Microscopy (SEM) analyses were performed with an environmental microscope (FEI-Quanta 200 type).

2.9. Transmission electron microscopy

Transmission electron microscopy analysis of PLA–EG was provided by a LEO 922 apparatus at 200 kV. The samples were 70 nm thick and prepared with a LEICA EM FC6 cryo-ultramicrotome at 25 °C.

2.10. X-ray diffraction

X-ray diffraction (XRD) experiments were performed in an INELFRANCE diffractometer. Samples were scanned in the reflection mode using the Cu K α 1 radiation (wavelength: 1.5405 Å).

3. Results and discussion

3.1. Molecular weight characterization

PLA, as most of polyesters, is sensitive to its environment during melt processing (mainly to water, impurities, temperature and shear). To minimize moisture content, intensive drying of all components is a first essential step to reduce the losses by hydrolysis and to maintain the polyester molecular weights as high as possible.

Murariu et al. showed recently that the polydispersity index of PLA is poorly affected by EG addition upon melt-blending. The addition of EG in low percentage (2–4 wt. %) leads only to a slight decrease of Mn. At higher percentage of EG (≥ 6 wt. %) it was observed that the decrease of the molecular weight was more pronounced [13]. It is important to notice that their experiments were performed in different equipment at different processing conditions.

To evaluate the impact of the processing conditions on the molecular masses of PLA–3wt.% EG, size exclusion chromatography (SEC) analysis were performed (Table 1). In our case, the average molecular weight (Mn) of the pure PLA decreases slightly from 77 000 g/mol (granules) to 65 000 g/mol for the sample processed in the most severe conditions (150 rpm, 10 min). The addition of 3wt.% of EG has an unexpected effect on PLA molecular weight. Indeed, GPC chromatograms display two molecular weight distributions, one at Mn values higher than PLA's Mn and a second at around 28 000 g mol^{−1} (not shown in the table). This can be mainly attributed to the presence of impurities such as acidic species, peroxide groups, metallic ions or other residual products that can provoke the degradation of PLA during melt-mixing. Indeed, by EDS, we detected the presence of titanium impurities that can induce chain branching leading to the increase of the molecular weight. The mechanism leading to chain scissions seems to be

minor, unlike the observation made by Murariu et al. [13]. One can conclude that there is no general behaviour of the expanded graphite towards a polymer matrix in which it is introduced. It will mainly depend on the nature of the impurities present in EG and/or on the processing conditions. Moreover, the nature of the impurities is associated to the method used to prepare the expanded graphite.

3.2. Morphology and dispersion characterization

To investigate the detailed morphological changes of the EG when melt-blended with PLA at different processing conditions, X-ray diffraction (Waxs mode), Raman spectroscopy and SEM were used.

X-ray diffraction patterns of the EG and PLA/EG composites obtained after extrusion are presented in Fig. 1. It was observed that PLA/EG composites exhibited a broad amorphous hallow scattering and a sharp peak at 2θ of $\sim 26.5^\circ$ which corresponds to the stacking of single graphene layers at a distance of 0.335 nm, regardless the processing conditions. The presence of the sharp peak at 26.5° confirms the presence of pure graphite based on stacks of parallel graphene sheets, and also the fact that even in advanced mixing conditions applied using the DSM extruder, exfoliation or complete separation of the graphene layers is not reached and some sheets still exist in the aggregate form. Because EG is fragile and breaks down during blending with different polymers, it is generally assumed that in polymer-EG composites it is difficult to completely delaminate the nanofiller and even in advanced mixing conditions a dense stacking of single graphene layers still exists. However, a partial delamination could take place. To check this hypothesis, several techniques of characterization are used such as SEM and TEM.

SEM images, show that EG stacks are dispersed homogenously in PLA matrix in soft (50 rpm, 5 min) as well as in severe (100 rpm, 10 min) melt-blending conditions (Fig. 2a,b).

A significant improvement of EG dispersion is observed when increasing reasonably the screw speed and the residence time. Furthermore, thinner layers and smaller aggregations are noticed in the composite melt-blended at 100 rpm during 10 min, indicating that the increase of the screw speed and the residence time leads to a better but partial separation of the multiple graphite layers. Indeed, the increase of the screw speed induces an increase of the shear leading to the delamination of EG and the longer is the

Table 1
Molecular weights (Mn and Mw) of all samples based PLA.

Samples	Mn (g mol ^{−1})	Mw (g mol ^{−1})	Polydispersity index
PLA (granules)	77,000	204,300	2.65
PLA: 100 rpm, 10 min	65,400	202,300	3.92
PLA: 150 rpm, 10 min	61,600	194,500	3.15
PLA–3EG: 50 rpm, 5 min	93,000	227,200	2.44
PLA–3EG: 50 rpm, 10 min	96,500	228,400	2.36
PLA–3EG: 100 rpm, 10 min	119,000	243,000	2.04
PLA–3EG: 150 rpm, 10 min	121,700	249,200	2.05

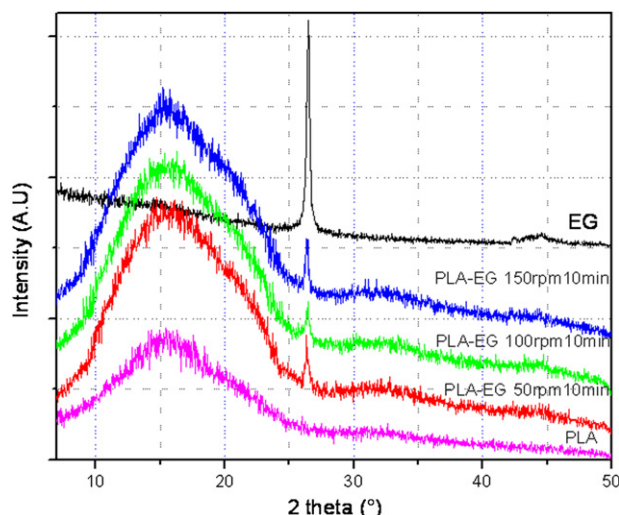


Fig. 1. XRD patterns of pure EG and PLA/3 wt. % EG nanocomposites.

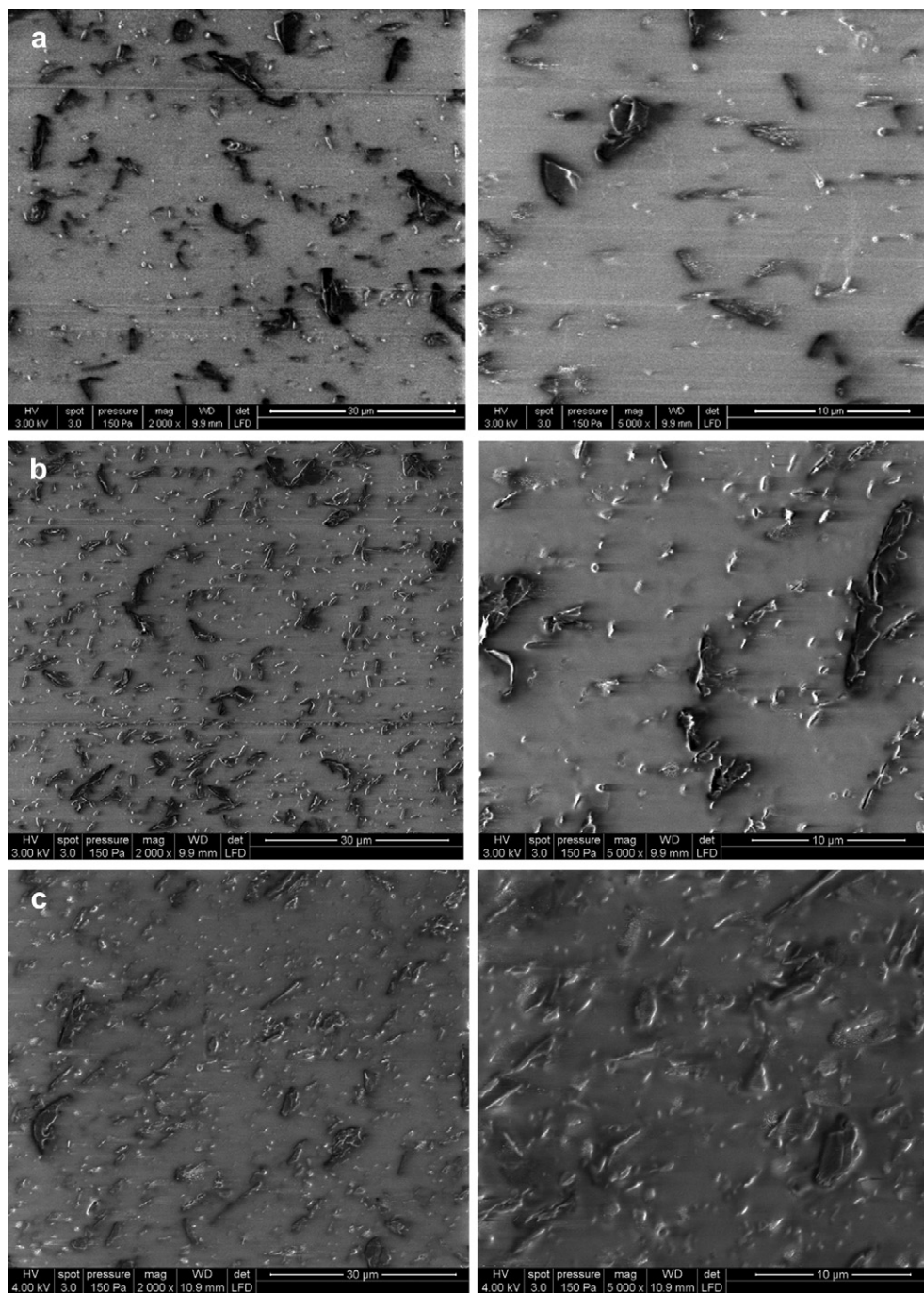


Fig. 2. SEM images of PLA–3EG nanocomposites melt-blended at a) 50 rpm, 5 min, b) 100 rpm, 10 min, c) 150 rpm, 10 min.

process the better it is. The coexistence of graphite with various numbers of layers is fully consistent with the strong peak observed at 26.5° in the XRD patterns. TEM micrographs obtained on the same samples (Fig. 3a,b) at a magnification of $1\ \mu\text{m}$ confirmed the observations made on SEM images.

It is necessary to mention that despite the fact SEM and TEM images can give good information about the dispersion state of the fillers in polymer matrix, this depends on the analyzed zone and the interpretation is based on a visual examination. For these reasons, it is essential to find out another technique that is capable to confirm the observations made by these microscopic techniques.

Additional information concerning the structure of PLA/EG was obtained through Raman spectroscopy analyses. Visible Raman

spectroscopy is a suitable tool for characterization of graphene/graphite nanocomposites, because visible excitation always resonates with the π states of carbon layers [14]. The spectral structure of these intense signatures is directly linked to the carbon sheets organization which is respectively specific to graphene, graphite, nanotube or fullerene structure. In particular, in graphene and graphite Raman spectra most of the vibrations modes are sensitive to the number of stacked carbon layers. Especially, the 2D band structure clearly evolves with the number of layers and can be used to identify graphene and graphite samples and to highlight a delaminating process efficiency [15].

The Raman spectrum obtained from EG is shown in Fig. 4. The G band is present at $1560\ \text{cm}^{-1}$ and the 2D band around $2700\ \text{cm}^{-1}$. In

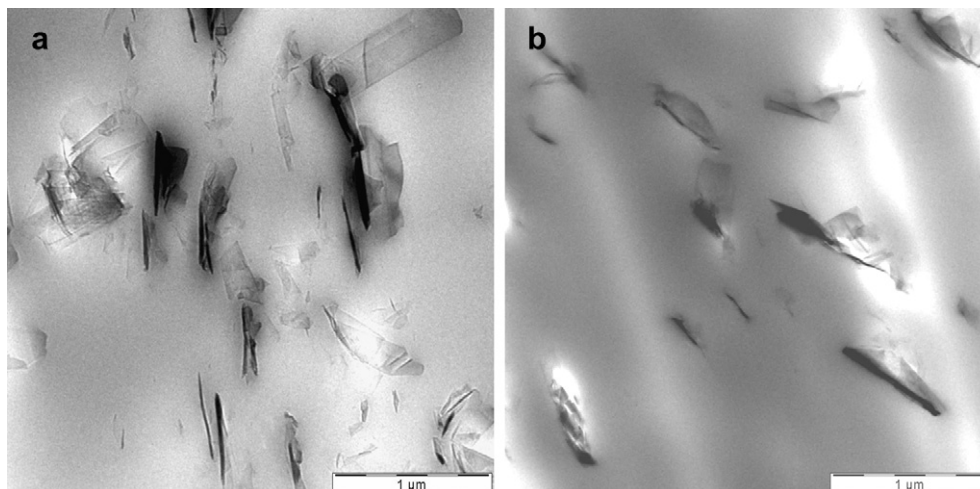


Fig. 3. TEM images of PLA–3EG nanocomposites melt-blended at a) 50 rpm, 5 min, b) 100 rpm, 10 min.

a basic molecular description the G band is attributed to the bond stretching and the 2D band, which is the second order of the D band, is attributed to breathing modes of sp^2 atoms in rings. Compared to a graphite spectrum, the 2D band of EG is downshifted with a frequency close to the graphene 2D band, around 2700 cm^{-1} [15], and with band shape similar to the graphene 2D band shape. The difference between EG 2D band and graphene 2D band is the full width at half maximum (FWHM). The measured FWHM of EG is 80 cm^{-1} and usual FWHM of graphene is around 30 cm^{-1} [15]. The FWHM of EG is close to FWHM of graphite. As the 2D band is related

to the stacking structure, the results show a singular spectral behaviour of EG between usual graphite and graphene: less interaction between carbon layers than graphite which explains the graphene like 2D band profile with a multilayer structure as the high FWHM value suggests. Then, the specific 2D band of EG can be considered as a probe of layers exfoliation efficiency during the extrusion process.

Raman spectra of PLA/3% EG composites are presented in Fig. 4 at different speed rates and for two different residence times: (a) 5 min, (b, c) 10 min. At first, no modification of the PLA CH_2 and CH_3

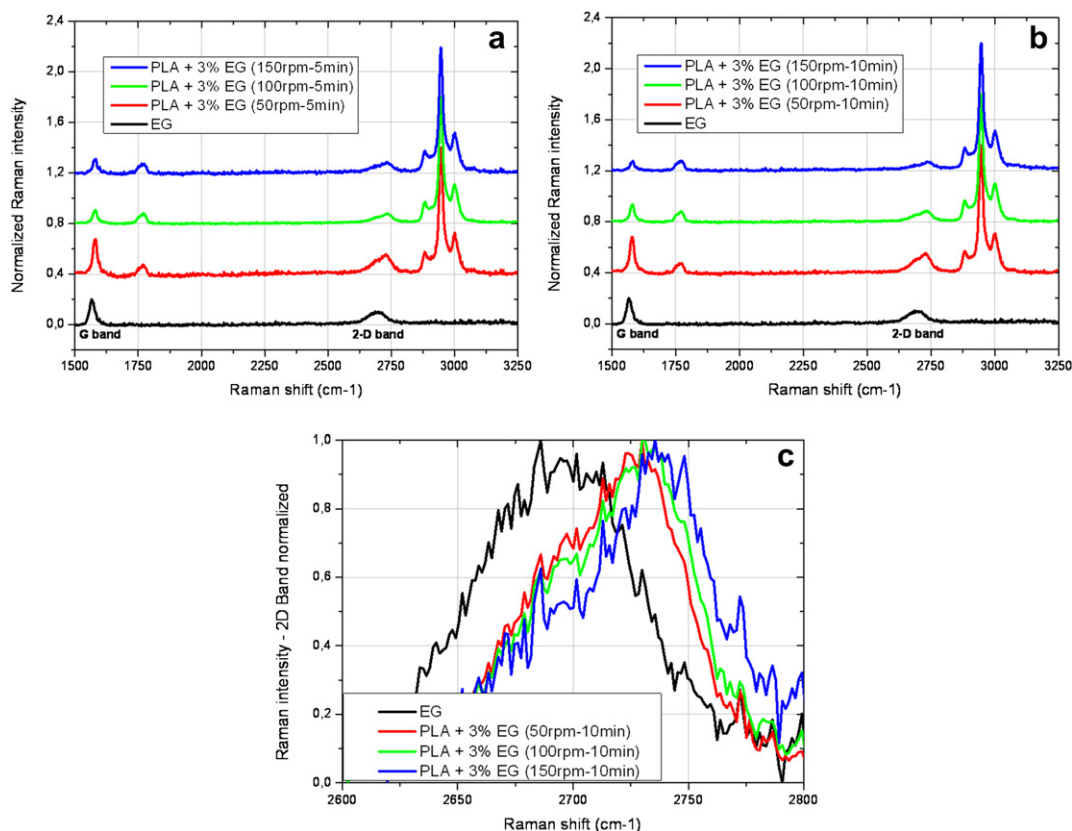


Fig. 4. Raman spectra of PLA–EG nanocomposites at three different speed rates and at two different residence times: 5 min (a) and 10 min (b). The Raman spectrum of EG before incorporation in PLA is given as reference. (c) Normalized 2D band of EG and PLA–EG nanocomposites.

stretching bands around 3000 cm^{-1} is observed for all spectra which indicates that the polymer matrix hasn't been damaged or under strain after extrusion.

Compared to the pure EG Raman spectrum, the G and 2D bands of the PLA/3% EG composites are upshifted with Raman shifts close to the graphite ones. Also, the shape of the 2D band is the typical profile of the 2D band in graphite samples [16] which suggests an increase of the interaction between carbon layers. As no modification was observed in XRD measurements, this result indicates a fillers aggregation process during extrusion. Fig. 4c presents the normalized 2D bands of EG and PLA/3% EG for different speed rates. As the speed rate increases the right side of the 2D band is slightly upshifted, the aggregation process of graphite in the stacking direction is then encourage.

Moreover, Raman intensities of the G and 2D bands decrease as the screw speed increases (Fig. 4a,b). This behaviour is related to a better dispersion of the fillers in the polymer host. At low speed rate, 50 rpm, only small delaminated EG pieces coexist with larger EG aggregates. As the screw speed rate increases the fillers distribution tend to be linear in size, from small to larger EG pieces. This screw speed effect on fillers size distribution is confirmed in SEM images (Fig. 2).

These Raman results highlighted two processes which can occur simultaneously. At first, aggregation process with an increase of the graphite number of layers, these flakes could be then delaminated by the screw in smaller ones. At the same time a crushing of these large planes occur which produces smaller graphite clusters. Raman spectra of PLA/3% EG at residence times of 5 min and 10 min are identical, the effect of the residence time has no influence on the carbon fillers structure in PLA.

3.3. Thermal stability

In order to better understand the effect of EG and its dispersion state on the thermal stability of PLA matrix, TGA analysis was operated to investigate the thermal degradation of PLA and PLA–EG nanocomposites. The thermal degradation of PLA–EG nanocomposites has been compared with that of pristine PLA. Fig. 5 shows the TG curves for PLA and PLA–EG nanocomposites at three different speed rates and at two different residence times, respectively 5 and 10 min. The 50% weight loss temperatures (T_{50}) for each sample are listed in Table 2. All TG curves of PLA and PLA–EG nanocomposites exhibit similar tendency. At 50 rpm and 5 min, the T_{50} of PLA–EG nanocomposite is similar to that of pristine PLA ($355\text{ }^{\circ}\text{C}$). As the addition of more shear strength and the residence time during mixing EG and PLA, the T_{50} continuously

Table 2

TGA data under air at $10\text{ }^{\circ}\text{C}/\text{min}$ for PLA and its nanocomposites with EG.

Samples	$T_{50\%}$ ($^{\circ}\text{C}$) at 5 min	$T_{50\%}$ ($^{\circ}\text{C}$) at 10 min
PLA (100 rpm)	355	355
PLA–3EG (50 rpm)	355	357
PLA–3EG (100 rpm)	359	362
PLA–3EG (150 rpm)	358	362

increase to $362\text{ }^{\circ}\text{C}$ for PLA–EG nanocomposite at 100 rpm and 10 min. Note that any increase of T_{50} was observed after 100 rpm. Indeed, the T_{50} of PLA–EG nanocomposite at 150 rpm and 10 min remains constant ($362\text{ }^{\circ}\text{C}$). From these TGA experimental data, it can be clearly seen that the optimum extruder parameter is 100 rpm and 10 min. Secondly, these results indicate that the incorporation of EG with well dispersion into PLA can improve the thermal stability of the nanocomposites as those reported in the literatures [13].

Kinetic analysis has been carried out in order to better understand the effect of the dispersion state of the EG on the degradation mechanism of PLA by using the isoconversional analysis.

The isoconversional analysis implies a kinetic model in the form of:

$$\frac{\partial \alpha}{\partial t} = f(\alpha) \cdot k_{\alpha} \cdot \exp\left(-\frac{E_{\alpha}}{RT}\right) \quad (3)$$

where:

- α is the conversion degree of the degradation reaction
- E_{α} is the apparent activation energy (J mol^{-1}) at α
- K_{α} is the pre-exponential factor (s^{-1}) at α
- $f(\alpha)$ is the reaction model

In this study we have used a model-free analysis, such as the well-known Friedman analysis [17], providing the plot of the activation energy versus the conversion rate. Starting from the TGA curves obtained for the degradation of pure PLA and PLA–EG nanocomposites at various heating rates: 2, 5 and $10\text{ }^{\circ}\text{C min}^{-1}$, E_{α} can be determined at any particular value of the conversion degree α (Fig. 6).

For PLA, the activation energy curve versus the conversion degree reveals that the activation energy is not constant, but continuously decreases from 187 to 132 kJ mol^{-1} between $0.1 < \alpha < 0.5$ and increases from 132 to 196 kJ mol^{-1} between $0.1 < \alpha < 0.5$. This indicates that the degradation does not take place as a single step reaction, but involves several competitive reactions as exposed in the literature [18].

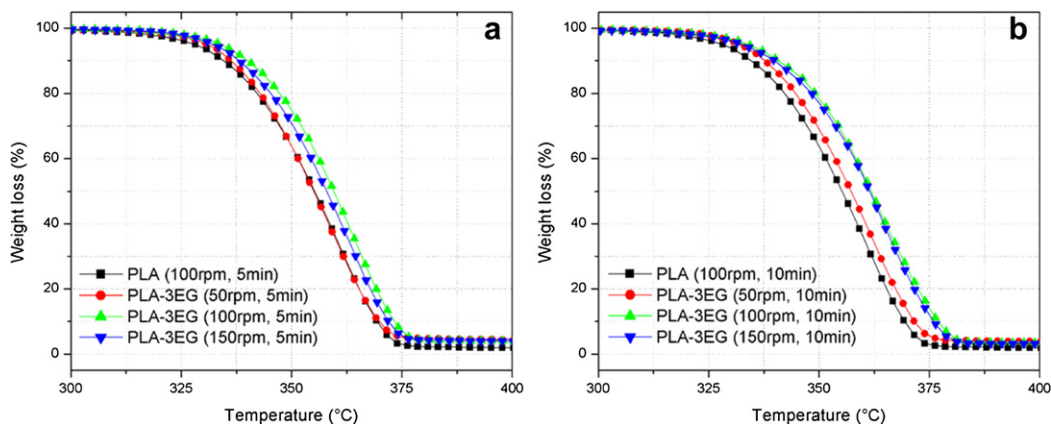


Fig. 5. TG curves for PLA and PLA–EG nanocomposites at three different speed rates and at two different residence times (5 min (a) and 10 min (b)).

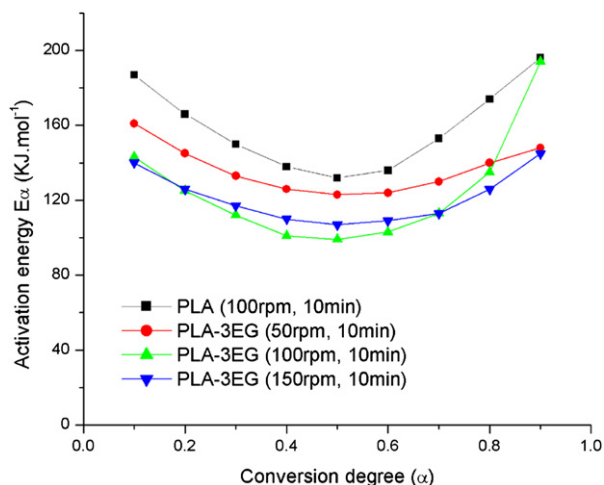


Fig. 6. Activation energy (E_a) versus conversion degree (α) determined using the Friedman analysis for PLA and PLA–EG nanocomposites at three different speed rates and at 10 min as residence time.

For PLA–EG nanocomposites, Fig. 6 shows that the addition of EG into PLA does not change the degradation mechanism of the matrix as the shape of E_a curve is the same as that obtained for pure PLA. However, a slight decrease of E_a of PLA in the presence of EG is observed. The raise of the shearing force by increasing the screw speed of the extruder up to 100 rpm leads to a more significant shift of E_a towards lower values. For screw speeds higher than 100 rpm, no supplementary decrease of E_a is noticed. The decrease of the E_a in presence of EG can be explained by a catalytic effect of this latter

on the emission of volatile products. In contrast, TGA curves do not show this catalytic effect as a shift of the degradation temperature to higher values is observed indicating the stabilizing effect of EG (Fig. 5). It seems that EG exhibits two different functions (catalytic and stabilizing effect) that could be related to its morphology. Indeed, based on Raman analysis, two dispersion states which can occur simultaneously are highlighted (partial delamination and aggregation). This phenomenon has been previously observed in metallic oxide fillers [19]. It is essential to emphasize that the catalytic effect of EG remains minor compared to its stabilizing effect. It could be attributed to the presence of impurities or aggregates.

Some of the known reasons of the thermal stability improvement when nanofillers are added to polymers are clearly exposed in the literature [20]. The rate of thermal decomposition can be influenced by: (i) chemical parameters (molecular weight, cross-linking...); (ii) physical parameters (viscosity, compactness, heating rate, temperature gradient, thermal diffusivity...).

Thermal diffusivity is the ability of a material to transmit heat rather than to absorb it. Investigating this intrinsic property will help to get a better knowledge about the impact of EG fillers on the thermal properties of composites. Measurements of thermal diffusivity of PLA and PLA–EG nanocomposites as a function of temperature are presented in Fig. 7. Thermal conductivity (k) can be inferred from thermal diffusivity by knowing the heat capacity (C_p) and the density of each material according to equation (2). The heat capacity was measured by DSC (Fig. 7). The values of thermal conductivities calculated from this equation are presented in Fig. 7. Thermal diffusivity decreases with temperature and the decrease is speeding up around the glass transition temperature ($T_g \sim 60^\circ\text{C}$), following the increase in heat capacity of the composite. It means that the heat takes longer to pass through the material for

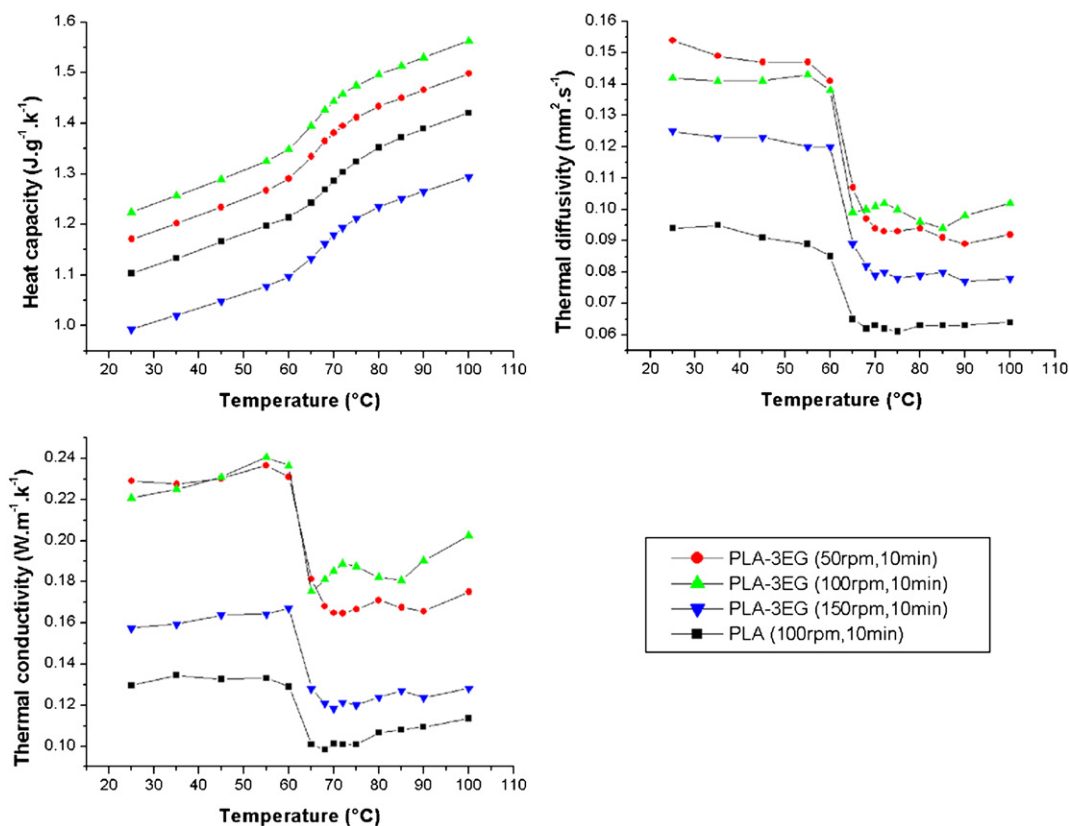


Fig. 7. Heat capacity, thermal diffusivity and thermal conductivity of PLA and PLA–EG nanocomposites at three different speed rates and at 10 min as residence time.

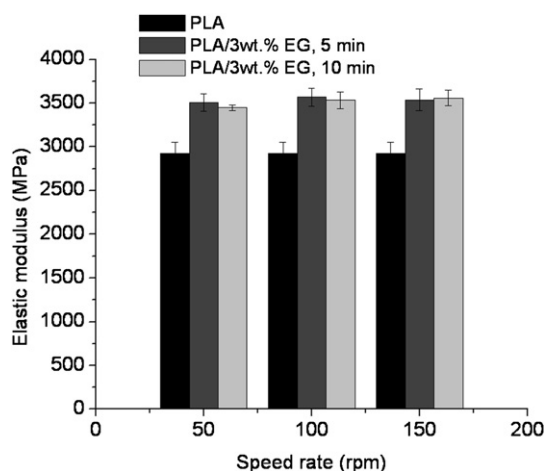


Fig. 8. Elastic modulus (E') for PLA and its nanocomposites with EG measured by DMA.

temperatures above the T_g . In the studied temperature range (25 °C–100 °C), the thermal diffusivity and thermal conductivity of PLA–EG nanocomposites are higher than that of pure PLA. However, the heat capacity and the thermal diffusivity both decrease when the screw speed increases from 100 to 150 rpm, consequently causing a significant drop in the thermal conductivity of PLA–EG nanocomposite.

The decomposition temperature shift observed on TGA curves could be due:

- (i) To the intrinsic temperature gradient in the samples: the higher the gradient, the longer time it takes for the heat to reach the core of the sample leading to a higher increase of the surface temperature which undergoes a faster decomposition. Thermal diffusivity directly influences thermal gradients: the higher it is, the less time it takes for the heat to pass through the material, therefore the thermal gradient between the two sides of the sample is getting lower and finally less heat builds up on the surface slowing down the decomposition,
- (ii) To the barrier effect of EG leading to the decrease of release rate of volatile products generated during the thermal degradation.

3.4. Thermo-mechanical properties

To understand the impact of the processing conditions on the thermo-mechanical performance of PLA–EG composites, the samples were submitted to stress in a temperature range (25–100 °C) and compared to the pure PLA. The average storage modulus (E') of PLA after extrusion (pure PLA) regardless the processing conditions applied is about 2960 MPa. Fig. 8 represents the changes of the E' of PLA–EG as a function of the screw speed and of the residence time. It shows that the addition of expanded graphite increases E' in all cases by the same value, at least within experimental errors. The increase of the average molecular weight of PLA when the speed screw and the residence time are raised up as well as the partial exfoliation of EG highlighted by Raman spectroscopy do not seem to have any supplementary effect on the elastic modulus. The possible positive effect brought by the partial

Table 3

Glass transition temperature (T_g) for PLA and its nanocomposites with EG measured by DMA.

Samples	T_g (°C) at 5 min	T_g (°C) at 10 min
PLA (100 rpm)	61	61
PLA–3EG (50 rpm)	63	62
PLA–3EG (100 rpm)	62	64
PLA–3EG (150 rpm)	62	66

exfoliation of EG may have been inhibited by the presence of EG aggregates.

However, a slight increase of the glass transition temperature (T_g) can be noticed compared to pure PLA (Table 3). The increase of the T_g when the dispersion of EG is optimized can be attributed to i) the restriction of macromolecular chain motions when the aspect ratio of EG increases (strong interface EG–PLA confirmed by TEM images), ii) the higher steric hindrance, iii) the decrease of the free volume.

4. Conclusions

A study of the dispersion of EG in PLA matrix melt-processed in a DSM Xplore twin-screw micro-extruder was performed using new approach based on Raman spectroscopy. We have shown that the Raman spectroscopy combined with more conventional techniques such as scanning electron microscopy, transmission electron microscopy and X-ray diffraction provides good and complete information about the dispersion and delamination/aggregation of EG. Indeed, the delamination of the filler occurring during the melt-blending was highlighted allowing an accurate optimization of the process. In particular, we have demonstrated that Raman spectroscopy could be a useful technique to study carbon fillers in polymer matrices. In this case, Raman measurements can be directly done at the extruder outlet to control fillers structure and distribution. The effect of the EG partial delamination and dispersion on the thermal and thermo-mechanical properties of PLA could therefore be explained.

References

- [1] Fukushima H, Drzal LT. Annu Tech Conf – Soc Plast Eng; 2003;2230.
- [2] Kalaitzidou K, Fukushima H, Drzal LT. Composites: Part A 2007;38:1675.
- [3] Kalaitzidou K, Fukushima H, Drzal LT. Carbon 2007;45:1446.
- [4] Soldano C, Mohamed A, Dujardin E. Carbon 2010;48:2127.
- [5] Zhang YB, Small JP, Pontius WV, Kim P. Appl Phys Lett 2005;86:073104.
- [6] Viculis LS, Mack JJ, Mayer OM, Hahn HT, Kaner RB. J Mater Chem 2005;15:974.
- [7] Carr KE. Carbon 1970;8:155.
- [8] Chen G, Wu D, Weng W, Wu C. Carbon 2003;41:619.
- [9] Pan Y-X, Yu Z-Z, Ou Y-C, Hu G-H. J Polym Sci Part B Polym Phys 2000;38:1626.
- [10] Kalaitzidou K, Fukushima H, Drzal LT. Compos Sci Technol 2007;67:2045.
- [11] Zheng W, Wong S-C, Sue H-J. Polymer 2002;43:6767.
- [12] Kim I-H, Jeong YG. J Polym Sci Part B Polym Phys 2010;48:850.
- [13] Murariu M, Dechief AL, Bonnaud L, Paint Y, Gallos A, Fontaine G, et al. Polym Degrad Stab 2010;95:889.
- [14] Ferrari AC, Robertson J. Philos Trans R Soc Ser A 2004;362:2267.
- [15] Ferrari AC, Meyer JC, Scardaci V, Casiraghi C, Lazzeri M, Mauri F, et al. Phys Rev Lett 2006;97:187401.
- [16] Cancado LG, Takaia K, Enokia T, Endob M, Kimb Y, Mizusakib H, et al. Carbon 2008;46:272.
- [17] Friedman HL. J Polym Sci 1965;6:183.
- [18] Li J, Zheng W, Li L, Zheng Y, Loua X. Thermochimica Acta 2009;493:90.
- [19] Liufu S-C, Xiao H-N, Li Y-P. Polym Degrad Stab 2005;87:103.
- [20] Laachachi A, Ferriol M, Cochez M, Ruch D, Lopez-Cuesta JM. Polym Degrad Stab 2008;93:1131.

Grégory Mertz

Department of Advanced
Materials and Structures,
CRP Henri Tudor, 66 rue de Luxembourg,
L-4002 Esch-sur-Alzette, Luxembourg;
Institut Jean Lamour - UMR CNRS 7198,
Ecole des Mines de Nancy,
Parc de Saurupt,
F-54042 Nancy cedex, France

Fatima Hassouna¹

e-mail: fatima.hassouna@tudor.lu

Valérie Toniazzo

Department of Advanced
Materials and Structures,
CRP Henri Tudor, 66 rue de Luxembourg,
L-4002 Esch-sur-Alzette, Luxembourg

Abdesselam Dahoun

Institut Jean Lamour - UMR CNRS 7198,
Ecole des Mines de Nancy, Parc de Saurupt,
F-54042 Nancy cedex, France

David Ruch

Department of Advanced
Materials and Structures,
CRP Henri Tudor, 66 rue de Luxembourg,
L-4002 Esch-sur-Alzette, Luxembourg

Effect of Coated Rutile TiO₂ and Disazopyrazolone Dye Additives on Unvulcanized Styrene Butadiene Rubber During Photo-Ageing

The effect of coated rutile titanium dioxide (TiO₂) and a disazopyrazolone dye (azo dye) on the mechanism and the kinetic of photo-oxidation of unvulcanized styrene butadiene rubber (SBR) composites under accelerated UV-visible irradiation ($\lambda > 290$ nm at 35 °C) has been investigated using several techniques such as infrared spectroscopy, UV-visible spectrophotometry, and gel fraction measurements. Different photo-products resulting from the photo-ageing such as alcohol, ketone, or acids as well as cross-linked network were identified. The incorporation of TiO₂ rutile and an azo dye into the matrix did not modify the mechanism of photo-oxidation. However, they have a significant effect on the kinetic of photoproducts accumulation. Both fillers protect the matrix from photo-oxidation. TiO₂ rutile, thanks to its inorganic coating at the surface, dissipates part of the UV-visible radiation received by the polymer. The activity mechanism of azo dye consisting of a combination of its function as an antioxidant and light absorber, presents a better stabilizing effect compared with TiO₂ rutile. [DOI: 10.1115/1.4005418]

Keywords: styrene butadiene rubber, TiO₂ rutile, dye, fillers, photo-ageing

1 Introduction

Styrene butadiene rubber (SBR) is a versatile synthetic rubber widely used for tires, belt, footwear, industrial products, and others [1]. As many polymers, during their lifetime, they suffer from the attacks of different external factors such as thermal, radiations, rain, acid, or alkaline medium [2–5]. The degradation that occurs implies a loss of properties and these materials become unsuitable for their uses [6–8]. In fact, among these degrading factors, oxygen and UV-visible radiations are known to degrade these materials by a photo-oxidative ageing mechanism [9–12]. Moreover, SBR is very sensitive to oxidative degradation due to the presence of weak C-H bonds in α position of the double bonds of the diene units [3,13,14]. The mechanism of degradation of pristine SBR has been established [11,12]. It is the same than that of polybutadiene rubber, showing that the presence of styrene group does not affect the mechanism of photo-oxidation of SBR [15]. As in any nonabsorbing polymer, defects or impurities act initially as intrinsic chromophores, and radicals are formed in the material [16,17]. These radicals attack the hydrogen atom in allylic position of the double bond and lead to an alkyl radical. Atmospheric oxygen reacts with these latter leading to the formation of hydroperoxides. Hydroperoxides being photochemically and thermally unstable decompose into alkoxy and hydroxyl radicals. These latter radicals can evolve following several routes. They lead to the formation of oxygenated photoproducts such as α , β unsaturated acids, due to the permeability of oxygen through the film [2]. Stable products such as alcohol, ketone, acid, and ester are also generated. Moreover, unsaturated

radicals could react with double bonds to form either ether bridge or link between two polymeric chains by creation of C-C bond. This leads to the formation of a three dimensional network by crosslinking process. The oxidation mechanism and crosslinking process for diene rubber lead to a physicochemical modification of the matrix and a loss of mechanical properties [18,19].

Many additives could be incorporated inside the polymer and can either protect the polymer or degrade it during ageing [20–22]. For example, the incorporation of carbon black [23,24] or TiO₂ may play a role of UV absorber and protect the matrix from photo-oxidative degradation [25–30]. Jubete et al. [31] investigated the effect of talc filler and coated TiO₂ pigment during the photo-oxidation of carboxylated styrene butadiene rubber. TiO₂ significantly retarded the surface photo-oxidation evidenced by a slow growth of the carbonyl absorption bands in infra-red spectra. Alumina and zirconia form a barrier at surface of TiO₂ acting as a space in which deactivation and recombination of electrons and holes take place, this played a role of screen effect. The presence of talc highlights a UV protective effect, but higher talc level decreases the stability against photo-oxidation due to presence of iron impurities. Stevenson et al. [32] studied the influence of SiO₂ fillers on the irradiation ageing of silicone rubbers. They observed a higher crosslink density for filled elastomers since links at the polymer-silica interfaces have been created as a result of irradiation. Concerning the influence of fillers during ageing of polymers, no general trends can be concluded from the literature [32].

Many scientists devoted their research topics to the determination of the mechanism of stabilization or degradation of polymer composites in the presence of some fillers such as TiO₂, carbon black or talc, but few articles dealt with the effect of organic dyes or the effect of the association of fillers during photo-ageing [33].

The present work describes the influence of coated TiO₂ rutile and disazopyrazolone dye (used to impart colour to the material)

¹Corresponding author.

Contributed by the Materials Division of ASME for publication in the JOURNAL OF ENGINEERING MATERIALS AND TECHNOLOGY. Manuscript received May 27, 2011; final manuscript received July 28, 2011; published online December 12, 2011. Assoc. Editor: Dongsheng Li.

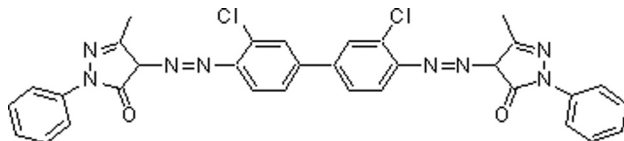


Fig. 1 Structure of disazopyrazolone orange dye

on the photo-oxidation of SBR composites. A possible mechanism of stabilization of the azo dye attributed to its properties of radical traps is proposed based on the results of Ivanov et al. [34,35] and Sabaa et al. [36,37].

2 Experimentation

2.1 Materials. Styrene butadiene rubber (5% of styrene units, Molecular weight about 200,000 g/mol) was purchased from Scientific Polymer Products (sp²). The purification of rubber was done by soxhlet extraction in methanol at 125 °C during 24 h. The polymer was then dried in vacuum oven at 60 °C during 24 h to remove all traces of solvent. TiO₂ rutile and azo dye were provided by Mondo S.A. Luxembourg and used without any further purification. TiO₂ used was a coated rutile form with a median particle size between 1 and 3 μm. The coating is constituted by a mixture of alumina and silica submitted to an organic treatment. The inorganic coating forms a physical barrier (screen effect) and organic layers provide dispersibility in polymer. The dye used was disazopyrazolones group in Fig. 1.

SBR deposits were prepared by dissolving the polymer in tetrahydrofuran (THF) in presence and in absence of fillers. Thin deposits of approximately 40 μm were obtained by spin coating a drop of each solution on KBr substrate. Three formulations were prepared: neat SBR, SBR + 5 phr dye, SBR + 5 phr TiO₂ rutile.

The main absorption bands of SBR are listed in Table 1 [2].

The insoluble fraction of the samples was evaluated by gravimetric measurements (gel fraction) for different times of irradiation on SBR films. Thin, 80 μm, films were obtained by the evaporation of polymer solutions prepared in tetrahydrofuran.

2.2 Photo-Oxidation. SBR deposits were exposed to UV-visible irradiation in a Suntest device at 35 °C in the presence of oxygen. This ageing device allows an accelerated ageing in artificial conditions relevant to natural ageing. It is equipped with a xenon lamp for irradiation at wavelength longer than 290 nm. A black panel controls the irradiance at 400 W/m².

2.3 Chemical Characterization. Infrared spectra were recorded using a BRUKER Tensor 27. Spectra were obtained using a summation of 32 scans and a resolution of 4 cm⁻¹.

UV-visible spectra were recorded on a Perkin-Elmer model lambda 35 equipped with an integrating sphere between 700 and 200 nm with slit of 2 nm.

Table 1 Principal absorption bands in SBR

Wavenumbers (cm ⁻¹)	Attribution
3073	CH of -CH=CH ₂ vinyl
3006	C-H of CH=CH ₂ cis
2918	C-H of -CH ₂
2844	C-H of -CH ₂
1639	C=C
1437	CH ₂ of -CH ₂
966	CH of -CH=CH- trans
911	CH of -CH=CH ₂ vinyl
759	Aromatic ring vibration
728	CH of -CH=CH- cis
700	Aromatic ring vibration

Raman spectra were recorded using a Horiba Jobin Yvon-LabRam microscope with a 5 mW He-Ne laser and a 50× objective.

After 120 h of ageing, SBR/dye composite film was immersed in an excess of dimethylformamide solvent (DMF) for 48 h in a sealed vial in the dark to extract the dye. The solution containing the dye was then investigated.

2.4 Physical Characterization. The insoluble fraction of the samples was evaluated by gravimetric measurements for different times of irradiation. After each exposure time, 0.100 g of SBR film was immersed into a glass tube with THF, a solvent of SBR. The tubes were then hermetically sealed and hidden from the daylight for 72 h. The gel obtained is filtered and dried until constant weight. The gel fraction is defined as the ratio between the weight of the dry gel after filtration and the initial weight of the sample in Eq. (1) [38]

$$\text{Gel fraction : } G_f = \frac{[M_{\text{insoluble}}]}{[M_{\text{total}}]} \times 100 \quad (1)$$

3 Results and Discussions

3.1 Infrared Analysis of Composites Based SBR. Irradiation of SBR composites under polychromatic light obtained from Suntest xenon lamps ($\lambda > 290$ nm, 400 W/m², T = 35 °C) in the presence of air, led to noticeable changes of the IR spectra of the exposed samples. The IR spectra showed an important increase of absorbance in the carbonyl, hydroxyl, and ether vibration domains and a significant decrease of the intensity of the double bands absorption.

In the carbonyl region [1900–1500] cm⁻¹ at weak conversion degree (see Fig. 2), the photo-oxidation led to the formation of a narrow absorption band with a maximum at 1697 cm⁻¹ attributed to α , β unsaturated acids [2,11,12] and a broader absorption band with a maximum at 1717 cm⁻¹. As photo-oxidation proceeds, the intensity of this latter band increased and the band shifted, while from 8 h, the band at 1697 cm⁻¹ became more difficult to observe in the IR spectra (see Fig. 2).

In the [1400–1000] cm⁻¹, frequency range represented by very complex C-O stretching vibration region, an increase of different bands was noticed. Several maxima were noted in the different spectra, such as 1060, 1175 cm⁻¹. Absorption band at 1060 cm⁻¹ has been assigned to crosslinking ether bridge [2,11,12]. The absorption band matched that of an α , β -unsaturated ether [2,11,12]. However, polyethers were known to be very oxidized structures and Piton and Rivaton [2] suggested that this band fits also with α , β unsaturated alcohols. The bands at 1175 cm⁻¹ has been assigned to lactone structures [2].

IR spectra for all samples showed the same photoproducts formation during photo-oxidation (see Fig. 2.) The addition of fillers such as TiO₂ rutile and azo dye did not seem to affect the mechanism of photo-oxidation of SBR proposed by Adam et al. [11,12] and represented in Fig. 3.

However, one can notice that the kinetic of photo-products formation was different.

The kinetic curves of SBR photo-oxidation are given in Fig. 4. The kinetic of photoproducts formation at 1717 cm⁻¹ (carbonyl C=O stretching mode considered as an indication of the degree of oxidation [39]) and decrease of 966 cm⁻¹ (unsaturation groups) was followed as a function of the ageing time. After a slight induction period, a rapid increase of the oxidation rate is observed, before the absorbance values reached a quasi-stationary state. The induction period was slightly longer in SBR composites (10 h) compared with neat SBR (5 h). The presence of coated TiO₂ rutile led to the decrease of the kinetic of carbonyl photoproducts formation, compared with neat SBR. This showed the role of coated TiO₂ in the protection of the matrix from the photo-oxidation. Jubete et al. [31] who worked on the degradation of carboxylated SBR composites at $\lambda > 254$ nm in presence of coated

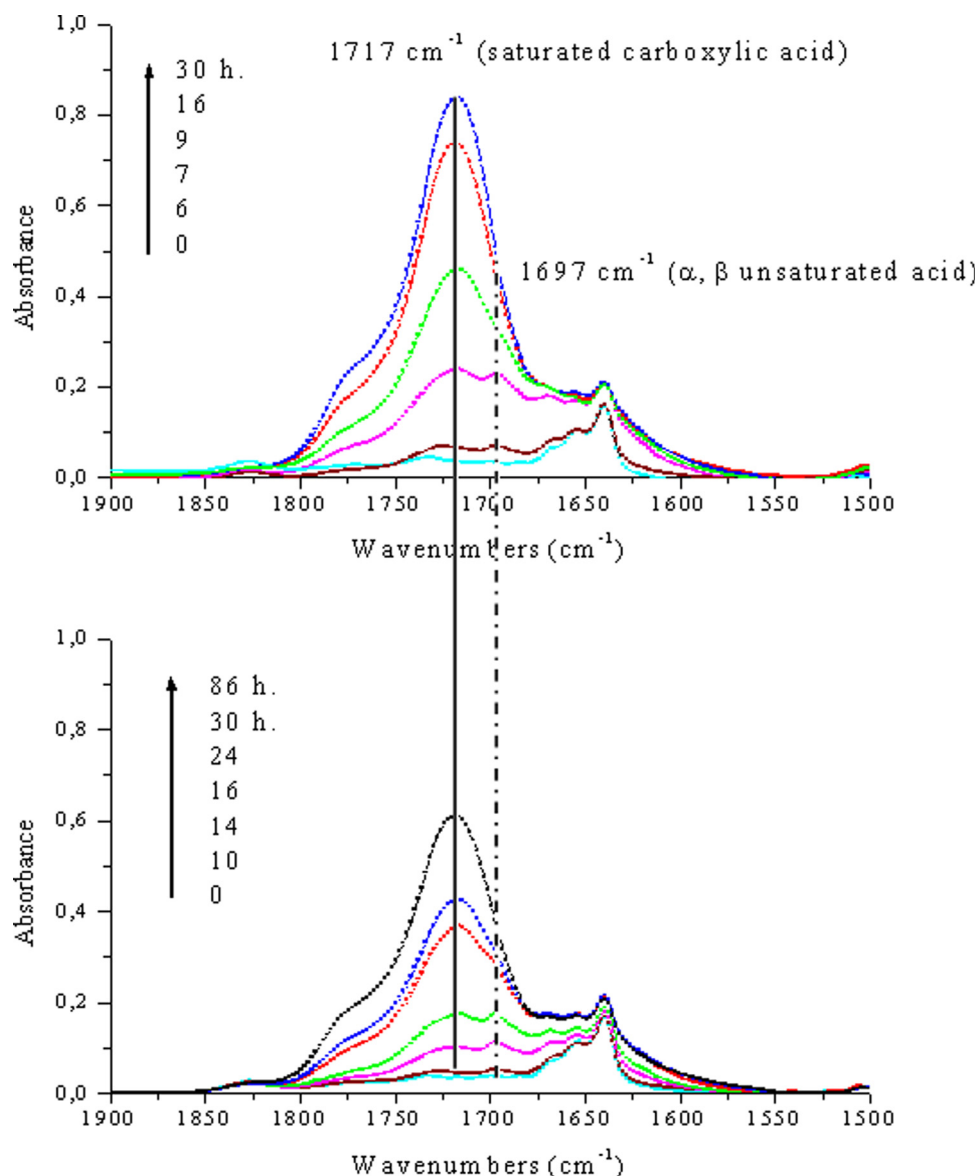


Fig. 2 FTIR spectra of carbonyl region of SBR (a) and SBR-TiO₂ rutile deposit (b), evolution of absorbance during photo-ageing

TiO₂ pigment observed that TiO₂ protect the matrix by absorbing UV radiation. Moreover, TiO₂ rutile particles present some UV protective properties due to the energy of the band gap located in the UV range [26].

By absorbing a wavelength below 385 nm, an electron in the valence band is ejected to the conductive band, generating an electron-hole pair. Normally, these two particles react with molecules at the surface of TiO₂ to form different radicals such as O₂^{•-} and •OH (see Fig. 5). The latter are very reactive and increase the kinetics of degradation [26]. However, barrier coating on TiO₂ particles traps electrons and holes and reaction (3) in Fig. 5 can take place. In this case, these latter cannot promote the formation of additional radicals, which would accelerate photo-oxidation process, and coated titania play as an UV absorber that leads to a protective effect.

An interesting fact was observed when disazopyrazolone dye is incorporated to SBR. Indeed, Fig. 4 showed that the kinetic of photoproducts formation was slower than that in presence of TiO₂ rutile. The azo dye seems to be a better photostabilizer than TiO₂ rutile from SBR matrix.

To elucidate the mechanism of dye light-stabilization, the dye was extracted from aged SBR composite and was submitted to

different physicochemical characterization (IR and Raman spectroscopy, and LDI-ToF mass spectrometry.) The obtained results were compared with those of pristine dye before and after exposure to Suntest light during 120 h (see Fig. 6).

The results indicated that the fingerprint of the extracted dye was the same that the pristine dye before and after ageing. No indication of the photo-oxidation of the dye has been observed; concluding that the industrial azo dye studied here is stable from photo-oxidation process within the irradiation time range and exhibits a protective effect from the matrix. The dye seems to behave as an anti-oxidant from SBR during the photo-ageing. Moreover, the UV-visible spectrum of the dye exhibiting a broad absorption band between 200 and 600 nm, which did not change during the irradiation. Since the azo dye strongly absorbs light in the UV and visible region, the second important factor responsible for its high effectiveness could be its screening capacity [34]. The azo dye acts probably simultaneously by two mechanism: as an anti-oxidant and as an absorber of light. This deduction is reinforced by the results obtained by Ivanov et al. [34,35]. Indeed, Ivanov et al. investigated the effect of some azo compounds during photo-oxidation on polydiene materials. They observed a photoprotective effect of the azo compounds acting as inhibitor and

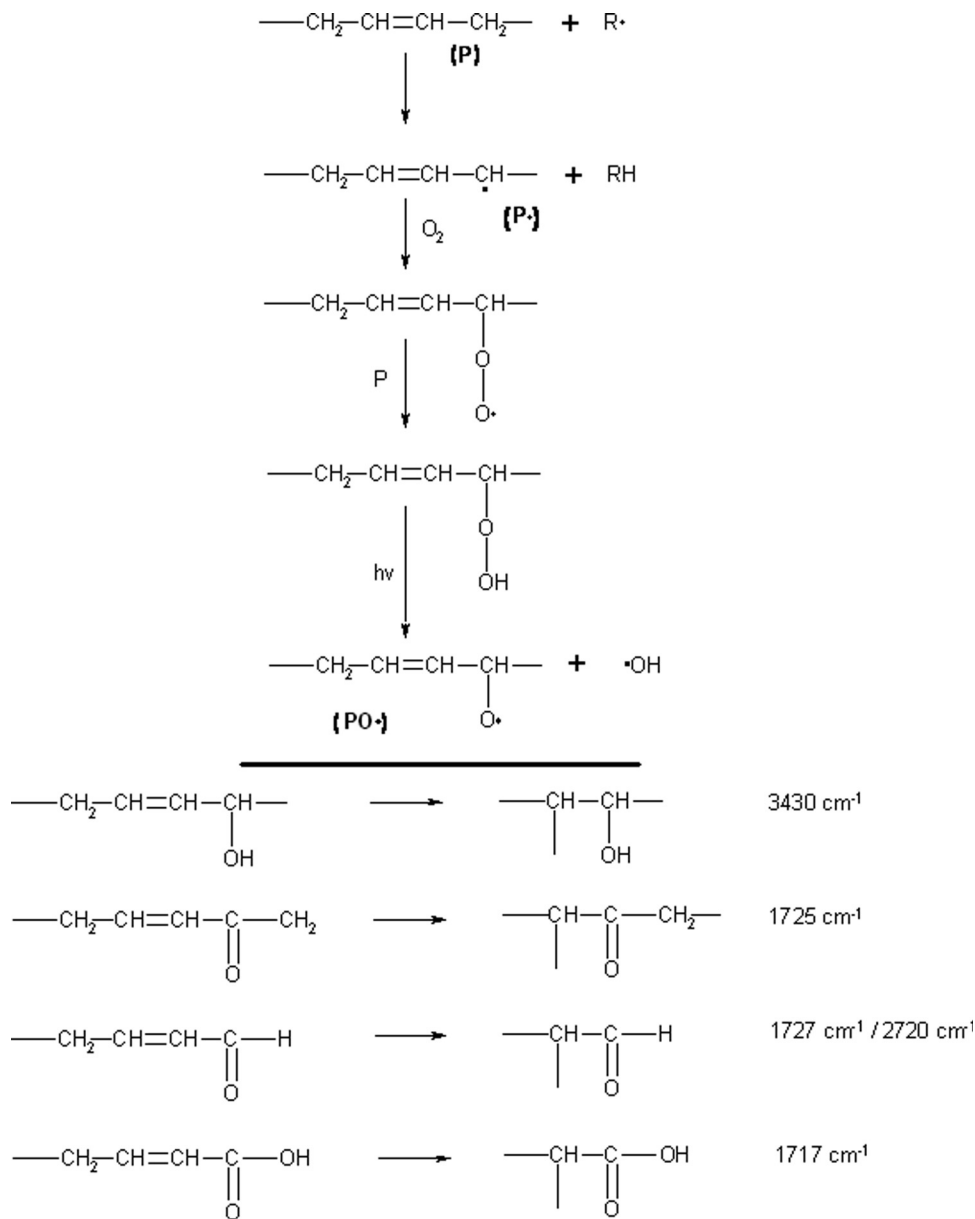


Fig. 3 Different steps of SBR photo-oxidation [2,11,12]

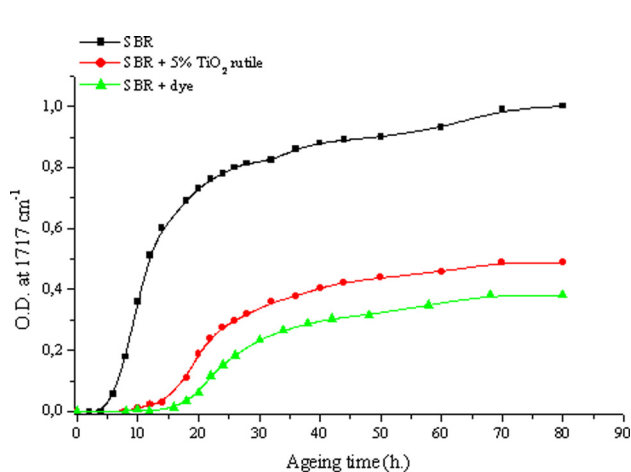


Fig. 4 Kinetic of photoproducts formation at 1717 cm^{-1} versus irradiation time

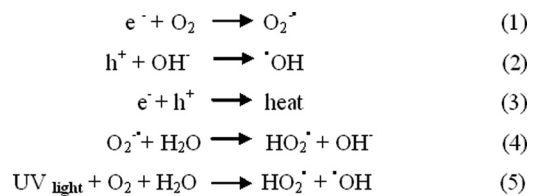


Fig. 5 Reactions occurring at the surface of TiO_2 particle in the presence of UV light and O_2

absorber of light at relatively low concentrations compared with ours. A mechanism of antioxidant photoprotection was suggested to explain the inhibiting activity of the azo dyes [34,35]. The azo compounds can react with peroxy radicals (PO_2^\bullet) produced during photo-oxidation by transferring its labile hydrogen to the radical to form a hydroperoxide and therefore disturb the cycle of oxidation as follow (see Fig. 7): where PH is the polymer, InH is the inhibitor, in this case, the azo compounds and In^\bullet are represented in Fig. 8.

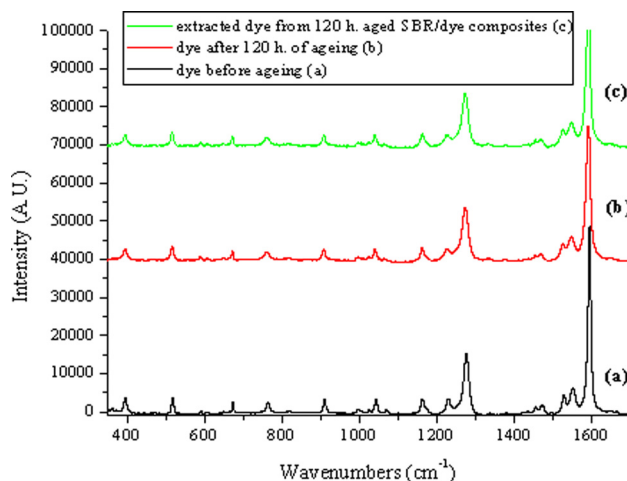


Fig. 6 Raman spectra of the dye before ageing (a), dye after 120 h of ageing (b), and dye extracted from 120 h aged SBR/dye composite (c)

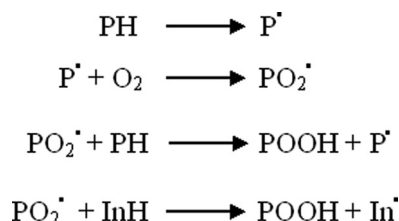


Fig. 7 Mechanism of action of antioxidant [34,35,40]

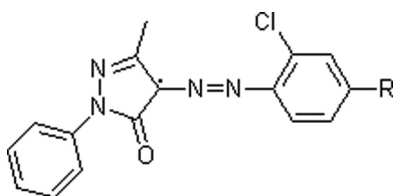


Fig. 8 Representation of pyrazolone radical inside the dye

The hydrogen on the carbon located on the α position to the carbonyl group is the most labile atom, and, therefore, the most sensitive to radical attack [36,37] (see Fig. 8). Sabaa et al. who investigated the effect of pyrazolone derivatives as efficient photostabilizers for rigid polyvinyl chloride (PVC), proposed a radical mechanism to explain their protective effect. They demonstrated

that the stabilizing efficiency of pyrazolone derivatives is attributed to their radical trapping property, which takes place during the degradation process of PVC, due to their ability to block newly formed radicals on the polymeric chains. This leads to the disruption of ageing cycle.

In our case, we cannot imagine the same mechanism because we did not detect oxidized dye. Indeed, the dye did not seem to have reacted with oxygenated radicals to give rise to oxidized dye.

3.2 Gel Fraction Measurement of Composites Based SBR Matrix. IR spectra showed a significant decrease in intensity of the absorption bands attributed to the three microstructures (1,4-trans unsaturation at 966 cm^{-1} , 1,4-cis at 728 cm^{-1} , and 1,2-vinyl at 910 cm^{-1}) throughout photo-oxidation at $\lambda > 300\text{ nm}$, 35°C . It has been previously reported that the decrease of the double bonds is due to the formation of network between polymer chains by crosslinking [2,41].

The decrease in the concentration of the three microstructures (1,4-cis, 1,4-trans, and 1,2-vinyl) has been reported to lead to a plateau [2,11]. Adam et al. [11,12] have attributed the limitation of the photo-oxidation to the decrease of permeability to oxygen: In the irradiated sample, it was shown that oxygen no longer diffused through the crosslinked surface layers [11]. Piton and Rivaton [2] have explained that the loss of unsaturation may occur through a crosslinking process (see Fig. 9).

The gel fraction of SBR has been determined as a function of irradiation time to investigate the crosslinked part. The evolution of the insoluble fraction upon irradiation is represented in Fig. 10. During the first 25 h of irradiation of neat SBR, a continuous increase of insoluble fraction was observed. The ratio of the insoluble part increased up to a plateau corresponding to 100% of insoluble fraction. A good correlation between the decrease of double bonds absorption and the gel fraction formation as a function of irradiation time was obtained. As the radiation time moves forward, the concentration of the double bonds decreased and, as a consequence, the crosslinking density increased generating a three-dimensional crosslinked insoluble and infusible network (see Fig. 9). In Fig. 9 showed that only butadiene group was involved in the crosslinking process.

The addition of fillers disturbed the formation of the crosslinked network more or less depending on the nature of the filler. The rate of formation of the insoluble fraction was slower in presence of fillers and the ranking of filler's effect was the same than oxidized photoproducts formation: dye + SBR < TiO_2 + SBR < neat SBR. Three different slopes were observed in presence of fillers: the first 5 h of irradiation was characterized by a very slow rate, followed by a significant increase of the gel content. After that, the ratio of the insoluble part increased up to a plateau corresponding to 80% (in presence of TiO_2 rutile) and 70% (in presence of dye) of gel content.

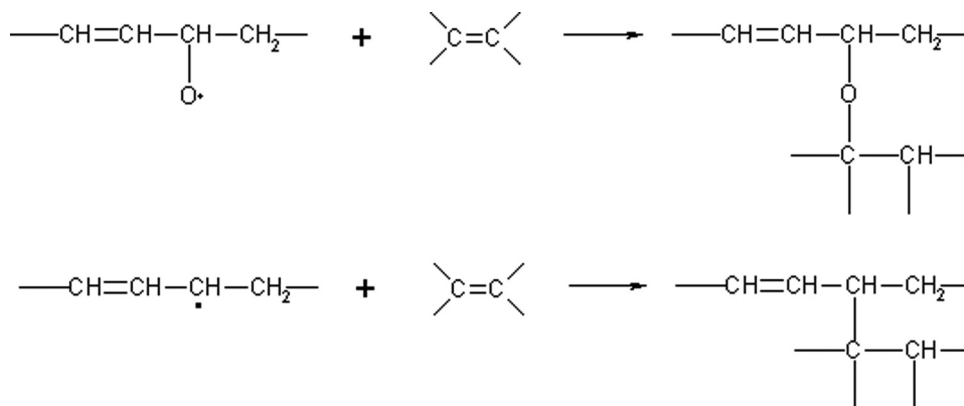


Fig. 9 Proposed crosslinking mechanism of SBR [2,11,12]

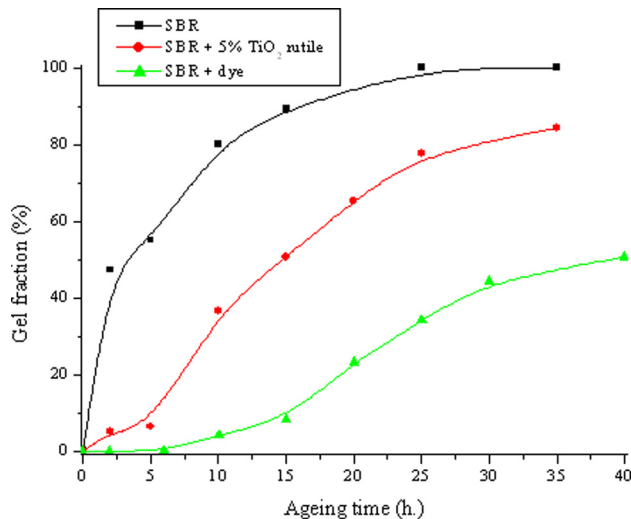


Fig. 10 Evolution of crosslinked network during photo-oxidation of SBR composites

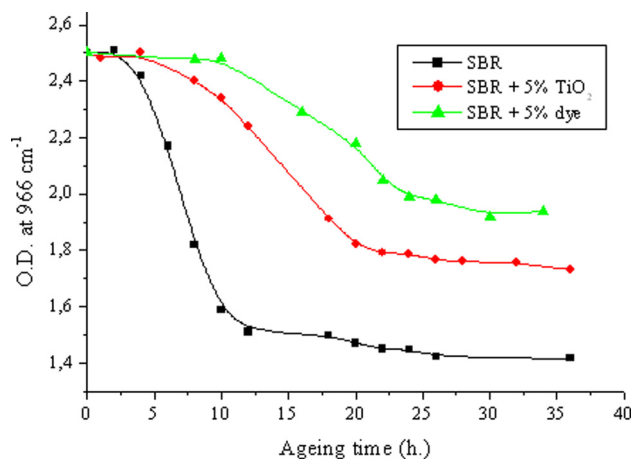


Fig. 11 Kinetic of evolution of vinyl-double band at 966 cm⁻¹ versus irradiation time for different composites

Moreover, a correlation between the evolution of the gel fraction and the optical density of the double bands at 966 cm⁻¹ during irradiation time was made. The variation of the absorbance at 966 cm⁻¹ in presence and in absence of fillers as a function of irradiation time was presented in Fig. 11. First of all, the curves in Fig. 11 showed clearly that the rate of disappearance of the double bonds was much higher in neat SBR and slowed down in presence of fillers following the same order as the rate of formation of gel content (see Fig. 10): dye + SBR < TiO₂ rutile + SBR < neat SBR. The good correlation obtained between the decrease of double bands (see Fig. 11) and the increase of insoluble part (see Fig. 10) was due to the fact that during ageing, loss of unsaturation of α , β unsaturated products occurred through crosslinking [2]. As already described above, coated TiO₂ protects the matrix from crosslinking, and more generally, from photo-oxidation by absorbing part of UV-visible radiation. In the case of azo dye, the photo-protective effect is even much more important compared with TiO₂. The activity mechanism of this compound consisting of a combination of its function as an antioxidant and light absorber, disturbs the cycle of SBR ageing and therefore the crosslinking network formation (see Fig. 9). In this case, the azo dye by influencing the formation of radicals perturbs the crosslinking mechanism showing a slower kinetic of network formation.

4 Conclusions

Mechanistic and kinetic aspects of the photo-oxidation of SBR composites are established and discussed. Although, the mechanism of oxidized products formation is similar to that of neat SBR, the kinetic of the accumulation of the photoproducts is different as well as the rate of the generation of the crosslinked network. Both fillers protect the matrix from photo-oxidation although they are usually incorporated in the polymer to color the material. TiO₂ rutile thanks to the inorganic coating at the surface dissipate a part of the UV-visible rays received by the polymer. The activity mechanism of disazopyrazolone dye, consisting of a combination of its function as an antioxidant and light absorber, slows down the cycle of SBR ageing. In fact, we observed a decrease of photoproducts formation and a decrease of gel formation by crosslinking process compared with neat SBR. We proposed a mechanism to highlight this protective effect. Moreover, it is interesting to note that the protection from the matrix is better than coated TiO₂ rutile, which is known to be a good stabilizer for polymer. The next work will be devoted to the photo-oxidation of vulcanized composites based SBR. The evolution of physico-chemical and mechanical properties of the composite rubbers will be investigated.

Acknowledgment

The authors gratefully acknowledge the financial support of the Fonds National de la Recherche (FNR) from Luxembourg. The authors wish to thanks Dr. Chapron from LMOPS (University Paul Verlaine at Metz in France) for his helpful analysis and discussion about Raman spectroscopy.

References

- [1] Marzocca, A. J., Rodriguez, A. L., Sorichetti, P., and Mosca, H. O., 2010, "Characterization Of Photodegradation of Polybutadiene and Polyisoprene: Chronology of Crosslinking and Chain-Scission," *Polym. Test.*, **29**(4), pp. 477–482.
- [2] Piton, M., and Rivaton, A., 1996, "Photooxidation of Polybutadiene at Long Wavelengths ($\lambda > 300$ nm)," *Polym. Degrad. Stab.*, **53**(3), pp. 343–359.
- [3] Bussière, P. O., Gardette, J. L., Lacoste, J., and Baba, M., 2005, "Characterization of Photodegradation of Polybutadiene and Polyisoprene: Chronology of Crosslinking and Chain-Scission," *Polym. Degrad. Stab.*, **88**(2), pp. 182–188.
- [4] Delor-Jestin, F., Lacoste, J., Barrois-Oudin, N., Cardinet, C., and Lemaire, J., 2000, "Photo-, Thermal and Natural Ageing of Ethylene-Propylene-Diene Monomer (EPDM) Rubber Used in Automotive Applications. Influence of Carbon Black, Crosslinking and Stabilizing Agents," *Polym. Degrad. Stab.*, **67**(3), pp. 469–477.
- [5] Commereuc, S., and Verney, V., 2002, "New Insights into Crosslinking of Elastomers Through Photo-Oxidation," *Polym. Degrad. Stab.*, **78**(3), pp. 561–569.
- [6] Li, G. Y., and Koenig, J. L., 2005, "A Review of Rubber Oxidation," *Rubber Chem. Technol.*, **78**(3), pp. 355–390.
- [7] Gardette, J. L., Baba, M., Mailhot, B., Morlat-Thérias, S., and Rivaton, A., 2008, "Photodégradation des Matériaux Polymères," *L'Actualité Chimique*, n°317, pp. 25–30.
- [8] Feldman, D., 2002, "Polymer Weathering: Photo-Oxidation," *J. Polym. Environ.*, **10**(4), pp. 163–173.
- [9] Luengo, C., Allen, N., Edge, M., Wilkinson, A., Dolores, M., and Ruiz Santa, V., 2006, "Photo-Oxidative Degradation Mechanisms in Styrene-Ethylene-Butadiene-Styrene (SEBS) Triblock Copolymer," *Polym. Degrad. Stab.*, **91**(4), pp. 947–956.
- [10] Bousquet, J. A., Fouassier, J. P., 1987, "Photo-oxidation of a Random Styrene-Butadiene Copolymer: Role of Hydroperoxides and Behaviour of Butenyl Segments," *Eur. Polym. J.*, **23**(5), pp. 367–376.
- [11] Adam, C., Lacoste, J., and Lemaire, J., 1989, "Photo-Oxidation of Elastomeric Materials. Part I-Photo-Oxidation of Polybutadienes," *Polym. Degrad. Stab.*, **24**(3), pp. 185–200.
- [12] Adam, C., Lacoste, J., and Lemaire, J., 1990, "Photo-Oxidation Of Elastomeric Materials: Part IV-Photo-Oxidation of 1,2-Polybutadiene," *Polym. Degrad. Stab.*, **29**(3), pp. 305–320.
- [13] Paoli, M. A., 1983, "The Chemical Effects of Photo-Oxidation on Butadiene Rubber," *Eur. Polym. J.*, **19**(9), pp. 761–768.
- [14] Beavan, S. W., and Phillips, D., 1973, "Mechanistic Studies on the Photo-Oxidation of Commercial poly(butadiene)," *Eur. Polym. J.*, **10**(7), pp. 593–603.
- [15] Adam, C., Lacoste, J., and Lemaire, J., 1989, "Photo-Oxidation of Elastomeric Materials: Part II-Photo-Oxidation of Styrene-Butadiene Copolymer," *Polym. Degrad. Stab.*, **26**(3), pp. 269–284.

- [16] Boutamdja, M., 2006, "Synthesis and Characterization of UV Absorber: 2-Hydroxy-4'-Vinyl Benzophenone," Ph.D. thesis, University of Hadj Lakhder de Batna, Batna, Algeria.
- [17] Bottino, F. A., Cinquegrani, A., Di Pascale, G., Leonardi, L., and Pollicino, A., 2004, "Chemical Modifications, Mechanical Properties and Surface Photo-Oxidation of Films of Polystyrene (PS)," *Polym. Test.*, **23**(4), pp. 405–411.
- [18] Guzzo, M., and De Paoli, M., 1992, "The Photo-Oxidation of EPDM Rubber: Part V—Mechanical Properties Degradation of Vulcanized Filled Samples," *Polym. Degrad. Stab.*, **38**(1), pp. 41–45.
- [19] Coran, A. Y., 2003, "Chemistry of the Vulcanization and Protection of Elastomers: A Review of the Achievements," *J. Appl. Polym. Sci.*, **87**(1), pp. 24–30.
- [20] Saron, C., Zulli, F., Giordano, M., and Felisberti, M., 2006, "Influence of Copper-Phthalocyanine on The Photodegradation of Polycarbonate," *Polym. Degrad. Stab.*, **91**(12), pp. 3301–3311.
- [21] Klemchuk, P., 1983, "Influence of Pigments on The Light Stability of Polymers: A Critical Review," *Polym. Photochem.*, **3**(1), pp. 1–27.
- [22] Allen, N., 1994, "Photofading And Light Stability of Dyed and Pigmented Polymers," *Polym. Degrad. Stab.*, **44**(3), pp. 357–374.
- [23] Delor, F., Lacoste, J., Lemaire, J., Barrois-oudin, N., and Cardinet, C., 1996, "Photo- and Thermal Ageing of Polychloroprene: Effect of Carbon Black and Crosslinking," *Polym. Degrad. Stab.*, **53**(3), pp. 361–369.
- [24] Mostafa, A., Abouel-Kasem, A., Bayoumi, M. R., and El-Sebaie, M. G., 2009, "The Influence of CB Loading on Thermal Aging Resistance of SBR and NBR Rubber Compounds Under Different Aging Temperature," *Mater. Des.*, **30**(3), pp. 791–795.
- [25] Arantes, T., Leao, K., and Camargo, E. R., 2009, "NMR Study of Styrene-Butadiene Rubber (SBR) and TiO₂ Nanocomposites," *Polym. Test.*, **28**(5), pp. 490–494.
- [26] Allen, N. S., Bullen, D. J., and McKellar, J. F., 1977, "Photo-Oxidation of Commercial Polyethylene Containing Titanium Dioxide (rutile)/Antioxidant Systems," *J. Mater. Sci.*, **12**(7), pp. 1320–1324.
- [27] Allen, N., Edge, M., Corrales, T., and Catalina, F., 1998, "Stabiliser Interactions in the Thermal and Photooxidation of Titanium Dioxide Pigmented Polypropylene films," *Polym. Degrad. Stab.*, **61**(1), pp. 139–149.
- [28] Zeynalov, E. B., and Allen, N.S., 2004, "An Influence of Micron and Nano-Particle Titanium Dioxides on the Efficiency of Antioxidant Irganox 1010 in a Model Oxidative Reaction," *Polym. Degrad. Stab.*, **86**(1), pp. 115–120.
- [29] Delor-Jestin, F., Barrois-Oudin, N., Cardinet, C., Lacoste, J., and Lemaire, J., 2000, "Thermal Ageing of Acrylonitrile-Butadiene Copolymer," *Polym. Degrad. Stab.*, **70**(1), pp. 1–4.
- [30] Silva, V. P., Paschoalino, M. P., Gonçalves, M. C., Felisberti, M. I., Jardim, W.F., and Yoshida, I. V. P., 2009, "Silicone Rubbers Filled With TiO₂: Characterization and Photocatalytic Activity," *Mater. Chem. Phys.*, **113**(1), pp. 395–400.
- [31] Jubete, E., Liauw, C. M., Jacobson, K., and Allen, N. S., 2007, "Degradation Of Carboxylated Styrene Butadiene Rubber Based Water Born Paints. Part 1: Effect of Talc Filler and Titania Pigment on UV Stability," *Polym. Degrad. Stab.*, **92**(8), pp. 1611–1621.
- [32] Stevenson, I., David, L., Gauthier, C., Arambourg, L., Davenas, J., and Vigier, G., 2001, "Influence of SiO₂ Fillers on the Irradiation Ageing of Silicone Rubbers," *Polym. Degrad. Stab.*, **42**(22), pp. 9287–9292.
- [33] Saron, C., Zulli, F., Giordano, M., and Felisberti, M., 2006, "Influence of Copper-Phthalocyanine on the Photodegradation of Polycarbonate," *Polym. Degrad. Stab.*, **91**(12), pp. 3301–3311.
- [34] Efremkin, A. F., and Ivanov, V. B., 1984, "Light Protective Action of Azo Compounds in Polydienes," *Polym. Photochem.*, **4**(3), pp. 179–205.
- [35] Ivanov, V. B., Efremkin, A. F., Arinich, L. V., Gorelik, M. V., Shlyapintokh, V. Ya., 1982, "Structure of Azo Compounds and Effectiveness of Their Light-Screening Effect in Elastomers," *Russ. Chem. Bull.*, **31**(9), pp. 2019–2023.
- [36] Sabaa, M. A., Oraby, E. H., Abdel Naby, A. S., and Mohamed, R. R., 2006, "N-Phenyl-3-Substituted 5 Pyrazolone Derivatives as Organic Stabilizers for Rigid Poly(vinyl chloride) Against Photodegradation," *J. Appl. Polym. Sci.*, **101**(3), pp. 1543–1555.
- [37] Sabaa, M. A., Oraby, E. H., Abdel Naby, A. S., and Mohamed, R. R., 2006, "Organic Thermal Stabilizers For Rigid Poly(Vinyl Chloride). Part XII: N-Phenyl-3-Substituted-5-Pyrazolone Derivatives," *Polym. Degrad. Stab.*, **91**(4), pp. 911–923.
- [38] Khoylou, F., and Hassanpour, S., 2005, "The Effect of Environmental Conditions on Electron Beam Cross-linked Agricultural Polyethylene Films," *Iran. Polym. J.*, **14**(10), pp. 875–879.
- [39] Schnabel, W., Levchik, G. F., Wilkie, C. A., Jiang, D. D., and Levchik, S. V., 1999, "Thermal Degradation of Polystyrene, Poly(1,4-butadiene) and Copolymers of Styrene and 1,4-Butadiene Irradiated Under Air or Argon With ⁶⁰Co-γ-rays," *Polym. Degrad. Stab.*, **63**(3), pp. 365–375.
- [40] Zweifel, H., Maier, R. D., and Schiller, M., 2009, *Plastics Additives Handbook*, Hanser Verlag, Munich.
- [41] Li, G. Y., and Koenig, J. L., 2003, "FTIR Imaging of Oxidation of Polyisoprene 2. The Role of N-Phenyl-N'-Dimethyl-Butyl-p-Phenylenediamine antioxidant," *Polym. Degrad. Stab.*, **81**(3), pp. 377–385.



New development on plasticized poly(lactide): Chemical grafting of citrate on PLA by reactive extrusion

Fatima Hassouna^{a,*}, Jean-Marie Raquez^b, Frédéric Addiego^a, Valérie Toniazzo^a, Philippe Dubois^b, David Ruch^a

^a Department of Advanced Materials and Structures, Centre de Recherche Public Henri Tudor, Rue Luxembourg 66, L-4221 Esch-sur-Alzette, Luxembourg

^b Laboratory of Polymeric and Composite Materials, Center of Innovation and Research in Materials & Polymers (CIRMAP), University of Mons, Place du Parc 23, B-7000 Mons, Belgium

ARTICLE INFO

Article history:

Received 5 July 2011

Received in revised form 28 November 2011

Accepted 1 December 2011

Available online 13 December 2011

Keywords:

Poly(lactide)

Tributyl citrate (TbC)

Mechanical properties

Reactive extrusion

Aging

ABSTRACT

New plasticization ways based on low molecular plasticizers from citrates family were investigated to improve the ductility of poly(lactide) (PLA). Grafting reactions between anhydride-grafted PLA (MAG-PLA) copolymer with hydroxyl-functionalized citrate plasticizer, i.e. tributyl citrate (TbC), were so-carried out through reactive extrusion. TributylO-acetylcitrate (ATbC) was used as a non-functionalized reference. Both plasticizers drastically decreased the T_g of PLA. However, the grafting reaction of TbC into MAG-PLA revealed a shift of PLA T_g toward higher values. After 6 months of aging, no phase separation was observed. However, plasticizer leaching was noticed in the case of PLA/ATbC materials, leading to the shift of T_g toward lower temperatures. In contrast, no major leaching phenomenon was noticed in PLA/TbC and PLA/MAG-PLA/TbC blends, indicating that the mobility restriction derived from the hydrogen bonding that can occur between PLA and TbC as well as the grafting reaction of TbC into MAG-PLA enabled to reduce leaching phenomena.

© 2011 Elsevier Ltd. All rights reserved.

1. Introduction

Poly(lactide) has received much attention in the research of alternative biodegradable polymers [1–3]. Its low toxicity, along with its environmentally benign characteristics, has made PLA an ideal material for food packaging and film wrap, as well as for other consumer products [4–6]. PLA is characterized by excellent optical properties and high tensile-strength but unfortunately, it is rigid and brittle at room temperature due to its glass transition temperature (T_g) close to 55 °C [2]. Previous works suggested that the brittleness of PLA is due to the low entanglement density (V_e) and the high value of characteristic ratio (C_∞), a measure of chain stiffness [7,8], limiting its melt-processability and its end-use mechanical performance. In the frame of packaging materials a high ductility at room

temperature is required and thus, there is no tolerance for the polymer film tearing or cracking when subjected to stresses during package manufacturing or use [2,9]. For such application, other requirements include transparency and low crystallinity. To improve the ductility of PLA-based materials, a large number of investigations have been performed to modify PLA properties *via* plasticization. However, an enormous number of variables, i.e. the nature of the PLA matrix, the type and optimal percentage of plasticizer, the thermal stability at the processing temperature, etc. must be taken into account. Unfortunately, poor mechanical properties are often reported and the relationships between the thermo-mechanical properties and the molecular parameters are far from being elucidated. In this paper, we focus on the plasticizer type that is believed to predominantly influence the final thermo-mechanical properties of the modified PLA. Rather than lactide, many kinds of ester-like plasticizers for PLA have been studied such as bishydroxymethyl malonate (DBM) [10], glucose

* Corresponding author. Tel.: +352 42 59 91 594.

E-mail address: fatima.hassouna@tudor.lu (F. Hassouna).

monoesters and partial fatty acid esters, citrates [11], etc. However, the low molecular weight plasticizers have the problem of migrating, owing to their high mobility within the PLA matrix. Therefore, plasticizers with rather high molecular weight and low mobility are suitable such as poly(ethylene glycol) (PEG) [11–13], poly(propylene glycol) (PPG) [14], atactic poly(3-hydroxybutyrate) (a-PHB) [15,16] and oligoesteramide (DBM-oligoesteramide) [10,17,18]. On the other hand, the choice of plasticizer used as a modifier for PLA is limited by the legislative or technical requirements of the application, and in this context, its selection becomes more difficult [10,18]. In fact, the plasticizer used for PLA has to be biodegradable, non-toxic for food contact (for packaging) and/or biocompatible (for medical applications). In general, amounts ranging from 10 to 20 wt.% of plasticizers are required to provide both a substantial reduction of T_g of the PLA matrix and adequate mechanical properties. In sustainable issues, the preferred plasticizer for PLA is biodegradable/bioresorbable, sufficiently non-volatile, with a relatively low molecular weight to produce the desired decrease of the Young's modulus value and increase of the impact strength. Moreover, the addition of more than 20–30% (depending on the plasticizer) of plasticizers into the PLA matrix leads to a phase separation. The plasticization is thus limited by the amount of plasticizer to be blended with PLA. Recently, we have developed new ways of plasticizing PLA with low molecular poly(ethylene glycol) (PEG) to improve the ductility of PLA while maintaining the plasticizer content at maximum 20 wt.% PLA [19]. The *in situ* reactive grafting of hydroxy terminated poly(ethylene glycol) (PEG) plasticizer onto the maleic anhydride modified PLA in PLA/PEG blends lowered significantly the glass transition temperature compared to the blends where no grafting could occur (neat PLA + PEG) and had a positive impact on the mechanical properties. Indeed, absence of yield peak was observed for PLA + 10% MAG-PLA + 20% PEG. In the present work, we applied the same strategy developed for the *in situ* reactive grafting of hydroxy terminated poly(ethylene glycol) (PEG) plasticizer into PLA to graft citrate plasticizers. The objectives of the present study is to verify if the strategy consisting in the grafting of a fraction of the plasticizer can be applied to citrate family (tributylO-acetylcitrate and tributyl citrate) to further improve the PLA ductility compared to what is done so far, while maintaining the plasticizer content at a maximum of 20 wt.% (to avoid phase separation). The strategy chosen consists in grafting a fraction of hydroxyl-functionalized citrate plasticizer (tributyl citrate) onto a PLA backbone by reactive extrusion in order to create more interactions between the functionalized polyester matrix and the remaining fraction of non-grafted plasticizer.

To this end, a reactive blending of maleic anhydride-grafted PLA (MAG-PLA) copolymer with hydroxyl-functionalized TbC was performed. Physico-chemical, thermal and mechanical properties of the extruded blends were studied in order to assess the compatibility of the plasticizer with the PLA. TributylO-acetylcitrate was used as a reference as this plasticizer does not possess any reactive group able to react with anhydride functions in melt temperature.

2. Experimental part

2.1. Materials

Poly(lactide) (PLA) was provided by NatureWorks LLC under the reference 4042D. (i) 2,5-Dimethyl-2,5-di-(tert-butylperoxy)hexane organic peroxide (Lupersol 101), (ii) maleic anhydride (MA) and (iii) tributylO-acetylcitrate 98% (ATbC) were purchased from Sigma–Aldrich. Tributyl citrate 99 + % (TbC) was provided by Acros Organics. The properties of the used plasticizers are listed in Table 1 [20].

2.2. Processing

All melt (reactive) blending were performed on a Leistritz corotating intermeshing twin-screw extruder ($L/D = 45$). The temperature profile was 160/180/180/180/180/180/180/180 from the feed throat to the die, and the melt temperature was 181 °C. The employed screw speed was 80 rpm. A two-hole filament die, 3 mm in diameter and equipped with a cooling sleeve, was assembled to the extruder. PLA was dried overnight at 40 °C in a vacuum oven before processing. Dry TbC and ATbC were used with any particular precaution.

Maleation of poly(lactide) (MAG-PLA) was carried out by reactive extrusion. PLA, MA and Lupersol 101 (L101) were hand-mixed together before extrusion.

The percentage of Lupersol added is based on a PLA weight (0.5 wt.%), while 2 wt.% of MA (PLA basis) is chosen for this maleation procedure [21]. Neat PLA and PLA + 10 wt.% MAG-PLA are mixed, added at a rate of 2.0 kg/h to the feed zone and submitted to extrusion using the same conditions than the grafting step. TbC or ATbC plasticizers are introduced to the extruder using a calibrated pump. The contents of plasticizer (TbC and ATbC) are chosen to be 10 and 20 wt.%, based on the total weight of the mixture. Table 2 summarizes the composition of each formulation.

For the mechanical study (tensile tests and dynamical mechanical analysis), $110 \times 110 \times 4$ mm³ plates of PLA were compression-molded using a Carver laboratory press and a specific rectangular mold. The procedure utilized was as follows: (i) extruded PLA was first heated at 190 °C for 3 min, (ii) PLA was then compressed during 30 s with a pressure of 15 MPa and (iii) under the same pressure (15 MPa) PLA was cooled by means of a room temperature water circulation.

2.3. Characterization

Fourier transform infrared (FTIR), Nuclear Magnetic Resonance (NMR), potentiometric titration and soxhlet

Table 1
Properties of the used plasticizers [20].

Plasticizer	Molecular weight (g mol ⁻¹)	Density (g mL ⁻¹)	Solubility parameters (J cm ³) ^{1/2}
Tributyl citrate (TbC)	360	1.104	18.8
TributylO-acetylcitrate (ATbC)	402	1.046	18.7

Table 2

Summary of (reactive) blending composition.

	PLA (wt.%)	Maleic anhydride (MA) (wt.%)	Lupersol (L101) (wt.%)
Anhydride-grafted PLA (MAG-PLA)	97.5	2	0.5
	PLA(wt.%)	MAG-PLA(wt.%)	TbC or ATbC(wt.%)
PLA + (TbC or ATbC)	90		10
	80		20
PLA + MAG-PLA + (TbC or ATbC)	80	10	10
	70	10	20

extraction were used to characterize the efficiency of the grafting reaction.

2.4. Fourier transform infrared spectrometer

Chemical structure modification of PLA was evaluated by Fourier transform infrared spectroscopy (FTIR) using the transmission mode. The signal was recorded from 400 to 4000 cm^{-1} with a Bruker Optics Tensor 27 spectrometer. This characterization was done on 100 μm -thick films prepared by hot-pressing. To this end, samples with a weight comprised between 20 and 30 mg were compressed between two sheets of poly(tetrafluoroethylene) (PTFE) Teflon films utilizing a Carver laboratory press (temperature: 180 $^{\circ}\text{C}$, pressure: 5 MPa).

2.5. Nuclear Magnetic Resonance

Nuclear Magnetic Resonance ^1H NMR spectra were recorded on a Bruker AMX-300 apparatus at room temperature in CDCl_3 at a sample concentration of 30 mg/0.6 mL. All chemical shifts and coupling constants are reported in ppm and Hz, respectively.

2.6. Potentiometric titration

The extent of maleation for samples grafted with MA can be determined by titration [21]. Since the initial percent of MA reacted is quite low (2 wt.%), it can be assumed that the actual percent grafted onto the PLA backbone is very small. A direct titration of these samples would probably be inaccurate as a small discrepancy such as a contaminant could result in a large error; therefore, a back-titration of the sample is necessary. A back-titration consists of adding a known excess of base and then titrating the remaining base with acid. The base reacts with both the maleated sample and the acid. The amount of anhydride attached to the PLA backbone can be then determined.

A potentiometric titration was done using a potentiometer. A first-derivative analysis was used to determine the equivalence point of the sample by the following method: (1) remove unreacted MA by drying in a vacuum oven at 80 $^{\circ}\text{C}$ for 24 h; (2) dissolve 1 g of the sample (containing a maximum of 2 wt.% MA) in 20 mL of CHCl_3 -MeOH (5:1); (3) after 1 h or when the samples are completely dissolved, add 2.0 mL of morpholine solution (0.05 N in MeOH); (4) let the mixture reacting for 10 min and (5) titrate the samples with 0.01 N HCl using the autotitrator. The HCl solution was titrated against a known NaOH standard. The morpholine solution was then titrated against

the HCl to get a blank reading. The calculation for determining the quantity of grafted anhydride is as follows:

$$\% \text{Anhydride} = (V_{\text{mor}} N_{\text{mor}} - V_{\text{HCl}} N_{\text{HCl}}) \times \frac{98.06 \text{ g mol}^{-1}}{W_{\text{sample}}} \times 100$$

2.7. Size exclusion chromatography

Size exclusion chromatography (SEC) tests were conducted with an Agilent Technologies series 1200 operating with a differential refractive index detection and a linear column (PLgel Mixed-D 5 and 3 μm , 200 Da < M_w < 200 kDa in chloroform 1 mL min^{-1}). SEC analyses were carried out to follow the evolution of the molecular weight of PLA before and after grafting and upon melt-blending with plasticizers. It is also to be noted that SEC tests were run at room temperature (polymer concentration 2 mg mL^{-1}).

2.8. Tensile tests

Tensile behavior of PLA was investigated by means of a servo-hydraulic testing machine MTS 810 equipped with the optical extensometer “VidéoTraction” (7 markers mode). This special extensometer provided the true stress – true strain curve of the materials at constant strain rate of a representative volume element located in the center of tensile specimens. Hence, the necking process was taken into account in the measured mechanical behavior. Mechanical tests were performed at the temperature of 23 $^{\circ}\text{C}$ and at the strain rate of 0.001 s^{-1} . Rectangular tensile specimens were machined from the 4 mm-thick plates using a computer-controlled milling machine (CharlyRobot CRA4). The calibrated zone of tensile specimens was a parallelepiped of $34 \times 7.6 \times 4 \text{ mm}^3$. Note that the median region of the calibrated zone had a reduced width of 6.8 mm and a local radius of curvature of 15 mm to localize necking process in this zone. Seven black ink markers were carefully printed in the form of a cross on the front flat face of the sample. More details about this method are given in a previous paper [22].

2.9. Dynamic mechanical analyzer

The influence of the plasticizer on viscoelastic properties of PLA was analyzed by means of a dynamic mechanical analyzer (DMA) Netzsch DMA 242 C. For this study, we used $50 \times 10 \times 4 \text{ mm}^3$ rectangular specimens machined from the compression-molded plates. They were subjected to double cantilever mode of flexural loading with a maximum displacement of 40 μm in the tempera-

ture range -60 – 120 °C (rate 10 °C min^{-1}) and a frequency of 1 Hz.

2.10. Differential scanning calorimeter

Differential scanning calorimetry thermograms of PLA were recorded by means of a Netzsch DSC 204 F1 Phoenix apparatus operating in inert atmosphere (nitrogen), and with a heating rate of 10 °C min^{-1} . The samples (10 – 20 mg) were placed into alumina crucibles and were subjected to the following temperature program: (i) a first heating step from -100 to 200 °C, (ii) a cooling step from 200 to -100 °C and (iii) a second heating step from -100 to 200 °C. We report in this study results arising from the second heating step since this second step is well-known to remove the effect of the thermal history of a polymer.

2.11. Wide-angle X-ray scattering

We performed wide-angle X-ray scattering (WAXS) experiments to investigate crystalline properties of the materials. WAXS experiments were conducted on the as-pressed 4 mm-thick specimens by means of an X'Pert Pro MPD diffractometer from PANalytical, with a copper α radiation (1.54 Å) generated at 45 kV and 40 mA. We used the transmission mode of the equipment on which was mounted a parallel mirror (divergence slit $1/2^\circ$, antiscatter slit $1/2^\circ$ and soller slit 0.04 rad) as incident beam optic and a PIXcel detector (antiscatter slit $1/32^\circ$, soller slit 0.04 rad) as diffracted beam optic. The specimens were tested with a revolution time of 4 s to put the higher number of planes in diffraction position. The weight index of crystallinity of PLA was measured from background-corrected curves as the ratio of total crystalline peaks area to total scattering area (calculation was performed by means of the software PeakFit from Systat Software Inc.).

2.12. Thermogravimetric analyzer

Thermogravimetric analyses were performed with a on a Netzsch TG 409 PC Luxx device operating in nitrogen (80 mL min^{-1}) and oxygen (20 mL min^{-1}) environment in alumina crucibles (150 mL) containing 20 – 25 mg of sample. The runs were carried out in dynamic conditions. They were heated up to 600 °C at the constant heating rate of 20 K min^{-1} .

2.13. Soxhlet extraction

The plasticizer was extracted from plasticized PLA using soxhlet to determine the amount and the nature of the ex-

tracted fraction. The samples were placed in a thimble-holder that was gradually filled with condensed fresh extractant (methanol) from a distillation flask. When the liquid reached the overflow level, a siphon aspirated the solute from the thimble-holder and unloaded it back into the distillation flask, thus carrying the extracted analytes into the liquid. This operation was repeated until extraction was complete. Solid fraction (PLA) was dried overnight at 60 °C and weighed. Methanol was then evaporated from the solution fraction and the obtained product was characterized by FTIR and NMR.

3. Results and discussion

3.1. Reactive extrusion grafting and plasticizing of PLA

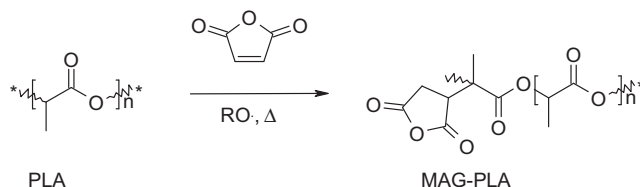
Grafting of MA onto PLA by reactive extrusion (Scheme 1) was characterized by FTIR and quantified by titration after elimination of the unreacted MA. The amount of anhydride attached to the PLA backbone was determined by back-titration. The addition of 0.5 wt.% of L101 and 2 wt.% of MA to PLA leads to the melt-grafting of 0.6 wt.% of MA. Moreover, the addition of MA has a slight negative effect on the molecular weight of PLA. It leads to a slight decrease of the number-average molecular weight (M_n) from $77,300$ to $66,950$ g mol^{-1} (Table 3) [19,21]. This step was already described in previous works and a grafting mechanism of maleic anhydride onto PLA was accordingly established [23].

The choice of the plasticizers to be used as modifiers for PLA is limited by the requirements of packaging and medical applications. Only non-toxic substances approved for food contact can be considered in these applications. In addition, the substance must be biodegradable. The plasticizers chosen for the present investigation displayed good plasticizing abilities when blended with PLA [20].

In order to react easily with the anhydride functions grafted in resulting PLA chains and to improve the compatibility with PLA, tributyl citrate (TbC) bearing a tertiary hydroxyl group was selected as plasticizer. Tributyl 0-ethylcitrate, free of hydroxyl group was also used in PLA

Table 3
Molecular weights (M_n and M_w) of PLA-based samples.

Sample	M_n (g mol^{-1})	M_w (g mol^{-1})	Polydispersity index
PLA	77,300	94,350	1.2
PLA after extrusion	77,850	93,850	1.2
MAG-PLA	66,950	87,300	1.3
PLA + 10% MAG-PLA	73,600	90,550	1.2



Scheme 1. Mechanism of reactive extrusion grafting of maleic anhydride (MA) onto PLA.

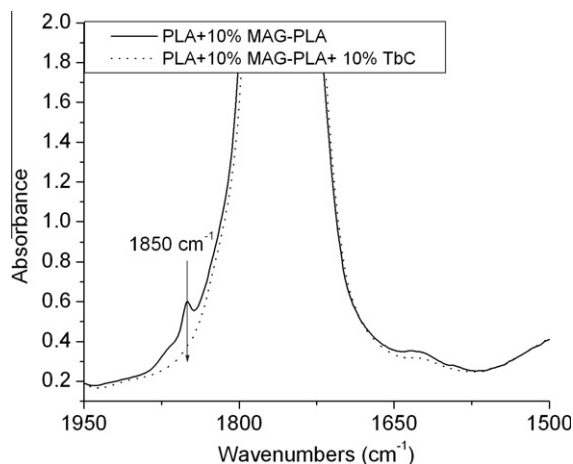


Fig. 1. Zoom over FTIR spectra of PLA films before and after reactive blending with TbC.

plasticization to study the effect of the citrate covalent grafting.

It was shown by FTIR that melt-blending TbC (10% or 20%) with PLA + 10% MAG-PLA leads to the grafting of a fraction of TbC onto the anhydride functions. Indeed, a decrease of the absorption band intensity at 1850 cm^{-1} corresponding to anhydride functions is noticed, evidencing the reaction between the anhydride functionalities and hydroxyl group of TbC (Fig. 1, Scheme 2). It is worth pointing out that reaction between carboxylic anhydride and hydroxyl groups via esterification reaction represents a very efficient reactive way for compatibilizing polymer blends [23].

The molecular weight characterization shows that the melt blending of PLA or PLA + MAG-PLA with TbC or ATbC did not affect the PLA molecular weight ($M_n = 73,600\text{ g mol}^{-1}$) during processing. Therefore, under adequate processing conditions, melt reactive extrusion and melt-blending of PLA with TbC or ATbC does not induce any significant drop of PLA molecular weight by thermal degradation or hydrolysis of the polyester chains.

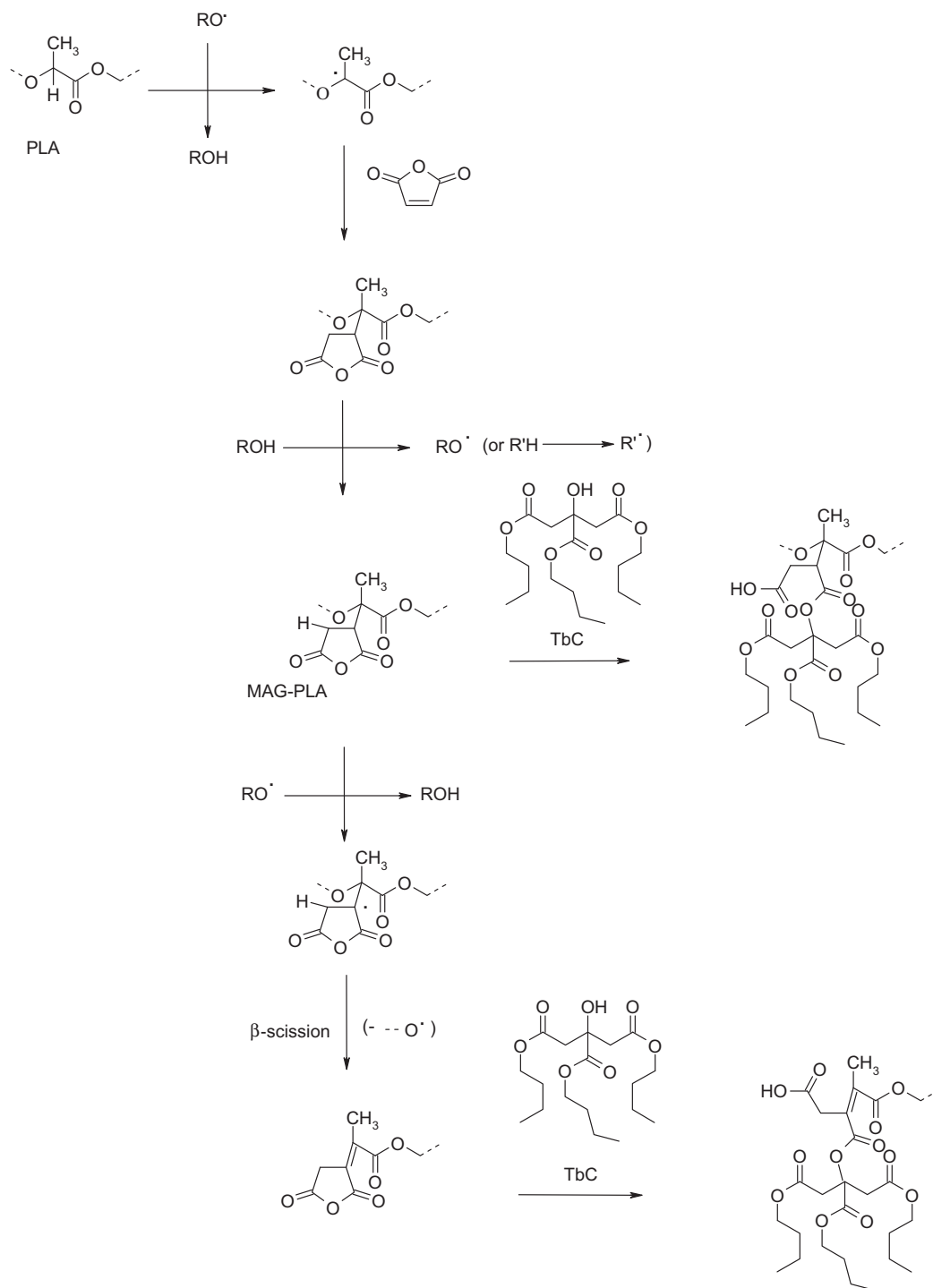
TGA measurements were also carried out on the different formulations (Fig. 2) to determine the impact of such plasticizers on the thermal stability of PLA. Indeed, it is believed that the choice of the most adequate processing conditions (residence time, temperature, etc.) and of thermally stable PLA compositions could lead to improved end-use characteristics. TGA measurements reveals that the decomposition temperature of the citrate plasticizers is quite high (decomposition temperature at 50% weight loss is about 330°C) compared to the extrusion temperature (180°C). The addition of citrates affects the thermal stability of PLA at high temperature ranges (higher than 250°C), which are not reached during processing. The grafting of TbC into MAG-PLA does not influence the thermal stability of the blends.

3.2. Thermal and physical characterization

Table 4 and Fig. 3(a and b) summarize the thermal properties of neat, modified and blended PLA during the second

heating scan ranging from -100 to 200°C . First it comes out that DSC runs for the neat and modified PLA show that the grafting of 0.6 wt.% anhydride functions onto PLA chains does not modify significantly the thermal properties of PLA [19]. It is also to be mentioned here that is all the investigated materials, the melting enthalpy (ΔH_m) of the materials is about equal to the enthalpy of cold crystallization (ΔH_{cc}). This implies that all the investigated materials are totally amorphous once the thermal history was removed. Both PLA and MAG-PLA thermograms display a shift in the signal baseline related to the glass transition around 60°C , an exothermic peak of cold crystallization centered at 124°C and an endothermic melting peak centered at 154°C . The addition of 10% of MAG-PLA to PLA does not influence the thermogram of PLA (not shown here). However it is observed a slight increase of melting enthalpy from 18 to 21 J/g . When a plasticizer (TbC or ATbC) is added to the blend PLA + 10% MAG-PLA, (i) T_g decreases from 60.5 to a minimum of 26°C , (ii) T_{cc} decreases from 126 to a minimum of 89°C and (iii) T_m decreases from 154 to a minimum of 149°C with increasing the amount of plasticizer up to 20 wt.%, while the melting enthalpy increases from 21 to $25\text{--}26\text{ J/g}$ independently of the amount of plasticizer (note that the crystallization enthalpy has the opposite tendency). Similar tendencies are obtained when a plasticizer is added to as-extruded PLA. Nevertheless, in the case of PLA/TbC systems, the decrease of T_g and T_{cc} are more marked than in the case of PLA/MAG-PLA/TbC systems. The DSC measurements did not reveal any additional T_g at low temperature that could indicate any phase separation within the blends, at least within experimental errors.

As expected, the addition of plasticizer significantly decreases the T_g of PLA due to higher chain mobility. This tendency does not depend on the type of plasticizer. When TbC is melt blended with PLA in presence of MAG-PLA, a reactive extrusion grafting of TbC onto the anhydride functions occurs, leading to the decrease of the amount of free TbC. The decrease of the amount of free TbC responsible for PLA plasticization explains the shift of T_g toward higher values in the case of PLA/MAG-PLA/TbC systems compared to PLA/TbC systems. The decrease of T_{cc} is considered to be directly related to the motion ability of the PLA chains. Indeed, the increase of PLA chain motion due to the amount of citrates (lower T_g) allows an easier rearrangement of the polyester chains in order to crystallize. For instance, the higher the concentration of citrate, the higher the motion and the lower the $T_{cc,PLA}$. The evolution of T_{cc} is highly dependent on the concentration, the nature and the presence of grafted plasticizer. The drop in T_{cc} observed in Table 4 and Fig. 3a is found at lower values with an increasing concentration of TbC or ATbC. In addition as it can be seen in Table 4 and Fig. 3b the presence of PLA grafted TbC leads to a slight increase of T_{cc} values compared to the PLA-g-TbC-free blends. As aforementioned for T_g , the amount of free TbC is lower in the case of PLA/MAG-PLA/TbC systems, which leads to less chain mobility and hence an increased T_{cc} compared to PLA/TbC systems. An increase of ΔH_m can be due to (i) the presence of higher amount of short chains that contribute to the crystallization of PLA, (ii) crystallization of PLA on cooling, weak enough not to produce a sig-



Scheme 2. Mechanism of reactive extrusion grafting of tributyl citrate (TbC) onto anhydride functionalized PLA copolymer (MAG-PLA).

nificant peak on a cooling thermogram, (iii) recrystallization of PLA cold-crystallized crystals during post-crystallization heating in DSC. This is directly linked to an increased mobility for short-range motion of the PLA chains. As a consequence a large portion of the amorphous

phase got allowed to crystallize in the plasticized PLA [18]. This is demonstrated by the presence of shoulders in the melting peaks of PLA blends (Fig. 4). At the same time, the decrease of T_m can be related to the decrease in the average lamella thickness. Therefore, the addition of plasti-

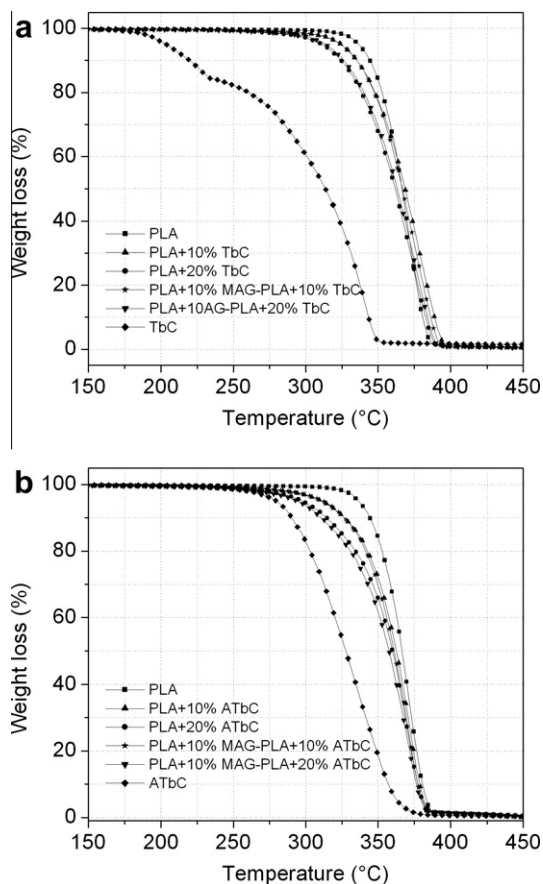


Fig. 2. TGA under N_2/O_2 flow of: (a) PLA + MAG-PLA + TbC and (b) PLA + MAG-PLA + ATbC systems.

cizer generates a higher number of lamellae but thinner lamellae during the cold-crystallization step. It can be also related to the fact that during melting in blends and copolymers, in addition to the entropy increase as a result of the transformation from an ordered crystalline state to a more disordered melt state, there is another positive contribution to the system entropy because crystallites of one component melt into a mixed phase of both compo-

nents. This additional effect causes a depression of T_m in comparison to that of a neat polymer or homopolymer with crystals of the same thickness. It can be further complicated by the fact that double melting exotherms indicate possibility of thickening of crystals prior to melting.

The effect of the grafting of a fraction of TbC onto PLA on the thermal properties of this latter is very different from what was noted in the case of PEG grafting [19]. Indeed, the *in situ* reactive grafting of PEG into MAG-PLA in PLA/20% PEG blends showed a clear effect on the thermal properties of PLA. In this latter case, the T_g displayed by the reactive blend was shifted to even lower temperatures at around 14 °C, while the T_g of neat PLA blended with 20 wt.% PEG was about 23 °C. The behavior of PLA grafted PEG chains (PLA-g-PEG) is completely different from the chains grafted TbC. This discrepancy between PLA-g-PEG and PLA-g-TbC behavior toward the evolution of T_g value can be related to their respective conformations. Indeed, we suspect a difference of conformation between PLA-g-PEG and PLA-g-TbC that can have a direct impact on PLA chain mobility. It is believed that PLA-g-PEG conformation generates a lower mobility restriction *via* a higher free-volume of PLA chains than in the case of PLA-g-TbC [19].

WAXS diagrams of PLA and its derived blends are plotted in Fig. 4. These tests were performed on the as-pressed plates, which imply that we characterized specimens influenced by the processing thermal history. Except for the materials containing 20% of TbC or ATbC, no diffraction peaks are observed, indicating that PLA is amorphous. For the materials containing 20% of TbC or ATbC, one notes the presence of crystalline peaks centered at 15.0°, 16.5° and 18.9°, corresponding to the planes (010), (200)/(110) and (203)/(113) of orthorhombic α phase [24,25]. We obtain a crystallinity of about 10 ± 2 wt.% for the crystalline PLA blends (in comparison with DSC results (Table 4), neat PLA, PLA + 10% TbC, PLA + 10% MAG-PLA + 10% TbC, PLA + 10% ATbC and PLA + 10% MAG-PLA + 10% ATbC are amorphous whatever the thermal history imposed to the material. In contrast, the final crystallinity of PLA + 20% TbC, PLA + 10% MAG-PLA + 20% TbC, PLA + 20% ATbC and PLA + 10% MAG-PLA + 20% ATbC is sensitive to the thermal history. Intrinsically, these four blends are amorphous as shown by DSC (Table 4), but the presence of a high content of plasticizer (20%) coupled with a spe-

Table 4

Thermal features of PLA systems measured by DSC.

Material	T_g (°C)	T_m (°C)	T_{cc} (°C)	$ \Delta H_m \approx \Delta H_{cc} $ (J/g)
PLA after extrusion (reference)	60	154	124	18
MAG-PLA	59.5	153	124	21
PLA + 10% MAG-PLA	60.5	154	126	21
PLA + 10% TbC	41	153	101	25
PLA + 20% TbC	26	149	87	26
PLA + 10% MAG-PLA + 10% TbC	44	153	105	26
PLA + 10% MAG-PLA + 20% TbC	30	150	89	25
PLA + 10% ATbC	42	153	110	25
PLA + 20% ATbC	26	149	95	25
PLA + 10% MAG-PLA + 10% ATbC	41	152	108	26
PLA + 10% MAG-PLA + 20% ATbC	26	149	91	25

T_g : glass transition temperature; T_m : melt temperature of PLA; T_{cc} : cold crystallization temperature of PLA; ΔH_m : heat of melting of PLA; ΔH_{cc} : heat of cold crystallization of PLA.

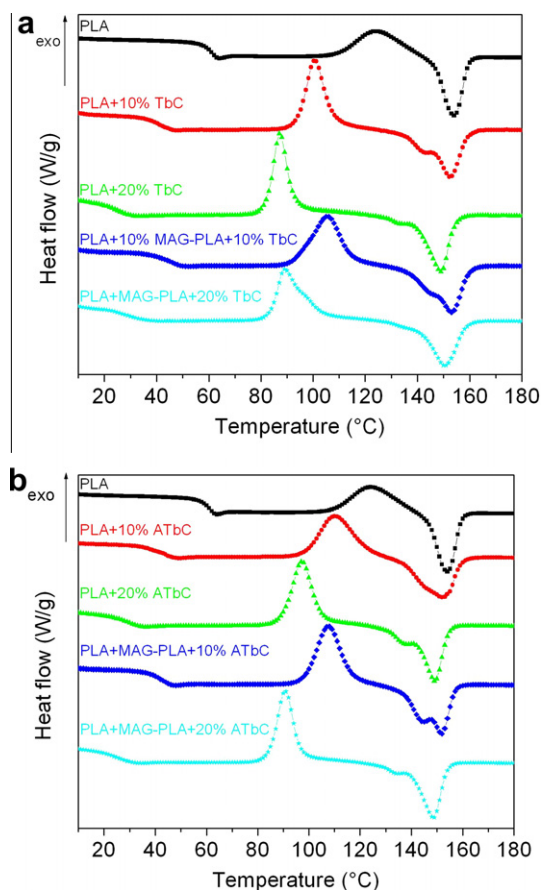


Fig. 3. DSC thermograms recorded during the second heating step: (a) plasticized PLA with TbC; (b) plasticized PLA with ATbC.

cific processing thermal history leads to the formation of PLA crystals. This is due to the low T_g of these blends that is equal to 26 °C (Table 4) and hence is near to room temperature. Therefore, as suggested by Labrecque et al. [22], crystallization occurs during the storage. The mechanical properties of the blends were evaluated from materials having the same thermal history than those investigated by WAXS.

3.3. Mechanical properties

The effect of temperature on storage modulus, E' and loss modulus, E'' is shown in Fig. 5 and 6 for neat and plasticized PLA. The dynamic mechanical measurements were carried out at 1 Hz.

The T_g values are here defined as the temperature of the maximum of the loss modulus, E'' , obtained for α relaxation (associated with the glass transition) at the frequency 1 Hz.

Accordingly, neat PLA has a T_g equal to 60 °C and, as expected, all the plasticized PLA display a lower glass transition temperature compared to neat PLA. It is to be noted that the systems PLA/TbC have a lower T_g than the systems PLA/MAG-PLA/TbC due to a higher concentration of free TbC. DMA results are hence in line with DSC results

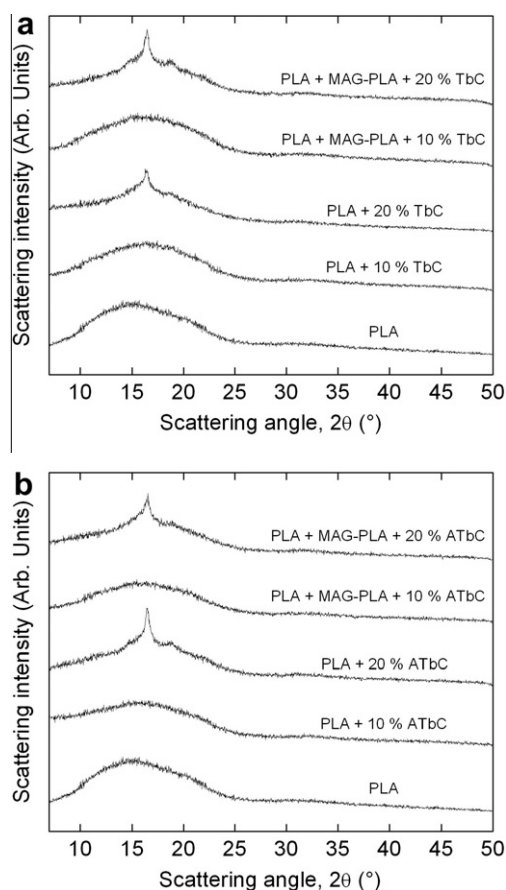


Fig. 4. WAXS diagrams of neat PLA and its derived blends, (a) PLA/MAG-PLA/TbC systems and (b) PLA/MAG-PLA/ATbC systems.

(Table 4) regarding the evolution of T_g . In the temperature-dependent E'' curves of plasticized PLA with TbC and ATbC, some phase separation occurs at low temperature as highlighted by the presence of a small shoulder at around 60 °C. However, the most interesting result is that cold-crystallization processes are observed after the glass transition relaxation. This is shown by the presence of several low intensity peaks between 60 and 120 °C that confirms DSC results. The storage modulus curves for PLA/TbC, PLA/MAG-PLA/TbC, PLA/ATbC and PLA/MAG-PLA/ATbC samples display no secondary peaks at temperatures around the respective T_g values of the neat plasticizers (−89 °C for the plasticizers). The curves in Fig. 5 were thus truncated at −60 °C. At the lowest investigated temperature, −60 °C, the plasticized PLA have a storage modulus E' ranging between 2450 and 3470 MPa, while that of neat PLA is equal to 2500 MPa. With increasing temperature up to the onset of glass transition relaxation, a 70% decrease of the storage modulus of plasticized PLA is noted. In the same temperature range, a much less marked decrease in E' occurs for neat PLA (17%). The storage modulus E' measured at room temperature, 23 °C, is reported in Tables 5 and 6 for the studied materials. Neat PLA has a modulus E' that is equal to 2190 MPa. When 10% of TbC or 10% ATbC are added to neat PLA, the storage modulus E' increases.

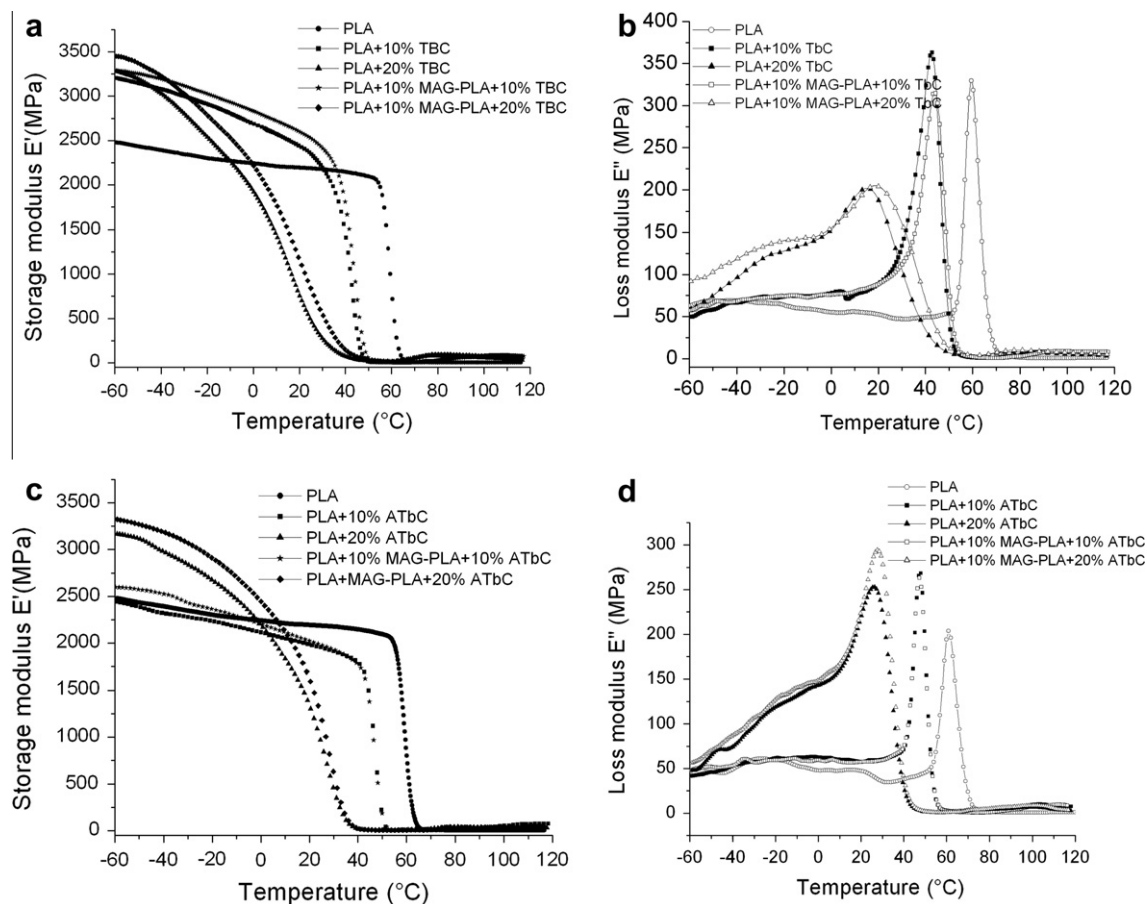


Fig. 5. Temperature dependence of storage modulus E' and loss modulus E'' for neat PLA (a, b, c and d), PLA/TbC and PLA/MAG-PLA/TbC blends (a and b), PLA/ATbC and PLA/MAG-PLA/ATbC blends (c and d) DMA tests performed at 1 Hz.

Table 5

Mechanical features of neat PLA and plasticized PLA with TbC measured by DMA and tensile tests.

Material	Storage modulus E' at 23° (MPa)	T_g by DMA (°C)	Yield stress σ_{33}^y (MPa)	Yield strain ϵ_{33}^y	Ultimate stress σ_{33}^u (MPa)	Ultimate strain ϵ_{33}^u
Neat PLA	2190	60	67.8	0.02	55.3	0.07
PLA + 10% TbC	2403	42	–	–	38.5	0.025
PLA + 20% TbC	572	15	1.7	0.02	>65.6	>1.3
PLA + 10% MAG-PLA + 10% TbC	2564	44	–	–	47.2	0.04
PLA + 10% MAG-PLA + 20% TbC	950	19	6.65	0.02	>60.0	>1.2

Table 6

Mechanical features of neat PLA and plasticized PLA with ATbC measured by DMA and tensile tests.

Material	Storage modulus E' at 23° (MPa)	T_g by DMA (°C)	Yield stress σ_{33}^y (MPa)	Yield strain ϵ_{33}^y	Ultimate stress σ_{33}^u (MPa)	Ultimate strain ϵ_{33}^u
Neat PLA	2190	60	67.8	0.02	55.3	0.07
PLA + 10% ATbC	1970	47	49.0	0.02	17	0.2
PLA + 20% ATbC	1120	26	–	–	>70	>1.35
PLA + 10% MAG-PLA + 10% ATbC	1991	47	44	0.02	15	0.1
PLA + 10% MAG-PLA + 20% ATbC	1328	27	–	–	>63	>1.3

The melt blending of 10% MA-grafted PLA (MAG-PLA) with 10% ATbC shows E' slightly higher than that of PLA + 10% ATbC, and the blend PLA + 10% MAG-PLA + 10% TbC exhib-

its a higher E' when compared to PLA + 10% TbC. The decrease of the amount of free TbC responsible for PLA plasticization due to the grafting of a fraction of the

plasticizer can explain the shift of E' toward higher values. The materials containing 20% of TbC or ATbC have the lowest moduli E' that are comprised between 572 and 950 MPa and between 1120 and 1328 MPa, respectively. After the glass transition relaxation, a weak but significant increase of E' occurs for the plasticized PLA. This process is linked to the cold-crystallization also observed in temperature-dependent E'' curves.

True tensile behavior of neat PLA and plasticized PLA systems is collected in Fig. 5a and c, while the measured characteristics (yield stress σ_{33}^y , yield strain ε_{33}^y , ultimate stress σ_{33}^u and ultimate strain ε_{33}^u) are listed in Tables 5 and 6. It is important to note that the accuracy of the optical extensometer used was not high enough in the initial part of stress–strain curve to determine an elastic modulus with sufficient precision. Neat PLA is characterized by a high yield point ($\sigma_{33}^y = 67.8$ MPa and $\varepsilon_{33}^y = 0.02$) and after this point is reached, a marked stress drop occurs until the material breaks at an ultimate strain of 0.07. As a result, neat PLA has a limited viscoplastic stage. For materials containing 20% plasticizer, it was not possible to record the tensile curve above the axial strain 1.3 due to a destruction of the markers. Indeed, if the markers break into several parts, the image analysis procedure cannot be pursued with the used version of VideoTracion. When compared to neat PLA, plasticized PLA materials exhibit different tensile behaviors. The blends PLA + 10%TbC and PLA + 10% MAG-PLA + 10% TbC have a purely viscoelastic behavior and hence does not display any yield point. The blends PLA + 20% TbC and PLA + 10% MAG-PLA + 20% TbC are characterized by a lower yield point comprised between 1.7 and 6.65 MPa and a longer viscoplastic stage (ultimate strain >1.2) than neat PLA. However such a behavior is close to that of a rubber, that is, purely viscoelastic. Regarding PLA + 10% ATbC and PLA + 10% MAG-PLA + 10% ATbC systems, one notes a decrease of yield stress from 67.8 to 44–49 MPa and an increase of ultimate strain from 0.07 to 0.1–0.2 in comparison with neat PLA. In the case of PLA + 20% ATbC and PLA + 10% MAG-PLA + 20% ATbC, a purely rubber-like behavior is obtained characterized by viscoplastic stage, a very marked hardening and an important viscoelastic stage (ultimate strain >1.3).

As shown by Fig. 5 and 6 and Tables 5 and 6, the viscoelastic and viscoplastic behavior of PLA are drastically influenced by the plasticization methodology. It is believed that the materials PLA + 20% ATbC, PLA + 10% MAG-PLA + 20% ATbC, PLA + 20% TbC and PLA + 10% MAG-PLA + 20% TbC, i.e. the materials containing 20 wt.% of plasticizers, are rubbery during the tensile tests performed at 23 °C. This is due to the marked increase of chain mobility induced by the plasticization process. As a result, they are mainly viscoelastic (no or little viscoplastic stage as is the case for PLA + 20% TbC and PLA + 10% MAG-PLA + 20% TbC), and exhibit an important hardening process and elongation. This means that (i) these materials are rubbery at 23 °C (glass temperature below 23 °C) or that (ii) the glass transition of these materials is achieved during the early stage of stretching. DMA results demonstrate that the T_g of the materials containing 20% of plasticizer is comprised between 15 and 27 °C, which proves that the two assumptions mentioned above are possible. It is to be

noted that DSC data (Table 4) provide higher glass transition temperature. This is due to the fact that relaxation processes of polymers strongly depend on solicitation mode (temperature, load + temperature, electrical field + temperature...), solicitation rate or frequency and the way how it is quantified from the experimental data (peak position, inflection of the curve...). DSC and DMA are techniques based on different solicitation modes and hence their results cannot be compared. The other materials, neat PLA and PLA containing 10% of TbC or ATbC, have a brittle tensile behavior with no (PLA + 10% TbC, PLA + 10% MAG-PLA + 10% TbC) or little (neat PLA, PLA + 10% ATbC and PLA + 10% MAG-PLA + 10% ATbC) viscoplasticity. It is also to be noted that neat PLA and PLA containing 10% of plasticizer exhibit crazes, whose propagation and coalescence may be at the origin of the specimen fracture. It is stipulated that the macroscopic stresses that are dissipated locally can be due to a competition between chain orientation mechanisms and damage mechanisms by crazing. For neat PLA or PLA containing a low amount of plasticizer, the chain mobility is not high enough to induce stress dissipation by chain orientation. Damage mechanisms are hence

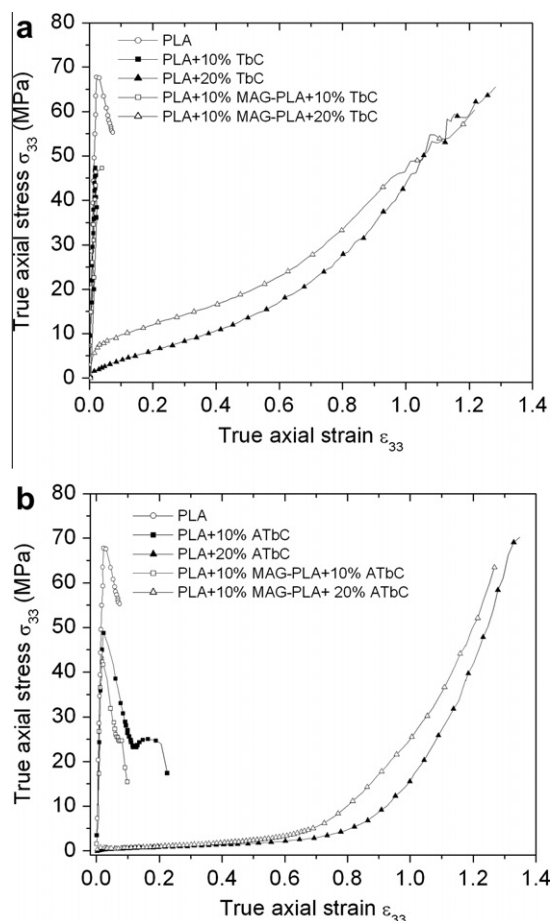


Fig. 6. True axial stress σ_{33} as a function of true axial strain ε_{33} for neat PLA (a and b), PLA/TbC and PLA/MAG-PLA/TbC blends (a), PLA/ATbC and PLA/MAG-PLA/ATbC blends (tensile tests performed at 23 °C and 10^{-3} s $^{-1}$).

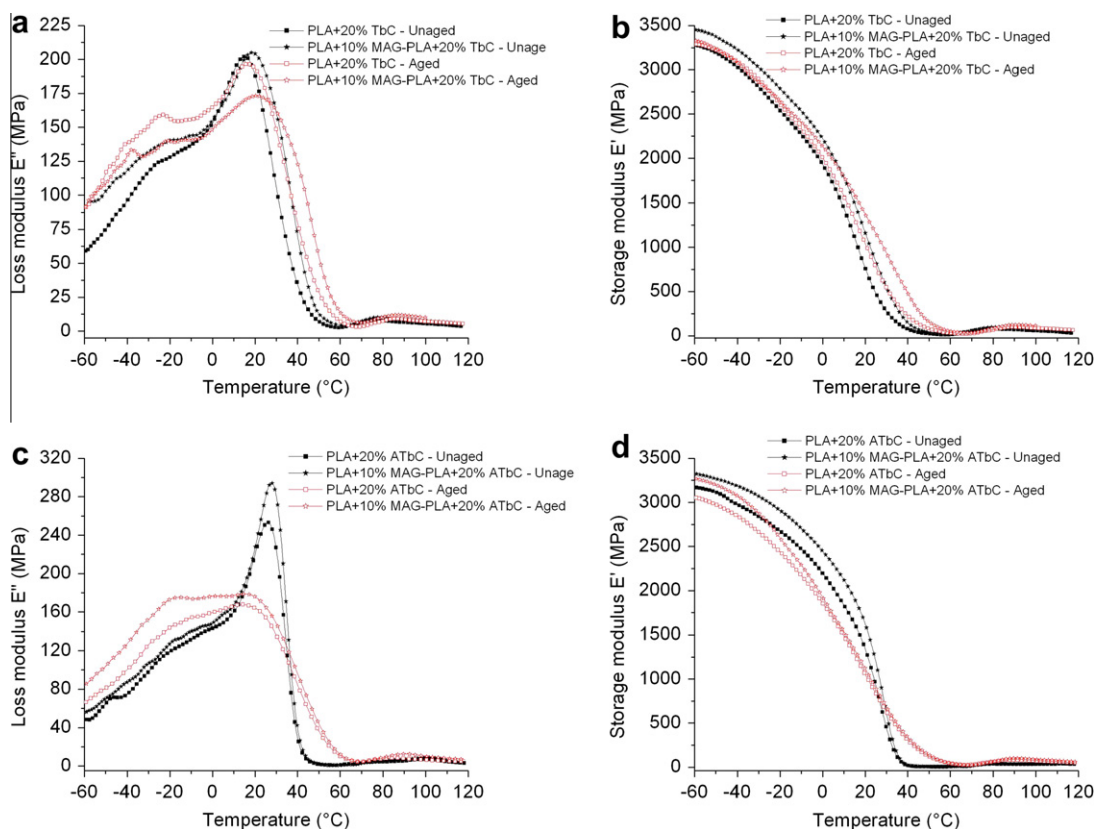


Fig. 7. Temperature dependence of storage modulus E' and loss modulus E'' for unaged and aged PLA/TbC and PLA/MAG-PLA/TbC blends (a and b), PLA/ATbC and PLA/MAG-PLA/ATbC blends (c and d) DMA tests performed at 1 Hz.

promoted, which leads to a brittle tensile behavior. However, we did not expect that PLA + 10% TbC and PLA + 10% MAG-PLA + 10% TbC would have exhibited less viscoplasticity than neat PLA. As indicated by DMA results (Table 5 and Fig. 6a), these two materials have a higher elastic modulus than neat PLA at 23 °C. The elastic modulus of plasticized PLA, exceeding that of neat PLA, was reported also in other papers [26]. This increase in matrix rigidity is not due to a crystallization process since PLA + 10% TbC and PLA + 10% MAG-PLA + 10% TbC are amorphous as the neat matrix prior to tensile test, based on WAXS results. The blends containing 10% of TbC are homogenous. We think that the mobility of the plasticizer below T_g of the blends is restricted by its interaction with PLA. The increase of the storage modulus can thus be related to interactions between the blends components on the molecular level.

The PLA/TbC and PLA/ATbC samples were naturally aged at room temperature (approximately 20 °C) for 6 months to investigate their morphological stability. Fig. 7 displays storage and loss modulus as a function of temperature to compare the aged and unaged blends. The unaged blends (Fig. 7a, b, c and d) seem to be compatible with PLA without any sign of phase separation. Indeed, DMA results did not display any additional T_g that could be attributed to the plasticizer as a consequence of phase separation. After 6 months of aging, T_g (associated with the

glass transition) of the blends PLA/TbC and PLA/MAG-PLA/TbC remained quasi-constant overtime. Moreover, no phase separation that could lead to the migration of the plasticizer to the surface was observed by SEM images. The fraction of TbC grafted into PLA does not seem to have any influence on the aging of the materials. Hydrogen bonding that TbC can generate via the –OH pending functions with the ester groups of PLA should prevent from the migration of the plasticizer to the surface and therefore avoid the phase separation. Furthermore, in PLA/MAG-PLA/TbC blends, the mobility restriction derived from the grafting reactions between hydroxyl moieties from the tributyl citrate and the anhydride moieties from MAG-PLA enabled to reduce the leaching phenomena.

The PLA/ATbC samples, however exhibit an unexpected effect on aging. Indeed, after 6 months of aging, the T_g is shifted to lower temperatures, from 26 to 16 °C for PLA + 20% ATbC and from 27 to 17 °C for PLA + MAG-PLA + 20% ATbC. This behavior, considered as an aging effect, even though it led to an improvement of ductility, can be explained by the fact that unlike TbC, ATbC does not have any function capable of creating hydrogen bonding with PLA, and being unable to be grafted onto PLA, will follow the classical route of plasticizer aging. Indeed, since T_g being at around room temperature, it provided an increased segmental mobility PLA chains, allowing them to rearrange and slowly to crystallize and therefore expulse

a certain fraction of plasticizer. However, unlike what could be expected, ATbC expelled from the blend during the crystallization process of PLA contributed to plasticize even more the amorphous phase and therefore reduced further the T_g . This is in correlation with SEM images that confirmed that no phase separation occurred on aging.

4. Conclusion

New plasticization strategies were studied to improve the ductility of poly(lactide) (PLA) following the use of low molecular plasticizers from citrates family (tributylO-acetyl citrate and tributyl citrate) for plasticizer content at maximum 20 wt.% PLA. In this regard, the *in situ* reactive grafting of hydroxyl-functionalized TbC with MAG-PLA was carried out *via* reactive extrusion in PLA/TbC blends. For sake of clarity, non-functional ATbC was used as a reference. FTIR analyses confirmed the grafting reactions between hydroxyl moieties from TbC and anhydride moieties from MAG-PLA, leading to the decrease of the amount of free TbC within PLA/MAG-PLA/TbC blends. As a consequence, DSC measurements revealed the shift of T_g toward higher values in the case of PLA/MAG-PLA/TbC systems compared to both PLA/TbC and PLA/ATbC systems. The temperature related with cold-crystallization of PLA was also increased after grafting reactions, confirming this restriction of mobility of as-grafted TbC. Moreover, WAXS, DMA and tensile analyses confirmed that as-plasticized PLA materials were amorphous at ambient temperature whichever the plasticizers used.

After aging during 6 months at ambient temperature, plasticizer leaching was noticed in the case of PLA/ATbC materials, as shown by the shift of T_g toward lower temperatures (as determined by DMA) for the corresponding PLA materials. This was explained by the re-concentration of plasticizers into the amorphous phase as well as the cold-crystallization of PLA-based materials, therefore reducing T_g . In contrast, in the case of PLA/TbC and PLA/MAG-PLA/TbC blends, no major leaching phenomenon was noticed, indicating that the mobility restriction derived from the hydrogen bonding that can be generated between PLA ester groups and TbC hydroxyl functions as well as grafting reactions between hydroxyl moieties from TbC and anhydride moieties from MAG-PLA enabled to reduce leaching phenomena.

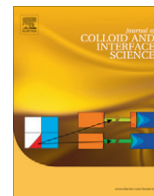
Acknowledgements

CIRMAP authors are grateful to the “Région Wallonne” and European Community (FEDER, FSE) in the frame of “Pôle d'Excellence Materia Nova” for their financial support. They thank the “Belgian Federal Government Office Policy of Science (SSTC)” for general support in the frame of the PAI-6/27. A.-L. J.-M. Raquez is “chargé de recherche” by the F.R.S.-FNRS.

AMS authors thank the European commission FEDER of the financial support in the frame of Matintello project.

References

- [1] Garlotta D. A literature review of poly(lactide). *J Polym Environ* 2001;9:63–84.
- [2] Lim LT, Auras R, Rubino M. Processing technologies for poly(lactide). *ProgPolymSci* 2008;33:820–52.
- [3] Vroman I, Tighzert L. Biodegradable polymers. *Materials* 2009;2:307–44.
- [4] Auras R, Harte B, Selke S. An overview of poly(lactides) as packaging materials. *MacromolBiosci* 2003;4:835–64.
- [5] Rabetafika HN, Paquot M, Dubois P. Les polymères issus du végétal : matériaux à propriétés spécifiques pour des applications ciblées en industrie plastique. *BiotechnolAgronSoc Environ* 2006;10(3):185–96.
- [6] Weber CJ, Haugaard V, Festersen R, Bertelsen G. Production and applications of biobased packaging materials for the food industry. *Food AdditContam* 2002;19:172–7.
- [7] Grijpma DW, Penning JP, Pennings AJ. Chain Entanglement, mechanical properties and drawability of poly(lactide). *Colloid PolymSci* 1994;271:1068–81.
- [8] Tonelli AE, Flory PJ. The Configuration Statistics of random poly(lactide) chains I. Experimental results. *Macromolecules* 1969;2(3):225–7.
- [9] Anderson KS, Schreck KM, Hillmyer MA. Toughening poly(lactide). *Polym Rev* 2008;48 (1):85–108.
- [10] Ljungberg N, Wesslén B. Preparation and properties of plasticized poly(lactide) films. *Biomacromolecules* 2005;6:1789–96.
- [11] Jacobsen S, Fritz HG. Plasticizing poly(lactide)-the effect of different plasticizers on the mechanical properties. *PolymEngSci* 1999;39:1303–10.
- [12] Hu Y, Hu YS, Topolkaraev V, Hiltner A, Baer E. Crystallization and phase separation in blends of high stereoregular poly(lactide) with poly(ethylene glycol). *Polymer* 2003;44:5681–9.
- [13] Hu Y, Rogunova M, Topolkaraev V, Hiltner A, Baer E. Ageing of poly(lactide)/poly(ethylene glycol) blends. Part 1. Poly(lactide) with low stereoregularity. *Polymer* 2003;44:5701–10.
- [14] Kulinski Z, Piorkowska E, Gadzinowska K, Stasiak M. Plasticization of poly(lactide) with poly(propylene glycol). *Biomacromolecules* 2006;7:2128–35.
- [15] Focarete ML, Dobrzynski MS, Kowalczyk M. *Macromolecules* 2002;35:8472–7.
- [16] Blumm E, Owen AJ. *Polymer* 1995;36:4077–81.
- [17] Ljungberg N, Andersson T, Wesslén B. Film extrusion and film weldability of poly(lactide) plasticized with triacetate and tributyl citrate. *J ApplPolymSci* 2003;88:3239–47.
- [18] Ljungberg N, Wesslén B. Tributyl citrate oligomers as plasticizers for poly(lactide): thermo-mechanical film properties and aging. *Polymer* 2003;44:7679–88.
- [19] Hassouna F, Raquez JM, Addiego F, Dubois P, Tonniaro V, Ruch D. *EurPolym J* 2011;47:2134–44.
- [20] Labrecque LV, Kumar RA, Davé V, Gross RA, McCarthy SP. Citrate esters as plasticizers for poly(lactic acid). *J ApplPolymSci* 1997;66:1507–13.
- [21] Carlson D, Nie L, Narayan R, Dubois P. Maleation of poly(lactide) (PLA) by reactive extrusion. *J ApplPolymSci* 1999;72:477–85.
- [22] Addiego F, Dahoun A, G'Sell C, Hiver JM. *Polymer* 2006;47:4387–99.
- [23] Baker WE, Hu G-H, Scott CE. Reactive polymer blending. München: Hanser; 2001.
- [24] Ou K, Cakmak M. Influence of biaxial stretching mode on the crystalline texture in polylactic acid films. *Polymer* 2008;49: 5344–52.
- [25] Kokturk GS, erhatkulu TF, Cakmak M, Piskin E. Evolution of phase behavior and orientation in uniaxially deformed polylactic acid films. *ProgPolymSci* 2002;42:1619–28.
- [26] Pluta M, Paul MA, Alexandre M, Dubois P. Plasticized poly(lactide)/Clay nanocomposites. I. The role of filler content, its surface organo-modification on the physico-chemical properties. *J PolymSci Part B: PolymPhys*, 2006; 44: 299–311.



Peculiar reduction of graphene oxide into graphene after diffusion in exponentially growing polyelectrolyte multilayers

F. Hassouna^a, S. Kashyap^a, A. Laachachi^a, V. Ball^{a,*}, D. Chapron^b, V. Toniazzi^a, D. Ruch^a

^aAdvanced Materials and Structures, Centre de Recherche Public Henri Tudor, 66 rue de Luxembourg, L-4002 Esch-sur-Alzette, Luxembourg

^bLaboratoire Matériaux Optiques Photonique et Systèmes, Université Paul Verlaine, Metz. 2 Rue Edouard Belin, F-57070 Metz, France

ARTICLE INFO

Article history:

Received 26 December 2011

Accepted 19 March 2012

Available online 28 March 2012

Keywords:

Graphene oxide

Polyelectrolyte multilayer films

Electrical conductivity

Raman spectroscopy

ABSTRACT

In the present work, in situ reduction of graphene oxide (GO) into graphene was preformed, after diffusion in exponentially growing polyelectrolyte multilayers, using sodium citrate as the reducing agent. First, the graphene oxide was obtained by treating a commercial grade of Expanded Graphite (EG). Based on XRD and Raman spectroscopy results, a complete exfoliation of graphene nanopellets down to one layer was achieved during the oxidation process. Secondly, the diffusion of GO was carried out in an exponentially growing polyelectrolyte multilayer film made from poly(diallyldimethylammonium chloride) as the polycation and from poly(acrylic acid) as the polyanion. Electrical conductivity of the GO based films was measured during the reduction process as a function of time. The conductivity reached values of the order of $10^{-4} \text{ S cm}^{-1}$, whereas the pristine polyelectrolyte multilayer was highly insulating ($\sim 10^{-8} \text{ S cm}^{-1}$). The conductivity also reached a maximal value after about 24 h of reduction and decreased for longer reduction duration. Some tentative explanations for this peculiar finding will be given.

© 2012 Elsevier Inc. All rights reserved.

1. Introduction

Graphene is the “new star” in nanotechnology since its discovery in 2004 and even more since the attribution of the Nobel Prize in Physics to Geim and Novoselov in 2009. The success of this 2D material is due to its high specific surface area (a theoretical value of $2600 \text{ m}^2 \text{ g}^{-1}$), its mechanical properties, and electrical conductivity (24 S cm^{-1} has been obtained for a powder issued from reduced graphene oxide [1]).

Graphene finds applications in the design of supercapacitors [2], in hydrogen storage [3], in magnetoconductive layers [4], and in many kinds of sensors like pH [5] or glucose sensors [6]. But to extend the properties of this fascinating material to large scale applications, it needs to be produced in largely scalable manner. Unfortunately, this is not possible using the micromechanical cleavage technique or chemical vapor deposition which leads to the best quality of graphene sheets, namely those having the highest fraction of sp^2 hybridized carbon atoms. Hence, most often, graphene is oxidized to graphene oxide in solution using strong oxidants to obtain graphene oxide (GO) before its subsequent reduction to graphene sheets. Unfortunately, those sheets undergo association in solution due to strong van der Waals and π – π interactions. This makes the processing of the exfoliated graphene

difficult. One way to overcome this problem is to use suited capping agents establishing strong interactions with both the reduced graphene sheets (GSs) and the solvent.

Besides strong reducing agents as hydrazine, hydrogen sulfide and sodium borohydride, many recent papers describe the reduction of GO using soft organic molecules, like sodium citrate, ascorbic acid [7], or extracts from green tea [8] or even solvents like pyrrole (reaction time and temperature were of 12 h and 95°C , respectively) [9]. In this latter case, the oxidation product of pyrrole, most probably poly(pyrrole) was adsorbed on the surface of the GS to allow for their stabilization. In a similar approach, dopamine can be used as the reducing agent in basic conditions: dopamine is oxidized to “polydopamine,” whereas GO is reduced to GS which is capped with hydrophilic “polydopamine” [10].

The chemistry of GO as well as the emerging methods to produce monodisperse graphene dispersions has been recently reviewed [11,12].

Since graphene (G) becomes now available in large scale amounts, one of its major interests comes in its incorporation as a nanofiller in composite materials. A polystyrene-G composite reaches a percolation threshold for electrical conductivity at only 0.2% in mass fraction [13].

An interesting method to produce composite films with high control of the content of the inorganic filler as well as its distribution within the composite is the Layer-by-layer deposition (LBL) of charged polymers and oppositely charged inorganic fillers

* Corresponding author.

E-mail address: vincent.ball@tudor.lu (V. Ball).

[14]. Polyelectrolyte multilayered films (PEMs) made using the Layer-by-layer (LBL) deposition method [15] made from 10 layer pairs of poly(diallyldimethylammonium chloride) (PDADMAC) and from graphite oxide (GO) had a resistance of 32 M Ω between 2 mm separated parallel gold stripes. Upon reduction of GO in G in the presence of hydrogen as the reducing agent, the resistance dropped to 12 k Ω [16].

Many other attempts have been made to incorporate G [17] or even GO [18] in PEM films. A spectacular increase in the elastic modulus from 1.5 GPa for a pristine film up to 20 GPa, as measured in a bulging test, was obtained by incorporating a single layer of GO by means of Langmuir–Blodgett deposition (at a surface pressure of 0.5 mN m⁻¹) in between a lower (PAH–PSS)₉–PAH stratum and an upper symmetrical (PAH–PSS)₉–PAH film. The Langmuir–Blodgett deposition method offered the advantage to obtain nonaggregated graphene sheets, an optimal situation for the improvement of mechanical properties. Such a remarkable improvement in the mechanical properties for free standing membranes only 50 nm in thickness was reached with only 3–8% of the film's volume due to GO.

However, to our knowledge, the possibility to load PEM films with GO by single diffusion of the platelets in the films has not yet been investigated. The feasibility of this concept has been shown for the incorporation of zero-dimensional CdTe nanoparticles [19] and one-dimensional carbon nanotubes [20] in films made from PDADMAC and poly(acrylic acid). Herein, we wish to check whether this concept holds true for quasi 2D materials, namely GO. We also wish to provide some electrical conductivity to the insulating and highly swollen (PDADMAC–PAA)_n films by in situ reduction of the incorporated GO.

2. Experimental

2.1. Deposition of PEM films

PDADMAC (ref 409014 from Aldrich, MW between 1 and 2 $\times 10^5$ g mol⁻¹) was dissolved in MilliQ water ($\rho = 18.2$ M Ω cm, Millipore) at a concentration of 0.5%, whereas PAA was dissolved in water which pH was previously adjusted to 3 ± 0.1 with diluted hydrochloric acid. The PEM films were deposited on cleaned quartz slides (Thuét, Blodelsheim, France) by alternated dipping in the polycation (PDADMAC) solution, in water, in the polyanion solution (PAA), and in water. Such a dipping cycle leads to the deposition of one “layer pair”. The whole film is made from the deposition of n such “layer pairs”. At the end of the deposition, the film was dried in an oven at 80 °C overnight.

Each dipping and rinsing step lasted over 1 min as in a previous investigation [19].

2.2. Preparation of GO suspensions

In the present method, the graphene oxide is obtained by treating a commercial grade Expanded Graphite (EG) supplied by ECO-PHIT G [21].

The expanded graphite powder (20 g) is placed into cooled concentrated H₂SO₄ (460 mL) at 0 °C and stirred for about 30 min. KMnO₄ (60 g) is added gradually with stirring and cooling, so that the temperature of the mixture is not allowed to reach more than 20 °C. The magnetic stirring is then kept for 30 min. The reaction between H₂SO₄ and KMnO₄ leads to the formation of metal and sulfate ions which help in exfoliating the EG layers [11]. The mixture is then stirred at 35 °C for more than 30 min, and deionized water (920 mL) is gradually added. After 60 min of stirring, the reaction is terminated by the addition of a large amount of deionized water (2.8 L) and 30% H₂O₂ solution (50 mL), causing violent

effervescence and an increase in temperature up to 100 °C, after which the color of the suspension changes to bright yellow. The suspension is then washed with 1:10 HCl solution (5 L) in order to remove metal ions by filter paper and funnel. The paste collected from the filter paper is dried at 60 °C, until it becomes an agglomerate. This agglomerate is dispersed into deionized water in static state for 2–3 h and slightly stirred by glass bar. The suspension is washed with much deionized water several times until the pH reaches a value of 7. The paste collected is dispersed into water by ultrasonication for about 1 h. The obtained brown GO hydrosol is then subjected to centrifugation at 4000 rpm for 30 min in order to remove any unexfoliated GO.

Sulfuric acid (H₂SO₄) (95–98%), potassium permanganate (KMnO₄) (327 mesh, 97%), and hydrogen peroxide (H₂O₂) (30%, p.a $\geq 30\%$, RT) were all purchased from Sigma Aldrich and used without further purification. Fuming hydrochloric acid (HCl) (37%) was purchased from Merck.

2.3. In situ reduction of GO in the PEM films

PEM films are placed in 25 mL GO (0.1 mg/mL) for a period of incubation of 24 h. The time of incubation has been optimized using UV–visible spectrophotometry.

The loaded PEM films with GO are then immersed in 25 mL of sodium citrate (4.65×10^{-3} mol L⁻¹) solution for different reaction times starting from 3 h up to 72 h at 80 °C and under reflux.

2.4. Characterization methods

X-ray photoelectron spectroscopy measurements were carried out with a SPECS spectrometer (Hemispherical Energy Analyzer PHOIBOS 150). A focused monochromatic Al K α source ($h\nu = 1486.7$ eV) was used, operating at 200 W with an anode voltage of 12 kV. The full width at half maximum (FWHM) of the Si_{2p} line was of 0.75 eV under the recording conditions. The pressure in the analysis chamber was set at 5.10^{-9} mbar. The analyzed area was of 3 mm \times 1 mm, and all measurements were carried out with a 0° takeoff angle with respect to the normal direction of the surface. The pass energies were set to 80 eV and 20 eV for survey and higher resolution scans, respectively. The binding energy scale was calibrated from the carbon contamination using the C_{1s} peak at 284.6 eV. Core peaks were analyzed using a nonlinear Shirley-type background.

Atomic force microscopy was performed with a Pico SPM microscope in the tapping mode and in air. The scanning frequency of the cantilever was of 1 Hz and all images were acquired with a resolution of 512×512 pixels. The cantilever tips were in silicon, and the cantilevers had a spring constant of 10 mM m⁻¹ as indicated by the furnisher. The films were needle scratched before imaging in order to evaluate their thickness and surface roughness.

Conductivity measurements were performed in a 4 point configuration with an Ecopia HMS-3000 device applying a magnetic field of 0.54 T for the Hall effect measurements. The applied currents were of 5×10^{-9} A in all our experiments. This means that for a film thickness of about 500 nm, an electrode to electrode distance of about 1 cm and a conductivity of 10^{-4} S cm⁻¹, the maximal applied electric field is of the order of 1 V cm⁻¹.

Raman scattering experiments were performed at room temperature with a LabRam spectrometer (Horiba JobinYvon). All spectra were recorded in backscattered geometry using a diffraction grating with 1800 grooves mm⁻¹. A spectral resolution of 1 cm⁻¹ was achieved. Both incident and scattered beams were collected through an Olympus confocal microscope using a 100 \times objective lens (NA = 0.9). Rayleigh scattering was blocked with a holographic Notch filter. The laser excitation wavelength was 514 nm, and the

laser power was less than 2 mW to avoid sample damage. The samples were analyzed without any further preparation.

The structural modification of EG to GO was also investigated by Fourier transform infrared Spectroscopy (FTIR) in the transmission mode. The signal was recorded from 400 cm^{-1} to 4000 cm^{-1} with a Bruker Optics Tensor 27 spectrometer. This characterization was done on powdered GO flakes incorporated in KBr pellets.

UV–visible spectroscopy in the absorption mode was carried on a PerkinElmer Lambda 35 UV spectrophotometer to analyze the PEM films and the composite PEM–GO films. The spectrophotometer was fitted with one Deuterium lamp (190–400 nm) and one Tungsten lamp (400–1100 nm).

X-ray diffraction (XRD) experiments were performed with an INELFRANCE diffractometer. Samples were scanned in the reflection mode using the Cu $K\alpha 1$ radiation (wavelength: 1.5405 \AA).

3. Results and discussion

3.1. Preparation of graphene oxide

Graphene oxide obtained by treating a commercial grade Expanded Graphite (EG) was characterized using several techniques. In a qualitative manner, oxygen-containing functional groups are most apparent in the FTIR spectra of GO with respect to that of the EG precursor powders. The spectrum of EG displays only few skeletal vibrations from the graphitic domains (Fig. 1). In contrast, Fig. 1 shows the appearance of new absorption bands after oxidation of EG. The band at 1706 cm^{-1} corresponds to the stretching vibrations from carbonyl groups ($\text{C}=\text{O}$), and the band at 1225 cm^{-1} is attributed to the stretching vibration mode of the $\text{O}-\text{H}$ band of $\text{CO}-\text{H}$ [22].

XPS analysis performed on EG and GO allowed to confirm the observations made by FTIR, namely a strong oxidation. Initially, the $\text{C}1\text{s}$ spectrum of EG (Fig. 2) indicates only the skeletal vibrations from graphitic domains as sp^3 peak, and the aromatic domains as sp^2 peaks due the graphitic structure. However, the $\text{C}1\text{s}$ spectrum for GO (Fig. 2) indicates a considerable degree of oxidation with four spectral components that correspond to carbon atoms in various redox states: the presence of $\text{C}-\text{C}$ or $\text{C}-\text{H}$ bonds, the C atoms present in $\text{C}-\text{O}$ bonds, the carbonyl $\text{C}=\text{O}$, and the carboxylate carbon atoms ($\text{O}-\text{C}=\text{O}$) [23]. Although the $\text{C}1\text{s}$ XPS spectrum of EG (Fig. 2) also exhibits these same oxygen functionalities, their peak intensities are much smaller than those observed in GO.

Raman spectroscopy is strongly sensitive to the electronic structure of carbon structures and it has proven to be a crucial technique to characterize graphite and graphene like materials [11]. During the transition from graphite to graphene, there are a

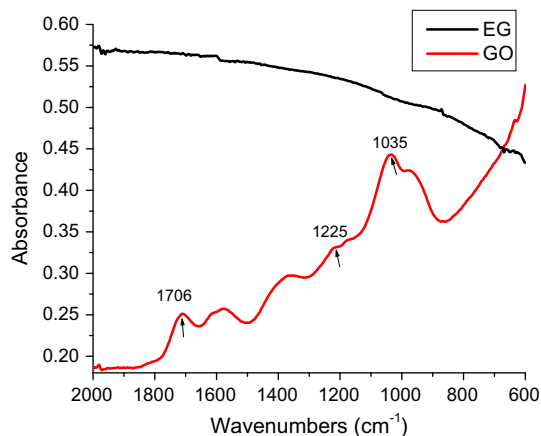


Fig. 1. Infrared spectra of EG and GO. The attribution of the main bands of GO is discussed in the text.

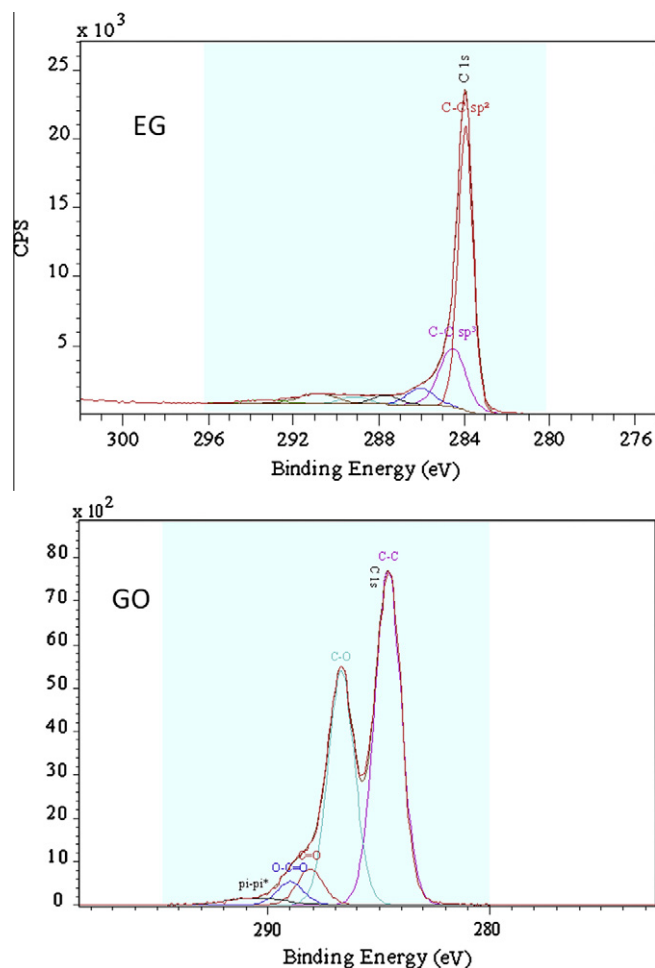


Fig. 2. $\text{C}1\text{s}$ core XPS spectra of EG and of GO.

large number of defects appearing in the 2D structures. The appearance of such defects and disorders can be observed by using Raman spectroscopy. Tuinstra and Koenig [24] had first pioneered the Raman spectra for nanocrystalline graphite, commonly known as graphene. They reported the so-called G and D peaks lying around 1580 cm^{-1} and 1380 cm^{-1} .

The G peak corresponds to the E_{2g} phonons located at the center of the first Brillouin zone. The D peak is due to the breathing mode of sp^2 rings and requires a defect for its activation [25]. Fig. 3 shows

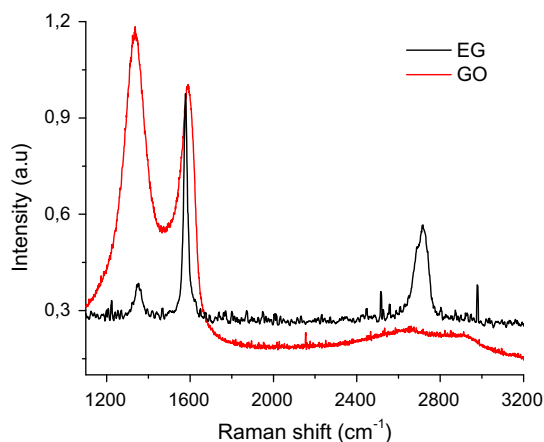


Fig. 3. Raman spectra of EG and of GO.

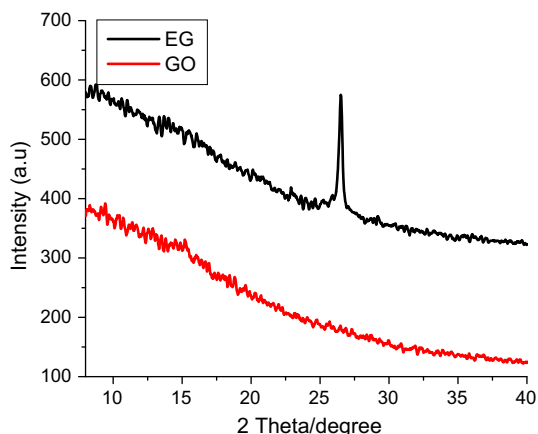


Fig. 4. X-ray diffractograms of EG and GO powders measured in the reflexion mode.

the Raman spectra for EG and GO normalized by considering that the stacking structure (G band) for both EG and GO remains the same. The Raman spectrum of GO shows that the G band is broadened and is shifted from 1577 to 1590 cm^{-1} . In addition, the D band at 1341 cm^{-1} becomes prominent, indicating the size reduction of the sp^2 domains possibly due to extensive oxidation. A weak smeared 2D band along with the D + G combination bands induced by disorder at around 2752 and 2939 cm^{-1} is also observed in the GO sample as a result of second order features, whereas EG has only a low intensity narrow peak at the G band position.

When compared with EG, observation of such distinct Raman peaks in the GO sample reflects that some defects arise along the transformation from EG to GO. Specifically, the intensity of the G and the D bands increases and the G band shifts to higher frequencies as already described in the literature [26].

X-ray diffraction patterns are used to further study the structural changes in EG after its oxidation process. GO is formed when the layers of EG/Graphite are exfoliated to such extents that the weak forces existing between them are destroyed completely. Hence, as a prerequisite for the synthesis of GO, it was required to destroy the crystalline nature of EG. Then, the successful conversion of EG to GO can be followed by X-ray diffraction. Fig. 4 shows powder XRD diffractograms of EG and GO. EG is characterized by a strong 002 peak centered at $2\theta = 26^\circ$ [27]. After its oxidation, the obtained GO powder displays a diffraction pattern where all the graphitic peaks are suppressed. The loss of the out-of-plane reflection in GO is attributed to the complete rupture of all Van Der Waals forces existing between the layers of the initially used EG. Indeed, the appearance of oxygen-containing functional groups attached on both sides of the graphene sheet (carboxylate, hydroxyl, and epoxide moieties) distorted the carbon networks. In contrast, several authors have proved the existence of a broad peak at around $2\theta = 10^\circ$ corresponding to an average interlayer spacing of $\sim 0.9\text{ nm}$, corresponding to a graphite oxide composed of around three layers [27]. Thus, it can be concluded from the XPS and XRD data that a complete exfoliation of graphene nanopellets down to one layer is achieved during the oxidation process. To our knowledge, this was unobserved so far in the literature. Such one layered GO sheets are well suited to interact with polyelectrolyte multilayers displaying anion exchange capacities as the (PDADMAC–PAA) $_n$ films [19].

3.2. In situ reduction of GO in polyelectrolyte multilayers

The GO suspension at 0.1 mg mL^{-1} was allowed to interact with PEM films made from the alternated deposition of PDADMAC and PAA. Such films are highly swollen and allow for the incorporation

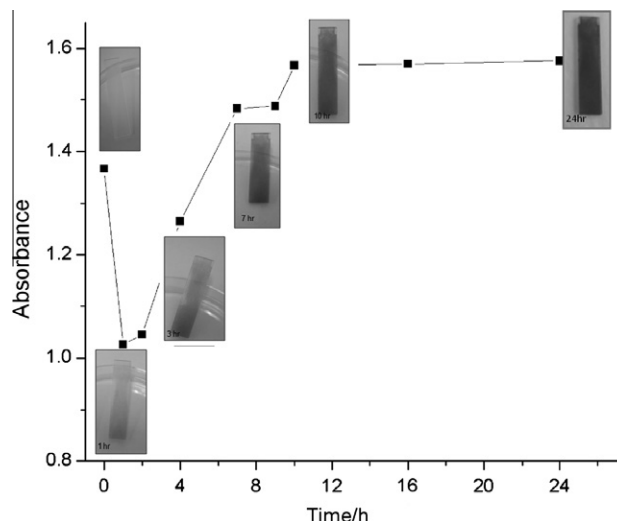


Fig. 5. Evolution of the absorbance (at $\lambda = 500\text{ nm}$) of a (PDADMAC–PAA) $_{15}$ film when put in contact with a solution containing 0.1 mg mL^{-1} of GO at pH 7.0 as a function of time. The pictures have been taken on a given quartz plate covered with a PEM film, put in contact with the GO solution for a time t and then dried in an oven at 60°C before taking each picture.

of either cadmium telluride nanoparticles capped with thioglycolic acid [19] or carbon nanotubes [20]. The loading of GO in the PEM is well confirmed by the UV–Vis spectra (Fig. 5) as well as by a single observation of the PEM coated glass slides (insets of Fig. 5). To optimize the film for maximum loading of GO, the UV–visible analysis is carried out after every hour. Note that the absorbance at $\lambda = 500\text{ nm}$ initially decreased when the PEM film was put in contact with a solution containing 0.1 mg mL^{-1} of GO, before increasing again in parallel with a marked change in color. The initial decrease in absorbance may be due a structural change in the film which was of milky appearance after its deposition and drying in an oven. This structural change will be confirmed later on by means of atomic force microscopy. The optimal time to reach complete filling of the (PDADMAC–PAA) $_{15}$ films followed by UV–vis spectroscopy was found to be of 24 h. The fact that the absorbance does not increase anymore after 24 h does not mean that the film is homogeneously filled with GO through its whole thickness. In a previous investigation, it was shown by means of laser confocal scanning microscopy (LCSM) that cadmium telluride nanoparticles fill (PDADMAC–PAA) $_{100}$ films in an homogeneous manner at the resolution of LCSM, namely about $1\text{ }\mu\text{m}$ [19]. Unfortunately, such an investigation is not possible with GO which does not display fluorescent emission and for films as thin as (PDADMAC–PAA) $_{15}$. In a future investigation, we will investigate the distribution of GO in similar but thicker PEM films by means of confocal Raman microscopy. This is important because the distribution of GO through the film thickness is important for the control of its electrical conductivity.

AFM topographies of the (PDADMAC–PAA) $_{15}$ films reveal the presence of doughnut structures in the film (Fig. 6a). Such doughnuts are not an exceptional case in polyelectrolyte multilayer films. However, their formation entirely depends on the experimental conditions of film growth [28]. The appearance of such nonuniform doughnuts (micron sized-rings) in our experiment could contribute to the diffusion of GO in the film.

The average thickness of the film made from 15 layer pairs is around 600 nm as measured by AFM before interaction with the GO containing solution (Fig. 6b). The morphology of the PEM films was profoundly modified during the incorporation of GO. Indeed, Fig. 6c shows an AFM topography obtained after 24 h of contact between the GO solution and the film; it shows a decrease in the

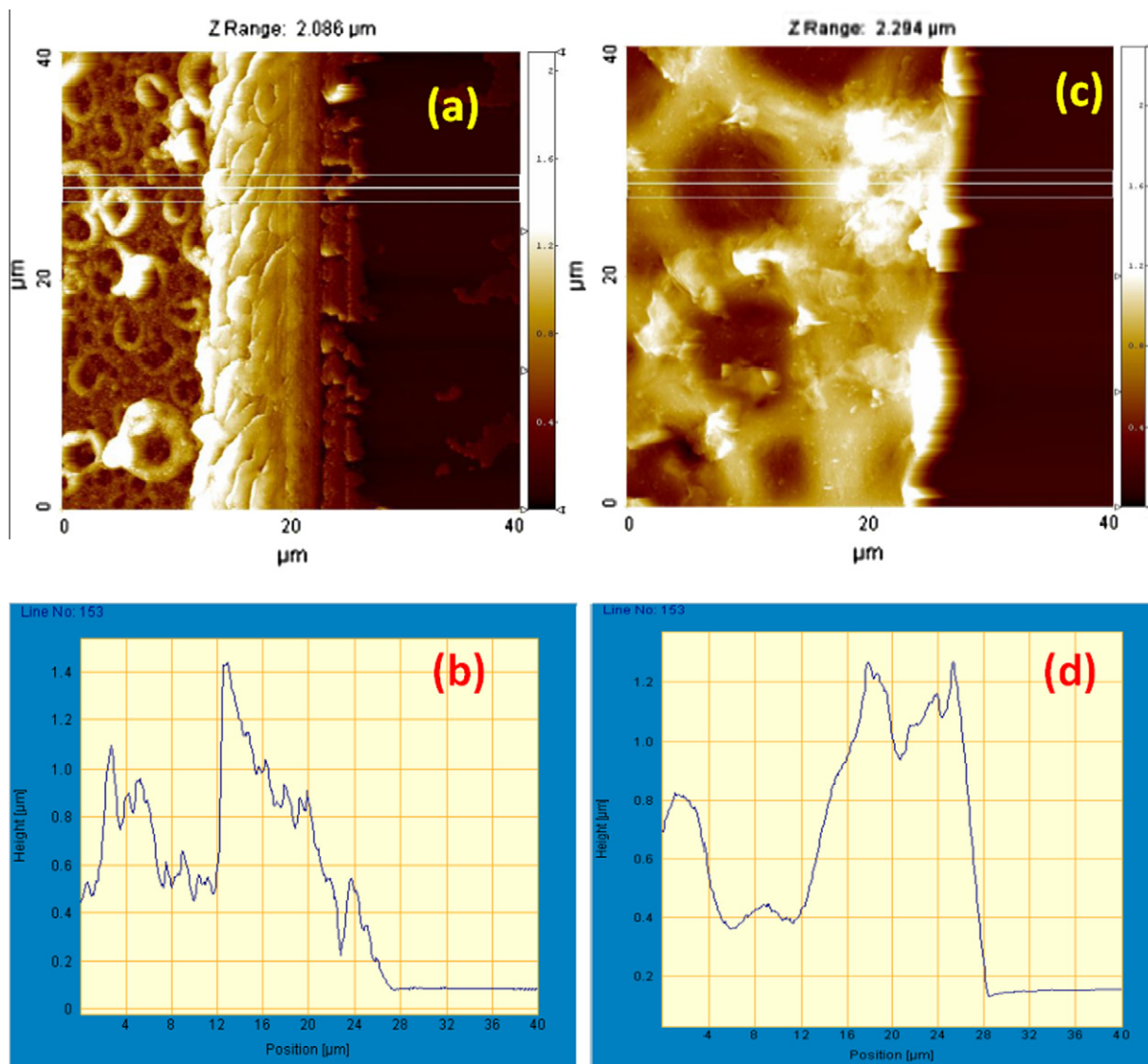


Fig. 6. AFM topographies of (PDADMAC-PAA)₁₅ films before (a) and after 24 h of exposure to a solution at 0.1 mg mL⁻¹ in GO (c). (b) and (d) correspond to the average of 30 line scans of the topographies represented in (a) and (c), respectively. The extreme of these lines are represented in white in (a) and (c). The films have been needle scratched before imaging. The scratched region corresponds to the right part of the images.

number of doughnut structures and an increase of their size. Hence, the interaction of GO with the PEM film induces a profound structural modification thereof. In addition, a partial film erosion and a smoothing effect are observed as the average film thickness decreases after exposure to the GO solution for 24 h. Indeed, the mean squared roughness decreases from 45 to 39 nm after incubation in the GO solution during 24 h (Fig. 6d).

In situ reduction of the incubated GO in PEM film has been carried out using sodium citrate (4.65×10^{-3} mol L⁻¹) at 80 °C. The electrical conductivity of PEM-GO films has been measured during the reduction process as a function of time (Fig. 7). The conductivity of the PEM films upon incorporation of GO increased from $(2.6 \pm 1) \times 10^{-8}$ S cm⁻¹ for the pristine film to $(5 \pm 1) \times 10^{-6}$ S cm⁻¹ after 24 h of contact with the GO suspension, the time duration required to ensure optimal filling of the film with GO (Fig. 5). The subsequent treatment of the PEM-GO film with sodium citrate (4.65×10^{-3} mol L⁻¹) at 80 °C allowed for an increase in conductivity up to a few 10^{-4} S cm⁻¹ after few hours of reduction (Fig. 7). When several successive measurements are performed on the same film, the conductivity values fluctuate within $\pm 25\%$ around the average value, but without a systematic

drift in the direction of a conductivity decrease or increase. This stability in the conductivity measurements suggests that the small applied electric fields (about 1 V over a distance of 1 cm, in the case where the films are 500 nm thick and display a conductivity of about 5×10^{-5} S cm⁻¹) are not sufficient to induce some structural changes and some migration of charged species inside of the PEM films.

It would have been interesting to relate the obtained conductivity values to the mass fraction of GO in the film as in other studies [13]. Unfortunately, analysis by thermogravimetry was not possible owing to the difficulty to obtain a mass of PEM film sufficient to reach a minimal value of 5 mg.

Surprisingly, higher contact times of the film with the sodium citrate solution, more than 24 h, induced a decrease in the film's conductivity. It has to be noted that the film did not dissolve upon this prolonged reduction time in the hot sodium citrate solution as shown by means of AFM (data not shown) and single visual inspection of the quartz substrate. Since citrate anions will be transformed into acetone dicarboxylic acid in the conditions employed in this investigation (80 °C under reflux for up to 72 h) and that this anionic molecule may change the structure of the PEM film, we

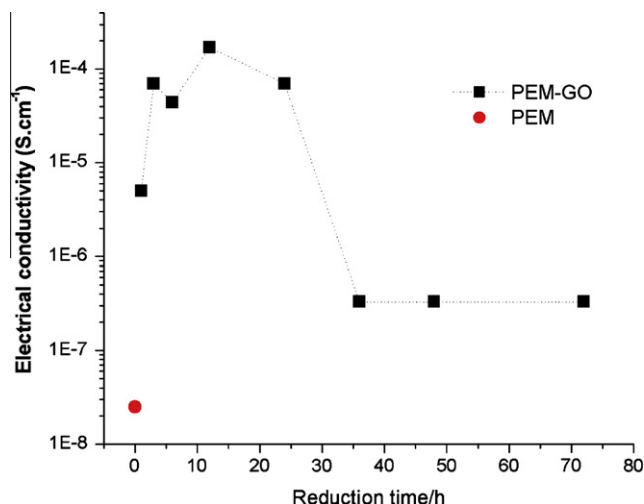


Fig. 7. Evolution of the conductivity with reduction time (in the presence of sodium citrate at $4.65 \times 10^{-3} \text{ mol L}^{-1}$ and at 80°C) for (PDADMAC-PAA)₁₅ films loaded with GO during 24 h and measured with the 4 point technique. The error bars for the conductivity on the pristine film is about $\pm 1.10^{-8} \text{ S cm}^{-1}$, it is of about $\pm 2.10^{-6} \text{ S cm}^{-1}$ in the case of the films put in the presence of GO and hot sodium citrate. Hence, the relative standard deviation is of the order of 20% for each data point. Each data point corresponds to an individual experiment and the quartz substrates used for each conductivity measurement were not incubated in the sodium citrate solution anymore.

cannot exclude that the changes in conductivity observed in Fig. 7 are simply due to the contact of the film with sodium citrate. Hence, we performed some control experiments in which the conductivity of the PEM films, not put in the presence of GO, was measured as a function of the interaction time with a sodium citrate solution (at $4.65 \times 10^{-3} \text{ mol L}^{-1}$ and 80°C). No measurable change in conductivity was found after rinse with water and drying of the film, for all reaction times in between 1 and 72 h. This shows that the conductivity changes observed in Fig. 7 are related to some transformations undergone by the incorporated GO.

To try to understand this nonmonotonous but reproducible change in the conductivity of the PEM-GO film as a function of the reduction time in the presence of sodium citrate solution, we performed some Raman spectroscopy measurements of the GO loaded films. This spectroscopic technique allows to follow the degree of reduction of GO by a measurement of the intensity ratio between the D and G bands (Fig. 8) [29]. It has to be noted that Raman spectroscopy was the only method allowing us to show in situ a partial and progressive reduction of GO in the PEM films. We could not use XPS spectroscopy for this aim because of the simultaneous presence of citrate anions and carboxylic groups from the used polyanions in the PEM film. Both species would contribute to the C1s core spectrum impeding to investigate the transformation of GO into graphene as shown for GO in solution (Fig. 2).

The I_D/I_G ratio increases during the first hours of GO reduction in the presence of sodium citrate solution which is indeed expected to occur during the reduction of GO. Each point in Fig. 8 corresponds to an individual PEM film loaded with GO during 24 h and put in contact with the hot sodium citrate solution during a time duration t . After 24 h, a sharp decrease of the I_D/I_G ratio is noticed.

A good correlation between the variation of the I_D/I_G ratio and the electrical conductivity as a function of reduction time is observed (Fig. 8). We now try to propose some mechanisms allowing to explain the simultaneous occurrence of a maximum in electrical conductivity and in the I_D/I_G ratio during the incubation of the (PDADMAC-PAA)₁₅ films loaded with GO in a hot sodium citrate solution. The increases of the electrical conductivity during the first 24 h of reduction can be explained by the reduction of GO in presence of sodium citrate as confirmed by Raman analysis. Sodium citrate as a weak reducing agent allows for a partial reduction of GO, leading to a significant improvement of the conductivity by two orders of magnitude (Fig. 7). However, as the reduction time increases, sodium citrate has tendency to act as a surfactant for rGO and therefore limits the achievement of large scale contacts between adjacent G domains. In this case, the conductivity would reach a constant value and should then decrease for increased reduction times. This explanation is straightforward in the case of the conductivity data but is not obvious in

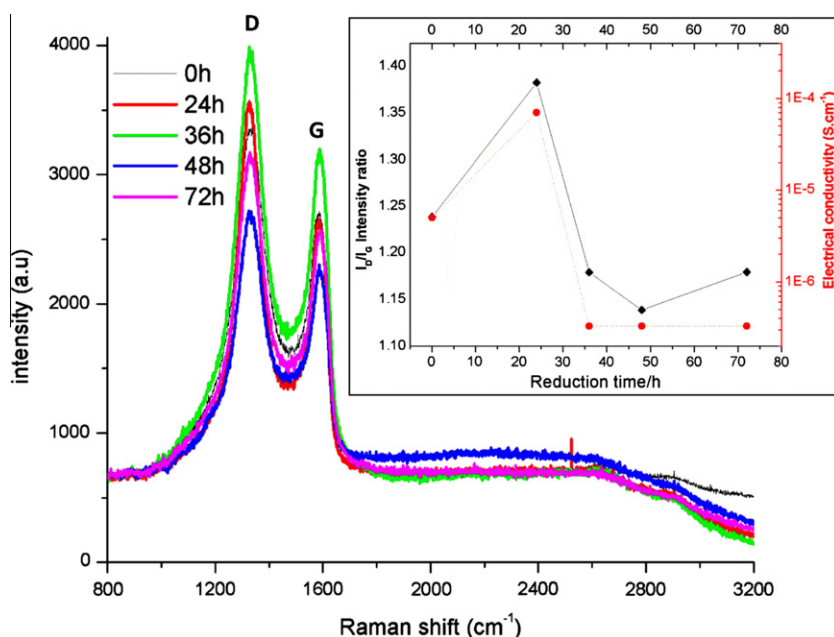


Fig. 8. Evolution of the Raman spectra of (PDADMAC-PAA)₁₅ films loaded with GO during 24 h and put in the presence of sodium citrate ($4.65 \times 10^{-3} \text{ mol L}^{-1}$) at 80°C as a function of time (24, 36, 48 and 72 h of reduction). The D and G bands are labeled, whereas the 2D bands ($2600\text{--}2800 \text{ cm}^{-1}$) are very weak. The inset represents the evolution of the I_D/I_G ratio (●, left hand scale), as calculated from the spectra, in parallel with the evolution of the film conductivity (●, right hand scale).

the case of the I_D/I_G ratio which also decreases after 24 h of reduction. In the later case, one would expect a *constant* value for longer reaction times. Indeed, the reduced GO cannot be oxidized again in the absence of strong oxidants, and hence, a decrease in the I_D/I_G ratio is hard to explain. The fact that citrate anions probably act as a surfactant for the reduced graphene implies some binding of citrate anions in the films or close to the graphene sheets and hence some increase in the absorption bands near 1600 cm^{-1} which are uniquely attributed to the graphene oxide. Indeed, in the framework of this explanation, the increase in the intensity of the vibration bands near 1600 cm^{-1} would be due to the binding of citrate anions and not to an intrinsic change in the GO material. We did some control experiments in which (PDADMAC–PAA)₁₅ films not loaded with GO were incubated with a hot sodium citrate solution: no signal due to sodium citrate was detected by Raman spectroscopy around 1600 cm^{-1} after 24 h of incubation in the sodium citrate solution ($4.65 \times 10^{-3}\text{ mol L}^{-1}$). This makes the previous assumption highly unlikely but is not an absolute proof, because the presence of GO in the film may modify its interaction with citrate anions.

In addition, AFM topographies show an important change in the film morphology as a function of reduction time with a total

disappearance of the doughnut structures (Fig. 9) confirming the impact of the presence of sodium citrate on the film morphology.

It might well be that such morphological changes are due to some aggregation of rGO (partially reduced graphene oxide) leading also to a clustering of rGO and a decrease in the number of electrically conductive pathways through the film (Scheme 1).

Such an explanation is reasonable because at longer reaction times with sodium citrate, the electrical conductivity of the pristine film is restored. The aggregation of isolated graphene sheets into graphitic structures should be associated with a decrease in the I_{2D}/I_G intensity ratio [30]. Hence, to confirm the assumption that graphene reassociates when GO is partially reduced in the PEM structure, we tried to calculate the I_{2D}/I_G intensity ratios from the measured Raman spectra (Fig. 8). Unfortunately, the signal to noise ratio for the 2D bands ($2600\text{--}2800\text{ cm}^{-1}$) was very low and did not allow an accurate quantification of the I_{2D}/I_G intensity ratios. Thus, our assumption of an aggregation process occurring during the partial reduction of GO and explaining the occurrence of a maximal film conductivity and a maximal value in the I_D/I_G ratio cannot be rigorously demonstrated in the framework of this investigation. We did some trials by investigating cross sections of PEM films loaded with GO and treated with sodium citrate, but these

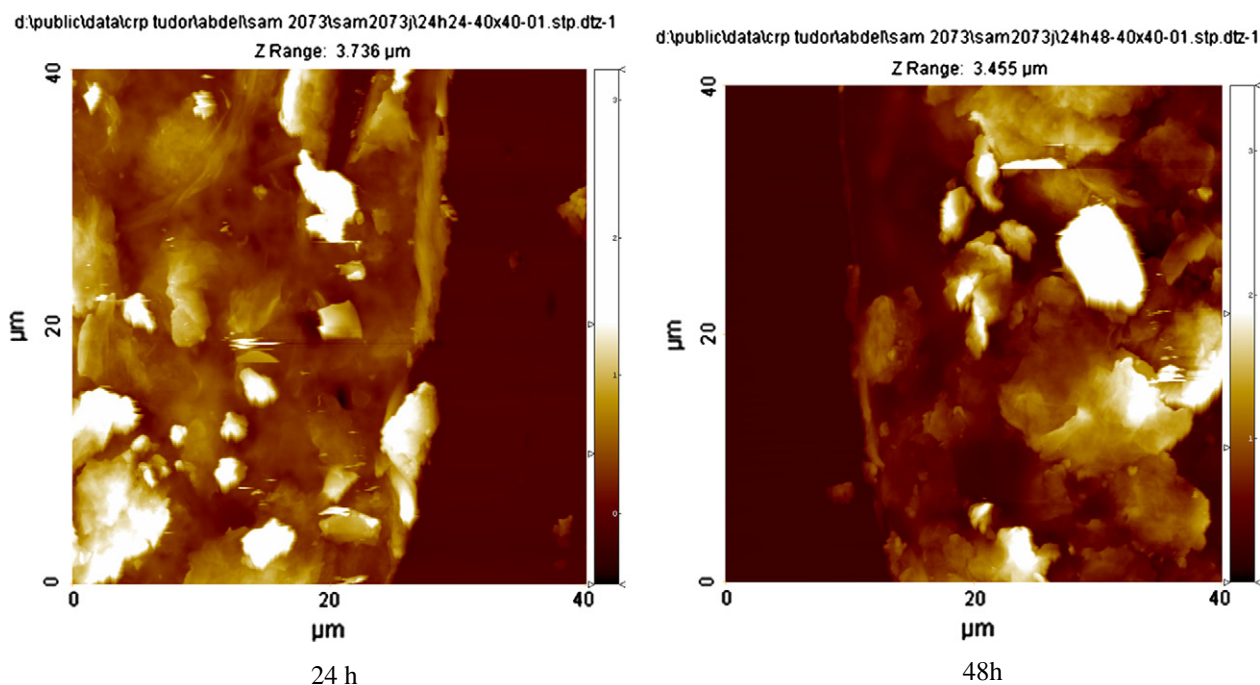
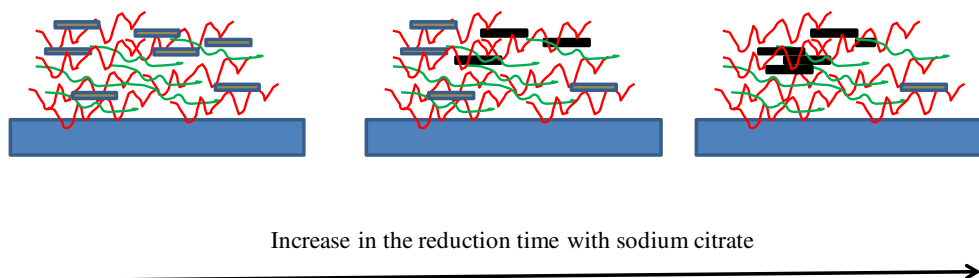


Fig. 9. AFM topographies of (PDADMAC–PAA)₁₅ films loaded with GO during 24 h and subsequently put in the presence of sodium citrate ($4.65 \times 10^{-3}\text{ mol L}^{-1}$) at $80\text{ }^{\circ}\text{C}$ during 24 h (left) and 48 h (right). Each film was needle scratched before imaging to emphasize the difference between the film and the quartz substrate. (For interpretation of the references to color in this figure legend, the reader is referred to the web version of this article.)



Scheme 1. Schematic representation of the influence of sodium citrate on the reduction of GO (brown platelets) into partially reduced GO (black platelets) and its subsequent reagglomeration in the PEM film made from PDADMAC (in red) and PAA (in green). (For interpretation of the references to color in this figure legend, the reader is referred to the web version of this article.)

images (not shown) were not conclusive enough to demonstrate a change in the agglomeration state of graphene like material in the film. The diffusion and agglomeration of graphene like material in highly swollen PEM films is however not unlikely. Indeed, it has been found that polyelectrolytes and proteins embedded in PEM films can have diffusion coefficients close to those measured in solution [31], meaning that these species are highly mobile in the PEM architecture.

Complementary, as an alternative to sodium citrate, hydrazine was used as a stronger reducing agent of GO incubated in PEM film. We expected that a much stronger reducing agent would allow for a complete and rapid reduction of GO in a time significantly shorter than needed for the obtained graphene to undergo diffusion and agglomeration in the film. Unfortunately, after only few minutes in contact with hydrazine, the film completely deteriorated and detached from the substrate and fell down into small parts.

The maximal electrical conductivity we reach after 24 h of reduction in the presence of sodium citrate, $1\text{--}2 \times 10^{-4} \text{ S cm}^{-1}$ is pretty low in comparison with the value obtained by Tang et al. for PEM film containing poly(sodium-4-styrene sulfonate) and reduced graphene oxide capped with cetyltrimethyl ammonium bromide [17]. They obtained conductivities of the order of 100 S cm^{-1} for PEM films made by alternated spin coating of PSS and the surfactant decorated graphene sheets. The high conductivity value they got is certainly related to the influence of the spin coating process in the alignment of graphene sheets parallel to the substrate. In our study, GO was allowed to diffuse in an already deposited and highly swollen (PDADMAC–PAA)₁₅ film. The probability for GO sheets to lie flat and parallel to the substrate is thus considerably reduced which has the consequence to decrease the probability to reach a percolation threshold upon reduction of GO into graphene.

Nevertheless, our approach allows providing some measurable electrical conductivity to insulating and highly swollen polyelectrolyte multilayer films in a three step method without the need to deposit surfactant capped graphene every layer pair.

Even if our investigation is of preliminary nature, because we lack of clear explanations for the occurrence of a decrease in conductivity for reduction times longer than 24 h as well as a knowledge of the mass fraction of GO in the films, we opened a new area of research: the interaction of graphene oxide with swollen polymer films and gels. We also showed the possibility to confer some measurable electrical conductivity to such insulators by in situ reduction processes of the embedded GO.

4. Conclusions

In the present article, we show the possibility to load polyelectrolyte multilayer films made from PDADMAC as the polycation and from PAA as the polyanion with GO that has been totally exfoliated in the form of single sheets. The loading kinetics of the film with the negatively charged GO is pretty slow as it takes 24 h to reach saturation of the film as inferred from UV–vis spectroscopy and is accompanied by a profound morphological change of the film. The GO embedded in the PEM films can be subsequently partially reduced in graphene, as found by means of Raman spectroscopy with a concomitant increase in the film conductivity by two

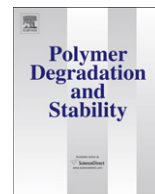
orders of magnitude from about $10^{-6} \text{ S cm}^{-1}$ for the film loaded with GO to about $10^{-4} \text{ S cm}^{-1}$ after 24 h of in situ reduction. Surprisingly, after 24 h of reduction, the film conductivity as well as the I_D/I_G ratio decreases again. Further investigations are required to investigate the distribution profile of GO and its reduced form in the direction perpendicular to the substrate and to know the average mass fraction of GO in the PEM films

Acknowledgments

We thank Dr. J. BOUR for performing and analyzing the XPS spectra. This project has been founded in the framework of the FEDER program “Compétitivité régionale et emploi” 2007–2013, CAPTOCHEM Project N° 2009-02-039-35.

References

- [1] S. Stankovich, D.A. Dikin, R.D. Piner, K.A. Kohlhaas, A. Kleinhammes, Y. Jia, Y. Wu, S.T. Nguyen, R.S. Ruoff, *Carbon* 45 (2007) 1558–1565.
- [2] J.J. Yoo, K. Balakrishnan, J. Huang, V. Meunier, B.G. Sumpter, A. Srivastava, M. Conway, A.L.M. Reddy, J. Yu, R. Vajtai, P.M. Ajayan, *Nano Lett.* 11 (2011) 1423–1427.
- [3] Z. Jin, W. Lu, K.J. O'Neill, P.A. Parilla, L.J. Simpson, C. Kittrell, J.M. Tour, *Chem. Mater.* 23 (2011) 923–925.
- [4] H. Paul, D. Mohanta, *Appl. Phys. A* 103 (2011) 396–399.
- [5] P.K. Ang, W. Chen, A.T. Schen Wee, K.P. Loh, *J. Am. Chem. Soc.* 130 (2008) 14392–14393.
- [6] C. Shan, H. Yang, J. Song, D. Han, A. Ivaska, L. Niu, *Anal. Chem.* 81 (2009) 2378–2382.
- [7] J. Gao, F. Liu, Y. Liu, N. Ma, Z. Wang, X. Zhang, *Chem. Mater.* 22 (2010) 2213–2218.
- [8] Y. Wang, Z. Shi, J. Yin, *ACS Appl. Mater. Interf.* 3 (2011) 1127.
- [9] C.A. Amarnath, C.E. Hong, N.H. Kim, B.-C. Ku, T. Kuila, J.H. Lee, *Carbon* 49 (2011) 3497–3502.
- [10] S.M. Kang, S. Park, D. Kim, S.Y. Park, R.S. Ruoff, H. Lee, *Adv. Funct. Mater.* 21 (2011) 108–112.
- [11] D.R. Dreyer, S. Park, C.W. Bielawski, R.S. Ruoff, *Chem. Soc. Rev.* 39 (2010) 228–240.
- [12] A. Green, A.M.C. Hersam, *J. Phys. Chem. Lett.* 1 (2010) 544–549.
- [13] S. Stankovich, D.A. Dikin, G.H.B. Dommett, K.M. Kohlhaas, E.J. Zimney, E.A. Stach, R.D. Piner, S.T. Nguyen, R.S. Ruoff, *Nat. Nanotechnol.* 4 (2009) 217–224.
- [14] E.R. Kleinfield, G.S. Ferguson, *Science* 265 (1994) 370–373.
- [15] G. Decher, *Science* 277 (1997) 1232–1237.
- [16] N.A. Kotov, I. Dékány, J.H. Fendler, *Adv. Mater.* 8 (1996) 637–640.
- [17] Q. Tang, Z. Tang, J. Wu, J. Lin, I. Oh, J. Mater. Chem. 21 (2011) 5378–5385.
- [18] D.D. Kulkarni, I. Choi, S.S. Singamaneni, V.V. Tsukruk, *ACS Nano* 8 (2010) 4667–4676.
- [19] S. Srivastava, V. Ball, P. Podsiadlo, J. Lee, P. Ho, N.A. Kotov, *J. Amer. Chem. Soc.* 130 (2008) 3748–3749.
- [20] S. Srivastava, P. Podsiadlo, K. Critchley, J. Zhu, M. Qin, B.S. Shim, N.A. Kotov, *Chem. Mater.* 21 (2009) 4397–4400.
- [21] T. Chen, B. Zeng, J.L. Liu, J.H. Dong, X.Q. Liu, Z. Wu, X.Z. Yang, Z.M. Li, *J. Phys.: Conf. Ser.* 188 (2009) 012051. doi:[10]1088/1742-6596/188/1/012051.
- [22] J. Shen, N. Li, N. Shi, Y. Hu, M. Ye, *J. Colloid Interf. Sci.* 348 (2010) 377–383.
- [23] D. Briggs, G. Beamson, *High resolution XPS of Organic Polymers: The Scienta ESCA 3000 database*, John Wiley and Sons, New York, 1992.
- [24] F. Tuinstra, J.L. Koenig, *J. Chem. Phys.* 53 (1970) 1126–1130.
- [25] S. Stankovich, D.A. Dikin, R.D. Piner, K.A. Kohlhaas, A. Kleinhammes, Y. Jia, Y. Wu, S.T. Nguyen, R.S. Ruoff, *Carbon* 45 (2007) 1558–1565.
- [26] R.B. Best, G. Hummer, *J. Am. Chem. Soc.* 130 (2008) 3748–3749.
- [27] G. Srinivas, Y. Zhu, R. Piner, N. Skipper, M. Ellerby, R. Ruoff, *Carbon* 48 (2010) 630–635.
- [28] H. Flores, J.L. Menchaca, F. Tristan, C. Gergely, E. Pérez, F.J.G. Cuisinier, *Macromolecules* 38 (2005) 521–526.
- [29] S. Stankovich, D.A. Dikin, R.D. Piner, K.A. Kohlhaas, A. Kleinhammes, Y. Jia, Y. Wu, S.T. Nguyen, R.S. Ruoff, *Carbon* 45 (2007) 1558–1565.
- [30] A. Das, B. Chakraborty, A.K. Sood, *Bull. Mater. Soc.* 31 (2008) 579–584.
- [31] L. Jourdainne, S. Lécuyer, Y. Arntz, C. Picart, P. Schaaf, B. Senger, J.-C. Voegel, P. Lavalley, T. Charitat, *Langmuir* 24 (2008) 7842–7847.



Correlation between (nano)-mechanical and chemical changes occurring during photo-oxidation of filled vulcanised styrene butadiene rubber (SBR)

Grégory Mertz^{a,b}, Fatima Hassouna^{a,*}, Philippe Leclère^b, Abdesselam Dahoun^c, Valérie Toniazzi^a, David Ruch^a

^a Department of Advanced Materials and Structures, CRP Henri Tudor, 66, rue de Luxembourg, L-4002 Esch-sur-Alzette, Luxembourg

^b Université de Mons, Chimie des Matériaux nouveaux, 20 Place du Parc, B-7000 Mons, Belgium

^c Institut Jean Lamour, UMR CNRS 7198, Ecole des Mines de Nancy, Parc de Saurupt, F-54042 Nancy cedex, France

ARTICLE INFO

Article history:

Received 24 April 2012

Received in revised form

10 August 2012

Accepted 13 August 2012

Available online 23 August 2012

Keywords:

Styrene butadiene rubber

Vulcanisation

TiO₂

Photo-oxidation

Depth profiling

Mechanical properties

ABSTRACT

Photo-oxidation at $\lambda > 290$ nm was performed on vulcanised styrene butadiene rubber (SBR) designed for flooring applications. The effect of the presence of coated titanium dioxide (TiO₂), used as a pigment, was evaluated. The chemical and nano-mechanical changes occurring at the surface during irradiation were studied by micro-FTIR spectroscopy and atomic force microscopy (AFM). Both techniques were used to obtain the oxidation profiles in the depth of the composites (in the absence and presence of TiO₂) to characterise the oxidative layer formation. The nano-mechanical and chemical profiles were superimposed for both composites (SBR and SBR/TiO₂) suggesting a correlation between both properties. Indeed, the increase of the DMT modulus determined by AFM reflects the crosslinking reactions which occur simultaneously with the formation of oxidised photo-products.

Moreover, during irradiation, the mechanical properties were followed at low and high degree of deformation by means of dynamic mechanical analysis (DMA) and tensile test until break, respectively. We demonstrate that the physico-chemical properties of the oxidised layer which represents 20 μm of the 600 μm of the material can explain the loss of mechanical properties for both composites based on vulcanised SBR and SBR/TiO₂ during irradiation at $\lambda > 290$ nm. We also demonstrate a different mechanical behaviour in presence of TiO₂ compared to neat SBR that could be due to a competition between formation of photo-products and the filler-rubber debonding during photo-oxidation.

© 2012 Elsevier Ltd. All rights reserved.

1. Introduction

During their outdoor exposure, all polymeric materials and especially elastomeric materials containing diene units are subjected to different environmental factors [1–4]. It has been demonstrated that oxygen and UV radiation are among the most important factors degrading polymeric materials by a chemical modification at the molecular scale due to their high sensibility towards oxidation known as photo-oxidation mechanism [5–7]. The formation of oxidised groups involves chain scissions and the formation of new covalent bonds between the chains known as crosslinking, resulting in the deterioration of the engineering properties of the polymeric materials [8]. The competition between these two opposite phenomenon depends on several factors including the conditions of ageing and the chemical structure of the

polymer [9]. To follow the changes occurring during the photo-oxidation, several characterisation methods are used to investigate the chemical, thermal, mechanical and rheological behaviour of the polymeric material. However, in most of the cases, the degradation produced by the oxidative ageing is heterogeneous due to the oxygen diffusion effect, and/or the attenuation of the UV light passing through the polymer [10]. In this case, a fine analysis of the photo-oxidised systems becomes more difficult. Consequently, analysis at the microscopic level is required [11]. The degradation profiles produced by oxidation can be investigated by depth-profiling analysis using infrared spectroscopy (micro-FTIR, photo acoustic and step scan) [12] and recently by AFM nano-indentations [11]. Celina et al. showed during thermo-ageing of nitrile rubber a heterogeneous reaction linked to oxygen diffusion and to UV–visible light penetration through the material leading to the formation of a so-called oxidative layer [10]. This oxidative layer is characterised by different physico-chemical properties than in the core of the material. Celina et al. devoted a part of their work to characterise the oxidative layer during thermo-ageing of nitrile

* Corresponding author. Tel.: +352 42 59 91 594; fax: +352 42 59 91 555.

E-mail address: fatima.hassouna@tudor.lu (F. Hassouna).

rubber by means of IR spectroscopy and modulus profiling in order to correlate how the increase of modulus is linked to chemical changes.

The recent use of AFM combined to micro-FTIR to follow the changes of surface properties after ageing or UV curing has shown that these two techniques are complementary [11]. The comparison of the chemical analysis (micro-FTIR) with the nano-mechanical analysis (AFM nano-indentations) provides new information about the ageing behaviour. Mailhot et al. used a method of depth profiling by AFM nano-indentations for the characterization of the heterogeneity of the nano-mechanical properties of photo-oxidized tetramethyl bisphenol-A polycarbonate (TMPC) [11]. Moreover, the comparison of the chemical analysis (micro-FTIR) with the mechanical measurements (AFM nano-indentation) provided new information about the ageing behaviour.

The aim of the present paper is to characterize the chemical changes occurring at the molecular level by micro-FTIR profiling and the nano and macro-mechanical behaviour during photo-oxidation of vulcanised SBR. A new generation of AFM is used to obtain quantitative nano-mechanical properties in terms of elastic modulus or stiffness in the depth of the materials [13]. Styrene butadiene rubber (SBR) appeared to be a good candidate for the study since the mechanisms of photo-ageing of diene rubber has been widely described in the literature [2–4]. During irradiation, there is a formation of oxidized photo-products hydroperoxides, α , β -unsaturated species and finally saturated carboxylic acid groups as well as the generation of crosslinked network. Afterwards, the mechanical response of the material during irradiation was measured using DMA technique and tensile tests. The results of the mechanical properties obtained were compared with micro-FTIR and AFM analysis and interpreted in the light of the chemical mechanism of photo-oxidation. The impact of the presence of the filler (coated rutile TiO_2 widely used as colouring agent in the polymer) on the photo-ageing mechanism of vulcanised SBR was also investigated. This kind of studies has not been previously attempted for these materials in vulcanised state probably due to their complexity (presence of a too many additives).

2. Experimental

2.1. Materials

Styrene butadiene rubber (SBR) was kindly provided by Materia Nova (Belgium) with a content of 23% w/w of styrene. The titanium dioxide (TiO_2) used was a coated rutile form with a median particle size between 1 and 3 μm provided by Mondo S.A. Luxembourg. The coating is constituted by a mixture of alumina and silica submitted to an organic treatment. The inorganic coating forms a physical barrier (screen effect) and the organic layers provide dispersibility in polymer matrix.

The vulcanisation of SBR rubber was performed as follow: 100 phr (per hundred part of rubber) of SBR, 1.4 phr sulphur, 2 phr 1,3-Diphénylguanidine (DPG), 3 phr ZnO , 2 stearic acid, 1.7 phr N-cyclohexylbenzthiazylsulphenamide (CBS), 0 and 5 phr of TiO_2 were mixed by means of Brabender® at 40 °C during 12 min. Afterwards, a compression moulding step at 170 °C and 50 bars is performed to obtain a sheet of approximately 600 μm thick.

2.2. Irradiation

SBR samples were exposed to UV–visible radiation by means of a Suntest device at 35 °C in presence of oxygen. Only the upper side of the sample is exposed. This ageing device allows an accelerated ageing in artificial conditions relevant to natural ageing. It is

equipped with a xenon lamp for irradiation at wavelengths longer than 290 nm. A black panel controls the irradiance at 400 W/m^2 .

2.3. Measurements

2.3.1. ATR-IR analysis

The spectra were recorded using a BRUKER Tensor 27 Fourier transform infrared (FTIR) coupled with an ATR diamond crystal. The spectra were obtained from 32 scans at a resolution of 4 cm^{-1} between 4000 and 600 cm^{-1} .

2.3.2. Depth profiling

Before profiling, the oxidized samples were microtomed in the irradiation section (cross section) by a microtome Leica EM UC6 at –60 °C. The slices obtained (approximately 30 μm thick) were then analysed by micro-FTIR (chemical profiling) in ATR mode and by AFM (nano-mechanical profiling).

2.3.2.1. Chemical profiles. Chemical profile experiments were performed on a Nicolet iN10 MX Infrared Imaging Microscope (micro-ATR). A slice of the material was deposited on Germanium crystal. The spectra were monitored with successive shifts of 6.25 μm through a window of 5 μm width, during 2.6 s and with a resolution of 4 cm^{-1} .

2.3.2.2. Nano-mechanical profiles. Nano-mechanical profiles were performed by means of a new generation of Bruker AFM, PeakForce QNM on the cross section of the sample at the ambient conditions. Peak force tapping was done with Si tips on SiN cantilevers (scana-syst-air). This new device allows to obtain a modulus mapping using a DMT model [13]. A scan of 50 \times 50 μm was performed on the cross section.

2.3.3. Mechanical properties

2.3.3.1. Dynamic mechanical analysis. Dynamic mechanical analysis (DMA) were carried out on vulcanised rubber during irradiation, using DMA 242C (Netzsch) operating in tension mode from –120 to 0 °C with a dynamic temperature sweep at 2 °C min^{-1} . Measurements were performed using tensile mode at a frequency of 1 Hz.

2.3.3.2. Elongation at break. Elongation at break values were measured on MTS 4/ML apparatus at a speed of 100 mm min^{-1} , while the initial gauge length of the sample was 25 mm. The size of the sample is represented in Fig. 1. For all mechanical measurements, at least four specimens were tested.

2.3.4. Scanning electron microscopy

SEM analyses were carried out on a QUANTA 200 FEG from FEI equipped with a spectrometer X GENESIS XM 4i EDS supplied by EDAX. This microscope is a Variable Pressure SEM (VP-SEM) that enables to observe insulating samples directly without additional

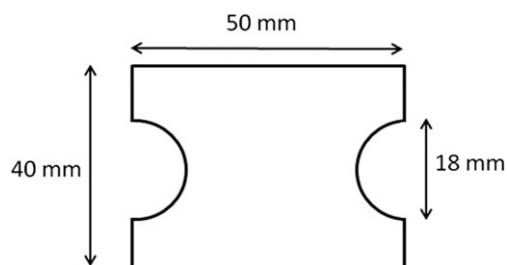


Fig. 1. Representation of the tensile specimen.

coating. Analyses were performed with a chamber pressure of 150 Pa and a working distance of 9 mm.

3. Results

SBR films were exposed to wavelengths longer than 290 nm in the presence of air. The chemical changes occurring during the photo-ageing are followed by ATR-IR to identify the nature of the photo-products and by depth profiling using micro-FTIR to characterise the degradation profile produced by oxidation. Depth profiling using AFM was also performed to determine the nano-mechanical changes of the surface properties. Afterwards, the macro-mechanical response of the material during irradiation was measured using DMA technique and tensile tests.

3.1. ATR-IR analysis

Irradiation of vulcanized SBR films leads to noticeable changes of chemical functions followed by ATR-IR measurements (Fig. 2). In fact, changes occur in the hydroxyl ($3000\text{--}3400\text{ cm}^{-1}$) and carbonyl ($1600\text{--}1800\text{ cm}^{-1}$) domains and in the complex region of C–O stretching vibrations ($1000\text{--}1500\text{ cm}^{-1}$). The main absorption bands formed during irradiation were attributed to hydroxyl and hydroperoxide groups at 3400 cm^{-1} and to carbonyl functions at 1709 cm^{-1} either in presence or in absence of TiO_2 . The consumption of double bonds correlated to the formation of crosslinked network was also evidenced at 964 , 910 and 722 cm^{-1} . The same photoproducts were observed on unvulcanized SBR rubbers [2,14]. It seems that the same photo-products are generated during photo-oxidation of vulcanized and unvulcanized SBR rubbers is similar. The consumption of double bonds due to the formation of crosslinked network disturbs the baseline and unfortunately does not allow to draw the kinetic of the photo-products formation.

The quantitative analysis of the formation of photo-products is not achievable by ATR-IR technique. Moreover, the results obtained by ATR-IR provide chemical information at the extreme surface of the material (first micrometres). Therefore, the competition between chain scission and crosslinking occurring in vulcanized SBR during the photo-ageing becomes difficult to estimate. Moreover, it is well established that oxygen diffusion and UV light absorption through the material generates an influential oxidative

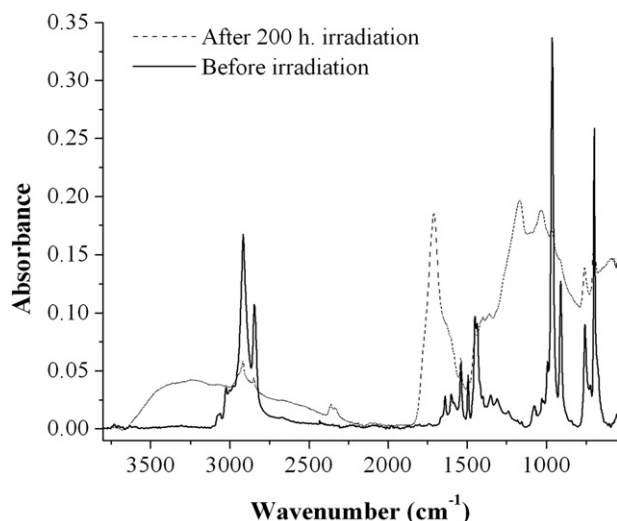


Fig. 2. IR spectra of vulcanized SBR before and after 250 h of irradiation.

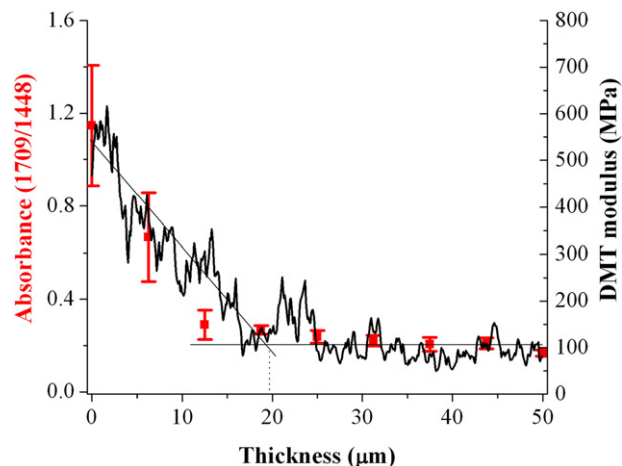


Fig. 3. Change of carbonyl profile (■) and DMT modulus (—) as a function of the thickness for vulcanized SBR after 250 h of irradiation.

layer [10]. In order to characterise the changes that can occur inside such complex materials as vulcanized rubbers, we performed depth profiling analysis using micro-FTIR and AFM in the cross section of the materials after 250 h of irradiation to reach the chemical changes and the nano-mechanical properties occurring during the photo-ageing.

3.2. Micro-FTIR and AFM profiling

Figs. 3 and 4 show the photo-oxidation profiles measured by micro-FTIR and AFM of vulcanized SBR and SBR/ TiO_2 , respectively, irradiated during 250 h. The concentration of the photo-oxidised products at 1709 cm^{-1} corresponding to the carbonyl functions is followed by micro-FTIR spectroscopy. We followed this band as an indication of the degree of oxidation [15]. One can recall that carbonyl groups are usually used as probe for chain scission. However, since both crosslinking and scissions occur at the same place inside the polymer matrix and that there are closely interconnected together, we believe that the concentration of the photo-oxidised products corresponding to the carbonyl functions can be followed as an indication of the degree of oxidation and

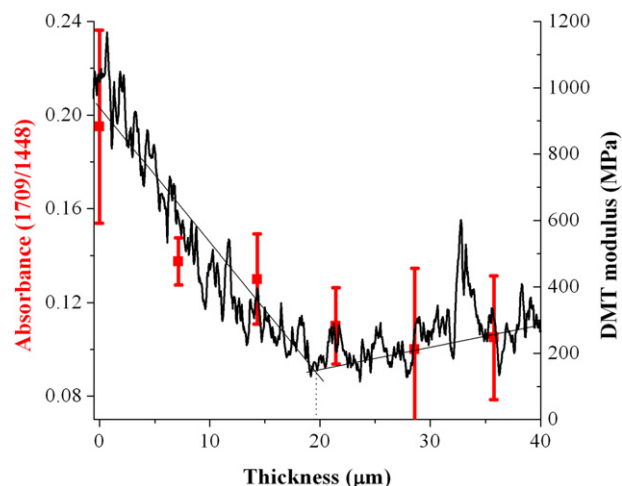


Fig. 4. Change of carbonyl profile (■) and DMT modulus (—) in function of the thickness for SBR/ TiO_2 after 250 h of irradiation.

consequently can bring a good indication about the stiffness of the material after ageing.

As shown in Fig. 3, the photoproducts are situated only in the first 20 μm of the film and their concentration decreases from the surface to the bulk. Correspondingly, in the same first 20 μm , we observed by AFM a decrease of the DMT modulus referring to the stiffness of the SBR film from the surface to the bulk [16]. Beyond 20 μm the DMT modulus of aged SBR becomes invariant and it corresponds to the modulus of the non-aged SBR. The comparison of micro-FTIR and AFM profiles of vulcanised SBR highlights a concordance of the results. The absorbance and the stiffness evolve in the same way. The stiffness increases from the bulk to the surface reflecting the crosslinking reactions which occur simultaneously with the formation of oxidised photo-products.

Fig. 4 indicates that AFM and micro-FTIR profiles of vulcanised SBR/TiO₂ are superimposable. As in vulcanised SBR, the depth of oxidation is limited to the first 20 μm . In this case, the presence of TiO₂ filler does not seem to affect the formation and the nature of the oxidative layer as it does not have any influence in the photo-products formation during photo-oxidation. Nevertheless, a small difference appears concerning the value of DMT modulus of both samples. In fact, for example, at a distance of 40 μm from the surface corresponding to non-aged part of SBR films, the values of DMT modulus are 100 and 200 MPa for SBR and SBR/TiO₂, respectively. The higher modulus value obtained for SBR/TiO₂ compared to SBR can be explained by the fact that the profile is obtained by averaging the values of the modulus of the rubber and the filler. As the modulus of the filler is very high with an order of magnitude of GPa, the resulting values of the compositae is about 200 MPa. To compare both the nano-mechanical behaviours of both films SBR and SBR/TiO₂, we introduced the notion of *variation* corresponding to the modulus difference between bulk and the surface, defined by:

$$\text{Variation}(\%) = \frac{V_f - V_i}{V_i} \times 100$$

with: V_i : DMT modulus value in the bulk corresponding to the non-aged value, V_f : DMT modulus value at the extreme surface

According to the Table 1, the increase of DMT modulus for both samples was approximately the same (about 500%). The increase of the modulus corresponding to the stiffness of the material can be correlated with the density of the crosslinked network generated during the photo-ageing. We suppose that in both cases, the crosslinking density is the same. The difference in DMT modulus values obtained for SBR and SBR/TiO₂ at the extreme surface after ageing, 600 and 1100 MPa, respectively, could be attributed to the presence of TiO₂ trapped inside the network resulting in a higher modulus values (Fig. 5).

To summarize, the shape of AFM profiles of SBR and SBR/TiO₂ indicates that the photo-ageing leads to the increase of the stiffness of the materials, which is attributed to the predominance of crosslinks. The observed heterogeneous oxidation can be explained by the decrease of the permeability to oxygen of SBR films during photo-oxidation due to the occurrence of crosslinking of polymer chains in the first layers. The comparison between AFM and micro-

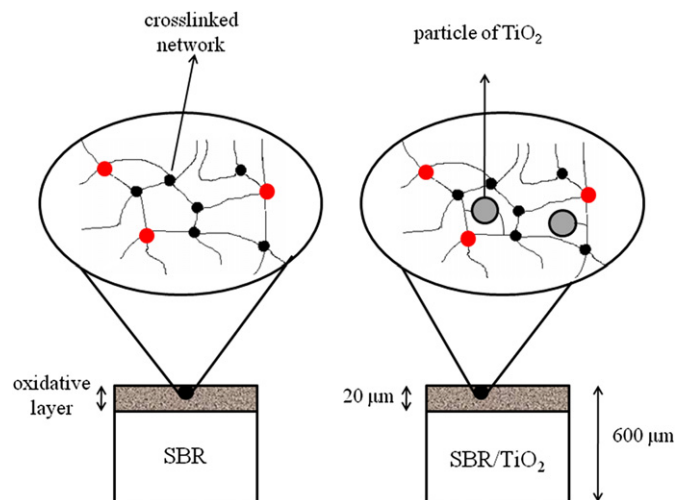


Fig. 5. Representation of the crosslinked network in oxidative layer for SBR and SBR/TiO₂, the red dots represent sulphur network due to vulcanisation step. (For interpretation of the references to colour in this figure legend, the reader is referred to the web version of this article.)

FTIR profiles highlights a nice correlation between chemical and nano-mechanical properties during irradiation at $\lambda > 290$ nm of vulcanized composites based SBR.

3.3. Mechanical properties

After having determined and highlighted a change in the chemical structure and in the nano-mechanical properties of vulcanised SBR during the photo-ageing and the effect of the presence of TiO₂ on the mechanisms of photo-oxidation of the polymer, we examined the influence of photo-ageing on the macro-mechanical properties of these materials at two levels of deformation. In fact, the mechanical properties of materials of vulcanised SBR and SBR/TiO₂ have been studied by DMA for small deformations and by tensile tests for higher deformations.

3.3.1. At small deformation

It is well known that the change of damping properties of materials during thermo-ageing is due to the changes in macromolecular chains conformations. For example, during thermo-ageing of rubber, the formation of three dimensional network by means of crosslinking leads to a decrease of the chain mobility and a decrease of the loss factor maximum ($\tan \delta_{\max}$) [17–19]. Moreover, this relation is predictable during thermo-ageing as in this case, the macromolecular changes occur in the whole material. However during photo-ageing, only a few micrometres at the surface of the exposed material are affected [7,12]. Thus, the change of $\tan \delta_{\max}$ is not so trivial than in the case of thermo-ageing. For instance, Delor et al. showed a weak change of $\tan \delta_{\max}$ during photo-oxidation at 60 °C in SEPAP ($\lambda > 300$ nm) of vulcanized EPDM compared to thermo-ageing wherein a decrease of the intensity of the main transition peak was higher [20]. In this case, changes in $\tan \delta_{\max}$ values would be a consequence of the presence of oxidative layer and not a property of the photo-aged material. During the present study, we tried to determine how this oxidative layer can impact the damping properties of the material.

Dynamic mechanical analysis was performed on both vulcanised SBR and SBR/TiO₂ films during photo-ageing. Fig. 6 shows the change of E' and the ratio E''/E' defined as $\tan \delta$ of both materials before and after 250 h of irradiation. A very weak increase of the storage modulus is observed for both SBR and SBR/TiO₂. The curves

Table 1
Properties of oxidative layer for SBR and SBR/TiO₂ obtained by AFM.

	DMT modulus at the extreme surface			Thickness (μm)
	Before ageing	After 250 h of irradiation (value at extreme surface)	Variation (%)	
SBR	100	600	500%	20 \pm 5
SBR/TiO ₂	200	1100	450%	20 \pm 5

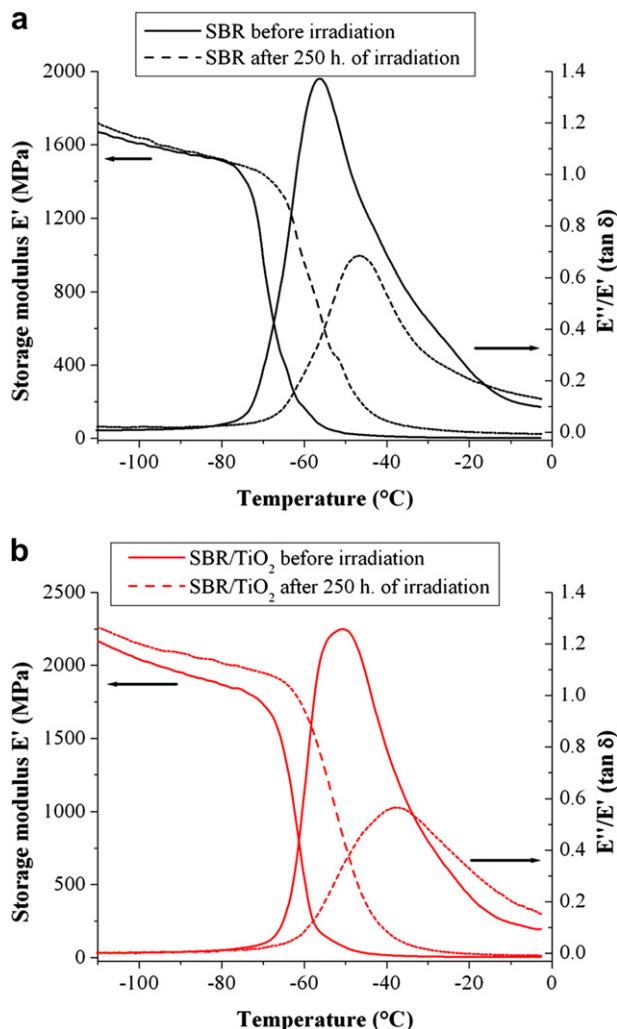


Fig. 6. Storage modulus (E') and $\tan \delta$ before and after irradiation as a function of irradiation time for (a) SBR and (b) SBR/TiO₂.

corresponding to the ratio E''/E' are shifted to higher temperatures by approximately 10 °C after ageing. Moreover, a drop of a factor 2 of $\tan \delta_{\max}$ is noticed. In this case, DMA suggests variations in the change of visco-elastic properties during photo-ageing of SBR

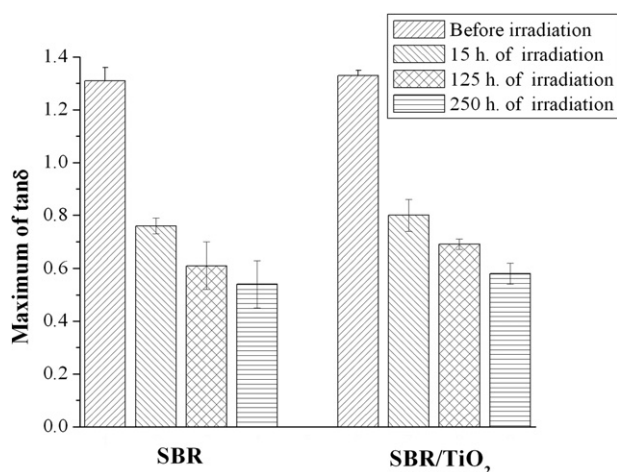


Fig. 7. Change of $\tan \delta_{\max}$ during irradiation for SBR and SBR/TiO₂.

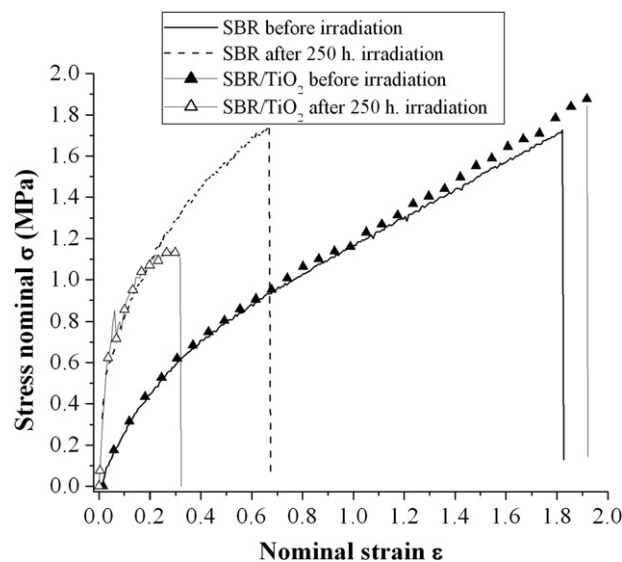


Fig. 8. Stress-strain curves of SBR before and after 250 h of irradiation at strain rate of 100 mm min⁻¹.

based materials. For deeper understanding, the change of $\tan \delta_{\max}$ has been studied at different ageing times and the results are depicted in Fig. 7 for both SBR systems.

During the first 15 h of irradiation of vulcanised SBR (Fig. 7), $\tan \delta_{\max}$ decreases from 1.3 to 0.75, followed by a slow decrease for higher irradiation times. The decrease of $\tan \delta_{\max}$ values as photo-oxidation proceeds characterises a change in macromolecular chain mobility of the polymeric material occurring in the oxidative layer. Indeed, as observed previously by micro-FTIR and AFM, during the photo-ageing, an oxidative layer of about 20 μm whose physico-chemical properties are different from that of the bulk is generated. The oxidative layer results from the formation of oxidised photo-products and a crosslinked network. DMA results suggest that this thin oxidised layer representing 3.3% of the volume of the material with stiffness higher than that of the core of the material influences the visco-elastic response of the overall material. This phenomenon could be compared to the core-shell effect where it is well known that the shell influences the response of the core. In our case, it is widely interesting to note that by DMA we demonstrated that the oxidative layer influences the mechanical response of the overall material.

The mechanical response of SBR/TiO₂ and SBR during irradiation is identical, both are characterised by similar peak maximum values E''/E' (Fig. 7). The oxidative layer for both SBR and SBR/TiO₂ influence in the same manner the visco-elastic response of the materials.

3.3.2. At high deformation

After investigating the mechanical behaviour at low degree of deformation of vulcanised rubbers, we focused on their behaviour at higher degree of deformation by means of tensile tests until break at a strain rate of 100 mm min⁻¹. Tensile behaviours of vulcanized SBR at different irradiation times are collected in Fig. 8. We can notice that SBR and SBR/TiO₂ before irradiation exhibit very similar strain-stress curves typical of elastomeric curve [16]. Before ageing, the strain at break is about 180% by taking into account the reproducibility tests and the associated errors. After ageing, the mechanical behaviour of these materials is different with a lower elongation at break, which is about 70% and 30% for SBR and SBR/TiO₂ respectively. During irradiation, both materials

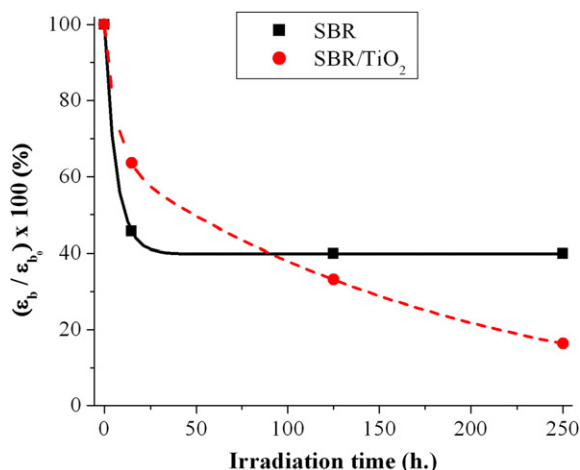


Fig. 9. ϵ_b/ϵ_{b0} as a function of irradiation time.

became more fragile highlighting the influence of the formation of the oxidized layer on the strain mechanisms.

For the sake of clarity, from the stress–strain curves, we followed the strain at the breaking point (ϵ_b) as a function of irradiation time (Fig. 9). We presented normalized strains by considering initial values (ϵ_{b0}) before irradiation equal to 100%.

Fig. 9 shows that SBR exhibits a rapid and important loss of the elongation at break during short exposure time of about 20 h the ϵ_b values decreased by 50% compared to the initial value ϵ_0 , after which the strain remains invariant. SBR/TiO₂ showed also a rapid loss of the elongation at break during first 20 h of irradiation of about 30%. However, unlike SBR, a quasi-linear loss is observed with a lower slope after 40 h of exposure in the case of SBR/TiO₂. For both SBR and SBR/TiO₂, the difference between the mechanical response of the non-aged and the aged materials is probably due to the formation of the oxidative layer during the photo-ageing. In fact, the hardening at the surface during irradiation linked to the formation of crosslinked network and oxidised photo-products produces a lack of mobility of the macromolecules [16]. These previous constraints at the surface of the material imply the formation of cracks during elongation which lead to a lower strain at break compared to non-aged material (Fig. 10).

Table 2

DMT modulus and elongation at break for SBR and SBR/TiO₂ after 250 h of irradiation.

	DMT modulus (MPa) at the surface after 250 h of irradiation	$\epsilon_b/\epsilon_{b(t0)}$ (%)
SBR	600	40
SBR/TiO ₂	1100	16

To better understand the variation of the elongation at break during irradiation for both SBR and SBR/TiO₂, we compared AFM results to those of tensile tests. Table 2 gathers the results of the elongation at break loss $\epsilon_b/\epsilon_{b(t0)}$ and DMT modulus of the extreme surface obtained by AFM after 250 h of exposure for both SBR samples. We can notice that SBR characterised by a lower DMT modulus exhibits a higher elongation at break compared to SBR/TiO₂. Indeed, the DMT modulus values determined by AFM at the extreme surface of the material aged during 250 h show that SBR/TiO₂ is distinguished by the highest modulus related to the existence a crosslinked network generated during UV–visible exposure and to the presence of the filler TiO₂ of a very high modulus giving rise to an increase apparent of stiffness at the extreme surface of the material. The presence of this oxidative layer makes the system much more fragile and influence the overall mechanical response.

It seems that the variation of DMT modulus measured by AFM and the elongation at break measured by tensile tests are correlated. Thus, our hypothesis on the properties of the oxidised layer obtained by AFM is directly linked to the decrease of the elongation at break during the tensile tests confirming the impact of this latter on the global macroscopic behaviour of the materials.

In addition, an interesting fact was observed in elongation at break of SBR/TiO₂ (Fig. 9). In fact, the normalised strain at break of SBR/TiO₂ at 15 h of irradiation was higher than that of SBR, 60 and 45% respectively. Previously, we concluded that the same formation of photo-products and crosslinked network are generated in both materials during ageing, which implied the increase of stiffness at the extreme surface (Fig. 5). However, the different values observed by AFM after 250 h irradiation for both materials were due to the presence of TiO₂ (Table 2). Indeed, the presence of this filler added to the crosslinked network presented the higher modulus which implied the lower elongation at break. However, we surprisingly observed at 15 h of irradiation opposite results for strain at break for SBR/TiO₂ sample compared to SBR (Fig. 9). In this case, we can suggest that during the first 15 h of irradiation, the properties of the oxidised layer have a lower influence on the mechanical response of the overall material in presence of TiO₂. We suppose the existence of a competition between formation of crosslinked network leading to a decrease of the elongation at break and the phenomena of filler–rubber debonding due to a weak interaction between TiO₂ and SBR matrix which involve an increase of elongation at break [21]. This competition will imply during the first times of irradiation a higher influence of the debonding mechanism on the formation of the oxidative layer which leads to a higher elongation at break. This influence will be likely inverted after 15 h of irradiation where the formation of the crosslinked network will be likely most preponderant.

4. Conclusions

The photo-oxidative degradation of vulcanised SBR was studied at $\lambda > 290$ nm at 35 °C. The effect of the presence of coated titanium dioxide (TiO₂) was examined. We first demonstrated that unvulcanised and vulcanised SBR and SBR/TiO₂ present similar photo-products generated during photo-oxidation. By means of micro-FTIR and AFM profiling, we were able to characterise the

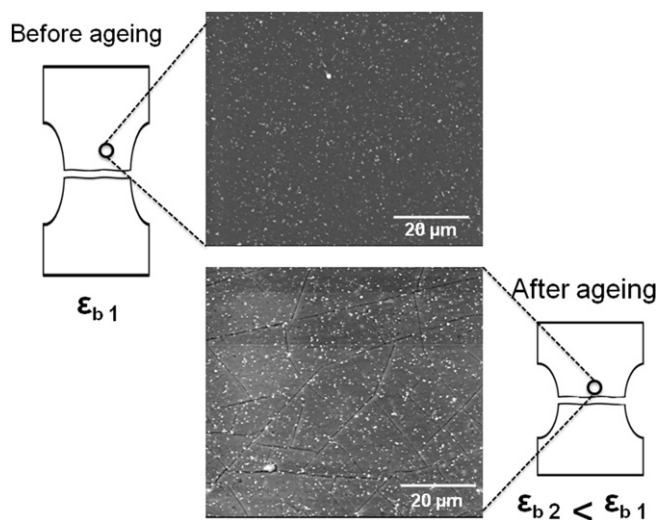


Fig. 10. SEM images obtained after the elongation at break at the surface of SBR/TiO₂ before and after 250 h of irradiation.

chemical changes and the nano-mechanical properties of the heterogeneous oxidative layer generated during the photo-ageing at the extreme surface of vulcanised SBR and SBR/TiO₂. The comparison between AFM and micro-FTIR profiles highlights a nice correlation between chemical and nano-mechanical properties during irradiation at $\lambda > 290$ nm of vulcanized composites based SBR.

Afterwards, we examined the influence of photo-ageing on the macro-mechanical properties of SBR and SBR/TiO₂ at two levels of deformation. The visco-elastic properties such as the loss factor ($\tan \delta$) and the elongation at break ϵ_b were followed during irradiation. It was shown that the change of visco-elastic properties during photo-ageing of SBR based materials was directly related to the formation of the oxidative layer. In our case we demonstrated that the physico-chemical properties of the oxidative layer can explain the loss of mechanical properties observed in the aged materials. In fact, the formation of photo-products and crosslinking network implies an increase of the stiffness of the material at the extreme surface. Therefore the material becomes brittle leading to the formation of cracks which lead to a faster breaking of the sample. We also demonstrated a different mechanical behaviour in presence of TiO₂ compared to neat SBR that could be due to a competition between formation of photo-products and the phenomena of filler-rubber debonding during photo-oxidation.

Acknowledgements

The authors would like to thanks Dr. Sophie Peeterbroeck from Materia Nova (Mons, Belgium) for allowing us to prepare our vulcanized samples in their research centre. We would like to thank also Mr. Regis Vaudemont and Dr. Frederic Addiego from CRP Henri Tudor at Luxembourg to the fruitful discussions exchanged with them regarding the mechanical properties results. The authors gratefully acknowledge the financial support of the Fonds National de la Recherche (FNR) from Luxembourg.

References

- [1] White JR. Polymer ageing: physics, chemistry or engineering? Time to reflect. *C R Chim* 2006;9(11):1396–408.
- [2] Piton M, Rivaton A. Photooxidation of polybutadiene at long wavelengths ($\lambda > 300$ nm). *Polym Deg Stab* 1996;53(3):343–59.
- [3] Adam C, Lacoste J, Lemaire J. Photo-oxidation of elastomeric materials. Part 1—Photo-oxidation of polybutadienes. *Polym Deg Stab* 1989;24(3):185–200.
- [4] Adam C, Lacoste J, Lemaire J. Photo-oxidation of elastomeric materials: Part II—photo-oxidation of styrene-butadiene copolymer. *Polym Deg Stab* 1989; 26(3):269–84.
- [5] Bussière PO, Gardette JL, Lacoste J, Baba M. Characterization of photo-degradation of polybutadiene and polyisoprene: chronology of crosslinking and chain-scission. *Polym Deg Stab* 2005;88(2):182–8.
- [6] Li GY, Koenig JL. A review of rubber oxidation. *Rubb Chem Technol* 2005; 78(3):355–90.
- [7] Delor F, Barrois-Oudin N, Duteurtre X, Cardinet C, Lemaire J, Lacoste J. Oxidation of rubbers analysed by HATR/IR spectroscopy. *Polym Deg Stab* 1998;62(2):395–401.
- [8] Bottino FA, Cinquegrani AR, Di Pasquale G, Leonardi L, Pollicino A. Chemical modifications, mechanical properties and surface photo-oxidation of films of polystyrene (PS). *Polym Test* 2004;23(4):405–11.
- [9] Jubete E, Liauw CM, Jacobson K, Allen NS. Degradation of carboxylated styrene butadiene rubber based water born paints. Part 1: effect of talc filler and titania pigment on UV stability. *Polym Deg Stab* 2007;92(8):1611–21.
- [10] Celina M, Wise J, Ottesen DK, Gillen KT, Clough RL. Oxidation profiles of thermally aged nitrile rubber. *Polym Deg Stab* 1998;60(2):493–504.
- [11] Mailhot B, Bussière PO, Rivaton A, Morlat-Thérias S, Gardette JL. Depth profiling by AFM nanoindentations and micro-FTIR spectroscopy for the study of polymer ageing. *Macromol Rapid Commun* 2004;25(2):436–40.
- [12] Kumar A, Commereuc S, Gonon L, Verney V. Depth-profile of photo-oxidation of polyoctenamer. *Polym Deg Stab* 2002;75(3):509–16.
- [13] Schön P, Bagdi K, Molnar K, Markus P, Pukanszky B, Vancso GJ. Quantitative mapping of elastic moduli at the nanoscale in phase separated polyurethanes by AFM. *Eur Polym J* 2011;47(4):692–8.
- [14] Mertz G, Hassouna F, Toniazio V, Dahoun A, Ruch D. Effect of coated rutile and disazopyrazolone dye additives on unvulcanised SBR during photo-ageing. *J Eng Mat Tech* 2012;134(1):0109031–7.
- [15] Schnabel W, Levchik GF, Wilkie CA, Jiang DD, Levchik SV. Thermal degradation of polystyrene, poly(1,4-butadiene) and copolymers of styrene and 1,4-butadiene irradiated under air or argon with 60Co- γ -rays. *Polym Degrad Stab* 1999; 63(3):365–75.
- [16] Guzzo M, De Paoli MA. The photo-oxidation of EPDM rubber: Part V—mechanical properties degradation of vulcanized filled samples. *Polym Degrad Stab* 1992;38(1):41–5.
- [17] Perera MCS, Ishiaku US, Ishak ZAM. Thermal degradation of PVC/NBR and PVC/ENR50 binary blends and PVC/ENR50/NBR ternary blends studied by DMA and solid state NMR. *Polym Deg and Stab* 2000;68(3):393–402.
- [18] Haward RN, editor. The physics of glassy polymers. New York: Wiley; 1973.
- [19] Chailan JF, Boiteux G, Chauchard J, Pinel B, Seytre G. Viscoelastic and dielectric study of thermally aged ethylene-propylene diene monomer (EPDM) compounds. *Polym Deg Stab* 1995;47(3):397–403.
- [20] Delor F, Lacoste J, Barrois-oudin N, Cardinet C, Lemaire J. Photo-, thermal and natural ageing of ethylene-propylene-diene monomer (EPDM) rubber used in automotive applications. Influence of carbon black, crosslinking and stabilizing agents. *Polym Deg Stab* 2000;67(3):469–77.
- [21] Poh BT, Ismail H, Tan KS. Effect of filler loading on tensile and tear properties of SMR L/ENR 25 and SMR L/SBR blends cured via a semi-efficient vulcanization system. *Polym Test* 2002;21(7):801–6.



Recent advances in high performance poly(lactide): from “green” plasticization to super-tough materials via (reactive) compounding

Georgio Kfoury^{1,2}, Jean-Marie Raquez², Fatima Hassouna^{1*}, Jérémy Odent², Valérie Toniazzo¹, David Ruch¹ and Philippe Dubois^{2*}

¹ Department of Advanced Materials and Structures, Public Research Center Henri Tudor, Hautcharage, Luxembourg

² Laboratory of Polymeric and Composite Materials, UMONS Research Institute for Materials Science and Engineering, Center for Innovation and Research in Materials and Polymers, University of Mons, Mons, Belgium

Edited by:

Alfonso Jiménez, University of Alicante, Spain

Reviewed by:

Alberto D'Amore, Second University of Naples, Italy
Michele Galizia, University of Texas at Austin, Italy

*Correspondence:

Fatima Hassouna, Department of Advanced Materials and Structures, Centre de Recherche Public Henri Tudor, Rue Bommel 5, Hautcharage 4940, Luxembourg
e-mail: fatima.hassouna@tudor.lu;
Philippe Dubois, Laboratory of Polymeric and Composite Materials, Center for Innovation and Research in Materials and Polymers, UMONS Research Institute for Materials Science and Engineering, University of Mons, Place du Parc 23, Mons, 7000, Belgium
e-mail: philippe.dubois@umons.ac.be

Due to its origin from renewable resources, its biodegradability, and recently, its industrial implementation at low costs, poly(lactide) (PLA) is considered as one of the most promising ecological, bio-sourced and biodegradable plastic materials to potentially and increasingly replace traditional petroleum derived polymers in many commodity and engineering applications. Beside its relatively high rigidity [high tensile strength and modulus compared with many common thermoplastics such as poly(ethylene terephthalate) (PET), high impact poly(styrene) (HIPS) and poly(propylene) (PP)], PLA suffers from an inherent brittleness, which can limit its applications especially where mechanical toughness such as plastic deformation at high impact rates or elongation is required. Therefore, the curve plotting stiffness vs. impact resistance and ductility must be shifted to higher values for PLA-based materials, while being preferably fully bio-based and biodegradable upon the application. This review aims to establish a state of the art focused on the recent progresses and preferably economically viable strategies developed in the literature for significantly improve the mechanical performances of PLA. A particular attention is given to plasticization as well as to impact resistance modification of PLA in the case of (reactive) blending PLA-based systems.

Keywords: poly(lactide), (reactive) compounding, mechanical properties, impact resistance, toughening

INTRODUCTION

Over the past decade, there has been a significant research interest on compostable and/or biodegradable polymers in order to alleviate solid waste disposal problems related with petro-based plastics (Lim et al., 2008). These biodegradable polymeric materials are increasingly used today in packaging, agricultural, medical, pharmaceutical, and other areas (Rabetafika et al., 2006; Vroman and Tighzert, 2009). Two main classes of biodegradable polymers can be distinguished (Vroman and Tighzert, 2009) (**Figure 1**):

- Natural and synthetic biodegradable polymers produced from feedstocks derived from biological or renewable resources available in large quantities;
- Synthetic biodegradable polymers produced from feedstocks derived from non-renewable petroleum resources.

Aliphatic polyesters represent a large part of biodegradable polymers. They are considered as hydrolytically degradable polymers due to the presence in their backbone of hydrolytically sensitive chemical bonds, that is, ester moieties (Li, 1999; Nair

and Laurencin, 2007). There are two routes generally used to chemically develop biodegradable polyesters; step (condensation) polymerization and ring-opening polymerization (ROP) (Nair and Laurencin, 2007). Due to the absence of any by-products released during condensation process, ROP is thereby the most used pathway to prepare biodegradable polyesters. Among them, the most extensively investigated polymers are the poly(α -hydroxyacid)s, which include poly(glycolic acid) and the stereoisomeric copolymers of poly(lactic acid). Due to the commercial and low cost production of high molecular weight polymers using ROP, poly(lactide) (PLA) is one of the most studied candidates (Lim et al., 2008). Indeed, this polymer represents one of the stiffest organic materials with a Young's modulus of ca. 3 GPa, together with good optical and thermal properties [melting temperature (T_m) of ca. 170°C and a glass transition temperature (T_g) of ca. 60°C]. In addition, PLA is directly derived from renewable resources, making it environmentally sustainable in terms of depletion of petroleum resources and CO₂-release. Due to these attributes, PLA holds tremendous promises as an alternative to the ubiquitous petroleum-based materials as shown in **Table 1**. For instance, compared with the general

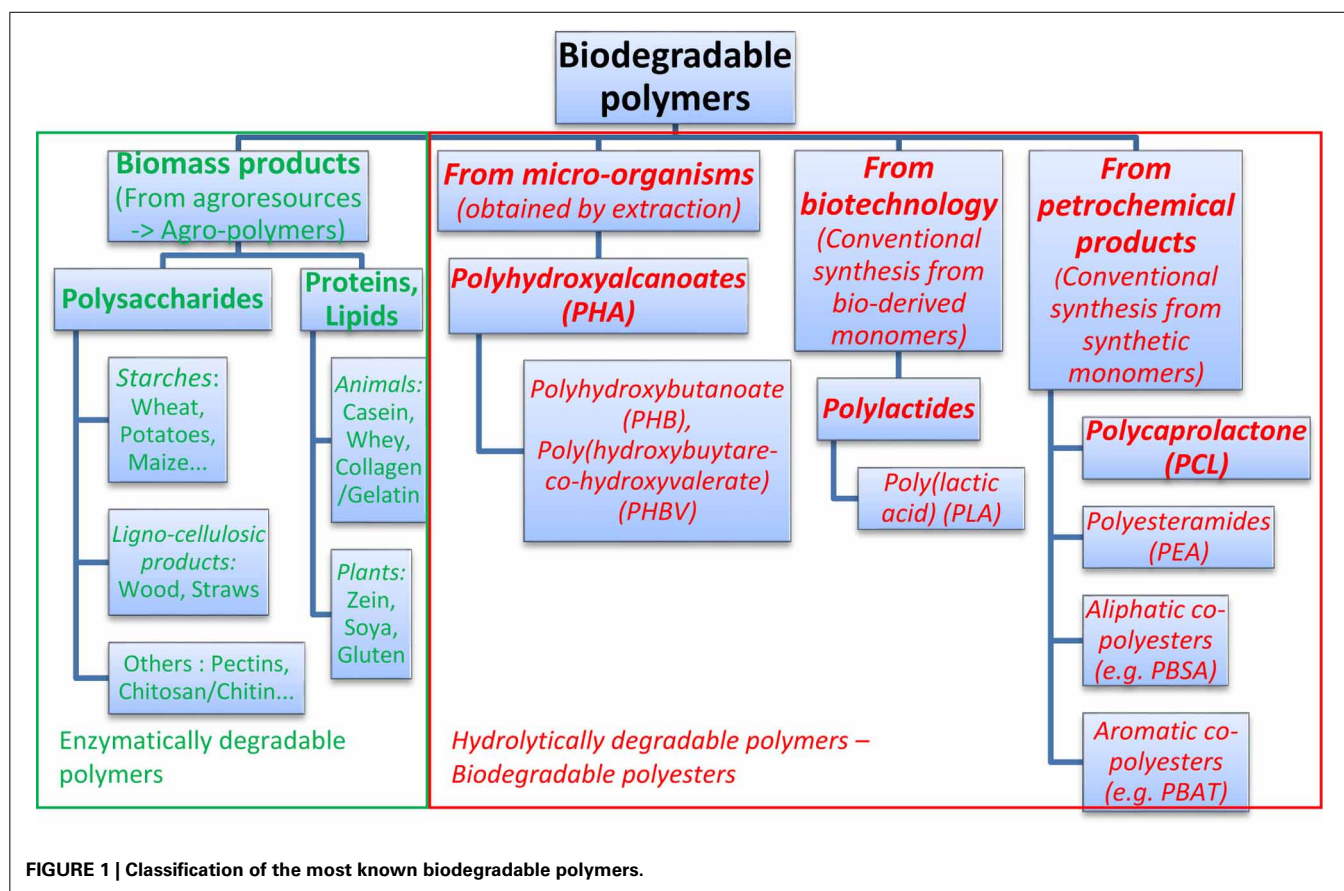


Table 1 | PLA mechanical properties compared to those of most common polymers used in commodity applications [Copyright ©(2011) Wiley and Sons; used with permission from Liu and Zhang (2011)].

	PLA	PET	PS	HIPS	PP
T_g (°C)	55–65	75	105	–	10
Tensile strength at break (MPa)	53	54	45	23	31
Tensile modulus (GPa)	3.4	2.8	2.9	2.1	0.9
Elongation at break (%)	6	130	7	45	120
Notched Izod impact strength (J/m)	13	59	27	123	27 (i-PP)
Gardner impact (J)	0.06	0.32	0.51	11.30	0.79
Cost (\$/lb) ^a	1–1.5	0.70–0.72	0.99–1.01	1.01–1.03	1.15–1.17

PET, Poly(ethylene terephthalate); PS, Polystyrene; HIPS, High-impact polystyrene; PP, Polypropylene; i-PP, Isotactic polypropylene homopolymer.

^aCost cited from "Plastic News", March 31, 2011 except PLA resin.

purpose polystyrene (GPPS), PLA has not only comparable tensile strength and modulus, but also exhibits very similar inherent brittleness (see **Table 1**). However, despite its numerous advantages such as good optical, physical, mechanical properties (high flexural and tensile moduli and strengths), the inherent brittleness significantly impedes its applications in many fields when a high level of mechanical strength is required.

The mechanical resistance of a material is its ability to withstand the application of a sudden load without failure by dissipation of energy of the impact blow. There are two general failure modes, namely *brittle fracture* and *ductile fracture*. While *brittle fracture*, usually resulting of highly concentrated *crazing*, is

characterized by a relatively low energy dissipation and a short nearly linear dependence of load–deformation before fracture, a *ductile fracture* is characterized by a high energy dissipation and a large-scale deformation (plastic yielding and plastic flow) (Bucknall, 1978; White, 1984; Argon and Cohen, 1990; Perkins, 1999). A *brittle-ductile transition* is accordingly defined as the point at which the fracture energy increases significantly with a mode of failure passing from brittle fracture to ductile fracture. The importance of this transition zone depends mainly on the strain nature and rate, the temperature gradient, and the specimen geometry (Perkins, 1999). For instance, the same material can exhibit higher brittleness at low temperatures and/or high

testing speeds. Mechanical resistance of polymers may be evaluated in terms of the energy absorbed by the specimen during testing by various methods including (Pearson Raymond, 2000):

- *Tensile testing*: The area under the stress strain curve is often used to quantify toughness. However, different stress-strain curve shapes indicating different mechanical behaviors and responses to the impact loading may dissipate the same impact energy.
- *Impact testing*: The energy required to break the sample which is usually entailed by a hammer is measured. The related impact strength is expressed in terms of the difference between the potential energy of the striker before and after the impact. It is generally obtained by dividing the energy required to break the sample by the sample width or cross-sectional area. For impact testing, three different tests are typically performed such as Izod (ASTM D256 where samples are clamped as a cantilever), Charpy (ASTM D6110 unclamped samples are supported at both ends) and Dynstat (DIN 53453 where samples are unclamped at the lower end), which can be done in either a notched or un-notched state.
- Falling weight tests where a projectile propelled onto the specimen or dropped on it under the force of gravity is used to measure the impact energy. Gardner impact tester is a well-known example of this type of instrument which offers the advantage over impact testing method that the fracture shape can be also analyzed.

Typically, like conventional brittle thermoplastics, the reason for brittleness of PLA is strain and stress localizations at its use temperature, which is usually below its glass transition and brittle to ductile transition temperature. Under mechanical loading PLA deforms involving highly localized *crazing mechanism*. As at room temperature its yield stress is superior to the critical stress value for crack formation and propagation, catastrophic damage and break can most likely occur at low deformation and in the elastic zone. The strain-localization can be suppressed namely by compounding the brittle polymer with various softening and toughening agents including plasticizers and rubbery polymers or impact modifiers. However, the most preferred way is to blend PLA with rubbery polymers in order achieve a good toughness-stiffness balance without largely scarifying its glass transition temperature. Like many tough polymer blends, PLA blends can undergo one or a combination of the most known toughening mechanisms, namely *multiple crazing, shear yielding, cavitation and debonding* (Petchwattana et al., 2012). The mechanical energy is therefore transferred to the plastic flow and dissipated through a large volume fraction of material. The energy dissipation mechanisms retard or stop crack initiation and propagation through the polymer, and ultimately result in a material with improved toughness. There are several factors that can influence the amount of toughening, mainly related to the matrix polymer (Kramer, 1983), the rubber phase (type, particle size, concentration, strength and morphology), and the rubber-matrix interfacial interaction. For instance, the correlations between the deformation morphologies (mainly under tensile and impact testing) and the resulting mechanical properties reveal that the blend

compatibility and related morphologies are important factors to influence the toughening mechanisms. The toughening mechanisms can be analyzed through several aspects, including stress whitening, matrix ligament thickness, microstructure evolution under testing, and morphology features of the fracture surface of the impacted sample. For instance, when the matrix ligament thickness is below the critical value, the blends deform to a large extent because of shear yield initiated by stress concentrations and interfacial de-bonding. This may result in the formation of fibers in both tensile and impact samples and the dissipation of a large amount of energy (Han and Huang, 2011).

Many strategies, namely the incorporation of a variety of soft polymers or rubbers, addition of rigid fillers and fibers, and modification of crystalline morphology, have been developed in the literature during the last decades in order to enhance the general toughness of PLA, while maintaining its stiffness-toughness balance acceptable (Anderson et al., 2008; Liu and Zhang, 2011). An optimal toughness balance can be obtained with 10–30% of toughening agents, even if little improvement can be seen by the addition of 5–10% of the latter (Mascia and Xanthos, 1992; Anderson et al., 2008; Liu and Zhang, 2011). In this regard, blending represents an economically viable approach such as plasticization, (reactive) compounding with a variety of flexible/soft polymers or rubbers and the addition of rigid fillers. In this report, an update on the strategies recently developed in the literature to significantly and effectively improve PLA's mechanical properties, will be discussed on its toughening and impact resistance properties.

APPROACHES FOR THE IMPROVEMENT OF PLA'S MECHANICAL PROPERTIES BY MODIFYING ITS INHERENT CRYSTALLINE STRUCTURE

The impact strength of semicrystalline polymers usually varies inversely with the percent crystallinity (Mercier et al., 1965). It is likely that crystallites act as stress concentrators, causing the stress acting on a small volume of the material to be much greater than the average stress applied to the whole sample. As a result, the material breaks at a stress that is less than the expected critical value. Also, crystallites are seen to reduce multiple crazing and shear yielding (Pecorini and Hertzberg, 1993), both energy-dissipative mechanisms of polymer matrices. The size and number of these crystalline structures have a profound influence on impact resistance. It is generally agreed that impact resistance and the brittle to ductile transition temperature are inversely related to spherulite size and morphology which can be tuned by controlling the cooling and drawing rates via thermal and mechanical treatments, respectively (Hammer et al., 1959; Ohlberg et al., 1959; Barish, 1962). This part of the study concerns the PLA matrix itself. In this regard we will report the main approaches that tune up the relationships “physical treatments—crystalline structure—mechanical properties” in order to improve the mechanical properties of PLA-based materials.

THERMAL TREATMENTS—ANNEALING

The effect of annealing treatment on thermal, mechanical and fracture behavior of PLA was investigated. Most of the studies demonstrated that the increase of PLA crystallinity usually leads

to; an improvement of its overall mechanical and heat resistance behaviors (Perego et al., 1996; Park et al., 2006; Yu et al., 2008; Nascimento et al., 2010). For instance, (Perego et al., 1996) evidenced that annealed PLA possess higher heat resistance, elastic moduli (tensional and flexural), Izod impact strength. Park et al. (2006) and Nascimento et al. (2010). Annealed PLA under different conditions to obtain several microstructures with varying spherulite size and density. They demonstrated that heat resistance is dramatically improved as crystallinity. Furthermore, the quasi-static fracture toughness of PLA decreases with increase of crystallinity corresponding to decrease of amorphous region; on the other hand, the impact fracture toughness tends to increase with crystallinity. The crack growth behaviors of the PLA specimens having different crystallinity exhibited that under quasi-static loading, disappearance of multiple crazes in the crack-tip region results in the decrease of the fracture toughness with crystallinity. On the contrary, under impact loading, the increase of the fracture toughness with crystallinity is considered to be related to the increase of fibril formation. Finally, for the amorphous PLA, the static toughness was higher than the impact one; mainly owing to extensive multiple craze formation at the static rate. On the contrary, for the crystallized PLA, the impact toughness became larger than the static one due to formation of fibril structure at the impact rate (Gamez-Perez, 2010). Gamez-Perez (2010) applied annealing treatment on two commercial grades of PLA from NatureWorks® (2002D and 4032D) of comparable average molecular weights (M_w) of 212 and 207 kDa, respectively, but they exhibited different optical purities, that is, d-lactic monomer contents of 4.25 and 2%, respectively (Natureworks®, 2005, 2006; Li and Huneault, 2007; Xiao et al., 2009; Carrasco et al., 2010). Annealing the sheets was performed using an oven at 60°C for 20 min, followed by a rapid quenching. The nomenclature

employed was “PLA-X” and “PLA-XT” for extruded and thermally treated films, respectively. “X” is set as 96 and 98 for PLAs for a content of 95.75 and 98% l-lactic monomer, respectively. From **Table 2**, it results that the heating at temperatures close to the glass transition temperature (T_g) with the subsequent quenching treatment produces a “de-aging effect,” with an increase of the free-volume of polymeric chains, as highlighted by the decrease of the T_g . The increase in the system potential energy was also shown by the disappearance of the endothermic peak at T_g . As a consequence, annealing promotes a brittle-to-ductile change in the fracture behavior of PLA with a decrease of the tensile strength and stiffness and yield stress, regardless the d-lactic isomer content. A shear yielding with a localized neck formation thereby appeared. The fracture parameters, assessed by the EWF method used to characterize the fracture toughness of PLA showed a great enhancement of the toughness after the annealing and quenching treatments. Regarding the influence of the D-lactic isomer content in PLA films, when they were in a glassy stage, no remarkable differences were noticed out in the mechanical properties and fracture behavior. Only when the films were in a de-aged form, the differences in the stiffness of both PLA grades had been revealed. The optical purity, the elastic modulus and the tensile strength were high. However, the deformation to break was still low, only passing from 17% (PLA-98) to 24% (PLA-96).

THERMOMECHANICAL TREATMENTS—SELF-REINFORCING POLYMERIC MATERIALS PROCEDURES (SRPMs)—ALIGNMENT AND ORIENTATION PROCEDURES

Although polymeric composites are referred to as multi-phase or hetero-composites, self-reinforced polymeric materials (SRPMs) are referred to as single-phase or homo-composites because

Table 2 | Effect of some (thermo)mechanical treatments and processing on the thermal and mechanical properties of PLA.

Material	$T_g(^{\circ}\text{C})$	$T_m(^{\circ}\text{C})$	$\Delta H_{cc}(\text{J/g})$	$\Delta H_m(\text{J/g})$	$X_c(\%)$	Yield stress σ_y (MPa)	Young's modulus E (GPa)	Elongation at break ϵ_b (%)	Charpy (KJ/m ²)	Izod impact (KJ/m ²)	References
PLA-96	60	148	–	1	1	56.2 ± 0.7	4.0 ± 0.2	24 ± 5			Gamez-Perez, 2010
PLA-98	61	164	29	31	2	58.4 ± 0.5	4.3 ± 0.1	17 ± 4			
PLA-96T	56	148	–	1	1	47.3 ± 1.1	3.3 ± 0.2	456 ± 100			
PLA-98T	57	165	31	34	3	53.4 ± 0.6	3.5 ± 0.3	422 ± 50			
Un-oriented						47.0	3.65	1.5	12.5	1.6	Grijpma et al., 2002
Oriented ($\lambda = 2.5$)						73.3	4.49	48.2	35.9	5.9	
Oriented ($\lambda = 3.4$)						66.3	3.74	21.8	No break	52.0	
PLA-I						65.6 ± 1.3	3.7 ± 0.1	4.0 ± 0.8			Carrasco et al., 2010
PLA-EI						65.2 ± 0.9	3.9 ± 0.1	5.4 ± 0.6			
PLA-IA						75.4 ± 0.9	4.1 ± 0.1	2.5 ± 0.2			
PLA-EIA						77.0 ± 1.1	4.1 ± 0.1	3.3 ± 0.3			

I, Injected; IA, Injected then Annealed; EI, Extruded then Annealed; EIA, Extruded then Injected then Annealed.

the same polymer forms both the reinforcing and the matrix phases. The basic concept of self-reinforcement is to create a one-, two- or three-dimensional alignment (1D, 2D, or 3D alignment, respectively) within the matrix to fulfill the role of matrix reinforcement. As a result, the generated structure has to possess a higher stiffness and strength than the matrix as well as to be “well-bonded” to the matrix polymer. Consequently, the stress can be transferred from the “weak” matrix to the “strong” reinforcing structure, according to the “working principle” of all composites. The reinforcing structure can be produced during one (*in situ*) or more processing steps (*ex situ*) (Kmetty et al., 2010). A driving force for SRPMs is the possibility of manufacturing lightweight parts and structures because the density of SRPMs is well-below those of traditional filled polymers, where the “heavier” reinforcements incorporated in the polymeric matrix are of, e.g., glass fibers (density: 2.5–2.9 g.cm⁻³), carbon fibers (density: 1.7–1.9 g.cm⁻³), basalt fibers (density: 2.7–3.0 g.cm⁻³), aramid fibers (density: 1.38–1.44 g.cm⁻³) and/or fillers like talc (density: 2.7–2.8 g.cm⁻³), chalk (density: 1.1–2.5 g.cm⁻³) and silica (density: 2.1–2.6 g.cm⁻³) (Kmetty et al., 2010). Furthermore, the ease of recycling SRPMs must be emphasized when reprocessing via re-melting is targeted. The concepts used to produce SRPMs can be also adapted to biodegradable polymers for improving their property profiles. Reinforcing a PLA matrix by embedding PLA fibers enables to respond the demands for high strength and stiffness required for many applications. The development of high-stiffness and high-strength polymeric fibers is essential to imparting superior mechanical properties for the resulting PLA SRCs (Matabola et al., 2009). The mechanical properties of fibers can be increased via molecular orientation during spinning and drawing (Alcock et al., 2006). The most commonly used methods to produce PLA fibers are melt-spinning and electro-spinning (Mäkelä et al., 2002; Tsuji et al., 2006; Li and Yao, 2008). Significantly improved interfacial bonding can be achieved in materials where both matrix and reinforcing elements have the same chemical structure (Törmälä, 1992). For example, SRCs consisting of oriented PLA fibers surrounded by a PLA matrix have improved strength and rigidity compared to non-reinforced PLA (Tormala et al., 1988; Majola et al., 1992; Wright-Charlesworth et al., 2005).

To control the impact performances, molecular orientation of amorphous poly(D,L-lactide) (PDLLA) chains was carried out through injection moulding techniques at $T < T_g$ or by non-conventional shear controlled orientation by injection moulding (SCORIM) process in which the melt is cooled under oscillating shear conditions. The latter allowed getting oriented PLA-based materials, leading to the elaboration of degradable devices with much improved mechanical properties compared to non-oriented materials (Grijpma et al., 2002). The brittle fracture mechanism of PDLLA via crazing changed from a fragile to a ductile energy dissipation mechanism upon orientation. Consequently, a significant increase in impact strength was obtained. In comparison to the brittle tensile behavior of un-oriented PDLLA, a much more ductile behavior was observed. This increase in toughness was not accompanied by a decrease in tensile strength and stiffness, as it is generally in the case of

plasticization and rubber modification. Due to orientation of the polymer chains in the direction of testing, fibrillation took place during the fracture process. Growing cracks got stopped in the anisotropic structure, and catastrophic failure could be postponed. The mechanical data are summarized in **Table 2**. However, in the perpendicular direction to the orientation, mechanical properties are much poorer and must be taken into account. The effects of operative SCORIM parameters were also investigated. The correlations between processing, morphology and mechanical properties of SCORIM-moulded PLLA were established and compared with conventional injection moulded CIM PLLA (Ghosh et al., 2008). The level of molecular orientation was assessed indirectly by hot recoverable strain HR test. The fracture surface-morphology assessed by optical microscopy and SEM technique showed that, at low mould temperature, the level of molecular orientation increased with shearing time. The SCORIM processing changed the typical heterogeneous skin-core morphology of CIM into a near homogeneous oriented structure. The extent of core-fibrillation increased with shearing time. Under the three-point flexural test, the higher oriented PLLA exhibited dual fractures where the crack initiation started in the skin and transferred to oriented core fraction without decreasing the modulus. At high mould temperatures, the orientation increased steadily with shearing time. However, the level of molecular orientation was lower than the corresponding low mould temperature conditions. The orientation of core-fraction increased steadily with shearing time. Depending on the level of molecular orientation, the SCORIM-processed PLLA products showed four distinct types of fracture surfaces under three-point flexural test: (i) the un-oriented core failed through crazing; (ii) the sub-skins failed either in smooth, rough or fibrillated fracture surfaces depending on the level of molecular orientation; (iii) the less oriented core failed with fibrillation through pronounced plastic deformation; and (iv) the highly oriented skins failed with smooth surface. All the SCORIM-processed PLLA exhibited higher toughness and higher maximum stress compared with conventional injection-moulded PLLA (**Table 2**). The overall increments in maximum stress and toughness were of 134% and 641%, respectively. The increase in maximum stress and toughness were higher in low mould temperatures (30°C) in contrast to high mould temperature temperatures (50°C). Unlike the traditional blending technique, the increments in mechanical performances were achieved without sacrificing the stiffness. The mechanical behavior namely toughness and maximum stress of PLLA processed by SCORIM could be tailored by controlling the melt stage, the in-mould shearing time and the cooling conditions. In another study (Bigg, 2005), biaxial orientation of PLLAs chains by extrusion induced a 5–10-fold increase in elongation and enhanced tensile strength at break, tensile toughness and tensile modulus (**Table 2**). The mechanical processing of PLA (injection and extrusion/injection) as well as annealing of processed materials were studied in order to analyse the variation of its chemical structure, thermal degradation and mechanical properties (Carrasco et al., 2010). Processing of PLA yielded a decrease of its molecular weight and melt-viscosity due to chain hydrolysis. PLA crystal structure was significantly recovered after annealing. The authors also confirmed by proton NMR

techniques that the chemical composition of PLA did change after processing, and the proportion of methyl groups from PLA matrix increased, more likely indicating the presence of a different molecular environment. The mechanical behavior was altered as well (**Table 2**). After annealing, the samples showed an increase in Young's modulus (5–11%) and in yield strength (15–18%), which had been explained by the higher degree of crystallinity of annealed materials, with its subsequent decrease in chains mobility. Extruded/injected materials showed a significant increase in elongation at break (32–35% higher), compared to injected materials. It is ascribed to the presence of low molecular-weight chains at high contents, due to hydrolysis reactions in reprocessed materials.

In general, the modification of chain orientation and crystallinity for PLA-based materials can improve its ductility and impact resistance to some extent. Some processing techniques may contribute efficiently to toughening PLA, without compromising its tensile properties. Orientation of chains by injection moulding and especially injection moulding with macroscopic oscillating shear force resulted, for instance, in an enhancement of tensile, Izod and Charpy impact in the orientation direction. In order to increase the crystallinity of PLA blends and therefore tune its mechanical properties, some routes may be considered (Battezzatore et al., 2011):

- *By chain orientation under stress;*
- *By applying thermal treatments (quenching and/or annealing);*
- *By minimizing the amount of the other lactide and mesolactide in the lactide used as the major monomer.* The crystallinity and crystallization rate of PLA decrease as the purity decreases. The crystallization half-time was found to increase by roughly 40% for every 1 wt.% increase in the mesolactide content of the polymerization mixture (Kolstad, 1996). In addition, it is known that a co-monomer content higher of 7 wt% with polymeric chains leads to an amorphous polylactide.;
- *By playing with the moulding conditions, in particular moulding temperature and cooling time.* Even at high L-lactide content, PLA crystallization is typically too slow to develop significant crystallinity unless it is induced by strain like processes used to manufacture bottles. In processes such as injection moulding, where the orientation is limited and the cooling rate is high, it is much more difficult to develop significant crystallinity and therefore formulation or process changes are required.;
- *By adding nucleating agent.*

Nevertheless, these techniques are not very industrially considered because they require increasing the processing time. In addition, studied alone, their influences are usually marginal and the resulting increase of toughness properties is insufficient [but sometimes quite enough because excellent stiffness-toughness balance was achieved in some cases (Gamez-Perez, 2010)] to satisfy the requirement of most applications. However, the combination of these factors with others such as compounding strategies (that will be discussed further) may bring more added-values in terms of the enhancement of PLA's mechanical properties and constitute more prospective routes to improve them.

APPROACHES TO INCORPORATING SOFT COMPONENTS INTO PLA MATRIX VIA COMPOUNDING/BLENDING

Blending polymers is as old as the polymer industry itself. Interestingly, using blending approach, PLA can be readily impact-modified, plasticized, filled, chemically modified and reactive blended and processed like many of other conventional polymers. There are two main ways to improving the ductility and the toughness of PLA materials namely through plasticization or incorporation of soft/rubbery polymers. Plasticization makes possible to achieve improved processing behaviors for polymeric materials, while providing better flexibility in the end-use product. As far as blending is concerned, blending PLA with immiscible polymers produces a new type of polymeric materials with different properties, in which each polymeric partner provide its own feature. Because of their impact-absorbing ability when well-dispersed with the convenient particle size distribution, rubbers should act as stress concentrators at many sites throughout the material. Therefore, they impart great ductility and impact strength to the material, resulting from dissipative micromechanisms initiated by the rubber particles. All of these phenomena are dependent on the deformation, toughening and fracture mechanisms, namely crazing, shear yielding, cavitation, or debonding as mostly reported in the literature (Kambour, 1973; Michler, 1989; Wu, 1990; Könczöl et al., 1992; Ikeda, 1993; Dompas et al., 1994; Lu et al., 1997; O'Connell and McKenna, 2002; Narisawa and Yee, 2006; Bucknall, 2007; Seelig and Van Der Giessen, 2009):

1. *Crazing mechanism* can be initiated in a material when the stress or hydrostatic tension is locally concentrated at a defect which can be a notch, voids, in-homogeneities or rubber particles. Therefore, interpenetrating micro-voids and highly drawn elongated micro-fibrils called *tufts* (usually a fraction of 1 μm in length, depending on the molecular weight of a polymer, several nanometers in diameter, and confined to a small volume of the material), are formed giving rise to macroscopic highly localized zones of plastic dilatational deformation (Kramer and Berger, 1990). Under sufficient mechanical loading, the local stress exceeds a critical value. Thus, the micro-fibrils elongate until breaking and cause the micro-voids growth and coalescence turning into micro-cracks. Crazing mechanism is dilatational in nature and consumes the predominant part of fracture energy in the case of many thermoplastics. Accordingly, crazing is to some extent a precursor to macroscopically brittle failure and is view as a damaging mechanism in the case of brittle polymers when the craze evolution into a micro-crack cannot be arrested. However, when blended with the brittle matrix, the rubbery impact modifier particles have two separate effects but equally important features as a response to load application. They first concentrate locally the stress where craze initiation takes place. The crazes then grow perpendicularly to the maximum applied stress direction. In a second step, the surrounding rubber particles play the role of "craze terminators," preventing the generation of micro-cracks. The result is that a large number of small crazes are formed, in contrast with the small number of large crazes (micro-cracks) within the same polymer

matrix in the absence of rubber particles. This multiple crazing that occurs throughout a comparatively large volume of rubbery-modified material explains the high energy absorption in fracture tests and the extensive stress whitening that accompanies deformation and failure (Perkins, 1999). Some matrices tend to craze because of low entanglement density while high molecular weight is needed to stabilize crazes.

- *Shear yielding mechanism* is highly localized plastic deformation characterized by appearance of oriented shear bands under uniaxial tension at 45°C to the direction of the applied stress. Shear yielding occurs approximately at constant volume while initiation of shear bands is affected by the hydrostatic tension (mean stress). In ductile polymers, shear-yielding is usually the major energy absorbing mechanism. There are also few polymers such as acrylonitrile butadiene styrene (ABS) and rubber-toughened PMMA that exhibit both shear yielding and crazing mechanisms. When the craze initiation stress of the matrix is lower than the yield stress, a polymer will tend to craze; if the yield stress is lower than the craze initiation stress, the matrix will fail by shear-yielding. Mixed crazing and shear yielding tends to occur when the craze initiation stress and the yield stress are comparable or when interactions occur between crazes and shear bands.
- *Cavitation* is void-expansion, which can occur in the matrix (generally coupling with crazing) or initiate inside the rubber particles, which is generally characterized by viewing stress-whitening zones. The essential conditions for void growth is an energy balance between the strain energy relieved by cavitation and the surface energy associated with the generation of a new surface. Cavitation is a precursor to other toughening mechanisms, thereby relieving the hydrostatic strain energy and initiating shear yielding of the matrix. It is assumed that internal rubber cavitation is an instantaneous process, which cannot occur for very small particles (less than 200 nm). In other words, rubber-cavitation mechanism is favored by increasing the particle size within rubber toughening materials or by decreasing the crosslinking density (which can suppress cavitation).
- *De-bonding* is the energy-dissipation due to the interfacial failure. The interface between the phases influences the final blends properties by efficient stress transfer between the two phases. However, interfacial de-bonding can be thought of as a secondary toughening mechanism being more important as a trigger for other induced mechanisms like shear yielding. Accordingly, low interfacial adhesion easily results in premature interfacial failure and hence rapid and catastrophic crack propagation, whereas very strong adhesion is unfavorable for de-bonding and also delays the occurrence of matrix yielding, involving the matrix-particle interface as an important factor that we need to control for optimum energy dissipation.

Toughening mechanisms and competition between both modes of fracture are mainly governed by a variety of factors such as mode of loading, environment, processing conditions, composition and behavior of the matrix, relaxation behavior of the dispersed phase, rubber content, blend morphology, rubber-matrix adhesion, etc. Being a suitable processing technique, reactive

extrusion for instance, represents a unique tool to manufacture biodegradable polymers upon different types of reactive modification in a cost-effective polymer processing (Michaeli et al., 1993; Mani et al., 1999). This technique enhances the commercial viability and cost-competitiveness of polymer materials, in order to carry out not only melt blending, but also chemical reactions including polymerization, grafting, compatibilization, branching, functionalization. . . (Michaeli et al., 1993; Mani et al., 1999). The *in situ* chemical modification of PLA by reactive extrusion has proven to be an effective promising way to elaborate tougher PLA-based materials with improved stiffness-toughness balance compared to neat PLA as it will be detailed later. Here, the forthcoming paragraphs will report the recent investigations on simple plasticization of PLA and blending PLA with rubbery/soft materials.

COMPOUNDING WITH PLASTICIZERS—MISCIBLE TO PARTIALLY MISCIBLE BLENDS

Plasticization is widely used to improve the polymers processability and/or other properties according to specific applications. Plasticizers can act by altering the intermolecular interactions among the host polymer chains to other interactions between the macromolecules and the plasticizer. This promotes conformational changes, resulting in increased mobility of plasticized chains. The Standard ISO427 (1988) define a plasticizer as being as a low or negligible volatility component, which is once incorporated to a plastic material, lowers its softening interval temperature, facilitates its processability and increases its flexibility and ductility. Its behavior can be explained by decreasing the viscosity of the molten plasticized polymer, the glass transition temperature and the elastic modulus of the plasticized materials. The evolution of the elongation at break can be also related to the ductility of a polymer and give information about the plasticization extent of polymers.

To be suitable with PLA, a plasticizer should fulfill the following characteristics (Liu and Zhang, 2011):

- To have an optimum molecular weight and loading level to be miscible with the polymer matrix. Miscibility of plasticizers in a polymer matrix is evaluated by solubility parameters (δ) and magnitude of interaction parameters (χ_T) (Pillin et al., 2006);
- Significantly lower the T_g of PLA and thus enhance tensile toughness;
- Preferably bio-sourced and biodegradable;
- Non-volatile;
- Non-toxic;
- Exhibit minimal even more negligible leaching/migration phase separation from the polymer matrix during ageing.

Many classes of plasticizers were reported by Liu and Zhang and will be discussed in the forthcoming part as follows (Liu and Zhang, 2011):

- Monomeric or small molecule plasticizers;
- Oligomeric and polymeric plasticizers;
- Mixed plasticizers.

In the review, a special emphasis is made on the impact behavior of plasticized PLA, because it has not received enough attention in the literature.

Monomeric or small molecule plasticizers

Many small molecules/monomeric plasticizers have been studied in order to evaluate their plasticization efficiency and their influence on the overall physical properties of PLA (Table 3). The optimal plasticizer content has to take into account the molecular weight, solubility δ and interaction parameters χ_T . For instance, most of the studies showed that between 10 and 20 wt.% of plasticizer content in PLA, all studied citrate esters (TEC, TBC, ATEC, ATBC) results in a higher elongation and lower T_g for the as-plasticized PLA materials compared to neat PLA.

Among the monomeric or small molecule plasticizers studied in the literature, lactide monomer (LA) possesses the best plasticization efficiency for PLA. However, due to its low molecular weight compared to the others, lactide tends to migrate toward the PLA surface. Therefore, the toughness of plasticized PLA tends to be reduced with time (Jacobsen and Fritz, 1999). LA can also volatilize during melt processing because of its low boiling point ($\sim 120^\circ\text{C}$). In terms of good stiffness-toughness balance, Dioctyl adipate (DOA) seems to be the most efficient one by significantly enhancing elongation with a slight depression of tensile modulus (Martino et al., 2009). The plasticizing efficiency of ATBC was higher compared to the others citrate-based plasticizers. Generally, the miscibility of plasticizers with a polymer decreases with increasing molecular weight of the plasticizers. Small molecule plasticizers are usually more efficient than larger ones in order to lower the host polymer's T_g because the mixing entropy is higher in the case of low M_w plasticizers. However, because of their low boiling point, small molecule plasticizers usually evaporate during melt processing (Labrecque et al., 1997; Ljungberg and Wesslén, 2003; Ljungberg et al., 2003; Martino et al., 2009) and have also a strong tendency to migrate toward the surface of the polymeric material (Ljungberg and Wesslén, 2003; Ljungberg et al., 2003, 2005; Martino et al., 2006). The driving force of the migration is ascribed to the enhanced crystallization ability of plasticized samples. Consequently, the ability of PLA to accommodate the plasticizer in the amorphous PLA phase diminishes (Ljungberg and Wesslén, 2002; Ljungberg et al., 2003, 2005; Martino et al., 2006; Pillin et al., 2006). In addition to the loss of the material toughness (plasticized PLA regains part of the brittleness of neat PLA); the plasticizer migration can, for example, contaminate the food or beverage in contact with plasticized PLA in food packaging applications. All monomeric plasticizers should be added in the range of 5–25% (depending on the plasticizer itself) in order to reduce the migration to the maximum, to maintain the optimum balance between tensile modulus, strength and elongation at break and reduce significantly the glass transition temperature of the host polymer. However, monomeric plasticizers cannot fulfill these requirements due to their high tendency to migrate and evaporate. In this regard, researches had been more widely focused on oligomeric and polymeric plasticizers.

Oligomeric and polymeric plasticizers

The common way to reduce plasticizers' migration and evaporation is to increase their molecular weight in such a way to retain their miscibility with the polymer matrix at the same time. In this respect, many researchers have investigated the effect of some oligomeric and polymeric molecules as plasticizers for PLA (Table 4).

For 20 wt% plasticizer content, ABA-type block copolymer of PDLLA and PEG400, that is, PDLLA-b-PEG400-b-PDLLA (10/2, molar ratio of D,L-LA monomer to PEG400 used in the feed) (COPO3) and poly(propylene glycol) (PPG720) provide a good stiffness-toughness balance. PPGs 425, 600 and 1000, Glyplast® 206/2 and Glyplast® 206/7 have a better plasticizing efficiency compared to the others. Adipates-based plasticizers are miscible with PLA until a critical concentration reached in function of the molar mass of adipate. A remarkable increase in elongation was achieved when the concentration of plasticizer reached 10 wt%, whereas the decreases in elastic modulus and tensile stress were noted for all the plasticizers investigated. Very recently, it has been shown that PLA can be efficiently plasticized and toughened by melt-blending with poly(1,2-propylene glycol adipate) (PPA) (Zhang et al., 2013b). Thermal and dynamic mechanical analysis revealed that PPA was partially miscible with PLA. In addition, morphological investigation of PLA/PPA blends showed that PPA was compatible with PLA. As a result, with the increase of PPA content (5–25 wt%), the blends showed a decrease in the tensile strength and the Young's modulus (Table 4); but the elongation at break and the impact strength dramatically increased due to the plastic deformation. The Izod notched impact strength reached 90 J/m when the PPA amount was of 20 wt%, and even exceeded 100 J/m when PPA amount was of 25 wt%. The plasticization effect of PPA was also highlighted by the lowering of dynamic storage modulus and viscosity in the melt stage of the blends compared with neat PLA. In another recent study, Gui et al. have successfully toughened PLA by melt-blending with poly(ethylene glycol-co-citric acid) (PEGCA) (Gui et al., 2013). The addition of PEGCA to PLA lowered the viscosity and the glass transition temperature of the resulting material. PEGCA was partially miscible in PLA and the blends exhibited a phase-separated morphology. The ductility and toughness of PLA were significantly improved in the presence of PEGCA. Whereas the impact resistance (Figure 2C) and the elongation at break (Figure 2B) of the blends were remarkably higher than those of neat PLA, the tensile and flexural strength and modulus of the blends (Figure 2A) monotonically dropped with increasing PEGCA content.

Hassouna et al. investigated new plasticization ways based on low molecular bio-plasticizers to improve the ductility of PLA. Grafting reactions between anhydride-grafted-PLA (MA-g-PLA) copolymer with hydroxyl-functionalized citrate plasticizer, i.e., tributyl citrate (TbC) (Hassouna et al., 2012), and poly(ethylene glycol) (Hassouna et al., 2011) were carried out through reactive extrusion. All plasticizers drastically decreased the T_g of PLA due to the mobility gained by the polymer chains within the plasticized blends. Regardless the nature of the plasticizer, the elastic modulus and yield stress decrease, while the ultimate strain increases for plasticized PLA. Very recently, we have investigated a novel and efficient pathway to

Table 3 | Plasticization effects on PLA with some monomeric plasticizers [Copyright ©(2011) Wiley and Sons; used with permission from Liu and Zhang (2011)].

Polymer	Molecular weight (g/mol)	Plasticizer	Molecular weight (g/mol)	Plasticizer content (wt%)	Solubility δ (MPa ^{0.5})	Interaction parameter χ_T	DSC T_g (°C)	Max. tensile strength (MPa)	Tensile modulus E (MPa)	Tensile elongation at break ϵ (%)	Notched impact strength (kJ/m ²)	References
PLA	–	LA	$M_n = 144$	1.3	–	–	–	51.7	1993	3	–	Sinclair, 1996
				17.3	–	–	–	15.8	820	288	–	
				19.2	–	–	32–40	29.2	658	536	–	
				25.5	–	–	–	16.8	232	546	–	
PLA	$M_w = 137000$	–	–	–	–	–	59.1	51.7	–	7	–	Labrecque et al., 1997
		TEC	$M_n = 276$	10	19.8	–	42.1	28.1	–	21.3	–	
				20	19.8	–	32.6	12.6	–	382	–	
		TBC	$M_n = 360$	30	19.8	–	–	$\sigma_b = 7.2$	–	610	–	Anderson et al., 2008
				10	18.8	–	40.4	22.4	–	6.2	–	Labrecque et al., 1997
				20	18.8	–	17.6	7.1	–	350	–	
		ATEC	$M_n = 318$	10	19.6	–	50.8	34.5	–	10	–	
				20	19.6	–	30.0	9.6	–	320	–	
		ATBC	$M_n = 402$	10	18.7	–	25.4	17.7	–	2.3	–	
				15	18.7	–	–	$\sigma_b = 21.3$	100	300	–	Anderson et al., 2008
				20	18.7	–	17.0	9.2	–	420	–	Labrecque et al., 1997
PLA ^a	$M_w = 204450$	–	–	–	–	–	58.01	41.69	3364	1.27	–	Sierra et al., 2010
		TBC ^a	$M_n = 360$	12.44	19.6 ^d	–	41.12 ^b	38.27	2542	2.14	–	
				12.99	–	–	37.61 ^b	12.44	1248	>100.23	–	
				15.58	–	–	32.1 ^b	6.39	53	>100.16	–	
				22.52	–	–	21.74 ^b	9.84	55	>102.77	–	
PLA ^c	$M_w = 204450$	–	–	–	–	–	–	41.69	3364	1.27	–	
		TBC ^c	$M_n = 360$	12.44	9.6 ^d	–	39.45	41.95	2301	3.43	–	
				12.99	–	–	36.97	19.97	1337	>99.98	–	
				15.58	–	–	30.37	7.67	313	>100.03	–	
				22.52	–	–	33.95	11.95	159	>100.08	–	
PLA	$M_n = 84000$	–	–	–	–	–	60	66	3300	1.8	–	Baiardo et al., 2003
		ATBC	$M_n = 402$	10	–	–	41	50.1	2900	7	–	
				20	–	–	24	23.1	100	298	–	

(Continued)

Table 3 | Continued

Polymer	Molecular weight (g/mol)	Plasticizer	Molecular weight (g/mol)	Plasticizer content (wt%)	Solubility δ (MPa) ^{0.5}	Interaction parameter χ_T	DSC T_g (°C)	Max. tensile strength (MPa)	Tensile modulus E (MPa)	Tensile elongation at break ϵ (%)	Notched impact strength (kJ/m ²)	References
PLA	$M_n = 74500$	-	-	-	20.1	-	62	66 ± 2	1020 ± 100	11 ± 3	2.6	Murariu et al., 2008a
		ATBC	$M_n = 402$	10	19.2	0.46	44	51 ± 1	970 ± 70	11 ± 4	2.4	
		DOA	$M_n = 370$	20	19.2	0.46	38	30 ± 1	270 ± 20	317 ± 4	4.6	
				10	17.6	1.33	45	29 ± 2	720 ± 90	36 ± 5	2.6	
				20	17.6	1.33	45	21 ± 1	670 ± 120	78 ± 33	28.7	
PLA	$M_n = 218$	GTA	$M_n = 218$	10	20.1	0.34	48	38 ± 3	760 ± 140	8 ± 2	2.7	
				20	20.1	0.34	29	24 ± 1	10 ± 3	443 ± 13	No Break	
				-	-	-	59.2	64.0 ± 1.5	2840 ± 50	3.0 ± 0.3	-	
				10	17.7	3.7	39.9	39.2 ± 4.0	2000 ± 80	2.3 ± 0.2	-	
				20	17.7	3.7	-66.9/26.1	23.1 ± 0.9	430 ± 50	269.0 ± 6.0	-	
PLA	$M_w = 316$	AGM	$M_w = 316$	10	18.5	1.5	45.8	52.1 ± 4.0	2240 ± 100	32 ± 2.1	-	Pillin et al., 2006
				20	18.5	1.5	-65.8/24.3	27.1 ± 3.1	35 ± 5	335.0 ± 2.3	-	
				-	-	-	58.2	47 ± 5	2000 ± 200	6 ± 2	-	
				10	16.67	-	40.8	27 ± 4	1600 ± 100	259 ± 64	-	
				20	16.67	-	40.1	17 ± 1	1400 ± 100	295 ± 89	-	
PLA	$M_n = 63000$	DOA	$M_n = 371$	-	-	-	61	52 ± 2	1800 ± 150	6 ± 1	2.6 ± 0.2	Lemmouchi et al., 2009
				20	-	-	20	20 ± 1	9 ± 1	320 ± 20	No Break	
				-	-	-	61	52 ± 2	1800 ± 150	6 ± 1	2.6 ± 0.2	
				20	-	-	20	20 ± 1	9 ± 1	320 ± 20	No Break	
				-	-	-	20	20 ± 1	9 ± 1	320 ± 20	No Break	

^a Material aged for 10 days.

^b Material aged for 20 days.

^c Material aged for 24 days.

^d (Ljungberg and Wesslén, 2003).

LA, Lactide; TEC, Triethyl citrate; TBC, Tributyl citrate; ATEC, Acetyl triethyl citrate; ATBC, Acethyl tributyl citrate; DOA, Dioctyl adipate (Bis(2-ethylhexyl) adipate); GTA, Glycerin triacetate (Triacetin); DBS, Dibutyl sebacate; AGM, Acetyl glycerol mono-laurate; σ_b , Tensile strength at break.

Table 4 | Table molecular weight and solubility parameters (δ) of some oligomeric and polymeric plasticizers and their Plasticization effects on PLA [Copyright ©(2011) Wiley and Sons; used with permission from Liu and Zhang (2011)].

Polymer	Molecular weight (g/mol)	Plasticizer	Molecular weight (g/mol)	Plasticizer content (wt%)	Solubility δ (MPa) ^{0.5}	Interaction parameter χ_T	DSC T_g (°C)	Max. tensile strength (MPa)	Tensile modulus E (MPa)	Tensile elongation at break ϵ (%)	Notched impact strength (kJ/m ²)	References
PLA	$M_n = 49000$	-	M	0	-	-	58	-	2050 \pm 44	9 \pm 2	-	Martin and Av��rous, 2001
		OLA	-	10	-	-	37	-	1256 \pm 38	32 \pm 4	-	
				20	-	-	18	-	744 \pm 22	200 \pm 24	-	
		PEG400	$M_w = 400$	10	-	-	30	-	1488 \pm 39	26 \pm 5	-	
		M-PEG	$M_w = 400$	20	-	-	12	-	976 \pm 31	160 \pm 12	-	
PLA	$M_n = 84000$			10	-	-	34	-	1571 \pm 51	18 \pm 2	-	Baiao et al., 2003
				20	-	-	21	-	1124 \pm 33	142 \pm 19	-	
		PEG400	$M_w = 400$	0	-	-	60	66	3300	1.8	-	
				10	-	-	23	32.5	1200	140	-	
		PEG1500	$M_w = 1500$	20	-	-	19	15.6	500	71	-	
PLA	$M_w = 74000$			10	-	-	42	46.6	2800	5	-	Pillin et al., 2006
				20	-	-	20	21.8	600	235	-	
		PEG10K	$M_w = 10000$	10	-	-	42	48.5	2800	2.8	-	
				20	-	-	34	22.1	700	130	-	
		PBOH	$M_w = 2100$	0	23.1	-	59.2	64.0 \pm 1.5	2840 \pm 50	3.0 \pm 0.3	-	
PLA *	$M_w = 160000$			10	21.3	2.3	476	56.3 \pm 1.9	2350 \pm 50	3.0 \pm 0.1	-	Hu et al., 2003b
				20	21.3	2.3	-48.5/30.1	30.2 \pm 1.1	350 \pm 20	302.5 \pm 32.0	-	
		PEG200	$M_w = 200$	10	23.5	0.0	35.8	30.0 \pm 4.1	1700 \pm 100	2.0 \pm 0.6	-	
		PEG400	$M_w = 400$	10	22.5	0.1	37.1	39.0 \pm 3.0	1920 \pm 53	2.4 \pm 0.3	-	
				20	22.5	0.1	-50.2/18.6	16.0 \pm 0.3	630 \pm 20	21.2 \pm 2.3	-	
		PEG1000	$M_w = 1000$	10	21.9	0.5	40.2	39.6 \pm 5.0	1970 \pm 120	2.7 \pm 0.3	-	
				20	21.9	0.5	-62.7/22.4	21.6 \pm 0.4	290 \pm 50	200.0 \pm 12.5	-	
		PEG8000	$M_w = 8000$	0	-	-	58	53 \pm 2	2200 \pm 50	14 \pm 1	-	
				10	-	-	36	23 \pm 1	950 \pm 30	200 \pm 10	-	
				15	-	-	30	16 \pm 1	630 \pm 20	260 \pm 10	-	
				20	-	-	21	5 \pm 1	180 \pm 20	300 \pm 20	-	
PLA *	$M_w = 160000$	PEG8000 ^a		30	-	-	9	-	5 \pm 1	500 \pm 20	-	(Continued)
		PEG8000 ^b		30	-	-	-	1 \pm 0.2	40 \pm 5	400 \pm 10	-	
		PEG8000 ^c		30	-	-	14 ⁺	2 \pm 0.2	100 \pm 10	340 \pm 10	-	
		PEG8000 ^d		30	-	-	-	7 \pm 0.3	220 \pm 20	300 \pm 20	-	
		PEG8000 ^e		30	-	-	22 ⁺	9 \pm 0.3	370 \pm 20	250 \pm 10	-	
		PEG8000 ^f		30	-	-	27 ⁺	9 \pm 0.3	400 \pm 20	240 \pm 20	-	

Table 4 | Continued

Polymer	Molecular weight (g/mol)	Plasticizer	Molecular weight (g/mol)	Plasticizer content (wt%)	Solubility δ (MPa) ^{0.5}	Interaction parameter χ_T	DSC T_g (°C)	Max. tensile strength (MPa)	Tensile modulus E (MPa)	Tensile elongation at break ϵ (%)	Notched impact strength (kJ/m ²)	References
PLA*	$M_w = 190000$	PEG8000	$M_w = 8000$	0	–	–	60	68 ± 2	2500 ± 200	3 ± 0.5	–	Hu et al., 2003a
				10	–	–	39	26 ± 1	900 ± 50	180 ± 10	–	
				20	–	–	21	4 ± 0.5	150 ± 20	260 ± 20	–	
				30	–	–	12	–	20 ± 2	300 ± 30	–	
		PEG8000 ^g		30	–	–	–	2.2 ± 0.3	80 ± 5	250 ± 20	–	
				30	–	–	–	3.8 ± 0.3	140 ± 10	230 ± 20	–	
				30	–	–	–	4.5 ± 0.6	150 ± 10	220 ± 10	–	
				30	–	–	–	5.0 ± 0.2	170 ± 15	170 ± 20	–	
PLA	$M_n = 11800$	PPG720	$M_w = 720$	10	–	–	51	52.2	1820	4.2	–	McCarthy and Song, 2002
				20	–	–	38	39.9	1296	260	–	
				10	–	–	42	50.5	2170	4.2	–	
				20	–	–	26	28.5	4.4	250	–	
		PPG640-E ⁱ	$M_w = 640$	0	–	–	–	65.6	2338	4.0	–	
				10	–	–	–	54.9	1827	4.3	–	
				20	–	–	–	33.1	1404	260	–	
				10	–	–	–	54.1	2081	3.9	–	
PLA	$M_w = 108000$	PPG425	$M_w = 530$	0	–	–	55.7	41.4 ± 1.5	–	64 ± 42	–	Kulinski et al., 2006
				10	–	–	33.1	21.0 ± 1.5	–	524 ± 66	–	
				10	–	–	34.0	23.1 ± 0.9	–	473 ± 111	–	
				10	19.93	–	31.3	18.5 ± 1.2	–	427 ± 42	–	
		PPG1000	$M_w = 1123$	0	–	–	–	–	–	–	–	
				10	–	–	–	–	–	–	–	
				10	–	–	–	–	–	–	–	
				10	–	–	–	–	–	–	–	
PLA	$M_n = 63000$	Glyplast® 206/2	$M_n = 1532$	0	21.91	–	58.2	47 ± 5	2000 ± 200	6 ± 2	–	Martino et al., 2009
				10	21.91	–	39.5	34 ± 2	1600 ± 100	5 ± 1	–	
				20	22.87	–	25.4	25 ± 4	200 ± 100	485 ± 65	–	
				10	22.87	–	42.1	36 ± 2	1700 ± 200	7 ± 5	–	
		Glyplast® 206/7	$M_n = 2565$	20	–	–	30.6	28 ± 2	500 ± 100	491 ± 34	–	
				5	–	–	–	77–84	2160–2313	160–200	–	
				–	–	–	–	–	–	–	–	
				–	–	–	–	–	–	–	–	

(Continued)

Table 4 | Continued

Polymer	Molecular weight (g/mol)	Plasticizer	Molecular weight (g/mol)	Plasticizer content (wt%)	Solubility ^{0.5} (MPa)	Interaction parameter χ_T	DSC T_g (°C)	Max. tensile strength (MPa)	Tensile modulus E (MPa)	Tensile elongation at break ϵ (%)	Notched impact strength (kJ/m ²)	References
PLA	$M_n = 81000$	PEG	$M_n = 18500$	10	-	-	-	57–59	1700–1786	180–210	-	Chen et al., 1997
				11	-	-	-	14.5 ± 2.8	423 ± 20	240 ± 21	-	
				20	-	-	-	24.1 ± 3.1	710 ± 21	204 ± 18	-	
		LA-co-PEG	$M_n = 17600$	0	-	-	61	52 ± 2	1800 ± 150	6 ± 1	2.6 ± 0.2	Lemmouchi et al., 2009
				20	-	-	29	21 ± 1	790 ± 180	170 ± 10	1.6 ± 0.6	
PLA	$M_n = 121400$	PPA	$M_n = 1900$	0	-	-	58.6	69.8 ± 3.2	1777 ± 42	6 ± 0.3	~5	Zhang et al., 2013b
				5	-	-	49.3	63.2 ± 3.1	1392 ± 34	6 ± 0.5	~5	
				10	-	-	40.6	49.6 ± 2.9	1305 ± 29	157 ± 28	<10	
				15	-	-	33.3	39.8 ± 2.7	822 ± 26	315 ± 35	<10	
				20	-	-	27.0	25.7 ± 2.2	554 ± 21	362 ± 39	~90	
				25	-	-	24.3	14.4 ± 1.5	374 ± 17	410 ± 44	>100	

An update of the Table 4 has been made by Kfoury et al. in the frame of this review.

*with low stereoregularity, T_g measured from E'' in DMA

^aaging for 6 h.

^baging for 30 h.

^caging for 120 h.

^daging for 500 h.

^eaging for 1800 h.

^faging for 2 h.

^gaging for 10 h.

^haging for 24 h.

ⁱaging for 120 h.

^jaging for 720 h.

^kaging for 3000 h.

LA, lactide; OLA, oligomeric lactic acid; PEG, poly(ethylene glycol), the subsequent number represents its nominal molecular weight; M-PEG, poly(ethylene glycol) monolaurate; PBOH, poly(1,3-butanediol); PPG, poly(propylene glycol), the subsequent number represents its nominal molecular weight; PPG-E, epoxy capped poly(propylene glycol); GlyplastVR 206/2 and GlyplastVR 206/7, two kinds of commercial polymeric adipates with molecular weight of 1532 and 2565 g/mol, respectively; COPO1 and COPO2, two kinds of AB-type block copolymers of DLLA and either PEG350 monomethyl ether or PEG750 monomethyl ether, that is, PDLLA-b-PEG350 (10/4, molar ratio of D,L-LA monomer to PEG350 used in the feed) and PDLLA-b-PEG750 (10/4, molar ratio of D,L-LA monomer to PEG750 used in the feed); COPO3, ABA-type block copolymer of PDLLA and PEG400, that is, PDLLA-b-PEG400-b-PDLLA (10/2, molar ratio of D,L-LA monomer to PEG400 used in the feed); COPO4, 3-star(PEG-b-PDLLA) block copolymer (10/1.3, molar ratio of D,L-LA monomer to 3-star-PEG used in the feed); COPO5, 4-star(PEG-b-PDLLA) block copolymer (10/1, molar ratio of D,L-LA monomer to 4-star-PEG used in the feed); PPA, Poly(1,2-propylene glycol adipate).

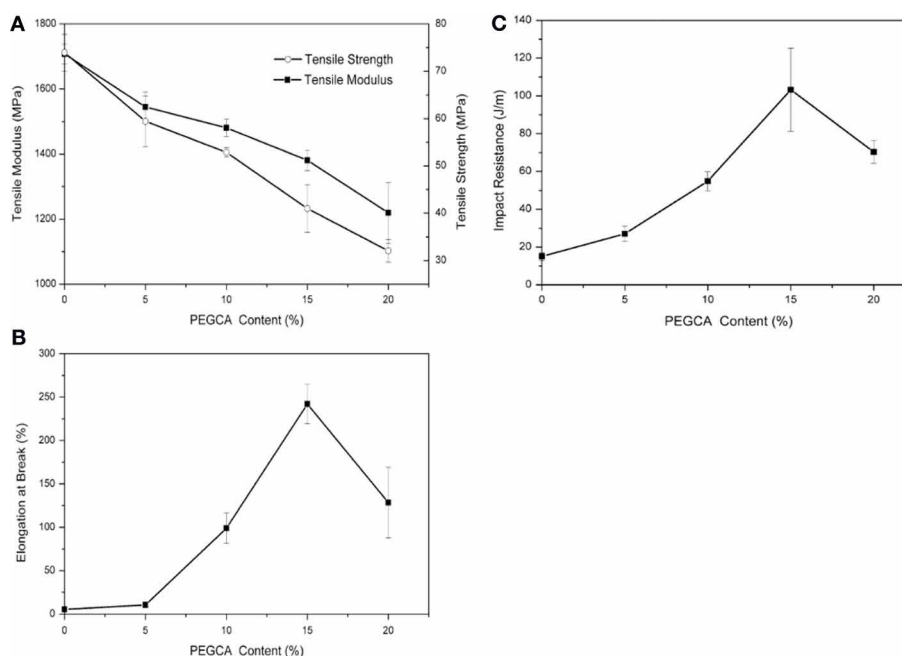


FIGURE 2 | (A) Tensile modulus, tensile strength, **(B)** elongation at break, and **(C)** of neat PLA and PLA/PEGCA blends (Gui et al., 2013, original copyright with kind permission from Springer Science and Business Media).

chemically modify PLA in the presence of “reactive” polyethylene glycol (PEG) derivatives via reactive extrusion (Kfoury et al. *Tunable and durable toughening of polylactide materials via reactive extrusion. Submitted*). In this purpose, polyethylene glycol methyl ether methacrylate (MAPEG) and polyethylene glycol methyl ether acrylate (AcrylPEG) were melt-mixed and extruded with PLA in the absence and in the presence of a free-radical di-tertiary alkyl peroxide, 2,5-dimethyl-2,5-di-(tert-butylperoxy)hexane (Luperox101 or L101). Molecular characterization revealed that in the case of PLA/MAPEG/L101 blends (79.5/20/0.5 wt/wt/wt), about 20% of the initially introduced MAPEG can be grafted onto PLA chains. The remaining fraction (80%) of the plasticizer was a mixture of unreacted/monomeric and “homo-oligomerized” MAPEG. As a result, an efficient plasticization effect was evidenced by a significant lowering of the glass transition temperature (T_g) and storage modulus E' as well as by a drastic increase of the tensile elongation at break of approximately 70 times as compared to neat PLA. More interestingly, in the case of PLA/AcrylPEG/L101 (79.5/20/0.5 wt/wt/wt), up to 65% of the initially introduced AcrylPEG reacted and was grafted onto the PLA chains. The remaining non-grafted AcrylPEG completely homo-oligomerized. As a result, an efficient toughening effect of the resulting materials was reached. This was especially marked by a drastic enhancement of the impact strength, ~ 36 times, and a significant improvement of the elongation at break, ~ 63 times.

Lapol®108 is a renewable bioplasticizer of PLA that can be processed using standard processes such as injection moulding, extrusion coating, thermoforming, and cast films (<http://www.lapol.net/>). It promotes toughness and flexibility without sacrificing modulus, while minimizing the reduction of glass

Table 5 | Comparison of flexural properties of Lapol® HDT blends vs. PLA (unannealed and annealed) (From <http://www.lapol.net/>).

Flexural properties	Modulus (MPa)	HDT ^b (°C)
PLA	3300	55
Annealed PLA ^a	3800	155
20% Lapol HDT in PLA	3800	165

^aPLA was annealed for 10 min at 110°C.

^bHeat deflection temperature is measured using a thermomechanical analyzer using a load of 0.2–0.3 N.

transition temperature. For the lowest plasticizer content (5–10 wt%), the bioplasticizer Lapol®108 seems to be the most convenient one to maintain a good stiffness-toughness balance among this list of investigated plasticizers (**Table 4**). Interestingly, the new Lapol® HDT additive used for increasing the heat deflection temperature of PLA is now available at pilot-production. For many high-performance applications, using PLA requires a high temperature resistance to deformation and deflection, i.e., a heat deflection temperature higher than 100°C. Compounding 20 wt.% of Lapol® HDT with PLA 3001D, 4032D, or 7000D can increase the heat deflection temperature of unannealed PLA from 55°C to about 160°C. This capability greatly expands the potential uses and applications to PLA. This increased heat-performance is achieved without adding inorganic fillers or other additives, although these additions may further enhance some other properties. **Table 5** shows typical flexural properties data for a blend of 20% Lapol® HDT in PLA compared to commercially available neat and annealed PLA.

PLA-based blends containing Lapol® HDT exhibit similar or higher flexural modulus than commercially available PLA (annealed and unannealed). Lapol® HDT may be compounded with an impact modifier to tailor the properties of PLA for specific applications.

Globally, these studies show that oligomeric and polymeric plasticizers are in general less efficient than monomeric ones in order to improve the elongation and reduce the glass transition temperature of resulting blend. However, they have more tendencies to give better stiffness-toughness balance for PLA material compared to small molecule plasticizers. Based on their complementary advantages, the combination of small molecule plasticizers with polymeric or oligomeric ones was also attempted in the literature.

Mixed plasticizers

These mixed plasticizers combine an oligomeric or polymeric plasticizer with a small molecule plasticizer. Therefore, they should lead to a medium level of depression in T_g and more balanced mechanical properties (elongation, modulus and strength) than the individual plasticizers. Some plasticizer combinations were studied. They are reported in Table 6.

In general, one can conclude on the behaviors of the plasticizers in PLA and their effect on the properties of the polymer as follows:

- The addition of 10–20% of plasticizers may be a successful way to remarkably reduce T_g and improve PLA flexibility/ductility/tensile elongation at the same time.
- Substantial reductions in tensile strength and modulus are unfortunately unavoidable.
- An excessive incorporation of plasticizer leads to the saturation of the plasticizer in the amorphous phase of PLA, resulting in a migration or phase separation depending on the plasticizer nature.
- Small molecule or monomeric plasticizers are more efficient in order to improve PLA flexibility/ductility/tensile elongation and decrease its T_g , but less efficient on tensile strength and modulus than oligomeric and polymeric plasticizers.
- The higher the molecular weight of the plasticizer, the lower the critical saturation concentration, at which phase separation begin to occur.
- Lower molecular weight PEGs exhibit good miscibility with PLA and result in more efficient reduction of T_g . This can lead to drastic improvement in ductility and/or impact resistance of PLA at low concentrations.
- After ageing for 1 month, the mechanical properties of the plasticized PLA did not change remarkably. This result indicated that PPG and PPG-E could prevent the physical ageing and the embrittlement of PLA.

Table 6 | Summary of effects of some mixed plasticizers on mechanical properties of PLA [Copyright © (2011) Wiley and Sons; used with permission from Liu and Zhang (2011)].

Polymer	Molecular weight (g/mol)	Plasticizer	Molecular weight (g/mol)	Plasticizer content (wt%)	DSC T_g (°C)	Max. tensile strength (MPa)	Tensile modulus E (MPa)	Tensile elongation at break ϵ (%)	Notched impact strength (kJ/m ²)	Reference
PLA	$M_n = 81000$	–	2	0	61	52 ± 2	1800 ± 150	6 ± 1	2.6 ± 0.2	Lemmouchi et al., 2009
		TBC	$M_n = 360$	20	20	20 ± 1	9 ± 1	320 ± 20	No break	
		COPO1	$M_n = 650$	20	29	21 ± 1	790 ± 180	170 ± 10	1.6 ± 0.6	
		COPO2	$M_n = 1000$	20	26	25 ± 1	300 ± 50	220 ± 20	8.3 ± 2.5	
		COPO3	$M_n = 1050$	20	36	30 ± 1	1700 ± 100	130 ± 20	1.9 ± 0.6	
		COPO4	$M_n = 1750$	20	35	24 ± 2	1150 ± 150	170 ± 10	1.9 ± 0.7	
		COPO1/TBC	–	10	42	40 ± 2	2000 ± 110	4 ± 1	2.7 ± 0.2	
				20	24	17 ± 1	9 ± 1	260 ± 20	6.4 ± 1.9	
		COPO2/TBC	–	10	–	27 ± 2	1480 ± 80	140 ± 20	2.4 ± 0.2	
				20	26	24 ± 1	19 ± 5	260 ± 10	No break	
		COPO3/TBC	–	10	–	37 ± 1	1850 ± 200	4 ± 1	–	
				20	25	16 ± 1	16 ± 7	300 ± 20	–	
		COPO4/TBC	–	10	41	39 ± 2	2000 ± 100	4 ± 1	2.5 ± 0.2	
				20	27	22 ± 1	150 ± 65	250 ± 10	5.5 ± 0.8	
		COPO5/TBC	–	10	47	37 ± 1	1950 ± 150	4 ± 1	2.5 ± 0.2	
				20	23	20 ± 1	400 ± 140	260 ± 20	3.8 ± 1.1	

TBC, tributyl citrate; COPO1 and COPO2, two kinds of AB-type diblock copolymers of PDLLA and either PEG350 monomethyl ether or PEG750 monomethyl ether, that is, PDLLA-b-PEG350 (10/4, molar ratio of D,L-LA monomer to PEG used in the feed) and PDLLA-b-PEG750 (10/4, D,L-LA monomer to PEG molar ratio used in the feed); COPO3, ABA-type triblock copolymer of DLLA and PEG400, that is, PDLLA-b-PEG400-b-PDLLA (10/2, molar ratio of D,L-LA monomer to PEG used in the feed); COPO4, 3-star-(PEG-b-PDLLA) block copolymer (10/1.3, molar ratio of D,L-LA monomer to PEG used in the feed); COPO5, 4-star-(PEG-b-PDLLA) block copolymer (10/1, molar ratio of D,L-LA monomer to PEG used in the feed).

- Whilst increasing the molecular weight of the plasticizer can slow down migration rate and thus improve morphological stability of PLA materials during storage, it also decreases its solubility and plasticizing efficiency. Additionally, high-molecular weight plasticizers are keen to phase-separation because of low saturation concentrations of plasticizers.

COMPOUNDING WITH FLEXIBLE/SOFT POLYMERS—PARTIALLY MISCIBLE TO IMMISCIBLE BLENDS—WAYS OF COMPATIBILIZATION

The term “blending” refers to the simple mixing of polymeric materials in the molten state. During the last three decades, polymer blends have become a very important part of the commercialization of polymers because one can tailor blend compositions to meet specific end-use requirements (Baker et al., 2001). Melt-blending polymers is a much more economical and convenient methodology at the industrial scale rather than synthesizing new polymers to achieve the properties unattainable with existing polymers. However, most polymer pairs are immiscible, which can lead to phase-separated materials. The latter has often three inherent problems if the morphology and the interfaces of the blend are not well-controlled: (1) poor dispersion of one polymer phase in the other one; (2) weak interfacial adhesion between the two phases; and (3) instability of immiscible polymer blends (Baker et al., 2001). However, immiscible polymer blends are much more interesting for commercial development because immiscibility allows maintaining the good features of each polymeric component of the blend. One of the most important challenges is thereby to develop compatibilization techniques that allow controlling both the morphology and the interfaces of phase-separated blends. In general, compatibilization in physical blends is tuned by the physical interactions (hydrogen bonds, Van der Waals interactions etc.) between the blend components.

PLA has been blended with various polymers for different purposes, namely for improving its stiffness-toughness balance. A variety of biodegradable and non-biodegradable soft polymers have been used as toughness modifiers for PLA. Recently, it has been shown that new impact modifiers can efficiently strengthen/toughen brittle/stiff PLA, due to their core-shell polymeric structure (a block copolymer). They form a soft or elastomeric block having high compatibility and miscibility with the toughening polymer, and surrounded with a rigid block copolymer, usually having a high compatibility and/or miscibility with the matrix polymer. When the softer component forms a second phase within the stiffer continuous phase, it may act as a stress concentrator, which enables ductile yield and prevents brittle failure (Babcock et al., 2008). At the same time, the core is “locked in” by slight crosslinking and grafting with its shell to avoid phase-separation during blending. Moreover, the adhesion between the two phases, core-shell polymer and polymer matrix, depends strongly on the degree of miscibility of the shell polymer with the matrix, *that is*, whether they are completely miscible, partially miscible, or immiscible. However, a partial miscibility between core-shell modifiers and polymeric matrix is often necessary to obtain blends of desired impact properties. From the literature, multiple crazing initiated from the dispersed rubber phase is recognized to be one of the main mechanisms, which increases

the toughness of glassy materials like polylactide-based materials (Ikeda, 1993; Bucknall, 2007; Mahajan and Hartmaier, 2012). Some authors have preferred to blend PLA with biodegradable flexible/soft polymers in order to preserve the overall biodegradability of resulting blends. Some of these blends are in this regard, finding short-term applications, namely packaging and mulch films for agriculture.

Flexible/soft (ϵ -Caprolactone)-based copolymers

As obtained by ring-opening polymerization of ϵ -caprolactone, poly(ϵ -caprolactone) (PCL) is a biodegradable and flexible/soft polyester with a melting temperature of 60°C and a glass transition temperature of -60°C. Due to the low glass transition temperature, PCL-based materials were considered as interesting impact modifiers. PCL and PLA blends have been extensively investigated over the past years. For instance, Broz et al. investigated the tensile properties of blends made of P(D,L-LA) and PCL at different content in PCL (Broz et al., 2003). Whilst the strain-at-failure decreases monotonically for PCL contents from 0.6 wt%, the modulus and tensile strength increased almost linearly with composition. This was more likely ascribed to some strengthening of the blend interface in this regime. However, DSC and NMR results suggested that PCL was able to crystallize to a certain extent within PCL/P(D,L-LA) blends, indicating that phase-separation was more pronounced under these conditions. However, as shown here, the simple melt blending of PLA and PCL usually results in a marginal toughness improvement because of their poor miscibility (López-Rodríguez et al., 2006). This can be more likely explained by the fact that PCL can readily crystallize within PLA/PCL blends, leading to the more pronounced phase-separation. Accordingly, the simple melt blending of PLA and PCL usually leads to a marginal improvement in toughness because of their immiscibility (López-Rodríguez et al., 2006; Vilay et al., 2009). In this regard, some of us have designed bio-sourced and hydrolytically degradable random copolyesters based on poly(ϵ -caprolactone) as a soft core component. (Co)polymerization of CL with other lactones affords an elegant way to modulate the thermal and mechanical properties of resulting PCL-based materials. The most interesting feature was that the overall crystallinity of these (co)polyesters decreased with the comonomer content, yielding rubbery-like materials at ambient temperature. When dispersed into glassy materials like PLA, it is well-known that rubbery microdomains can readily absorb the impact energy. In a first study (Odent et al., 2012), 10 wt.% of amorphous poly(ϵ -caprolactone-co- δ -valerolactone) (P[CL-co-VL]) random aliphatic copolyesters were thereby synthesized and investigated as biodegradable impact modifiers for commercial PLA using a microcompounder. The use of a high molar mass copolyester (M_n = ca. 60,000 g/mol) with a molar composition of 45/55 mol% (CL/VL) resulted in the optimal improvement in notched Izod impact strength for compression-moulded (vs. injection-moulded) PLA materials (7 kJ/m²) compared to 2.5 kJ/m² for PLA. According to the author, this improvement in toughness is also related to the mean size (0.7 μ m) and size distribution of the dispersed copolymer micro-domains throughout the PLA matrix. In a similar study (Odent et al., 2013b), the random biocopolyester was synthesized and used as impact

modifier is poly(ϵ -caprolactone-*co*-D,L-lactide) (P[CL-*co*-LA]). By varying the comonomer content, a phase inversion was noticed. A control of the affinity between PCL-based impact modifiers and PLA matrix gives access to a mixture of spherical microdomains with similar range of optimum particles diameter (i.e., 0.9 μ m) and nanosized oblong structures, involving a combination of shear yielding and multiple crazing mechanisms. As a result, PLA blended with 10 wt.% of the CL/LA composition 72/28 mol.% displayed a maximum impact strength of about 11.4 kJ/m² (Figure 3). The mean size of the rubbery micro-domains was 0.9 μ m in this case.

In the case of brittle polymers, spherical microdomains act as stress reservoirs and initiate crazing upon the microdomains size, i.e., larger microdomains size than 0.5 μ m are required to nucleate crazing mechanism and enhance fracture energy absorption (Donald and Kramer, 1982; Van Der Wal and Gaymans, 1999). Accordingly, an optimum particle size range (ca. 0.7–0.9 μ m) for PLA toughening was identified by correlating dispersed microdomains size with notched Izod impact strength (Gramlich et al., 2010; Liu et al., 2011). Wu and al. correlated rubber particle diameter with chain structure parameter of the matrix and claimed that the optimum particle size for toughening decreased as the matrix becomes less brittle (Wu, 1990). Kowalczyk et al. reported that rubbery poly[1,4-*cis*-isoprene] microdomains within PLA-based materials initiated crazing at the early stages of deformation, immediately followed by the cavitation phenomena inside rubbery microdomains. This latter promotes further shear yielding for PLA matrix (Kowalczyk and Piorkowska, 2012). More recently, some of us have elaborated ultratough PLA-based materials by synergistically adding PLA, rubber-like poly(ϵ -caprolactone-*co*-D,L-lactide) copolyester and silica nanoparticles using extrusion techniques (Odent et al., 2013a). A peculiar alteration for the phase-morphology of the rubbery phase within PLA matrix was achieved by co-adding copolyester and silica nanoparticles into

PLA matrix. It resulted that regularly obtained spherical nodules convert into almost continuous features after adding nanoparticles in the PLA-based melt-blend. In the latter, an enhancement of 15-fold impact strength was obtained by comparison to unfilled PLA.

The use of small molecule reactive additives during compounding has been demonstrated to be an effective way to improve the compatibility between PLA and PCL. Wang et al. (1998) investigated the tri-phenyl phosphate (TPP) as a catalyst or coupling agent for the preparation of PLA and PCL blends. The addition of 2 phr TPP to PLA/PCL (80/20, w/w) blend during processing resulted in a higher elongation (127 vs. 28%) and tensile modulus (1.0 GPa vs. 0.6 GPa) compared to the binary TPP-free blend. The balance between degradation of molecular weight and the formation of copolymer was believed to govern the final mechanical properties of the blends. Reaction time and molecular weight of PCL used were found to have remarkable effects on mechanical properties of the blends. Higher molecular weight PCL ($M_n = 80,000$ g/mol) and medium reaction time (15 min) promoted the largest improvement of the ductility. In another study, di-cumyl peroxide (DCP) was used to promote reactive compatibilization of the PLA/PCL blends (Semba et al., 2006). The results showed again that the addition of DCP increased the ductility of the final material. Further addition of DCP beyond the optimum amount had an opposite effect on elongation. AFM observation revealed that the diameter of the dispersed PCL domains decreased with increasing DCP content. The addition of 0.3 phr DCP to the optimum ratio PLA/PCL = 70/30 resulted in (1) an impact strength of 2.5 times more than that of neat PLA, (2) an improved blend compatibility, (3) an improved ultimate tensile strain (4) a yield point and ductile behavior under tensile test, and (5) mechanical properties comparable to those of HIPS and ABS. In contrast, the addition of DCP to PLA alone did not alter mechanical properties. It was suggested that DCP caused crosslinking of PLA with PCL and therefore improved interfacial adhesion. Depending on feeding procedure, addition of DCP *via* the splitting feeding method resulted in a higher reverse Izod impact strength than feeding at once through the main hopper (Semba et al., 2007). Lysine tri-isocyanate (LTI) as a reactive compatibilizer improved the compatibility of PLA and PCL, resulting in the reduction of size of PCL spherulites (Takayama and Todo, 2006; Takayama et al., 2006). Impact fracture toughness markedly improved by increasing LTI content, which was attributed to the strengthening structure of the blend as a consequence of crosslinking reactions. The compatibilizing effect of LTI was compared with four other reactive processing agents on the PLA/PCL (80/20, w/w) blends (Harada et al., 2008). The addition of 0.5 phr of each reactive agent resulted in an increase in the un-notched Charpy impact strength in the order of LTI > LDI (lysine diisocyanate) > Duranate TPA-100 [1,3,5-tris(6-isocyanatohexyl)- 1,3,5-triazinane-2,4,6-trione] > Duranate 24A-100 [1,3,5-tris(6-isocyanatohexyl)biuret] > Epiclon 725 (trimethylolpropane triglycidyl ether). It was assumed that the reaction of isocyanates group with both terminal hydroxyl and carboxylic groups of polyesters accounted for improved compatibility at the PLA/PCL interfaces and therefore the enhancement in the physical properties.

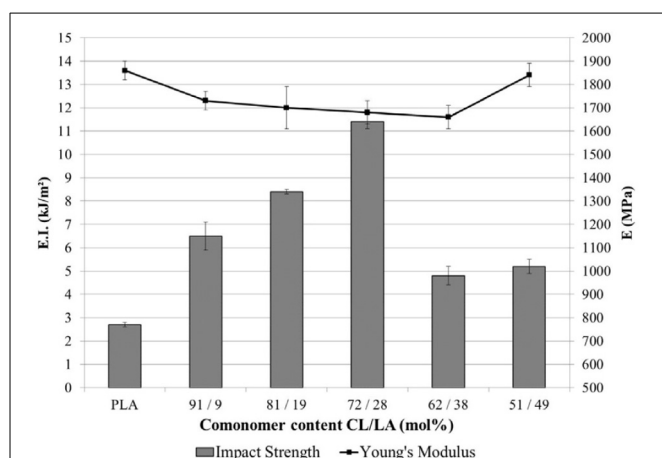


FIGURE 3 | Influence of the LA comonomer content of copolyester on the notched Izod impact strength and Young's modulus of PLA-based materials containing 10 wt.% of P[CL-*co*-LA]. [Reprinted from Odent et al. (2013b) with permission from Elsevier].

Polyhydroxyalkanoates (PHAs) and their copolyesters

Polyhydroxyalkanoates (PHAs) are biodegradable polyesters produced by bacterial fermentation of sugar or lipids (Steinbüchel and Valentin, 1995; Zinn et al., 2001; Poirier, 2002; Noda et al., 2005) when nutrient shortage is present. Since the range of monomers available is impressive within this family, the mechanical properties of PHAs can range from stiff thermoplastics to elastomers dependent on their pendent alkyl chain length (**Scheme 1A**). However, only one grade, i.e., Nodax™, was industrially implemented by Procter and Gamble Co., which correspond to copolymers of 3-hydroxybutyrate with a small amount of 3-hydroxyalkanoate as co-monomer (**Scheme 1B**) (Noda et al., 2004, 2005).

In this regard, Noda et al. (2004) melt-blended PLA with a poly(3-hydroxybutyrate-co-3-hydroxyhexanoate) copolymer, i.e., NodaxH6, containing 5 mol% of 3-hydroxyhexanoate (3-HH) unit. The PLA/NodaxH6 (90/10, w/w) blend exhibited a tensile toughness of 10 times more than that of neat PLA and an elongation superior to 100%. When NodaxH6 content was less than 20 wt % in the blends, its crystallization was largely restricted and thereby NodaxH6 was dispersed as rubbery amorphous droplets within PLA, suggesting that the material was toughened by craze-initiation. Furthermore, it was interesting that the inclusion of these small amounts of PHA did not compromise the optical clarity of PLA itself.

Schreck and Hillmyer investigated the impact toughness of blends of PLLA with a NodaxH6 containing 7 mol.% of 3-HH (Schreck and Hillmyer, 2007). The PLLA/NodaxH6 (85/15, w/w) blend demonstrated a twofold increase in notched Izod impact strength (44 J/m) compared with that of PLLA (22 J/m). Ma et al. toughened PLA by melt-compounding with fully bio-based and

bio-compostable poly(β -hydroxybutyrate-co- β -hydroxyvalerate) (PLA/PHBV) with high β -hydroxyvalerate content (40 mol%) (Ma et al., 2013). The blends displayed two separate glass transition temperatures and two separate phases, indicating that the PLA and PHBV were immiscible. The toughness and the ductility of PLA can be effectively improved by incorporation of 10–30 wt% of the PHBV as evidenced by a significant increase in the elongation at break and the impact toughness (**Table 8**). The local deformation mechanism revealed that fibrillation, partial interfacial de-bonding, cavitation and matrix yielding were involved in the toughening mechanism of the PLA/PHBV blends under impact and tensile testing conditions.

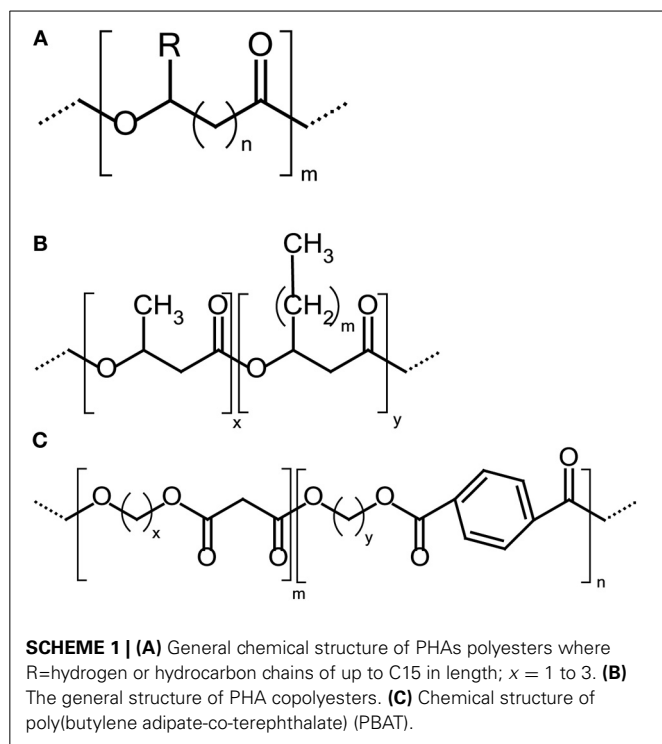
Biodegradable poly(butylene adipate) (PBA), poly(butylene succinate) (PBS), and poly(butylene adipate-co-butylene terephthalate) (PBAT)

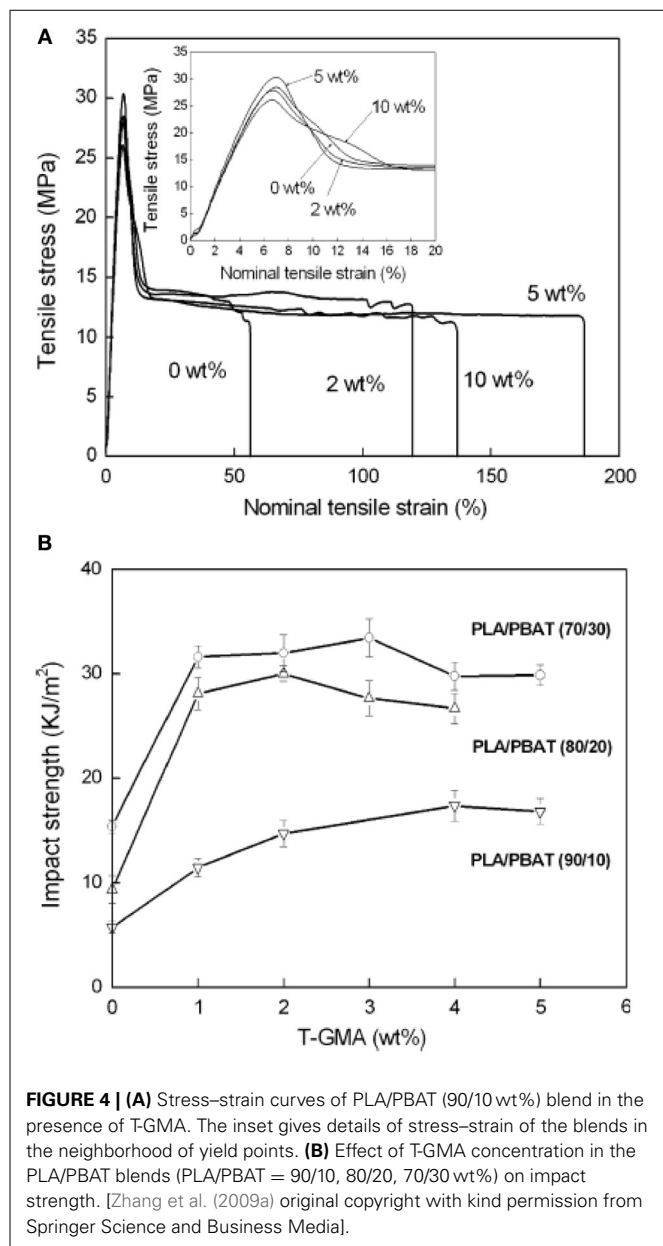
Poly(butylene adipate-co-terephthalate) (PBAT) is a fully biodegradable aliphatic–aromatic copolyester (**Scheme 1C**), which is commercially available under the trade name of EcoflexVR (BASF Co.).

PBAT has similar thermal properties to those of LDPE, but exhibits higher mechanical properties, more particularly higher flexibility and ductility (elongation > 700%). Even though PLA/PBAT blend are immiscible, PBAT could be dispersed in PLA with an average particle size of about 0.3–0.4 μm without use of compatibilizers in co-rotating twin-screw extruder (Jiang et al., 2006). The mechanical properties of the different PLA/PBAT blends are reported in **Table 8**. It was demonstrated that the de-bonding-induced shear yield was responsible for the remarkable high extensibility of the blends. Because of weak interfacial adhesion in the blends, impact toughness was slightly improved. Interestingly, the PLA/PBAT blends are now being commercially produced by BASF Co. under the trademark EcovioVR for film and extruded foam applications.

To improve the compatibility of PLA/PBAT blends, a random terpolymer of ethylene, acrylate ester, and glycidyl methacrylate (referred as “T-GMA”) was investigated as a reactive compatibilizer in melt compounding (Zhang et al., 2009a). Regardless the PLA/PBAT blends composition (70/30, 80/20 or 90/10 wt/wt), the increase of T-GMA content up to 5 wt% resulted in a great improvement of tensile nominal strain at break (**Figure 4A**) and the notched impact strength (**Figure 4B**) to reach more than 150% and 30 kJ/m², respectively, approximately two times that of the uncompatibilized binary blends. These results were correlated to the good miscibility and interfacial adhesion between PLA and PBAT, leading to a shear yielding mechanism when increasing the T-GMA content. The authors attributed the better interfacial adhesion to the *in situ* reactive compatibilization phenomena (**Scheme 2A**).

Lin et al. (2012) compatibilized the biodegradable blends poly(lactic acid) (PLA)/poly(butylene adipate-co-terephthalate) (PBAT) by *in situ* transesterification using various amounts of tetrabutyl titanate (TBT) as catalyst. The incorporation of 0.5% of TBT into PLA/PBAT blends not only improved their overall mechanical properties as well as gave values of tensile strength, elongation at break and impact strength of 45 MPa, 298% and 9 kJ/m² (**Figures 5A,B**), respectively. It was also demonstrated





that the storage modulus of the blends and glass transition temperature (Figure 5C) were enhanced compared to the binary blends free of TBT. The SEM micrographs demonstrated that the compatibility between PLA and PBAT was improved *via* transesterification during reactive melt-extrusion. The interfacial debonding and the yielding deformation were the most important mechanisms to improve toughness.

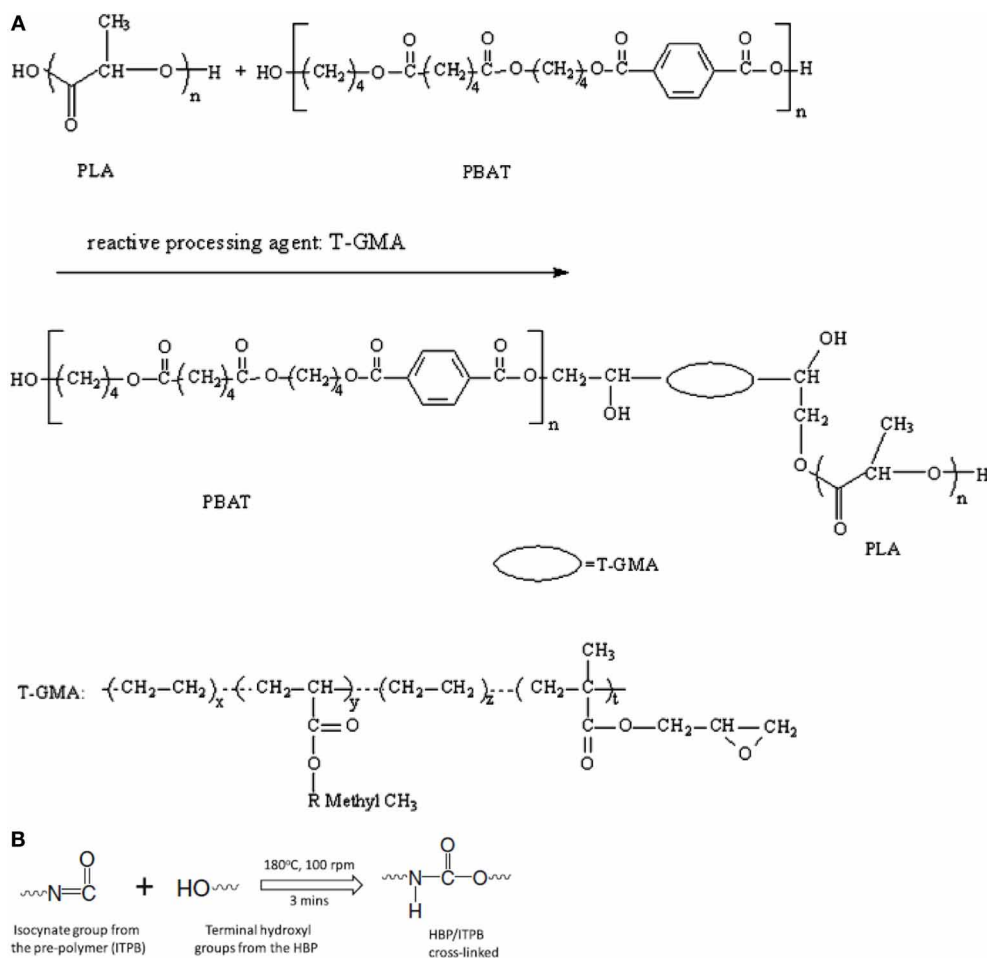
Poly(butylene succinate)s (PBS) and their copolyesters

PLA is immiscible with PBS. In some studies, a third *in situ* reactive component was incorporated to improve compatibility. PBS was melt blended with PLA without compatibilizer and using LDI and LTI as compatibilization agents (Harada et al., 2007). For all PLA/PBS compositions ranging from 90/10 to 80/20 wt.%, only the addition of 0.5 wt.% of LDI or 0.15 wt.% of LTI increased

the elongation at break to more than 150%. Impact strength also increased to reach 50–70 kJ/m². For PLA/PBS (80/20 wt/wt) with LTI, the un-notched samples did not break during the impact test. Furthermore, due to the addition of 0.15 phr LTI into the PLA/PBS (90/10, wt/wt) blend, the size of dispersed PBS particles was significantly reduced. Consequently, LTI was an effective reactive processing agent capable of increasing the toughness of the PLA/PBS blends. Similar results were observed by using LTI with PLA/PBSL (Vannaladsaysy et al., 2009) with effectively improved blend compatibility and higher energy dissipation during the initiation and propagation of crack growth. This results in the suppression of spherulite formation of PBSL and the formation of a firm structure made of entanglements between both PLLA and PBSL chains. DCP was also used for *in situ* compatibilization of the PLLA/PBS (80/20 wt/wt) blend (Wang et al., 2009). The uncompatibilized blend showed much higher elongation than PLLA (250 vs. 4%), but only slightly higher notched Izod impact strength (3.7 kJ/m² vs. 2.5 kJ/m² for PLA). Addition of 0.1 phr DCP greatly increased the impact strength of the blend to 30 kJ/m². Both strengths and moduli invariably decreased with increasing DCP content. It was found that the addition of DCP led to a reduction in the size of the PBS domains and improved interfacial adhesion between the PLLA and PBS phases. The toughening effect of the blends was considered to be related to the de-bonding initiated shear yielding. In a similar way, blending PLA with other polycondensates like biodegradable poly(butylene adipate) (PBA) and poly(butylene succinate) (PBS) was also investigated on the toughening effect. These results were compared with PBAT/PLA blends. Like PBAT, these (co)polyesters can be readily synthesized by melt-polycondensation (Zhao et al., 2010). As far as blends are concerned, a considerably high elongation at break with a moderate loss of strength was observed for all the blends, regardless the investigated copolyesters. For instance, the elongation at break and the impact strength increase with polyester content, until reaching maximum values (>600% and >35 KJ/m², respectively) at a PBA/PBS/PBAT content of 15 and 20%, respectively. The addition of PBA/PBS/PBAT into PLA improves the toughness, but reduces the stiffness of the latter. Moreover, the crystallization ability of PLA blends can be increased by the addition of a small amount of PBS/PBA/PBAT.

Poly(ethylene oxide-*b*-amide-12) (PEBA) or Pebax®

Biosourced and biodegradable poly(ethylene oxide-*b*-amide-12) (PEBA) was used as a toughening agent for PLA *via* melt compounding. PLA/PEBA blends are an immiscible system with a two-phase morphology (Han et al., 2013). By increasing the PEBA content, the binary blends displayed a marked improvement in toughness. All PLA/PEBA blends showed a clear stress yielding on the stress–strain curves with necking when the PEBA contents varied from 10 to 30%. For the blend with 20% PEBA, the elongation at break markedly increased to 346%, corresponding to a 50-fold increase compared with the elongation at break of neat PLA. The impact strength of the blend was significantly enhanced at 20% (or more) of added PEBA as well. The maximum impact strength reached was of 60.5 kJ/m², indicating that a significant toughening effect was achieved (Table 8). The phase morphology evolution in the PLA/PEBA blends during



SCHEME 2 | (A) Predicted reaction of PLA, PBAT, and T-GMA [Zhang et al. (2009a), original copyright with kind permission from Springer Science and Business Media]. **(B)** Schematic showing the proposed *in-situ* crosslinking of the terminal hydroxyl

groups from HBP or PLA with isocyanate groups from the ITPB during reactive blending in extruder at 180°C [Nyambo et al. (2012), original copyright with kind permission from Springer Science and Business Media].

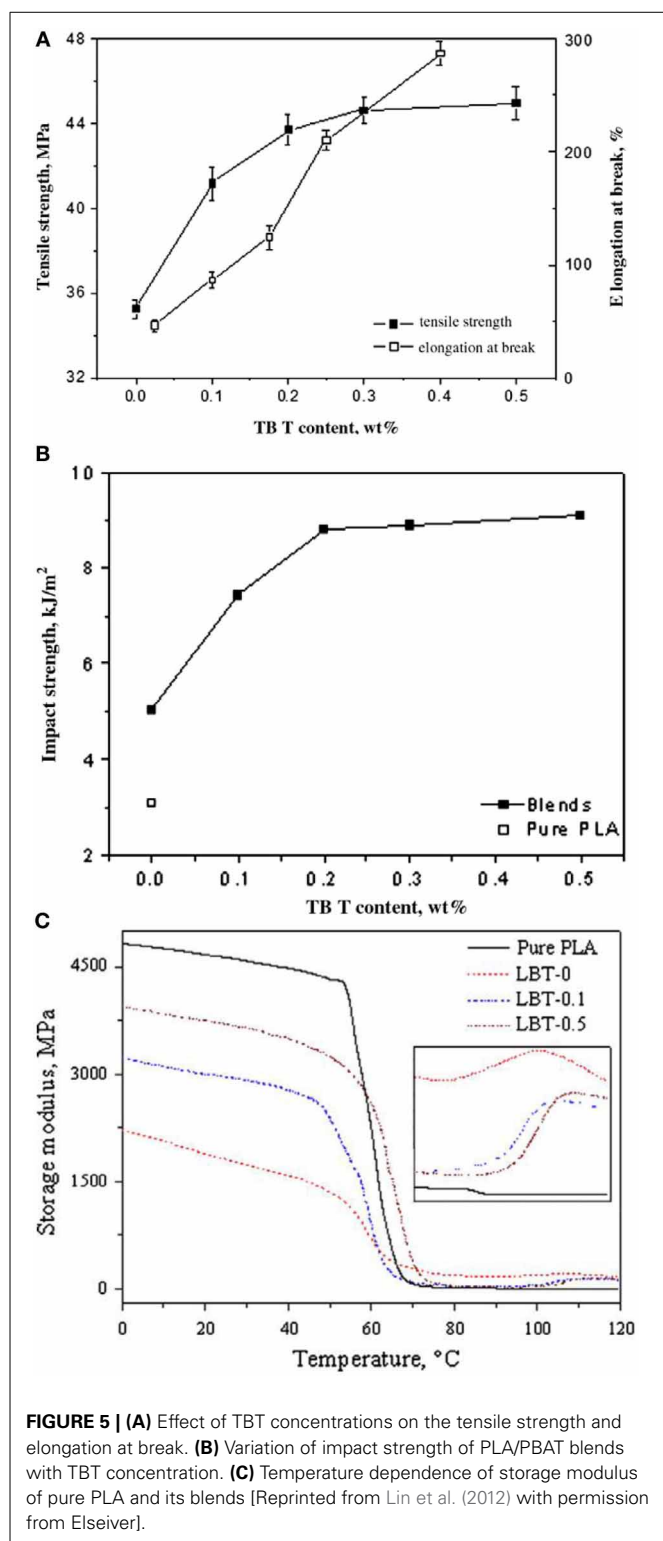
tensile and impact tests were investigated, and the corresponding toughening mechanism was discussed. Remarkably, a clear shear yielding bands perpendicular to the stretching direction and crack propagation along the tensile direction were observed during the tensile test. Moreover, the obvious plastic deformation in the blend was observed during the impact test. The shear yielding induced energy dissipation and therefore led to the improvement in toughness of the PLA/PEBA blends.

Polyurethane and polyamide elastomers

Feng et al. used a thermoplastic polyurethane (TPU) elastomer with a high strength, toughness and biocompatibility to prepare PLA/TPU blends suitable for a wide range of applications of PLA as general-purpose plastics (Feng and Ye, 2011). The morphological structure and mechanical properties of the PLA/TPU blends indicated that an obvious yield and neck formation was observed for the PLA/TPU blends (**Figure 6A**). The stress-strain curves of the blends exhibited an elastic deformation stress plateau, indicating the transition of PLA from brittle to ductile fracture.

The elongation at break and notched impact strength for the PLA/20 wt% TPU blend reached 350% and 25 kJ/m², respectively, without an obvious drop in the tensile strength (**Figure 6B**). The respective T_g 's of PLA and TPU in the blends also shifted to intermediate values, suggesting a partially miscible system due to the hydrogen bonding formed between the chains of TPU and PLA. Spherical particles of TPU dispersed homogeneously in the PLA matrix, and the fracture surface presented much roughness. With increasing TPU content, the blends exhibited increasing tough failure thanks to the improved crack initiation resistance and crack propagation resistance. It was evident that the use of TPU greatly improved the toughness of PLA.

In a similar study, Han et al. also investigated the toughness effect of TPU on PLA (Han and Huang, 2011). The study of the blends morphology as a function of TPU contents showed that PLA was incompatible with TPU. The spherical particles dispersed in PLA matrix, and the uniformity decreased with increasing TPU content. There existed long threads among some TPU droplets in blend with 30 wt.% TPU. After addition of



30 wt.% TPU, the elongation at break of the blend reached about 600% (Figure 7), and the samples could not be broken up in the notched Izod impact tests at room temperature. The toughening mechanism was analyzed through three aspects, including the stress whitening, matrix ligament thickness, and observation of

the fracture surface of the impacted sample. The matrix ligament thickness of the PLA/TPU blends was below the critical value, and the blends deformed to a large extent because of shear yield initiated by stress-concentrations and interfacial de-bonding. This resulted in the formation of fibers in both tensile and impact samples and the dissipation of a large amount of energy.

Some other blends with polyurethane (PU) and polyamide elastomers (PAE) were elaborated in order to study their mechanical properties (Table 7). PLA/PU blends were found to be partially miscible, and PU was dispersed in PLA within domain sizes at the submicrometer scale. It was demonstrated that matrix shear yielding initiated by de-bonding at the matrix/particle interface was considered to be responsible for the improved toughness. Their mechanical properties are reported in Table 8.

Dynamic mechanical analysis (DMA) demonstrated a good compatibility between PAE and PLA blends. A good tough dispersion of PAE in PLA matrix was shown in SEM images. When the PAE content was fixed to 10%, the tensile strength of blend was similar to that of neat PLA, and the elongation increased significantly to 194.6%. Remarkably, the blends showed a wonderful shape-memory effect. PAE domains act as stress concentrators in system with the stress release locally and lead to energy-dissipation process. This prevents PLA matrix from breaking under high deformation, and lead to the PLA molecular orientation. Consequently, the blends submitted to deformation upon tensile load, and heating up the material reform the shape back to the original shape. Table 8 lists the obtained results.

Natural rubber

Natural rubber (NR) can be a good impact modifier candidate for PLA because it is derived from renewable resource. However, because of its incompatibility with PLA, it does not provide the desired improvement of PLA toughness. It has also several properties and appearance issues. Interestingly, epoxidized natural rubber (ENR) is more compatible with PLA. The toughness of the final material is dependent on the level of epoxy functions present in the ENR. Bitinis et al. investigated some formulations of natural rubber (NR)–PLA blends (Bitinis et al., 2011). The rubber phase was uniformly dispersed in the continuous PLA matrix with a droplet size ranging from 1.1 to 2.0 μm . The ductility of PLA was significantly improved from 5% for neat PLA to 200% by adding 10 wt.% NR as reported in Table 8. At this concentration, the rubber droplets provided an optimum balance between their coalescence and their beneficial effect provided on the material's physical and mechanical behavior, without sacrificing totally the transparency of the material. Moreover, the small molecules contained in the elastomeric phase could be acting as nucleating agent, favoring the crystallization ability of PLA. According to the authors, these materials are, therefore, very promising for industrial applications.

Zhang et al. toughened PLA with epoxidized natural rubber (ENR) by melt-blending in an internal mixer (Zhang et al., 2013a). Whilst the stiffness of the material was slightly reduced, the impact strength of the latter could be improved to 6-fold values as compared to that of pure PLA. Again, the authors attributed this enhancement to a good interfacial adhesion between ENR and PLA.

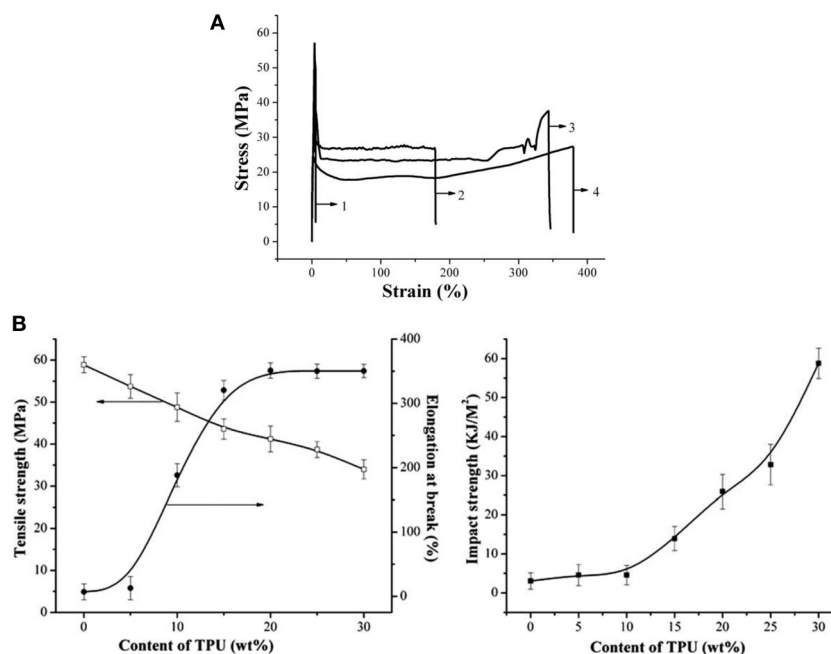


FIGURE 6 | (A) Tensile stress–strain curves of the PLA/TPU blends: (1) PLA/TPU (100/0), (2) PLA/TPU (90/10), (3) PLA/TPU (80/20), and (4) PLA/TPU (70/30). **(B)** Mechanical properties of the PLA/TPU blends as a function of the TPU content. Copyright (2010) Wiley; used with permission from Feng and Ye (2011).

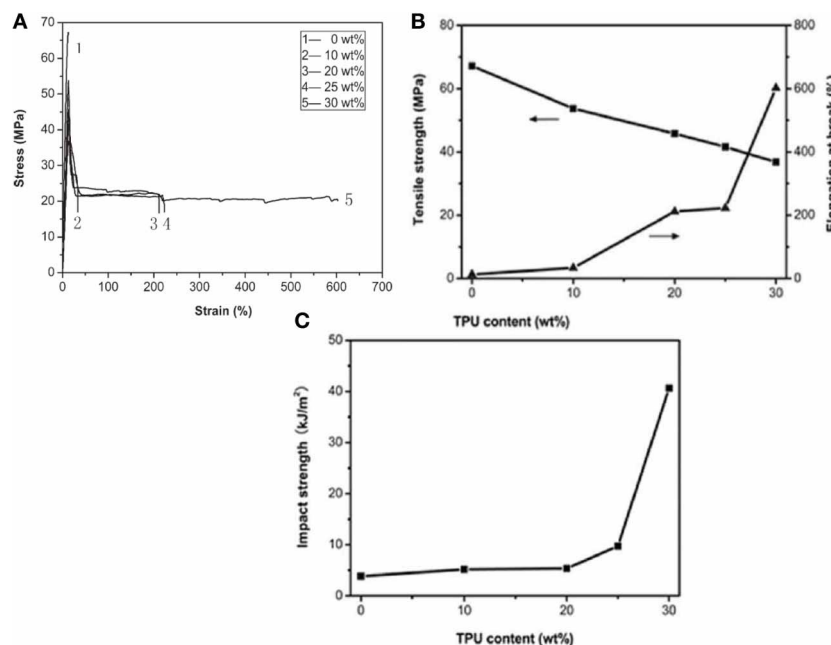


FIGURE 7 | (A) Stress–strain curves, **(B)** Tensile properties, and **(C)** Impact strength of PLA/TPU blends with different TPU contents. Copyright (2011) Wiley; used with permission from Han and Huang (2011).

Ge et al. blended PLA with glycerol monostearate (GMS) (Ge et al., 2013) (**Figure 8**). SEM micrographs of the impact fracture surfaces of PLA/GMS blends had a relatively good separation and this phenomenon was in good agreement with their higher impact strength. The result showed that the addition of GMS

enhanced the flexibility of PLA/GMS blends as compared to neat PLA. The impact strength changed from 4.7 kJ/m² for neat PLA to 48.2 kJ/m² for 70/30 PLA/GMS blend (**Table 8**).

Ma et al. studied the influence of vinyl acetate (VA) content in ethylene-*co*-vinyl acetate copolymer (EVA) rubbers (Levapren®)

Table 7 | Blends with biodegradable elastomers and rubbers.

Elastomer category	Elastomer name	PLA/Elastomer (wt/wt)	Tensile strength (MPa)	Tensile modulus E (GPa)	Tensile elongation ϵ (%)	Izod impact strength (J/m)	References
–	–	100/0	65	–	4	64 (Unnotched) 27 (Notched)	Li and Shimizu, 2007
Biodegradable PU Elastomer	Thermoplastic Poly(ether)urethane	70/30	31.5	–	363	315 (Unnotched)	Natureworks LLC, 2007
	Pellethane™2102-75A	70/30	–	–	410	769 (Notched)	
–	–	100/0	46.8	1.8	5.1	–	Zhang et al., 2009b
Biodegradable Polyamide Elastomer	Thermoplastic PAE	5	48.1	1.5	161.5	–	
		20	23.4	–	184.6	–	

on toughening mechanisms of PLA-based materials (Ma et al., 2012) (**Figure 9**). They showed that the increase of VA content improves the compatibility between the components of the blend, since PLA is miscible with PVAc (no phase separation). The toughness of the PLA/EVA (80/20 wt/wt) blends firstly increased with VA content up to 50 wt.% and then declined. At high VA content, it resulted the formation of small EVA particles that could not cavitate under impact testing, whereas at low VA content, large EVA particle size was achieved. However, in the latter, there had a weak interfacial adhesion, affecting the toughness of the PLA/EVA blends. As a result, the optimum toughening efficiency of EVA on PLA was obtained at VA content of 50–60 wt.%. The EVA with VA content of 50 wt.% (i.e., EVA50) was selected to study the toughening effect of EVA content in the PLA/EVA blends. Even 5 wt.% EVA50 could already make PLA ductile ($\epsilon_b \approx 300\%$). However, the notched Izod impact toughness of this blend was not obviously improved due to a strain-rate dependence of the rubber cavitation (Dompas and Groeninckx, 1994; Jansen et al., 1999). Interestingly, the notched Izod impact toughness of the PLA/EVA50 blends was considerably improved in presence of 15 wt.% EVA50. By further increasing the EVA50 content, super-tough PLA/EVA50 blends could be obtained. The reason for brittleness of amorphous polymers is strain-localization, which could be delocalized by the dispersed rubber phase via a (pre)cavitation process. The morphology of PLA/EVA blends could be tuned by the VA content in the EVA copolymers as well as with the EVA content within the blends. The moderate particle size and the low modulus of the non-crosslinked EVA rubber particles are suitable for cavitation in the presence of tri-axial strain/stress [66, (Bucknall and Paul, 2009)]. Consequently, internal EVA rubber cavitation in the PLA matrix occurred under both the impact and tensile testing. Meanwhile, no obvious crazes were observed after deformation. In this regard, internal rubber cavitation in combination with matrix yielding is proposed to be the dominant toughening mechanism for the PLA/EVA blends.

To improve its toughness and crystallization, Zhang et al. (2013c) melt-blended PLA with ethylene/methyl acrylate/glycidyl

methacrylate terpolymer (EGA) containing relatively high-concentration of epoxide groups (8 wt%). Although we cannot exclude any coupling reaction between epoxide groups and end-functionality (hydroxyl) from PLA chains, the addition of EGA accelerated the crystallization rate and increased the final crystallinity of PLA in the blends. Significant enhancements in both toughness and flexibility of PLA were achieved by the incorporation of 20–30 wt% EGA. The impact strength increased from 3 kJ/m² of neat PLA to 60 kJ/m² and the elongation at break increased from 5 to 232% (**Table 11**). The failure mode changed from brittle to ductile fracture of the blend. The phase separated morphology with relatively good interfacial adhesion played an important role in the improvement in crystallization and toughness of the blend.

Petchwattana et al. (2012) utilized ultrafine rubbery particles as toughening agent to reduce the brittleness of PLA. Elastomeric particles of acrylate rubber were added to PLA in the range from 0.1 to 10 wt% (**Figure 10**). Maximum reduction of the flexural modulus and the tensile modulus was achieved by 20 and 45% respectively, when the acrylate rubber content was of 10 wt%. However, under stress, the rubber-modified PLA could be uniaxially deformed to elongation at break of nearly 200%, accounting for an increase by 50 times in comparison to PLA. The toughening efficiency of the ultra-fine rubber particles was also reflected through the significant increase in the impact strength by a four-fold factor. Fractographs of the acrylate rubber-modified PLA revealed a plastic deformation and a good dispersion and adhesion of the rubber particles within the PLA matrix. Therefore, they played an important role in dissipating the energy by formation of multiple crazes. The crazing mechanism was found to be the major impact mechanism of the acrylate rubber modified PLA system.

Jiang et al. (2006) and Li and Shimizu (2007) attributed the toughening behavior of the PLA-based blends to debonding at the matrix/particle interface during deformation, which released the hydrostatic stress and facilitated shear yielding to occur.

Table 8 | Mechanical properties of different PLA blends with biodegradable flexible/soft polymers.

Formulation (wt.%)	E_t (MPa)	σ_y (MPa)	ϵ_b (%)	NIE (KJ/m ²)			
PLA/PHBV (Ma et al., 2013)					U-NIE (KJ/m ²)	E_f (GPa)	σ_f (MPa)
100/0		68	4	2.5	16	3.5	109
95/5		62	5	2.7	15	3.4	96
90/10		53	220	3.1	23	3.0	85
80/20		42	230	11	150n.f.	2.5	66
70/30		35	260	10	127n.f.	2.0	51
50/50		15	15	6	41	1.2	21
0/100		9	12	48	45n.f.	0.5	11
PLA/PBAT (Jiang et al., 2006)							
100/0	3400	63	3.7	2.6			
95/5	–	–	~115	–			
80/20	2600	47	>200	4.4			
PLA/PEBA (Han et al., 2013)							
100/0	1170 ± 42	60.0 ± 1.1	6.7 ± 0.4	4.5 ± 0.6			
95/5	1151 ± 75	49.3 ± 1.2	13.7 ± 0.8	7.1 ± 0.3			
90/10	1156 ± 44	46.8 ± 0.4	283 ± 18	7.4 ± 0.4			
85/15	1062 ± 48	42.5 ± 0.9	313 ± 2	9.1 ± 0.4			
80/20	1011 ± 41	42.4 ± 1.0	346 ± 18	39.3 ± 2.2			
70/30	911 ± 54	36.8 ± 0.6	335 ± 5	60.5 ± 1.0			
PLA/PAE (Zhang et al., 2009b)					E_s (MPa)	T_g PAE(°C)	T_g PLA(°C)
100/0	1814	46.8	5.1		2460		79.48
95/5	1517	48.1	161.5		2116	–47.31	77.85
90/10	1633	40.9	194.6		2017	–53.87	75.97
80/20	1240	23.7	184.6		1442	–57.89	74.47
70/30	1050	24.6	367.2		1395	–60.26	73.84
PLA/NR (Bitinis et al., 2011)							
Pristine PLA	2900 ± 100	63.1 ± 1.1	3.3 ± 0.4				
Processed PLA	3100 ± 40	58.0 ± 1.5	5.3 ± 0.7				
95/5	2500 ± 60	50.4 ± 1.6	48 ± 22				
90/10	2000 ± 50	40.1 ± 1.5	200 ± 14				
80/20	1800 ± 80	24.9 ± 0.9	73 ± 45				
PLA/GMS (Ge et al., 2013)							
100/0	1777 ± 42	69.8 ± 3.2	5.7 ± 0.3	4.7 ± 0.2			
95/5	1570 ± 44	44.8 ± 1.3	4.5 ± 0.5	8.1 ± 0.4			
90/10	1200 ± 12	41.9 ± 4.6	7.6 ± 2.4	8.5 ± 0.5			
85/15	1270 ± 36	39.7 ± 1.0	11 ± 5.0	15.5 ± 0.3			
80/20	1210 ± 17	35.1 ± 2.1	9.5 ± 6.5	36.7 ± 0.3			
75/25	1190 ± 24	32.4 ± 1.8	11 ± 3.1	46.1 ± 2.9			
70/30	695 ± 38	29.9 ± 2.6	45 ± 15.8	48.2 ± 4.6			

E_t , Tensile modulus; σ_y , Tensile yield stress; ϵ_b , Tensile elongation at break; NIE, Notched Izod Impact Energy; U-NIE, Un-Notched Izod Impact Energy; E_f , Flexural modulus; σ_f , Flexural stress; E_s , Storage modulus; T_g , Glass transition temperature by DMA; n.f., Not (completely) fractured.

Zhao et al. (2013) (Figure 11) used a unique ultrafine full-vulcanized powdered ethyl acrylate rubber (EA-UFPR) as toughening modifier for PLA. Largely improved tensile toughness was successfully achieved by the incorporation of only 1 wt% EA-UFPR, while the tensile strength and modulus of the blends were almost the same as pure PLA. The highly efficient toughening of

UFPR on PLA could be mainly ascribed to the strong interfacial interaction between PLA and UFPR as well as a good dispersion of UFPR particles in PLA matrix. This induces de-bonding cavitation at the PLA/UFPR interfaces during stretching, leading to an extensive energy dissipation and superior tensile toughness. It should be highlighted that this work provided an effective

toughening method to largely improve the mechanical properties of PLA without sacrificing its stiffness, which is very important for the wide application of PLA materials.

Taib et al. (2012) toughened PLA with a commercially available ethylene acrylate copolymer impact modifier. PLA/impact modifier blends were partially miscible as confirmed by dynamic mechanical analysis. With increasing the impact modifier content, the stress-strain curves showed that the brittle behavior of PLA changed to ductile-failure. The blends showed some improvement in the elongation at break and notched impact strength, highlighting the toughening effects provided by the impact modifier again. In contrast, the yield stress and tensile modulus decreased with the increase in the impact modifier content (Figure 12A). Scanning electron microscopy micrographs revealed that the impact mechanisms among others involved shear-yielding or plastic deformation of the PLA matrix induced

by interfacial de-bonding between the PLA and the impact modifier domains. In addition to shear-yielding of PLA, extensive deformation of the impact modifier domains was observed on the fractured surface, which accounts for the “partial” break of the blend after the impact test (Figure 12B).

PLA with polyethylene using PLLA-b-PE diblock copolymers as a compatibilizer (Anderson et al., 2003; Anderson and Hillmyer, 2004)

The addition of PLLA-b-PE block copolymers into the binary blend PLA/LLDPE resulted in improved interfacial adhesion and finer dispersion of LLDPE in PLA matrix. With the addition to the blend PLA/LLDPE (80/20, w/w) of 5 wt% of the block copolymer [with molecular weights for the PLA block above its entanglement molecular weight M_c , that is, PLLA-b-PE (30–30 w/w)], the impact strength was drastically increased to 460 J/m (Figure 13). This difference was attributed to the superior ability of the block copolymer from the long PLLA block to suppress the coalescence of dispersed phase. Table 9 lists the impact strength properties as a function of the blend composition as well as some explanations of the occurring phenomena.

By increasing the amounts of PLLA-b-PE (30–30 wt/wt) block copolymer in the PLLA/LLDPE (80/20, wt/wt) blends, the size of dispersed LLDPE particles was gradually reduced. At 3 wt.% of block copolymer, the size of the dispersed LLDPE particles began leveling off at less than 1.0 μm , and the impact resistance drastically increased (Figure 14 and Table 10).

Meng et al. successfully synthesized poly(butyl acrylate) (PBA) in order to melt-blend with PLA using a Haake Rheometer (Meng et al., 2012). Dynamic rheology, SEM and DSC results showed that PLA was partially miscible with PBA. The crystallinity of PLA increased with the content of PBA (<15 wt.%). By increasing PBA content, the tensile strength and modulus of the blend decreased slightly, while the elongation at break and toughness dramatically increased (Table 11). The failure mode changes from brittle to ductile fracture of the blend with PBA as well. SEM micrographs revealed that a de-bonding-initiated shear yielding mechanism is

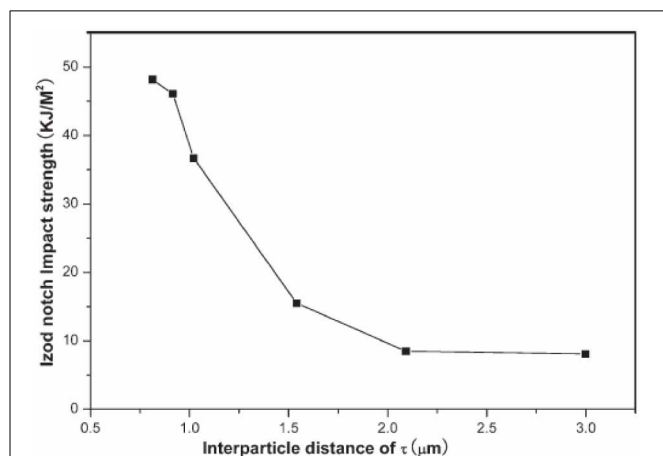


FIGURE 8 | The impact strength as a function of inter-particle distance of GMS. Copyright (2012) Wiley; used with permission from Ge et al. (2013).

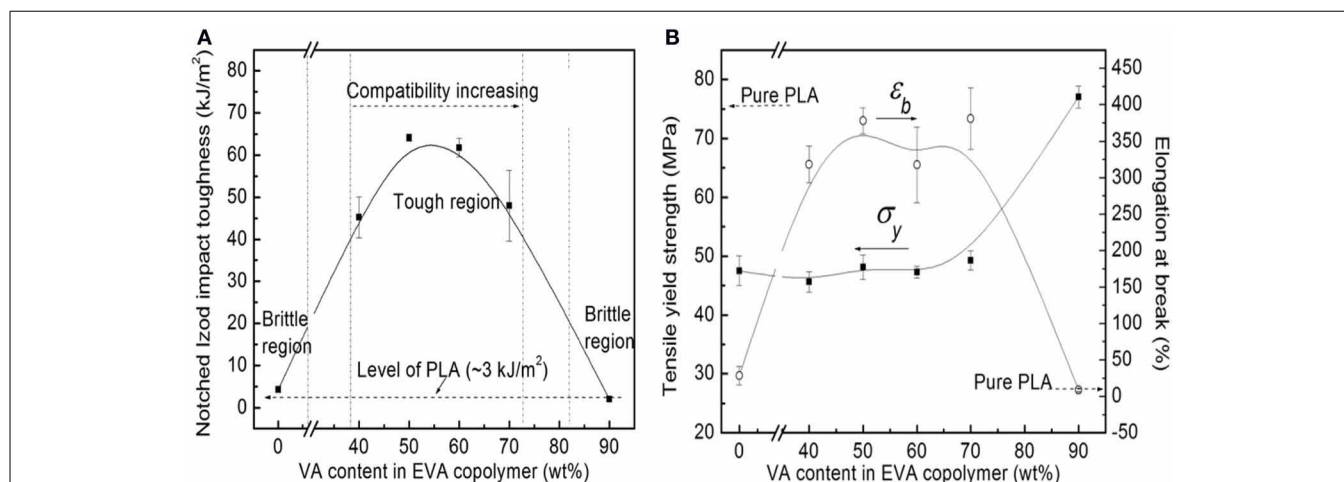


FIGURE 9 | (A) Impact toughness and (B) tensile properties of the PLA/EVA (80/20) blends as a function of VA content in the EVA copolymers [Reprinted from Ma et al. (2012) with permission from Elsevier].

involved in the toughening of the blend. Rheological investigation revealed that a phase segregation occurred at loading above 11 wt.% PBA. UV-vis light transmittance showed that PLA/PBA blends had a high transparency, but the transparency slightly decreased with the amount of PBA.

Commercially available impact modifiers for PLA. Recently, several polymeric impact modifiers have been specifically produced and commercialized in order to toughen brittle PLA (Table 12). These impact modifiers may be based on either linear thermoplastics/elastomers having a low glass transition temperature or crosslinked core-shell block copolymers, where the core is mainly a rubbery soft block encapsulated by a glassy and rigid shell that brings a good interfacial compatibilization with the matrix. In the optimal conditions (dispersion, compatibilization/adhesion, size and size distribution...), they dissipate the mechanical energy, retarding the initiation and propagation of micro-cracks through the polymer matrix.

Recently, Scaffaro et al. (2011) have compared toughening effects of OnCap™ BIO Impact T and Sukano® PLA im S550 on PLA. Both modifiers were immiscible with PLA, but Sukano® PLA im S550 displayed a more homogeneous dispersion in the PLA matrix. It was found that none of the impact modifiers

brought obvious increase in elongation to PLA. The maximum Izod impact strength of 141 J/m was achieved by adding 8 wt.% Sukano® PLA im S550, while the impact strength increased only to 124 J/m even with the addition of OnCap™ BIO Impact T. Murariu et al. (2008b) studied toughening effects of Biomax Strong® 100 on PLA and high-filled PLA/b-calcium sulphate anhydrite (AII) composites. Notched Izod impact strength of PLA containing 5 and 10 wt.% Biomax Strong® 100 increased from 2.6 kJ/m² of the neat PLA to 4.6 and 12.4 kJ/m², respectively. Elongation at break was more than 25% for the blend containing 10 wt.% of the impact modifier, while tensile strength and modulus of PLA gradually decreased with the addition of the impact modifier. Addition of 5 and 10 wt% of the impact modifier to the PLA/AII (70/30, wt/wt) composite also increased their impact strength to 4.5 and 5.7 kJ/m², respectively. Impact strength slightly decreased with further increase of the filler loading to 40 wt.%, but remained higher than that of both the unmodified composites and the neat PLA. On the other hand, for the PLA composites containing 40% of filler, tensile strength and elongation markedly decreased with the incorporation of the impact modifier. Zhu et al. (2009) studied the films of PLA blends containing either Biomax Strong® 100 or Sukano® PLA im S550 as a toughening agent. It was shown that the modulus decreased when increasing the concentration of Biomax Strong® 100 modifier, but was relatively independent of the concentration of Sukano® PLA im S550. The maximum elongation was of 255% in presence of 12 wt.% of BiomaxVR Strong 100 and of 240% in presence of 8 wt.% of Sukano® PLA im S550, while elongation at break of neat PLA was of about 90%. For a given composition, the latter impact modifier gave a clearer film than Biomax® Strong 100, but the clarity of films decreased as the concentration increased for both toughening agents. Afrifah and Matuana (2010) investigated the toughening mechanisms of PLA blended with an ethylene/acrylate copolymer (EAC) to show a mode of fracture through crazing or microcracking and debonding of impact modifier particles with the matrix. This resulted in brittle failure at low content. Higher impact modifier content than 10 wt% revealed fracture mechanisms including impact modifier debonding, fibrillation,

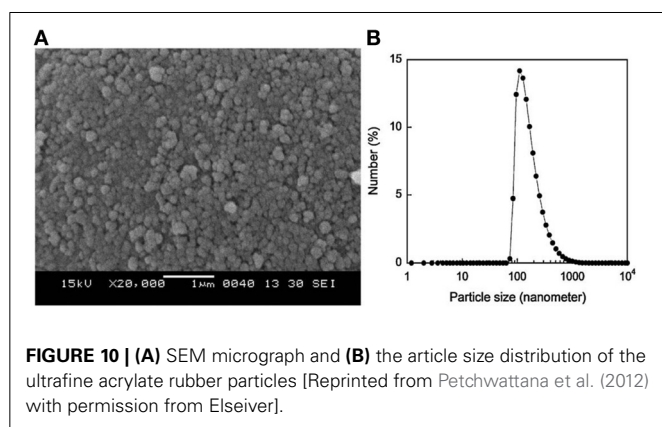


FIGURE 10 | (A) SEM micrograph and **(B)** the particle size distribution of the ultrafine acrylate rubber particles [Reprinted from Petchwattana et al. (2012) with permission from Elsevier].

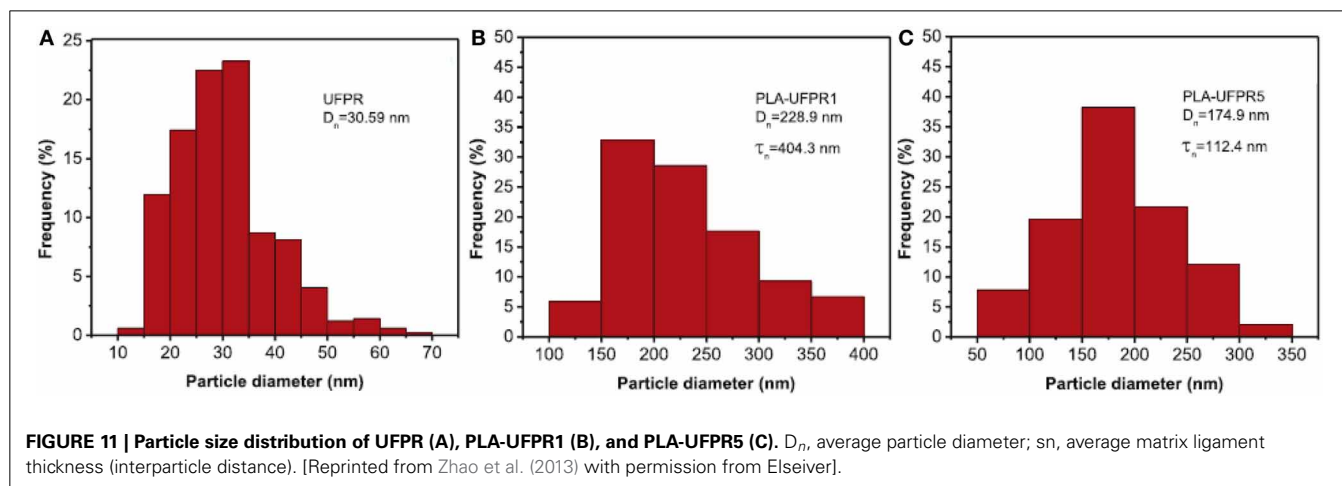


FIGURE 11 | Particle size distribution of UFPR (A), PLA-UFPR1 (B), and PLA-UFPR5 (C). D_n, average particle diameter; τ_n, average matrix ligament thickness (interparticle distance). [Reprinted from Zhao et al. (2013) with permission from Elsevier].

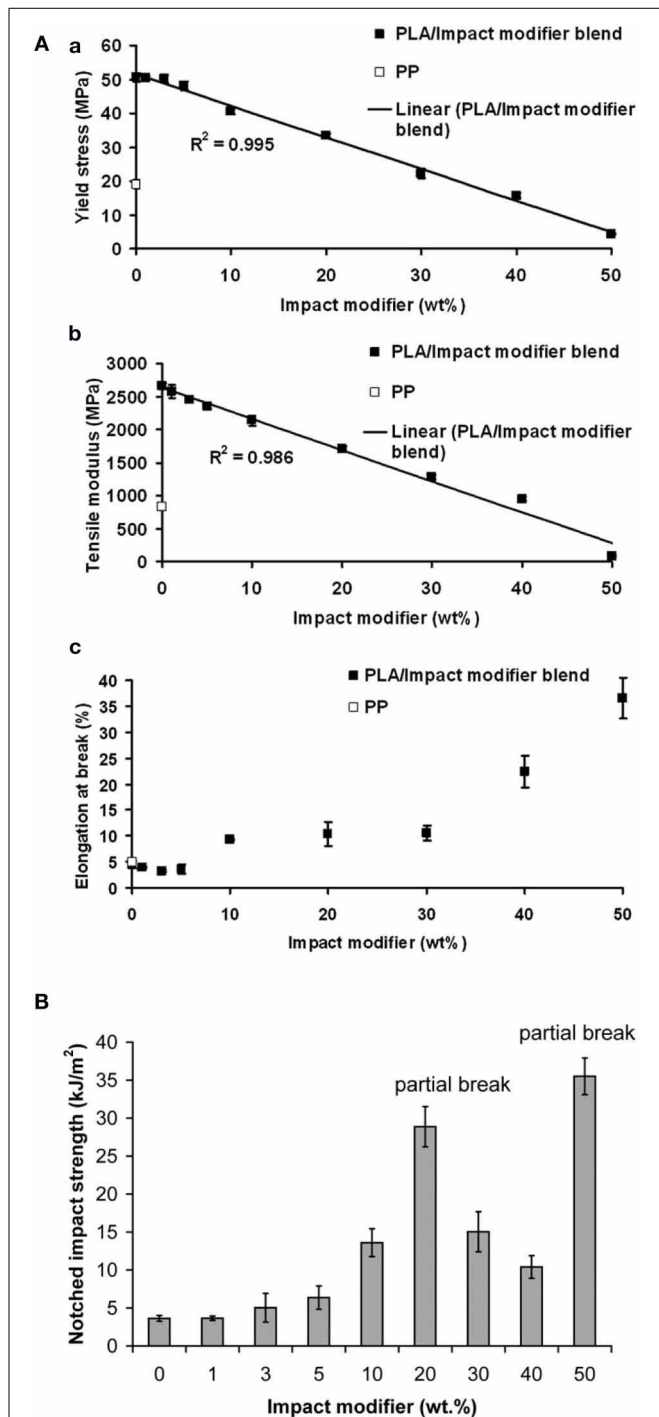


FIGURE 12 | (A) Tensile properties of PLA and PLA/impact modifier blends. **(a)** Yield stress; **(b)** tensile modulus; and **(c)** elongation at break. **(B)** Notched impact strength of PLA and PLA/ impact modifier blends. Notched impact strength for PP = 7.81 ± 1.50 kJ/m². Copyright (2011) Wiley; used with permission from Taib et al. (2012).

crack bridging, and matrix shear yielding, resulting in a ductile behavior. They also demonstrated that Biomax® Strong 100 yielded superior toughening on semi-crystalline PLA over amorphous PLA. With 40 wt.% of the toughening agent, the notched

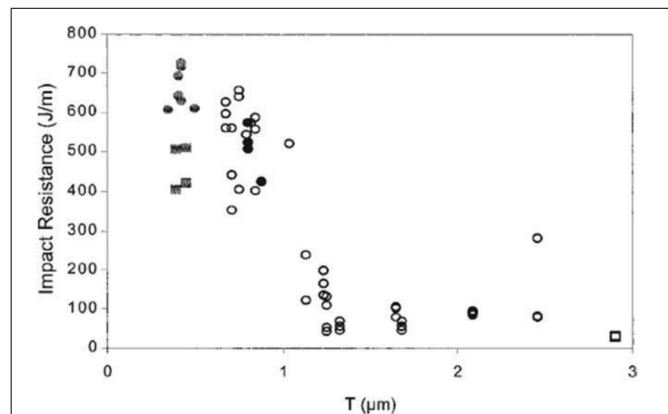


FIGURE 13 | Relationship between matrix ligament thickness (MLT) and impact resistance for: 80:20 PLLA/LLDPE binary blend (open circles); 80:20:5 PLLA/LLDPE/PLLA-PE(5-30) (black circles); 80:20:5 PLLA/LLDPE/PLLA-b-PE(30-30) (gray circles); 80:20 (w/w) PLA/LLDPE binary blend (open squares); and 80:20:5 (w/w) PLA/LLDPE/PLLA-b-PE(30-30) (gray squares). Copyright (2003) Wiley; used with permission from Anderson et al. (2003).

Izod impact strength of the semi-crystalline PLA increased from 16.9 J/m for amorphous PLA to 248.4 J/m for semi-crystalline PLA. In addition, the presence of 15 wt.% Biomax® Strong 100 reduced the brittle-to-ductile transition temperature of PLA, as revealed by the notched Izod impact test data from the frozen specimens. Ito et al. (2010) investigated the fracture mechanism of neat PLA and PLA blends toughened with an acrylic core-shell modifier. The acrylic modifier was composed of a crosslinked alkyl acrylate rubber core and PMMA shell, and the particle size was in the range of 100–300 nm. Plane strain compression testing of PLA clearly showed strong softening after yielding. Because the stress for craze nucleation was close to that of yield stress, brittle fracture occurred for neat PLA. Addition of the acrylic modifier significantly lowered the yield stress and formed many microvoids. The release of strain constrained by microvoiding and the decrease of yield stress led to the relaxation of stress concentration, and therefore the toughness was improved moderately. **Table 9** summarizes the reported mechanical properties of some of highly toughened PLA blends prepared *via* melt-blending. From **Table 9**, it results that in order for a rubbery polymer to impart toughness to PLA or any other polymer, several criteria must be encountered as follows (Natureworks LLC, 2007):

- the rubber must be distributed as small domains (usually 0.1–1.0 μm) in the matrix polymer;
- the rubber must have a good interfacial adhesion to PLA;
- the glass transition temperature of the rubber must be at least 20°C lower than the test/use temperature;
- the molecular weight of the rubber must not be too low;
- the rubber should not be miscible, to a certain extent, with the polymer matrix;
- and the rubber must be thermally stable to PLA processing temperatures.

Table 9 | Results summary and explanation.

Blend system	Compatibilizer (PLLA-b-PE)	Impact strength (J/m)	Explanation
a-PLA	–	12	
a-PLA/LLDPE (80wt%/20wt%)	–	34	
a-PLA/LLDPE (80wt%/20wt%)	5 wt% ^a	36	The difference is attributed to superior ability of the PLLA-b-PE from the longer PLLA block to suppress the coalescence of the dispersed phase
a-PLA/LLDPE (80wt%/20wt%)	5 wt% ^b	460	
PLLA	–	20	
PLLA/LLDPE (80wt%/20wt%)	–	350	Adhesion test showed a superior interfacial adhesion when used semicrystalline PLLA instead of amorphous a-PLA
PLLA/LLDPE (80wt%/20wt%)	5 wt% ^a	510	The tacticity effects on either the M_c of PLA or the miscibility degree of PLA matrix with LLDPE phase accounted for the difference between the two binary blends
PLLA/LLDPE (80wt%/20wt%)	5 wt% ^b	660	

a-PLA, amorphous PLA; PLLA, semicrystalline PLA; LLDPE, linear low density polyethylene.

^a The molecular weight of PLLA block in PLLA-b-PE is 5 kg/mol < M_c = 9 kg/mol.

^b The molecular weight of PLLA block in PLLA-b-PE is 30 kg/mol > M_c = 9 kg/mol.

M_c = 9 kg/mol is the critical entanglement molecular weight of PLLA block in PLLA-b-PE.

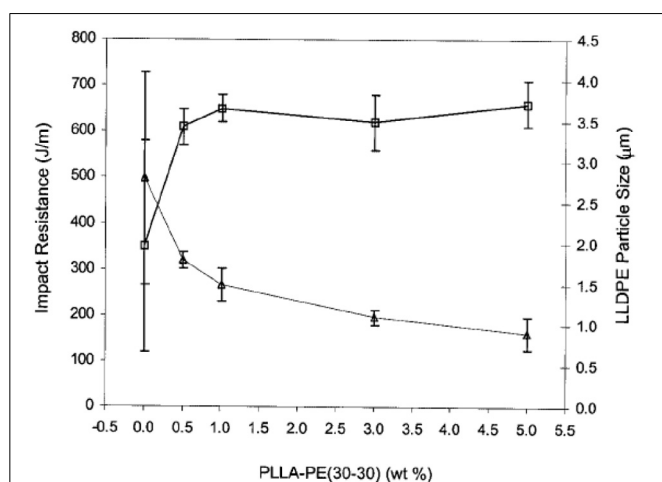


FIGURE 14 | Effect of the amount of PLLA-PE(30-30) block copolymer on the impact resistance (squares) and the LLDPE particle size (triangles) of 80: 20 PLLA/LLDPE blends. Copyright (2003) Wiley; used with permission from Anderson et al. (2003).

These factors will allow the rubber to induce energy dissipation mechanisms in PLA, which retard crack-initiation and propagation and ultimately result in a material with improved toughness. PLA is similar to many polymers that can undergo plastic flow mechanisms, initiated by dispersed rubber domains. The increase in toughness comes from the transfer of the impact energy to plastic flow, either in the form of crazing or shear yielding mechanisms through a large volume fraction of polymer. In PLA, excellent toughness balance can be obtained with 15–25% of impact modifier, even if little improvement can be seen by the addition of 3–5% of impact modifier. Typically like most conventional thermoplastics, PLA can be toughened after blending

Table 10 | Particle size analysis and impact resistance of PLLA homopolymer and blends [Copyright (2003) Wiley; used with permission from Anderson et al. (2003)].

PLLA/LLDPE/ PLLA-PE block	PLLA-PE block	LLDPE particle size (μm)	Izod impact resistance (J/m)
100/0/0			20 ± 2
80/20/0		2.8 ± 1.3	350 ± 230
80/20/5	5–30	1.9 ± 0.2	510 ± 60
80/20/5	30–30	0.9 ± 0.2	660 ± 50

with rubbery polymers such as low modulus polyesters, linear elastomers, or cross-linked core-shell impact modifiers, which have been observed to impart the highest degree of toughening in PLA. These modifiers typically consist of a low T_g crosslinked rubbery core (T_g < -10°C) encapsulated by a glassy shell polymer (T_g > 50°C) that has good interfacial adhesion with the matrix polymer. When well-dispersed, these modifiers act as nanoscale or microscale rubbery domains that dissipate mechanical energy to retard or arrest crack initiation and propagation through the polymer. Some possible major drawbacks resulting from blending PLA with impact modifiers are the dispersion of the micro-domains in the PLA matrix and the transparency of the resulting material. The latter case depends to some extent on the dispersion of the micro-domains and their size. The addition of impact modifier to PLA often results in a substantial decrease in clarity of the toughened blend, although high clarity is required for many PLA applications. To retain the good clarity and transparency of PLA, for instance, small dispersed particles have to have a similar refractive index as PLA as well as the particle size has to be inferior to the visible light wavelength. The use of very small rubber particles with refractive indexes

Table 11 | Mechanical properties of different PLA blends with non-biodegradable flexible/soft polymers.

Formulation (wt.%)	E_t (MPa)	σ_y (MPa)	ϵ_b (%)	NIIIE (KJ/m ²)			
PLA/EVA50 (Ma et al., 2012)					Hardness (Shore D)	E_f(GPa)	σ_f (MPa)
100/0		75	9	3	86	3.7	105
95/5		68	310	2	85	3.3	90
90/10		61	390	5	84	2.9	75
85/15		54	430	32	82	2.7	70
80/20		45	340	64	80	2.4	65
70/30		37	400	83	76	1.9	50
PLA/EGA (Zhang et al., 2013c)							
100/0	1745 ± 39	60.0 ± 3.0	4.9 ± 0.3	3.0 ± 0.4			
90/10	1530 ± 35	44.3 ± 2.1	23.4 ± 3.6	3.9 ± 0.3			
80/20	1154 ± 42	33.8 ± 2.4	232.0 ± 26	59.8 ± 5.1			
70/30	945 ± 49	24.9 ± 1.3	126.0 ± 21	53.2 ± 8.4			
PLA/PEBA (Petchwattana et al., 2012)				NIIIE (J/m)			
100/0	2750 ± 120	61.22 ± 1.42	3.46 ± 1.42	23.66 ± 1.33			
99.9/0.1	2660 ± 60	61.69 ± 1.99	3.53 ± 0.19	26.62 ± 1.87			
99.7/0.3	2680 ± 80	61.57 ± 1.76	5.01 ± 0.34	33.18 ± 2.01			
99.5/0.5	2550 ± 70	58.34 ± 0.94	8.94 ± 1.82	36.89 ± 2.43			
99.3/0.7	2310 ± 140	58.17 ± 1.83	15.1 ± 2.07	38.12 ± 1.95			
99/1	2350 ± 380	58.69 ± 0.91	19.8 ± 4.97	52.15 ± 2.57			
97/3	2050 ± 120	53.89 ± 0.84	53.7 ± 4.93	64.59 ± 3.46			
95/5	2150 ± 220	54.22 ± 0.97	124 ± 25.9	86.95 ± 4.65			
93/7	2040 ± 210	50.31 ± 0.93	167 ± 24.4	96.21 ± 4.99			
90/10	2000 ± 250	48.98 ± 1.79	198 ± 31.7	101.0 ± 5.63			
PLA/UFPR (Zhao et al., 2013)							
100/0	2062 ± 12	68.05 ± 1.42	6.08 ± 0.36	1.60 ± 0.21			
99.5/0.5	1922 ± 66	67.53 ± 1.99	106.60 ± 15.08	2.00 ± 0.15			
99/1	1896 ± 2	66.26 ± 1.76	219.93 ± 2.64	2.2 ± 0.23			
97/3	1768 ± 54	65.67 ± 0.94	231.45 ± 20.55	2.6 ± 0.37			
95/5	2029 ± 129	65.39 ± 1.83	215.63 ± 12.21	3.20 ± 0.19			
PLA/PBA (Meng et al., 2012)					Tensile toughness^a (MJ/m³)		
100/0	3510	68	4.52		2.13		
95/5	1540	51.77	31.52		3.7		
92/8	1490	44.79	74.62		17.0		
89/11	1440	40.82	173.98		41.74		
85/15	1330	41.01	174.52		47.02		

E_t , Tensile modulus; σ_y , Tensile yield stress; ϵ_b , Tensile elongation at break; NIIIE, Notched Izod Impact Energy; E_f , Flexural modulus; σ_f , Flexural stress.

^aCalculated as the area under stress-strain curve.

comparable to that of PLA can help maintaining transparency (refractive index in the range of from 1.430 to 1.485). This can be achieved if the added rubber is slightly compatible with PLA. Moreover, a poor compatibility and interfacial adhesion can also result in partially dispersed and large cluster-like domains responsible for the de-bonding of the rubber phase, void-formation, and a premature failure in a brittle mode. The main negative consequence resulting from the incorporation of toughening agents into PLA is the reduction of the material stiffness (elastic modulus). Accordingly, many researchers have investigated the

incorporation of rigid fillers in order to compensate the loss of stiffness.

Generally, fillers or fibers are incorporated in PLA to either reduce the cost or modify the physical, rheological, or optical properties of the polymer. Starch is for instance an excellent example, which is available at less than \$ 0.10/pound and which retains both renewability and biodegradability characteristics of PLA while enhancing some structural and mechanical properties at room or elevated temperature. Some additives (e.g., talc), can increase the nucleation rates and crystallinity, and

Table 12 | Injection moulded properties of PLA containing various commercial impact modifiers.

Manufacturer	Impact modifier (IM)	Nature	Characteristics of PLA/IM	Optimal load in PLA	IM loading (%)	Notched izod impact (J/m)	Tensile yield (MPa)	Elongation ^a (%)
Sukano	Sukano® PLA im S550 (Sukano Co., 2008; Scaffaro et al., 2011)	Linear elastomer	Transparent, compostable, cost effective, immiscible	4% (impact resistance improved by a factor of 10)	8	141 (87)		8 (3)
	Sukano® PLA im S555 (Co, 2010)	Linear elastomer	Transparent, compostable, cost effective					
PolyOne	OnCap™ BIO Impact T (http://www.polyone.com/en-us/docs/Documents/OnCap%20BIO%20Impact%20T.pdf . Accessed on 2008.; http://www.polyone.com/en-us/news/Press%20Release%20Attachments/Chinaplas%20OnCap%20BIO%20Impact%20T.pdf . Accessed on April 19, 2010.; Scaffaro et al., 2011)	Linear elastomer	Transparent, tear resistant, immiscible		12.5	124 (87)		8 (3)
DuPont	Biomax® Strong 100 (DuPont Co., 2010). Biomax® Strong 120 Hytrel™3078	Ethylene-acrylate copolymer Ethylene-acrylate copolymer Aliphatic/aromatic copolyester	Non-food applications Food packaging Very compatible	<5% for good toughness and clarity 5–10% (High elongation at break and impact properties)	12 30	198 (27)	34 (62)	255 430 (10)
Rohm and Hass	Polaroid™ BPM-500 Polaroid™ KM 334 Polaroid™ BTA 753 Polaroid™ EXL 3691A Polaroid™ EXL 2314	Acrylic-based	Transparent	3–5% (dart drop impact increased by four time with respect to neat PLA)	15 20 20 20	59 (27) 112 (27) 64 (27) 53 (27)	37 (62) 36 (62) 43 (62) 38 (62)	165 (10) 300 (10) 280 (10) 250 (10)

(Continued)

Table 12 | Continued

Manufacturer	Impact modifier (IM)	Nature	Characteristics of PLA/IM	Optimal load in PLA	IM loading (%)	Notched izod impact (J/m)	Tensile yield (MPa)	Elongation ^a (%)
Dow chemical company	Polaroid™ BPM-515	Acrylic-based	Transparent	1% (higher efficiency than Polaroid™ BPM-500)				
	Pellethane™2102-75A				30	769 (27)	42 (62)	410 (10)
Arkema	Biostrongth™ 130	Acrylic core-shell structure	Transparent	2–6 wt. %				
	Biostrongth™ 150	MMA-butadiene-styrene core-shell structure	Opaque	2–6 wt. %				
	Biostrongth™ 280	Acrylic core-shell structure	Transparent	2–6 wt. %				
Procter and gamble metabolix	Nodax™	Aliphatic copolyester (PHA)		10–20 wt. % (rubber domains size 0.2–1.0 μm)				
Karton polymers LLC.	Karton™FG 1901X	Functionalized Elastomer			20	-	33 (62)	100 (10)
BASF	Ecoflex™	Aliphatic/aromatic copolyester	Very compatible	5–10% (High elongation at break and impact properties)	30	128 (27)	43 (62)	100 (10)
Showa higher polymer	Bionelle™3001	Aliphatic polyester			15	48 (27)	59 (62)	230 (10)
Crompton corporation	Blendex™ 415				15	48 (27)	44 (62)	230 (10)
	Blendex™ 360				20	107 (27)	47 (62)	280 (10)
	Blendex™ 338	ABS resin (70% of butadiene)			20	518 (27)	43 (62)	281 (10)
Reference	PLA				0			10

^a According to ASTM D-638 at 2.0 inch/min.

thereby improve heat resistance of PLA-based materials (Bopp and Whelan, 2003). Fillers and fibers can also increase the stiffness of PLA and, to some extent, enhance the toughness of PLA materials. This can be explained by the fact that the crystallization extent of PLA is enhanced on incorporation of fillers, and therefore yielding a ductile behavior for the resulting PLA-based materials (Urayama et al., 2003). In order to get the maximum benefits from the fibers or fillers, several factors must be considered. For instance, optimizing the extruder screw configuration, through-put rate, screw speed, temperature and other process parameters are necessary. The optimal particle size of the filler is generally in the range of 0.1–12 μm (Ikado et al., 1997). A good and uniform dispersion must be achieved as well. This is normally obtained by controlling the addition of the compatibilizers during processing (Kjeschke et al., 2001), which help the dispersion of filler/fiber as well as minimizes micro-defects in blends that can cause embrittlement. For instance, the affinity of organically modified clay in PLLA/PBS blends was found to be critical for the properties enhancement of resulting composites (Chen et al., 2005). When a commercially available nanoclays, i.e., 10 wt% Cloisite® 25A was used as compatibilizer into the PLLA/PBS (75/25, w/w) blend, the tensile modulus of blends increased from 1.08 GPa to 1.94 GPa, but the elongation at break was sacrificed from 71.8 to 3.6% at the same time, which was even lower than that of neat PLLA (6.9%). In contrast, using an epoxy-functionalized organoclay (TFC) at the same amounts that was able to react with the extremities (carboxylic/hydroxylic) of both polyesters, not only retained high tensile modulus, but

also increased elongation to 118%. Similar compatibilizing effect of TFC on the PLA/PBSA (75/25 w/w) blends were reported (Chen and Yoon, 2005). Odent et al. reported immiscible polymer blends made of PLA toughened with Biomax Strong® 100 in order to elaborate ultratough PLA-based materials mediated with nanoparticles (ref. Odent et al., 2013c). The co-addition of 10 wt% of Biomax Strong® 100 and 10 wt% of silica nanoparticles (CAB-O-SIL TS-530 from CABOT) provided an increase from 2.7 kJ/m² to 30.2 kJ/m², which is related to the formation of peculiar morphologies (from round-like nodules to elongated structure) mediated by the localization of nanoparticles at the interface PLA/impact modifier. Same improvement was also reached by replacing silica with organomodified layered aluminosilicate (clay), with value of 32.6, 37.6 and 21.9 kJ/m² with only 1 wt% of Cloisite 20A, Cloisite 25A, and Cloisite 30B, respectively. Coupling agents are often used with glass fibers (Mochizuki and Suzuki, 2004) or coated fillers to enhance the interfacial adhesion of the additive to the matrix polymer, more particularly when polar additives are combined with non-polar polymers. Silane and titanate coupling agents with various structures, which depends on the polymer to be blended, are often embedded onto glass fibers and inorganic particulate fillers. These coupling agents can have beneficial effects on dispersion, toughness and rheology, and often allow higher levels of incorporation. However, the desired beneficial effects from the addition of fillers and fibers can have some negative consequences. High levels of fillers/fibers can significantly increase viscosity, cause shear heating and degradation (molecular weight loss and color formation), and

Table 13 | Mechanical properties of some fillers blended with PLA (http://www.natureworkslc.com/~media/Technical_Resources/Properties_Documents/PropertiesDocument_Fillers-and-Fibers_pdf.pdf).

PLA filled with	Filler loading (%)	Flex modulus ^a (MPa)	Dart impact at 23°C (KJ/m ²)	IZOD impact ^b (notched) (J/m)	IZOD impact ^b (un-notched) (KJ/m ²)
Specialty minerals MTAGD609 Talc	1.5	3940	123	43	331
	10	5002	112	27	272
	30	9248	69	27	176
Vicron 15–15 CaCO ₃	1.5	3809	107	32	272
	10	4287	128	27	288
	30	5606	128	32	187
Specialty minerals Mica 5040	1.5	4009	123	32	256
	10	5366	139	27	198
	30	9874	85	32	123
Synthetic silicate	1.5	3855	144	32	304
	10	4345	117	27	214
	30	5761	96	21	112
Specialty minerals EMforce™ Bio	1.5	3876	128	32	203
	10	4457	134	32	171
	30	5687	1057	123	294
Unmodified NatureWorkx™ PLA 4032D		3651	160	37	235

^aASTM D 790.

^bASTM D 256-92.

affect the ability to fill thin walled parts. In the case of natural fibers, they contain high levels of moisture, requiring to apply extensive drying step before processing. It is worth noting that adding large amounts of natural fiber into the extruder requires using side-feeders for uniform extrusion operations. The batch-to-batch variation in natural fiber composition and quality can lead to consistency problems in the final blend as well (http://www.natureworkslc.com/~media/Technical_Resources/Properties_Documents/PropertiesDocument_Fillers-and-Fibers_.pdf.pdf).

Visual problems are also an issue with flow lines, poor colorability, and opacity. **Table 13** is listing the mechanical properties of some fillers blended with PLA.

Jiang et al. (Long et al., 2009) compared the effects of organo-modified montmorillonite (OMMT) and nanosized precipitated calcium carbonate (NPCC) on the mechanical properties of PLA/PBAT/nanofiller ternary composites. Mechanical testing demonstrated that the composites containing OMMT exhibited higher tensile strength and Young's modulus, but with lower elongation, as compared to those containing NPCC. When 25 wt.% PLA was replaced by maleic anhydride grafted PLA (PLA-g-MA), the elongation of the ternary composites was substantially increased, possibly as a result of the improved dispersion of the nanoparticles and enhanced interfacial adhesion from maleic anhydride moieties along the PLA backbone. Among these composites, PLA/10 wt.% PBAT/2.5 wt.% OMMT/25 wt.% PLA-g-MA demonstrated the best overall properties with 87% retention of tensile strength of pure PLA, slightly higher modulus and significantly improved elongation at break (16.5 times than that of neat PLA). Teamsinsungvon et al. (2010) also reinforced PLA/PBAT blends using micro-sized precipitated CaCO_3 and achieved similar toughening effects on PLA/PBAT (80/20, wt/wt) blends. The incorporation of talc particles significantly accelerated the crystallization process of the PLA matrix (Battezzore et al., 2011). The presence of crystals improved the thermo-mechanical properties. Talc provides both reinforcing and toughening effects on PLA (Yu et al., 2012). The reinforcing effect of talc particles can be mainly ascribed to the good interfacial adhesion between PLA matrix and the orientation of talc layers during processing. Interfacial debonding of PLA/talc composite can induce massive crazing, meanwhile talc particles diffused in PLA matrix can prevent from the void coalescence and propagation of the crazes, which increase the toughness of PLA. Additionally, talc layers aligned along the tensile direction make its toughening effect on PLA more significant in tensile test because they

induce more advantageous shear yielding and prevent microcracks from propagation along fracture direction. Some aggregation of talc particles can appear in composites at higher talc content, which act as a stress concentration points or weak points and cause poor toughness of PLA/talc composites. Recently, NatureWorks® has succeeded to develop the Ingeo™ 3801X grade by co-adding impact modifier, crystal accelerant, reinforcing agent and nucleating agent into PLA. This PLA-based grade is a high heat and impact resistance material. **Table 14** shows its composition.

The bio-content of this material is of 70%. It was designed for non-food, opaque, semi-durable, and non-compostable applications. Due to its high crystallinity and rapid crystallization rate, the resulting blend has good thermal and dimensional stability. It is designed to be processed at fast cycle times. Its mechanical properties are summarized in **Table 15**.

Physical compounding of low or high molecular weight compounds offers a convenient approach to modifying biopolymers. Whether a good compatibility/affinity is present between both partners, the resulting blends exhibit good properties, being intermediate from that of each polymeric partner. However, only few biopolymer pairs are miscible or even compatible with each other. Therefore, chemical routes such as chemical modification or reactive compatibilization are required. Reactive blending has proven to be a simple, economically viable, and reliable technology for designing complex nanostructured polymeric blends. In this part, it will be pointed out, by reviewing the recent advances, that reactive extrusion technology represents the most promising approaches to tune the stiffness-toughness balance of bio-sourced polymeric materials. Reactive extrusion enables to manufacture biodegradable polymers through different routes of

Table 15 | Thermal and mechanical properties of the Ingeo™ 3801X grade (http://www.biocom.iastate.edu/workshop/2010workshop/2010workshop/presentations/dan_sawyer.pdf).

Mechanical properties	Value	ASTM standard
Tensile Modulus (MPa)	2980	D638
Tensile yield strength (MPa)	25.9	D638
Tensile elongation at break (%)	8.1	D638
Notched Izod impact (J/m)	144	D256
HDT B at 0.45 MPa (°C)	65	E2092
HDT at 0.114 MPa (°C)	140	E2092

Table 14 | Formulation of the Ingeo™ 3801X grade (http://www.biocom.iastate.edu/workshop/2010workshop/presentations/dan_sawyer.pdf).

Material	Commercial name	Supplier	Chemical	Formula weight fraction	25°C density [g/ml]
Matrix	Ingeo™ 3001D	NatureWorks LCC	PLA	0.711	1.24
Impact modifier	Biostrength® 150	Arkema Inc.	Proprietary core-shell copolymer	0.100	1.00
Crystal accelerant	Plasthall® DOA	The HallStar Company	Dioctyl adipate	0.090	0.98
Reinforcing agent	ULTRATALC® 609	Specialty Minerals Inc.	<0.9 µm particle 3MgO.4SiO ₂ .2H ₂ O	0.090	2.8
Nucleating agent	LAK-301	Takemoto Oil & Fat Co. LTD	Aromatic sulfonate derivative	0.009	1.00

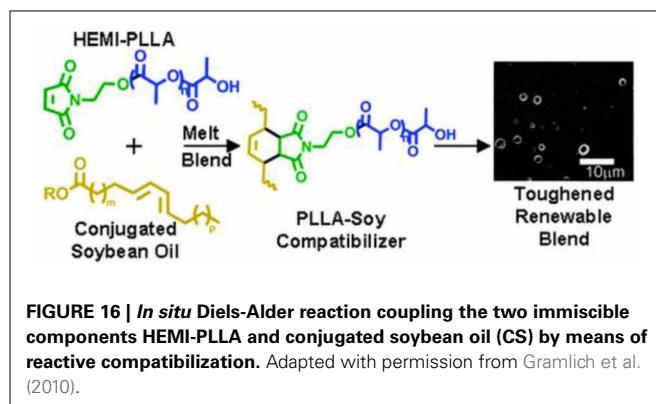
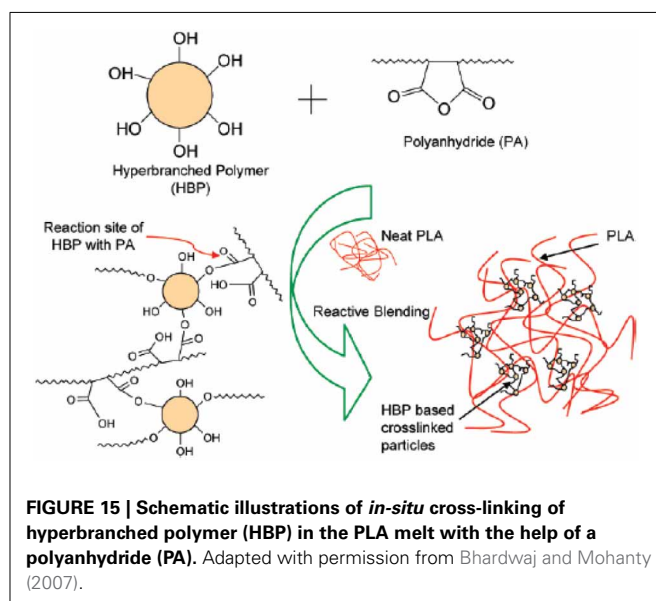
reactive modification (polymerization, grafting, compatibilization, branching, functionalization,...) in a cost-effective polymer processing (Michaeli et al., 1993; Mani et al., 1999). Most of the researchers employ this technology for the reactive compatibilization of PLA with a rubbery modifier in order to impart toughness to PLA. In the review, the *in situ* reactive compatibilization is defined here as the melt-blending process in which two polymers containing mutually reactive functionalities react with each other at the interface to combine them during melt blending, generating *in situ* block or graft copolymer. The *in situ* generated block or graft copolymer will be then able to compatibilize the blend by reducing the interfacial tension and by improving the interfacial adhesion. This leads to a significantly improved dispersibility of the rubber into much smaller particles (Baker et al., 2001). Compatibility is defined in this context as the ability of the rubber modifier to finely disperse into the main PLA phase in order to form stable morphologies of fine rubber particle dispersions with reduced interfacial tension and improved adhesion to resist delamination. Early patent literature recognized the need for some types of grafting reactions or an associative interaction between the polymeric components of the blend to obtain sufficient compatibility for good impact modification (Kray and Bellet, 1968; Seddon et al., 1971; Murch, 1974; Mason and Tuller, 1983). Interfacial compatibilization and toughening is achieved through grafting copolymers generated *in situ* at the interface during the melt blending. There are four fundamental requirements to be addressed for the *in situ* reactive compatibilization in an extrusion device:

- Sufficient mixing to achieve the desired distribution and dispersion of one polymer into another polymer;
- The presence of reactive functionalities in each phase capable of reacting together across the interphase;
- Reaction to take place within the available residence time in the processing device;
- Formation of stable bonds during processing.

In the case of polymers with no reactive chemical function (such as polyolefins), peroxides are used to create free polymeric macroradicals in the blend. Like in some cases the compatibilization cannot be achieved through the direct reaction between the free polymeric macro-radicals, low molecular weight (macro)monomers, or a mixture of low molecular weight (macro)monomers have to be grafted on the free polymeric radicals in order to functionalize the polymeric chains. The role of these grafted chemical functions is to (1) stabilize the macro-radicals, and thereby avoid any undesirable free radical side-reactions by localizing the free radical reactions at the polymers' interface, and (2) interact at the interface between the polymer components of the blend for compatibilization. PLA has been blended and reactive compatibilized with several biodegradable and non-biodegradable polymer modifiers that will be discussed here. We have to mention that other researchers have attempted using reactive extrusion technique to *in situ* synthesize the toughening agent for PLA.

Biodegradable hyperbranched polymers (HBP)

Hyperbranched polymer-based nanostructures (HBPs) have a globular molecular architecture with cavernous interiors, many peripheral functional end-groups, and low hydrodynamic volume and viscosity. They may have better miscibility with other polymers than the linear analogous (Seiler, 2002). Due to their inherently high surface area—volume ratio, structures engineered at the nano-meter length scales are increasingly played key-roles in the enhancement of the materials mechanical properties. In this regard, they have demonstrated a high potential to be used as impact modifiers for mechanical performances in a variety of industrial applications after a reactive process (Liu and Zhang, 2011). For instance, non-reactive melt-blending (physical compatibilization via H-bonding) of a hyperbranched biodegradable poly(ester amide) with PLA modestly enhance, yield strength. Moreover, the tensile failure mode changed from brittle to ductile fracture and led to a maximum tensile elongation at break of 50% compared to 3.7% for neat PLA using 20 wt.% HBP (Lin et al., 2007). This was explained by the fact that the dispersion of hyperbranched biodegradable poly(ester amide) was not fine enough



to get its maximum benefits. In this respect, Bhardwaj and Mohanty (2007) proposed and demonstrated a new industrially relevant methodology to develop PLA-based materials, having outstanding stiffness-toughness balance through *in situ* cross-linking reactions. They *in-situ* cross-linked a hydroxyl functional hyperbranched polymer (HBP) with a polyanhydride (PA) in the

PLA matrix during melt-processing (**Figure 15**). Transmission electron microscopy (TEM) and atomic force microscopy (AFM) revealed the sea-island morphology of PLA-cross-linked HBP reactive blend. The domain size of cross-linked HBP particles in the PLA matrix was less than 100 nm. Compared to unmodified neat PLA, the PLA/HBP/PA (92/5.4/2.6, wt/wt/wt)

Table 16 | Physical properties of melt blends of CS with PLLA-49 and HEMI-PLLA-67 (Adapted with permission from Gramlich et al. (2010)).

Matrix polymer	W _{CS0} (%) ^a	W _{CS} (%) ^b	E (GPa) ^c	σ _b (MPa) ^d	ε _b (%) ^e	X _{HBP} (%) ^f	X _{CS} (%) ^g	d _{lm} (μm) ^h	σ _{lm} (μm) ⁱ	MLT (μm) ^j
PLLA-49			2.4 ± 0.3	58 ± 3	5 ± 2					
HEMI-PLLA-67			3.0 ± 0.2	67 ± 9	4 ± 1					
PLLA-49	15	9	2.4 ± 0.3	28 ± 4	22 ± 7			1.81	1.8	3.1
HEMI-PLLA-67	15	7	2.0 ± 0.5	34 ± 2	50 ± 30	100	14	0.91	2.0	2.2
PLLA-49	5	4	2.1 ± 0.3	38 ± 1	30 ± 10			1.17	2.0	3.6
HEMI-PLLA-67	5	7	2.5 ± 0.2	37 ± 2	70 ± 30	98	44	0.70	2.1	2.0
PLLA-49/HEMI-PLLA-67 ^k	5	6	2.3 ± 0.3	36 ± 3	20 ± 10	96	39	0.96	1.8	2.1
PLLA-49	2	2	2.6 ± 0.1	51 ± 1	5 ± 2			0.30	2.0	1.3
HEMI-PLLA-67	2	3	2.5 ± 0.2	54 ± 5	4 ± 2	66	70	0.35	1.3	0.5

^aWeight fraction of CS added to melt mixer.

^bWeight fraction of CS incorporated into blends, by ¹HNMR spectroscopy.

^cElastic modulus.

^dStress at break.

^eElongation to break.

^fConversion of HEMI end-groups for blends with HEMI-PLLA-67.

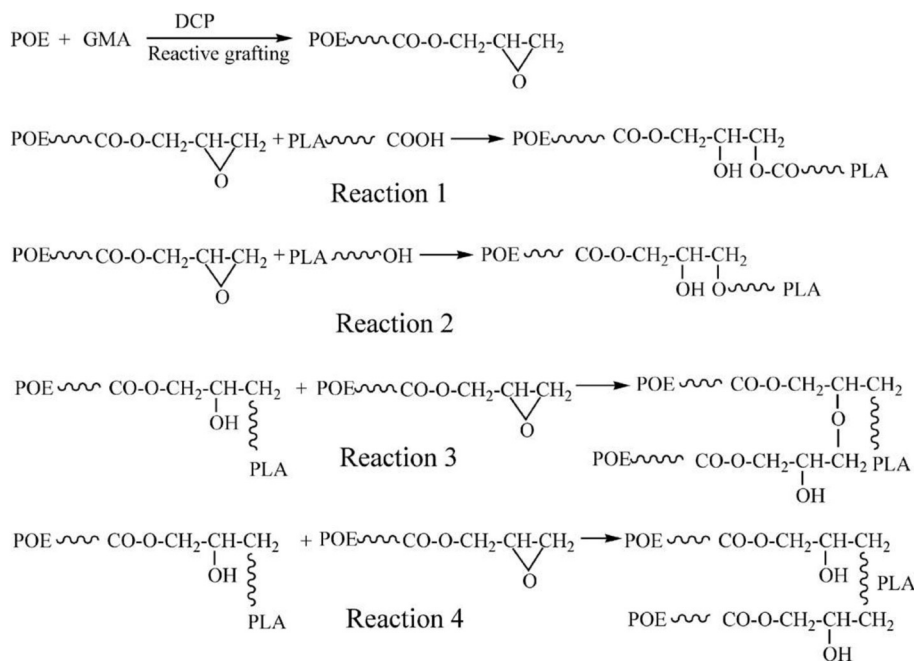
^gConversion of E,E isomers of CS added to mixer.

^hLog-mean average CS droplet diameter.

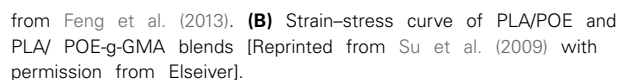
ⁱLog-mean CS droplet size distribution parameter.

^jMatrix ligament thickness.

^kMatrix polymer was a 50/50 blend of PLLA-49 and HEMI-PLLA-67.



SCHEME 3 | The possible reactions in the melt reactive blends [Reprinted from Su et al. (2009) with permission from Elsevier].



blend exhibited $\sim 570\%$ and $\sim 847\%$ improvement in the tensile toughness (17.4 MJ/m^3 vs. 2.6 MJ/m^3 for neat PLA) and elongation at break (48.3% vs. 5.1% for neat PLA), respectively. However, tensile modulus and strength of the blend slightly decreased from 3.6 GPa (neat PLA) to 2.8 GPa and from 76.6 MPa (neat PLA) to 63.9 MPa , respectively. The authors ascribed the increase in the ductility of modified PLA to the stress-whitening and the multiple crazing initiated in the presence of cross-linked HBP particles. As revealed by rheological data, the formation of a networked interface was associated with enhanced compatibility of the PLA-cross-linked HBP blend as compared to the PLA/HBP blend.

The effects on mechanical properties of hydroxyl-terminated hyperbranched poly(ester amide) (HBP) and isocyanate-terminated prepolymer of butadiene (ITPB), alone and in combination, were investigated with the aim to make tough PLA (Nyambo et al., 2012). The glass transition temperature did not change from that of neat PLA. Interestingly, due to synergistic effects, impact strength and elongation at break of the PLA/HBP/ITPB ternary blend were improved by over 86 and 100%, respectively. Physical and chemical interactions between the hydroxyl-terminated HBP and the ITPB (**Scheme 2B**) may be responsible for the synergistic effect on the improvements in impact strength without scarifying the tensile modulus and strength. Scanning electron microscopy (SEM) images on impact fractures showed evidence of stretched and course surface,

which indicated a change in fracture behavior from brittle to ductile behavior after chemical modification. Accordingly, the impact strength of PLA can be easily enhanced using low additive loadings of 10 wt% *via* reactive extrusion with HBP and a suitable reactive compatibilizer such as ITPB. The modified PLA can address most issues related to neat brittle PLA, since it can exhibit a better stiffness–toughness balance and has the potential for use in durable commercial applications.

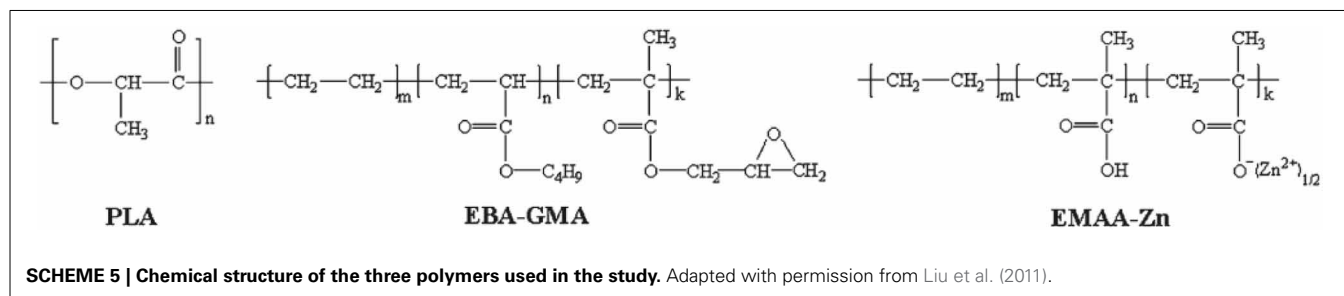
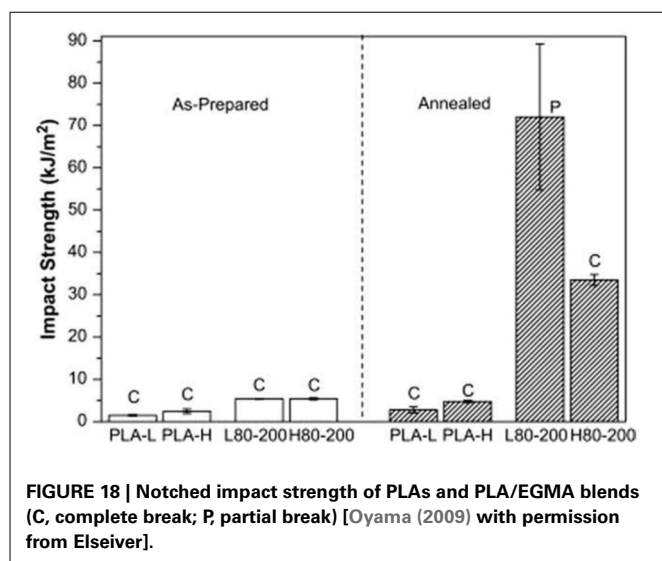
Soybean oil

PLLA/soybean oil binary blends containing unmodified soybean oil undergoes phase inversion at even low concentrations of soybean oil, leading to the release of the oil during blending. Therefore, the blends must be compatibilized (Chang et al., 2009). Ali et al. (2009) demonstrated that moderate improvements in the elongation at break of PLLA were gained by the addition of epoxidized soybean oil.

Robertson et al. (2010) explored how the polymerization and the optimization of soybean oil characteristics prior to blending improved its level of incorporation into PLLA and increased toughness compared to PLLA. They also demonstrated moderate improvements in the PLA/polysoybean oil blends regarding elongation at break and toughness of four and six times greater than those of unmodified PLLA, respectively. Gramlich et al. (2010) studied a more effective approach to toughen PLA consisting in the reactive compatibilization of conjugated soybean oil with PLLA. In a first step, bulk ring-opening polymerization via reactive extrusion (REx) of L-lactide using N-2-hydroxyethylmaleimide (HEMI) as a difunctional initiator and tin (II) 2-ethylhexanoate as a catalyst produced a high molecular weight reactive end-functionalized PLA (HEMI-PLLA). In a second step, REx of HEMI-PLLA and conjugated soybean oil (CS) was carried out through a Diels-Alder reaction in order to couple the two immiscible components *via* reactive compatibilization (**Figure 16**). Blends of HEMI-PLLA and 5 wt.% CS resulted in a greater than 17-fold increase in elongation to break compared to PLLA homopolymer and more than twice the elongation to break compared to a 5 wt.% CS blend with unreactive PLLA (**Table 16**). Analysis of the blend morphology indicated that the *in situ* formation of the compatibilizer at the HEMI-PLLA/CS interface decreased the CS droplet diameter to an optimal value ($0.7 \mu\text{m}$) compared to unreactive binary blends, explaining the toughening PLLA with CS.

Use of glycidyl methacrylate (GMA) and its copolymers

The grafting effect on mechanical properties of poly(ethylene octene) (POE) with PLA via glycidyl methacrylate (GMA) was

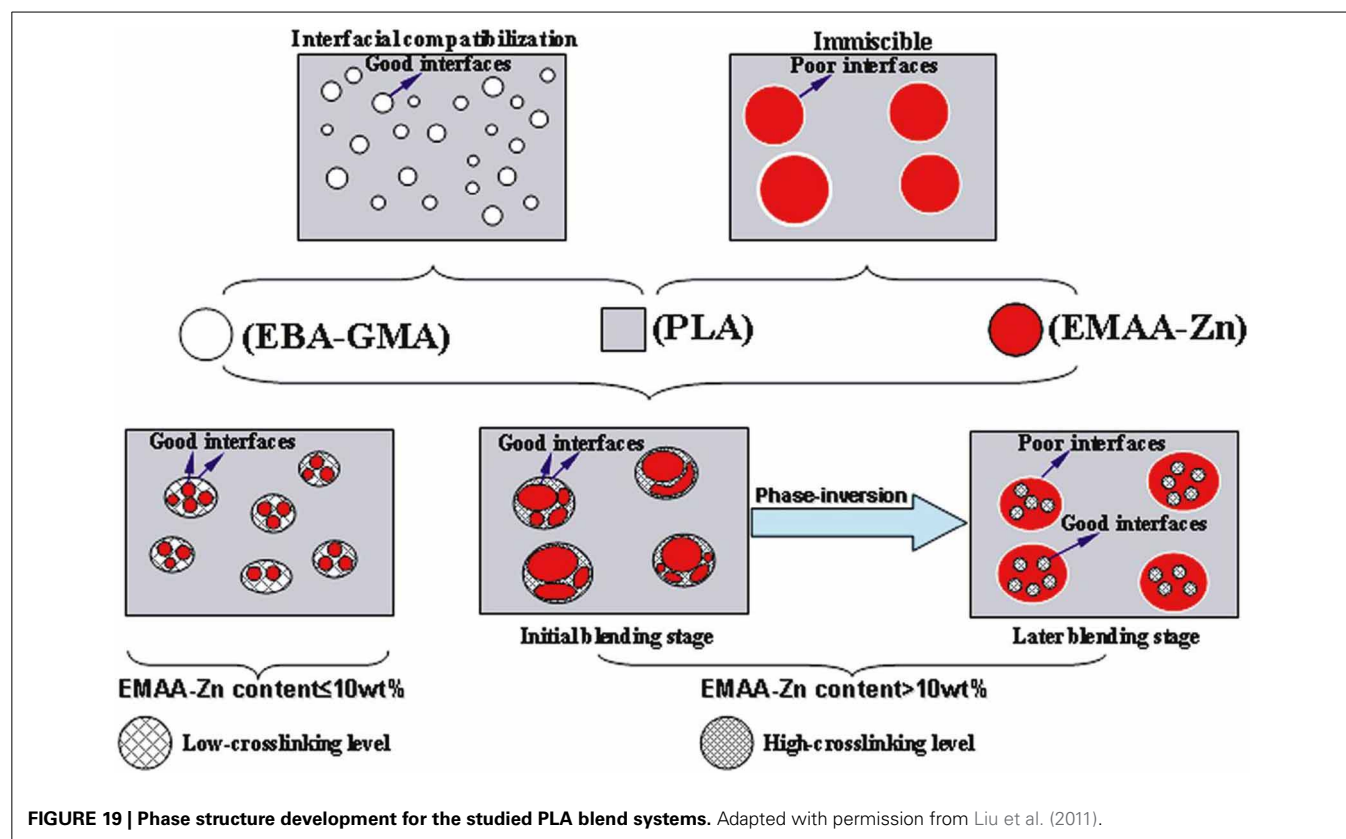


investigated (Su et al., 2009; Feng et al., 2013). POE-g-GMA was used to prepare high impact modified PLA/POE-g-GMA reactive blends (**Scheme 3**). The presence of GMA moieties enhanced the blends compatibility due to the coupling reactions between the carboxyl and hydroxyl end-groups from PLA and the epoxy groups from POE-g-GMA (**Scheme 3**). Moreover, morphology analysis demonstrated better wetting of the dispersed phase by the PLA matrix and finer dispersed particles by reactive blending. Accordingly, the effective interfacial compatibilization promoted by the grafting reaction was mainly responsible for the significant improvement of PLA toughening (**Figures 17A,B**). Interestingly, the highest toughening effect was obtained at lower particle size and interparticle distance, which were submicronic (**Figure 17A**).

PLLA and acrylonitrile-butadiene-styrene copolymer (ABS) are thermodynamically immiscible and incompatible by simply melt blending them. Styrene acrylonitrile-glycidyl methacrylate copolymer (SAN-GMA) as a reactive compatibilizer and ethyltriphenyl phosphonium bromide (ETPB) as a catalyst were thereby introduced during the reactive melt blending of PLA/ABS96 (Li and Shimizu, 2009). The epoxide group of SAN-GMA reacted with PLLA end-groups under the mixing conditions, and the addition of ETPB accelerated the reaction (**Scheme 4**). As a result, it was found that the size of the “salami-like” ABS domains in PLLA matrix significantly decreased and their dispersion improved by the addition of the reactive compatibilizer. A significant shift of glass transition temperatures for both PLLA and ABS indicated the improvement of the

compatibility between PLLA and ABS. As a result, the compatibilized PLLA/ABS blends exhibited a very nice stiffness-toughness balance, i.e., an improvement of the impact strength and the elongation at break with a slight reduction in the modulus. For instance, the addition of 5 phr of SAN-GMA to the PLLA/ABS (70/30 wt/wt) blend increased elongation at break from 3.1 to 20.5% and impact strength from 63.8 to 81.1 kJ/m². By further incorporating 0.02 phr ETPB, the elongation at break and impact strength of the blend increased to 23.8% and 123.9 kJ/m², respectively.

Low and high molecular weight PLA (L-PLA and H-PLA, respectively) were blended with 20% of poly(ethylene-co-glycidyl methacrylate) (EGMA) (Oyama, 2009). The resulting blend had a high elongation above 200% compared to 5% for neat PLA. The notched Charpy impact was only 2 times that of neat PLA. After annealing, the injection-moulded specimens of the L-PLA/EGMA (80/20 wt/wt) blend at 90°C for 2.5 h showed that the impact strength significantly increased to 72 kJ/m², about 50 times that of neat L-PLA. Moreover, the improvement in strength and modulus of the blend was accompanied by a significant decrease in elongation at break. With the higher molecular weight PLA (H-PLA) as matrix, such positive effect of annealing on impact strength appeared relatively less prominent (**Figure 18**). The author argued that the crystallization of the PLA matrix played a key-role in such significant improvement. It was demonstrated that the interfacial reaction (reactive compatibilization) between the polymeric components improved not



only the dispersion of the second component but also the bonding between the particles and matrix to expect combination of crazing and shear yielding, contributing to the formation of the super-touch PLA materials, superior to commercially available acrylonitrile-butadiene-styrene (ABS) resins. Furthermore, these improvements in mechanical properties were achieved without scarifying the heat resistance of the material. The material highlights again the importance of interface control in the preparation of multicomponent materials.

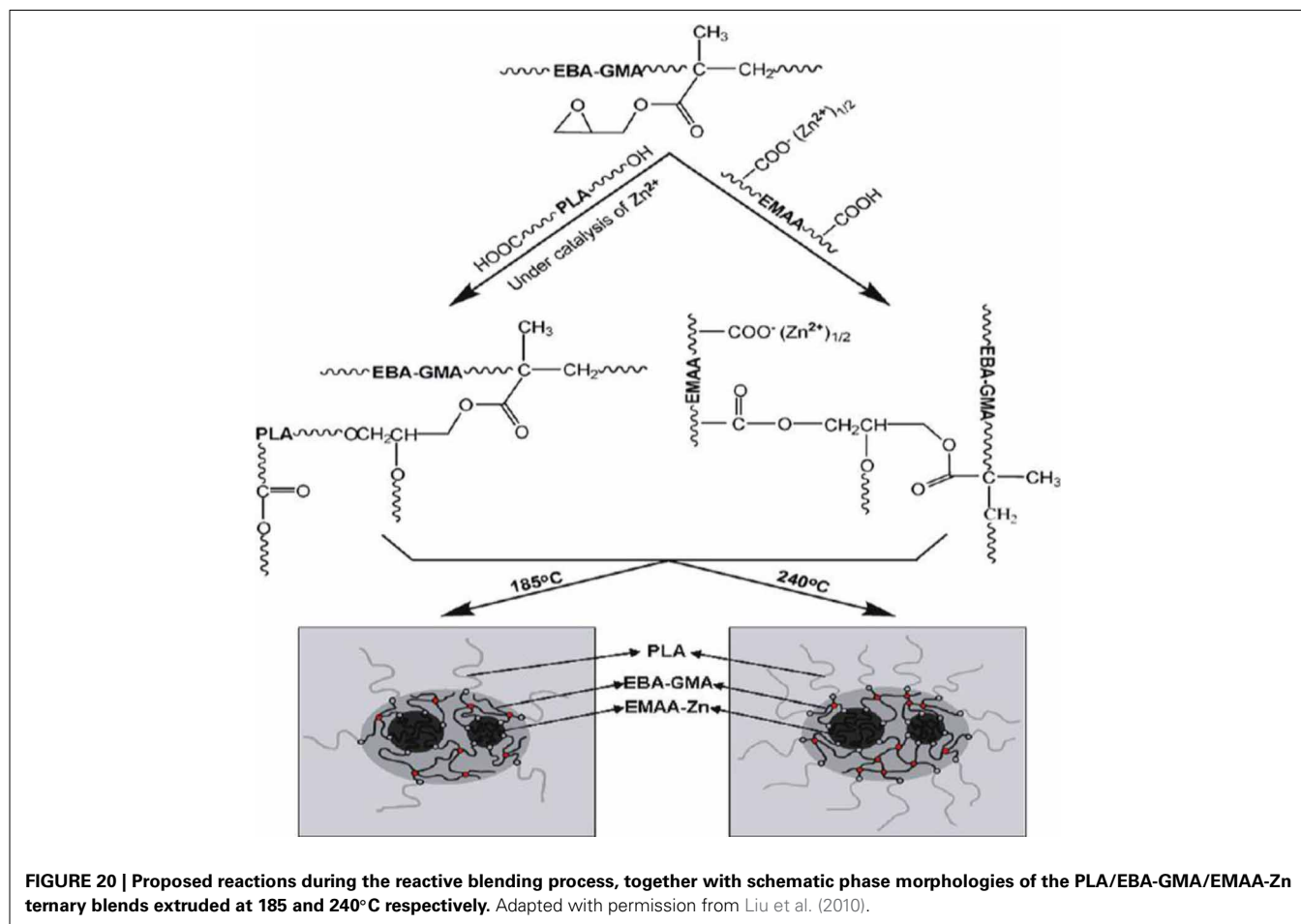
Liu et al. (2010, 2011) and Song et al. (2012) studied extensively the reactive ternary blends of PLA with ethylene/n-butyl acrylate/glycidyl methacrylate (EBA-GMA) terpolymer and a zinc ionomer of ethylene/methacrylic acid (EMAA-Zn) using a Leistritz ZSE 18 twin-screw extruder having a L/D ratio of 40. The three polymeric components are represented in **Scheme 5** and **Figure 19**.

The influence of the simultaneous dynamic vulcanization (crosslinking) and interfacial compatibilization and adhesion on mechanical and impact performance of the reactive PLA-based ternary blends was investigated. It was demonstrated that the EBA-GMA/EMMA-Zn ratio played a crucial role in determining the phase-morphology. Interestingly, the increase of the EMAA-Zn content gradually turned the phase of the latter from occluded sub-inclusions into a continuous phase within the “salami”-like

micro-structure (domain-in-domain morphology) as revealed by TEM in the case of the ternary blends. It was reasonably proposed that when the EMAA-Zn content exceeded 10%, a phase inversion within the sub-structure of the dispersed phase domains could likely take place, which would account for the pronounced deterioration in interfacial wetting of the dispersed particles by the PLA matrix in these cases. The phase structure development for the studied PLA blend systems are schematized in **Figure 20**. The EMAA-Zn domains were finally occluded inside the EBA-GMA particles which were homogeneously dispersed in PLA.

Interestingly, it was demonstrated that at higher extrusion temperature (240 vs. 185°C), not only the carboxyl groups in the EMAA-Zn ionomer were able to trigger more cross-linking reactions *via* the epoxy groups in the EBA-GMA phase, but also more PLA macromolecules were grafted at the interface between PLA and the elastomer (**Figure 20**). The Zn ions further catalyzed the reactions. According to the SEM micrographs, this was confirmed by the better wetting of the dispersed phase by PLA matrix at higher blending temperature. Accordingly, effective interfacial compatibilization and adhesion were achieved at higher compounding temperature.

As a result, although increasing the extrusion temperature did not significantly influence the tensile properties (**Figure 21B**), both blending temperature and elastomer/ionomer ratio were



found to play key-roles in achieving super-toughness (great improvement of impact strength and strain at break) of the PLA-based ternary reactive blends (**Figure 21A**). This can be attributed to the effective interfacial compatibilization at higher temperature (240°C).

The correlation between the particle size and impact toughness had revealed that there existed an optimum submicronic range of particle sizes of the dispersed domains for PLA super-toughening in this ternary blend system (**Figure 22**). Preliminary analysis of micromechanical deformation suggested that the high impact toughness observed for some ternary blends was attributed to the low cavitation resistance of the dispersed particles coupled with suitable interfacial adhesion. It was found that debonding mainly occurred around the relatively large particles together with fibrillated crazes and no cavitation when blended with an ethylene/n-butyl acrylate/glycidyl methacrylate terpolymer (EBA-GMA). Addition of a zinc ionomer of ethylene/methacrylic acid copolymer (EMAA-Zn) within the PLA/EBA-GMA blend

gradually turned the morphology into a salami-like phase structure, which provides a low cavitation resistance coupled with suitable interfacial adhesion. Therefore, internal cavitation of the dispersed particles followed by the matrix shear yielding was predominant and resulted in the optimum impact strength. All of these examples regarding toughening mechanisms within PLA are not exhaustive but strengthen that toughness of PLA is a complex function which implies all of the described mechanisms (crazing, shear yielding, cavitation and debonding) and mode of fracture.

In a complementary study, Song et al. (2012) investigated the effect of the ionomer characteristics on reactions and properties of the PLA-based reactive ternary blends studied above (**Schemes 6A,B**). The ionomer was prepared by neutralizing the EMAA ionomer precursor with ZnO. It came out that the reactivity of the system and the interfacial compatibilization were drastically enhanced by increasing both the degree of neutralization (DN) of the ionomer and the methacrylic acid (MAA) content of ionomer precursor. As a result, the particle size and polydispersity of the dispersed phase reached the right optimum to greatly improve the impact toughness and tensile elongation at break of the material (**Figures 23A,B**).

Super-tough PLA alloy with greatly improved heat resistance

Hashima et al. (2010) toughened PLA by blending it with hydrogenated styrene-butadiene-styrene block copolymer (SEBS) with the aid of reactive compatibilizer, poly(ethylene-co-glycidyl methacrylate) (EGMA). The high temperature property (HDT) and thermal ageing resistance were improved by further incorporating a ductile polymer with a high glass transition temperature, that is, polycarbonate (PC). Based on TEM, differential scanning calorimetry (DSC), and dynamic mechanical analysis (DMA), the author explained that the origin of the outstanding toughness and ageing resistance of the 4 component alloy; e.g., PLA/PC/SEBS/EGMA 40/40/5/5 (wt.% ratio), seems

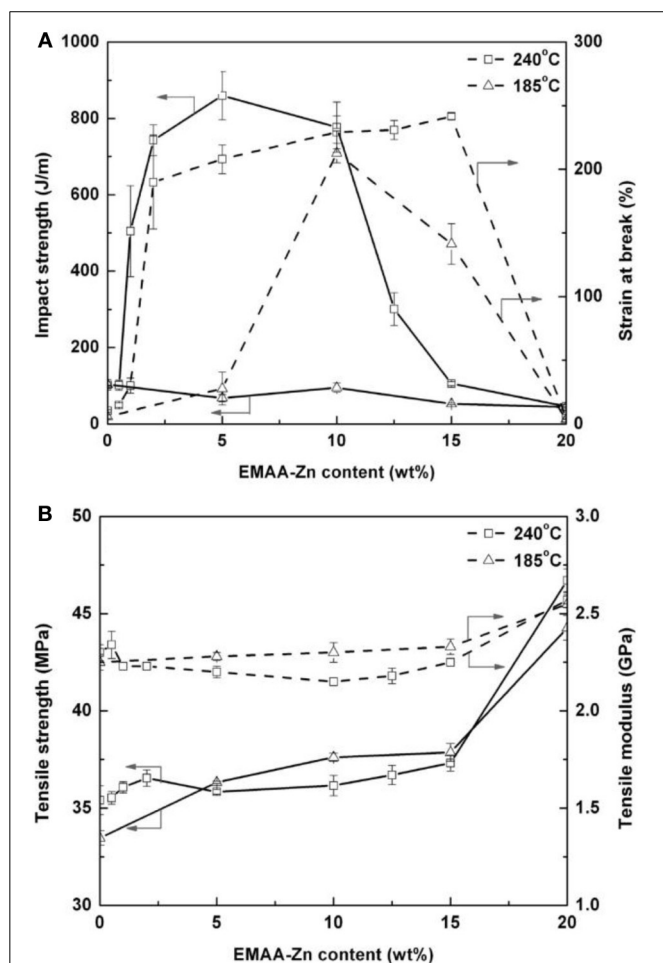


FIGURE 21 | Mechanical properties of PLA/EBA-GMA/EMAA-Zn (80/x/y in weight, $x + y = 20$) blends as functions of weight content of added EMAA-Zn under 240°C vs. 185°C: (A) impact strength (solid line) and strain at break (%) (dashed line); (B) tensile strength (solid line) and tensile modulus (dashed line). Liu et al. (2010).

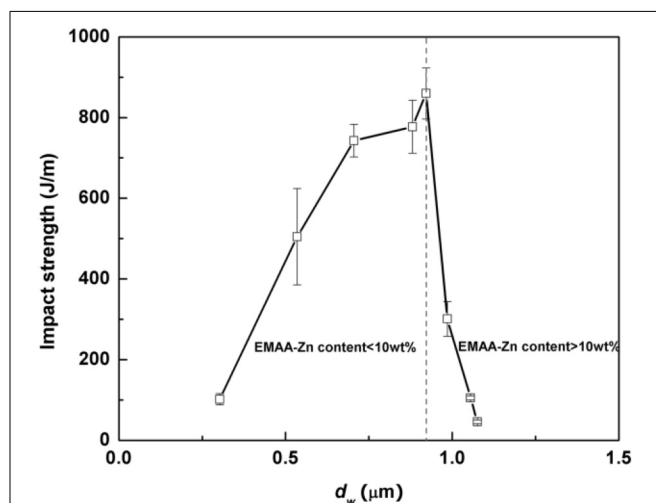
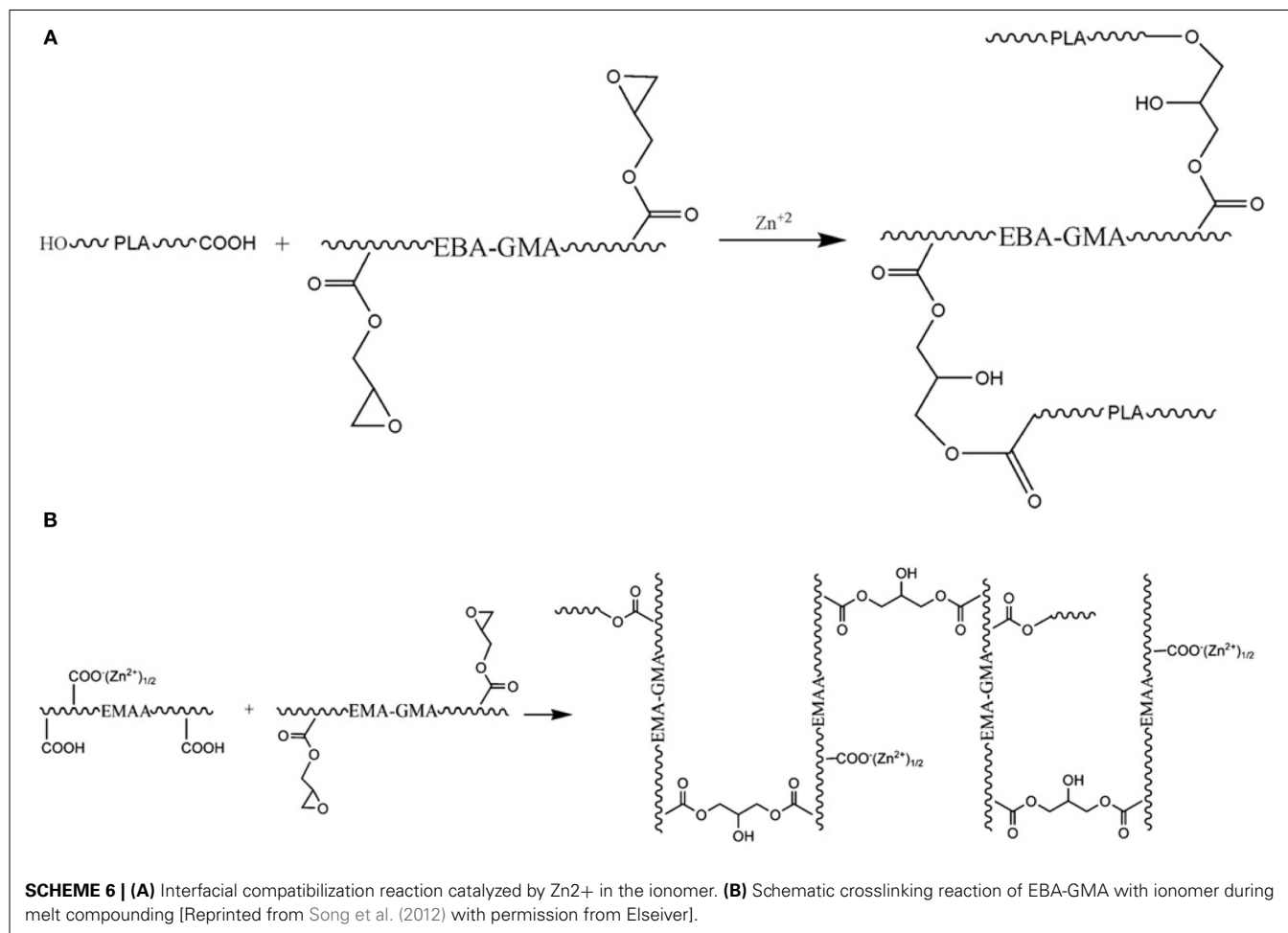


FIGURE 22 | Izod impact strength of PLA/EBA-GMA/EMAA-Zn (80/20-x/x) blends with total content of both modifiers fixed at 20 wt% as a function of weight-average particle diameter (d_w). Adapted with permission from Liu et al. (2011).



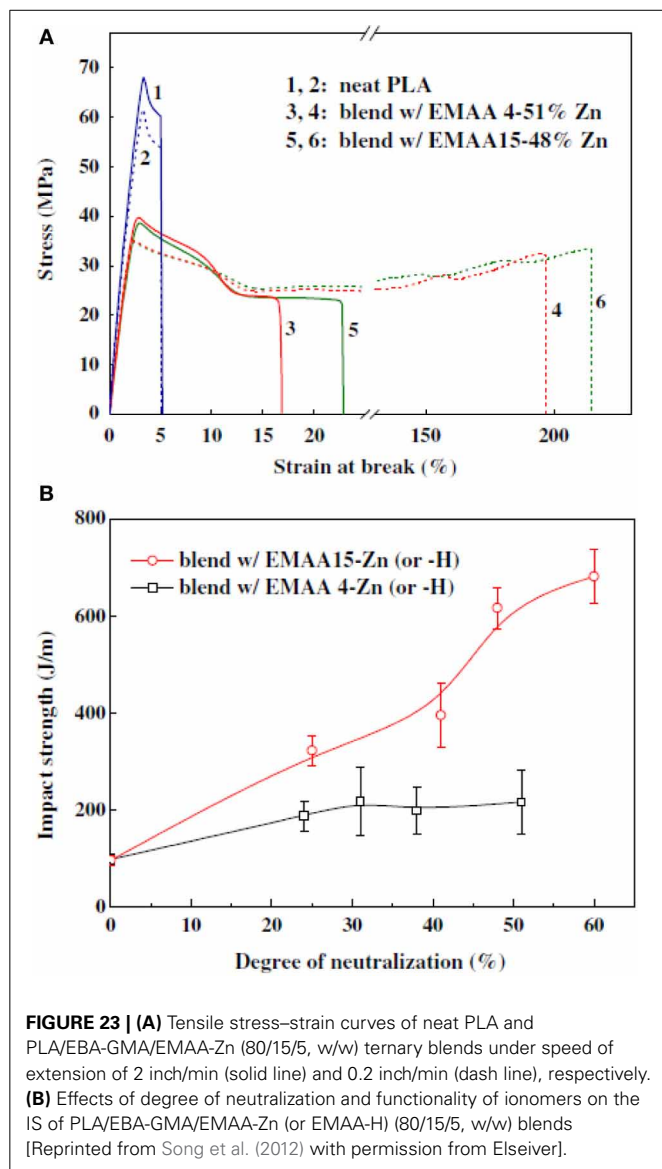
to come from the negative pressure effect of SEBS that dilates the plastic matrix consisting of PLA and PC to enhance the local segment motions. The phenomenon is briefly summarized in **Figure 24**.

Jiang et al. (2012) blended PLA with various commercial rubber components, i.e., poly (ethylene-glycidyl methacrylate) (EGMA), maleic anhydride grafted poly(styrene-ethylene/butylene-styrene) triblock elastomer (m-SEBS), and poly(ethylene-co-octene) (EOR) and compared their toughening effect on PLA (**Figure 25**). It was observed that: (i) EGMA was highly compatible due to its reaction with PLA, (ii) m-SEBS was less compatible with PLA, and (iii) EOR was incompatible with PLA. SEM and TEM revealed that a fine 3-D co-continuous microlayer structure was formed in the injection-moulded PLA/EGMA blends. This led to polymer blends with high toughness and very low linear thermal expansion both in the flow direction and in the transverse direction. The microlayer thickness of rubber in PLA blends was found to play key-roles in reducing the linear thermal expansion and achieving high toughness of the blends. Therefore, PLA blends with the notched impact strength over 20 times higher (ca. 90 kJ/m^2) than that of the neat PLA (ca. 4 kJ/m^2) were obtained by reactive blending of PLA and EGMA at 40 wt.% of rubber loading. It should be

highlighted that the PLA/EGMA blend having both high impact resistance and low thermal expansion coefficient is of great importance in applications.

CONCLUSION

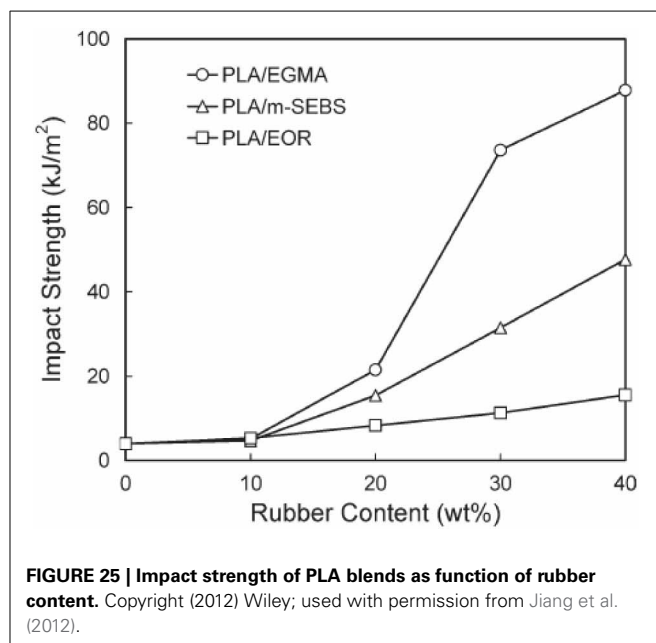
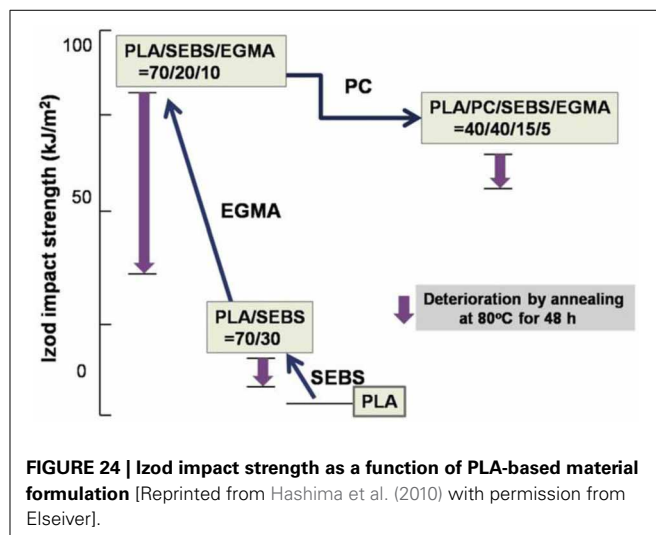
In comparison with many other commodity thermoplastics, PLA presents many advantages, mainly its renewability, biodegradability, high stiffness and competitive cost production. The main problem for this biopolyester is its inherent brittleness due to a crazing deformation mechanism through which the polymer fails upon tensile and impact testing. Since many applications require high impact resistance and flexibility bio-based and/or biodegradable materials, several approaches aiming at toughening PLA has been investigated over the last decades. First of all, understanding the effect of the pristine microstructure modification on the mechanical performances was established. It has been demonstrated that de-aging and molecular orientation can improve the mechanical properties of PLA. However, such strategies require long and specific processes, which are not cost effective for an economical production of high performance PLA materials. Classically, compounding with softer polymers seems to be the best option for toughening PLA in



costless way. The toughening effects of PLA blends are complicated as many parameters are concerned including the high interfacial adhesion between the matrix and the toughener, the domain size of the dispersed phase that should be ideally between 0.1 and 1.0 μm to improve the blend compatibility. The most common compatibilization way consists on the incorporation of block copolymers. Recently, chemical compatibilization *via* reactive extrusion has proven to be a very promising technology and more effective in improving the toughness of PLA blends. In some cases, outstanding toughness was successfully achieved, but accompanied with a compromise of the biodegradability and the initial stiffness of PLA. Therefore, the challenge pursues to develop a fully bio-based and biodegradable PLA-based material with a balance of outstanding mechanical properties.

ACKNOWLEDGMENTS

Authors from CIRMAR are grateful to the “Région Wallonne” and European Community (FEDER, FSE) in the frame of “Pôle



d'Excellence Materia Nova” for their financial support. CIRMAR thanks the “Belgian Federal Government Office Policy of Science (SSTC)” for general support in the frame of the PAI-6/27. Jean-Marie Raquez is “chercheur qualifié” by the F.R.S.-FNRS. Authors (from AMS and CIRMAR) thank the Fonds National de la Recherche-Luxembourg and the Centre de Recherche Public Henri Tudor for financial supports.

REFERENCES

- Afrifah, K. A., and Matuana, L. M. (2010). Impact modification of polylactide with a biodegradable ethylene/acrylate copolymer. *Macromol. Mater. Eng.* 295, 802–811. doi: 10.1002/mame.201000107
- Alcock, B., Cabrera, N. O., Barkoula, N. M., Loos, J., and Peijs, T. (2006). The mechanical properties of unidirectional all-polypropylene composites. *Compos. Part A Appl. Sci. Manuf.* 37, 716–726. doi: 10.1016/j.compositesa.2005.07.002
- Ali, F., Chang, Y.-W., Kang, S. C., and Yoon, J. Y. (2009). Thermal, mechanical and rheological properties of poly (lactic acid)/epoxidized soybean oil blends. *Polym. Bull.* 62, 91–98. doi: 10.1007/s00289-008-1012-9

- Anderson, K. S., and Hillmyer, M. A. (2004). The influence of block copolymer microstructure on the toughness of compatibilized polylactide/polyethylene blends. *Polymer* 45, 8809–8823. doi: 10.1016/j.polymer.2004.10.047
- Anderson, K. S., Lim, S. H., and Hillmyer, M. A. (2003). Toughening of polylactide by melt blending with linear low-density polyethylene. *J. Appl. Polym. Sci.* 89, 3757–3768. doi: 10.1002/app.12462
- Anderson, K. S., Schreck, K. M., and Hillmyer, M. A. (2008). Toughening polylactide. *Polymer Reviews* 48, 85–108. doi: 10.1080/15583720701834216
- Argon, A. S., and Cohen, R. E. (1990). “Crazing and toughness of block copolymers and blends,” in *Crazing in Polymers* Vol. 2, ed H. H. Kausch (Berlin Heidelberg: Springer), 301–351.
- Babcock, L. M., Henton, D. E., and Tadesse, F. A. (2008). *Impact Modified Polylactide Resins*, U.S. Pat. WO 2008/051443 A1 patent application.
- Baiardo, M., Frisoni, G., Scandola, M., Rimelen, M., Lips, D., Ruffieux, K., et al. (2003). Thermal and mechanical properties of plasticized poly(L-lactic acid). *J. Appl. Polym. Sci.* 90, 1731–1738. doi: 10.1002/app.12549
- Baker, W. E., Scott, C. E., and Hu, G.-H. (2001). *Reactive Polymer Blending*, Cincinnati: Hanser Publishers; Munich Hanser Gardner Publications, Inc.
- Barish, L. (1962). The study of cracking and fracturing of spherulitic isotactic polypropylene. *J. Appl. Polym. Sci.* 6, 617–623. doi: 10.1002/app.1962.070062403
- Battegazzore, D., Bocchini, S., and Frache, A. (2011). Crystallization kinetics of poly(lactic acid)-talc composites. *eXPRESS Polym. Lett.* 5, 849–858. doi: 10.3144/expresspolymlett.2011.84
- Bhardwaj, R., and Mohanty, A. K. (2007). Modification of Brittle Polylactide by Novel Hyperbranched Polymer-Based Nanostructures. *Biomacromolecules* 8, 2476–2484. doi: 10.1021/bm070367x
- Bigg, D. M. (2005). Polylactide copolymers: effect of copolymer ratio and end capping on their properties. *Adv. Polym. Technol.* 24, 69–82. doi: 10.1002/adv.20032
- Bitinis, N., Verdejo, R., Cassagnau, P., and Lopez-Manchado, M. A. (2011). Structure and properties of polylactide/natural rubber blends. *Mater. Chem. Phys.* 129, 823–831. doi: 10.1016/j.matchemphys.2011.05.016
- Bopp, R., and Whelan, J. (2003). U.S. Pat. WO 200316015 A1 patent application.
- Broz, M. E., Vanderhart, D. L., and Washburn, N. R. (2003). Structure and mechanical properties of poly(D,L-lactic acid)/poly(ϵ -caprolactone) blends. *Biomaterials* 24, 4181–4190. doi: 10.1016/S0142-9612(03)00314-4
- Bucknall, C. (1978). “Fracture and failure of multiphase polymers and polymer composites,” in *Failure in Polymers*, ed E. H. Andrews (Berlin, Heidelberg: Springer), 121–148.
- Bucknall, C. B. (2007). Quantitative approaches to particle cavitation, shear yielding, and crazing in rubber-toughened polymers. *J. Polym. Sci. B Polym. Phys.* 45, 1399–1409. doi: 10.1002/polb.21171
- Bucknall, C. B., and Paul, D. R. (2009). Notched impact behaviour of polymer blends: Part 1: new model for particle size dependence. *Polymer* 50, 5539–5548. doi: 10.1016/j.polymer.2009.09.059
- Carrasco, F., Pagès, P., Gámez-Pérez, J., Santana, O. O., and MasPOCH, M. L. (2010). Processing of poly(lactic acid): characterization of chemical structure, thermal stability and mechanical properties. *Polym. Degrad. Stab.* 95, 116–125. doi: 10.1016/j.polymdegradstab.2009.11.045
- Chang, K., Robertson, M. L., and Hillmyer, M. A. (2009). Phase inversion in polylactide/soybean oil blends compatibilized by poly(isoprene-*b*-lactide) block copolymers. *ACS Appl. Materials and Interfaces* 1, 2390–2399. doi: 10.1021/am900514v
- Chen, G.-X., Kim, H.-S., Kim, E.-S., and Yoon, J.-S. (2005). Compatibilization-like effect of reactive organoclay on the poly(l-lactide)/poly(butylene succinate) blends. *Polymer* 46, 11829–11836. doi: 10.1016/j.polymer.2005.10.056
- Chen, G.-X., and Yoon, J.-S. (2005). Morphology and thermal properties of poly(L-lactide)/poly(butylene succinate-co-butylene adipate) compounded with twice functionalized clay. *J. Polym. Sci. B Polym. Phys.* 43, 478–487. doi: 10.1002/polb.20345
- Chen, X., McCarthy, S. P., and Gross, R. A. (1997). Synthesis and characterization of [L]-lactide-ethylene oxide multiblock copolymers. *Macromolecules* 30, 4295–4301. doi: 10.1021/ma970385e
- Co, S. (2010). *Biogoes functional—Sukano biobased masterbatches put performance into PLA [Online]*. Available: <http://www.sukano.com/pdf/PC022010BIOBM.pdf> (Accessed February, 2010).
- Dompas, D., and Groeninckx, G. (1994). Toughening behaviour of rubber-modified thermoplastic polymers involving very small rubber particles: 1. A criterion for internal rubber cavitation. *Polymer* 35, 4743–4749. doi: 10.1016/0032-3861(94)90727-7
- Dompas, D., Groeninckx, G., Isogawa, M., Hasegawa, T., and Kadokura, M. (1994). Toughening behaviour of rubber-modified thermoplastic polymers involving very small rubber particles: 2. Rubber cavitation behaviour in poly(vinyl chloride)/methyl methacrylate-butadiene-styrene graft copolymer blends. *Polymer* 35, 4750–4759. doi: 10.1016/0032-3861(94)90728-5
- Donald, A. M., and Kramer, E. J. (1982). Craze initiation and growth in high-impact polystyrene. *J. Appl. Polym. Sci.* 27, 3729–3741. doi: 10.1002/app.1982.070271009
- DuPont Co. (2010). Website. Product Data Sheet. Biomax Strong 100. Available online at: http://www2.dupont.com/Biomax/en_US/assets/downloads/biomax_strong_100.pdf. Accessed on January 12, 2010.
- Feng, F., and Ye, L. (2011). Morphologies and mechanical properties of polylactide/thermoplastic polyurethane elastomer blends. *J. Appl. Polym. Sci.* 119, 2778–2783. doi: 10.1002/app.32863
- Feng, Y., Hu, Y., Yin, J., Zhao, G., and Jiang, W. (2013). High impact poly(lactic acid)/poly(ethylene octene) blends prepared by reactive blending. *Polym. Eng. Sci.* 53, 389–396. doi: 10.1002/pen.23265
- Gamez-Perez, J. (2010). Fracture behaviour of quenched poly(lactic acid). *eXPRESS Polym. Lett.* 5, 82–91. doi: 10.3144/expresspolymlett.2011.9
- Ge, H., Yang, F., Hao, Y., Wu, G., Zhang, H., and Dong, L. (2013). Thermal, mechanical, and rheological properties of plasticized poly(L-lactic acid). *J. Appl. Polym. Sci.* 127, 2832–2839. doi: 10.1002/app.37620
- Ghosh, S., Viana, J. C., Reis, R. L., and Mano, J. F. (2008). Oriented morphology and enhanced mechanical properties of poly(L-lactic acid) from shear controlled orientation in injection moulding. *Mater. Sci. Eng. A* 490, 81–89. doi: 10.1016/j.msea.2008.01.003
- Gramlich, W. M., Robertson, M. L., and Hillmyer, M. A. (2010). Reactive compatibilization of poly(l-lactide) and conjugated soybean oil. *Macromolecules* 43, 2313–2321. doi: 10.1021/ma902449x
- Grijpma, D. W., Altpeter, H., Bevis, M. J., and Feijen, J. (2002). Improvement of the mechanical properties of poly(D,L-lactide) by orientation. *Polym. Int.* 51, 845–851. doi: 10.1002/pi.988
- Gui, Z., Xu, Y., Cheng, S., Gao, Y., and Lu, C. (2013). Preparation and characterization of polylactide/poly(polyethylene glycol-co-citric acid) blends. *Polym. Bull.* 70, 325–342. doi: 10.1007/s00289-012-0810-2
- Hammer, C. F., Koch, T. A., and Whitney, J. F. (1959). Fine structure of acetal resins and its effect on mechanical properties. *J. Appl. Polym. Sci.* 1, 169–178. doi: 10.1002/app.1959.070010207
- Han, J.-J., and Huang, H.-X. (2011). Preparation and characterization of biodegradable polylactide/thermoplastic polyurethane elastomer blends. *J. Appl. Polym. Sci.* 120, 3217–3223. doi: 10.1002/app.33338
- Han, L., Han, C., and Dong, L. (2013). Morphology and properties of the biosourced poly(lactic acid)/poly(ethylene oxide-*b*-amide-12) blends. *Polym. Compos.* 34, 122–130. doi: 10.1002/pc.22383
- Harada, M., Iida, K., Okamoto, K., Hayashi, H., and Hirano, K. (2008). Reactive compatibilization of biodegradable poly(lactic acid)/poly(ϵ -caprolactone) blends with reactive processing agents. *Polym. Eng. Sci.* 48, 1359–1368. doi: 10.1002/pen.21088
- Harada, M., Ohya, T., Iida, K., Hayashi, H., Hirano, K., and Fukuda, H. (2007). Increased impact strength of biodegradable poly(lactic acid)/poly(butylene succinate) blend composites by using isocyanate as a reactive processing agent. *J. Appl. Polym. Sci.* 106, 1813–1820. doi: 10.1002/app.26717
- Hashima, K., Nishitsuji, S., and Inoue, T. (2010). Structure-properties of super-tough PLA alloy with excellent heat resistance. *Polymer* 51, 3934–3939. doi: 10.1016/j.polymer.2010.06.045
- Hassouna, F., Raquez, J.-M., Addiego, F., Dubois, P., Toniazio, V., and Ruch, D. (2011). New approach on the development of plasticized polylactide (PLA): Grafting of poly(ethylene glycol) (PEG) via reactive extrusion. *Eur. Polym. J.* 47, 2134–2144. doi: 10.1016/j.eurpolymj.2011.08.001
- Hassouna, F., Raquez, J.-M., Addiego, F., Toniazio, V., Dubois, P., and Ruch, D. (2012). New development on plasticized poly(lactide): Chemical grafting of citrate on PLA by reactive extrusion. *Eur. Polym. J.* 48, 404–415. doi: 10.1016/j.eurpolymj.2011.12.001
- Hu, Y., Hu, Y. S., Topolkaraev, V., Hiltner, A., and Baer, E. (2003a). Aging of poly(lactide)/poly(ethylene glycol) blends. Part 2. Poly(lactide) with high stereoregularity. *Polymer* 44, 5711–5720. doi: 10.1016/S0032-3861(03)00615-3

- Hu, Y., Rogunova, M., Topolkaraev, V., Hiltner, A., and Baer, E. (2003b). Aging of poly(lactide)/poly(ethylene glycol) blends. Part 1. Poly(lactide) with low stereoregularity. *Polymer* 44, 5701–5710.
- Ikado, S., Kobayashi, N., Kurokit, T., Saruwatarim, M., Suzuki, K., and Wanibe, H. (1997). European Patent 776927 A1, assigned to Mitsui Toatsui Chem, Inc.
- Ikeda, R. M. (1993). Shear yield and crazing stresses in selected glassy polymers. *J. Appl. Polym. Sci.* 47, 619–629. doi: 10.1002/app.1993.070470406
- Ito, M., Abe, S., and Ishikawa, M. (2010). The fracture mechanism of polylactic acid resin and the improving mechanism of its toughness by addition of acrylic modifier. *J. Appl. Polym. Sci.* 115, 1454–1460. doi: 10.1002/app.31292
- Jacobsen, S., and Fritz, H. G. (1999). Plasticizing polylactide – the effect of different plasticizers on the mechanical properties. *Polym. Eng. Sci.* 39, 1303–1310. doi: 10.1002/pen.11517
- Jansen, B. J. P., Rastogi, S., Meijer, H. E. H., and Lemstra, P. J. (1999). rubber-modified glassy amorphous polymers prepared via chemically induced phase separation. 3. influence of the strain rate on the microscopic deformation mechanism. *Macromolecules* 32, 6283–6289. doi: 10.1021/ma981406n
- Jiang, J., Su, L., Zhang, K., and Wu, G. (2012). Rubber-toughened PLA blends with low thermal expansion. *J. Appl. Polym. Sci.* 128, 3993–4000. doi: 10.1002/app.38642
- Jiang, L., Wolcott, M. P., and Zhang, J. (2006). Study of biodegradable polylactide/poly(butylene adipate-co-terephthalate) blends. *Biomacromolecules* 7, 199–207.
- Kambour, R. P. (1973). A review of crazing and fracture in thermoplastics. *J. Polym. Sci. Macromol. Rev.* 7, 1–154. doi: 10.1002/pol.1973.230070101
- Kjeschke, K., Timmermann, R., and Voight, M. (2001). German Patent De 100279 A1, assigned to Bayer Ag.
- Kmetty, Á., Bárány, T., and Karger-Kocsis, J. (2010). Self-reinforced polymeric materials: a review. *Prog. Polym. Sci.* 35, 1288–1310. doi: 10.1016/j.progpolymsci.2010.07.002
- Kolstad, J. J. (1996). Crystallization kinetics of poly(L-lactide-co-meso-lactide). *J. Appl. Polym. Sci.* 62, 1079–1091.
- Könczöl, L., Döll, W., and Michler, G. H. (1992). Study of the toughening mechanism of crazing in rubber modified thermoplastics. *Colloid Polym. Sci.* 270, 972–981. doi: 10.1007/BF00655966
- Kowalczyk, M., and Piorkowska, E. (2012). Mechanisms of plastic deformation in biodegradable polylactide/poly(1,4-cis-isoprene) blends. *J. Appl. Polym. Sci.* 124, 4579–4589. doi: 10.1002/app.35489
- Kramer, E. (1983). “Microscopic and molecular fundamentals of crazing,” in *Crazing in Polymers*, ed H. H. Kausch (Berlin, Heidelberg: Springer), 1–56.
- Kramer, E., and Berger, L. (1990). “Fundamental processes of craze growth and fracture,” in *Crazing in Polymers*, Vol. 2, ed H. H. Kausch (Berlin, Heidelberg: Springer), 1–68.
- Kray, R. J., and Bellet, R. J. (1968). U.S. Pat. 3,388,186 patent application.
- Kulinski, Z., Piorkowska, E., Gadzinowska, K., and Stasiak, M. (2006). Plasticization of Poly(L-lactide) with Poly(propylene glycol). *Biomacromolecules* 7, 2128–2135. doi: 10.1021/bm060089m
- Murch, L. E. (1974). U.S. Pat. 3,845,163 patent application.
- Labrecque, L. V., Kumar, R. A., Davé, V., Gross, R. A., and McCarthy, S. P. (1997). Citrate esters as plasticizers for poly(lactic acid). *J. Appl. Polym. Sci.* 66, 1507–1513.
- Lapol, L. W. (2009). *Getting Started with LapolVR 108 Bioplasticizer* [Online]. Available online at: http://www.lapol.net/images/Lapol_Getting_Started_Guide_and_Essential_Documentation_100930.pdf
- Lemmouchi, Y., Murariu, M., Santos, A. M. D., Amass, A. J., Schacht, E., and Dubois, P. (2009). Plasticization of poly(lactide) with blends of tributyl citrate and low molecular weight poly(d,l-lactide)-b-poly(ethylene glycol) copolymers. *Eur. Polym. J.* 45, 2839–2848. doi: 10.1016/j.eurpolymj.2009.07.006
- Li, H., and Huneault, M. A. (2007). Effect of nucleation and plasticization on the crystallization of poly(lactic acid). *Polymer* 48, 6855–6866. doi: 10.1016/j.polymer.2007.09.020
- Li, R., and Yao, D. (2008). Preparation of single poly(lactic acid) composites. *J. Appl. Polym. Sci.* 107, 2909–2916. doi: 10.1002/app.27406
- Li, S. (1999). Hydrolytic degradation characteristics of aliphatic polyesters derived from lactic and glycolic acids. *J. Biomed. Mater. Res.* 48, 342–353.
- Li, Y., and Shimizu, H. (2007). Toughening of polylactide by melt blending with a biodegradable poly(ether)urethane elastomer. *Macromol. Biosci.* 7, 921–928. doi: 10.1002/mabi.200700027
- Li, Y., and Shimizu, H. (2009). Improvement in toughness of poly(l-lactide) (PLLA) through reactive blending with acrylonitrile–butadiene–styrene copolymer (ABS): morphology and properties. *Eur. Polym. J.* 45, 738–746. doi: 10.1016/j.eurpolymj.2008.12.010
- Lim, L. T., Auras, R., and Rubino, M. (2008). Processing technologies for poly(lactic acid). *Prog. Polym. Sci.* 33, 820–852. doi: 10.1016/j.progpolymsci.2008.05.004
- Lin, S., Guo, W., Chen, C., Ma, J., and Wang, B. (2012). Mechanical properties and morphology of biodegradable poly(lactic acid)/poly(butylene adipate-co-terephthalate) blends compatibilized by transesterification. *Mater. Des.* 36, 604–608. doi: 10.1016/j.matdes.2011.11.036
- Lin, Y., Zhang, K.-Y., Dong, Z.-M., Dong, L.-S., and Li, Y.-S. (2007). Study of hydrogen-bonded blend of polylactide with biodegradable hyperbranched poly(ester amide). *Macromolecules* 40, 6257–6267. doi: 10.1021/ma070989a
- Liu, H., Chen, F., Liu, B., Estep, G., and Zhang, J. (2010). Super toughened poly(lactic acid) ternary blends by simultaneous dynamic vulcanization and interfacial compatibilization. *Macromolecules* 43, 6058–6066. doi: 10.1021/ma101108g
- Liu, H., Song, W., Chen, F., Guo, L., and Zhang, J. (2011). Interaction of microstructure and interfacial adhesion on impact performance of polylactide (PLA) ternary blends. *Macromolecules* 44, 1513–1522. doi: 10.1021/ma1026934
- Liu, H., and Zhang, J. (2011). Research progress in toughening modification of poly(lactic acid). *J. Polym. Sci. B Polym. Phys.* 49, 1051–1083. doi: 10.1002/polb.22283
- Ljungberg, N., Andersson, T., and Wesslén, B. (2003). Film extrusion and film weldability of poly(lactic acid) plasticized with triacetone and tributyl citrate. *J. Appl. Polym. Sci.* 88, 3239–3247. doi: 10.1002/app.12106
- Ljungberg, N., Colombini, D., and Wesslén, B. (2005). Plasticization of poly(lactic acid) with oligomeric malonate esteramides: dynamic mechanical and thermal film properties. *J. Appl. Polym. Sci.* 96, 992–1002. doi: 10.1002/app.21163
- Ljungberg, N., and Wesslén, B. (2002). The effects of plasticizers on the dynamic mechanical and thermal properties of poly(lactic acid). *J. Appl. Polym. Sci.* 86, 1227–1234. doi: 10.1002/app.11077
- Ljungberg, N., and Wesslén, B. (2003). Tributyl citrate oligomers as plasticizers for poly(lactic acid): thermo-mechanical film properties and aging. *Polymer* 44, 7679–7688. doi: 10.1016/j.polymer.2003.09.055
- Long, J., Bo, L., and Jinwen, Z. (2009). Properties of poly(lactic acid)/poly(butylene adipate-co-terephthalate)/nanoparticle ternary composites. *Ind. Eng. Chem. Res.* 48, 7594–7602. doi: 10.1021/ie900576f
- López-Rodríguez, N., López-Arraiza, A., Meaurio, E., and Sarasua, J. R. (2006). Crystallization, morphology, and mechanical behaviour of polylactide/poly(ϵ -caprolactone) blends. *Polym. Eng. Sci.* 46, 1299–1308. doi: 10.1002/pen.20609
- Lu, F., Cantwell, W. J., and Kausch, H. H. (1997). The role of cavitation and debonding in the toughening of core-shell rubber modified epoxy systems. *J. Mater. Sci.* 32, 3055–3059. doi: 10.1023/A:1018626012271
- Ma, P., Hristova-Bogaerds, D. G., Goossens, J. G. P., Spoelstra, A. B., Zhang, Y., and Lemstra, P. J. (2012). Toughening of poly(lactic acid) by ethylene-co-vinyl acetate copolymer with different vinyl acetate contents. *Eur. Polym. J.* 48, 146–154. doi: 10.1016/j.eurpolymj.2011.10.015
- Ma, P., Spoelstra, A. B., Schmit, P., and Lemstra, J. P. (2013). Toughening of poly(lactic acid) by poly(β -hydroxybutyrate-co- β -hydroxyvalerate) with high β -hydroxyvalerate content. *Eur. Polym. J.* 49, 1523–1531. doi: 10.1016/j.eurpolymj.2013.01.016
- Mahajan, D. K., and Hartmaier, A. (2012). Mechanisms of crazing in glassy polymers revealed by molecular dynamics simulations. *Phys. Rev. E* 86, 021802. doi: 10.1103/PhysRevE.86.021802
- Majola, A., Vainionpää, S., Rokkanen, P., Mikkola, H. M., and Törmälä, P. (1992). Absorbable self-reinforced polylactide (SR-PLA) composite rods for fracture fixation: strength and strength retention in the bone and subcutaneous tissue of rabbits. *J. Mater. Sci. Mater. Med.* 3, 43–47. doi: 10.1007/BF00702943
- Mäkelä, P., Pohjonen, T., Törmälä, P., Waris, T., and Ashammakhi, N. (2002). Strength retention properties of self-reinforced poly l-lactide (SR-PLLA) sutures compared with polyglyconate (MaxonR) and polydioxanone (PDS) sutures. An *in vitro* study. *Biomaterials* 23, 2587–2592. doi: 10.1016/S0142-9612(01)00396-9
- Mani, R., Bhattacharya, M., and Tang, J. (1999). Functionalization of polyesters with maleic anhydride by reactive extrusion. *J. Polym. Sci. A Polym. Chem.* 37, 1693–1702.

- Martin, O., and Avérous, L. (2001). Poly(lactic acid): plasticization and properties of biodegradable multiphase systems. *Polymer* 42, 6209–6219. doi: 10.1016/S0032-3861(01)00086-6
- Martino, V. P., Jiménez, A., and Ruseckaite, R. A. (2009). Processing and characterization of poly(lactic acid) films plasticized with commercial adipates. *J. Appl. Polym. Sci.* 112, 2010–2018. doi: 10.1002/app.29784
- Martino, V. P., Ruseckaite, R. A., and Jiménez, A. (2006). Thermal and mechanical characterization of plasticized poly (L-lactide-co-D,L-lactide) films for food packaging. *J. Therm. Anal. Calorim.* 86, 707–712. doi: 10.1007/s10973-006-7897-3
- Mascia, L., and Xanthos, M. (1992). An overview of additives and modifiers for polymer blends: facts, deductions, and uncertainties. *Adv. Polym. Technol.* 11, 237–248. doi: 10.1002/adv.1992.060110402
- Mason, C. D., and Tuller, H. W. (1983). *High impact nylon composition containing copolymer esters and ionic copolymers*. U.S. Pat. 4,404,325 A patent application. Available online at: <http://www.google.nl/patents/US4404325>.
- Matabola, K. P., De Vries, A. R., Moolman, F. S., and Luyt, A. S. (2009). Single polymer composites: a review. *J. Mater. Sci.* 44, 6213–6222. doi: 10.1007/s10853-009-3792-1
- McCarthy, S., and Song, X. (2002). Biodegradable plasticizers for polylactic acid. *J. Appl. Med. Polym.* 6, 64–69.
- Meng, B., Deng, J., Liu, Q., Wu, Z., and Yang, W. (2012). Transparent and ductile poly(lactic acid)/poly(butyl acrylate) (PBA) blends: structure and properties. *Eur. Polym. J.* 48, 127–135. doi: 10.1016/j.eurpolymj.2011.10.009
- Mercier, J. P., Aklonis, J. J., Litt, M., and Tobolsky, A. V. (1965). Viscoelastic behaviour of the polycarbonate of bisphenol A. *J. Appl. Polym. Sci.* 9, 447–459. doi: 10.1002/app.1965.070090206
- Michaeli, W., Höcker, H., Berghaus, U., and Frings, W. (1993). Reactive extrusion of styrene polymers. *J. Appl. Polym. Sci.* 48, 871. doi: 10.1002/app.1993.070480512
- Michler, G. H. (1989). Crazes in amorphous polymers I. Variety of the structure of crazes and classification of different types of crazes. *Colloid Polym. Sci.* 267, 377–388. doi: 10.1007/BF01410182
- Mochizuki, T., and Suzuki, F. (2004). U.S. Patent Application 20040180990 A1, Assigned to Fuji Photo Co Ltd.
- Murariu, M., Da Silva Ferreira, A., Alexandre, M., and Dubois, P. (2008a). Polylactide (PLA) designed with desired end-use properties: 1. PLA compositions with low molecular weight ester-like plasticizers and related performances. *Polym. Adv. Technol.* 19, 636–646. doi: 10.1002/pat.1131
- Murariu, M., Ferreira, A. D. S., Duquesne, E., Bonnaud, L., and Dubois, P. (2008b). Polylactide (PLA) and highly filled PLA - calcium sulfate composites with improved impact properties. *Macromol. Symp.* 272, 1–12. doi: 10.1002/masy.200851201
- Nair, L. S., and Laurencin, C. T. (2007). Biodegradable polymers as biomaterials. *Prog. Polym. Sci.* 32, 762–798. doi: 10.1016/j.progpolymsci.2007.05.017
- Narisawa, I., and Yee, A. (2006). “Crazing and fracture of polymers,” in *Materials Science and Technology* (Yonezaga; Ann Arbor: Wiley-VCH Verlag GmbH and Co. KGaA). doi: 10.1002/9783527603978.mst0146
- Nascimento, L., Gamez-Perez, J., Santana, O. O., Velasco, J. I., MasPOCH, M. L., and Franco-Urquiza, E. (2010). Effect of the Recycling and Annealing on the Mechanical and Fracture Properties of Poly(Lactic Acid). *J. Polym. Environ.* 18, 654–660. doi: 10.1007/s10924-010-0229-5
- Natureworks® (2005). PLA Polymer 2002D – Data Sheet. Available online at: <http://www.unicgroup.com/upfiles/file01170656495.pdf>
- Natureworks® (2006). PLA Polymer 4032D – Data Sheet. Available online at: http://www.natureworkslc.com/~media/Technical_Resources/Technical_Data_Sheets/TechnicalDataSheet_4032D_films.pdf
- Natureworks LLC (2007). Technology Focus Report: Toughened PLA. Available online at: http://www.natureworkslc.com/~media/Technical_Resources/Properties_Documents/PropertiesDocument_Toughened-Ingeo_pdf.pdf
- Noda, I., Green, P. R., Satkowski, M. M., and Schechtman, L. A. (2005). Preparation and properties of a novel class of polyhydroxyalkanoate copolymers. *Biomacromolecules* 6, 580–586. doi: 10.1021/bm049472m
- Noda, I., Satkowski, M. M., Dowrey, A. E., and Marcott, C. (2004). Polymer Alloys of Nodax Copolymers and Poly(lactic acid). *Macromol. Biosci.* 4, 269–275. doi: 10.1002/mabi.200300093
- Nyambo, C., Misra, M., and Mohanty, A. (2012). Toughening of brittle poly(lactide) with hyperbranched poly(ester-amide) and isocyanate-terminated prepolymer of polybutadiene. *J. Mater. Sci.* 47, 5158–5168. doi: 10.1007/s10853-012-6393-3
- O’Connell, P. A., and McKenna, G. B. (2002). “Yield and crazing in polymers,” in *Encyclopedia of Polymer Science and Technology* (Lubbock, Texas: Texas Tech University; John Wiley and Sons, Inc.). Available online at: http://onlinelibrary.wiley.com/book/10.1002/0471440264/homepage/Editors_Contributors.html. doi: 10.1002/0471440264.pst463
- Odent, J., Habibi, Y., Raquez, J.-M., and Dubois, P. (2013a). *Ultra-tough polylactide-based materials synergistically designed in the presence of rubbery ε-caprolactone-based copolyester and silica nanoparticles*. Composites Science and Technology. doi: 10.1016/j.compscitech.2013.05.003
- Odent, J., Leclère, P., Raquez, J.-M., and Dubois, P. (2013b). Toughening of polylactide by tailoring phase-morphology with P[CL-co-LA] random copolymers as biodegradable impact modifiers. *Eur. Polym. J.* 49, 914–922. doi: 10.1016/j.eurpolymj.2012.12.006
- Odent, J., Habibi, Y., Raquez, J.-M., and Dubois, P. (2013c). “A new paradigm for the toughening of polylactide-based materials,” in *Proceedings of the Polymer Processing Society 28th Annual Meeting ~ PPS-28*. Pattaya
- Odent, J., Raquez, J.-M., Duquesne, E., and Dubois, P. (2012). Random aliphatic copolymers as new biodegradable impact modifiers for polylactide materials. *Eur. Polym. J.* 48, 331–340. doi: 10.1016/j.eurpolymj.2011.11.002
- Ohlberg, S. M., Roth, J., and Raff, R. A. V. (1959). Relationship between impact strength and spherulite growth in linear polyethylene. *J. Appl. Polym. Sci.* 1, 114–120. doi: 10.1002/app.1959.070010118
- Oyama, H. T. (2009). Super-tough poly(lactic acid) materials: Reactive blending with ethylene copolymer. *Polymer* 50, 747–751. doi: 10.1016/j.polymer.2008.12.025
- Park, S. D., Todo, M., Arakawa, K., and Koganemaru, M. (2006). Effect of crystallinity and loading-rate on mode I fracture behaviour of poly(lactic acid). *Polymer* 47, 1357–1363. doi: 10.1016/j.polymer.2005.12.046
- Pearson Raymond, A. (2000). “Introduction to the Toughening of Polymers,” in *Toughening of Plastics*, eds A. Pearson Raymond, H.-J. Sue, and A. F. Yee (Lehigh University; Texas A&M University; The University of Michigan: American Chemical Society), 1–12.
- Pecorini, T. J., and Hertzberg, R. W. (1993). The fracture toughness and fatigue crack propagation behaviour of annealed PET. *Polymer* 34, 5053–5062. doi: 10.1016/0032-3861(93)90248-9
- Perego, G., Cella, G. D., and Bastioli, C. (1996). Effect of molecular weight and crystallinity on poly(lactic acid) mechanical properties. *J. Appl. Polym. Sci.* 59, 37–43.
- Perkins, W. G. (1999). Polymer toughness and impact resistance. *Polym. Eng. Sci.* 39, 2445–2460. doi: 10.1002/pen.11632
- Petchwattana, N., Covavisaruch, S., and Euapanthasate, N. (2012). Utilization of ultrafine acrylate rubber particles as a toughening agent for poly(lactic acid). *Mater. Sci. Eng. A* 532, 64–70. doi: 10.1016/j.msea.2011.10.063
- Pillin, I., Montrelay, N., and Grohens, Y. (2006). Thermo-mechanical characterization of plasticized PLA: Is the miscibility the only significant factor? *Polymer* 47, 4676–4682. doi: 10.1016/j.polymer.2006.04.013
- Poirier, Y. (2002). Polyhydroxyalkanoate synthesis in plants as a tool for biotechnology and basic studies of lipid metabolism. *Prog. Lipid Res.* 41, 131–155. doi: 10.1016/S0163-7827(01)00018-2
- Rabetafika, H. N., Paquot, M., and Dubois, P. (2006). Les polymères issus du végétal matériaux à propriétés. *Biotechnol. Agron. Soc. Environ.* 10, 185–196.
- Robertson, M. L., Chang, K., Gramlich, W. M., and Hillmyer, M. A. (2010). Toughening of polylactide with polymerized soybean oil. *Macromolecules* 43, 1807–1814. doi: 10.1021/ma9022795
- Scaffaro, R., Morreale, M., Mirabella, F., and La Mantia, F. P. (2011). Preparation and Recycling of Plasticized PLA. *Macromol. Mater. Eng.* 296, 141–150. doi: 10.1002/mame.201000221
- Schreck, K. M., and Hillmyer, M. A. (2007). Block copolymers and melt blends of polylactide with Nodax™ microbial polyesters: preparation and mechanical properties. *J. Biotechnol.* 132, 287–295. doi: 10.1016/j.jbiotec.2007.03.017
- Seddon, J. D., Hepworth, S. J., and Priddle, J. E. (1971). United Kingdom 1,241,361 patent application.
- Seelig, T., and Van Der Giessen, E. (2009). A cell model study of crazing and matrix plasticity in rubber-toughened glassy polymers. *Comput. Mater. Sci.* 45, 725–728. doi: 10.1016/j.commatsci.2008.05.024
- Seiler, M. (2002). Dendritic polymers – interdisciplinary research and emerging applications from unique structural properties. *Chem. Eng. Technol.* 25, 237–253. doi: 10.1002/1521-4125(200203)25:3<237::AID-CEAT237>û3.0.CO;2-4

- Semba, T., Kitagawa, K., Ishiaku, U. S., and Hamada, H. (2006). The effect of crosslinking on the mechanical properties of polylactic acid/polycaprolactone blends. *J. Appl. Polym. Sci.* 101, 1816–1825. doi: 10.1002/app.23589
- Semba, T., Kitagawa, K., Ishiaku, U. S., Kotaki, M., and Hamada, H. (2007). Effect of compounding procedure on mechanical properties and dispersed phase morphology of poly(lactic acid)/polycaprolactone blends containing peroxide. *J. Appl. Polym. Sci.* 103, 1066–1074. doi: 10.1002/app.25311
- Sierra, J., Noriega, M., Cardona, E., and Ospina, S. (2010). *Proceedings of Annual Technical Conference of the Society of Plastics Engineers (ANTEC 2010)* (Orlando, FL).
- Sinclair, R. G. (1996). The case for polylactic acid as a commodity packaging plastic. *J. Macromol. Sci. A Pure Appl. Chem.* 33, 585–597. doi: 10.1080/10601329608010880
- Song, W., Liu, H., Chen, F., and Zhang, J. (2012). Effects of ionomer characteristics on reactions and properties of poly(lactic acid) ternary blends prepared by reactive blending. *Polymer* 53, 2476–2484. doi: 10.1016/j.polymer.2012.03.050
- Steinbüchel, A., and Valentin, H. E. (1995). Diversity of bacterial polyhydroxyalkanoic acids. *FEMS Microbiol. Lett.* 128, 219–228. doi: 10.1016/0378-1097(95)00125-0
- Su, Z., Li, Q., Liu, Y., Hu, G.-H., and Wu, C. (2009). Compatibility and phase structure of binary blends of poly(lactic acid) and glycidyl methacrylate grafted poly(ethylene octane). *Eur. Polym. J.* 45, 2428–2433. doi: 10.1016/j.eurpolymj.2009.04.028
- Sukano Co. (2008). Website. SUKANOVR announces unique transparent impact modifier for PLA. Available online at: http://www.sukano.com/downloads/newsletter/english/2008_02_PLA_IM_EN.pdf. Accessed on February 2008.
- Taib, R. M., Ghaleb, Z. A., and Mohd Ishak, Z. A. (2012). Thermal, mechanical, and morphological properties of polylactic acid toughened with an impact modifier. *J. Appl. Polym. Sci.* 123, 2715–2725. doi: 10.1002/app.34884
- Takayama, T., and Todo, M. (2006). Improvement of impact fracture properties of PLA/PCL polymer blend due to LTI addition. *J. Mater. Sci.* 41, 4989–4992. doi: 10.1007/s10853-006-0137-1
- Takayama, T., Todo, M., Tsuji, H., and Arakawa, K. (2006). Effect of LTI content on impact fracture property of PLA/PCL/LTI polymer blends. *J. Mater. Sci.* 41, 6501–6504. doi: 10.1007/s10853-006-0611-9
- Teamsinsungvon, A., Ruksakulpiwat, Y., and Jarukumjorn, K. (2010). *Mechanical and morphological properties of poly(lactic acid)/poly (butylene adipate-co-terephthalate)/calcium carbonate composite. 18th international conference on composite materials*. Available online at: [http://www.iccm-central.org/Proceedings/ICCM18proceedings/data/3.%20Poster%20Presentation/Aug23\(Tuesday\)/P2-18~35%20Green%20Composites/P2-27-IF1477.pdf](http://www.iccm-central.org/Proceedings/ICCM18proceedings/data/3.%20Poster%20Presentation/Aug23(Tuesday)/P2-18~35%20Green%20Composites/P2-27-IF1477.pdf)
- Törmälä, P. (1992). Biodegradable self-reinforced composite materials; Manufacturing structure and mechanical properties. *Clin. Mater.* 10, 29–34. doi: 10.1016/0267-6605(92)90081-4
- Tormala, P., Rokkanen, P., Laiho, J., Tamminmaki, M., and Vainionpää, S. (1988). Material for osteosynthesis devices. *US Patent Application 4,473,257*
- Tsuji, H., Nakano, M., Hashimoto, M., Takashima, K., Katsura, S., and Mizuno, A. (2006). Electrospinning of Poly(lactic acid) Stereocomplex Nanofibers. *Biomacromolecules* 7, 3316–3320. doi: 10.1021/bm060786e
- Urayama, H., Ma, C., and Kimura, Y. (2003). Mechanical and thermal properties of poly(L-lactide) incorporating various inorganic fillers with particle and whisker shapes. *Macromol. Mater. Eng.* 288, 562–568. doi: 10.1002/mame.200350004
- Van Der Wal, A., and Gaymans, R. J. (1999). Polypropylene–rubber blends: 5. Deformation mechanism during fracture. *Polymer* 40, 6067–6075. doi: 10.1016/S0032-3861(99)00216-5
- Vannaladsaysy, V., Todo, M., Takayama, T., Jaafar, M., Ahmad, Z., and Pasomsouk, K. (2009). Effects of lysine triisocyanate on the mode I fracture behaviour of polymer blend of poly (L-lactic acid) and poly (butylene succinate-co-L-lactate). *J. Mater. Sci.* 44, 3006–3009. doi: 10.1007/s10853-009-3428-5
- Vilay, V., Mariatti, M., Ahmad, Z., Pasomsouk, K., and Todo, M. (2009). Characterization of the mechanical and thermal properties and morphological behaviour of biodegradable poly(L-lactide)/poly(ϵ -caprolactone) and poly(L-lactide)/poly(butylene succinate-co-L-lactate) polymeric blends. *J. Appl. Polym. Sci.* 114, 1784–1792. doi: 10.1002/app.30683
- Vroman, I., and Tighzert, L. (2009). Biodegradable polymers. *Materials* 2, 307–344. doi: 10.3390/ma2020307
- Wang, L., Ma, W., Gross, R. A., and McCarthy, S. P. (1998). Reactive compatibilization of biodegradable blends of poly(lactic acid) and poly(ϵ -caprolactone). *Polym. Degrad. Stab.* 59, 161–168. doi: 10.1016/S0141-3910(97)00196-1
- Wang, R., Wang, S., Zhang, Y., Wan, C., and Ma, P. (2009). Toughening modification of PLLA/PBS blends via *in situ* compatibilization. *Polym. Eng. Sci.* 49, 26–33. doi: 10.1002/pen.21210
- White, E. F. T. (1984). *Fracture behaviour of polymers*. Edited by A. J. Kinloch and R. J. Young, Applied Science Publishers, London and New York, 1983. Pp xxv + 496, Price £30.00. ISBN 0853341869. *Br. Polym. J.* 16, 114. doi: 10.1002/pi.4980160231f
- Wright-Charlesworth, D. D., Miller, D. M., Miskioglu, I., and King, J. A. (2005). Nanoindentation of injection moulded PLA and self-reinforced composite PLA after *in vitro* conditioning for three months. *J. Biomed. Mater. Res. A* 74A, 388–396. doi: 10.1002/jbm.a.30353
- Wu, S. (1990). Chain structure, phase morphology, and toughness relationships in polymers and blends. *Polym. Eng. Sci.* 30, 753–761. doi: 10.1002/pen.760301302
- Xiao, H., Lu, W., and Yeh, J.-T. (2009). Effect of plasticizer on the crystallization behaviour of poly(lactic acid). *J. Appl. Polym. Sci.* 113, 112–121. doi: 10.1002/app.29955
- Yu, F., Liu, T., Zhao, X., Yu, X., Lu, A., and Wang, J. (2012). Effects of Talc on the Mechanical and Thermal Properties of Polylactide. *J. Appl. Polym. Sci.* 125, E99–E109. doi: 10.1002/app.36260
- Yu, L., Liu, H., Xie, F., Chen, L., and Li, X. (2008). Effect of annealing and orientation on microstructures and mechanical properties of polylactic acid. *Polym. Eng. Sci.* 48, 634–641. doi: 10.1002/pen.20970
- Zhang, C., Wang, W., Huang, Y., Pan, Y., Jiang, L., Dan, Y., et al. (2013a). Thermal, mechanical and rheological properties of polylactide toughened by expoxidized natural rubber. *Mater. Des.* 45, 198–205. doi: 10.1016/j.matdes.2012.09.024
- Zhang, H., Fang, J., Ge, H., Han, L., Wang, X., Hao, Y., et al. (2013b). Thermal, mechanical, and rheological properties of polylactide/poly(1,2-propylene glycol adipate). *Polym. Eng. Sci.* 53, 112–118. doi: 10.1002/pen.23238
- Zhang, N., Wang, Q., Ren, J., and Wang, L. (2009a). Preparation and properties of biodegradable poly(lactic acid)/poly(butylene adipate-co-terephthalate) blend with glycidyl methacrylate as reactive processing agent. *J. Mater. Sci.* 44, 250–256. doi: 10.1007/s10853-008-3049-4
- Zhang, W., Chen, L., and Zhang, Y. (2009b). Surprising shape-memory effect of polylactide resulted from toughening by polyamide elastomer. *Polymer* 50, 1311–1315. doi: 10.1016/j.polymer.2009.01.032
- Zhang, X., Li, Y., Han, L., Han, C., Xu, K., Zhou, C., et al. (2013c). Improvement in toughness and crystallization of poly(L-lactic acid) by melt blending with ethylene/methyl acrylate/glycidyl methacrylate terpolymer. *Polym. Eng. Sci.* 53, 2498–2508. doi: 10.1002/pen.23507
- Zhao, P., Liu, W., Wu, Q., and Ren, J. (2010). Preparation, mechanical, and thermal properties of biodegradable polyesters/poly(lactic acid) blends. *J. Nanomater.* 2010. doi: 10.1155/2010/287082
- Zhao, Q., Ding, Y., Yang, B., Ning, N., and Fu, Q. (2013). Highly efficient toughening effect of ultrafine full-vulcanized powdered rubber on poly(lactic acid)(PLA). *Polym. Test.* 32, 299–305. doi: 10.1016/j.polymertesting.2012.11.012
- Zhu, S., Rasal, R., and Hirt, D. (2009). *Annual Technical Conference of the Society of Plastics Engineers (ANTEC 2009)*, (Chicago, Illinois), 1616–1620.
- Zinn, M., Witholt, B., and Egli, T. (2001). Occurrence, synthesis and medical application of bacterial polyhydroxyalkanoate. *Adv. Drug Deliv. Rev.* 53, 5–21. doi: 10.1016/S0169-409X(01)00218-6

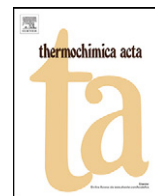
Conflict of Interest Statement: The authors declare that the research was conducted in the absence of any commercial or financial relationships that could be construed as a potential conflict of interest.

Received: 09 September 2013; paper pending published: 06 November 2013; accepted: 21 November 2013; published online: 17 December 2013.

Citation: Kfoury G, Raquez J-M, Hassouna F, Odent J, Toniazio V, Ruch D and Dubois P (2013) Recent advances in high performance poly(lactide): from “green” plasticization to super-tough materials via (reactive) compounding. *Front. Chem.* 1:32. doi: 10.3389/fchem.2013.00032

This article was submitted to Polymer Chemistry, a section of the journal *Frontiers in Chemistry*.

Copyright © 2013 Kfoury, Raquez, Hassouna, Odent, Toniazio, Ruch and Dubois. This is an open-access article distributed under the terms of the Creative Commons Attribution License (CC BY). The use, distribution or reproduction in other forums is permitted, provided the original author(s) or licensor are credited and that the original publication in this journal is cited, in accordance with accepted academic practice. No use, distribution or reproduction is permitted which does not comply with these terms.



Experimental and multiscale modeling of thermal conductivity and elastic properties of PLA/expanded graphite polymer nanocomposites

Bohayra Mortazavi^{a,b,*}, Fatima Hassouna^a, Abdelghani Laachachi^a, Ali Rajabpour^c, Said Ahzi^b, David Chapron^d, Valérie Toniazzi^a, David Ruch^a

^a Centre de Recherche Public Henri Tudor, Department of Advanced Materials and Structures, 66, rue de Luxembourg BP 144, L-4002 Esch/Alzette, Luxembourg

^b Institut de Mécanique des Fluides et des Solides (IMFS), University of Strasbourg, 2 Rue Boussingault, 67000 Strasbourg, France

^c Department of Mechanical Engineering, Imam Khomeini International University, Qazvin 34149-16818, Iran

^d LMOPS, Université Paul Verlaine Metz, Supélec, 2 Rue Edouard, Belin F-57070 Metz, France

ARTICLE INFO

Article history:

Received 27 September 2012

Received in revised form

13 November 2012

Accepted 14 November 2012

Available online 23 November 2012

Keywords:

Expanded graphite

Nanocomposites

Thermal conductivity

Elastic modulus

Multiscale

ABSTRACT

We developed experimental as well as theoretically based hierarchical multiscale procedures for the evaluation of effective elastic modulus and thermal conductivity of poly-lactide (PLA)/expanded graphite (EG) nanocomposites. The incorporation of EG fillers into PLA was carried out by a twin-screw micro-extruder. The dispersion/delamination of EG in PLA was studied using Raman spectroscopy, SEM and TEM. In the multiscale modeling, the thermal conductivity constants and stiffness tensor of EG were first acquired by the means of molecular dynamics (MD) simulations. Using the fillers' properties obtained by the MD, we developed finite elements (FE) models to evaluate the effective thermal conductivity and elastic modulus of PLA/EG nanocomposites. Our results, for a wide range of temperatures revealed the efficiency in thermal and mechanical reinforcement of PLA by incorporation of EG nanoparticles.

© 2012 Elsevier B.V. All rights reserved.

1. Introduction

The addition of fillers within a polymer matrix is an efficient way to create materials with advanced properties for engineering applications (electronic devices, automotive parts, etc.). In recent years, considerable research effort has been devoted to the processing and characterization of nanocomposites with graphite nanofillers or graphene to improve mechanical, thermal, electrical, and gas barrier properties of polymers [1–5]. The exploit of graphite with its combination of extraordinary high physical properties such as exceptional electron transport, mechanical properties, thermal conductivity and high surface area [6–10] has created a new class of polymer nanocomposites.

The reinforcement is achieved, not only by using the intrinsic properties of the nanofillers, but more importantly by optimizing the dispersion, the loading, interface chemistry and nanoscale morphology to take advantage of the immense surface area per unit volume that nanofillers cover. Indeed, a lot of efforts have

been recently developed to exfoliate and optimize the dispersion of graphite sheets using intercalation with alkali metals [11] or exposing them to severe acidic conditions [12–14]. Expansion of layer spacing takes place via heat treatment [11,13] or exposure to microwave radiation followed by mechanical grinding [15]. As a result of the expansion, the surface area of graphite is enhanced considerably.

As a biodegradable thermoplastic derived from sustainable sources, poly-lactide (PLA) has received considerable attention for conventional use [16,17]. In the next years, PLA production and consumption is expected to increase exponentially. Therefore, there is a need to better understand and improve its properties. Some investigations suggested that the addition of expanded graphite nanofillers improved the tensile and storage modulus as well as the thermal conductivity of PLA based materials [2,18,19]. However, depending upon the processing conditions and characteristics of both the polymer matrix and filler, the in situ dispersion of the fillers inside the host polymer by melt blending can be more or less achieved, leading to intercalated or exfoliated nanocomposites. The effect of the resulting microstructure on mechanical and thermal properties is not well established.

Recently, the optimization of the melt-processing conditions of 3 wt.% PLA/EG using DSM Xplore twin screw micro-extruder was achieved to improve the dispersion and the delamination of the fillers [19]. It was shown that the combination of techniques

* Corresponding author at: Centre de Recherche Public Henri Tudor, Department of Advanced Materials and Structures, 66, rue de Luxembourg BP 144, L-4002 Esch/Alzette, Luxembourg. Tel.: +33 0 6 03 59 96 08; fax: +33 0 3 68 85 29 36.

E-mail addresses: bohayra.mortazavi@tudor.lu, bohayra.mortazavi@gmail.com (B. Mortazavi).

such as scanning electron microscopy (SEM), transmission electron microscopy (TEM), X-ray diffraction and Raman spectroscopy provides good and complete information about the dispersion and particularly the delamination of the fillers. Based on the optimized conditions, the effect of the expanded graphite concentration on the structure, morphology, thermal stability and thermo-mechanical properties of the composites are investigated. The correlation between the morphology and the physical properties was established.

Due to difficulties in experimental characterization of nano-structured materials, analytical and numerical simulations are getting more attractive as alternatives. To this aim, the prediction and analysis of materials behavior by numerical tools such as finite element (FE) and molecular dynamics (MD) simulations are now widely considered. This is mainly due to the fact that if the computer simulation results could be used to substitute experimental studies, the design costs and quality for a particular product will be improved. On another viewpoint, the predictability of a particular material property by computer simulations could be a sign for the validity of the simulation procedures and related assumptions as well.

In this way, we have also developed theoretically based hierarchical multiscale procedures for the evaluation of the effective elastic modulus and thermal conductivity of PLA/EG nanocomposites. In this frame, first we have developed molecular dynamics models for the evaluation of stiffness and conductivity tensors of the expanded graphite. The validity of the proposed modeling scheme was verified by comparing the simulation results with experimental results available in the literature. In the final step, using the transversely isotropic materials properties acquired by molecular dynamics simulations, we have developed 3-dimensional (3D) finite element models to evaluate the thermal conductivity and elastic modulus of the nanocomposite structures. In the finite element modeling, disc structures were chosen for describing the EG geometries inside the PLA. The diameter to thickness ratio of the platelets, which is commonly called as aspect ratio (AR), is the adjustable and independent parameter in our finite element modeling. Comparison of modeling results with experimental measurements reveals the good efficiency in thermal and mechanical reinforcement of PLA by incorporation of EG particles using the herein presented experimental procedure.

2. Experimental part

2.1. Materials and processing

Poly-lactide was supplied by Nature Works LLC (grade 4042D) with density of 1.25 g/cm³, elastic modulus of 2.7 GPa and thermal conductivity of 0.13 W/m-K at room temperature. Expanded graphite was supplied from ECOPEX G. According to the technical sheet, the principal characteristics of the specific grade of EG used GFG 5 are: real density = 2.25 g/cm³, mean diameter (d₅₀ = 5–7 μm). It was used without any further purification. Before processing by melt-blending, PLA and EG were dried at 40 °C under vacuum to minimize the water content. PLA/EG nanocomposites were prepared by mixing, in an appropriate ratio, the molten PLA pellets and the EG using a twin-screw extruder (DSM Xplore), at 180 °C at speed rate of 100 rpm for 10 min. The EG content in PLA/EG composites was set to 3.0 wt.% and 6.75 wt.%. For comparison, the neat PLA was processed in similar conditions of melt-blending like the composites.

In thermomechanical study (dynamical mechanical analysis) plates of filled PLA were compression-molded using a Carver press and a specific mold. The procedure used was as follow: a) extruded PLA/EG pellets were introduced within the mold, b) PLA material

was heated at 190 °C for 3 min, c) The composite was compressed for 30 s with a pressure of 15 MPa, and d) under the same pressure (15 MPa), the material was cooled by room temperature water circulation.

2.2. Characterizations

2.2.1. Raman spectroscopy

Raman scattering experiments were performed at room temperature with a LabRam spectrometer (Horiba Jobin Yvon). All spectra were recorded in backscattered geometry using a 1800 grooves per mm as the diffraction grating and a spectral resolution of 1 cm⁻¹ was achieved. Both incident and scattered beams were collected through an Olympus confocal microscope using a 100x objective lens (NA = 0.9). Rayleigh scattering was blocked with a holographic Notch filter. The laser excitation wavelength was 514 nm and the laser power was less than 2 mW to avoid sample damage.

2.2.2. Transmission electron microscopy

Transmission electron microscopy analysis of PLA/EG were provided by a LEO 922 apparatus at 200 kV. The samples were 70 nm thick and prepared with a LEICA EM FC6 cryo-ultramicrotome at 25 °C.

2.2.3. Dynamic mechanical analyzer

The influence of the expanded graphite on viscoelastic properties of filled and non-filled PLA was analyzed by means of a dynamic mechanical analyzer (DMA) Netzsch DMA 242 C. For this study, we used 50 × 10 × 1 mm³ rectangular specimens machined from the compression-molded plates. They were subjected to double cantilever mode of flexural loading with a maximum displacement of 40 μm in the temperature range 25 to 100 °C (rate 2 °C/min) and a frequency of 1 Hz.

2.2.4. Flash laser

The thermal diffusivity of PLA and nanocomposites were measured from room temperature to 100 °C using a laser flash technique (Netzsch LFA 457 MicroflashTM) under inert atmosphere (argon flow: 100 mL.min⁻¹). Samples were plane and parallel disks with 12.7 mm in diameter and about 1.1 mm thick. Owing to the PLA translucency, prior to measurements, graphite was sprayed on both sample surfaces to avoid the penetration of the laser light through the sample and to improve the signal-to-noise ratio of the infrared detector signal. Graphite was also used due to its high thermal diffusivity, allowing the propagation of heat through the samples. Their front side was heated by a short laser pulse (0.5 ms). The induced heat propagates through the sample and causes a temperature increase on the rear surface. This temperature rise is measured versus time using the IR-detector. The thermal diffusivity is then determined using the “half-rise-time” (t_{1/2}) corresponding to the time for the back face temperature to reach 50% of its maximum value. The thermal diffusivity can be calculated using:

$$\alpha = \frac{1.38L^2}{\pi^2 t_{1/2}} \quad (1)$$

where L is the specimen thickness. For each sample and condition, measurements were repeated three times in order to collect meaningful data between room temperature and 100 °C. Laser Flash Analysis is a direct measurement method for measuring thermal diffusivity and an indirect one for measuring of thermal conductivity.

Thermal conductivity (k) can be calculated using:

$$k(t) = \alpha C_p \rho \quad (2)$$

Table 1

Comparison of the elastic constants of graphite from MD simulation and experimental studies (GPa).

	C ₁₁	C ₁₂	C ₁₃	C ₃₃	C ₄₄	C ₆₆
Present MD study	970	95	8	26	–	449
Ultrasonic and static tests [25]	1060	180	15	36.5	4	440
Inelastic neutron scattering [26]	1440	–	–	37.1	4.6	460
Inelastic X-rays [27]	1109	139	0	38.7	5	485

where C_p is the heat capacity determined by Differential Scanning Calorimetry and ρ is the density measured with a densimeter. The thermal conductivity experiments were performed for five times for each volume concentration and the mean values were calculated.

3. Multiscale modeling

In the current study, theoretically based hierarchical multiscale homogenization procedure is presented for the modeling of thermal conductivity and elastic modulus of PLA/EG nanocomposite. In the first step, molecular dynamics modeling are utilized for the evaluation of thermal conductivity and elastic stiffness tensors of expanded graphite as a transversely isotropic material. In the next step, we developed two-phase continuum modeling tools by means of finite elements for the evaluation of thermal conductivity and elastic modulus of a representative volume element (RVE) of PLA/EG nanocomposites. In this modeling, the material properties acquired by the MD simulations are used for introducing the properties of EG. Moreover, as a common assumption, the isotropic properties of the matrix were assumed to be the same as those of bulk and non-filled PLA.

3.1. Molecular dynamics modeling

In the current study, classical molecular dynamics simulations were carried out in order to evaluate the thermal conductivity and stiffness tensors of expanded graphite as the reinforcement part in the continuum modeling. To this aim, LAMMPS [20] package is used for the atomistic modeling. The expanded graphite is the multilayer form of graphene which is the planar structure of honeycomb lattice of sp^2 carbon atoms. The carbon-carbon bonded interaction in this study is modeled by the optimized Tersoff potential developed by Lindsay and Broido [21]. In the multilayer graphene (MLG) structures, the carbon atoms at different layers are not covalently bonded together and they only present van der Waals interactions. Commonly, the nonbonded interactions are expressed by Lennard–Jones (LJ) potential. In this study, we used the LJ potential type with the parameterization suggested by Girifalco et al. [22]. To the best of our knowledge, this has been the mostly used potential [22] for the modeling of nonbonded interaction of carbon atoms which also satisfies the density of bulk graphite (2.2 gr/cm³).

In Fig. 1, the equilibrated MD model for the evaluation of EG properties is shown. The EG was constructed by putting the graphene sheets up together with a spacing distance of 3.4 Å. In the MD simulations in this study, we applied the periodic boundary conditions (PBC) in the planar directions (X and Y directions in Fig. 1). Thus, these simulations are representative of infinite multilayer graphene sheets. In the evaluation of bulk graphite properties, we also applied the periodic boundary conditions along the thickness direction (Z directions in Fig. 1). It is worth noting that in all of the simulations in this study, prior to the step for properties evaluation, the structure was allowed to relax to zero pressure at 300 K in all directions using constant pressure-temperature (i.e. NPT ensemble) simulations by Nosé–Hoover barostat and thermostat method. Then the final equilibrated structure was obtained by

performing constant energy (i.e. NVE ensemble) simulations. The time increment of the simulations was set to 0.5 fs.

3.1.1. Elastic constants

Our recent molecular dynamics study [23] has shown the limited dependency of the multi-layer graphene mechanical properties on the number of atomic planes. It was shown that further increasing of the number of layers from six does not influence the in-plane elastic modulus of multilayer graphene. In other word, it was found that the six-layers graphene structure presents the same in-plane elastic modulus as that of bulk graphite. In this way, we developed a six layer graphene structure (as illustrated in Fig. 1) for the evaluation of expanded-graphite elastic constants at room temperature. Calculation of elastic constants at finite temperature is always challenging. One way to do this is to measure the change in average stress tensor at constant temperature NVT simulations when the simulation box undergoes finite deformations [24]. By performing the MD simulations, the elastic constants of expanded graphite compared to different experimental studies are listed in Table 1. We have also verified that the EG presents transversely isotropic behavior [23].

Generally speaking, the obtained elastic constants by the optimized Tersoff potential are close to the experimental results. It should be mentioned that due to the uncertainties observed in the evaluation of C_{44} , we preferred not to report any value and in our continuum modeling we used the average value of the experimental studies (4.5 GPa).

3.1.2. Thermal conductivity

The equilibrium molecular dynamics (EMD) method is used for the evaluation of thermal conductivity of EG. The EMD method relies on relating the ensemble average of the heat current autocorrelation function (HCACF) to the thermal conductivity K , via the Green-Kubo expression:

$$K_a = \frac{1}{3VK_B T^2} \int_0^\infty \langle J_a(t) J_a(0) \rangle dt \quad (3)$$

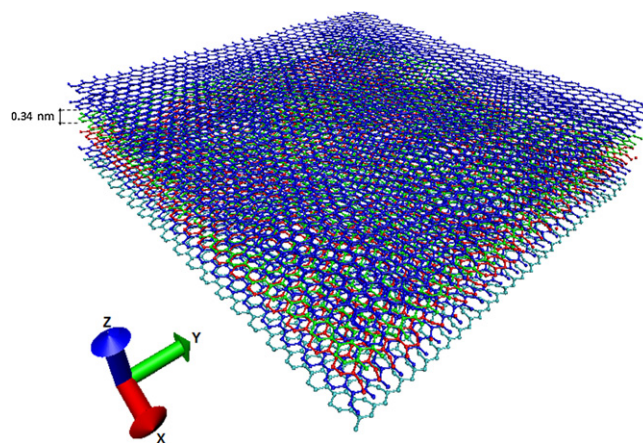


Fig. 1. The constructed six-layer graphene structure for evaluation of thermal conductivity and stiffness tensors of expanded graphite by molecular dynamics.

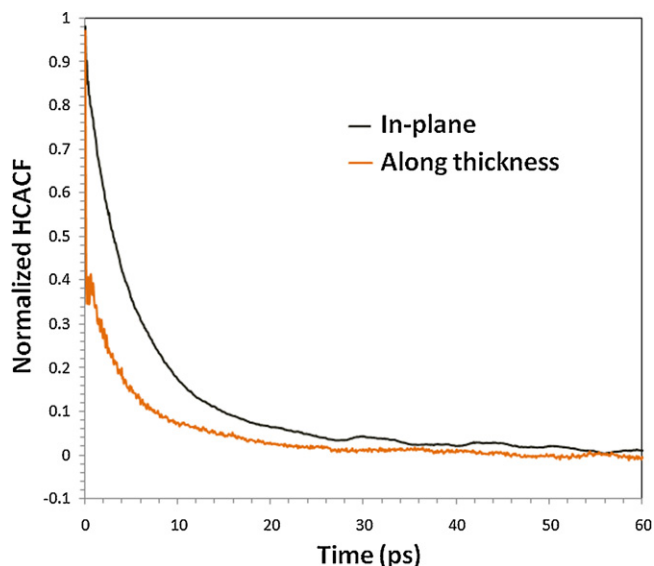


Fig. 2. Average in-plane and along the thickness normalized heat current auto-correlation function (HCACF) obtained from MD simulations for bulk graphite.

where α denotes the three Cartesian coordinates, K_B is the Boltzmann's constant, V and T are the volume and temperature of the system respectively. The auto-correlation functions of the heat current $\langle J_a(t)J_a(0) \rangle$ (HCACF) can be calculated using the heat current $\vec{J}(t)$ as expressed by [24]:

$$\vec{J}(t) = \sum_i \left(e_i \vec{v}_i + \frac{1}{2} \sum_{i < j} (\vec{f}_{ij} \cdot (\vec{v}_i + \vec{v}_j)) \vec{r}_{ij} \right) \quad (4)$$

Here, e_i and v_i are the total energy and velocities of atom i respectively, f_{ij} and r_{ij} are respectively the interatomic forces and position vector between atoms i and j . The in-plane thermal conductivity of EG is obtained by averaging the thermal conductivity along the X and Y directions. We found that the thermal conductivities along the X and Y directions are considerably close to each other, thus, the thermal conductivity of EG also presents transversely isotropic nature. It is worth noting that in order to minimize the statistical errors, the thermal conductivity is calculated based on the average HCACF, calculated from eight independent MD runs with different initial atomic velocities.

Fig. 2 depicts the in-plane and along the thickness normalized HCACF obtained from MD simulation for bulk graphite. It shows a decay behavior over the entire time range. The thermal conductivity is calculated by performing the integration of HCACF using Eq. 3. By direct integration of HCACF over the time range, the in-plane and out of plane thermal conductivity of graphite are obtained to be 1200 ± 100 W/m-K and 2.2 ± 0.2 W/m-K, respectively. The size independency of the obtained results was verified by performing the simulations for different length, ranging between 3 to 8 nm and different number of layers from 6 to 8. We also performed the same study on 5 layers graphene sheets (no PBC along the Z direction) and we found that the in-plane thermal conductivity falls within the obtained range for bulk graphite. It is worth mentioning that the latest experimental results [28] suggest a continuous decline of in-plane thermal conductivity of graphene from single-layer (4100 ± 540 W/m-K) to four-layer graphene (1230 ± 160 W/m-K) structures. Further increase of graphene number of atomic planes does not change the reported in-plane thermal conductivity values. The in-plane thermal conductivity of graphite has also been reported to be in the range between 800–2000 W/m-K [28]. Using the optimized

Tersoff potential, we have recently [29] calculated the thermal conductivity of single-layer graphene to be 3000 ± 100 W/m-K. It is worth mentioning that the thermal conductivity of a single-layer graphene is predicted to be 350 W/m-K [30], by REBO [31] potential and 800 W/m-K [32], by Tersoff [33] potential. As it is clear, the predictions by optimized Tersoff potential are in better agreement with experimental results in comparison with other available results in the literature.

3.2. Finite element modeling

Now-a-days finite element (FE) modeling is regarded as a versatile technique for modeling and simulations of a wide range of engineering problems. In the present study, we carried out 3-dimensional (3D) FE modeling for the evaluation of thermo-mechanical properties of PLA/EG nanocomposites. There have been numerous studies using FE for modeling of thermal and mechanical properties of nanocomposites [34–40]. For platelets inclusions like graphene, graphite and clay, one may use the 2-dimensional (2D) finite element models [34,36]. The main advantage of 2D models in comparison with 3D FE models is their lower computational costs and simplicities in the modeling. However, it was shown that 2D finite element models underestimate the predictions by 3D models [36]. Furthermore, the 2D finite element models could not accurately describe the transversely isotropic behavior of EG platelets. Due to computational cost of FE modeling, the simulations are limited to modeling of a representative volume element (RVE) of the composite. The FE simulations in this study were carried out using ABAQUS/Standard (Version 6.10). In our FE models, EG are modeled as discs with the effective mechanical and thermal properties obtained from MD simulation. In the constructed RVE, the EG platelets were randomly distributed-and-oriented in the PLA matrix. As discussed earlier, the EGs are a transversely isotropic material. For the modeling of a randomly distributed material with transversely isotropic properties, there are two available approaches. The first approach is to define a local coordinate system for each platelet and then assign the transversely isotropic properties for each platelet along this local coordinate. The definition of local coordinate systems for each platelet results in the complexity of the modeling and imposes difficulties on applying the boundary condition. The second approach which is used in this study is to define anisotropic material properties for each platelet along the RVE global coordinate system. In ABAQUS, the full anisotropic elastic and thermal conductivity properties are defined by introducing 21 and 6 constants, respectively. These constants are obtained by transformation of each platelet's transversely isotropic stiffness and thermal conductivity tensors along their local coordinate to the RVE global coordinate. This method is physically acceptable for the evaluation of thermal conductivity. In the evaluation of mechanical properties, such a technique is valid only for evaluating the elastic constants at low strain levels because the rotations of inclusions are neglected.

The bonding between the EG discs and the polymer material was assumed to be perfect. The dimensions of all the EGs in the RVE are equal and it is introduced by definition of diameter to thickness ratio, called Aspect Ratio (AR). The aspect ratio of the inclusions plays an important role in the load bearing capabilities of the nanocomposite. A sample of 3D cubic RVE of a nanocomposite containing 2 volume percent of EG platelets with aspect ratio of 100 and its elements are shown in Fig. 3. The RVE was modeled in a way to satisfy the periodicity criterion. This means that if a filling disc is cut by a boundary face of RVE, the remaining part of that particle should continue from the opposite face. In this way, by putting these RVE cubes together side by side, no discontinuity will be observed in the constructed sample. Such a RVE was constructed in ABAQUS by developing a Python user subroutine.

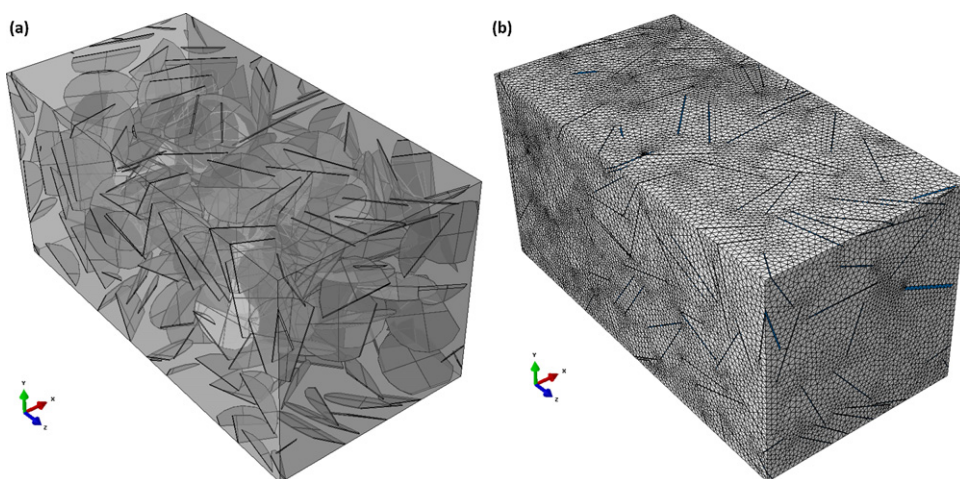


Fig. 3. Developed 3D periodic finite element RVE for evaluation of effective thermal conductivity and elastic modulus of PLA/EG nanocomposites, (a) wire-frame model (b) meshed model.

We also developed a C++ program for creating the random distribution of platelets inside the RVE and obtaining the anisotropic materials constants in the RVE global coordinates. The provided information by the C++ code was used as input data for Python script for the construction of the final models in the ABAQUS. The specimen was meshed using the 4-node linear tetrahedron shape elements, 3-Dimensional stress (C3D4) elements are used for elastic analysis and heat transfer (DC3D4) elements are used in thermal conductivity modeling.

In the evaluation of elastic properties, a small uniform strain was applied on one of the surfaces along the Z direction and the other surfaces were fixed only in their normal directions. The reaction forces on each surface were computed to calculate the corresponding stresses. Using Hooke's law for an isotropic material, the effective elastic modulus and Poisson's ratio of the nanocomposite RVE was estimated.

For the evaluation of thermal conductivity, a constant heating surface heat flux (+q) was exerted on one of the surfaces along the Z direction and on the opposite surface the same magnitude cooling surface heat flux (-q) was applied. The applied steady state heat fluxes, establish a temperature gradient along the Z direction in the RVE. The temperature gradient, $\frac{dT}{dz}$, was calculated by introducing the dT as the average temperature differences between the hot and cold surfaces. The effective thermal conductivity of the nanocomposite was obtained by using the one-dimensional form of the Fourier law, $(K = q \frac{dz}{dT})$.

4. Results and discussions

4.1. Morphological and structural characterization of PLA/EG nanocomposites

To investigate the detailed morphological of PLA/EG nanocomposites, several techniques have been used including X-ray diffraction, Raman spectroscopy SEM and TEM (see details in [19]). It was observed by X-ray diffraction [19] that PLA/EG nanocomposites exhibited a peak at 2θ of 26.5° which corresponds to the stacking of single graphene layers at a distance of 0.335 nm. The presence of this peak confirms that the complete exfoliation of EG is not reached and some sheets still exist in the aggregate form. However, SEM images show clearly that EG stacks are dispersed homogeneously in the PLA matrix (Fig. 4). As it can be observed, TEM image do not show the presence of any interphase between EG and PLA (Fig. 5 TEM). In addition, IR analysis performed on EG powder shows the absence of oxidized functions [19]. In this case, the

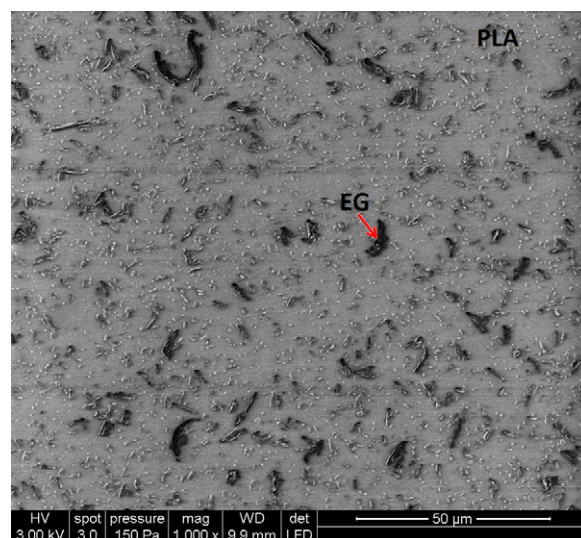


Fig. 4. SEM image of PLA + 3 wt.% EG nanocomposites.

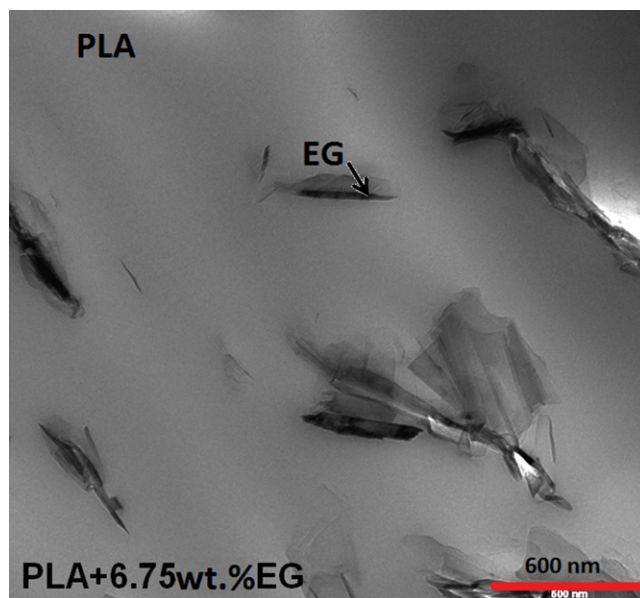


Fig. 5. TEM image of PLA/6.75 wt.% EG.

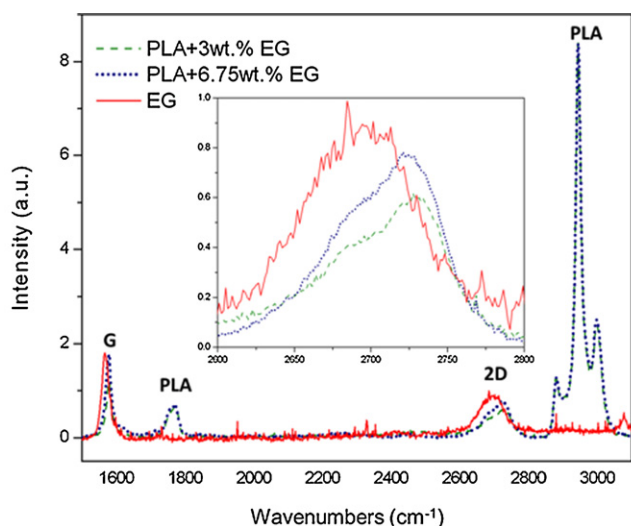


Fig. 6. Raman spectra: Comparison of the 2D band for PLA nanocomposites with EG concentrations of 3 wt.% and 6.75 wt.% respectively.

interaction between PLA (hydrophobic polymer) and EG is expected to be strong.

Additional information concerning the structure of PLA/EG was obtained through Raman spectroscopy analyses [19]. Raman spectra can provide qualitative and quantitative information on host polymer matrix and fillers: concentrations, purities, residual strains, fillers homogeneity and orientation, etc. Then, some vibration modes of the carbon lattice can be used as probe to characterize physical properties of the nanocomposites. Fig. 6, shows the Raman spectra of EG and the PLA/EG composites at two EG concentrations: 3 wt.% and 6.75 wt.%. At first, no modification of the PLA CH_2 and CH_3 stretching bands around 3000 cm^{-1} is observed for all spectra which indicates that the polymer matrix was not damaged or under strain after extrusion. Spectra are thus normalized based on PLA peak. EG is characterized by the G band at 1560 cm^{-1} and the 2D band around 2700 cm^{-1} . In a basic molecular description, the G band is attributed to the bond stretching and the 2D band, which is the second order of the D band, is attributed to breathing modes of sp^2 atoms in rings. The 2D band, second order of the D band is allowed by the selection rule and its shape is sensitive to the number of carbon layers and could be used to distinguish graphene from graphite. The 2D bands of EG in PLA have a graphite shape with relative intensities proportional to the fillers concentrations. A slight upshift around 5 cm^{-1} is observed for the lower EG concentration. The 2D band shape and Raman shift value do not show the presence of graphene in the PLA/EG composite. It means that

in the delamination process during the extrusion, we could not get to carbon monolayers. Some graphene sheets may exist, but with no significant concentration. This upshift, from EG concentration of 6.75 wt.% to 3 wt.%, indicates a small compression of carbon rings as results of mechanical constraint, which disrupts carbon atoms vibrations. This compression is probably due to mechanical compression of the polymer on the carbon fillers. At high EG concentration, the carbon rings vibration modes are similar to bulk graphite ones. Thus, the polymer has no effect on these breathing modes which means the existence of a normal interaction between carbon layers and small concentration of PLA-carbon interface. On contrary, at lower EG concentration, the polymer matrix induces a compression on carbon rings which suggests a higher density of interface PLA-carbon which could be explained as a result of delamination process. The mechanical effect of PLA on EG fillers indicates a good and strong interface PLA-EG which could also be confirmed by TEM images.

4.2. Convergence of finite element results

There are always computational limitations in generating of large RVEs. According to the RVE definition, the calculated effective results must be independent of the RVE size. Otherwise, obtained properties could not be used as estimations of bulk properties. To address this issue, we developed different RVEs with different number of platelets and different configuration of inclusions to investigate the independency of the reported results to the RVE size. Fig. 7 shows the predicted elastic modulus and thermal conductivity of the nanocomposite for different RVE sizes (number of EG platelets), containing 1.7 volume percent (3 wt.%) of EG platelets with aspect ratio of 50. As expected, by increasing the RVE size, the variation band of FE results decreases. We could conclude that the predicted results by the RVE with 70 platelets of EG shows acceptable size independency and accuracy as well. In this way, in the FE results reported in this study we included at least 70 EG platelets in the modeling. This also shows that modeling of limited number of particles by 3D finite element models could be efficiently used for prediction of thermal conductivity and elastic properties of two phase composite materials.

4.3. Comparison between experimental and multiscale modeling

The comparison between experimental and multiscale predictions of elastic modulus of PLA/EG nanocomposites is shown in Fig. 8. The experimental results are reported for two different EG concentrations of 3 wt.% and 6.75 wt.%, which are equivalent with 1.7 vol.% and 4 vol.%, respectively. As it can be observed, in the case of 3 wt.% concentration of EG at low temperatures (below

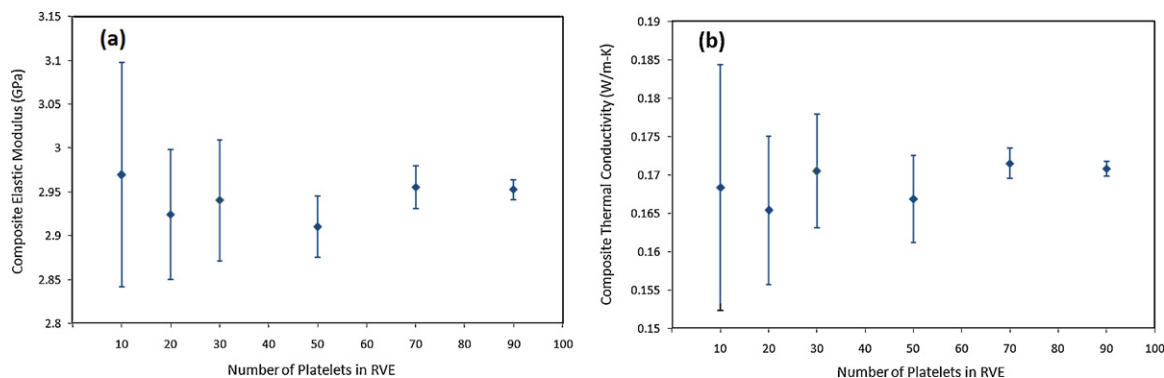


Fig. 7. Size dependency (number of platelets inside RVE) of the finite element results for prediction of (a) elastic modulus and (b) thermal conductivity of PLA/EG nanocomposites.

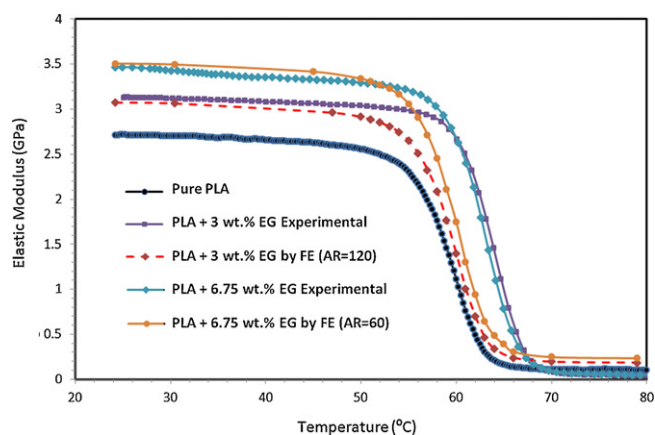


Fig. 8. Experimental and predicted elastic modulus of the PLA nanocomposites with EG concentrations at 3 wt.% and 6.75 wt.%, respectively.

glass transition), finite element results for the elastic modulus with effective aspect ratio of 120 for EG platelets match fairly well the experimental results. For PLA with 6.75 wt.% concentration of EG and at temperatures below the glass transition, the finite element results with effective aspect ratio of 60 fall close to the experimental elastic modulus. We should remark that for the platelet inclusions, the modeling results are strongly dependent on the effective aspect ratio of the inclusions inside the polymer [41]. In a fabricated random nanocomposite material, the inclusions shape would not be similar. Therefore, considering similar geometries for all of the EG platelets inside the polymer matrix in our finite element modeling could not be considered as a realistic construction of nanocomposite sample. However, the comparison with finite element results could be used to verify the efficiency of EG platelets distributions and delamination inside the PLA. The agreement of finite element results with aspect ratio of 120 with experimental results could be used as a sign of well distributed and delaminated EG platelets inside PLA. On the other hand, by increasing the volume concentration of EG platelets, the finite element results with effective aspect ratio of 60 match the experiments, accordingly, this could imply the decline of the quality of EG distributions and less delamination of EG inside PLA. This is in accord with the experimental observations. It is worth mentioning that in the finite element modeling presented here we did not include the interphase effect as a third phase. This two-phase finite element modeling could be convincing for herein fabricated PLA/EG nanocomposite, since the IR, TEM images and Raman spectroscopy did not reveal any significant sign for the formation of interphase between EG platelets and PLA matrix.

The strong mechanical interaction between carbon atoms of EG and polymer atoms could satisfy our perfect bonding assumption in finite element modeling for elastic modulus. As it is illustrated on Fig. 8, the finite element results are close to the experimental measurements from room temperature to 50 °C. At this point, the finite element results deviate from experimental ones. We note that the basic assumption that we made in our finite element modeling is that the nanocomposite structure is a perfectly elastic solid. In the case of polymer materials this assumption is no longer valid if the specimen temperature approaches or gets higher than the glass transition temperature. It is important to underline a shift of the glass transition temperature toward lower values (4–5 °C) in the theoretical curve compared to the experimental one. This discrepancy could be explained by the fact that in the theoretical model did not take into account the impact of EG on the polymer chain mobility responsible of the increase of the glass transition temperature of PLA.

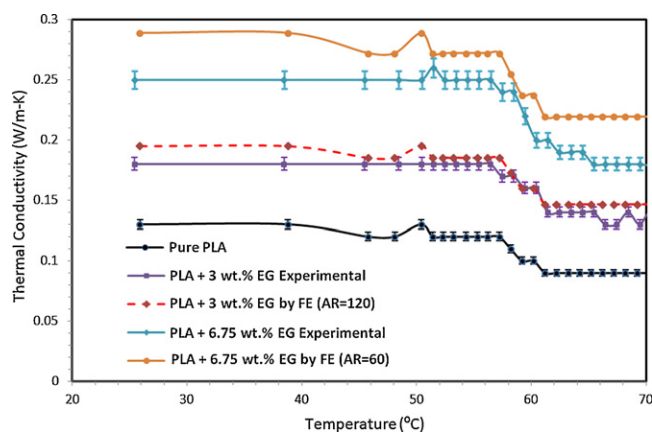


Fig. 9. Experimental and predicted thermal conductivity of the nanocomposite with EG concentrations at 3 wt.% and 6.75 wt.%, respectively.

Despite strong bonding between EG platelets and the polymer material, perfect heat flux transfer could not be physically acceptable, which is due to the existence of thermal boundary resistance between the fillers and the matrix [42]. Moreover, the thermal conductivity of graphene is much more sensitive to chemical doping and defects [29] in comparison with mechanical properties [43]. Therefore, we could expect the overestimation of thermal conductivity of PLA/EG nanocomposite by the finite element method as shown by our predicted results in Fig. 9. We should remark that the experimental procedure for the evaluation of thermal boundary resistance at the interface between inclusion and matrix at nanoscale is considerably difficult and complex. For these cases, the virtual computer simulations using the molecular dynamics method seems promising.

We should note that there exist a variety of analytical approaches such as Halpin-Tsai [44], and Mori-Tanaka [45] methods for the evaluation of thermal conductivity and elastic modulus of composite materials. These two methods cannot accurately consider the interactions between adjacent inclusions. Moreover, they cannot evaluate the micro-stresses involving with individual inclusion. The priority of the 3D finite element modeling in the evaluation of thermal and elastic properties of composite materials in comparison with micromechanical and statistical methods is elaborately discussed in our recent study [41]. In recent works [47], micromechanical models have been developed to include microstructural features of polymer nanocomposites such as matrix/fillers interphase and their relative strengths as well as the shifts of the glass transition due to the addition of nanofillers.

5. Conclusion

We developed experimental and theoretically based multiscale approaches for the investigating of the thermal and mechanical reinforcement of poly (lactide) by addition of expanded graphite platelets. Due to high stiffness as well as thermal conduction properties of graphite, we could observe considerable improvement in PLA thermal conductivity and elastic modulus by incorporation of expanded graphite particles. The experimental characterizations of nanocomposite samples were performed using Infrared and Raman spectroscopy, dynamic mechanical analyzer, flash laser for evaluation of thermal conductivity and transmission electron microscopy. The Infrared spectroscopy and transmission electron microscopy images reveal the strong bonding between expanded graphite and PLA atoms and also verify the negligible interphase effects. The efficiency of expanded graphite distribution inside the PLA using twin-screw micro-extruder procedure was also concluded by computers modeling. In the multiscale modeling, first, we evaluated the

thermal conductivity and stiffness tensor of graphite by means of molecular dynamics simulations. The molecular dynamics results are in close agreement with experimental results available in the literature. Next, we developed 3D finite element models for the evaluation of thermal conductivity and elastic modulus of the nanocomposites. Our study proposes the combination of molecular dynamics and 3D finite element modeling as a characterization technique for the evaluation and prediction of thermal conductivity and elastic modulus of nanocomposite materials.

Acknowledgment

The authors acknowledge the financial support of the FNR of Luxembourg via the AFR Grants (PHD-09-016).

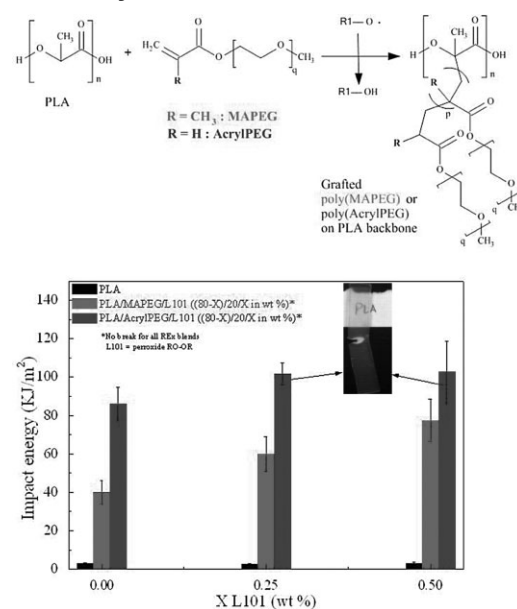
References

- [1] H. Kim, A.A. Abdala, C.W. Macosko, Graphene/polymer nanocomposites, *Macromolecules* 43 (2010) 6515–6530.
- [2] I.H. Kim, Y.J. Joong, Poly(lactide)/exfoliated graphite nanocomposites with enhanced thermal stability, mechanical modulus, and electrical conductivity, *J. Polym. Sci. Part B: Polym. Phys.* 48 (2010) 850–858.
- [3] M. Murariu, A.L. Dechief, L. Bonnaud, Y. Paint, A. Gallos, G. Fontaine, S. Bourbigot, P. Dubois, The production and properties of poly(lactide) composites filled with expanded graphite, *Polym. Degrad. Stab.* 95 (2010) 889–900.
- [4] A. Yasmin, J.J. Luo, I.M. Daniel, Processing of expanded graphite reinforced polymer nanocomposites, *Compos. Sci. Technol.* 66 (2006) 1182–1189.
- [5] W. Zheng, S.C. Wong, Electrical conductivity and dielectric properties of PMMA/expanded graphite composites, *Compos. Sci. Technol.* 63 (2003) 225–235.
- [6] T. Ramanathan, A.A. Abdala, S. Stankovich, D.A. Dikin, M. Herrera-Alonso, R.D. Piner, A.D.H. Adamson, H.C. Schniepp, X. Chen, R.S. Ruoff, S.T. Nguyen, I.A. Aksay, R.K. Prud'Homme, L.C. Brinson, Functionalized graphene sheets for polymer nanocomposites, *Nat. Nanotechnol.* 3 (2008) 327–331.
- [7] K.R. Ratina, W.R. Yang, S.P. Ringer, F. Braet, Toward ubiquitous environmental gas sensors-capitalizing on the promise of grapheme, *Environ. Sci. Technol.* 44 (2010) 1167–1176.
- [8] C. Soldano, A. Mahmood, E. Dujardin, Production, properties and potential of grapheme, *Carbon* 48 (2010) 2127–2150.
- [9] H. Fukushima, L.T. Drzal, Carbon nanotube alternative: graphite nanoplatelets as reinforcements for polymers, *Annu. Tech. Conf. – Soc. Plast. Eng.* (2003) 2230.
- [10] Y.B. Zhang, J.P. Small, W.V. Pontius, P. Kim, Fabrication and electric field dependent transport measurements of mesoscopic graphite devices, *Appl. Phys. Lett.* 86 (2005) 073104.
- [11] L.S. Viculis, J.J. Mack, O.M. Mayer, H.T. Hahn, R.B. Kaner, Intercalation and exfoliation routes to graphite nanoplatelets, *J. Mater. Chem.* 15 (2005) 974–978.
- [12] K.E. Carr, Intercalation and oxidation effects on graphite of a mixture of sulphuric and nitric acids, *Carbon* 8 (1970) 155–158.
- [13] G. Chen, D. Wu, W. Weng, C. Wu, Exfoliation of graphite flake and its nanocomposites, *Carbon* 41 (2003) 619–621.
- [14] Y.X. Pan, Z.Z. Yu, Y.C. Ou, G.H. Hu, A New Process of Fabricating Electrically Conducting Nylon 6/Graphite Nanocomposites via Intercalation Polymerization, *J. Polym. Sci. Part B: Polym. Phys.* 38 (2000) 1626.
- [15] K. Kalaitzidou, H. Fukushima, L.T. Drzal, A new compounding method for exfoliated graphite–polypropylene nanocomposites with enhanced flexural properties and lower percolation threshold, *Compos. Sci. Technol.* 67 (2007) 2045–2051.
- [16] D. Garlotta, A literature review of poly(lactide), *J. Polym. Environ.* 9 (2001) 63–84.
- [17] L.T. Lim, R. Auras, M. Rubino, Processing technologies for poly(lactide), *Prog. Polym. Sci.* 33 (2008) 820–852.
- [18] M. Murariu, A. Da Silva Ferreira, M. Alexandre, Poly(lactide) (PLA) designed with desired end-use properties: 1. PLA compositions with low molecular weight ester-like plasticizers and related performances, *Polym. Adv. Technol.* 19 (2008) 636–646.
- [19] F. Hassouna, A. Laachachi, D. Chapron, Y. El Mouedden, V. Toniazzo, D. Ruch, Development of new approach based on Raman spectroscopy to study the dispersion of expanded graphite in poly(lactide), *Polym. Degrad. Stab.* 96 (2011) 2040–2047.
- [20] S. Plimpton, Fast parallel algorithms for short-range molecular dynamics, *J. Comput. Phys.* 117 (1995) 1–19.
- [21] L. Lindsay, D.A. Broido, Optimized Tersoff and Brenner empirical potential parameters for lattice dynamics and phonon thermal transport in carbon nanotubes and graphene, *Phys. Rev. B* 82 (2010) 209903.
- [22] L.A. Girifalco, M. Hodak, R.S. Lee, Carbon nanotubes, buckyballs, ropes, and a universal graphitic potential, *Phys. Rev. B* 62 (2000) 13104–13110.
- [23] B. Mortazavi, Y. Rémond, S. Ahzi, V. Toniazzo, Thickness and chirality effects on tensile behavior of few-layer graphene by molecular dynamics simulations, *Comput. Mater. Sci.* 53 (2012) 298–302.
- [24] LAMMPS user manual, <http://lammps.sandia.gov/doc/Manual.html>
- [25] O.L. Blakslee, D.G. Proctor, E.J. Seldin, G.B. Spence, T.T. Weng, Elastic constants of compression-annealed pyrolytic graphite, *J. Appl. Phys.* 41 (1970) 3373–3382.
- [26] R. Nicklow, N. Wakabayashi, H.G. Smith, Lattice dynamics of pyrolytic graphite, *Phys. Rev. B* 5 (1972) 4951–4962.
- [27] A. Bosak, M. Krisch, M. Mohr, J. Maultzsch, C. Thomsen, Elasticity of single-crystalline graphite: inelastic x-ray scattering study, *Phys. Rev. B* 75 (2007) 153408.
- [28] S. Ghosh, W. Bao, D.L. Nika, S. Subrina, E. Pokatilov, C.N. Lau, A.A. Balandin, Dimensional crossover of thermal transport in few-layer graphene, *Nat. Mater.* 7 (2010) 555–558.
- [29] B. Mortazavi, A. Rajabpour, S. Ahzi, Y. Rémond, S. Mehdi Vaez Allaei, Nitrogen doping and curvature effects on thermal conductivity of graphene: a non-equilibrium molecular dynamics study, *Solid State Commun.* 152 (2012) 261–264.
- [30] J. Thomas, R. Iutzi, A. Mcgaughey, Thermal conductivity and phonon transport in empty and water-filled carbon nanotubes, *Phys. Rev. B* 81 (2010) 45413.
- [31] D.W. Brenner, O.A. Shenderova, J.A. Harrison, S.J. Stuart, B. Ni, S.B. Sinnott, A second-generation reactive empirical bond order (REBO) potential energy expression for hydrocarbons, *J. Phys.: Condens. Matter* 14 (2002) 783–802.
- [32] Z. Wei, Z. Ni, K. Bi, M. Chen, Y.i. Chen, In-plane lattice thermal conductivities of multilayer graphene films, *Carbon* 49 (2011) 2653–2658.
- [33] J. Tersoff, New empirical approach for the structure and energy of covalent systems, *Phys. Rev. B* 37 (1988) 6991–7000.
- [34] N. Sheng, M.C. Boyce, D.M. Parks, G.C. Rutledge, J.I. Abes, R.E. Cohen, Multiscale micromechanical modeling of polymer/clay nanocomposites and the effective clay particle, *Polymer* 45 (2004) 487–506.
- [35] R.S. Fertig, M.R. Garnich, Influence of constituent properties and microstructural parameters on the tensile modulus of a polymer/clay nanocomposite, *Compos. Sci. Technol.* 64 (2004) 2577–2588.
- [36] K. Hbaieb, Q.X. Wang, Y.H.J. Chia, B. Cotterell, Modelling stiffness of polymer/clay nanocomposites, *Polymer* 48 (2007) 901–909.
- [37] H. Liu, L.C. Brinson, Reinforcing efficiency of nanoparticles: a simple comparison for polymer nanocomposites, *Compos. Sci. Technol.* 68 (2008) 1502–1512.
- [38] B. Mortazavi, J. Bardon, S. Ahzi, A. Ghazavizadeh, Y. Rémond, D.D. Ruch, Atomistic-continuum modeling of the mechanical properties of silica/epoxy nanocomposite, *J. Eng. Mater. Technol.* 134 (2012) 010904.
- [39] S.-T. Tu, W.-Z. Cai, Y. Yin, X. Ling, Numerical simulation of saturation behavior of physical properties in composites with randomly distributed second-phase, *J. Compos. Mater.* 39 (2005) 617–631.
- [40] M. Baniassadi, B. Mortazavi, H.A. Hamedani, H. Garmestani, S. Ahzi, M. Fathi-Torbaghan, et al., Three-dimensional reconstruction and homogenization of heterogeneous materials using statistical correlation functions and FEM, *Comput. Mater. Sci.* 51 (2012) 372–379.
- [41] B. Mortazavi, M. Baniassadi, J. Bardon, S. Ahzi, Modeling of two-phase random composite materials by finite element, Mori-Tanaka and strong contrast methods, *Compos. Part B: Eng.* 45 (2013) 1117–1125.
- [42] K.M.F. Shahil, A.A. Balandin, Graphene-multilayer graphene nanocomposites as highly efficient thermal interface materials, *Nano Lett.* 12 (2012) 861–867.
- [43] B. Mortazavi, S. Ahzi, V. Toniazzo, Y. Rémond, Nitrogen doping and vacancy effects on the mechanical properties of graphene: a molecular dynamics study, *Phys. Lett. A* 376 (2012) 1146–1153.
- [44] J.C. Halpin, Stiffness and expansion estimates for oriented short fiber composites, *J. Compos. Mater.* 3 (1969) 732–734.
- [45] T. Mori, K. Tanaka, Average stress in matrix and average elastic energy of materials with misfitting inclusions, *Acta Mater.* 21 (1973) 571–574.
- [47] R. Matadi Boumbimba, S. Ahzi, N. Bahlouli, D. Ruch, J. Gracio, Dynamic mechanical properties of PMMA/organoclay nanocomposite: experiments and modeling, *J. Eng. Mater. Technol.* 133 (2011) 030908.

Tunable and Durable Toughening of Polylactide Materials Via Reactive Extrusion

Georgio Kfoury, Fatima Hassouna,* Jean-Marie Raquez, Valérie Toniazzi, David Ruch, Philippe Dubois*

To tune the toughness of PLA, a novel pathway to chemically modify PLA via reactive extrusion in the presence of “reactive” PEG derivatives is proposed. PEG methyl ether methacrylate (MAPEG) and PEG methyl ether acrylate (AcrylPEG) are melt-mixed and extruded with PLA in the presence of 2,5-dimethyl-2,5-di(*tert*-butylperoxy)hexane (L101) as a free-radical initiator. Molecular characterization reveals that about 20 and 65%, respectively, of the initially introduced MAPEG and AcrylPEG can be grafted onto the PLA backbone. The plasticization effect is demonstrated by a significant decrease of the glass transition temperature and storage modulus together with a significant increase of the elongation at break as compared to neat PLA.



1. Introduction

Poly(lactide) (PLA) is the most extensively studied biodegradable thermoplastics derived from renewable resources for commodity applications, due to its industrial imple-

mentation. High-molecular-weight PLA can be readily obtained at low cost production via ring-opening polymerization (ROP) of lactide (LA).^[1] Due to its inherent brittleness, the use of PLA is limited as it cannot fulfil the applications where high ductility is required compared to the others.^[2,3] In order to improve the mechanical properties of PLA, plasticizing PLA with low-molecular-weight compounds has been intensively investigated.^[4–6] To get all the benefits in terms of its processability, flexibility/ductility, and impact strength,^[7] the plasticizer should be miscible with the polymer at the required loadings. Depending on their molecular weight, two main classes of plasticizers can be distinguished as reported by Liu and Zhang;^[8] the first type includes monomers or small molecule plasticizers and the second one includes oligomeric or polymeric plasticizers. Many small molecules/monomeric biodegradable compounds, mainly based on

G. Kfoury, Dr. F. Hassouna, Dr. V. Toniazzi, Dr. D. Ruch
Department of Advanced Materials and Structures (AMS), Centre de Recherche Public Henri Tudor, Rue Bommel 5 4940, Hautcharage, Luxembourg
E-mail: fatima.hassouna@tudor.lu
G. Kfoury, Dr. J.-M. Raquez, Prof. P. Dubois
Laboratory of Polymeric and Composite Materials (LPCM), Centre d'Innovation et de Recherche en Matériaux Polymères (CIRMAP), UMONS Research Institute for Materials Science and Engineering, Université de Mons (UMONS), Place du Parc 23, B-7000 Mons, Belgium
E-mail: philippe.dubois@umons.ac.be

the family of citrate derivatives and LA monomer have been investigated. By comparison with oligomeric or polymeric plasticizers, the small molecule plasticizers are more miscible and efficient in order to decrease the T_g of the PLA polymer for their higher mixing entropy contribution. However, because of their low boiling point, small molecule plasticizers can get evaporated during melt processing^[3,9–11] as well as have a strong tendency to migrate toward the surface of the polymeric material,^[9,11–13] reducing the toughness of PLA-based materials. This can be explained by the tendency of the plasticized PLA to crystallize with time, which reduces the amorphous fraction able to retain the plasticizer molecules in the polymer.^[11–15] In addition, the plasticizer migration can have some risks of food contaminations in packaging applications. In this regard, oligomeric and polymeric plasticizers are more preferred in order to plasticize the polymer matrix, while reducing the extent of the plasticizer migration. However, the plasticization extent with oligomeric and polymeric plasticizers has not been satisfactory yet, because they can yield macrophase separation at high loadings with time in the PLA-based blends.

To overcome this problem, Hassouna et al.^[16,17] have succeeded to graft hydroxylated PEG and citrate plasticizers in the presence of maleic anhydride moieties grafted onto PLA chains using reactive extrusion (REx), resulting in a very tough material. A partial grafting of hydroxylated PEG through maleic anhydride moieties was evidenced, reducing the tendency of PEG to phase-separate in the blends. In this work, we hence propose to chemically modify PLA matrix through the free-radical grafting of PEG derivatives bearing (meth)acrylates moieties using REx in order to finely tune the toughness of PLA-based materials. The free-radical grafting of unsaturated monomers onto PLA backbone has thereby shown to be an efficient way to functionalize, but also to enhance the stiffness of the PLA matrix.^[18] This latter is very important because toughness of PLA is significantly reduced after plasticization.

Interestingly, REx has proven to be an ecological, cost-effective, and versatile process to design novel and high performance bioplastics.^[19] Luperox 101 (L101) was used as free-radical initiator with two unsaturated low-molecular-weight poly(ethylene glycol)s (PEGs), i.e., poly(ethylene glycol) methyl ether methacrylate (MAPEG) and poly(ethylene glycol) methyl acrylate (AcrylPEG). Interestingly, depending on the nature of the PEG derivatives and the concentration of the free-radical initiator, it was possible to achieve tough to highly-plasticized materials. The L101 amount in the ternary REx blends PLA/MAPEG/L101 and PLA/AcrylPEG/L101 was investigated in this regard. A thorough molecular characterization was performed in order to provide some mechanistic insights. Thermal and mechanical properties

of the so-produced materials were determined, namely in terms of impact strength and tensile properties.

2. Experimental Section

2.1. Materials and Reagents

4042D (NatureWorks®) grade PL-LA [\overline{M}_n (PS) \approx 129 000 g mol⁻¹, D-(–)-LA monomer content (as determined by selective enzymatic titration) = 4.6%] was provided by NatureWorks LLC. 2,5-dimethyl-2,5-di-(*tert*-butylperoxy)hexane organic peroxide (Luperox101 or L101), MAPEG, $\overline{M}_n \approx$ 300 g mol⁻¹, and AcrylPEG, $\overline{M}_n \approx$ 480 g mol⁻¹ were purchased from Sigma-Aldrich. L101 was chosen as the initiator for several reasons. A half-lifetime of 1 min at 180 °C and 13 s at 200 °C was reported by the supplier, which indicates a complete decomposition of the peroxide at the operating temperatures and residence times of our process. L101 is also recognized by the FDA as a food additive (Code of Regulations; Title 21 “Food and Drugs” part 170 under “Food Additives”).

2.2. Reactive Extrusion and Sample Elaboration

All melt (reactive) blends were performed using a twin screw DSM Xplore Research micro-compounder under nitrogen atmosphere. Barrel temperature was set at 180 °C. Melt temperature was measured before and during the process (\approx 170–175 °C). Screw speed was fixed to 100 rpm and the residence time to 5 min. 15 g in total per batch were introduced into the micro-compounder. PLA was first dried for at least 12 h at 60 °C in a vacuum oven (Thermo scientific–Heraeus) before processing. During experiments, the liquids (MAPEG, AcrylPEG, and L101) were kept in dark, cool, and inert atmosphere in a closed Dewar vase containing liquid nitrogen to prevent any potential photo-polymerization and any degradation of the plasticizers by contact with the ambient humidity. PLA was first introduced and melted in the extruder. MAPEG (or AcrylPEG) and L101 were mixed in a small glass vial then injected into the extruder using a syringe. The evolution of the force (N) during REx was recorded. Standard samples of resulting PLA-based materials were then prepared by compression molding using a Carver manual press (25 × 25 cm² plates) at 180 °C during 10 min.

2.3. Characterization Methods

2.3.1. Soxhlet Extraction in Methanol

This extraction technique was used to separate and quantify the residues of the liquid fraction (soluble in methanol) from the PLA matrix. Approximately 1 g of each extruded sample was placed in a thimble-holder that was gradually filled with condensed methanol from a distillation flask constantly heated at 120 °C. When the liquid reached the overflow level, a siphon aspirated the solute from the thimble-holder and unloaded it back into the distillation flask, carrying the extracts into the bulk liquid. This operation was repeated until extraction was complete (\approx 24 h). Solid fraction was dried overnight at 70 °C under vacuum and weighed after being kept at ambient conditions for at least 15 h in order to reabsorb

the ambient humidity. Methanol was evaporated from the solution fraction by Rotavapor technique, and dried overnight under vacuum at 50 °C. Extracted fraction (EF in wt%) was calculated according to $EF = \frac{\text{before Soxhlet(g)} - \text{after Soxhlet and drying(g)}}{\text{before Soxhlet(g)}} \times 100$. Soxhlet extraction was repeated at least two times for each sample. Average and standard deviation were calculated and the results were plotted.

The residues of the soluble fraction as well as the insoluble fraction from PLA-based blends were characterized by FTIR and SEC.

2.3.2. Fourier-Transform Infrared (FTIR) Spectroscopy

The changes in the chemical structure of PLA, MAPEG, and AcrylPEG were evaluated by FTIR spectroscopy in attenuated total reflectance (ATR) mode from 400 to 4000 cm^{-1} using a Bruker Optics Tensor 27 spectrometer.

2.3.3. Size Exclusion Chromatography (SEC)

SEC was performed in order to characterize the molecular weight change of PLA, MAPEG, and AcrylPEG in the presence of different concentrations of L101. Sample preparation was performed by dissolving the material to be analyzed in chloroform at a concentration of 2 $\text{mg} \cdot \text{mL}^{-1}$. This was followed by the filtration of the prepared material solution using a syringe and an acrodisk (0.45 μm). SEC used was an Agilent Technologies series 1200 working with a differential refractive index detection and a linear column (PLgel 5 μm Mixed-D, 200 Da < M_w < 400 kDa).

2.3.4. Proton Nuclear Magnetic Resonance (^1H NMR)

The changes in the chemical structure of PLA, MAPEG, and AcrylPEG were evaluated by ^1H NMR. Sample preparation was performed by dissolving the material to be analyzed in deuterated chloroform CDCl_3 (containing 0.03% of trimethylsilane) at a concentration of 50 $\text{mg} \cdot \text{mL}^{-1}$. ^1H NMR spectra were recorded using a BRUKER AMX-300 spectrometer working at a frequency of 300 MHz in a magnetic field of 7 T. The delay between the scans was 10 s. A BRUKER AMX-500 spectrometer was also used where higher precision and sensitivity were required. The latter worked at a frequency of 500 MHz in a magnetic field of 11.6 T.

2.3.5. Differential Scanning Calorimetry (DSC)

5–10 mg of each sample was subjected to thermal characterization using a TA instrument Q2000 DSC under nitrogen atmosphere. A “heat/cool/heat” program was used and the lower and the upper temperatures were fixed to –80 and +200 °C and both the cooling and the heating rates were fixed to 10 °C min^{-1} .

2.3.6. Dynamic Mechanical Thermal Analysis (DMTA)

The viscoelastic properties of elaborated PLA-based materials were analyzed by means of a dynamic mechanical analyzer (DMA) TA Instrument Q800. For this study, three rectangular specimens (60 × 12 × 2 mm^3) per sample were prepared by compression-moulding then conditioned for at least 24 h at 20 °C and 50% of relative humidity before testing. They were subjected to double

cantilever mode of flexural loading with amplitude of 20 μm in the temperature range from –60 to +120 °C at a heating rate of 2 °C $\cdot \text{min}^{-1}$ and a frequency of 1 Hz.

2.3.7. Tensile Tests

Tensile properties were determined according to ASTM D638 procedure using a Zwickline tensile bench. At least four tensile specimens per sample (narrow section dimensions: 16 × 3 × 3 mm^3) were prepared by compression moulding. They were conditioned for at least 24 h at 20 °C and 50% of relative humidity before testing. After measuring the dimensions of the narrow section, each specimen was fixed between the grips of both the fixed and the movable members. The test was performed according to ASTM D638 procedure at 5 $\text{mm} \cdot \text{min}^{-1}$ till break under the same temperature and relative humidity conditions. The data acquisition was managed by testXpert II software.

2.3.8. Notched Izod Impact

At least four rectangular specimens (62 × 12 × 3 mm^3) per sample were prepared by compression moulding and notched on a Ray Ran 1900 notching apparatus according to ASTM D256 specifications. The angle of the notch was 45° and the radius is 2.5 mm. Before testing, specimens were conditioned at 20 °C and 50% of relative humidity for at least 24 h. Ray Ran 2500 pendulum impact tester was used. Each specimen was held as a vertical cantilever beam and was broken by a single swing of the pendulum. The line of initial contact was at a fixed distance from the specimen clamp and from the center-line of the notch and on the same face as the notch. The results of all test methods were reported in terms of energy absorbed per unit of specimen cross-sectional area under the notch. Testing conditions were: impact velocity: 3.46 $\text{m} \cdot \text{s}^{-1}$; hammer weight: 0.668 kg; energy: 3.99 J.

3. Results and Discussion

The influence of free-radical grafting reactions of PLA with MAPEG and AcrylPEG at 20 wt% was assessed over the force evolved during REX at 180 °C. For a sake of comparison, a simple blending between PLA and unsaturated PEG derivatives was carried out, i.e., in the absence of free-radical initiator. The evolution of the REX force as a function of time was recorded and plotted in Figure 1.

Irrespective of the plasticizer, the liquid injection in the viscous PLA matrix resulted in a fast and significant drop of the extrusion force from ≈6 000 to 2 000–3 000 N. This observation can be ascribed to the dramatic decrease of the material viscosity due to the high plasticizer loading (20 wt%). From Figure 1, two different REX force evolutions can be noticed in function of the plasticizer. When MAPEG was extruded with PLA (in the presence or in the absence of L101), the initial extrusion force fluctuated slightly as MAPEG was incorporated in the PLA matrix before leveling off after 2 min. Moreover, the extrusion force and to some extent, the blend-viscosity

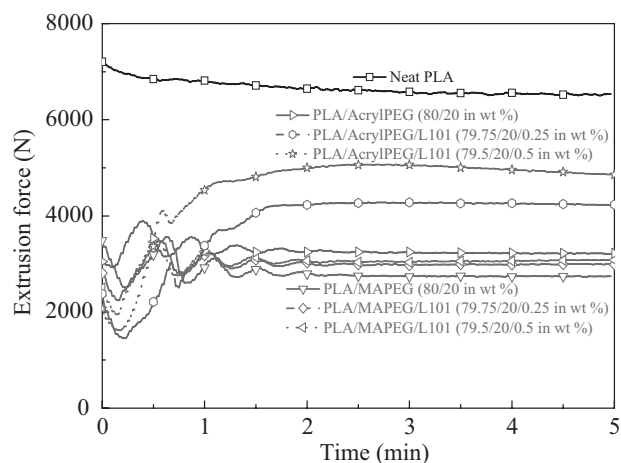


Figure 1. REx force evolution as a function of time for different REx PLA/MAPEG/L101 and PLA/AcrylPEG/L101 blends.

slightly increased by ≈ 500 N with the addition of L101. A similar REx force trend is noticed for the simple blend of PLA/AcrylPEG, except that slightly higher values are obtained with respect to all PLA/MAPEG/L101 blends. When L101 was added to PLA/AcrylPEG blend, the REx force remarkably increases during the first 2 min of REx before reaching a plateau. The extrusion force at the plateau is considerably enhanced with the addition of 0.25 and 0.5 wt% of L101, passing from 3 250 for PLA/AcrylPEG to 4 300 and 5 000 N for PLA/AcrylPEG/L101 blends, respectively. This attests for the substantial modifications of the length (higher molecular weight) and/or topology (chain branching) of the polymer chains as evidenced on the molecular characterization of the polymer blends so-produced by REx.

3.1. Molecular Characterization

The plasticizers were extracted from the PLA matrix by means of Soxhlet technique from methanol as a solvent. Figure 2 displays the evolution, as a function of the added L101 amount, of the residues from the soluble fraction (in wt%) for the different blends investigated. Up to 19 wt% of plasticizer was extracted from the simple blends made of MAPEG and AcrylPEG. This indicates that all plasticizer introduced, either MAPEG or AcrylPEG, remained unreacted in PLA matrix. Interestingly, the residues amount from the soluble fraction decreases with the L101 amount. For instance, when 0.5 wt% L101 was added in the case of PLA/MAPEG/L101 blends, only ca. 16 wt% of residues from the soluble fraction was extracted out. This value (ca. 7 wt%) was lower in the case of PLA/MAPEG/L101 blend containing 0.5 wt% of L101. This can be explained by the fact that in presence of L101, a certain fraction of plasticizer can be grafted onto PLA

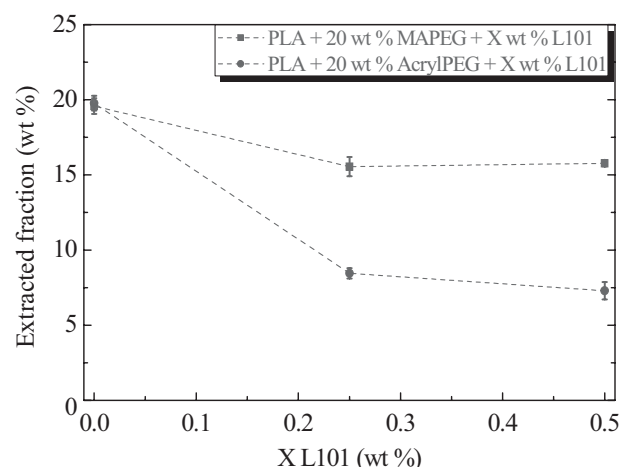


Figure 2. Extracted fraction by Soxhlet in methanol from the different REx blends plotted as a function of the L101 amount. —■— for PLA/MAPEG/L101 and —●— for PLA/AcrylPEG/L101.

backbone, and therefore decreasing the amount of the residues from the soluble fraction. Moreover, the grafting extent of AcrylPEG onto PLA is much higher than that with MAPEG.

To support these statements, the resulting PLA-based materials as well as the corresponding residues of liquid fractions were characterized by means of FTIR and SEC techniques (Figure 3 for the PLA/MAPEG/L101 blends and Figure 4 for the PLA/AcrylPEG/L101 blends). The relative molecular weights (\bar{M}_n and \bar{M}_w , \bar{D} and $D\bar{P}_n$) of all samples were thereby determined by SEC analysis according to polystyrene standards and are summarized in Table 1. The average degree of polymerization ($D\bar{P}_n$) is defined as the molecular weight of distribution of the PEG plasticizer after REx (homo-oligomers) per the molecular weight distribution of the neat reactive plasticizer. Figure 3F and Figure 4F show that the chromatograms of the materials recovered just after extrusion is bimodal (MWD) in both simple blends containing either MAPEG or AcrylPEG (not added with L101). These two molecular weight distributions are ascribed to PLA [$MWD_{(PLA)}$] and to the plasticizers [$MWD_{(MAPEG)}$ for MAPEG in PLA/MAPEG, and $MWD_{(AcrylPEG)}$ for AcrylPEG in PLA/AcrylPEG] by comparison with the chromatograms of the reference materials (neat PLA, MAPEG, and AcrylPEG, separately). In other terms, no reaction occurred between PLA and the plasticizers during the extrusion process as previously demonstrated by Soxhlet extraction (Figure 2). In the case of the reactively modified REx PLA/MAPEG/L101 blends, adding L101 leads to the decrease of $MWD_{(MAPEG)}$ of MAPEG, together with the appearance of a new molecular weight distribution $MWD_{(oligo-MAPEG)}$ between $MWD_{(MAPEG)}$ (MAPEG) and $MWD_{(PLA)}$. In the case of the REx PLA/AcrylPEG/L101 blends, adding L101 also leads to the appearance of a new molecular weight distribution

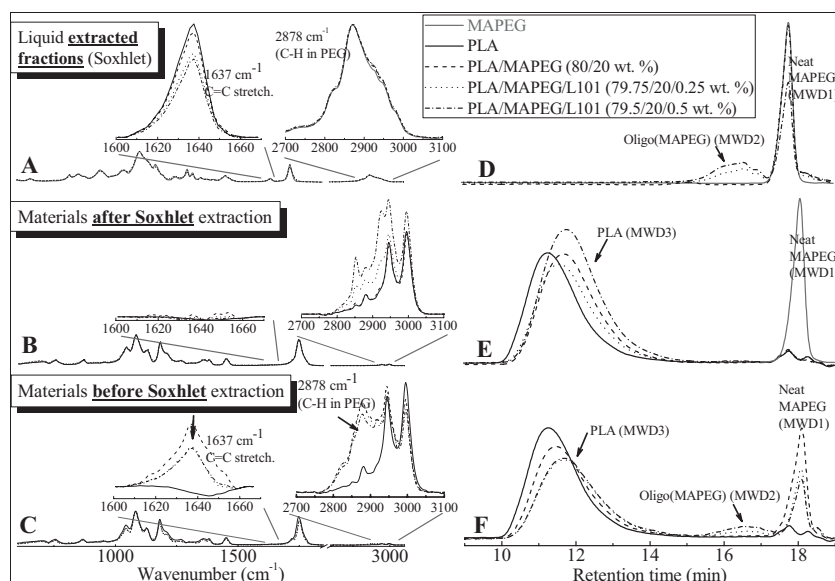


Figure 3. Left: A) FTIR spectra of the residue from the liquid fractions, B) solid fraction recovered after Soxhlet extraction, and C) materials before extraction. Right: D) SEC chromatograms of the residue from the liquid fractions, E) solid fraction recovered after Soxhlet extraction, F) and materials before extraction.

containing 0.5 wt% of L101) as compared to neat PLA ($\bar{M}_w = 260\,580\text{ g}\cdot\text{mol}^{-1}$ and $\bar{D} = 1.8$; Table 1). Although we cannot exclude any recombination of PLA macroradicals, this can be more likely explained by the grafting of AcrylPEG macroradicals onto PLA backbone during the REx process. In Figure 3C and Figure 4C, we observe that the characteristic absorption bands of PLA, MAPEG, and AcrylPEG in the FT-IR spectra of all the investigated (REx) blends. The FTIR spectrum of residues of the soluble fractions from the PLA/MAPEG/L101 blends is very similar to the spectrum of neat MAPEG. However, the intensity of the absorption band at $1\,637\text{ cm}^{-1}$ corresponding to the double-bond moieties from methacrylate derivatives decreases with the increase of L101 amount (Figure 3A). Furthermore, SEC analysis performed on the same samples (Figure 3D) show the presence of two molecular weight distributions:

$MWD_{(\text{oligo-AcrylPEG})}$, but the AcrylPEG macroinitiator was almost reacted as evidence by the quasi-total disappearance of $[MWD_{(\text{AcrylPEG})}]$. In addition, a significant broadening of $MWD_{(\text{PLA})}$ was noticed, indicating the PLA weight-average molecular weight \bar{M}_w and dispersity \bar{D} increase ($\bar{M}_w = 1\,296\,400\text{ g}\cdot\text{mol}^{-1}$ and $\bar{D} = 10$ for the blend

$MWD_{(\text{MAPEG})}$ corresponding to neat MAPEG and $MWD_{(\text{oligo-MAPEG})}$. One can notice a decrease of $MWD_{(\text{MAPEG})}$ and an increase of $MWD_{(\text{oligo-MAPEG})}$ as the amount of L101 increases. The evolution of the absorption band at $1\,637\text{ cm}^{-1}$ determined by FTIR analysis can be therefore correlated with the evolution of the molecular weight distribution $MWD_{(\text{MAPEG})}$ of the MAPEG plasticizer measured by SEC. Indeed, the decrease of the band intensity of the double-bond moieties from methacrylate derivatives ($1\,637\text{ cm}^{-1}$) with the increased amount of L101 observed by FTIR corresponds to the decrease of $MWD_{(\text{MAPEG})}$ and an increase of $MWD_{(\text{oligo-MAPEG})}$ as observed by SEC. Furthermore, Table 1 shows that the molecular weight distribution $MWD_{(\text{oligo-MAPEG})}$ is characterized by a dispersity \bar{D} of about 1.2, while \bar{D} of MAPEG is just slightly higher than 1. In other terms, the $MWD_{(\text{oligo-MAPEG})}$ population can be ascribed to the in situ free-radical homo-oligomerization of MAPEG derivatives. Accordingly, the residues from the soluble fraction from the PLA/MAPEG/L101 blends can be identified as a mixture of MAPEG and its oligomers.

According to these results, we may suggest a multi-stage process during free-radical grafting of PLA with MAPEG

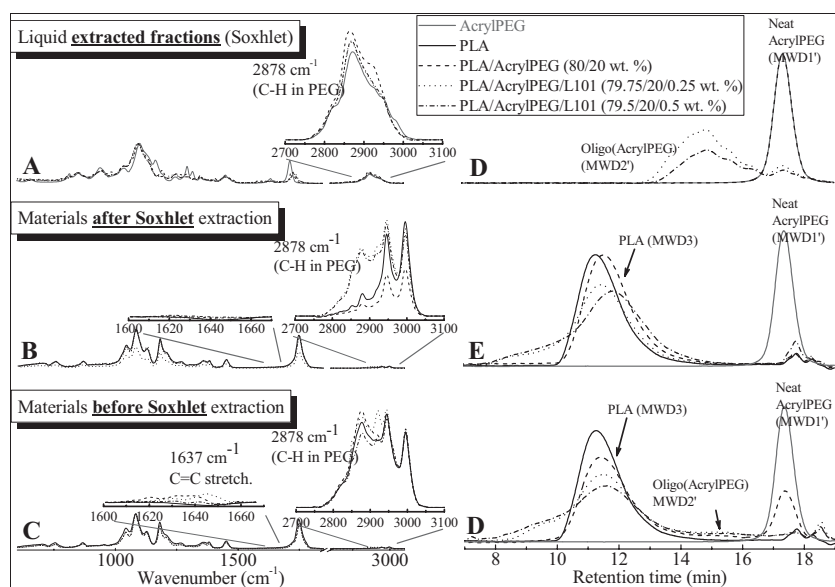


Figure 4. Left: A) FTIR spectra of the residue from the liquid fractions, B) the solid fraction recovered after Soxhlet extraction, and C) materials before extraction. Right: D) SEC chromatograms of the residue from the liquid fractions, E) the solid fraction recovered after Soxhlet's extraction, and F) materials before extraction.

Table 1. Molecular weights, dispersity (\bar{D}) and number-average degree of polymerization (\overline{DP}_n) as determined by SEC on all the investigated materials.

X	PLA/X/L101 [wt.%]	\bar{M}_n (PS) [g mol ⁻¹]			\bar{M}_w (PS) [g mol ⁻¹]			$\bar{D} = \bar{M}_w/\bar{M}_n$			\overline{DP}_n ^{a)}
		X	oligo-X	PLA	X	oligo-X	PLA	X	oligo-X	PLA	oligo-X
–	100/0/0 ^{b)}			145 400			260 580			1.79	
–	100/0/0 ^{c)}			132 310			241 550			1.83	
MAPEG	0/100/0	420			430			1.03			
MAPEG	80/20/0	422	–	102 760	435	–	195 010	1.03	–	1.90	–
MAPEG	79.75/20/0.25	425	1 660	120 460	440	1960	247 830	1.03	1.19	2.28	4
MAPEG	79.5/20/0.5	424	1 756	121 890	437	2142	280 370	1.03	1.22	2.30	4
AcrylPEG	0/100/0	830			940			1.13			
AcrylPEG	80/20/0	840	–	113 750	930	–	234 580	1.11	–	2.06	–
	79.75/20/0.25	–	6 736	123 130	–	11 368	518 960	–	1.69	4.21	8
AcrylPEG	79.5/20/0.5	–	5 700	129 390	–	9 380	1 296 400	–	1.65	10.01	7

^{a)} $\overline{DP}_n = \frac{\bar{M}_n \text{ of oligo-MAPEG or oligo-AcrylPEG}}{\bar{M}_n \text{ of MAPEG or AcrylPEG}}$; ^{b)}Neat PLA; ^{c)}Extruded PLA.

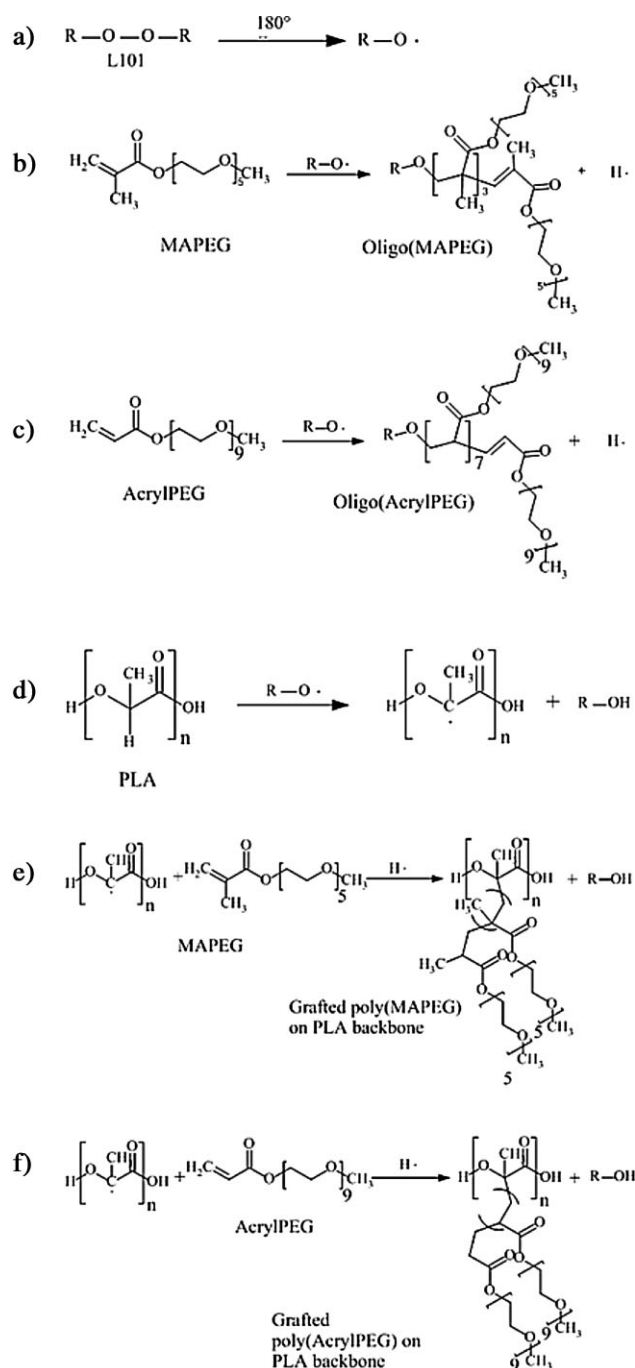
during the REx process (Scheme 1). L101 is a difunctional di-tertiary alkyl peroxide. The free-radicals as generated during the thermal decomposition of L101 can initiate the polymerizations of unsaturated monomers.^[20–22] During reactive melt processing, L101 generates free-radicals in the medium (decomposition half-time at 180 °C \approx 1 min) (Scheme 1a). The L101 free radicals activate the methacrylic carbon-carbon double bonds.^[23] The resulting tertiary MAPEG free radicals may then combine with other MAPEG species, i.e., oligomerization of MAPEG. Based on FTIR and SEC analyses, the oligomerization of MAPEG (Scheme 1b) is the main reaction taking place during the REx process.

One should note that the infrared absorption band (peak at 2 878 cm⁻¹) related to the C-H single bonds from the PEO segment remained unmodified, indicating that the PEO segment itself did not participate to free-radical grafting of PLA with MAPEG. However, the grafting reaction of MAPEG onto PLA can be partly considered to take place during the melt processing. Indeed, FTIR analysis performed on PLA/MAPEG/L101 materials after Soxhlet extraction (Figure 3B) reveals a total disappearance of the C=C groups (1 637 cm⁻¹), but still the presence of the absorption band at 2 878 cm⁻¹ corresponding to C-H single bonds from the PEO segments of MAPEG. Similarly, SEC analysis performed on the same materials shows the presence of a single molecular weight distribution confirming the absence of the starting MAPEG. The molecular weight distribution can be ascribed to a mixture of PLA and PLA-graft-MAPEG.

However, one can notice that further addition of L101, i.e., at 0.25 and 0.5 wt%, had a slight negative effect on the

molecular weight of PLA. This decrease can be explained by a slight degradation of PLA through free-radical induced β -scission of the polyester chain.^[24]

The residues of soluble fractions from the PLA/AcrylPEG/L101 materials were also characterized. All the residues of soluble fractions from the PLA/AcrylPEG/L101 materials exhibited FTIR spectra similar to neat AcrylPEG. However, the absorption band corresponding to the carbon-carbon double bond at 1 637 cm⁻¹ disappeared in presence of L101 (Figure 4A). SEC analysis carried out on the same samples shows the quasi-total disappearance of the peak corresponding to neat AcrylPEG molecular weight distribution [MWD_(AcrylPEG)] and the appearance of a new peak at higher molecular weight [MWD_(AcrylPEG)] (Figure 4D). Furthermore, Table 1 shows that the material corresponding to MWD_(AcrylPEG) is characterized by a dispersity \bar{D} of about 1.7, while \bar{D} of neat AcrylPEG [MWD_(AcrylPEG)] is 1.1. Consequently, by comparison to the residues of the soluble fractions from the blends PLA/MAPEG/L101, MWD_(AcrylPEG) is more likely the result of an in situ free-radical homo-oligomerization reaction of the acrylic functional end-groups of AcrylPEG in presence of L101. The residue of the soluble fraction from the PLA/AcrylPEG/L101 blends can be identified as AcrylPEG oligomers [oligo_(AcrylPEG)]. A mechanism of homo-oligomerization of AcrylPEG in presence of L101 during the REx process is proposed in Scheme 1a and c, in this regard. L101 free-radicals formed during the melt processing attacks the acrylic carbon-carbon double bonds. The formed secondary AcrylPEG free-radical may then combine with other AcrylPEG molecules. FTIR and SEC results suggest clearly that the oligomerization of AcrylPEG is the main reaction



Scheme 1. In situ chemical reactions taking place during the reactive extrusion of the ternary reactive blends PLA/MAPEG/L101 and PLA/AcrylPEG/L101.

taking place during the REx process and again, the grafting reaction of AcrylPEG onto PLA cannot be neglected. Indeed, FTIR analysis performed on the PLA/AcrylPEG/L101 blends after Soxhlet extraction (Figure 4B) show the presence of the absorption band at 2878 cm^{-1} attributed to the C–H single bonds from the PEO segment of AcrylPEG and the

absence of the band at 1637 cm^{-1} (double bonds), attesting for the complete derivatization of AcrylPEG, as observed by Soxhlet. Indeed, Soxhlet extractions performed on PLA/AcrylPEG/L101 showed the decrease of the EF for the plasticizer with increasing the amount of L101 (i.e., 13 wt% of non-extracted plasticizer in the blend containing 0.5 wt% of L101).

^1H NMR spectra (Figure 5) of PLA/AcrylPEG/L101 blends after Soxhlet extraction (79.75/20/0.25 and 79.5/20/0.5 in wt%) confirms the absence of C=C functions (absence of the doublet at $\delta = 5.50$ and 6.50 attributed to the protons of the acrylic end-groups) and the presence of unreacted PEG (peaks between $\delta = 3.00$ and 4.50 attributed to the CH_2 and CH_3 units in PEG chains). Moreover, SEC analysis carried out on the same blends indicates the presence of only one molecular weight distribution $[\text{MWD}_{(\text{PLA})}]$ (Figure 4E), which remains the same before and after Soxhlet extraction (Figure 4F). Accordingly, the PEG observed by FTIR and quantified by Soxhlet (non-EF) must be grafted onto the PLA backbone (Scheme 1d,f). The molecular characterization can be correlated with the REx force evolution. Indeed, when the plasticizer grafting extent is high (as in the case of the REx PLA/AcrylPEG/L101 blends), the molecular weight of the resulting modified PLA chains increases as reported in Table 1 (a drastic increase of \bar{M}_w and \bar{D}) and in Figure 4C (broadening of the PLA MWD due to the formation of high-molecular-weight chains). Accordingly, the viscosity of the melt blends and to some extent the REx force are expected to increase by comparison with the simple (non-reactive) blend.

Overall, the above results show a clear difference of reactivity toward MAPEG, AcrylPEG and PLA in presence of peroxide during the REx process. The grafting efficiency onto PLA chains proved remarkably higher with AcrylPEG rather than MAPEG. This could be explained by the nature of the free radicals generated from MAPEG and AcrylPEG. Indeed, AcrylPEG can generate secondary free radicals with lower stability as compared to the tertiary ones generated by MAPEG.^[25]

3.2. Thermal and Mechanical Properties

Thermal and structural behaviors of the investigated blends were characterized by means of DSC using a heat/cool/heat cycle. Neat PLA did not display any significant differences in its thermal profile between the first (not shown here) and the second heating (Figure 6B). They both correspond to an amorphous material with a glass transition temperature (T_g) at ca. 60°C . This can be explained by the fact that the studied PLA matrix contains 4.6% of D-LA isomer, reducing its crystallization ability. In the case of the simple PLA/MAPEG blend (not added with L101), the addition of 20 wt% of MAPEG to PLA leads to the shift of the glass transition to 16°C as well as the

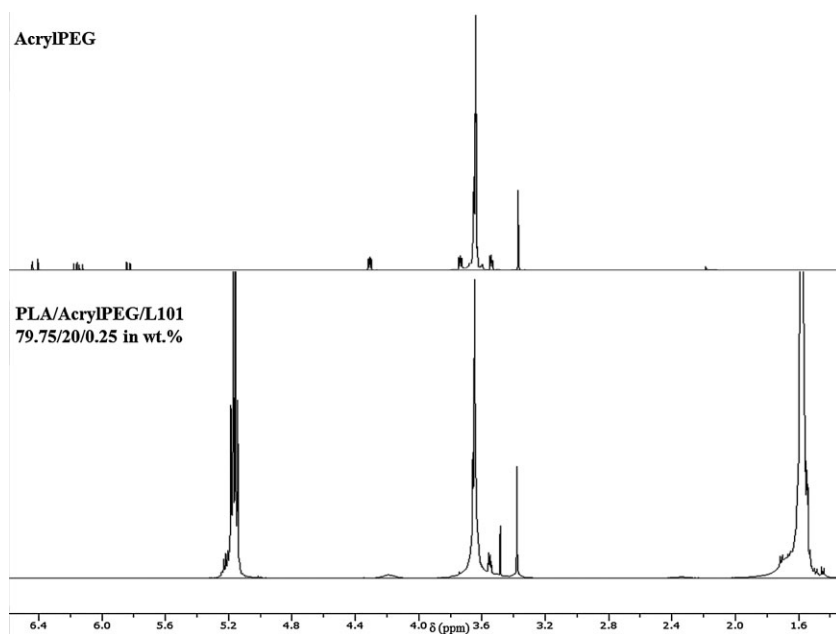


Figure 5. Proton NMR spectra of AcryIPEG and PLA/AcryIPEG/L101 (79.75/20/0.25 wt.%).

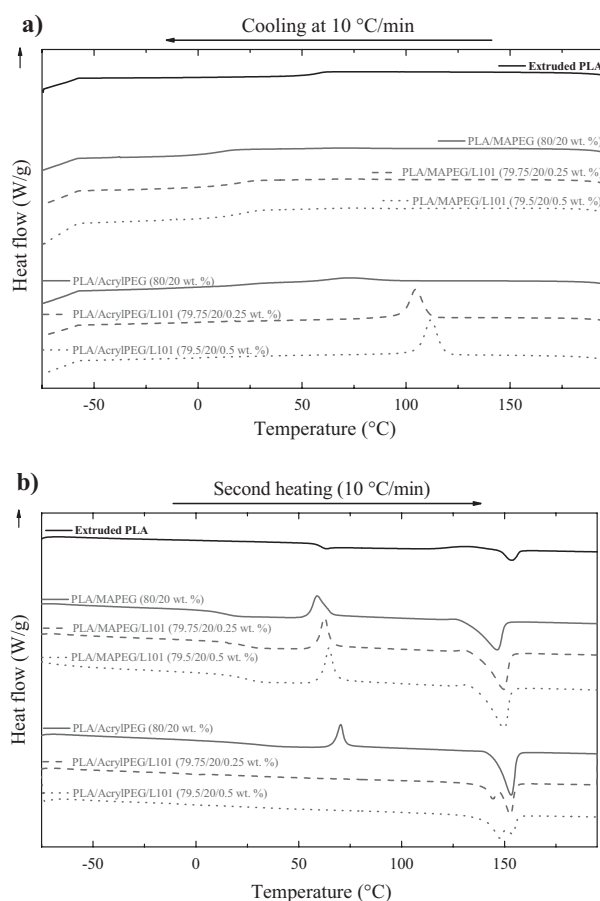


Figure 6. A) Cooling and B) second heating DSC thermograms of all the investigated materials.

appearance of a cold-crystallization peak and a melting peak ($T_{cc} \approx 59^\circ\text{C}$ and $T_m = 146^\circ\text{C}$). This can be attributed to the higher chain mobility of PLA chains as a result of the presence of the large amount of low-molecular-weight plasticizer as reported elsewhere. It is worth noting that these binary blends behave as any conventionally plasticized PLA materials since no reactions were observed between the polyester matrix and the plasticizing agent. The presence of L101 in the ternary PLA/MAPEG/L101 blend shifts to higher values both T_g (up to 25°C), T_{cc} (to $\approx 64^\circ\text{C}$), and T_m (to $\approx 150^\circ\text{C}$) with respect to the reference PLA/MAPEG blend. This result is considered to be directly related with the motion ability of the PLA chains.^[14,25] Indeed, in the simple PLA/MAPEG blend, MAPEG did not homopolymerize and only low-molecular-weight MAPEG participated more efficiently to the plasticization of

PLA materials in contrast to higher molecular weight oligo(MAPEG) obtained in the case of the REx PLA/MAPEG/L101 blends. It is also to be mentioned here that for all the investigated materials, i.e., PLA/MAPEG and PLA/MAPEG/L101, the melting enthalpy (ΔH_m) of the materials is about equal to the enthalpy of cold crystallization (ΔH_{cc}). This implies that all the investigated materials are globally amorphous at room temperature.

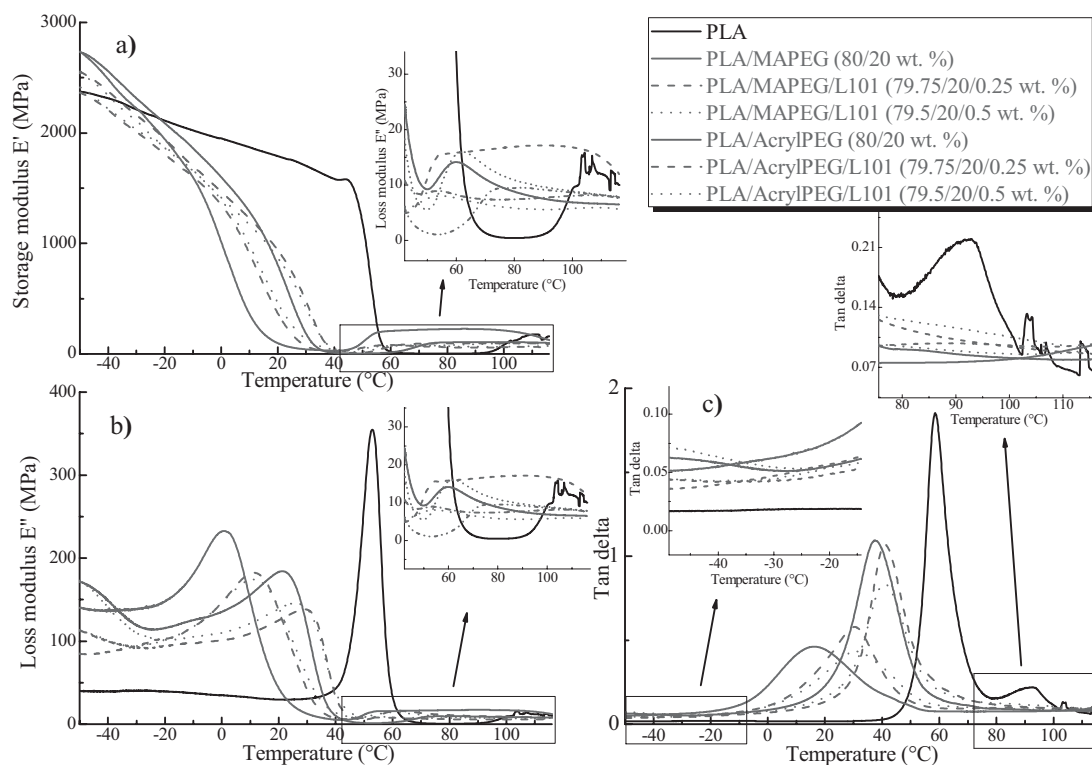
Similar tendencies are obtained when AcryIPEG plasticizer was added to as-extruded PLA. Nevertheless, in the case of simple PLA/AcryIPEG blend, the decrease of T_g , T_{cc} , and T_m shown to be lower than in the case of simple PLA/MAPEG blend ($T_g = 29^\circ\text{C}$, $T_{cc} = 70^\circ\text{C}$, and $T_m = 153^\circ\text{C}$). The addition of L101 to PLA/AcryIPEG leads to the disappearance of the T_g and T_{cc} and to the appearance of shoulders in the melting peaks ($T_m = 153^\circ\text{C}$) of PLA blends at lower temperatures (144 and 148°C in the blends containing 0.25 and 0.5 wt% of L101, respectively). Moreover, the degree of crystallinity calculated by DSC indicates that the addition of 0.25 and 0.5 wt% of L101 to PLA/AcryIPEG enhanced the crystallization of PLA by about 25 and 27%, respectively, while the simple PLA/AcryIPEG blend exhibited an amorphous behavior. The crystallization process of PLA in PLA/AcryIPEG/L101 took place during the cooling step (crystallization peaks at 104 and 111°C for the materials containing 0.25 and 0.5 wt% of L101, respectively; Figure 6A). The crystallization process of PLA observed in the materials containing relatively high amount of L101 (i.e., 0.25 and 0.5 wt%) can be explained by the fact that the PLA-graft-poly(acryIPEG) generated during the REx processing played the

role of nucleating agent and enabled the crystal growth.^[26]

Interestingly, it can be suggested that a new crystalline phase with a lower melting temperature appeared due to the grafting of AcrylPEG onto the PLA chains. Interestingly enough, when the grafting of AcrylPEG is higher (with higher amount of L101), the new melting temperature increases from 144 to 148 °C. As a result, the amorphous phase was therefore reduced and any glass transition temperature (T_g) could not be detected by DSC. T_g could not be detected in the blends containing relatively high amount of L101 for two main reasons: (i) formation of a significant crystalline phase leading to the reduction of the amorphous phase content and hindering the polyester chain motions, (ii) a drastic increase of the molecular weight of the modified PLA chains (highly branched system) as observed by SEC and REX force evolution reduces the polyester chain motions.

The thermo-mechanical behaviors of the blends were investigated by means of DMTA to reveal the influence of the grafting extent on the mechanical characteristics of the blends. The temperature effect on the storage modulus E' , loss modulus E'' , and damping factor $\tan \delta$ of resulting blends is represented in Figure 7A–C, respectively. The glass transition temperature T_g has been also estimated by means of DMTA (coined as T_α) and was associated to the temperature at the maximum of the $\tan \delta$ peak [$(\tan \delta)_{\max}$].

At –60 °C, the materials have a storage modulus E' between 2 300 and 2 800 MPa (Figure 7A). Neat PLA displays the lowest loss modulus E'' and damping factor $\tan \delta$, while the non-reactive binary PLA/MAPEG and PLA/AcrylPEG blends the highest values. The curves of the reactively modified REX blends are located in between them. Accordingly, PLA seems to have a high elastic behavior, and the simple blends can thus dissipate more energy as a response to deformation when the temperatures are below T_g . With increasing the temperature up to the onset of glass transition relaxation, $\approx 50\%$ decrease of the storage modulus of plasticized PLA is noted. This observation indicates that the rigidity and the elastic behavior of the modified PLA decrease rapidly as a function of the temperature increase. In the same temperature range, a much less marked decrease in E' occurred for PLA ($\approx 15\%$). The glass transition temperature range of the plasticized PLA-based materials is lower and wider than the one of PLA. The glass transition temperature, as measured as T_α , as well as the storage modulus E' measured at 20 °C are reported in Table 2 for the studied materials. Neat PLA has a storage modulus E' measured at 20 °C of about 1 776 MPa and displays a T_α at 59 °C. E' of neat PLA displayed a sharp decrease around T_α . As expected, the addition of MAPEG and AcrylPEG to PLA provokes a dramatic decrease of the storage modulus E' at 20 °C down to 72 and 643 MPa, respectively, as reported in



■ Figure 7. Temperature dependence of a) storage modulus, b) loss modulus, and c) damping factor $\tan \delta$ of all the investigated blends.

Table 2. Overall thermal and mechanical properties of all the investigated materials.

X	PLA/X/L101 [wt.%]	T_g^a [°C]	T_{cc}^a [°C]	T_m^a [°C]	ΔH_{cc}^a [J g ⁻¹]	ΔH_{cc}^a [J g ⁻¹]	χ_c^b [%]	T_α^c [°C]	E' ^{d)} [MPa]	ϵ^e [%]	I.E. ^{f)} [kJ m ⁻²]
–	100/0/0 ^{g)}	61	132	153	7	8	1	59	1 776 ± 17	4 ± 1	2.8 ± 0.3
MAPEG	80/20/0	16	59	146	25	26	1	17	72 ± 3	313 ± 15	39.9 ± 6.3
MAPEG	79.75/20/0.25	25	63	150	25	26	1	28	289 ± 63	241 ± 3	60.0 ± 9.1
MAPEG	79.5/20/0.5	25	64	150	26	28	2	29	302 ± 51	279 ± 3	77.5 ± 11.0
AcrylPEG	80/20/0	29	67	149	23	25	2	35	643 ± 46	230 ± 35	86.0 ± 8.6
AcrylPEG	79.75/20/0.25	n.d. ^{h)}	n.d. ^{h)}	144, 153	n.d. ^{h)}	23	25	41	820 ± 77	254 ± 9	101.6 ± 5.6
AcrylPEG	79.5/20/0.5	n.d. ^{h)}	n.d. ^{h)}	148, 153	n.d. ^{h)}	23	25	41	827 ± 109	199 ± 47	102.6 ± 16.3

^{a)}Glass transition temperature from the second heating DSC scans; ^{b)} χ_c = crystallinity = $\frac{\Delta H_m - \Delta H_{cc}}{\Delta H_m^0} \times 100$ where ΔH_m^0 of 100% pure PLA is 93.4 J g⁻¹; ^{c)}Alpha transition temperature at maximum tan δ peak (DMTA); ^{d)}Storage modulus at 20 °C (DMTA); ^{e)}Tensile elongation at break at 20 °C according to ASTM D638 (test speed 5 mm · min⁻¹); ^{f)}Notched Izod impact energy at 20 °C according to ASTM D256; ^{g)}Extruded PLA; ^{h)}Not detected.

Table 2. The addition of L101 to PLA/MAPEG and PLA/AcrylPEG shows an important increase of the storage modulus at 20 °C of about 302 and 827 MPa, respectively. After the glass transition relaxation, a weak increase of E'' occurs for all the investigated blends. This process can be related to the cold crystallization process,^[27] also observed in DSC thermograms. It should be noted that except for the PLA/AcrylPEG/L101 blends, the plasticizer leaching was observed for all the other investigated blends (PLA/MAPEG, PLA/AcrylPEG, and PLA/MAPEG/L101) at the end of DMTA analysis. The leaching phenomenon occurring during DMTA tests could be explained by the increase of PLA chain motion under thermo-mechanical solicitation. This allowed an easier rearrangement of polyester chains to crystallize and therefore expelling a certain fraction of plasticizer out of PLA matrix because of the crystallization of the material.^[11–15]

Regarding the temperature dependence of loss modulus E'' and the damping factor tan δ , PLA displayed low damping properties below the onset of its T_g , which confirm its highly elastic behavior as described previously. Therefore, PLA chain segments are highly immobilized due to their linear structure, yielding a very stiff material at low temperature ($T < T_g$). In the temperature range of the glass transition, PLA displayed a sharp, high, and narrow E'' and tan δ peaks, respectively. Further heating the material above the onset value of its T_g allowed the PLA chains to gain very high segmental mobility. Indeed the addition of low-molecular-weight plasticizer like MAPEG and AcrylPEG allowed segmental motions even at low temperature as the binary PLA/MAPEG and PLA/AcrylPEG blends displayed higher loss modulus and tan δ at lower temperature as compared to neat PLA. In the range of their glass transition shifted to the lower temperature with respect to PLA, the binary blends displayed wider

and lower E'' and tan δ peaks. The addition of L101 to PLA/MAPEG and PLA/AcrylPEG narrowed the glass transition temperature range, increased the intensity and shifted the peaks to higher temperature as compared to the simple PLA/MAPEG and PLA/AcrylPEG blends. Indeed, as aforementioned, the presence of L101 is responsible for the oligomerization and the grafting of a fraction of the plasticizers onto PLA chains. This leads to the partially replacement of the highly plasticized PLA with high molecular weight PEG derivatives grafted to PLA backbone. Accordingly, the free volume and therefore the segmental motions in the REx blends containing the peroxide L101 would be reduced in comparison with the same blends without the peroxide.

Moreover, DMTA is a good tool to provide information about polymers miscibility.^[28] Generally, an immiscible polymer blend exhibits in the temperature-dependence of the tan δ curve several damping peaks corresponding to the T_g 's of individual polymers.^[29] The curves of a highly miscible blend show^[30] only a single peak in between the transition temperatures of the component polymers, whereas broadening of the transition occurs in the case of partially miscible systems. In the case of miscible or partially miscible blends, the T_g 's are shifted to higher or lower temperatures as a function of composition. Furthermore, the area under the tan δ curve has been shown to be related to the activation enthalpy of relaxation transition process of the backbone motion in magnitude.^[31] Accordingly, for a given area, the height of the tan δ peak is dependent on the breadth of the transition and hence the range of different relaxation processes contributing to the overall transition. In this regard, both plasticizers were miscible with PLA as the corresponding simple blends displayed one loss modulus and tan δ peak, respectively. The blends containing MAPEG

had the lowest temperature at maximum peak ($T_{\alpha} = 17, 28$, and 29°C), the lowest peak intensity and the broadest $\tan \delta$ peaks. The width, height, and position of $\tan \delta$ peaks of the blends containing AcrylPEG are between those of the blends containing MAPEG and the one of neat PLA. In this regard, higher degree of dynamic heterogeneity appeared in the blends containing MAPEG, meaning a good miscibility. The addition of L101 further narrowed the loss and damping peaks. The mechanisms leading to the narrowing of the loss and damping peaks are unclear. Nevertheless, the evolution of the interaction between PLA chains and the plasticizer as a function of L101 content due to the homo-oligomerization and grafting reactions of the plasticizer onto PLA chains could be at the origin of this phenomenon. This shift is even more pronounced in the case of the reactively modified REX PLA/AcrylPEG/L101 blends.

Indeed, the shift of $\tan \delta$ toward higher values is related to the grafting of the plasticizer on PLA backbone, which limits the PLA segmental motions. Furthermore, in comparison to the corresponding simple blends (MAPEG or AcrylPEG), the area under the loss modulus curves is smaller than in the case of the related ternary REX blends. Any restriction to the main chain mobility is expected within the area under the loss modulus vs. temperature curve. This trend reflected in the intensity of the $\tan \delta$ peak at the glass transition temperature, which is considered to reflect the extent of mobility of the macromolecular chain segments at that temperature.

Nominal tensile axial stress/strain behavior at 20°C of all plasticized/modified PLA materials is plotted in Figure 8. Tensile elongation at break as a function of L101 amount is reported in Table 2. PLA specimens exhibited a purely brittle tensile behavior, with an elastic axial deformation $<4\%$ and without displaying neither a yield point, nor a plastic deformation. Regardless the

added amount of L101, the presence of 20 wt% MAPEG and AcrylPEG, has intrinsically changed the uniaxial deformation (tensile elongation) of the modified materials to highly ductile behavior. No more yield point was noticed, and the stress continuously increased as a function of the deformation (strain) during the entire test. Over $\approx 150\%$ of elongation, a light whitening of the specimen was noticed and attributed to a crystallization process under stress with a kind of drawing (orientation) process. This can be attributed to a globally elastic/rubbery tensile behavior, because of the absence of the yield peak (necking of the specimen) at the transition between the viscoelastic and the viscoplastic behaviors. In addition, the materials are soft and flexible because of the plasticization. Accordingly, a very low tensile modulus and a very high elongation at break (200–300%) were reported in comparison with 4% for brittle PLA. These observations are for instance in accordance with those reported in literature in terms of elongation at break for the PEG content used in this study.^[32] The viscoelastic deformation was ascribed to an initial elastic expansion of the materials influenced by the phenomena described above. Subsequently, the stresses are dissipated by conformational changes of glassy amorphous PLA chains that lead to segmental orientation and disentanglement. Orientation can also occur in crystalline phase of PLA, proving that shear mechanisms of crystalline lamellae took place in PLA. The development of crazes in amorphous layers occurred in the plasticized PLA blends studied since whitening phenomena were noted at macroscopic scale.

Finally, the influence of the plasticizer and its grafting yield on the notched Izod impact energy (measured according to ASTM D256) is reported in Table 2. The grafting had a positive effect on the enhancement of the impact resistance of the tested specimens. It should be mentioned that all the specimens did not break due to their high flexibility/ductility. It could be seen that the impact strength significantly increased with the addition of L101 amount.

4. Conclusion

In this work, we could demonstrate the high interest of the REX process to design a new biodegradable polyester based on the in situ solvent-free chemical modification of PLA. Two unsaturated molecular weight (meth)acryl functional (reactive) poly(ethylene glycol) plasticizers could be successfully homo-oligomerized and grafted onto the PLA chains. This was evidenced by the increase of the melt viscosity (extrusion force), the decrease of the plasticizer EF from the so-produced materials (Soxhlet), and finally by an extensive molecular characterization demonstrating that the presence of L101 in the ternary

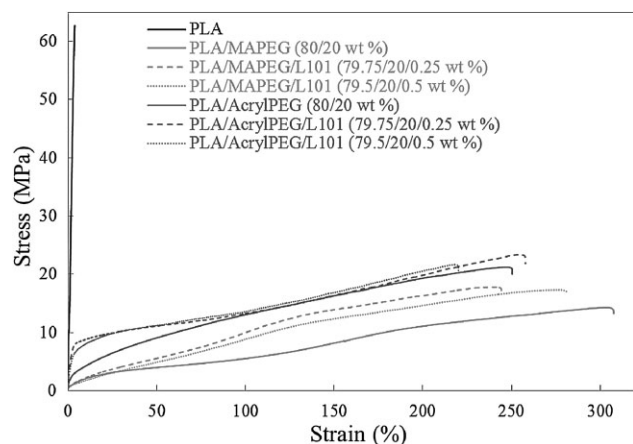


Figure 8. Tensile strain/stress curves of the different blends investigated.

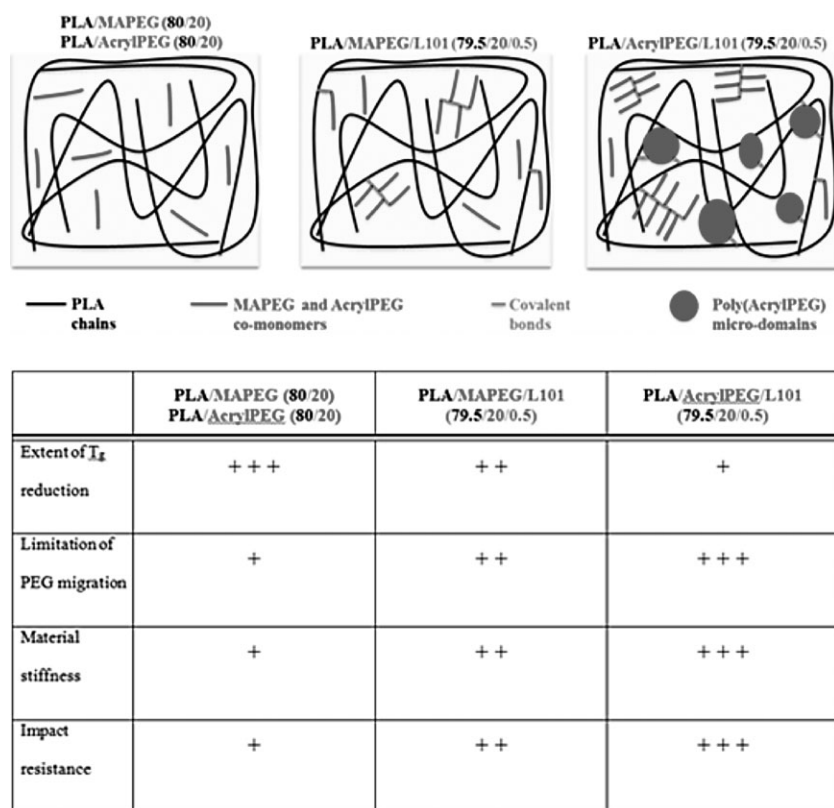


Figure 9. Schematic representation summarizing the effect on some physical properties and the reactive behavior of the different ternary blends compared to the corresponding non-reactive binary blends.

REx PLA/MAPEG/L101 and PLA/AcrylPEG/L101 blends played a key role to graft the plasticizers onto PLA backbone. Interestingly, the plasticizer functional end-group displayed a significant effect on the grafting efficiency mainly because of the difference in the reactivity between the methacrylic and the acrylic functional groups (Figure 9).

Accordingly, a much higher grafting efficiency could be reached when using AcrylPEG. The organic peroxide played a key role in promoting free-radical reactions that took place in the melt during REx. As a result, where only up to 4 wt% of MAPEG could be grafted onto PLA chains, up to 13 wt% of AcrylPEG (20 wt% were initially introduced) could be reacted and grafted onto PLA chains when the L101 amount was high enough (0.5 wt%). In both cases, the non-grafted fraction of plasticizer that could be extracted (by Soxhlet) from the material have been identified as a mixture made of unreacted monomeric MAPEG and "homologomerized" MAPEG ($\overline{DP}_n = 4$). In the case of PLA/AcrylPEG/L101 (79.5/20/0.5 in wt%) however, the remaining 7 wt% of AcrylPEG that could be extracted (by Soxhlet) from the material have been identified as completely homologomerized AcrylPEG ($\overline{DP}_n \approx 7$). The two plasticizers used were very efficient in terms of lowering the T_g from 59 °C for neat PLA to 41 °C for PLA/AcrylPEG/L101 (79.5/20/0.5 in

wt%), and improving the PLA's ductility at room temperature (more than 200% of tensile elongation at break). By comparison to the "conventionally" plasticized binary blends PLA/MAPEG and PLA/AcrylPEG, grafting the plasticizers on PLA increased the T_g of the plasticized reactive blends, permitted to regain a part of PLA homopolymer stiffness, and further improved the impact resistance of the materials while conserving the plasticized blend flexibility. By comparison to the plasticization methods developed in the literature, the added value of this approach is its capability of avoiding the migration of the plasticizer out of the PLA matrix (no migration could be noticed after DMTA in the case of the reactively modified REx PLA/AcrylPEG/L101) blends. This permanent plasticizer needs to be validated and quantified by further physical aging tests.

Acknowledgements: The authors from CIRMAP are grateful to the "Région Wallonne" and European Community (FEDER, FSE) in the frame of "Pôle d'Excellence Materia Nova" for their financial support. CIRMAP thanks the "Belgian Federal Government Office Policy of Science (SSTC)" for general support in the frame of the PAI-6/27. J.-M. Raquez is "chercheur qualifié" by the F.R.S.-FNRS. The authors (from AMS and CIRMAP) thank the Fonds National de la Recherche-Luxembourg and the Centre de Recherche Public Henri Tudor for financial support.

Received: July 2, 2013; Revised: August 13, 2013; Published online: October 15, 2013; DOI: 10.1002/mame.201300265

Keywords: grafting; mechanical toughness; plasticizers; poly(lactide)s; reactive extrusion

- [1] R. Datta, M. Henry, *J. Chem. Technol. Biotechnol.* **2006**, *81*, 1119.
- [2] Z. Kulinski, E. Piorkowska, K. Gadzinowska, M. Stasiak, *Biomacromolecules* **2006**, *7*, 2128.
- [3] V. P. Martino, A. Jiménez, R. A. Ruseckaite, *J. Appl. Polym. Sci.* **2009**, *112*, 2010.
- [4] D. W. Grijpma, H. Altpeter, M. J. Bevis, J. Feijen, *Polym. Int.* **2002**, *51*, 845.
- [5] D. M. Bigg, *Adv. Polym. Technol.* **2005**, *24*, 69.
- [6] D. W. Grijpma, A. J. Pennings, *Macromol. Chem. Phys.* **1994**, *195*, 1649.
- [7] L. Mascia, M. Xanthos, *Adv. Polym. Technol.* **1992**, *11*, 237.
- [8] H. Liu, J. Zhang, *J. Polym. Sci., Part B: Polym. Phys.* **2011**, *49*, 1051.

- [9] N. Ljungberg, B. Wesslén, *Polymer* **2003**, *44*, 7679.
- [10] L. V. Labrecque, R. A. Kumar, V. Davé, R. A. Gross, S. P. McCarthy, *J. Appl. Polym. Sci.* **1997**, *66*, 1507.
- [11] N. Ljungberg, T. Andersson, B. Wesslén, *J. Appl. Polym. Sci.* **2003**, *88*, 3239.
- [12] V. P. Martino, R. A. Ruseckaite, A. Jiménez, *J. Therm. Anal. Calorim.* **2006**, *86*, 707.
- [13] N. Ljungberg, D. Colombini, B. Wesslén, *J. Appl. Polym. Sci.* **2005**, *96*, 992.
- [14] I. Pillin, N. Montrelay, Y. Grohens, *Polymer* **2006**, *47*, 4676.
- [15] N. Ljungberg, B. Wesslén, *J. Appl. Polym. Sci.* **2002**, *86*, 1227.
- [16] F. Hassouna, J. M. Raquez, F. Addiego, V. Toniazio, P. Dubois, D. Ruch, *Eur. Polym. J.* **2012**, *48*, 404.
- [17] F. Hassouna, J. M. Raquez, F. Addiego, P. Dubois, V. Toniazio, D. Ruch, *Eur. Polym. J.* **2011**, *47*, 2134.
- [18] M. Rätzscha, M. Arnoldb, E. Borsigc, H. Buckaa, N. Reichelta, *Prog. Polym. Sci.* **2002**, *27*, 1195.
- [19] J. M. Raquez, R. Narayan, P. Dubois, *Macromol. Mater. Eng.* **2008**, *293*, 447.
- [20] Y. Minoura, M. Ueda, S. Mizunuma, M. Oba, *J. Appl. Polym. Sci.* **1969**, *13*, 1625.
- [21] D. Suwanda, R. Lew, S. T. Balke, *J. Appl. Polym. Sci.* **1988**, *35*, 1019.
- [22] *Organic Dialkyl Peroxides*, Arkema Inc, Philadelphia.
- [23] B. Dogan, S. Catak, V. Van Speybroeck, M. Waroquier, V. Aviyente, *Polymer* **2012**, *53*, 3211.
- [24] D. Carlson, P. Dubois, L. Nie, R. Narayan, *Polym. Eng. Sci.* **1998**, *38*, 311.
- [25] S. G. Roos, A. H. E. Müller, K. Matyjaszewski, *Macromolecules* **1999**, *32*, 8331.
- [26] H. T. Oyama, *Polymer* **2009**, *50*, 747.
- [27] Z. Kulinski, E. Piorkowska, *Polymer* **2005**, *46*, 1029.
- [28] D. J. Walsh, J. S. Higgins, C. Zhikuan, *Polymer* **1982**, *23*, 336.
- [29] S. George, K. T. Varughese, S. Thomas, *J. Polym. Sci. Part B: Polym. Phys.* **1997**, *35*, 2309.
- [30] K. T. Varughese, G. B. Nando, P. P. De, S. K. De, *J. Mater. Sci.* **1988**, *23*, 3894.
- [31] M. C. O. Chang, D. A. Thomas, L. H. Sperling, *J. Appl. Polym. Sci.* **1987**, *34*, 409.
- [32] M. Baiardo, G. Frisoni, M. Scandola, M. Rimelen, D. Lips, K. Ruffieux, E. Wintermantel, *J. Appl. Polym. Sci.* **2003**, *90*, 1731.

Processing of Nanocomposites PLA/Graphite Using a Novel Elongational Mixing Device

Rigoberto Ibarra-Gómez,¹ René Muller,² Michel Bouquey,² Jérôme Rondin,² Christophe A. Serra,² Fatima Hassouna,³ Yamna El Mouedden,³ Valérie Toniazio,³ David Ruch³

¹ Centro de Investigación en Materiales Avanzados S.C, Miguel de Cervantes 120, Complejo Industrial Chihuahua, Chihuahua 31109, México

² Institut de Chimie et Procédés pour l'Energie, l'Environnement et la Santé (ICPEES), ECPM, Université de Strasbourg, 25 rue Becquerel, 67087 Strasbourg, France

³ Centre de Recherche Public Henri Tudor, 5 rue Bommel, ZAE Robert Steichen, L-4940 Hautcharage, Luxembourg

Expanded graphite (EG) was added to polylactic acid (PLA) and then fully mixed in a novel elongational mixing device (RMX) to obtain PLA/EG nanocomposites. The operation of the new mixer device is based on the induced multiple passages of material (by means of reciprocating pistons) at different flow speeds through a short capillary die, thus creating convergent/divergent elongational flows. Highly homogeneous materials were obtained at all mixing conditions and particle size ranged from hundred to several hundreds of nanometers. Also, X-ray diffractograms showed different intensity of the characteristic peak of EG (3% wt/wt EG was kept constant), suggesting partial exfoliation. Furthermore, the molecular weight of processed neat PLA samples was assessed in order to correlate the PLA degradation to morphology and reinforcement mechanisms in the nanocomposites, as a function of the RMX parameters. As well, final flow properties of neat PLA and EG compounds were obtained by dynamic rheology. Thermo-mechanical degradation of PLA was found to play a major role in the rheology of mixing. On the other hand, PLA nanocomposites presented a storage modulus between 20 and 40% higher than neat PLA. Finally, morphology comparison between the RMX and an internal mixer, at the same mixing energy input, demonstrated a higher dispersive mixing efficiency for the RMX. *POLYM. ENG. SCI.*, 55:214–222, 2015. © 2014 Society of Plastics Engineers

INTRODUCTION

Polymer/Graphite Nanocomposites

With the advent of graphene in the last decade [1], research on polymer/graphite nanocomposites has been gaining relevance since graphite is a natural source of this revolutionary material. Graphene is a honeycomb shaped atomic thick monolayer of sp² hybridized carbon and it is the primary constituent of graphite and carbon black particles. Literature has remarkably emphasized its properties [2]. Back to graphite, this is one of the most common forms of carbon and, as silicates, its layered structure makes it a natural filler candidate for the elaboration of polymer nanocomposites. It has the susceptibility to undergo exfoliation under proper conditions, that is, to render pristine tactoids into graphite nanoplatelets (GNP, several layers stacks) and/or graphene. Actually, there is a large volume of work in the literature

devoted to describe different ways to sustainably obtain GNP and graphene from graphite, in their basic and modified versions (named, in general, chemically modified graphene, CMG). Derived from such research, a series of graphitic materials is to be considered as precursor or structural fillers for the elaboration of polymer nanocomposites, i.e. expanded graphite (EG), graphite intercalation compounds (GIC), graphite oxide (GO), graphene oxide (G-O), functionalized graphene sheets (FGS), chemically reduced GO (R-GO), thermally reduced GO (TrGO), polymer modified GO (P/GO), and others [2, 3].

Up to now, there are three main methods to prepare graphene or GNP-based polymer nanocomposites: solvent blending, in situ polymerization, and melt compounding. The first and second methods have been, so far, the most successful to produce compounds with filler inclusion in the range of monolayers to several layers thick. In this regard, Stankovich et al. [4] and Brinson and coworkers [5] have reported remarkable results at working on polystyrene (PS) and polymethylmethacrylate (PMMA) solution-made nanocomposites, respectively. In the former case, the authors found an electrical percolation threshold as low as about 0.1% vol/vol of graphene. In the latter, it was found a glass transition temperature (T_g) around 25°C higher than the neat polymer. Nevertheless, despite these promising results, important limitations arises concerning chemical or solvent approaches: the use of monomers and/or solvents, laborious procedures, small amounts of final material, and limited capability to expand to a larger scale. In view of this, melt compounding continues to be a strong alternative to produce polymer/graphite nanocomposites in a more reliable manner, even though results obtained by this method have been so far not that remarkable. However, the great interest in melt compounding lies in that it presents very significant advantages, for instance, it may involve continuous, semi-continuous, and batch processes that yield high production of material; the use of solvents is normally avoided and operation is simple and economic. Furthermore, large and intensive research on clay-based nanocomposites via melt blending provides an important and fundamental reference since the morphology of this type of filler i.e., montmorillonite possess layered microstructure similar to graphite.

Melt Compounding

The main challenge in melt processing about the inclusion of nanostructured particles is to attain good dispersion and distribution at the nanoscale level, searching for the maximum improvement in properties. In this regard, literature on polymer/graphite

Correspondence to: Rigoberto Ibarra-Gómez; e-mail: ibarragomez@unistra.fr
DOI 10.1002/pen.23869

Published online in Wiley Online Library (wileyonlinelibrary.com).

© 2014 Society of Plastics Engineers

nanocomposites has reported the employment of diverse graphitic materials and strategies to disperse them. For example, Steurer et al. [6] used TrGO as filler into different engineering matrixes by solution masterbatches in a first step and subsequent melt blending using a twin screw microcompounder. Independently of polymer polarity, large exfoliated nanocomposites were obtained. Wilkie and coworkers [7] found that virgin and EG composites did not undergo exfoliation and presented a slight improvement of the mechanical properties when blended with acrylonitrile butadiene styrene (ABS) and high impact polystyrene (HIPS) using an internal mixer. Also, Murariu et al. [8] utilized an internal mixer for melt blending of polylactic acid (PLA) and EG; they obtained a composite with heterogeneous graphite morphology consisting of discrete domains of exfoliated graphite and large particulates. Katbab et al. [9] compared dispersion of natural graphite, G, GIC, and EG in polypropylene (PP)/ethylene-propylene-diene rubber (EPDM) blends, employing concentrated masterbatch of functionalized PP, followed by dilution with rubber phase; both steps done by internal mixer. GIC gave the best results when it came to exfoliation. Macosko and coworker [10] compared dispersion of graphite and FGS in polycarbonate using a twin-screw microcompounder, finding that FGS nanocomposites form a filler network at very low concentrations that imparts a strong elastic character to the melt of the nanocomposite. Nevertheless, a result that seems unexpected is that tensile modulus was fairly comparable between the two types of composites at similar range of concentration. On the other hand, Zhao et al. [11] worked on polyphenylene sulfone (PPS)/EG systems by means of an internal mixer. The authors argue that low viscosity of PPS allows for the molecular diffusion into the pores of EG, giving place to intercalated systems and, thus, matrix reinforcement.

Flow Geometry

From the literature above, and more elsewhere, it has been strongly demonstrated the key role of particle pre-treatment before mixing and processing to succeed in obtaining GNP/graphene nanocomposites. However, surprisingly nothing or little is said about the specific influence of the flow geometry in the final dispersion of the compounds. As it is known, high shear contributions to dispersive mixing are common in conventional mixing devices, as those just mentioned in the literature. This is because sustained shear flow is easy to build up using relatively simple geometries compared to elongational flow field, also present at a different extent and whose contribution depends on the type of mixer. Nonetheless, on the other hand, it has to be pointed out that shear stresses necessary for filler dispersion often involve ranges of high shear rates that considerably reduce the polymer viscosity in the shear thinning zone, which demands high energy inputs to reach reasonable dispersion efficiency. Also, this efficiency is affected by the rotational component of the shear flow that offers no contribution to filler dispersive mixing. In this context, it has been stated that a way to highly improve dispersive mixing is to enhance the contributions of elongational flow fields in the overall mixing process [12, 13]. Accordingly, greater hydrodynamic stresses are generated in elongational flow and stresses are transferred more efficiently to the agglomerates because rotational motion is absent in pure elongational flow (irrotational flow); as a consequence, the

energy consumption is expected to be less in elongational flow relative to shear flow [12]. This is why, in the present work, a new mixer design with predominantly elongational flow contribution (RMX) has been used as a different approach to obtain polymer/graphite nanocomposites.

Elongational Flow Mixer and Reactor

In the last two decades, new designs have been developed to create strong elongational flow to improve dispersive mixing. Developments have been principally applied on the existing continuous systems like single and twin-screw extruders. Among these improvements are the tapered slots in screw flights, optimized kneading configuration for twin-screw extruders, and static elements like screens. In the operation of these mixers, a critical feature is the multiple passage of the material through the points of elongational stresses, which compensates for the relative low velocities needed to develop the elongational flow field. Also, the idea of promoting elongational flow for enhancing mixing efficiency has given place to the development of devices specifically designed to study elongational flow. In particular, Meller et al. [14] studied the deformation and break up of dispersed droplets in molten polymer blends of different viscosities. They used a capillary rheometer equipped with dies having different entry profiles and showed that the mixing efficiency in the converging flow zone was dependent on both the shape of the convergence and the flow rate. This kind of works has enabled some authors to revisit and to bring back old mixers designs like those by Hausman [15] and Westover [16] concerning the concept of flow between two chambers. Mackley et al. [17] adapted this geometry to design their so-called “multipass rheometer” in which the influence of the number of passes through the central die on the rheological properties can be studied. Recently, Son et al. [18] have shown that the concept of multipass rheometer can be adapted to design a batch mixer in which an unlimited number of convergent/divergent flows can be applied to the material to be mixed.

The RMX is based on similar principles described in the literature just mentioned. In this mixer, the material is induced to pass throughout a central die from opposites cylindrical chambers in a back and forth fashion. An unlimited number of convergent/divergent flows can be produced at different speed, allowing the generation of elongational flow in an efficient manner. A mixing sequence is defined simply by the piston velocity (v) and the number of cycles (N); the pressure in one of the chambers is continuously measured during the mixing sequence by a pressure transducer. Figure 1 [19] shows a general view of the mixer.

Polylactic Acid

The selected polymer matrix for this work was PLA, given the great interest at present on biodegradable polymers and those derived from renewable sources. The diversity of PLA properties makes it attracting to many applications, like packaging, films, textiles, biomedical products, tableware, etc. being some of them typically covered by well-known petroleum-based thermoplastics like polyethylene terephthalate (PET). PLA belongs to a family of biodegradable polyesters which are characterized for their potentially hydrolysable ester bonds [20]. It is synthesized through ring opening polymerization of lactide, an

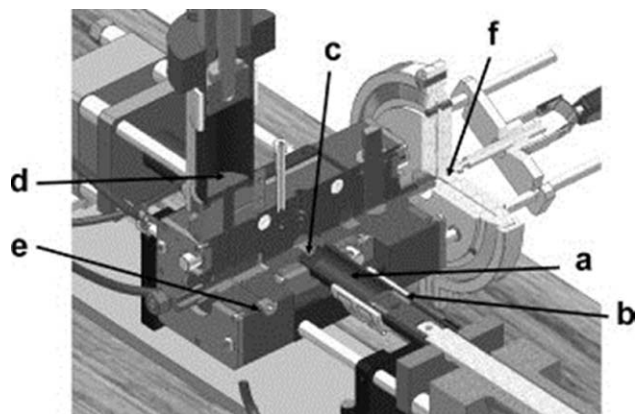


FIG. 1. Three-dimensional view of the RMX: (a) chamber, (b) piston and seal, (c) mixing element, (d) feeding unit for melts, (e) feeding channel for liquids, and (f) optional mold (from ref. 19).

intermediary form of lactic acid stereoisomers, which can be obtained by fermentation of carbohydrate rich substances coming from agricultural by-products. In general, properties of PLA depends on the final stereoisomer structure: poly(L-lactide) (PLLA), poly(D-lactide) (PDLA), and poly(DL-lactide)(PDLLA). For instance, polymers with stereo regular chain microstructure present a medium degree of crystallinity unlike amorphous PDLLA with racemic mixture of D- and L-lactide. As a consequence, some physical properties varies in the same way but, it can be said that some of them like elastic modulus, impact resistance, dimensional stability, and gas barrier remain low in comparison with equivalent thermoplastics for similar applications. Because of that, a lot of interest is still being devoted to improve this property by the inclusion of nanofillers like silicates and different types of carbon particles as described by some recent results: Carreau and coworkers [21] obtained PLA/clay nanocomposites with improved mechanical and barrier properties, avoiding PLA degradation through the addition of chain extenders. Tait et al. [22] compared the effect of carbon nanofibers and GNP on PLA using extrusion and injection molding. A more significant increase in elastic modulus was attributed to GNP and flexural strength to carbon nanofibers. Also, injection molding was the most efficient method of improvement. Murariu et al. [8] increased the elastic modulus of PLA in a significant way using EG.

On the other hand, even though degradability is the most important feature for PLA as eco-friendly material, it is precisely this characteristic that, along with low thermo-mechanical properties, limits its use up to now. As a matter of fact, kinetics of PLA degradation, promoted by hydrolysis of the ester groups and chain scission, is strongly catalyzed at temperatures needed for mixing and processing operations. Cordari et al. [23] found that the value of the kinetics constants for the hydrolysis of ester groups presented at least a threefold increase for every 20°C of temperature increment. That is why in the present project, the assessment of RMX performance is accompanied by key considerations on the degradative process of PLA during the compounding process. This is possible to do in a much more controlled manner compared to conventional systems since RMX defines very specific operational parameters, as speed and number of cycles, from which residence times are very simple to calculate and to correlate with viscosity and molecular weight changes in PLA.

EXPERIMENTAL

Materials

Amorphous PLA grade 4042D from NatureWorks® was used as polymer matrix with average molecular weight, M_w , 157,000 g/mol, M_n , 71,000 g/mol, and polydispersity 2.21. The mol% of D-isomer units in PLA is 4.3 [23] and density, $\rho = 1.24 \text{ g/cm}^3$ (technical data sheet). As filler, it was used EG Ecophit® from SGL Group, The Carbon Company, Germany; carbon content $\geq 95\%$, $D_{50} \sim 5\text{--}7 \text{ }\mu\text{m}$, $\rho_{\text{powder}} \sim 0.115\text{--}0.135 \text{ g/cm}^3$, $\rho_{\text{real}} = 2.25 \text{ g/cm}^3$, moisture content ≤ 2 (technical data sheet).

Characterization

Rheological characterization was carried out in both Bohlin Inst capillary rheometer HR2000 and Anton Paar MCR301 rheometer. In the first one, shear and elongational viscosities of pristine PLA in the range of the selected RMX speeds were obtained, as well as the global shear power law index, n . In order to estimate elongational properties from capillary measurements, Cogswell approach [24] is commonly used:

$$\eta_e = \frac{9}{32} \cdot \frac{(n+1)^2}{\eta} \cdot \left(\frac{\Delta P_e}{\dot{\gamma}} \right)^2 \quad (1)$$

$$\sigma_e = \frac{3}{8} \cdot (n+1) \cdot \Delta P_e \quad (2)$$

$$\dot{\epsilon} = \frac{\sigma_e}{\eta_e} \quad (3)$$

where η_e is the elongational viscosity, η is the shear viscosity, ΔP_e is the entrance pressure drop, $\dot{\gamma}$ is the shear rate and σ_e and $\dot{\epsilon}$ are the elongational stress and elongational strain rate, respectively.

In the Anton Paar rheometer, by using oscillation mode, the complex viscosity, η^* , of pristine, neat processed PLA, and PLA/EG samples as a function of frequency (0.1–600 rad/sec) was measured. Characterization by X-ray diffraction (XRD) was done in a Siemens 5000 diffractometer (Cu-K α radiation) $\lambda = 1.54 \text{ }\text{\AA}$, generator voltage of 35 kV, and current 25 mA. A 2 theta sweep from 10° to 30° was applied. Morphology characterization was realized by transmission electron microscopy (TEM) in an electronic microscope Hitachi 7500. Also, for the assessment of molecular weight and polydispersity of pristine and neat processed PLA, gel permeation chromatography (GPC) measurements were carried out in an Agilent Technologies® Chromatograph 1200 employing a refraction index detector (RDI) and chloroform as a solvent. Dynamical mechanical properties were evaluated in a DMA Nietzsche 202D in a three point bending geometry.

Melt Compounding

Previous to blending, PLA and EG were dried under vacuum at 80°C for 12 h. Before feeding of the RMX with the raw materials, the powder was incorporated into the polymer by means of an internal mixer Haake Rheomix 600 Thermo Electron® at 200°C and 20 rpm for 5 min. Afterwards, the integrated material was cut into pieces to be introduced into the RMX. This integration step was considered to be necessary since the RMX, at the moment, does not count on an effective powder feeding system. However, it has to be pointed out that the selected conditions for this

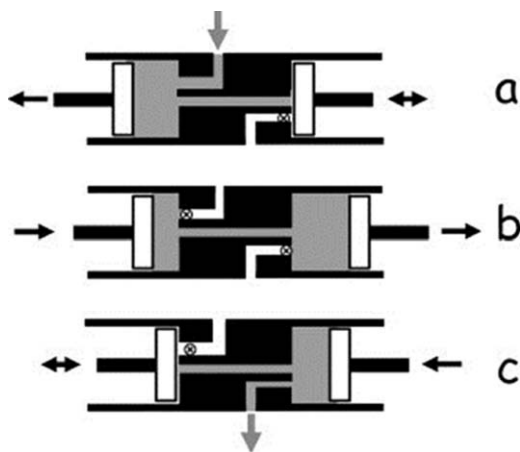


FIG. 2. Schematic description of the RMX operation principle. (a) Alimentation, (b) mixing sequence, (c) discharge (from Ref. 19).

TABLE 1. RMX mixing conditions.

	v (mm/sec)	N (cycles)
Neat PLA	10	40
	20	10
	40	10
	40	20
PLA/EG	10	10
	10	20
	10	30
	10	40
	20	10
	40	10

incorporation stage were kept mild in order to avoid a significant influence in the final morphology of RMX composites. Discussion on morphology goes back to this point.

The mixing operation was carried out in the RMX which presents the next main features: controlled pistons speed (v) range of 3–180 mm/sec which corresponds, using cylinders of 3.2 cm diameter, to volumetric flow (Q) values in the range of 2.4–125 cm³/sec. A basic scheme of its operation is presented in Fig. 2 [19]. Samples were prepared at 200°C, the concentration of EG was kept constant at 3% wt/wt and different combinations of pistons speed, v (mm/sec) and number of cycles, N , were employed according to Table 1. In general, these conditions were selected to cover in a first approach a relatively low range of speeds and number of cycles with respect to the RMX capacity, trying to prevent large PLA degradation. Also, since the RMX configuration is analogous to capillary rheometer geometry, corresponding shear rates at the different speeds were calculated applying the Rabinowitsch equation to non-Newtonian flow,

$$\dot{\gamma} = \frac{4Q}{\pi R^3} \cdot \frac{3n+1}{4n} \quad (4)$$

where $\dot{\gamma}$ is the true or corrected shear rate, Q is the volumetric flow, R is the radius of the die, and n is the power law index, that, at the processing temperature is 0.285. The mixing element used in the RMX was a round die of $\phi = 4$ mm and $L/D = 7$.

Also, a following up of the pressure, P , during the mixing sequence was considered to be fundamental as to describe the flow behavior within the RMX in real time. Data acquisition of P values during the RMX mixing sequence was done by Data-Xport[®] software. For the sake of morphology comparison and evolution as a function of the different mixing conditions, a reference sample was prepared at the lowest piston speed allowed by the mixer, 3 mm/sec without mixing sequence. Finally, a mixing efficiency comparison between the RMX and an internal mixer Haake Rheomix 600 was carried out by preparing samples at the same specific mechanical energy input (SMEI), calculated for each mixer as follows:

$$W_{\text{INT}} = \frac{\Omega T t}{m} \quad (5)$$

$$W_{\text{RMX}} = \frac{\Delta P \times N}{\rho} \quad (6)$$

where N is the number of cycles, ρ is the polymer density, m , mass of polymer, t , time, Ω , the angular speed, and T , torque.

RESULTS AND DISCUSSION

Effect of RMX Mixing Conditions on Flow Properties and PLA Integrity

A basic understanding of neat PLA flow behavior under certain mixing conditions in the RMX was considered to be fundamental in order to address the role of the degradative phenomenon of PLA.

Rheology and Molecular Weight Assessment. Figure 3 presents the shear and elongational viscosity behavior of neat PLA as a function of shear rate as obtained by capillary rheometry. It can be observed that shear viscosity, η , decreases in a more significant way than the elongational viscosity, η_e , thus making the ratio η_e/η higher as shear rate increases. This fact is important since the elongational to shear ratio remains also high (Fig. 4) toward shear rates ranges estimated to be reached in the RMX. Intensive or dispersive mixing of components with significant cohesive strength is said to be dependent on the magnitude of

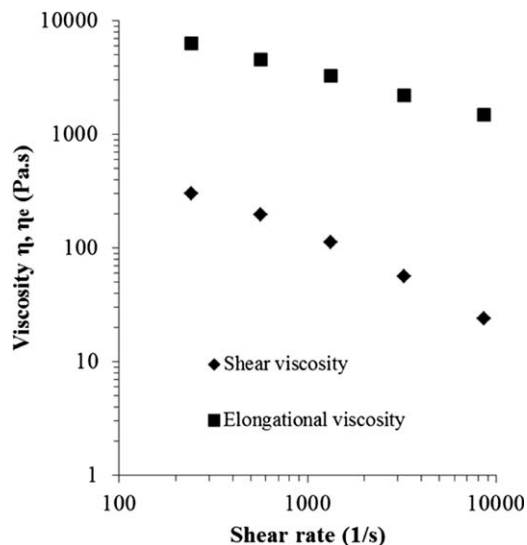


FIG. 3. Shear and elongational viscosity of pristine PLA.

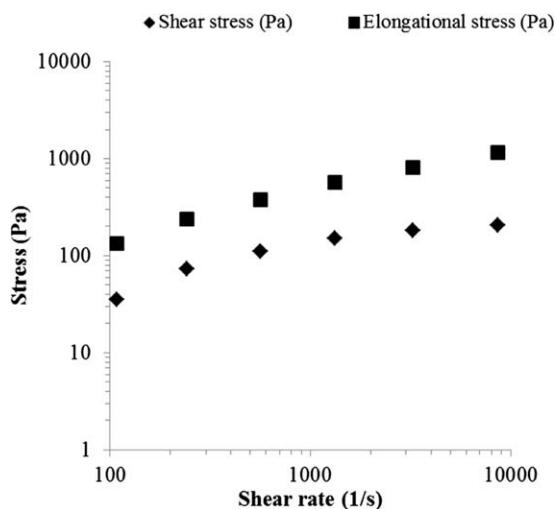


FIG. 4. Shear and elongational stress as a function of shear rate obtained from capillary measurements for the pristine PLA.

shear and elongational stresses [12, 13, 25], contributing the last to a greater dispersion efficiency. In conventional mixers, an important constraint is to reach significant rates of elongation for the built-up of critical elongational stresses, whereas in the RMX, due to the easiness with which elongational flow is produced, this limitation is thought to be far surpassed.

As it was described above, the RMX architecture resembles that of a capillary rheometer; thus, capillary measurements were useful to correlate the piston speed, v , one of the main parameters of the RMX, to corresponding shear and elongational strain rates, $\dot{\gamma}$ and $\dot{\epsilon}$, respectively, during mixing. This was possible by approximating convergence ratios, ϕ/ϕ_d (diameter of the reservoir to that of the die), for both, the capillary rheometer and the RMX. So that, we can observe in Fig. 5 that, on superimposing data of two different convergence ratios (15/2 and 15/1) used in

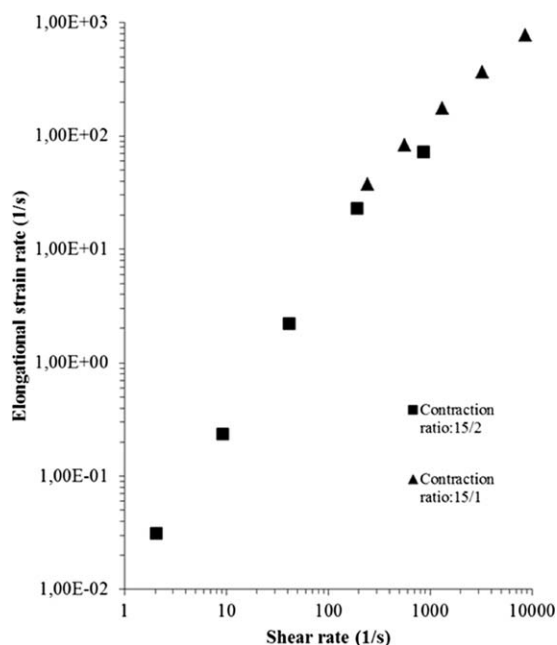


FIG. 5. Elongational strain rate vs. shear rate of pristine PLA at two different contraction ratios in a capillary rheometer.

TABLE 2. Estimated shear and elongational strain rates at different RMX mixing conditions.

	v (mm/sec)	N	$\dot{\gamma}_{\text{corr}}$ (sec^{-1})	$\dot{\epsilon}$ (sec^{-1})
Neat PLA	10	40	2070	265
	20	10	4140	530
	40	10	8280	1060
	40	20	8280	1060
PLA/EG	10	10	2070*	265*
	10	20	2070	265
	10	30	2070	265
	10	40	2070	265
	40	10	8280	1060
	40	10	8280	1060

*assumed strain rates for compounds

the capillary rheometer, corresponding data series seem to describe an almost linear relationship between $\dot{\gamma}$ and $\dot{\epsilon}$ at least in the vicinity of this ratio values. According to that, once a true $\dot{\gamma}$ is estimated in the RMX by means of the Rabinowitsch equation and, keeping a similar convergence ratio to that of the capillary rheometer (32/4), Fig. 5 leads to the estimation of the correspondent $\dot{\epsilon}$ value in the mixer. The whole values are shown in Table 2. Thus, for the selected RMX conditions it is possible to have an estimation of the balance between shear and elongational strain permitting to envisage better correlations mixing/properties for the compounds.

On the other hand, it was also necessary to address the effect of the number of cycles, N , in the PLA melt flow at specific shear and elongational strain rates. In order to do this, a following up of the pressure, P , for every passage was done in the RMX for 10/40 and 40/10 (v/N) samples, since P is a response of the system directly related to flow. A transducer fixed in one of the chambers senses the overall pressure. Figures 6 and 7 show the total pressure cycle as a function of the piston displacement, forward (high P) and backward (low P). Even though the general trajectory of P is clearly dependent on the piston speed, v , from both figures it can be suggested a three stage pattern as a function of the piston forward displacement: an initial pressure increase because of the induction of the material to get into the die; a stable zone derived from the well-

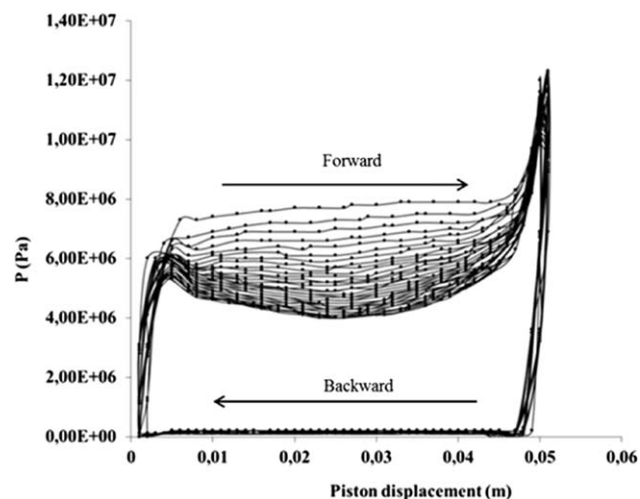


FIG. 6. RMX pressure trajectory during the mixing sequence of neat PLA at 10 mm/sec and 40 cycles.

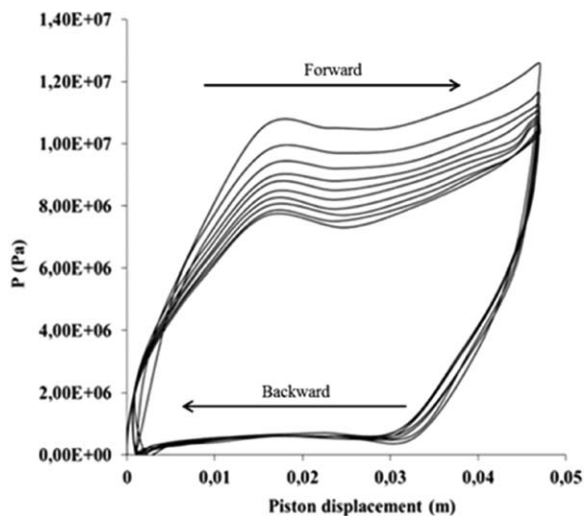


FIG. 7. RMX pressure trajectory during the mixing sequence of neat PLA at 40 mm/sec and 10 cycles.

developed flow inside the die and, a pressure shot possibly due to over compacting of the last portion of material. The subsequent decrease and constant low value of P corresponds to the filling stage of the chamber or retracting movement of the piston. However, it is evident a great difference of pressure behavior especially in the steady flow regimes between samples. On this respect, we can say that at high piston speeds, sample 40/10 (8220 sec^{-1}), there is not time enough to develop steady flow in contrast to sample 10/40 (2070 sec^{-1}), where pressure stabilizes at a large displacement range in the first cycles. A large difference in shear viscosity at the corresponding shear rates (Fig. 3) may also contribute to this behavior.

A second significant finding from Figs. 6 and 7 is the decrease in P at each cycle as mixing sequence evolves. Total P losses of about 50% and 30% for mixing conditions at 10/40 and 40/10, respectively, were estimated at the end of the sequence. Based on these results and, considering the principle of multiple passage of the RMX as well as the sensitivity of PLA to degradation, the effect of viscous heating as a result of the number of cycles was addressed. This phenomenon is thought to be especially significant at high strain rates and/or cycles number [17]. Accordingly, the estimation of the average adiabatic temperature rise (ΔT) was done using the next relationship from Ref. 17]:

$$\Delta T = \frac{\Delta P}{\rho_{\text{PLA}} C_{p\text{PLA}}} \quad (7)$$

where ΔP is the pressure difference between chambers, ρ_{PLA} and $C_{p\text{PLA}}$ are the density and the specific heat of PLA at the reference temperature, respectively. It is worthy to mention that P values from Figs. 6 and 7 were approached to ΔP in Eq. 7, given a very low P in the opposite chamber. Also, P values were taken from the assumed “steady state” region of the curves. Finally, an accumulated ΔT of about 65°C for the sample 10/40 and 35°C for the sample 40/10 were estimated at the end of the mixing sequence. High shear contributions, according to $\Delta T \propto \eta \dot{\gamma}^2$ [26] accounts for large ΔT increments at relatively high piston speed (40 mm/sec), whereas a high number of passages (40) produces even a much higher viscous heating in spite of employing a relatively low shear rate. Moreover, viscous heating seems to be

greater in the first cycles, what is especially noteworthy in the sample at 10/40. For example, after the first 10 cycles, differences in P are much smaller, almost disappearing when approaching the end of the mixing sequence. Also, if we consider a very large decrease in viscosity, at those conditions subsequent viscous heating may be limited in turn by $\Delta T \propto \eta \dot{\gamma}^2$. Another observation that calls the attention is the minimum in the trajectory of P as N increases; it can be argued that additional effects of viscous heating and PLA degradation in flow stability.

Figure 8 depicts the balance of PLA in terms of complex viscosity, η^* , and correspondent weight molecular weight average, M_w , after being subjected to different RMX conditions. First, the large drop in both, η^* and M_w for all samples, indicates that ΔP decrements observed during the mixing sequence in the RMX was a direct result of PLA degradation. Secondly, somewhat surprisingly, v (related to shear rate) seems to have a little bit more influence in PLA degradation than N (related to residence time) given a lower M_w for the sample 40/10 with respect to the sample 10/40; although, at the end, degradation phenomenon is a combination of both. On the other hand, effects of mild and hard mixing conditions are clearly identified since low v and N tend to preserve M_w (sample 20/10) and, on the contrary, high v and N promotes large M_w detriments (sample 40/20).

PLA/EG Nanocomposites

Flow Properties. Figure 9 shows the corresponding η^* behavior of EG filled PLA. Because of the presence of EG, results are somewhat not aligned to those of neat processed PLA. As an illustrative example of this, the sample at highest v (40/10) presents the highest η^* even though neat PLA at these conditions reported the lowest M_w . A possible explanation could lie on the ease of diffusion and/or interlocking of shorter polymer molecules, as a result of chain scission, into the high porosity of EG particles, enhancing hydrodynamic effect on viscosity. On the other hand, samples at increasing N (10/20, 10/30, and 10/40) exhibit lower η^* than those of high v , also in contrast to the

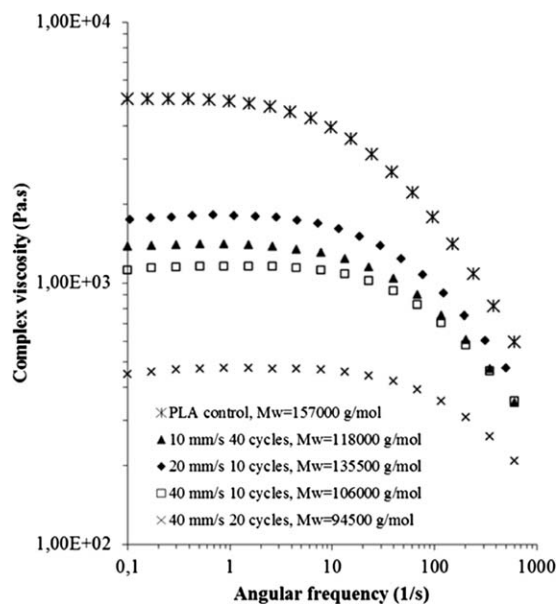


FIG. 8. Complex viscosity as a function of frequency for processed samples of neat PLA at different RMX mixing conditions.

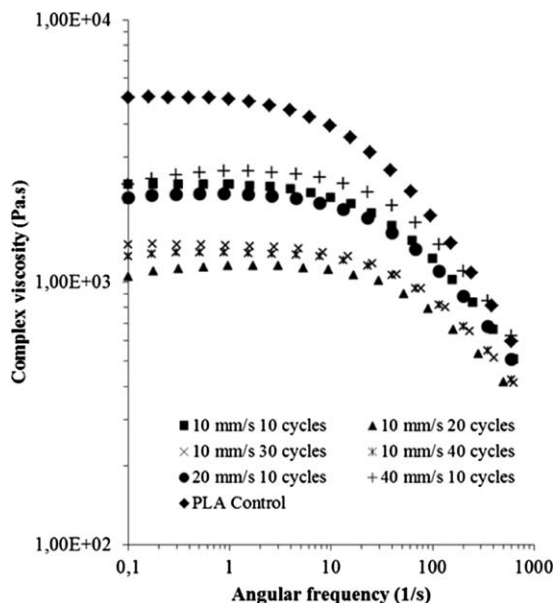


FIG. 9. Complex viscosity as a function of frequency for PLA/EG samples at different RMX mixing conditions.

observations of the precedent section. In this regard we could state that, because of the increase in viscosity of filled samples, degradation by viscous heating during mixing at long times becomes predominant. Samples 10/10 and 20/10, in turn, processed at mild mixing conditions, are expected to preserve in a greater extent the structural integrity of the polymer matrix and, hence, show higher η^* .

Morphology. XRD. Figure 10 presents XRD diffractograms of PLA/EG samples, focusing only on the small 2 theta range of the characteristic peak of graphite (2 theta $\sim 26.38^\circ$) since it is expected to be modified as a function of mixing conditions. For the sake of a valid comparison, a reference sample was processed at the lowest RMX specification speed, 3 mm/sec, and 1 cycle to try to preserve the EG structure. On one hand, when comparing, the 2 theta value of the graphite diffraction peak for all samples remains practically the same (26.40–26.52) which states the lack of intercalated structures. On the other hand, we can observe very important differences in peak intensities as a function of mixing conditions. In this respect, diffraction peak intensity is related to the amount of graphitic layers that scatter, it means, to the mass fraction of crystalline phase [27]. Thus, differences observed may obey to the development of different dispersion patterns, even partial exfoliation, as a function of mixing [28], where the reference sample is expected to present a much more agglomerated or preserved filler microstructure, which coincides with the highest peak. Also, although a tendency about the influence of v or N in the signal intensity is not clear in the processed samples, it is noteworthy that those at an extreme (40/10) and mild (10/10) mixing condition presents the highest and lowest peak, respectively. It can be said that differences in molecular weight of the PLA matrix as a function of mixing (Fig. 8) may strongly account for the development of a different filler dispersion pattern for each sample, situation to be clarified in the subsequent sections.

TEM. Morphology was tried to be complemented by TEM. Figures 11 and 12 show different samples processed by the RMX

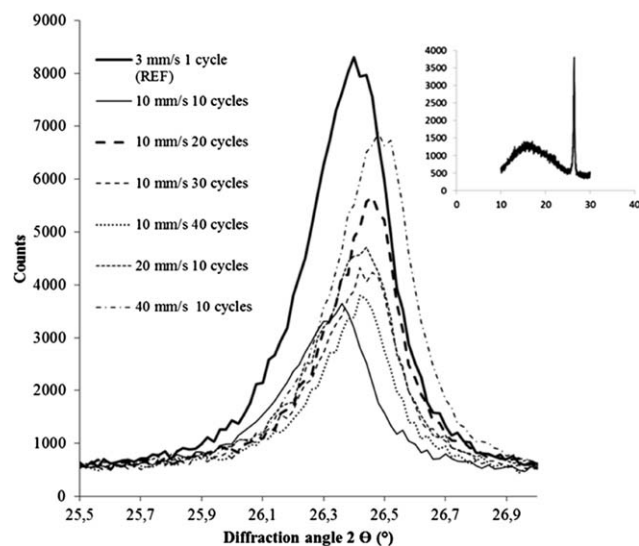


FIG. 10. XRD diffractograms showing the graphite characteristic peak for different PLA/EG samples. The small graphic inside shows the general pattern of all samples, in order to point out that the amorphous character of the PLA matrix was preserved.

and compared to the reference. The image of the reference sample shows very large EG particles, suggesting that the previous incorporation step carried out in the Haake mixer had not a striking effect or contribution to the mixing process in terms of morphology. An improvement of filler distribution and dispersion is clearly observed in the RMX processed samples, which evidence also a lack of filler networking at this concentration. In general, most of the samples presented a broad distribution of particle sizes, ranging roughly from 100 nm to 1 μ m thick. However, in many cases, the identification of particles much thinner than 100

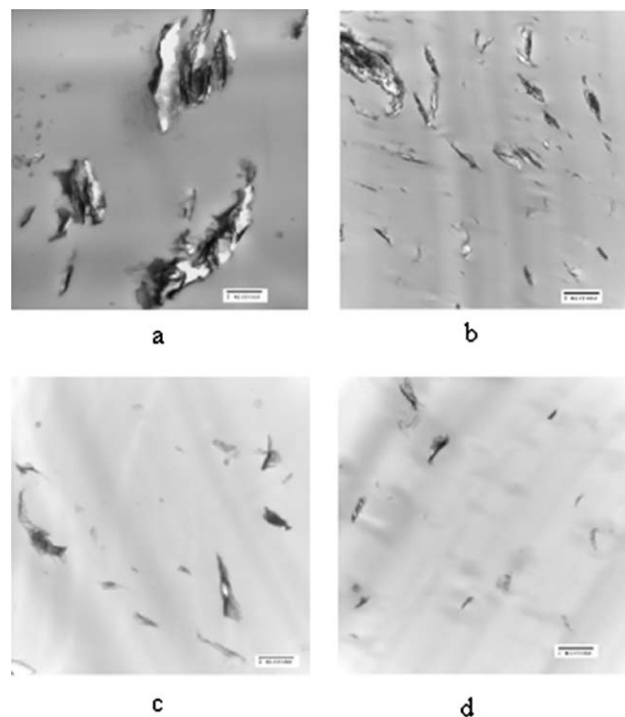


FIG. 11. TEM microphotographs of: (a) Reference sample, (b) 10/20, (c) 10/30, and (d) 10/40. 10,000 \times (bar = 2 μ m).

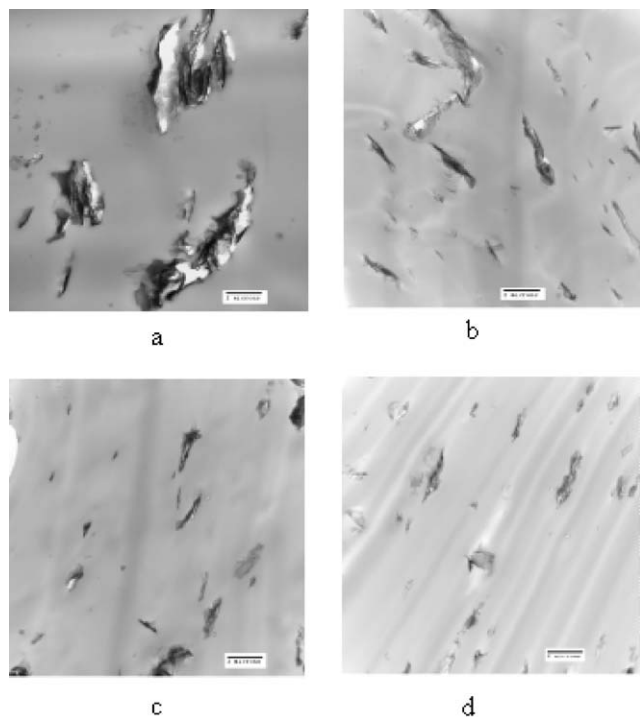


FIG. 12. TEM microphotographs of: (a) Reference sample, (b) 10/10, (c) 20/10, and (d) 40/10. 10,000 \times (bar = 2 μ m).

nm could be evident, giving support to X-ray results about partial exfoliation. Even though direct comparison between samples at different mixing conditions did not report great visual differences, samples at higher v and/or N seem to exhibit, in general, lower particle size but, again, it is not possible to establish a tendency in this sense. It is important to mention that special difficulties arose to carry out a more accurate morphology assessment, since the high hardness of the samples, made it that thin EG edges have been slightly oriented in the sense of the cut. More work has to be done on this.

Mixing Efficiency. With the aim of having a qualitative reference to ponder the RMX performance, for the particular system studied, two PLA/EG blends were prepared by means of an internal mixer and their morphology were compared to RMX samples at the same estimated specific mixing energy inputs (SMEI) as described in the experimental section. Figure 13 presents micrographs from the two mixing devices at the lowest (62 J/g) and highest (246 J/g) energy inputs used in the RMX. In both cases, direct comparison evidences a less homogeneous EG particles distribution and significantly higher particle size for the internal mixer blends.

Physical Properties. In order to obtain a basic look at the physical behavior of PLA/EG compounds, Table 3 is presented. A general remarkable increase of elastic modulus, from 20 up to 38%, was found. It must be recalled that a fixed concentration of only 3% wt/wt of EG has been used; therefore, only the influence of mixing on properties is addressed. In a closer look to the effects, the particular results and comparison between different RMX conditions indicate several scenarios that would have to do with the issue of molecular weight role in polymer reinforcement. As it has been stated above, M_w changes at every commanded mixing condition. About this matter, it is known that, under

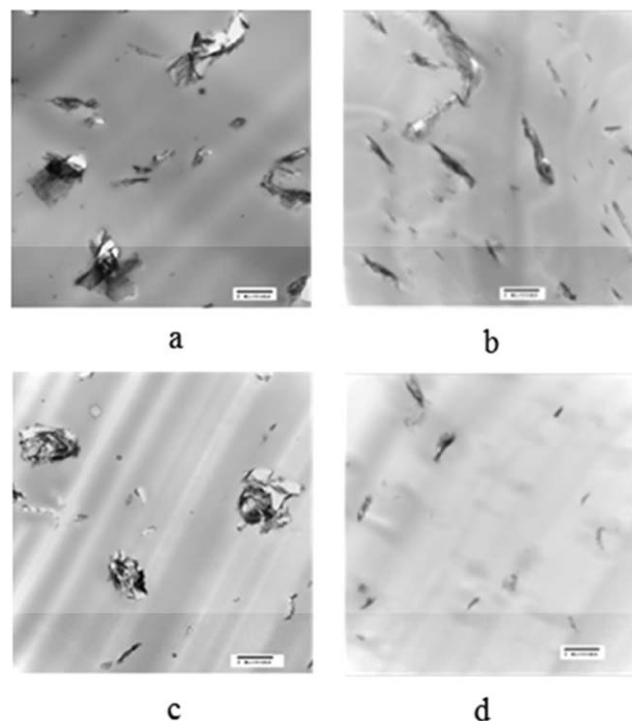


FIG. 13. TEM characterization: Photographs (a, b), internal mixer sample and RMX sample 10/10, respectively, at 62 J/g. Photographs (c, d) internal mixer sample and RMX 10/40, respectively, at 246 J/g. 10,000 \times (bar = 2 μ m).

proper compatibility between components, high molecular weight and viscosity of the polymeric matrix leads to the generation of high shear and elongational stress needed to effectively disperse and/or exfoliate the filler particles [25, 29], thus improving mechanical properties through the high increase of interfacial area. But, on the other hand, low molecular weight promotes better chain diffusion into particle galleries (interlocking) what is said to also promote reinforcing and exfoliation [30, 31]. In the present case, this could be better explained starting out from samples at extreme v/N conditions. For example, sample at the mildest condition, 10/10, expected to have the highest molecular weight, presents the second largest E' increment, around 31%. On the other hand, sample at the highest speed, 40/10, with the lowest M_w of the series surprisingly presents the largest E' increment, 38%. Evidently, reinforcement mechanisms in terms of molecular weight role are different, suggesting for the first one a predominant shear/elongational stress contribution to dispersion and reinforcement and, for the second one, a more diffusional, molecular interlocking phenomenon. Although, samples just described seem to adhere in a greater extent to one mechanism or another, it is

TABLE 3. Physical properties of PLA/EG nanocomposites.

Sample (v/N)	E' (MPa)	% $\Delta E'$	T_g ($^{\circ}$ C)
PLA ref	2750	—	60
10/10	3600	30.9	65
10/20	3350	21.8	64
10/30	3400	23.6	65
10/40	3300	20	64
20/10	3400	23.6	63
40/10	3800	38.2	61

difficult to discuss in more detail on mechanisms for samples at relatively medium conditions, having among them a similar E' increment of about 20%. In this point, the work by Bousmina [31] gives an important insight; it points out to a balance between mechanical stresses and diffusion process that requires rather low medium viscosity as to favor the best level of exfoliation in, for example, clay-based nanocomposites. In the present system, a range of viscosities coming up from the mixing process, and resultant degradation, favors different balances between the two mechanisms, diffusion and stress dependent dispersion and, thus, reinforcement. In spite of the aim to ponder the importance of flow geometry in dispersion, it is not possible to assess so far the punctual role of elongational flow contribution since the drastic effect of viscous heating in PLA produces significant changes in the rheology of the system in the very same mixing sequence, specifically, the elongational to shear flow ratios. It is remarkable, nevertheless, that good morphology/properties of nanocomposites are attained in a relatively small window of experimental conditions and using an extremely sensitive polymer, which represents a solid starting point to continue doing new and promising research on this field.

CONCLUSIONS

A very acceptable performance of the RMX (good distributive and dispersive mixing) was evidenced, to obtain PLA/EG nanocomposites with remarkable reinforcement (high modulus) at low weight concentration of filler. An apparently wide distribution of particle size in a similar range for all samples suggests that selected mixing conditions could be below those of a possibly break-through morphology (high degree of exfoliation) as a function of the RMX capacity. However, for this particular system, PLA degradation is indeed a limiting factor to further expand the experimental design. On the other hand, thermo-mechanical degradation of PLA plays a key role during the compounding of PLA/EG nanocomposites in the RMX. It seems that chain diffusion as a function of molecular weight reduction during the mixing sequence dictates at some extent the dispersion and reinforcement mechanisms and, thus, the efficacy of filler on final PLA physical properties. Even though it is difficult so far to establish punctual elongational and shear contributions to the RMX mixing efficiency, because of the drastic rheology changes during mixing, this proved to be higher than that of an internal mixer at values in the relatively low to medium RMX capacity. Furthermore, the specific influence of v and N in the final dispersion and reinforcement of nanocomposites strongly depends on the direct effect of the mixing parameters on PLA molecular weight.

ACKNOWLEDGMENT

The authors acknowledge Cathy Royer, Neurosciences Centre, University of Strasbourg, for all her kindly support on TEM characterization.

REFERENCES

1. A.K. Geim and K.S. Novoselok, *Nat. Mater.*, **6**, 183 (2007).
2. S. Park and R.S. Ruoff, *Nat. Nanotechnol.*, **4**, 217 (2009).

3. R. Sengupta, M. Bhattacharya, S. Bandyopadhyay, and A.K. Bhowmick, *Prog. Polym. Sci.*, **36**, 638 (2011).
4. S. Stankovich, D.A. Dikin, G.H.B. Dommett, K.M. Kohlaas, E.J. Simney, E.A. Stach, R.D. Piner, S.T. Nguyen, and R.S. Ruoff, *Nature*, **442**, 282 (2006).
5. T. Ramanathan, A.A. Abdala, S. Stankovich, D.A. Dikin, M. Herrera-Alonso, R.D. Piner, D.H. Adamson, H.C. Schniepp, X. Chen, R.S. Ruoff, S.T. Nguyen, I.A. Aksay, R.K. Prud'homme, and L.C. Brinson, *Nat. Nanotechnol.*, **3**, 327 (2008).
6. P. Steurer, R. Wissert, R. Thomann, and R. Mülhaupt, *Macromol Rapid Commun.*, **30**, 316 (2009).
7. F.M. Ohl, Q. Yao, and C.A. Wilkie, *Polym. Adv. Technol.*, **16**(7), 533 (2005).
8. M. Muriaru, A.L. Dechief, L. Bonnaud, Y. Paint, A. Gallos, G. Fontaine, S. Bourbigot, and P. Dubbois, *Polym. Degrad. Stab.*, **95**(5), 889 (2010).
9. A.A. Katbab, A.N. Hrymak, and K. Kasmadjian, *J. Appl. Polym. Sci.*, **107**, 3425 (2008).
10. H. Kim and C.W. Macosko, *Polymer*, **50**, 3797 (2009).
11. Y.F. Zhao, M. Yiao, S.J. Wang, X.C. Ge, and Y.Z. Meng, *Compos. Sci. Technol.*, **67**, 2528 (2007).
12. C. Rauwendall, *Plast. Add. Comp.*, **1**, 4, 21 (1999).
13. I. Manas-Zloczower, Z. Tadmor, Eds., *Mixing and Compounding of Polymers, Theory and Practice*, 2nd ed., Carl Hanser Verlag, Munich (2009).
14. M. Meller, A. Luciani, A. Sarioglu, and J.A.E. Manson, *Polym. Eng. Sci.*, **42**(3), 611 (2002).
15. J.M. Hausman, U.S. Patent, 2,948,920 (1960).
16. R.F. Westover, *Soc. Plast. Eng. Trans.*, **1**, 14 (1961).
17. M.R. Mackley, R.T.J. Marshall, and J.B.A.F. Smeulders, *J. Rheol.*, **39**, 1293 (2005).
18. Y. Son, *J. Appl. Polym. Sci.*, **112**, 609 (2009).
19. M. Bouquey, C. Loux, R. Muller, and G. Bouchet, *J. Appl. Polym. Sci.*, **119**, 482 (2010).
20. K. Madhavan Nampoothiri, N. Rajendran Nair, and R. Pappy John, *Bioresour. Technol.*, **101**, 8493 (2010).
21. Q. Meng, M.C. Hezvey, and P.J. Carreau, *Polym. Degrad. Stab.*, **97**, 2010 (2012).
22. M. Tait, A. Pergoretti, A. Dorigato, and K. Kalaitzidou, *Carbon*, **49**, 4280 (2011).
23. F. Cordari, S. Lazzari, M. Soos, G. Storti, M. Morbidelli, and D. Moscatelli, *Polym. Degrad. Stab.*, **97**(11), 2460 (2012).
24. F.N. Cogswell, *Trans. Soc. Rheol.*, **16**(3), 383 (1972).
25. T.D. Fornes, P.J. Yoon, H. Keskkula, and D.R. Paul, *Polymer*, **42**, 9929 (2001).
26. H.M. Laun, *Rheol. Acta*, **43**, 509 (2004).
27. R.A. Vaia, K.D. Jandt, E.J. Kramer, and E.P. Giannelis, *Macromolecules*, **28**, 8080 (1995).
28. A. Yasmin, J.-J. Luo, and I. M. Daniel, *Compos. Sci. Technol.*, **66**, 1179 (2006).
29. T.D. Fornes and R.D. Paul, *Cièn. Technol.*, **13**, 212 (2003).
30. F.J. Rodriguez, A. Coloma, M.J. Galotto, A. Guarda, and J.E. Bruna, *Polym. Degrad. Stab.*, **97**, 1996 (2012).
31. M. Bousmina, *Macromolecules*, **39**, 4259 (2006).

Toughening of Poly(lactide) Using Polyethylene Glycol Methyl Ether Acrylate: Reactive Versus Physical Blending

Georgio Kfoury,^{1,2} Jean-Marie Raquez,² Fatima Hassouna,¹ Philippe Leclère,³ Valérie Toniazio,¹ David Ruch,¹ Philippe Dubois²

¹ Department of Advanced Materials and Structures (AMS), Centre de Recherche Public Henri Tudor, 4940 Hautcharage, Luxembourg

² Research Institute for Materials Science and Engineering, Laboratory of Polymeric and Composite Materials (LPCM), Centre of Innovation and Research in Materials and Polymers (CIRMAP), University of Mons (UMONS), B-7000 Mons, Belgium

³ Research Institute for Materials Science and Engineering, Laboratory for Chemistry and Novel Materials (LCNM), CIRMAP, University of Mons (UMONS), B-7000 Mons, Belgium

To design high-performance poly(lactide)-based materials (PLA-based) with improved toughness, two approaches based on the reactive extrusion (REx) process are investigated and compared in the present study. The first approach relies upon a two-step procedure using a REx-polymerized poly(ethylene glycol) methyl ether acrylate, i.e., poly(AcrylPEG), as a highly-branched and compatible impact modifier for PLA. The free-radical polymerization proves to be very efficient with a peroxide initiator concentration of 1 wt%. The as-produced poly(AcrylPEG) is then melt-blended with PLA by extrusion. The resulting materials exhibit largely increase impact resistance (ca. 35 kJ/m²) in presence of 20 wt% poly(AcrylPEG) in comparison with neat PLA (2.7 kJ/m²), while moderate ductility (tensile elongation at break <40%) and limited plasticization effect are observed. The second “one-step” approach consists in in situ grafting of AcrylPEG onto PLA backbone via a one-stage REx. The resulting materials exhibit substantially improved impact resistance (ca. 102 kJ/m²) for AcrylPEG loading of 20 wt%, high ductility (tensile elongation at break of ca. 150%) and efficient plasticization. A detailed characterization of the morphology of the materials has been performed using PF-QNM-AFM to better elucidate the structure-property relationships. POLYM. ENG. SCI., 55:1408–1419, 2015. © 2015 Society of Plastics Engineers

INTRODUCTION

Poly(lactide) (PLA) is one of the most promising bio-based thermoplastic resins to compete with petroleum-based polymers for many applications, not only because of its high strength and stiffness, but also due to its excellent transparency and biodegradability when required. Unfortunately, its inherent brittleness is a major drawback that limits its range of applications [1]. Typically, like most conventional glassy thermoplastics, the brittleness of PLA is due to strain- and stress-localizations when

deformed below the brittle-to-ductile transition temperature, that is, under glass transition temperature. Under mechanical loading, PLA thereby deforms via a highly localized strain and crazing mechanism. In this regard, the strain-localization can be suppressed namely by compounding the brittle polymer with various softening and toughening agents including plasticizers and rubbery polymers or impact modifiers. For instance plasticized PLA blends are fully miscible, and the resulting materials exhibit very high ductility and low stiffness [2–19]. In addition the glass transition temperature of PLA-based materials decreases after adding these plasticizers into PLA matrix, so-increasing the disentanglement ability of PLA chains. However, the major drawback of these plasticizers is their high ability to migrate out toward the material surface, resulting in the reduction of the material flexibility and regaining its brittleness [20]. Accordingly, the most preferred way is to blend PLA with an impact modifier in order achieve a good toughness-stiffness balance without scarifying its glass transition temperature. Most of the polymeric impact modifiers that have been investigated to toughen PLA are based on either thermoplastic polyesters/elastomers, or cross-linked core-shell block copolymers [21–42]. They have low modulus and low glass transition temperature to impart toughness to PLA even at low temperatures. Unlike the plasticizers, the impact modifiers usually display a phase-separated morphology within the PLA matrix, because of their poor or partial miscibility in most cases. Their degree of compatibility via interfacial adhesion depends on the chemical nature of the blend components [43]. A poor compatibility can result into ill-dispersed and large cluster-like domains responsible for the de-bonding of the rubber phase, void-formation, and premature failure in a brittle mode. As of yet, a good compatibility can impart with well-distributed/dispersed particles as sub-micronic domains [41, 44, 45] with low extent of internal cavitation of the rubber under mechanical testing. This results in an optimum toughening efficiency [26, 27, 32, 39, 46, 47]. To address this issue, we hence propose to investigate melt-blending PLA with as-polymerized poly(ethylene glycol) methyl ether acrylate poly(AcrylPEG) as highly-branched and compatible impact modifiers on the impact resistance of PLA materials [48]. In our previous work, to finely tune the toughness of PLA, we proposed a novel pathway to chemically modify PLA in presence of “reactive” polyethylene glycol (PEG) derivatives via reactive extrusion. Luperox 101 (L101) was used as free-radical initiator with two unsaturated low molecular weight PEGs, i.e.

Correspondence to: Fatima Hassouna; e-mail: fatima.hassouna@tudor.lu or Philippe Dubois; e-mail: philippe.dubois@umons.ac.be

Contract grant sponsors: “Région Wallonne” and European Community (FEDER, FSE) (to G.K., J.-M.R. P.D., and P.L.), Belgian Federal Government Office Policy of Science (SSTC), F.R.S.-FNRS (to J.-M.R.), Fonds National de la Recherche-Luxembourg, and the Centre de Recherche Public Henri Tudor (to G.K., F.H., V.T., D.R.).

DOI 10.1002/pen.24085

Published online in Wiley Online Library (wileyonlinelibrary.com).

© 2015 Society of Plastics Engineers

poly(ethylene glycol) methyl ether methacrylate (MAPEG) and poly(ethylene glycol) methyl acrylate (AcrylPEG). Interestingly, depending on the nature of the PEG derivatives and the concentration of the free-radical initiator (from 0.1 to 0.5 wt%), it was possible to achieve tough to highly-plasticized materials. The L101 amount in the ternary REx blends PLA/MAPEG/L101 and PLA/AcrylPEG/L101 was investigated in this regard. A thorough molecular characterization was performed to provide some mechanistic insights. Thermal and mechanical properties of the so-produced materials were determined, namely in terms of impact strength and tensile properties.

We demonstrated that acryl-functionalized poly(ethylene glycol) (AcrylPEG) can effectively react and graft *in situ* onto PLA chains via reactive extrusion (REx) in the presence of a free-radical peroxide. In both cases, plasticization effect was demonstrated by a significant decrease of the glass transition temperature and storage modulus, together with a significant increase of the elongation at break as compared with neat PLA. However, the best improvement in terms of impact strength and elongation at break was achieved in the case of PLA/AcrylPEG/L101 (79.5/20/0.5 wt%).

In the present study, we highlight the added value of reactive blending for *in situ* designing PLA-based bioplastics having either only high impact resistance, or both high impact resistance and ductility, using the reactive AcrylPEG and. For this purpose, two approaches are investigated and compared. This study comprises a detailed morphological characterization of the materials using PF-QNM-AFM to better elucidate the structure-property relationships. The first approach consists in the synthesis of a rubbery polymeric impact modifier (poly(AcrylPEG)) by free-radical polymerization of the reactive AcrylPEG in presence of 1wt% of free-radical initiator at full conversion via REx. The polymerization proved to be very efficient with a peroxide initiator concentration of 1wt%. The so-produced poly(AcrylPEG) was then melt-blended with PLA. On the other hand, the second approach consists on a one-step synthesis of PLA-graft-poly(acrylPEG), by *in situ* free-radical grafting and polymerization of AcrylPEG on PLA backbone via extrusion following the procedure reported in our previous work [49]. The effect of the (reactive) melt processing approaches on the material morphology and microstructure was established. The morphological and microstructural features are correlated to the mechanical properties of the recovered blends to understand the toughening mechanisms involved in the enhancement of PLA mechanical properties.

EXPERIMENTAL

Materials and Reagents

PLA grade 4042D (average M_n (PS) $\sim 129,000$ g/mol, D(-)lactide monomer content (as determined by selective enzymatic titration) = 4.6%) was provided by NatureWorks LLC. 2,5-dimethyl-2,5-di-(tert-butylperoxy)hexane organic peroxide (Luperox101 or L101), and poly(ethylene glycol) methyl ether acrylate (AcrylPEG), $M_n \sim 480$ g/mol were purchased from Sigma-Aldrich. L101 was chosen as the initiator for several reasons. A low half-life of 1 min at 180°C and 13 s at 200°C was reported by the supplier, matching with the operating temperatures and residence times of the REx process. L101 is also recog-

nized by FDA as a food additive (Code of Regulations; Title 21 “Food and Drugs” part 170 under “Food Additives”).

Processing and Elaboration

Polymerization of AcrylPEG via Rex. Fifteen grams of the liquid reactive blend AcrylPEG/L101 (99/1 in wt%) premixed in a beaker were injected in the running (100 rpm) and preheated (180°C) DSM Xplore microcompounder (15 mL). After 10 min of mixing time, the as-produced poly(AcrylPEG) got exited out of the machine, collected in a beaker and cooled under ambient conditions. It is worth noting that these prevailing conditions enabled us to achieve the full conversion/polymerization of the macroinitiator into poly(AcrylPEG).

Melt processing of PLA/Poly(AcrylPEG) and PLA/L101/AcrylPEG Blends and Specimen Preparation for Mechanical Testing.

All melt and reactive blends were performed using a twin screw DSM Xplore Research micro-compounder under nitrogen atmosphere. Barrel temperature was set at 180°C. Screw speed was fixed to 100 rpm. Melt-temperature was measured before and during the process (~ 170 – 175°C); 15 g in total per batch were introduced into the micro-compounder. PLA was first dried for at least 12 h at 60°C in a vacuum oven (Thermo scientific—Heraeus) before processing. The liquids (AcrylPEG and L101) were kept in the dark, cooled (to prevent any potential photopolymerization), and under inert atmosphere (to prevent any degradation of the macromonomer by contact with ambient humidity) in a closed Dewar vessel filled with liquid nitrogen.

Two processing procedures were performed to improve PLA impact strength. In the first one, PLA was introduced and melted into the extruder. 10 or 20 wt% of AcrylPEG, and 1 wt% of L101 were hand-mixed in a small glass vial and then injected into the extruder using a dedicated syringe. In the second approach, 10 or 20 wt% of the separately produced poly(AcrylPEG) were melt blended with PLA.

In both cases, the evolution of the force (N) required to mix the blends during the (reactive) extrusion was recorded.

Standard samples of resulting PLA-based materials were then prepared by compression molding at 180°C for 10 min. The compression-moulding procedure was as following: (i) the material was heated at 180°C for 3 min without any pressure to insure its complete melting; (ii) the sample was degased by alternating and repeating a compression and decompression manipulation during 2 min; (iii) the sample was increasingly compressed under heat from 2 to 10 metric tons during 5 min; (iv) finally, under the same pressure (10 metric tons) the sample was cooled using the “cold” Carver press under a cold water circulation ($\sim 15^\circ\text{C}$).

Characterization

Soxhlet Extraction. This extraction technique enables to separate (and quantify) the liquid fractions soluble in methanol from the PLA matrix (insoluble in methanol) or to separate the soluble fraction of poly(AcrylPEG) in chloroform from the insoluble one in order to characterize the as-produced poly(AcrylPEG). Approximately 1 g of sample was placed in a thimble-holder that was gradually filled with condensed solvent from a distillation flask constantly heated at 120°C. When the liquid reached the overflow level, a siphon aspirates the solution from the

thimble-holder and unloads it back into the distillation flask, thus carrying the extracts into the liquid container. This operation is repeated until extraction is complete (after ~24 h). The insoluble fraction is dried overnight at 70°C under vacuum and weighed after being kept at ambient conditions for at least 15 h in order to re-equilibrate the samples. The solvent was evaporated from the solution fraction by Rotavapor technique, and dried overnight under vacuum at 50°C. Extracted fraction (EF, in wt%) was calculated with the following equation:

$$EF = \frac{\text{Before Soxhlet}(g) - \text{After Soxhlet \& drying}(g)}{\text{Before Soxhlet}(g)} \times 100$$

Soxhlet extraction was repeated at least two times for each sample. Average values and standard deviation were calculated and the results were plotted.

Fourier Transform-Infrared (FT-IR) Spectroscopy. The changes in the chemical structure of PLA and AcrylPEG were evaluated by Fourier Transform-Infrared (FT-IR) spectroscopy in attenuated total reflectance (ATR) mode from 400 cm^{-1} to 4000 cm^{-1} using a Bruker Optics Tensor 27 spectrometer.

Size Exclusion Chromatography (SEC). SEC was performed in order to characterize the molecular weight change of AcrylPEG after (reactive) extrusion. Sample preparation was performed by dissolving the material to be analyzed in chloroform at a concentration of 2 mg/mL. This was followed by the filtration of the prepared material solution using a syringe and an acrodisc-branded filter (0.45 μm). SEC equipment used was an Agilent Technologies series 1200 working with a differential refractive index detection and two linear columns (PLgel 5 μm Mixed-D, 200 Da < M_w < 400 kDa) in addition to a protection column.

Proton Nuclear Magnetic Resonance (^1H NMR). The chemical structure of AcrylPEG was evaluated by proton nuclear magnetic resonance (^1H NMR). Sample was prepared by dissolving the material to be analyzed in deuterated chloroform (CDCl_3 containing 0.03% of TMS) at a concentration of 50 mg/mL. ^1H NMR spectra were recorded using a BRUKER AMX-500 spectrometer operating at a frequency of 500 MHz in a magnetic field of 7 T.

Differential Scanning Calorimetry (DSC). Five to 10 mg of each sample was subjected to thermal characterization using a TA instrument Q2000 DSC under nitrogen atmosphere. A “heat/cool/heat” program was used between -80°C and 200°C at both the cooling and the heating rates of $10^\circ\text{C}/\text{min}$. The error about the transition temperature was of about $\pm 0.1^\circ\text{C}$ and that of melting/crystallization enthalpies was of ± 0.1 J/g (not explicitly reported along the manuscript).

Dynamic Mechanical Thermal Analysis (DMTA). The viscoelastic properties of elaborated PLA-based materials were analyzed by means of a dynamic mechanical analyzer (DMA) TA Instrument Q800. For this study, three rectangular specimens ($60 \times 12 \times 2$ mm^3) per sample were prepared by compression-molding and conditioned for at least 24 h at 20°C and 50% of relative humidity before testing. They were subjected to double cantilever mode of flexural loading with amplitude of 20 μm in the temperature range from -60 to 120°C at a heating rate of

$2^\circ\text{C}/\text{min}$ and a frequency of 1 Hz. The error about the transition temperature was of about $\pm 0.5^\circ\text{C}$ and that of the storage/loss modulus was of ± 5 MPa (not explicitly reported along the manuscript).

Tensile Tests. Tensile properties were determined according to ASTM D638 procedure using a Zwick-line tensile bench. Five tensile specimens per sample (narrow section dimensions: $16 \times 3 \times 3$ mm^3) were prepared by compression molding. They were conditioned for at least 24 h at 20°C and 50% of relative humidity before testing. After measuring the dimensions of the narrow section, each specimen was fixed between the grips of both the fixed and the movable members. The test was performed according to ASTM D638 procedure at 5 mm/min until break occurs under the same temperature and relative humidity conditions. The data acquisition was mastered by testXpert II software.

Notched Izod Impact. At least four rectangular specimens ($62 \times 12 \times 3$ mm^3) per sample were prepared by compression moulding and notched on a Ray Ran 1900 notching apparatus according to ASTM D256 specifications. The notching angle was of 45° and the radius was of 2.5 mm. Before testing, specimens were conditioned at 20°C and 50% of relative humidity for at least 24 h. Ray Ran 2500 pendulum impact tester was used. Each specimen was held as a vertical cantilever beam and got broken by a single swing of the pendulum. The line of initial contact was at a fixed distance from the specimen clamp and from the center-line of the notch and on the same side as the notch. The results of all test methods were reported in terms of energy absorbed per unit of specimen cross-sectional area under the notch. Testing conditions were: impact velocity: 3.46 m s^{-1} ; Hammer weight: 0.668 kg; energy: 3.99 J.

Scanning Electron Microscopy (SEM). Room-temperature impact-fractured and microtome surfaces of specimens were examined to morphological analysis using a pressure controlled Quanta 200 Field Effect Gun scanning electron microscope from Philips-FEI. The microscope is coupled with an EDAX GENESIS XM 4i EDS. Low voltage (<5 kV) and low vacuum (150 Pa) conditions were applied during the measurements in order to avoid the sample degradation.

Atomic Force Microscopy (AFM). Atomic force microscopy (AFM) was carried out on a Bruker Dimension Icon using Peak Force Tapping mode (PFT) based on real time force distance curve analysis recorded at a frequency of about 2 kHz [50]. This allows locally measuring various mechanical properties of the material surface at nanoscale such as Young's modulus (from data analysis based on DMT model), adhesion, deformation, and dissipation, simultaneously to the height image. This technology also provides equal or higher resolution than a Tapping mode image. In addition, Peak Force QNM controls the force applied to the sample by the tip, this decreases the contact area between the tip and sample and deformation depths. There is a minimal damage to the probe or sample. The samples were microtomed at -100°C using a Leica UCT microtome before imaging.

RESULTS AND DISCUSSION

The synthesis of a rubbery polymeric impact modifier (poly(AcrylPEG)) by random free-radical polymerization of

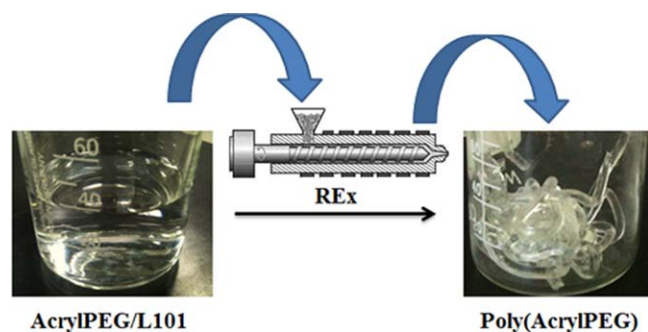


FIG. 1. Poly(AcryIPEG) as synthesized by reactive extrusion (REx) of AcryIPEG in presence of 1 wt% L101 free-radical precursor. [Color figure can be viewed in the online issue, which is available at wileyonlinelibrary.com.]

AcryIPEG was carried out from the following mixture of AcryIPEG/L101 (99/1 wt%) at 180°C for 10 min in the DSM micro-compounder (Fig. 1). After their introduction (AcryIPEG and L101), the extrusion force remained constant at 50 N during the first 3 min on melt blending (see Fig. 4) and then continuously increased to reach 340 N after 10 min of REx. This indicates an increase of the medium viscosity due to the occurrence of free-radical polymerization of AcryIPEG. The as-produced gel-like poly(AcryIPEG) material is transparent and sticky at room temperature (Fig. 1).

Performing Soxhlet extraction from chloroform on the as-polymerized poly(AcryIPEG) enabled to extract 60 wt% as soluble fraction. Moreover, the insoluble fraction had been able to swell 50-times in chloroform. Both soluble and insoluble fractions of poly(AcryIPEG) have been characterized by means of FT-IR technique (Fig. 2a). By comparison with the FT-IR spectrum of the starting AcryIPEG macromonomer, all the infrared absorption bands corresponding to the acrylic carbon-carbon double bond (at 811, 986, 1194, 1273, 1296, and 1408 cm^{-1}) disappeared after the REx polymerization of AcryIPEG (Fig. 2a), attesting for the good conversion of AcryIPEG macromonomer into polymer. In addition, SEC analysis performed on the soluble fraction reveals the presence of many overlapped molecular weight distributions, indicating that the presence of a microgel structure (Fig. 2b). This is further confirmed by proton NMR spectra (Fig. 3), where the peaks (between 5.6 and

6.4 ppm) corresponding to the protons on the acrylic carbon-carbon double bond in the AcryIPEG macromonomer disappeared after the REx polymerization.

According to the literature, the following reaction mechanism (Scheme 1) may suggest the free-radical polymerization of AcryIPEG and the branching of the resulting polymer following inter- and intra-molecular free-radical transfer reactions. [51–58] During the initiation step, L101 decomposition generates free-radicals under heat. The free-radical homopolymerization of AcryIPEG leads to the formation of linear macromolecules (Scheme 1). Inter- or intramolecular free-radical (and hydrogen radical) transfer can lead to a highly self-branched material as reported previously. [49]

Melt (Reactive) Extrusion of the PLA-Based Blends

After the melting step of PLA in the DSM micro-compounder, either AcryIPEG/L101 or the previously produced poly(AcryIPEG) were separately introduced. A higher drop of the viscosity was observed for the blends containing higher contents of AcryIPEG and poly(AcryIPEG) (Fig. 4). While the viscosity did not increase as a function of time in the case of PLA/poly(AcryIPEG) blends, it drastically increased from about 2000 N to about 7000 N in PLA/L101/AcryIPEG (79/1/20 in wt%) and to about 9000 N in PLA/L101/AcryIPEG (89/1/10 wt%) after less than 2 min of extrusion before starting to decrease. One can notice that higher viscosities were reached in the reactive blends (PLA/L101/AcryIPEG) with respect to PLA/poly(AcryIPEG) blends. The substantial increase of the viscosity in the reactive blends (PLA/L101/AcryIPEG) attests for some substantial modifications of the length (higher molecular weight) and/or topology (chain branching) of the polymer chains during REx.

The Soxhlet extractions of the soluble fractions of AcryIPEG and poly(AcryIPEG) from the PLA matrix were performed in methanol for better molecular characterization of the blends after the (reactive) extrusion. The results are presented in Fig. 5.

Figure 5 shows that the extracted fractions from PLA/Poly(AcryIPEG) blends are higher than those from PLA/L101/AcryIPEG, for an equivalent amount of added plasticizer/modifier. Moreover, while the extracted fraction from PLA/Poly(AcryIPEG) (90/10 wt%) (ca. 6 wt%) represents approximately 50% of the extracted fraction from PLA/Poly(AcryIPEG)

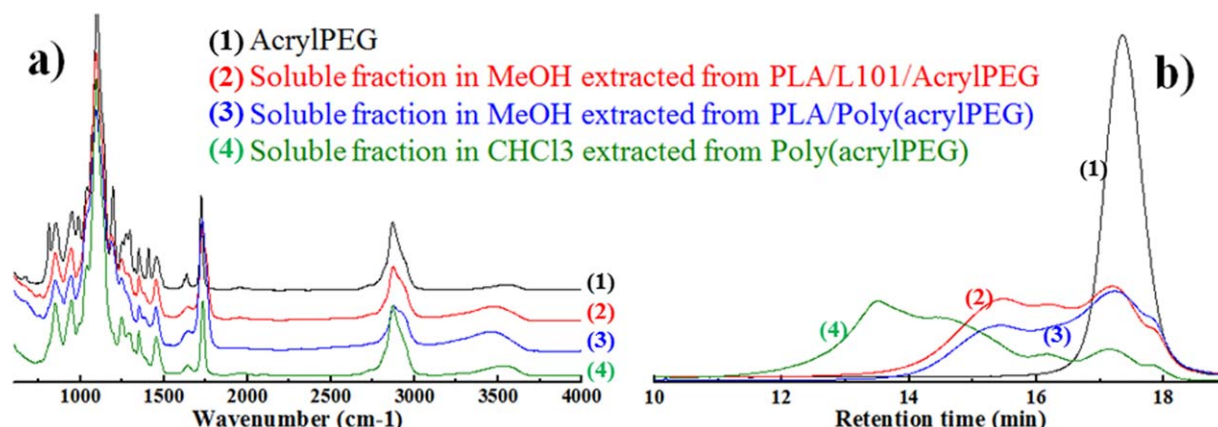


FIG. 2. FT-IR spectra (a) and SEC chromatograms (b) of AcryIPEG and Soxhlet extracted fractions of poly(AcryIPEG) produced by REx of the blend AcryIPEG/L101 (99/1 wt%). [Color figure can be viewed in the online issue, which is available at wileyonlinelibrary.com.]

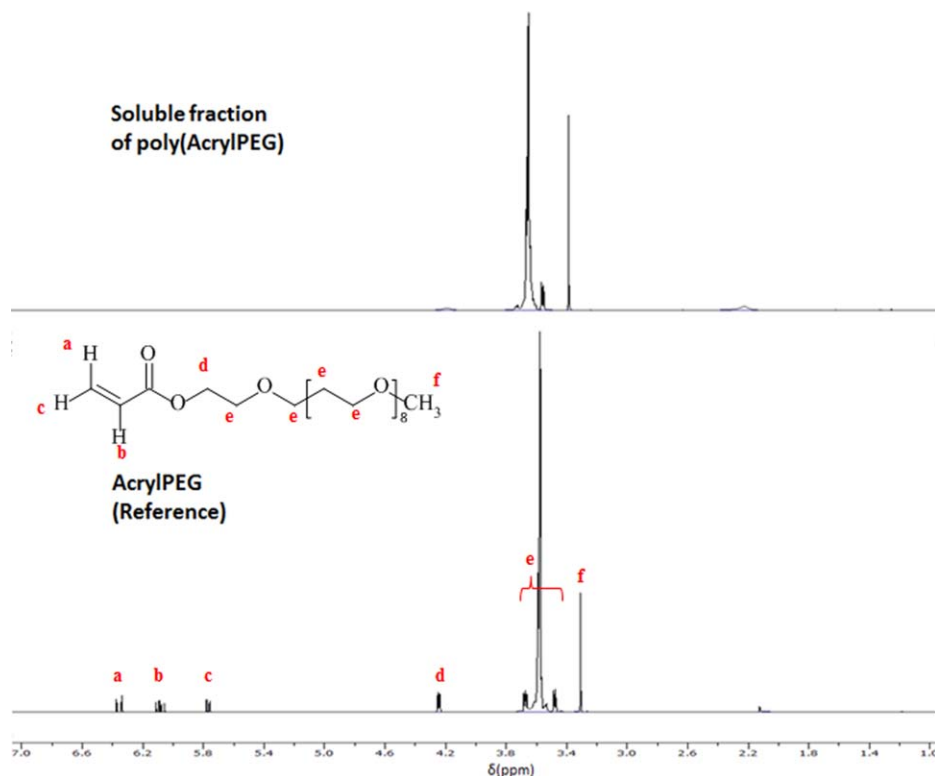


FIG. 3. Proton NMR spectra of AcrylPEG (reference) and soluble fraction of poly(AcrylPEG). [Color figure can be viewed in the online issue, which is available at wileyonlinelibrary.com.]

(80/20 wt%) (ca 12.4 wt%), the extracted fraction from PLA/L101/AcrylPEG (89/1/10 wt%) (ca. 1.5 wt%) represents only about 16% of the extracted fraction from the PLA/L101/AcrylPEG (79/1/20 wt%) (ca. 8 wt%). The bigger difference observed in the latter case (between the reactive blends) is due to the difference in the starting L101/AcrylPEG ratio. In PLA/L101/AcrylPEG blends, L101 can activate and promote higher reactive interfacial compatibilization between PLA and AcrylPEG. This is explained by the grafting of AcrylPEG on PLA, leading to the formation of PLA-graft-Poly(AcrylPEG) as well as by the PLA chains coupling [49]. Therefore, for the same amount of L101, the reactivity is higher in the blend containing the lowest amount of AcrylPEG (10 wt%). Finally, by contrast to the reactive blends PLA/L101/AcrylPEG, the extracted fractions from the PLA/Poly(AcrylPEG) physical blends is proportional to the initially added amount of poly(AcrylPEG), confirming the absence of chemical reactions in those systems during the processing. FT-IR and SEC data depicted in Fig. 2 and the proton NMR spectrum shown in Fig. 3 indicate that for all studied blends, the extracted fractions are identified as a mixture of AcrylPEG macromonomers and some related oligomers. Differential scanning calorimetry (DSC) measurements were performed on as-polymerized poly(AcrylPEG). During the first (not shown here) and the second heating (Fig. 6b, Table 1), poly(AcrylPEG) displayed a mid-set glass transition temperature (T_g) at about -61°C and a sharp melting peak at about 2°C (with a melting enthalpy $\Delta H_m \sim 43 \text{ J/g}$), ascribed to the crystalline properties of poly(AcrylPEG). Therefore poly(AcrylPEG) is a semicrystalline rubbery polymer, being fully amorphous at temperatures higher than 2°C . The melt-blending of PLA/poly(AcrylPEG) compositions 90/10 and 80/20 in wt% was then

carried out. For the sake of comparison, reactive blends between PLA/L101/AcrylPEG were carried out as reported elsewhere [49]. In the case of PLA/poly(AcrylPEG) blends 90/10 and 80/20 in wt%, it results in materials with T_g of about 50 and 42°C , respectively. This can be related to the slightly increase of the mobility of PLA chains due to the some affinity between poly(-AcrylPEG) and PLA. Some immiscibility extent can be noticed with the presence of a small melting peak at about -4°C on the second heating DSC thermogram of the PLA/Poly(AcrylPEG) blend (80/20 in wt%). It should be noted that this melting peak was hardly detected in the blend containing 10 wt% of

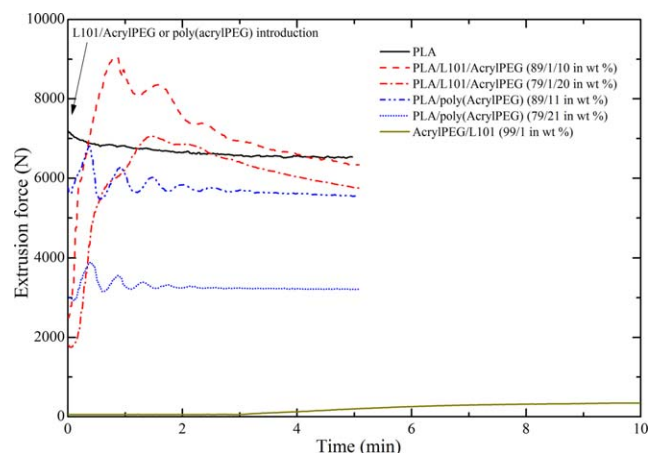
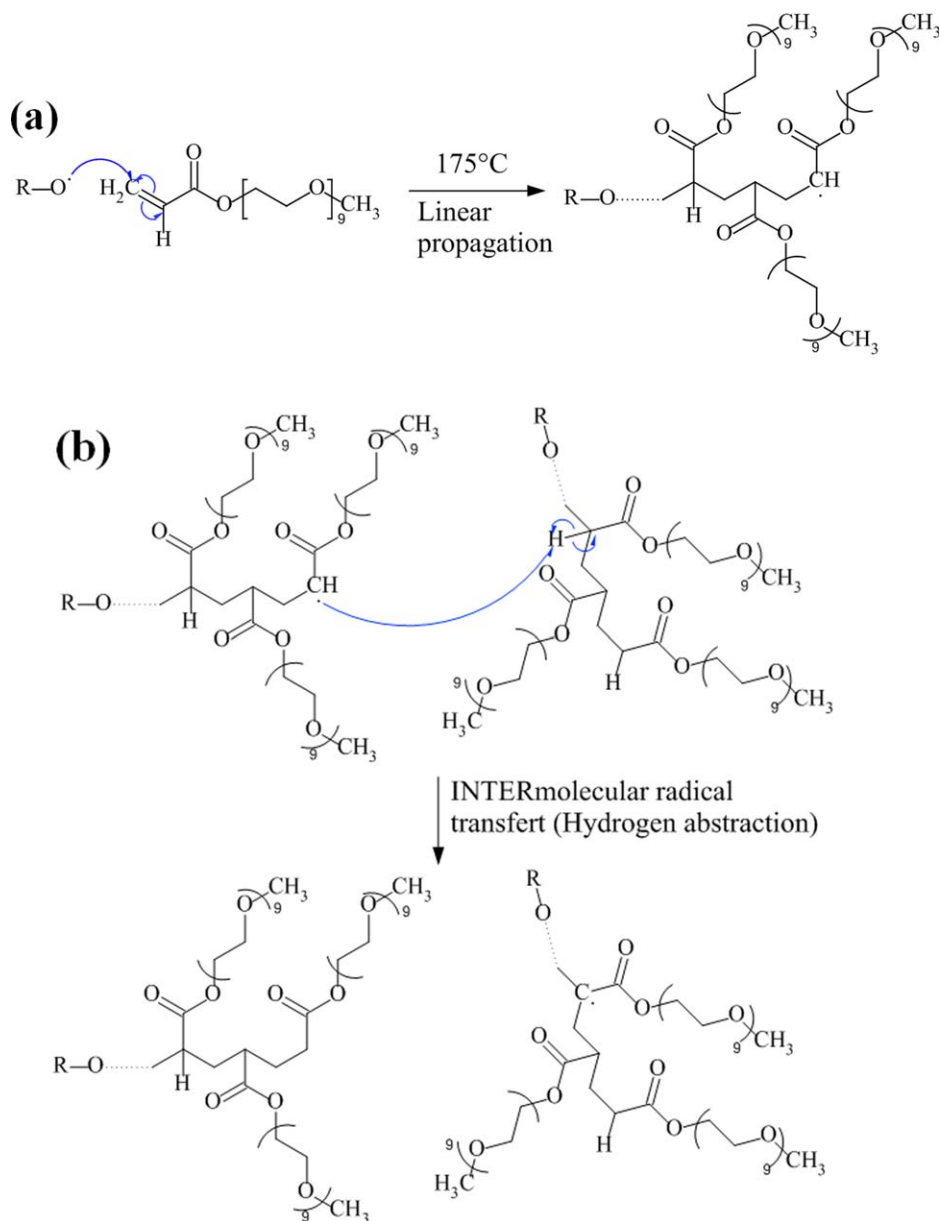


FIG. 4. Extrusion force evolution as a function of mixing time. [Color figure can be viewed in the online issue, which is available at wileyonlinelibrary.com.]



SCHEME 1. Free-radical initiation and linear propagation (a); intermolecular free radical hydrogen abstraction and radical transfer (b). [Color figure can be viewed in the online issue, which is available at wileyonlinelibrary.com.]

poly(AcrylPEG) because of its lower relative content. In contrast, both plasticization and miscibility extents proved to be more pronounced in the case of reactive blends. For instance, no T_g can be detected in the PLA/L101/AcrylPEG reactive blends (where the glass transitions were hardly detected during the second heating scan of DSC analyses). The degree of crystallinity significantly increased to about 32% for the reactive blends PLA/L101/AcrylPEG, although neat PLA and the binary PLA/poly(AcrylPEG) blends exhibit much lower crystallinity degree. The crystallization process of PLA/L101/AcrylPEG reactive blends took readily place during the cooling step (crystallization peaks at ca. 85 and $100^\circ C$ for the materials containing 20 and 10 wt% of AcrylPEG, respectively) (Fig. 6a, Table 1). This can be explained by the branched structure of PLA-g-AcrylPEG. Compared with the linear structure of neat PLA, a branched PLA has a higher free volume caused by the higher number of

chain ends [59] which can explain the T_g depression and the improved crystallization ability of the materials during cooling. In addition, the PLA-graft-Poly(AcrylPEG) phase is most likely acting as a nucleating agent. One should mention that the crystalline phase should hamper the amorphous phase from any molecular/segmental motion, thus the glass transition could not be detected by DSC during the second heating cycle.

The thermomechanical behavior of the (reactive) blends was assessed by means of DMTA. The effects of the temperature and the oscillatory deformation in flexion mode on the storage modulus E' and the loss modulus E'' are presented in Fig. 7a and b, respectively. The alpha transition temperatures determined by DMTA and reported in Table 1 can be associated to the temperature at the maximum of the loss modulus peak. Glassy and elastic PLA at room temperature is characterized by a unique alpha transition temperature (T_α) at about $58^\circ C$.

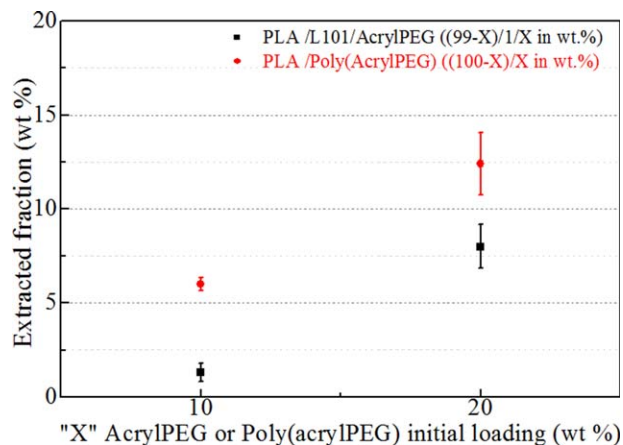


FIG. 5. Soxhlet extracted fractions in methanol from the different blends plotted as a function of the initially added AcryIPEG and poly(AcryIPEG) amount. --■-- for PLA/L101/AcryIPEG and --●-- for PLA/Poly(AcryIPEG). [Color figure can be viewed in the online issue, which is available at wileyonlinelibrary.com.]

However, all the other materials, namely PLA/poly(AcryIPEG) and PLA/L101/AcryIPEG display two distinct alpha transition temperatures, indicating the occurrence of a phase-separation [60, 61]. The first alpha transition temperature (T_{α}) is equal to -60 and -55°C for PLA/Poly(AcryIPEG) and PLA/L101/AcryIPEG, respectively. $T_{\alpha} = -60^{\circ}\text{C}$ is ascribed to the poly(AcryIPEG) rubbery phase (according to the previous DSC results) in the PLA/Poly(AcryIPEG) physical blend. However, the increase of T_{α} by 5°C from -60 in the PLA/Poly(AcryIPEG) physical blend to -55°C in the PLA/L101/AcryIPEG reactive blend may be explained by the grafting of AcryIPEG moieties onto PLA chains (PLA-graft-Poly(AcryIPEG)), so-limiting segmental motions of poly(AcryIPEG) in situ generated during the REX process and so-improving the blend compatibility. Moreover, it is reported that the peak area of loss modulus is proportional to the concentration of the component (poly(AcryIPEG)) in the composition [62]. In this regard, Fig. 7b shows that the peak area of loss modulus in the case of the PLA/L101/AcryIPEG reactive blends (peak at -55°C) is smaller than the peak area of loss modulus in the case of the PLA/Poly(AcryIPEG) physical blends (peak at -60°C) for the same initial composition of AcryIPEG or Poly(AcryIPEG), respectively. It can be attested that the generation of PLA-graft-Poly(AcryIPEG) in the case of the PLA/L101/AcryIPEG reactive blends reduces the free-content in poly(AcryIPEG). Accordingly and as attested by the smaller T_{α} peaks for poly(AcryIPEG) as in situ generated during the REX in PLA/L101/AcryIPEG whichever the initial AcryIPEG content, some higher miscibility can be further confirmed by the decrease of the effective volume of the dispersed phase due to the grafting of AcryIPEG on PLA [62]. The second alpha transition (T_{α}) is located between 40 and 55°C . In the case of the PLA/poly(AcryIPEG) nonreactive blends, T_{α} is about 52°C and 48°C for the formulations 90/10 and 80/20 in wt%, respectively. These values are inferior to that of neat PLA (ca. 58°C). The decrease of T_{α} as compared with neat PLA can be attributed, to some extent, to the local plasticization effect of the PLA matrix by the AcryIPEG oligomers present in poly(AcryIPEG), providing higher free volume and segmental motions. In the case of the PLA/L101/AcryIPEG reactive blends,

the shift of T_{α} toward lower values (-55°C) in comparison with -60°C for the physical blending PLA/Poly(AcryIPEG) can be ascribed to two phenomena taking place: (i) the enhanced miscibility between the dispersed poly(AcryIPEG) phase and the PLA matrix after the grafting reactions (leading to the in situ formation of PLA-graft-Poly(AcryIPEG)), (ii) the global plasticization effect of the PLA matrix brought by the oligomeric AcryIPEG moieties fully miscible within the PLA matrix.

The storage modulus E' measured at 20°C of neat PLA is about 1776 MPa (Table 1). As expected, PLA/poly(AcryIPEG) materials displayed a decrease of the storage modulus E' at 20°C from 1776 MPa to about 1416 and 1125 MPa for the compositions 90/10 and 80/20 in wt%, respectively. The E' drop is more important in the case of the PLA/L101/AcryIPEG reactive blends with about 1247 and 1000 MPa for the formulations 89/1/10 and 79/1/20 in wt%, respectively. Indeed the latter blends are highly plasticized and miscible. It should be noted that no leaching phenomenon of the plasticizer was noticed for all the materials after DMTA analysis.

Peak-Force AFM in tapping mode was performed to investigate the bulk-morphology including the phase-miscibility and separation of the micro-domains within the PLA-based blends. Figure 8 shows the blends morphology with respect to the surface deformation as assessed by Peak-Force AFM in tapping mode. The dark zones correspond to low deformation and rigid surface, while the clear zones are assigned to high deformation

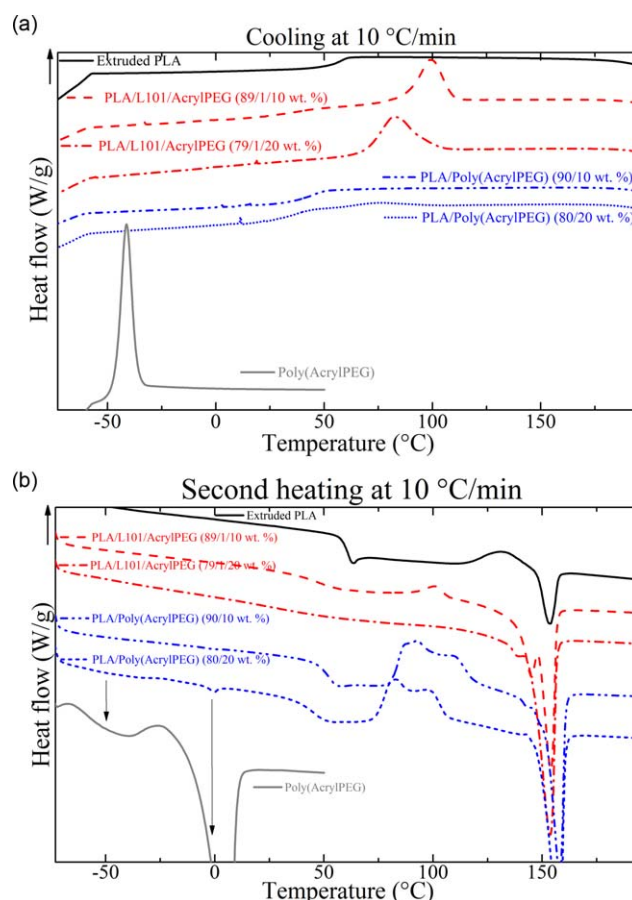


FIG. 6. Cooling (a) and second heating (b) DSC thermograms of all investigated materials. [Color figure can be viewed in the online issue, which is available at wileyonlinelibrary.com.]

TABLE 1. Overall thermal and mechanical properties of all studied materials.

Blend composition (in wt%)	T_g^a (°C)	T_{cc}^a (°C)	T_m^a (°C)	$(\Delta H_m - \Delta H_{cc})^a$ (J/g)	χ_c^b (°C)	T_α^c (°C)	E'^d (MPa)	E_t^e (MPa)	σ_y^e (MPa)	ε_b^e (%)	I.E. ^f (kJ/m ²)
Extruded PLA	61	132	153	7	0	58	1776	2243 ± 40	—	4 ± 0	2.8 ± 0.3
Poly(AcrylPEG)	−63	−25	2	43	—	—	—	—	—	—	—
PLA/L101/ AcrylPEG											
90/1/10	—	97	151	29	31	−55 & 44	1247	1750 ± 44	40 ± 2	150 ± 21	4.2 ± 0.5
80/1/20	—	—	149	31	33	−55 & 41	1000	653 ± 27	—	155 ± 27	101.6 ± 5.6 (Partial Break)
PLA/Poly(AcrylPEG)											
90/10	50	82 88 106	153	1	1	−60 & 52	1416	1900 ± 82	42 ± 1	28 ± 5	8.2 ± 0.5
80/20	42	77 95	−4 & 153	5	6	−60 & 48	1125	1500 ± 85	27 ± 3	37 ± 12	35.5 ± 5.6

^aThermal properties from the second heating DSC scans.

^b $\chi_c = \text{Crystallinity} = \frac{\Delta H_m - \Delta H_{cc}}{\Delta H_m} \times 100$ where ΔH_m of 100% crystalline PLLA is 93.4 J/g.

^cAlpha transition temperature at maximum $\tan \delta$ peak (DMTA).

^dStorage modulus at 20°C (DMTA).

^eTensile properties at 20°C according to ASTM D638 (test speed 5 mm/min).

^fNotched Izod impact energy at 20°C according to ASTM D256.

ND: not detected.

zones. The main differences between PLA/poly(AcrylPEG) (80/20 wt%) (Fig. 8a) and PLA/L101/AcrylPEG (79/1/20 wt%) (Fig. 8b) are related to the size of the microdomains and the rigidity of the matrix. With respect to the contrast, while both blends displayed “salami-like” or “domains-in-domains” morphologies, the continuous phase of PLA/poly(AcrylPEG) blend seems to be more rigid than that of PLA/L101/AcrylPEG blend (where the latter is more plasticized according to the previously discussed DMTA results). Moreover, the microdomains in the

latter case are clearly smaller ($<1 \mu\text{m}$) than in the former case ($>1 \mu\text{m}$). Similar blend morphologies have been reported for high impact polystyrene [63] and the reactive ternary blends of PLA with ethylene/*n*-butyl acrylate/glycidyl methacrylate (EBA-GMA) terpolymer and a zinc ionomer of ethylene/methacrylic acid (EMAA-Zn) extensively studied by Liu et al.[64, 65] and Song et al. [66]. Accordingly, the microdomains are composed by rigid PLA-rich submicrodomains (dark color) and soft poly(AcrylPEG)-rich submicrodomains (clear color). While in

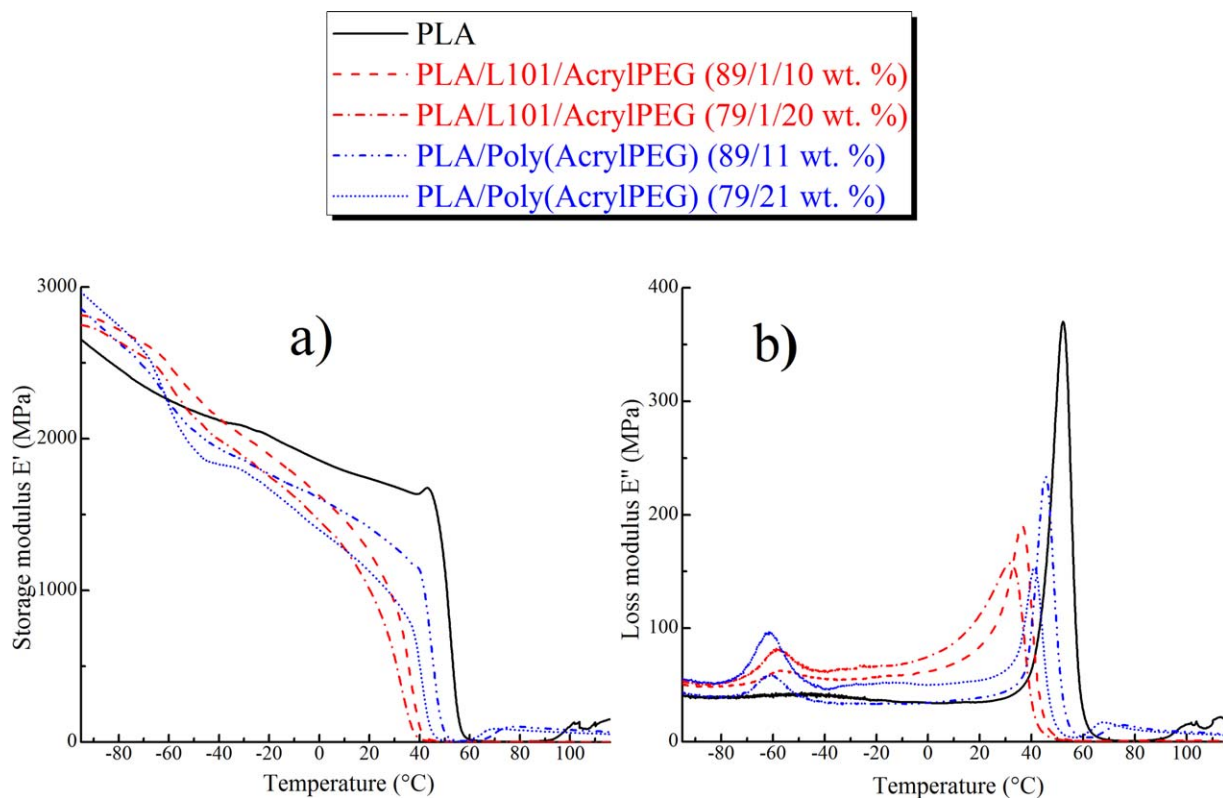


FIG. 7. Temperature-dependence of the storage modulus and the loss modulus of all investigated blends. [Color figure can be viewed in the online issue, which is available at wileyonlinelibrary.com.]

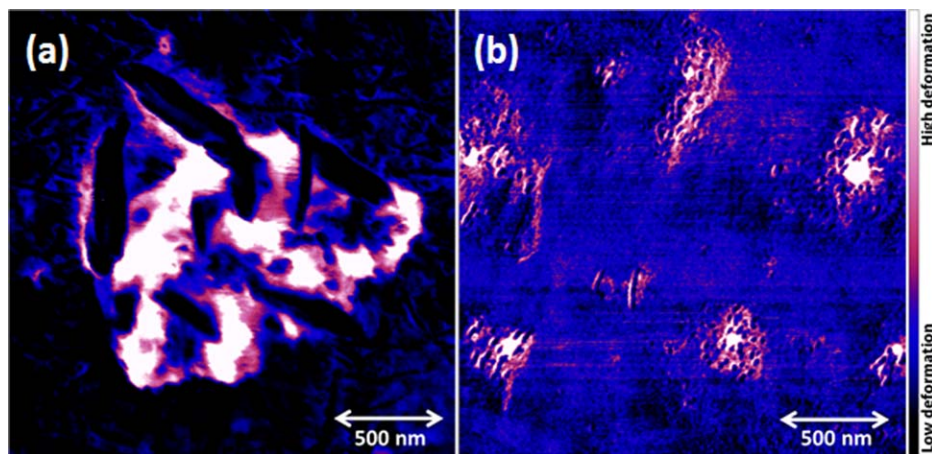


FIG. 8. Peak force AFM images showing the blends morphology with respect to the surface deformation. (a) Corresponds to PLA/poly(AcrylPEG) 80/20 in wt% and (b) to PLA/L101/AcrylPEG 79/1/20 in wt%. [Color figure can be viewed in the online issue, which is available at wileyonlinelibrary.com.]

the case of the PLA/poly(AcrylPEG) (Fig. 8a), the boundary interfaces between PLA and poly(AcrylPEG) submicrodomains are very well defined, “immiscibility gradient” characterizes the PLA/L101/AcrylPEG reactive blend (Fig. 8b) where the boundary interfaces are less well-defined. Regarding the degree of miscibility, these morphological features are in total agreement with the DMTA results detailed earlier. As the L101 has a decomposition time of 1 minute at the REX temperature of about 180°C, it is suggested that the excellent solubility of the AcrylPEG macromonomer in the PLA matrix during the reactive extrusion process prior to the free-radical grafting reactions and polymerization of AcrylPEG onto PLA backbone. This leads to a better and finer dispersion of the microdomains. It therefore results in the presence of submicrodomains as obtained after grafting AcrylPEG onto the PLA backbone in Fig. 8b. In the case of the non-reactive blends, as poly(AcrylPEG) was synthesized prior to melt-blending with PLA, larger size and size distribution microdomains are obtained when compared with the (PLA/L101/AcrylPEG) reactive blends. Moreover, the miscible AcrylPEG oligomers present in poly(AcrylPEG) are mostly confined in the immiscible poly(AcrylPEG) microdomains indicating that the compounding could not enable the good dispersion of poly(AcrylPEG) into the PLA matrix under the processing parameters used. This explains the limited plasticization efficiency of the non-reactive binary blends with respect to the ternary reactive blends.

Tensile axial stress-strain behaviors of all modified PLA materials are plotted in Fig. 9. The corresponding tensile properties are reported in Table 1. PLA exhibited high tensile modulus and strength at failure (ca. 2.2 GPa and 63 MPa, respectively), a low elongation at break (<4%) and no yield strength. Indeed yielding cannot occur in inherently brittle polymers as they break in their elastic zone before reaching their very high yield stress [67]. Accordingly, highly localized crazing mechanism is responsible for the catastrophic damage and break of PLA like any other brittle polymer below its brittle-to-ductile transition temperature. Regardless of the added amount of AcrylPEG in the reactive blends or poly(AcrylPEG) in the physical blends, a ductile behavior can be clearly evidenced at room temperature by the appearance of the yielding and necking right after the

elastic zone. Indeed, the yield stress depends on the poly(AcrylPEG) and AcrylPEG initial loadings. Higher initial loading of AcrylPEG results in lower yield stress. After the yielding point, the reactive blends exhibited much higher ductility and elongation at break (ϵ_b ca. 150%) than the physical blends (ϵ_b <40%). These observations are in accordance with those reported in literature in terms of elongation at break for the PEG content used in this study [68]. The viscoelastic deformation was ascribed to an initial elastic expansion of the materials. Subsequently, the stresses are dissipated by conformational changes of glassy amorphous PLA chains that lead to segmental orientation [69]. Orientation can also occur in crystalline phase of PLA, proving that shear mechanisms of crystalline lamellae took place in PLA. Because the stress for craze nucleation and crack propagation in PLA is lower than its yield stress at room temperature, brittle fractures result. The addition of AcrylPEG or poly(AcrylPEG) to PLA significantly lowered the yield stress and may formed voids inside the rubbery domains. The release of the strain constraint due to the formation of many voids and the decrease of yield stress resulted in the relaxation of stress concentration, and the toughness was improved [33, 70–72]. A whitening of the specimen was noticed. The whitening in plasticized PLA containing rubbery inclusions can be due to (i) structural transformation within PLA matrix as crystallization and/or (ii) cavitation of rubbery inclusions. In the two cases, scattering of the light may be explained by the formation of domains with size on the order of the light wavelength (0.4–0.8 μm) engendering a variation of the refractive index compared with the rest of the material. In addition, the materials PLA/L101/AcrylPEG are soft and flexible because of the plasticization. Accordingly, low tensile modulus and very high elongation at break (thus very ductile materials) are reported for the PLA/L101/AcrylPEG reactive blends in comparison with brittle PLA.

Figure 10 shows the cryofractured surface in the direction of tensile drawing of the different materials investigated. The PLA/L101/AcrylPEG blends (Fig. 10a for 79/1/20 and Fig. 10c for 89/1/10 in wt%) display much higher deformation extents than the PLA/poly(AcrylPEG) physical blends (Fig. 10b for 80/20 and Fig. 10d for 90/10 in wt%). These results are in complete agreement with the tensile elongation at break values reported

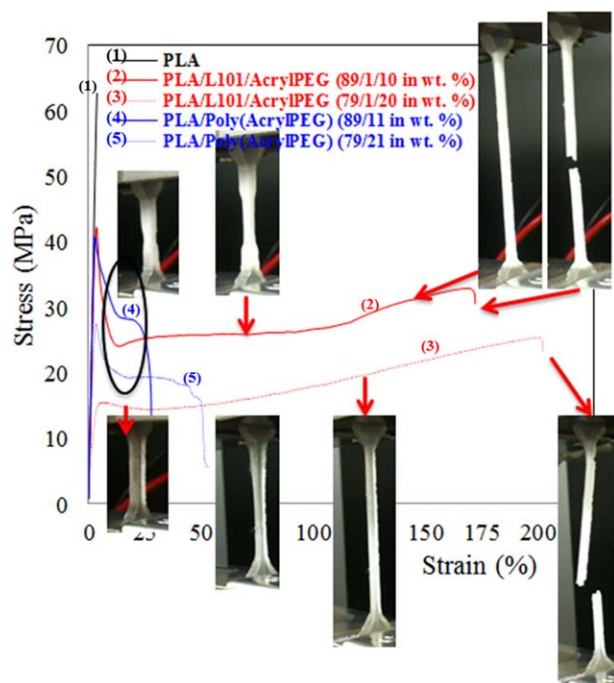


FIG. 9. Tensile strain–stress curves of the different materials. [Color figure can be viewed in the online issue, which is available at wileyonlinelibrary.com.]

in Table 1. The much larger ductility of the samples PLA/L101/AcryIPEG (Fig. 10a for 79/1/20 and Fig. 10c for 89/1/10 in wt%) is namely explained by the high deformation rates of both the plasticized PLA matrix and the microdomains. Indeed, the plasticized matrix with oligo(AcryIPEG) together with the high interfacial adhesion between the matrix and the microdomains (due to the reactive compatibility thanks to the higher grafting rate) are playing the key-role for making the materials very ductile and tough. In contrast, in the case of the PLA/poly(AcryIPEG) non reactive blends (Fig. 10b and d), much lower deformation rates of about 53 and 28% for the compositions 80/20 and 90/10 in wt%, respectively, are noticed because the PLA matrix in these latter cases is not sufficiently plasticized as most of the oligo(AcryIPEG) moieties are confined in the poly(-AcryIPEG) microdomains. Interestingly, matrix ligaments and fibrillation process can be noticed on Fig. 10a and c. The ligament thickness appears to be larger in Fig. 10a than in Fig. 10c. This larger ligament thickness can be attributed to a greater plasticized matrix and to a higher grafting rate of the acrylic dispersed phase onto the PLA matrix. It should be noted that in all cases, no de-bonding of the acrylic microdomains from the matrix was noticed. Once again, the exact origin of the macroscopic specimen whitening observed during the tensile testing (Fig. 9) can not be elucidated at this stage of the study. Advanced mechanical characterization of the reactive material is required to attempt elucidating the mechanism of whitening.

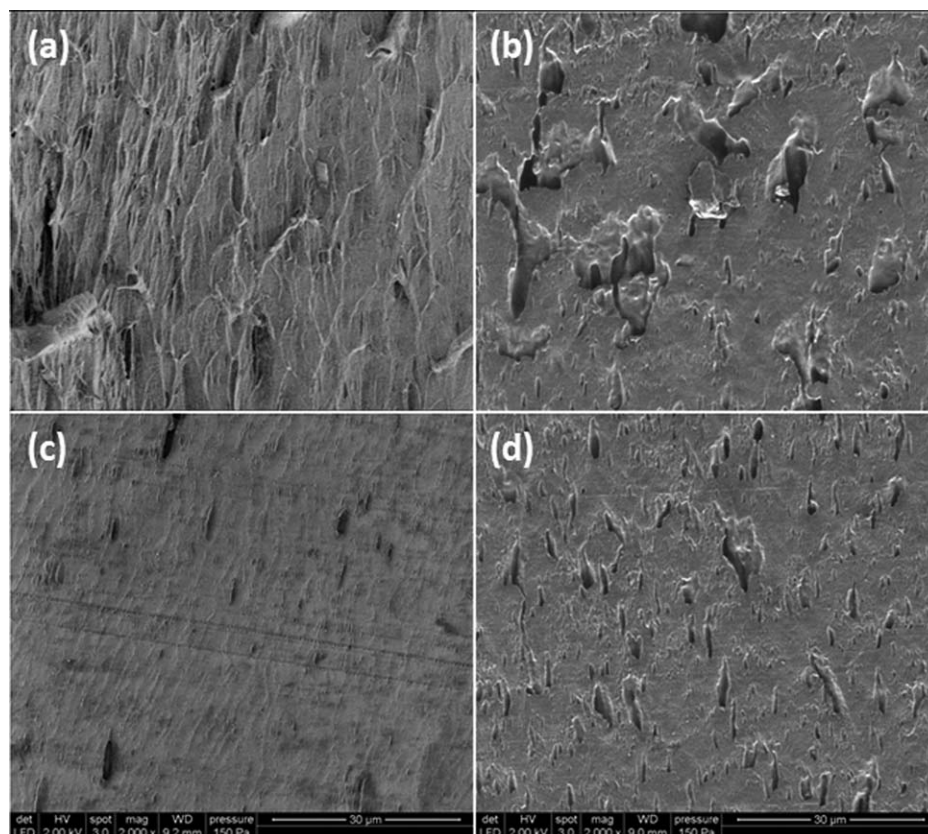


FIG. 10. SEM images on cryofractured surfaces in the direction of tensile drawing of (a) PLA/L101/AcryIPEG (79/1/20 wt%); (b) PLA/poly(AcryIPEG) (80/20 wt%); (c) PLA/L101/AcryIPEG (89/1/10 wt%); (d) PLA/poly(AcryIPEG) (90/10 wt%).

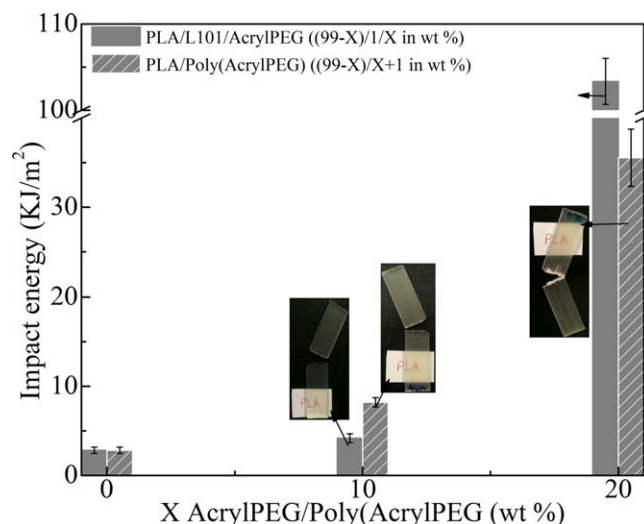


FIG. 11. Notched Izod impact energy reported as a function of the AcrylPEG and the poly(AcrylPEG) relative content in PLA matrix. [Color figure can be viewed in the online issue, which is available at www.interscience.wiley.com.]

Finally, the influence of the grafting yield and the polymerization of acrylPEG on the notched Izod impact energy (measured according to ASTM D256) is plotted in Fig. 11 and the related values are reported in Table 1. Regarding the (non-reactive) physical blends, while the addition of 10 wt% of the so-produced poly(AcrylPEG) impact modifier leads to an improvement of the impact energy to about 8 kJ/m², the addition of 20 wt% of the same impact modifier resulted in a material with an impact energy of about 35 kJ/m² in comparison with 2.7 kJ/m² for neat PLA. Regarding the reactive blends on the other hand, while a moderate improvement of the impact energy to about 4 kJ/m² is observed due to the presence of 10 wt% of AcrylPEG, the impact resistance of PLA material reaches about 102 kJ/m² and the notched samples did not break due to the addition of 20 wt% of AcrylPEG. Indeed, in addition to impact modification, the PLA matrix in the PLA/L101/AcrylPEG reactive blends is also plasticized due to the presence of AcrylPEG oligomers. Accordingly, the grafting has a positive effect on the enhancement of not only the impact resistance, but also the ductility of the specimen tested.

CONCLUSION

This study highlights the added value and the high interest of reactive extrusion (REx) as a versatile technology in designing high performance PLA-based bio-plastics. Indeed, two approaches are investigated and compared. As a two-step procedure, the first approach consists in ex situ synthesizing the impact modifier, namely poly(AcrylPEG), by random free-radical polymerization of AcrylPEG via REx. The so-produced poly(acrylPEG) is then melt-blended with PLA. The resulting materials exhibited good (ca. 8 kJ/m²) to high (ca. 35 kJ/m²) impact resistance depending on the poly(AcrylPEG) loading (10 wt% and 20 wt%, respectively), while limited ductility (tensile elongation at break <40%) and poor plasticization effect were observed. Dynamic mechanical thermal analysis (DMTA) revealed a clear phase separation in the materials. Furthermore, peak force quantitative nanomechanical atomic force microscopy

(PF-QNM-AFM) together with gel fraction determination permitted to suggest that the soluble AcrylPEG oligomers remain confined inside the insoluble poly(AcrylPEG) gel fraction rather than being dispersed in the PLA matrix, thus limiting the plasticization of the latter. Multiple crazing is most likely the predominant toughening mechanism that is taking place. On the other hand, as a one-step procedure, the second approach consists in in situ synthesis of a rubbery impact modifier, namely PLA-graft-poly(AcrylPEG), by in situ free radical grafting and polymerization of AcrylPEG on PLA backbone via REx. The resulting materials exhibited improved (ca. 4 kJ/m²) to very high (ca. 102 kJ/m²) impact resistance depending on the AcrylPEG initial loading (10 wt% and 20 wt%, respectively), and high ductility (tensile elongation at break of ca. 150%) and efficient plasticization. An immiscibility gradient between the PLA matrix and the “salami-like” domains-in-domains is revealed by Peak-Force Quantitative Nano-Mechanical Atomic Force Microscopy (PF-QNM-AFM).

ACKNOWLEDGMENTS

Authors are also thankful to Dr. Frédéric Addiego for the fruitful discussion about the mechanical properties of the studied materials.

REFERENCES

1. L.T. Lim, R. Auras, and M. Rubino, *Prog. Polym. Sci.*, **33**, 820 (2008).
2. I. Pillin, N. Montrelay, and Y. Grohens, *Polymer*, **47**, 4676 (2006).
3. V.P. Martino, A. Jiménez, and R.A. Ruseckaite, *J. Appl. Polym. Sci.*, **112**, 2010 (2009).
4. F. Hassouna, J.-M. Raquez, F. Addiego, P. Dubois, V. Toniazzi, and D. Ruch, *Eur. Polym. J.*, **47**, 2134 (2011).
5. Y. Hu, Y.S. Hu, V. Topolkaraev, A. Hiltner, and E. Baer, *Polymer*, **44**, 5711 (2003).
6. Y. Hu, M. Rogunova, V. Topolkaraev, A. Hiltner, and E. Baer, *Polymer*, **44**, 5701 (2003).
7. M. Baiardo, G. Frisoni, M. Scandola, M. Rimelen, D. Lips, K. Ruffieux, and E. Wintermantel, *J. Appl. Polym. Sci.*, **90**, 1731 (2003).
8. O. Martin, and L. Avérous, *Polymer*, **42**, 6209 (2001).
9. Z. Kulinski, E. Piorkowska, K. Gadzinowska, and M. Stasiak, *Biomacromolecules*, **7**, 2128 (2006).
10. S. McCarthy, and X. Song, *J. Appl. Med. Polym.*, **6**, 64 (2002).
11. H. Zhang, J. Fang, H. Ge, L. Han, X. Wang, Y. Hao, C. Han, and L. Dong, *Polym. Eng. Sci.*, **53**, 112 (2013).
12. Z. Gui, Y. Xu, S. Cheng, Y. Gao, and C. Lu, *Polym. Bull.*, **70**, 325 (2013).
13. Lapol. *Getting Started with Lapol® 108 Bioplasticizer*, (2009). Available at: http://www.lapol.net/images/Lapol_Getting_Started_Guide_and_Essential_Documentation_100930.pdf. Accessed on March 13, 2011.
14. F. Hassouna, J.-M. Raquez, F. Addiego, V. Toniazzi, P. Dubois, and D. Ruch, *Eur. Polym. J.*, **48**, 404 (2012).
15. Y. Lemmouchi, M. Murariu, A.M.D. Santos, A.J. Amass, E. Schacht, and P. Dubois, *Eur. Polym. J.*, **45**, 2839 (2009).
16. J. Sierra, M. Noriega, E. Cardona, and S. Ospina, *Proceedings of Annual Technical Conference of the Society of*

- Plastics Engineers (ANTEC)*, Orlando, Florida, May 16–20, 127 (2010).
17. K.S. Anderson, K.M. Schreck, and M.A. Hillmyer, *Polym. Rev.*, **48**, 85 (2008).
 18. L.V. Labrecque, R.A. Kumar, V. Davé, R.A. Gross, and S.P. McCarthy, *J. Appl. Polym. Sci.*, **66**, 1507 (1997).
 19. R.G. Sinclair, *J. Macromol. Sci. Pure*, **33**, 585 (1996).
 20. S. Jacobsen, and H.G. Fritz, *Polym. Eng. Sci.*, **39**, 1303 (1999).
 21. P. Ma, A.B. Spoelstra, P. Schmit, and P. J. Lemstra, *Eur. Polym. J.*, **49**, 1523 (2013).
 22. I. Noda, P.R. Green, M.M. Satkowski, and L.A. Schechtman, *Biomacromolecules*, **6**, 580 (2005).
 23. I. Noda, M.M. Satkowski, A.E. Dowrey, and C. Marcott, *Macromol. Biosci.*, **4**, 269 (2004).
 24. K.M. Schreck, and M.A. Hillmyer, *J. Biotechnol.*, **132**, 287 (2007).
 25. J. Ren, P. Zhao, W. Liu, and Q. Wu, *J. Nanomater.*, **8** (2010).
 26. J. Odent, J.-M. Raquez, E. Duquesne, and P. Dubois, *Eur. Polym. J.*, **48**, 331 (2012).
 27. J. Odent, P. Leclère, J.-M. Raquez, and P. Dubois, *Eur. Polym. J.*, **49**, 914 (2013).
 28. L. Han, C. Han, and L. Dong, *Polym. Compos.*, **34**, 122 (2013).
 29. J.-J. Han and H.-X. Huang, *J. Appl. Polym. Sci.*, **120**, 3217 (2011).
 30. F. Feng and L. Ye, *J. Appl. Polym. Sci.*, **119**, 2778 (2011).
 31. N. Bitinis, R. Verdejo, P. Cassagnau, and M.A. Lopez-Manchado, *Mater. Chem. Phys.*, **129**, 823 (2011).
 32. C. Zhang, W. Wang, Y. Huang, Y. Pan, L. Jiang, Y. Dan, Y. Luo, and Z. Peng, *Mater. Des.*, **45**, 198 (2013).
 33. M. Ito, S. Abe, and M. Ishikawa, *J. Appl. Polym. Sci.*, **115**, 1454 (2010).
 34. Z. Cygan, M. Singh, S. Seshadri, *Annual Technical Conference of the Society of Plastics Engineers (ANTEC)*, Society of Plastics Engineers (SPE), Cincinnati, OH, 3071 (2007).
 35. K.A. Afrifah, and L.M. Matuana, *Macromol. Mater. Eng.*, **295**, 802 (2010).
 36. S. Zhu, R. Rasal, and D. Hirt, *Annual Technical Conference of the Society of Plastics Engineers (ANTEC)*, Society of Plastics Engineers (SPE), Chicago, IL, 1616 (2009).
 37. M. Murariu, A. Da Silva Ferreira, E. Duquesne, L. Bonnaud, and P. Dubois, *Macromol. Symp.*, **272**, 1 (2008).
 38. R. Scaffaro, M. Morreale, F. Mirabella, and F.P. La Mantia, *Macromol. Mater. Eng.*, **296**, 141 (2011).
 39. X. Zhang, Y. Li, L. Han, C. Han, K. Xu, C. Zhou, M. Zhang, and L. Dong, *Polym. Eng. Sci.*, **53**, 2498 (2013).
 40. N. Petchwattana, S. Covavisaruch, and N. Euapanthasate, *Mater. Sci. Eng. A.*, **532**, 64 (2012).
 41. Q. Zhao, Y. Ding, B. Yang, N. Ning, and Q. Fu, *Polym. Test.*, **32**, 299 (2013).
 42. B. Meng, J. Deng, Q. Liu, Z. Wu, and W. Yang, *Eur. Polym. J.*, **48**, 127 (2012).
 43. B. Imre and B. Pukansky, *Eur. Polym. J.*, **49**, 1215 (2013).
 44. K.S. Anderson and M.A. Hillmyer, *Polymer*, **45**, 8809 (2004).
 45. K.S. Anderson, S.H. Lim, and M.A. Hillmyer, *J. Appl. Polym. Sci.*, **89**, 3757 (2003).
 46. D. Dompas and G. Groeninckx, *Polymer*, **35**, 4743 (1994).
 47. B.J.P. Jansen, S. Rastogi, H.E.H. Meijer, and P.J. Lemstra, *Macromolecules*, **32**, 6283 (1999).
 48. J.-M. Raquez, R. Narayan, and P. Dubois, *Macromol. Mater. Eng.*, **293**, 447 (2008).
 49. G. Kfoury, F. Hassouna, J.-M. Raquez, V. Toniazio, D. Ruch, and P. Dubois, *Macromol. Mater. Eng.*, **299**, 583 (2014).
 50. B. Pittenger, N. Erina, and C. Su, “Quantitative Mechanical Properties Mapping at the Nanoscale with PeakForce QNM,” Bruker Application Note #128 (2011).
 51. N.M. Ahmad, B. Charleux, C. Farcet, C.J. Ferguson, S.G. Gaynor, B.S. Hawkett, F. Heatley, B. Klumperman, D. Konkolewicz, P.A. Lovell, K. Matyjaszewski, and R. Venkatesh, *Macromol. Rapid Commun.*, **30**, 2002 (2009).
 52. C. Barner-Kowollik, *Macromol. Rapid. Commun.*, **30**, 1961 (2009).
 53. J. Barth, M. Buback, P. Hesse, and T. Sergeeva, *Macromol. Rapid. Commun.*, **30**, 1969 (2009).
 54. T. Junkers, and C. Barner-Kowollik, *J. Polym. Sci. Part A: Polym. Chem.*, **46**, 7585 (2008).
 55. A.M. van Herk, *Macromol. Rapid. Commun.*, **30**, 1964 (2009).
 56. W. Wang, A.N. Nikitin, and R.A. Hutchinson, *Macromol. Rapid Commun.*, **30**, 2022 (2009).
 57. R.X.E. Willemse, A.M. van Herk, E. Panchenko, T. Junkers, and M. Buback, *Macromolecules*, **38**, 5098 (2005).
 58. C. Quan, *High-Temperature Free-Radical Polymerization of n-Butyl Acrylate*, PhD Thesis, Drexel University, Philadelphia, PA (2002).
 59. S. Saeidlou, M.A. Huneault, H. Li, and C.B. Park, *Progr. Polym. Sci.*, **37**, 1657 (2012).
 60. D.J. Walsh, J.S. Higgins, and C. Zhikuan, *Polymer*, **23**, 336 (1982).
 61. N.N. George, S. Varughese, and S. Thomas, *J. Polym. Sci. Part B: Polym. Phys.*, **35**, 2309 (1997).
 62. H. Yang, X. Zhang, C. Qu, B. Li, L. Zhang, Q. Zhang, and Q. Fu, *Polymer*, **48**, 860 (2007).
 63. M. Vonka, L. Šeda, and J. Kosek, *Macromol. Symp.*, **302**, 151 (2011).
 64. H. Liu, F. Chen, B. Liu, G. Estep, and J. Zhang, *Macromolecules*, **43**, 6058 (2010).
 65. H. Liu, W. Song, F. Chen, L. Guo, and J. Zhang, *Macromolecules*, **44**, 1513 (2011).
 66. W. Song, H. Liu, F. Chen, and J. Zhang, *Polymer*, **53**, 2476 (2012).
 67. W.G. Perkins, *Polym. Eng. Sci.*, **39**, 2445 (1999).
 68. M. Baiardo, G. Frisoni, M. Scandola, M. Rimelen, D. Lips, K. Ruffieux, E. Wintermantel, *J. Appl. Polym. Sci.*, **90**, 1731 (2003).
 69. X. Yang, S. Kang, Y. Yang, K. Aou, and S.L. Hsu, *Polymer*, **45**, 4241 (2004).
 70. B.W. Cherry and T.S. Hin, *Polym. Commun.*, **22**, 1610 (1981).
 71. L. Farge, S. André, A. Pawlak, C. Baravian, S.C. Irvine, and A.-M. Philippe, *J. Polym. Sci. Part B: Polym. Phys.*, **51**, 826 (2013).
 72. A. Blaise, C. Baravian, J. Dillet, L.J. Michot, and S. André, *J. Polym. Sci. Part B: Polym. Phys.*, **50**, 328 (2012).

Strain-induced deformation mechanisms of polylactide plasticized with acrylated poly(ethylene glycol) obtained by reactive extrusion

Kui Wang,^a Berit Brüster,^a Frédéric Addiego,^{a*} Georgio Kfoury,^a Fatima Hassouna,^a David Ruch,^a Jean-Marie Raquez^b and Philippe Dubois^b

Abstract

This work aimed at identifying the tensile deformation mechanisms of an original grade of plasticized polylactide (pPLA) obtained by reactive extrusion. This material had a glass transition temperature of 32.6 °C and consisted of a polylactide (PLA) matrix grafted with poly(acryl-poly(ethylene glycol)) (poly(Acryl-PEG)) inclusions. pPLA behaved like a rubber-toughened amorphous polymer at 20 °C, and its tensile behavior evolved toward a rubbery semicrystalline polymer with increasing temperature. The drawing of pPLA involved orientation of amorphous and crystalline chains, crystallization, and destruction of crystals. It was found that crystal formation and crystal destruction were in competition below 50 °C, resulting in a constant or slightly decreasing crystallinity with strain. Increasing temperature enhanced crystal formation and limited crystal destruction, resulting in an increased crystallinity with the strain level. Drawing yielded a transformation of the initial spherical poly(Acryl-PEG) inclusions into ellipsoids oriented in the tensile direction. This mechanism may engender the formation of nanovoids within the inclusions due to a decreased density, assumed to be responsible for the whitening of the specimen.

© 2015 Society of Chemical Industry

Keywords: polylactide; plastification; tensile testing; chain orientation; crystallinity

INTRODUCTION

Polylactide (PLA) is one of the most attractive biosourced polymers due to its renewability, biodegradability, high biocompatibility and low production cost.¹ This polymer is characterized by a low tendency to crystallize, as it usually contains between 2 and 4 mol% of D-isomeric units randomly distributed along its predominantly L-isomeric backbone. PLA possesses a glass transition temperature (T_g) of around 60 °C and is characterized by a high rigidity (Young's modulus of about 4 GPa at room temperature).² When it is semicrystalline, its melting point is of the order of 160 °C. PLA is mainly used for packaging, textile, agriculture and biomedical applications and is being viewed as a promising green alternative to synthetic non-degradable polyolefin commodities like polypropylene. In this respect, one of the main challenges of PLA is to achieve a high tensile strength and a high toughness or impact resistance within a wide range of temperatures. An understanding of PLA tensile deformation mechanisms, which are controlled by its composition, processing and structure, is of high importance to identify the key parameters to control its tensile strength.

The tensile deformation mechanisms of neat PLA at different temperatures were previously elucidated by wide-angle X-ray scattering (WAXS) for amorphous and semicrystalline grades.^{3–7} Depending on the initial crystallinity and testing temperature, the drawing of PLA involves (i) ordering of the amorphous phase resulting in the formation of a metastable mesomorphic phase

and/or formation of the α' and α crystalline phases, (ii) transformation of the initial α crystalline phase into mesophase and/or α' crystalline phase, and (iii) damage by cavitation. To increase its toughness and impact resistance, PLA is generally plasticized with plasticizing agents such as poly(ethylene glycol),^{8,9} poly(propylene glycol)¹⁰ and citrate.^{11,12} However, after long-term storage migration of the plasticizer toward the material's surface is observed in the case of low molecular weight plasticizers. In contrast, high molecular weight plasticizers have a lower mobility and therefore have less tendency to leach out. However, they significantly reduce the rigidity of PLA compared to low molecular weight plasticizer, which is not desirable. A relevant strategy to stabilize low molecular weight plasticizers within PLA is the chemical grafting of functional plasticizer onto the PLA backbone

* Correspondence to: Frédéric Addiego, Department of Materials Research and Technology (MRT), Luxembourg Institute of Science and Technology (LIST), ZAE Robert Steichen, 5 Rue Bommel, L-4940 Hautcharage, Luxembourg. E-mail: frederic.addiego@list.lu

a Department of Materials Research and Technology (MRT), Luxembourg Institute of Science and Technology (LIST), ZAE Robert Steichen, 5 Rue Bommel, L-4940, Hautcharage, Luxembourg

b Laboratory of Polymeric and Composite Materials, Centre d'Innovation et de Recherche en Matériaux Polymères (CIRMAP), Université de Mons, Place du Parc 20, B-7000, Mons, Belgium

by reactive extrusion.^{13,14} By this methodology, Kfoury *et al.*¹⁵ have recently developed a transparent plasticized grade of PLA (pPLA) derived from grafting reactions of PLA with acrylated poly(ethylene glycol) (Acryl-PEG) as reactive plasticizer in the presence of a free-radical initiator, i.e. 2,5-dimethyl-2,5-di(tert-butylperoxy)hexane (Luperox 101, L101). After grafting Acryl-PEG onto the PLA backbone, pPLA exhibited an original morphology, leading to the formation of rubbery poly(Acryl-PEG)-based inclusions. The amount of grafted Acryl-PEG was proved by Soxhlet extraction: the extracted fraction (non-grafted Acryl-PEG) was less than 10 wt%; therefore it was considered that about half of the plasticizer was grafted onto the PLA matrix. The T_g of this novel pPLA (PLA/Acryl-PEG/L101 79.5/20/0.5 wt%) was about 40 °C and its elastic modulus was about 0.8 GPa at room temperature, as determined via dynamic mechanical analysis.¹⁵ The tensile deformation mechanisms of this original pPLA have not been elucidated to date. The objective of this work was to identify the strain-induced chain orientation, phase transformation and possible damage mechanisms of pPLA during drawing carried out at different temperatures and strain rates. WAXS, SEM and DSC investigations were conducted to assess the deformation mechanisms of pPLA compared with neat PLA.

EXPERIMENTAL

Materials and processing

PLA was supplied by NatureWorks (Minnetonka, MN, USA) under the reference 4042D and contained 4.2 mol% D-isomeric units. For the reactive extrusion, Acryl-PEG ($\bar{M}_n \approx 480 \text{ g mol}^{-1}$) from Sigma-Aldrich (Steinheim, Germany) was utilized as plasticizer, while Luperox 101 (L101) from Sigma-Aldrich (Steinheim, Germany) was used as free-radical initiator. The reactive processing was performed using a twin-screw DSM XPlore 15 mL micro-compounder (Geleen, The Netherlands) at 180 °C with a nitrogen purge to remove oxygen from the extruder housing. It should be noted that L101 offers a half-life time of 1 min at 180 °C.¹⁶ The screw speed was adjusted to 100 rpm, while the overall residence time was 5 min. 15 g in total per batch was introduced into the micro-compounder. PLA pellets were first dried for 12 h at 60 °C in a vacuum oven (Heraeus, Thermo Scientific, Langensfeld, Germany) before processing. PLA was introduced and melted in the micro-compounder. Acryl-PEG and L101 were then mixed in a small glass vial and injected into the extruder using a syringe. PLA/Acryl-PEG/L101 systems with the compositions 79/20/1 and 100/0/0 (in wt%) were chosen for this study and are denoted pPLA and PLA, respectively. The extruded rods of pPLA and PLA were ground and hot-pressed with a Carver manual press (Wabash, IN, USA) to obtain tensile specimens based on ASTM D638-10 with sample type V. The specimen had an overall length of 63.5 mm and a thickness of 3 mm. The gauge section of the specimen had a length of 25 mm and a minimum width of 3 mm. The hot-pressing procedure consisted in (i) heating the material at 180 °C for 3 min without any pressure to ensure its complete melting and inter-pellet chain diffusion, (ii) degassing the material by several successive compression and decompression procedures for 2 min, (iii) compressing the material at 180 °C by progressively increasing the pressure from 0.3 to 1.5 MPa during 5 min to ensure good consolidation, and (iv) cooling the material with water circulation within the press plates (water temperature of about 15 °C) under 1.5 MPa.

Tensile testing

The quasi-static uniaxial tensile testing was done with a universal testing machine Instron model 5967 (Norwood, MA, USA) equipped with an environmental chamber. To get the same experimental condition for each testing, at each change of temperature the chamber was first heated without specimen for 30 min to obtain a uniform temperature. Then, the specimen was placed in the chamber for 15 min to allow thermal equilibration, and finally was tested. The engineering axial stress σ versus axial strain ϵ curves were recorded at constant crosshead rates of 0.6, 6 and 60 mm min⁻¹. Based on the tensile specimen gauge length of 25 mm, the corresponding initial strain rates $\dot{\epsilon}$ were $4 \times 10^{-4} \text{ s}^{-1}$, $4 \times 10^{-3} \text{ s}^{-1}$ and $4 \times 10^{-2} \text{ s}^{-1}$, respectively. For each strain rate, tensile testing was carried out at temperatures T of 20 °C, 50 °C and 80 °C. As usually noted for polymers, PLA and pPLA samples underwent a non-uniform deformation process inducing a necking that generally initiated at geometrical, structural and/or mechanical defects.¹⁷ Because of technical limitations, we were not able to measure the local mechanical variables at the necking level. Special attention was paid to the influence of the experimental conditions (T and $\dot{\epsilon}$) on Young's modulus E , the yield stress σ_y , the ultimate strain ϵ_u and the ultimate stress σ_u of the materials. The plastic flow activation volume v was calculated from the Eyring equation based on a previous paper:¹⁸

$$\sigma_y = \frac{E_0}{v} + \frac{kT}{v} \times \ln \frac{2\dot{\epsilon}}{\dot{\epsilon}_0} \quad (1)$$

where σ_y is the yield stress, $\dot{\epsilon}$ is the strain rate, E_0 is the activation energy barrier for plastic deformation, k is Boltzmann's constant, T is temperature and $\dot{\epsilon}_0$ is a pre-exponential factor. A plot of σ_y versus $\ln(\dot{\epsilon})$ allowed the determination of v via the resulting slope which was equal to kT/v . Note that we decided to use Boltzmann's constant k instead of the gas constant R in Eqn (1) as was done in the previous study.¹⁸ The characterization of the specimens was conducted *ex situ* at different strain levels. Each strain considered corresponded to the maximum strain reached at the end of the loading stage. Then, the specimen strain was kept constant during 30 min in a stress relaxation stage (at the same time the specimen was rapidly cooled to 20 °C for testing conducted at 50 °C and 80 °C), and finally the specimen was quickly analyzed by the different techniques described below. Some optical pictures of the deformed specimens were recorded with a stereomicroscope Leica MZ 125 (Heerbrugg, Switzerland) to observe the whitening mechanism.

WAXS measurements

The WAXS technique was selected to reveal the structural features of PLA and pPLA as a function of strain. Testing was done with a Panalytical X'Pert Pro MPD equipment (Almelo, The Netherlands) configured in the transmission mode and using Cu K α radiation (wavelength $\lambda = 1.54 \text{ \AA}$) generated at 40 kV and 40 mA. The samples were cut from the center of the drawn tensile specimen. The diffractograms were recorded at room temperature in the 2θ range 5° – 40°. As primary optics, a focusing mirror was used with specific slits to allow high resolution in the 2θ range of interest. As secondary optics, a PIXcel detector (Panalytical) was utilized to record the scattering intensity. The specimen was positioned on a spinner that enabled different azimuthal angles ϕ to be analyzed. When the angle ϕ was equal to 0° detection was performed perpendicular to the tensile axis, and when the angle ϕ was equal to 90° detection was performed parallel to

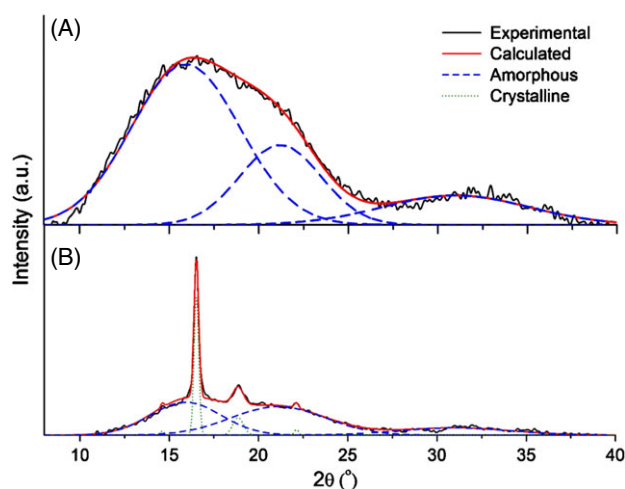


Figure 1. WAXS diagram deconvolution of (A) PLA and (B) pPLA in the non-deformed state exhibiting in the two cases three amorphous halos at $2\theta = 15.0^\circ$, 21.2° and 31.0° and in the case of pPLA four crystalline peaks at $2\theta = 14.6^\circ$, 16.5° , 18.8° and 22.2° engendered by the (010), (110/200), (203) and (210) reflections, respectively.

the tensile axis. The analyzed volume corresponded to an irradiated surface of $0.6\text{ mm} \times 2\text{ mm}$ multiplied by the specimen thickness which depended on the deformation state. Note that the final thickness of each specimen was systematically measured by means of digital calipers. The scattering intensity $I(2\theta)$ was first corrected by means of the Beer–Lambert relationship by considering an absorption coefficient of 9.23 cm^{-1} for PLA and pPLA and the sample thickness. The absorption coefficient for the PLA repeating unit $-(\text{C}_3\text{H}_4\text{O}_2)_n-$ was calculated as the sum of the atomic mass coefficients considering their weight fraction in the repeating unit. The atomic mass coefficients used for Cu K α radiation of C, H and O were $4.51\text{ cm}^2\text{ g}^{-1}$, $0.391\text{ cm}^2\text{ g}^{-1}$ and $11.5\text{ cm}^2\text{ g}^{-1}$, respectively.¹⁹ Then the WAXS curves were treated with the software PeakFit (Systat Software, Framingham, MA, USA) to perform background subtraction by means of an exponential function and peak deconvolution by means of Gaussian functions (Fig. 1). To this end, we considered three amorphous halos located at a 2θ angle of around 15.0° , 21.2° and 31.0° (Fig. 1(A)). The first two scattering halos were attributed to interchain periodicities, while the last scattering halo was attributed to an intrachain periodicity (distance between methyl groups).⁵ Concerning crystalline phases, we attributed the peaks centered at 2θ angles of 14.6° , 16.5° , 18.8° and 22.2° (Fig. 1(B)) to the (010), (110/200), (203) and (210) reflections, respectively.^{5,20} Since it is generally not possible to unambiguously distinguish between the crystalline phases α and α' , we only considered one crystalline phase for all the WAXS analyses.⁴ In the case of PLA, an amorphous to mesomorphic phase transformation can occur when drawing the material resulting in the formation of a broad peak centered at 16.5° .⁷ For a given azimuthal ϕ direction, the weight fraction of crystallinity X_c was calculated as the ratio between the total crystalline peak area to the overall peak area. The average crystallinity $\langle X_c \rangle$ was calculated using the equation^{21,22}

$$\langle X_c \rangle = \frac{\int_0^{\pi/2} X_c(\phi) \times \sum A(\phi) \times \sin(\phi) \times d(\phi)}{\int_0^{\pi/2} \sum A(\phi) \times \sin(\phi) \times d(\phi)} \quad (2)$$

where $X_c(\phi)$ is the crystallinity obtained for a given azimuthal angle ϕ , while $\sum A(\phi)$ is the sum of the area of all the peaks (amorphous, crystalline and mesomorphic phases) for a given azimuthal angle ϕ . The same methodology was used to calculate the weight fraction of the mesophase $\langle X_{\text{mes}} \rangle$. In particular, we found that the average crystallinity of non-deformed PLA and pPLA was 0 wt% and 15.4 wt%, respectively (Fig. 1).

The Herman orientation function was calculated for the three amorphous halos, the two main crystalline peaks (110/200) and (203) and the mesomorphic peak based on

$$f_{i,z} = \frac{3 \langle \cos^2 \phi_{i,z} \rangle - 1}{2} \quad (3)$$

where i is the considered case and $\langle \cos^2 \phi_{i,z} \rangle$ is the average of the cosine squared angle between the normal of the scattering planes i considered (evolved by the crystalline diffractions or by the amorphous molecular scatterings) and the drawing direction z . In the rest of the paper, $f_{1,z}$ corresponds to the amorphous halo positioned at 15.0° , $f_{2,z}$ corresponds to the amorphous halo positioned at 21.2° , $f_{3,z}$ corresponds to the amorphous halo positioned at 31.0° , $f_{(110/200),z}$ corresponds to the crystalline peak (110/200), $f_{(203),z}$ corresponds to the crystalline peak (203) and $f_{\text{mes},z}$ corresponds to the mesophase. $\langle \cos^2 \phi_{i,z} \rangle$ was calculated from

$$\langle \cos^2 \phi_{i,z} \rangle = \frac{\int_0^{\pi/2} I_i(\phi) \times \sin(\phi) \times \cos^2(\phi) \times d(\phi)}{\int_0^{\pi/2} I_i(\phi) \times \sin(\phi) \times d(\phi)} \quad (4)$$

where $I_i(\phi)$ corresponds to the scattering intensity of the i objects considered (crystalline peaks or amorphous halos) for a given azimuthal ϕ direction.

DSC measurements

DSC testing was carried out using a Netzsch DSC 204 F1 instrument (Selb, Germany) as a complementary investigation to WAXS. For DSC experiments, samples with mass $5 \pm 1\text{ mg}$ were heated from 10°C to 180°C with a heating rate of $10^\circ\text{C min}^{-1}$ under a nitrogen gas flow. All the measurements were conducted during the first heating. Special attention was paid to measurement of the glass transition temperature of PLA (T_g), the cold-crystallization temperature of PLA (T_{cc}), the melting temperature of PLA (T_m) and the melting temperature of the PLA mesophase (T_{mes}). The crystallinity enthalpy of PLA was calculated from its melting enthalpy (ΔH_m) subtracted by its cold-crystallization enthalpy (ΔH_{cc}) based on the equation

$$X_c = \frac{\Delta H_m - \Delta H_{cc}}{\Delta H_m^0} \quad (5)$$

where ΔH_m^0 is the enthalpy of a 100% crystalline PLA polymer taken to be equal to 93 J g^{-1} .²³ For pPLA, X_c was calculated using Eqn (5) but in this case ΔH_m^0 was multiplied by the effective fraction of PLA which was 0.79. The mesophase content in neat PLA was determined by using the mesophase enthalpy ΔH_{mes} based on the equation

$$X_{\text{mes}} = \frac{\Delta H_{\text{mes}}}{\Delta H_{\text{mes}}^0} \quad (6)$$

where ΔH_{mes}^0 is the heat of fusion for a 100% mesophase PLA taken to be equal to 70 J g^{-1} .⁶

SEM observations

The microstructure of PLA and pPLA induced by drawing was studied by means of a pressure-controlled scanning electron microscope model Quanta FEG 200 from FEI (Eindhoven, The Netherlands). The materials were first observed with the large field detector (LFD) at a water pressure of 150 Pa from polished samples in the case of PLA and cryo-surfaced samples in the case of pPLA. Cryo-surfacing consisted in removing very thin specimen sections at -30°C with a cryo-ultramicrotome Leica EM UC6/UF6 (Wien, Austria) equipped with a glass knife. Observations were conducted at the center of the specimen necking characterized by the highest deformation level. pPLA was also investigated with the transmission mode of the scanning electron microscope called the STEM mode from 80 nm-thick specimens prepared with the cryo-ultramicrotome. To this end, a small specimen volume was first extracted and grossly trimmed with a razor blade from the center of the tensile specimen. The specimen was afterwards sectioned at -30°C parallel to the tensile direction with a glass knife and subsequently with a diamond blade (Diatome Cryo 35°, Hatfield, PA, USA). STEM images were recorded with the bright field detector enabling phase contrast imaging.

RESULTS AND DISCUSSION

Tensile behavior

The influence of temperature and strain rate on the tensile behavior of pPLA is shown in Fig. 2, while the extracted mechanical parameters are reported in Table 1. As a reference, the same mechanical investigation was conducted on the untreated PLA grade. At 20°C and $4 \times 10^{-2} \text{ s}^{-1}$ (Figs 2(A) and 2(B)), the tensile behavior of pPLA exhibited three stages: (i) an initial viscoelastic stage where the stress increased drastically with strain up to a maximum point related to the yield point $\sigma_y = 25 \text{ MPa}$ characterized by a Young's modulus of 865 MPa ; (ii) the onset of the viscoplastic stage characterized by a drop in stress; and (iii) a final increase of the stress until the break point at the ultimate strain $\epsilon_u = 165\%$. Under the same conditions, PLA exhibited a brittle tensile behavior without any viscoplastic stage characterized by a Young's modulus $E = 3123 \text{ MPa}$ and an ultimate strain $\epsilon_u = 2\%$. In the case of pPLA, with increasing temperature or decreasing strain rate, a decrease of Young's modulus, yield stress and ultimate stress were noted. At the same time, an increase of the ultimate strain was observed (Table 1). For example, at 80°C and $4 \times 10^{-4} \text{ s}^{-1}$, $E = 63.5 \text{ MPa}$, $\sigma_y = 4 \text{ MPa}$ and $\epsilon_u = 470\%$ for pPLA. It must also be mentioned that the intensity of the stress drop at the beginning of the viscoplastic stage decreased with decreasing strain rate from $4 \times 10^{-2} \text{ s}^{-1}$ to $4 \times 10^{-4} \text{ s}^{-1}$ and increasing temperature from 20°C to 80°C . For PLA, on increasing the temperature from 20°C to 50°C a viscoplastic stage appeared with an ultimate strain of 298% (Figs 2(A) and 2(B)). The yield activation volume of the materials was calculated using the Eyring equation (Eqn (1)) from the yield stress (Table 1). As PLA was brittle at room temperature and exhibited no plasticity, no activation volume was determined for this condition. It was found that the activation volume of pPLA at 50°C (9.2 nm^3) was higher than that of PLA (0.2 nm^3). At 80°C , the activation volume of PLA was higher than that of pPLA (27.6 nm^3 versus 19.7 nm^3). For the two materials, the activation volume increased with temperature.

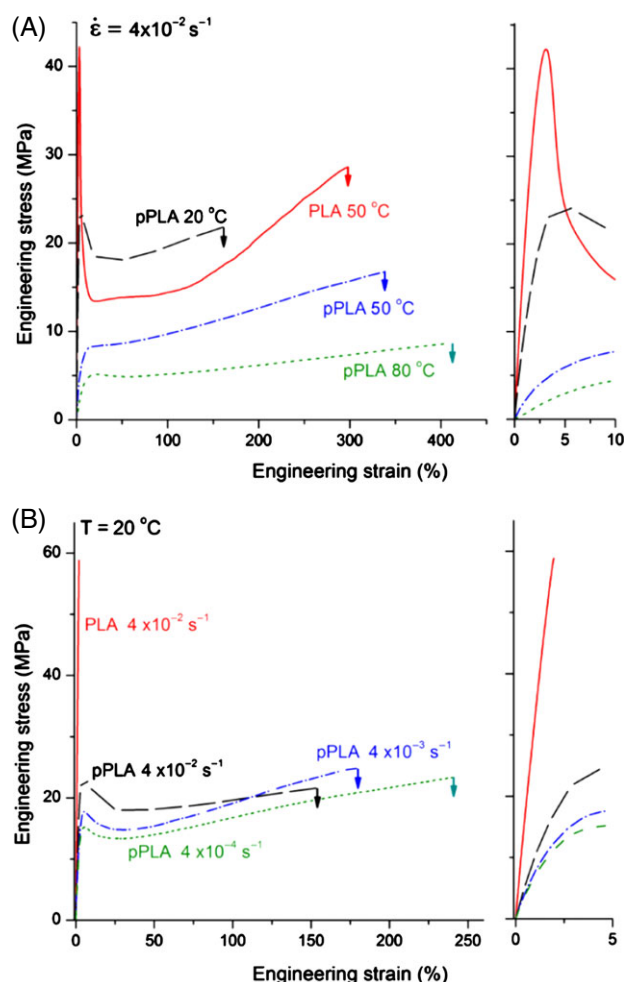


Figure 2. Influence of the temperature at $4 \times 10^{-2} \text{ s}^{-1}$ (A) and of the strain rate at 20°C (B) on the tensile behavior of pPLA including a zoom-in view of the initial part of the curves (some reference curves of PLA are also plotted for comparison).

Some optical microscope images of pPLA recorded for different strain levels and strain rates are presented in Fig. 3. For characterization of the whitening intensity, the average grey level of the optical image was calculated by means of the software ImageJ (National Institutes of Health, USA) from a $1.5 \text{ mm} \times 1.5 \text{ mm}$ area at the center of the specimen. The average grey level ranged from 0 (black) to 255 (white). In the non-deformed state (Fig. 3(A)), pPLA was quite transparent (but less transparent than untreated PLA) with a grey level of 102.5. With increasing strain level at 20°C and $4 \times 10^{-4} \text{ s}^{-1}$, a progressive whitening of the samples was observed (Fig. 3(A)). Indeed, the grey level increased from 102.5 in the non-deformed state to 254 for a strain of 240% . Note that at a strain of 150% the grey level was equal to 191.8 for the same strain rate. Increasing the strain rate to $4 \times 10^{-2} \text{ s}^{-1}$ led to a weak increase of the whitening at a strain of 150% as the grey level increased from 191.8 at $4 \times 10^{-4} \text{ s}^{-1}$ to 208.8 at $4 \times 10^{-2} \text{ s}^{-1}$ (Fig. 3(B)). After a recovery period of 1 week at an initial strain of 150% obtained at $4 \times 10^{-2} \text{ s}^{-1}$, a partial disappearance of the whitening related to a grey level of 123.8 was observed (Fig. 3(C)). When the strain rate was decreased to $4 \times 10^{-4} \text{ s}^{-1}$, the whitening was more permanent than for $4 \times 10^{-2} \text{ s}^{-1}$ (images not shown here). Concerning PLA, some whitening phenomena were also noted at the highest

Table 1. Young's modulus E , yield stress σ_y , ultimate strain ϵ_u and ultimate stress σ_u of PLA and pPLA as a function of temperature and strain rate extracted from tensile testing curves and yielding the activation volume determined from the Eyring equation

Material	Temperature T (°C)	Strain rate $\dot{\epsilon}$ (s ⁻¹)	Young's modulus E (MPa)	Yield stress σ_y (MPa)	Yielding activation volume V (nm ³)	Ultimate strain ϵ_u (%)	Ultimate stress σ_u (MPa)
PLA	20	4×10^{-2}	3123	Brittle	n.m.	2	58.8
		4×10^{-3}	2839	Brittle		1.7	47.3
		4×10^{-4}	2766	Brittle		1.6	45.8
	50	4×10^{-2}	1748	42.2	0.9	298.2	28.6
		4×10^{-3}	1297	29.2		327.0	26.3
		4×10^{-4}	922	18.2		366.1	24.9
	80	4×10^{-2}	2.0	0.9	27.6	845.4	7.7
		4×10^{-3}	1.2	0.4		1114.1	1.6
		4×10^{-4}	n.m.	0.1		n.m.	n.m.
pPLA	20	4×10^{-2}	865	24.5	2.0	165.1	21.9
		4×10^{-3}	626	17.7		179.6	24.8
		4×10^{-4}	567	15.2		239.8	23.3
	50	4×10^{-2}	174	8.4	9.2	342.3	16.8
		4×10^{-3}	134	6.9		372.8	16.9
		4×10^{-4}	123	6.1		419.5	16.4
	80	4×10^{-2}	67	5.1	19.7	409.9	8.6
		4×10^{-3}	64.9	4.4		452.5	9.0
		4×10^{-4}	63.5	4.0		469.7	8.3

n.m., not measurable.

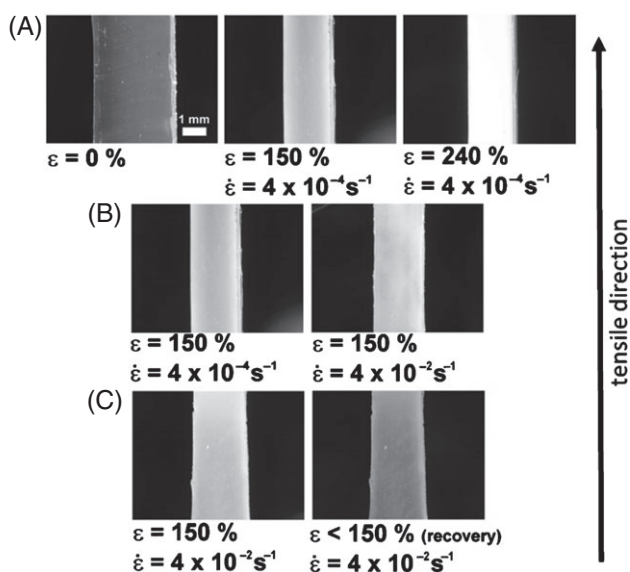


Figure 3. Optical microscope images of pPLA deformed in tension at 20 °C showing the effect of strain level at 4×10^{-4} s⁻¹ (A), the effect of strain rate at a strain level of 150% (B) and the effect of relaxation after 1 week (C). The images were recorded at the center of the tensile specimens.

strain rate of 4×10^{-2} s⁻¹ and 50 °C (images not shown here), and in this case it was permanent even after several weeks.

To understand the macroscopic behavior of pPLA, its initial glass transition temperature T_g and crystallinity X_c were first determined. By DSC, we found a T_g of 32.6 °C for pPLA and 59.8 °C for PLA (see the next section). Note that the T_g of poly(Acryl-PEG) was found to be -61 °C by DSC in a previous study,²⁴ and hence the inclusions were considered to have a rubbery behavior between 20 °C and 80 °C. Based on WAXS measurements, X_c was equal to 0 wt% for PLA and 15.4 wt% for pPLA. The tensile behavior of pPLA

is therefore influenced by the glassy/rubbery state, the presence of the rigid crystalline phase and the presence of the rubbery poly(Acryl-PEG) inclusions. At 20 °C, the tensile curve of pPLA is similar to that of rubber-toughened amorphous polymers such as high-impact polystyrene drawn below their T_g .^{25,26} In this case, the tensile curve is characterized by an initial viscoelastic stage where the stress drastically increases with strain until the yield point. At the onset of the viscoplastic stage the stress drops resulting in a strain-softening stage and then finally increases resulting in a strain-hardening stage. Despite the glassy state of the molecular network, these materials exhibit ductility due to the vicinity of the testing temperature to their glass transition temperature and to the presence of the rubbery poly(Acryl-PEG) inclusions. In other words, pPLA has enough mobility to withstand the set strain, exhibiting plasticity. The presence of the crystalline phase in pPLA is expected to increase Young's modulus, to increase the tensile strength and to decrease the ductility compared to neat PLA. In contrast, the presence of rubbery poly(Acryl-PEG) inclusions is expected to get the opposite effect. The yield in pPLA may be induced by the activation of shearing mechanisms in crystalline lamellae (crystal plasticity), as commonly considered for semicrystalline polymers.²⁷ To prove the effective role of crystalline lamellae on the mechanical behavior of PLA, stress transfers have to be active between the amorphous phase and crystalline lamellae. This point was further investigated by WAXS. In parallel, the presence of rubbery poly(Acryl-PEG) inclusions in pPLA may also play a role on the activation of the material plasticity by yielding internal cavitation.²⁸ It is important to note that in the case of neat PLA stretched below its T_g the onset of the viscoplastic stage can be associated with cavitation mechanisms within the polymer matrix.³ The measurement of the yielding activation volume of the materials may provide information about the molecular mechanisms involved in the plastic flow (Table 1). At 50 °C, the higher activation volume of pPLA compared to PLA may be explained by a lower chain mobility in PLA compared to pPLA as neat PLA is

in its glassy state. It can also be explained in pPLA by the presence of crystalline lamellae and the inclusions that are expected to contribute to the plastic flow, increasing the number of molecular segments involved in the yielding process of pPLA compared to PLA. Increasing temperature generally increases the molecular mobility, which may be at the origin of the increased activation volume for PLA and pPLA. Note that this increase in mobility appears more marked for PLA than for pPLA resulting in a higher activation volume for PLA than for pPLA at 80 °C.

The possible cavity formation during the viscoplastic stage in neat or rubber-toughened amorphous polymers may induce marked variation in the refractive index compared to the matrix, and consequently visible light can be scattered off. If cavities have a micrometer size, like visible light wavelengths, they can induce a whitening phenomenon as they scatter approximately the same amount of light for all the visible spectrum wavelengths.^{29–31} For pPLA and PLA, whitening was observed upon drawing (Fig. 3). Whitening was non-reversible for PLA and reversible for pPLA, indicating different underlying mechanisms. The presence of cavities in PLA and pPLA will be verified below.

For pPLA, the yield stress and the strain-softening intensity decreased with increasing temperature or decreasing strain rate (Fig. 2 and Table 1). These results can be explained by enhanced molecular relaxation and orientation of the amorphous chains, and at the same time enhanced shearing mechanisms of the crystalline lamellae. As a result, the material may exhibit less resistance to the imposed strain. The influence of rubbery poly(Acryl-PEG) inclusions on the yield of pPLA is also expected to decrease with increasing temperature yielding less cavitation. From 50 °C, the tensile curve of pPLA is similar to that observed for semicrystalline polymers drawn above their glass transition temperature characterized by a rubbery amorphous phase.^{21,22} At 80 °C, the yield stress of pPLA was higher than that of PLA due to the presence of the crystalline phase in pPLA, which may significantly increase the tensile strength above T_g .

DSC investigation

DSC thermograms of non-deformed PLA and pPLA exhibited crystallinity for pPLA ($X_c = 25.4$ wt%), while PLA was totally amorphous (Fig. 4). The glass transition and cold-crystallization temperatures were greater for PLA ($T_g = 59.8$ °C and $T_{cc} = 128.5$ °C) than for pPLA ($T_g = 32.6$ °C and $T_{cc} = 73.2$ °C), indicating that the plastification of PLA by reactive extrusion effectively increased the molecular mobility of the matrix. The drawing process significantly modified the thermograms of the two materials. In the case of pPLA, the melting temperature was lower for non-deformed pPLA compared with deformed pPLA for all experimental conditions, showing that deformation induced smaller crystalline lamellae. At 50 °C and $4 \times 10^{-2} \text{ s}^{-1}$, pPLA had an increased crystallinity at a strain state of 300% compared to the non-deformed state, reaching a maximum of 30.5 wt%. At 20 °C and $4 \times 10^{-3} \text{ s}^{-1}$, pPLA had a decreased crystallinity with a strain of 100% compared to the non-deformed state, reaching a minimum of 14.1 wt%. Therefore, strain significantly changes the crystallinity of pPLA, and hence crystalline lamellae participate in the overall deformation mechanisms of the material. The deformation mechanisms of the crystalline phase are investigated in more detail in the next section. The glass transition temperature increased from 32.6 °C to a maximum at 45.6 °C ($T = 50$ °C, $\epsilon = 300\%$, $\dot{\epsilon} = 4 \times 10^{-2} \text{ s}^{-1}$) comparing non-deformed pPLA with deformed pPLA, and at the same time the cold-crystallization temperature decreased from 73.2 °C to a minimum of 59.6 °C ($T = 50$ °C, $\epsilon = 300\%$, $\dot{\epsilon} = 4 \times 10^{-3} \text{ s}^{-1}$). It is

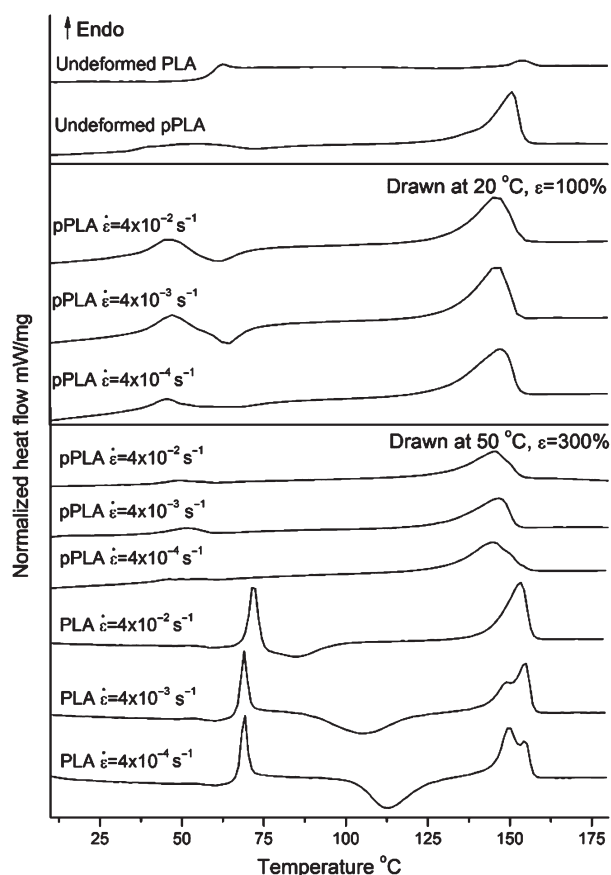


Figure 4. DSC curves of PLA and pPLA at various strain levels and temperatures.

generally admitted that the glass transition involves cooperative motions in one chain that are influenced by intramolecular interactions and intermolecular interactions. A certain dynamic free volume is required enabling conformational change of the chain.³² In the case of pPLA, the grafting of the plasticizer is expected to space out the chains and hence may increase the free volume and decrease T_g . The increase in T_g with imposed strain may be explained by a chain ordering process by orientation that globally reduces the free volume and hence hinders the glass transition process. It was found, however, that the free volume in the vicinity of the chain ends increased with stretching, indicating more mobility in these regions for the glass transition.³³ The strain-induced ordering of the chains may facilitate the cold-crystallization of pPLA, which can explain the decrease in T_{cc} for non-deformed pPLA compared with deformed pPLA. No significant effect of the strain rate was noted on the thermal properties of pPLA for stretching at 20 °C and 50 °C. Concerning PLA, the imposed strain again caused an increase in T_g and a decrease in T_{cc} compared to the non-deformed state, which can be explained in the same way. An original aspect of stretched PLA is the occurrence of an endothermic peak positioned at about 70 °C that is attributed to the melting of the mesomorphic phase.⁶ For the same strain level of 300% at 50 °C, we found a fraction of mesophase that increased from 9.5 wt% to 12.0 wt% when the strain rate was increased from $4 \times 10^{-4} \text{ s}^{-1}$ to $4 \times 10^{-2} \text{ s}^{-1}$. The formation of the mesophase in the case of neat PLA induced by drawing at 50 °C may be due to its low chain mobility that does not enable the more ordered α or α' crystalline phase to be created.

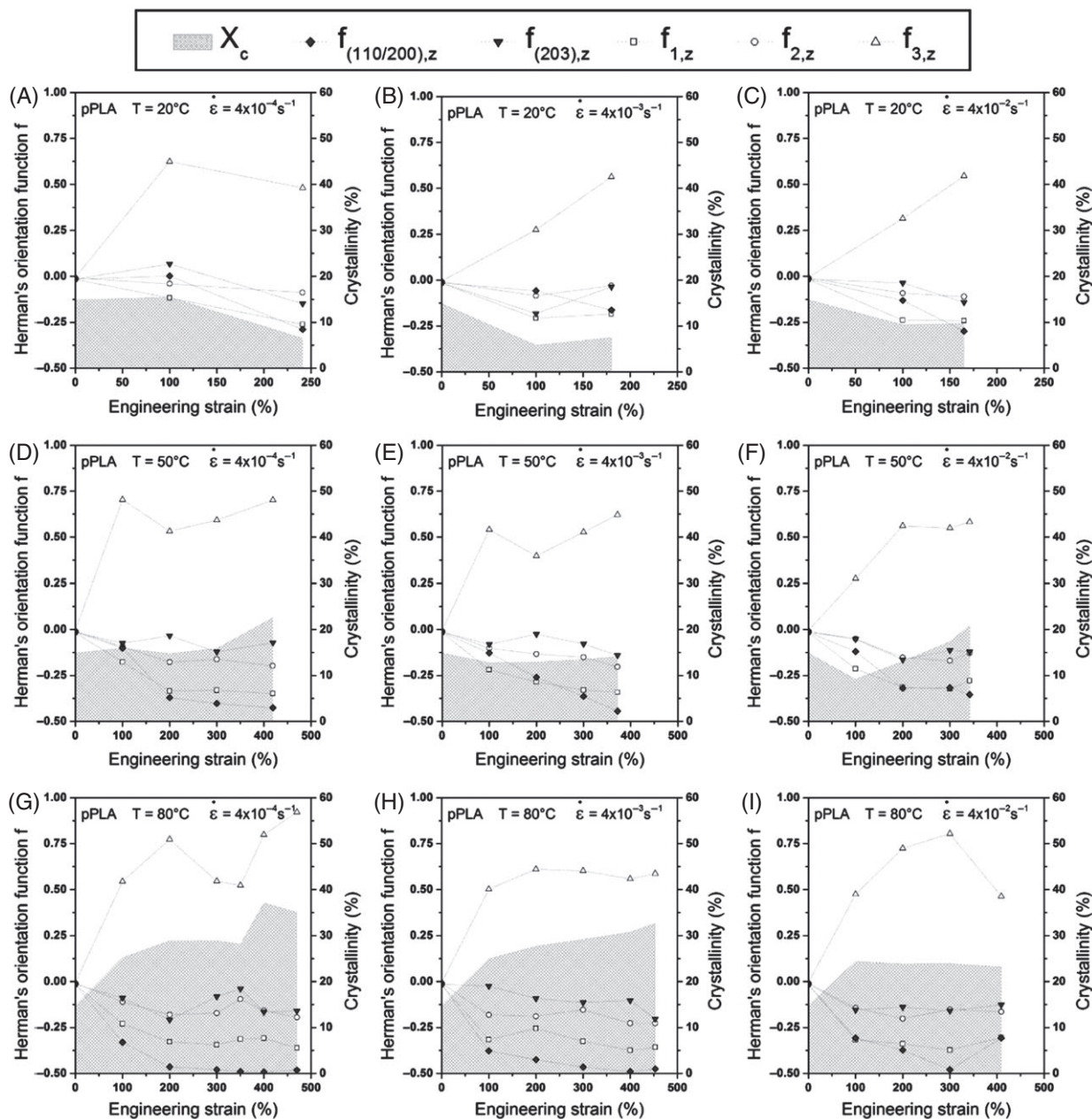


Figure 5. WAXS investigation of pPLA showing the evolution of the orientation function of the three amorphous halos (labeled 1 to 3) and of the two main crystalline peaks (labeled (110/200),z and (203),z) (left-hand axis) and of the crystallinity (right-hand axis) as a function of strain. Tensile testing was conducted at different temperatures (20 °C (A) – (C), 50 °C (D) – (F) and 80 °C (G) – (I)) and different strain rates ($4 \times 10^{-4} \text{ s}^{-1}$ (A), (D) and (G); $4 \times 10^{-3} \text{ s}^{-1}$ (B), (E) and (H); and $4 \times 10^{-2} \text{ s}^{-1}$ (C), (F) and (I)).

WAXS investigation

The evolutions of crystallinity and of the orientation functions with the strain level of pPLA and PLA subjected to tension are represented in Figs 5 and 6, respectively. Crystallinity found by DSC analyses was higher compared with WAXS results. This variation is due to the fact that these two techniques rely on different methods and in addition each of them has inherent uncertainties. It must be noted that, by DSC analyses, drawing did not yield the formation of a mesophase in the case of pPLA for all the temperatures and strain rates investigated. In the case of PLA, drawing induced the formation of a mesophase only at 50 °C. At 20 °C, pPLA had a decreased crystallinity with increasing strain level whatever the strain rate. In particular, X_c evolved from 15.4 wt% in the non-deformed state

to 6.6 wt% at a strain level of 240% obtained with a strain rate of $4 \times 10^{-4} \text{ s}^{-1}$. At 50 °C, the crystallinity of pPLA was stable or slightly decreased with strain level and then increased with high strain levels. At 80 °C, the crystallinity of pPLA increased with strain level. In particular, X_c reached a maximum of 37 wt% for a strain of 400% at a strain rate of $4 \times 10^{-4} \text{ s}^{-1}$. These results demonstrate that during the drawing of pPLA a competition between crystal destruction and crystal formation is present. Crystal destruction may be due to the shearing and subsequent fragmentation of the initial crystalline lamellae,²¹ while crystal formation may be due to the ordering of the amorphous chains. The deformation of the crystalline phase by shearing is shown in pPLA by decrease of the orientation functions $f_{(110/200),z}$ and $f_{(203),z}$ with strain for all

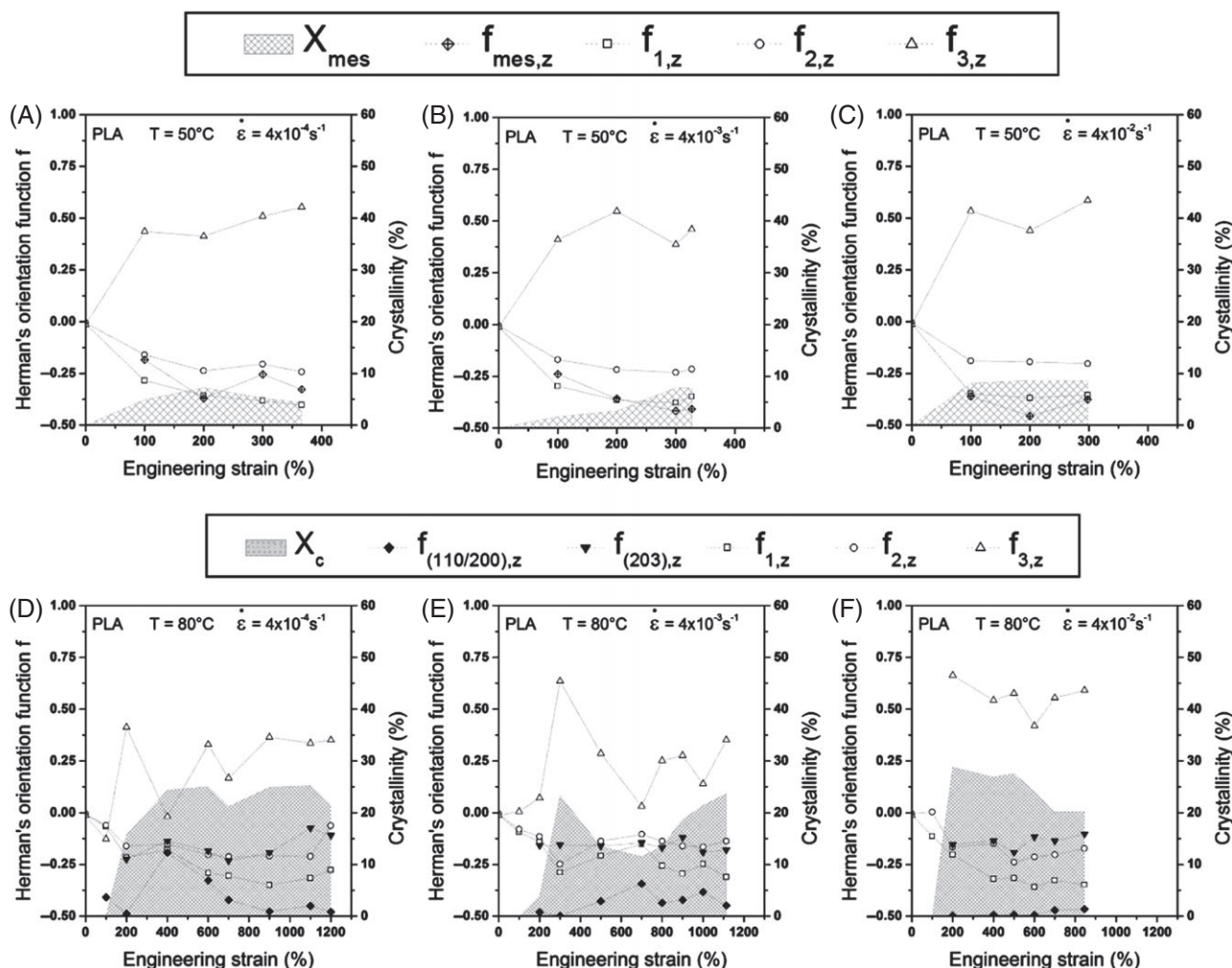


Figure 6. WAXS investigation of PLA showing the evolution of the orientation function of the three amorphous halos (labeled 1 to 3), of the mesophase peak (labeled mes, just at 50 °C) and of the two main crystalline peaks (labeled (110/200) and (203), just at 80 °C) (left-hand axis) and of the crystallinity (right-hand axis) as a function of strain. Tensile testing was conducted at different temperatures (50 °C (A) – (C) and 80 °C (D) – (F)) and different strain rates ($4 \times 10^{-4} \text{ s}^{-1}$ (A), (D); $4 \times 10^{-3} \text{ s}^{-1}$ (B), (E); and $4 \times 10^{-2} \text{ s}^{-1}$ (C), (F)). At 50 °C, the crystallinity is based on the mesophase peak.

temperatures and strain rates. At the same time, the ordering of the amorphous chains is proved by the evolution of the orientation functions $f_{1,z}$, $f_{2,z}$ and $f_{3,z}$ from 0 to values above 0.5 for $f_{3,z}$, from 0 to values below -0.125 for $f_{2,z}$ and from 0 to values below -0.25 for $f_{1,z}$. With increasing temperature from 20 °C to 80 °C, it appears that the intensity of the orientation of the crystalline chains increased considering the orientation function of the main crystalline peak (110/200) at a strain of 100%. For example, $f_{(110/200),z}$ decreased from 0.00 to -0.33 when the temperature was increased from 20 °C to 80 °C at $4 \times 10^{-4} \text{ s}^{-1}$. This result shows that crystal shearing is facilitated with increasing temperature and that fragmentation may hence be restricted, resulting in no or limited crystalline destruction. At the same time, the intensity of the orientation of the amorphous chains increased as shown by the values of the orientation function of the main amorphous halo 1 positioned at 15.0° . For example, at a strain of 100%, $f_{1,z}$ evolved from -0.12 to -0.23 with increasing temperature from 20 °C to 80 °C at $4 \times 10^{-4} \text{ s}^{-1}$. Therefore crystal formation in pPLA is enhanced when the tensile testing temperature is increased. This WAXS investigation proves that in pPLA both amorphous and crystalline phases exhibit chain orientation during drawing, demonstrating that deformation mechanisms involve these two phases

and that stress transfers are effective between them. Concerning PLA, the formation of the mesomorphic phase was observed at 50 °C whatever strain rate was investigated, confirming the DSC results. The fraction of the mesomorphic phase reached 5.2 wt% at a strain of 300% and for a strain rate of $4 \times 10^{-4} \text{ s}^{-1}$. At 80 °C, PLA exhibited formation of the α or α' crystalline phase for all strain rates. With increasing temperature, the ordering of the amorphous chains upon drawing increased in the case of PLA as an amorphous to mesophase transformation evolved to an amorphous to crystalline transformation. At 50 °C and 80 °C, PLA was characterized by an increase in the orientation of its amorphous and non-amorphous chains (crystalline or mesomorphic phases) with strain. It must be noted that for pPLA and PLA no significant effect of the strain rate was observed on the evolution of crystallinity/mesophase fraction and on the orientation functions with the strain level.

Morphological investigation

The morphology of deformed PLA and pPLA observed by SEM is represented in Fig. 7. PLA exhibited some micro-sized primary cavities having an ellipsoid shape with major axis oriented in the tensile direction (Fig. 7(A)). Based on image analysis of SEM

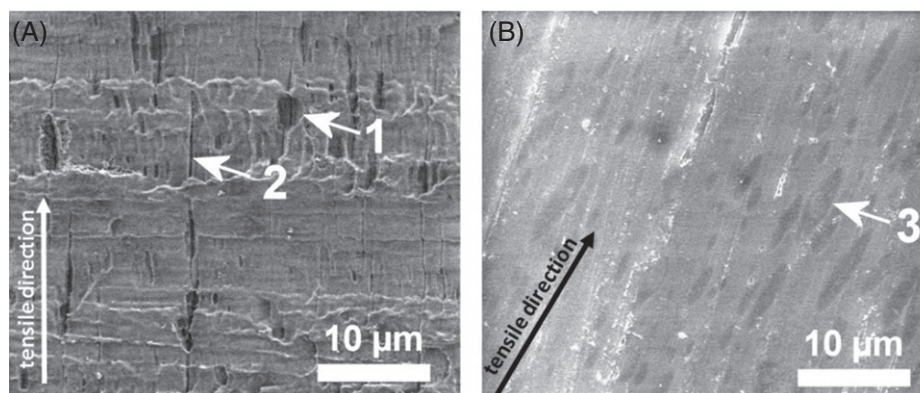


Figure 7. SEM observations with the LFD mode of deformed (A) PLA (strain of 298% obtained at 50 °C with a strain rate of $4 \times 10^{-2} \text{ s}^{-1}$) and (B) pPLA (strain of 165% obtained at 20 °C with a strain rate of $4 \times 10^{-2} \text{ s}^{-1}$): 1, primary cavities containing a secondary cavity; 2, secondary cavities; 3, drawn poly(Acryl-PEG) micrometer inclusions.

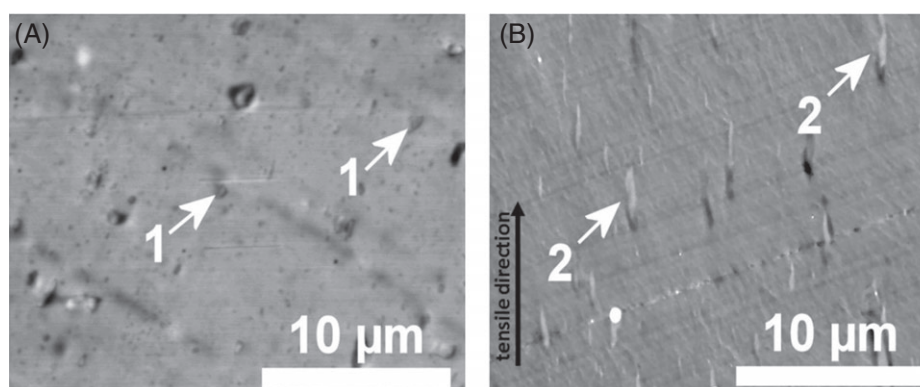


Figure 8. STEM observations of (A) non-deformed pPLA and (B) deformed pPLA (strain of 165% obtained at 20 °C with a strain rate of $4 \times 10^{-2} \text{ s}^{-1}$): 1, initial poly(Acryl-PEG) inclusions with high density; 2, drawn poly(Acryl-PEG) micrometer inclusions with decreased density.

images with the software ImageJ (National Institutes of Health), the average ellipsoid height and width were found to be 2.2 μm and 0.6 μm , respectively, corresponding to a shape factor of 3.7. We also noted an original damage aspect here that was the presence of secondary cavities oriented in the tensile direction that seemed to interact with the primary cavities. Indeed, some primary cavities clearly contained a secondary cavity passing through their center. To our best knowledge, damage mechanisms in neat PLA subjected to tension have not been described in detail in the literature. In the work of Rezgui *et al.*,³ the presence of primary cavities in drawn semicrystalline PLA was noted but no secondary cavity was observed. The micrometric cavities in PLA may induce variation in the refractive index compared with the matrix, and hence visible light can be scattered yielding the whitening. In contrast, pPLA did not exhibit cavities at the scale of observation but elongated poly(Acryl-PEG) inclusions forming ellipsoids with major axis oriented in the tensile direction (Fig. 7(B)). Moreover, with the LFD mode which provided topographical contrast, inclusions appeared as dark grey, which can indicate the presence of voids that emit few or no electrons. By image analysis with ImageJ, we found that the average ellipsoid height and width were 2.8 μm and 0.65 μm , respectively. Therefore, their shape factor was about 4.3. In the non-deformed state, poly(Acryl-PEG) inclusions had a spherical shape with an average diameter of about 0.7 μm (SEM image not shown here). To get complementary information about the deformation mechanism of poly(Acryl-PEG) inclusions

in pPLA, some micrographs were recorded with the STEM configuration of the microscope (Fig. 8). The contrast observed here is a phase contrast linked to the difference in electron scattering by the specimen areas. On STEM images, areas appearing in dark grey correspond to areas having a high density, and inversely. Based on Figs 8(A) and 8(B), the density of the poly(Acryl-PEG) significantly decreases with deformation as the grey level of the inclusions evolved from dark grey to light grey. This result indicates that the volume of these inclusions increased with strain level on assuming that they have a constant mass, confirming their increased size on SEM images (Fig. 7(B)). It is thought that the deformation of poly(Acryl-PEG) involved the formation of nanovoids that are not visible by SEM and STEM explaining their increased volume. These voids may be generated by the separation of poly(Acryl-PEG) chains from each other in molecular regions characterized by a high free volume.³⁴ However, to scatter visible light voids must have a micrometric size of visible light wavelengths. It is hence thought that whitening is not due to the scattering by each nanovoid but to scattering by each micron inclusion containing the nanovoids.^{30,31} After strain recovery, the whitening partially disappeared demonstrating that it is not permanent (Fig. 3(C)). In particular, the rubbery inclusions may shrink during the recovery stage resulting in a partial disappearance of the nanovoids. Further investigations are needed to identify with more detail the deformation mechanisms of the inclusions at the molecular level.

CONCLUSIONS

The tensile behavior of pPLA (initial crystallinity of 15.4 wt% based on WAXS) was assessed for temperatures ranging from 20 °C to 80 °C and strain rates ranging from $4 \times 10^{-4} \text{ s}^{-1}$ and $4 \times 10^{-2} \text{ s}^{-1}$, while the underlying deformation mechanisms were identified by DSC, WAXS and SEM. At 20 °C, the stress–strain curve of pPLA was typical of a rubber-toughened amorphous polymer drawn below its glass transition temperature exhibiting a strain-softening stage after the yield point and a certain ductility. With increasing temperature, the tensile behavior of pPLA evolved towards the behavior of a rubbery semicrystalline polymer, especially when passing its glass transition temperature of 32.6 °C. With increasing temperature or decreasing strain rate, the yield stress and the strain-softening intensity decreased, while the ultimate strain increased. pPLA exhibited a progressive whitening during the drawing that partially disappeared after a recovery period. Neat PLA also showed whitening upon drawing but in this case the whitening was permanent.

The evolution of the crystallinity and of the orientation functions of amorphous and crystalline chains with strain level was carefully studied by WAXS. The crystallinity of pPLA was stable or slightly decreased with strain at low temperature, while it increased with strain at high temperature. A competition between crystal destruction due to shearing and subsequent fragmentation of the lamellae and crystal formation due to amorphous chain ordering was noted. The shearing of the lamellae was proved by a decrease of the orientation functions of the crystalline peaks (110/200) and (203) with strain. The ordering of the amorphous chains was demonstrated by an increase or decrease of the orientation functions of the three amorphous halos with strain. With increasing temperature from 20 °C to 80 °C, the intensity of the orientation of the crystalline and amorphous chains increased for a strain of 100%. Therefore, crystal shearing is facilitated with increasing temperature and fragmentation may hence be restricted resulting in no or limited crystalline destruction. At the same time, crystal formation in pPLA was enhanced by the increased amorphous chain ordering. The restricted fragmentation and enhanced ordering may explain the increased crystallinity when pPLA is drawn at high temperature compared to low temperature. The WAXS study demonstrates that in the case of pPLA both amorphous and crystalline chains exhibit orientation during the drawing, and hence stress transfers are effective between them.

By DSC analyses, it was shown that the melting temperature systematically decreased comparing non-deformed with deformed pPLA, indicating that deformation induces smaller crystalline lamellae. DSC measurements also indicated that pPLA crystallinity decreased with strain at low stretching temperature, while it increased with strain for high stretching temperature. Therefore, DSC confirmed that the crystalline phase was involved in the tensile deformation mechanisms of pPLA. It was also observed that in the case of pPLA the glass transition temperature increased and the cold-crystallization temperature decreased with the strain level. These results were explained by a possible decrease in the free volume of the chains with the drawing that may hinder the glass transition relaxation and by the strain-induced chain ordering that may facilitate the crystallization, respectively. For neat PLA that was initially amorphous, DSC revealed that stretching induced the formation of a mesomorphic phase at 50 °C, while the formation of this phase did not occur for pPLA.

The morphological investigation by SEM showed that pPLA exhibited an elongation of the initial poly(Acryl-PEG) inclusions forming ellipsoids with major axis oriented in the tensile direction. This mechanism may engender a decrease in inclusion density resulting in possible nanovoid formation inside the inclusions and specimen whitening. The presence of these nanovoids was not experimentally proved, however. In the case of PLA, drawing induced the formation of micron cavities that are expected to scatter visible light and hence may cause specimen whitening.

The current work provides new aspects about plasticized biosourced polymer deformation mechanisms that could be the basis of a physically based model enabling the tensile curve of these materials to be predicted. To go further, the detailed molecular deformation mechanisms of the rubbery poly(Acryl-PEG) inclusions have to be assessed with attention focusing on their possible voiding.

ACKNOWLEDGEMENTS

The authors acknowledge the Fonds National de la Recherche Luxembourg (FNR) for CORE project funding. The authors also thank the Belgian Federal Government Office Policy of Science (BELSPO) for its support in the framework of the PAI-6/27. J.-M. Raquez is a research associate of the F.R.S.-FNRS.

REFERENCES

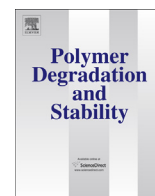
- Nair LS and Laurencin CT, *Prog Polym Sci* **32**:762–798 (2007).
- Gómez-Pérez J, Velázquez-Infante JC, Franco-Urquiza E, Pages P, Carrasco F, Santana OO *et al.*, *Express Polym Lett* **5**:82–91 (2011).
- Rezgui F, Swistek M, Hiver JM, G'Sell C and Sadoun T, *Polymer* **46**:7370–7385 (2005).
- Stoclet G, Seguela R, Vanmansart C, Rochas C and Lefebvre J-M, *Polymer* **53**:519–528 (2012).
- Stoclet G, Seguela R, Lefebvre JM, Elkoun S and Vanmansart C, *Macromolecules* **43**:1488–1498 (2010).
- Stoclet G, Seguela R, Lefebvre J-M and Rochas C, *Macromolecules* **43**:7228–7237 (2010).
- Stoclet G, Séguéla R, Lefebvre JM, Li S and Vert M, *Macromolecules* **44**:4961–4969 (2011).
- Martin O and Avérous L, *Polymer* **42**:6209–6219 (2001).
- Hu Y, Hu YS, Topolkaraev V, Hiltner A and Baer E, *Polymer* **44**:5681–5689 (2003).
- Kulinski Z, Piorkowska E, Gadzinowska K and Stasiak M, *Biomacromolecules* **7**:2128–2135 (2006).
- Ljungberg N and Wesslén B, *J Appl Polym Sci* **86**:1227–1234 (2002).
- Ljungberg N and Wesslén B, *Polymer* **44**:7679–7688 (2003).
- Hassouna F, Raquez JM, Addiego F, Dubois P, Toniazio V and Ruch D, *Eur Polym J* **47**:2134–2144 (2011).
- Hassouna F, Raquez J-M, Addiego F, Toniazio V, Dubois P and Ruch D, *Eur Polym J* **48**:404–415 (2012).
- Kfoury G, Hassouna F, Raquez J-M, Toniazio V, Ruch D and Dubois P, *Macromol Mater Eng* **299**:583–595 (2014).
- Debaud F, Defrancisci A and Palys LH, Available at: <http://www.luperox.com/export/sites/organicperoxide/content/medias/downloads/literature/sp-technologies.pdf> [29/04/2015] (2004).
- G'Sell C, Aly-Helal NA, Semiatin SL and Jonas JJ, *Polymer* **33**:1244–1254 (1992).
- Díez-Pascual AM and Naffakh M, *Mater Chem Phys* **141**:979–989 (2013).
- Prince E, *International Tables for Crystallography, Mathematical, Physical and Chemical Tables*, 3rd edition, ed. by King SE and Ashcroft NJ. Kluwer Academic, Dordrecht, The Netherlands (2004).
- Choi K, Choi M-C, Han D-H, Park T-S and Ha C-S, *Eur Polym J* **49**:2356–2364 (2013).
- Addiego F, Dahoun A, G'Sell C and Hiver J-M, *Polymer* **47**:4387–4399 (2006).
- Eddoumy F, Addiego F, Dhieb H, Célis J-P, Muller R, Toniazio V *et al.*, *Polym Int* **62**:867–877 (2013).

- 23 Fischer BEW, Sterzel HJ and Wegner G, *Kolloid-Z u Z Polym* **251**:980–990 (1973).
- 24 Kfoury G, *High Impact Bioplastics by Reactive Extrusion of Poly(lactide)*. PhD Thesis, University of Mons, Belgium (2014).
- 25 Castellani L and Maestrini C, *Polymer* **31**:2278–2286 (1990).
- 26 Choi JH, Ahn KH and Kim SY, *Polymer* **41**:5229–5235 (2000).
- 27 Brooks NW, Ghazali M, Duckett RA, Unwin AP and Ward IM, *Polymer* **40**:821–825 (1999).
- 28 Lazzeri A and Bucknall CB, *Polymer* **36**:2895–2902 (1995).
- 29 Cherry BW and Hin TS, *Polymer* **22**:1610–1612 (1981).
- 30 Farge L, Andre S, Pawlak A, Baravian C, Irvine SC and Philippe AM, *J Polym Sci B Polym Phys* **51**:826–841 (2013).
- 31 Blaise A, Baravian C, Dillet J, Michot LJ and André S, *J Polym Sci B Polym Phys* **50**:328–337 (2012).
- 32 Halary JL, Laupretre F and Monnerie L, *Polymer Materials: Macroscopic Properties and Molecular Interpretations*. Wiley, Hoboken, NJ (2011).
- 33 Dong H and Jacob KI, *Macromolecules* **36**:8881–8885 (2003).
- 34 Rozanski A, Galeski A and Debowska M, *Macromolecules* **44**:20–28 (2011).



Contents lists available at ScienceDirect

Polymer Degradation and Stability

journal homepage: www.elsevier.com/locate/polydegstab

Thermo-mechanical degradation of plasticized poly(lactide) after multiple reprocessing to simulate recycling: Multi-scale analysis and underlying mechanisms

B. Brüster^a, F. Addiego^{a,*}, F. Hassouna^b, D. Ruch^a, J.-M. Raquez^c, P. Dubois^c^a Department Materials Research and Technology (MRT) and National Composite Centre - Luxembourg (NCC-L), Luxembourg Institute of Science and Technology (LIST), ZAE Robert Steichen, 5 Rue Bommel, L-4940 Hautcharage, Luxembourg^b Department of Chemical Engineering, University of Chemistry and Technology (UCT) Prague, Technická 3, Prague 6 – Dejvice, 166 28, Czech Republic^c Laboratory of Polymeric and Composite Materials (LPCM), Centre d'Innovation et de Recherche en Matériaux Polymères (CIRMAP), Université de Mons, Place du Parc, 20, B-7000 Mons, Belgium

ARTICLE INFO

Article history:

Received 26 February 2016

Received in revised form

27 May 2016

Accepted 21 July 2016

Available online 25 July 2016

Keywords:

Poly(lactide)

Plasticization

Thermo-mechanical degradation

Reprocessing

Mechanical properties

ABSTRACT

The thermo-mechanical recycling of poly(lactide) (PLA) by reprocessing was recently considered as a new end-of-life scenario for this biosourced and biodegradable polymer. With this regard, the degradation mechanisms of plasticized PLA (pPLA) engendered by multiple reprocessing were little investigated to date, and hence, the relevancy of its reprocessing was not assessed. They were identified in this paper by a multiscale approach in the case of a lab-developed grade of pPLA obtained by the reactive extrusion of PLA with acrylated poly(ethylene glycol) (acryl-PEG) as reactive plasticizer. pPLA structure consisted of a semi-crystalline PLA matrix in which grafted poly(acryl-PEG) micro-inclusions were dispersed. Up to 5 successive processing cycles including extrusion and compression-molding, the tensile and impact properties drastically dropped indicating an embrittlement of pPLA. Structural analyses revealed that reprocessing caused these mechanisms: chain scission of PLA, crystallization of PLA, damaging of the inclusions, decrease of the size of poly(acryl-PEG) phases within the inclusions, and cracking of PLA. At the same time, the amount of grafted poly(acryl-PEG) was not influenced by the reprocessing. Inclusion damaging and matrix cracking are believed to be responsible for the embrittlement of pPLA after multiple reprocessing, which makes it not suitable for being reused for its initial application.

© 2016 Elsevier Ltd. All rights reserved.

1. Introduction

Poly(lactide) (PLA) currently raises hope to replace petroleum-based polymers due to its lower environmental impact concerning production related to its renewability, and waste management related to its biodegradability [1]. The end-of-life scenarios of PLA include composting, but also incineration and chemical recycling, all these scenarios provide a low carbon dioxide footprint [2]. Recently, it was shown that thermo-mechanical recycling by reprocessing and reuse of PLA could further reduce energy and renewable resource consumption compared to the end-of-life scenarios indicated above [3]. While the thermo-mechanical recycling of common petroleum-based polymers like high-density

polyethylene (HDPE) [4], polypropylene (PP) [5], and polyethylene terephthalate (PET) [6] was intensively investigated with well-identified degradation mechanisms, degradation of PLA was scarcely studied. Pillin et al. [7] reprocessed PLA by injection molding up to seven times and observed a decrease of the glass transition temperature from 66 °C to 57 °C. The initial molecular weight decreased to 50% already after three reprocessing steps and the viscosity dropped from initial 3960 Pa.s to 25 Pa.s after seven cycles. At the same time, the crystallinity increased to values over 50%. Concerning mechanical properties, Pillin et al. [7] also showed that recycling had no impact on the tensile modulus of PLA after seven cycles, while at the same time its stress at break drastically decreased from 65 MPa to 25 MPa. It was explained that the raised crystallinity in combination with the lower molecular weight dropped the ultimate strain during reprocessing. Badia et al. [8] confirmed the previous work [7] and justified the chain scission

* Corresponding author.

E-mail address: frederic.addiego@list.lu (F. Addiego).

with increasing crystallization enthalpy, while the cold crystallization temperature decreased by nearly 10 °C. Furthermore, in this particular study PLA stayed amorphous during the recycling and by FTIR no significant change in functional groups was observed. Another study [9] dealt with the impact of multiple extrusions on PLA properties. On the one side, the tensile strength, the tensile stress at break and the impact strength decreased slightly by less than 10% and the Young's modulus did not vary. On the other side, the glass transition temperature was not influenced, but the cold crystallization temperature decreased. Since the crystallization and melting enthalpy increased equally, the material was considered to remain amorphous, despite the increased cold crystallization ability. All studies dealing with the recycling or reprocessing of PLA came to the same conclusion. The main degradation mechanism was proved to be chain scission engendering a change of thermal properties and a decrease of mechanical performance. It was concluded that PLA material cannot be re-used for the same applications unless virgin pellets of PLA are mixed with a maximum of 50% of recycled ones [10] or stabilizers are used in the initial formulation [7].

Compared to PET or HDPE, the low thermal stability and the low impact resistance at room temperature of PLA limit its application range. One common way to improve PLA's impact resistance is its plasticization by dispersing a plasticizer within PLA matrix [11]. However, phase separation and plasticizer migration toward PLA surface occur in the case of low molecular weight plasticizer, which is at the origin of the interest for the grafting between PLA backbone and the plasticizer by reactive extrusion [12–16]. Processing of PLA with an acrylated poly(ethylene glycol) (acryl-PEG) by this method lowered the glass transition temperature significantly (up to 20 °C lower). Concerning mechanical properties, plasticized PLA obtained by reactive extrusion had a decreased elastic modulus at room temperature (around 25% lower), increased the ultimate strain at room temperature (up to 165% higher), and increased impact energy at room temperature (more than 30 times higher) compared to neat PLA [15–17]. Special attention was paid to the original structure of this modified PLA. In the study conducted by Kfoury et al. [16], the reactive extrusion at 180 °C of PLA with acryl-PEG and 2,5-bis(tert-buthylperoxy)-2,5-dimethylhexane used as free-radical initiator (half-life time of 1 min at 180 °C [18]) formed a material composed of a plasticized PLA matrix, free (non-grafted) poly(acryl-PEG), and on the PLA backbone grafted poly(acryl-PEG) micro-inclusions that led to partial cross-linking of PLA. The appearance of partially grafted inclusions was proved by Soxhlet extraction highlighting an extracted fraction of poly(acryl-PEG) comprised between 5 wt% and 8 wt% for an initial acryl-PEG amount of 20 wt% [15,16].

To the best of our knowledge, just a few studies dealt with the thermo-mechanical recycling of modified or plasticized PLA. Scafaro et al. [19] analyzed the degradation mechanisms of PLA containing 8% of a commercial impact modifier after multiple injection molding procedures and reached the same conclusions as for neat PLA: the main degradation mechanism was chain scission leading to poor mechanical properties, although the crystallinity was improved. However, little details were provided in this pioneer work that lacks microstructural and molecular characterization of the recycled modified PLA, as well as no comparison with the reference neat PLA. Further works are needed to identify the degradation mechanisms of the impact modifier itself, and to understand the effective influence of the impact modifier on the degradation mechanisms of PLA.

The objective of this work was to identify the degradation mechanisms engendered by multiple reprocessing of a plasticized PLA (pPLA) grade obtained by grafting/polymerizing acryl-PEG within PLA via reactive extrusion, and of a neat PLA grade as

reference. Due to the complexity of the pPLA structure, a multi-scale characterization approach was considered. In particular, the viscoelastic, tensile, and impact behaviors were first assessed as a function of the processing number. Thermal characterization of the materials by differential scanning calorimetry (DSC) was also conducted. To understand these macroscopic aspects, the microstructure of the as-(re)processed materials was analyzed by scanning electron microscopy (SEM) and atomic force microscopy (AFM). Last, attention was focused on the molecular scale in terms of i) chemical structure by nuclear magnetic resonance (¹H NMR) spectroscopy, ii) chemical functions by Fourier transform infrared (FTIR) spectroscopy, and iii) molecular weight by size exclusion chromatography (SEC) and rheology testing. To provide details about the degradation mechanisms of pPLA, some separations between the non-grafted plasticizer and the PLA matrix phase were conducted by Soxhlet extraction, and the extracted material fractions were analyzed at the molecular scale.

2. Experimental

2.1. Materials

Poly(lactide) (PLA) reference 4042D (4.2% D-lactide content) was purchased from NatureWorks LLC (Minnetonka, MN, USA). PLA did not contain neither stabilizer nor antioxidant. The plasticizer poly(ethylene glycol) methyl ether acrylate (acryl-PEG, Mn 480 g/mol) and the free-radical initiator 2,5-bis(tert-buthylperoxy)-2,5-dimethylhexane (Luperox101 or L101) were ordered from Sigma-Aldrich (Steinheim, Germany). At the investigated processing temperature (180 °C) the initiator offered a half-life time of 1 min that was suitable to produce significant reaction [16,18].

2.2. Processing

2.2.1. Extrusion

Processing and reprocessing of PLA and pPLA were simulated with laboratory equipment, meaning with small material quantities and specific machines with operating conditions that may only partially reflect industrial realities. Nevertheless, lab-scale simulation of recycling appeared as a fast and cost-effective procedure to get first information about recycling-induced degradation mechanisms of the materials enabling to optimize an eventual scale-up study of their recycling.

Before the first extrusion, neat PLA was dried in a vacuum oven (Thermo-Scientific Heraeus, Waltham, MA, USA) at 50 °C for 12 h. The two materials, PLA (PLA/acryl-PEG/L101 with weight composition 100/0/0) and plasticized pPLA (PLA/acryl-PEG/L101 with weight composition 79/20/1) were extruded using a twin screw micro-compounder reference Xplore 15 cc from DSM (Geleen, Netherlands) with a nitrogen purge. The melting temperature was set to 180 °C and the screw speed was adjusted to 50 rpm. In total 12 g per batch were introduced within the micro-compounder for a total extrusion time of 5 min (with recirculation) to produce strands of diameter 3–5 mm. For pPLA reactive extrusion, acryl-PEG and L101 were first mixed in a glass vial and then injected within the micro-compounder by means of a syringe after the PLA was melted in the extruder. In the rest of the manuscript, (p)PLA stands for PLA or pPLA.

2.2.2. Compression molding

Before shaping by compression molding, the extruded strands were cut by hand into 5 mm-long pellets. Compression molding was conducted on a Carver manual press (Wabash, IN, USA) equipped with heating plates. (p)PLA pellets were placed in a tile mold Carver (Wabash, IN, USA) enabling to produce plates of

10 cm × 10 cm × 0.2 cm and then were melted at 180 °C for 10 min without applying any pressure. After several degassing steps by successive compressing/decompressing procedures with a maximum applied load of 7 metric tons, the materials were compressed with a constant applied load of 7 metric tons at 180 °C for 10 min. The plates were cooled down under the same pressure during 10 min by a room temperature water circulation within the press plates.

2.2.3. Reprocessing

After the shaping by compression molding, the recycling was simulated by several cutting/extrusion/cutting/compression-molding procedures, as represented in Fig. 1. Each cutting step was done by hand using a sharp tile nipper. Before each re-extrusion, pPLA pellets were dried at 30 °C in a vacuum oven for 12 h, while PLA pellets were dried at 50 °C under the same conditions due to the T_g difference between the two materials. All samples were named starting with their material type (PLA, pPLA) and finishing with the number of compression molding steps (CM1, CM3, CM5). It is to be noted that the characterization was systematically conducted from the shaped plates of (p)PLA.

2.3. Characterization

2.3.1. Dynamic mechanical analysis

The viscoelastic response of (p)PLA was assessed by dynamic mechanical analysis (DMA) using a Netzsch DMA 42 C equipment (Selb, Germany). For this measurement, samples with dimensions 10 mm × 60 mm × 2 mm were machined from compression-molded plates. DMA testing was conducted with the double cantilever mode of flexural loading in the temperature range from −100 °C to 120 °C with a heating rate of 2 K/min. The specimens were subjected to a loading amplitude of 20 μm and frequencies of 1, 5, 10, 50 and 100 Hz. Attention was focused on the evolution of storage modulus E' , and loss factor $\tan \delta = E''/E'$ (E'' was the loss modulus) as a function of the temperature. All the materials were tested twice.

2.3.2. Tensile testing

The elastoviscoplastic response of (p)PLA at different temperatures was obtained by tensile testing. Dumbbell specimens were machined from the 2 mm-thick compression-molded plates to obtain ASTM D638-10 sample type V specimens. The quasi-static uniaxial tensile testing was measured with a universal testing machine Instron model 5967 (Norwood, MA, USA) equipped with an environmental chamber at the temperatures 20 °C, 50 °C and 80 °C. First, the environmental chamber was heated to the targeted testing temperature and then was left to this temperature for temperature homogenization during 30 min. The specimen was mounted and left 15 min at the chamber temperature for thermal equilibration before being tested. The engineering axial stress σ –axial strain ϵ curves were recorded at the constant crosshead speed of 60 mm/min. Based on the tensile specimen gauge length of 25 mm, the corresponding initial strain rate $\dot{\epsilon}$ was $4 \times 10^{-2} \text{ s}^{-1}$. It is important to note that the deformation of (p)PLA was non-uniform and led to necking due to geometrical, structural, and/or mechanical defects [20]. Our reported engineering axial stress σ –axial strain ϵ tensile curves did not take into account localization of strain because of technical limitations. The tensile modulus E , the yield stress σ_y , the ultimate strain ϵ_u and the ultimate stress σ_u of the materials were calculated as a function of the number of recycling cycles and the temperature. For every condition at least three specimens were tested.

2.3.3. Impact testing

For impact testing, specimen of dimensions 62 mm × 8 mm × 2 mm were machined from compression molded plates. The specimen were notched with an Instron Ceast Motorized Notchvis machine (Norwood, MA, USA). The radius of the notch was 25 mm, while its angle was 45°. The samples were tested on an impact pendulum Instron Ceast 9050 (Norwood, MA, USA) at room temperature according to ISO 180 standard. The exact specimen dimensions were measured and the impact energy was calculated by the integrated software of the pendulum machine. At least 5 specimens were tested per condition.

2.3.4. Differential scanning calorimetry

The glass transition temperature (T_g), the melting temperature (T_m), the melting enthalpy (ΔH_m), and the cold crystallization enthalpy (ΔH_{cc}) of (p)PLA were obtained by differential scanning calorimetry (DSC) from samples with weight comprised between 3 mg and 5 mg. DSC measurements were done by using a Netzsch DSC 204 F1 (Selb, Germany), while the curves were analyzed with the Software Netzsch Proteus Thermal Analysis. The samples were cooled down to −100 °C and then were heated to 180 °C. The selected heating and cooling rates were 10 K/min and −10 K/min, respectively. All the thermal properties (T_g , T_m , ΔH_m , and ΔH_{cc}) were calculated from the heating stage. The crystallinity was calculated based on equation (1), where $x_{\text{acryl-PEG}}$ was the total amount of acryl-PEG, and $\Delta H_{m,0}$ was the melting enthalpy of a 100% crystalline PLA determined to be $H_{m,0} = 93 \text{ J/g}$ [21].

$$X_c = \frac{\Delta H_m - \Delta H_{cc}}{(1 - x_{\text{acryl-PEG}}) \Delta H_{m,0}} \quad (1)$$

2.3.5. Scanning electron microscopy

The microstructure of pPLA was studied by means of a pressure-controlled scanning electron microscope (SEM) model Quanta FEG 200 from FEI (Eindhoven, The Netherlands). The samples were cut from compression molded plates and prepared by polishing the surface with a manual polishing machine. SEM observations were done at a water pressure of 150 Pa, with an accelerating voltage $\leq 7 \text{ kV}$ to limit the pPLA surface degradation and with the large field detector for topographical contrast imaging.

2.3.6. Atomic force microscopy

The morphology of the samples was characterized by means of an atomic force microscope (AFM) in acoustic mode on an Agilent 5100 from Agilent Technologies (Santa Clara, CA, USA). The scanned pictures consisted of 512 pixels × 512 pixels images obtained at a scanning speed comprised between 0.9 and 1.1 lines per second. As operating parameters, a cantilever free amplitude of 2 μm and a resonance frequency of 285.8 kHz were selected. The samples were prepared with a cryo-ultramicrotome Leica EM UC6/UF6 (Vienna, Austria) at −50 °C by cutting small surfaces first with a glass knife and polishing the surface subsequently with a diamond blade (Diatome Cryo 35°, Hatfield, PA, USA).

2.3.7. Size exclusion chromatography

The molecular weight and molecular weight distribution of PLA were assessed by size exclusion chromatography (SEC). To this end, samples were dissolved in chloroform to a concentration of 1.5 mg/ml and filtered with a nylon acrodisc syringe filter (pore size 0.45 μm). SEC was performed on an Agilent Technologies series 1200 (Santa Clara, CA, USA) working with a differential refractive index detection and two linear columns (PLgel 5 μm Mixed-D,

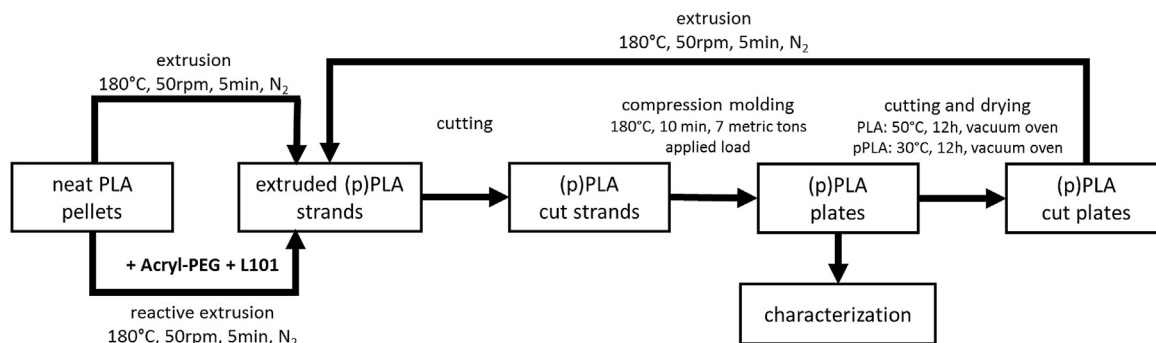


Fig. 1. Processing and reprocessing procedures of (p)PLA including the main experimental conditions.

200 Da < MW < 400 kDa) in addition to a protection column. The number average (M_n) and weight average molecular (M_w) weights standardized to polystyrene and the dispersity index ($D = M_w/M_n$) were determined for all the samples. At least 3 samples were tested for each material and the average with standard deviation was calculated from these 3 values. Note that pPLA samples were not totally soluble in chloroform, so that no SEC measurement on this material could be performed.

2.3.8. Fourier transform infrared spectroscopy

The chemical functions of (p)PLA were characterized by Fourier transform infrared spectroscopy (FTIR). Such analyses were conducted on a Bruker Tensor 27 (Ettlingen, Germany) in attenuated total reflection (ATR) mode. First, a background spectrum was recorded and subtracted from the sample spectrum in the area from 4000 cm^{-1} to 400 cm^{-1} .

2.3.9. Nuclear magnetic resonance spectroscopy

The chemical structure of (p)PLA was analyzed by nuclear magnetic resonance spectroscopy (NMR). In particular, the samples were dissolved in deuterated chloroform (CDCl_3 , containing 0.03% of tetramethylsilane (TMS)) to obtain a concentration of about 50 mg/ml. ^1H NMR spectra were recorded with a Bruker AMX-500 (Karlsruhe, Germany) at a frequency of 500 MHz and in a magnetic field of 11.6 T. Peak positions and integrals (PLA: CH_3 doublet at 1.58 ppm and CH at 5.16 ppm; poly(acryl-PEG): CH_2 singlet at 3.59 ppm) were determined with the software MestReNova (Mestrelab Research S.L., Santiago de Compostela, Spain) and the acryl-PEG weight content was determined by equation (2):

$$\text{wt\%(PEG)} = \frac{\frac{\text{area}_{\text{PEG}}}{N_{\text{H,PEG}}} \cdot M_{\text{PEG}}}{\frac{\text{area}_{\text{PLA}}}{N_{\text{H,PLA}}} \cdot M_{\text{PLA}} + \frac{\text{area}_{\text{PEG}}}{N_{\text{H,PEG}}} \cdot M_{\text{PEG}}} \quad (2)$$

2.3.10. Rheology

The rheology measurements were conducted to obtain from the viscosity values qualitative information about the molecular weight of cross-linked pPLA samples. To this end, testing was conducted on an ARES Rheometer from Rheometrics (Piscataway, NJ, USA) at 180 °C. The gap for the sample was 0.5 mm and the diameter of the plates was 25 mm. The measurements were conducted on the same samples in two modes. Strain sweep mode at a frequency of 1 Hz was conducted in the strain range 100%–0.01%, while frequency sweep mode at a strain of 1% (if 1% contained in the linear area of strain sweep) was conducted from 100 Hz to 0.01 Hz. For both measurement modes, 30 points per decade were recorded.

2.3.11. Soxhlet extraction

The non-grafted fraction of poly(acryl-PEG) within pPLA was extracted and quantified by Soxhlet extraction with methanol. An extraction thimble was filled with about 1.5 g of (p)PLA (m_o) sample and put in a 100 ml Soxhlet extractor. The extractor was set between a 500 ml round-bottom flask filled with 350 ml of methanol and a reflux condenser. The soluble fraction was extracted for 24 h under reflux. The remaining solid fraction was dried at 50 °C in a vacuum oven over night and the methanol was evaporated from the extracted fraction and extracted fraction was also dried at 50 °C in a vacuum oven over night. The percentage of extracted fraction (EF) was calculated from the mass of extracted fraction (m_{EF}) based on equation (3) and this fraction was further characterized by SEC and ^1H NMR.

$$\text{EF} = \frac{m_{\text{SF}}}{m_o} \quad (3)$$

3. Results and discussion

3.1. Influence of the reprocessing on the macroscopic behaviors

The viscoelastic behavior of pPLA (PLA/acryl-PEG/L101 79/20/1 in wt%) and of the neat reference PLA (PLA/acryl-PEG/L101 100/0/0 in wt%) processed under the same conditions were studied by DMA analysis. For the case pPLA CM5, it was not possible to machine DMA specimen that systematically broke during the machining, highlighting a certain brittleness of the materials. Fig. 2 illustrated the viscoelastic responses of pPLA and PLA in the temperature range from –100 °C to 120 °C at a frequency of 5 Hz. Briefly, in the temperature range –30 °C to 50 °C, the plasticizing led to a decrease of PLA storage modulus and an increase of PLA loss factor, indicating a lower ability to restore mechanical energy and a higher ability to dissipate it, respectively. These findings confirmed previous results where the differences between PLA and pPLA were discussed in details [16]. The glass transition temperature T_g was defined as the corresponding peak position in the $\tan \delta$ – temperature T curves. T_g was equal to 50 °C for pPLA CM1 and 65 °C for PLA CM1. Consequently, the reactive extrusion of PLA with acryl-PEG led to a decrease of T_g of about 15 °C in comparison with neat PLA. Based on all the DMA data obtained at different frequencies, no important impact of recycling was noted on the E' – T , E'' – T and $\tan \delta$ – T curves. However, recycling caused a weak shift of the cold-crystallization peak toward lower temperatures for pPLA when comparing CM1 with CM3 (Fig. 2 (a)) and for PLA when comparing CM1 with CM3 or CM5 (Fig. 2 (b)). Recycling also engendered a decrease of the storage modulus of PLA when comparing CM1 with CM3 or CM5 demonstrating a lower ability of

PLA to restore mechanical energy after reprocessing (Fig. 2 (a)).

The typical tensile behavior of PLA and pPLA assessed at 50 °C was represented in Fig. 3, while the extracted mechanical parameters at all the temperatures were reported in Table 1. In this part, we decided to test all the materials at 50 °C and 80 °C, while at 20 °C only PLA CM1, pPLA CM1 and pPLA CM3 were tested. This is due to the fact that tensile testing is material-consuming especially for repeatability, it was hence chosen to promote tensile testing at high temperatures for which PLA and pPLA may exhibit a high ductility. At 20 °C, the tensile modulus of PLA CM1 was higher than that of pPLA CM1 (3062.0 MPa vs. 1134.7 MPa), as was the case in the evolution of the storage modulus E' as a function of temperature in DMA measurement (Fig. 2 (a)). Moreover, plasticization improved the ductility as shown by the increase of elongation at break from 4.1% for neat PLA CM1 to 54.1% for pPLA CM1 yielding a material having a wide elastoviscoplastic stage at 20 °C, as described in a previous work [17]. At the same time, the plasticization decreased the tensile resistance as shown by the decrease of ultimate stress σ_u from 71.9 MPa for PLA CM1 to 19.4 MPa for pPLA CM1, and the decrease of yield stress σ_y from 77.9 MPa for PLA CM1 to 26.6 MPa for pPLA CM1. For the non-recycled materials, the tensile modulus E decreased, the yield stress σ_y decreased, the ultimate strain ε_u increased and the ultimate stress σ_u decreased with increasing temperature. It is to be noted that PLA was very soft at 80 °C with a tensile modulus of about 2 MPa, and hence, achieved the displacement limit of the machine corresponding to 800% of elongation with no breaking point. pPLA was more ductile than PLA

only at room temperature, for the other temperatures the opposite case was noted. The tensile modulus of pPLA did not significantly vary with recycling, as noted for the storage modulus measurements by DMA (Fig. 2 (a)). In contrast, pPLA ultimate strain markedly decreased with recycling at all the temperatures, demonstrating an important embrittlement of the material that exhibited no or limited elastoviscoplasticity (Table 1). For example, between CM1 and CM5, ε_u decreased from 142.3% to 5.2% at 50 °C, and from 221.8% to 2.8% at 80 °C. Excepted at 20 °C, the ultimate stress σ_u of pPLA was quite constant with recycling (CM1 to CM3), σ_u of pPLA markedly decreased too with the recycling number. Concerning PLA, recycling engendered a decrease of the tensile modulus when comparing CM1 with CM3 or CM5 at 50 °C, as noted by DMA for the storage modulus measurements (Fig. 2 (a)). Contrary to pPLA, no embrittlement was noted in the case of PLA with recycling. Only a decrease of the tensile resistance was observed through the decrease of σ_u when comparing the non-recycled material with the materials processed 3 times or 5 times at 50 °C and 80 °C.

The impact testing, carried out at 20 °C, showed for PLA a slight decrease from the first to the third recycling cycle, but no change up to the fifth (Table 1). Concerning pPLA, it was again not possible to machine impact testing specimen that systematically broke during the machining of the notch, showing again a certain brittleness of the materials. pPLA CM1 exhibited a higher impact energy (4.7 kJ/m² compared to 3.6 kJ/m² for PLA CM1), but after three recycling cycles the impact energy of pPLA decreased to 2.1 kJ/m² (pPLA CM3), which was below that of the recycled PLA samples PLA CM3 (2.4 kJ/m²). Therefore, after 3 processing, the toughness of pPLA decreased by 55.3%, while that of PLA decreased by 33.3%. The toughness decrease was hence more marked for pPLA than for PLA. It is important to mention here that due to different processing conditions, we did not attain the toughness of pPLA indicated in a previous study (101.6 kJ/m² for PLA/acryl-PEG/L101 79/20/1 wt%) [22]. Indeed, due to a motor torque limitation of the extruder it was not possible to mix the same amount of material (12 g instead of 15 g) and use the same speed (50 rpm instead of 100 rpm). Our processing conditions certainly lead to a less intense elongational flow in the extruder compared to the previous study. It is thought, that decreasing elongational flow yields to a lower dispersion state of the plasticizer and free-radical initiator within PLA matrix, and hence, to a non-optimal dispersion of the inclusions limiting the toughness increase.

The thermal properties of PLA and pPLA were analyzed by DSC and the extracted results were summarized in Table 2. pPLA exhibited a higher crystallinity compared to PLA ($X_c = 31.2\%$ vs. $X_c < 1\%$) that was considered as amorphous. An important finding was that pPLA crystallinity increased slightly from 31.2% to 35.6% with recycling. At the same time, PLA remained amorphous whichever the processing number was. The determined crystallinity was confirmed by x-ray diffraction (XRD) testing based on the methodology reported in a previous work [14] (curves not shown here). Another important finding was the presence of a double melting peak for pPLA that is transformed into a simple melting peak with recycling, while it was the opposite situation for neat PLA. Furthermore, the main melting peak was positioned at $T_m = 151.0$ °C for pPLA and $T_m = 155.8$ °C for PLA, indicating thinner lamellae in the case of pPLA compared to PLA during the melting. Based on the study of Ma et al. [23], the double melting peak in pPLA can be interpreted as the presence of thin crystals with different extent of perfection due to the grafting of plasticizer [24], while for PLA, crystals may have a higher perfection and hence may be thicker. Recycling caused a disappearance of the double peak for pPLA indicating a higher perfection compared to pPLA processed one time. On the contrary, recycling induced crystal imperfection in

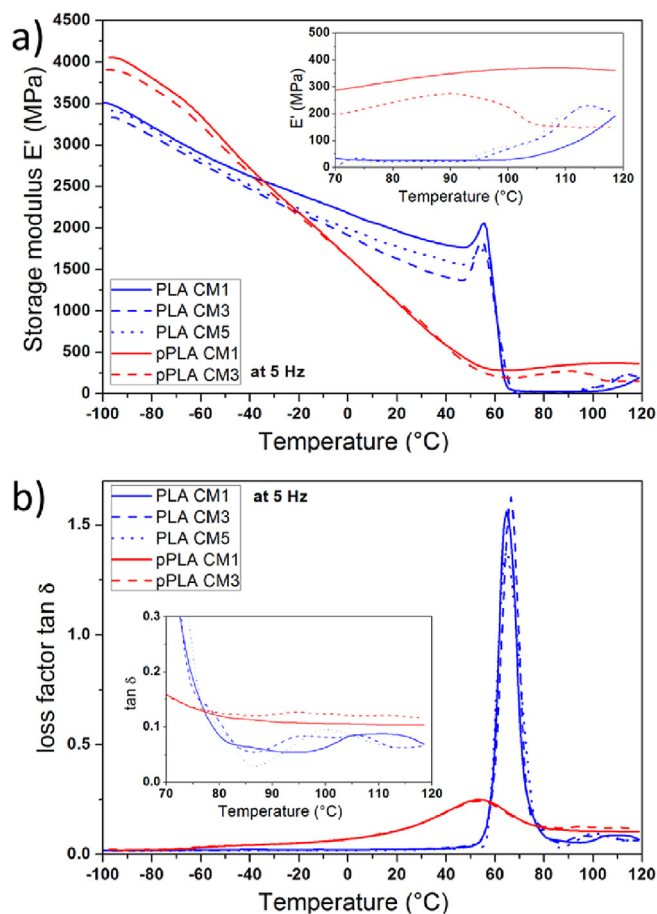


Fig. 2. DMA analysis of PLA and pPLA after 1, 3, and 5 processing cycles in the temperature range from –100 °C to 120 °C at 5 Hz with some high temperature close-up views: a) storage modulus E' , and b) loss factor $\tan \delta$.

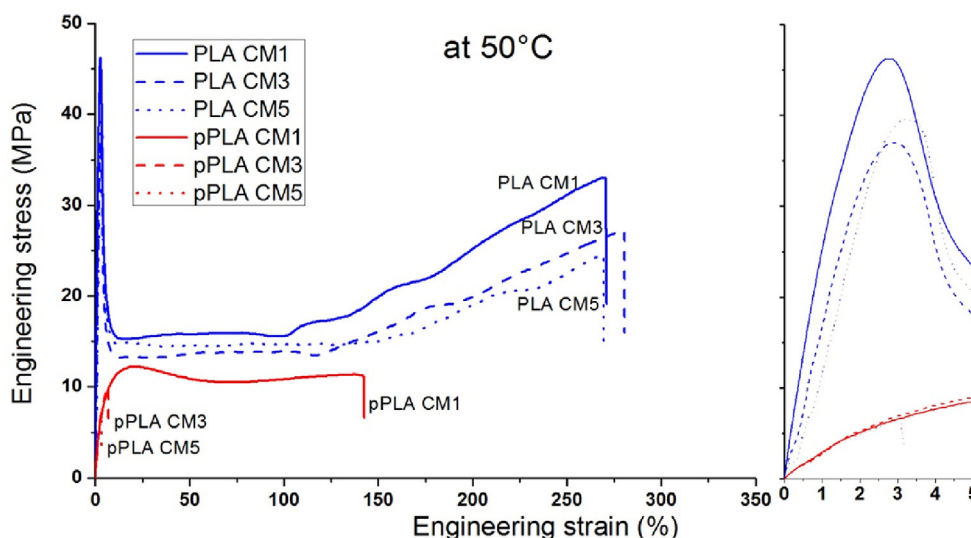


Fig. 3. Influence of the processing cycle on the tensile curves engineering stress – engineering strain of pPLA and PLA as reference including a zoom-in view of the initial part of the curves at 50 °C.

Table 1

Mechanical parameters with standard deviation obtained from tensile testing at 20 °C, 50 °C and 80 °C, and impact testing for pPLA and PLA as reference (n.t. stands for non-tested, n.m. stands for non-measurable, no b.p. stands for no breaking point at the maximum crosshead displacement of the tensile machine).

Temperature	Material	Recycling cycle	Tensile modulus E (MPa)	Yield stress σ_y (MPa)	Ultimate strain ϵ_u (%)	Ultimate stress σ_u (MPa)	Impact energy (kJ/m ²)
20 °C	PLA	CM1	3062.0 (± 17.3)	77.9 (± 2.3)	4.1 (± 0.3)	71.9 (± 0.1)	3.6 (± 0.8)
		CM3	n.t.				2.4 (± 0.1)
		CM5	n.t.				2.4 (± 0.1)
	pPLA	CM1	1134.7 (± 56.1)	26.6 (± 0.4)	54.1 (± 9.7)	19.4 (± 1.0)	4.7 (± 0.7)
		CM3	1212.7 (± 36.3)	2.3 (–)	3.2 (± 2.3)	22.5 (± 3.8)	2.1 (± 0.2)
		CM5	n.t.				n.t.
50 °C	PLA	CM1	2511.5 (± 2.4)	46.2 (± 1.0)	272.0 (± 2.0)	34.1 (± 1.3)	
		CM3	1930.4 (± 242.6)	42.2 (± 4.5)	217.5 (± 55.5)	22.5 (± 4.2)	
		CM5	1458.0 (± 296.8)	39.0 (± 1.9)	233.7 (± 92.5)	22.4 (± 6.8)	
	pPLA	CM1	297.1 (± 10.4)	12.3 (± 0.1)	142.3 (± 9.5)	11.5 (± 0.2)	
		CM3	273.4 (± 18.6)	7.1 (± 0.3)	6.6 (± 0.5)	9.5 (± 0.4)	
		CM5	285.5 (± 7.3)	5.3 (–)	5.2 (± 4.7)	5.3 (± 0.6)	
80 °C	PLA	CM1	2.9 (± 0.5)	1.0 (± 0.0)	>800, no b.p.	>11.9, no b.p.	
		CM3	2.7 (± 0.1)	0.7 (± 0.0)	>800, no b.p.	>4.1, no b.p.	
		CM5	2.5 (± 0.2)	0.7 (± 0.0)	>800, no b.p.	>1.5, no b.p.	
	pPLA	CM1	131.6 (± 12.5)	n.m.	221.8 (± 75.6)	6.9 (± 0.1)	
		CM3	147.8 (± 19.5)	4.5 (± 0.4)	5.8 (± 0.4)	5.8 (± 0.7)	
		CM5	148.8 (± 6.5)	n.m.	2.8 (± 0.5)	3.5 (± 0.6)	

the case of PLA. PLA melting temperature (T_m) increased slightly when comparing PLA CM1 with PLA CM3 or PLA CM5, while that of pPLA was quite constant. Furthermore, for PLA the cold crystallization enthalpy (ΔH_{cc}) increased with the processing number, while the cold crystallization temperature (T_{cc}) decreased. In contrast to PLA, pPLA did not exhibit any cold crystallization peak in DSC unlike in DMA. Cold crystallization results from sufficient chain mobility that leads to chain orientations. Zhang et al. [25] demonstrated that the simple addition (without grafting) of amorphous phase of poly(3-hydroxybutyrate-co-3-hydroxyvalerate) (PHBV) and poly(butylene succinate) (PBS) could activate the chain mobility of PLA and enhance the cold crystallization. pPLAs structure was earlier described by Kfoury et al. [13] as a PLA matrix plasticized with partially grafted poly(acryl-PEG) that formed partially cross-linked inclusions. The bonds between the PLA matrix and the plasticizer phase can reduce the PLA chain mobility and hinder the cold crystallization, while the crystallization from the melted state is possible. It is to be noted that cold crystallization of pPLA was observed by DMA testing that was conducted at a lower heating rate (2 K/min) compared to DSC

(10 K/min). As shown in previous works [15,16], pPLA had a lower glass transition temperature ($T_g = 34$ °C) compared to amorphous PLA ($T_g = 60$ °C). After recycling, pPLA glass transition was little visible and the exact glass transition temperature could not be determined by DSC, but DMA measurement showed already that recycling had no influence on T_g up to three processing. The glass transition temperature of PLA (T_g) stayed stable with increasing the recycling number (Fig. 4).

Based on their macroscopic behaviors, PLA and pPLA undergo different degradation mechanisms, and hence, the plasticization has an influence on the thermo-mechanical degradation of PLA. Concerning molecular relaxations, DMA showed nearly no effect of the recycling for pPLA, while PLA underwent a decrease of storage modulus. A shift of cold-crystallization relaxation toward lower temperatures was however observed for PLA and pPLA with recycling. Tensile testing highlighted no change of tensile modulus for pPLA with recycling (as observed in DMA), but at the same time this material was characterized by an important loss of ductility and hence an embrittlement. Concerning PLA, tensile testing showed a decrease of tensile modulus (as observed by DMA for the storage

Table 2

Data from DSC measurements with standard deviation.

Material	T _g (�C)	T _{cc} (�C)	T _m (�C)	�H _{cc} (J/g)	�H _m (J/g)	X _c (wt%)
PLA CM1	59.8 (�0.9)	127.4 (�1.9)	155.8 (�1.1)	9.0 (�3.6)	9.6 (�2.8)	0.6 (�1.2)
PLA CM3	58.9 (�1.1)	122.0 (�4.0)	158.8 (�1.2)	24.2 (�5.7)	25.3 (�4.6)	0.7 (�3.9)
PLA CM5	61.3 (�3.0)	118.4 (�1.5)	159.6 (�1.2)	30.0 (�3.4)	32.7 (�2.6)	1.8 (�2.2)
pPLA CM1	34.0 (�8.9)	63.3 (�5.5)	151.0 (�0.2)	2.2 (�0.8)	25.1 (�1.0)	31.2 (�1.5)
pPLA CM3	hardly visible	no peak	152.4 (�0.5)	1.5 (�0.6)	26.1 (�1.8)	33.5 (�2.7)
pPLA CM5	hardly visible	no peak	151.5 (�0.5)	3.2 (�1.7)	29.4 (�1.0)	35.6 (�1.1)

modulus), and a decrease of tensile resistance. Impact testing indicated a more marked decrease of toughness for pPLA than for PLA with increasing the number of processing. The variation of mechanical properties can be explained by variation of microstructure and molecular structure. For pPLA, the microstructure is linked to the quantity, size and morphology of poly(acryl-EPG) inclusions [16], crystal quantity and morphology, and possible defects/damage. The molecular structure is linked to molecular weight, chemical structure, and chemical functions.

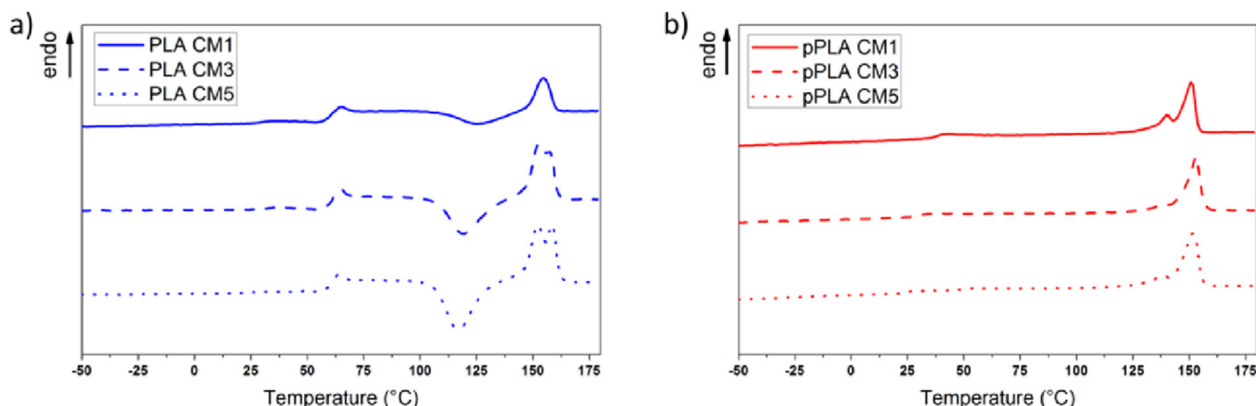
DSC testing provided first information enabling to understand the effect of recycling on the microstructure and molecular structure of PLA and pPLA. The increase of the cold-crystallization enthalpy of PLA is attributed to chain scission mechanisms, so that shorter chains enhance the possibility of cold crystallization [4–7]. However, Pillin et al. [4] recycled PLA up to seven times and reported an increase of cold crystallization enthalpy, reaching a plateau after the second recycling, and a decrease of  H_{cc} afterwards. They explained this behavior by a decrease of the molecular weight and defined 132,000 g/mol as the critical molecular weight. Below this molecular weight, the cold crystallization enthalpy decreased again. In our study, PLA's molecular weight may be higher than this critical value, since the crystallization enthalpy increased up to the fifth processing. This increase of cold crystallization enthalpy was accompanied by a decrease of the corresponding cold crystallization temperature for PLA and the decrease of PLA molecular weight can explain the decrease of tensile/storage modulus, tensile resistance and toughness observed in the mechanical testing. Indeed, in the case of an amorphous matrix, elasticity, tensile strength, and toughness decreased when the entanglement density decreased or when the molecular weight between entanglements increased [26,27]. Such changes of molecular structure may be induced by chain scission mechanisms, as reported in Ref. [28]. Considering that chain scission would be active in pPLA during recycling, as indicated by the shift of cold-crystallization relaxation toward lower temperatures in the DMA study, this mechanism would be in competition with the increase of

crystalline perfection and fraction for the control of mechanical properties. Indeed, a higher crystallinity and more perfect crystals would increase the storage/tensile modulus, tensile resistance and toughness. It is believed that chain scission mechanisms and crystallization mechanisms are in equilibrium concerning their influence on the viscoelastic properties of pPLA (tensile modulus or storage modulus) that are constant with increasing the recycling number. However, other mechanisms may be active during the viscoelastic stage of pPLA that worsen the mechanical properties of pPLA. These mechanisms will be identified in the next sections dedicated to pPLA microstructure and molecular structure.

3.2. Influence of the reprocessing on the microstructure

Although the PLA matrix and the poly(acryl-PEG) inclusions had a similar chemical structure and an exact differentiation in SEM of both phases was complicated, Fig. 5 showed some topographical differences when comparing non-recycled with recycled pPLA. After the first cycle, pPLA exhibited some white areas, and hence, some peaks scattering numerous secondary electrons (Fig. 5 (a)). These white areas are probably the edges of the soft inclusions that are deformed along the polishing direction. With increasing recycling the edges of poly(acryl-PEG) phase seemed to be better dispersed within the PLA matrix indicating that the inclusions may be smaller (Fig. 5 (b)). For the last recycling cycle, the difference between the two phases was less obvious than the previous cases (Fig. 5 (c)). The dispersion of the inclusions seemed even higher since the white edges were less visible (smaller inclusions), but at the same time cracks appeared in the material. The latter are obviously detrimental for the mechanical properties of the materials.

AFM allowed a more detailed look on the evolution of the poly(acryl-PEG) inclusions of pPLA with recycling. Fig. 6 showed the inclusions in the plasticized PLA matrix after the first, third and fifth cycle. Again, the structures of PLA and poly(acryl-PEG) lacked a strong difference in AFM, but the evolution of inclusions was

**Fig. 4.** Representative DSC curves of a) PLA and b) pPLA after 1, 3, and 5 processing cycles.

visible. First the inclusions embedded within the polymer matrix were quite round and homogeneous, while the matrix/inclusions interface seemed to be poor despite the existence of grafting. After three processing steps (Fig. 6 (b)) the inclusions were hardly observable, and appeared deformed and porous. Note that some of the pores were ellipsoids with long axis oriented in the same direction indicating shearing forces. In the last image (Fig. 6 (c)) a high porosity was visible in the inclusion that appeared totally fibrillated, and hence almost destroyed. This damage mechanism may explain why inclusions edges were less visible in the SEM investigation (Fig. 5 (c)). Recycling causes a deformation and a damage of the inclusions that appear larger than in the non-recycled pPLA but at the same time, we can obviously suppose that the remaining fragments of poly(acryl-PEG) phases within the inclusions have a reduced size. Some remaining fragments of poly(acryl-PEG) phase were visible in Fig. 6 (c) for pPLA CM5. The observed transformation of the inclusions may explain the matrix cracking observed in the SEM study. Indeed, the inclusion damage/fibrillation may significantly decrease the physical interactions between the poly(acryl-PEG) phases and the PLA matrix. PLA matrix is supposed to be hydrophobic, while PEG polymers are supposed to be more hydrophilic [29,30]. This mechanism may lead to local internal stress at the interface between poly(acryl-PEG) and PLA and may create cracks. Another possible explanation may rely on important chain scission mechanisms of the matrix that generate local shrinkage, and finally cracking [31].

SEM and AFM studies reveal that poly(acryl-PEG) micro-inclusions in pPLA suffer from shape deformation, intrinsic damage by the formation of porosity and finally fibrillation, which contribute to create weak areas in pPLA. These weak areas may localize mechanical stress and engender material breaking explaining the reported brittleness of pPLA with recycling (Fig. 3, Table 1). The interaction between i) the initial poor interface between the matrix and the inclusions (Fig. 6 (a)), ii) the porosity in the inclusions (Fig. 6 (b)), iii) the fibrillation of the inclusions (Fig. 6 (c)) and iv) the matrix cracking (Fig. 5 (c)) was not assessed to date, but it is hypothesized that these mechanisms may interact one to another one during the matrix cracking and sample breaking. It is to be noted that for other materials, recycling caused a decrease of the inclusion size without damaging. For example, Wang et al. [5] studied a material consisting of a polypropylene (PP) matrix with dispersed ethylene octene copolymer inclusions. Likewise PLA during recycling, PP matrix underlay mainly chain scission mechanisms, but a diminishment of the inclusion size was observed without porosity formation. Beside an increase of PP crystallinity, the decrease of inclusion size was held responsible for improvement or stabilization of the mechanical properties compared to the neat matrix material. In this previous study, the inclusions were not grafted to the polymer matrix, which may indicate that in our case the inclusion grafting may be at the origin of the severe damage of the poly(acryl-PEG) micro-inclusions.

3.3. Influence of the reprocessing on the molecular structure

First it is important to confirm, that chain scission is the main degradation mechanism in PLA. Based on SEC measurement, the weight average molecular weight of PLA decreased from 289,000 g/mol (CM1) to 154,000 g/mol (CM5), whereas the dispersity did not vary during recycling (Table 3). The diminution of the molecular weight with stable dispersity affirms the suggestion of a random chain scission mechanisms through the formation of free radicals, which was described earlier and in the literature as the main mechanisms in PLA degradation [10]. Due to the absence of moisture in the materials that were systematically dried before processing and reprocessing, it is supposed that hydrolysis is not active during recycling. Furthermore, FTIR and ^1H NMR analyses attest a simple chain scission mechanism, since no functional group different from the original PLA structure was observed (results not shown here). In ^1H NMR, PLA possessed two signals: one doublet at 1.58 ppm and a quartet at 5.16 ppm dedicated to the CH_3 group and the CH group, respectively. PLA oligomers, with a lower molecular weight, also provided a peak at 4.37 ppm dedicated to the end-groups [32]. Even the recycled materials missed a peak dedicated to the end-groups, leading to the assumption that chain scission mechanisms suffice a reduction of molecular weight but no formation of oligomers. FTIR analysis provides as well no change after recycling. The main peaks of PLA were the asymmetric and symmetric C–H stretching of the CH_3 group and the CH_2 deformation vibration at 2995 cm^{-1} , 2945 cm^{-1} , and 1452 cm^{-1} , respectively. The chemical structure of PLA gave strong bands of oxygen functions, especially in the carbonyl band region $1700\text{--}1750\text{ cm}^{-1}$ and the observation of oxidation was not possible [33,34].

It is important to mention, that SEC analysis of pPLA was not possible, which was presumably due to a partial cross-linking during the reactive extrusion. The pPLA samples could not be dissolved in the SEC solvent sufficiently. Likewise PLA, no change of chemical functions was observed in ^1H NMR (spectra not shown here) and FTIR for pPLA (Fig. 7). However, the amount of plasticizer did not change after several recycling cycles. In ^1H NMR, the ratio between the PLA-protons (doublet at 1.58 ppm or quartet at 5.16 ppm at ppm) and PEG-protons (singlet at 3.59 ppm) remained stable. The calculation of the acryl-PEG amount from ^1H NMR results, led to amounts of 14.8 wt%, 14.6 wt%, and 14.3 wt% for the samples after 1, 3, and 5 cycles, respectively. The lower detected amount of acryl-PEG compared to the initially added amount of 20 wt% could assist the assumption of a partial cross-linking. The sample was partially dissolved and not the whole sample was detected in NMR. It is to be noted that the assumption of cross-linking was approved by gel formation. PLA and pPLA pellets were swollen in chloroform for 48 h. While the PLA was dissolved completely, pPLA formed a gel. The gel was not stable enough to be separated, but the test proved the existence of cross-link bonds in pPLA even after 5 recycling cycles.

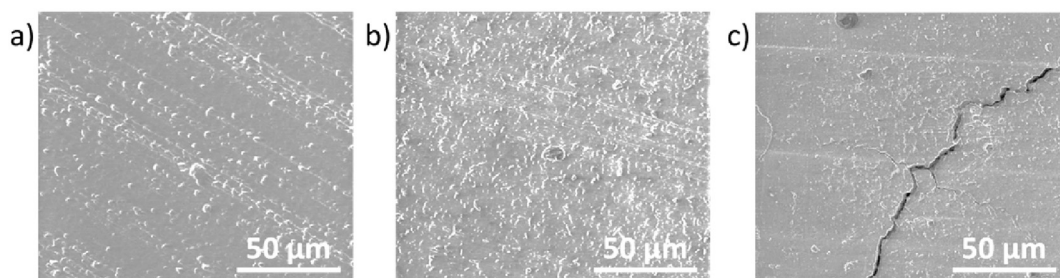


Fig. 5. SEM images of pPLA after a) 1, b) 3, and c) 5 processing cycles.

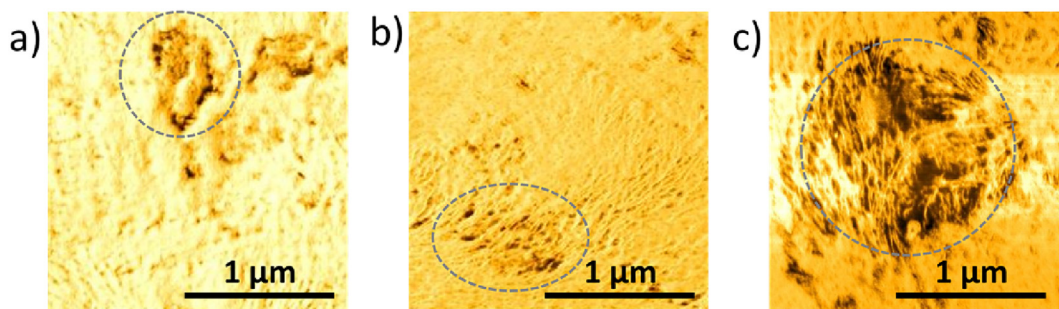


Fig. 6. AFM phase images of pPLA inclusions: a) initial inclusions in pPLA CM1, b) slightly deformed inclusions with porosity in pPLA CM3, and c) strongly deformed inclusions with fibrillation and high porosity in pPLA CM5 (inclusions were surrounded on each image).

Fig. 8 illustrated the frequency depending viscosity for PLA and pPLA from rheology measurements. The viscosity for pPLA CM1 was lower than for PLA CM1, which could be reasoned to a higher dispersity in pPLA due to the radical grafting reaction. It is evident, that the viscosity for both materials decreased with recycling indicating a degradation of the material with reprocessing. The SEC results for PLA indicated a decrease of the molecular weight and at the same time an unchanged dispersity index. In general, a decrease of the molecular weight is related to a decrease in the viscosity. Assuming that the matrix in pPLA underlies the same degradation mechanisms like PLA, the dispersity index is stable and the decreasing viscosity indicates a decrease of molecular weight with recycling. For both materials, PLA and pPLA, the curves show a Newtonian plateau. Despite the cross-linking in pPLA the plateau is visible, which leads to the assumption that the cross-linking exists in a low quantity. It is important to mention that pPLA CM3 and CM5 showed scattering of the viscosity at low frequencies, which indicates important degradation mechanisms. In particular, this finding shows that degradation is more marked for pPLA than for PLA from the recycling number 3 since no scattering of viscosity value was noted for PLA.

The calculation of chain scission number (s) gave a qualitative information about the degradation and can be calculated with the initial molecular weight (M_w^i) and the molecular weight after a recycling step (M_w) (equation (4)). Accordingly, the chain scission number for PLA CM3 and CM5 was calculated with the molecular weights from SEC measurements. Since a direct determination of the molecular weight of pPLA was not possible with SEC due to insufficient solubility, the molecular weight was substituted by viscosity from the Mark-Houwink equation (equation (5)). This equation gave a correlation between the viscosity η and the molecular weight M with the system depended parameters k and a .

$$s = \frac{M_w^i}{M_w} \quad (4)$$

$$\eta = kM^a \quad (5)$$

The parameter k was considered to be not influenced by the recycling. Therefore, the chain scission number could be described by equation (6). The a value was determined for PLA by an optimization to obtain the same values for the chain scission as

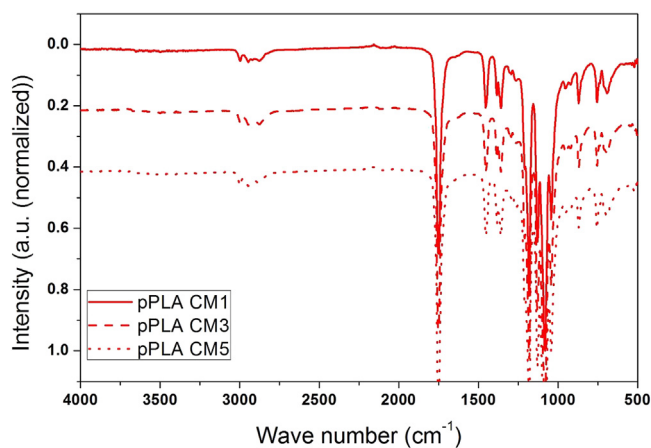


Fig. 7. FTIR spectra of pPLA after 1, 3, and 5 processing cycles.

determined with the molecular weight from SEC. The optimized a value was taken to calculate the chain scission number for pPLA.

$$s = \frac{\sqrt[a]{\frac{\eta_i}{k}}}{\sqrt[a]{\frac{\eta_f}{k}}} - 1 = \sqrt[a]{\frac{\eta_i}{k} \cdot \frac{k}{\eta_f}} - 1 = \sqrt[a]{\frac{\eta_i}{\eta_f}} - 1 \quad (6)$$

The calculation of s pPLA reported in Table 4 was just an approach for the given assumptions, that PLA matrix in pPLA behaved like PLA and that the parameters from Mark-Houwink equation were the same. Nevertheless, the calculation supported the hypothesis that the PLA matrix was stronger damaged in pPLA than in PLA. The chain scission number for pPLA was nearly double (0.85 for pPLA and 0.44 for PLA) after 3 recycling steps compared to the PLA material without plasticizer and increased to 1.48 for pPLA CM5, which means that more chains are cut during the recycling process. In particular, the molecular of pPLA weight is stronger decreased and the material becomes more brittle compared to PLA with recycling.

Soxhlet extraction with methanol allowed a separation of the non-grafted amount of plasticizer from the plasticized and partially cross-linked PLA matrix [15,16]. Non grafted poly(acryl-PEG) was soluble in methanol and hence was extracted, while the PLA matrix

Table 3

Molecular weight (M_w) and dispersity (D) with standard deviation for PLA after 1, 3, and 5 processing cycles from SEC (with polystyrene standard).

	PLA CM1	PLA CM3	PLA CM5
M_w (g/mol)	$2.89 \text{ E}+5 \pm 0.03 \text{ E}+5$	$1.99 \text{ E}+5 \pm 0.04 \text{ E}+5$	$1.54 \text{ E}+5 \pm 0.10 \text{ E}+5$
D (M_w/M_n)	2.21 ± 0.21	2.25 ± 0.13	2.20 ± 0.16

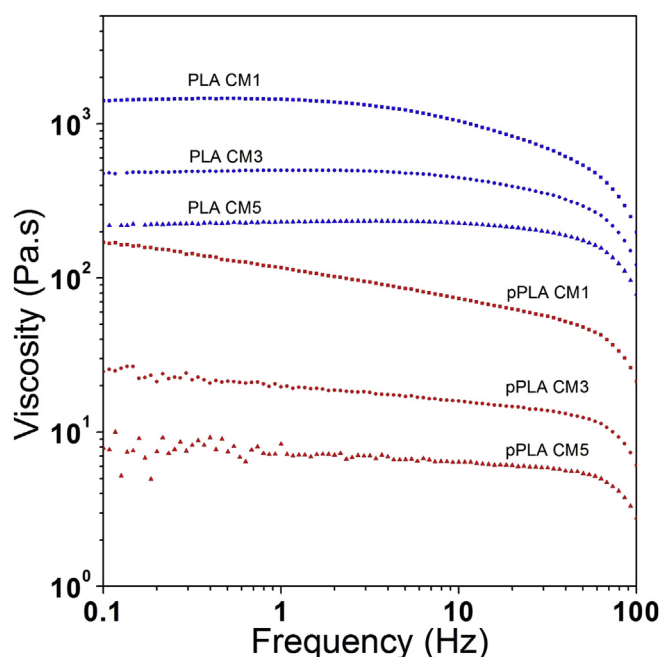


Fig. 8. Viscosity measurements in dependency on the frequency for PLA and pPLA after 1, 3, and 5 processing cycles.

was insoluble. The amount of extracted fraction ascended from 7.3 wt% after the first cycle to 9.0 wt% after the third cycle to 10.7 wt% after 5 cycles (Table 5). Even though, in the ^1H NMR of the whole sample no formation of PLA oligomers was observed, the analysis of the extracted fraction by ^1H NMR showed an increasing amount of PLA from 3.3 wt% after the first reprocessing to 24.7 wt% after the fifth reprocessing. The real values of extracted PEG fraction were calculated from this data (Table 5) and indicated just a small increase from 7.1 wt% to 8.1 wt% after 1 and 5 processing, respectively. Contrary to the above mentioned assumption, that the PLA matrix was not disturbed by the extraction, these results prove that PLA is partially extracted. Methanolysis of PLA was proved to occur in presence of catalysts [35,36], but the results of Soxhlet extraction create the impression, that the presence of poly(acryl-PEG) enhances methanolysis as well. With increasing recycling number, the amount of extractable PLA in pPLA increased, while in the samples of neat PLA no increase of this fraction was observed (extracted fraction for PLA CM1, CM3 and CM5 \approx 0.3 wt%). These findings lead to the assumption that the plasticizer phase increases the degradation of PLA matrix. Concerning the poly(acryl-PEG) inclusions, on the one side the partial cross-linking remained, which was proved by the solubility (SEC), the unchanged amount of soluble PEG (^1H NMR), and the possibility of gel formation after recycling. On the other side a slightly higher amount of poly(acryl-PEG) was extracted with average molecular weights between 6800 g/mol and 590 g/mol (Fig. 9). The peak of higher molecular weight belonged to the oligomers of acryl-PEG, which were not grafted and could be extracted easily. The second peak was associated to PEG oligomers, which did not graft during the reactive extrusion or were unhinged from the poly(acryl-PEG) inclusions. With increasing recycling the peak of single units became broader and more molecules with molecular weight between 580 g/mol and 6800 g/mol were extracted. Since the partial cross-linking endure the recycling, the extracted poly(acryl-PEG) was part of the inclusions before recycling and hence, the amount of bonded poly(acryl-PEG) in inclusions seem to be diminished. Furthermore, the observed porosity in AFM (Fig. 6) could simplify the extraction of PEG units from the

poly(acryl-PEG) inclusions. As mentioned above PLA with a high molecular weight could not be extracted by methanol, but low molecular weight PLA (like lactic acid monomer) seemed to be extracted by hot methanol. The peak with the higher average molecular weight increased with recycling and became broader. The extracted PLA seemed to be in this molecular weight range (around and below 6800 g/mol). From these results we conclude two important parts of the degradation mechanisms of pPLA. First, poly(acryl-PEG) phase size in the PLA matrix is diminished confirming AFM investigation, while the cross-linking remains, and second, PLA is degraded to low molecular weight PLA by chain scission and can be extracted with hot methanol. These findings confirm the observed higher degradation for pPLA in rheology measurements and could be reasoned by a higher hydrophilicity induced by PEG based polymers that was already described in the literature [37].

3.4. Degradation scheme of plasticized PLA

Despite the initial assumption, the PLA matrix in pPLA is differently affected by recycling than unmodified PLA matrix. Fig. 10 illustrates the main degradation mechanisms in pPLA during multiple processing affecting the matrix and the inclusions. The degradation of PLA matrix leads to shorter PLA chains, and at the same time its crystallinity increases. Furthermore, the initial spherical inclusions are deformed, damaged and fibrillated engendering a decrease of poly(acryl-PEG) phase size and leading to a high porosity in the material. It is important to mention that the inclusion grafting and cross-linking endure the recycling. For high recycling number, a crack formation occurs within the polymer matrix. Cracking may be due to the loss of physical interaction between the PLA matrix and the poly(acryl-PEG) phases, and the important chain scission mechanisms of the matrix yielding to local shrinkage and then cracking. The damage of the inclusions engendering porosity, and the polymer matrix cracking are believed to be responsible for the material brittleness observed during tensile and impact testing.

The main difference between the recycling mechanisms of PLA and pPLA is the damage of the PLA matrix. In PLA the matrix seems to be more stable and just simple chain scission occurs, which just lowers the tensile resistance and toughness, while PLA remained ductile. In contrary, in pPLA the PLA matrix underlies a stronger degradation in comparison with neat PLA. In particular, chain scission was accelerated and the molecular weight decreased strongly, so that low molecular weight PLA was extracted by methanol in the case of pPLA. Indeed, the ^1H NMR analysis proved an increasing amount of PLA in the extracted fraction and SEC showed that the extracted fraction has molecular weights between 580 g/mol and 6800 g/mol, so that PLA degraded to short chains. This phenomenon could be reasoned by the different hydrophobicity of the materials. The more hydrophilic nature of pPLA compared to PLA could support the hydrolytically induced degradation of the PLA matrix [37,38].

4. Conclusions

The work aimed at identifying the different degradation mechanisms occurring during the thermo-mechanical recycling of a plasticized PLA (pPLA) grade and to compare them to those of a neat PLA grade. The pPLA consisted of a plasticized PLA matrix with dispersed inclusions of poly(acryl-PEG) that were partially grafted onto the PLA backbone yielding to a partial cross-linking of the PLA matrix. Both materials were characterized at the macroscopic scale by mechanical and thermal testing, at the microstructure scale, and at their molecular scale after 1, 3 and 5 processing cycles.

Table 4
Chain scission number for PLA calculated with molecular weight from SEC and chain scission number for PLA and pPLA calculated with the viscosity from rheology measurements at 1 Hz and an optimized value $a = 2.9$ (n.m. stands for non-measurable).

		s from GPC	s from rheology (with $a = 2.9$)
PLA	CM3	0.45	0.44
	CM5	0.88	0.88
pPLA	CM3	n.m.	0.85
	CM5	n.m.	1.48

Table 5
Extracted fraction EF (in wt%) for PLA and pPLA after Soxhlet extraction with methanol.

	Soxhlet extraction EF in wt%	Amount of PLA in the extracted fraction in wt%	Amount of extracted PEG in wt%
pPLA CM1	7.9	3.3	7.1
pPLA CM3	9.4	14.7	7.7
pPLA CM5	10.5	24.7	8.1

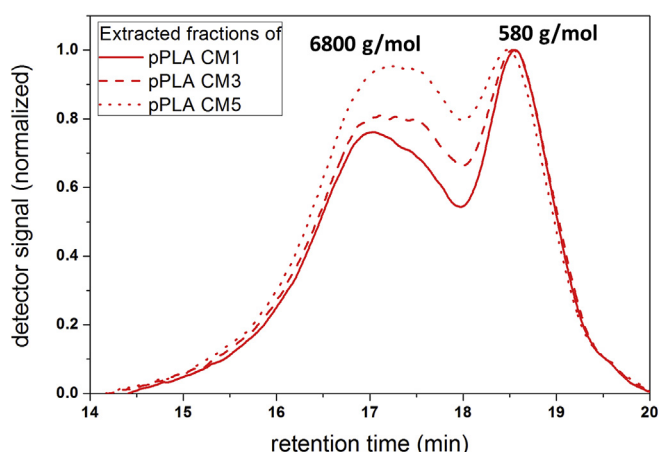


Fig. 9. SEC of soluble fraction after Soxhlet extraction with methanol.

a differentiated look on different components interacting one each other. The mechanical properties worsened from the first processing to the third processing strongly and the material became brittle since it markedly loosed tensile ductility and its toughness dropped. Note that the viscoelastic properties of pPLA were unaffected by the recycling (constant storage modulus and tensile modulus). SEM and AFM imaging proved that the inclusions of poly(acryl-PEG) underwent a marked transformation with reprocessing characterized by a deformation of their shape, damaging mechanisms through the formation of porosity, and fibrillation leading to a decrease of their size. For the highest number of processing, SEM highlighted the formation of cracks in the polymer matrix. The origin of these cracks was not completely clarified. They can be due to the coupling of poly(acryl-PEG) phase size reduction and porosity formation that may decrease the physical interactions between the matrix and poly(acryl-PEG). They can also be due to chain scission mechanisms of the polymer matrix inducing chain shrinkage and finally cracks. While FTIR and ^1H NMR analysis exposed again no change in the chemical functions, the conduction of SEC was not possible due to cross-linking that survived reprocessing up to 5 times. The increase of crystallinity after reprocessing proved a higher mobility due to chain scission, but the lack of cold crystallization noted in DSC measurements supports the assumption that cross-linking may endure the reprocessing. Since the viscosity decreased for pPLA with the recycling, a degradation of the PLA matrix in pPLA by a chain scission mechanism seemed to dominate here as well. By the calculation of the chain scission number s from the rheology data, it was shown that the pPLA matrix underlies a stronger degradation than the neat PLA. The chain scission number was nearly double for pPLA compared to PLA. Only after separation of the plasticized matrix phase and the non-grafted plasticizer by Soxhlet extraction with methanol, it was

For PLA, the main degradation mechanism was a simple random chain scission. The molecular weight gain from $289,000 \text{ g mol}^{-1}$ to $154,000 \text{ g mol}^{-1}$ was proved by SEC and led to a higher chain mobility that was confirmed by a higher ability of cold crystallization in DSC. At the same time PLA remained amorphous as shown by DSC measurements. The analysis of chemical structure by FTIR and ^1H NMR indicated no additional chemical function (end groups of PLA) compared to the non-recycled PLA. So, only a random chain scission mechanism was active during PLA recycling and was believed to be responsible for the decrease of storage modulus and tensile modulus, decrease of tensile resistance and decrease of toughness.

In pPLA, the clarification of the degradation mechanisms needed

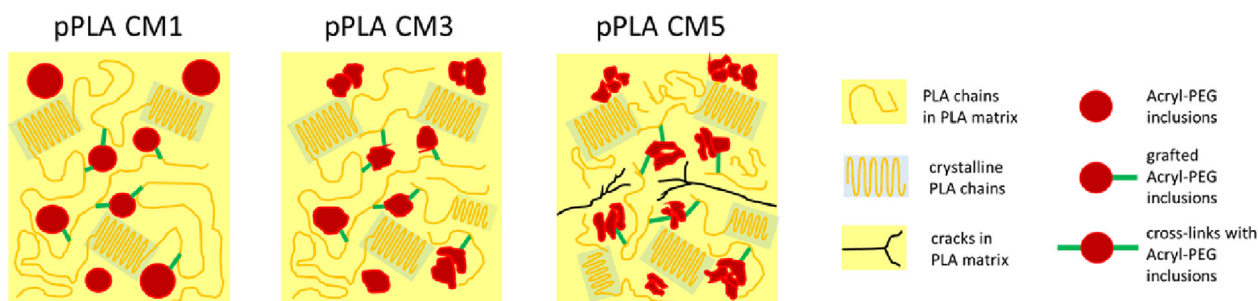


Fig. 10. Schematic degradation of pPLA after 1, 3, and 5 processing cycles.

possible to further identifying the degradation mechanisms of pPLA. While the cross-linking and poly(acryl-PEG) grafting were not influenced, the amount of extracted fraction increased and a higher amount of PLA in the extracted fraction was detected by ^1H NMR. These results show on the one side, that poly(acryl-PEG) phase size was diminished, since the extracted PEG fraction increased, and on the other side, that the PLA matrix was strongly degraded, since the molecular weight decreased to a value that the PLA can be extracted by methanol. It was concluded that the increase of pPLA crystallinity and chain scission mechanisms were in equilibrium in controlling the viscoelastic properties of the material that were constant with recycling. Concerning elastovisco-plastic properties of pPLA, the matrix cracking and the inclusions damage were believed to be responsible for the observed embrittlement. A general scheme summarizing the degradation mechanisms of pPLA was proposed.

The current work exhibits new facets about the thermo-mechanical recycling of plasticized bio-based polymers obtained by reactive extrusion. At the actual state, plasticized PLA by reactive extrusion cannot be recycled and reused for the same application. The identification of the degradation mechanisms of such multi-phase systems should be taken into account for the development of new plasticized materials that could endure the thermo-mechanical constraints of recycling. As other perspective of this work, the thermo-mechanical recycling of bio-based polymers has to better reflect industrial realities. To this end, we are currently simulating their recycling by developing scale-up extrusion procedures.

Acknowledgement

The authors are grateful to the Fonds National de la Recherche Luxembourg (FNR) for CORE project funding under reference C13/MS/5837188. Thanks also go to the Belgian Federal Government Office Policy of Science (BELSPO) for its support in the framework of the PAI-6/27. J.-M. Raquez is a research associate of the F.R.S.-FNRS.

References

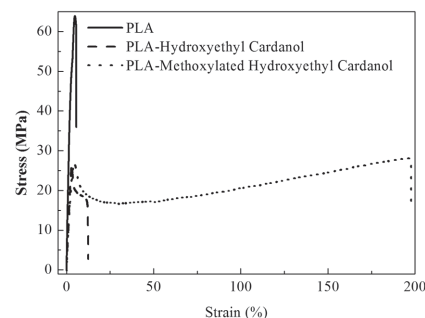
- [1] L.S. Nair, C.T. Laurencin, Biodegradable polymers as biomaterials, *Prog. Polym. Sci.* 32 (2007) 762–798, <http://dx.doi.org/10.1016/j.progpolymsci.2007.05.017>.
- [2] S. Papong, P. Malakul, R. Trungkavashirakun, P. Wenunun, T. Chom-In, M. Nithitanakul, et al., Comparative assessment of the environmental profile of PLA and PET drinking water bottles from a life cycle perspective, *J. Clean. Prod.* 65 (2014) 539–550, <http://dx.doi.org/10.1016/j.jclepro.2013.09.030>.
- [3] V. Piemonte, Bioplastic wastes: the best final disposition for energy saving, *J. Polym. Environ.* 19 (2011) 988–994, <http://dx.doi.org/10.1007/s10924-011-0343-z>.
- [4] T. Kealy, Rheological analysis of the degradation of HDPE during consecutive processing steps and for different processing conditions, *J. Appl. Polym. Sci.* 112 (2009) 639–648.
- [5] K. Wang, F. Addiego, N. Bahloul, S. Ahzi, Y. Rémond, V. Toniazzi, et al., Analysis of thermomechanical reprocessing effects on polypropylene/ethylene octene copolymer blends, *Polym. Degrad. Stab.* 97 (2012) 1475–1484, <http://dx.doi.org/10.1016/j.polymdegradstab.2012.05.005>.
- [6] J.D. Badia, F. Vilaplana, S. Karlsson, A. Ribes-Greus, Thermal analysis as a quality tool for assessing the influence of thermo-mechanical degradation on recycled poly(ethylene terephthalate), *Polym. Test.* 28 (2009) 169–175, <http://dx.doi.org/10.1016/j.polymtest.2008.11.010>.
- [7] I. Pillin, N. Montrelay, A. Bourmaud, Y. Grohens, Effect of thermo-mechanical cycles on the physico-chemical properties of poly(lactic acid), *Polym. Degrad. Stab.* 93 (2008) 321–328, <http://dx.doi.org/10.1016/j.polymdegradstab.2007.12.005>.
- [8] J.D. Badia, E. Strömberg, S. Karlsson, A. Ribes-Greus, Material valorisation of amorphous polylactide. Influence of thermo-mechanical degradation on the morphology, segmental dynamics, thermal and mechanical performance, *Polym. Degrad. Stab.* 97 (2012) 670–678, <http://dx.doi.org/10.1016/j.polymdegradstab.2011.12.019>.
- [9] M. Żenkiewicz, J. Richert, P. Rytlewski, K. Moraczewski, M. Stepczyńska, T. Karasiewicz, Characterisation of multi-extruded poly(lactic acid), *Polym. Test.* 28 (2009) 412–418, <http://dx.doi.org/10.1016/j.polymtest.2009.01.012>.
- [10] A. Soroudi, I. Jakubowicz, Recycling of bioplastics, their blends and bio-composites: a review, *Eur. Polym. J.* 49 (2013) 2839–2858, <http://dx.doi.org/10.1016/j.eurpolymj.2013.07.025>.
- [11] O. Martin, L. Averous, Poly (lactic acid): plasticization and properties of biodegradable multiphase systems, *Polymer* 42 (2001) 6209–6219, [http://dx.doi.org/10.1016/S0032-3861\(01\)00086-6](http://dx.doi.org/10.1016/S0032-3861(01)00086-6).
- [12] J.-M. Raquez, R. Narayan, P. Dubois, Recent advances in reactive extrusion processing of biodegradable polymer-based compositions, *Macromol. Mater. Eng.* 293 (2008) 447–470, <http://dx.doi.org/10.1002/mame.200700395>.
- [13] F. Hassouna, J.-M. Raquez, F. Addiego, P. Dubois, V. Toniazzi, D. Ruch, New approach on the development of plasticized polylactide (PLA): grafting of poly(ethylene glycol) (PEG) via reactive extrusion, *Eur. Polym. J.* 47 (2011) 2134–2144, <http://dx.doi.org/10.1016/j.eurpolymj.2011.08.001>.
- [14] F. Hassouna, J.-M. Raquez, F. Addiego, V. Toniazzi, P. Dubois, D. Ruch, New development on plasticized poly(lactide): chemical grafting of citrate on PLA by reactive extrusion, *Eur. Polym. J.* 48 (2012) 404–415, <http://dx.doi.org/10.1016/j.eurpolymj.2011.12.001>.
- [15] K. Choi, M.-C. Choi, D.-H. Han, T.-S. Park, C.-S. Ha, Plasticization of poly(lactic acid) (PLA) through chemical grafting of poly(ethylene glycol) (PEG) via in situ reactive blending, *Eur. Polym. J.* 49 (2013) 2356–2364, <http://dx.doi.org/10.1016/j.eurpolymj.2013.05.027>.
- [16] G. Kfoury, F. Hassouna, J.-M. Raquez, V. Toniazzi, D. Ruch, P. Dubois, Tunable and durable toughening of polylactide materials via reactive extrusion, *Macromol. Mater. Eng.* 299 (2014) 583–595, <http://dx.doi.org/10.1002/mame.201300265>.
- [17] K. Wang, B. Brüster, F. Addiego, G. Kfoury, F. Hassouna, D. Ruch, et al., Strain-induced deformation mechanisms of polylactide plasticized with acrylated poly(ethylene glycol) obtained by reactive extrusion, *Polym. Int.* 64 (2015) 1544–1554, <http://dx.doi.org/10.1002/pi.4927>.
- [18] F. Debaud, A. Defrancisci, L.H. Palys, SP and CST Technologies – a new generation of cost saving curatives in rubber processing, 2004.
- [19] R. Scaffaro, M. Morreale, F. Mirabella, F.P. La Mantia, Preparation and recycling of plasticized PLA, *Macromol. Mater. Eng.* 296 (2011) 141–150, <http://dx.doi.org/10.1002/mame.201000221>.
- [20] C. G'Sell, N.A. Aly-Helal, S.L. Semiatin, J.J. Jonas, Influence of deformation defects on the development of strain gradients during the tensile deformation of polyethylene, *Polymer* 33 (1992) 1244–1254, [http://dx.doi.org/10.1016/0032-3861\(92\)90770-W](http://dx.doi.org/10.1016/0032-3861(92)90770-W).
- [21] B.E.W. Fischer, H.J. Sterzel, G. Wegner, Investigation of the structure of solution grown crystals of lactide copolymers by means of chemical reactions, *Kolloid-Z uZ Polym.* 251 (1973) 980–990, <http://dx.doi.org/10.1007/BF01498927>.
- [22] G. Kfoury, J.-M. Raquez, F. Hassouna, P. Leclère, V. Toniazzi, D. Ruch, et al., Toughening of poly(lactide) using polyethylene glycol methyl ether acrylate: reactive versus physical blending, *Polym. Eng. Sci.* 55 (2015) 1408–1419, <http://dx.doi.org/10.1002/pen>.
- [23] P. Ma, L. Jiang, T. Ye, W. Dong, M. Chen, Melt free-radical grafting of maleic anhydride onto biodegradable poly(lactic acid) by using styrene as a comonomer, *Polym. (Basel)* 6 (2014) 1528–1543, <http://dx.doi.org/10.3390/polym6051528>.
- [24] K.I. Ku Marsilla, C.J.R. Verbeek, Modification of poly(lactic acid) using itaconic anhydride by reactive extrusion, *Eur. Polym. J.* 67 (2015) 213–223, <http://dx.doi.org/10.1016/j.eurpolymj.2015.03.054>.
- [25] K. Zhang, A.K. Mohanty, M. Misra, Fully biodegradable and biorenewable ternary blends from polylactide, poly(3-hydroxybutyrate-co-hydroxyvalerate) and poly(butylene succinate) with balanced properties, *ACS Appl. Mater. Interfaces* 4 (2012) 3091–3101, <http://dx.doi.org/10.1021/am3004522>.
- [26] D.W. Grijpma, A.J. Pennings, (Co) polymers of L-lactide, 2. Mechanical properties, *Macromol. Chem. Phys.* 195 (1994) 1649–1663, <http://dx.doi.org/10.1002/macp.1994.021950516>.
- [27] L. Monnerie, J.L. Halary, H.H. Kausch, Deformation, yield and fracture of amorphous polymers: relation to the secondary transitions, *Adv. Polym. Sci.* 187 (2005) 215–364, <http://dx.doi.org/10.1007/b136957>.
- [28] B. Fayolle, E. Richaud, X. Colin, J. Verdu, Review: degradation-induced embrittlement in semi-crystalline polymers having their amorphous phase in rubbery state, *J. Mater. Sci.* 43 (2008) 6999–7012, <http://dx.doi.org/10.1007/s10853-008-3005-3>.
- [29] J. Israelachvili, The different faces of poly(ethylene glycol), *Proc. Natl. Acad. Sci. U. S. A.* 94 (1997) 8378–8379, <http://dx.doi.org/10.1073/pnas.94.16.8378>.
- [30] G.L. Siparsky, K.J. Voorhees, J.R. Dorgan, K. Schilling, Water transport in polylactide acid (PLA), PLA/polycaprolactone copolymers, and PLA/polyethylene glycol blends, *J. Environ. Polym. Degrad.* 5 (1997) 125–136, <http://dx.doi.org/10.1007/BF02763656>.
- [31] B. Fayolle, L. Audouin, G.A. George, J. Verdu, Macroscopic heterogeneity in stabilized polypropylene thermal oxidation, *Polym. Degrad. Stab.* 77 (2002) 515–522, [http://dx.doi.org/10.1016/S0141-3910\(02\)00110-6](http://dx.doi.org/10.1016/S0141-3910(02)00110-6).
- [32] A. Gratia, D. Merlet, V. Ducruet, C. Lythaud, A comprehensive NMR methodology to assess the composition of biobased and biodegradable polymers in contact with food, *Anal. Chim. Acta* 853 (2015) 477–485, <http://dx.doi.org/10.1016/j.aca.2014.09.046>.
- [33] J.D. Badia, L. Monreal, V. Sáenz de Juano-Arbona, A. Ribes-Greus, Dielectric spectroscopy of recycled polylactide, *Polym. Degrad. Stab.* 107 (2014) 21–27, <http://dx.doi.org/10.1016/j.polymdegradstab.2014.04.023>.
- [34] D. Rasselet, A. Ruellan, A. Guinault, G. Miquelard-Garnier, C. Sollogoub, B. Fayolle, Oxidative degradation of polylactide (PLA) and its effects on

- physical and mechanical properties, *Eur. Polym. J.* 50 (2014) 109–116, <http://dx.doi.org/10.1016/j.eurpolymj.2013.10.011>.
- [35] X. Song, X. Zhang, H. Wang, F. Liu, S. Yu, S. Liu, Methanolysis of poly(lactic acid) (PLA) catalyzed by ionic liquids, *Polym. Degrad. Stab.* 98 (2013) 2760–2764, <http://dx.doi.org/10.1016/j.polymdegradstab.2013.10.012>.
- [36] A. Carné Sánchez, S.R. Collinson, The selective recycling of mixed plastic waste of polylactic acid and polyethylene terephthalate by control of process conditions, *Eur. Polym. J.* 47 (2011) 1970–1976, <http://dx.doi.org/10.1016/j.eurpolymj.2011.07.013>.
- [37] S.M. Li, I. Rashkov, J.L. Espartero, N. Manolova, M. Vert, Synthesis, characterization, and hydrolytic degradation of PLA/PEO/PLA triblock copolymers with long poly (L -lactic acid) blocks, *Macromolecules* 29 (1996) 57–62.
- [38] K.-M. Choi, S.-W. Lim, M.-C. Choi, Y.-M. Kim, D.-H. Han, C.-S. Ha, Thermal and mechanical properties of poly(lactic acid) modified by poly(ethylene glycol) acrylate through reactive blending, *Polym. Bull.* 71 (2014) 3305–3321, <http://dx.doi.org/10.1007/s00289-014-1251-x>.

Design of New Cardanol Derivative: Synthesis and Application as Potential Biobased Plasticizer for Poly(lactide)

Fatima Hassouma,* Iulia Mihai, Ludivine Fetzter, Thierry Fouquet, Jean-Marie Raquez, Abdelghani Laachachi, Hicham Ibn Al Ahrach, Philippe Dubois

A novel biobased plasticizer made of cardanol is designed for poly(lactide) (PLA). This cardanol-derived plasticizer, i.e., methoxylated hydroxyethyl cardanol (MeCard), is synthesized through methoxylation of the double bonds on the side chain of cardanol, and characterized by ^1H NMR and mass spectrometry. The plasticization effect of MeCard on the molecular structure, morphology, thermal and mechanical properties of PLA is evaluated and compared to that of a commercial cardanol, i.e., hydroxyethyl cardanol (pCard). The plasticization efficiency of MeCard is demonstrated by a substantial decrease of the glass transition temperature and storage modulus together with a significant increase of the elongation at break as compared to neat PLA. Moreover, MeCard exhibits higher plasticization performance than pCard toward PLA. Such behavior is related to a higher miscibility and compatibility between PLA and MeCard thanks to the methoxylation of the double bonds on the side chain of cardanol as shown by SEM micrographs.



Dr. F. Hassouma

Department of Chemical Engineering
University of Chemistry and Technology (UCT)
Prague, Technická 3, Prague 6 – Dejvice 166 28, Czech Republic
Dr. I. Mihai, Dr. L. Fetzter, Dr. A. Laachachi, Dr. H. Ibn Al Ahrach,
Prof. P. Dubois

Materials Research and Technology Department
Luxembourg Institute of Science and Technology (LIST) – 5
Rue Bommel, ZAE Robert Steichen
L-4940 Hautcharage, Luxembourg
E-mail: fatima.hassouna@vscht.cz

Dr. T. Fouquet
National Institute of Advanced Industrial Science
and Technology (AIST)

Environmental Measurement Technology Group
Environmental Management Research Institute
Onogawa 16-1, Tsukuba, Ibaraki 305-8569, Japan
Dr. J.-M. Raquez, P. Dubois

Laboratory of Polymeric and Composite Materials
Center of Innovation and Research in Materials
& Polymers – CIRMAP – University of Mons – UMONS
Place du Parc, 23, B-7000 Mons, Belgium

1. Introduction

During the last decade, much effort has been provided to the use of renewable resources due to increasing environmental concern and depletion of petrochemical resources. Cardanol oil is a renewable and organic natural resource that is obtained via the vacuum distillation of roasted cashew nut shell liquid (CNSL) obtained from the spongy mesocarp of cashew nut shells, a byproduct of cashew nut processing.^[1] Owing to its versatile chemical structure and low cost, cardanol and its derivatives are considered as a promising raw material to develop new derived-biobased materials. In fact, the chemistry of cardanol is being an interesting area in the framework of academic and industrial research, mainly for the preparation of new ecofriendly chemicals, composites, and functional organic materials.^[2,3] Cardanol and its derivatives found major applications in biocomposites, synthetic resins, epoxy curing agents, and coatings.^[3,4] Cardanol is composed of

3-*n*-pentadecylphenol (20%–30%), 3-(pentadeca-8-enyl)-phenol (70%–80%), 3-(penta-deca-8,11- dienyl)-phenol (nearly 5%), and 3-(pentadeca-8,11,14-trienyl) phenol (less than 5%).^[2] Peculiar properties of cardanol and its derivatives, such as the relatively high solubility in non-polar environments and good processability, can be ascribed to the presence of the C15 chain attached to the meta-position of the phenolic ring.^[2] The intrinsically reactive alkyl chain constitutes an interesting platform for chemical modification and functionalization.^[4–6] For instance, cardanol-grafted rubbers have been produced by chemical grafting through the C15 side chain and has shown significant plasticizing effect.^[7–9] Furthermore, phosphorylated cardanol has been shown to be an efficient plasticizer for ethylene-propylene-diene rubber, polychloroprene and polybutadiene rubber, natural rubber/EPDM terpolymer blends, and LLDPE/EVA copolymer blends.^[7,9–11] Greco et al. have also reported that cardanol acetate and epoxidated cardanol acetate, the esterified derivatives of cardanol, are effective plasticizers for poly(vinyl chloride) (PVC).^[12,13] Indeed, it was shown that esterification of the hydroxyl group of the cardanol molecule is necessary in order to achieve a good miscibility of cardanol with PVC. Miscibility between cardanol and PVC can be further enhanced by insertion of an epoxy bond on the side chain of cardanol.^[4,12,13]

Poly(lactide) (PLA), a well-known biodegradable and biobased polyester, has attracted growing interest in different markets, such as packaging, biomedical, electronic and automotive industries.^[14–19] Despite its numerous advantages such as high strength and high modulus, high optical properties, and biocompatibility, PLA has some inherent brittleness, which limits its application.^[20] Plasticization is commonly used to improve the processability of thermoplastics or to increase the flexibility and toughness as well as impact strength of glassy polymers.^[21–24] Though blending PLA with plasticizers enhances its mechanical properties, most of these plasticizers are petroleum-based compounds.^[25] Hence, there is a high need to look at alternative sources of plasticizers derived from biobased resources to design fully renewable polymeric blends.

The purpose of the present study is to propose a novel family of biobased plasticizers made of cardanol for PLA. The plasticizers should not compromise the biobased, biodegradable, and sustainable nature of PLA-based materials and they should be able to improve PLA mechanical properties. To the best of our knowledge, this is the first time cardanol and its derivatives are used as potential plasticizers for PLA.

In this work, a novel cardanol-derived plasticizer was synthesized through methoxylation of the double bonds on the side chain of cardanol (C15 chain attached to the meta position of the phenolic ring). The motivation

behind designing methoxylated cardanol, i.e., methoxylated hydroxyethyl cardanol (5) (MeCard), lies on the improvement of the compatibility properties with PLA. Indeed, as clearly demonstrated in this paper, a lack of miscibility between the commercial pCard and PLA is observed. Hence, MeCard is expected to improve the plasticizing effect and mechanical properties of PLA as compared to non-modified cardanol. Finally, the plasticization effect of pCard versus MeCard on the chemical structure, morphology, thermal and mechanical properties of PLA was evaluated.

2. Experimental Section

2.1. Materials

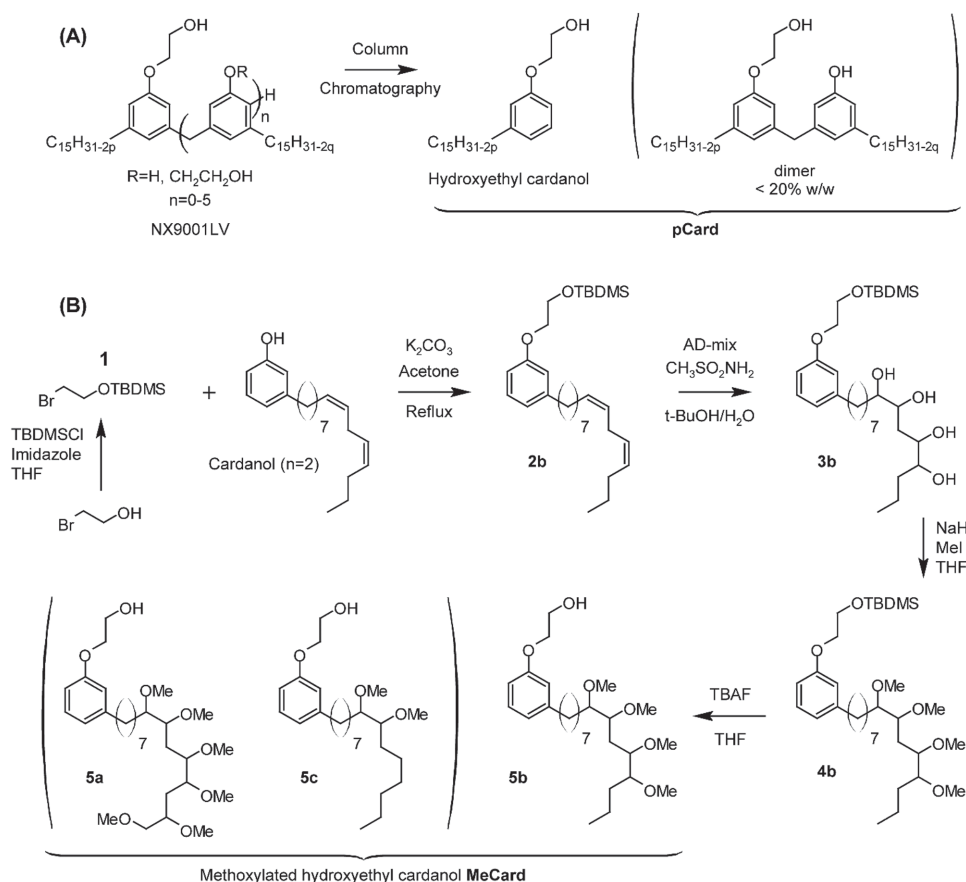
Poly(lactide) (PLA) was supplied by NatureWorks LLC under the reference 4042D. Cardanol as well as hydroxyethyl cardanol (NX9001LV) were obtained from Cardolite. 2-Bromoethanol, *tert*-butyldimethylsilyl chloride (TBDMSCl), imidazole, potassium carbonate (K_2CO_3), AD-mix α , methanesulfonamide ($CH_3SO_2NH_2$), *tert*-butanol (*t*-BuOH), sodium sulfite (Na_2SO_3), sodium hydride (NaH), iodomethane, tetrabutyl ammonium fluoride (TBAF), and chloroform ($CHCl_3$) were purchased from Sigma Aldrich. Tetrahydrofuran (THF) was obtained from Chem-Lab Analytical. *n*-Heptane and ethyl acetate were purchased from Fisher Scientific. All reagents were used as received without preliminary purification.

2.2. Preparation and Synthesis

The purification of the commercial NX9001LV to recover pure hydroxyethyl cardanol and the synthesis of a methoxylated hydroxyethyl cardanol from cardanol are summarized in Scheme 1a,b, respectively. Details about each step are provided below.

2.2.1. Purification of Hydroxyethyl Cardanol

NX9001LV is an industrial “polyol” resin grade. Its generic structure is depicted in Scheme 1a. The main constituent is a hydroxyethyl cardanol ($n = 0$, Scheme 1a), while dimers and larger oligomers of hydroxyethyl cardanol ($R=CH_2CH_2OH$) and/or cardanol ($R=H$) polymerized with formaldehyde are also present for half of the weight. A purified version of NX9001LV—further noted pCard—was obtained after purification over silica gel column chromatography using heptane/ethyl acetate (8/2 to 7/3). The oil isolated after purification was a mixture of saturated, mono-, di-, and triunsaturated congeners of the targeted hydroxyethyl cardanol (>80%, w/w) while a dimeric impurity (hydroxyethyl cardanol/cardanol) still remains for less than 20% w/w (Scheme 1a). 1H NMR (400 MHz, $CDCl_3$): $\delta = 7.19$ (t, 1H, $J_{HH} = 7.8$ Hz, $1H_{Ar}$), 6.81–6.73 (m, $3H_{Ar}$), 5.87–5.77 (ddt, 0.46H, $J_{HH} = 10.14$ Hz, $J_{HH} = 17.04$ Hz, $J_{HH} = 6.18$ Hz, $CH=CH_2$), 5.48–5.30 (m, 4.19H, $CH=$), 5.05 (dq, 0.51H, $J_{HH} = 17.12$ Hz, $J_{HH} = 1.86$ Hz, $CH_2=CH$), 4.99 (dq, 0.51H, $J_{HH} = 10.15$ Hz, $J_{HH} = 1.59$ Hz, $CH_2=CH$), 4.08 (m, 2H, CH_2-O), 3.96 (m, 2H, CH_2-O), 2.81 (m, 2.55H, $CH=CH-CH_2-CH=CH$), 2.56 (m, 2.66H, CH_2-Ar),



Scheme 1. A) Structures of the commercial polyol resin NX9001LV and its purified version noted pCard composed of hydroxyethyl cardanol and a hydroxyethyl cardanol/cardanol dimeric residual impurity. B) Synthesis route to produce a methoxylated hydroxyethyl cardanol (noted MeCard) from pure cardanol (lite2023).

2.03 (m, 5.04H, $\text{CH}_2\text{—CH=}$), 1.61 (m, 2.96H, $\text{CH}_2\text{—CH}_2\text{—Ar}$), 1.43–1.26 (m, 17.48H, $(\text{CH}_2)_n$), 0.90 (m, 2.59H, CH_3) (Figure S1 in the Supporting Information).

2.2.2. Synthesis of Methoxylated Hydroxyethyl Cardanol (5)

Compound numbers **1–5** and congeners **a–c** (tri-, di-, and mono-unsaturated congeners of cardanol, respectively) refer to Scheme 1b.

2-Bromoethoxy-tert-butyldimethylsilane (1): 2-Bromoethanol (15 g, 8.5 mL, 0.12 mol) was dissolved in tetrahydrofuran (500 mL) and placed in a 1 L round-bottom flask. Imidazole (10.6 g, 0.16 mol) and *tert*-butyldimethylsilyl chloride (23.5 g, 0.16 mol) were added under stirring. After one night at room temperature, the reaction was quenched by adding 400 mL of a saturated solution of ammonium chloride. The aqueous layer was washed with ethyl acetate and the organic layer with a saturated aqueous solution of sodium chloride. The organic layer was then dried over magnesium sulfate and filtered. The solution was concentrated under vacuum. The crude product was purified under silica gel column chromatography using heptane/dichloromethane (9/1 to 7/3) as eluent to provide **1** (17.6 g, 70 mmol, 61%). ^1H NMR (400 MHz, CDCl_3): δ = 3.89 (t, 2H, J_{HH} = 6.55 Hz, CH_2OTBDMS), 3.39 (t, 2H, J_{HH} = 6.55 Hz, CH_2Br), 0.90 (s, 9H, *tert*-Bu), 0.09 (s, 6H, 2Me) (Figure S2a in the Supporting Information).

Cardoxyethoxy-tert-butyldimethylsilane (2): Cardanol (7 g, 23 mmol) was diluted in acetone (300 mL). **1** (16.8 g, 70 mmol) and potassium carbonate (29 g, 0.2 mol) were added. After 48 h at reflux, the mixture was cooled to room temperature and a saturated solution of ammonium chloride (250 mL) was added. The aqueous phase was washed with ethyl acetate and the organic phase was washed with saturated solution of sodium chloride and dried over magnesium sulfate. The crude product was purified under silica gel column chromatography using pentane/dichloromethane (8/2 to 6/4) as eluent. ^1H NMR (400 MHz, CDCl_3): δ = 7.17 (m, 1H_{Ar}), 6.77–6.71 (m, 3H_{Ar}), 5.81 (ddt, 0.32H, J_{HH} = 10.06 Hz, J_{HH} = 17.11 Hz, J_{HH} = 6.31 Hz, CH=CH_2), 5.47–5.30 (m, 3.08H, CH=), 5.05 (dq, 0.35H, J_{HH} = 17.08 Hz, J_{HH} = 1.75 Hz, $\text{CH}_2\text{=CH}$), 4.98 (dq, 0.35H, J_{HH} = 10.09 Hz, J_{HH} = 1.55 Hz, $\text{CH}_2\text{=CH}$), 4.03 (m, 2H, $\text{CH}_2\text{—O}$), 3.97 (m, 2H, $\text{CH}_2\text{—O}$), 2.81 (m, 2H, $\text{CH=CH—CH}_2\text{—CH=CH}$), 2.57 (m, 2H, $\text{CH}_2\text{—Ar}$), 2.03 (m, 3.15H, $\text{CH}_2\text{—CH=}$), 1.60 (m, 2.55H, $\text{CH}_2\text{—CH}_2\text{—Ar}$), 1.42–1.26 (m, 12.83H, $(\text{CH}_2)_n$), 0.91 (m, 10.33H, $\text{CH}_3 + \text{tBuSi}$), 0.10 (s, 6H, 2 CH_3Si) (Figure S2b in the Supporting Information).

Hydroxylated Carboxyethoxy-tert-butyldimethylsilane (3): A room temperature mixture of AD-mix α (56 g) in *tert*-butanol/ H_2O 1/1 (450 mL) was stirred until both phases became clear. Methanesulfonamide (1.8 g, 19 mmol) was added and the mixture was cooled to 0 °C. A solution of **2** (9 g, 19 mmol)

in *tert*-butanol/H₂O 1/1 (50 ml) was added and the reaction mixture was stirred vigorously at 0 °C overnight. Sodium sulfite (56 g) was added and the mixture was stirred for 30 min. The mixture was diluted with ethyl acetate and H₂O. The organic phase was washed with 20% aqueous sodium hydroxide solution and saturated aqueous sodium chloride solution. The organic layer was then dried over magnesium sulfate and filtered. The solution was concentrated under vacuum. ¹H NMR (400 MHz, CDCl₃): δ = 7.17 (m, 1H_{Ar}), 6.73 (m, 3H_{Ar}), 4.04–3.60 (m, 8.6H, CH₂–O+CH–OH+CH₂–OH), 2.55 (m, 2H, CH₂–Ar), 2.07–1.25 (m, 19.7H, (CH₂)_n), 0.91 (m, 10.8H, CH₃ + *t*BuSi), 0.10 (s, 6H, 2 CH₃Si) (Figure S2c in the Supporting Information).

Methoxylated Carboxyethoxy-*tert*-butyldimethylsilane (4): Sodium hydride (4.1 g, 0.17 mol) was added to a stirred solution of **3** (10.6 g, 20 mmol) in tetrahydrofuran (125 mL) at 0 °C. After 5 min, iodomethane (21 mL, 0.34 mol) was added. After 10 min, the cooling bath was removed and the reaction mixture stirred at room temperature overnight. Brine (200 mL) was slowly added and the organic layer was extracted with ethyl acetate. The combined organic layers were dried over magnesium sulfate and filtered. The solution was concentrated under vacuum. The crude product was purified under silica gel column chromatography using heptane/ethyl acetate (7/3 to 0/10) as eluent. ¹H NMR (400 MHz, CDCl₃): δ = 7.16 (m, 1H, H_{Ar}), 6.73 (m, 3H_{Ar}), 4.04–3.94 (m, 4H, 2 CH₂–O), 3.55–3.15 (m, 15H, CH₃–O, CH–OCH₃), 2.56 (m, 2H, CH₂–Ar), 1.89–1.23 (m, 21H, (CH₂)_n), 0.91 (m, 12H, CH₃ + *t*BuSi), 0.10 (s, 6H, 2 CH₃Si) (Figure S2d in the Supporting Information).

Methoxylated Hydroxyethyl Cardanol (5): A mixture of tetrabutyl ammonium fluoride 1 M solution in tetrahydrofuran (150 mL, 150 mmol, 10 eq) and **4** (9.6 g, 15 mmol) were stirred at room temperature overnight. After removal of solvent, the residue was diluted with water and extracted with ethyl acetate. The organic layer was washed with brine, dried over magnesium sulfate and concentrated. The crude product was purified under silica gel column chromatography using heptane/ethyl acetate (2/8 to 0/10) as eluent.

The methoxylated hydroxyethyl cardanol (MeCard) was a mixture of four constituents with different unsaturation degrees on the side chain. The saturated, mono-, di-, and triene derivatives have a natural occurrence around 5%, 49%, 16%, and 30%, respectively. ¹H NMR (400 MHz, CDCl₃): δ = 7.18 (t, 1H, *J*_{HH} = 7.68 Hz, H_{Ar}), 6.76 (m, 3H_{Ar}), 4.08 (m, 2H, CH₂–O), 3.95 (m, 2H, CH₂–O), 3.56–3.15 (m, 15H, CH₃–O + CH–OCH₃), 2.57 (t, 2H, *J*_{HH} = 7.76 Hz, CH₂–Ar), 1.85–0.86 (m, 25H, (CH₂)_n, CH₃) (Figure S2e in the Supporting Information).

2.3. Processing

Before processing by melt-blending, PLA pellets were first dried overnight at 50 °C in a vacuum oven (Heraeus, Thermo Scientific) to minimize the water content for melt-blending. Dry pCard and MeCard were used without any particular precaution.

All melt blends PLA-pCard and PLA-MeCard were performed using a co-rotating twin screw micro-compounder (DSM Xplore Research) under argon atmosphere. Barrel temperature was set at 180 °C. Melt temperature was measured before and during the process (≈170 °C–175 °C). Screw speed was fixed to 100 rpm and the residence time to 5 min. The content of plasticizer (pCard

and MeCard) is chosen to be 20 wt% (after an optimization step), based on the total weight of the mixture. For the melt-blending procedure, PLA was first introduced and melted in the preheated micro-compounder. Dry pCard and MeCard were then injected into the extruder using a syringe. For comparison, pure PLA was processed in similar conditions of melt-blending.

Standard samples of the resulting PLA based materials were then prepared by injection molding machine (Model HAAKE MiniJet II, Thermo Scientific) at 180 °C and 700 bar during 5 s.

It is worth mentioning that the melt blending of non-purified hydroxyethyl cardanol (NX9001LV) with PLA was attempted without success. Indeed, a macroscopic phase separation between the two components was observed immediately after blending. The purification step of hydroxyethyl cardanol is therefore essential.

2.4. Characterizations

2.4.1. Proton Nuclear Magnetic Resonance

The ¹H nuclear magnetic resonance (¹H NMR) characterization was performed on a Avance 400 spectrometer (Bruker Biospin, Wissembourg, France) equipped with a 9.4 T Ascend magnet, operating at a proton frequency of 400 MHz. Samples were dissolved in deuterated chloroform (CDCl₃) with all peaks referenced relative to tetramethylsilane.

2.4.2. Mass Spectrometry

Mass spectra were recorded using a Autoflex III mass spectrometer (Bruker) equipped with a frequency-tripled Nd-YAG laser (λ = 355 nm) operating at a pulse rate of 50 Hz. The time-of-flight analyzer was operated in reflectron mode. External calibrations were performed using monodisperse poly(ethylene glycol) PEG (600, 1500, and 4000 g mol^{−1}, Sigma-Aldrich). FlexControl software version 3.0 (Bruker) was used for instrument control and data acquisition while both FlexAnalysis software version 3.0 (Bruker) and mMass version 5.5 15 were used for data processing. Mass analyses were conducted using a surface-assisted laser desorption/ionization technique in the positive ion mode (SALDI(+)-MS) with carbon nanofibers as “active” surface. Samples were dissolved in THF and mixed with a suspension of carbon nanofibers GANF (Grupo Antolin) in acetone and lithium trifluoroacetic acid (LiTFA, Sigma-Aldrich) in THF. The mixture deposited on the target and allowed to air dry before the mass analysis. For the particular characterization of the purified version of NX9001LV (pCard), fractions of interest (containing either the targeted hydroxyethyl cardanol or the dimeric side product) were collected from the SEC elution directly after the detector, the solvent allowed to evaporate for a few minutes and further submitted to the same SALDI procedure.

2.4.3. Differential Scanning Calorimetry

The thermal properties were carried out on a Netzsch DSC 204 F1 instrument under a nitrogen gas flow, with a heating rate of 10 °C min^{−1} between −100 °C and 200 °C to observe the glass transition process. Samples (5–10 mg) were sealed in hermetic aluminum pans and were subjected to the following temperature program:

i) a first heating step from $-100\text{ }^{\circ}\text{C}$ to $200\text{ }^{\circ}\text{C}$, ii) a cooling step from $200\text{ }^{\circ}\text{C}$ to $-100\text{ }^{\circ}\text{C}$ and iii) a second heating step from $-100\text{ }^{\circ}\text{C}$ to $200\text{ }^{\circ}\text{C}$. The T_g value was measured at the second ramp.

2.4.4. Size Exclusion Chromatography

For the size exclusion chromatography (SEC) analyses of cardanol derivatives, the apparatus consisted of a 600E controller & pumping units (Waters, Versailles, France) followed by a 486 tunable UV/Vis detector (Waters). Separation was performed on a unique mixed bed column (PLgel Mixed-D $300 \times 7.5\text{ mm}$, particle size $5\text{ }\mu\text{m}$, Agilent) with precolumn (PLgel Mixed-D $50 \times 7.5\text{ mm}$) at room temperature. THF was used as eluent at a flow rate of 1 mL min^{-1} . $20\text{ }\mu\text{L}$ of 1 g L^{-1} and 15 g L^{-1} resin solution were injected for SEC and SEC-SALDI analyses with satisfactory S/N ratio in a single run, respectively. For the PLA-based materials, the molecular weight change tests were conducted with an Agilent Technologies series 1200 operating with a differential refractive index detection and a linear column (PLgel Mixed-D 5 and $3\text{ }\mu\text{m}$, $200\text{ Da} < M_w < 200\text{ kDa}$ in chloroform 1 mL min^{-1}). Sample preparation was performed by dissolving the material to be analyzed in chloroform at a concentration of 2 mg mL^{-1} . This was followed by the filtration of the prepared material solution using a syringe and an acrodisk-branded filter (pore size $0.45\text{ }\mu\text{m}$). All analyses were run at room temperature.

2.4.5. Thermogravimetric Analysis

The thermal stability was investigated with a thermogravimetric analyzer model STA 409PC Luxx from NETZSCH. $15\text{--}20\text{ mg}$ of sample in an aluminum pan was heated from RT up to $600\text{ }^{\circ}\text{C}$ under nitrogen (80 mL min^{-1}) and oxygen (20 mL min^{-1}) gas flow. The runs were carried out in dynamic conditions. The experiments were carried out at a heating rate of $10\text{ }^{\circ}\text{C min}^{-1}$.

2.4.6. Scanning Electron Microscopy

The morphology was observed by using a pressure-controlled scanning electron microscope (SEM) Quanta Field Effect Gun 200 from FEI. To this end, samples were characterized with particular preparation. All the samples were fractured after immersion in liquid nitrogen for about 5 min to observe the fracture surface of the materials.

2.4.7. Dynamic Mechanical Analysis

The viscoelastic properties were evaluated by means of a dynamic mechanical analyzer (DMA) using a Netzsch equipment model DMA 242C. For this study, rectangular specimens ($60 \times 11 \times 3\text{ mm}^3$) were processed by injection molding machine. They were conditioned for at least 24 h at $20\text{ }^{\circ}\text{C}$ and 50% of relative humidity before testing. Subsequently, they were subjected to double cantilever mode of flexural loading with amplitude of $30\text{ }\mu\text{m}$ in the temperature range from $-60\text{ }^{\circ}\text{C}$ to $120\text{ }^{\circ}\text{C}$ at a heating rate $2\text{ }^{\circ}\text{C min}^{-1}$ and a frequency of 1 Hz .

2.4.8. Tensile Tests

The quasi-static uniaxial tensile testing was done with a universal testing machine Instron model 5967. The extruded rods

of materials were processed by injection molding machine to obtain tensile specimens based on ASTM D638 with sample type V. The specimen had an overall length of 63.5 mm and a thickness of 3 mm . The gauge section of the specimen had a length of 25 mm and a minimum width of 3 mm . The specimens were conditioned for at least 24 h at $20\text{ }^{\circ}\text{C}$ and 50% of relative humidity before testing. The engineering axial stress versus axial strain curves were recorded at room temperature at a constant cross-head rate of 1 mm min^{-1} until break occurs.

3. Results and Discussion

3.1. Preparation and Synthesis

3.1.1. Purification and Characterization of a Commercial Poly(hydroxyethyl cardanol) Resin

NX9001LV (Cardolite, see Experimental Section) is commercialized as a “polyol” resin and has been found to be composed of oligomers of hydroxyethyl cardanol and formaldehyde (i.e., a Novolac-like resin replacing phenol by a cardanol derivative moiety). Despite the fact that its content in oligomers has been drastically reduced, this low viscosity version of the NX9001 resin remains an industrial grade product and contains dimers, trimers, and larger oligomers of hydroxyethyl cardanol, uncapped cardanol, and formaldehyde (Scheme 1a for its generic structure with a $\text{Ph-CH}_2\text{-Ph}$ linkage). SEC chromatogram of NX9001LV is depicted in Figure 1a (black line, top) and peaks assigned according to a previous work.^[26] Following the purification over silica gel column, the so-called “pCard” sample has been re-analyzed by SEC under the same conditions, the resulting SEC chromatogram being depicted in Figure 1b (red line, bottom). The largest oligomeric components (trimers and above) have been successfully removed and the “monomer” is now the main component of this newly produced pCard. A residual dimer peak is still observed but accounting for less than 20%, w/w of the sample according to the peak areas (Scheme 1a). To ensure a proper molecular characterization, fractions containing the “monomer” and “dimer” peaks have been collected and submitted to surface-assisted laser desorption ionization mass spectrometry (SALDI). The SALDI(+)-MS spectrum of the “monomer” peak is depicted in Figure 1b. A pure hydroxyethyl cardanol adducted with lithium cation is readily detected at $m/z\ 349$ (tri-unsaturated congener of cardanol), $m/z\ 351$ (di-unsaturated congener), and $m/z\ 353$ (mono-unsaturated congener), constituting the so-called unsaturation pattern of cardanol. A slight distortion of this unsaturation pattern in terms of relative abundance is nevertheless observed when comparing the theoretical pattern computing from the natural occurrence of the three constituents (inset in Figure 1b, bottom). The tri-unsaturated congener is indeed prone to elute with the more polar dimers and trimers during the

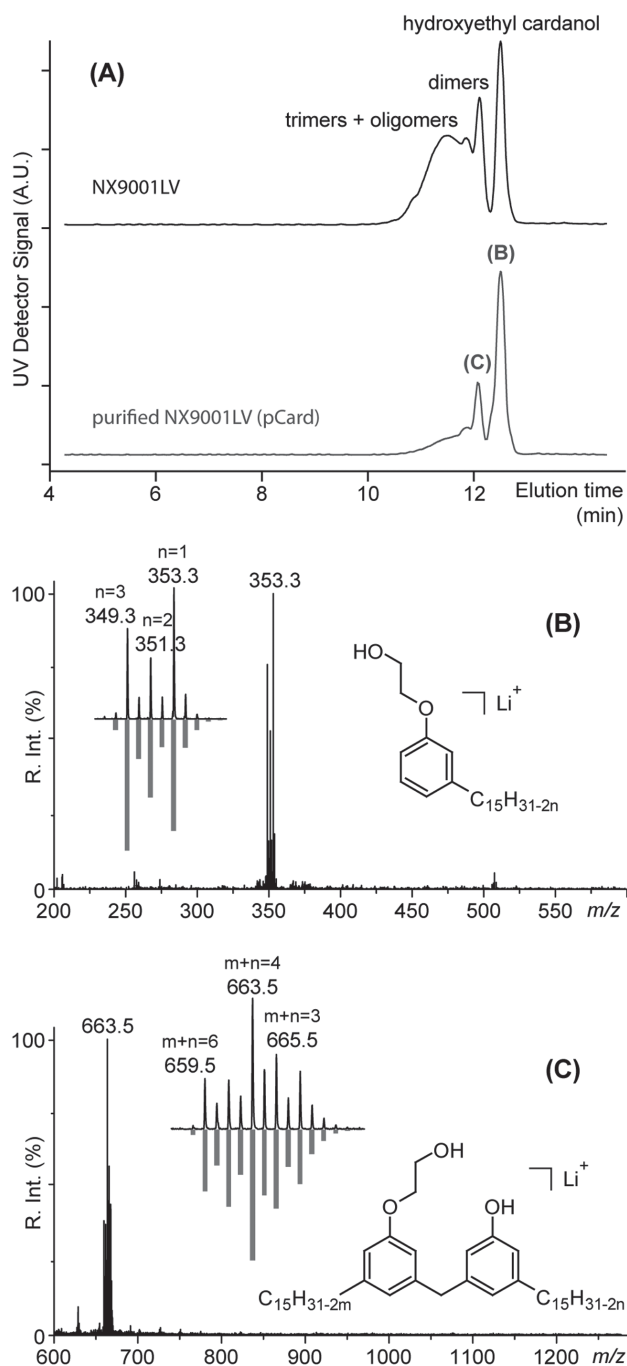


Figure 1. SEC chromatograms of the commercial polyol resin NX9001LV (black line, top) and the purified sample (further noted pCard) isolated from NX9001LV by column chromatography (red line, bottom). SALDI(+)-MS spectra of B) the "monomer" peak and C) the minor "dimer" peak (<20%, w/w) collected from the SEC elution of pCard (offline coupling).

purification step by column chromatography, accounting for the depletion of its signal in SALDI(+)-MS. The properties of pCard have been considered not to drastically change in spite of this segregation effect. A unique dimeric species is eventually detected in the SALDI(+)-MS spectrum

of the minor "dimer" fraction (Figure 1c) at m/z 663 (+ congeners depending on the number of unsaturations along the two C15 side chains). Based on its elemental composition, this dimer could be described as a hydroxyethyl cardanol linked to a pristine cardanol moiety (no ethoxy capping) by a $\text{Ph-CH}_2\text{-Ph}$ linkage (Novolac-like dimer with one cardanol moiety in lieu of a hydroxyethyl cardanol). As for the unsaturation pattern change, such impurity is thought to be of limited impact on the overall properties of the pCard sample, further considered as a pure hydroxyethyl cardanol for sake of simplicity. ^1H NMR characterization of pCard confirms those first results (Figure S1 in the Supporting Information). In particular, the amount of dimeric impurity has been evaluated to $\approx 17\%$ based on the areas of the aromatic protons (four for the targeted hydroxyethyl cardanol, six for the dimer) and protons from the ethoxy arm (four in both cases because of the missing ethoxy capping in the dimeric structure), in agreement with the evaluation from SEC.

3.1.2. Synthesis and Characterization of a Methoxylated Hydroxyethyl Cardanol

The methoxylated hydroxyethyl cardanol has been synthesized following the synthesis route depicted in Scheme 1b. Starting from the capping of bromoethanol by TBDMS (protecting group of the alcohol function) to yield **1**, its coupling with cardanol produces a hydroxyethyl cardanol capped with TBDMS (noted **2**). The dihydroxylation of the double bonds of the C15 side chain has been quantitatively done in one step using AD-mix α as catalyst (compound **3**). Hydroxyl functions were then methylated using iodomethane and sodium hydride to yield the methoxylated TBDMS-hydroxyethyl cardanol **4**. The deprotection of the hydroxyethyl arm was eventually conducted using a 1 M tetrabutyl ammonium fluoride solution and the targeted methoxylated hydroxyethyl cardanol **5** finally isolated.

The SALDI mass spectra of the four cardanol-containing products **2–5** are depicted in Figure 2. The three tri-unsaturated, di-unsaturated and mono-unsaturated congeners forming the hydroxyethyl cardanol capped with TBDMS are detected in that order at m/z 463, m/z 465, and m/z 467 (Figure 2a). The unsaturation pattern and its simulation based on the theoretical abundances in cardanol are mirror depicted in inset and in good agreement. Contrary to the purification of NX9001LV to produce pCard, the synthesis of MeCard is conducted using pure cardanol and ratios of tri-, di-, and mono-unsaturated congeners are not biased. The hydroxylation of the C15 chain is highlighted by the detection of a di-hydroxylated (**3c**) at m/z 501, a tetra-hydroxylated (**3b**) at m/z 533, and a hexa-hydroxylated congener (**3a**) at m/z 565 (lithium adducts). Hydroxylating the side chain leads to the degeneracy of the "unsaturation

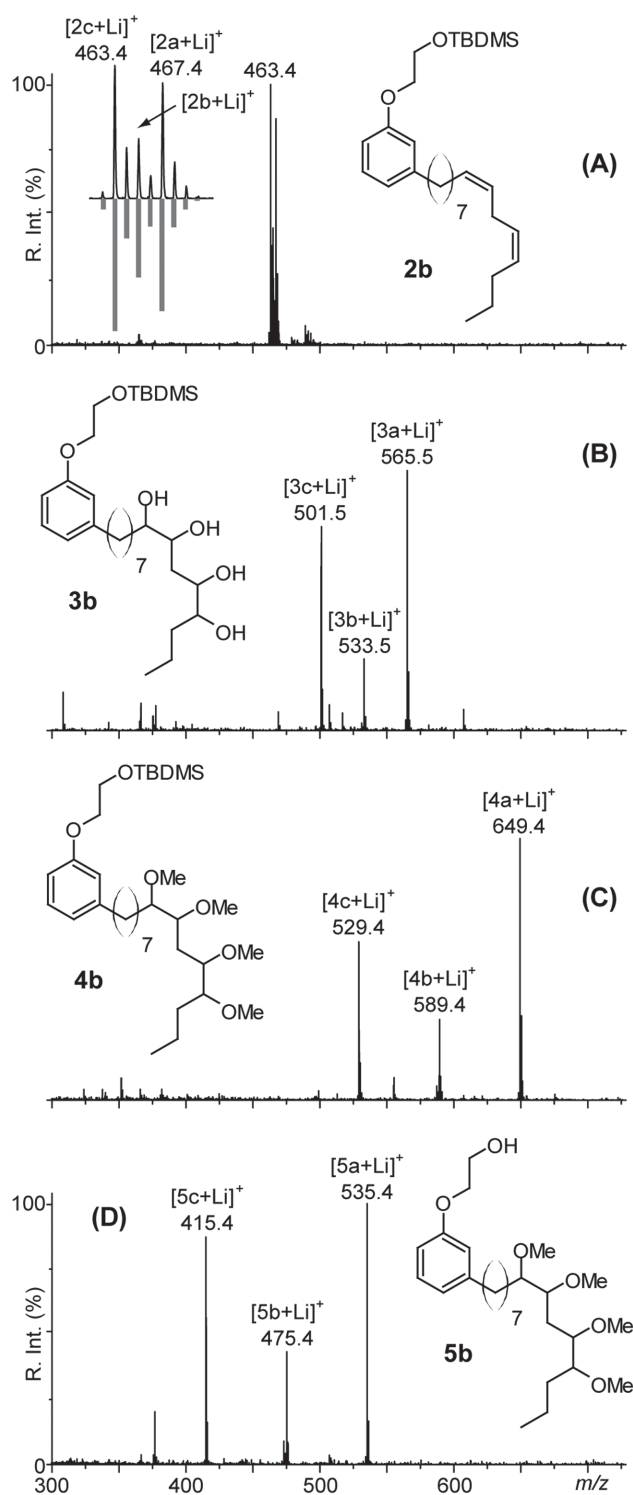


Figure 2. SALDI(+)-MS spectra of A) hydroxyethyl cardanol capped with TBDMS noted 2, B) hydroxylated hydroxyethyl cardanol capped with TBDMS noted 3, C) methoxylated hydroxyethyl cardanol capped with TBDMS noted 4, and D) the targeted methoxylated hydroxyethyl cardanol noted 5. Structures of the di-unsaturated, tetrahydroxylated, and tetramethoxylated congeners “b” are depicted in insets.

pattern.” The tri-unsaturated cardanol is detected at the lowest m/z ratio, while the hexa-hydroxylated cardanol made from the former is detected at the highest m/z ratio, and 32 Da now separates each congeners ($2 \times 17 \text{ Da} - 2\text{H} = 32 \text{ Da}$) when pristine cardanol congeners are shifted by 2 Da (2H per unsaturation). The next step of the synthesis leads to the methylation of the hydroxyl pendant groups to produce methoxy functions along the C15 side chain. The targeted products are detected as lithiated adducts at m/z 529 (di-methoxylated congener 4c), m/z 589 (tetra-methoxylated congener 4b), and m/z 649 (hexa-methoxylated congener 4a) in the associated SALDI mass spectrum (Figure 2c). The 60 Da shift between each congener reflects the occurrence/absence of two methoxy groups ($2 \times 31 \text{ Da} - 2\text{H} = 60 \text{ Da}$). The mass analysis of the product from the last step to eventually form the methoxylated hydroxyethyl cardanol upon the release of the protecting group TBDMS provides the mass spectrum depicted in Figure 2d. The three congeners bearing two (compound 5c), four (compound 5b), and six methoxy groups (compound 5a) are readily seen at m/z 415, m/z 475, and m/z 535, respectively (lithium adducts), shifted of 114 Da from the previous m/z values ($-\text{Si}(\text{CH}_3)_2\text{C}_4\text{H}_9 + \text{H} = -115 + 1 = -114 \text{ Da}$). Note the relative abundance of the three species is still in accordance with the theoretical values (hexa-methoxylated > di-methoxylated > tetra-methoxylated, equivalent to tri-unsaturated > mono-unsaturated > di-unsaturated for the pristine cardanol, Figure 2a). In inset of all the four spectra is depicted the “b” congener (di-unsaturated, tetra-hydroxylated, and tetra-methoxylated) for sake of simplicity (Scheme 1b).

The ^1H NMR spectra of the five products synthesized in this procedure are depicted and thoroughly commented in the Figure S2 (Supporting Information). ^1H NMR and SALDI spectra are in good agreement and confirm the successful synthesis of the targeted methoxylated hydroxyethyl cardanol “MeCard” with no residual impurities. The final product “MeCard” is a transparent liquid while pCard is an orange oily liquid.

3.2. Modification of PLA Molecular Characteristics

As most of polyesters, PLA is sensitive to melt processing conditions, i.e., particularly to water, temperature, and shear. In several cases, the mixing of PLA with additives such as plasticizers leads to a decrease of the molecular weights, with a possible negative effect on the thermomechanical properties of the polymer material.

SEC analyses used to determine the apparent molecular weight (M_n and M_w) of all samples according to polystyrene standards are summarized in Table 1. Melt blending of PLA with 20 wt% of pCard does not have any impact on PLA molecular weight. However, a slight

■ Table 1. Molecular weights and dispersity (\bar{D}) as determined by SEC on all the investigated materials.

Blend composition [W/W]	\bar{M}_n [g mol ⁻¹] (PS)		\bar{M}_w [g mol ⁻¹] (PS)		Dispersity \bar{D} (M_w/M_n)	
	PLA	Card ^{a)}	PLA	Card ^{a)}	PLA	Card ^{a)}
PLA after extrusion	1 18 120		2 44 280		2	
pCard		430		680		2
MeCard		502		522		1
PLA-pCard (80/20)	1 15 710	434	2 34 120	720	2	2
PLA-MeCard (80/20)	88 560	465	1 87 000	519	2	1

^{a)}Card refers to either pCard or MeCard.

shift of M_w and M_n toward lower molecular weights is observed when melt blended with MeCard. PLA chain scissions are however very limited. This could be due to some degradation of methoxy groups at high temperature leading to the formation of some methanol molecules, known for their reaction with the ester functions spread along the PLA chains. It is worth noting that dispersity is not affected by the presence of both cardanol derivatives. Moreover, overall, the molecular weight characterization seems to evidence, that under adequate melt processing conditions, melt-blending of PLA with pCard and MeCard does not induce any dramatic drop of PLA molecular weight by thermal degradation or hydrolysis of polyester chains.

3.3. Thermal Characterizations

3.3.1. Thermal Stability

TGA measurements were performed on the different PLA-based materials (Figure 3) to determine the effect of such novel plasticizers on the thermal stability of PLA. Indeed, the choice of the most adequate processing conditions (residence time, temperature, etc.) and of thermally stable PLA compositions could lead to enhanced end-use features.

Figure 3 shows the TG curves for neat PLA and PLA plasticized with either pCard or MeCard as recorded under air atmosphere at 10 °C min⁻¹. In the presence of each plasticizer, the decomposition onset temperature of plasticized PLA is slightly shifted to lower temperature with respect to neat PLA. However, no effect of the plasticizers was observed on the decomposition temperature at 50% weight loss. The addition of pCard or MeCard affects the thermal stability of PLA at higher temperature ranges (higher than 300 °C), which are never reached during the melt processing. Interestingly enough the methoxylation of the double bonds on the side chain of cardanol does not seem to lead to measurable weight loss of PLA, even though a slight decrease of the molecular weight of

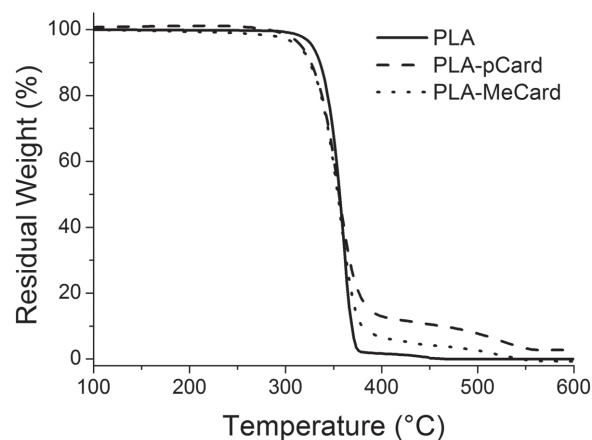
PLA is observed by SEC when melt blended with MeCard (Table 1).

3.3.2. Thermal and Morphological Properties

Thermal and structural behaviors of the investigated PLA-based materials have been examined by means of DSC using a heat/cool/heat cycle. Table 2 and Figure 4 summarize the thermal properties of neat and plasticized PLA during the second heating scan ranging from -100 °C to 200 °C. The second heating eliminates the uncertainties that arise when the behavior of the material may depend on the thermal history of the materials.

Foremost, it is worth emphasizing that DSC analysis performed on neat pCard and MeCard indicate glass transition temperature (T_g) values ≈ 46 °C and -59 °C, respectively.

Neat PLA did not exhibit substantial differences in its thermal behavior between the first and the second heating. They both attest for the semicrystallinity of the PLA matrix with T_g at ≈ 60 °C, an exothermic peak of cold crystallization (T_{cc}) ≈ 124 °C and an endothermic melting



■ Figure 3. TG curves for PLA-based materials under air atmosphere (heating rate: 10 °C min⁻¹).

■ Table 2. Overall thermal and mechanical properties of all the materials investigated.

Blend composition [in wt%]	T_g^a [°C]	T_{cc}^a [°C]	T_m^a [°C]	$(\Delta H_m - \Delta H_{cc})^a$ [J g ⁻¹]	χ_c^b [%]	T_g^c [°C]	E'^d [MPa]	E''^e [MPa]	σ_y^e [MPa]	ϵ_b^e [%]
Extruded PLA	60	124	154	0	0	60	1850	1860	63	5.7
PLA-pCard (80/20)	38	92	138 152	0.8	0	41	1435	1035	26.5	12
PLA-MeCard (80/20)	27	79	152	0.5	0	33	1235	710	27	198

^{a)}Glass transition temperature from the second heating DSC scans; ^{b)} χ_c = Crystallinity = $\frac{\Delta H_m - \Delta H_{cc}}{\Delta H_m^0} \times 100$ where ΔH_m^0 of 100% crystalline

PLLA is 93.4 J g⁻¹; ^{c)}Glass transition temperature at maximum E'' peak (DMA); ^{d)}Storage modulus at 20 °C (DMTA); ^{e)}Tensile properties at 20 °C according to ASTM D638 (test speed 5 mm min⁻¹).

ND: Not Detected.

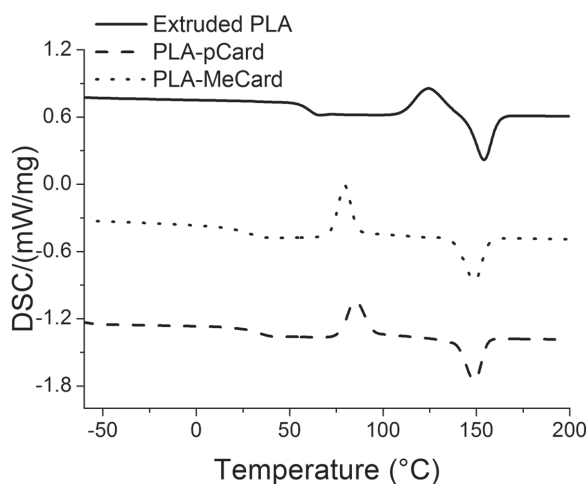
peak centered at 154 °C. This can be explained by the fact that the studied PLA matrix possesses 4.6% of D-lactide isomer, reducing its crystallization ability. It must be stated out here that for all the investigated materials, i.e., neat PLA but also PLA-pCard and PLA-MeCard, the melting enthalpy (ΔH_m) of the materials is about equal to the enthalpy of cold crystallization (ΔH_{cc}). This suggests that all the studied materials are amorphous at room temperature.

The addition of 20 wt% of pCard leads to the shift of the glass transition as well as the cold-crystallization peak and the melting peak to lower values (T_g 38 °C, $T_{cc} \approx 92$ °C, and $T_m = 152$ °C). This can be attributed to the higher chain mobility as a result of the presence of a high amount of low molecular weight plasticizer. The decrease of T_{cc} is considered to be directly related to the motion ability of PLA chains. Indeed, the increase of PLA chain motion due to the amount of pCard (lower T_g) well dispersed in the polyester matrix.

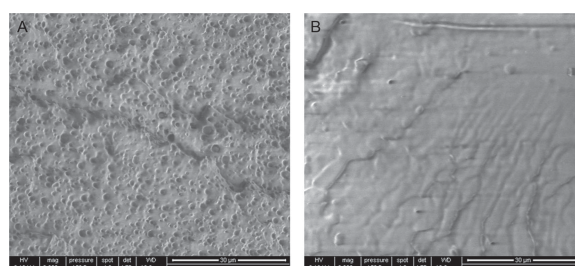
More interesting, when 20 wt% MeCard are melt blended with PLA, the T_g and T_{cc} of the blend are shifted to

even lower temperatures at ≈ 27 °C and 79 °C, respectively, as compared to PLA/pCard blend.

The plasticizing performance of MeCard as compared to pCard can be attributed to the intermolecular interaction and compatibility between the cardanol derivative plasticizers and PLA. Indeed, the methoxylation of the double bonds on the side chain of cardanol (C15 chain attached to the meta position of the phenolic ring) seems to improve the compatibility properties with PLA. To verify this assumption, morphological analysis were performed on both PLA-pCard and PLA/MeCard materials using SEM technique (Figure 5). Indeed, miscibility, immiscibility, and some other characteristics, such as roughness and defects, can be assessed through morphology analysis. SEM image of PLA-pCard blend shows clearly the presence of two distinct phases, in which fine and regular pCard droplets are dispersed in PLA matrix. The same morphology was observed in the systems containing lower amounts of pCard, i.e., PLA-pCard 90/10 and 85/15% w/w (not shown here), confirming a lack of miscibility of pCard with PLA. On the other hand, homogeneous morphological features without any phase separation are observed in PLA-MeCard micrograph, confirming that the interaction between PLA and MeCard is enough for providing miscibility. This interaction takes place between the methyl side groups present on PLA chains and the methoxy groups on the side chain of cardanol. Therefore, it can be concluded that methoxylation of the double



■ Figure 4. DSC traces recorded for PLA based materials during the second heating.



■ Figure 5. SEM images of A) PLA-pCard, B) PLA-MeCard.

bonds on the side chain of cardanol does improve its compatibility properties with PLA.

It is worth mentioning that even though DSC analysis displayed only one glass transition temperature in the blends PLA-pCard and PLA-MeCard, this does not state straight away for full miscibility of the polymer and the plasticizer. PLA-pCard blend is a perfect illustration of that. In fact, DSC transition parameters such as T_g and enthalpy are very much dependent on the sensitivity limits of the calorimeter.

3.4. Mechanical Properties

The impact of temperature on storage modulus (E') and loss modulus (E'') is shown in Figure 6a,b for neat and plasticized PLA. The dynamic mechanical measurements were carried out at 1 Hz. T_g values are defined as the temperature of the maximum of the loss modulus (E'') obtained for α relaxation (associated with the glass transition) at the frequency 1 Hz.

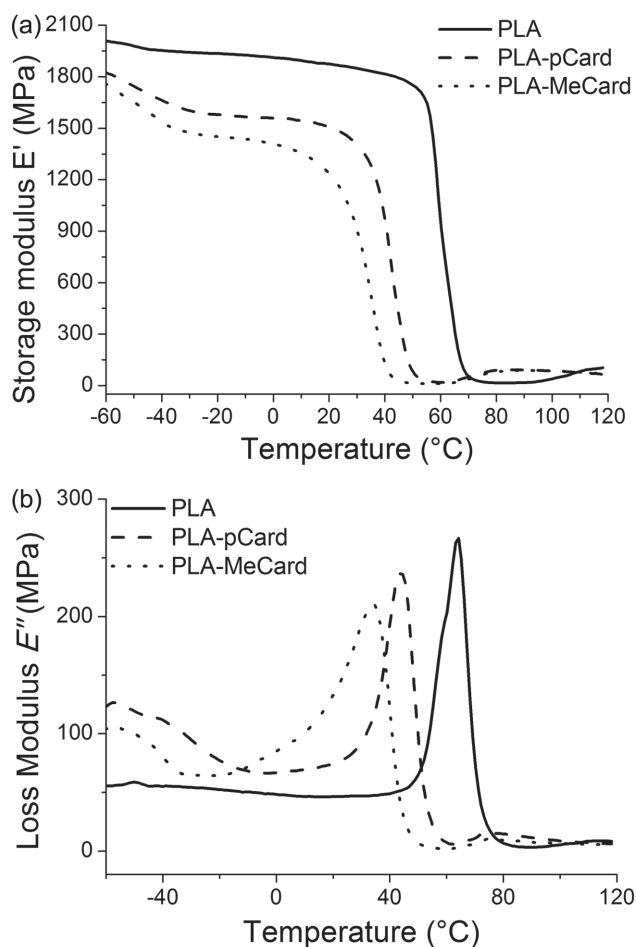


Figure 6. Temperature dependence of a) storage modulus E' ; b) loss modulus E'' for PLA-based materials.

Neat PLA has a T_g equal to ≈ 60 °C and, as expected, all the plasticized PLA exhibit lower glass transition temperature compared to neat PLA. Moreover, the T_g of the blend PLA-MeCard is lower than that of PLA-pCard (33 °C and 41 °C, respectively). DMA results are hence in line with those obtained with DSC. It is to be noted that DSC analysis provide lower T_g values. This is explained by the fact that relaxation processes of polymers are strongly dependent on sollicitation mode (temperature, load + temperature...), sollicitation rate or frequency, and the way it is quantified from the experimental data (peak position, inflection of the curve...). DSC and DMA are two methods based on different sollicitation modes and therefore their results cannot be directly compared.

In the temperature-dependent E'' curves of PLA based materials, cold-crystallization processes are observed after the glass transition relaxation. This is shown by the presence of low intensity peaks between 60 °C and 130 °C, thereby confirming DSC results.

The storage modulus E' curves for PLA is higher than that of plasticized PLA-pCard and PLA-MeCard, and E' of PLA-pCard is higher than that of MeCard in a very large range of temperatures from -60 °C to 75 °C ($E'_{\text{PLA}} > E'_{\text{PLA-pCard}} > E'_{\text{PLA-MeCard}}$). At the lowest investigated temperature, at -60 °C, neat PLA, PLA-pCard, and PLA-MeCard have E' of 1935, 1825, and 1745 MPa, respectively. With increasing the temperature up to the onset of glass transition relaxation, a $\approx 25\%$ – 30% decrease of the storage modulus of plasticized PLA is noted, while $\approx 15\%$ decrease of the storage modulus of neat PLA is recorded. The storage modulus E' measured at room temperature, 20 °C, is reported in Table 2. As expected, the storage modulus value E' at 20 °C of neat PLA is the highest (1850 MPa) and that of PLA-MeCard is the lowest (1235 MPa). At temperature above the glass transition relaxation, that is to say between 60 °C and 130 °C, a weak but significant increase of E' occurs for all PLA-based materials. This process is also linked to the cold-crystallization observed in temperature-dependent E'' curves.

Overall, the addition of 20 wt% of MeCard to PLA leads to a decrease of the storage modulus E' and the loss modulus E'' of the PLA-MeCard blend to lower values as compared to pCard-based system, therefore highlighting a higher extent of miscibility between PLA and MeCard owing to the methoxylation of the double bonds on the side chain of cardanol.

Nominal tensile axial stress–strain behavior at 20 °C of all PLA-based materials is plotted in Figure 7, while the measured characteristics (tensile modulus, yield stress σ_y , and tensile elongation at break ϵ_b (ultimate strain)) are listed in Table 2. Neat PLA exhibited a purely brittle tensile failure and behavior characterized by a high tensile modulus (1860 MPa), a high yield point (63 MPa) and a very low elastic axial deformation $< 6\%$. Neat PLA failure takes

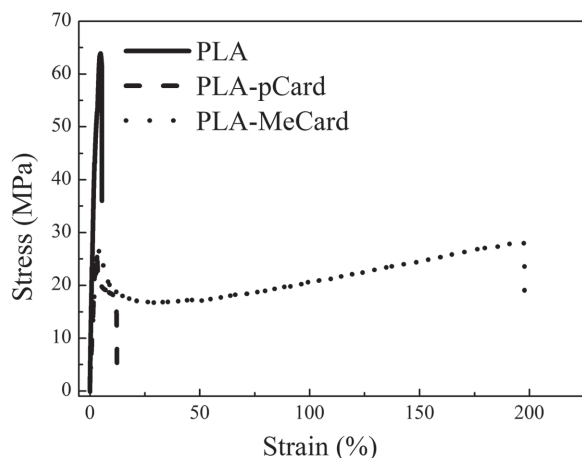


Figure 7. Tensile strain-stress curves for PLA-based materials.

place by crazing or micro-cracking where the cracks propagate facily and freely. Therefore, neat PLA has a limited viscoplastic stage. When compared to neat PLA, plasticized PLA specimens display a lower tensile modulus, a lower yield stress and a higher strain at break. Moreover, plasticized PLA specimens yielded stable necking showing cold-drawing behavior. These blends underwent tensile deformation with a light whitening of the specimen due to the development of crazes in the amorphous phase, confirming the toughening and plasticizing effect of cardanol derivatives. However, PLA-MeCard specimens display a much higher ductility as compared to PLA-pCard counterpart. Indeed, the tensile modulus and the strain at break measured for PLA-MeCard are 710 MPa and 198%, respectively, while those displayed by PLA-pCard specimens are 1037 MPa and 12%, respectively. Thus, the presence of 20 wt% MeCard modifies more radically the uniaxial deformation (tensile elongation) of PLA resulting in highly ductile behavior. This enhanced ductility highlights a high level of miscibility between PLA and MeCard owing to the methoxylation of the double bonds on the side chain of cardanol.

It is also to be noted that neat PLA displays crazes, whose propagation and coalescence can be at the origin of the specimen fracture. It is agreed that the macroscopic stresses that are dissipated locally can be due to a competition between chain orientation mechanisms and damage mechanisms by crazing. For neat PLA, the chain mobility is probably not high enough to provoke stress dissipation by chain orientation.^[27,28] Damage mechanisms are therefore promoted.

In the case of plasticized PLA specimens, the stresses are dissipated by conformational changes of glassy amorphous PLA chains that lead to segmental orientation and disentanglement.^[27,28] However, these phenomena are more pronounced in PLA-MeCard blend, thanks to the higher miscibility between MeCard and PLA.

4. Conclusions

A novel family of biobased plasticizers made of cardanol was designed for PLA. This novel cardanol-derived plasticizer, was synthesized, through methoxylation of the double bonds on the side chain of cardanol (C15 chain attached to the meta position of the phenolic ring). The motivation behind designing methoxylated cardanol, i.e., methoxylated hydroxyethyl cardanol (MeCard), lies on the improvement of the compatibility properties with PLA. The plasticization effect of MeCard on the chemical structure, morphology, thermal and mechanical properties of PLA was evaluated and compared with that of a commercial hydroxyethyl cardanol (pCard).

A five-step synthetic route was employed to obtain MeCard at high yield. Molecular characterizations and TGA analyses revealed that both cardanol derivatives (pCard and MeCard) do not alter the processability of PLA after blending. Interestingly the plasticizer performances were first highlighted using DMA and DSC measurements. Addition of 20 wt% of pCard leads to the shift of the glass transition as well as the cold-crystallization peak and the melting peak to lower values ($T_g = 38^\circ\text{C}$, $T_{cc} \approx 92^\circ\text{C}$, and $T_m = 152^\circ\text{C}$) due to the presence of a high amount of low molecular weight plasticizer. The decrease of T_{cc} is considered to be directly related to the motion ability of PLA chains. More interesting, when 20 wt% MeCard are melt blended with PLA, the T_g and T_{cc} of the blend are shifted to even lower temperatures at $\approx 27^\circ\text{C}$ and 79°C , respectively, as compared to PLA-pCard blend. Such behavior can be related to the good miscibility between PLA and MeCard thanks to the methoxylation of the double bonds on the side chain of cardanol as shown by SEM images. Positive effects were noticed on the mechanical properties of the resulting blends. DMA results indicate that the addition of 20 wt% of MeCard to PLA leads to a decrease of the storage modulus E' and the loss modulus E'' of the blend PLA-MeCard to lower values as compared to pCard, therefore highlighting a much better miscibility and compatibility between PLA and MeCard. The enhanced ductility of blends containing MeCard again highlights a high miscibility and compatibility between PLA and MeCard.

Supporting Information

Supporting Information is available from the Wiley Online Library or from the author.


Acknowledgements: J.M.R. is "chercheur qualifié" of the F.R.S.-FNRS, Belgium.

Received: April 19, 2016; Revised: May 19, 2016;
Published online: ; DOI: 10.1002/mame.201600190

Keywords: cardanol derivatives; extrusion; mechanical properties; plasticization; poly(lactide)

- [1] G. Vasapollo, G. Mele, R. Del Sole, *Molecules* **2011**, *16*, 6871.
- [2] E. Bloise, L. Carbone, G. Colafemmina, L. D'Accolti, S. E. Mazzetto, G. Vasapollo, G. Mele, *Molecules* **2012**, *17*, 12252.
- [3] F. Jaillet, E. Darroman, A. Ratsimihety, R. Auvergne, B. Boutevin, S. Caillol, *Eur. J. Lipid Sci. Technol.* **2014**, *116*, 63.
- [4] J. Chen, Z. Liu, J. Jiang, X. Nie, Y. Zhou, R. E. Murray, *RSC Adv.* **2015**, *5*, 56171.
- [5] V. S. Balachandran, S. R. Jadhav, P. K. Vemula, G. John, *Chem. Soc. Rev.* **2013**, *42*, 427.
- [6] C. Voirin, S. Caillol, N. V. Sadavarte, B. V. Tawade, B. Boutevin, P. P. Wadgaonkar, *Polym. Chem.* **2014**, *5*, 3142.
- [7] S. Mohapatra, G. B. Nando, *Ind. Eng. Chem. Res.* **2013**, *52*, 5951.
- [8] M. Alexander, E. T. Thachil, *J. Appl. Polym. Sci.* **2006**, *102*, 4835.
- [9] S. Mohapatra, G. B. Nando, *RSC Adv.* **2014**, *4*, 15406.
- [10] A. R. R. Menon, L. L. Y. Visconte, *J. Appl. Polym. Sci.* **2006**, *102*, 3195.
- [11] A. R. R. Menon, T. A. Sonia, J. D. Sudha, *J. Appl. Polym. Sci.* **2006**, *102*, 5123.
- [12] A. Greco, D. Brunetti, G. Renna, G. Mele, A. Maffezzoli, *Polym. Degrad. Stab.* **2010**, *95*, 2169.
- [13] E. Calò, A. Greco, A. Maffezzoli, *Polym. Degrad. Stab.* **2011**, *96*, 784.
- [14] D. Garlotta, *J. Polym. Environ.* **2001**, *9*, 63.
- [15] L. T. Lim, R. Auras, M. Rubino, *Prog. Polym. Sci.* **2008**, *33*, 820.
- [16] I. Vroman, L. Tighzert, *Materials* **2009**, *2*, 307.
- [17] R. Auras, B. Harte, S. Selke, *Macromol. Biosci.* **2003**, *4*, 835.
- [18] H. N. Rabetafika, M. Paquot, P. Dubois, *Biotechnol., Agron., Soc. Environ.* **2006**, *10*, 185.
- [19] C. J. Weber, V. Haugaard, R. Festersen, G. Bertelsen, *Food Addit. Contam.* **2002**, *19*, 172.
- [20] K. S. Anderson, K. M. Schreck, M. A. Hillmyer, *Polym. Rev.* **2008**, *48*, 85.
- [21] K. Anderson, K. Schreck, M. Hillmyer, *Polym. Rev.* **2008**, *48*, 85.
- [22] H. Liu, J. Zhang, *J. Polym. Sci., Part B: Polym. Phys.* **2011**, *49*, 1051.
- [23] G. Kfoury, J. M. Raquez, F. Hassouna, J. Odent, V. Toniazzo, D. Ruch, P. Dubois, *Front. Chem.* **2013**, *1*, 32.
- [24] L. Mascia, M. Xanthos, *Adv. Polym. Technol.* **1992**, *11*, 237.
- [25] W. M. Gramlich, M. L. Robertson, M. A. Hillmyer, *Macromolecules* **2010**, *43*, 2313.
- [26] T. Fouquet, L. Fetzer, G. Mertz, L. Puchot, P. Verge, *RSC Adv.* **2015**, *5*, 54899.
- [27] F. Hassouna, J.-M. Raquez, F. Addiego, P. Dubois, V. Toniazzo, D. Ruch, *Eur. Polym. J.* **2011**, *47*, 2134.
- [28] F. Hassouna, J. M. Raquez, F. Addiego, P. Dubois, V. Toniazzo, D. Ruch, *Eur. Polym. J.* **2012**, *48*, 404.

Reactive Plasticization of Poly(lactide) with Epoxy Functionalized Cardanol

Iulia Mihai,¹ Fatima Hassouna ,² Thierry Fouquet,³ Abdelghani Laachachi,¹ Jean-Marie Raquez,⁴ Hicham Ibn El Ahrach,¹ Philippe Dubois⁴

¹ Materials Research and Technology Department, Luxembourg Institute of Science and Technology (LIST) –5, Rue Bommel, ZAE Robert Steichen, Hautcharage, L-4940, Luxembourg

² Department of Chemical Engineering, University of Chemistry and Technology (UCT) Prague, Dejvice, 166 28, Czech Republic

³ Research Institute for Sustainable Chemistry, National Institute for Advanced Industrial Science and Technology (AIST), Tsukuba, 305-8565, Japan

⁴ Laboratory of Polymeric and Composite Materials, Center of Innovation and Research in Materials and Polymers, CIRMAP, University of Mons, B-7000, Belgium

New biobased plasticizers made of di-functional glycidyl ether epoxy cardanol (ECard) were investigated to improve the ductility of renewable poly(lactide) (PLA). Compatibility between PLA and ECard was achieved out through *in situ* reactive grafting strategy catalyzed with Ethyltriphenyl phosphonium bromide (ETPB) using twin-screw extruder. In absence of catalyst, ECard forms domain ill-dispersed in the PLA matrix due to the high incompatibility between both phases. When ETPB is added as catalyst domain size distribution of the plasticizer decreased, indicating an enhanced compatibility due to the reactive grafting of a fraction of ECard plasticizer onto PLA backbone. Although all plasticized PLA specimens exhibit lower glass transition temperature, lower elastic/tensile modulus, lower yield stress, and higher strain at break, the reactive blend containing the lowest amount of catalyst, that is, 0.02 phr, exhibited the highest ductility behavior. POLYM. ENG. SCI., 00:000–000, 2017. © 2017 Society of Plastics Engineers

INTRODUCTION

Among biodegradable and biobased polymers available, poly(lactide) (PLA) is the most prevalent one on the market and cost-competitive compared to lots of conventional petroleum-based polymers. It has attracted growing interest in different markets, such as packaging, biomedical, electronic, and automotive industries [1–6]. Despite its numerous advantages such as high strength and high modulus, high optical properties, resistance to moisture and grease, flavor and odor barrier characteristics, biocompatibility, non-volatility, and nontoxicity, PLA presents some inherent brittleness, which limits its application [7]. Thus, PLA displays some drawbacks in terms of properties (poor impact strength, low elongation at break, low heat deflection temperature...) and processability [7]. PLA rigidity and

brittleness at room temperature are the result of its high glass transition temperature (T_g) close to 60°C [2]. Like most conventional glassy thermoplastics, the brittleness of PLA is due to strain- and stress-localizations when deformed below the brittle-to-ductile transition temperature, that is, under glass transition temperature. Under mechanical loading, PLA deforms via a highly localized strain and crazing mechanism [8]. To improve the properties of PLA, many strategies are already investigated including plasticization, polymer blending, copolymerization, surface modification [7, 9, 10]. Plasticization is commonly used to improve the processability of thermoplastics or to increase the flexibility as well as impact strength of glassy polymers [7, 9–11]. Several plasticizers for PLA are reported in the literature including cyclic lactides and oligolactic acids [12–14], bis(hydroxymethyl) malonate (DBM) [15], glucose esters and fatty acid esters [16–19], citrates [14, 20], polyethylene glycol (PEG) [13, 15, 16], poly(propylene glycol) [21, 22], atactic poly(3-hydroxybutyrate) [18, 19], polyester diol as poly(diethylene adipate) [23], tributyl citrate-oligoester (TbC-oligoesters), diethyl bis(hydroxymethyl) malonate oligoester (DBM-oligoester), and oligoesteramide (DBM-oligoesteramide) [15, 24, 25], modified soybean oil [16, 17]. Toughening through reactive extrusion with plasticizers such as PEG derivatives and citrate derivatives was also established [8, 16, 26–28].

Although blending PLA with plasticizers improves its mechanical properties, most of them are petroleum based compounds [16]. Hence, research towards a fully renewable plasticizer and therefore a fully renewable blend is of a high interest. The main goal of this study is to develop novel bioplasticizers that do not compromise the biodegradable and sustainable nature of PLA based materials at the same time as they can be produced in large scale from inedible biomass resources. Cardanol derivatives are thereby one of such renewable resource. Cardanol is a renewable and inexpensive organic natural resource that is obtained *via* the vacuum distillation of roasted cashew nut shell liquid obtained from the spongy mesocarp of cashew nut shells, a byproduct of cashew nut processing [29]. The chemistry of cardanol and its derivatives is becoming an interesting area in academic and industrial research, mainly for the preparation of new eco-friendly chemicals, composites, and functional organic materials [30, 31]. Indeed cardanol, is a mixture of 3-*n*-pentadecylphenol (20–30%), 3-(pentadeca-8-enyl)phenol (70–80%), 3-(penta-deca-8,11-dienyl)-phenol (nearly 5%), and

Additional Supporting Information may be found in the online version of this article.

Correspondence to: Dr. F. Hassouna; e-mail: fatima.hassouna@vscht.cz

Contract grant sponsor: Science Policy Office of the Belgian Federal Government (PAI 7/5); contract grant sponsor: European Commission/Walloon Region (FEDER – BIORGEL RF project – Valicell); contract grant sponsor: Belgian National Fund for Scientific Research (FNRS).

DOI 10.1002/pen.24647

Published online in Wiley Online Library (wileyonlinelibrary.com).

© 2017 Society of Plastics Engineers

3-(pentadeca-8,11,14-trienyl) phenol (<5%) [30]. Specific properties of cardanol and its derivatives, such as the relatively high solubility in nonpolar milieu and good processability, can be attributed to the presence of the -C15- chain attached to the meta position of the phenolic ring [30]. Cardanol and its derivatives find major applications in biocomposites, synthetic resins, epoxy curing agents, and coatings [31, 32]. Recently, cardanol has been used as a plasticizer for poly(vinyl chloride) and rubber, with or without chemical modification, and has revealed significant plasticizing effects [32, 33].

Epoxidized cardanol (ECard) is one of such cardanol derivatives, which is produced on an industrial scale and is being used for polymers, coatings, and adhesives. Recently, some of us have synthesized a novel cardanol-derived plasticizer, that is, methoxylated hydroxyethyl cardanol, through methoxylation of the double bonds on the side chain of cardanol (C15 chain thus attached to the meta position of the phenolic ring) [34]. The plasticization efficiency of methoxylated hydroxyethyl cardanol was demonstrated by a substantial decrease of the glass transition temperature and storage modulus together with a significant increase of the elongation at break as compared with neat PLA. Moreover, methoxylated hydroxyethyl cardanol exhibited higher plasticization performance than the commercial hydroxyethyl cardanol (pCard) toward PLA.

Interestingly, reactive extrusion has proven to be an ecological, cost effective, and versatile process to design novel and high performance bioplastics. In the present study, the potential for application of ECard as plasticizer for PLA is investigated. *In situ* reactive grafting strategy has been employed to improve the compatibility between PLA and ECard using co-rotating twin-screw extruder. The reactive plasticization effect on the chemical structure, morphology, thermal, and mechanical properties of PLA/ECard was evaluated.

EXPERIMENTAL

Materials

PLA (4042D) was supplied by NatureWorks LLC (Minnetonka, USA). Epoxidized cardanol (ECard) NC-514 S Cashew Liquid Resin was obtained from Cardolite Chemical Zhuhai CO (Guangdong, China) and used as supplied. Ethyltriphenyl phosphonium bromide (ETPB) and chloroform were purchased from Sigma Aldrich (St Louis, MO) and used as received.

Processing

Several compositions were prepared using a 15 cc twin-screw micro-extruder DSM XPlore with *L/D* ratio 18 (Geleen, The Netherlands). The following PLA/ECard/ETPB materials were considered as: 100/0/0 (wt%), 80/20/0 (wt%), 80/20/0.02 phr (per hundred parts of resin), 80/20/0.06 phr, and 80/20/0.1 phr. In fact, the amount of plasticizer ECard was fixed to 20% after an optimization step. The processing conditions were also set up after an optimization step. Therefore, the barrel temperature was set at 180°C, screw speed was fixed to 100 rpm and the residence time to 5 min. PLA pellets were first dried overnight at 50°C before processing. PLA was first introduced and melted in the preheated micro-extruder. Dry ECard and ETPB were mixed and then injected into the extruder using a syringe.

Standard samples of the resulting materials were then prepared by injection molding machine (Model HAAKE MiniJet II, Thermo Scientific) at 180°C and 700 bar during 5 s.

Characterization

Fourier-Transform Infrared (FTIR) Spectroscopy . The changes in the chemical structure of PLA were evaluated by FTIR spectroscopy in attenuated total reflectance mode from 400 to 4000 cm^{-1} using a Bruker Optics Tensor 27 spectrometer.

Differential Scanning Calorimetry (DSC) . DSC measurements were performed on Netzsch DSC 204 F1 instrument (Selb, Germany) under nitrogen gas flow, with a heating rate of 10°C min^{-1} . Samples (5–10 mg) were sealed in hermetic aluminum pans and were subjected to the following temperature program: (i) a first heating step from –100 to 200°C, (ii) a cooling step from 200 to –100°C, and (iii) a second heating step from –100 to 200°C. T_g values were measured at the second ramp. The second heating eliminates the uncertainties due to the thermal history of the materials and therefore allows evaluating the inherent properties of the materials.

Size Exclusion Chromatography . Molecular weight change analyses were conducted with Agilent Technologies series 1200 operating with a differential refractive index detection and a linear column (PLgel Mixed-D 5 and 3 μm , 200 Da < Mw < 200 kDa in chloroform 1 ml min^{-1}). Sample preparation was performed by dissolving the material to be analyzed in chloroform at a concentration of 2 mg ml^{-1} . This was followed by the filtration of the prepared material solution using a syringe and an acrodisc-branded filter (pore size 0.45 μm). All analyses were run at room temperature.

For SEC analyses with UV detection, the apparatus consisted of 600E controller & pumping units (Waters, Versailles, France) followed by 486 tunable UV/Vis detector (Waters). Separation was performed on a unique mixed bed column (PLgel Mixed-D 300 \times 7.5 mm, particle size 5 mm, Agilent) with precolumn (PLgel Mixed-D 50 \times 7.5 mm) at room temperature. THF was used as eluent at a flow rate of 1 ml min^{-1} . Twenty microliters of a 1 and a 15 g L^{-1} resin solution were injected for SEC and SEC-SALDI analyses with satisfactory *S/N* ratio in a single run, respectively.

Thermogravimetric Analysis . Thermal stability of the plasticized PLA materials was investigated by means of thermogravimetric analyzer (TGA) model STA 409PC from NETZSCH; [15–20] mg of sample in an aluminum pan was heated from room temperature up to 600°C under air (100 ml min^{-1}) gas flow. The runs were carried out in dynamic conditions at a heating rate of 10°C min^{-1} .

Scanning Electron Microscopy (SEM) . Microstructure of plasticized PLA materials was studied by means of pressure controlled SEM Quanta Field Effect Gun 200 from FEI (Eindhoven, The Netherlands). To this end, all samples were fractured after immersion in liquid nitrogen for about 5 min to observe the fracture surface of the materials.

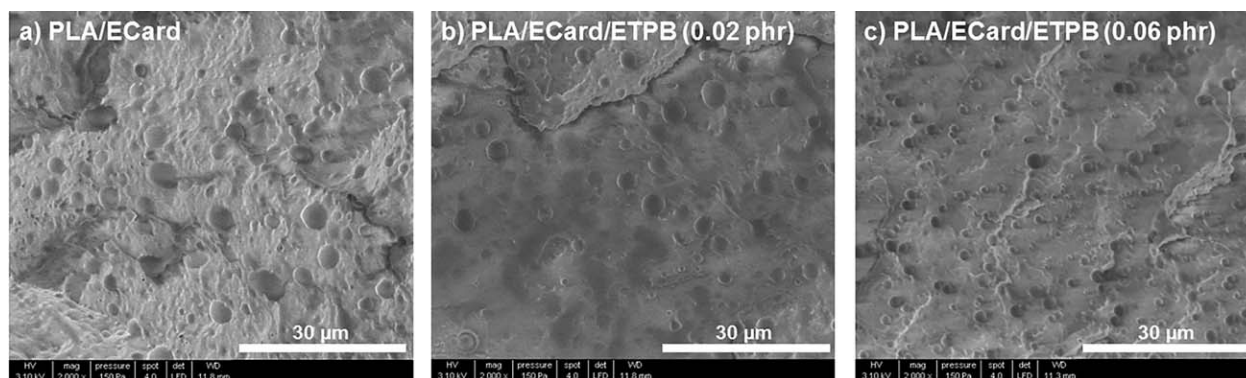


FIG. 1. SEM images of a) PLA-ECard, b) PLA- PLA-ECard-ETPB 0.02 phr, c) PLA-ECard-ETPB 0.06 phr.

Dynamic Mechanical Analysis (DMA) . The viscoelastic properties were evaluated by means of DMA using a Netzsch equipment model DMA 242C. Rectangular specimens ($60 \times 11 \times 3 \text{ mm}^3$) were used. They were conditioned for at least 24 h at 20°C and 50% of relative humidity before testing. Subsequently, they were subjected to double cantilever mode of flexural loading with amplitude of $30 \mu\text{m}$ in the temperature range from -60 to 120°C at a heating rate 2°C min^{-1} and a frequency of 1 Hz.

Tensile Tests . The quasi-static uniaxial tensile testing was done with a universal testing machine Instron model 5967 (Norwood, MA). Tensile specimens based on ASTM D638 with sample type V were used. The specimen had an overall length of 63.5 mm and a thickness of 3 mm. The gauge section of the specimen had a length of 25 mm and a minimum width of 3 mm. The specimens were conditioned for at least 24 h at 20°C and 50% of relative humidity before testing. The engineering axial stress versus axial strain curves were recorded at room temperature at a constant crosshead rate of 1 mm min^{-1} until break.

RESULTS AND DISCUSSION

Reactive Extrusion Modification and Plasticizing of PLA

In situ reactive grafting strategy has been employed to improve the compatibility between PLA and ECard by reactive extrusion.

Figure 1 shows the SEM images of the PLA-ECard blends. In absence of ETPB, ECard forms microsized domains dispersed in the PLA matrix (Fig. 1a). ECard domain average size is about $5 \mu\text{m}$. The weakness of the interface between PLA and ECard is evident, highlighting a high incompatibility between both phases. In order to decrease ECard domain size and strengthen the interface between PLA and the plasticizer, ETPB was added as a catalyst [35]. Indeed, the epoxide groups present in Ecard chemical structure can react either with $-\text{COOH}$ or with $-\text{OH}$ of the PLA end groups under the catalytic effect of ETPB to form some grafted copolymer that can function as compatibilizer between PLA and ECard. The grafting of a fraction of ECard plasticizer onto PLA backbone by reactive extrusion is expected to lead to the creation of more interactions between the so-functionalized polyester matrix and the remaining fraction

of nongrafted plasticizer [26, 27]. Therefore, different concentrations of ETPB were introduced into PLA/Ecard blend and their effect was investigated.

Figure 1b and c show that the domain size distribution of the plasticizer decreases in presence of ETPB. This decrease is accentuated with the increase of the catalyst amount (3 and $1 \mu\text{m}$ in presence of 0.02 and 0.06 phr, respectively). This morphological trend can be explained by a grafting of a fraction of ECard plasticizer onto PLA backbone by reactive extrusion leading to the creation of more interactions between the so-functionalized polyester matrix and the remaining fraction of nongrafted plasticizer. The grafting rate being proportional to the amount of ETPB, it has a direct impact on the domain size distribution of the plasticizer.

Grafting of ECard plasticizer onto PLA backbone by reactive extrusion was characterized by FTIR and SEC-MALDI-MS. **Figure 2** shows the FTIR spectra within the region of epoxy absorption. The intensity of the peak at 912 cm^{-1} attributed to epoxy groups of ECard decreases markedly with the addition of ETPB, suggesting reactions of epoxy groups during the reactive extrusion [35]. The reaction mechanism of $-\text{COOH}$ and $-\text{OH}$

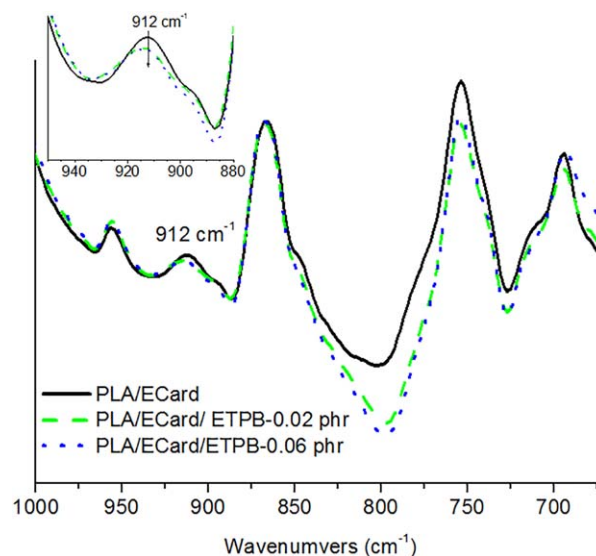
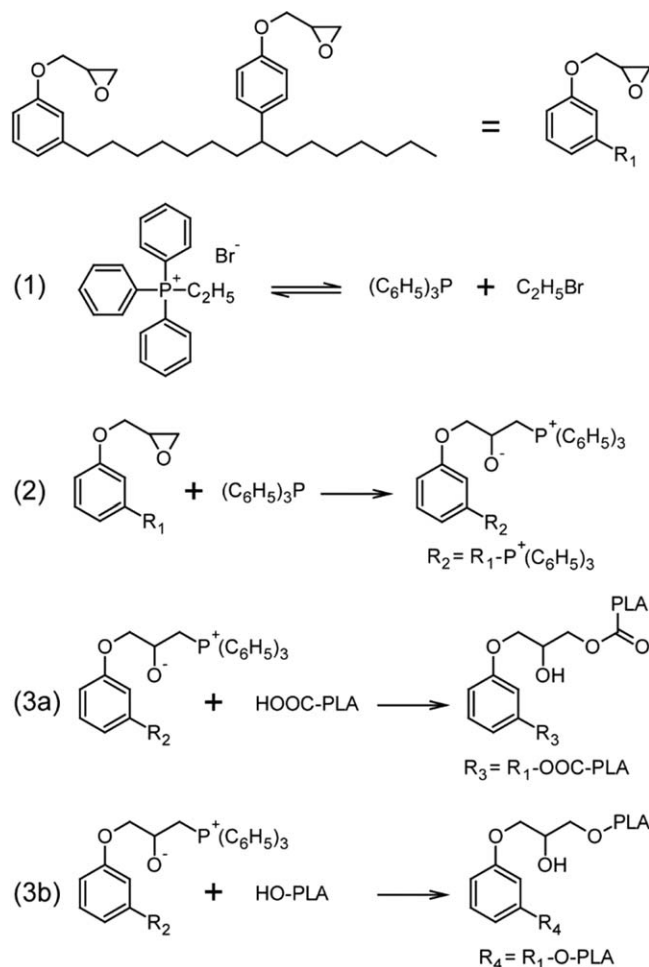


FIG. 2. FTIR spectra of plasticized PLA-based materials. [Color figure can be viewed at wileyonlinelibrary.com]



SCHEME 1. Reaction of PLA end groups with Ecard under the catalytic effect of ETPB.

groups with epoxy groups in presence of catalysts is already established [36]. It is established that ETPB dissociates easily under the mixing conditions and proceeds through a nucleophilic attack, which opens the epoxy ring in Ecard to generate an intermediate product. This product has high reactivity toward $-\text{COOH}$ and $-\text{OH}$ of PLA end chain groups, leading to the formation of PLA-g-Ecard copolymer. It is expected that the formed copolymer can act as an efficient compatibilizer for PLA/Ecard blends. The reaction scheme for Ecard with PLA in presence of ETPB is shown in **Scheme 1**.

In Addition to FTIR characterization, SEC analyses were also conducted on a device equipped with a UV detector. Cardanol moiety is indeed UV active at 280 nm [37] while PLA is transparent at such wavelength. Since PLA is of higher molecular weight than Ecard, any peak detected at a short retention time in the SEC chromatogram of a PLA/Ecard/ETPB sample would highlight any grafting of cardanol on the PLA backbones. As compared to the SEC chromatogram of Ecard (Fig. 3a), the chromatograms of three PLA/Ecard/ETPB 80/20/*X* samples with *X* = 0.02 (Fig. 3a), *X* = 0.06 (Fig. 3b) and *X* = 0.1 (Fig. 3c) display a distinct broad peak detected in the shortest elution volumes (~ 6 – 9 ml), validating the presence of high molecular weight compounds bearing UV-active groups. The two main peaks at the longer retention times are assigned to epoxidized

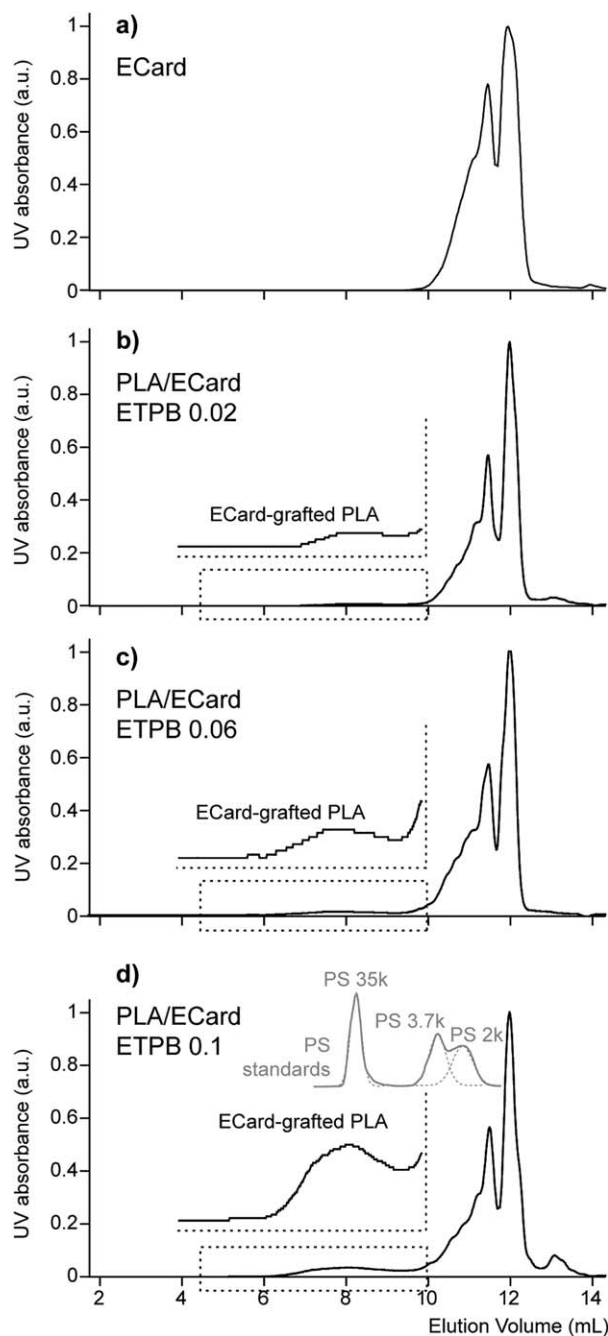


FIG. 3. SEC chromatograms of (a) Ecard and PLA/Ecard/ETPB in THF (b) 80/20/0.02, (c) 80/20/0.06, and (d) 80/20/0.1 recorded using a UV detector set at 280 nm. Insets in (b–d) Ecard-grafted PLA peaks (normalized). The SEC chromatogram of a mixture of three PS standards 35,000, 3,700, and 2,000 g/mol (UV detection, 254 nm) is depicted in inset of d).

cardanol and dimers as already characterized for NC514 [37] (NC514S named Ecard in this work is a purified grade of NC514—see **Figure S1** in the Supporting Information—but of similar chemical nature). Note that the decrease of intensity of the dimer peak for the three formulated samples are compared to the pristine Ecard. Dimers contain more epoxy groups and are more prone to react with PLA than the monomer of Ecard.

The SEC elution of three PS standards 35,000, 3,700, and 2,000 g mol⁻¹ is depicted in inset of Fig. 3d (light gray line). The PS 35,000 g mol⁻¹ standard and the Ecard-grafted PLA

TABLE 1. Molecular weights and dispersity as determined by SEC on all the investigated materials.

Blend composition (W/W)	\bar{M}_n (g/mol) (PS)		\bar{M}_w (g/mol) (PS)		Dispersity \bar{D} (M_w/M_n)	
	PLA	ECard*	PLA	ECard*	PLA	ECard*
Extruded PLA	118,120		244,280		2	
ECard		756		1,188		1.5
PLA/ECard (80/20)	113,460	793	224,540	1,266	2	1.5
PLA/ECard/ETPB (80/20/0.02 phr)	105,570	799	217,260	1,271	2	1.5
PLA/ECard/ETPB (80/20/0.06 phr)	91,500	682	182,000	1,106	2	1.5
PLA/ECard/ETPB (80/20/0.1 phr)	51,700	691	101,000	1,125	2	1.5

peak maxima have similar retention volumes (~ 8.1 ml), while the PLA peak is broad and some species elute in a much shorter time. The molecular weight of these polymeric chains thus ranges approximately between 100,000 and 20,000 g mol⁻¹ (PS equivalent) and could thus be seen as “intact” PLA backbones carrying epoxidized cardanol grafted on the end-group(s) upon ring opening of the epoxy group. One should also note the increase of the relative abundance of the ECard-PLA peak with the increase of the catalyst molar ratio (from 0.02 to 0.1) as evidenced in the insets of Fig. 3b–d. Increasing the amount of initiator tends to favor the grafting of the epoxidized cardanol in a noticeable extent under relatively given molar ratio limits. An attempt has been conducted using a PLA/ECard/ETPB formulation at 80/20/0.1. The appearance of the extruded mixture strongly suggested the PLA has been degraded. Its SEC chromatogram depicted in **Figure S2a** (Supporting Information) confirms this observation with a broad peak convoluted with the oligomers of ECard readily detected with an associated molecular weight comprised between 30,000 and 1,500 g mol⁻¹ (according to the elution volumes of the PS standards, inset in **Figure S2a**). A SEC-MALDI-MS coupling on this last PLA/ECard/ETPB 80/20/0.1 assessed the PLA nature of the broad polymeric distribution by the 72 Da shift between consecutive oligomers (C₃H₄O₂, the repeating unit of a PLA chain). The degradation of the PLA sample, i.e. cleavage of bonds upon thermo-oxidative processes leading to the mass reduction, and the complexity of ECard (expected to be a diepoxidized cardanol but most likely containing residual phenol groups instead of epoxy and dimers as impurities [37] account for the occurrence of several mass distributions. The detection of a complex isotopic pattern for each oligomer in **Figure S2c** is in accordance with the presence of at least one cardanol moiety along the backbone (consecutive peaks spaced by 2 Da owing to the polyunsaturated side chain [38] constituting a preliminary clue at a molecular level for the grafting of NC514S on PLA chains.

In addition to the SEC analyses conducted on device equipped with a UV detector to highlight the reactive grafting of ECard onto PLA backbone, SEC analyses were also conducted on another device equipped with RI detector to check at any changing of the molecular weight of PLA. SEC analyses used to determine the apparent molecular weight (M_n and M_w) of all samples according to polystyrene standards are summarized in **Table 1**.

Melt blending of PLA with 20 wt% of ECard does not have any impact on PLA molecular weight. The addition of 0.02 phr of ETPB does not affect the molecular weight of the polymer when taking into account the uncertainty of SEC measurements (ca., 10%). However, for higher ETPB concentrations (>0.02

phr), a significant shift of M_w and M_n toward lower molecular weights is observed, thus highlighting a concordance with the results obtained with SEC-MALDI-MS. The presence of high amount of catalyst leads to PLA chain scissions. PLA chain scissions can be attributed to a nucleophilic attack of the dissociated ETPB species under melt blending as explained above.

Besides the chain scission mechanism, branching/crosslinking reactions also occur during the reactive extrusion. The branching/crosslinking can be explained by the presence of difunctional epoxy groups in ECard, which can play a role of crosslinker. The crosslinked moiety could not be analyzed by SEC as it became insoluble [35].

Therefore, an excessive amounts of catalyst is not recommended as it can have a negative impact on PLA molecular weights.

Overall, the morphological analysis combined with FTIR and SEC-MALDI-MS show that the addition of ETPB catalyst leads to the creation of PLA-g-ECard copolymer. This latter takes an effective role in compatibilizing PLA/ECard. Even though the increase of the catalyst content has a positive impact on the enhancement of the compatibility between the polymer and the catalyst, it is clearly shown that at higher catalyst content (>0.02 phr), PLA chain scission occurs, therefore deteriorating the overall properties of PLA based materials.

Thermal Behavior

TGA and DSC were used to examine the thermal properties of all PLA based materials after melt processing.

The effect of the plasticizer on the thermal stability of the polymeric matrix is not often considered when studying plasticization of polymers. To investigate the effect of the presence of

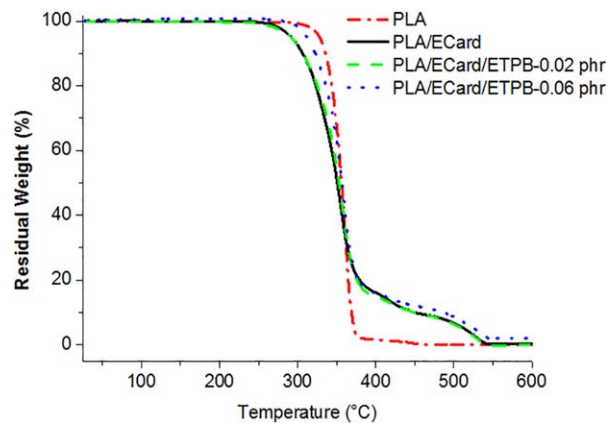


FIG. 4. TG curves for neat and plasticized PLA-based materials under air atmosphere. [Color figure can be viewed at wileyonlinelibrary.com]

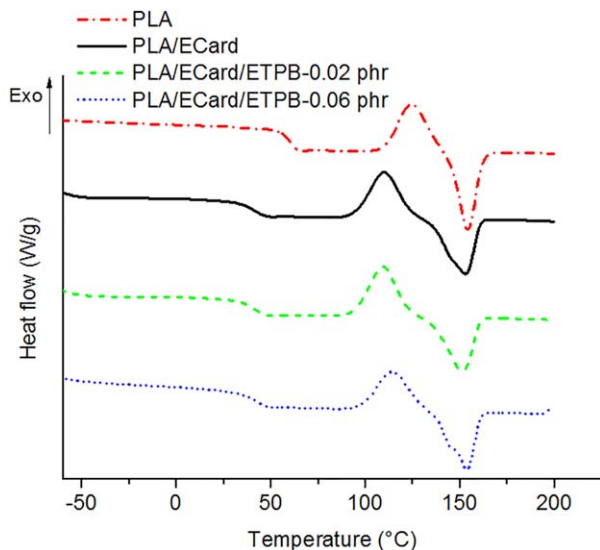


FIG. 5. DSC curves recorded for neat and plasticized PLA-based materials during the second heating. [Color figure can be viewed at wileyonlinelibrary.com]

ECard and the reactive grafting of a fraction of this latter on the thermal stability of PLA matrix, TGA measurements were performed on the elaborated formulations (Fig. 4). The thermal stability of plasticized PLA was compared with that of neat PLA. **Figure 4** shows the TG curves for PLA and plasticized PLA with ECard in absence and in presence of ETPB (0, 0.02, and 0.06 phr). The addition of ECard to PLA matrix leads to a slight shift of the decomposition onset temperature to lower temperatures with respect to neat PLA. However, the reactive grafting of a fraction of ECard onto PLA backbone after addition of 0.02 phr of catalyst does not seem to have any impact on the thermal decomposition temperature of plasticized PLA as compared with the nonreactive system PLA/ECard. However, in a highly reactive system containing 0.06 phr of catalyst, a lower decrease of the decomposition onset temperature is displayed. This could be due to the PLA molecular mobility restriction caused by high grafting rate of ECard. However, it should be noted that no effect related to the presence of ECard and its reactive grafting on PLA backbone was observed on the decomposition temperature at 50% weight loss. Overall, the addition of ECard in absence and in presence of catalyst did affect the thermal stability of PLA only at higher temperature ranges

(above 270°C), which are far away from the temperatures used during the melt processing.

Thermal behaviors of the investigated PLA/ECard materials were examined by means of DSC. **Table 2** and Fig. 5 summarize the thermal properties of neat and plasticized PLA.

DSC thermogram of neat PLA displays a glass transition temperature (T_g) at about 60°C, an exothermic peak of cold crystallization around 124°C and an endothermic melting peak at 154°C. Furthermore, the melting enthalpy (ΔH_m) of neat PLA is about equal to the enthalpy of cold crystallization (ΔH_{cc}), indicating that neat PLA is entirely amorphous. This is due to the fact that the investigated PLA contains 4.6% of D-lactide isomer, which reduces its capability to crystallize.

The addition of 20 wt% ECard leads to the shift to lower values of the glass transition and the cold-crystallization peak ($T_g = 41^\circ\text{C}$, $T_{cc} = 110^\circ\text{C}$). This shift is probably due to enhanced PLA chain mobility as a consequence of the presence of a high amount of low molecular weight plasticizer. Moreover, besides the main melting peak (T_m) at 153°C, a shoulder at 142°C appeared. Multiple melting peaks are typically observed in semi-crystalline polymers due to melt-recrystallization, and for PLA, corresponds to melting of initial lamellae and that of thicker, more perfected crystals formed during heating [39]. In this particular case, in the presence of ECard, this is directly linked to an increased mobility for short-range motion of the PLA chains. As a consequence a large portion of the amorphous phase got allowed to crystallize in the plasticized PLA [24], demonstrated by the presence of the shoulder (142°C) in the melting peaks of PLA blends. The reactive grafting of a fraction of ECard in presence of 0.02 phr of catalyst does not affect the overall thermal properties of plasticized PLA as T_g , T_{cc} , and T_m remained constant. However, even though no sensitive evolution is observed on the T_g and T_m of the reactive blend containing three times more of catalyst (0.06 phr), T_{cc} did shifted toward higher values (114°C). The evolution of T_{cc} as a function of the presence of ECard and catalyst is as follows: $T_{cc}\text{-PLA} > T_{cc}\text{-PLA/ECard/ETPB-0.06 phr} > T_{cc}\text{-PLA/ECard} \approx T_{cc}\text{-PLA/ECard/ETPB-0.02 phr}$. The origin of this trend is not clear as many processes occur at the same time during reactive extrusion (grafting, branching, crosslinking, chain scission...). However, two explanations can be stated out: (i) It is known from the literature that grafting may increase the crystallization temperature as the result of increased chain interaction, making it more difficult for these chains to disentangle from each other to crystallize

TABLE 2. Overall thermal and mechanical properties of all the materials investigated.

Blend composition (in wt%)	T_g^a (°C)	T_{cc}^a (°C)	T_m^a (°C)	$(\Delta H_m - \Delta H_{cc})^a$ (J/g)	T_g^b (E''_{\max}) (°C)	E^c (MPa)	E_t^d (MPa)	σ_y^d (MPa)	ε_b^d (%)
Extruded PLA	60	124	154	0	60	1,850	1,861	63	5.7
Epoxidized Cardanol (ECard)	−46	—	—	—	—	—	—	—	—
PLA/ECard 80/20	41	110	153	2.2	−45 and 50	1,488	1,361	28	32
			144						
PLA/ECard/ETPB (80/20/0.02 phr)	41	109	153	2.8	−45 and 46	1,377	1,110	34	49
			143						
PLA/ECard/ETPB (80/20/0.06 phr)	41	114	154	0.5	−45 and 46	1,510	1,425	31	11
			145						

^aGlass transition temperature from the second heating DSC scans.

^bGlass transition temperature at maximum E'' (DMA).

^cStorage modulus at 20°C (DMA).

^dTensile properties at 20°C according to ASTM D638 (test speed 5 mm min^{−1}).

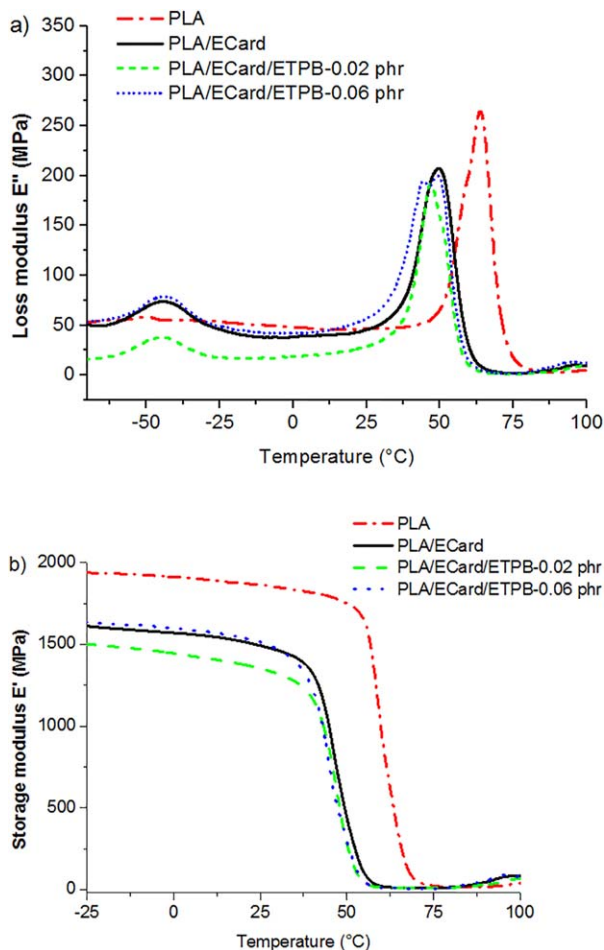


FIG. 6. Temperature dependence of (a) loss modulus E'' and (b) storage modulus E' for neat and plasticized PLA-based materials. [Color figure can be viewed at [wileyonlinelibrary.com](#)]

[40]. In the systems PLA/ECard/ETPB, this trend is observed only in the most reactive blend (at high grafting rate). (ii) ECard, being a difunctional glycidyl ether epoxy cardanol, crosslinking/branching reactions should take place simultaneously between the epoxy groups of the plasticizer and the carboxyl and hydroxyl end groups of PLA chains during reactive extrusion. As a consequence, the ability of PLA chains to crystallize can be hindered.

Mechanical Properties

Dynamic mechanical measurements were performed at 1 Hz to reveal the impact of plasticization and reactive grafting of ECard on the mechanical characteristics of the blend. The temperature effect on the storage modulus E' and loss modulus E'' is depicted Fig. 6a and b and the extracted mechanical parameters are summarized in **Table 2** for neat and plasticized PLA. T_g values are defined as the temperature of the maximum of the loss modulus (E'') obtained for α relaxation.

Neat PLA exhibits one T_g equal to 60°C while all plasticized blends display two distinct T_g , indicating the occurrence of a phase-separation. The first T_g , is equal to -45°C for free ECard, while the second value above 40°C corresponds to the T_g of plasticized PLA chains. Plasticized PLA chains in all blends display lower T_g as compared with neat PLA. Moreover, unlike DSC

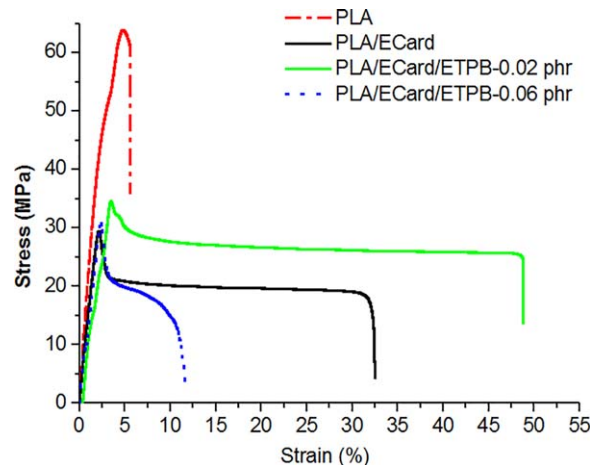


FIG. 7. Tensile strain-stress curves for neat and plasticized PLA-based materials. [Color figure can be viewed at [wileyonlinelibrary.com](#)]

results, DMA shows the reactive grafting effect of ECard on the T_g of the blends. Indeed, the reactive systems PLA/ECard/ETPB display lower T_g (46°C) than the nonreactive one PLA/ECard (T_g = 50°C). Similar behaviour was observed in our previous study, in which the reactive blend PLA + 10% MAG-PLA + 20% PEG [MAG-PLA: anhydride grafted PLA, PEG: poly(ethylene glycol)] displayed lower T_g as compared with the nonreactive one PLA + 20% PEG [26]. It is commonly admitted that the glass transition implies cooperative motions in one chain that are governed by intramolecular interactions as well as by intermolecular interactions [41]. A certain dynamic free volume is required allowing conformational change of the chain. Therefore, further decrease of T_g in the reactive blend can be caused by the enhancement of PLA chain disentanglement due to the presence of PLA-g-ECard which will space out the chains, thereby leading to the expansion of the free volume. The conformation of PLA-g-ECard formed during the reactive extrusion can be at the origin of the increase of PLA chain disentanglements. Physical interactions between grafted and free ECard could be also considered when describing the decrease of the T_g . Indeed, as discussed above, the formation of PLA-g-ECard copolymer improves probably the interfacial adhesion and the compatibility in PLA blends and thus the plasticizing efficiency of ECard.

As stated by Piorkowska et al. [42], the curve loss modulus E'' – temperature gives information about the dispersion/distribution of ECard within amorphous PLA phase. The existence of an additional low temperature peak in the plasticized PLA suggests the formation of ECard-rich phase. Moreover, a broadening of the width of the peak reflecting the glass transition is due to a plasticizer concentration gradient in all PLA blends.

Differences in results observed between DSC and DMA are in general due to the fact that these two techniques are based on different solicitation modes and thus their results cannot be systematically compared.

When looking at the storage modulus E' curves as a function of temperature for neat and plasticized PLA (Fig. 6b and **Table 2**), one can notice that E' measured at 20°C, for neat PLA is higher (1850 MPa) than that of the plasticized blends. However, among the plasticized blends, the reactive blend containing the lowest amount of catalyst, that is, 0.02 phr, displayed the lowest storage modulus (1377 MPa). When increasing the content of

the catalyst, that is, 0.06 phr, the storage modulus of the material increased from 1377 MPa (PLA/ECard/ETPB-0.02 phr) to 1510 MPa. Therefore, the evolution of E' as a function of the presence of ECard and catalyst is as follows: E' -PLA > E' -PLA/ECard/ETPB-0.06 phr > E' -PLA/ECard > E' -PLA/ECard/ETPB-0.02 phr. A clear correlation between the increase of E' and the increase of T_{cc} in the most reactive blend, that is, PLA/ECard/ETPB-0.06 phr as compared with PLA/ECard/ETPB-0.02 phr can be made. Even though these two reactive blends display the same T_g according to DSC and DMA, they do exhibit different viscoelastic properties.

Nominal tensile axial stress-strain behavior at room temperature, 20°C, of neat and plasticized PLA materials is depicted Fig. 7. The corresponding tensile properties are reported in Table 2 [tensile modulus E_t , yield stress σ_y and tensile elongation at break ϵ_b (ultimate strain)]. Neat PLA exhibits a purely brittle tensile failure and behavior characterized by a high tensile modulus (1860 MPa), a high yield point (63 MPa) and a very low elastic axial deformation <6%. Indeed, neat PLA reveal crazes, whose propagation and coalescence can lead to the specimen fracture. It is well established that the macroscopic stresses that are dissipated locally may be due to a competition between damage mechanisms by crazing and chain orientation mechanisms. For neat PLA, the chain motion is definitely not high enough to initiate stress dissipation by chain orientation [26, 27]. Damage mechanisms are thus favored. Damage mechanisms are generally observed in brittle polymer below its brittle-to-ductile transition temperature [43].

All plasticized PLA specimens exhibit lower tensile modulus, lower yield stress, and higher strain at break as compared to neat PLA. Furthermore, all plasticized PLA specimens yielded stable necking, showing cold-drawing behavior. They were subjected to tensile deformation accompanied by whitening of the specimen due to the development of crazes in the amorphous phase, highlighting the plasticizing efficiency of ECard. Nevertheless, the plasticizing effect is very much dependent on the presence and the amount of the catalyst (reactivity of the materials). In fact, the reactive blend containing the lowest amount of catalyst, *i.e.*, 0.02 phr, exhibited the highest ductility behavior characterized with lower tensile modulus and higher strain at break. Indeed, the tensile modulus and the strain at break measured for PLA/ECard/ETPB-0.02 phr are 1110 MPa and 49%, while those displayed for the physical blend PLA/ECard and for the most reactive blend PLA/ECard/ETPB-0.06 phr are 1361 MPa and 32%, and 1425 MPa and 11%, respectively. Further increase of the amount of the catalyst has tendency to deteriorate the overall mechanical properties of the material. The same trend was observed by DMA. As mentioned above, ECard, being a difunctional glycidyl ether epoxy cardanol, crosslinking/branching reactions should take place simultaneously between the epoxy groups of the plasticizer and the carboxyl and hydroxyl end groups of PLA chains during reactive extrusion. As a consequence, the tensile/elastic modulus in the reactive blend PLA/ECard/ETPB-0.06 phr increases (Scheme 1).

Unlike neat PLA, in all plasticized PLA specimens molecular relaxation is enhanced and the stresses are dissipated by conformational changes of glassy amorphous PLA chains, leading to segmental orientation and disentanglement [26, 27]. These phenomena are more prominent in the reactive blend containing the lowest content of catalyst, that is, PLA/ECard/ETPB-0.02 phr blend.

CONCLUSIONS

In this study, plasticization of PLA with a new biobased plasticizer, di-functional glycidyl ether epoxy cardanol, is described. In situ reactive grafting strategy has been employed to improve the compatibility between PLA and ECard in presence of ETPB as a catalyst using twin-screw extruder. In absence of catalyst, ECard forms micron-sized domain dispersed in the PLA matrix. The weakness of the interface between PLA and ECard highlights a high incompatibility between both phases. Domain size distribution of the plasticizer decreases in presence of ETPB. This decrease is accentuated with the increase of the catalyst amount. This morphological trend can be explained by the fact that the reactive grafting of a fraction of ECard plasticizer onto PLA backbone leads to the creation of more interactions between the so-functionalized polyester matrix and the remaining fraction of non-grafted plasticizer. Although all plasticized PLA specimens exhibit lower glass transition temperature, lower elastic/tensile modulus, lower yield stress, and higher strain at break, the reactive blend containing the lowest amount of catalyst, that is, 0.02 phr, exhibited the highest ductility behavior. Indeed, it is clearly demonstrated in this study that at higher catalyst content (>0.02 phr), PLA chain scission and crosslinking/branching reactions occur, therefore deteriorating the overall properties of PLA based materials.

REFERENCES

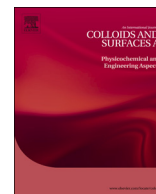
1. D. Garlotta, *J. Polym. Environ.*, **9**, 63 (2001).
2. L.T. Lim, R. Auras, and M. Rubino, *Prog. Polym. Sci.*, **33**, 820 (2008).
3. I. Vroman, and L. Tighzert, *Materials*, **2**, 307 (2009).
4. R. Auras, B. Harte, and S. Selke, *Macromol. Biosci.*, **4**, 835 (2004).
5. H.N. Rabetafika, M. Paquot, and P. Dubois, *Biotechnol. Agronomie Soc. Environ.*, (2006).
6. C.J. Weber, V. Haugaard, R. Festersen, and G. Bertelsen, *Food Addit. Contam.*, **19**, 172 (2002).
7. K. Anderson, K. Schreck, and M. Hillmyer, *Polym. Rev.*, **48**, 85 (2008).
8. G. Kfoury, J.-M. Raquez, F. Hassouna, P. Leclère, V. Toniazzi, D. Ruch, and P. Dubois, *Polym. Eng. Sci.*, **55**, 1408 (2015).
9. H. Liu, and J. Zhang, *J. Polym. Sci. Part B: Polym. Phys.*, **49**, 1051 (2011).
10. G. Kfoury, J.M. Raquez, F. Hassouna, J. Odent, V. Toniazzi, D. Ruch, and P. Dubois, *Front. Chem.*, **1**, 32 (2013).
11. L. Mascia, and M. Xanthos, *Adv. Polym. Tech.*, **11**, 237 (1992).
12. P.R. Gruber, J.J. Kolstad, C.M. Ryan, R.S.E. Conn, and E.S. Hall, U.S. Patent 6355772 (2002).
13. R.G. Sinclair, U.S. Patent 5180765 (1993).
14. S. Jacobsen, and H.G. Fritz, *Polym. Eng. Sci.*, **39**, 1303 (1999).
15. N. Ljungberg, and B. Wesslén, *Biomacromolecules*, **6**, 1789 (2005).
16. W.M. Gramlich, M.L. Robertson, and M.A. Hillmyer, *Macromolecules*, **43**, 2313 (2010).
17. S. Vijayarajan, S.E.M. Selke, and L.M. Matuana, *Macromol. Mater. Eng.*, **299**, 622 (2014).
18. E. Azwar, B. Yin, and M. Hakkarainen, *J. Chem. Technol. Biotechnol.*, **88**, 897 (2013).

19. C.M. Buchanan, N.L. Buchanan, K.J. Edgar, and J.L. Lambert, U.S. Patent 2003171458 A1, (2003).
20. L. Dobircan, N. Delpouve, R. Herbinet, S. Domenek, L. Le Pluart, L. Delbreilh, V. Ducruet, and E. Dargent, *Polym. Eng. Sci.*, **55**, 858 (2015).
21. Z. Kulinski, E. Piorkowska, K. Gadzinowska, and M. Stasiak, *Biomacromolecules*, **7**, 2128 (2006).
22. H. Zhang, J. Fang, H. Ge, L. Han, X. Wang, Y. Hao, C. Han, and L. Dong, *Polym. Eng. Sci.*, **53**, 112 (2013).
23. K. Okamoto, T. Ichikawa, T. Yokohara, and M. Yamaguchi, *Eur. Polym. J.*, **45**, 2304 (2009).
24. N. Ljungberg, and B. Wesslén, *Polymer*, **44**, 7679 (2003).
25. N. Ljungberg, T. Andersson, and B. Wesslén, *J. Appl. Polym. Sci.*, **88**, 3239 (2003).
26. F. Hassouna, J.M. Raquez, F. Addiego, P. Dubois, V. Tonniazzo, and D. Ruch, *Eur. Polym. J.*, **47**, 2134 (2011).
27. F. Hassouna, J.M. Raquez, F. Addiego, V. Tonniazzo, P. Dubois, and D. Ruch, *Eur. Polym. J.*, **48**, 404 (2012).
28. G. Kfoury, F. Hassouna, J.-M. Raquez, V. Tonniazzo, D. Ruch, and P. Dubois, *Macromol. Mater. Eng.*, **299**, 583 (2014).
29. G. Vasapollo, G. Mele, and R. Del Sole, *Molecules*, **16**, 6871 (2011).
30. E. Bloise, L. Carbone, G. Colafemmina, L. D'Accolti, S.E. Mazzetto, G. Vasapollo, and G. Mele, *Molecules*, **17**, 12252 (2012).
31. F. Jaillet, E. Darroman, A. Ratsimihety, R. Auvergne, B. Boutevin, and S. Caillol, *Eur. J. Lipid Sci. Technol.*, **116**, 63 (2014).
32. J. Chen, Z. Liu, J. Jiang, X. Nie, Y. Zhou, and R.E. Murray, *RSC Adv.*, **5**, 56171 (2015).
33. M. Alexander, and E.T. Thachil, *J. Appl. Polym. Sci.*, **102**, 4835 (2006).
34. F. Hassouna, I. Mihai, L. Fetzer, T. Fouquet, J.-M. Raquez, A. Laachachi, H. Ibn Al Ahrach, and P. Dubois, *Macromol. Mater. Eng.*, **301**, 1267 (2016).
35. Y. Li, and H. Shimizu, *Eur. Polym. J.*, **45**, 738 (2009).
36. H.T. Oyama, T. Kitagawa, T. Ougizawa, T. Inoue, and M. Weber, *Polymer*, **45**, 1033 (2004).
37. T. Fouquet, L. Fetzer, G. Mertz, L. Puchot, and P. Verge, *RSC Adv.*, **5**, 54899 (2015).
38. P. Verge, T. Fouquet, C. Barrère, V. Tonniazzo, D. Ruch, and J.A.S. Bomfim, *Compos. Sci. Technol.*, **79**, 126 (2013).
39. R. Pantani, F. De Santis, A. Sorrentino, F. De Maio, and G. Titomanlio, *Polym. Degrad. Stab.*, **95**, 1148 (2010).
40. K.I. Ku Marsilla, and C.J.R. Verbeek, *Eur. Polym. J.*, **67**, 213 (2015).
41. J.L. Halary, F. Laupretre, and L. Monnerie, *Polymer Materials: Macroscopic Properties and Molecular Interpretations*, Wiley, Hoboken, NJ (2011).
42. E. Piorkowska, Z. Kulinski, A. Galeski, and R. Masirek, *Polymer*, **47**, 7178 (2006).
43. W.G. Perkins, *Polym. Eng. Sci.*, **39**, 2445 (1999).



Contents lists available at ScienceDirect

Colloids and Surfaces A

journal homepage: www.elsevier.com/locate/colsurfa

An environmentally benign methodology to elaborating polymer nanocomposites with tunable properties using core-shell nanoparticles and cellulose nanocrystals



Fatima Hassouna^{a,*}, Johana Korbelářová^a, Baptiste Jaquet^b, Edith Mawunya Kutorglo^a, Dušan Kopecký^c, Pavel Ulbrich^d, Michal Fulem^e, Zdeněk Hrdlička^f, Miroslav Šoos^a

^a Department of Chemical Engineering, University of Chemistry and Technology Prague, Technická 3, 166 28 Prague 6, Dejvice, Czech Republic

^b Institute for Chemical and Bioengineering, Department of Chemistry and Applied Biosciences, ETH Zurich, Vladimir-Prelog-Weg 1, 8093 Zurich, Switzerland

^c Department of Physics and Measurements, University of Chemistry and Technology Prague, Technická 3, 166 28 Prague 6, Dejvice, Czech Republic

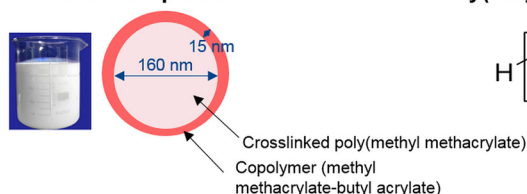
^d Department of Biochemistry and Microbiology, University of Chemistry and Technology Prague, Technická 3, 166 28 Prague 6, Dejvice, Czech Republic

^e Department of Physical Chemistry, University of Chemistry and Technology Prague, Technická 5, 166 28 Prague 6, Dejvice, Czech Republic

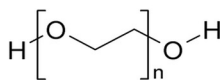
^f Department of Polymers, University of Chemistry and Technology Prague, Technická 5, Prague 6, Dejvice, 166 28, Czech Republic

GRAPHICAL ABSTRACT

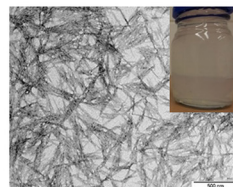
Core-shell nanoparticles



Poly(ethylene glycol) (PEG)



Cellulose nanocrystals (CNC)



ARTICLE INFO

Keywords:

Core-shell latex nanoparticles

Cellulose nanocrystals

Colloidal suspension

Nanocomposite

Morphology

Thermo-mechanical properties

ABSTRACT

An environmentally benign concept based on waterborne systems is developed for preparation of novel nanocomposite materials with tunable properties. The designed nanocomposites are based on combination of core-shell latex nanoparticles, cellulose nanocrystals (CNC) and polyethylene glycol (PEG). First, core-shell latex nanoparticles from copolymer (methyl methacrylate-ethylene glycol dimethacrylate)-core and copolymer (methyl methacrylate-butyl acrylate)-shell (CS15) are prepared by starved emulsion polymerization. Likewise, incorporation of CNC aqueous suspension into the core-shell latex without any further chemical modification of the nanofiller while assuring good compatibility between both entities is achieved. PEG is effectively added to the suspension to assure multiple functions in the final material. After mixing of the ternary systems, the nanocomposites are prepared by three approaches, i.e. solution casting, solution casting followed by compression molding, and freeze drying followed by compression molding. SEM analysis shows that compression molding

* Corresponding author.

E-mail address: fatima.hassouna@vscht.cz (F. Hassouna).

<https://doi.org/10.1016/j.colsurfa.2018.05.054>

Received 5 December 2017; Received in revised form 11 May 2018; Accepted 18 May 2018

Available online 19 May 2018

0927-7757/ © 2018 Published by Elsevier B.V.

processes lead to the highest degree of coalescence of CS15 nanoparticles. This effect is however reduced in presence of PEG or PEG/CNC. It is further observed that the presence of PEG helps protecting CNC from thermal degradation. Thermal and thermo-mechanical analyses prove a high plasticizing performance of PEG and its good confinement between the nanoparticles and at interstitial spaces. Furthermore, it is revealed that the level of material reinforcement by CNC depends strongly on the ratio between CNC and PEG due to the establishment of strong interactions via hydrogen bonding between both components, which can affect the formation of CNC percolating network. These findings allow tuning the microstructure and related properties of the nanocomposites.

1. Introduction

In recent years, replacing petroleum-based products with materials obtained from renewable resources is of a high importance in terms of economic and ecological perspectives [1]. Indeed, an increasing interest has been concentrated on the development of biobased materials in different sectors to overcome the environmental concerns and inevitable dwindling of petroleum-based resources. The development of polymers as well as nanofillers derived from renewable resources allowed the advances made in this trend. Among the biobased nanofillers, cellulose nanocrystals (CNC), extracted from cellulose, have emerged as very promising materials for the design of environmentally friendly materials thanks to their renewability, biodegradability, needle-like morphology, low specific density and exceptional mechanical properties [2–10]. Indeed, the CNC Young's modulus is in the range of 130 and 250 GPa (depending on the variety and the source of cellulose as well as on the method of extraction) [6]. Thanks to their remarkable mechanical properties, nanoscale size and high aspect ratios, CNC fulfill all features necessary for ideal nanofiller for preparation of polymeric nanocomposites [2–10].

One of the disadvantages associated to the utilization of cellulose nanoparticles for preparation of polymer nanocomposites as a reinforcement material is their difficulty to disperse in most of polymeric matrices and particularly in hydrophobic matrices, or in non-polar solvents due to polar nature of their surface, thus leading to the aggregation of nanofillers [4,6].

To overcome all these issues, chemical modification of the surface of CNC is used such as polymer chain grafting that can play a role of compatibilizer, mainly, when they are of the same nature as the matrix [2,6–9] and hence improving the final mechanical properties of the nanocomposite materials. However, the disadvantage of this approach is the use of many toxic chemicals.

To minimize these drawbacks, few studies recently reported the use of new methodology based on the preparation of nanocomposites with a polymeric latex as a matrix and CNC as a reinforcing agent. When they are homogeneously dispersed in the polymer matrix, they provide an outstanding reinforcing effect [11–14]. In fact, polymer aqueous suspensions, so-called latexes, have attracted enormous interest. This area has been stimulated by environmental concerns and governmental directives to move from solvent-based to water-borne systems as well as the scientific challenges that still need to be addressed. Further processing of the generated latex can be performed by solution casting or by lyophilization (also called freeze drying) followed by conventional thermoforming processes (injection molding, compression molding, extrusion, etc.) [11–14]. It is well known that the standard model for latex film formation follows three stages including evaporation of water and packing of latex particle; particle deformation along with the loss of the interstitial voids between latex particles; and the inter-diffusion of polymer chains between the residual particles achieving the final mechanical properties of the film [15]. When using water-born systems, several recent studies showed the possibility to mix different kinds of latexes with different organic and inorganic suspensions [13,15]. Therefore, it becomes very convenient to incorporate CNC aqueous suspension into latex suspension, without any further chemical modification of the nanofiller to assure a good compatibility. Favier et al. [13,14] are the first authors who reported the processing by casting of composite materials

based on aqueous suspensions of CNC and latex synthesized by copolymerization of the monomers butyl acrylate (65% (w/w)) and styrene (35% (w/w)). They observed enhancement of the mechanical properties (shear modulus) in the rubbery state of the polymer due to the presence of CNC. Different types of mechanical models were developed to describe this effect. It was deduced that CNC create a rigid network, most likely linked together by hydrogen bonds. It is believed that the percolation mechanism is at the origin of the formation of this network [13,14]. More recently, Annamalai et al. [11] prepared biomimetic, stimuli-responsive polymer nanocomposites from an aqueous styrene – butadiene rubber (SBR) latex and CNC aqueous suspensions. The final nanocomposite materials were made by three different processes, i.e. i) solution casting, ii) solution casting followed by additional reshaping by compression molding, and iii) infusion of SBR solution in CNC organogel template and subsequent drying and thermoforming by compression molding of the gel. The study highlighted the advantage of using CNC as a reinforcing agent for polymeric matrix obtained out of latex. It was also shown that the method of preparation of the final nanocomposites out of mixtures of SBR latex with CNC aqueous dispersion influenced the properties of the materials.

The purpose of this study aims at extending and exploring the concept of Latex based nanocomposite materials to core-shell polymeric latex characterized by crosslinked hard core and soft shell to design new and innovative materials that can find applications in different domains. Tailored core-shell latex nanoparticles can offer a variety of properties and similar advantages as homogeneous nanoparticles and avoid the disadvantage of organic solvent release during the preparation of the film [16]. CNC are used as a biobased reinforcing agent thanks to their enormous Young's modulus (up to 250 GPa) [6]. Low molecular weight PEG is used as a plasticizing agent. The combination of the three components exhibiting different properties (thermal, rheological, mechanical etc.) are expected to tailor the properties of the final ternary nanocomposites. Furthermore, fundamental aspects governing the behavior of such hybrid polymer nanocomposites are still not well understood since they were barely investigated. Therefore, the present study will contribute to better understand the physical and chemical interactions occurring between the phases of the nanocomposites. It will also contribute to better understand the relationship between the morphological features and the final properties of the material (thermal and thermo-mechanical properties).

Therefore, in the present study core-shell latex nanoparticles from copolymer (methyl methacrylate-ethylene glycol dimethacrylate)-core and copolymer (methyl methacrylate-butyl acrylate)-shell (CS15) were synthesized by starved emulsion polymerization. The core-shell nanoparticles should exhibit soft shell will low glass transition temperature (T_g) and a hard crosslinked core. In fact, soft shell is expected to allow the coalescence/compaction of the nanoparticles during the film formation (via solution casting or compression molding. A hard cross-linked core is expected to allow retaining the particle-structure while enhancing the mechanical properties of the subsequent film (higher modulus). Using CS15 as a matrix, CNC isolated from ramie fibers as a biobased reinforcing agent and polyethylene glycol (PEG) as a plasticizing agent, a new family of nanocomposite materials with tunable properties were prepared. The nanocomposite films were elaborated using three different approaches including solution casting, solution casting followed by compression molding, and freeze drying followed

by compression molding. The addition of both PEG and CNC allowed to tailor the microstructure and related properties of the ternary system CS15/PEG/CNC. Moreover, the effect of the processing techniques, *i.e.* solution casting versus compression molding on properties of the materials was examined. The impact of the ratio of CS15/PEG/CNC on the morphology, thermal and thermo-mechanical properties of the elaborated materials was evaluated.

2. Experimental section

2.1. Materials

Sodium hydroxide was purchased from Penta. Sulfuric acid (96% *p.a.*), polyethylene glycol (PEG) ($M_n = 700 \text{ g mol}^{-1}$), methyl methacrylate (MMA) (Aldrich, 99%), iso-butyl acrylate (BA) (Aldrich, $\geq 99\%$), Ethylene glycol dimethylacrylate (EGDMA) (Aldrich, 98%), potassium persulfate (Aldrich, 99.99%) and sodium dodecyl sulfate (SDS) (Fluka, $> 96\%$) were used as received. Ramie fiber was kindly offered by Stucken Melchers GmbH & Co. KG (Germany). Deionized water was further treated by using a Millipore Simpact 2 purification device for the synthesis part.

2.2. Synthesis of core-shell nanoparticles

The core-shell nanoparticles were prepared by starved emulsion polymerization [17,18] using LABMAX. The synthesis was performed in a 4 l jacketed reactor at 70 °C under nitrogen atmosphere. The reactor was firstly filled with MQ water (2.405 l) and SDS (0.80 g in 20 ml MQ-water) and heated. Solution of KPS used as initiator ((2.5 g in 75 ml MQ-water) was then added, and the feed of 5% w/w monomer mixture (20% EGDMA / 80% MMA) at 2.5 ml/min (125 ml total) started. 30 min after the end of monomer addition, 10 ml of 20% SDS solution were added and the reaction was allowed to proceed. The conversion reaction and the size of the particles were monitored using gravimetric analysis and dynamic light scattering (DLS), respectively. Once the core of the particles was reached with the desired diameter, approximately 160 nm, additional 1.25 g KPS was added into the reactor followed by the feed of 100 ml of 70% BA / 30% MMA with the feeding rate of 0.5 ml/min to generate the shell. The monomer feed was stopped when the shell of the nanoparticles reached the size of 15 nm-thick. A latex (CS15) with core-shell nanoparticles characterized by a core diameter of 160 nm and shell thickness of 15 nm were used as prepared. Their average size distribution was analysed in the ZetaSizer (Malvern ZetaSizer Nano-ZS) (Fig. S1 in the Supporting Information). It is worth mentioning that core-shell nanoparticles with different shell thickness were prepared, *i.e.* 5, 10 and 15 nm. A shell thickness of 15 nm was necessary to prepare films with good mechanical properties.

2.3. Preparation of cellulose nanocrystals

The method used to prepare cellulose nanocrystals (CNC) was adopted from Habibi et al. [19]. 30 g of clean ramie fibers were mechanically cut into small segments. Subsequently, they were treated with 500 ml of a 4% of sodium hydroxide solution at 80 °C for 2 h to eliminate residual contaminations. The fibers were then immersed in 400 ml of sulfuric acid solution (64 wt.%) at 50 °C for 45 min. They were subjected to a continuous mechanical stirring for an efficient acid hydrolysis. After the acid hydrolysis was completed, the hydrolysis was stopped by the addition of cold deionized water. The obtained suspension was filtered to take away unhydrolyzed fibers. The suspension was carefully and repeatedly washed with deionized water by centrifugation at 12 300 rpm at 10 °C for 20 min until neutral pH was reached. Lastly, dialysis was performed against deionized water for 10 days to eliminate residual sulfuric acid. Aqueous suspension of CNC was then sonicated for 30 min using ultrasonic probe (Bandelin Sonoplus).

2.4. Preparation of nanocomposites

Well-defined amounts of the CNC suspension were incorporated into the CS15 latex. The resulting mixtures of CS15/CNC were magnetically stirred during 3 h and sonicated in sonication bath (Bandelin Sonorex) for 1 h with ice cubes. Addition of plasticizing agent *i.e.* PEG to the formulation CS15/CNC was also performed. Amounts of PEG ranging from 10 to 20 wt.% based on the total weight of the mixture were added to the CS15/CNC water mixture while magnetically stirring over 1 h. The nanocomposite films were processed by the approaches described below.

2.4.1. Solution casting (SC) and solution casting followed by compression-molding (SC-CM)

When solution approach was applied, the resulting mixture suspensions (CS15, CS15/CNC or CS15/CNC/PEG) were cast on Teflon Petri-dishes and placed in a ventilated oven at 40 °C during 3 days to ensure complete water evaporation, hence leading to the formation of nanocomposite films.

When solution casting followed by compression molding approach is applied, compression-molding of the films prepared by solution casting was carried out in a hydraulic press SHP 20, ZDB Hydraulics, Ltd., (CR 2000) between Teflon sheets for 3 min at 165 °C. Under these optimized conditions non shrinking, self-standing films were obtained.

Reference samples of neat CS15 films were also elaborated following aforementioned approaches.

2.4.2. Freeze drying followed by compression molding (CM)

The mixtures (CS15, CS15/CNC or CS15/CNC/PEG) were subsequently freeze dried for 48 h (freeze dryer Christ Alpha 1–2 LD plus equipped with vacuum pump Vacuubrand RZ 2.5). The resulting powders were further compression-molded in a hydraulic press (SHP 20, ZDB Hydraulics, Ltd., (CR 2000)). $50 \times 50 \times 1 \text{ mm}^3$ square plates of CS15 (reference sample), CS15/CNC or CS15/CNC/PEG were compression molded using a definite mold. The followed procedure includes several steps: i) the powder was placed inside the mold, ii) it was heated at 165 °C during 2 min, iii) then it was compressed during 1 min with a pressure of 4 MPa, and iv) CS15, CS15/CNC or CS15/CNC/PEG were cooled in a second cooling hydraulic press by means of water circulation (15 °C).

2.5. Characterization

2.5.1. Transmission electron microscopy

CNC size and shape were determined using Transmission electron microscope (TEM). The measurement was carried out by JEM-1010 (JEOL, Ltd; Japan) equipped with a CCD camera MegaView III Olympus SIS (Germany). Drops of aqueous dispersions of CNC (about 10 μl) were applied to a copper electron microscopic grid, covered by very thin layer of carbon, left to adhere for about 5 min and excess of solution was sucked out with a filter paper. Then, the grid was placed on a drop of 1% uranyl acetate in ethanol for about 2–5 minutes to contrast the sample. The grid was again dried by filter paper and inserted into the microscope for subsequent observation. Microscopy was carried out at an acceleration voltage of 80 kV. The pictures were evaluated by Image Analysis Software v.3.2. and the dimensions of nanoparticles were measured about 30 times on, at least, 3 independent fields on the grid (*i.e.* taken pictures).

2.5.2. Scanning electron microscopy

Scanning electron microscope (SEM) was used to observe the surface and cross-section of the nanocomposites. The samples were coated by the 5 nm thin layer of gold and measured by electron microscope Mira 3 LMH (Tescan Brno, s.r.o.; Czech Republic) equipped with Shottky cathode.

2.5.3. Fourier transform infrared spectroscopy

The chemical structure of freeze dried cellulose nanocrystals was characterized by Fourier transform infrared (FTIR) spectroscopy in attenuated total reflectance (ATR) mode using a Thermo Scientific Nicolet iZ10-FTIR spectrometer, working with OMNIC Software. Spectra were obtained using 64 scans summation and 4 cm^{-1} resolution.

2.5.4. X-ray diffraction

The crystalline structure of CNC was determined using X-ray diffraction of cellulose powder obtained by freeze drying. The composite films were characterized by same methodology. X-ray powder data were measured at room temperature on a θ - θ powder diffractometer X'Pert3Powder in Bragg-Brentano para-focusing geometry using wavelength $\text{CuK}\alpha$ radiation ($\lambda = 1.5418\text{ \AA}$, $U = 40\text{ kV}$, $I = 30\text{ mA}$). Data were scanned using an ultrafast detector 1D PIXcel angular range 5 – 50° (2θ) with a step size of 0.039° (2θ) and a counting time of 175.185 s per step. Data evaluation was done by HighScorePlus 4.0.

2.5.5. Differential scanning calorimetry

The thermal properties were investigated with a differential scanning calorimeter TA Q1000, TA Instruments, USA under a nitrogen gas flow. The heating rate was adjusted to $10^\circ\text{C}/\text{min}$. Samples (3 – 5 mg) were placed in a well-sealed aluminum pans and were exposed to three cycles: i) first heating from -90 to 165°C , ii) then cooling from 165 to -90°C and iii) finally heating from -90 to 165°C .

2.5.6. Dynamic mechanical thermal analysis

The viscoelastic behaviors of the materials were assessed by means of dynamic mechanical thermal analyzer (DMTA) DX04 T model (RMI, Czech Republic). Rectangular specimens ($50 \times 10 \times 1\text{ mm}^3$) were used. Before testing, they were conditioned for 24 h at 50% of relative humidity and at 20°C . Afterward, they were subjected to single cantilever (two-point bending) testing with dynamic deformation (deformation amplitude) of 0.25 mm and static deformation (pre-strain) of 0 mm at a heating rate $2^\circ\text{C}/\text{min}$ and a frequency of 1 Hz . Temperature range was set between -80 to 140°C .

3. Results and discussion

3.1. Characterization of CNC

The CNC utilized in this study were extracted from bleached ramie fibers by acidic hydrolysis following the procedure described by Habibi et al. [20]. TEM images shown in Fig. 1a revealed that CNC were well individualized into rod-like nanoparticles. From TEM images, an average length of $172 \pm 47\text{ nm}$ and an average diameter of $7 \pm 1.8\text{ nm}$ were measured. An aspect ratio of 25.5 was calculated from these CNC size parameters. The dimensions of CNC are in accordance with previously published data reported for ramie CNC prepared under the same conditions. FTIR and XRD confirmed the successful extraction of CNC (Fig. 1b and c). FTIR spectrum of CNC showed peaks typical for cellulose bond stretching at 3336 cm^{-1} ($-\text{OH}$ groups), 1650 cm^{-1} ($\text{C}=\text{O}$ carbonyl groups), 1100 cm^{-1} ($\text{C}-\text{O}-\text{C}$ glycosidic ether groups) and 1161 cm^{-1} ($\text{C}-\text{C}$ ring breathing band). XRD

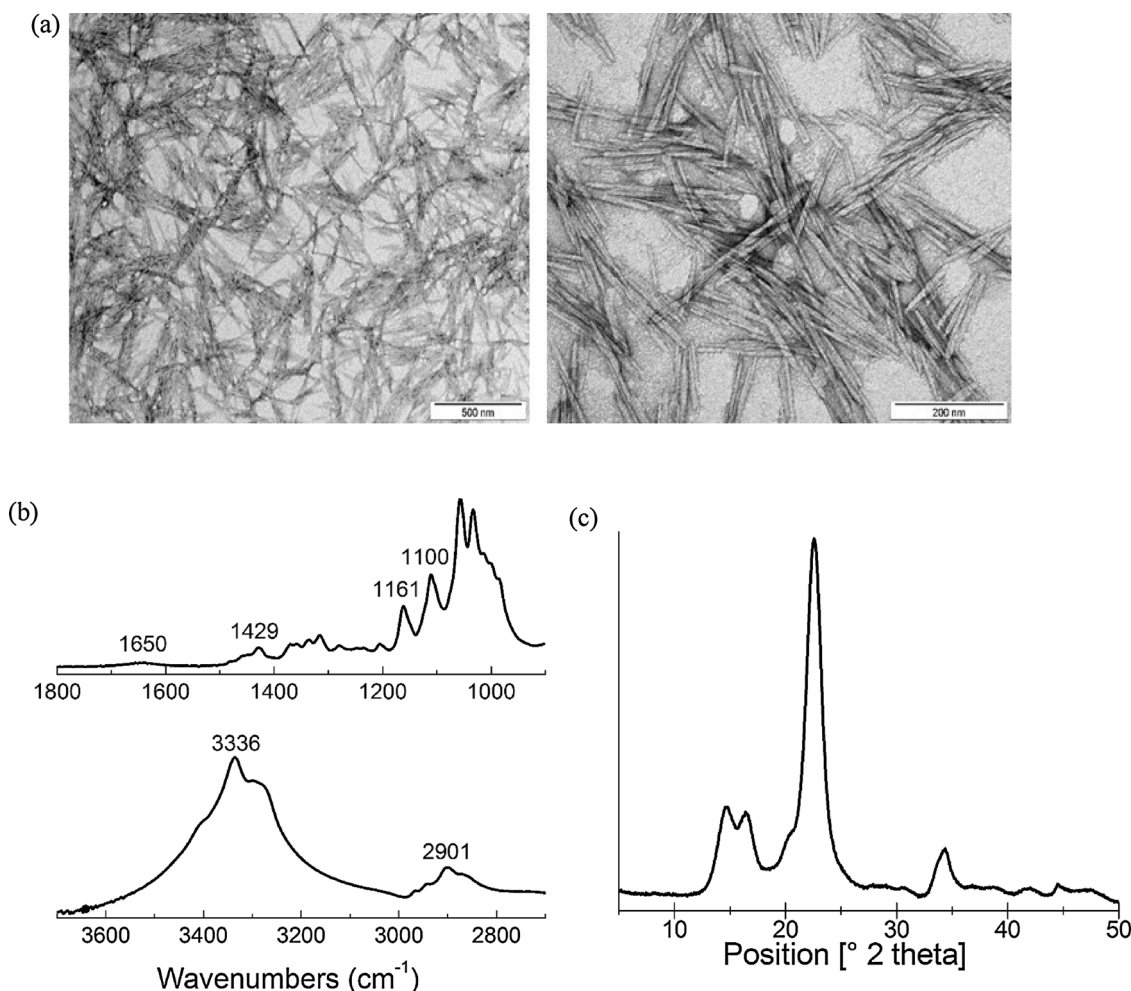


Fig. 1. a) TEM image, b) FTIR spectrum and c) XRD pattern of ramie CNC.

diffractogram of CNC showed peaks at $2\theta = 16.7$, 22.6 , and 33.7° attributed to (110), (200), and (004) planes, which are typical of cellulose-I structure [21,22].

3.2. Preparation and morphology of CS15/PEG/CNC nanocomposite films

Nanocomposite films based on CS15 latex, 0–14% CNC and 0–20% PEG were first prepared by solution casting. Water was slowly evaporated at room temperature. Film of neat CS15 prepared by this method developed a lot of cracks due to limited compaction properties between the nanoparticles (Fig. 2A). It is worth noting that drying at higher temperature up to 50°C did not improve the quality of the films. The addition of 8% of CNC to CS15 leads to the formation of more compact films with less cracks (Fig. 2A), highlighting a good compatibility between CNC and CS15, thanks to the SDS surfactant present at the surface of the latex nanoparticles. However, as the amount of CNC increases, the film becomes brittle again due to the reinforcing effect of CNC, though the film becomes more transparent due to the outstanding optical properties of CNC (Fig. 2A).

Interestingly, combination of PEG and CNC brings better compaction and transparency to the final latex based films, particularly at high PEG loading, i.e. 20–30 wt.% (Fig. 3A). It is worth noting that in absence of CNC, CS15/PEG films exhibited some cracks and two visible phases, even at higher PEG loading. Therefore, a combination of CNC and PEG is beneficial for producing CS15 free-standing films by solution casting, presumably due to CNC network formation. This also indirectly states for an establishment of interactions between CNC and PEG. Recently Cheng et al highlighted the process of adsorption of PEG was recently reported by Cheng et al. [23].

Though the combination of CNC and PEG helped improving the quality of the CS15 based films, some cracks were still visible. In order to achieve high degree of coalescence/compaction with desired thickness, films prepared by solution casting were further compression-molded at 165°C (Figs. 2B and 3B). Transparent free-standing films were obtained due to the softening of the shell during the heat, leading to a very high degree of coalescence of the shell of the polymeric nanoparticles. However, visual observation of the compression-molded materials shown in Fig. 2B allowed providing clear information about the thermal stability of CNC. In fact, the CS15-based films were

brownish when loaded with CNC, while unfilled CS15 remained colorless after similar heat-processing treatment (compression molding). This visual observation indicates that the thermal degradation of CNC was probably occurring during the compression molding step. Indeed, as already reported in the literature the presence of sulfate groups the surface of CNC reduces their thermal stability [2]. Hence, the temperature applied in this case during the compression molding must be close to the temperature at which CNC begins to undergo some thermal decomposition [2]. In contrast, CS15-based films containing CNC and PEG appear colorless and transparent. This is another clear indication that PEG chains adsorbed at the surface of CNC and played a role of a protective shell around the nanofillers, thus preventing their thermal decomposition during the compression molding at relatively high temperature.

Fig. 4 gathers representative morphologies and microstructural aspects of the CS15 based materials prepared by different approaches. As shown in Fig. 4a, SEM micrographs of the films formed by solution casting showed the establishment of a coalescence between CS15 nanoparticles in CS15 film. Indeed during evaporation of water (continuous phase), these interactions and all forces resisting particle deformation should be weakened to allow the establishment of the interparticle coalescence [11]. SEM analysis allowed also to confirm the establishment of better compaction between CS15 nanoparticles in presence of CNC (Fig. 4b and c). Moreover, a higher degree of compaction is achieved by increasing the content of CNC in CS15/CNC nanocomposites. This compaction is enhanced by the addition of PEG to the binary blend CS15/CNC (Fig. 4d). The ternary systems CS15 / 20% PEG / 8% CNC displayed a co-continuous morphology in which two phases can be distinguished. In the main phase, very high degree of compaction of the CS15 nanoparticles is attained thanks to the presence of PEG and CNC. The minor phase is dispersed in the main one in a co-continuous manner. This minor phase is most likely PEG and CNC-rich. This co-continuous morphology observed in solution casted films is a consequence of concentration gradient of PEG/CNC formed in the CS15 based materials during the evaporation of water.

According to previous studies [24–26], the increase of compaction in presence of additives such as block copolymers, in this case CNC and PEG, suggests a decrease for the coalescence of the nanoparticles through steric hindrance by PEG and/CNC at the interface. Milner et al.

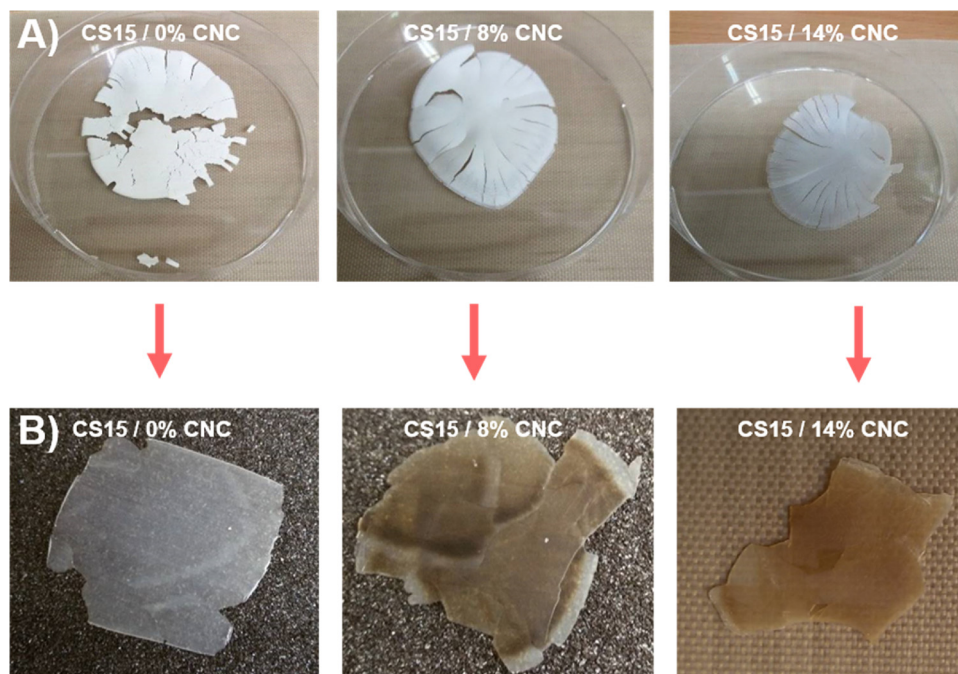


Fig. 2. Nanocomposite films of CS15/CNC prepared by A) solution casting, B) solution casting followed by compression molding.

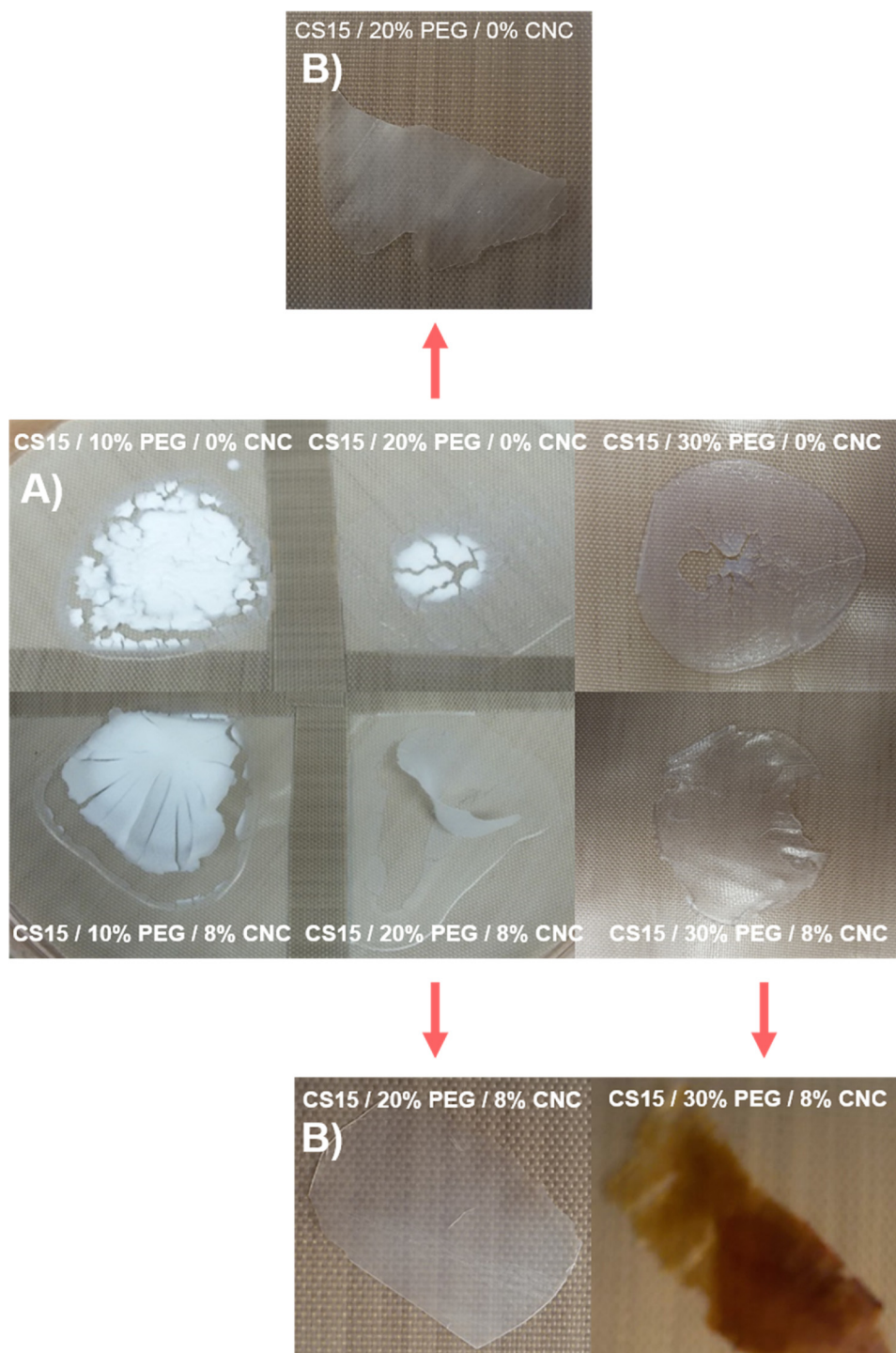


Fig. 3. Nanocomposite films of CS15/PEG/CNC prepared by A) solution casting, B) solution casting followed by compression molding.

suggested that suppression of coalescence is because of a force arising from surface tension gradient (referred as the Marangoni force) caused by a gradient of the polymeric additive concentration at the interfaces, in this case PEG and CNC. The gradient is engendered by flow between the approaching nanoparticles [27]. When two nanoparticles get closer to each other, the matrix between them is squeezed out (film drainage). This squeezing flow transports the additives at the interface out from the particle gap generating a gradient of concentration [24].

Besides the solution casting, SEM micrographs of the films elaborated by solution casting followed by compression molding (Fig. 4e) allowed also to confirm the positive effect of compression molding on

the coalescence of CS15 nanoparticles due to the softening of the shell during the heat while retaining their particle-structure due to a hard crosslinked core. In addition, few small nano-objects appeared in the ternary systems. These nano-objects observed on the film surface may originate from the phase separation under heat between the two co-continuous phases observed in the solution casted films. Indeed, during heat at 165 °C, the motion ability of PEG in the PEG/CNC-rich phase will significantly increase allowing an easier rearrangement of the CS15 nanoparticles to coalesce due to the inter-diffusion of the shell polymeric chains. In addition, the resistance to coalescence arising from the steric repulsive force induced by compression of the layers of additives

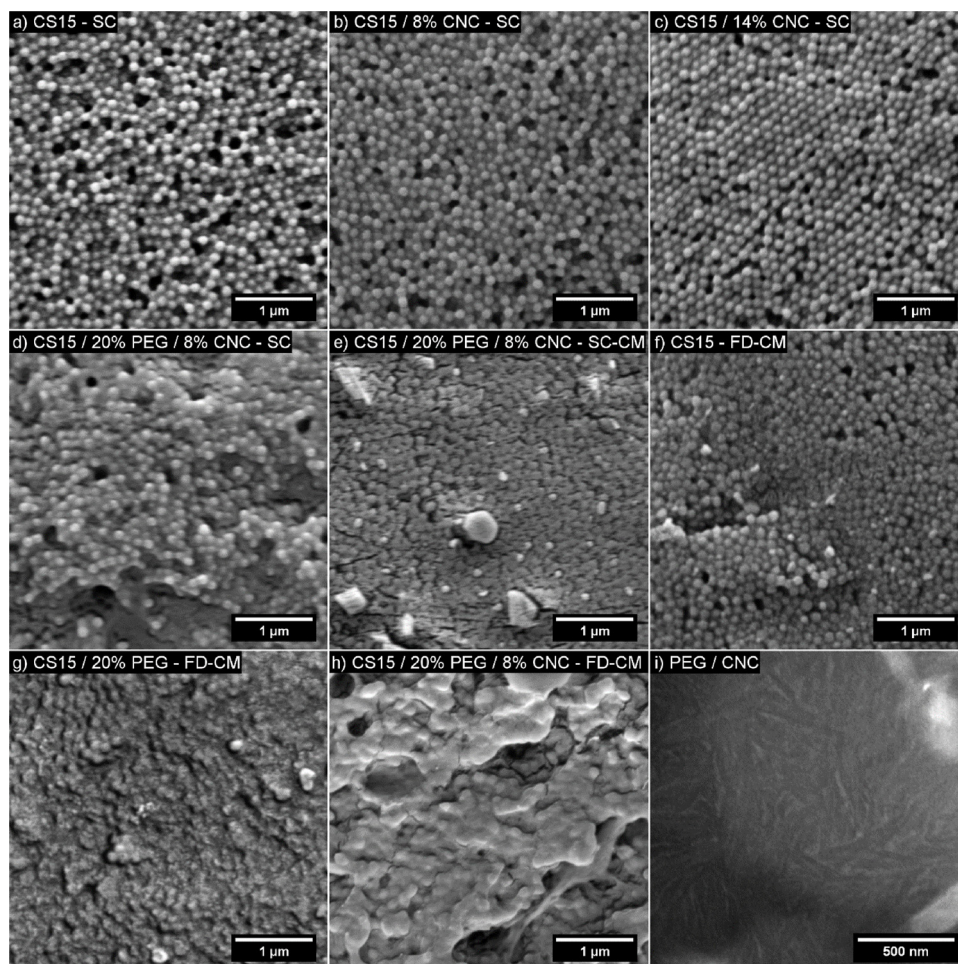


Fig. 4. SEM images of nanocomposite films made of a, b, c) CS15/CNC prepared by solution casting (CNC content: 0, 8 and 14 wt.%), d, e) CS15/PEG/CNC prepared by solution casting and by solution casting followed by compression molding, f, g, h) CS15/PEG/CNC prepared by freeze drying followed by compression molding (FD-CM) and i) PEG/CNC.

(PEG and CNC in this case) surrounding the surface of two approaching nanoparticles becomes weak at very high temperatures, i.e. 165 °C [24–26]. Therefore, excess of PEG/CNC is excluded from the composite matrix, leading to the formation of few nano-objects on the film surface. In fact, a good compatibility between CNC and PEG was confirmed by

preparing a mixture of PEG/CNC (ratio 2/5) using the same conditions as CS15 based materials followed by the subsequent film formation. As can be seen from Fig. 4i, SEM image of PEG/CNC film shows that CNC are homogeneously dispersed in PEG matrix, confirming the good compatibility between both phases, which is in good agreement with



Fig. 5. CS15/PEG/CNC specimen prepared by freeze drying followed by compression molding.

the recent results reported by Cheng et al. [23].

To further improve the processability of the nanocomposite films based on CS15 latex, another approach was tested. This approach consisted of the freeze drying of the desired mixtures (CS15, CS15/CNC or CS15/CNC/PEG) followed by compression molding. As can be seen from Fig. 4f, a high degree of coalescence of CS 15 nanoparticles in CS15 film is achieved while retaining their particle-structure due to a hard crosslinked core. While the addition of 10 wt.% PEG did not show a discernable impact on the morphology of CS 15/PEG film (SEM image not shown here), the highest level of compaction of the material could be attained in presence of 20 wt.% PEG (Fig. 4g). In fact, at higher PEG loading, it becomes difficult to discriminate clearly the particle-structure shape of CS15 in CS15 / PEG 20% as PEG seems to fully occupy the interstitial spaces and the interface, thus covering CS 15 nanoparticles.

As depicted in Fig. 5, visual observation of the films elaborated by freeze drying and subsequent compression molding confirmed the thermal sensitivity of CNC in CS15/CNC films highlighted by the darkening of the film. The addition of PEG to CS15-based materials allows on one hand to enhance the transparency of CS15 films which increases with the increase of PEG content and on the other hand to protect CNC from thermal degradation. The protecting effect of PEG seems to be very much dependent on the ratio PEG / CNC and on the total sum of amount of PEG and CNC. In fact, the ternary blends CS15 / PEG / CNC containing more than 30% of PEG + CNC are yellowish, i.e. CS15 / 20% PEG / 14% CNC and CS15 / 30% PEG / 8% CNC. Surprisingly, the addition of very high amount of PEG, above 20%, to the material containing the lowest amount of CNC, i.e. 8 wt.% produces the reverse effect in which the protective role of PEG is slightly reduced. This unexpected behavior is probably related to the leaching phenomena observed in the films containing 30% PEG, evidenced by their sticky surface. Probably under such a high amount of plasticizer, leaching phenomenon can occur by expelling the plasticizer from the blend [28]. The yellowish color in the overloaded materials could be explained by leaching of a fraction of PEG covering CNC (PEG / CNC leaching). To verify this hypothesis, a mixture of CNC / PEG (ratio 2/5) was compression molded under the same conditions as the ternary systems. The obtained film became very brown (data not shown), at-testing for an insufficient protective effect of PEG towards CNC when the mixture CNC / PEG is not confined within the polymeric matrix. Therefore, due to their lack of stability overtime, the systems containing 30 wt.% PEG were not considered for further investigation. Based on the above results, the approach consisting of freeze drying followed by compression molding is preferred as it offers a number of advantages such as absence of residual moisture, processability of high amount of material, fast processing speed, easy control of the thickness and the shape of the films etc.

As it is well described in the literature, the morphology of the films prepared from latex materials is dependent on the degree of the “coalescence”. The mechanism of coalescence of latex nanoparticles that are generally stabilized by steric or/and electrostatic interactions through charged polymers or adsorbed surfactants [11] implicates compaction, deformation, cohesion and inter-diffusion of polymer chains from the distinct nanoparticles. In the case of the solution casting, upon evaporation of water phase, all interactions resisting particle deformation can be surmounted for an achievement of a maximum level of coalescence which is dependent on evaporation rate, and therefore on casting temperature. According to SEM analysis, in the films prepared by compression molding, a coalescence, i.e. inter-diffusion of the polymeric chains of the shell (copolymer (methyl methacrylate-butyl acrylate)) occurs. A significant advantage of using core-shell nanoparticles, such as CS15, is that this coalescence is limited only to the shell, while hard core helps to retain the particle structure of the original nanoparticles. Due to this feature, the mechanical properties of the final film are mainly governed by the shell coalescence. Furthermore, as indicated by SEM analysis of the blends, the coalescence of the shell is significantly affected by the presence of CNC and PEG. When

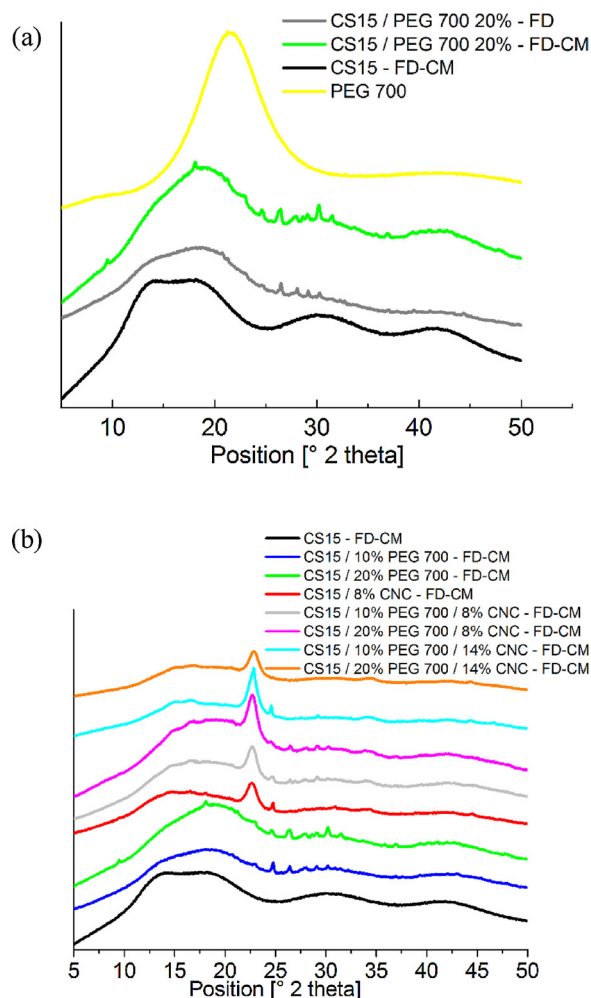


Fig. 6. (a) WAXS diagrams of PEG, CS15 / 20% PEG prepared by freeze drying (FD) and prepared by freeze drying followed by compression molding (FD-CM), (b) WAXS diagrams of CS15 based materials.

coalescence occurs, CNC and PEG must be concentrated within the interstitial space, leading to an improvement of the reinforcement effect, than in the case where optimal dispersion of CNC in a polymeric matrix is obtained. Similar behavior was reported previously by Dubief et al. [12] and by Annamalai et al. [11].

For a deeper understanding of the morphological properties, X-ray patterns of the CS15 based materials were collected and plotted in Fig. 6a, b. In fact, though SEM analyses highlight the impact of the presence of CNC on the morphology of the nanocomposites, it is difficult to observe precisely such small nanoobjects (diameter of 7 ± 1.8 nm) with this technique, particularly in the interstitial spaces. XRD analyzes were carried out on the as-pressed films, which means that the characterized materials are certainly affected by the processing thermal history. Except for CS15 film, diffraction peaks are observed in all other materials, indicating that CS15 film is amorphous. The addition of 10–20 wt.% PEG to CS15 lead to the appearance of residual crystals. These residual crystals are also observed in the freeze dried blends CS15/PEG as shown in Fig. 6a, suggesting a crystallization of a residual fraction of PEG at low temperatures. Further tiny peaks are observed after the compression molding of the blends CS15/PEG due to PEG chain rearrangement as a result of the processing effect. Therefore, PEG residual crystals are probably formed during the cooling step of the compression molded specimen in the hydraulic press. They are probably confined between the CS15 nanoparticles. Indeed, though according to XRD (Fig. 6a) PEG is amorphous at room temperature, this

latter can easily crystallize below 20 °C as it will be highlighted further below by the results of DSC analysis.

CS15 based materials containing CNC show the presence of crystalline peak centered at $2\theta = 16.7$ and 22.6° assigned to (110), (200), and (004) planes, which are typical of cellulose-I structure [21,22], attesting for a good preservation of CNC from thermal degradation at high temperatures. Except for the material CS15 / 20% PEG / 14% CNC, the intensity of the crystalline peaks of cellulose-I structure increases when increasing CNC amount from 8 to 14 wt.%, therefore indicating again the good conservation of CNC during the melt processing at 165 °C, even at higher CNC loading. The material CS15 / 20% PEG / 14% CNC exhibits lower peak intensities of cellulose-I as compared to CS15 / 10% PEG / 14% CNC. Moreover, one can also notice the disappearance of the residual peaks attributed to PEG, which is most probably caused by thermal degradation observed on Fig. 5.

3.3. Thermal and thermo-mechanical properties

The thermal properties of PEG and CS15 based materials evaluated by DSC are depicted in Fig. 7a, b, respectively. DSC thermograms of PEG depicted in Fig. 7a indicate its crystallization at 18 °C during the cooling cycle followed the melting of the formed crystals during the second cycle of the heat demonstrated by the presence of a melting peak with a maximum at 30 °C and a shoulder at 22 °C. DSC results highlight the aptitude of the PEG to crystallize below room temperature. This indicates, that the residual crystals observed by XRD in CS15 based materials do belong to PEG and they are most probably formed during the cooling of the compression molded specimen in the hydraulic press.

According to DSC thermograms of CS15 based materials shown in

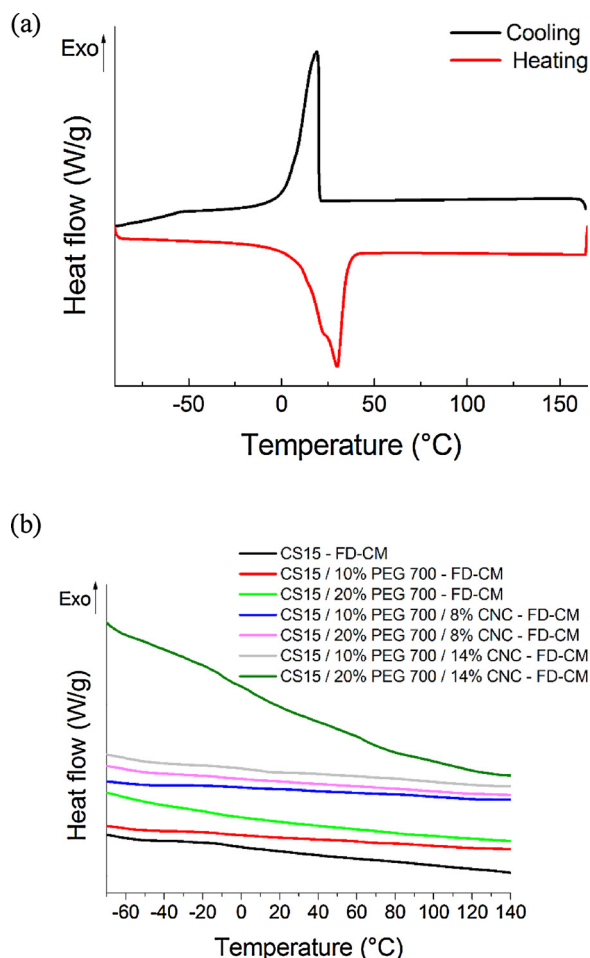


Fig. 7. DSC traces recorded for (a) PEG and (b) CS15 based materials.

Fig. 7b, all polymeric components constituting CS15 based materials, i.e. CS15 and PEG, are amorphous. The residual crystals of PEG observed by XRD (Fig. 6a, b) were not detected by DSC due to the sensitivity limit of the technique. In addition, the absence of the T_g of PEG from the thermograms of all CS15 materials containing PEG indicates on one side that PEG is very well confined between the nanoparticles and at the interstitial spaces, thus limiting its motion ability, and on the other side confirms the absence of large-scale phase separation between PEG and the other components within the nanocomposite.

It is worth mentioning that the materials containing 30 wt.% of PEG in which a leaching phenomenon was noticed exhibited a melting peak with a maximum at 25 °C and a shoulder at 22 °C (Fig. S2 in the Supporting Information). This melting peak belongs to PEG, thus indicating a clear phase separation of a fraction of PEG from the blends. Clearly under such a high amount of plasticizer, leaching phenomenon does occur by expelling a fraction of the plasticizer, i.e. PEG from the blend as advanced aforementioned [28].

To study the impact of CNC and PEG on the thermo-mechanical properties of CS15 based material, the changes of the storage modulus (E') and the loss modulus (E'') as a function of temperature were probed by DMTA. Fig. 8a, b show the E' and E'' versus temperature, respectively, of all CS15 based materials. The thermo-mechanical parameters extracted at room temperature (25 °C) are gathered in Table 1. It is worth recalling that α relaxation associated with the glass transition temperature (T_g) is described as the temperature at the maximum of the loss modulus (E''). The E' curve of CS15 shows a typical behavior of high molecular weight amorphous polymers characterized by E' of about 2260 MPa in the glassy state (-60°C), and a rubbery plateau, where E' drops with increasing temperature (ca. 667 MPa at 25 °C) (Fig. 8a). For this material, a T_g of 1 °C is recorded and it is associated to the segmental chain motion capability of the copolymer (methyl methacrylate-butyl acrylate)-shell. At the lowest recorded temperature (-60°C) corresponding to the glassy regime, the plasticizing effect of PEG is emphasized by the decrease of the E' . Nevertheless, though the value of the E' of CS15 / 20% PEG (2086 MPa) is inferior to that of CS15 (2260 MPa), it still remains superior to the E' of CS15 / 10% PEG (1433 MPa). In fact, in the glassy state, PEG can easily crystallize below room temperature as already observed in DSC thermograms of PEG (Fig. 6a). As expected, addition of CNC to the blend containing the lowest amount of PEG (CS15 / 10% PEG) leads to the increase of E' . This increase follows the increase of CNC content, i.e. 1433 and 1817 MPa for CS15 / 10% PEG / 8% CNC and CS15 / 10% PEG / 14% CNC, respectively. Interestingly, a high depression of E' values occurs when CS15 is blended with 20 wt.% PEG and from 8 to 14 wt.% CNC, from 2260 to 730–750 MPa, respectively. One can also notice that there is no further decrease of E' with the increase of CNC content. High plasticizing ability of 20 wt.% PEG in presence of CNC at the lowest temperature (-60°C) is difficult to understand. It comes out that more complex phenomena are occurring in these materials than a simple good and homogeneous dispersion of CNC network. The origin of this phenomenon is obscure, nevertheless one can assume that it might be caused by a quasi-total coverage of CNC surface by PEG, therefore reducing a crystallization ability of PEG and at the same time suppressing the reinforcing agent role of coated CNC. Indeed, the reinforcing effect of CNC is often ascribed to the establishment of a percolating network of CNC [11,29,30]. Several percolation models describing the level of CNC reinforcement [11,29,30] consider that when the modulus of the rigid percolating network generated by the nanofiller is much higher than that polymeric matrix, the value of the tensile storage modulus E' of the nanocomposite material depends mainly on the volume fraction as well as the modulus of the nanofiller of the rigid percolating network. When CNC are fully coated with PEG the formation of the percolating network is probably compromised. In this case coated CNC play probably a role of their corresponding coating agent, in other terms plasticizing agent role, leading to a significant decrease of the E' . This hypothesis is supported by the behavior of the systems containing

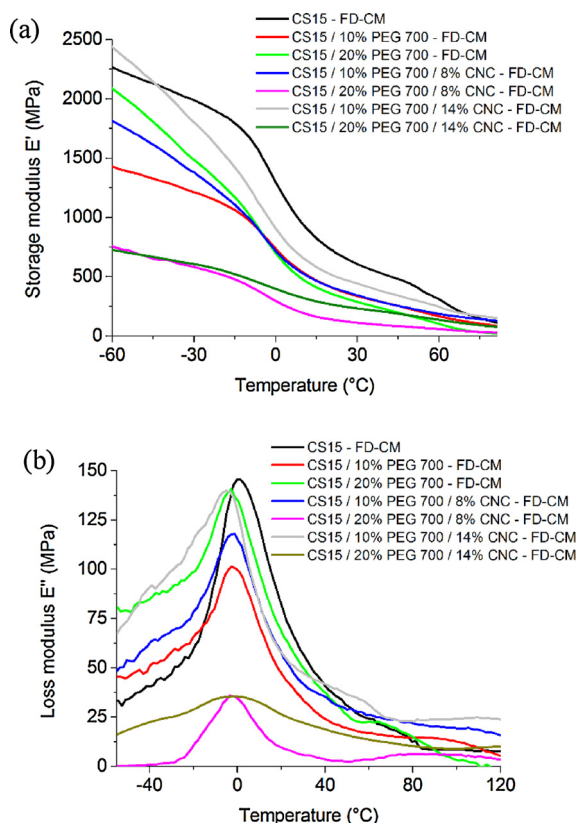


Fig. 8. DMTA curves of a) storage modulus E' and b) loss modulus E'' for CS15 based materials.

Table 1

Overall thermal and mechanical properties of all the materials investigated.

Blend composition (in wt. %)	T_g (E''_{max}) (°C) ^a	E' (MPa) (25 °C)	E' (MPa) (-60 °C)
CS15	1	667	2260
CS15/(10%)PEG	-3	365	1433
CS15/(20%)PEG	-3	320	2086
CS15/(10%)PEG/(8%)CNC	-3	365	1817
CS15/(20%)PEG/(8%)CNC	-3	125	740
CS15/(10%)PEG/(14%)CNC	-3	475	2451
CS15/(20%)PEG/(14%)CNC	-3	247	730

lower amounts of PEG, in which the degree of coating of CNC is more likely lower than in those containing higher amounts of PEG, and therefore leading to the creation of percolating network capable of increasing the overall E' of the system.

In the rubbery regime at room temperature (25 °C), as expected, the increase of PEG content leads to the noticeable decrease of the E' of the materials. However, the level of reinforcement of CNC recorded in the systems containing 10 wt.% PEG is much less marked in the rubbery regime. Indeed, high amounts of CNC were necessary (< 8 wt.%) to detect a reinforcement effect by DMTA, with a notable increase of E' from 365 MPa for CS15 / 10% PEG to 475 MPa for CS15 / 10% PEG / 14% CNC for instance. Thus, an increase of E' by 23% is reached in the rubbery regime, while an increase of 41% in the glassy regime was measured. One possible explanation could be linked with the morphology of PEG which has tendency to crystallize below room temperature, therefore leading to an increase of E' in the glassy regime as the crystallinity reduces the degree of freedom for the macromolecular chains to move.

However, as is seen in the glassy regime, raising the plasticizer content to 20 wt.% in presence of 8 wt.% of CNC induces a further drop

of the E' as compared to the blend free of CNC (CS15 / 20 wt.% PEG), from 320 to 125 MPa. Interestingly, a visible reinforcement can be achieved at higher CNC loading (CS15 / 20% PEG / 14% CNC) reflected by an increase of E' to 247 MPa as compared to CS15 / 20% PEG / 8% CNC, thus an increase of 50% is obtained in the rubbery regime. Though some more complex phenomena are occurring in these materials than a simple homogenous dispersion of PEG and CNC network, the reinforcement effect observed in the rubbery regime for the system suggests the creation of percolating CNC network capable of increasing the overall E' of the system. When compared to the system free of CNC (CS15 / 20% PEG), it is clear that this reinforcing effect of CNC in CS15 / 20% PEG / 14% CNC is weak and the percolating network is very much compromised by the adsorption of PEG at the surface of most of CNC.

Concerning the variation of loss modulus E'' as a function of temperature (Fig. 7b), one can notice a broadening of the peak corresponding to the T_g of the shell of CS15 nanoparticles (copolymer methyl methacrylate-butyl acrylate) in the case of the blends CS15/PEG and CS15/PEG/CNC with respect to neat CS15. More interesting, a shift of this peak from 1 °C for neat CS15 to lower temperatures at around -3 °C for all blends is noticed, highlighting the plasticizing effect of PEG on the shell of copolymer methyl methacrylate-butyl acrylate-shell. According to Pillin et al, this also states for a good miscibility of the copolymer and the plasticizer [31]. The increase of the amount of PEG from 10 to 20 wt.% does not lead to supplementary decrease of the T_g of the shell. However it does accentuate the broadening of the peak. Moreover, though the presence of CNC does not affect the T_g of the shell of CS15, it does show an effect on the broadening of the E'' peak. The broadening of the width of the peak reflecting the T_g can be correlated with the presence of a plasticizer concentration gradient in all the CS15 based materials as confirmed by SEM analysis. As aforementioned, the plasticizer concentration gradient in CS15 based materials must be affected by the presence of CNC due to the strong interaction via probably hydrogen bonding that can be generated between hydroxyl functions of CNC and hydroxyl terminated groups of PEG.

4. Conclusions

In this study, we first synthesized a core-shell nanoparticles from copolymer (methyl methacrylate-ethylene glycol dimethacrylate)-core and copolymer (methyl methacrylate-butyl acrylate)-shell (CS15). Using CS15 as a matrix, CNC isolated from ramie fibers as a reinforcing agent as well as a biobased source and PEG as a plasticizing agent, novel nanocomposite materials with tunable properties were prepared. The nanocomposite films were processed following three different methods, i.e. solution casting, solution casting followed by compression molding, and freeze drying followed by compression molding. SEM analysis showed that the approaches involving compression molding displayed the highest degree of coalescence of CS15 nanoparticles. Nevertheless, in presence of PEG or PEG/CNC, the highest level of compaction of the material was attained as PEG or PEG/CNC fully occupied the interstitial spaces and the interface, hence limiting the coalescence mechanism. Moreover, it was observed that the presence of PEG helps protecting CNC from thermal degradation. It was shown that this protective effect is dependent on the ratio between CNC and PEG.

DSC analysis revealed that PEG is very well confined between the nanoparticles and at the interstitial spaces and is present in amorphous form in all CS15 based materials containing less than 30 wt.% of PEG. Nevertheless XRD thanks to its higher sensitivity did detected the presence of residual crystals of PEG formed during the processing of the blends at low temperatures.

The microstructure and related properties of the ternary nanocomposite CS15 / PEG / CNC were tailored by monitoring the concentration of the different components. Indeed, according to the DMTA extracted thermo-mechanical parameters at 25 °C, the storage modulus (E') of CS15 was 743 MPa and the glass transition temperature (T_g) of

the shell was 1 °C. When adding 20 wt.% PEG, E' and T_g of the materials noticeably decreased to 320 MPa and -3 °C, respectively. On the other hand, high amounts of CNC were necessary (< 8 wt.%) to detect a reinforcement effect by DMTA.

Acknowledgements

The authors thank the Czech Science Foundation (GAČR project 16-22997S (2016/2019)) and specific university research (MSMT No 20-SVV/2017) for the financial support. The authors thank also MSc. D. Čadek from University of Chemistry and Technology Prague for his assistance on the use of the compression molding machine. The authors are grateful to Dr. Y. Habibi from Luxembourg Institute of Science and Technology (LIST) for the fruitful discussions around the synthesis of CNC.

Appendix A. Supplementary data

Supplementary material related to this article can be found, in the online version, at doi:<https://doi.org/10.1016/j.colsurfa.2018.05.054>.

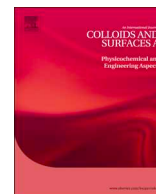
References

- [1] M. Patel, I. Bartle, C. Bastioli, K. Doutlik, J. Ehrenberg, D. Johansson, Towards the integration of renewable raw materials in EU climate policy. Part 1, *Agro Food Ind. Hi-Tech* 13 (2002) 28–31.
- [2] A.L. Goffin, J.M. Raquez, E. Duquesne, G. Siqueira, Y. Habibi, A. Dufresne, P. Dubois, From interfacial ring-opening polymerization to melt processing of cellulose nanowhisker-filled polylactide-based nanocomposites, *Biomacromolecules* 12 (2011) 2456–2465.
- [3] A. Dufresne, Processing of polymer nanocomposites reinforced with polysaccharide nanocrystals, *Molecules* 15 (2010) 4111–4128.
- [4] P. Tingaut, C. Eyholzer, T. Zimmermann, Functional Polymer Nanocomposite Materials from Microfibrillated Cellulose *Advances in Nanocomposite Technology*, Chapter 14, pages 319–334, Edited by Abbass Hashim, InTech, July, 2011, ISBN 978-953-307-347-7.
- [5] Y. Habibi, L.A. Lucia, O.J. Rojas, Cellulose nanocrystals: chemistry, self-assembly, and applications, *Chem. Rev.* 110 (2010) 3479–3500.
- [6] G. Siqueira, J. Bras, A. Dufresne, Cellulosic bionanocomposites: a review of preparation, properties and applications, *Polymers* 2 (2010) 728–765.
- [7] J.M. Raquez, Y. Murena, A.L. Goffin, Y. Habibi, B. Ruelle, F. Debuy, P. Dubois, *Compos. Sci. Technol.* 72 (2012) 544–549.
- [8] A.L. Goffin, J.M. Raquez, E. Duquesne, G. Siqueira, Y. Habibi, A. Dufresne, P. Dubois, Poly(caprolactone) based nanocomposites reinforced by surface-grafted cellulose nanowhiskers via extrusion processing: morphology, rheology, and thermo-mechanical properties, *Polymer* 52 (2011) 1532–1538.
- [9] Y. Habibi, A.-L. Goffin, N. Schiltz, E. Duquesne, P. Dubois, A. Dufresne, *J. Mater. Chem.* 18 (2008) 5002–5010.
- [10] R.-J. Moon, A. Martini, J. Nairn, J. Simonsen, J. Youngblood, *Chem. Soc. Rev.* 40 (2011) 3941–3994.
- [11] P.K. Annamalai, K.L. Dagnon, S. Monemian, E.J. Foster, S.J. Rowan, C. Weder, Water-responsive mechanically adaptive nanocomposites based on styrene-butadiene rubber and cellulose nanocrystals—processing matters, *ACS Appl. Mater. Interfaces* 6 (2014) 967–976.
- [12] D. Dubief, E. Samain, A. Dufresne, Polysaccharide microcrystals reinforced amorphous poly(β -hydroxyoctanoate) nanocomposite materials, *Macromolecules* 32 (1999) 5765–5771.
- [13] V. Favier, G.R. Canova, J.Y. Cavaille, H. Chanzy, A. Dufresne, C. Gauthier, Nanocomposite materials from latex and cellulose whiskers, *Polym. Adv. Technol.* 6 (1995) 351–355.
- [14] V. Favier, H. Chanzy, J.Y. Cavaille, Polymer nanocomposites reinforced by cellulose whiskers, *Macromolecules* 28 (1995) 6365–6367.
- [15] K. Wood, The advantages of networking, *Eur. Coat. J.* (2005) 48.
- [16] D. Juhue, J. Lang, Film formation from dispersion of core-shell latex particles, *Macromolecules* 28 (1995) 1306–1308.
- [17] S. Lazzari, B. Jaquet, L. Colonna, G. Storti, M. Lattuada, M. Morbidelli, Interplay between aggregation and coalescence of polymeric particles: experimental and modeling insights, *Langmuir* 31 (2015) 9296–9305.
- [18] S. Sajjadi, Particle formation under monomer-starved conditions in the semibatch emulsion polymerization of styrene. I. Experimental, *J. Polym. Sci. A: Polym. Chem.* 39 (2001) 3940–3952.
- [19] J.O. Zoppe, M.S. Peresin, Y. Habibi, R.A. Venditti, O.J. Rojas, Reinforcing poly(epsilon-caprolactone) nanofibers with cellulose nanocrystals, *ACS Appl. Mater. Interfaces* 1 (2009) 1996–2004.
- [20] Y. Habibi, A. Dufresne, Highly filled bionanocomposites from functionalized polysaccharide nanocrystals, *Biomacromolecules* 9 (2008) 1974–1980.
- [21] A.D. French, Idealized powder diffraction patterns for cellulose polymorphs, *Cellulose* 21 (2013) 885–896.
- [22] Q. Lu, Z. Cai, F. Lin, L. Tang, S. Wang, B. Huang, Extraction of cellulose nanocrystals with a high yield of 88% by simultaneous mechanochemical activation and phosphotungstic acid hydrolysis, *ACS Sustain. Chem. Eng.* 4 (2016) 2165–2172.
- [23] D. Cheng, Y. Wen, L. Wang, X. An, X. Zhu, Y. Ni, Adsorption of polyethylene glycol (PEG) onto cellulose nano-crystals to improve its dispersity, *Carbohydr. Polym.* 123 (2015) 157–163.
- [24] S.T. Milner, H. Xi, How copolymers promote mixing of immiscible homopolymers, *J. Rheol.* 40 (1996) 663–687.
- [25] G.H. Fredrickson, S.T. Milner, Time-dependent reactive coupling at polymer–polymer interfaces, *Macromolecules* 29 (1996) 7386–7390.
- [26] B. O'Shaughnessy, U. Sawhney, Reaction kinetics at polymer–polymer interfaces, *Macromolecules* 29 (1996) 7230–7239.
- [27] S. Yukioka, T. Inoue, Ellipsometric analysis on the in situ reactive compatibilization of immiscible polymer blends, *Polymer* 35 (1994) 1182–1186.
- [28] N. Ljungberg, B. Wesslén, Tributyl citrate oligomers as plasticizers for poly(lactic acid): thermo-mechanical film properties and aging, *Polymer* 44 (2003) 7679–7688.
- [29] S. Camarero Espinosa, T. Kuhnt, E.J. Foster, C. Weder, Isolation of thermally stable cellulose nanocrystals by phosphoric acid hydrolysis, *Biomacromolecules* 14 (2013) 1223–1230.
- [30] M.N. Anglès, A. Dufresne, Plasticized Starch/Tunicin whiskers nanocomposites. 1, *Struct. Anal. Macromol.* 33 (2000) 8344–8353.
- [31] I. Pillin, N. Montrelay, Y. Grohens, Thermo-mechanical characterization of plasticized PLA: Is the miscibility the only significant factor? *Polymer* 47 (2006) 4676–4682.



Contents lists available at ScienceDirect

Colloids and Surfaces A

journal homepage: www.elsevier.com/locate/colsurfa

Synthesis of conductive macroporous composite polymeric materials using porogen-free method

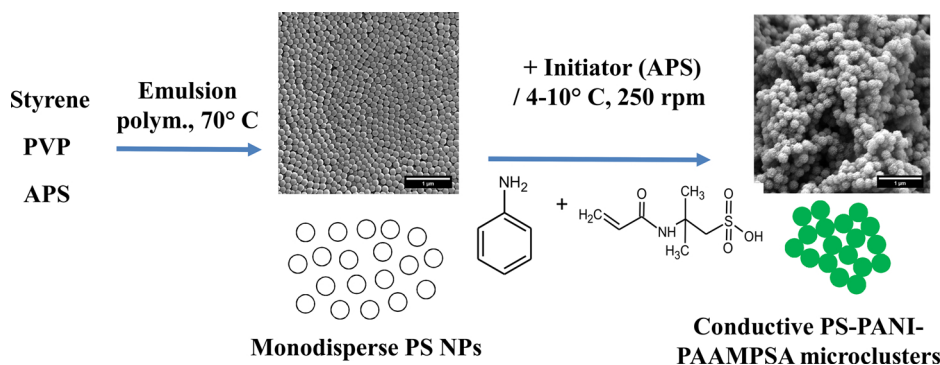
Edith Mawunya Kutorglo^{a,*}, Fatima Hassouna^a, Dušan Kopecký^b, Ladislav Fišer^b,
Ivona Sedlářová^c, Aleš Zadrazil^a, Miroslav Šoos^{a,*}

^a Department of Chemical Engineering, University of Chemistry and Technology, Technická 3, 166 28 Prague 6, Dejvice, Czech Republic

^b Department of Physics and Measurements, University of Chemistry and Technology, Technická 3, 166 28 Prague 6, Dejvice, Czech Republic

^c Department of Inorganic Technology, University of Chemistry and Technology, Technická 3, 166 28 Prague 6, Dejvice, Czech Republic

GRAPHICAL ABSTRACT



ARTICLE INFO

Keywords:
Polyaniline
Macroporous microclusters
Conductive polymers
Porogen-free method

ABSTRACT

We report the synthesis of stable conductive macroporous materials by chemical oxidative polymerization of aniline-(2-acrylamido-2-methylpropanesulfonic acid) in the presence of polystyrene nanoparticles (PS-NPs). The presented method allows, without using any pore generating agent, to prepare conductive highly porous materials with tunable properties. In particular, by changing the composition, i.e. ratio between poly(aniline-(2-acrylamido-2-methylpropanesulfonic acid)) (PANI-PAAMPSA) and PS-NPs, we were able to modulate structure moieties of PANI-PAAMPSA on the surface of PS-NPs as well as the size and internal structure of the formed microclusters. The materials exhibited high porosities up to 80% and surface areas up to 18 m²/g depending on the ratio between PS and PANI-PAAMPSA. In addition, by differential scanning calorimetry (DSC), it was observed that the PANI-PAAMPSA coating serves as a thermal barrier for PS-NPs. Such a high thermal stability of the prepared microclusters, up to 350 °C, was confirmed by the thermal gravimetric analysis (TGA). Despite the presence of non-conductive PS-NPs, the synthesized composite materials exhibited specific conductivities in the order of 10⁻³ S cm⁻¹, comparable to aniline-based conductive polymers studied in the literature.

* Corresponding authors.

E-mail addresses: kutorgle@vscht.cz (E.M. Kutorglo), miroslav.soos@chem.ethz.ch (M. Šoos).

<http://dx.doi.org/10.1016/j.colsurfa.2017.10.082>

Received 28 August 2017; Received in revised form 24 October 2017; Accepted 29 October 2017

Available online 31 October 2017

0927-7757/ © 2017 Elsevier B.V. All rights reserved.

1. Introduction

Over the last decade, there has been increased interest in the development of new functional materials using intrinsically conducting polymers (ICPs) [1,2]. This reflects the growing demands in technologies such as electrorheological fluids [3], organic lightweight batteries, conductive packaging [4], smart sensors and switches [5], energy storage materials [6] etc. ICPs are an interesting class of materials that combine the electrical, optical and magnetic properties typical of metals with the mechanical properties, chemical stability and processability typical of conventional polymers [7–11]. Because they offer additional properties such as lightweight, ease of preparation and low cost as compared to metallic conductors, these polymers are being considered as substitutes for inorganic semiconductors [12]. Recent studies have combined ICPs with polymers, inorganic materials, or even metals to form composites in the form of individual coated particles [1,2]. This approach combines the good characteristics of two or more constituent materials usually yielding functionalities superior to those of the individual materials [13]. Additionally, due to the fact that the content of the core and outer coating can be manipulated independently [14,15], they offer the flexibility to tune the properties of the final materials.

The common approach to the preparation of coated particles from conductive polymers involves first the preparation of colloidal particles from a non-conducting inorganic or vinyl polymer [11] that provides the material with good mechanical or structural properties. Subsequently, a coating of the preferred conductive polymer is deposited onto the surface of the colloidal particle. This results in materials with entirely new properties or an improvement in a particular – mechanical, thermal, or optical property [16,17]. Several researchers have synthesized conductive polymer-coated particles for use as particulate fillers in anisotropic conductive films [7] or electrorheological applications [3]. The deposition of conductive polymers on sacrificial core materials has also been used to prepare hollow particles after removal of the core [18–20]. These materials have applications including photonic crystals, insulation materials, materials for controlled delivery and separations.

Despite the efforts made in the controlled deposition of conductive polymers onto the surfaces of colloidal particles for applications in solution or films, it has been very challenging assembling such coated nanoparticles into ordered 3-D structures [21]. For certain applications, particularly catalysis, chromatography and chemical sensing, the individual coated particles are not suitable. This is because they possess only small or no diffusive pores that lead to mass transport problems. Additionally, many materials display certain functionalities only when they get assembled into specific 3-D structures or morphologies [22]. Many researchers have focused on devising ways of assembling nanoparticle building blocks into 3-D porous structures with larger pores and large surface areas [23–26]. To our knowledge, there has not been any study based on a simple approach to obtain such hierarchically structured materials from conductive polymers with controlled pore properties. Additionally, the systematic investigation of the porous properties of these 3-D materials has not yet been reported elsewhere.

In this paper, applying a combination of the concepts of supramolecular and colloidal chemistry, we describe the fabrication of 3-D conductive macroporous materials using porogen-free method based on chemical oxidative polymerization of aniline-(2-acrylamido-2-methylpropanesulfonic acid) in the presence of polystyrene nanoparticles (PS-NPs), used as building blocks. PS is selected as the model core polymer due to its high glass transition temperature (T_g), which gives rigid and non-deformable particles that make the composites mechanically stronger than they would be by using PANI without a support [3,19,27,28]. Polyaniline (PANI) remains one of the most investigated conjugated polymers, not only because of its high electrical conductivity but also its multiple electronic states, electrical tuneability, nontoxicity, low manufacturing costs and relative environmental stability [12,29–34]. Incorporation of (2-acrylamido-2-methylpropanesulfonic acid) (AAMPSA) during the synthesis of PANI confers several

advantages on the materials. This includes the maintenance of pH around 2 during the aniline polymerization, which is crucial for the synthesis of the conductive form of PANI [35,36]. Additionally, due to the conjugated bond system, PANI is rigid and mechanically brittle thus the incorporation of polymer acids such as PAAMPSA or poly (amic acid) with lower glass transition, improves the flexibility of the final material [37]. Use of polymeric acid in PANI synthesis, would also preserve the electrical conductivity of the materials, since it has been reported that small-molecule acid dopants e.g. hydrochloric acid could leach out of the materials leading to a loss in conductivity over time [38].

The novelty of our work lies on several aspects. We prepared 3-D materials having large porosity and not individually coated particles. Additionally, unlike other approaches to macroporous materials, which involve multiple complicated steps, our approach involves only two simple steps that result in the formation of microclusters. It is also important to note that the coating of the PS-NPs with polyaniline-poly-(2-acrylamido-2-methylpropanesulfonic acid) PANI-PAAMPSA and their formation into the porous structures occur in a single reaction medium without using any pore generating agent. Due to its chemical composition and 3D porous structure, the produced material can find applications in catalysis.

2. Experimental section

2.1. Materials

Styrene (Sty, > 99%), ammonium peroxydisulfate (APS, 98%), poly (vinyl pyrrolidone) (PVP, Mw = 40000 g/mol), aniline (ANI, ACS reagent, > 99.5%), 2-acrylamido-2-methyl-1-propanesulfonic acid (AAMPSA, 99%) were all purchased from Sigma Aldrich and used as received. All aqueous solutions were prepared with deionized water.

2.2. Synthesis of monodisperse polystyrene nanoparticles (PS-NPs)

With the intention to make clusters of conductive polymer-coated nanoparticles, the PS-NPs were first prepared by a radical emulsion polymerization of styrene using APS as initiator and PVP as stabilizer in a radical emulsion polymerization system. The ratio between monomer, initiator and surfactant was adopted from the work of Davodi et al. [34] and was equal to 6 g: 0.06 g: 0.5 g, respectively. The detailed steps are as follows: The aqueous phase was prepared by dissolving PVP (0.5 g) in deionized water (90 mL) followed by the addition of styrene (6 g). The mixture was stirred in an ice bath using ultraturrax (IKA® T25 digital) at 15000 rpm for 30 min. The resulting emulsion was transferred into a three-neck round bottom flask, equipped with a reflux condenser and degassed by applying sequential vacuum/nitrogen cycles while mixing with a magnetic stirrer at 350 rpm for about 15–20 min. The reaction mixture was then heated to 70 °C, while the temperature in the reactor was monitored with a standard thermometer inserted directly into the solution through a septum. When the temperature of the solution reached 70 °C, aqueous initiator solution (0.06 g APS in 4 mL of DI water) was injected. The polymerization was carried out for 8 h and the resulting latex was allowed to cool down and stored for further experiments.

2.3. Synthesis of PANI-PAAMPSA-PS NPs composite microclusters

For preparation of the microclusters, aniline-(2-acrylamido-2-methylpropanesulfonic acid) (ANI-AAMPSA) was polymerized by chemical oxidative route in the presence of the PS-NPs. The PS-NPs concentration was kept constant at 1 wt.% while varying the amount of ANI-AAMPSA according to the composition in Table 1. (The samples were named PS – PANI-PAAMPSA 1–4 depending on the ratio between the PS-NPs and PANI-PAAMPSA).

The procedure is as follows: ANI-AAMPSA solution was prepared

Table 1
Parameters for synthesizing the PS/PANI-PAAMPSA microclusters.

Parameter/Sample name	Composition
Weight of PS-NPs [%]	1
Ratio (AAMPSA/ANI)	5.6
Ratio of Monomer/initiator	2.7
PANI-PAAMPSA	(0 wt.% PS: 1 wt.% PANI-PAAMPSA)
PS – PANI-PAAMPSA 1	(1 wt.% PS: 0.25 wt.% PANI-PAAMPSA)
PS – PANI-PAAMPSA 2	(1 wt.% PS: 0.5 wt.% PANI-PAAMPSA)
PS – PANI-PAAMPSA 3	(1 wt.% PS: 1 wt.% PANI-PAAMPSA)
PS – PANI-PAAMPSA 4	(1 wt.% PS: 2 wt.% PANI-PAAMPSA)

and the PS-NPs were added. The solution was stirred for 15 min to allow the ANI-AAMPSA to adsorb onto the PS-NP surface. The solution was then cooled to 4 °C in an ice water bath. The initiator solution (APS) was slowly added using a syringe pump at a rate of 0.3 mL/min. The polymerization was run at 4 °C for the first 8 h and then stirring continued for another 16 h at 20 °C to ensure complete conversion. The initial solution of monomers was colorless and then turning blue after some minutes upon addition of the initiator. As the reaction proceeded, the blue color changed to dark green indicating the formation of the conductive salt of PANI-PAAMPSA (See Fig. SI. 1 in Supporting Information). Part of the resulting suspension of microclusters was oven-dried at 60 °C for 24 h to obtain dry product.

3. Characterizations

3.1. Fourier Transform Infrared Spectroscopy

Fourier Transform Infrared Spectroscopy (Nicolet iZ10 FTIR module with ATR accessory) was used to evaluate the chemical bonds and structures in the obtained materials. Spectra were averaged over 64 scans.

3.2. Scanning electron microscopy

The morphology of the synthesized nanoparticles and porous materials was analyzed using scanning electron microscopy (SEM) (Mira 3 LMH, Tescan Company). The samples were sputter-coated with a thin layer of gold prior to SEM observation. The accelerating voltage of Schottky cathode was 3 kV. Secondary electrons were detected by the Everhart-Thornley type secondary electron detector or by the in-lens detector (In-Beam). An attempt was also made to obtain a rough estimate of the thickness of the polyaniline coating on the surface of the PS-NPs. This was done by calculating the difference in the mean diameter between the uncoated PS-NPs and the coated particles in the PS-PANI-PAAMPSA samples using image analysis of SEM pictures.

3.3. Dynamic and static light scattering

The average size of the PS nanoparticles was determined by dynamic light scattering (DLS, Malvern Zetasizer Nano). The same device was used to evaluate the zeta potential of the PS-NPs through the Smoluchowski model. Because the sizes of the microclusters were in the micrometer range, the analysis of their size and internal structure was, after necessary dilution to avoid multiple light scattering, performed using static light scattering technique (Malvern, Mastersizer 2000). Obtained data were used to evaluate the aggregate mean radius of gyration, $\langle R_g \rangle$ as well as fractal dimension d_f . More information about data treatment can be found in Supporting Information (A.2)

3.4. N_2 sorption and Hg intrusion porosimetry

Micromeritics AutoPore IV 9500 analyzer was used to characterize the porosity of the materials while the specific surface area was

determined by physisorption of nitrogen and calculated from the BET model (Nova 2200 e surface area analyzer, Quantachrome).

3.5. Thermogravimetric analysis

The thermal stability and degradation behavior of the materials were investigated by Thermogravimetric Analysis (TGA). The TGA measurements were carried out using Stanton-Redcroft TG 750 in air (20 mL min^{-1}) at a heating rate of 10 °C/min from room temperature to 700 °C.

3.6. Differential scanning calorimetry

The thermal properties of the materials were investigated by means of differential scanning calorimetry (DSC). Samples (5–15 mg) were sealed in hermetic aluminum pans. DSC analysis was done under a nitrogen gas flow with a heating rate of 10 °C/min from 20 °C to 180 °C for PS-NPs. For PS – PANI-PAAMPSA composites, the first heating was done from 20 °C to 180 °C, the samples were cooled to 20 °C and subsequently heated again up to 350 °C and thermograms for second heating were recorded (Fig. SI 2 supporting information). The second heating excludes the uncertainties that arise when the behavior of the material may depend on the thermal history of the samples.

3.7. Conductance measurements

Specific conductance measurements were carried out using an apparatus constructed according to Medek et al. [39]. Detailed description of the measurement is presented in A.1 in Supporting Information. Values of specific conductance were evaluated from Ohm's law and known geometrical dimensions.

4. Results and discussion

The process of preparing the 3-D conductive porous materials involved 2 main steps. First, monodisperse PS-NPs were synthesized by emulsion polymerization with PVP as steric stabilizer. The average size of the prepared PS-NPs was 185 nm and polydispersity index (PDI) of 0.01 as measured by dynamic light scattering. The PDI is a dimensionless measure of the broadness of the size distribution and it was obtained from the intensity correlation function [40]. The PDI typically has values less than 0.07 for a monodisperse test sample of spherical particles, thus a PDI of 0.01 confirmed that monodisperse PS particles were obtained. Furthermore, these particles have a zeta potential of –29 mV indicating good colloidal stability. In a second step, the PS-NPs were dispersed in ANI-AAMPSA solution and addition of APS initiates the polymerization of ANI-AAMPSA onto the PS-NPs surface, which subsequently formed the porous structures.

The uniform coating of the individual PS-NPs with PANI-PAAMPSA and their subsequent formation into the porous structures could be explained by the following effects: (i) Presence of PVP on the surface of the PS-NPs helps in the stabilization of the particles at the low pH of ANI-AAMPSA solution. This low pH is crucial for the successful synthesis of the conductive form of PANI and thus it is important that the NPs are stable in the acidic pH solution. This was confirmed by similar particle size distribution measured for PS-NPs and PS-NPs in the presence of ANI-AAMPSA solution prior to initiating the polymerization (supporting information Fig. SI 3). Keeping the particles stable before aniline polymerization begins will ensure that each individual particle gets coated with the conductive polymer before they assemble into the porous structures to ensure homogeneity. Particles stabilized by SDS on the other hand, rapidly aggregated upon addition to the ANI-AMPSA solution, and thus the probability of the inner part of the aggregates not fully coated with polyaniline is high and could lead to inhomogeneity in the structure and lower mechanical properties of the final materials. (ii) In acidic AAMPSA solution, ANI is protonated with the $-\text{NH}_2$ group on

aniline carrying a positive charge, which electrostatically interacts with negatively charged PS-NPs (iii) Thirdly, AAMPSPA is very polar and because PVP binds easily to polar molecules, ANI-AAMPSPA is able to adsorb onto the PVP stabilized PS-NPs and thus help to assemble the PS-NPs into 3D porous structure. This effect would be similar to that reported by Han et al. [17] where PVP was behaving as a link between poly(butyl methacrylate) (PBMA) core particles and polyaniline (PANI) shell around them. (iv) The last effect could come from the properties of PAAMPSPA, which has been used in adhesives and hydrogels for its high water uptake. Thus, in this case the PAAMPSPA would be acting as a glue to aid the formation of the porous structures. The use of PAAMPSPA in these materials is also important for improving their chemical stability [38,41] and maintaining the conductive form even during their application over a wide pH range. This is because PAAMPSPA, perfluoro-octane sulfonic acid and dodecyl benzene-sulfonic acid have been reported to overcome the problem of losing the counter ion from small molecular weight acid dopants (e.g. HCl) and maintain PANI in conductive state over wider pH range. It was observed that protons stay attached to the PANI backbone due to the fact that the negatively charged PAAMPSPA counter ions make it energetically favorable even under alkaline pH [42].

As already indicated, the pH at which aniline polymerization occurs is one of the critical parameters considered [43]. Because both the monomer (AAMPSPA) and polymer (PAAMPSPA) are strong acids in aqueous solution, synthesis of PANI in the presence of AAMPSPA ensures that the pH of the polymerization medium is maintained between 1 and 2 [35]. The AAMPSPA/ANI ratio of 5.6 was chosen according the capability to keep the pH values around 2, which was required for the synthesis (See Fig. SI 4 in supporting information). This is supported by Zhao et al. [36] who observed that polymerization in mildly acidic medium only yielded aniline oligomers without the formation of PANI.

4.1. Analysis of chemical composition

The chemical structure of the synthesized materials, i.e., PS-NPs and the PS – PANI-PAAMPSPA aggregates was carried out using FTIR-ATR and the spectra are displayed in the 4000–1000 cm^{-1} region (Fig. 1). FTIR spectrum of PS-NPs indicates absence of the peak at 1630 cm^{-1} corresponding to C=C stretching vibration of the vinyl group, demonstrating a quasi-total reaction of styrene monomers (Fig. 1(a)). The main peaks of PS were observed at 3079, 3058, and 3025 cm^{-1} (C–H) aromatic stretching, triple bands; 2917, 2848 cm^{-1} (C–H aliphatic stretching); 1600, 1490, and 1450 cm^{-1} (C=C aromatic stretching). Moreover, a new peak belonging to PVP at 1660 cm^{-1} corresponding to the stretching vibration of the C=O group and new others between 1282 and 1492 cm^{-1} corresponding to the CH_2 -bending vibrations were also observed in the PS-NPs. These new peaks confirmed the adsorption of PVP on the surface of PS-NPs, providing high stability to the nanoparticles (Fig. 1(a)).

FTIR-ATR spectra of PANI-PAAMPSPA and PS – PANI-PAAMPSPA aggregates confirmed the successful synthesis of PANI-PAAMPSPA. Indeed, all spectra showed the presence of a weak peak at 1650, and a peak at 1036 cm^{-1} attributed to the vibration of the secondary amide C=O stretching and to the sulfonic acid group $-\text{SO}_3\text{H}$, respectively, originating from PAAMPSPA (Fig. 1(b)). The peaks at 1484 and 1573 cm^{-1} are associated with benzenoid and quinoid rings, respectively, of PANI [19,29,44]. Besides these main peaks attributed to PANI-PAAMPSPA, absorption bands with very low intensity attributed to PS and PVP functional groups were detected (Fig. 1(c) shows the PS and PVP peaks in PS-PANI-PAAMPSPA 1 and 2). Their intensity diminished as the content of PANI-PAAMPSPA increased, due to the increased thickness of PANI-PAAMPSPA coating. This trend could be observed because of the FTIR mode used, i.e., attenuated total reflection mode (ATR).

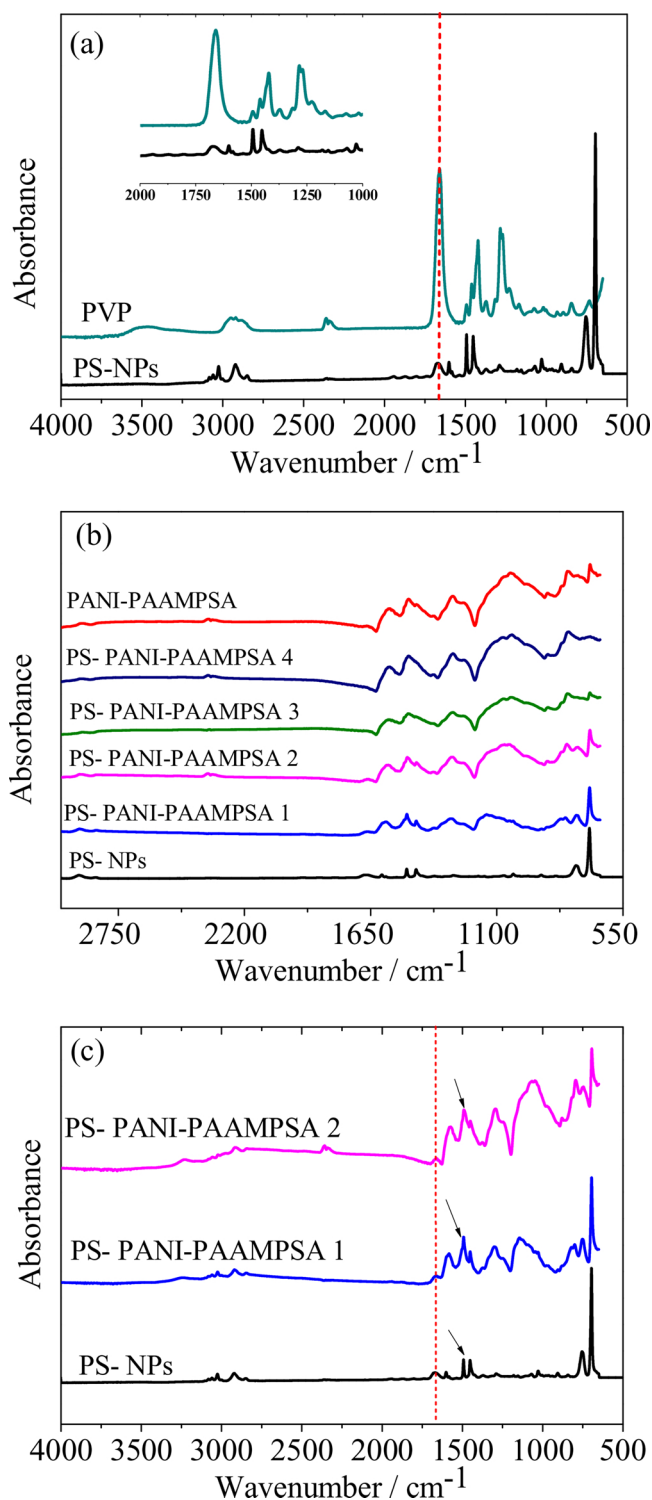


Fig. 1. FTIR spectra of PS NPs and composites (a) showing the chemical groups corresponding to PVP and PS, (b) PS and PANI-PAAMPSPA and (c) PS effect in PS-PANI-PAAMPSPA 1 and 2 which have thinner PANI-PAAMPSPA coating.

4.2. Morphology of the particles and composite microclusters

The morphology of the PS-NPs and the porous materials was analyzed by means of SEM as shown in Fig. 2(a)–(f). The image shown in Fig. 2(a) provided evidence that monodisperse PS-NPs were obtained. This was also confirmed by dynamic light scattering (DLS), which displayed an average size of 185 nm and polydispersity index of 0.01. These particles with zeta potential of -29 mV were highly

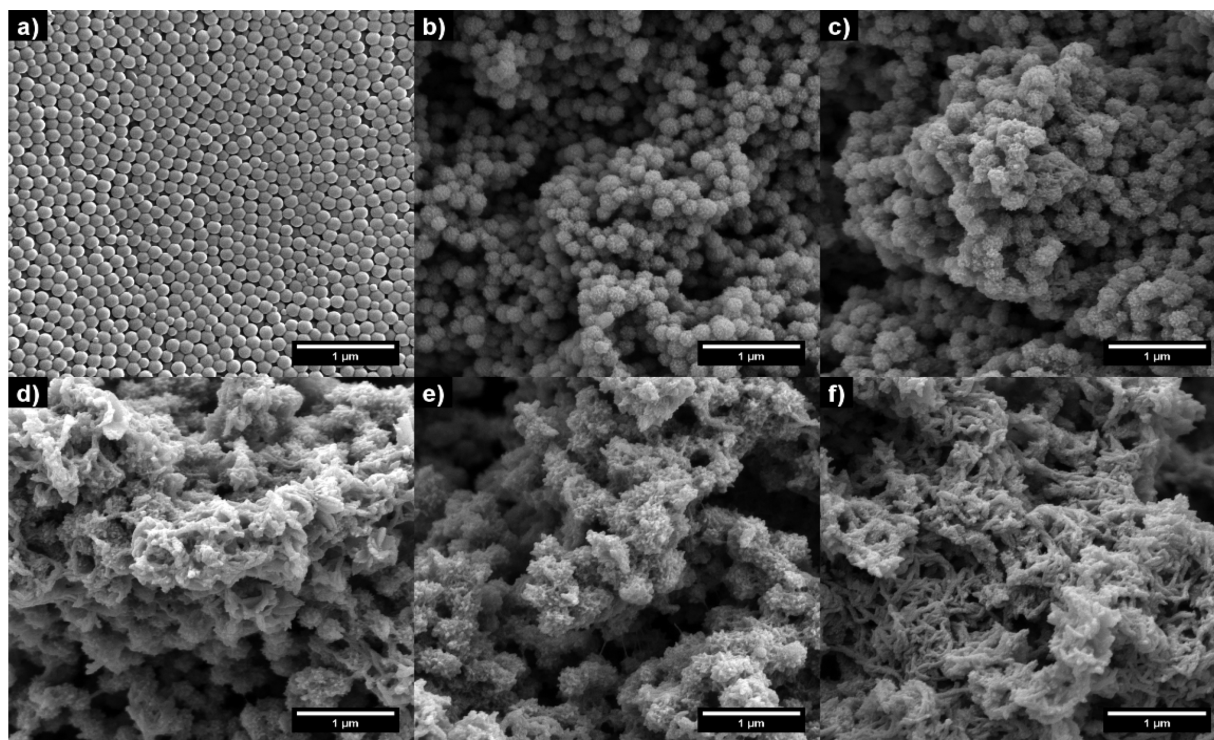


Fig. 2. SEM pictures of PS nanoparticles before and after coating with different amounts of PANI-PAAMPSA (a) PS NPs (b) PS – PANI-PAAMPSA 1 (c) PS – PANI-PAAMPSA 2 (d) PS – PANI-PAAMPSA 3 (e) PS – PANI-PAAMPSA 4 (f) PANI-PAAMPSA.

stable in water for over a year. When comparing the morphology of PS-NPs (Fig. 2(a)) to that of the PS – PANI-PAAMPSA composites (Fig. 2(b)–(e)), a significant modification of the surface morphology was observed after coating with the conductive polymer. The uncoated PS-NPs display a smooth surface morphology with a well-defined interface whereas the PS – PANI-PAAMPSA composites show some roughening on the surface, as a result of the growth of tiny PANI-PAAMPSA structures on the surface of the PS-NPs.

PANI-PAAMPSA alone is shown in Fig. 2(f) for comparison, exhibiting fibrillar morphology, which may be due to the long chain structure of the PAAMPSA. SEM images confirmed that the individual PS-NPs were uniformly pre-coated with ANI-AAMPSA, and then later locked together by the precipitating PANI-PAAMPSA leading to the formation of 3-D porous structures. An increase in the sizes of the individual building units (coated PS-NPs) was a further confirmation of successful coating. From this observation, an attempt was made to estimate the thickness of the PANI-PAAMPSA coating on the surface of the PS-NPs. This was done by determining the difference in the mean diameter between the uncoated PS-NPs and the coated particles in the aggregates using image analysis of the SEM pictures. According to this analysis, the increase of the coating thickness in the range from 16 to 50 nm was observed as the amount of PANI-PAAMPSA with respect to the PS-NPs increased, covering the range 1:0.25, 1:0.5, 1:0.75 and 1:1, respectively (Fig. 3). For the samples with higher weight fraction of PANI-PAAMPSA than PS, there was no more well defined spherical shape of the building blocks after the coating and therefore, the thickness could not be properly evaluated.

The SEM results alone cannot provide precise information about the size and internal structure of the microclusters, as such, static light scattering (SLS) analysis was used to obtain the mean radius of gyration $\langle R_g \rangle$ and the fractal dimension d_f [45]. It can be seen from the double logarithmic plot of the structure factor $\langle S(q) \rangle$ plotted as a function of scattering wave vector q , that as the amount of PANI-PAAMPSA increases, the bending of the curve (i.e. Guinier region used to extract $\langle R_g \rangle$) is shifted more to the left (larger aggregates), indicating the improved mechanical stability of the formed aggregates (Fig. 4(a)). This

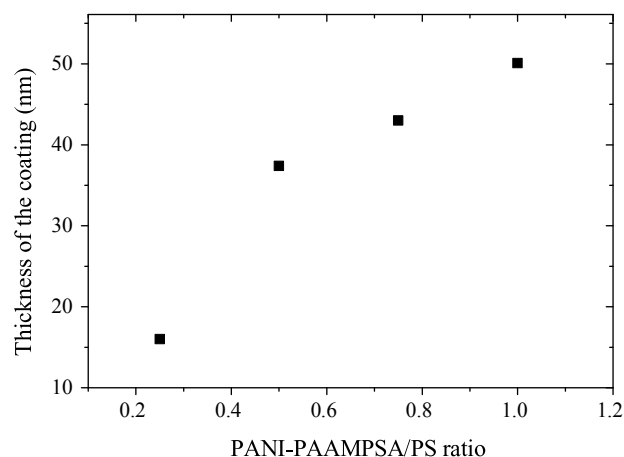


Fig. 3. Dependence of the coating thickness on PANI-PAAMPSA/PS ratio.

is furthermore supported by the increase of the d_f as obtained from the slope of the power law region of $\langle S(q) \rangle$ up to PS-PANI-PAAMPSA ratio of 1:0.75, indicating formation of more compact, and therefore, more resistant aggregates [23–25,46–52,53]. Above the PANI-PAAMPSA/PS ratio equal to 1 wt.%, the fractal dimension decreases probably due to the fact that not enough PS NPs were present in comparison to PANI-PAAMPSA to support the PANI-PAAMPSA into compact 3-D structure. It is therefore worth stating the role of PS NPs in enhancing the strength of the aggregates. Nevertheless, the materials show some huge through pores, which accounted for their high porosities as illustrated in Fig. SI 5 in Supporting Information. This result agrees with observations of other authors published recently in the literature [24,25,46].

From the plots of $\langle R_g \rangle$ and d_f as a function of the amount of PANI-PAAMPSA present in the composite, it was observed that the $\langle R_g \rangle$ values of the microclusters increased with an increase of the PANI-PAAMPSA amount up to 1 wt.% (Fig. 4(b)). Above this value there was no further increase of the microcluster size with increasing PANI-PAAMPSA

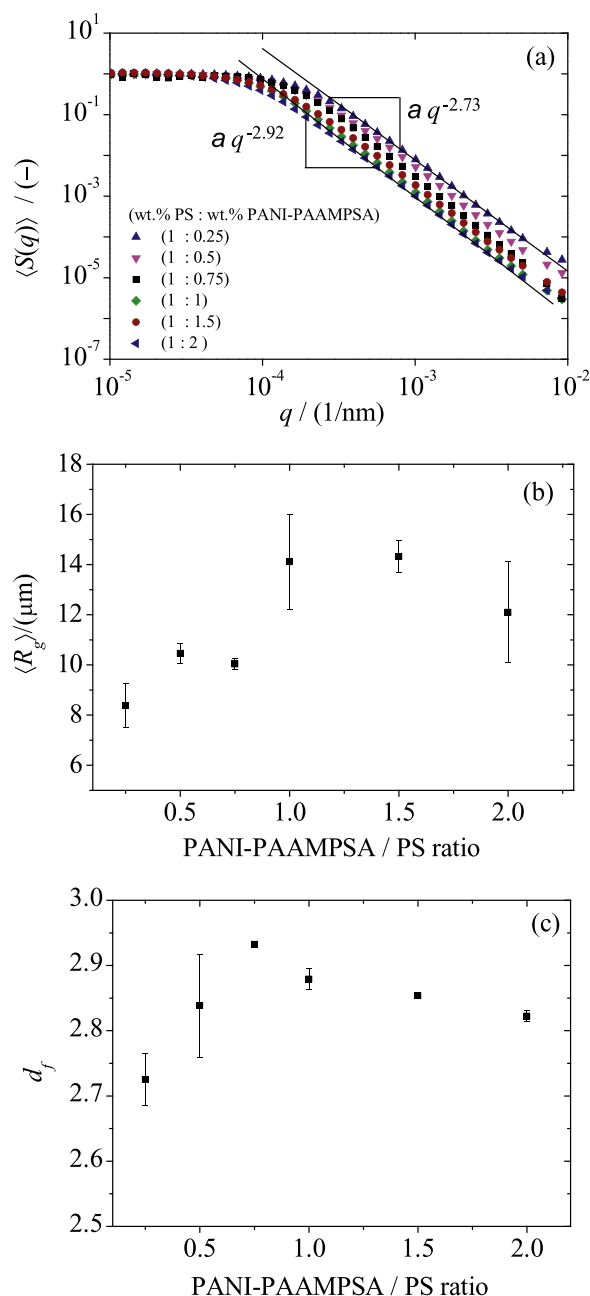


Fig. 4. Double logarithmic plot $\langle S(q) \rangle$ vs q of the composites (a), $\langle R_g \rangle$ (b) and d_f (c) as a function of PANI-PAAMPSA/PS ratio.

amount. This is related to an increase in the coating thickness as the amount of PANI-PAAMPSA increased resulting in bigger aggregates. Similar effect was observed also on the evolution of d_f , which increases from value of about 2.7–2.9 as the PANI-PAAMPSA amount increases from 0.25 to 1 wt.%, without further rise of d_f for 1.5 and 2 wt.% (Fig. 4(c)). Similar increase of d_f was also observed in the works of Lamprou et al. [24,25] and Brand et al. [46] and it was related to the interpenetration of the primary particles during the production of the porous material. This is comparable to our case where there is buildup of a solid bridge of PANI-PAAMPSA between PS-NPs.

To confirm the observed porous nature of the microclusters (see Figs. 2 and Fig. SI 5 in Supporting Information) and to determine their surface areas, mercury porosimetry and N_2 -adsorption/desorption were conducted. The obtained results are summarized in Fig. 5(a)–(d). For all prepared materials the N_2 sorption isotherms were of the type II according to the Bruner-Deming-Deming-Teller classification [54]

exhibiting a slight hysteresis in the range of relative pressures above 0.7 (Fig. 5(a)). The type II isotherms are typical of non-porous or macroporous materials. The latter case describes our materials, which are, aggregated particles [4,54]. The presence of H3-type hysteresis (according to IUPAC classification) indicates mesoporous condensation due to the presence of small pores with interconnected porosity [54]. However, the microclusters also possess very large pores (> 50 nm), a property that is in good agreement with SEM images as well as with their porosity data. The corresponding pore size distribution obtained from the Barret-Joyner-Halenda (BJH) method is also shown in Fig. 5(c), indicating the range of pore diameters in the microclusters. This was confirmed by lower magnification SEM images of the microclusters showing the large pores as was described previously in Fig. SI 5 in Supporting Information.

The isotherm from Hg porosimetry is shown in Fig. 5(b). The volume of Hg intruded increased as the pressure augmented until a plateau was reached at around 50 MPa for PS – PANI-PAAMPSA 3 and 4. For PS – PANI-PAAMPSA 1 and 2, two different plateaus were observed. In fact, first the volume increased as the pressure increased until about 4.5 MPa when the value remained nearly constant increasing just slightly. Upon increasing the pressure further, the intruded volume increased again until a second plateau was observed at around 50 MPa. The appearance of two distinct plateau regimes points out the existence of two different populations of pores in the microclusters possessing lower amounts of PANI-PAAMPSA (PS-PANI-PAAMPSA 1 and 2). The first plateau could correspond to the large interspaces between the clusters due to drying effect while the second plateau could be as a result of the porosities of individual coated particles. We think this could come from the drying effect as the individual aggregates come together during the drying process creating larger interspaces between them.

The surface areas and porosities obtained from both BET and Hg porosimetry data are presented in Table 2. It was observed that the surface areas increased as the amount of PANI-PAAMPSA decreased, a trend observed from both N_2 sorption and Hg porosimetry data. This could be due to the smaller size of the formed clusters at lower PANI-PAAMPSA concentrations, which means higher contact surface area. However, on the whole, the observed BET surface areas of the materials were relatively low (ranged from 13 to $18 \text{ m}^2/\text{g}$) while the total pore areas evaluated from Hg porosimetry data were slightly higher ($17\text{--}32 \text{ m}^2/\text{g}$). The differences could be due to the assumption of cylindrical pores in evaluating the data from mercury porosimetry and considering the irregular nature of the pores in the materials, this evaluation accounted for the differences in results. Nevertheless, the trend was the same in both cases.

Furthermore, from the porosity data, it was clearly observed that the increase of the porosity of the materials is associated with the amount of PANI-PAAMPSA present, as evidenced by the fibrillar morphology of PANI-PAAMPSA providing additional porosity compare to the inter-particle porosity.

4.3. Thermal behavior

TGA and DSC were used to examine the thermal properties of PS – PANI-PAAMPSA microclusters.

TG curve, the derivative of the TG curve and DSC curve for PS NPs, PANI-PAAMPSA and PS – PANI-PAAMPSA composites show the thermal behavior and stabilities of the microclusters (Fig. 6(a)–(c) respectively). In particular, TG curve for PS-NPs displays an onset decomposition temperature at 411°C , where 95% of the weight loss occurred during the first stage. The second degradation stage which starts from 577°C and ranged to 650°C represents 5% of the weight loss probably the second stage of PS decomposition and also thermal decomposition of the PVP. This demonstrated that the majority of the decomposition occurs in the first cycle (Fig. 6(b)). In contrast, due to the highly hygroscopic nature of polyaniline, PANI-PAAMPSA has two

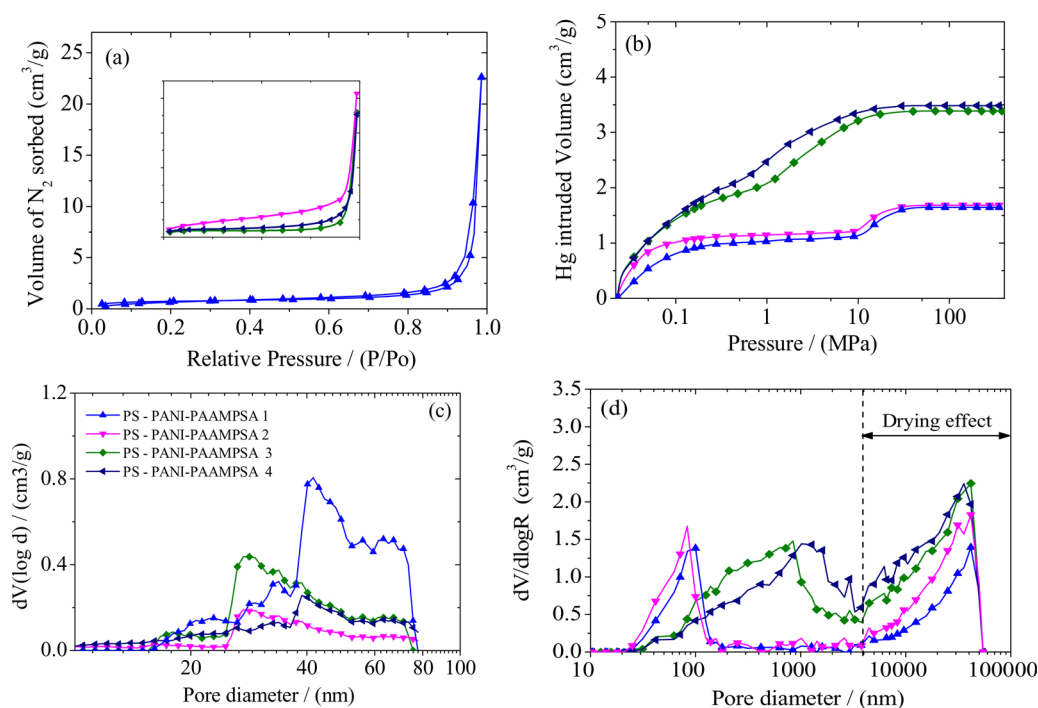


Fig. 5. (a). Nitrogen adsorption-desorption isotherm of PS-PANI-PAAMPSA 1 (inset shows similar adsorption curves for other compositions), (b) mercury intrusion isotherm of the microclusters (c) differential pore size distribution from N₂ sorption data and (d) differential pore size distribution from Hg porosimetry data.

Table 2
Properties of the produced microclusters.

Samples and ratios	Porosity (Hg Porosimetry)	S _{BET} [m ² /g]	Total Pore area H _g [m ² /g]
PS – PANI-PAAMPSA 1	0.59	18	32
PS – PANI-PAAMPSA 2	0.65	16	26
PS – PANI-PAAMPSA 3	0.79	15	23
PS – PANI-PAAMPSA 4	0.80	13	17

weight loss stages. An initial weight loss of about ~10% was observed from room temperature to 110 °C, which was attributed to the release of moisture. The onset of the main decomposition stage occurs earlier at 318 °C, compared to that of PS-NPs, which is seen as a small shoulder peak in the DTG curve in Fig. 6(b). This early onset of decomposition is due to the loss of the doping acid, PAAMPSA, a similar case was observed by other researchers [55]. Then two other peaks occurring at 412 and 500 mark the main decomposition stages of PANI-PAAMPSA. Though the initial onset decomposition temperature of PANI-PAAMPSA is much lower, the overall degradation spans a wide temperature range up to 700 °C. Therefore, the thermal decomposition of PANI-PAAMPSA is much slower process than that of PS-NPs.

Comparing the TG curves of PS-NPs and PS – PANI-PAAMPSA, a systematic shift can be seen, which is caused by the presence of the PANI-PAAMPSA coating on the surface of PS-NPs. This is evidenced by the overlap of PS-NPs and PS – PANI-PAAMPSA 1 curves in the temperature range room temperature to 300 °C. The microclusters containing higher amounts of PANI-PAAMPSA (> 0.25 wt.%) have three stages. The first stage corresponds to moisture release as also observed in PANI-PAAMPSA. The second stage is caused mainly by the thermal decomposition of PS-NPs but also by the initiation of the thermal decomposition of PANI-PAAMPSA. The onset decomposition temperature of the second stage was slightly shifted to lower temperatures compared to PS-NPs (370, 370, 372 and 373 °C for PS – PANI-PAAMPSA 1–4 respectively) as the amount of PANI-PAAMPSA increased. On the other hand, the weight loss at the third stage corresponding to PANI-PAAMPSA thermal degradation increased with the increase of the content of this latter. The decomposition temperatures of the second stage decreased as the amount of PANI-PAAMPSA increased, 570, 562,

552 and 554 °C PS – PANI-PAAMPSA 1–4 respectively. The TG curves of PANI-PAAMPSA and of the microcluster exhibiting the highest amount of PANI-PAAMPSA (PS – PANI-PAAMPSA 4) are quasi-superposed. Overall, the weight loss of the PS – PANI-PAAMPSA composites was more shifted to higher temperatures as compared to PS-NPs. Therefore the PANI-PAAMPSA coating greatly improved the thermal stability of the microclusters.

As can be seen from the DSC curves of PS-NPs and PS – PANI-PAAMPSA microclusters (Fig. 6(c)), the PS-NPs display a glass transition temperature (T_g) at ca. 108 °C. This value is comparable to that of typical high molecular weight pristine PS (T_g (PS) = 100 °C). The slight shift of the T_g of PS-NPs towards higher values as compared to pristine PS can be due to the presence of PVP layer at the surface of the nanoparticles. Reported increase in T_g values by 5 °C upon formation of PS-b-PVP copolymers were attributed in part to the incorporation of the rigid block of PVP [56]. Similar higher T_g was observed for polystyrene-polystyrene sulfonate-Na core-shell particles, which was attributed to the stiffness caused by the sulfonate group of polystyrene-polystyrene sulfonate-Na [57]. For the samples PS – PANI-PAAMPSA containing lower amounts of PANI-PAAMPSA i.e. 0.25 and 0.5 wt.%, similar T_g values to those measured for PS-NPs (Table SI 1 in supporting information) were also recorded though the intensity of the glass transition decreased in presence of PANI-PAAMPSA (Fig. 6(c)). Nevertheless, for PS – PANI-PAAMPSA microclusters containing higher amount of PANI-PAAMPSA i.e. 1–2 wt.%, the T_g was barely detected. Overall, as the amount of PANI-PAAMPSA increased in the PS – PANI-PAAMPSA microclusters, the intensity of the T_g peak decreased until it became hard to measure. This interesting thermal behavior of the nanoparticles could be explained by the presence of crystalline PANI-PAAMPSA coating at the surface of PS nanoparticles leading to hindering of the amorphous PS chain motions. This phenomenon is amplified as the thickness of the coating increased and acted as a thermal and as a mechanical barrier material, which limited the mobility of the PS chains. More details about the TG analysis can be found in Supporting Information (Section A.3).

4.4. Electrical conductivity

The electrical properties of the macroporous materials were also

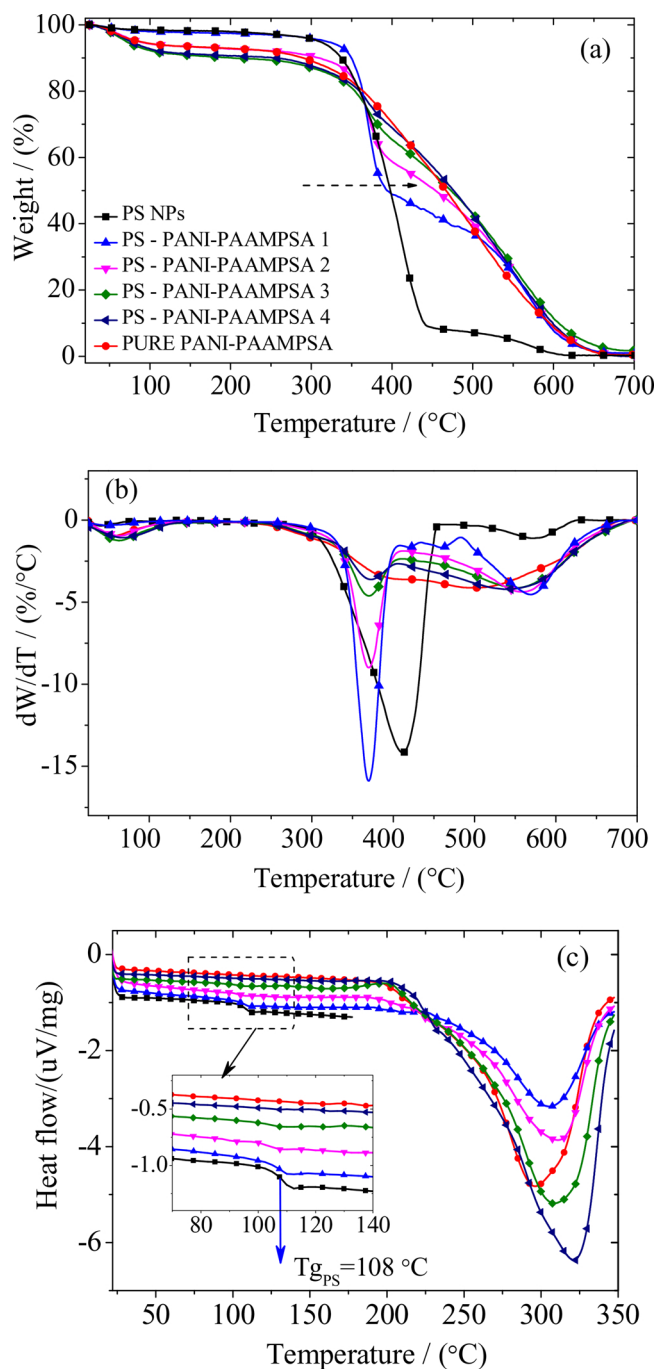


Fig. 6. (a) TGA curves and (b) DTG curves and (c) DSC curves for PS NPs, PANI-PAAMPSA and PS – PANI-PAAMPSA composite microclusters.

measured to evaluate their potential for electronic applications. An increase in the electrical conductivity was observed as the amount of PANI-PAAMPSA increased (Fig. 7). Sample (e) which is pure PANI-PAAMPSA (1 wt.%) exhibited the highest conductivity of $11.4 \times 10^{-3} \text{ S cm}^{-1}$ while PS – PANI-PAAMPSA 1 with the least amount of PANI-PAAMPSA showed the least conductivity of $0.22 \times 10^{-3} \text{ S cm}^{-1}$. This trend in conductivity is associated with the different morphologies of the materials. The conductivity is highest for pure PANI-PAAMPSA because of better interconnectivity of the PANI chains due to the fact that there is only PANI-PAAMPSA present on all surfaces. Additionally, this interconnectivity is seen in the fibrillar nature of the PANI-PAAMPSA material (Fig. 2(f)). For the PS – PANI-PAAMPSA composites, the conductivity was increasing linearly with the amount of PANI-PAAMPSA and also the

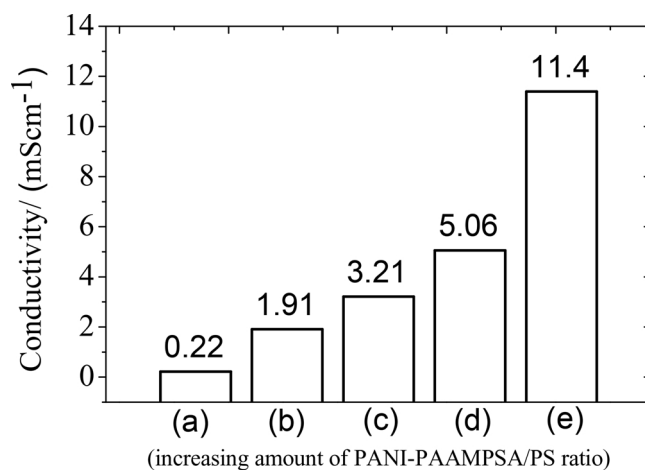


Fig. 7. Conductivities of composites (a) 1 wt.% PS: 0.25 wt.% PANI-PAAMPSA (b) 1 wt.% PS: 0.5 wt.% PANI-PAAMPSA. (c) 1 wt.% PS: 1 wt.% PANI-PAAMPSA (d) 1 wt.% PS: 2 wt.% PANI-PAAMPSA (e) 1 wt.% PANI-PAAMPSA.

size of the aggregates. Similar results were observed by Zhang et al. [55] where they observed higher conductivities at higher aspect ratios of PANI nanostructures while the same nanostructures with smaller aspect ratios exhibited lower conductivities. Nevertheless, all the materials exhibited conductive properties in the scale of 10^{-3} S/cm , which is in the range of semiconductor materials.

5. Conclusions

In this work we demonstrated the synthesis of stable conductive macroporous composite materials by chemical oxidative polymerization of aniline-(2-acrylamido-2-methylpropanesulfonic acid) (PANI-PAAMPSA) in the presence of polystyrene nanoparticles (PS-NPs) building blocks. Due to its nature, the presented method does not require to use any pore generating agent and is suitable for preparation of 3D porous material with porosity up to 80% having specific surface areas between 13 and $18 \text{ m}^2/\text{g}$. The morphology and properties of the resultant microclusters were found to depend strongly on the composition (PANI-PAAMPSA/PS-NPs ratio). In particular, by varying PANI-PAAMPSA/PS-NPs ratio from 0.25 to 1 under stirring conditions, we were able to prepare porous microclusters with diameter in the range from 15 to $30 \mu\text{m}$ with thickness of PANI-PAAMPSA moieties on the surface of PS NPs ranging from 15 to approximately 50 nm. Furthermore, PANI-PAAMPSA coating on the surface of PS NPs makes the microclusters highly thermally stable up to $350\text{ }^{\circ}\text{C}$, as confirmed both by thermal gravimetric analysis and differential scanning calorimetry. Measured conductivities in the order of $10^{-3} \text{ S cm}^{-1}$ confirms continuous character of the PANI-PAAMPSA coating over the entire 3D structure of the microclusters, which opens doors to new applications for which hierarchically-structured materials combined with conductivity will be required.

Acknowledgments

The authors are grateful for support provided by a Czech Science Foundation (GACR) grant 16-22997S and a specific university research grant (MSMT No 20/2015).

Appendix A. Supplementary data

Supplementary data associated with this article can be found, in the online version, at <http://dx.doi.org/10.1016/j.colsurfa.2017.10.082>.

References

- [1] T.K. Das, S. Prusty, Review on conducting polymers and their applications, *Polym. Plast. Technol. Eng.* 51 (2012) 1487–1500.
- [2] Y. Tao, J. Li, A. Xie, S. Li, P. Chen, L. Ni, Y. Shen, Supramolecular self-assembly of three-dimensional polyaniline and polypyrrole crystals, *Chem. Commun.* 50 (2014) 12757–12760.
- [3] D. Kim, Y. Tian, H.J. Choi, Seeded swelling polymerized sea urchin-like core-shell typed polystyrene/polyaniline particles and their electric stimuli-response, *RSC Adv.* 5 (2015) 81546–81553.
- [4] A.M. Youssef, Morphological studies of polyaniline nanocomposite based meso-structured TiO₂ nanowires as conductive packaging materials, *RSC Adv.* 4 (2014) 6811.
- [5] U. Lange, N.V. Roznyatovskaya, V.M. Mirsky, Conducting polymers in chemical sensors and arrays, *Anal. Chim. Acta* 614 (2008) 1–26.
- [6] J.W. Jeon, Y. Ma, J.F. Mike, L. Shao, P.B. Balbuena, J.L. Lutkenhaus, Oxidatively stable polyaniline:polyacid electrodes for electrochemical energy storage, *Phys. Chem. Chem. Phys.* 15 (2013) 9654–9662.
- [7] L. Wang, J. Xu, Y. Chen, S. Cheng, L.-J. Fan, Preparation and characterization of polyaniline coated microspheres for potential application in anisotropic conductive film, *J. Polym. Res.* 18 (2011) 2169–2174.
- [8] S. Bhadra, D. Khashtgir, N.K. Singha, J.H. Lee, Progress in preparation, processing and applications of polyaniline, *Prog. Polym. Sci.* 34 (2009) 783–810.
- [9] A.G. MacDiarmid, Synthetic metals: a novel role for organic polymers (Nobel lecture), *Angew. Chem. Int. Ed.* 40 (2001) 2581–2590.
- [10] Y.S. Negi, P.V. Adhyapak, Development in polyaniline conducting polymers, *J. Macromol. Sci. Polym. Rev.* 42 (2002) 35–53.
- [11] D.B. Cairns, S.P. Armes, Synthesis and characterization of submicrometer-sized polypyrrole-polystyrene composite particles, *Langmuir* 15 (1999) 8052–8058.
- [12] I.Y. Sapurina, M.A. Shishov, Oxidative polymerization of aniline: molecular synthesis of polyaniline and the formation of supramolecular structures, in: A. De Souza Gomes (Ed.), *New Polymers for Special Applications*, InTech, 2012, pp. 251–312.
- [13] F. Caruso, Nanoengineering of particle surfaces, *Adv. Mater.* 13 (2001) 12.
- [14] K. Chatterjee, S. Sarkar, K. Jagajjanani Rao, S. Paria, Core/shell nanoparticles in biomedical applications, *Adv. Colloid Interface Sci.* 209 (2014) 8–39.
- [15] H.-P. Hentze, M. Antonietti, Porous polymers and resins, in: K.S.W.S. Ferdi Schuth, Jens Weitkamp (Eds.), *Handbook of Porous Solids*, Wiley-VCH Weinheim, Germany, 2002, pp. 1964–2013.
- [16] X. Sun, M. Gan, L. Ma, H. Wang, T. Zhou, S. Wang, W. Dai, H. Wang, Fabrication of PANI-coated honeycomb-like MnO₂ nanospheres with enhanced electrochemical performance for energy storage, *Electrochim. Acta* 180 (2015) 977–982.
- [17] M.G. Han, J. Sperry, A. Gupta, C.F. Huebner, S.T. Ingram, S.H. Foulger, Polyaniline coated poly(butyl methacrylate) core-shell particles: roll-to-roll printing of templated electrically conductive structures, *J. Mater. Chem.* 17 (2007) 1347–1352.
- [18] X.-y. Dai, X. Zhang, Y.-f. Meng, P.-k. Shen, Preparation of hollow carbon spheres by carbonization of polystyrene/polyaniline core-shell polymer particles, *New Carbon Mater.* 26 (2011) 389–395.
- [19] S. Bousalem, S. Benabderrahmane, Y.Y.C. Sang, C. Mangeney, M.M. Chehimi, Covalent immobilization of human serum albumin onto reactive polypyrrole-coated polystyrene latex particles, *J. Mater. Chem.* 15 (2005) 3109.
- [20] H.C. Zeng, Synthesis and self-assembly of complex hollow materials, *J. Mater. Chem.* 21 (2011) 7511.
- [21] X.C. Jiang, Q.H. Zeng, C.Y. Chen, A.B. Yu, Self-assembly of particles: some thoughts and comments, *J. Mater. Chem.* 21 (2011) 16797.
- [22] A. Thomas, Functional materials: from hard to soft porous frameworks, *Angew. Chem. Int. Ed.* 49 (2010) 8328–8344.
- [23] A. Lamprou, A.F. Gavrilidou, G. Storti, M. Soos, M. Morbidelli, Application of polymeric macroporous supports for temperature-responsive chromatography of pharmaceuticals, *J. Chromatogr. A* 1407 (2015) 90–99.
- [24] A. Lamprou, I. Kose, Z.P. Aguirre, G. Storti, M. Morbidelli, M. Soos, Macroporous polymer particles via reactive gelation under shear: effect of primary particle properties and operating parameters, *Langmuir* 30 (2014) 13970–13978.
- [25] A. Lamprou, I. Kose, G. Storti, M. Morbidelli, M. Soos, Synthesis of macroporous polymer particles using reactive gelation under shear, *Langmuir* 30 (2014) 6946–6953.
- [26] I.T. Papadas, I. Vamvasakis, I. Tamiolakis, G.S. Armatas, Templated self-assembly of colloidal nanocrystals into three-dimensional mesoscopic structures: a perspective on synthesis and catalytic prospects, *Chem. Mater.* 28 (2016) 2886–2896.
- [27] C.F. Mangeney, M. Fertani, S. Bousalem, M. Zhicai, S. Ammar, F. Herbst, P. Beaunier, A. Elaissari, M.M. Chehimi, Magnetic Fe₂O₃-Polystyrene/PPy core/shell particles: Bioreactivity and self-assembly, *Langmuir* 23 (2007) 10940–10949.
- [28] D.B. Cairns, M.A. Khan, C. Perruchot, A. Riede, S.P. Armes, Synthesis and characterization of polypyrrole-coated poly(Alkyl methacrylate) latex particles, *Chem. Mater.* 15 (2003) 233–239.
- [29] W. Shao, R. Jamal, F. Xu, A. Ubul, T. Abdiryim, The effect of a small amount of water on the structure and electrochemical properties of solid-state synthesized polyaniline, *Materials* 5 (2012) 1811–1825.
- [30] Y. Sheng, J.-d. Chen, D.-q. Zhu, C. Carrot, J. Guillet, Synthesis of conductive polyaniline via oxidation by MnO₂, *Chin. J. Polym. Sci.* 22 (2004) 269–277.
- [31] H. Gu, J. Guo, H. Wei, Y. Huang, C. Zhao, Y. Li, Q. Wu, N. Haldolaarachchige, D.P. Young, S. Wei, Z. Guo, Giant magnetoresistance in non-magnetic phosphoric acid doped polyaniline silicon nanocomposites with higher magnetic field sensing sensitivity, *Phys. Chem. Chem. Phys.* 15 (2013) 10866–10875.
- [32] V.V. Abalyaeva, N.N. Dremova, N.N. Vershinin, The effect of Ce³⁺ cations on polyaniline morphology and electric properties, *Russ. J. Electrochem.* 49 (2013) 863–869.
- [33] P. Bober, M. Trchová, J. Prokeš, M. Varga, J. Stejskal, Polyaniline–silver composites prepared by the oxidation of aniline with silver nitrate in solutions of sulfonic acids, *Electrochim. Acta* 56 (2011) 3580–3585.
- [34] B. Davodi, M.S. Lashkenari, H. Eisazadeh, Fabrication and thermal degradation behavior of polystyrene nanoparticles coated with smooth polyaniline, *Synth. Met.* 161 (2011) 1207–1210.
- [35] J.E. Yoo, J.L. Cross, T.L. Bucholz, K.S. Lee, M.P. Espe, Y.-L. Loo, Improving the electrical conductivity of polymer acid-doped polyaniline by controlling the template molecular weight, *J. Mater. Chem.* 17 (2007) 1268.
- [36] Y. Zhao, E. Tomsik, J. Wang, Z. Moravkova, A. Zhigunov, J. Stejskal, M. Trchova, Self-assembly of aniline oligomers, *Chem. Asian J.* 8 (2013) 129–137.
- [37] S. Chen, H. Lee, Structure and properties of poly(acrylic acid)-doped polyaniline, *Macromolecules* 28 (1994) 2858–2866.
- [38] H.-S. Moon, J.-K. Park, Structural effect of polymeric acid dopants on the characteristics of doped polyaniline composites: effect of hydrogen bonding, *J. Polym. Sci. Part A: Polym. Chem.* 36 (1998) 1431–1439.
- [39] J. Medek, Z. Weishauptova, Determination of resistivity of solids in powdered form, *Powder Technol.* 80 (1994) 183–190.
- [40] Malvern instruments limited, Zetasizer Nano Series User Manual, MANO317, (2004) England.
- [41] J.E. Yoo, J. Bae, The influence of aniline to acid composition on the electrical conductivity of PANI-PAAMPSA, *Bull. Korean Chem. Soc.* 34 (2013) 3825–3828.
- [42] P. Bober, P. Humpolíček, J. Pachernik, J. Stejskal, T. Lindfors, Conducting polyaniline based cell culture substrate for embryonic stem cells and embryoid bodies, *RSC Adv.* 5 (2015) 50328–50335.
- [43] J. Stejskal, I. Sapurina, M. Trchová, Polyaniline nanostructures and the role of aniline oligomers in their formation, *Prog. Polym. Sci.* 35 (2010) 1420–1481.
- [44] L. Hechavarria, Polyaniline-poly(2-acrylamido-2-methyl-1-propanesulfonic acid) composite thin films: structure and properties, *Thin Solid Films* 441 (2003) 56–62.
- [45] M. Soos, A. Moussa, L. Ehrl, J. Sefcik, H. Wu, M. Morbidelli, Effect of shear rate on aggregate size and morphology investigated under turbulent conditions in stirred tank, *J. Colloid Interface Sci.* 319 (2008) 577–589.
- [46] B. Brand, M. Morbidelli, M. Soos, Shear-induced reactive gelation, *Langmuir* 31 (2015) 12727–12735.
- [47] L.S. Ehrl, M. Soos, M. Morbidelli, Dependence of aggregate strength, structure, and light scattering properties on primary particle size under turbulent conditions in stirred tank, *Langmuir* 24 (2008) 3070–3081.
- [48] L.S. Ehrl, M. Soos, H. Wu, M. Morbidelli, Effect of flow field heterogeneity in coagulators on aggregate size and structure, *AIChE J.* 56 (2010) 2573–2587.
- [49] Y.M.L. Harshe, M. Lattuada, M. Soos, Experimental and modeling study of breakage and restructuring of open and dense colloidal aggregates, *Langmuir* 27 (2011) 5739–5752.
- [50] M. Kroupa, M. Vonka, M. Soos, J. Kosek, Size and structure of clusters formed by shear induced coagulation: modeling by discrete element method, *Langmuir* 31 (2015) 7727–7737.
- [51] M. Soos, L. Ehrl, M.U. Bäbler, M. Morbidelli, Aggregate breakup in a contracting nozzle, *Langmuir* 26 (2010) 10–18.
- [52] A.S. Moussa, M. Lattuada, B.O. Conchuir, A. Zacccone, M. Morbidelli, M. Soos, Flow-induced aggregation and breakup of particle clusters controlled by surface nanoroughness, *Langmuir* 29 (2013) 14386–14385.
- [53] M. Soos, M. Lattuada, J. Sefcik, M. Morbidelli, Interpretation of light scattering and turbidity measurements in aggregated systems: effect of intra-cluster multiple-light scattering, *J. Phys. Chem. B* 113 (2009) 14962–14970.
- [54] F. Rouquerol, J. Rouquerol, K. Sing, Adsorption by Powders and Porous Solids Principles, Methodology and Applications, Academic Press, New York, 1999.
- [55] X. Zhang, J. Zhu, N. Haldolaarachchige, J. Ryu, D.P. Young, S. Wei, Z. Guo, Synthetic process engineered polyaniline nanostructures with tunable morphology and physical properties, *Polymer* 53 (2012) 2109–2120.
- [56] M.A. Farias, M.d.C. Gonçalves, Synthesis and applications of polystyrene-block-poly(N-vinyl-2-pyrrolidone) copolymers, *Polímeros* 26 (2016) 1–10.
- [57] N. Yeole, D. Hundiware, T. Jana, Synthesis of core-shell polystyrene nanoparticles by surfactant free emulsion polymerization using macro-RAFT agent, *J. Colloid Interface Sci.* 354 (2011) 506–510.



Contents lists available at ScienceDirect

Chemical Engineering Journal

journal homepage: www.elsevier.com/locate/cej

Nitrogen-rich hierarchically porous polyaniline-based adsorbents for carbon dioxide (CO₂) capture

Edith Mawunya Kutorglo^{a,*}, Fatima Hassouna^a, Anna Beltzung^b, Dušan Kopecký^c,
Ivona Sedlářová^d, Miroslav Šoos^{a,*}

^a Department of Chemical Engineering, University of Chemistry and Technology, Technická 3, 166 28 Prague 6 – Dejvice, Czech Republic

^b Institute for Chemistry and Bioengineering, Department of Chemistry and Applied Biosciences, ETH Zurich, Vladimir-Prelog-Weg 1-5/10, 8093 Zürich, Switzerland

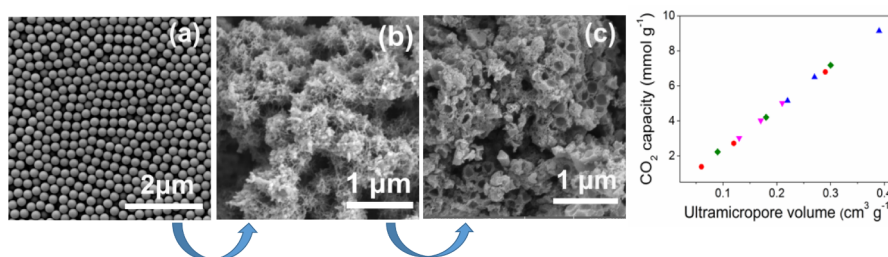
^c Department of Physics and Measurements, University of Chemistry and Technology, Technická 3, 166 28 Prague 6 – Dejvice, Czech Republic

^d Department of Inorganic Technology, University of Chemistry and Technology, Technická 5, 166 28 Prague 6 – Dejvice, Czech Republic

HIGHLIGHTS

- Hierarchically porous materials were synthesized using an easy and new concept.
- The materials were prepared from cheap precursors and applied in CO₂ capture.
- The pore size distribution was easily tuned by changing the size of nanoparticles.
- The high CO₂ sorption capacity is among the highest reported for carbon materials.
- The approach provides a strategy serving as a guide to the design of new CO₂ capture sorbents.

GRAPHICAL ABSTRACT



ARTICLE INFO

Keywords:

Hierarchical pore structure
Carbon dioxide capture
Nitrogen rich
Polyaniline
Adsorption
Porous materials

ABSTRACT

The development of new materials and technologies for CO₂ capture has attracted a lot of interest due to the growing concerns about global warming and climate change. Herein, we prepared hierarchically porous materials from cheap precursors – polyaniline and polystyrene nanoparticles (PS NPs) using an easy and new concept based on the removal of the PS NPs during a pre-carbonization step followed by chemical activation. The pore size distribution was easily tuned by varying the size of the sacrificial PS NPs and the intensity of chemical treatment. We obtained an outstanding CO₂ capture capacity of our optimum material (9.14 mmol g⁻¹ at 273.15 K and 1 bar). The findings suggest that these materials are promising CO₂ sorbents and the approach provides a strategy to design new high-capacity polymer-based carbons for CO₂ capture.

1. Introduction

The heavy reliance on fossil fuels for energy has led to a drastic rise in atmospheric CO₂ emissions. This has raised a lot of concerns given the steady increase in global temperatures, commonly known as global

warming, of which anthropogenic CO₂ emissions have been directly implicated [1–3]. Carbon capture and storage (CCS) from large emission sources is considered as immediate and most realistic solution to minimize CO₂ emissions while searching for long-term sustainable energy sources to replace fossil fuels [4,5]. Among the CO₂ capture

* Corresponding authors.

E-mail addresses: kutorgle@vscht.cz (E.M. Kutorglo), soosm@vscht.cz (M. Šoos).

<https://doi.org/10.1016/j.cej.2018.10.133>

Received 20 July 2018; Received in revised form 21 September 2018; Accepted 13 October 2018

1385-8947/ © 2018 Elsevier B.V. All rights reserved.

options available, post-combustion capture is the most widely adopted method, thanks to its flexibility and the fact that it can be easily retrofitted to already existing fossil fuel power plants [1,6]. For more than 60 years, aqueous amine absorption has been an efficient technology for the removal of CO₂ from natural gas. However, this technique has several drawbacks, such as corrosion of equipment and high amounts of energy are needed for regeneration of the solvents making the process expensive [2,5,7]. The main challenge for realizing practical carbon capture lies with the design of new sorbents from cheap materials, with high capacity and easy recyclability.

Over the past few decades, a number of solid sorbents e.g. molecular sieves, porous carbon, porous silica, metal organic frameworks etc., are emerging as good alternatives to replace liquid amines, given their well developed porosity, easy handling and lower energy requirements for regeneration [7–9]. Based on the materials studied so far, it has been found that efficient CO₂ sorption performance depends on a combination of diffusion and adsorption selectivity [10–12]. Therefore, a good CO₂ sorbent comprises high microporosity with suitable pore sizes (ultramicropores with diameters < 0.7 nm), coupled with the presence of bigger pores, to enhance efficient diffusion [13]. An additional parameter reported to influence CO₂ sorption is the presence of appropriate surface functionalities (nitrogen or other heteroatoms). Many different mechanisms have been proposed to explain the increase of CO₂ sorption on nitrogen-doped carbon materials such as Lewis acid-Lewis base interaction [14–16], quadrupolar interaction [17,18] and hydrogen bonding interaction [19]. Specifically, it was previously reported that the pyrrolic and amine nitrogen functionalities have the strongest interactions with CO₂ molecules [15,20,21].

Several authors have attempted to explain the differences in the mechanisms of CO₂ adsorption in micropores and in the presence of nitrogen functionalities. When a sorbent material is highly ultramicroporous, where their pore aperture is similar to the size of CO₂ molecules, adsorption occurs mainly by physisorption mechanisms such as capillary condensation and molecular sieving and the role of nitrogen functionalities becomes less obvious. When the materials are mesoporous, and therefore the capillary effect diminishes, it is then the chemisorption binding mechanisms dominate and nitrogen functionalities play the major role [7]. Additionally, because CO₂ is a weak Lewis acid, its adsorption capacity is influenced by the surface chemistry [6], suggesting that a synergistic contribution between the hierarchical porosity (micro- and mesopores) coupled with appropriate surface chemistry (nitrogen functionalities) is essential to achieve high sorption capacities. This may be the reason why it has been difficult to make a direct correlation between the simultaneous contribution of nitrogen and textural properties in the same material towards its CO₂ uptake capacity, especially if the material has a hierarchical pore structure with contributions from both micro- and mesopores.

From these findings, a lot of research has been focused on designing new sorbents using two main approaches: (i) post-synthetic functionalization to incorporate nitrogen or oxygen groups onto the porous framework and (ii) direct carbonization and activation of nitrogen-containing polymers [13,19,22]. The latter approach is more promising since it allows better control over the chemical composition and eliminates the usually complicated post-treatments to incorporate nitrogen or other functional groups [10,23], which usually results in the blockage of the diffusion channels to the active sites present on the materials [24,25]. Moreover, there have been reports of amine degradation and leaching after multiple CO₂ capture cycles leading to instability of these materials and limiting their long-term use [8,26,27]. Recently several N-bearing microporous carbon sorbents have been prepared from N-based precursors such as polyacrylonitrile [28], polyaniline [29], polypyrrole [22], and other renewable resources such as soya bean dregs [30] and saw dust [31] by various methods, mainly using KOH as activating agent. These materials have been shown to exhibit high sorption capacities and are promising for CO₂ capture applications. Specifically, Wickramarante et al. [32] successfully

synthesized phenolic resin-based activated carbon spheres with the optimum material CS*-P-A exhibiting high surface area ($S_{\text{BET}} = 2400 \text{ m}^2/\text{g}$) and a corresponding high CO₂ capacity of 8.9 mmol g^{-1} at 1 bar and 273 K. Similarly, Lee et al. [11] prepared polypyrrole-based porous materials and the materials exhibit high microporosity and high sorption capacities up to 7.30 mmol g^{-1} for their optimized material (600-2). Many of these experimental studies have been supported by molecular simulations on CO₂ adsorption behavior, which attribute high CO₂ capacities to high microporosity and the presence of surface functionalities (nitrogen, oxygen and sulfur) [13,33–35]. The incorporation of heteroatoms into carbon framework is thought to enhance uptake due to increased polarity of the carbon surface. However, tuning the diffusion and adsorption selectivity in these materials is not synergistic. Generally, the conditions required for generating high amount of small pores (high temperature and chemical treatment e.g. using KOH) results in the loss of surface functionalities [36–38]. For instance, Xing et al. [19] prepared a series of N-doped carbons from bean dreg by chemical activation and observed an inverse relationship between the nitrogen content and both the KOH amount and activation temperature. In a similar study, the content of sulfur in nanoporous carbon was found to decrease whereas the porosity increased upon air oxidation at 350 °C [39]. Moreover, it has been known that porous materials consisting solely of micropores suffer from diffusion problems, suggesting that the optimally designed sorbent should have a hierarchical pore structure. Therefore, it still remains a challenge to design the perfect combination of a material framework and surface chemistry. In other words, materials comprising all three types of pores i.e. abundant micropores (for high CO₂ adsorption), mesopores and macropores (to facilitate efficient CO₂ diffusion into and out of the adsorption sites) coupled with appropriate surface functionalities [40,41], will be the optimal sorbent.

In our earlier work, we reported the preparation of 3-D macroporous polyaniline (PANI) materials with very high porosities by a simple approach using polystyrene nanoparticles (PS NPs) as support blocks onto which PANI can easily adsorb and form 3-D networks [42]. To create a material comprising all three types of pores while preserving surface functional groups, we used a simple approach involving sacrificial PS NPs to prepare stable hierarchically porous materials with high surface areas and abundant surface groups and tested their application in CO₂ capture. Our strategy, which is based on an extension of our previous synthetic approach, involves the removal of sacrificial PS NPs during a pre-carbonization step followed by chemical activation using KOH. By changing the size of the PS NPs and KOH/C ratio for activation, it is possible to tune the pore size distribution and sorption capacity of the materials. The optimized material achieved very high CO₂ capacity (9.14 mmol g^{-1}) at 273.15 K and 1 bar, which is among the highest reported for carbon-based sorbents in the literature.

2. Materials and methods

2.1. Materials

Styrene (St, > 99%), ammonium peroxydisulfate (APS, 98%), poly(vinyl pyrrolidone) (PVP, $M_w = 40000 \text{ g mol}^{-1}$), aniline (ANI, ACS reagent, > 99.5%), phytic acid solution 50% (w/w) in H₂O were all purchased from Sigma Aldrich and used without modification or purification.

2.2. Synthesis of monodisperse PS nanoparticles and the 3-D microclusters

The PS-NP building blocks were prepared by radical emulsion polymerization according to the procedure described in Kutorglo et al. [42]. The recipe for preparing 370 nm PS NPs is presented in Table 1(A) while that for the preparation of PANI and crosslinked PANI is shown in Table 1(B). Aniline (ANI) was polymerized by chemical oxidative route in aqueous medium at 4 °C in an ice water bath in the presence of the PS

Table 1

Recipe for the preparation of (A) monodisperse 370 nm PS NPs by emulsion polymerization and (B) PS-PANI aggregates.

Parameter	Composition
<i>(A) PS-NPs</i>	
Solid content	20 wt%
Ratio styrene/PVP	56.25 (-)
Ratio monomer/initiator	100 (-)
<i>(B) PANI Microclusters</i>	
Solid content	5 wt%
Ratio of PS NPs/aniline (ANI)	1 (-)
Ratio of initiator (APS)/ANI	2.5 (-)
Ratio of phytic acid/ANI	2 (-)
Concentration of APS solution	1.56 mol L ⁻¹
Rate of addition of APS solution	0.5 mL min ⁻¹

NPs. APS was used as initiator and HCl as dopant, which was also used to maintain the pH of the polymerization medium in acidic range. Additionally, polymerization of ANI was done without PS NPs, with or without phytic acid as crosslinker for comparison. In a typical synthesis, ANI was added to HCl solution (1 M) under stirring followed by addition of phytic acid. After stirring at 250 rpm using a magnetic stirrer for some time (approx. 15 min), PS NPs were added to the mixture and stirred for another 10 min. APS was then dissolved in HCl solution (1 M) and added to the ANI-PS mixture slowly using a syringe pump. The polymerization was allowed to run overnight for at least 16 h. The resulting suspension of microclusters was freeze dried to obtain dry product for further characterization and testing.

2.3. Carbonization and activation

The freeze-dried materials prepared in Section 2.2. were carbonized in a tube furnace at 500 °C at a heating rate of 5 °C/min and under nitrogen flow of 25 L/h. The samples were then dispersed in KOH solution for at least 10 h under stirring. Different ratios of KOH/Carbonized material = 1, 2, 3 and 4 were used to find the optimum condition for the generation of the desired pore structures. The KOH treated materials were vacuum filtered and oven dried at 60 °C. This was followed by activation in a tube furnace at 750 °C for 1 h at a heating rate of 5 °C/min and under nitrogen flow of 25 L/h. The samples were then washed with 1 M HCl solution and followed by washing with distilled water until the pH was around 7. The resulting materials were oven dried at 60 °C overnight and characterized by a combination of several analytical techniques.

2.4. Characterization

The Fourier transform infrared spectroscopy (FTIR) spectra were recorded on a Nicolet iZ10 FTIR spectrometer with attenuated total reflectance (ATR) accessory from 4000 cm⁻¹ to 400 cm⁻¹ to evaluate the chemical bonds and structures in the obtained materials. Spectra were averaged over 64 scans. The morphology of the synthesized nanoparticles and hierarchically porous materials was observed with a scanning electron microscopy (SEM) (Mira 3 LMH, Tescan Company). The samples were sputter-coated with a thin layer of gold prior to SEM observation. The accelerating voltage of Schottky cathode was 3 kV. Secondary electrons were detected by the Everhart-Thornley type secondary electron detector or by the in-lens detector (In-Beam). The average size of the PS nanoparticles was determined by dynamic light scattering (DLS, Malvern Zetasizer Nano). The same device was used to evaluate the zeta potential of the PS NPs through the Smoluchowski model. The thermal stability of the materials was evaluated by thermal gravimetric analysis (TGA) using an STA-780 series Thermal Analyzer (Stanton-Redcroft, UK) under nitrogen flow (20 mL min⁻¹) at a heating rate of 10 °C min⁻¹ from room temperature to 850 °C. To assess the

textural properties of the materials, i.e. porosities and pore size distribution, these were measured by Hg porosimetry using Micromeritics AutoPore IV 9500 analyzer. For the surface areas, conventional nitrogen isotherms at 77 K were measured using Nova 2200 e surface area analyzer (Quantachrome). From this analysis, surface areas were obtained from the Brunauer-Emmett-Teller (BET) equations. The total pore volumes were measured at the relative pressure of 0.985 and the pore size distribution was determined based on density functional theory (DFT) model. For a more accurate characterization of the micropores, CO₂ adsorption at 273.15 K was performed on all samples using a Quadrasorb-SI gas adsorption analyzer (Quantachrome, USA). Using the DFT model (based on statistics and provided by the software) and assuming slit pore geometry, the corresponding pore size distributions were computed. With this method, it is possible to access the ultramicropores (sizes < 1 nm). The surface areas from CO₂ sorption were based on the BET model and were computed using the data collected in the range of values of relative pressures P/P_0 from 0.013 to 0.019. All the samples were degassed under vacuum (0.1 mbar) at 115 °C for at least 10 h before the measurements. Elemental composition (C, H, N) of the samples was determined with an Elementar vario EL Cube analyser (Elementar, Germany). XPS measurements were done on Omicron Nanotechnology with monochrome radiation of Al lamp with energy 1486.7 eV in constant analyser energy (CAE) mode. Measured spectra were evaluated by software Casa XPS where after intensity calibration the area of peaks and relative sensitivity factors (RSF) from database are used for determination of concentrations.

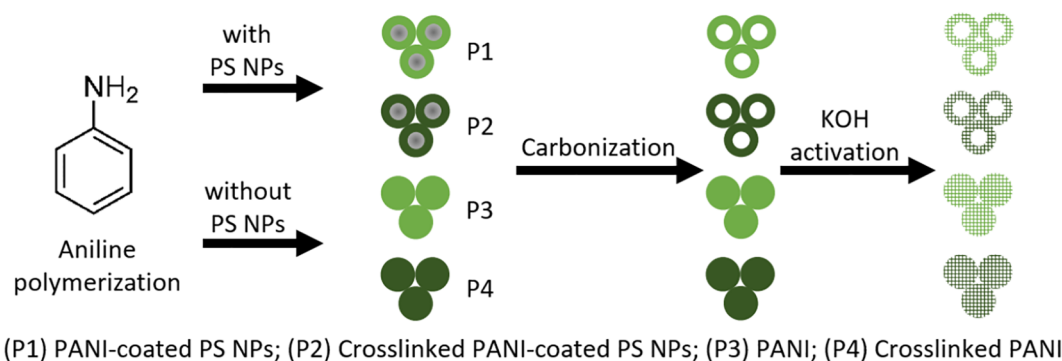
2.5. CO₂ adsorption measurements

CO₂ adsorption measurements of the hierarchically porous materials were characterized using a Quadrasorb-SI gas adsorption analyzer (Quantachrome, USA) according to the procedure described in Beltzung et al. [28] Specifically, all the samples were degassed at 115 °C for a minimum of 10 h to remove moisture and adsorbed gases from the pores before the measurements. The adsorption in moles per unit mass of adsorbent was calculated using the volumetric measurement and assuming ideal gas behavior at 1 atm and 273.15 K.

3. Results and discussion

3.1. Synthetic approach to the hierarchical porosity

The proposed strategy for designing the stable hierarchically porous materials was aimed at creating in the same material a range of pore sizes while retaining a good amount of nitrogen functionalities on the carbon framework, given its reported affinity towards CO₂. The creation of different pore sizes was necessary to facilitate efficient gas diffusion, while simultaneously enhancing the CO₂ adsorption capacity. Polyaniline (PANI), one of the most studied conductive polymers was selected as starting polymer, thanks to its high nitrogen content, easy synthesis and low cost [43–45]. The intrinsic presence of nitrogen in the molecule of aniline (the monomer), made it certain to have nitrogen groups homogeneously distributed in the carbon based final materials. The spherical PS NPs were chosen as building blocks, based on their high glass transition temperature (T_g), which gave rigid and non-deformable support to the 3-D framework [42,46–49] and later on as sacrificial template. Upon carbonization and removal of PS NPs we expected to create additional pores and increase the surface area and pore volume of the final materials. In order to investigate the effect of crosslinking the polymer on the results of heat treatment and final CO₂ capture, PS coated PANI (P1) and PS coated crosslinked PANI (P2) were prepared. Similar synthesis was performed but without PS NPs and were named P3 (PANI) and P4 (crosslinked PANI) to demonstrate the importance of the PS NPs in the creation of the hierarchical porosity. The synthesis procedure is depicted in Scheme 1 for clarity. The carbonized materials treated at 500 °C were denoted P1_CAR, while the



Scheme 1. Parameters for synthesizing the 3-D porous materials.

KOH activated samples were named P1_X, where X denotes the mass ratio between KOH and the pre-carbonized material (i.e. 1, 2, 3 or 4) used for the activation step.

3.2. Morphology and porous properties of the as-synthesized materials

Before the activation process, the as-synthesized materials showed a mesh-like structure indicating the growth of PANI nanostructures on the PS NPs support forming 3-D structures (Fig. 1a). The rigid monodisperse PS NPs preserved the outer PANI structure upon crosslinking without significant deformation or shrinkage (P2, Fig. 1b) exhibiting inter-particle channels. With the control samples prepared without PS on the other hand, a more globular structure with large grain sizes was obtained upon crosslinking (P3 and P4, Fig. 1 c and d) indicating limited porous structure. The large clusters of P3 and P4 are more

prevalent at lower magnification (5 μm) (Fig. SI 1, Supporting Information). During the polymerization of aniline, the initiator solution was added slowly to control the polymerization rate such that PANI nanostructures get deposited onto PS NP building blocks forming a 3-D mesh-like structure. For comparison, we also prepared porous materials by addition of APS as a shot instead of slow addition. Obtained results confirmed that this approach led to the rapid polymerization of PANI forming larger granular structures instead of PANI nanostructures obtained from our standard approach (see Fig. SI 2, Supporting Information).

To track the evolution of the pore formation, the textural properties of the as-synthesized materials were evaluated by means of N_2 sorption at 77 K and Hg intrusion porosimetry. The surface areas were calculated using the Brunauer-Emmett-Teller (BET) equation, whereas the pore size distributions were calculated using the density functional theory

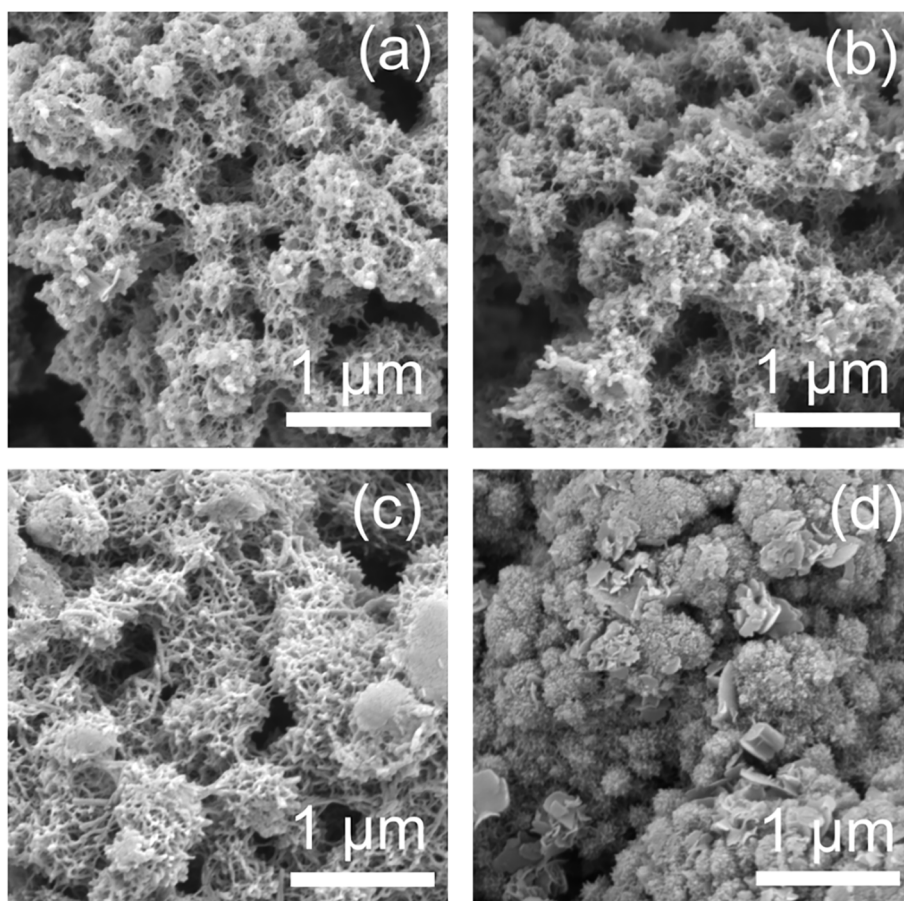


Fig. 1. SEM images of as-synthesized porous materials at 5 wt% solid content (a) P1 (b) P2 (c) P3 and (d) P4.

(DFT) from the N_2 adsorption isotherm. As shown in the N_2 sorption isotherms (Fig. SI 3 (a), Supporting Information), the as-synthesized materials before the chemical activation step all showed typical type II isotherm according to the Bruner-Deming-Deming-Teller classification [50,51], with low surface areas ($S_{BET} < 32 \text{ m}^2 \text{ g}^{-1}$), which corresponded to macroporous structures with low or inexistent microporosity. As the relative pressure increased above 0.6, there was a uniform increase in the uptake of nitrogen coupled with a minor hysteresis loop, which can be attributed to the mesoporosity. From the Hg porosimetry data, we observed clearly the hierarchical porosity for P1 and P2 with two different pore size ranges indicating the inter-particle meso- and macroporosity due to the presence of PS NPs. In the case of the samples prepared without PS NPs (P3 and P4), a single broad pore size distribution was observed (Fig. SI 3 (d), Supporting Information). As seen in Table SI 1 in Supporting Information, the porosity only decreased slightly from 87% in P1 to 85% in P2 upon crosslinking, which we believe was due to the rigid PS NPs maintaining the 3-D structure of the material. With the PS-free samples, the porosity decreased from 82% in P3 to 73% in P4, demonstrating the impact of PS NPs to maintain the 3-D structure, while avoiding the loss of porosity when the material was crosslinked.

3.3. Pore-generation: effect of carbonization and activation conditions on material properties

For the various sorbents that have been reported as the most promising in terms of CO_2 sorption performance, two main parameters have been identified as crucial for enhancing their performance: (1) optimized size of accessible pores usually below 0.7 nm and (2) presence of accessible surface functionalities on the porous material matrix, which can improve CO_2 uptake and selectivity. Generally, N-doped porous sorbents with different porosities, nitrogen and oxygen contents and sorption properties were obtained depending on the synthesis approach as well as the different carbonization and activation conditions used [6,52]. As such, the temperatures for carbonization and activation were selected to keep a balance between textural properties and surface chemistry based on similar investigations reported in the literature. Although higher pyrolysis temperatures could generally yield higher surface areas, it may also lead to a compromised opening up of narrow micropores with resulting increase in mesopore volumes and a loss in surface functionalities [13,15,53,54]. With the aim of generating a hierarchical pore structure with a high amount of micropores while also retaining a reasonable amount of surface functionalities, the as-synthesized materials were subjected to a first heating treatment at 500°C at a rate of 5°C min^{-1} . This step, known as the carbonization step, was important to slowly decompose the PS NPs and carbonize the PANI frameworks. Thermal gravimetric analysis (TGA) revealed a major decomposition between 400 and 500°C (Fig. 2) which corresponded to the degradation of PS NPs with the weight of PS NPs nearing 0%. This was followed by a chemical activation at 750°C using potassium hydroxide (KOH). This is the most used agent for the activation of carbon materials due to its low energy demand and less impact on the environment when compared to other activating agents [6]. Its presence enhances the pore development process, for example, samples carbonized in the presence of KOH exhibited more developed porosity compared to samples carbonized in the absence of it, clearly indicating its role in formation of small pores [53]. During the KOH activation process, potassium ions are released, which intercalate into the amorphous part of the graphitic fingers of the carbon, reacting with it and producing large number of fine pores under high diffusion and pyrolysis action. This results in an increase in the surface area and pore volume [13,55]. We observed that the high surface hierarchically structured materials were only obtained after the activation step and there was no significant increase in surface area and pore volume of the materials after stopping at the carbonization step (Table SI 2, in Supporting Information).

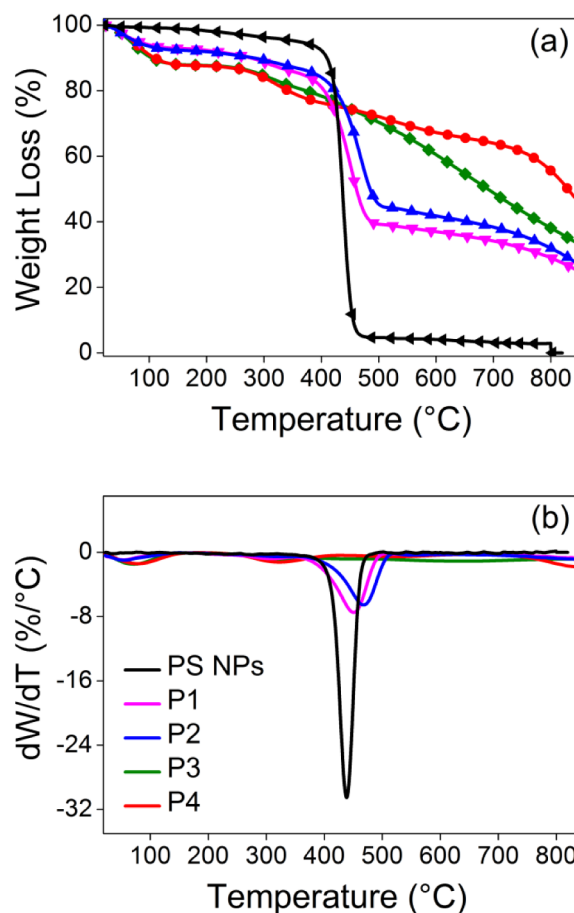


Fig. 2. Thermal behaviour of PS NPs and PANI microclusters measured by TGA under nitrogen atmosphere (a) Weight vs. temperature TG curve (b) DTG curve, derivative of the TG curves (▼) P1 = PANI-coated PS NPs; (▲) P2 = Crosslinked PANI-coated PS NPs; (◆) P3 = PANI; (●) P4 = Crosslinked PANI; (◄) PS-NPs.

Overall, a higher carbon mass remained for all the crosslinked materials in comparison to non-crosslinked materials (Fig. 2, Table SI 3 in Supporting Information). The weight difference is due to the thermal stability of the crosslinker, phytic acid, which undergoes dehydration and carbonization and therefore slightly increasing the weight of the crosslinked materials.

Examples of SEM images of the activated materials are shown in Fig. 3(a–d). It was observed that the skeleton of the PS-PANI microclusters contain interconnected spherical pores left by the removal of PS NPs, which created additional porosity for easy diffusion of CO_2 (see Fig. 3(a) and (b)). Comparatively, as shown in Fig. 3(c) and (d), the PANI microclusters prepared without PS NP building blocks showed globular rather than the hierarchically porous structures.

The formation of the high surface area hierarchically porous materials after the carbonization and activation steps was further confirmed by the change in the adsorption isotherms from type II to type I (Fig. SI 4, Supporting Information), typical of microporous materials with significant adsorption at low relative pressures. Moreover, transmission electron microscopy (TEM) images of the optimum material are presented in Fig. 4, clearly showing the porosity of the carbon, which is important for efficient gas diffusion.

Using various KOH/C ratios (1, 2, 3 and 4) for activation, a series of nitrogen-doped carbons were produced where the textural and surface chemistry were well tuned. It was observed that treatment with the KOH/C ratio of 1 mostly resulted in non-microporous materials with low surface areas. This may be due to the less efficient pore generating process at low KOH amounts resulting in predominantly mesoporous

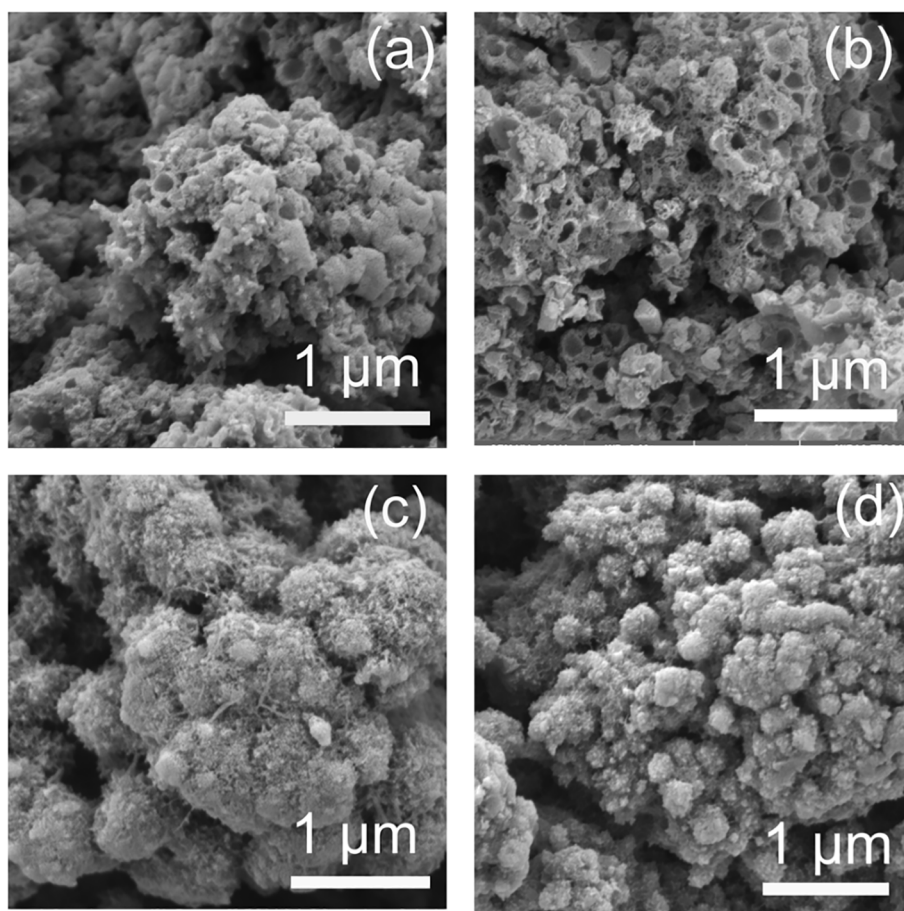


Fig. 3. SEM images of KOH activated materials (a) P1 (b) P2 (c) P3 (d) P4, magnification = 50 kX.

materials. Generally, the lower KOH/C ratios lead to less efficient pore generation whereas too high KOH/C ratios result in harsh activation and the resultant pore widening or degradation of the 3D structure. It was therefore concluded that this ratio was not sufficient to generate the desired micropore sizes for CO₂ capture. Samples treated with KOH/C ratios of 2, 3 and 4 were highly microporous to various degrees depending on their composition with enhanced surface area and pore volume. The high N₂ uptake of the activated samples at low relative pressures $P/P_0 < 0.01$ confirmed the predominantly microporous nature of the materials (IUPAC definition pore diameters < 2 nm). Moreover, the isotherms showed slight hysteresis loops (type H4),

indicating the presence of some mesopores. This was also clearly reflected in their corresponding pore size distributions (PSDs) obtained by the non-local density functional theory (NLDFT) shown in (Fig. SI 4 (b), (d) and (f), Supporting Information). Complete report of the measured specific surface areas, total volume and average pore diameter are reported in Table SI 2 in Supporting Information. Although the activated materials also contain ultramicropores (with pore diameters < 0.7 nm), they were too narrow for N₂ to diffuse into them at 77 K. As such these were not optimally determined using N₂ sorption as evidenced by the incomplete pore size distributions in the micropore range. These smaller pores were subsequently evaluated from CO₂ sorption analysis.

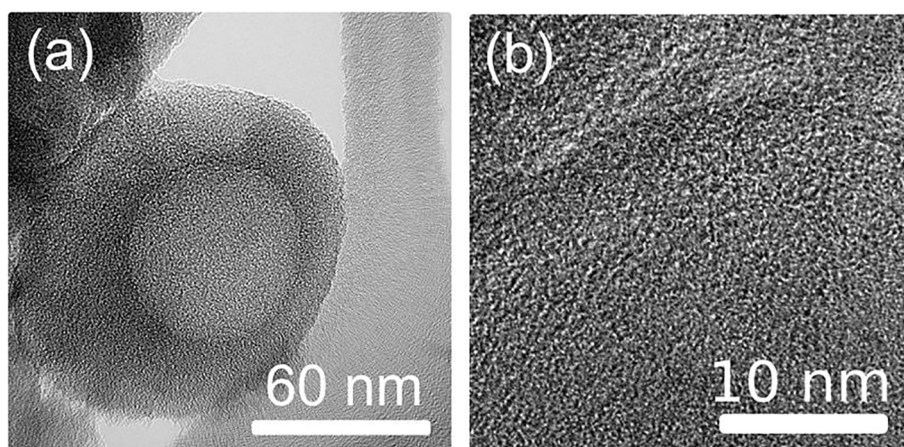


Fig. 4. TEM images of the optimum porous carbon P2₃ with two different magnifications.

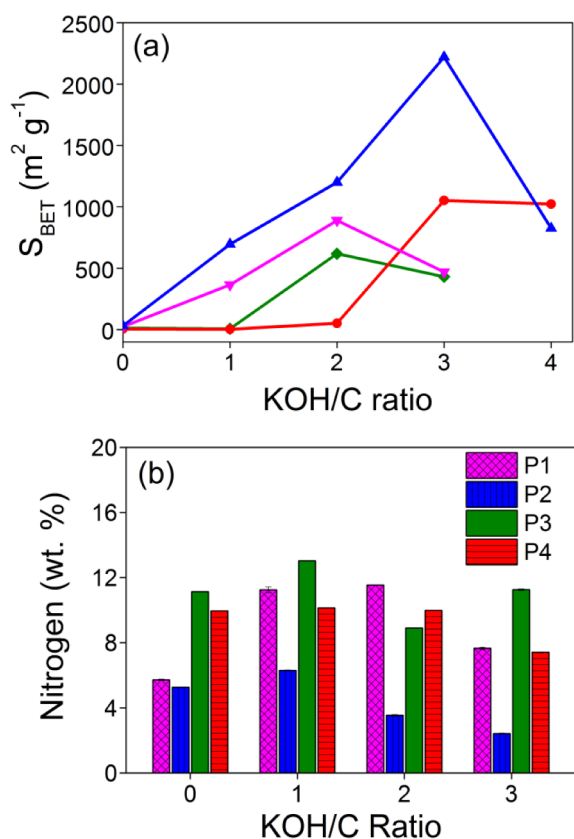


Fig. 5. (a) Trend in the evolution of BET surface areas of the microclusters obtained from N_2 sorption and (b) Nitrogen content in relation to KOH/C ratio (▼) P1 = PANI-coated PS NPs; (▲) P2 = Crosslinked PANI-coated PS NPs; (◆) P3 = PANI; (●) P4 = Crosslinked PANI.

The trend in evolution of BET surface areas with different KOH treatments as displayed in Fig. 5(a) showed that increasing the KOH/C ratio from 1 to 3 resulted in the formation of new pores and thus to higher surface areas. This effect was more pronounced for the materials, which were crosslinked with phytic acid. The phytic acid networks ensured maximum KOH adsorption of the carbonized material, and thus a well-developed porosity in the subsequent activation step due to the pore-generation property of KOH [13]. When the ratio KOH/C 4 was used for the crosslinked materials, we observed a generation of wider pores with an increase in the average pore sizes (Fig. SI 5 (a and b) in Supporting Information, BET results in Table SI 2), which was in line with previous reports which indicated the generation of too large pores and almost complete removal of nitrogen functionalities when $KOH/C \geq 4$ were used for activation [13,22,32]. Even though the sample P4 treated with $KOH/C = 4$ did not show a huge decrease in BET surface area compared to sample P2 treated with $KOH/C = 4$, the SEM images confirmed the creation of large pores. From these results, the KOH/C ratio of 3 was the optimum condition for the crosslinked materials.

For the non-crosslinked samples, increasing the KOH/C ratio from 1 to 2 resulted in a significant increase in the surface area whereas a further increase of KOH/C to 3 resulted in a huge decrease in the surface areas. The reason for such observation is likely due to weaker structure in the absence of phytic acid leading to the complete destruction of the 3-D structure at higher KOH amounts (Fig. SI 5 (c), Supporting Information), with a corresponding decrease in the surface areas and pore volumes. As such, the optimum treatment for the non-crosslinked materials was KOH/C ratio of 2. The final hierarchically porous materials exhibited an optimized N_2 BET surface area of up to $2200 m^2 g^{-1}$ (P2) and total pore volumes as large as $1.21 cm^3 g^{-1}$ (P2) with pore diameters $< 1.8 nm$. The difference observed in surface areas

and pore volumes of the porous materials as prepared, after the carbonization and KOH activation steps, was an evidence of the role of KOH in the generation of high number of micropores (See Table SI 2, Supporting Information for the detailed textural properties).

Previous investigations have indicated a strong link between N-functional groups and CO_2 sorption capacity. Therefore, the nitrogen content of the prepared materials was analyzed by organic elemental analysis as shown in Fig. 5(b). All the materials retained high amounts of nitrogen reaching up to $\sim 13 wt\%$ after the activation step, which was far higher compared to similar materials prepared through chemical activation methods [13,38]. Apart from the material composed of pure PANI, generally, the nitrogen content decreased with an increase in the KOH/C ratio, which is in agreement with previous reports [22,53]. It was observed that the nitrogen content of the carbons before KOH treatment was lower than the nitrogen content of materials treated with $KOH/C = 1$. The reason for this observation was the change of the material composition during the thermal treatments. Throughout the material treatments from carbonization up to KOH activation, certain groups (O, C and N groups) were removed from the polymer structure causing the overall N content, which was calculated based on the total number of elements, to increase. Moreover, comparing the carbon, hydrogen and nitrogen content before and after activation indicated that the activation process altered the groups to different degrees for each sample without any trend, which could be due to the heterogenous distribution of the groups on the surface with some embedded in the bulk of the material. The full elemental composition of the as-synthesized and activated samples under different KOH/C treatments is shown in Table SI 4 in Supporting Information. The optimized material (P2,3) obtained at the highest KOH/C ratio of 3, however had the lowest amount of nitrogen because of the opposite effects of the activation conditions on microporosity and nitrogen content [11,19,22].

3.4. Chemical structure by FTIR-ATR spectroscopy

In order to understand the structural changes of the materials during the thermal treatment process, the evolution of the structure was studied using FTIR-ATR. The FTIR spectra of the as prepared, carbonized and activated materials are shown in Fig. 6, where “CAR” and “ACT” after the name P1-4 are abbreviations of carbonized and activated, respectively. The characteristic absorption bands at about 1518 and $1620 cm^{-1}$ were observed for all the materials. This corresponded to the carbon-carbon aromatic ring stretching vibrations of benzenoid and vibration of quinoid rings of PANI, respectively. The band at $1340 cm^{-1}$ was attributed to the C–N stretching vibrations of secondary aromatic amines and the peaks at 1194 and $843 cm^{-1}$ are noted for the C–H in-plane and out-of-plane bending. The fact that similar peaks were observed in all the PANI and PS-PANI microclusters was an indication that the PS NPs were uniformly covered by PANI. After carbonization at $500^\circ C$, the two main peaks assigned to the benzenoid and quinoid rings broadened and became weaker and less sharp, which was due to the strong absorption of carbon [22]. The disappearance of the maximum peak at $1194 cm^{-1}$ was due to the deprotonation of the materials at high temperatures. In the activated samples, the broad peak with maximum at $1677 cm^{-1}$ corresponded to the G band (graphite-like structure) of carbon [56]. The spectrum of the final activated samples confirmed the synthetic approach resulting in the conversion of the polymeric material to carbon. It was also observed that the C–N absorption band decreases as the materials are carbonized and activated, hence highlighting the loss of some of these functional groups during these latter treatments. In order to follow quantitatively the evolution of nitrogen, oxygen and carbon atoms before and after activation, XPS analysis was carried out as reported in the subsequent sections of the manuscript (Section 3.6.3).

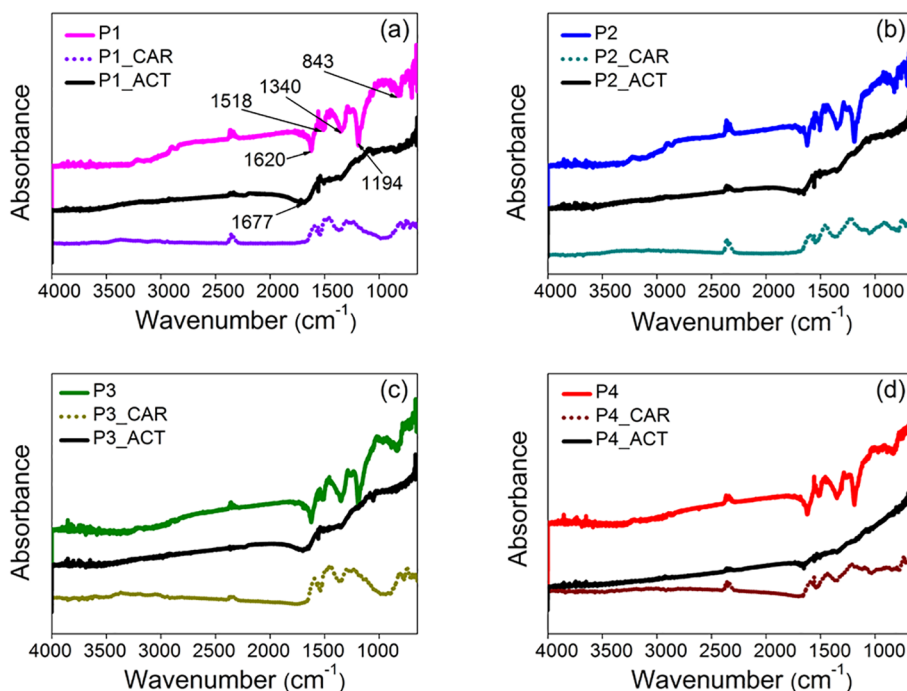


Fig. 6. FTIR spectra of the materials as-synthesized carbonized at 500 °C and activated at 750 °C. CAR and ACT after the sample names are abbreviations for carbonized and activated respectively.

3.5. CO₂ capture performance

Due to the creation of abundant micropores and the high amounts of nitrogen functionalities measured in the prepared materials, their CO₂ sorption capacities were evaluated. The CO₂ capacity was evaluated by measuring the entire adsorption isotherm at 1 atm and at 273.15 K by volumetric method. This pressure (1 atm) was used because post-combustion CO₂ capture is typically carried out at low pressures. To estimate the values of uptake of CO₂ in mmol g⁻¹, the highest values of adsorbed volume have been considered assuming ideal gas behavior. The CO₂ sorption capacity measured at 273.15 K and 1 atm also enabled the evaluation of the narrow micropores, since these were not properly obtained in the N₂ sorption measurements. An example of the CO₂ sorption isotherms measured for four optimally performing samples in each sample class are presented in Fig. 7(a). Complete results for the different KOH/C ratios and their corresponding pore size distribution (PSD) curves are shown in Fig. SI 6 and 7 in Supporting Information. All the isotherms displayed type I curves with slight hysteresis loops indicating the presence of both micropores and mesopores. The corresponding PSD curves in Fig. 7(b) showed that all the materials possess a significant amount of micropores ranging from 0.3 to 1 nm, with a maximum around 0.5–0.6 nm.

With the exception of materials activated at KOH/C = 1, all the other materials exhibited high CO₂ sorption capacities, which pointed to the fact that the CO₂ capture capacities were closely related to the narrow microporosity of the carbons, which was developed at KOH/C of 2 and 3. The results are summarized in Table 2 or its graphical representation in Fig. SI 8, Supporting Information).

For the crosslinked materials (P2 and P4), the higher the KOH/C ratio, the higher the surface area and pore volume, and the higher the corresponding CO₂ capacity. For the non-crosslinked materials (P1 and P3), at the optimum KOH/C of 2, the highest CO₂ sorption capacity was obtained. When the KOH/C ratio increased to 3, it resulted in a decrease in the surface areas and pore volumes with a corresponding decrease in the CO₂ capture capacity. This trend was in good agreement with that observed in the case of surface areas in Fig. 5(a). The textural properties (obtained from CO₂ sorption data), and CO₂ adsorption capacities of the

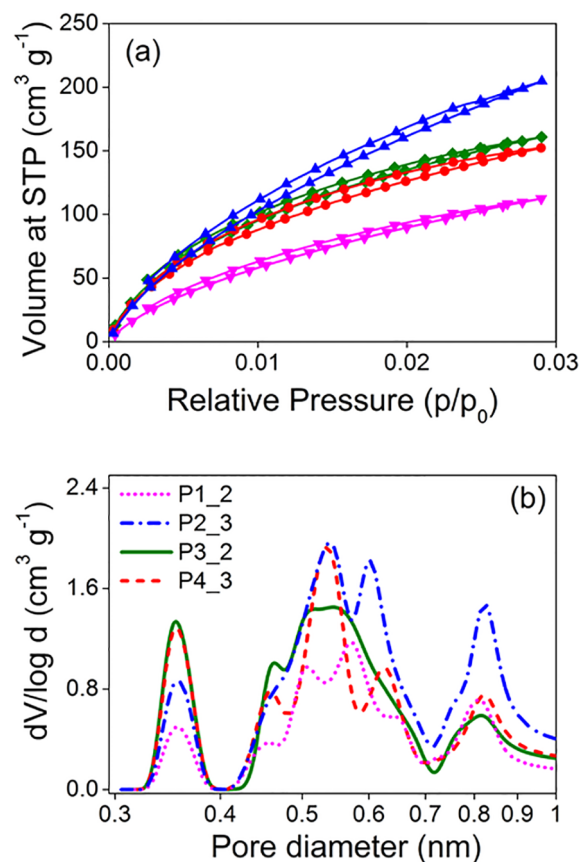


Fig. 7. (a) CO₂ adsorption and desorption isotherm of the optimum material at 273.15 K and 1 bar (b) Corresponding pore size distribution (▼ P1_2; ▲ P2_3; ◆ P3_2; ● P4_3).

Table 2

Textural properties and CO₂ capacities of the materials measured at 273.15 K and 1 bar.

Material	S _{BET} from CO ₂ [m ² g ⁻¹]	Total V _{pore} (CO ₂) [cm ³ g ⁻¹]	V _{pore} for pores < 0.7 nm [cm ³ g ⁻¹]	CO ₂ Capacity [mmol g ⁻¹]
P1_1	524	1.19	0.13	3.02
P1_2	1080	2.35	0.21	5.02
P1_3	717	1.66	0.17	4.02
P2_1	1115	2.47	0.22	5.15
P2_2	1537	3.24	0.27	6.50
P2_3	2036	4.36	0.39	9.14
P3_1	309	0.62	0.09	2.23
P3_2	1280	2.90	0.30	7.18
P3_3	700	1.58	0.18	4.21
P4_1	309	0.75	0.06	1.38
P4_2	427	0.95	0.12	2.72
P4_3	1219	2.81	0.29	6.80

Table 3

Textural properties, nitrogen content and CO₂ sorption capacity of our optimum materials in comparison to those reported in the literature measured at similar conditions (1 bar, 273 K).

Material (Sample name)	S _{BET} from N ₂ [m ² g ⁻¹]	V _{total} ^[a] /V _{ultra} ^[b] (ultramicropore) ^[b]	N content [%]	CO ₂ Capacity [mmol g ⁻¹]	Ref.
NC-800	263	0.38	5.58	2.65	[57]
SG-MOP-5	807	2.80	38.1	3.37	[58]
S3	390	—	6.82	3.56	[28]
SU-AC-400	4196 ^[c]	2.26/[0.25]	0.55	4.30 (298 K)	SI of [13]
1000CDC	1887	—	2.5	4.67	[59]
HMT-80-900	809	0.34	2.0	5.6	[8]
600-2	2003	1.2	8.95	7.30	[11]
CS ⁺ -P-A	2400	1.07/0.27 ^[d]	0	8.90	[32]
P3_2	618	0.35/[0.30]	8.9	7.18	This work
P2_3	2220	1.21/[0.39]	2.42	9.14	This work

^[a] Total pore volume obtained from N₂ sorption at 77 K.

^[b] The pore volume of ultramicropores (pores < 0.7 nm) was obtained from CO₂ sorption data at 273 K.

^[c] S_{BET} evaluated from Ar adsorption at 87 K and P/P₀ = 0.999.

^[d] Cumulative pore volume calculated in the range up to 0.8 nm, the nitrogen content (N %) is obtained by elemental analysis

hierarchically porous materials are presented (Table 2). Overall, all the materials possess a high amount of micropores below 1 nm with high cumulative ultramicropore (pores with diameters < 0.7 nm) and corresponding volumes ranging from 0.12 to 0.39 cm³ g⁻¹. The comparison of CO₂ sorption capacity of two of our optimum materials with the highest-performing materials in the literature is presented in Table 3.

It was observed that the CO₂ capture capacity of our best sample, P2_3 at 1 bar is among the highest reported values for most carbon materials. It is believed that the high CO₂ capacity of the materials at low pressure was mainly due to the synergistic effect of the hierarchical porosity (ultramicropores, mesopores and macropores in the same material). This facilitates the efficient diffusion of CO₂ for easy accessibility to the micropores, coupled with the high CO₂ adsorption in the ultramicropores.

3.6. Effects of textural properties and surface chemistry on CO₂ capture capacity

The contribution of textural properties and surface chemistry (nitrogen functionalities) to the CO₂ sorption performance of various

porous sorbents has been debated by many researchers [32,36]. Gas physisorption is generally believed to be directly influenced by large specific surface areas and high pore volumes of adsorbents [54]. However, recent studies of some solid sorbents have revealed that high surface areas and large pore volumes do not necessarily lead to high uptake capacity [19,27]. While many reports have indicated the strong influence of surface chemistry of activated carbon on adsorption capacity, with enhanced CO₂ uptake upon nitrogen doping [6,25,60,61], a few other works have reported the opposite that nitrogen functionalities do not influence CO₂ adsorption under conventional operation conditions of temperatures 0–25 °C and pressures between 0 and 1 bar [32,36]. Overall, the most efficient CO₂ sorbents reported were those exhibiting two main characteristics: large number of properly sized narrow micropores to enhance efficient CO₂ uptake coupled with nitrogen functionalities in the structure to improve CO₂ affinity [10,22,62,63]. To understand the influence of the textural properties and surface chemistry on the CO₂ capture capacity of the materials, the CO₂ adsorption capacities were correlated with the textural properties (obtained from CO₂ sorption data) and the nature and content of nitrogen functionalities of the materials (obtained from organic elemental analysis).

3.6.1. Effect of pore sizes on CO₂ capture capacity

It was observed that there was no direct relationship between the BET specific surface area obtained from CO₂ sorption data and the CO₂ adsorption capacities (Table 2). Because the BET equation does not describe the CO₂ adsorption at 273.15 K most appropriately, the use of BET equation for evaluating surface areas resulted in a much lower surface areas than those obtained from N₂ sorption at 77 K (See Table SI 2 in Supporting Information). However, these values were evaluated in the same manner and were therefore used as a comparison among the different samples. Application of the Langmuir model in evaluating the surface areas was avoided because it can lead to overestimation of the surface area especially in this case, where the adsorption is not strictly by monolayer.

Although no direct relationship was observed between the specific surface area and the CO₂ sorption capacities, the sorption capacity was strongly correlated with the ultramicropore volume especially pores between 0.3 and 0.7 nm (considering that the kinetic diameter of CO₂ is 0.33 nm). In fact, the best performance in terms of CO₂ sorption capacity (9.14 mmol g⁻¹) was correlated with the highest ultramicropore volume of 0.39 cm³ g⁻¹. Additionally, among the optimum materials, the sample P3_2 with the second highest sorption capacity exhibited the second highest ultramicropore volume of 0.3 cm³ g⁻¹ compared to P2_2 (0.27 cm³ g⁻¹) although P2_2 (1537 m² g⁻¹) had a higher specific surface area than P3_2 (1280 m² g⁻¹). Similar effect was seen in the case of P3_1 and P4_1, which both show the same specific surface area of (309 m² g⁻¹) but different microporosity, where P3_1 showed higher pore volume between pore size range of 0.3 and 0.4 nm than P4_1. This suggested that the micro and narrow mesopores were mainly responsible for the high CO₂ sorption performance of the materials at low pressure. It was interesting to note that when plotting CO₂ sorption capacity as a function of ultramicropore volume for all prepared materials, a linear relationship was observed (Fig. 8), confirming the strong influence of the ultramicropores in enhancing CO₂ capture. This linear correlation of CO₂ sorption capacity at low pressure with ultramicropore volume is in agreement with previous reports [13,36]. The enhanced uptake of CO₂ with higher ultramicropore volume has been attributed to increasing adsorption potential with decreasing pore width, resulting in complete filling of narrow micropores at low relative pressures.

3.6.2. Effect of nanoparticle size on the porous material properties

To further tune and evaluate the impact of pore sizes, we selected the optimum sample and condition for the activation (P2 activated using KOH/C = 3 at 750 °C) and evaluated the effect of the

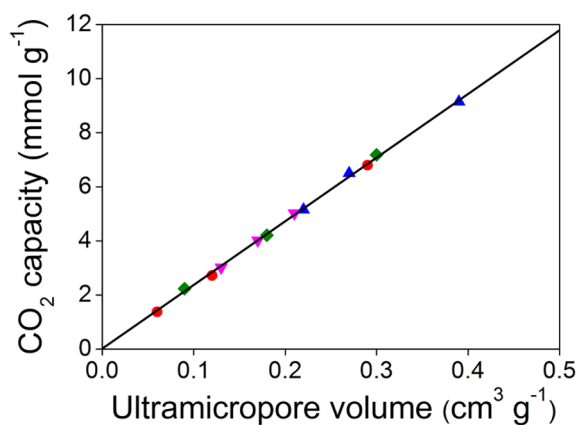


Fig. 8. Trends in ultramicropore volume (pores < 0.7 nm) in relation to CO₂ capture capacity; ratio (▼) P1 = PANI-coated PS NPs; (▲) P2 = Crosslinked PANI-coated PS NPs; (◆) P3 = PANI; (●) P4 = Crosslinked PANI. Line represents the best fit to the data.

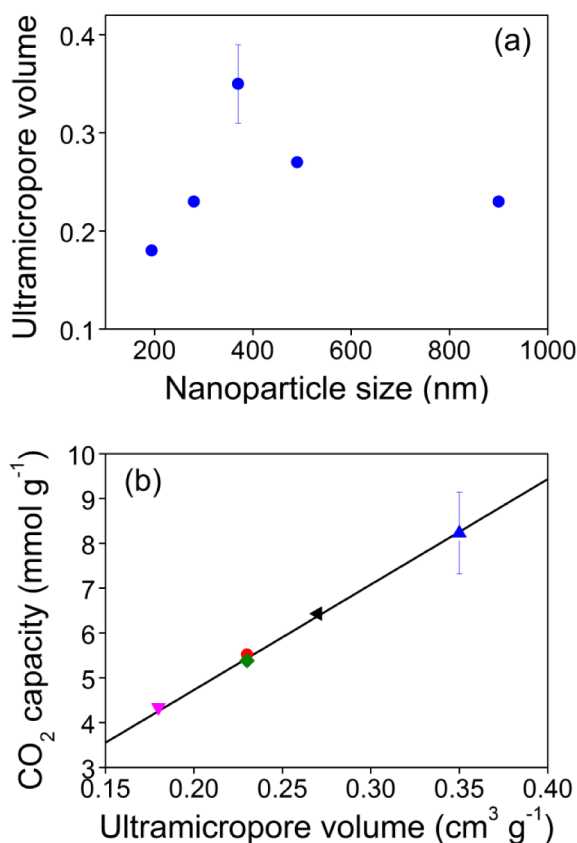


Fig. 9. (a) Effect of nanoparticle size on ultramicropore volume and (b) relationship between the ultramicropore volume and CO₂ sorption capacity (▼) 194 nm; (●) 280 nm; (▲) 370 nm; (◄) 490 nm; (◆) 900 nm, Line represents the best fit to the data.

nanoparticle sizes on the pore properties and subsequently on the CO₂ sorption capacity. Interestingly, the ultramicropore volume increased with increasing size of the particles up to an optimum of 370 nm and then a further increase in the size resulted in the decrease in the ultramicropore volumes (see Fig. 9 or the sorption isotherms depicted in Fig. SI 9 and the textural properties in Table SI 5, in Supporting Information). The observed trend could be due to the fact that with increase in the nanoparticle sizes, the porosity increases enabling effective KOH penetration for micropore generation. However with too large pores, the carbonization step, which removes PS NPs leaves very

large pores. This most probably caused at least partial collapse of the hierarchical structure and the drop in the ultramicropore volumes. Similar to the trend observed in Section 3.6.1 and Fig. 8, the CO₂ capture capacity was linearly correlated to the ultramicropore volume (Fig. 9b), once again confirming the strong influence of this parameter on CO₂ capture capacity.

3.6.3. Effect of surface functionalities (nitrogen and oxygen) on CO₂ capture capacity

The CO₂ adsorbents prepared in this work consist mainly of nitrogen and oxygen atoms on the surface of carbon; therefore we investigated the effects of nitrogen and oxygen on the CO₂ capture capacity. The nitrogen content of the microclusters were quantified by organic elemental analysis (Table SI 4 in Supporting Information) and correlated to the sorption capacities of the materials. There was no obvious trend between the CO₂ capacity and the total nitrogen content of the microclusters (Fig. SI 10, Supporting Information). Although the sample P3.1 had the highest nitrogen content (13.03 wt%), its sorption capacity was far lower than the optimum material, P2.3, which had only 2.42 wt% of nitrogen. Considering the fact that the sample with the highest CO₂ sorption capacity had the lowest amount of nitrogen, this led us to conclude that at low pressures, the CO₂ capture behavior was mainly controlled by adsorption in narrow micropores, with no evidence on the contribution from the surface chemistry.

To further understand the contribution of the chemical interactions towards the high CO₂ sorption, XPS analysis was carried out on the optimally performing materials in each class to study the nature of the specific surface groups. Fig. SI 11 in Supporting Information shows the full XPS spectrum of the materials with three main peaks at binding energies of 284.98, 399.38 and 531.78 eV corresponding to carbon (C), nitrogen (N) and oxygen (O), respectively. The high resolution C1s spectra (Fig. 10) comprised of five different overlapping peaks at binding energy 284.7 eV showing presence of sp³ carbon (–C–C–), 287.0 eV (–C–O(N)–), 288.3 eV (–C=O), 289.2 eV (–O–C=O) and 285.7 eV sp²(–C=C–). Generally, all the samples presented the same type of carbon functionalities, with graphitic carbon being the major component.

Quantitative XPS analysis of the nitrogen groups revealed that P1, P2, P3 and P4 contained 5.45, 5.89, 9.39 and 6.62 wt% of total nitrogen, respectively. Although the amount of nitrogen reduced upon activation, all the samples retained a good amount of the nitrogen functionalities considering the amount in the as-synthesized samples (Table 4). These values were lower than those obtained by organic elemental analysis (Table SI 4, Supporting Information). The slight difference was due to the fact that XPS evaluates only surface nitrogen groups while organic elemental analysis takes into account the bulk nitrogen fraction. N1s core spectra allows us to obtain a better understanding of the types and local environment of the nitrogen atoms present in the material. The deconvoluted N1s spectra (Fig. 11) revealed the bonding of N with C and the existence of 4 types of nitrogen at the following binding energies: 399.3 eV (amine, –NH₂), 400.7 eV (pyrrolic, –N–H) 398.3 eV (pyridinic, =N–H) and 401.6 eV (quaternary/graphitic, =N⁺–H) present in all the activated samples as illustrated.

The relative peak areas of each nitrogen species arranged in order of highest CO₂ sorption capacity to the lowest are summarized in Table 4. It was observed that for all materials analyzed, the amine and pyrrolic nitrogen groups were the most stable and abundant, and could contribute to the high CO₂ capture. Similar to our findings, many researchers have identified the pyrrolic or amine nitrogens to have stronger interactions with CO₂ molecules [15,20,21]. Although there was no obvious contribution from nitrogen functionalities, it is worth noting that because of the tendency of gas desorption at higher temperatures, microporous materials without any CO₂-philic sites present may not be appropriate for practical CO₂ capture applications [7,21,64]. Moreover, it was recently reported by Xing et al. [19] that

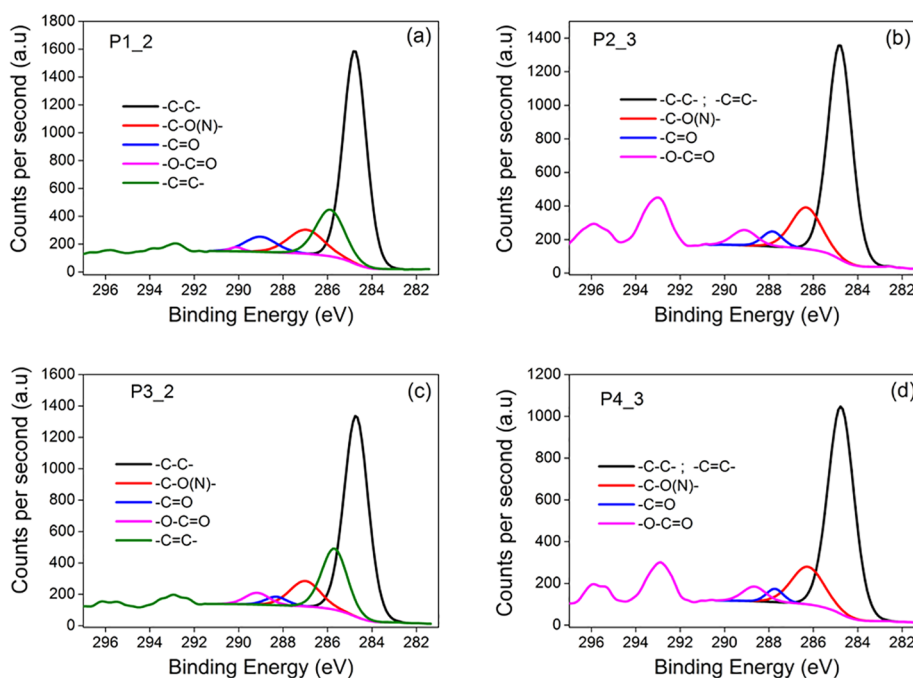


Fig. 10. C 1s core-level spectra of the activated carbons.

the CO₂ capture capacity of carbons can be further increased by an additional interaction. They found that the introduction of nitrogen into carbon facilitated hydrogen-bonding interactions between the carbon surface and CO₂ molecules, accounting for high CO₂ uptakes. This could explain why the presence of even a small amount of nitrogen (2.42 wt% measured by elemental analysis) in our optimized material (P2_3) could contribute to the high CO₂ sorption capacity significantly. However, this phenomenon needs further investigation.

As the surface oxygen functionalities on the surface have also been indicated to contribute to enhanced CO₂ sorption [65], the oxygen content detected from XPS was correlated with the CO₂ sorption capacity of the optimum materials (Fig. 12a). Although there was no obvious trend between the oxygen content and the CO₂ sorption capacity, it was observed that for all materials, the oxygen content was higher than the nitrogen content (Fig. 12b). Comparing the oxygen content before and after activation (Fig. 12c) indicated that the activation process altered the oxygen content to different degrees for each sample, which could be due to the heterogeneous distribution of oxygen on the surface. Additionally, an attempt was made to ascertain whether there was an optimum N/O ratio, which favoured high CO₂ uptake. From Fig. 12(d), no correlation was observed with N/O ratio, this again could be due to the heterogeneous distribution of oxygen in the surface and bulk. Similar to these results, He et al.[13] found no correlation between CO₂ sorption capacity and the oxygen content of their materials.

3.7. Considerations for industrial applications: sorbent regeneration

In designing a low-cost CO₂ capture sorbent that can replace aqueous amine-based CO₂ capture systems. The sorbent should (i) be prepared from cheap materials by a simple approach, (ii) have a hierarchical pore structure for high adsorption capacity and efficient diffusion, (iii) be mechanically and thermally stable and (iv) exhibit a minimum CO₂ capture capacity of 2–3.0 mol/kg of sorbent and high CO₂/N₂ selectivity, (v) be easily regenerable and with minimal or preferably no environmental impact to enable wide-scale application [3,7,41,66].

So far, the most important technological challenge for large scale application of post-combustion CO₂ capture to industrial units is the potential to lower the costs of capture. Therefore, sorbent regeneration capability is very crucial as it determines the lifetime and replacement frequency of the sorbent, which affects the overall cost of capture. In this regard, porous carbons are advantageous compared to other solid sorbents because they are easily regenerated. Fig. 13 shows the CO₂ sorption capacities per cycle of the optimized sample (P2_3) for eight subsequent cycles with simple vacuum regeneration at 115 °C after each cycle. The detailed textural properties and the sorption isotherms are shown in Table SI 6 and 7 and Fig. SI 12 and 13 respectively. To consider realistic deviation between repetitions, the sorption capacity graph is accompanied with the error bars, which were calculated for first four cycles as 2x standard deviation, thus considering 95% confident interval. Due to lack of repetitions for 5 to 8 cycles, these were estimated as an average of the error bars calculated for first 4 cycles.

Table 4

Proportion of oxygen content and nitrogen types (N1s) from XPS spectra of the as-synthesized and activated materials.

Material	Total oxygen as-prepared	Total oxygen-activated	Total N ^[a] [wt. %]	Total N ^[b] [wt. %]	PLN [%]	PDN [%]	QN [%]	NH [%]
P2_3	16.73	19.28	5.89	1.90	23.24	17.88	22.16	36.72
P3_2	10.12	8.68	9.39	7.58	15.75	15.55	15.54	53.17
P4_3	15.96	19.01	6.62	6.08	32.89	24.53	15.19	27.39
P1_2	18.00	10.96	5.46	4.36	44.18	22.81	15.35	17.67

^[a] Nitrogen content in the as-synthesized materials.

^[b] Nitrogen content in the activated materials, PLN (Pyrrolic nitrogen at position 400.70 eV), PDN (pyridinic nitrogen at 398.27 eV), QN (Quaternary Nitrogen at 401.63 eV) and (NH) amine at position 399.33 eV.

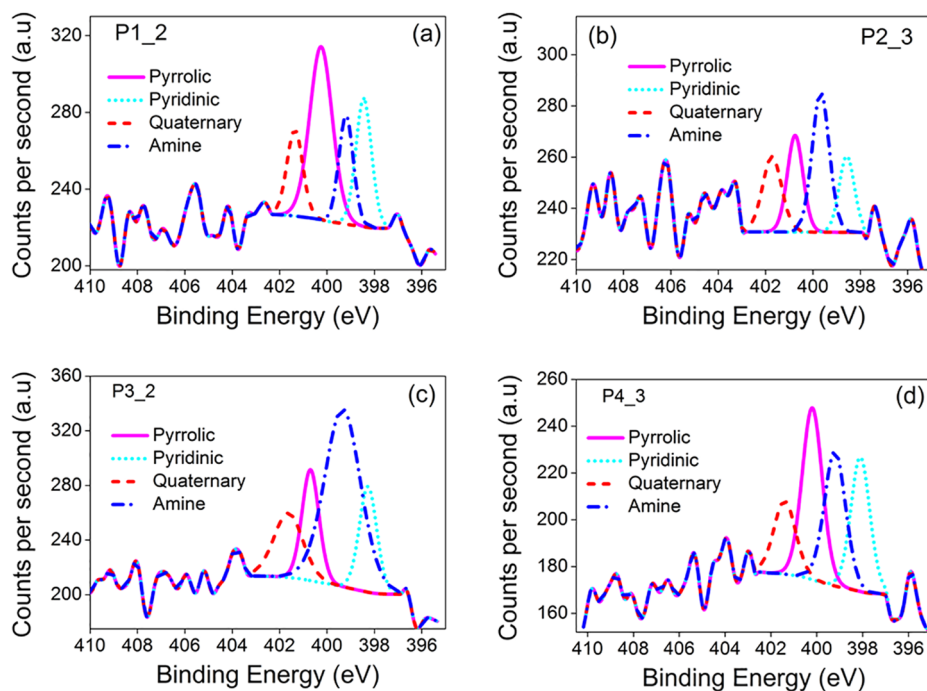


Fig. 11. N 1s core-level spectra of the activated carbons.

Based on the obtained results of regeneration, we observed the highest reduction in sorption capacity after the first cycle, whereas further cycles within statistical uncertainty of the measured data did not show significant reduction of the sorption capacity. From the CO₂ sorption isotherms measured after each regeneration cycle (Fig. SI 13), we observed a change in PSD after the first regeneration while other distributions were rather similar to each other independent on the number of regeneration cycle. There was no significant difference in the chemical composition of all tested materials (see Fig. SI 14 and 15) indicating that physical adsorption in ultramicropores (physisorption)

is the main binding mode. However, the loss in sorption capacity, despite no change in composition suggested that there were small changes to the material porosity. In fact, when plotting all measured data of CO₂ sorption capacity as a function of ultramicropore volumes including regeneration cycles, all of them follow the same linear relationship (Fig. SI 16 in Supporting Information).

Practically, since the binding mechanism of our materials is only by physisorption, we believe this requires lower amount of energy for regeneration compared to aqueous amine absorption process, where CO₂ is reacting with amine molecules (chemisorption). In addition, it was

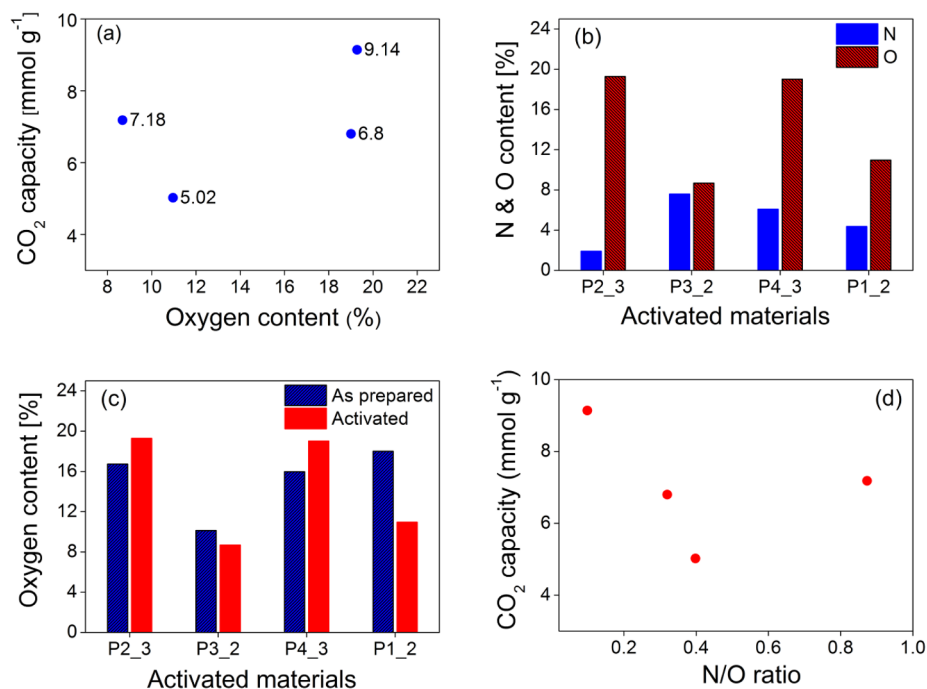


Fig. 12. (a) Effect of oxygen content on CO₂ capacity (b) comparison between nitrogen and oxygen content (c) effect of activation on oxygen content (d) effect of N/O ratio on CO₂ capacity.

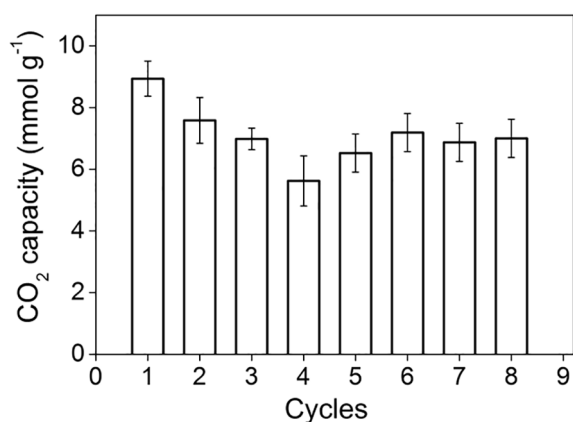


Fig. 13. (a) CO₂ capacities (273.15 K, 1 bar) for the optimized material P2_3 after eight cycles C1 – C8, the sorbent was degassed under vacuum at 115 °C after each cycle.

already reported that amine solutions are less stable and undergo degradation, which is not the case of solid sorbents, which are durable over several cycles (proven also for our material).

4. Conclusions

Stable hierarchically porous nitrogen-rich sorbents were prepared using cheap precursors, through a simple approach for application in post-combustion CO₂ capture. The synthetic approach using PS NPs building blocks resulted in superior textural properties and CO₂ capture capacity compared to the materials prepared without PS NPs. The presented method, though simple, is suitable for preparation of 3-D hierarchically porous materials with high porosities, specific surface areas and pore volumes. The optimized material achieved very high CO₂ capacity (9.14 mmol g⁻¹) at 273.15 K and 1 bar, which is among the highest reported for carbon-based sorbents in the literature. It is evident that this high CO₂ capture capacity was mainly due to the hierarchical pore structure, which enhanced the diffusion of CO₂ into the inner micropores. By analyzing the CO₂ capture capacity of the different materials with varying textural properties and nitrogen contents, we conclude that the CO₂ capture capacity at low pressure is primarily controlled by the presence of micropores with diameter smaller than 0.7 nm. Nevertheless, in designing materials for practical applications, it is important to tune both the pore structure (pore size distribution) and surface chemistry (nitrogen functionalities) simultaneously to combine their advantages. These materials are promising CO₂ sorbents and we believe the described approach will serve as a guide to the development of new polymer-based carbons for CO₂ capture. Because industrial sorbents are required to withstand multiple adsorption/desorption cycles, future work will focus on evaluating the stability of these sorbents under various industrial conditions.

Acknowledgments

This work was supported by a Czech Science Foundation (GACR) grant [16-22997S]. Financial support from specific university research grants [MSMT No. 20/2017] and [MSMT No 21-SVV/2018] are gratefully acknowledged. The authors are also grateful to Prof. Dr. Giuseppe Storti from ETH Zurich for helpful discussions.

Appendix A. Supplementary data

Supplementary data to this article can be found online at <https://doi.org/10.1016/j.cej.2018.10.133>.

References

- [1] B. Dutcher, M. Fan, A.G. Russell, Amine-based CO₂ capture technology development from the beginning of 2013-a review, *ACS Appl. Mater. Interfaces* 7 (2015) 2137–2148.
- [2] J.D. Figueroa, T. Fout, S. Plasynski, H. McIlvried, R.D. Srivastava, Advances in CO₂ capture technology-the U.S. department of energy's carbon sequestration program, *Int. J. Greenhouse Gas Control* 2 (2008) 9–20.
- [3] M. Songolzadeh, M. Soleimani, M. Takht Ravanchi, R. Songolzadeh, Carbon dioxide separation from flue gases: a technological review emphasizing reduction in greenhouse gas emissions, *Sci. World J.* 828131 (2014) 1–34.
- [4] Y. Li, Z.-Y. Fu, B.-L. Su, Hierarchically structured porous materials for energy conversion and storage, *Adv. Funct. Mater.* 22 (2012) 4634–4667.
- [5] J.A. Martens, A. Bogaerts, N. De Kimpe, P.A. Jacobs, G.B. Marin, K. Rabaey, M. Saey, S. Verhelst, The chemical route to a carbon dioxide neutral world, *ChemSusChem* 10 (2017) 1039–1055.
- [6] A.L. Yauri, M.Z.A. Bakar, B.H. Hameed, Recent advances in functionalized composite solid materials for carbon dioxide capture, *Energy* 124 (2017) 461–480.
- [7] H.A. Patel, J. Byun, C.T. Yavuz, Carbon dioxide capture adsorbents: chemistry and Methods, *ChemSusChem* 10 (2017) 1303–1317.
- [8] L. Liu, Q.-F. Deng, X.-X. Hou, Z.-Y. Yuan, User-friendly synthesis of nitrogen-containing polymer and microporous carbon spheres for efficient CO₂ capture, *J. Mater. Chem.* 22 (2012) 15540–15548.
- [9] Z. Liu, Z. Du, H. Song, C. Wang, F. Subhan, W. Xing, Z. Yan, The fabrication of porous N-doped carbon from widely available urea formaldehyde resin for carbon dioxide adsorption, *J. Colloid Interface Sci.* 416 (2014) 124–132.
- [10] W. Shen, W. Fan, Nitrogen-containing porous carbons: synthesis and application, *J. Mater. Chem. A* 1 (2013) 999–1013.
- [11] D. Lee, C. Zhang, C. Wei, B.L. Ashfeld, H. Gao, Hierarchically porous materials via assembly of nitrogen-rich polymer nanoparticles for efficient and selective CO₂ capture, *J. Mater. Chem. A* 1 (2013) 14862–14867.
- [12] C. Pevida, M.G. Plaza, B. Arias, J. Feroso, F. Rubiera, J.J. Pis, Surface modification of activated carbons for CO₂ capture, *Appl. Surf. Sci.* 254 (2008) 7165–7172.
- [13] J. He, J.W.F. To, P.C. Psarras, H. Yan, T. Atkinson, R.T. Holmes, D. Nordlund, Z. Bao, J. Wilcox, Tunable polyaniline-based porous carbon with ultrahigh surface area for CO₂ capture at elevated pressure, *Adv. Energy Mater.* 6 (1502491) (2016) 1–11.
- [14] D. Guo, R. Shibuya, A. Akiba, S. Saji, T. Kondo, J. Nakamura, Active sites of nitrogen-doped carbon materials for oxygen reduction reaction clarified using model catalysts, *Science* 351 (2016) 361–365.
- [15] G.P. Hao, W.C. Li, D. Qian, A.H. Lu, Rapid synthesis of nitrogen-doped porous carbon monolith for CO₂ capture, *Adv. Mater.* 22 (2010) 853–857.
- [16] Y. Xia, R. Mokaya, G.S. Walker, Y. Zhu, Superior CO₂ adsorption capacity on n-doped, high-surface-area, microporous carbons templated from zeolite, *Adv. Energy Mater.* 1 (2011) 678–683.
- [17] J. Wang, Y. Lin, Q. Yue, K. Tao, C. Kong, L. Chen, N-rich porous carbon with high CO₂ capture capacity derived from polyamine-incorporated metal-organic framework materials, *RSC Adv.* 6 (2016) 53017–53024.
- [18] X. Zhu, S. Chai, C. Tian, P.F. Fulvio, K.S. Han, E.W. Hagaman, G.M. Veith, S.M. Mahurin, S. Brown, H. Liu, S. Dai, Synthesis of porous, nitrogen-doped adsorption/diffusion carbonaceous membranes for efficient CO₂ separation, *Macromol. Rapid Commun.* 34 (2013) 452–459.
- [19] W. Xing, C. Liu, Z. Zhou, L. Zhang, J. Zhou, S. Zhuo, Z. Yan, H. Gao, G. Wang, S.Z. Qiao, Superior CO₂ uptake of N-doped activated carbon through hydrogen-bonding interaction, *Energy Environ. Sci.* 5 (2012) 7323–7327.
- [20] M. Peyravi, Synthesis of nitrogen doped activated carbon/polyaniline material for CO₂ adsorption, *Polym. Adv. Technol.* 29 (2018) 319–328.
- [21] A. Sanchez-Sanchez, F. Suarez-Garcia, A. Martinez-Alonso, J.M. Tascon, Influence of porous texture and surface chemistry on the CO₂ adsorption capacity of porous carbons: acidic and basic site interactions, *ACS Appl. Mater. Interfaces* 6 (2014) 21237–21247.
- [22] M. Sevilla, P. Valle-Vigon, A.B. Fuentes, N-doped polypyrrole-based porous carbons for CO₂ capture, *Adv. Funct. Mater.* 21 (2011) 2781–2788.
- [23] E.V. Shlyakhova, L.G. Bulusheva, M.A. Kanygin, P.E. Plyusnin, K.A. Kovalenko, B.V. Senkovskiy, A.V. Okotrub, Synthesis of nitrogen-containing porous carbon using calcium oxide nanoparticles, *Phys. Status Solidi* 251 (b) (2014) 2607–2612.
- [24] F. Liu, K. Huang, Q. Wu, S. Dai, Solvent-free self-assembly to the synthesis of nitrogen-doped ordered mesoporous polymers for highly selective capture and conversion of CO₂, *Adv. Mater.* 29 (1700445) (2017) 1–8.
- [25] L. Zhou, J. Fan, G. Cui, X. Shang, Q. Tang, J. Wang, M. Fan, Highly efficient and reversible CO₂ adsorption by amine-grafted platelet SBA-15 with expanded pore diameters and short mesochannels, *Green Chem.* 16 (2014) 4009–4016.
- [26] C.S. Srikanth, S.S. Chuang, Spectroscopic investigation into oxidative degradation of silica-supported amine sorbents for CO₂ capture, *ChemSusChem* 5 (2012) 1435–1442.
- [27] D.M. D'Alessandro, B. Smit, J.R. Long, Carbon dioxide capture: prospects for new materials, *Angew. Chem. Int. Ed. Engl.* 49 (2010) 6058–6082.
- [28] A. Beltzung, A. Klauke, C. Colombo, H. Wu, G. Storti, M. Morbidelli, Polyacrylonitrile nanoparticle-derived hierarchical structure for CO₂ capture, *Energy Technol.* 6 (2018) 718–727.
- [29] Z. Rozlívková, M. Trchová, M. Exnerová, J. Stejskal, The carbonization of granular polyaniline to produce nitrogen-containing carbon, *Synth. Met.* 161 (2011) 1122–1129.
- [30] M. Olivares-Marín, M.M. Maroto-Valer, Development of adsorbents for CO₂ capture from waste materials: a review, *Greenhouse Gases: Sci. Technol.* 2 (2012) 20–35.

- [31] M. Sevilla, A.B. Fuertes, Sustainable porous carbons with a superior performance for CO₂ capture, *Energy Environ. Sci.* 4 (2011) 1765–1771.
- [32] N.P. Wickramaratne, M. Jaroniec, Importance of small micropores in CO₂ capture by phenolic resin-based activated carbon spheres, *J. Mater. Chem. A* 1 (2013) 112–116.
- [33] X. Li, T. Guo, L. Zhu, C. Ling, Q. Xue, W. Xing, Charge-modulated CO₂ capture of C₃N nanosheet: Insights from DFT calculations, *Chem. Eng. J.* 338 (2018) 92–98.
- [34] X. Li, Q. Xue, D. He, L. Zhu, Y. Du, W. Xing, T. Zhang, Sulfur-Nitrogen codoped graphite slit-pore for enhancing selective carbon dioxide adsorption: insights from molecular simulations, *ACS Sustainable Chem. Eng.* 5 (2017) 8815–8823.
- [35] X. Li, L. Zhu, Q. Xue, X. Chang, C. Ling, W. Xing, Superior selective CO₂ Adsorption of C₃N Pores: GCMC and DFT simulations, *ACS Appl. Mater. Interfaces* 9 (2017) 31161–31169.
- [36] M. Sevilla, J.B. Parra, A.B. Fuertes, Assessment of the role of micropore size and N-doping in CO₂ capture by porous carbons, *ACS Appl. Mater. Interfaces* 5 (2013) 6360–6368.
- [37] A.J. Rennie, P.J. Hall, Nitrogen-enriched carbon electrodes in electrochemical capacitors: investigating accessible porosity using CM-SANS, *Phys. Chem. Chem. Phys.* 15 (2013) 16774–16778.
- [38] C. Liu, W. Xing, J. Zhou, S.-P. Zhuo, N-containing activated carbons for CO₂ capture, *Int. J. Smart Nano Mater.* 4 (2013) 55–61.
- [39] M. Seredych, J. Jagiello, T.J. Bandoz, Complexity of CO₂ adsorption on nanoporous sulfur-doped carbons – is surface chemistry an important factor? *Carbon* 74 (2014) 207–217.
- [40] J.H. Lee, H.J. Lee, S.Y. Lim, B.G. Kim, J.W. Choi, Combined CO₂-philicity and ordered mesoporosity for highly selective CO₂ capture at high temperatures, *J. Am. Chem. Soc.* 137 (2015) 7210–7216.
- [41] B. Li, Y. Duan, D. Luebke, B. Morreale, Advances in CO₂ capture technology: a patent review, *Appl. Energy* 102 (2013) 1439–1447.
- [42] E.M. Kutorglo, F. Hassouna, D. Kopecký, L. Fišer, I. Sedlářová, A. Zadrazil, M. Šoós, Synthesis of conductive macroporous composite polymeric materials using porogen-free method, *Colloids Surf. A: Phys. Eng. Aspects* (2017), <https://doi.org/10.1016/j.colsurfa.2017.10.082>.
- [43] T.K. Das, S. Prusty, Review on conducting polymers and their applications, *Polym. Plast. Technol. Eng.* 51 (2012) 1487–1500.
- [44] S. Bhadra, D. Khastgir, N.K. Singha, J.H. Lee, Progress in preparation, processing and applications of polyaniline, *Prog. Polym. Sci.* 34 (2009) 783–810.
- [45] C. Dhand, M. Das, M. Datta, B.D. Malhotra, Recent advances in polyaniline based biosensors, *Biosens. Bioelectron.* 26 (2011) 2811–2821.
- [46] D. Kim, Y. Tian, H.J. Choi, Seeded swelling polymerized sea urchin-like core-shell typed polystyrene/polyaniline particles and their electric stimuli-response, *RSC Adv.* 5 (2015) 81546–81553.
- [47] S. Bousalem, S. Benabderrahmane, Y.Y.C. Sang, C. Mangeney, M.M. Chehimi, Covalent immobilization of human serum albumin onto reactive polypyrrole-coated polystyrene latex particles, *J. Mater. Chem.* 15 (2005) 3109–3116.
- [48] C. Mangeney, M. Fertani, S. Bousalem, M. Zhicai, S. Ammar, F. Herbst, P. Beaunier, A. Elaissari, M.M. Chehimi, Magnetic Fe₂O₃-polystyrene/PPy core/shell particles: bioreactivity and self-assembly, *Langmuir* 23 (2007) 10940–10949.
- [49] D.B. Cairns, M.A. Khan, C. Perruchot, A. Riede, S.P. Armes, Synthesis and characterization of polypyrrole-coated poly(alkyl methacrylate) latex particles, *Chem. Mater.* 15 (2003) 233–239.
- [50] A.M. Youssef, Morphological studies of polyaniline nanocomposite based meso-structured TiO₂ nanowires as conductive packaging materials, *RSC Adv.* 4 (2014) 6811.
- [51] F. Rouquerol, J. Rouquerol, K. Sing, Adsorption by Powders and Porous Solids. Principles, Methodology and Applications, Academic Press, London, 1999, pp. 166–168.
- [52] M. Sevilla, C. Falco, M.-M. Titirici, A.B. Fuertes, High-performance CO₂ sorbents from algae, *RSC Adv.* 2 (2012) 12792–12797.
- [53] J. Kou, L.-B. Sun, Fabrication of nitrogen-doped porous carbons for highly efficient CO₂ capture: rational choice of a polymer precursor, *J. Mater. Chem. A* 4 (2016) 17299–17307.
- [54] L.Y. Meng, S.J. Park, Effect of heat treatment on CO₂ adsorption of KOH-activated graphite nanofibers, *J. Colloid Interface Sci.* 352 (2010) 498–503.
- [55] A.-N.A. El-Hendawy, An insight into the KOH activation mechanism through the production of microporous activated carbon for the removal of Pb²⁺ cations, *Appl. Surf. Sci.* 255 (2009) 3723–3730.
- [56] S. Mentus, G. Ciric-Marjanovic, M. Trchova, J. Stejskal, Conducting carbonized polyaniline nanotubes, *Nanotechnology* 20 (245601) (2009) 1–10.
- [57] J. Wang, I. Senkovska, M. Oschatz, M.R. Lohe, L. Borchardt, A. Heerwig, Q. Liu, S. Kaskel, Imine-linked polymer-derived nitrogen-doped microporous carbons with excellent CO₂ capture properties, *ACS Appl. Mater. Interfaces* 5 (2013) 3160–3167.
- [58] F.Q. Liu, L.L. Wang, G.H. Li, W. Li, C.Q. Li, Hierarchically structured graphene coupled microporous organic polymers for superior CO₂ capture, *ACS Appl. Mater. Interfaces* 9 (2017) 33997–34004.
- [59] E. Zera, W. Nickel, G.P. Hao, L. Vanzetti, S. Kaskel, G.D. Sorarù, Nitrogen doped carbide derived carbon aerogels by chlorine etching of a SiCN aerogel, *J. Mater. Chem. A* 4 (2016) 4525–4533.
- [60] A.K. Mishra, S. Ramaprabhu, Nanostructured polyaniline decorated graphene sheets for reversible CO₂ capture, *J. Mater. Chem.* 22 (2012) 3708–3712.
- [61] M.S. Shafeeyan, W.M.A.W. Daud, A. Houshmand, A. Arami-Niya, Ammonia modification of activated carbon to enhance carbon dioxide adsorption: effect of pre-oxidation, *Appl. Surf. Sci.* 257 (2011) 3936–3942.
- [62] A.P. Katsoulidis, M.G. Kanatzidis, Phloroglucinol based microporous polymeric organic frameworks with –OH functional groups and high CO₂ capture capacity, *Chem. Mater.* 23 (2011) 1818–1824.
- [63] M.G. Schwab, B. Fassbender, H.W. Spiess, A. Thomas, X. Feng, K. Mullen, Catalyst-free preparation of melamine-based microporous polymer networks through schiff base chemistry, *J. Am. Chem. Soc.* 131 (2009) 7216–7217.
- [64] M.G. Plaza, F. Rubiera, J.J. Pis, C. Pevida, Ammonoxidation of carbon materials for CO₂ capture, *Appl. Surf. Sci.* 256 (2010) 6843–6849.
- [65] W. Xing, C. Liu, Z. Zhou, J. Zhou, G. Wang, S. Zhuo, Q. Xue, L. Song, Z. Yan, Oxygen-containing functional group-facilitated CO₂ capture by carbide-derived carbons, *Nanoscale Res. Lett.* 9 (189) (2014) 1–8.
- [66] M.L. Gray, J.S. Hoffman, D.C. Hreha, D.J. Fauth, S.W. Hedges, K.J. Champagne, H.W. Pennline, Parametric study of solid amine sorbents for the capture of carbon dioxide, *Energy Fuels* 23 (2009) 4840–4844.